

BULGARIAN CHEMICAL COMMUNICATIONS

2015 Volume 47 / Number 1

*Journal of the Chemical Institutes
of the Bulgarian Academy of Sciences
and of the Union of Chemists in Bulgaria*

80th ANNIVERSARY FOR PROF. IVAN SCHOPOV, DSC



On March 16, 2015, eighty years from the birth of Prof. Ivan Schopov were marked. Prof. Ivan Schopov is a prominent scientist in the field of polymer science with broad international recognition and fundamental merits for its development in Bulgaria. He is one of the pioneers in the research of electroactive polymers. Together with his co-workers he has synthesized a variety of polymers with conjugation and he has studied the correlation between their structure and specific properties. Very important are his contributions in studying the electric and magnetic properties of a new class of “segment polymers”, proposed by him.

He and his co-workers discovered a new “carbonyl-olephine” reaction enabling the production of various polymers with conjugation. It is important to note his research on destruction of polymers by singlet oxygen and its inhibition by poly-conjugated polymers.

Prof. Schopov is an author and co-author of more than 120 scientific papers, 23 Bulgarian and 4 international patents. He has been invited to deliver lectures in different universities around the world, in Germany, France, the United States, Japan, the United Kingdom, etc.

He has given lectures for undergraduate students in Bulgaria for 10 years. He has been invited lecturer in specialized training courses for students

in the Free University in West Berlin, the Technical University in Graz, Austria and the Max Planck Institute for Polymer Research in Mainz, Germany.

Prof. Schopov has had very intensive activity among the college of Bulgarian chemists. He has been very active member in the Union of Chemists in Bulgaria, being organizer of all its regular and traditional events. He was its president for ten years. He is the founder of the Bulgarian Polymer Society, a member of the European Polymer Federation.

He was very active as a member of the Union of Scientists in Bulgaria, being a member of its steering body.

Prof. Schopov played very important role for the association of the Bulgarian science in the structures of the European Union in the 1990s. He was national coordinator for all scientific programs for three years until the Bulgarian Ministry for Science and Education took its duties. Later he was Bulgarian representative in the Framework Programs 5, 6 and 7, as well as in the Program Committee of the “Marie Curie” program.

Prof. Ivan Schopov was a Head of the Institute of Polymers at the Bulgarian Academy of Sciences for the period of 1989 to 2003.

He is faithful to the best Bulgarian traditions for enhancement in science and education. He established in 2004 a personal prize for “Prominent young scientist” in the field of polymer science, annually awarded. It turned into one of the most valuable events for the Bulgarian polymer college.

His participation in new research projects, training and stimulation of young scientists and social activities does not stop.

Let us greet him cordially for his 80th anniversary and wish him much health and creative powers during the next decades.

From the Union of Chemists in Bulgaria

A facile catalyst-free Knoevenagel condensation of pyridinecarbaldehydes and active methylene compounds

M.H. Moemeni, M.A. Amrollahi*, F. Tamaddon

Department of Chemistry, Yazd University, Yazd, Iran, P.O. Box 89195-741

Received June 18, 2013; Revised May 7, 2014

This paper reports a study of the facile catalyst-free Knoevenagel condensation of pyridinecarbaldehydes and active methylene compounds like malononitrile, cyanoacetamide, ethyl cyanoacetate, and methyl cyanoacetate. The reaction occurs in a H₂O:EtOH mixture at room temperature to give high yields of electron-deficient alkenes with E-selectivity.

Keywords: Active methylene compounds, Catalyst-free, Knoevenagel condensation, Pyridinecarbaldehydes

INTRODUCTION

Catalysts play an important role in organic synthesis. In spite of its importance, at the end of a reaction, the catalyst should be separated from the products. This usually needs an organic solvent. Recently, green chemistry has tried to decrease the use of toxic solvents. With the increasing interest in developing environmentally benign reactions, the atom-economic catalytic processes, along with the use of approximately green solvents, are considered as ideal processes in organic chemistry [1]. There are some reports on catalyst-free reactions in organic synthesis such as the preparation of dithiocarbamates [1], thiosemicarbazones [2], nitrogen heterocycles [3] and vinyl sulfides [4].

Knoevenagel condensation is one of the most useful C=C bond forming reactions in organic synthesis [5,6]. Although other organic reactions, like Heck and Wittig reactions, yield alkenes, Knoevenagel condensation has the advantage of being a simple and easy reaction to perform. This is because water is the only side product and no unstable reactive intermediates are involved. These elements make this reaction environmentally friendly. Furthermore, the products of this reaction are usually E-alkenes. In contrast, Wittig reaction produces a mixture of Z/E-alkenes [5]. Knoevenagel condensation is applied to the synthesis of therapeutic drugs [7], natural products [8], herbicides, insecticides, functional polymers [9], and fine chemicals [10]. It is usually performed in organic solvents in the presence of common bases such as piperidine [11]. However, certain alternative approaches such as aqueous media [7],

high pressure [11], microwave [12], and ultrasound [13] have been employed. Also, a wide range of catalysts have been used. They include Lewis acids [14], zeolites [15], solid bases [16], heterogeneous catalysts [17], amines immobilized on polymers [18], ionic liquids [19], and amino acids [20]. The development of facile and environmentally benign methods for Knoevenagel condensation would be of value and is still required for green organic synthesis. In this paper, we report a facile uncatalyzed synthetic approach to prepare a series of new electron-deficient alkenes with operational simplicity, economic viability, and greater E-selectivity *via* Knoevenagel condensation. This condensation reaction was carried out in a H₂O:EtOH mixture at room temperature. The structures of the products were determined by IR, ¹H-, and ¹³C-NMR spectra.

EXPERIMENTAL

Instrumentms

IR spectra were recorded on a Bruker Equinox 55 spectrometer. ¹H- and ¹³C-NMR spectra were obtained using a Bruker Avance 500 MHz spectrometer (DRX). The elemental analysis was done on a Costech ECS 4010 CHNS-O analyzer. The melting points were determined on a Büchi melting point B-540 apparatus.

General experimental procedure

At room temperature, active methylene compound (1mmol) was added to a magnetically stirred solution of pyridinecarbaldehyde (1 mmol, 0.1 g) in H₂O:EtOH (5 ml). The progress of the reaction was monitored by TLC using CHCl₃:MeOH 90:10 as an eluent. After completion of the

*To whom all correspondence should be sent:
E-mail: mamrollahi@yazd.ac.ir

reaction, the corresponding solid product was filtered off. The sole product was obtained after simple recrystallization in a 50% H₂O:EtOH mixture in excellent yields (90-95%).

Selected spectroscopic data

2-(Pyridin-4-ylmethylene)malononitrile (Table 2, Entry 1): White solid; mp 100-101 °C; IR: 3023, 2233, 1610, 1590, 1548, 1416, 1403, 1236, 1219, 1067, 947, 933, 819,771, 621. ¹H-NMR (500 MHz, CDCl₃): 7.69 (d, *J* = 5.3 Hz, 2H, ArH); 7.83 (s, 1H, vinyl H); 8.88 (d, *J* = 5.3 Hz, 2H, ArH). ¹³C-NMR (125 MHz, CDCl₃): 89.0; 111.8; 112.9; 123.1; 137.4; 151.9; 158.0. Anal. calc. for C₉H₅N₃: C 69.67, H 3.25, N 27.08; Found: C 69.59, H 3.54, N, 26.96.

2-(Pyridin-3-ylmethylene)malononitrile (Table 2, Entry 2): White solid; mp 81-83 °C; IR: 3035, 2226, 1589, 1412, 1263, 1234, 1023, 974, 856, 802, 692, 650, 618. ¹H-NMR (500 MHz, CDCl₃): 7.53 (dd, *J* = 8.2 Hz, *J* = 4.8 Hz, 1H, ArH); 7.86 (s, 1H, vinyl H); 8.48 (d, *J* = 4.8 Hz, 1H, ArH); 8.83 (d, *J* = 4.8 Hz, 1H, ArH); 8.91 (s, 1H, ArH); ¹³C-NMR (125 MHz, CDCl₃): 86.1; 112.5; 113.4; 124.7; 127.4; 136.1; 152.8; 155.1; 156.1. Anal. calc. for C₉H₅N₃: C 69.67, H 3.25, N 27.08; Found: C 69.42, H 3.53, N 27.05.

(E)-Methyl-2-cyano-3-(pyridin-4-yl)acrylate (Table 2, Entry 3). White solid, mp 124-125 °C; IR: 3029, 2227, 1725, 1615, 1596, 1547, 1434, 1418, 1274, 1236, 1197, 1099, 969, 847, 816, 795, 763. ¹H-NMR (500 MHz, CDCl₃): 3.99 (s, 3H, CH₃); 7.77 (d, *J* = 6.1 Hz, 2H, ArH); 8.22 (s, 1H, vinyl H); 8.83 (d, *J* = 6.3 Hz, 2H, ArH). ¹³C-NMR (125 MHz, CDCl₃): 54.2; 97.3; 114.6; 123.7; 138.4; 151.5; 152.8; 162.2. Anal. calc. for C₁₀H₈N₂O₂: C 63.82, H 4.28, N 14.89; Found: C 63.73, H 4.18, N 14.74.

(E)-Methyl-2-cyano-3-(pyridin-3-yl)acrylate (Table 2, Entry 4): White solid; mp 127-128 °C; IR: 3035, 2226, 1731, 1612, 1584, 1564, 1475, 1429, 1236, 1264, 1196, 1089, 1044, 1023, 937, 814, 793, 757, 703, 626. ¹H-NMR (500 MHz, CDCl₃): 3.95 (s, 3H, CH₃); 7.52 (dd, *J* = 8.1 Hz, *J* = 4.8 Hz, 1H, ArH); 8.31 (s, 1H, vinyl H); 8.61 (d, *J* = 8.1 Hz, 1H, ArH); 8.80 (d, *J* = 4.8 Hz, 1H, ArH); 8.96 (s, 1H, ArH). ¹³C-NMR (125 MHz, CDCl₃): 54.1; 95.7; 115.2; 124.5; 127.9; 136.5; 151.9; 153.2; 153.8; 162.6. Anal. calc. for C₁₀H₈N₂O₂: C 63.82, H 4.28, N 14.89; Found: C 63.69, H 4.20, N 14.90.

(E)-Ethyl-2-cyano-3-(pyridin-4-yl)acrylate (Table 2, Entry 5): White solid; mp 99-100 °C; IR: 3032, 2224, 1725, 1618, 1596, 1542, 1416, 1365, 1260, 1236, 1192, 1087, 1014, 853, 830, 764. ¹H-NMR (500 MHz, CDCl₃): 1.40 (t, *J* = 7.0 Hz, 3H,

CH₃); 4.40 (q, *J* = 7.0 Hz, 2H, CH₂); 7.74 (d, *J* = 6.2 Hz, 2H, ArH); 8.19 (s, 1H, vinyl H); 8.81 (d, *J* = 6.2 Hz, 2H, ArH). ¹³C-NMR (125 MHz, CDCl₃): 14.5; 63.7; 98.7; 114.6; 123.6; 138.5; 151.5; 152.5; 161.6. Anal. calc. for C₁₁H₁₀N₂O₂: C 65.34, H 4.98, N 13.85; Found: C 65.45, H 4.86, N 13.52.

(E)-Ethyl-2-cyano-3-(pyridin-3-yl)acrylate (Table 2, Entry 6): White solid; mp 78-80 °C; IR: 3023, 2221, 1728, 1611, 1584, 1419, 1363, 1250, 1225, 1092, 1014, 896, 852, 763, 705, 632. ¹H-NMR (500 MHz, CDCl₃): 1.43 (t, *J* = 7.1, 3H, CH₃), 4.43 (q, *J* = 7.1, 2H, CH₂), 7.50 (dd, *J* = 8.2, *J* = 4.7, 1H, ArH), 8.28 (s, 1H, vinyl H), 8.59 (d, *J* = 8.2, 1H, ArH), 8.78 (d, *J* = 4.7, 1H, ArH), 8.95 (s, 1H, ArH); ¹³C-NMR (125 MHz, CDCl₃): 14.5; 63.5; 96.1; 115.3; 124.3; 128.0; 136.4; 151.7; 153.3; 153.9; 162.1. Anal. calc. for C₁₁H₁₀N₂O₂: C 65.34, H 4.98, N 13.85; Found: C 65.62, H 4.92, N 13.76.

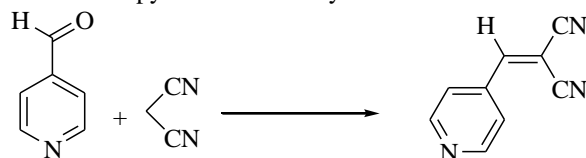
(E)-2-Cyano-3-(pyridin-4-yl)acrylamide (Table 2, Entry 7): White solid; mp 209-211 °C; IR: 3427, 3325, 3027, 2216, 1697, 1598, 1414, 1360, 1240, 1004, 974, 808, 668. ¹H-NMR (500 MHz, CDCl₃): 7.76 (d, *J* = 5.9, 2H, ArH); 8.05 (brs, 2H, NH₂); 8.18 (s, 1H, vinyl H); 8.79 (d, *J* = 5.9, 2H, ArH). ¹³C-NMR (125 MHz, CDCl₃): 89.5; 116.3; 123.8; 139.9; 149.1; 151.6; 162.7. Anal. calc. for C₉H₇N₃O: C 62.42, H 4.07, N 24.27; Found: C 62.01, H 4.10, N 24.26.

(E)-2-Cyano-3-(pyridin-3-yl)acrylamide (Table 2, Entry 8): White solid; mp 228-231 °C; IR: 3415, 3331, 3029, 2220, 1687, 1594, 1419, 1380, 1257, 1225, 1029, 803, 693. ¹H-NMR (500 MHz, CDCl₃): 7.61 (dd, *J* = 7.9, *J* = 4.8, 1H, ArH); 7.98 (brs, 2H, NH₂); 8.24 (s, 1H, vinyl H); 8.37 (d, *J* = 7.9, 1H, ArH); 8.72 (d, *J* = 4.8, 1H, ArH); 8.97 (s, 1H, ArH). ¹³C-NMR (125 MHz, CDCl₃): 109.8; 116.9; 125.0; 129.08; 136.83; 148.6; 152.1; 153.2; 163.0. Anal. calc. for C₉H₇N₃O: C 62.42, H 4.07, N 24.27; Found: C, 62.31, H, 4.11, N 24.21.

RESULTS AND DISCUSSION

Knoevenagel condensation produced some products that can be regarded as Michael acceptors in Michael or Aza-Michael reaction, as dienophiles in Diels-Alder and hetero Diels-Alder reactions, and as monomers in anionic polymerization. This condensation reaction was also applied to the synthesis of bioactive molecules. In this work, we report an environmentally benign procedure for the synthesis of some new electron-deficient alkenes *via* Knoevenagel condensation of pyridine-carbaldehydes and active methylene compounds.

At first, for the optimization of the reaction conditions, the condensation of 4-pyridine-

Table 1. Condensation of 4-pyridinecarbaldehyde with malononitrile in various conditions ^{a)}

Entry	Solvent	Temperature. (°C)	Time (h)	Yield (%) ^{b)}
1	MeCN	r. t.	24	20
2	MeCN	reflux	24	35
3	EtOH	r. t.	24	50
4	EtOH	70	24	65
5	H ₂ O	r. t.	-	- ^c
6	Solvent-free	r. t.	-	- ^c
7	H ₂ O:EtOH (25:75)	r. t.	2	92
8	H ₂ O:EtOH (50:50)	r. t.	0.5	95
9	H ₂ O:EtOH (75:25)	r. t.	1.5	90
10	H ₂ O:EtOH (50:50)	70	0.5	94

^{a)} 4-Pyridinecarbaldehyde (1 mmol), malononitrile (1 mmol). ^{b)} Yield refers to isolated yield. ^{c)} Black stick.

carbaldehyde with malononitrile was studied as a model reaction in various solvents at room temperature. The reaction in an aprotic solvent such as MeCN and in EtOH, as a protic one, did not proceed well and produced 2-(pyridin-4-ylmethylene)malononitrile with low yield after long reaction time even in refluxing conditions. As environment consciousness imposes the use of water for organic processes from both industrial and academic points of view [21-24], we decided to study the model reaction in pure water. The reactants were consumed promptly and a black sticky mixture was obtained in water. The black stick was also obtained in solvent-free conditions. In order to avoid this problem, the reaction was performed in a H₂O:EtOH mixture, and the ratio of the solvents was optimized. Fortunately, in a 50% H₂O:EtOH solution, this condensation was took place in a short reaction time (30 min) to produce 2-(pyridin-4-ylmethylene)malononitrile with an excellent yield under catalyst-free conditions (Table 1).

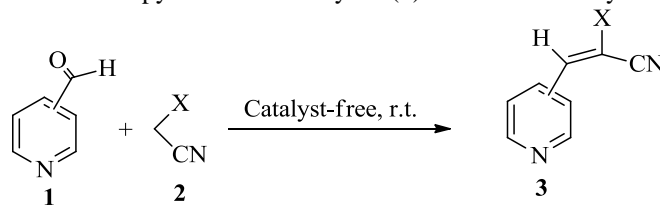
To examine the generality of the procedure, we checked the Knoevenagel condensation of various pyridylcarbaldehydes and active methylene compounds under optimized reaction conditions. The results summarized in Table 2 show that malononitrile is more active than cyanoacetamide, ethyl cyanoacetate, and methyl cyanoacetate due to the electron-withdrawing ability of CN groups. Ethyl and methyl cyanoacetates are more active than cyanoacetamide and readily react with pyridinecarbaldehydes. The Knoevenagel condensation of 4-pyridinecarbaldehyde with active methylene compounds is faster than that of 3-pyridinecarbaldehyde. It is because of the the resonance electron-withdrawing effect. The

reaction of 2-pyridinecarbaldehyde is also faster than that of 3-pyridinecarbaldehyde and 4-pyridinecarbaldehyde due to both resonance and induced effects of nitrogen in a pyridine ring.

All aforementioned reactions proceeded well enough and delivered high to excellent yields (Table 2). One of the advantages of this method, as mentioned in the experimental section, is that the product is precipitated, as the reaction proceeds and is isolated by simple filtration after the reactant is consumed. Thus, the reaction can be conducted without using any reaction workup method. Furthermore, we applied this green method for the condensation of malononitrile with an aromatic aldehyde such as benzaldehyde, 4-nitrobenzaldehyde, and 4-cyanobenzaldehyde with a view to compare with pyridinecarbaldehydes (Table 3).

According to the results, the Knoevenagel condensation of pyridinecarbaldehydes with malononitrile is much faster than the condensation of the same active methylene compound with benzaldehyde, 4-nitrobenzaldehyde, 4-cyanobenzaldehyde, and even 4-nitrobenzaldehyde in the presence of pyridine. These results also show that the pyridine ring has dual activity. One is to activate the methylene compounds by attracting the proton from the methylene *via* a non-bonding electron pair of nitrogen in the pyridine ring. The second is to activate the carbonyl group in the fourth position of the pyridine ring. A possible mechanism is denoted in the Scheme 1.

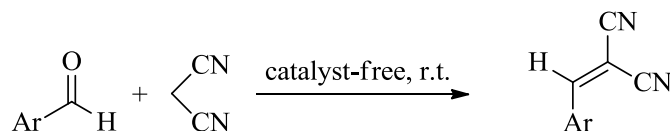
After the catalysts have accelerated the rate of a reaction in many cases, they should be separated at the end of the reaction. Catalyst-free reactions usually occur by reflux, microwave or other energetic methods while, in this work, we perform the catalyst-free reaction at room temperature.

Table 2. Condensation of pyridinecarbaldehydes (**1**) with active methylene compounds (**2**)^a

Entry	Pyridinecarbaldehyde	X	Product	Time(min)	Yield % ^b	Mp (°C)
1		CN		30	95	100-101
2		CN		40	93	81-83
3		CO ₂ Me		45	92	124-125
4		CO ₂ Me		55	92	127-128
5		CO ₂ Et		50	91	99-100
6		CO ₂ Et		65	93	78-80
7		CONH ₂		80	90	209-211
8		CONH ₂		95	92	228-231

^a Reaction conditions: pyridinecarbaldehyde (1 mmol), active methylene compound (1 mmol), H₂O:EtOH (1:1).^b Yields refer to isolated pure products which were characterized by their Mp, IR, ¹H- and ¹³C-NMR spectra and elemental analysis.

Table 3. Comparison of different arylaldehydes in a catalyst-free Knoevenagel reaction ^{a)}

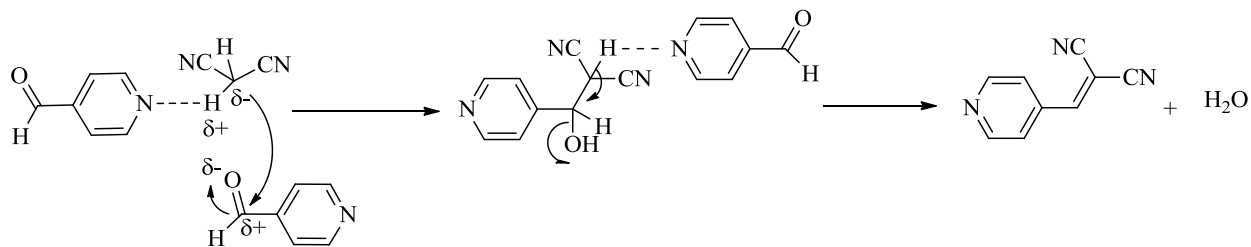


Entry	Ar	Time(min)	Yield (%)
1	C ₆ H ₅	240	93
2	4-CN- C ₆ H ₄	160	85
3	4-NO ₂ - C ₆ H ₄	160	91
4	4-NO ₂ - C ₆ H ₄ ^{b)}	110	92
5	2-Pyridyl	Very fast	-
6	3-Pyridyl	40	93
7	4-Pyridyl	30	95

^{a)} Reaction conditions: arylaldehyde (1 mmol), malononitrile (1 mmol), H₂O:EtOH (1:1).

^{b)} Pyridine was added to the reaction media.

Scheme 1. The proposed mechanism of synthesizing 2-(Pyridin-4-ylmethylene)malononitrile



Scheme 1

Acknowledgments: Authors thank the Research Council of Yazd University for financial support.

REFERENCES

1. M. R. Saidi, N. Azizi, F. Aryanasab, L. Torkiyan, A. Ziyaei, *J. Org. Chem.*, **71**, 3634 (2006).
2. S. Cunha, T. L. Silva, *Tetrahedron Lett.*, **50**, 2090 (2009).
3. V. Polshettiwar, R. S. Varma, *Tetrahedron Lett.*, **49**, 7165 (2008).
4. C. M. Chuy, Z. Tuy, P. Wu, C. C. Wang, J. T. Liu, C. W. Kuo, Y. H. Shin, C. F. Yao, *Tetrahedron*, **65**, 3878 (2009).
5. F. Freeman, *Chem. Rev.*, **80**, 329 (1980).
6. L. F. Tietze, *Chem. Rev.*, **96**, 115 (1996).
7. G. A. Kraus, M. E. Krolski, *J. Org. Chem.*, **51**, 3347 (1986).
8. L. F. Tietze, *Pure Appl. Chem.*, **76**, 1967 (2004).
9. F. Liang, Y. Pu, T. Kurata, J. Kido, H. Nishide, *Polymer*, **46**, 3767 (2005).
10. M. Zahouily, M. Salah, B. Bahlaouane, A. Rayadh, A. Houmam, E. A. Hamed, S. Sebti, *Tetrahedron*, **60**, 1631 (2004).
11. M. L. Deb, P. J. Bhuyan, *Tetrahedron Lett.*, **46**, 6453 (2005).
12. G. Jenner, *Tetrahedron Lett.*, **42**, 243 (2001).
13. J. S. Yadav, B. V. S. Reddy, A. K. Basak, B. Visali, A. V. Narsaiah, K. Nagaiah, *Eur. J. Org. Chem.*, **3**, 546 (2004).
14. J. McNulty, J. A. Steere, S. Wolf, *Tetrahedron Lett.*, **39**, 8013 (1998).
15. P. Leelavathi, S. R. Kumar, *J. Mol. Catal. A: Chem.*, **99**, 240 (2005).
16. T.I. Reddy, R. S. Varma, *Tetrahedron Lett.*, **38**, 1721 (1997).
17. Y. Goa, P. Wu, T. Tatsumi, *J. Catal.*, **224**, 107 (2004).
18. S. Nakamura, H. Hirao, T. Ohwada *J. Org. Chem.*, **69**, 4309 (2004).
19. B. Tamami, A. Fadavi, *Catal. Commun.*, **6**, 747 (2005).
20. A. Rahmati, K. Vakili, *Amino Acids*, **39**, 911 (2010).

21. (a) P. T. Anasta, J. C. Warner, *Green Chemistry: Theory and Practice*. Oxford University Press, Oxford, 1998. (b) P. A. Grieco, *Organic Synthesis in Water*. Blacky Academic and Professional, London, 1998. (c) C. J. Li, T. H. Chan, *Comprehensive Organic Reactions in Aqueous Media*. Wiley & Sons, New York (1999).
22. H. C. Kolb, M. G. Finn, K. B. Sharpless, *Angew. Chem. Int. Ed.*, **40**, 2004 (2001).
23. (a) M. Shiri, M. A. Zolfigol, *Tetrahedron*, **65**, 587 (2009). (b) C. J. Li, *Chem. Rev.*, **105**, 3095 (2005). (c) S. Narayan, J. Muldoon, M. G. Finn, V. V. Fokin, H. C. Kolb, K. B. Sharpless, *Angew. Chem. Int. Ed.*, **44**, 3275 (2005).
24. (a) J. H. Fendler, E. J. Fendler, *Catalysis in Micellar and Macromolecular Systems*. Academic Press, London, 1975. (b) P. M. Holland, D. N. Rubingh, *Mixed Surfactant Systems*. American Chemical Society, Washington, DC, 1992. (c) C. J. Cramer, D. G. Truhlar, *Structure and Reactivity in Aqueous Solution*. American Chemical Society, Washington, DC, 1994. (d) D. A. Sabatini, R. C. Knox, J. H. Harwell, *Surfactant-Enhanced Subsurface Remediation*. American Chemical Society, Washington, DC, 1994.

ПРОСТА КНОЕВЕНАГЕЛ'ОВА КОНДЕНЗАЦИЯ НА ПИРИДИН-КАРБАЛДЕХИДИ И АКТИВНИ МЕТИЛЕНОВИ СЪЕДИНЕНИЯ БЕЗ КАТАЛИЗАТОР

М.Х. Моемени, М.А. Амролахи, Ф. Тамадон

Департамент по химия, Колеж по наука, Университет Язд, Иран

Постъпила на 18 юни 2013 г.; коригирана на 7 май 2014 г.

(Резюме)

В статията се съобщава за изследване на една проста Knoevenagel'ова кондензация без катализатор на пиридин-карбалдехиди и активни метиленови съединения, като малонитрил, цианацетамид, етил-цианоацетат и метил-цианоацетат. Реакцията протича в смес от вода и етанол при стайна температура с високи добиви на производни на пиридил-метилен-малонитрила с Е-селективност.

Kinetics and mechanism of Ru (III) catalysed and uncatalysed oxidation of DL-alanine by N-bromosuccinimide

R.Venkata Nadh*, M.Sireesha,

Vignan University, Vadlamudi, India

Received August 15, 2013; Revised May 11, 2014

The kinetics of Ru(III) catalysed and uncatalysed oxidation of DL-alanine by N-bromosuccinimide (NBS) was studied in aqueous acetic acid and in the presence of perchloric acid and Hg (II). In both Ru(III) catalysed and uncatalysed oxidations, the kinetic orders were: first order in NBS, fractional order in substrate. The rate of the reaction decreased with the increase in perchloric acid concentration and addition of halide ions. The reactions were of fractional order with respect to Ru (III). Addition of Os(VIII) had no effect on the rate of oxidation of DL-alanine by NBS. The presence of catalysis with Ru (III) and the absence of catalysis with Os(VIII) in NBS oxidations was traced to different factors. A factor other than complexation could be a more powerful oxidant species like Ru (V) which accelerates the NBS oxidations. The effect of temperature was also investigated. By varying the solvent composition it was found that the reaction rate decreased with the decrease in dielectric constant of the solvent. All kinetic features were explained by postulating suitable mechanisms and rate laws.

Keywords: kinetics, oxidation, ruthenium(III), DL-alanine, N-bromosuccinimide

INTRODUCTION

Amino acids can undergo many types of reactions depending on whether a particular amino acid contains non-polar groups or polar substituents. The oxidation of amino acids is of interest as the oxidation products differ for different oxidants. These oxidation reactions display diverse reaction mechanisms, oxidative deamination and decarboxylation [1]. Thus, the study of amino acids becomes important because of their biological significance and selectivity towards the oxidant. Oxidation of alanine has received much attention because it is a degraded product of nucleic acids and is involved in biological processes such as stability of glucose in the system and is associated with chronic fatigue as well as Epstein–Barr virus, when alanine level becomes excessive [2]. Ruthenium complexes are mutagenic, capable of binding to nitrogen sites on DNA bases (as octahedral Ru (III) complexes are inert, they are activated *in vivo* by reduction to active Ru (II) complexes), suppress the immune response by inhibiting the proliferation of T cells by short-circuiting electron transfer pathways and serve as prodrugs by coordinating with biomolecules (for example as potential anticancer pharmaceuticals). As ruthenium mimics iron in binding to plasma proteins, transportation and sequestration of ruthenium into tumour cells may be mediated *via* protein transport and receptor mediated uptake [3].

Attention has been paid to N-halo oxidants due to their wide range of properties [4]. Oxidation of alanine was carried out by different hypohalous agents like N-bromophthalimide in presence of sodium dodecyl sulfate [5], NBS in alkaline medium [6], chloramine-T in absence of catalyst, in presence of catalyst and in presence of micellar aggregates [7]. Silver (I) catalysed oxidation of alanine by cerium (IV) in perchloric acid medium [8] and sulfuric acid medium [9] was well studied. The oxidation of DL-alanine by permanganate ions has been studied by Verma *et al.* [10] in concentrated acid solutions and Refat *et al.* [11] in dilute acid solutions. Oxidation of L-alanine by permanganate in acidic solvent was studied by Maria *et al.* [12] and Andres *et al.* [13]. In alkaline medium, the oxidation of alanine was studied using different oxidants like Os(VIII) [14], Ag(III) complex [15], hexacyanoferrate(III) [16] and diperiodatoargentate(III) [17].

The above literature survey shows that various oxidizing agents have been studied for the oxidation of amino acids, but catalyzed oxidations using transition metals as catalysts have not been studied in detail by using co-oxidants like N-halo compounds. The present investigation was undertaken using N-bromosuccinimide (NBS) as an oxidant to clarify whether oxidations of DL-alanine are catalyzed by transition metal catalysts like Ru (III) and Os (VIII) or whether the catalysis is selective to transition metal catalysts like Ru (III). Hence, a systematic investigation was done in acetic acid – perchloric acid mixtures to throw light on the nature of reaction orders and mechanistic sequences.

* To whom all correspondence should be sent:
E-mail: doctornadh@yahoo.co.in

EXPERIMENTAL

Materials

The reagents employed were DL-alanine (Loba Chemie), N-bromosuccinimide (G.R., Merck), ruthenium (III) chloride (Johnson Matthey, London), osmium tetroxide (Johnson Matthey), mercuric acetate (G.R., Merck), other reagents used were of analytical grade. All solutions were prepared with doubly distilled water. Stock solutions of N-bromosuccinimide were prepared in pure acetic acid and standardized iodometrically.

Kinetic measurements

Kinetic studies were carried out in perchloric acid medium at a temperature of 313K under pseudo first order conditions with a large excess of DL-alanine over NBS. The progress of the reaction

was followed by determining N-bromosuccinimide concentrations iodometrically in aliquots withdrawn after suitable time intervals [18].

From the titer values, plots of log [NBS] vs. time were drawn and from their slopes the pseudo first order rate constants $k_1(\text{min}^{-1})$ were obtained. To evaluate k_1 , generally 8–10 values at least up to 80% completion of the reaction were used. Average values of at least two independent determinations of k_1 were taken for analysis. All first order plots were linear, with a correlation coefficient of 0.995–0.998. The obtained rate constants were reproducible within the experimental error of $\pm 4\%$.

The kinetics of both uncatalysed and Ru(III) catalysed oxidation of DL-alanine by N-bromosuccinimide (NBS) were studied in acetic acid-perchloric acid medium. The kinetic rate data are given in Tables 1 and 2.

Table 1. Kinetic data for the uncatalysed oxidation of DL-alanine by NBS

[NBS] = 0.001 M [DL-Alanine] = 0.01 M [HClO₄] = 0.25 M
 AcOH – H₂O = 20% - 80 % (v/v) [Hg (OAc)₂] = 0.02M Temp = 40°C

Variant	Concentration of Variant	$k_1 \times 10^4 \text{ min}^{-1}$
NBS	$0.5 \times 10^{-3}\text{M}$	128.1
	$1.0 \times 10^{-3}\text{M}$	129.3
	$2.0 \times 10^{-3}\text{M}$	124.7
DL-alanine	$1.25 \times 10^{-3}\text{M}$	41.3
	$2.50 \times 10^{-3}\text{M}$	56.3
	$5.00 \times 10^{-3}\text{M}$	97.5
	$10.00 \times 10^{-3}\text{M}$	125.3
	$20.00 \times 10^{-3}\text{M}$	174.7
	$40.00 \times 10^{-3}\text{M}$	305.0
H ⁺	0.10	319.6
	0.25	125.3
	0.50	67.4
	1.00	34.6
	2.00	14.8
Acetic Acid	5 : 95	224.3
	10 : 90	199.9
	20 : 80	125.3
	40 : 60	69.1
	60 : 40	25.3
Temperature	30°C	46.0
	40°C	125.3
	50°C	426.9
Os (VIII) at [HClO ₄] = 0.5M	0.0	67.4
	$6.40 \times 10^{-5}\text{M}$	83.4
	$12.80 \times 10^{-5}\text{M}$	73.4
	$19.20 \times 10^{-5}\text{M}$	66.4
	$25.60 \times 10^{-5}\text{M}$	55.2
Addition of salt at [HClO ₄] = 0.5M	No salt	67.4
	0.02 M KF	79.1
	0.02 M KCl	30.7
	0.02M KBr	No Reaction

Table 2. Arrhenius parameters for the uncatalysed reaction at 313°K

ΔE^\ddagger	ΔH^\ddagger	$\log_{10} PZ$	$-\Delta S^\ddagger$	ΔG^\ddagger
KJmol^{-1}	KJmol^{-1}		$\text{JK}^{-1} \text{mol}^{-1}$	KJmol^{-1}
92.544	89.942	11.764	28.415	98.835

Factors influencing the rate of oxidation of DL-alanine by NBS, such as effects of (i) [NBS], (ii) [DL-alanine], (iii) [H⁺], (iv) ionic strength, (v) dielectric constant, and (vi) temperature, both in absence and presence of Ru (III) catalyst were studied. Rate and activation parameters were evaluated.

RESULTS AND DISCUSSION

Uncatalysed reactions

Effect of [NBS]

The kinetics of oxidation of DL-alanine was investigated under pseudo first order conditions, keeping the concentrations of DL-alanine in a large excess (nearly tenfold) over that of [NBS]. When log [NBS] was plotted against 'time', very good straight line plots were obtained indicating that the reaction was of first order with respect to [NBS] (Table 1). Effect of varying [NBS] on the rate of oxidation was studied at constant [DL-alanine], [H⁺], %AcOH, [mercuric acetate] and temperature. The pseudo first order rate constants k_1 were found to be independent of [NBS], confirming the first order dependence of rate on [NBS].

Effect of [DL-alanine]

At constant [NBS], [H⁺], [AcOH], [mercuric acetate] and temperature the kinetic runs were carried out with various initial concentrations of DL-alanine, which yielded rate constants whose values depended on [DL-alanine]. The pseudo first order rate constants k_1 (min⁻¹) thus obtained were found to increase with [DL-alanine] (Table 1) over the range of [DL-alanine] used. The plot of log k_1 versus log [alanine] was a straight line with fractional slope showing that the reaction obeys a fractional order with respect to [DL-alanine]. The formation of the complex was kinetically proven by Michaelis – Menten plot, that is, a non-zero

$$F = kT \ln \beta = -\frac{\mu}{r^3} \left[\frac{D-1}{2D+1} \right]$$

Introducing a non-electrostatic term, this becomes

$$F = kT \ln \beta = -\frac{\mu}{r^3} \left[\frac{D-1}{2D+1} \right] + \phi$$

For the reaction under consideration, the equation for the specific velocity constant k will be

intercept of the plot of 1/rate vs. 1/[S]. The complex formation between oxidant and substrate was also reported in the literature [19].

Effect of acid

A change in the kinetic rate of the reaction with the change in the concentration of perchloric acid was observed in the present investigation. The first order rate constants decreased with the increase in perchloric acid concentration. The plot of log k_1 versus log [H⁺] is linear and yields a fractional slope.

Effect of solvent

In order to determine the effect of dielectric constant (polarity) of the medium on the rate, the oxidation of DL-alanine by NBS was studied in aqueous acetic acid mixtures of various compositions (Table 1). The rate of the reaction decreased with increase in the percentage of acetic acid in the mixture. In other words, decrease in the dielectric constant of the medium lowers the rate of reaction. This indicates that there is a charge development in the transition state involving a more polar activated complex than the reactants [20]. Amis showed that in a straight line plot of logarithm k_{obs} versus 1/D, a positive slope indicates a positive ion–dipole reaction, while a negative slope indicates the involvement of two dipoles or a negative ion–dipole reaction [21]. In this investigation a plot of logarithm k_{obs} versus 1/D gives straight lines with negative slopes; these results clearly support the involvement of two dipoles in the rate determining step.

For the dipole-dipole type of reaction, Laidler and Eyring treatment can be applied [22]. Laidler and Eyring derived an expression for the free energy transfer of a polar molecule with a dipole moment μ from vacuum to a medium of dielectric constant D. This equation is in the following form for a molecule of radius 'r' which has symmetrical charge distribution.

$$\ln k = \ln \left[x \frac{kT}{h} k_0 \right] - \frac{1}{kT} \left[\frac{D-1}{2D+1} \right] \left[\frac{\mu_A^2}{r_A^3} + \frac{\mu_B^2}{r_B^3} + \frac{\mu_m^{2*}}{r_m^3} \right] + \left[\frac{\phi_A + \phi_B - \phi_M^*}{kT} \right]$$

A plot of $\log k$ versus $\frac{D-1}{2D+1}$ will be linear if non-electrostatic terms are negligibly small. In the present investigation the plots of $\log k_1$ versus $\frac{D-1}{2D+1}$ are linear confirming the dipole - dipole nature of the reaction. The two neutral molecules participating in the reaction are NBS and amine.

Test for free radicals

To test for free radicals, the reaction mixture containing stabilizer-free acrylonitrile was kept for 24 hours in an inert atmosphere [23]. On diluting the reaction mixture with methanol no precipitate was observed. This indicates that no free radicals intervene in the reaction.

Rate and activation parameters

The effect of temperature on the rate of the reaction was studied in the range (303 – 323 K) and the results are shown in Table 2. From the Arrhenius plot, the value of energy of activation (ΔE^\ddagger), enthalpy (ΔH^\ddagger), entropy ($-\Delta S^\ddagger$) and free energy (ΔG^\ddagger) were computed. A large negative value of entropy ($-\Delta S^\ddagger$) was obtained, which can be attributed to the severe restriction of solvent molecules (electrostriction) around the transition state [24]. It also indicates that the complex is more ordered than the reactants [25]. The modest activation energy and sizeable entropy of activation supports a complex transition state in the reaction.

Effect of added salt

Different potassium halides were added to the reaction mixture and the reaction rates were determined. Addition of potassium bromide (Table 1) did not increase the kinetic rate as expected but rather stopped the reaction. This finding seems to be at variance to earlier published work [26, 27], where molecular bromine formed on addition of bromide to the system was considered to be more reactive than N-halo compounds and hence acceleration was expected. The present result of stopping the reaction may be due to the following reasons:

There is no doubt that molecular bromine is formed on addition of higher concentrations of Br⁻ ions.

The question to be decided is whether bromine in molecular form is always a powerful oxidant

whatever may be the substrate. The observed differential rate points to the fact that molecular bromine is probably not a powerful oxidant in the present reaction compared to N-halo compounds, Br⁻ or HOBr, the likely species in this reaction.

This seems to be quite in order, as seen from the work of de la Mare and our earlier work where it has been observed that NBS or HOBr or H₂OBr⁻ or Br⁻ are more reactive than molecular bromine in partially aqueous systems with aromatic substrates [28, 29]. Hence, in the present investigation extending the argument to aliphatic amino acids, the formed molecular bromine is not effective compared to the other reactive species. So, it is not surprising that the addition of Br⁻ did not result in an increase in the rate.

It was observed that the change in the concentration of added mercuric acetate had negligible effect on the rate. The function of the added mercuric acetate is therefore only to fix up Br⁻ formed in the course of the reaction as HgBr₂ or $HgBr_4^{2-}$.

Product Analysis

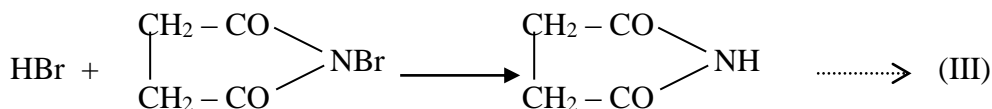
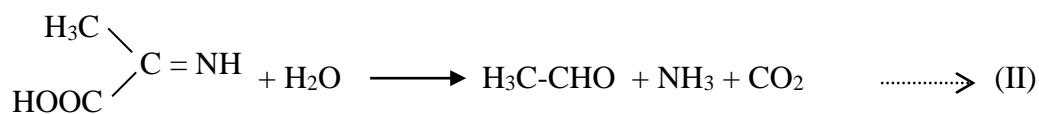
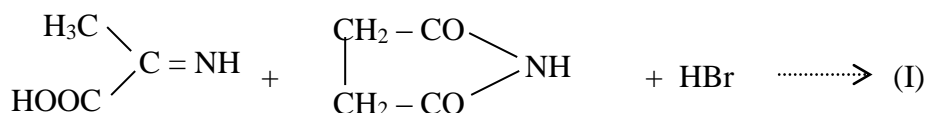
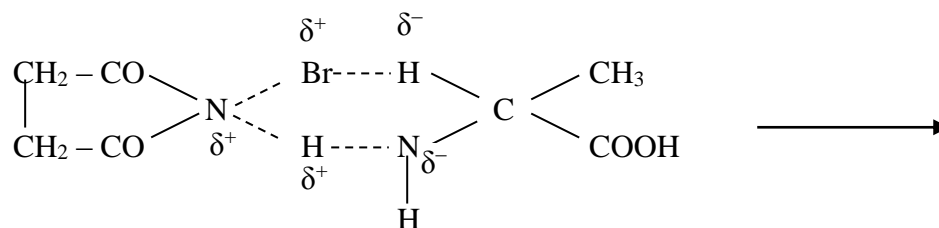
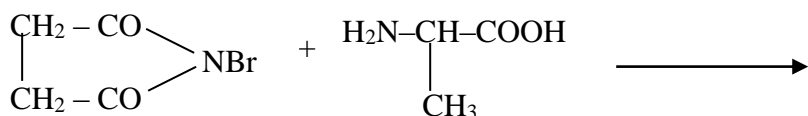
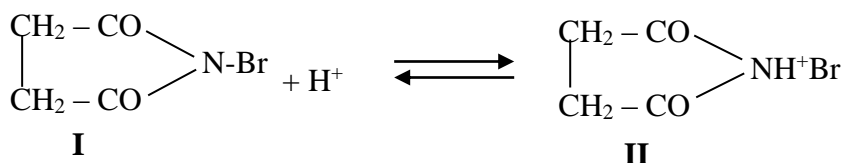
The product analysis was carried out under kinetic conditions. In a typical experiment, DL-alanine (0.05M) and NBS (0.01M) were made up to 100 ml in 1:1 (V/V) acetic acid-water mixture and the reaction mixture was allowed to stay in the dark for about one day to ensure completion of the reaction. The main reaction products were succinimide, acetaldehyde, ammonia, and CO₂. Liberated ammonia was identified by Nessler's reagent where a brownish color was observed indicating a deamination reaction [30]. Carbon dioxide was identified by freshly prepared lime water; and the solution turned milky, indicating a decarboxylation reaction [31].

The solution was then treated with an excess (200 ml) of a saturated solution of 2,4-DNP in 2M HCl and kept overnight in a refrigerator. The precipitated 2,4-DNP was filtered off, dried, weighed, recrystallized from ethanol, and weighed again. The yields of DNP before and after crystallization were 94% and 89%, respectively. The DNP was found to have identical melting point and spectral data as the DNP of acetaldehyde. Further, the aldehyde group was confirmed with a qualitative test such as Tollen's reagent [32] and spot tests [33]. Similarly, Verma *et al.* [10] and Rao *et al.* [34] indicated that ammonia and acetaldehyde are two of the reaction products from the oxidation of DL-alanine by MnO₄⁻ ions.

Mechanism

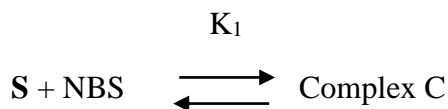
It is reported that the oxidation of amino acids involves the cleavage of N-H and C-H bonds in the rate determining step [35]. The rate of oxidation of

DL-alanine by NBS is inhibited by the addition of H⁺ ions. This may be explained by assuming the equilibrium (I=II) to be present and that the unprotonated species (I) is the reactive one.

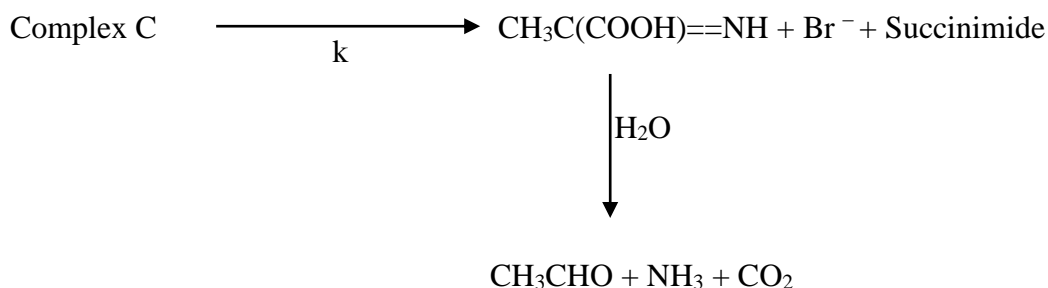


However in presence of mercuric acetate the reaction (Eq. III) does not take place.

Rate law



Where S = alanine = CH₃ CH (NH₂) COOH



$$\begin{aligned} \text{Rate} &= k [\text{Complex}] \\ &= k K^1 [\text{S}] [\text{NBS}] \longrightarrow (1) \end{aligned}$$

$$\begin{aligned} [\text{NBS}]_T &= [\text{NBS}] + [\text{Complex}] + [\text{NBSH}^+] = [\text{NBS}] + K^1 [\text{NBS}] [\text{S}] + K [\text{NBS}] [\text{H}^+] \\ &= [\text{NBS}] \{1 + K^1 [\text{S}] + K [\text{H}^+]\} \longrightarrow (2) \end{aligned}$$

from (1) and (2)

$$\text{rate} = \frac{k K^1 [\text{NBS}]_T [\text{S}]}{1 + K^1 [\text{S}] + K [\text{H}^+]} \longrightarrow (3)$$

The above rate law explains the first order in oxidant, the fractional order in substrate and the inverse first order in acid.

Ru (III) Catalysed reactions

Ruthenium (III) chloride accelerates the oxidation of DL-alanine by NBS in acetic acid – perchloric acid medium (Table 3), whereas osmium (VIII) does not catalyze the oxidation of DL-alanine (Table 1). N-bromosuccinimide oxidation of DL-alanine catalyzed by Ru (III) was carried out in aqueous acetic acid - perchloric acid mixtures.

Effect of variation of concentration of NBS

The reaction is of first order in NBS as evidenced by the linear plots of log (a-x) versus time. Increase of concentration of NBS yields constant first order rate constants

confirming the first order dependence on NBS (Table 3).

Effect of increase of concentration of substrate:

An increase in the concentration of DL-alanine increased the kinetic rate (Table 3). A plot of log k₁ versus log [S] is linear with a slope of nearly 0.5 indicating a fractional order dependence on DL-alanine.

Effect of increase in concentration of Ru (III)

The oxidation of DL-alanine by NBS is of fractional order with respect to Ru(III). The first order rate constants at different concentrations of Ru (III) are presented in Table 3. The plot of log k₁ versus log [Ru (III)] is linear and has a slope of 0.63 indicating that the reactions are of fractional order with respect to Ru (III).

Table 3. Kinetic data for the Ru(III) catalysed oxidation of DL-alanine by NBS

[NBS] = 0.001 M [DL-alanine] = 0.01 M Temp = 40°C
 [HClO₄] = 1.0 M [Hg(OAc)₂] = 0.02M [Ru (III)]=0.95×10⁻⁵M.
 AcOH – H₂O = 20% - 80% (v/v)

Variant	Concentration of Variant	k ₁ × 10 ⁴ min ⁻¹
NBS at [HClO ₄] = 0.5 M	1.0 × 10 ⁻³ M	98.6
	2.0 × 10 ⁻³ M	99.6
	4.0 × 10 ⁻³ M	100.3
DL-alanine at [Ru (III)]=3.8×10 ⁻⁵ M	0.625 × 10 ⁻³ M	41.4
	1.25 × 10 ⁻³ M	49.8
	2.5 × 10 ⁻³ M	59.1
	5.0 × 10 ⁻³ M	98.3
	10.0 × 10 ⁻³ M	145.8
	20.0 × 10 ⁻³ M	192.3
	40.0 × 10 ⁻³ M	272.6
Ru(III)	0.0	34.6
	0.95 × 10 ⁵ M	66.9
	1.90 × 10 ⁵ M	111.9
	3.80 × 10 ⁵ M	145.8
	7.60 × 10 ⁵ M	243.1
	15.20 × 10 ⁵ M	271.0
H ⁺	0.25	239.9
	0.5	98.6
	1.0	66.9
	2.0	27.9
	4.0	No Reaction
Acetic Acid : Water at [Ru(III)] = 3.8×10 ⁻⁵ M	5 : 95	197.2
	10 : 90	164.2
	20 : 80	145.8
	40 : 60	111.6
	60 : 40	36.00
Temperature at Ru(III)] = 3.8×10 ⁻⁵ M	30°C	28.7
	40°C	145.8
	50°C	387.6
	60°C	1545.2

Effect of variation of [H⁺]

The effect of acid concentration on the reaction kinetics was studied and the first order rate constants are presented in Table 3. The rate constants decrease with the increase in the concentration of perchloric acid. A linear plot with a slope of -1.045 indicates an inverse unit dependence on [H⁺]. As the reaction rate decreased with the increase in H⁺, free alanine molecules are probably the predominant species.

Effect of variation of solvent composition

The reactions were carried out at various solvent compositions to find the effect of change in dielectric constant and the rate constants are listed in Table 3. The reaction rate decreases with the decrease in dielectric constant as required for dipole-dipole reactions, as the major reaction is between free alanine and free NBS molecules.

Effect of variation of temperature

The reactions were carried out at four different temperatures: 30°C, 40°C, 50°C and 60°C and reaction rate constants are recorded. Plot of log k₁ versus 1/T is linear. Arrhenius parameters are calculated (Table 4).

Nature of Ru (III) species

The electronic spectrum of ruthenium (III) chloride shows that it probably exists as [Ru(H₂O)₆]³⁺ under acid conditions [36, 26] while species like [RuCl₅.H₂O]²⁻, [RuCl(H₂O)₅]²⁺, [RuCl₄(H₂O)₂]⁻, [RuCl₃(H₂O)₃], [RuCl₂(H₂O)₄]⁺, [RuCl(H₂O)₅]²⁺ and [Ru(H₂O)₆]³⁺ are present in aqueous solutions. The most active species is [Ru(H₂O)₆]³⁺ in acid medium which is formed due to the following equilibrium:

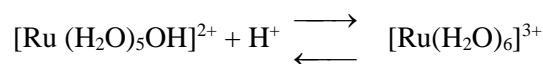
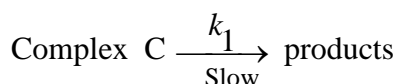
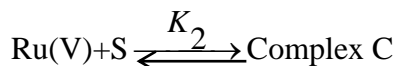
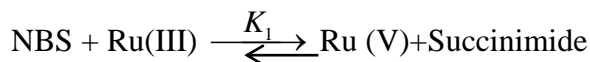
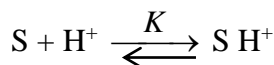


Table 4. Arrhenius parameters for the catalysed reaction at 313^oK

ΔE^\ddagger KJmol ⁻¹	ΔH^\ddagger KJmol ⁻¹	$\log_{10} PZ$	ΔS^\ddagger JK ⁻¹ mol ⁻¹	ΔG^\ddagger KJmol ⁻¹
102.117	99.515	14.4	3.431	98.441

Mechanism and rate law for Ru (III) catalyzed oxidation of DL-alanine by NBS



$$S_T = S + S H^+ + \text{Complex} = S + K [S] [H^+] + K_1 K_2 [S] [NBS] [Ru(III)]$$

$$= [S] \{1 + K[H^+] + K_1 K_2 [NBS] [Ru(III)]\}$$

$$[S] = \frac{S_T}{1 + K[H^+] + K_1 K_2 [NBS] [Ru(III)]}$$

$$\text{Rate} = k_1 C$$

$$= k_1 K_2 [Ru(V)][S] = k_1 K_1 K_2 [NBS] [Ru(III)][S]$$

$$= \frac{k_1 K_1 K_2 [NBS] [Ru(III)] S_T}{1 + K[H^+] + K_1 K_2 [NBS] [Ru(III)]}$$

The above rate law explains the apparent first order in N-bromosuccinimide, the fractional order in Ru (III), the fractional order in alanine and the inverse unit order in [H⁺].

CONCLUSIONS

In summary, the following points can be delineated in the oxidation of DL-alanine by NBS in acid medium.

a) Alanine can be classified as a substrate which is not catalysed by Os (VIII). The reason may be the

absence of direct complex formation between Os (VIII) and alanine.

b) The presence of catalysis with Ru (III) and absence of catalysis with Os(VIII) in NBS oxidations could be traced to different factors. The factor other than complexation could be a more powerful oxidant species like Ru (V) which accelerates the NBS oxidations.

Hence, Ru (V) participation is responsible for the catalysis observed for compounds like alanine in NBS oxidations.

REFERENCES

- 1.S. Huo, C. Song, J. Shan, S. Shen, H. Sun, *J. Iran. Chem. Soc.*, 6(2), 243 (2009).
2. Shanmugam, *Fundamentals of Biochemistry for Medical students*, Published by the Author, Madras, 1998.
- 3.(a) M.J. Clarke, *Coord. Chem. Reviews* 236, 209 (2003). (b) C.S. Allardyce, P.J. Dyson, J. Coffey, N. Johnson, *Mass Spectrom.*, 16(10), 933 (2002). (c) M. Pongratz, P. Schluga, M. Jakupec, V. Arion, C. Hartinger, G. Allmaier, *J. Anal. At. Spectrom* 19(1), 46 (2004).
- 4.(a) R.V. Nadh, B.S. Sundar and P.S. Radhakrishnamurti, *Russ. J. Phy. Chem.*, 75(2), 174 (2001). (b) R.V. Nadh, B.S. Sundar and P.S. Radhakrishnamurti, *Oxid. Commun.*, 23(1) 102, (2000). (c) V. Neeraja, R.V. Nadh, B.S. Sundar and P.S. Radhakrishnamurti, *Oxid. Commun.*, 21(3), 369 (1998)
5. Y.R. Katre, G.K. Joshi, A.K. Singh, *Kinet. Catal.*, 50(3), 367 (2009).

6. K. Neelu, G. Neeti, S.K. Upadhyaya, *J. Ind. Chem. Soc.*, 79(12), 939 (2002).
7. (a) S.M. Ramachandran, S.T. Vivekanandam, *Bull. Chem. Soc. Japan.*, 60(9), 3397(1987). (b) R.A. Singh, V.K. Srivastava, *Proc. Nat. Acad. Sci. Ind. Sec-A.*, 75(1), 17(2005). (c) E. Pandey, S.K. Upadhyay, *Colloids and Surfaces A: Physicochemical and Engineering Aspects.*, 269(1-3), 7 (2005).
8. D. Vijay, *J. Ind. Chem. Soc.*, 82(4), 290 (2005).
9. T. Sumathi, P. Shanmuga Sundaram, G. Chandramohan, *Arab. J. Chem.*, 4(4), 427 (2011).
10. R.S. Verma, M.J. Reddy, V.R. Shastry, *J. Chem. Soc. Perkin Trans.*, 2, 469 (1976).
11. R.M. Hassan, *Can. J. Chem.*, 69, 2018 (1991).
12. M.J. Insausti, F. Mata-Pérez, M.P. Alvarez-Macho, *Collect. Czech. Chem. Commun.*, 59(3), 528 (1994).
13. J. de Andres, E. Brillas, J.A. Garrido, J.F. Perez-Benito, *J. Chem. Soc. Perkin Trans.*, 2, 107 (1988).
14. M. B. Yadav, D. Vijay, A. Rani, *J. Ind. Chem. Soc.*, 87(7), 823 (2010).
15. Ch. Song, L. Chen, J. Shan, *Res. Lett. Inorg. Chem.*, 4 pages, Article ID 786857, doi:10.1155/2008/786857, (2008)
16. P.K. Chourasia, N.C. Bhattacharjee, T.K. Singh, *J. Ind. Chem. Soc.*, 86(4), 364 (2009).
17. V. Seregar, T.M. Veeresh, S.T. Nandibewoor, *Trans. Met. Chem.*, 34(6), 647 (2009).
18. C. Srinivasan, A. Chellamani, *React. Kinet. Catal. Lett.*, 18(1-2), 187 (1981).
19. J. Richard, L. Emmett, *A manual of paper chromatography and paper electrophoresis*, 2nd edition, Academic Press Inc., New York, 1958.
20. I. Sharma, D. Vijai, G. Divya, C.M. Gangwas, P.D. Sharma, *Int. J. Chem. Kinet.*, 27, 311(1995),
21. E.S. Amis, *J. Chem. Educ.*, 30, 351 (1953).
22. K.J. Laidler, H. Eyring, *N.Y. Ann. Acad. Sci.*, 39, 303 (1939).
23. S.M. Desai, N.N. Halligudi, S.T. Nandibewoor, 27(2), 207 (2002).
24. S.S. Anis, *J. Chim. Phy. Phy.-Chim. Biol.*, 89, 659 (1992).
25. D.C. Hiremath, T.S. Kiran, S.T. Nandibewoor, *Int. J. Chem. Kinet.*, 39, 1 (2007).
26. N. Venkata Subramanian, V. Thiagarajan, *Tetra. Lett.*, 35, 3349 (1967).
27. C.K. Ingold, *Structure and Mechanism in Organic Chemistry*, 2nd edition, G.Bell and Sons Ltd., London, 1969.
28. P.B.D. de la Mare, J. H. Ridd, *Aromatic Substitution*, Butterworths Scientific Pubs., London, 1959.
29. R.V. Nadh, B.S. Sundar, P.S. Radhakrishnamurti, *Oxid. Commun.*, 28(1), 81 (2005)
30. R.K. Patil, S.A. Chimatadar, S.T. Nandibewoor, *Ind. J. Chem.*, 48A, 357 (2009).
31. G. Svehla, *Vogel's Qualitative Inorganic Analysis*, Pearson Education India, 1996.
32. Ch. Shivamurti, V. Madawale Shankar, T. Nandibewoor Sharanappa, *Trans. Met. Chem.*, 32(5), 634 (2007).
33. V.S. Rao, B. Sethuram, T.N. Rao, *Ind. J. Chem. Kinet.*, 11, 165 (1975).
34. R. Shukla, S.K. Upadhyay, *Ind. J. Chem.*, 47A, 551 (2008).
35. F. Feigl, *Spot Tests in Organic Analysis*, Elsevier, New York, USA, 1956.
36. R.E. Connick, D.A. Fine, *J. Amer. Chem. Soc.* 82, 4187 (1960).

КИНЕТИКА И МЕХАНИЗЪМ НА ОКИСЛЕНИЕТО НА DL-АЛАНИН С N-БРОМОСУКЦИНИМИД С И БЕЗ РУТЕНИЕВ Ru (III)-КАТАЛИЗАТОР

Р. Венката Надх *, М. Сирееша

Университет Вигнан, Вадламуди, Андра Прадеш, Индия

Получена на 15 август 2013 г.; ревизирана на 11 май, 2014 г.

(Резюме)

Изследвана е кинетиката на окислението на DL-аланин с N-бромосукцинимид (NBS) с и без рутениев Ru (III)-катализатор във водна среда и в присъствие на перхлорна киселина и Hg (II). И в двата случая (с и без катализатор) реакциите са с кинетика от първи порядък по отношение на NBS и от дробен порядък по отношение на субстрата. Скоростта на реакцията се понижава с нарастване на концентрацията на перхлорната киселина и добавянето на халогениден йон. Реакцията е от дробен порядък по отношение на Ru(III). Добавянето на Os(VIII) няма ефект върху скоростта на окисление. Наличието на катализа при Ru(III) и отсъствието при Os(VIII) може да се търси в други фактори. Освен комплексообразуването ускоряването на окислението на NBS може да търси в по-мощни окислителни, като Ru (V). Изследван е и ефекта на температурата. Установено е, че промените в състава на разтворителя промяната на скоростта на реакцията се свързва с промяна в диелектричната константа на средата.

Всички кинетични ефекти са обяснени с приети подходящи механизми и кинетични закони.

Determination of complex 12-grade phytic acid dissociation constants

H. Zhang, H. Xue *, J. Yang, L. Liang

Department of Chemistry, Bengbu Medical College, Bengbu, P. R. China

Received September 17, 2013; Revised November 30, 2013

The potentiometric method was used to titrate hydrochloric acid with sodium phytate using a combined pH electrode. Four groups of 12-grade dissociation constants, cumulative dissociation constants and ionization degrees of phytic acid were calculated according to the changes in the pH value and the related substance concentration in the titration process. A group of 12-grade relatively reasonable dissociation constants K_a , cumulative dissociation constants β and ionization degrees α of phytic acid was selected, with K_a values between 10^{-10} and 10^{10} , β values in the range of 10^{-12} to 10^{27} , and α values from 10^{-5} to 1. The data are relatively objective and reasonable and provide a theoretical basis for in-depth research on phytic acid.

Keywords: phytic acid; potentiometric titration; dissociation constants; cumulative dissociation constants; ionization degrees

INTRODUCTION

Phytic acid ($C_6H_{18}O_{24}P_6$), also known as myoinositol hexaphosphate, is present in most cereal grains, legumes, nuts, oilseeds, tubers, pollen, spores and organic soils [1-3]. It has been the subject of several reviews [4] owing to the following physical and chemical properties: light yellow or light brown syrupy liquid with relative molecular mass of $660.04 \text{ g mol}^{-1}$, strong acid, soluble in water, 95% ethanol and acetone, insoluble in anhydrous diethyl ether, benzene, hexane, chloroform, etc., decomposed easily by heating, more stable at higher concentrations. Phytic acid in plant sources is natural, non-toxic to human and green to environment, more secure and reliable compared with synthetic food additives. It is a superior example of green food additives because of its unique chemical properties, special physiological, pharmacological and health functions [5, 6]. At present, it covers various fields of industry [7], agriculture, food [8], pharmaceuticals, chemicals, metal corrosion [9, 10],

gradually showing more new features and getting involved in the whole process of human life [11].

The structure of the phytic acid molecule is shown in Figure 1. As can be seen, phytic acid molecule with 12 acidic hydrogen atoms has 12-grade different dissociation constants.

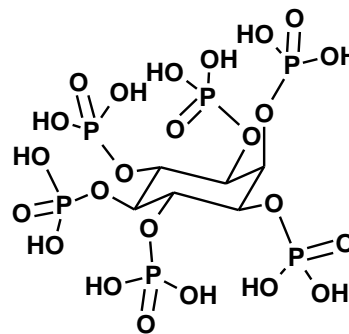


Fig. 1 Structure of phytic acid

On the basis of previous research, 12-grade dissociation constants were obtained by Evans *et al.* [12] in 1982; the results between 10^{12} and 10^{-11} acquired by the application of acid-base titration were relatively objective. However, these results were not accurate according to phytic acid structure, and there are no more accurate reports of phytic acid dissociation constants at all levels in the latest literature.

* To whom all correspondence should be sent:

E-mail: hongbaoxueqhd@126.com

The objectives of this study were to apply the method of potentiometric titration of hydrochloric acid with sodium phytate using a combined pH electrode. The dissociation constants, accumulated dissociation constants and ionization degrees of phytic acid at all levels were calculated from the pH titration curve. The reliability of the obtained results is confirmed by the analysis of phytic acid structure, and provides a theoretical basis for further research and development of phytic acid from natural product.

EXPERIMENTAL

Chemical reagents and apparatus

Titration was carried out using a ZD-2A automatic potentiometric titrator (Shanghai Dapu instrument Co., Ltd. China) equipped with 405-60-SC-P-PA- K19/120/3mMETTLER pH/ORP electrode (Shenzhen TRT technology Co., Ltd. China). Weighing was performed on a FA/JA series precision electronic balance (Accuracy: 0.0001 g, Tianjin Tianma hengji instrument Co., Ltd. China). Ultrasound (KQ-100 NC ultrasonic cleaning machine, Kunshan ultrasonic instruments Co., Ltd. China) was used to promote the dissolution of phytic acid in water. DZF-6050B vacuum drying oven (Shanghai Qixin technology instrument Co., Ltd. China) was used to dry sodium borate.

Sodium phytate was purchased from Sigma-Aldrich Corporation. Sodium borate and concentrated HCl were obtained from Shanghai Reagent Co. All reagents were of analytical grade. Deionized water from an ultrapure Milli-Q system (Millipore, Molsheim, France) was used.

Experimental Methods

Sample preparation:

100 mL sodium borate solution was prepared by dissolving 2.8612 g of sodium borate in deionized water. 3.8 mL of concentrated HCl was diluted to 250 mL for calibration. 100 mL standard solution of sodium phytate was obtained by dissolving 9.6584 g of sodium phytate in water.

Calibration of the HCl standard solution:

The concentration of the HCl solution was calibrated by titration. The 10.00 mL standard sodium borate solution was titrated with the HCl solution until the end point of pH = 5.27. The volume of consumed hydrochloric acid was recorded. The above operation was repeated 3 times. The average concentration of the HCl standard solution was calculated to be $0.1250 \text{ mol}\cdot\text{L}^{-1}$. Measurement of 12-grade dissociation constants of phytic acid:

The HCl standard solution and the sodium phytate solution were used for the pH measurements. The temperature of all operations was maintained at $25.0\pm 0.1^\circ\text{C}$.

Data Processing

The experimental data obtained were processed by Excel, statistical analysis using Origin 8.0 software.

RESULTS AND DISCUSSION

Calculation of phytic acid dissociation constants

The results presented in Figure 2 demonstrate that the pH values of the solution varied from 0.74 to 9.67 in the titration process, because the gradually increasing volume of the solution led to a dilution effect, and the concentrations of sodium phytate and HCl changed accordingly (see Figure 3). The hydrogen ion calibration concentration, namely stoichiometric concentration, was denoted as concentration 1. On the other hand, the corrected concentration of hydrogen ion, denoted as concentration 2, includes the activity factors, in other words, this hydrogen ion concentration was calculated according to the electrode potential value. The pH value, the sodium phytate concentration and the HCl concentration were selected in line with the stoichiometric point corresponding to concentration 1 and concentration 2, substituted into the following formula to calculate.

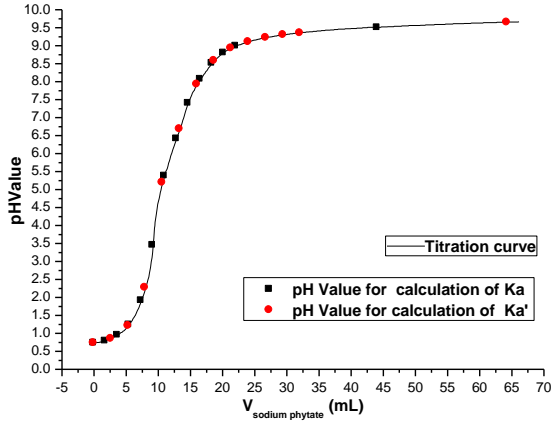


Fig. 2. Curves of sodium phytate titration of HCl

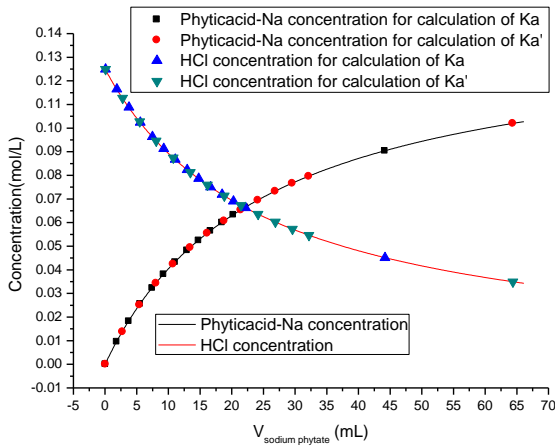
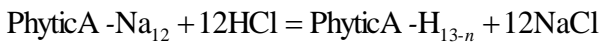


Fig. 3. Concentrations of sodium phytate and HCl

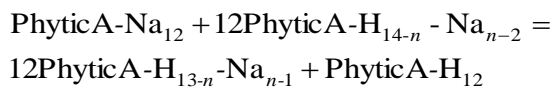
In the titration process, it was assumed that every step of the acid-base titration proceeded completely, the chemical reaction equations being as follows:

When the molar ratio of sodium phytate and HCl was kept at 1:12, the following reaction took place:



Where n is equal to 1.

While the molar ratio of sodium phytate and HCl was kept at 2 : 12, 3 : 12, , 12 : 12, the following reactions occurred:



where n is equal to 2, 3, , 11 or 12.

According to the change in pH values during the titration process, the hydrogen ion concentration

satisfied the following formula:

$$[\text{H}^+]_n = \sqrt{\frac{\prod_{i=n}^{12} K_{ai} \cdot [\text{PhyticA} - \text{H}_{13-n} - \text{Na}_{n-1}]}{[\text{PhyticA} - \text{Na}_{12}]}}$$

From the material balance of the titration process of sodium phytate it follows that:

$$c_{\text{PhyticANa}_{12}} = [\text{PhyticA} - \text{Na}_{12}] + [\text{PhyticA} - \text{H}_{13-n} - \text{Na}_{n-1}]$$

Based on the material balance of the titration process of HCl it follows that:

$$[\text{PhyticA} - \text{H}_{13-n} - \text{Na}_{n-1}] = \frac{c_{\text{HCl}}}{13-n}$$

$$[\text{PhyticA} - \text{Na}_{12}] = c_{\text{PhyticANa}_{12}} - \frac{c_{\text{HCl}}}{13-n}$$

Reactions (1) ~ (12) merged, that is:

from (1)+(2)+(3)+.....+(11)+(12), was derived:



When the reactions were completed, and sodium phytate was added dropwise, no chemical reaction occurred, PhyticA - Na₁₂ and

PhyticA - H - Na₁₁ existed only in the buffer

solution, and the hydrogen ion concentration at this time could be expressed by the following relationship:

$$[\text{H}^+]_{13} = \frac{K_{a12}[\text{PhyticA} - \text{H} - \text{Na}_{11}]}{[\text{PhyticA} - \text{Na}_{12}]}$$

$$c_{\text{PhyticANa}_{12}} = [\text{PhyticA} - \text{Na}_{12}] + [\text{PhyticA} - \text{H} - \text{Na}_{11}]$$

$$[\text{PhyticA} - \text{H} - \text{Na}_{11}] = c_{\text{HCl}}$$

$$[\text{PhyticA} - \text{Na}_{12}] = c_{\text{PhyticANa}_{12}} - c_{\text{HCl}}$$

According to the amount of sodium phytate consumed in the titration process, the concentrations of PhyticA-Na, HCl, [PhyticA-H_{13-n}-Na_{n-1}], [PhyticA-Na₁₂], [H⁺] in the reaction (1), (2), (3), (11), (12) are listed in Table 1. No chemical reactions occurred again after the reaction (12) was completed. PhyticA - Na₁₂

and PhyticA - H - Na₁₁ consisted of buffer solution, but the proportion of the two compositions changed in the buffer solution system with the addition of PhyticA - Na₁₂. Therefore, the concentrations of PhyticA-Na, HCl, PhyticA-H_{13-n}-Na_{n-1}, [PhyticA-Na₁₂], [H⁺] varied correspondingly, the results are shown in Table 1. On the basis of the above formula and the data in Table 1, 12-grade dissociation constants K_a , cumulative dissociation constants β and ionization degrees α of phytic acid were calculated, according to which Figure 4, Figure 5 and Figure 6 were obtained.

*Reasonable analysis of phytic acid K_a , β
 α*

Analysis of K_a

In Figure 4, it is seen that $pK_{a1} \sim pK_{a4}$ were gradually decreasing, and $pK_{a5} \sim pK_{a10}$ increasing according to the stoichiometric concentration. The results were not related to the excessive quantities of sodium phytate in the titration process. When the quantities of sodium phytate in the solution were

excessive, pK_{a12}' and pK_{a11}' , adjacent to pK_{a10}' and pK_{a9}' that were computed according to the concentrations of all species had relatively large errors (Figure 4). In other words, there was no clear downward trend from pK_{a12}' to pK_{a9}' , contrarily, pK_{a12}' was too high, and pK_{a11}' too low. This set of data was unreasonable and was given up. Furthermore, pK_a (corrected) calculated by the corrected concentrations showed a distinct downward trend from pK_{a12} to pK_{a3} , but a sharply upward trend from pK_{a3} (corrected) to pK_{a1} (corrected). So pK_{a3} (corrected) had a minimum value. Compared with pK_a calculated by uncorrected concentrations, pK_{a3} (calibration) was so low that could reach around -24. It was largely different from both pK_{a2} (corrected) = -9 and pK_{a4} (corrected) = -6, so that they could be excluded. Consequently, pK_a in the experiment was more reasonable to have the same variational tendency as pK_a in ref. [12]. Decreasing tendency was displayed from pK_{a1} to pK_{a4} , and increasing from pK_{a5} to pK_{a12} . The changing scale of pK_a was smaller. This set of pK_a values was more reasonable than that reported in the literature. As the difference from pK_{a10} to pK_{a12} reported in the literature was greater than 0, it was concluded that except the last three

Table 1 Concentrations of each component from the 1st grade to the 12th grade of the titration reactions

n	$c(\text{mol}\cdot\text{L}^{-1})$ PhyticA - Na ₁₂	$c(\text{mol}\cdot\text{L}^{-1})$ HCl	[PhyticA- H _{13-n} -Na _{n-1}]	[PhyticA- Na ₁₂]	[H ⁺]
—	0.000000	0.125000	0.000000	0.000000	1.81972E-01
1	0.010001	0.116171	0.009681	0.000321	1.58489E-01
2	0.018255	0.108885	0.009899	0.008356	1.09648E-01
3	0.025534	0.102459	0.010246	0.015289	5.62340E-02
4	0.032341	0.096451	0.010717	0.021624	1.20230E-02
5	0.038091	0.091374	0.011422	0.026669	3.47000E-04
6	0.043267	0.086806	0.012401	0.030866	4.07000E-06
7	0.048196	0.082454	0.013742	0.034454	3.80000E-07
8	0.052431	0.078715	0.015743	0.036688	3.89000E-08
9	0.056504	0.075120	0.018780	0.037724	8.32000E-09
10	0.060033	0.072005	0.024002	0.036032	3.02000E-09
11	0.063281	0.069137	0.034569	0.028713	1.55000E-09
12	0.066441	0.066348	0.066348	0.000093	1.00000E-09
12 ^a	0.090370	0.045224	0.045224	0.045146	3.09000E-10

^a With PhyticA-Na₁₂ concentration increasing, no chemical reactions occur.

hydrogens in phytic acid which dissociated weakly, the other hydrogens dissociated strongly. This assumption was not proper, too. In our research, pK_{a1} , and pK_{a6} to pK_{a12} were greater than 0. The weak acid dissociation was self-evident including the 1st grade and the 6th grade to the 12th grade.

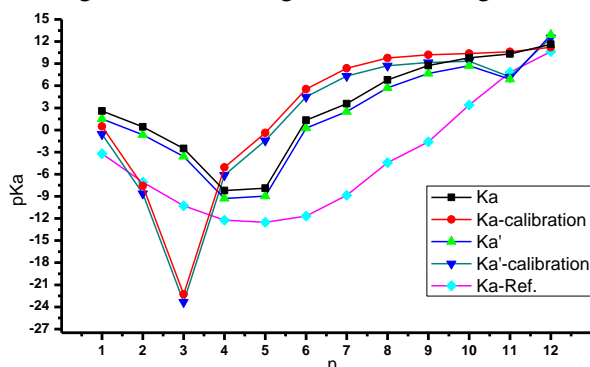


Fig. 4. 1st to 12th dissociation constants ($pK_{a1} \sim 12$) values of phytic acid

Analysis of β

The cumulative dissociation constants β were calculated from the corresponding dissociation constants of pK_a above. The results in Figure 5 show that the values of $p\beta_1$ to $p\beta_9$ in the literature were low, which pointed to strong acid dissociation. The values of $p\beta_{10}$ to $p\beta_{12}$ were greater than those of $p\beta_1$ to $p\beta_9$. The values of $p\beta_1$ to $p\beta_{12}$ were lower than -3, which assumed strong acid dissociation in every grade which contradicts with the phytic acid being a medium strong acid. From the results, it could be seen that the calculated cumulative dissociation constants β are certainly rational by comparison with the calculated results in the literature.

Analysis of α

The ionization degrees α in every grade were calculated from the corresponding dissociation constants of pK_a above. As shown in Figure 6, the values of α_1 to α_9 in the literature [12] were great enough to illustrate the full ionization of phytic acid from the 1st grade to the 9th grade. However, the values of α_{10} were dramatically lower. As strong

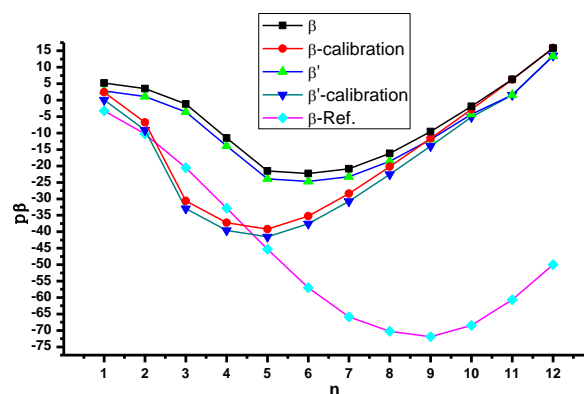


Fig. 5. 1st to 12th cumulative dissociation constants ($\beta_1 \sim 12$ values) of phytic acid

acidity was shown from the former 9 ionizations, and weak from the latter 3 ionizations, the data were not reasonable. The values of α_2 (corrected) to α_5 (corrected) calculated by corrected concentrations showed that phytic acid was almost completely ionized from the 2nd grade to the 5th grade. This statement is opposite to that of ionization from the 6th grade to the 12th grade, and the ionization degrees were close to 0. The unreasonable outcome illustrated that phytic acid molecule was composed of 5 strongly acidic hydrogens and 7 weak hydrogens. There had been a set of reasonable data calculated by uncorrected concentrations, according to which the value of α_1 was quite low, the values of α_2 to α_5 were close to 1, α_6 to α_7 lay between 0 and 1, and $\alpha_8 \sim \alpha_{12}$ were nearly equal to 0. It was concluded that the 1st hydrogen in the phytic acid molecule exhibited weak acidity, the 2nd to 5th hydrogens showed strong acidity, the 6th and 7th hydrogens - medium strong acidity, and the 8th to 12th hydrogens - weak acidity. The data indicated that the ionization degree values of phytic acid increased to 1 and then decreased to nearly 0 gradually, showing a certain regularity.

Analysis of phytic acid structures

The chemical structure of phytic acid is complex, and is different in aqueous solution from that in solid [13, 14]. This is seen in Figures 1 and 7 in the light of the earlier investigation of Johnson *et al.* [15]. Due to the presence of hydrogen bonds in aqueous solution, phosphorus oxygen double bonds (P=O) in the phytic acid molecule could bind water

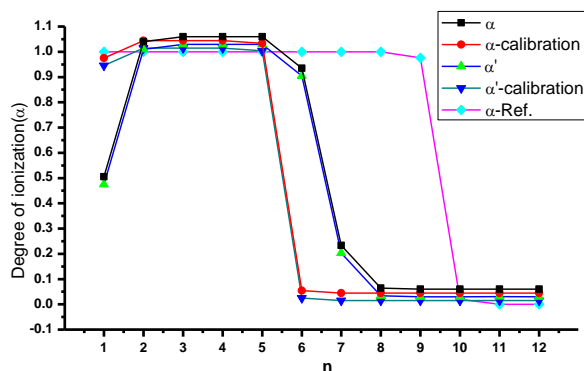


Fig. 6. 1st to 12th ionization degrees ($\alpha_1 \sim \alpha_{12}$ values) of phytic acid

molecules to form trihydrate phytic acid (Figure 7A). In this process, trigonal bipyramidal structure of phosphorus atoms is formed with the transformation from sp^3 hybridization to sp^3d [16], in which 3 hydroxy groups are attached to a phosphorus atom. In aqueous solution, the structure is so unstable that it is easy to dehydrate to form a stable sp^3 hybrid structure [12]. De-trihydrate inositol phosphate (Figure 7B) was obtained by dehydration of three water molecules. It was more appropriate that the structure was called phytic anhydride. Commonly, hydrogen bonds could form easily in strong polybasic acid. On the basis of analyzing the molecular structure, an assumption was proposed: as a hexa-basic acid, phytic anhydride could form intramolecular hydrogen bonds (Figure 7C). Two six-membered rings which were composed of two phosphorus atoms and one oxygen bridge atom were in chair conformation. This conformation similar to the structure of adamantane was chemically relatively stable (hydrogen ion could not easily dissociate).

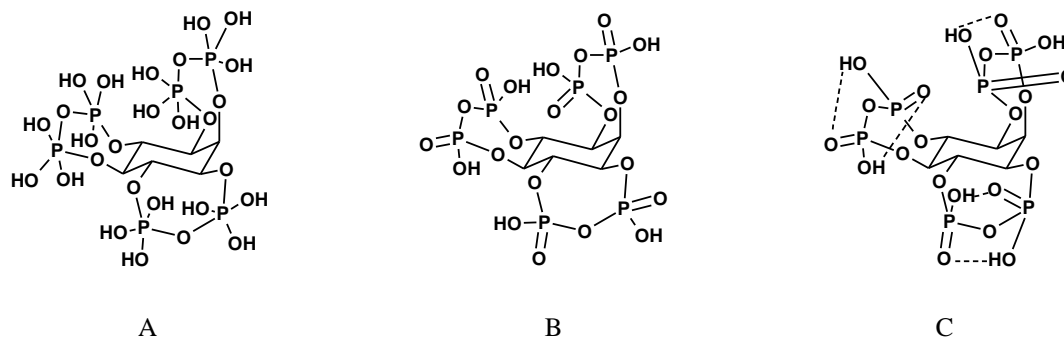


Fig. 7. Structures of phytic acid. A: Trihydrate phytic acid; B: Phytic acid anhydride; C: Phytic acid anhydride with intra-molecular hydrogen bonds

Therefore, the first-grade ionization degree α_1 of phytic acid is relatively smaller, with a value about 0.5. When one hydrogen ion from phytic acid anhydride is ionized, the presence of hydrogen ions would promote the destruction of the intramolecular hydrogen bonds, resulting in a relatively larger ionization degree between the second-grade to the sixth-grade $\alpha_2 \sim \alpha_6$ near to 1.0, and displaying strong acid ionization. At present, the six hydrogen in phytic acid anhydride ionized completely, and the framework structure of hexavalent phytic acid anhydride anion was formed (Figure 7B). In the process of further ionization of phytic acid anhydride, each molecule needs to combine three water molecules to form phytic acid (Figure 1), while phytic acid would further combine water molecules to generate trihydrate phytic acid (Figure 7A). Phytic acid and trihydrate phytic acid, which are weak acids, coexist in the equilibrium solution system. So, phytic acid of the 7th-grade to the 12th-grade ionization degrees $\alpha_7 \sim \alpha_{12}$ which were all below 0.2 was relatively smaller. Therefore, it was concluded that the ionization degrees in our works were more reasonable than those of the other 4 groups (including α) according to the assumed molecular structure and reported in the literature.

CONCLUSION

Potentiometric titration was used for titrating sodium phytate with hydrochloric acid using a combined pH electrode. Four groups of 12-grade dissociation constants, cumulative dissociation constants and ionization degrees of phytic acid

were calculated according to the changes of the pH value and the related substance concentrations in the titration process. A group of 12-grade relatively reasonable dissociation constants K_a , cumulative dissociation constants β and ionization degrees α of phytic acid was obtained compared with the corresponding literature values. The results shown in Table 2 are consistent with phytic acid structure. The data are relatively objective and reasonable and provide a theoretical basis for in-depth research on natural phytic acid.

Table 2 Dissociation constants, cumulative dissociation constants and ionization degrees at all levels of phytic acid

n	K_{an}	β_n	α_n
1	3.57735E-01	3.57735E-01	0.445415
2	4.92753E+01	1.76275E+01	0.980490
3	4.45596E+04	7.85476E+05	0.999978
4	2.17067E+10	1.70501E+16	1.000000
5	1.05257E+10	1.79464E+26	1.000000
6	6.12137E+00	1.09857E+27	0.874942
7	3.64539E-02	4.00470E+25	0.173570
8	2.16032E-05	8.65143E+20	0.004637
9	2.32527E-07	2.01169E+14	0.000482
10	2.07516E-08	4.17458E+06	0.000144
11	6.45879E-09	2.69628E-02	0.000080
12	3.08492E-10	8.31779E-12	0.000018

Acknowledgment: This research was financially supported by Anhui Province College Excellent Young Talents Foundation (No. 2013SQRL051ZD), Higher Education in Anhui Province Provincial Revitalization Plan (No. 2014zytz014), Anhui Research Project (No. KJ2011Z247), Anhui Engineering Technology Research Center of Biochemical Pharmaceutical Foundation (Nos. BYEC1202, BYEC1301) and Anhui Natural Science Foundation (No. 1308085QB24).

REFERENCES

1. A. M. Shamsuddin. *Int. J. Food Sci. & Tec.*, **37**, 769 (2002).
2. C. I. Febles, A. Arias, A. Hardisson, C. Rodriguez-Alvarez, A. Sierra, *J. Cereal Sci.*, **36**, 19 (2002).
3. H. Y. Zhang, Q. Y. Yang, H. T. Lin, X. F. Ren, L. N. Zhao, J. S. Hou, *LWT - Food Sci. Technol.*, **52**, 110 (2013).
4. G. E. Blank, J. Pletcher, M. Sax, *Biochem. Bioph. Res. Co.*, **44**, 319 (1971).
5. G. Frida, C. Munir, *J. Am. Oil Chem. Soc.*, **60**, 1761 (1983).
6. J. W. Erdman, *J. Am. Oil Chem. Soc.*, **56**, 736 (1979).
7. B. Liu, J. B. He, Y. J. Chen, Y. Wang, N. Deng, *Int. J. Hydrogen Energy*, **38**, 3130 (2013).
8. H. Wang, Y. M. Zhou, J. M. Ma, Y. Y. Zhou, H. Jiang, *Food Chem.*, **141**, 18 (2013).
9. H. W. Shi, E. H. Han, F. C. Liu, S. Kallip, *Appl. Surf. Sci.*, **280**, 325 (2013).
10. J. Chen, Y. W. Song, D. Y. Shan, E. H. Han, *Corros. Sci.*, **74**, 130 (2013).
11. A. Uzma, U. R. Haneef, A. U. Q. Shah, T. M. Zahida, *Carbohydr. Polym.*, **95**, 167 (2013).
12. W. J. Evans, E. J. Mccourtney, R. I. Shrager, *J. Am. Oil Chem. Soc.*, **59**, 189 (1982).
13. L. F. Johnson, M. E. Tate. *Can. J. Chem.*, **47**, 63 (1969).
14. K. M. Sureshan, T. Miyasou, S. Miyamori, Y. Watanabe, *Tetrahedron: Asymmetr.*, **15**, 3357 (2004).
15. Z. Szakács, M. Kraszni, B. Noszál, *Anal. Bioanal. Chem.*, **378**, 1428 (2004).
16. X. Z. Cao, T. Y. Song, X. Q. Wang, *Inorganic Chemistry*, Vol. 2, Eds.: 3, Higher Education Press, Beijing, p. 671(1994). (in Chinese).

ОПРЕДЕЛЯНЕ НА СЛОЖНА, ДВАНАДЕСЕТОСТЕПЕННА ДИСОЦИАЦИОННА КОНСТАНТА НА ФИТИНОВА КИСЕЛИНА

Х. Жанг, Х. Ксюе *, Дж. Янг, Л. Лианг

Департамент по химия, Медицински колеж Бенгбу, Бенгбу, Китай

Постъпила на 17 септември, 2013 г.; коригирана 30 ноември, 2013 г.

(Резюме)

Използван е потенциометричен метод за титруване на солна киселина с натриев фитат с комбиниран рН-електрод. Изчислени са четири групи от 12-степенни дисоциационни константи, кумулативни дисоциационни константи и йонизационни степени на фитиновата киселина според измененията на рН и съответните концентрации на титрувания субстрат. Подбрана е група от 12-степенни дисоциационни константи K_a , кумулативни дисоциационни константи β и степени на йонизация α за фитиновата киселина със стойности на K_a между 10^{-10} и 10^{10} , стойности на β в интервала от 10^{-12} до 10^{27} и стойности на α от 10^{-5} до 1. Данните са относително обективни, разумни и предлагат теоретична основа за по-задълбочени изследвания.

On the exact solution for peristaltic flow of couple-stress fluid with wall properties

S. Hina¹, M. Mustafa², T. Hayat^{3,4}

¹ Department of Mathematical Sciences, Fatima Jinnah Women University, Rawalpindi, Pakistan

² School of Natural Sciences (SNS), National University of Sciences and Technology (NUST), Islamabad, Pakistan

³ Department of Mathematics, Quaid-I-Azam University, Islamabad, Pakistan

⁴ Department of Mathematics, Faculty of Science, King Abdulaziz University, Jeddah, Saudi Arabia

Received November 19, 2013; Revised February 24, 2014

This communication reports the peristaltic motion of an electrically conducting couple-stress fluid in a channel with compliant walls. Mathematical model subjected to long wavelength and low Reynolds number approximations is presented. A closed form exact solution for the dimensionless stream function is derived. Behaviors of different physical parameters including Hartman number (M), couple-stress fluid parameter (γ), elastic parameters (E_1 , E_2 , E_3 , E_4 , E_5) and amplitude ratio (ε) are thoroughly examined through the graphical results for velocity and stream function. The study reveals that fluid velocity significantly increases with an increase in the couple-stress fluid parameter and decreases with an increase in the magnetic field strength.

Keywords: Couple-stress fluid, compliant wall, peristalsis, magnetic field, analytic solution.

INTRODUCTION

Peristaltic motion is the form of fluid transport that occurs due to the waves travelling along the walls of a channel/tube. This mechanism appears in many industrial and physiological processes including rollers and finger pumps to pump sanitary and corrosive fluids. The peristaltic activity is quite prevalent in the gastrointestinal tract for food bolus transportation. It also occurs in the urinary tract to transport urine from kidney to bladder, in small blood vessels to transport blood, spermatozoa transport in the *ductus efferentes*, etc. Haroun [1] studied the peristaltic flow of third grade fluid in an asymmetric channel. Peristaltic flow of fourth grade fluid in an inclined channel is also discussed by Haroun [2]. Kothandapani and Srinivas [3] presented the peristaltic flow of Newtonian fluid in an inclined asymmetric channel. Here, the fluid saturates the porous medium. Kothandapani and Srinivas [4] discussed the effect of magnetic field on the peristaltic flow of Jeffrey fluid in an asymmetric channel. Ebaid [5] studied the effects of magnetic field and wall slip conditions on the peristaltic transport of Newtonian fluid in an asymmetric channel. Muthuraj and Srinivas [6] presented the mixed convective heat and mass transfer effects on the

peristaltic flow in a vertical wavy channel with porous medium. Srinivas *et al.* [7] extended the work of Muthuraj and Srinivas [6] for an asymmetric channel. Srinivas and Muthuraj [8] discussed the effects of chemical reaction and space porosity on MHD mixed convective peristaltic flow in a vertical asymmetric channel. Heat transfer in the pulsatile flow through a vertical annulus was discussed by Elmaboud and Mekheimer [9]. Peristaltic flow of an electrically conducting micropolar fluid was described by Mekheimer [10].

It is now recognized that fluids involved in various industrial and physiological processes are non-Newtonian. In view of flow diversity in nature, all non-Newtonian fluids cannot be described by a single constitutive relationship between stress and shear rate. Due to this reason several constitutive equations describing the motions of such fluids have been proposed by the researchers. The associated equations are mathematically more complex and higher-ordered than the governing equations for a Navier-Stokes fluid. Couple-stress fluid is one of the non-Newtonian fluids that describe rheologically complex fluids such as liquid crystals, polymeric suspensions, infected urine, animal and human blood and many lubricants. Recently, many researchers discussed the peristaltic flow of couple-stress fluid. Mekheimer [11] analyzed the effect of induced magnetic field on the peristaltic flow of couple-stress fluid. Mekheimer and Elmaboud [12] studied the

* To whom all correspondence should be sent:
E-mail: address: quaidan85@yahoo.com

peristaltic flow of couple-stress fluid in an annulus. Nadeem and Akram [13] extended the work of Mekheimer [11] for an asymmetric channel. Rao and Rao [14] discussed the influence of heat transfer on the peristaltic transport of couple-stress fluid through a porous medium. Eldabe *et al.* [15] studied the (1)MHD peristaltic flow of couple-stress fluid with heat and mass transfer through a porous medium. Heat transfer analysis in the peristaltic flow of couple-stress fluid through asymmetric channel is performed by Elmaboud *et al.* [16].

In all above mentioned studies, the effect of wall properties is not taken into account. The consideration of wall properties of the channel in peristaltic motion is realistic. Due to this reason the peristaltic flow in a channel with wall properties has great importance in the natural processes that exist in industry and physiology. Muthu *et al.* [17] discussed the effect of wall properties on the peristaltic motion of micropolar fluid. Radhakrishnamacharya and Srinivasulu [18] studied the influence of wall properties on the peristaltic motion with heat transfer. Kumari and Radhakrishnamacharya [19] analyzed the effect of slip boundary condition on the peristaltic transport in an inclined channel with wall properties. Kothandapani and Srinivas [20] discussed the influence of wall properties on the MHD peristaltic flow with heat transfer and porous medium. Srinivas and Kothandapani [21] presented the heat and mass transfer on MHD peristaltic flow through a porous space with compliant walls. Hayat *et al.* [22] extended the work of Srinivas and Kothandapani [18] for the flow of second grade fluid. Hayat *et al.* [23] discussed the peristaltic flow of Maxwell fluid in an asymmetric channel with wall properties. Mustafa *et al.* [24] analyzed the effect of wall properties on the peristaltic transport of nanofluid. Mustafa *et al.* [25] extended their work [24] by considering the slip boundary conditions. Hina *et al.* [26] studied the peristaltic flow of pseudoplastic fluid in a curved channel with wall properties.

The objective here is to examine the magnetohydrodynamic (MHD) peristaltic flow of couple-stress fluid with wall properties. To our knowledge, no such attempt is made yet. Problem formulation is presented. Closed form exact solutions for velocity and stream function are constructed. Effects of couple-stress parameter, Hartman number and compliant wall parameters are also discussed in detail.

FORMULATION OF THE PROBLEM

Consider the peristaltic flow of couple-stress fluid in a compliant walls channel. The channel width is taken as $2d_1$. The x - and y - axes are along and perpendicular to the channel walls, respectively. An incompressible and electrically conducting fluid is considered. A uniform magnetic field of strength B_0 is applied in the y - direction. The flow is induced due to the sinusoidal waves on the compliant walls of the channel and the wave shapes are described as follows:

$$y = \pm \eta(x, t) = \pm \left[d_1 + a \sin \frac{2\pi}{\lambda}(x - ct) \right]. \quad (1)$$

In the above equation c is the wave speed, a the wave amplitude and λ the wavelength. The governing equations for the problem under consideration are

$$\frac{\partial u}{\partial x} + \frac{\partial v}{\partial y} = 0, \quad (2)$$

$$\rho \left[\frac{\partial}{\partial t} + u \frac{\partial}{\partial x} + v \frac{\partial}{\partial y} \right] u = - \frac{\partial p}{\partial x} + \mu \nabla^2 u - \eta \nabla^4 u - \sigma B_0^2 u, \quad (3)$$

$$\rho \left[\frac{\partial}{\partial t} + u \frac{\partial}{\partial x} + v \frac{\partial}{\partial y} \right] v = - \frac{\partial p}{\partial y} + \mu \nabla^2 v - \eta \nabla^4 v, \quad (4)$$

and the boundary conditions are

$$u = 0, \quad \frac{\partial^2 u}{\partial y^2} = 0 \text{ at } y = \pm \eta, \quad (5)$$

$$\left[-\tau \frac{\partial^3}{\partial x^3} + m \frac{\partial^3}{\partial x \partial t^2} + d \frac{\partial^2}{\partial t \partial x} + B \frac{\partial^5}{\partial x^5} + H \frac{\partial}{\partial x} \right] \eta = \mu \nabla^2 u - \eta_1 \nabla^4 u - \sigma B_0^2 u - \rho \left(\frac{\partial}{\partial t} + u \frac{\partial}{\partial x} + v \frac{\partial}{\partial y} \right) u \text{ at } y = \pm \eta. \quad (6)$$

In the above equations u and v denote the velocities in the x - and y - directions, respectively, $\nabla^2 = \partial^2 / \partial x^2 + \partial^2 / \partial y^2$, p denotes the pressure, σ is the electrical conductivity of the fluid, τ the elastic tension in the membrane, m the mass per unit area, d the coefficient of viscous damping, B the flexural rigidity of the plate, H the spring stiffness, η_1 the couple-stress fluid parameter, μ the dynamic viscosity and ρ the density.

We define the following dimensionless variables

$$\begin{aligned} u^* &= \frac{u}{c}, \quad v^* = \frac{v}{c}, \quad x^* = \frac{x}{\lambda}, \quad y^* = \frac{y}{d_1}, \quad t^* = \frac{ct}{\lambda}, \\ \gamma &= d_1 \sqrt{\frac{\mu}{\eta_1}}, \quad p^* = \frac{d_1^2 p}{c\lambda\mu}, \quad \eta^* = \frac{\eta}{d_1}. \end{aligned} \quad (7)$$

The problem statement in the dimensionless variables is given by

$$\text{Re} \left[\delta \frac{\partial}{\partial t} + u\delta \frac{\partial}{\partial x} + v \frac{\partial}{\partial y} \right] u = -\frac{\partial p}{\partial x} + \nabla^2 u - \frac{1}{\gamma^2} \nabla^4 u - M^2 u, \quad -\gamma^2 \left[E_1 \frac{\partial^3}{\partial x^3} + E_2 \frac{\partial^3}{\partial x \partial t^2} + E_3 \frac{\partial^2}{\partial t \partial x} + E_4 \frac{\partial^5}{\partial x^5} + E_5 \frac{\partial}{\partial x} \right] \eta, \quad (8)$$

$$\text{Re} \delta \left[\delta \frac{\partial}{\partial t} + u\delta \frac{\partial}{\partial x} + v \frac{\partial}{\partial y} \right] v = -\frac{\partial p}{\partial y} + \nabla^2 v - \frac{1}{\gamma^2} \nabla^4 v, \quad (9)$$

$$u = 0, \quad \frac{\partial^2 u}{\partial y^2} = 0 \quad \text{at } y = \pm \eta = \pm(1 + \varepsilon \sin 2\pi(x - ct)), \quad (10)$$

$$\begin{aligned} &\left[E_1 \frac{\partial^3}{\partial x^3} + E_2 \frac{\partial^3}{\partial x \partial t^2} + E_3 \frac{\partial^2}{\partial t \partial x} + E_4 \frac{\partial^5}{\partial x^5} + E_5 \frac{\partial}{\partial x} \right] \eta \\ &= \nabla^2 u - \frac{1}{\gamma^2} \nabla^4 u - M^2 u \\ &- \text{Re} \left(\delta \frac{\partial}{\partial t} + u\delta \frac{\partial}{\partial x} + v \frac{\partial}{\partial y} \right) u \quad \text{at } y = \pm \eta. \end{aligned} \quad (11)$$

In the above equations $\nabla^2 = \delta^2 \partial^2 / \partial x^2 + \partial^2 / \partial y^2$, ε ($= a / d_1$) is the amplitude ratio, δ ($= d_1 / \lambda$) the wave number, Re ($= cd_1 / \nu$) the Reynolds number, M ($= B_0 d_1 \sqrt{\sigma / \mu}$) the Hartman number, γ the couple-stress fluid parameter and E_1 ($= -\alpha d_1^3 / \lambda^3 \mu c$), E_2 ($= mcd_1^3 / \lambda^3 \mu$), E_3 ($= dd_1^3 / \lambda^2 \mu$), E_5 ($= Hd_1^3 / \lambda c \mu$) are the non-dimensional elasticity parameters.

Denoting the stream function $\psi(x, y, t)$ by

$$u = \frac{\partial \psi}{\partial y}, \quad v = -\delta \frac{\partial \psi}{\partial x}, \quad (12)$$

we can see that the equation of continuity (2) is automatically satisfied. Introducing stream function in the flow problem and then applying long wavelength and low Reynolds number approximations, we obtain

$$\frac{\partial^3 \psi}{\partial y^3} - \frac{1}{\gamma^2} \frac{\partial^5 \psi}{\partial y^5} - M^2 \frac{\partial \psi}{\partial y} = \frac{\partial p}{\partial x}, \quad (13)$$

$$\frac{\partial p}{\partial y} = 0, \quad (14)$$

with boundary conditions

$$\frac{\partial \psi}{\partial y} = 0, \quad \frac{\partial^3 \psi}{\partial y^3} = 0 \quad \text{at } y = \pm \eta, \quad (15)$$

$$= \frac{\partial^5 \psi}{\partial y^5} - \gamma^2 \frac{\partial^3 \psi}{\partial y^3} + M^2 \gamma^2 \frac{\partial \psi}{\partial y} \quad \text{at } (y = \pm \eta). \quad (16)$$

Equations (13) and (14) yield

$$\frac{\partial^6 \psi}{\partial y^6} - \gamma^2 \frac{\partial^4 \psi}{\partial y^4} + M^2 \gamma^2 \frac{\partial^2 \psi}{\partial y^2} = 0. \quad (17)$$

Solving equation (17) subject to the boundary conditions (15) and (16), we have

$$\psi = C_1 \sinh m_1 y + C_2 \sinh m_2 y + Ly, \quad (18)$$

$$u = m_1 C_1 \cosh m_1 y + m_2 C_2 \cosh m_2 y + L, \quad (19)$$

where

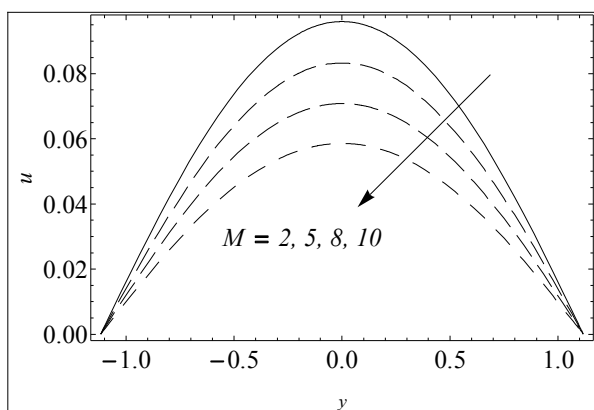
$$m_1 = \sqrt{\frac{\gamma^2 + \sqrt{\gamma^4 - 4M^2\gamma^2}}{2}}, \quad m_2 = \sqrt{\frac{\gamma^2 - \sqrt{\gamma^4 - 4M^2\gamma^2}}{2}},$$

$$C_1 = \frac{m_2^2 L}{m_1(m_1^2 - m_2^2) \cosh m_1 \eta}, \quad C_2 = \frac{-m_1^2 L}{m_2(m_1^2 - m_2^2) \cosh m_2 \eta},$$

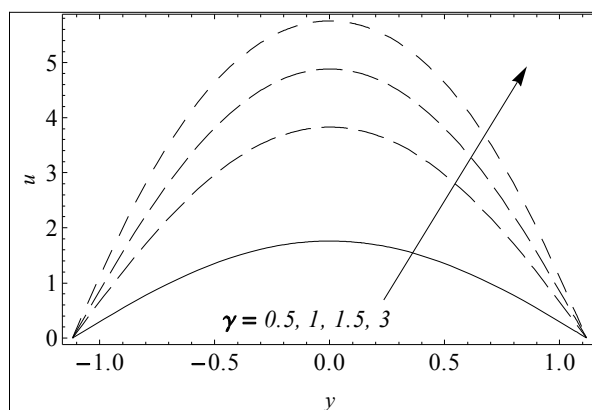
$$L = \frac{8\pi^3 \varepsilon}{M^2} \left\{ \left(E_1 + E_2 - 4\pi^2 E_4 - \frac{E_5}{4\pi^2} \right) \cos 2\pi(x-t) - \frac{E_3}{2\pi} \sin 2\pi(x-t) \right\}.$$

RESULTS AND DISCUSSION

This section discusses the variations of different emerging parameters on the axial velocity u and stream function ψ . The variation of Hartman number (M), amplitude ratio (ε), elastic tension in the membrane (E_1), mass per unit area (E_2), coefficient of viscous damping (E_3), flexural rigidity of the plate (E_4), spring stiffness (E_5) and couple-stress parameter (γ) are examined. Fig. 1 elucidates the behavior of different parameters involved in the axial velocity. Fig. 1a shows that velocity decreases with an increase in Hartman number M .



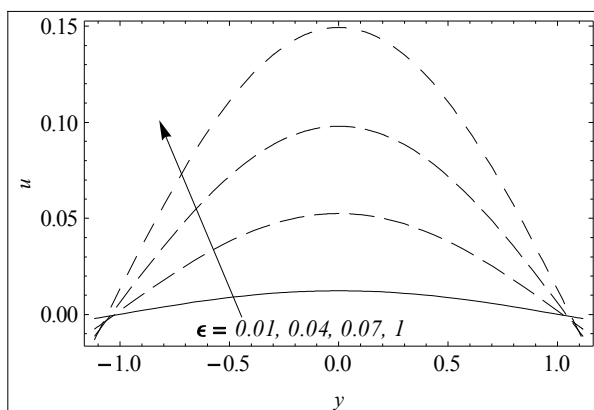
(1a)



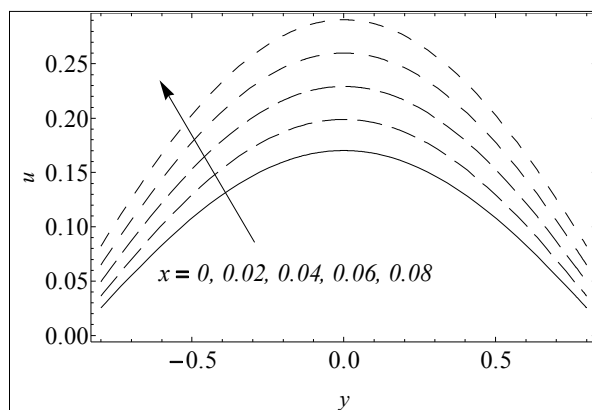
(1b)

Fig. 1(a). Variation of M on u when $E_1=1$; $E_2=0.2$; $E_3=0.5$; $E_4=0.01$; $E_5=0.01$; $\varepsilon=0.2$; $\gamma=0.1$; $x=0.2$; $t=0.1$.

Fig. 1(b). Variation of γ on u when $E_1=1$; $E_2=0.2$; $E_3=0.5$; $E_4=0.01$; $E_5=0.01$; $\varepsilon=0.2$; $M=2$; $x=0.2$; $t=0.1$.



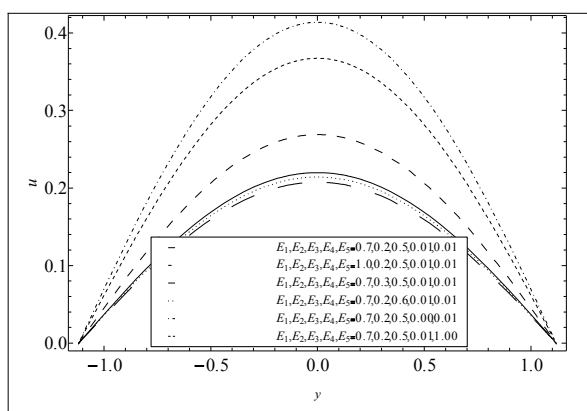
(1c)



(1d)

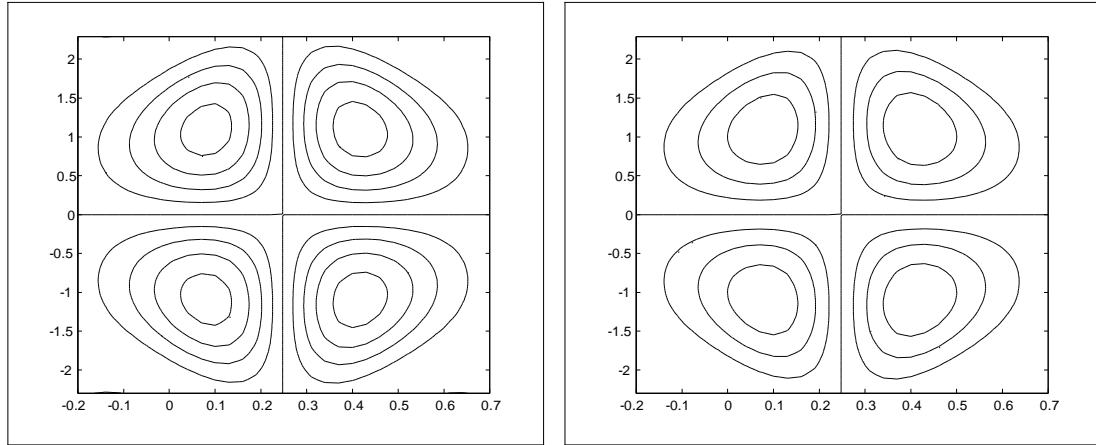
Fig. 1(c). Variation of ε when $E_1=1$; $E_2=0.2$; $E_3=0.5$; $E_4=0.01$; $E_5=0.01$; $\gamma=0.2$; $M=2$; $x=0.2$ $t=0.1$.

Fig. 1(d). Variation of x when $E_1=1$; $E_2=0.2$; $E_3=0.5$; $E_4=0.01$; $E_5=0.01$; $\varepsilon=0.2$; $\gamma=0.2$; $M=2$; $t=0.1$.



(1e)

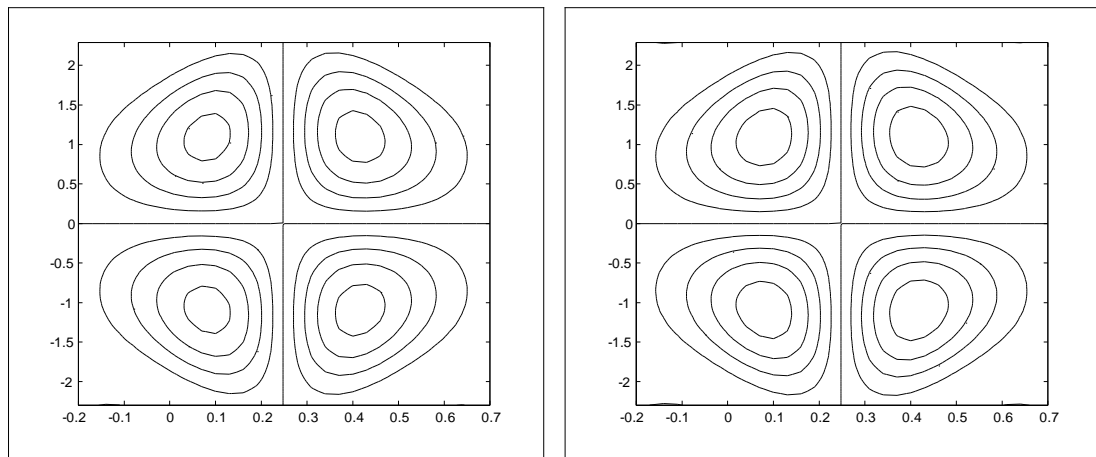
Fig. 1(e). Variation of compliant wall parameters when $\varepsilon=0.2$; $\gamma=0.2$; $M=2$; $x=0.2$; $t=0.1$.



(2a)

(2b)

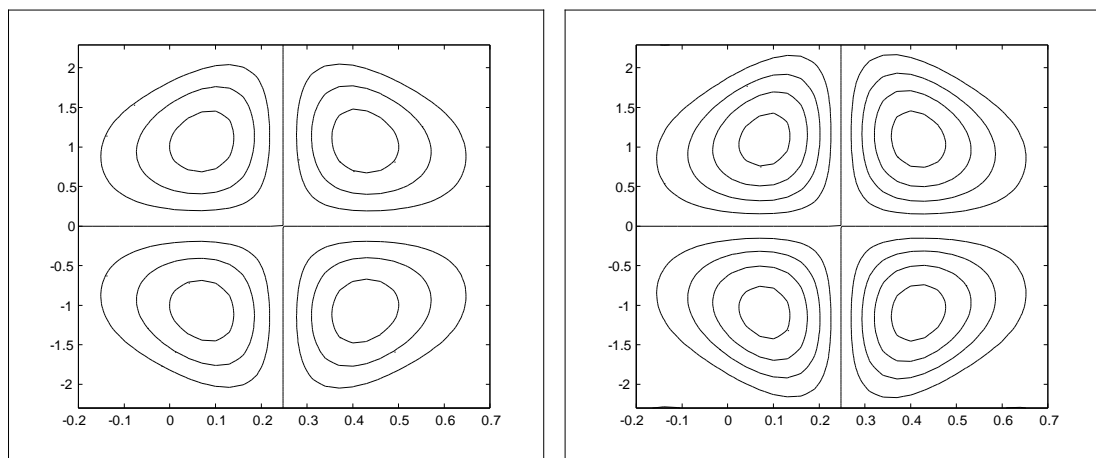
Fig. 2. Streamlines for $E_1 = 1$; $E_2 = 0.5$; $E_3 = 0.1$; $E_4 = 0.01$; $E_5 = 1$; $\varepsilon = 0.18$; $t = 0$; $\gamma = 0.02$;
(a): $M = 2$; (b): $M = 2.2$.



(3a)

(3b)

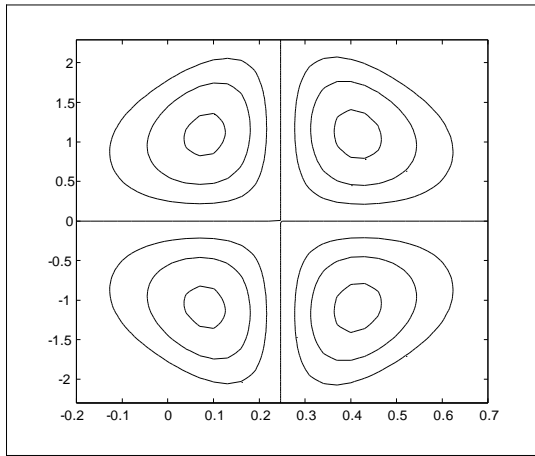
Fig. 3. Streamlines for $E_1 = 1$; $E_2 = 0.5$; $E_3 = 0.1$; $E_4 = 0.01$; $E_5 = 1$; $\varepsilon = 0.18$; $t = 0$; $M = 2$;
(a): $\gamma = 0.01$; (b): $\gamma = 0.03$.



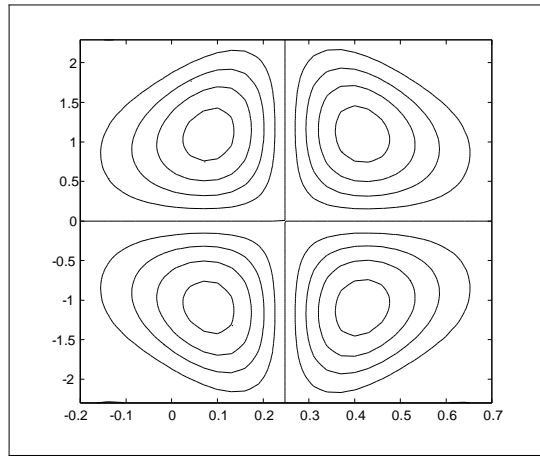
(4a)

(4b)

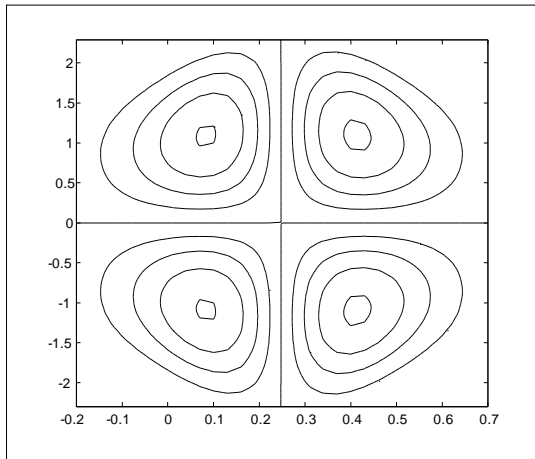
Fig. 4. Streamlines for $E_1 = 1$; $E_2 = 0.5$; $E_3 = 0.1$; $E_4 = 0.01$; $E_5 = 1$; $\gamma = 0.02$; $t = 0$; $M = 2$;
(a): $\varepsilon = 0.15$; (b): $\varepsilon = 0.18$.



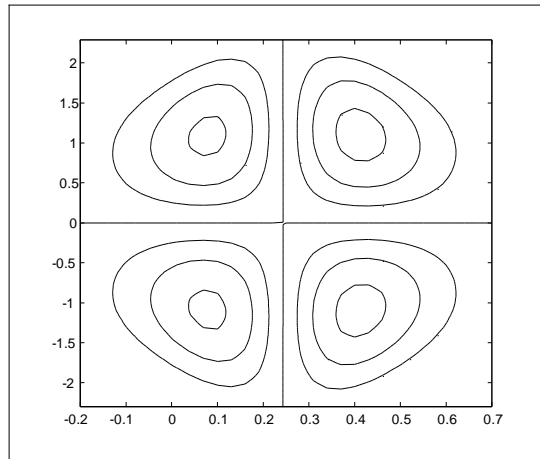
(5a)



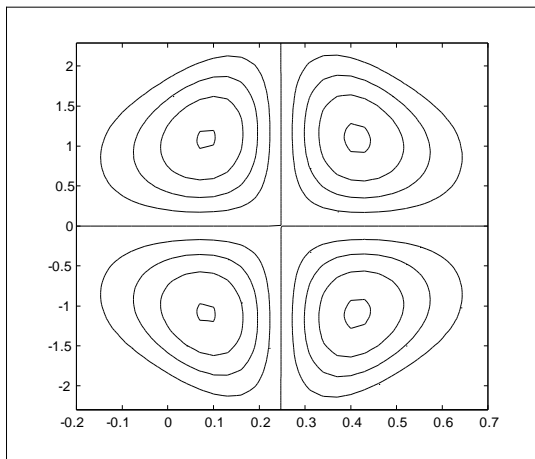
(5b)



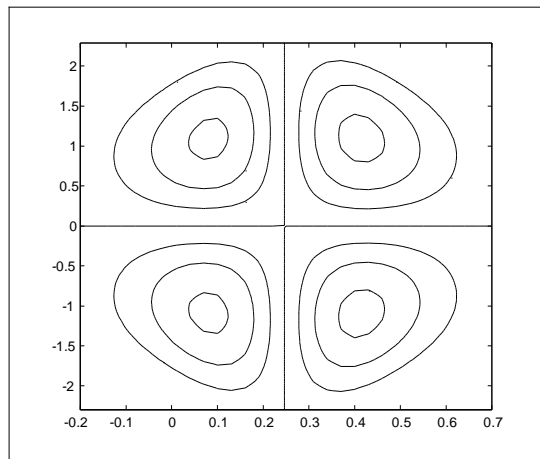
(5c)



(5d)



(5e)



(5f)

Fig. 5. Streamlines for $\varepsilon = 0.18$; $M = 2$; $\gamma = 0.02$; $t = 0$; (a): $E_1 = 0.7$; $E_2 = 0.5$; $E_3 = 0.1$; $E_4 = 0.01$; $E_5 = 1$; (b): $E_1 = 1$; $E_2 = 0.5$; $E_3 = 0.1$; $E_4 = 0.01$; $E_5 = 1$; (c): $E_1 = 0.7$; $E_2 = 0.7$; $E_3 = 0.1$; $E_4 = 0.01$; $E_5 = 1$; (d): $E_1 = 0.7$; $E_2 = 0.5$; $E_3 = 0.2$; $E_4 = 0.01$; $E_5 = 1$; (e): $E_1 = 0.7$; $E_2 = 0.5$; $E_3 = 0.1$; $E_4 = 0.005$; $E_5 = 1$; (f): $E_1 = 0.7$; $E_2 = 0.5$; $E_3 = 0.1$; $E_4 = 0.01$; $E_5 = 1.2$.

Hartman number is the ratio of magnetic force to viscous force. Magnetic force being transverse to the flow direction, causes resistance to the flow and hence slows down the fluid motion. Fig. 1b depicts that velocity increases by increasing the couple-stress fluid parameter. Fig. 1c analyzes the behavior of amplitude ratio ε on axial velocity. It is observed that by increasing the amplitude ratio the axial velocity increases. This is due to the fact that increasing values of the amplitude ratio ε correspond to an increase in the amplitude of the wave across the channel which thereby increases the fluid velocity within the channel. Fig. 1d is sketched to perceive the behavior of velocity distribution at different locations in the channel. It is seen that the axial velocity increases along the positive x - direction. The influences of compliant wall parameters (E_1, E_2, E_3, E_4 and E_5) on the velocity can be captured from Fig.1e. It is observed that the velocity distribution increases with an increase in E_1 and E_2 , whereas it decreases when E_3, E_4 and E_5 are increased. These observations may be inferred to the fact that increase in the elasticity of the channel walls assists the flow whereas damping and stiffness of the wall resists the flow.

Figs. 2-5 illustrate the behaviour of embedded parameters on the stream function

Generally, the shape of streamlines is analogous to the wave travelling along the walls of the channel. Under certain conditions these streamlines split and enclose a bolus which moves along with the wave across the channel. The circulation and size of the trapped bolus are presented in these Figs. Fig. 2 shows the impact of Hartman number or equivalently the magnetic field on the streamlines. It is observed that the size of trapped bolus and the number of circulations decrease with an increase in M . Fig. 3 shows that the size of bolus increases with an increase in couple-stress fluid parameter γ . Fig. 4 analyzes the effect of amplitude ratio ε on the stream function. It is clear that size of the trapped bolus and number of circulations are increased by increasing the amplitude ratio ε . Fig. 5 is plotted to examine the behavior of the wall elasticity parameters. It is observed that the size of trapped bolus increases by increasing E_1, E_2 and it decreases by increasing E_3, E_4 and E_5 .

CONCLUSIONS

In this article, MHD peristaltic motion of couple-stress fluid is discussed in a compliant walls channel. A closed form exact solution of the problem is presented after applying long wavelength and low Reynolds number assumptions. The effects of different parameters on the axial velocity and streamlines are thoroughly discussed. It is observed that the axial velocity and the size of trapped bolus decreases by increasing the Hartman number, wall damping parameters and wall stiffness parameters, whereas axial velocity and size of trapped bolus increases by increasing the couple-stress fluid parameter, amplitude ratio and wall elasticity parameters. The present study finds an important application in describing blood flow in arteries since the rheological properties of blood can be adequately described through the couple-stress fluid model. Moreover, the human arteries and veins possess the properties of elasticity, damping and stiffness which are also taken into consideration in this work.

REFERENCES

1. M.H. Haroun, *Comm. Nonlinear Sci. Numer. Simul.*, **12**, 1464 (2007).
2. M.H. Haroun, *Comput. Material Sci.*, **39**, 324 (2007).
3. M. Kothandapani and S. Srinivas, *Phys. Lett. A*, **372**, 1265 (2008).
4. M. Kothandapani and S. Srinivas, *Int. J. Non-Linear Mech.*, **43**, 915 (2008).
5. A. Ebaid, *Phys. Lett. A*, **372**, 4493 (2008).
6. R. Muthuraj and S. Srinivas, *Comp. Math. Applicat.*, **59**, 3516 (2010).
7. S. Srinivas, R. Gayathri and M. Kothandapani, *Comm. Nonlinear Sci. Numer. Simul.*, **16**, 1845 (2011).
8. S. Srinivas and R. Muthuraj, *Math. Comp. Model.*, **54**, 1213 (2011).
9. Y.A. Elmaboud and Kh. S. Mekheimer, *Z. Naturforsch.*, **67a**, 185 (2012).
10. Kh. S. Mekheimer, *Appl. Math.*, **23** (2008) Article ID 570825 doi:10.1155/2008/570825.
11. Kh.S. Mekheimer, *Phys. Lett. A*, **372**, 4271 (2008).
12. Kh.S. Mekheimer and Y. Abd elmaboud, *Physica A*, **387**, 2403 (2008).
13. S. Nadeem and S. Akram, *Arch. Appl. Mech.*, **81**, 97 (2011).
14. T.R. Rao and D.R.V.P. Rao, *Advances Appl. Sci. Research*, **3**, 2355 (2012).
15. N.T. Eldabe, S.M. Elshaboury, A.A. Hasan and M.A. Elogail, *Design and Engineering*, **3**, 51 (2012).
16. Y.A. elmaboud, Kh. S. Mekheimer and A. I. Abdellateef, *J. Heat Transf. ASME*, **135** (2013) 044502, doi:10.1115/1.4023127.
17. P. Muthu, B.V.R. Kumar and P. Chandra, *ANZIAM J.*, **45**, 245, (2003).
18. G. Radhakrishnamacharya and C. Srinivasulu, *C. R. Mecanique*, **335**, 369 (2007).

19. A.V.R. Kumari and G. Radhakrishnamacharya, *Int. J. Appl. Math. Mech.*, **7**, 1 (2011).
20. M. Kothandapani and Srinivas, *Phys. Lett. A*, **372**, 4586 (2008).
21. S. Srinivas and M. Kothandapani, *Appl. Math. Comput.*, **213**, 197 (2009).
22. T. Hayat, S. Hina and A. A. Hendi, *Heat Transfer-Asian Research*, **40**, 577 (2011).
23. T. Hayat, S. Hina, S. Asghar and S. Obaidat, *Int. J. Physical Sci.*, **7**, 2145 (2012).
24. M. Mustafa, S. Hina, T. Hayat and A. Alsaedi, *Int. J. Heat Mass Transfer*, **55**, 4871 (2012).
25. M. Mustafa, S. Hina, T. Hayat and A. Alseadi, *J. Heat Transfer*, **135**, 041701(1-7) (2013).
1. 26. S. Hina, M. Mustafa, T. Hayat and A. Alseadi, *J. Appl. Mech.*, **80**, 024501(1-7) (2013).

ОТНОСНО ТОЧНОТО РЕШЕНИЕ ЗА ПЕРИСТАЛТИЧНО ТЕЧЕНИЕ НА ФЛУИД СЪС СПРЕГНАТИ НАПРЕЖЕНИЯ И ПРОМЕНЛИВИ СВОЙСТВА НА СТЕНАТА

С. Хина¹, М. Мустафа², Т. Хаят^{3,4}

¹ Департамент по математика, Дамски университет "Фатима Джина", Равалпинди, Пакистан

² Колеж по природни науки, Национален университет по наука и технология, Исламабад, Пакистан

³ Департамент по математика, Университет Куаид-и-Азам, Исламабад, Пакистан

⁴ Департамент по математика, Научен факултет, Университет "Крал Абдулазис", Джеда, Саудитска Арабия

Получена на 19 ноември 2013 г.; коригирана на 24 февруари 2014 г.

(Резюме)

В тази работа се разглежда перисталтичното движение на електропроводящ флуид със спрегнати напрежения (couple-stress fluid) в канал със стени с променлива твърдост. Въведен е математичен модел за ламинарно вълново течение при голяма дължина на вълната. Получено е точно решение за безизмерната токова функция. Подробно са изследвани различни параметри, като числото на Hartman number (M), параметъра на спрегнати напрежения (γ), параметрите на еластичността (E_1 ; E_2 ; E_3 ; E_4 ; E_5) и отношението на амплитудите (ϵ) чрез резултатите за скоростта на течението и токовата функция. Изследването показва, че скоростта на течението се повишава значително с нарастване на параметъра на спрегнатите напрежения и се понижава, когато се приложи магнитно поле.

Cytotoxicity, antimicrobial and antioxidant activity of *Daucus carota* L., *Lycopersicon esculentum* Mill. and *Capsicum annuum* L.

J. Mladenović*¹, A. Radovanović², R. Pavlović¹, B. Radovanović³
J. Zdravković⁴, G. Aćamović-Đoković¹

¹ University of Kragujevac, Faculty of Agronomy, Cara Dušana 34, Čačak, Serbia

² University of Belgrade, Faculty of Chemistry, Karnegijeva 12-16, Belgrade, Serbia

³ University of Niš, Faculty of Natural Sciences and Mathematics, Višegradska 33, Niš, Serbia

⁴ Institute for Vegetable Crops, Karađorđeva 71, 26 000 Smederevska Palanka, Serbia

Received November 27, 2013; Revised February 24, 2014

The objective of this study was to evaluate the cytotoxicity, antimicrobial and antioxidant activities of extracts of *Daucus carota* L., *Lycopersicon esculentum* Mill. and *Capsicum annuum* L. grown in Central Serbia. The content of phenolic compounds in the extracts was determined using spectrophotometric and HPLC analysis. These plant extracts proved to be potent inhibitors of cell growth in the cell lines (FemX and LS 174). The IC₅₀ values against FemX and LS174 cell lines were 33.52 ± 1.08 and 40.22 ± 0.03 $\mu\text{g/mL}$, respectively. The highest antioxidant capacity was found in *C. annuum* L. (98.01 ± 0.72 $\mu\text{g AA/g}$) and *D. carota* L. (48.51 ± 1.18 $\mu\text{g AA/g}$) extracts. The test extracts showed strong to moderate antimicrobial activity (19.53 - 312.50 $\mu\text{g/mL}$). *D. carota* L., *L. esculentum* Mill. and *C. annuum* L. extracts can serve as new dietary and food supplements.

Keywords: *Capsicum annuum* L.; *Daucus carota* L.; *Lycopersicon esculentum* Mill.; Cytotoxicity; Antimicrobial activity; Antioxidant activity.

INTRODUCTION

The medicinal properties of plants have been investigated in the light of recent scientific developments throughout the world, due to their potent pharmacological activities and low toxicity [1,2]. Antimicrobial activity of herbs has been known and described for several centuries [3]. Many naturally occurring compounds found in edible and medicinal plants, herbs, and spices have been shown to possess antimicrobial functions and could serve as a source of antimicrobial agents against bacteria and fungi [4,5,6].

Several studies have pointed out the possibility to use essential oils and/or their components in medical and plant pathology, as well as in food industry for the control of microorganisms pathogenic to consumers and/or responsible for food spoilage [7]. Everyday, our body is exposed to a large number of foreign chemicals [8]. Most of them are man-made and our inability to properly metabolize them negatively affects our health by generation of free radicals. Free radicals are also generated during normal metabolism of aerobic cells [9,10]. The oxygen consumption inherent to cell growth leads to the generation of a series of oxygen free radicals. Highly active free radicals and their

uncontrolled production are responsible for numerous pathological processes such as cell tumor (prostate and colon cancers) and coronary heart diseases.

Antioxidants can significantly delay or prevent the oxidation of easily oxidizable substances [11]. According to their mechanism of action, natural antioxidants are classified as chain-breaking antioxidants which scavenge free radicals or inhibit the initiation step or interrupt the propagation step of lipid oxidation and as preventive antioxidants which slow the rate of oxidation by several actions but do not convert free radicals [12]. However, there have been concerns about synthetic antioxidants such as butylated hydroxyanisole (BHA) and butylated hydroxytoluene (BHT) because of their possible activity as promoters of carcinogenesis [13]. Fruits and vegetables contain antioxidant compounds broadly called polyphenols that are known to reduce oxidative stress and prevent chronic diseases [14,15,16]. The antioxidant properties of these compounds are responsible for their anticancer, antiviral and antimicrobial properties. There is growing interest in natural antioxidants from plant sources [17].

The aim of this study was to evaluate the cytotoxicity, antimicrobial and antioxidant activities of extracts of *Daucus carota* L., *Lycopersicon esculentum* Mill. and *Capsicum annuum* L. grown in Central Serbia.

* To whom all correspondence should be sent:
E-mail: jelenamala@kg.ac.rs

MATERIALS AND METHODS

Chemicals

All standards for HPLC analysis were of analytical grade and were purchased from Sigma Chemical Co. (St Louis, MO, USA) and Alfa Aesar (Karlsruhe, Germany). Acetonitrile and phosphoric acid were of HPLC grade (Tedia Company, USA). Ethanol was of analytical grade (Aldrich Chemical Co., Steinheim, Germany).

Plant Collection

The plants were cultivated under open field conditions during the autumn growing cycle in 2010 in an experimental field at Trbušani (Central Serbia).

Preparation of plant extracts

Plant samples (10.0 g) were extracted by 70% ethanol (100.0 ml) used as a solvent. The extraction process was carried out in an ultrasonic bath (Branson and Smith-Kline Company, B-220) at room temperature for 1 h. After filtration, 5 ml of the liquid extract was used for extraction yield determination. The solvent was removed by a rotary evaporator (Devarot, Elektromedicina, Ljubljana) under vacuum, and was dried to constant mass at 60°C. Dry extracts were stored in glass bottles at 4°C to prevent oxidative damage until analysis.

Determination of total phenolic content

Total phenols were estimated using the Folin-Ciocalteu method [18]. The extract was diluted to a concentration of 1 mg/ml, and aliquots of 0.5 ml were mixed with 2.5 ml of Folin-Ciocalteu reagent (previously diluted 10-fold with distilled water) and 2 ml of NaHCO₃ (7.5 %). The absorbance was measured at 765 nm using a UV/VIS spectrophotometer, after 15 min at 45°C. Total phenols were determined as gallic acid equivalents (mg GAE/g extract), and the values were presented as means of triplicate analyses.

Determination of flavonoid content

Total flavonoids were determined according to [19]. A total of 0.5 ml of 2 % aluminium chloride (AlCl₃) in methanol was mixed with the same volume of the methanol solution of the plant extract. After storage for 1 h at room temperature, the absorbance was measured at 415 nm in a spectrophotometer against a blank sample. Total flavonoids were determined as rutin equivalents (mg RE/g dry extract), and the values are presented as means of triplicate analyses.

HPLC analysis

Quantification of individual phenolic compounds was performed by reversed phase HPLC analysis, using a modified method [20,21]. HPLC analysis was performed on an Agilent 1200 HPLC equipped with a diode array detector (DAD), Chemstation software (Agilent Technologies), a binary pump, an online vacuum degasser, an autosampler and a thermostated column compartment, on an Agilent, Zorbax Eclipse Plus-C18, 1.8 µm, 600 bar, 2.1×50 mm column, at a flow rate of 0.8 mL/min. Gradient elution was performed by varying the proportion of solvent A (methanol) to solvent B (1% formic acid in water (v/v)) as follows: initial 0-2 min, 100% B; 2-4 min, 100-98% B; 4-6 min, 98-95% B; 6-7 min, 95-73% B; 7-10 min, 75-48% B; 10-12 min 48% B; 12-20 min, 48-40% B. The total running time and post-running time were 21 and 5 min, respectively. The column temperature was 30°C. The injection volume of samples and standards was 5 µL and injection was performed automatically using the autosampler. The spectra were acquired in the range 210–400 nm and chromatograms were plotted at 280, 330 and 350 nm with a bandwidth of 4 nm and a reference wavelength/bandwidth of 500/100 nm.

Cytotoxic activity

Cell lines

The human melanoma FemX and human colon carcinoma LS174 cell lines were obtained from the American Type Culture Collection (Manassas, VA, USA). Both cancer cell lines were maintained in the recommended RPMI-1640 medium supplemented with 10% heat-inactivated (56°C) fetal bovine serum, l-glutamine (3 mM), streptomycin (100 mg), penicillin (100 IU), and 25 mM HEPES and adjusted to pH 7.2 by bicarbonate solution. Cells were grown in a humidified atmosphere of 95% air and 5% CO₂ at 37°C.

Treatment of cell lines

Stock solutions (100 mg/mL) of extracts, made in dimethyl sulfoxide (DMSO), were dissolved in the corresponding medium to the required working concentrations. Neoplastic FemX cells (5000 cells per well) and neoplastic LS174 cells (7000 cells per well) were cultured in 96-well microtiter plates, and 24 h later, upon cell adherence, five different, double diluted concentrations of the test compounds were added to the wells. The final concentrations applied to the target cells were 200, 100, 50, 25 and 12.5 µg/mL, except to the control wells, where only nutrient medium was added to the cells. The nutrient medium was RPMI 1640 medium, supplemented with 1-

glutamine (3 mM), streptomycin (100 Ig/mL), and penicillin (100 IU/mL), 10% heat-inactivated (56°C) fetal bovine serum (FBS) and 25 mM Hepes, and was adjusted to pH 7.2 by bicarbonate solution. The cultures were incubated for 72 h.

Determination of cell survival (MTT test)

The effect of the extracts on cancer cell survival was determined by MTT test (microculture tetrazolium test) [22,23] 72 h upon addition of the compounds, as described earlier. Briefly, an aliquot of 20 µl of MTT solution (5 mg/mL PBS) was added to each well. The samples were incubated for further 4 h at 37°C in 5% CO₂ and humidified air atmosphere. Then, 100 µL of 10% SDS were added to extract the insoluble product formazan resulting from the conversion of the MTT dye by viable cells. The number of viable cells in each well was proportional to the intensity of the absorbance of light, which was then read in an ELISA plate reader at 570 nm. Absorbance (A) at 570 nm was measured 24 h later. To obtain cell survival (%), A of a sample with cells grown in the presence of various concentrations of the test extracts was divided with the control optical density (A of control cells grown only in nutrient medium), and multiplied by 100. It was implied that A of the blank was always subtracted from A of the corresponding sample with target cells. IC₅₀ concentration was defined as the concentration of an agent inhibiting cell survival by 50%, compared with a vehicle-treated control. Cis-diamminedichloroplatinum (Cis-DDP) was used as a positive control. All experiments were done in triplicate.

Determination of antioxidant activity

The total antioxidant activity of the plant extracts was evaluated by the phosphomolybdenum method [23]. The assay is based on the reduction of Mo (VI) – Mo (V) by antioxidant compounds and subsequent formation of a green phosphate/Mo (V) complex at an acidic pH. A total of 0.3 ml of the sample extract was combined with 3 ml of reagent solution (0.6 M sulfuric acid, 28 mM sodium phosphate and 4mM ammonium molybdate). The tubes containing the reaction solution were incubated at 95°C for 90 min. Then, the absorbance of the solution was measured at 695 nm using a UV/VIS spectrophotometer (MA9523-SPEKOL 211, Iskra, Horjul, Slovenia) against a blank after cooling to room temperature. Methanol (0.3 mL) in the place of extract was used as the blank. Ascorbic acid (AA) was used as the standard and total

antioxidant capacity was expressed as milligrams of ascorbic acid per gram of dry extract.

Determination of antimicrobial activity

Test microorganisms

The antimicrobial activity of the plant extract was tested *in vitro* against the following bacteria: *Staphylococcus aureus* ATCC 25923, *Klebsiella pneumoniae* ATCC 13883, *Escherichia coli* ATCC 25922, *Proteus vulgaris* ATCC 13315, *Proteus mirabilis* ATCC 14153, *Bacillus subtilis* ATCC 6633, and fungi: *Candida albicans* ATCC 10231 and *Aspergillus niger* ATCC 16404. The fungi were cultured on potato-glucose agar for 7 days at room temperature of 20 °C under alternating light and dark conditions. They were recultured on a new potato-glucose substrate for another 7 days. The culturing procedure was performed four times until pure culture was obtained. The identification of the test microorganisms was confirmed by the Laboratory of Mycology, Department of Microbiology, Torlak Institute, Belgrade, Serbia.

Minimum inhibitory concentration (MIC)

Minimum inhibitory concentrations (MIC) of the extract and cirsimarin against the test bacteria were determined by the microdilution method in 96 multi-well microtiter plates [24]. All tests were performed in Muller–Hinton broth (MHB) with the exception of the yeast, in which case Sabouraud dextrose broth was used. A volume of 100 µL stock solutions of oil (in methanol, 200 µL/mL) and cirsimarin (in 10 % DMSO, 2 mg/mL) was pipetted into the first row of the plate. Fifty µL of Mueller Hinton or Sabouraud dextrose broth supplemented with Tween 80 at a final concentration of 0.5 % (v/v) for analysis of oil was added to the other wells. A volume of 50 µL from the first test wells was pipetted into the second well of each microtiter line, and then 50 µL of scalar dilution was transferred from the second to the twelfth well. Ten µl of resazurin indicator solution (prepared by dissolution of a 270-mg tablet in 40 mL of sterile distilled water) and 30 µL of nutrient broth were added to each well. Finally, 10 µL of bacterial suspension (106 CFU/mL) and yeast spore suspension (3×10⁴ CFU/mL) was added to each well. For each strain, growth conditions and sterility of the medium were checked. The standard antibiotic amracin was used to control the sensitivity of the tested bacteria, whereas ketoconazole was used as control against the tested yeast. The plates were wrapped loosely with cling film to ensure that bacteria did not become dehydrated and were prepared in triplicate. Then, they were placed in an incubator at 37 °C for 24 h for the

bacteria and at 28 °C for 48 h for the yeast. Subsequently, color change was assessed visually. Any color change from purple to pink or colorless was recorded as positive. The lowest concentration at which color change occurred was taken as the MIC value. The average of 3 values was calculated, and the value obtained was taken as the MIC for the tested compounds and standard drug.

Statistical Analysis

The results are presented as mean ± standard deviations of three determinations. Statistical analyses were performed using Student's t-test and one-way analysis of variance. Multiple comparisons of means were done by LSD (least significant difference) test. A probability value of 0.05 was considered significant. All computations were made by employing the statistical software (SPSS, version 11.0).

RESULTS AND DISCUSSION

Phenolic compounds of plant extracts

The total phenolic content and total flavonoids expressed as mg/g of dry extracts of *Daucus carota* L., *Lycopersicon esculentum* Mill. and *Capsicum annuum* L. plants grown in an experimental field near Čačak (Central Serbia) are shown in Table 1.

The highest content of phenolic compounds was detected in the *D. carota* extract, 50.42 mg GAE/g. A similar content of total phenolic compounds was observed in the *L.esculentum* and *C. annum* extract, about 30 mg GAE/g of dry extract. Flavonoids are phenolic compounds that have the highest antioxidant activity due to their chemical structure [25]. The lowest flavonoid content was found in the *L.esculentum* extract, 17.45 mg RE/g of dry extract. A higher and similar content of total flavonoid compounds was observed in *D. carota* and *C. annum* extracts (around 23 mg RE/g) than in *L.esculentum* extracts.

In crude extracts, the following phenolic and hydroxycinnamic acids were identified and quantified using HPLC analysis: gallic acid, protocatechuic acid, caffeic acid, vanillic acid, chlorogenic acid, rosmarinic acid, ferulic acid, sinapic acid and syringic acid. Also, the flavonols: naringenin, myricetin, rutin and quercetin were identified (Figure 1. and Table 2.). The predominant components of *D. carota* extracts were chlorogenic acid and rosmarinic acid, while protocatechuic acid, sinapic acid and vanillic acid were found to be less dominant. The content of gallic acid, caffeic acid and ferulic acid was lower than 0.1 mg/g of dry extract. The predominant acids in *Lycopersicon esculentum* Mill. extract were gallic acid (0.37 mg/g) and caffeic acid (0.55 mg/g). The extract of *C. annum* had the highest concentration of myricetin (3.32 mg/g).

Antioxidant capacity of plant extracts

Phenols and flavonoids play a dual role in reducing the rate of oxidation, as they participate in iron chelation and trapping radicals [26]. The antioxidant capacity of the ethanolic extracts of *Daucus carota* L., *Lycopersicon esculentum* Mill. and *Capsicum annum* L. is presented in Table 1. A strong correlation between free radical scavenging and the phenolic content has been reported for many plants. The highest antioxidant capacity was found in *C. annum* L. (98.01 ± 0.72 µg AA/g) and *D. carota* L. (48.51 ± 1.18 µg AA/g) extracts. The ratio of total phenolic to total flavonoid content (TF/TP) in the *C. annum* extract was much higher than in the other two extracts, which is in agreement with literature data for these types of vegetables [27]. The effectiveness in reducing powers was in a descending order of *D. carota* > *L. esculentum* > *C. annum*.

D. carota extract shows the best antioxidant capacity and the highest content of phenolic compounds.

Table 1. Total phenols (TF), total flavonoids and their relationships (TF/TP), and antioxidant capacity of *Daucus carota* L., *Lycopersicon esculentum* Mill. and *Capsicum annum* L. ethanolic extracts*

Plant extracts	Total phenols (mg GAE/g d.e.)	Total flavonoids (mg RE/g of d.e.)	$\frac{TF}{TP} \cdot 100$ [%]	Antioxidant capacity (µg AA/g d. e.)
<i>D. carota</i> L.	50.42 ± 0.02	23.19 ± 0.54	45.99	48.51 ± 1.18
<i>L. esculentum</i> Mill.	32.96 ± 0.65	17.44 ± 0.39	52.93	72.20 ± 0.72
<i>C. annum</i> L.	33.34 ± 0.34	25.14 ± 0.32	75.41	98.01 ± 0.72

*Results are mean values ± SD from three experiments

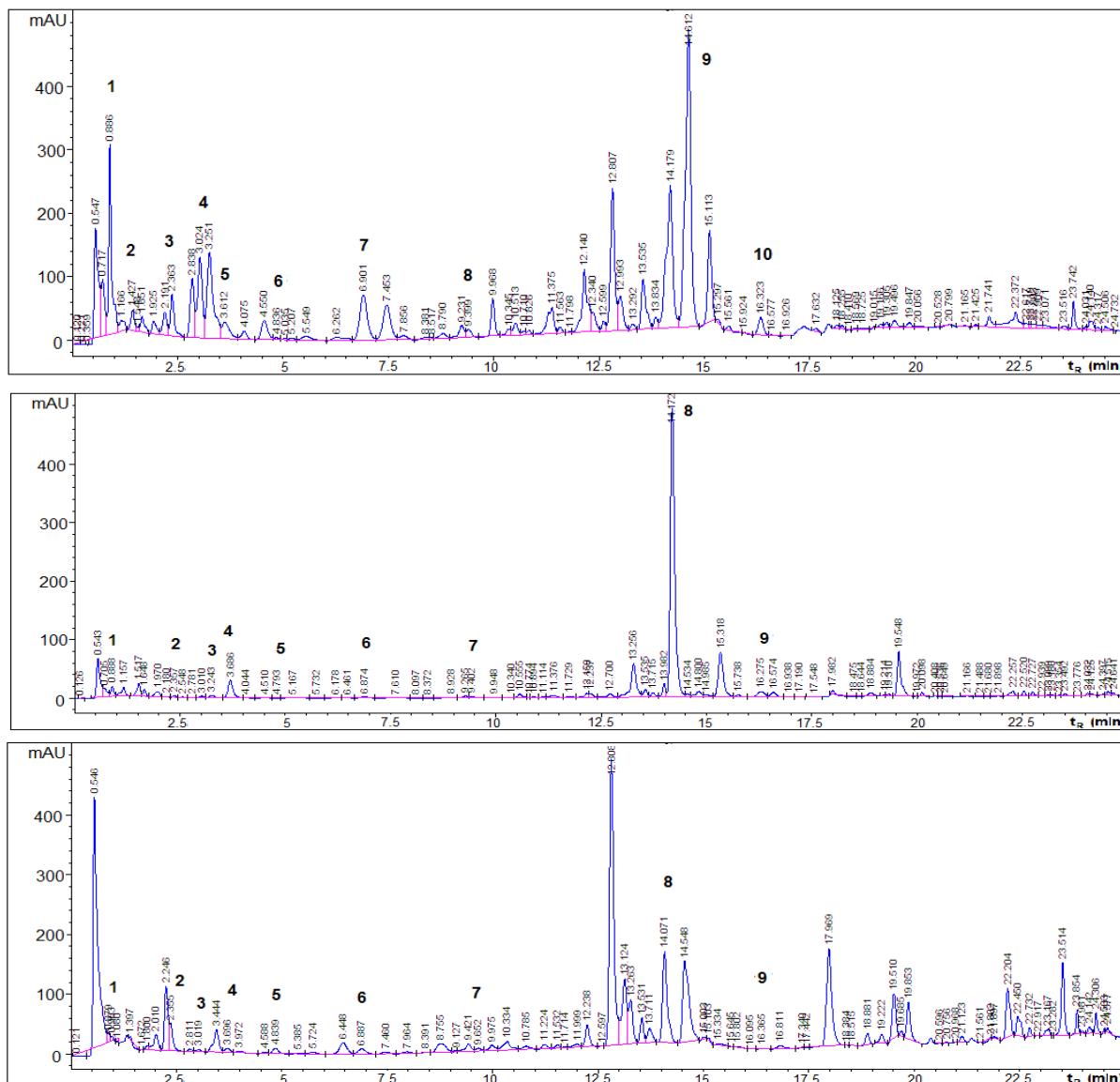


Fig. 1. HPLC chromatograms of the ethanolic extracts of *Daucus carota* L. (I), *Lycopersicon esculentum* Mill. (II) and *Capsicum annuum* L. (III)

Table 2. HPLC analysis of phenolic compounds of *Daucus carota* L. *Lycopersicon esculentum* Mill. and *Capsicum annuum* L. ethanolic extracts

	Phenolic compounds (mg/g of d. e.) of plant extracts		
	<i>D. carota</i> L.	<i>L. esculentum</i> Mill.	<i>C. annuum</i> L.
Gallic acid (1)*	0.09±0.01	0.37±0.02	0.17±0.01
Protocatechuic acid (2)	0.34±0.02	-	0.52±0.02
Caffeic acid (4)	0.06±0.02	0.55±0.02	-
Vanillic acid (5)	0.15±0.01	-	-
Chlorogenic acid (6)	0.80±0.02	-	-
Ferulic acid (9)	0.07±0.01	-	-
Sinapic acid (10)	0.25±0.01	-	-
Rosmarinic acid (13)	0.65±0.01	0.06±0.02	-
Syringic acid (8)	-	0.05±0.03	-
Cinnamic acid (14)	-	-	0.04±0.02
Myricetin (12)	-	-	3.32±0.01
Quercetin (15)	-	-	0.041±0.02
Naringenin (16)	-	-	0.02±0.01

*number corresponds to the peak

Cytotoxic activity of plant extracts

The tested extracts exhibited a strong cytotoxic activity against the target cells *in vitro* (Table 3.). The inhibitory concentration at 50% inhibition (IC₅₀) was the parameter used to compare the cytotoxic activity. A lower IC₅₀ meant better cytotoxic activity. *Daucus carota* L. showed the best cytotoxic activity. The IC₅₀ values against

Table 3. Growth inhibitory effects of the ethanolic extracts of *Daucus carota* L., *Lycopersicon esculentum* Mill. and *Capsicum annuum* L. on FemX and LS 174 cell lines

Plant extracts	IC ₅₀ (µg/mL)	
<i>Daucus carota</i> L.	33.52 ± 1.08	40.22 ± 0.03
<i>L.esculentum</i> Mill.	43.51 ± 0.05	30.29 ± 0.51
<i>Capsicum annuum</i> L	39.58 ± 0.38	22.23 ± 0.95
Cis-DDP	1.94 ± 0.55	7.41 ± 0.97

Antimicrobial activity of plant extracts

The results on minimum inhibitory concentrations (MIC) of the ethanolic extracts of *Daucus carota* L., *Lycopersicon esculentum* Mill. and *Capsicum annuum* L. for eight selected indicator strains are given in Table 4. The antimicrobial activity of the plants ranged from 19.53 µg/mL to 312.50 µg/mL. The extract of *D. carota* showed the highest antimicrobial susceptibility of the fungus *Aspergillus niger* (19.53 µg/mL). Intermediate antimicrobial susceptibility was exhibited by the yeast *Candida albicans* and the fungus *Aspergillus niger* to the *C. annuum* extract, by *Bacillus subtilis* to the *D. carota* extract and by *Bacillus subtilis* and the fungus *Aspergillus niger* to the *L.esculentum* Mill. extract (39.1

FemX and LS174 cell lines were 33.52 ± 1.08 and 40.22 ± 0.03 µg/ml, respectively. The extract of *Lycopersicon esculentum* Mill. also showed good cytotoxic activity against both cell lines. The IC₅₀ value was 43.51 ± 0.05 µg/mL against FemX cell and 30.29 ± 0.51 µg/ml against LS174 cell. *Capsicum annuum* L. exhibited slightly weaker cytotoxic activity. The IC₅₀ value was 39.58 ± 0.38 µg/ml for FemX cell and 22.23 ± 0.95 µg/ml for LS174 cell. µg/mL). The lowest antimicrobial susceptibility was shown by *Staphylococcus aureus* to the *C. annuum* extract (312.5 µg/ml).

CONCLUSIONS

Intensive research on novel and natural antioxidant, antimicrobial and antitumor sources is highly important as it can lead to the creation of new pharmaceutical products. Finding natural sources of antioxidants can serve as an alternative to the use of toxic artificial antioxidants in the food industry. As shown by the results, the positive control (Cis-DDP) exhibited slightly better cytotoxic activity compared to the ethanolic extracts of *Daucus carota* L., *Lycopersicon esculentum* Mill. and *Capsicum annuum* L. This study suggests that all plant extracts show good antioxidant and antimicrobial properties and can serve as new dietary and food supplements.

Acknowledgments: This study is part of the TR 31059, TR-34012 and 031020 projects financially supported by the Ministry of Science and Technological Development, Republic of Serbia.

Table 4. Minimum inhibitory concentrations (MIC, µg/mL) of the ethanolic extracts of *Daucus carota* L., *Lycopersicon esculentum* Mill. and *Capsicum annuum* L.

Microbial strains	<i>C.annuum</i> L.	<i>D. carota</i> L.	<i>L.esculentum</i> Mill.	MIC (µg/ml)	
				<i>Amracin</i>	<i>Ketoconazole</i>
<i>S. aureus</i> ATCC 25923	312.50	156.25	156.25	0.97	/
<i>K. pneumoniae</i> ATCC 13883	156.25	78.13	78.13	0.49	/
<i>E. coli</i> ATCC 25922	78.13	78.13	78.13	0.97	/
<i>P. vulgaris</i> ATCC 13315	78.13	156.25	78.13	0.49	/
<i>P. mirabilis</i> ATCC 14153	156.25	78.13	156.25	0.49	/
<i>B. subtilis</i> ATCC 6633	78.125	39.10	39.10	0.24	/
<i>C. albicans</i> ATCC 10231	39.10	78.13	78.13	/	1.95
<i>A. niger</i> ATCC 16404	39.11	19.53	39.11	/	0.97

REFERENCES

1. H. M. Sharma, A. Hanna, E. M. Kauffman, H. A. I. Newman, *Pharmacol. Biochem. Behav.*, **43**, 1175 (1992).
2. M. Kosanić, B. Ranković, *J. Med. Food*, **14**(12), 1624 (2011).
3. C.F. Begamboula, M. Uyttendaele, J. Debevere, *J. Food Prot.*, **66**, 668 (2003).
4. S.G. Deans, G.A. Ritchie, *Int. J. Food Microbiol.*, **5**, 165 (1987).
5. A. M. Janssen, J. J. C. Scheffer, A. Svendsen, Y. B. Martinus: Nijhoff Publishers, Dordrecht, The Netherlands 1985, p. 213.
6. J. Kim, M.R. Marshal, C. Wei, *J. Agric. Food Chem.*, **43**, 2839 (1995).
7. P. L. Cantore, V. Shanmugaiah, N.S. Iacobellis, *J. Agric. Food Chem.* **57**, 9461 (2009).
8. P. Santhakumari, A. Prakasam, K. V. Pugalendi, *Indian J. Pharm.*, **35**, 373 (2003).
9. M. M. Carmen, A. Florin, *Molecules* **14**, 480 (2009).
10. K. Ghaseme, Y. Ghasemi, M. A. Ebrahimzadeh, *Pakistan J. Pharm. Sci.*, **22**, 272 (2009).
11. A. Giacosa, R. Filiberti, M. J. Hill, J. Faivre, *Eur. J. Cancer. Prev.*, **6**, S54 (1997).
12. G. Cao, E. Sofic, R.L. Prior, *Free Rad. Biol. Med.*, **22**, 749 (1997).
13. O. Benavente-Garcia, J. Castillo, F.R. Marin, A. Ortuno, J.A. Del Rio, *J. Agric. Food Chem.*, **45**, 4505 (1997).
14. S.E. Gariballa, A.J. Sinclair, *Br. J. Nutr.*, **80**, 7 (1998).
15. D. Satyajit, L.N. Sarker, Y. Kumarasamy, *Methods*, **42** (4), 321 (2007).
16. V. Singleton, R. Orthofer, R.A. Lamuela-Raventos, *Methods Enzymol.*, 1999, p.152.
17. I.M.C. Brighente, M. Dias, L.G. Verdi, M.G. Pizzolatti, *Pharm. Biol.*, **45**, 156 (2007).
18. P.D. Duh, G.C. Yed, *Food Chemistry*, **6**, 639 (1997).
19. A.Č. Mišan, N.M. Mimica-Dukić, A.I. Mandić, M.B. Sakač, I.LJ. Milovanović, I.J. Sedej, *Centr. Eur. J. Chem.*, **9**, 133 (2011).
20. T. Mosmann, *J. Immunol Methods*, **65**, 55 (1983).
21. M. Ohno, T. Abe, *J. Immunol Methods*, **145**, 199 (1991).
22. B.N. Ames, L.S. Gold, W.C. Willett, *Proc. Natl. Acad. Sci. USA*, 1995, p. 5265.
23. B.N. Ames, M.K. Shigenaga, T.M. Hagen, *Proc. Natl. Acad. Sci. USA*, **90**, 7922, 1993.
24. M. Aviram, *Royal Society of Chemistry*, 1999, p.9.
25. H. Muller, A. Bub, B. Waltzl, G. Rechkemmer, *Eur. J. Nutr.*, **38**, 35 (1999).
26. M.P. Kähkönen, A.I. Hopia, H.J. Vuorela, J.P. Rauha, T.S. Kujala, M. Heinonen, *J. Agric. Food Chem.*, **47** (10), 3954 (1999).
27. Z. Ilic, F. Elazar, Dj. Mihal, Dj. Martinovski, R. Trajkovic: *Fiziologija i tehnologija čuvanja povrća i voća*, Novi Sad, 2007.

ЦИТОТОКСИЧНОСТ, АНТИМИКРОБНО И АНТИОКСИДАНТНО ДЕЙСТВИЕ НА *DAUCUS CAROTA* L., *LYCOPERSICON ESCULENTUM* MILL. AND *CAPSICUM ANNUUM* L.

Дж. Младенович *¹, А. Радованович², Р. Павлович¹, Б. Радованович³,
Дж. Здравкович⁴, Г. Ачанович-Джокович¹

¹ Универзитет в Крагуевац, Агрономически факултет, Цар Душан 34, Чачак, Србија

² Белградскиј универзитет, Факултет по хемија, Карнегиева 12-16, Белград, Србија

³ Универзитет в Ниш, Факултет Природни науки и математика, Вишеградска 33, Ниш, Србија
⁴ Институт за зеленчукови култури, Карађорђево 71, 26 000 Смедеревска паланка, Србија

Получена на 27 ноември 2013 г.; Ревизирана на 24 февруари, 2014 г.

(Резюме)

Целта на това проучване беше да се оцени цитотоксичноста, антимикробната и антиоксидантната активност на екстракти от *Daucus Carota* L., *Lycopersicon esculentum* Mill. и *Capsicum annuum* L. отгледани в централна Србија. Съдържанието на фенолни съединения в екстрактите се определяше чрез спектрофотометричен и HPLC анализ. Тези растителни екстракти се оказаха мощни инхибитори на клетъчния растеж в клетъчни линии (FemX и LS 174). Стойностите на IC50 срещу FemX и LS174 клетъчни линии бяха 33.52 ± 1.08 и 40.22 ± 0.03 мкг / мл, съответно. Най-високият антиоксидантен капацитет беше намерен в *C. Annuum* L. (98.01 ± 0.72 мкг АА / г) и *D. carota* L. (48.51 ± 1.18 мкг АА / г) екстракти. Тестваните екстракти показаха силна до умерена антимикробна активност (19.53 - 312.50 мкг / мл). Екстрактите от *D. carota* L., *L. esculentum* Mill. и *C. annuum* L. могат да служат като нови диетични и хранителни добавки.

Sympathovagal balance after application of N-modified nociceptin analogues

R. A. Girchev¹, P. P. Markova^{1*}, P.T.Todorov², E. D. Naydenova²,

¹ Department of Physiology, Medical University-Sofia, Sofia,

² Department of Organic Chemistry, University of Chemical Technology and Metallurgy, Sofia

Received December 5, 2013; Accepted February 26, 2014

The effects of two new N/OFQ(1-13)NH₂ derivatives in which the N-terminal Phe was replaced with 1-[(methoxyphosphono) methylamino]cycloalkanecarboxylic acids containing seven AFC7-N/OFQ(1-13)NH₂, (NC7) or eight-membered cycloalkane rings AFC8-N/OFQ(1-13)NH₂, (NC8) on the fast oscillations of the interpulse interval (IPI) as well as on the sympathovagal balance in conscious Wistar rats were investigated. The NC7 or NC8, was applied by i.v. bolus injection in dose 100 nmol/kg b.w. and its effects were studied for nine consecutive 10 minute long intervals. The spectrograms for IPI were derived by using Fast Fourier Transform algorithm. The spectral power (P) in the low (LF), mid (MF) and high (HF) frequency band typical for rats (20-195; 195-605; 605-3000 mHz, respectively) was studied. The sympathovagal balance was determined by the relation of power of mid to high frequency band P_{MF}/P_{HF}. Application of NC7 led to decrease of P_{MF}/P_{HF} from 0.52±0.04 to 0.31±0.08 (p<0.05); 0.24±0.06 (p<0.01) and to 0.23±0.07, (p<0.01) in the first three 10 min long intervals as a result of decrease of mainly sympathetic mediated oscillations of IPI (P_{MF}). Depended by parasympathetic branch of autonomic nervous system fast oscillations of IPI (P_{HF}) were not influenced. Application of NC8 did not affect fast oscillation of IPI as well as sympathovagal balance, but provoked a sustained decrease of heart rate in the course of 70 min, (p<0.05). Our results indicated that NC7 led to displacement of sympathovagal balance as a result of decrease of sympathetic determined fast oscillations, whereas NC8 involved a powerful mechanism responsible for long-lasting regulation of heart rate.

Keywords: heart rate variability, conscious rats, N-modified nociceptin analogues

INTRODUCTION

Heart rate variability analysis has been a prevalent technique to assess autonomic influences on the heart. Support for its utility as an index of autonomic tone comes from data which demonstrate that heart rate variability is virtually abolished after sympathetic and parasympathetic blockade [1]. Furthermore, under selected conditions, certain frequencies of heart rate variability are accentuated in response to sympathetic and parasympathetic stimulation [2]. Sympathovagal balance has emerged to describe the dual opposing effects of the sympathetic and parasympathetic nervous systems on the sinus node [3, 4, 5].

The understanding of the role of the N/OFQ - NOP receptor system depends upon the development of selective and highly potent peptide and non-peptide agonist and antagonist ligands [6]. Structure-activity relationship studies identified strategies to render N/OFQ ligands less susceptible to enzymatic degradation. Phosphonopeptides are phosphorus analogues of naturally occurring peptides containing a tetrahedral phosphorus atom. Their importance is obvious from the fact that they

are being widely used as enzyme inhibitors and as haptens in catalytic antibody research, because they can be considered as stable mimetics of tetrahedral transition states in ester and amide hydrolysis and formation [7, 8]. It has been established that N-terminal tridecapeptide sequence of nociceptin molecule is sufficient for its full biological activities [9]. The structure-activity relationship studies demonstrated that the N/OFQ sequence can be divided into a N-terminal tetrapeptide "message" critical for receptor activation and a C-terminal "address" important for receptor binding [10]. Recently structure-activity relationships of new N-modified analogues of N/OFQ(1-13)NH₂, with aminophosphonate moiety containing 5-, 7- and 8-membered cycloalkane rings have been reported [11, 12]. In our study we tested the effects of two new N/OFQ(1-13)NH₂ derivatives in which the N-terminal Phe was replaced with 1-[(methoxyphosphono) methylamino]cycloalkanecarboxylic acids containing seven AFC7-N/OFQ(1-13)NH₂, (NC7) or eight-membered cycloalkane rings AFC8-N/OFQ(1-13)NH₂, (NC8) on the fast oscillations of the interpulse interval, as well as on the sympathovagal balance in conscious Wistar rats.

* To whom all correspondence should be sent:
E-mail: pp.markova@gmail.com

EXPERIMENTAL

Synthesis of nociceptin analogues

The 1-[(dimethoxyphosphono) methylamino] cycloheptanecarboxylic acid and 1-[(dimethoxyphosphono) methylamino] cyclooctanecarboxylic acid were previously prepared using Kabachnik-Fields reaction [13]. The peptides AFC7-N/OFQ(1-13)NH₂ and AFC8-N/OFQ(1-13)NH₂, (Fig. 1) were obtained with good yield by solid phase peptide synthesis - Fmoc (9-fluorenylmethoxy-carbonyl) chemistry, according to the previously described procedure [11, 12]. Rink-amide resin was used as a solid-phase carrier, and 2-(1-OH-benzotriazole-1-yl)1,1,3,3-tetramethyl-carbamide tetrafluoroborate (TBTU) was used as a coupling reagent.

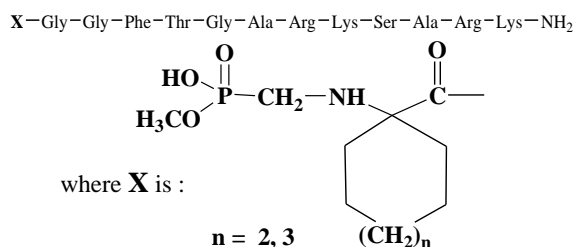


Fig. 1. Sequences of new N-modified analogues of the N/OFQ(1-13)NH₂ with aminophosphonate moiety containing 7- and 8-membered cycloalkane rings

The 3 equivalent of 1-[(dimethoxyphosphono) methylamino]cycloalkanecarboxylic acids were coupled to the growing peptide chain by using TBTU (3 equiv) in the presence of 1-hydroxy benzotriazole (HOBt) dissolved in DMF and in excess of N,N-diisopropylethylamine (DIEA). The coupling reaction time was 15 h. The cleavage of the synthesized peptide from the resin was done using a mixture of 95 % trifluoroacetic acid (TFA), 2.5 % triisopropylsilan (TIS) and 2.5 % water. During the cleavage, one of the methoxy groups from the cyclic aminophosphonic residue was removed. The crude peptides were purified by reversed-phase high-performance liquid chromatography (HPLC) and the molecular weights were determined using electrospray ionization mass-spectrometry.

Experimental design

Experiments were carried out on normotensive Wistar rats (W) at the age of 12-14 weeks, male in sex. The study was performed in accordance with the Convention on Animal Protection. The animals were housed under standard conditions: constant room temperature 22 °C; 12/12 h light /dark cycle; free access to standard rat chow and tap water. The

effects of the newly synthesized nociceptin analogues NC7 or NC8 were investigated in two different experimental groups each consisting of 10 animals. Under general anesthesia (Nembutal – Sigma, in dose 35 mg/kg b.w., i.p.) in the femoral artery for a continuous blood pressure measurement and in the femoral vein for drug application catheters were inserted. To avoid clotting, the catheters were previously flushed and after that filled with 20 IU/ml heparin in sterile saline. The catheters were tunneled subcutaneously and exteriorized at the back of the neck. The experiments were performed on conscious freely moving animals 24 hours after surgical intervention. The arterial blood pressure wave was registered by a Gould Statham transducer P23ID connected to computerized data acquisition system Biopac MP100WS through arterial catheter. The analog to digital converted signal was received and monitored by AcqKnowledge 3.8 software. Arterial blood pressure wave was registered during a 40 min control period. The N/OFQ(1-13)NH₂ analogue NC7 or NC8, was applied by i.v. bolus injection in dose 100 nmol/kg, dissolved in 200 µl 0.9 % NaCl. The effects of nociceptin analogues were studied five minutes after its application for nine consecutive 10 minute long intervals. In the blood pressure wave the values of inter-pulse interval (IPI) were determined by peak and rate detectors of the AcqKnowledge 3.8 software in terms of time between two consecutive diastolic minima of the blood pressure wave, thereafter heart rate was calculated. The obtained raw data of the investigated parameter were resampled for 10 Hz. The spectrograms for IPI were derived from 512 successive values through a virtual instrument developed in graphical programming environment Lab VIEW 3.1.1., by using Fast Fourier Transform algorithm. In the spectrogram the spectral power (P) in the low (LF), mid (MF) and high (HF) frequency band typical for rats (20-195; 195-605; 605-3000 mHz, respectively) was studied [14]. In IPI spectrograms the sympathovagal balance was determined by the relation of power of mid to high frequency band P_{MF}/P_{HF} . Statistical analysis was performed by Student's t-test. The results are presented as mean±SEM. Differences at a level $p < 0.05$ were considered statistically significant.

RESULTS AND DISCUSSION

Effects of NC7

Application of NC7 did not change the mean values of heart rate. In the control period the heart rate was 342.64±6.11 bpm. In the nine consecutive

10-min long investigated intervals after application of NC7 the mean values of heart rate were: 347.77±5.92 bpm; 347.00±9.95 bpm; 345.42±6.23 bpm; 342.75±4.80 bpm; 344.00±9.22 bpm; 337.17±7.34 bpm; 339.50±8.52 bpm; 344.00±5.20 bpm and 342.84±7.40 bpm, respectively. However, NC7 affected the fast oscillation of IPI spectrograms. Administration of NC7 provoked a decrease in P_{MF} from 1.04±0.13 ms² to 0.66±0.16 ms², ($p<0.05$) in the first; to 0.55±0.17, ($p<0.01$) in the second and to 0.28±0.05 ms², ($p<0.01$) in the third 10 minutes long interval (Fig. 2). In the course of the fourth investigated period after application of NC7 the spectral power in the mid frequency band returned to its control level.

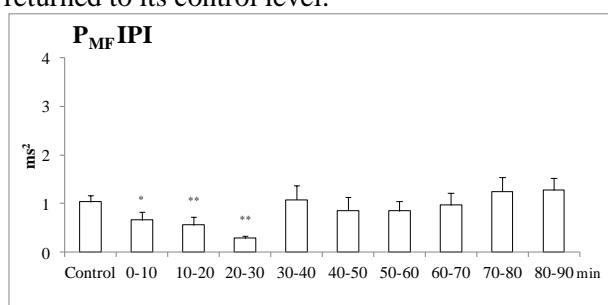


Fig. 2. Mid frequency spectral power (P_{MF}) in interpulse interval (IPI) spectrograms in control period (control) and after application of AFC7-NC(1-13)NH₂, (NC7) in nine consecutive 10 min long intervals

The P_{HF} in the IPI spectrograms did not change as a result of NC7 application: 1.93±0.23 ms² in the control period; 1.76±0.29 ms² in the first; 2.26±0.38 ms² in the second; 1.85±0.27 ms² in the third investigated period and till the end of experiment they remained at the same level. The P_{MF}/P_{HF} ratio decreased after NC7 application (Fig. 3) in the same intervals in which P_{MF} decreased: from 0.52±0.04 in the control period to 0.31±0.08 ($p<0.05$) in the first interval to 0.24±0.06 ($p<0.01$) in the second and to 0.23±0.07 ($p<0.01$) in the third investigated interval. In the fourth 10 minute interval the P_{MF}/P_{HF} ratio returned to its control level.

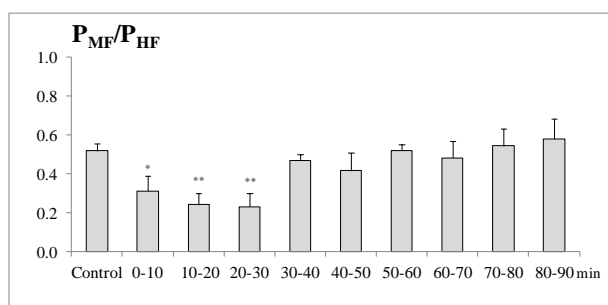


Fig. 3. The sympathovagal balance (P_{MF}/P_{HF}) in the control period (control) and after application of AFC7-NC(1-13)NH₂, (NC7) in nine consecutive 10 min long intervals

The change of sympathovagal balance is a result of decrease of mainly sympathetic mediated oscillations of the IPI spectrograms. Depended by parasympathetic branch of autonomic nervous system fast oscillations of IPI (P_{HF}) were not influenced by application of NC7. Application of NC7 did not affect the power of low frequency oscillations (P_{LF}) in IPI spectrograms neither. The P_{LF} in the control period was 5.21±0.65 ms². In the investigated nine consecutive 10-min long intervals during application of NC7 the values of P_{LF} were: 5.57±0.54 ms²; 5.06±0.64 ms²; 5.98±0.59 ms²; 5.87±0.47 ms²; 5.81±0.69 ms²; 5.25±0.50 ms²; 5.15±0.56 ms²; 5.80±0.57 ms² and 5.47±0.64 ms², respectively. The mid-frequency oscillations in the interpulse interval are mainly mediated by the sympathetic part of the autonomic nervous system [1, 14]. The power of oscillations in this spectral band, however, can also be modulated by baroreflex mechanisms [14], as well as by interactions of the sympathetic nervous system with different factors affecting the sympathetic nerves activity on a local and on a central level [1, 14, 15]. Our results show a decrease of power in mid frequency oscillations in IPI in the first three investigated intervals. The decrease of the relation P_{MF}/P_{HF} , characterized sympathovagal balance is a result of the decreased mid frequency oscillations in the IPI spectrograms. We suggest that the decreased power of the mid frequency oscillations of the inter-pulse interval is a result of a specific, short-term influence of the sympathetic nerve activity to the sinus node.

Effects of NC8

Differently from NC7, the application of NC8 led to a decrease in the mean values of heart rate in the intervals between 0-70 min (Fig. 4).

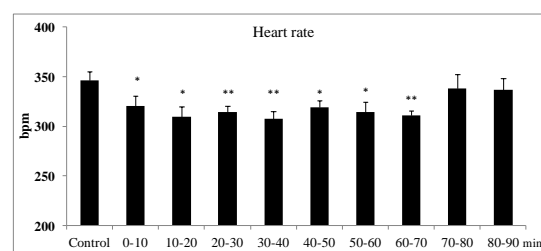


Fig. 4. Mean values of the heart rate in the control period (control) and after application of AFC8-NC(1-13)NH₂, (NC8) in nine consecutive 10 min long intervals

In the control period the heart rate was 346.5±8.7 bpm. As a result of NC8 application the heart rate decreased to 320.5±10.1 bpm, ($p<0.05$) in the interval 0-10 min; to 309.5±10.5 bpm, ($p<0.05$) in the interval 10-20 min; to 314.1±6.5

bpm, ($p < 0.01$) in the interval 20-30 min; to 307.3 ± 7.5 bpm, ($p < 0.01$) in the interval 30-40 min; to 319.2 ± 6.7 bpm, ($p < 0.05$) in the interval 40-50 min to 314.2 ± 10.4 bpm, ($p < 0.05$) in the interval 50-60 min and to 311.2 ± 4.8 bpm, ($p < 0.01$) in the interval 60-70 min. In the last two intervals 70-80 min and 80-90 min the mean values of the heart rate were restored to the control level: 338.00 ± 14.0 and 336 ± 11.9 bpm, respectively. Interestingly, in difference to NC7, the application of NC8 did not change the spectral characteristics of IPI and sympathovagal balance (Tabl. 1).

Table 1. Spectral power distribution in interpulse interval (IPI) spectrograms in the low (P_{LF}), mid (P_{MF}), and high (P_{HF}) frequency band as well as sympathovagal balance (P_{MF}/P_{HF}) in the control period (control) and after application of AFC8-NC(1-13)NH₂, (NC7) in nine consecutive 10 min long intervals

Investigated periods	P_{LF} (ms ²)	P_{MF} (ms ²)	P_{HF} (ms ²)	P_{MF}/P_{HF}
Control	5.60 ± 0.76	1.18 ± 0.29	2.13 ± 0.11	0.53 ± 0.09
0-10 min	5.93 ± 0.22	1.09 ± 0.25	2.66 ± 0.26	0.50 ± 0.12
10-20 min	5.81 ± 0.67	1.04 ± 0.09	2.71 ± 0.42	0.56 ± 0.10
20-30 min	5.52 ± 0.62	0.97 ± 0.08	2.38 ± 0.26	0.53 ± 0.06
30-40 min	5.43 ± 0.83	1.06 ± 0.09	2.27 ± 0.39	0.52 ± 0.08
40-50 min	6.02 ± 0.88	1.30 ± 0.19	2.44 ± 0.34	0.61 ± 0.08
50-60 min	5.71 ± 0.79	1.00 ± 0.12	1.95 ± 0.37	0.53 ± 0.09
60-70 min	5.79 ± 0.52	1.21 ± 0.34	2.43 ± 0.38	0.59 ± 0.08
70-80 min	6.08 ± 0.28	1.08 ± 0.28	2.00 ± 0.23	0.53 ± 0.07
80-90 min	6.05 ± 0.58	1.43 ± 0.21	2.79 ± 0.35	0.58 ± 0.06

In our previous investigations we have established that N/OFQ(1-13)NH₂, the smallest peptide in which the activity of the natural peptide is preserved, participated in the regulation of sympathovagal balance in normotensive Wistar rats [16]. Briefly, the application of N/OFQ(1-13)NH₂ led to a decrease in P_{MF} in the first three investigated intervals, did not affect the power of the high frequency oscillations and decreased the relation of P_{MF}/P_{HF} in the same intervals in which P_{MF} decreased. In our current study we established identical effects provoked by NC7 application on the fast oscillation in IPI. Application of NC7 provoked a decrease in P_{MF} , as well as a decrease in the P_{MF}/P_{HF} ratio in the first three 10 min long intervals. Both N/OFQ(1-13)NH₂ and NC7 did not change P_{HF} . On the other hand, application of NC8 did not lead to changes in the fast oscillation of IPI, as well as in the sympathovagal balance, but provoked a sustained decrease of heart rate in Wistar rats. Such an effect was not observed neither after the application of NC7, nor after applying N/OFQ(1-13)NH₂. The replacement of Phe in

position 1 of N/OFQ(1-13)NH₂ with 1-[(methoxyphosphono)methylamino]cycloheptanecarboxylic acid (NC7) did not provoke effects different from that established after application of N/OFQ(1-13)NH₂. In our experiments we established that the replacement of Phe1 of N/OFQ(1-13)NH₂ with 1-[(methoxyphosphono)methylamino]cyclooctanecarboxylic acid (NC8) abolished the action of N/OFQ(1-13)NH₂ on the fast oscillation of the interpulse interval. However, the NC8 administration provoked a decrease in the mean values of the heart rate. Despite of lack of effects of NC8 on the fast oscillation of the interpulse interval, NC8 involved a powerful mechanism responsible for long-lasting regulation of heart rate.

Acknowledgements: This work was supported by the National Science Fund by Grant DTK 02/61/2009, Sofia, Bulgaria.

REFERENCES:

1. S. Akselrod, D. Gordon, FA Ubel, DC Shannon, AC Berger, RJ Cohen, *Science*, **213**, 220, (1981).
2. A. Malliani, F. Lombardi, M. Pagani, *Br Heart J.*, **71**, 1, (1994).
3. J. J. Goldberger, *Am J Physiol.* **276**, H1273, (1999).
4. D.L. Eckberg, *Circulation.*; **96**, 3224, (1997).
5. S. Guzzetti, R. Magatelli, E. Borroni, S. Mezzetti, *Auton Neurosci.*, **90**, 102, (2001).
6. R. Guerrini, G. Caló, D.G. Lambert, G. Carrá, M. Arduin, T.A. Barnes, J. McDonald, D. Rizzi, C. Trapella, E. Marzola, D.J. Rowbotham, D. Regoli, S. Salvadori, *J Med Chem.*, **48**, 1421, (2005).
7. R. Hirschmann, A. B. 3rd Smith, C. M. Taylor, P. A. Benkovic, S. D. Taylor, K. M. Yager, P. A. Sprengeler, S. J. Benkovic, *Science*, **265**, 234, (1994).
8. E. Cunningham, M. Drag, P. Kafarski, A. Bell, *Antimicrob Agents Chemother.* **52**, 3221, (2008).
9. G. Calò, R. Guerrini, A. Rizzi, S. Salvadori, D. Regoli, *Br. J. Pharmacol.*, **129**, 1261 (2000).
10. R. Guerrini, G. Calò, A. Rizzi, C. Bianchi, L.H. Lazarus, S. Salvadori, P.A. Temussi, D. Regoli, *J Med Chem.* **40**, 1789, (1997).
11. E. Naydenova, P. Todorov, P. Mateeva, R. Zamfirova, N. Pavlov, S. Todorov, *Amino Acids*, **39**, 1537, (2010).
12. P. Todorov, P. Mateeva, R. Zamfirova, N. Pavlov, E. Naydenova, *Amino Acids*, **43**, 1217, (2012).
13. E. Naydenova, P. Todorov, M. Topashka-Ancheva, G. Momekov, T. Yordanova, S. Konstantinov, K. Troev, *Eur J Med Chem* **43**, 1199, (2008).
14. S. C. Malpas, *Am. J. Physiol.*, **282**, H6 (2002).
15. P. B. Persson, *Am J Physiol.*, **273**, R1201, (1997).
16. P. Markova, R. Girchev, E. Naydenova, L. Vezenkov, *Trakia Journal of Sciences*, **5**, 1, (2007)

СИМПАТИКО-ВАГУСОВ БАЛАНС СЛЕД ПРИЛОЖЕНИЕ НА N-МОДИФИЦИРАНИ НОЦИЦЕПТИНОВИ АНАЛОЗИ

Р. А. Гърчев¹, П. П. Маркова¹, П. Т. Тодоров², Е. Д. Найденова²

¹Катедра по физиология, Медицински университет-София, София

²Катедра по органична химия, Химикотехнологичен и металургичен университет, София

Получена на 5 декември, 2013 г.; приета на 26 февруари, 2014 г.

(Резюме)

Изследвани са ефектите на два новосинтезирани N/OAQ(1-13)NH₂ аналози в които N-крайната аминокиселина (фенилаланин) е заместена с 1-[(метоксифосфо)метиламино]циклоалканкарбоксилна киселина, съдържаща седем AFC7-N/OAQ(1-13)NH₂, (NC7) или осем членен циклоалканов пръстен AFC8-N/OAQ(1-13)NH₂, върху бързите колебания на интерпулсовия интервал (IPI) и върху симпатико-вагусовия баланс у будни нормотензивни плъхове Wistar. Ефектите на NC7 или на NC8, приложени i.v., бяха изследвани в 9 последователни 10 минутни интервала. Спектрограмите на IPI бяха получени чрез бърза Фурие трансформация. Бяха изследвани мощностите на колебания (P) в зоните на ниски (LF), средни (MF) и високи (HF) честоти, характерни за плъхове (20-195; 195-605; 605-3000 mHz). Симпатико-вагусовият баланс беше определен чрез отношението P_{MF}/P_{HF}. Приложението на NC7 предизвика понижение на стойността на отношението P_{MF}/P_{HF} от 0.52±0.04 на 0.31±0.08 (p<0.05); 0.24±0.06 (p<0.01) и на 0.23±0.07, (p<0.01) в първите три 10 минутни интервала, в резултат на понижението на предимно симпатиково медираните осцилации P_{MF} на IPI. Мощността на опосредстваните от парасимпатикуса колебания P_{HF} на IPI не бяха повлияни от приложението на NC7. Приложението на NC8 не засегна бързите колебания на IPI и симпатико-вагусовия баланс, обаче предизвика трайно понижаване на сърдечната честота в продължение на 70 минути, (p<0.05). Нашите резултати показват, че NC7 предизвиква изместване на симпатико-вагусовия баланс в резултат на понижаването на мощността на симпатиково медираните осцилации, докато NC8 въвлича механизми, отговорни за дълготрайната регулация на сърдечната честота.

Synthesis and crystal structure of 6-(1-benzyl-5-methyl-1H-1,2,3-triazol-4-yl)-4-(2-methoxyphenyl)-3,4-dihydropyrimidine-2(1H)-thione

S. Murugavel^{1*}, D. Lakshmanan², Sangaraiah Nagarajan³, Alagusundaram Ponnuswamy³

¹Department of Physics, Thanthai Periyar Government Institute of Technology, Vellore, Tamilnadu, India *

²Department of Physics, C. Abdul Hakeem College of Engineering & Technology, Melvisharam, Vellore, India,

³Department of Organic Chemistry, School of Chemistry, Madurai Kamaraj University, Madurai, Tamilnadu, India.

Received December 9, 2013; Revised February 22, 2014

The structure of 6-(1-benzyl-5-methyl-1H-1,2,3-triazol-4-yl)-4-(2-methoxyphenyl)-3,4-dihydropyrimidine-2(1H)-thione was determined by X-ray crystallography. The compound crystallizes as colourless needles shaped in the triclinic system, space group *P*1 with cell constants: *a* = 10.0624(5) Å, *b* = 10.3668(6) Å, *c* = 11.8773(9) Å, α = 91.865 (4)°, β = 114.838 (2)°, γ = 99.304 (3)°, *V* = 1102.58(12) Å³, *Z* = 2. The crystal structure was solved by direct methods and refined by full-matrix least-squares on *F*² to final values of *R*₁ = 0.0583 and *wR*₂ = 0.1930. In the crystal structure, supramolecular chains mediated by C–H...O contacts along the *a*-axis are linked into a double layer *via* N–H...S hydrogen bonds and π – π [ring centroid (pyrimidine)...ring centroid (triazole) distance = (3.508(1) Å] interactions. The resulting double layer stacks along the *b*-axis without any specific interactions.

Keywords: 1, 2, 3-triazole, Single-crystal X-ray diffraction, Crystal structure, Hydrogen bonding

INTRODUCTION

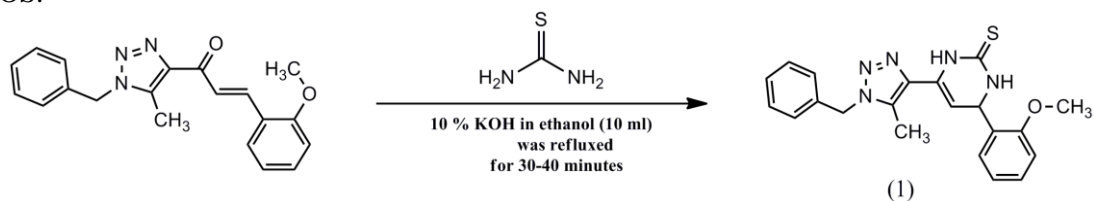
1,2,3-triazoles have found a wide range of important applications in pharmaceutical, polymer, and material fields [1]. In addition, they have shown a broad spectrum of biological properties such as antibacterial [2] anti-allergic [3], anti-HIV activity [4] and also serve as potential chemotherapeutic agents for various diseases [5]. On the other hand, substituted pyrimidine nuclei are found antiviral [6], anti-tubercular, antineoplastic, anti-inflammatory, diuretic, antimalarial and cardiovascular [7]. In view of these bioactivities of the individual heterocycles, it was envisaged that the synthesis of novel hybrid molecules containing two of the above said moieties in a single frame is worth attempting. Several similar structures related to the title compound have been synthesized and antibacterial activities are reported by our coauthors [8]. Here we present the crystal structure of 6-(1-benzyl-5-methyl-1H-1,2,3-triazol-4-yl)-4-(*o*-tolyl)-3,4-dihydropyrimidine-2(1H)-thione (**1**), C₂₁H₂₁N₅OS.

EXPERIMENTAL

Synthesis and characterization

The title compound (**1**) was obtained according to the reaction scheme 1.

A mixture of (*E*)-1-(1-benzyl-5-methyl-1H-1,2,3-triazol-4-yl)-3-(2-methoxyphenyl)prop-2-en-1-one (0.2 g, 0.58 mmol), thiourea (0.067 g, 0.88 mmol) and 10 % aq. KOH in ethanol (10 ml) was refluxed for 30-40 minutes and poured onto excess of crushed ice and neutralized with dilute hydrochloric acid. The precipitated 6-(1-benzyl-5-methyl-1H-1,2,3-triazol-4-yl)-4-(2-methoxyphenyl)-3,4-dihydropyrimidine-2(1H)-thione were filtered and recrystallized from ethanol. Needle-like colourless single crystals of the title compound **1**, suitable for single crystal X-ray diffraction analyses, grown in ethanolic solution by slow evaporation of the solvent at room temperature were collected (yield 2.58 g (93 %), m.p. 175-177 °C).



Scheme 1. Reaction scheme and chemical diagram of the title compound (**1**)

* To whom all correspondence should be sent:
E-mail: smurugavel27@gmail.com

X-ray – single crystal analyses

A crystal of the title compound having approximate dimensions of 0.30×0.24×0.10 mm³ was mounted on a glass fiber using cyanoacrylate adhesive. All measurements were made on a Bruker AXS Kappa Apex II single crystal X-ray diffractometer using graphite mono-chromated MoK α ($\lambda = 0.71071$ Å) radiation and CCD (Charge coupled device) detector. Diffraction data were collected at room temperature by the ω -scan technique. Accurate unit cell parameters and orientation matrix were obtained by a least-squares fit of several high angle reflections in the ranges $1.9^\circ < \theta < 26.3^\circ$ for the title compound.

The unit cell parameters were determined for 36 frames measured (0.5° phi-scan) from three different crystallographic zones and using the method of difference vectors. The intensity data were collected with an average four-fold redundancy per reflection and optimum resolution (0.75 Å). The intensity data collection, frames integration, Lorentz-polarization correction and decay correction were done using SAINT-NT (version 7.06a) software. Empirical absorption correction (multi-scan) was performed using SADABS [9] program. The structure was solved by direct methods using ShelxS [10] and refined by full-matrix least-square procedures on F^2 with ShelxL-97 [10]. All H atoms were positioned geometrically and constrained to ride on their parent atom with C—H = 0.93–0.97 Å and N—H = 0.86 Å, and with $U_{iso}(H) = 1.5 U_{eq}$ for methyl H atoms and $1.2 U_{eq}(C)$ for other H atoms. The investigated crystal was found to be a two-component rotational twin. The data for both components were integrated using SAINT and scaled with TWINABS. Final refinement was performed using a HKLF5 file generated by TWINABS with a BASF parameter (0.1666(1)). The crystal structure contained solvent accessible voids of 148 Å³, showed no electrons in the voids. This might indicate that the crystal lost its solvent during crystallization without collapsing the structure.

NMR

¹H NMR and ¹³C NMR spectra were recorded in CDCl₃ and DMSO-d₆ on a Bruker Advance 300 MHz spectrometer and the chemical shifts are reported as δ values in parts per million (ppm) relative to tetramethylsilane, with J values in Hertz. The splitting patterns in the ¹H NMR spectra are reported as follows: s = singlet; d = doublet; br s = broad singlet; br d = broad doublet; m = multiplet.

¹³C NMR data are reported with the solvent peak (CDCl₃ = 77.0 MHz) as the internal standard.

White solid; m.p. 175–177 °C; Yield:93%; ¹H NMR (300 MHz, CDCl₃): 8.51 (br s, 1H, NH), 7.35–6.84 (m, 9H, ArH), 6.84 (br s, 1H, NH), 5.63 (br s, 1H, -CH), 5.55 (m, 2H, -CH₂), 5.18 (br s, 1H, olefinic -CH), 3.86 (s, 3H, -OCH₃), 2.27 (s, 3H, -CH₃); ¹³C NMR (75 MHz, CDCl₃): 175.45, 156.09, 137.61, 134.16, 130.25, 129.54, 129.08, 128.51, 127.46, 127.09, 121.08, 110.59, 97.88, 55.41, 52.11, 50.48, 29.60, 9.47.

RESULTS AND DISCUSSION

The chemical diagram of the studied compound (**1**) is illustrated in Scheme 1 and experimental conditions are summarized in Table 1.

Selected bond distances and bond angles are listed in Table 2.

Table 1. Crystal data and structure refinement for **1**

<i>Crystal Data</i>	
Empirical formula	C ₂₁ H ₂₁ N ₅ O ₅
Formula weight	391.49 g mol ⁻¹
Temperature	293(2) K
Wavelength	0.71073 Å
Crystal system	Triclinic
Space group	P $\bar{1}$
Hall Symbol	- P 1
Unit cell dimensions	a = 10.0624(5) Å, b = 10.3668(6) Å, c = 11.8773(9) Å, $\alpha = 91.865(4)^\circ$, $\beta = 114.838(2)^\circ$, $\gamma = 99.304(3)^\circ$
Volume	1102.58(12) Å ³
Z	2
Calculated Density	1.179 Mg/m ³
Absorption coefficient	0.166 mm ⁻¹
F(000)	412
Crystal Color, habit	colourless, needle
Crystal size	0.30 × 0.24 × 0.10 mm ³
<i>Data Collection</i>	
Diffractometer	Bruker APEX II CCD area detector
θ range for data collection	1.9 to 26.3°
Index ranges	-12 ≤ h ≤ 12, -12 ≤ k ≤ 12, -14 ≤ l ≤ 14
Reflections collected	20070
Independent reflections	20070 [R(int) = 0.0000]
Completeness to theta = 26.28°	99.1 %
<i>Refinement</i>	
Refinement method	Full-matrix least-squares on F^2
Absorption correction	Multi-scan
Data / restraints / parameters	20070 / 0 / 256
Goodness-of-fit on F^2	1.143
Final R indices [I > 2 σ (I)]	R1 = 0.0583, wR2 = 0.1778
R indices (all data)	R1 = 0.0717, wR2 = 0.1930
Largest diff. peak and hole	0.314 and -0.261 e.Å ⁻³
CCDC Deposition number	974620

A diagram of the molecular structure with 50% probability and the atom numbering scheme are shown in Fig. 1.

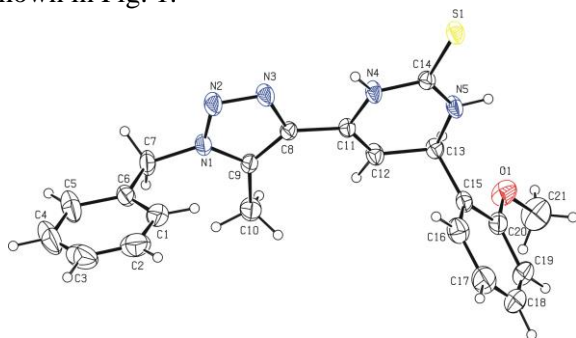


Fig. 1. View of the molecule with an atom-numbering scheme. Displacement ellipsoids for the non-H atoms are drawn at the 50% probability level. The H atoms are presented with spheres with arbitrary radii.

The data for publication were prepared with WinGX [11], ORTEP [12], Platon [13] and Mercury [14] program packages.

Hydrogen bonding geometry is presented in Table 3.

In the title compound, C₂₁H₂₁N₅OS, the essentially planar triazole (N1/N2/N3/C8/C9) ring [maximum deviation = 0.003(1) Å for the C9 atom] forms

dihedral angle of 7.7 (1)° with the pyrimidine (N4/N5/C11-C14) ring [maximum deviation = -0.032(1) Å for the C13 atom]. The methoxy phenyl ring attached to the pyrimidine ring is in equatorial position. The dihedral angle between the benzene rings is 61.9 (1)°. The methoxy group at C20 is almost coplanar with the attached benzene ring as evidenced by the torsion angle of C21–O1–C20–C19 = 1.7 (3)°. The phenyl group and triazole heterocycle are linked by methylene group at carbon atom C7 with C6–C7–N1 angle of 113.1 (1)° distorted from ideal tetrahedral geometry (109.7°). This can be attributed to steric factors of the adjacent cyclic system. The bond distances N3–C8, C8–C9, C9–N1, N1–N2 and N2–N3 are 1.362(2), 1.367(2), 1.358(2), 1.329(2) and 1.308(2) Å respectively, which agrees with C=C, N=N, C–N distances found in literature for compound having triazole heterocycles [15, 16].

The molecular conformation is stabilized by two weak intramolecular C13–H13...O1 and N4–H4A...N3 hydrogen bonds, both forming S(5) ring motifs [17] (Table 3).

Table 2. Bond lengths [Å] and angles [°] for 1

Bond distance			
C7 – N1	1.458(2)	C13 – C15	1.508(2)
C8 – N3	1.362(2)	C14 – N5	1.319(2)
C8 – C9	1.367(2)	C14 – N4	1.348(2)
C9 – N1	1.358(2)	C14 – S1	1.685(2)
C9 – C10	1.482(2)	C20 – O1	1.367(2)
C11 – C12	1.321(2)	C21 – O1	1.403(2)
C11 – N4	1.398(2)	N1 – N2	1.329(2)
C13 – N5	1.469(2)	N2 – N3	1.308(2)
Bond Angle			
N1 – C7 – C6	113.1(1)	N5 – C13 – C12	108.7(1)
N3 – C8 – C9	108.9(1)	N5 – C13 – C15	110.9(1)
N3 – C8 – C11	119.0(1)	C12 – C13 – C15	112.4(1)
C9 – C8 – C11	132.1(1)	N5 – C14 – N4	117.0(1)
N1 – C9 – C8	103.4(1)	N5 – C14 – S1	122.2(1)
N1 – C9 – C10	123.5(1)	N4 – C14 – S1	120.8(1)
C8 – C9 – C10	133.1(1)	O1 – C20 – C15	116.1(1)
C12 – C11 – N4	119.8(1)	O1 – C20 – C19	123.7(2)
N4 – C11 – C8	113.5(1)	C15 – C20 – C19	120.1(2)
N2 – N3 – C8	108.7(1)	N2 – N1 – C9	111.7(1)
C14 – N4 – C11	122.9(1)	N2 – N1 – C7	119.1(1)
C14 – N5 – C13	128.0(1)	C9 – N1 – C7	129.2(1)
C20 – O1 – C21	118.2(1)	N3 – N2 – N1	107.3(1)

Table 3. Hydrogen bond for 1(Å, °)

D–H...A	D–H	d(H...A)	d(D...A)	<(DHA)
C13–H13...O1	0.98	2.30	2.786(2)	109.0
N4–H4A...N3	0.86	2.31	2.690(2)	107.0
C7–H7B...S1 ⁱ	0.97	2.85	3.808(2)	169.8
N5–H5A...S1 ⁱⁱ	0.86	2.50	3.343(1)	166.1

Symmetry codes: (i) x-1, y, z; (ii) -x+2, -y+1, -z+1

In the crystal structure, C7–H7B...S1 contacts lead to the formation of a supramolecular chain along the *a*-axis. These chains are linked into a double layer *via* N5–H5A...S1 intermolecular hydrogen bonds forming $R_2^2(8)$ cyclic centrosymmetric dimers and intermolecular π – π interactions occur between inversion related molecules with $\text{Cg1} \dots \text{Cg2}^{iii} = 3.508(1)$ Å and $\text{Cg2} \dots \text{Cg1}^{iii} = 3.508(1)$ Å [Table 3 and Fig. 2; Cg1 and Cg2 are the centroids of the triazole (N1/N2/N3/C8/C9) ring and pyrimidine (N4/N5/C11–C14) ring, respectively, symmetry code: (iii) $1-x, 1-y, -z$].

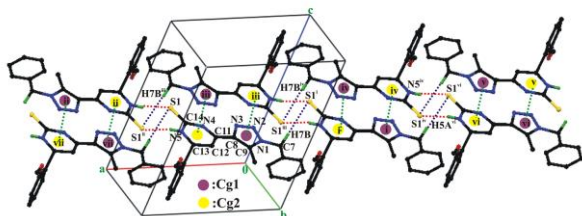


Fig. 2. View of the crystal packing showing supramolecular double layer along the *a*-axis, which involves the C–H...S (blue dotted lines), N–H...S (red dotted lines) and π – π (green dotted lines) interactions. [Cg1 and Cg2 are the centroids of the triazole (N1/N2/N3/C8/C9) ring and pyrimidine (N4/N5/C11–C14) ring, respectively, symmetry codes: (i) $-1+x, y, z$, (ii) $2-x, 1-y, 2-z$, (iii) $1-x, 1-y, 1-z$, (iv) $-x, 1-y, 1-z$, (v) $-1-x, 1-y, 1-z$, (vi) $-2+x, y, z$, (vii) $1+x, y, z$].

The resulting double layer stacks along the *b*-axis without any specific interactions (Fig. 3).

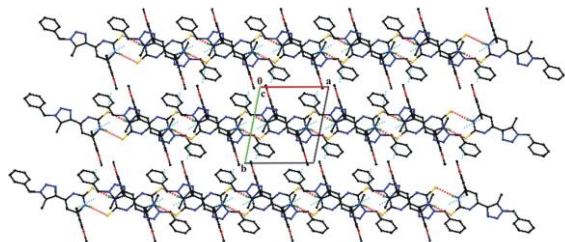


Fig. 3. View of the overall crystal packing highlighting the stacking of double layers along the *b*-axis.

CONCLUSION

The title compound was synthesized and confirmed by NMR and structural (single-crystal X-ray diffraction) techniques. The molecular conformation is stabilized by two weak intramolecular C–H...O and N–H...N hydrogen bonds. The crystal packing is stabilized by supramolecular chains mediated by C–H...O contacts along the *a*-axis linked into a double layer *via* N–H...S hydrogen bonds and π – π interactions.

SUPPLEMENTARY MATERIALS

CCDC 974620 contains the supplementary crystallographic data for this paper. The data can be obtained free of charge *via* www.ccdc.cam.ac.uk/data_request/cif, by e-mailing data_request@ccdc.cam.ac.uk, or by contacting The Cambridge Crystallographic Data Centre, 12 Union Road, Cambridge CB2 1EZ, UK; fax: +44(0)1223-336033.

Acknowledgements: The authors thank Dr. Babu Vargheese, SAIF, IIT, Madras, India, for his help with the data collection.

REFERENCES

1. J. Morales-Sanfrutos, M. Ortega-Munoz, J. Lopez-Jaramillo, F. Hernandez-Mateo, & F. Santoyo-Gonzalez, *J. Org. Chem.* **73**, 7768 (2008).
2. M.J. Genin, D.A. Allwine, D.J. Anderson, M.R. Barbachyn, D.E. Emmert, S.A. Garmon, D.R. Graber, K.C. Grega, J.B. Hester, D.K. Hutchinson, J. Morris, R.J. Reischer, C.W. Ford, G.E. Zurenko, J.C. Hamel, R.D. Schaadt, D. Stapert, & B.H. Yagi, *J. Med. Chem.* **43**, 953 (2000).
3. D.R. Buckle, C.J.M. Rockell, H. Smith, & B.A. Spicer, *J. Med. Chem.* **29**, 226 (1986).
4. M.J. Giffin, H. Heaslet, A. Brik, Y.C. Lin, G. Cauvi, C.H. Wong, D.E. McRee, J.H. Elder, C.D. Stout, & B.E. Torbett, *J. Med. Chem.*, **51**, 6263 (2008).
5. S. Wang, Q. Wang, Y. Wang, L. Liu, X. Weng, G.L.X. Zhang, & X. Zhou, *Bioorg. Med. Chem. Lett.*, **18**, 6505 (2008).
6. H.I. El-Subbagh, S.M. Abu-Zaid, M.A. Mahran, F.A. Badria, A.M. Al-Obaid, *J. Med. Chem.*, **43**, 2915 (2000).
7. A.R. Trivedi, D.K. Dodiya, N.R. Ravat, V.H. Shah, *Arkivoc.* **XI**, 131 (2008).
8. S. Nagarajan, M. Sathishkumar, P. Shanmugavelan, R.Ranganathan, A. Ponnuswamy, R. Venkatesn, V.Shanmugaiah, *Eur. J. Med. Chem.*, **58**, 464 (2012).
9. Bruker, *APEX-II and SAINT-Plus (Version 7.06a)*, Bruker AXS Inc. Madison, Wisconsin, USA, 2004.
10. G. M. Sheldrick, *Acta Cryst. A*, **64**, 112 (2008).
11. L. J. Farrugia, *J. Appl. Cryst.*, **32**, 837 (1999).
12. L. J. Farrugia, *J. Appl. Cryst.*, **30**, 565 (1997).
13. A.L. Spek, *J. Appl. Cryst.* **36**, 7 (2003).
14. I. J. Bruno, J.C. Cole, P. R. Edgington, M. Kessler, C. F. Macrae, P. McCabe, J. Pearson, R. Taylor, *Acta Cryst. B*, **58**, 389 (2002).
15. C.-C. Huang, F.-L. Wu, Y. H. Lo, W.-R. Lai and C.-H. Lin, *Acta Cryst.* **E66**, 1690 (2010).
16. J. I. Sarmiento-Sánchez, G. Aguirre and I. A. Rivero, *Acta Cryst.*, **E67**, o1856 (2011).
17. J. Bernstein, R.E. Davis, L. Shimoni, & N.-L. Chang, *Angew. Chem. Int. Ed. Engl.*, **34**, 1555 (1995).

СИНТЕЗ И КРИСТАЛНА СТРУКТУРА НА 6- (1-БЕНЗИЛ-5-МЕТИЛ-1Н-1, 2, 3-ТРИАЗОЛ-4-ИЛ) -4- (2-МЕТОКСИФЕНИЛ) -3,4-ДИГИДРОПИРИМИДИН-2 (1Н) - ТИОН

С. Муругавел¹ *, Д. Лакшманан², С. Нагараджан³, А. Понусвами³

¹ Катедра по физика, Правителствен институт по технологии „Тантаи Перияр“, Велор, Тамилнаду, Индия,

² Катедра по физика, Колеж по инженерство и технологии "С. Абдул Хакийм, Мелвишарам, Велор, Индия,

³ Катедра по органична химия, Факултет по химия, Университет „Мадурай Камарадже“, Мадурай, Тамилнаду, Индия.

Получена на 9 декември 2013 г.; Ревизирана на 22 февруари 2014 г.

(Резюме)

Структурата на 6- (1-бензил-5-метил-1Н-1,2,3-триазол-4-ил) -4- (2- methoxyphenyl) -3,4-дихидропиримидин-2 (1Н) -тион е определена чрез рентгенова кристалография. Съединението кристализира във вид на безцветни игли, оформени в триклинна система, пространствена група $P\bar{1}$ с клетъчните константи: $a = 10.0624(5) \text{ \AA}$, $b = 10.3668(6) \text{ \AA}$, $c = 11.8773(9) \text{ \AA}$, $\alpha = 91.865(4)^\circ$, $\beta = 114.838(2)^\circ$, $\gamma = 99.304(3)^\circ$, $V = 1102.58(12) \text{ \AA}^3$, $Z = 2$. Кристалната структура бе решена чрез директни методи и уточнена по пълната матрица на най-малките квадрати по F^2 до окончателни стойностите на $R_1 = 0.0583$ и $wR_2 = 0.1930$. В кристалната структура, супрамолекулярни вериги с посредничеството на С-Н ... О връзки по a -оста са свързани в двоен слой чрез НН ... S водородни връзки и π - π [разстоянието пръстенно центроиден (пиримидин) ... пръстенно центроиден (триазол) = $(3.508(1) \text{ \AA})$] взаимодействия. Получените двойни слоеве се подреждат по оста b без конкретни взаимодействия.

Green synthesis of 2-substituted benzothiazole derivatives under solvent-free conditions

G. Mohammadi Ziarani^{1*}, M. Shakiba Nahad¹, N. Lashgari²¹Department of Chemistry, Alzahra University, Tehran, Iran²School of Chemistry, College of Science, University of Tehran, Tehran, Iran

Received December 12, 2013; Revised July 19, 2014

A series of benzothiazole derivatives were efficiently synthesized in good to excellent yields *via* the reaction of 2-aminothiophenol with aromatic benzoyl chlorides under solvent-free conditions at room temperature in excellent yields and short reaction time.

Keywords: 2-aminothiophenol, benzothiazole derivatives, benzoyl chlorides, catalyst free, green synthesis, solvent free reaction.

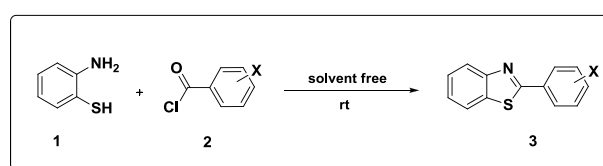
INTRODUCTION

Benzothiazole derivatives are known for different biological properties, including antitubercular, antimalarial, anticonvulsant, antihelmintic, analgesic, antidiabetic, antimicrobial, antibacterial, antifungal, herbicidal, antiproliferative and anti-inflammatory activities [1-3]. These compounds have antitumor activity against a range of human breast, ovarian, and colon cancers [4, 5]. They are also useful for the *in-vivo* diagnosis of Alzheimer's disease [6, 7].

Conventionally, 2-substituted benzothiazoles are synthesized by condensation of 2-aminothiophenol with aldehyde derivatives in different conditions. Various catalysts such as ZnO-beta zeolite [8], solid silica supported ferric chloride (SiO₂-FeCl₃) [9], glucose oxidase (GOX)/chloroperoxidase (CPO) [10], perchloric acid-doped polyaniline (HClO₄/PANI) [11], Sc(OTf)₃ [12], YCl₃ [13] and mixed metal oxide nano crystals of Al₂O₃-Fe₂O₃, Al₂O₃-V₂O₅ and Al₂O₃-CuO [14] were used in the synthesis of benzothiazoles. However, there is still room for improvement in the present methods so as to overcome the limitations and disadvantages of using organic solvents [9], long reaction times [10], low yields [11] and tedious work-up procedures [13]. In this paper we report our results on the development of an environmentally friendly protocol for the synthesis of 1,3-benzothiazole derivatives.

RESULTS AND DISCUSSION

Condensation of 2-aminothiophenol (1) with benzoyl chlorides (2) under solvent free conditions at room temperature gives 2-substituted benzothiazoles (3) (Scheme 1).



Scheme 1. Reaction of 2-aminothiophenol (1) with benzoyl chlorides (2)

At first, the reaction of 2-aminothiophenol (1) and 3-chlorobenzoyl chloride (2) was examined as a model experiment in different solvents such as polar protic (H₂O, EtOH, MeOH) and polar aprotic (CH₃CN, CH₂Cl₂, acetone, EtOAc) solvents at room temperature to get an insight into the solvent effect on the reaction yield. As shown in Table 1, in acetone the reaction yield was low (Table 1, entry 3), but in other solvents and also in solvent free conditions, product yield was quantitative.

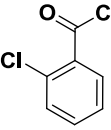
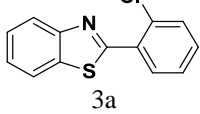
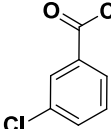
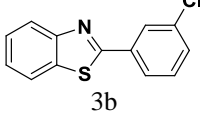
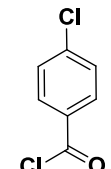
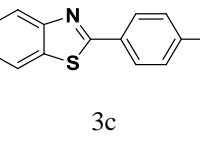
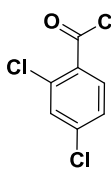
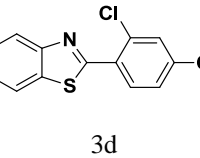
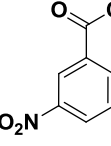
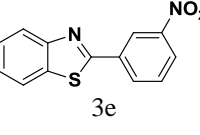
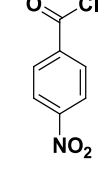
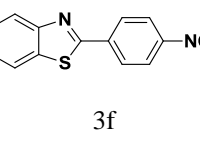
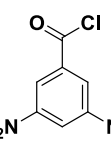
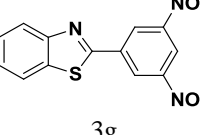
Table 1. Synthesis of benzothiazole derivatives in various solvents.

Entry	Solvent	Yield (%)
1	CH ₃ CN	quantitative
2	CH ₂ Cl ₂	99
3	Acetone	79
4	EtOAc	quantitative
5	H ₂ O	quantitative
6	EtOH	quantitative
7	MeOH	99
8	-	quantitative

Therefore, solvent-free condition at ambient temperature was selected as the optimal condition and was used to the synthesis of other derivatives. The results are summarized in Table 2.

* To whom all correspondence should be sent:
E-mail: gmziarani@hotmail.com

Table 2. Synthesis of benzothiazole derivatives under green conditions.

Entry	Benzoyl chloride	Product	Time (min)	Yield (%)	m.p. (°C)	m.p. (Ref.)
1		 3a	3	61	77-79	76-78 [15]
2		 3b	3	97	97-98	97-98 [16]
3		 3c	1-2	quantitative	118-119	117-118 [8]
4		 3d	1-2	quantitative	136-138	136 [17]
5		 3e	1	97	188 -189	186-188 [18]
6		 3f	2	quantitative	233-234	230-232 [18]
7		 3g	2	quantitative	237-238	-

These reactions were completed within 3 min. After completion of the reaction (monitored by TLC), the crude product was filtered and recrystallized in EtOH.

As shown in Table 2, in most cases, 2-aminothiophenol (1) reacted with a wide variety of substituted benzoyl chlorides (2) and afforded the corresponding benzothiazoles in good to excellent yields. Benzoyl chlorides with substituents at *ortho*, *meta*, and *para* positions were successfully employed to prepare the corresponding products, which shows the applicability of this protocol.

The suggested mechanism for the synthesis of 2-substituted benzothiazoles (3) is shown in Scheme 2. The NH₂ group of 2-aminothiophenol (1) attacks as nucleophilic reagent to the carbonyl group of the benzoyl chlorides (2) to give the intermediate (4). The nucleophilic attack of the SH group to the

carbonyl group of intermediate (4) resulted in ring closure followed by dehydration to create 2-benzothiazole derivatives (3) (Scheme 2).

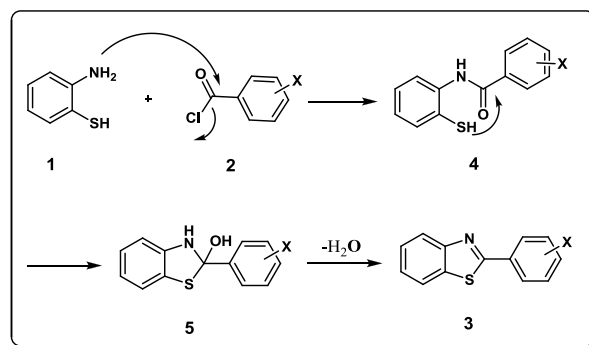
**Scheme 2.** Proposed mechanism

Table 3. Comparison of different conditions in the synthesis of benzothiazole derivatives (3).

Entry	Solvent	Catalyst	Condition	Time (h)	Yield (%)	Year	Ref.
1	1-Methyl-pyrrolidin-2-one	-	100 °C	1	75-95	1990	[16]
2	Pyridine	-	reflux	1	74-82	1996	[19]
3	Ethanol	SnCl ₂ .2H ₂ O	reflux	4	85-95	1996	[19]
4	Pyridine	-	multi step	2	12-85	1996	[20]
5	Toluene	-	r.t.	0.25-1	80-100	2005	[21]
6	-	-	r.t.	1-3 (min)	61-100		This work

The synthesis of benzothiazoles (**3**) with several catalysts in different solvents has been reported in the literature and the results are shown in table 3. In contrast with other existing methods, the present methodology which doesn't need any catalyst and solvent, offers several advantages, such as excellent yields, simple procedure, easy synthesis, simple work-up and greener conditions. The product structures were confirmed by IR, ¹H NMR and GC-mass data

EXPERIMENTAL SECTION

General information

GC-mass analysis was performed on a GC-mass model: 5973 network mass selective detector, GC 6890 Agilent. IR spectra were obtained with a Bruker 500 scientific spectrometer. ¹H NMR spectra of the products were recorded on a FT-NMR Bruker instrument at 250 MHz. Room temperature (r.t.) is 20–25 °C. Melting points were measured by the capillary tube method with an Electrothermal 9200 apparatus.

General procedure for the preparation of 2-(3-chlorophenyl) benzothiazole in various solvents (3b)

2-aminothiophenol (3.60 mmol, 0.38 mL) was dissolved in an appropriate solvent (5 mL) and 3-chlorobenzoyl chloride (3.60 mmol, 0.46 mL) was added to it. Then the mixture was stirred at room temperature for 5 min. After completion of the reaction (TLC: *n*-hexane/EtOAc, 2/1), the crude product was filtered and recrystallized from hot ethanol.

General procedure for the preparation of benzothiazole derivatives under solvent free conditions (3)

2-aminothiophenol (3.60 mmol, 0.38 mL) was placed in a flask and then benzoyl chloride (3.60 mmol) was added to it. The mixture was stirred at room temperature until completion of the reaction which was indicated by TLC (*n*-hexane/EtOAc,

1/1). The resulting crude product was recrystallized from EtOH. The spectroscopic and analytical data for selected compounds are presented in the following part.

Spectral Data of Products

2-(3-chlorophenyl)-1,3-benzothiazole (**3b**): IR (KBr): ν_{\max} = 3053, 1622, 1567, 1457, 759, 730, 674 cm⁻¹. ¹H NMR (250 MHz, DMSO-d₆): δ_{H} = 7.44-7.64 (m, 4H), 8.05 (t, 2H, *J* = 20 Hz), 8.02-8.13 (m, 2H) ppm.

2-(4-chlorophenyl)-1,3-benzothiazole (**3c**): IR (KBr): ν_{\max} = 3066, 1598, 1521, 1342, 851, 767, 728, 684 cm⁻¹. ¹H NMR (250 MHz, DMSO-d₆): δ_{H} = 7.43-7.64 (m, 4H), 8.04-8.16 (m, 4H) ppm. Mass (m/e): 245, 210, 122, 108.

2-(4-nitrophenyl)-1,3-benzothiazole (**3f**): IR (KBr): ν_{\max} = 3066, 1598, 1521, 1342, 851, 767, 728, 684 cm⁻¹. ¹H NMR (250 MHz, DMSO-d₆): δ_{H} = 7.52-7.62 (m, 2H), 8.12-8.23 (dd, 2H, *J* = 8 Hz), 8.32-8.36 (m, 4H) ppm.

2-(3,5-dinitrophenyl)-1,3-benzothiazole (**3g**): IR (KBr): ν_{\max} = 3099, 1626, 1541, 1451, 1342, 769, 726 cm⁻¹. ¹H NMR (250 MHz, DMSO-d₆): δ_{H} = 7.55-7.65 (m, 3H), 8.17-8.26 (dd, 2H, *J* = 8 Hz), 8.92 (s, 1H), 9.06 (s, 1H) ppm.

CONCLUSION

In summary, a novel and highly efficient method for quick synthesis of benzothiazoles was developed by the reaction of aromatic benzoyl chlorides with 2-aminothiophenol. The reactions were carried out at r.t. and high yields obtained were comparable to those reported in the literature. A major advantage of our procedure is the very short reaction time (1-3 min) without use of any catalyst or solvents. Other attractive features of this protocol are: simple procedure, high yields, simple workup and non-chromatographic purification of the products.

Acknowledgments: We gratefully acknowledge the financial support from the Research Council of Alzahra University.

REFERENCES

1. Z. Wang, X. H. Shi, J. Wang, T. Zhou, Y. Z. Xu, T. T. Huang, Y. F. Li, Y. L. Zhao, L. Yang, S. Y. Yang, L. T. Yu, Y. Q. Wei, *Bioorg. Med. Chem. Lett.*, **21**, 1097 (2011).
2. M. D. Altıntop, Z. A. Kaplancıklı, G. I. T. Zitouni, A. O. zdemir, F. Demirci, G. k. Is, can, G. Revial, *Synth. Commun.*, **41**, 2234 (2011).
3. P. Datta, D. Sardar, A. P. Mukhopadhyay, E. L. Torres, C. J. Pastor, C. Sinha, *J. Organomet. Chem.*, **696**, 488 (2011).
4. Y. Q. Yuan, S. R. Guo, *Synth. Commun.*, **41**, 2169 (2011).
5. T. H. Al-Tel, R. A. Al-Qawasmeh, R. Zaarour, *Eur. J. Med. Chem.*, **46**, 1874 (2011).
6. B. H. Yousefi, A. Manook, A. Drzezga, B. V. Reutern, M. Schwaiger, H. J. Wester, G. Henriksen, *J. Med. Chem.*, **54**, 949 (2011).
7. T. I. A. Gerber, K. C. Potgieter, P. Mayer, *Inorg. Chem. Commun.*, **14**, 1115 (2011).
8. S. S. Katkar, P. H. Mohite, L. S. Gadekar, K. N. Vidhate, M. K. Lande, *Chin. Chem. Lett.*, **21**, 421 (2010).
9. M. H. Mosslemin, A. Fazlinia, *Phosphorus, Sulfur Silicon Relat. Elem.*, **185**, 2165 (2010).
10. A. Kumar, S. Sharma, R. A. Maurya, *Tetrahedron Lett.*, **51**, 6224 (2010).
11. M. Abdollahi-Alibeik, S. Poorirani, *Phosphorus, Sulfur Silicon Relat. Elem.*, **184**, 3182 (2009).
12. T. Itoh, K. Nagata, H. Ishikawa, A. Ohsawa, *Heterocycles*, **62**, 197 (2004).
13. L.-J. Zhang, J. Xia, Y.-Q. Zhou, H. Wang, S.-W. Wang, *Synth. Commun.*, **42**, 328 (2012).
14. P. Bandyopadhyay, M. Sathe, G. K. Prasad, P. Sharma, M. P. Kaushik, *J. Mol. Catal. A: Chem.*, **341**, 77 (2011).
15. T. G. Deligeorgiev, S. Kaloyanova, A. Vasilev, J. J. Vaquero, *Phosphorus, Sulfur Silicon Relat. Elem.*, **185**, 2292 (2010).
16. A. Brembilla, D. Roizard, P. Lochon, *Synth. Commun.*, **20**, 3379 (1990).
17. D. S. Deshpande, N. V. S. Subbarao, *J. Sci. Ind. Research.*, **16 B**, 136 (1957).
18. A. A. Weekes, M. C. Dix, M. C. Bagley, A. D. Westwell, *Synth. Commun.*, **40**, 3027 (2010).
19. M. F. G. Stevens, D. F. Shi, A. Castro, *J. Chem. Soc., Perkin Trans.*, **1**, 83 (1996).
20. D. F. Shi, T. D. Bradshaw, S. Wrigley, C. J. McCall, P. Lelieveld, I. Fichtner, M. F. G. Stevens, *J. Med. Chem.*, **39**, 3375 (1996).
21. S. Rudrawar, A. Kondaskar, A. K. Chakraborti, *Synthesis*, 2521 (2005).

ЗЕЛЕНА СИНТЕЗА НА 2-СУБСТИТУИРАНИ ПРОИЗВОДНИ НА БЕНЗОТИАЗОЛА В ОТСЪСТВИЕ НА РАЗТВОРИТЕЛ

Г. Мохамеди Зиарани^{*1}, М. Шакиба Нахад¹, Н. Лашгари²

¹) Департамент по химия, Университет Алзахра, Техеран, Иран

²) Школа по химия, Колеж по наука, Университет в Техеран, Иран

Получена на 12 декември, 2013г.; коригирана на 19 юли, 2014 г.

(Резюме)

Успешно са синтезирани производни на бензотиазола чрез реакция на 2-аминофенол и ароматни бензоилхлориди в отсъствие на разтворител при стайна температура с отлични добиви и за кратко време.

Synthesis, characterization and study of photocatalytic activity of nanocomposites of oxides and sulfides of Ni(II) and Ni(III)

H. R. Pouretedal^{1*}, F. Momenzadeh²

¹ Faculty of Applied Chemistry, Malek-ashtar University of Technology, Shahin-Shahr, Iran,

² Department of Chemistry, Islamic Azad University, Shahreza Branch, Shahreza, Iran

Received December 21, 2013; Revised May 1, 2014

Nanoparticles of NiO, NiS, Ni₂O₃, Ni₂S₃, NiO_{0.5}S_{0.5} and Ni₂O_{1.5}S_{1.5} were synthesized by a controlled precipitation method. The prepared nanoparticles were calcined at temperature 700 °C. The X-ray diffraction patterns of the nanoparticles showed cubic structure for NiO, Ni₂O₃, Ni₂S₃, NiO_{0.5}S_{0.5} and Ni₂O_{1.5}S_{1.5}, while the nanosized NiS displayed cubic and hexagonal structure. The absorption peaks at wavenumbers of 600-400 cm⁻¹ in the FT-IR spectra showed the existence of S-Ni and S-Ni-S vibrations. A red shift of 30 nm was observed in the DRS UV-Vis spectra of NiO_{0.5}S_{0.5} and Ni₂O_{1.5}S_{1.5} nanocomposites with respect to the nanoparticles of oxide and sulfide of Ni (II) and Ni(III). The band-gap energies were 5.79, 5.71, 5.64, 5.51, 4.96 and 4.86 eV for Ni₂S₃, Ni₂O₃, NiO, NiS, NiO_{0.5}S_{0.5} and Ni₂O_{1.5}S_{1.5}, respectively. The TEM image showed that the size of the Ni₂O_{1.5}S_{1.5} nanocomposite was less than 70 nm. The existence of Ni, S and O atoms in the structure of Ni₂O_{1.5}S_{1.5} nanocomposite was proved by energy dispersive X-ray analysis. The photocatalytic activity of the prepared nanoparticles was studied in the photodegradation reaction of methyl blue dye. The trend of the photocatalytic activity of the prepared nanoparticles in photodegradation of methyl blue was: Ni₂O_{1.5}S_{1.5} > NiO_{0.5}S_{0.5} > NiS > NiO > Ni₂O₃ > Ni₂S₃. The pH of the point of zero charge of the nanocomposites was ~6.0. The optimized conditions of the photodegradation process were: pH 7, 0.5 g L⁻¹ of photocatalyst, 20 mg L⁻¹ of dye and irradiation time of 60 min.

Keywords: Nanocomposite, nanoparticle, photocatalyst, methyl blue, nickel.

INTRODUCTION

High-efficiency photocatalysts have been actively sought due to their potential applications in the decomposition of toxic and hazardous materials [1,2], in water splitting for hydrogen energy production [3,4] and in photoelectrochemical or solar cell devices [5,6]. There have been various kinds of efforts to develop more efficient versions of photocatalysts than the well-known TiO₂ [7].

Intense research activity is seen in recent years in advancing the synthesis and functionalization of various sizes and shapes of semiconductors as photocatalysts. The goal of these activities is to improve the performance and utilization of nanophotocatalysts in order to enhance the efficiency of advanced oxidation techniques (AOTs) [8]. The photocatalytic activity is dependent on the size and shape of the photocatalyst particles. Maximizing the efficiency of photoinduced charge separation in semiconductor systems remains a major challenge to the scientific community [9]. Obtaining insight into charge transfer processes is important to improve the photoconversion efficiencies in semiconductor-based nanoassemblies. Extending

the photoresponse of the particles is a common goal and improving efficiency by using various combinations of particle materials is often attempted. Quantization and its effects on charge transfer, the processes that are induced by charge separation at the particle surface are the focus of many of the current advances in the field and dual use of these materials, as well as combination of AOTs is often explored [10,11].

In recent years, research on the coupling of semiconductor photocatalysts as nanocomposite alloys has taken place for increasing the efficiency of AOTs. The coupling of photocatalyst nanoparticles is due to interfacial charge transfer between two different semiconductors with disparately favorable band edge energy levels [12,14].

Although charge transfer to adsorbate species is the desired behavior of electron-hole pairs (EHPs), the vast majorities recombine, creating a loss in photocatalytic efficiency often greater than 90%. This recombination process between the photoexcited electron and the hole can occur either in the bulk of the semiconductor particle or on its surface with a byproduct of heat release [15]. The EHP recombination process itself results when the electron-hole recombination time is shorter than the time needed by the carrier to diffuse to the surface.

* To whom all correspondence should be sent:
E-mail: hamidrezapouretedal@yahoo.com

The use of nanocomposite alloys as photocatalysts can extend the electron-hole recombination time. Thus, an increase in reactivity of electron/hole (e/h^+) pairs is observed with reduction of the rate of electron-hole recombination [16].

The most common semiconducting metal oxide is TiO_2 . However, other semiconducting metal oxides and metal sulfides such as NiO and NiS appear to be especially efficient as catalysts for wastewater pollution abatement. NiO is a p-type semiconductor characterized by a wide band gap between 3.1-3.5 eV that makes it suitable for photocatalytic processes [17,18].

NiS (a p-type semiconductor) is showing metal-insulator transition by doping or as a function of temperature and pressure. NiS semiconductor shows antiferromagnetic and paramagnetic properties in low and high temperature phases, respectively [19,20]. NiS films have been used as catalysts and coatings in photovoltaic cells. Catalysts have broad application in oil industry, for the separation of sulphur and nitrogen that often coexist with hydro-compounds from insulators. NiS is used as a holder in hydro-process catalysts [21,22].

The goal of this research is the synthesis of nanocomposites of oxides and sulfides of Ni(II) and Ni(III) as $NiO_{0.5}S_{0.5}$ and $Ni_2O_{1.5}S_{1.5}$. The photocatalytic activity of the prepared nanocomposites is studied in the photodegradation process of methyl blue dye and compared with the reactivity of NiO, NiS, Ni_2O_3 and Ni_2S_3 nanoparticles. The photocatalytic activity of the nanocomposites is discussed on the basis of the results of nanoparticles characterization.

EXPERIMENTAL

Preparation of nanocomposites

Nanosized powders of NiO, NiS, Ni_2O_3 , Ni_2S_3 , $NiO_{0.5}S_{0.5}$ and $Ni_2O_{1.5}S_{1.5}$ were prepared by precipitation and co-precipitation methods [23,24]. $Ni(NO_3)_2 \cdot 6H_2O$ was used as the precursor and ammonia (1:1) and $Na_2S \cdot 9H_2O$ were used as precipitants. The $Ni(OH)_2$ precipitate was formed with addition of ammonia solution to Ni^{2+} solution (50 ml 0.05 mol/L) at room temperature under vigorous stirring. The pH of the sample was maintained at pH=5.0. The sulfide solution (0.05 mol/L) was added drop-wise so that the Ni(II) ions were completely transformed to the precipitate NiS. The oxidizing agent $KClO_3$ was used to oxidize Ni(II) to Ni(III) for the preparation of Ni_2O_3 and Ni_2S_3 powders. Stoichiometric amounts of ammonia and/or Na_2S were added to a solution

containing 0.05 mol/L of Ni^{2+} and 0.1 mol/L of $KClO_3$. Then, the precipitates of $Ni(OH)_3$ and Ni_2S_3 were used to prepare nanoparticles of Ni_2O_3 and Ni_2S_3 , respectively. For preparation of $NiO_{0.5}S_{0.5}$ nanocomposite, stoichiometric amount of sulfide solution was added to Ni(II) solution so that half of the nickel ions was converted to NiS and then the pH of the samples was brought to 5 with addition of ammonia solution for conversion of the other half of Ni^{2+} ions to $Ni(OH)_2$ precipitate. The nanocomposite $Ni_2O_{1.5}S_{1.5}$ was prepared similarly to the $NiO_{0.5}S_{0.5}$ nanocomposite using $KClO_3$ to oxidize Ni(II) to Ni(III) ions.

The formed precipitates were filtered and washed with deionized water and ethanol. The wet powders were dried at about 100 °C and then calcined at a temperature of 700 °C in air for 4 h.

Characterization of the nanoparticles

The XRD patterns of the nanoparticles were obtained on a diffractometer Bruker D8 ADVANCE, Germany with Cu anode ($\lambda=1.5406 \text{ \AA}$ of Cu $K\alpha$) and Ni filter. A JEOL JEM-1200EXII transmission electron microscope (TEM) operating at 120 kV was used for estimation of nanoparticles size. The supporting grids were formvar-covered, carbon-coated 200-mesh copper grids. A Philips XL30 scanning electron microscope was used to observe the composition of the nanocomposites. The absorbance spectra of the prepared nanosized materials were recorded by a UV-Vis spectrophotometer Carry-100. Nicolet Impact 400D FT-IR spectrophotometer was used to record the IR-spectra of the prepared photocatalysts in the range 4000-400 cm^{-1} .

Photocatalytic activity

The photocatalytic activity of the prepared nanoparticles and nanocomposites was studied in the photodegradation reaction of methyl blue dye. The samples were irradiated in a photoreactor containing a 36 W mercury low-pressure lamp. A light path of 5.0 cm was used in the photoreactor cell. The photoreactor was filled with 100 ml of 20 mg/L of methyl blue and 0.1-3.0 g/L of the photocatalyst at a pH of 2-9. The pH of the samples was adjusted by sodium hydroxide and hydrochloric acid solutions of concentration 0.1 mol/L. A water-cooled jacket was applied outside the photoreactor to maintain the temperature at 30 °C. All reactants in the degradation reaction were stirred in the photoreactor cell by a magnetic stirrer for 30-180 min. A time of 30 min in dark was applied to set the adsorption/desorption

equilibrium of methyl blue on the surface of the heterogeneous catalysts.

A UV-Vis spectrophotometer Carry-100 was used to measure the absorbance of the samples before and after definite times of irradiation. The decoloration efficiency (%D) was obtained as: $\%D = 100 \times [(Co-Ct)/Co]$. The Co and Ct were the initial and the final concentration at a time, respectively. A centrifuge was used to separate suspended particles before absorbance measurement.

The pH of samples played an important role in the decoloration of dye. The pH of point of zero charge (pH of PZC) of nanocomposites was determined as follows. The initial pH values of several suspensions containing 1.0 g/L of the nanoparticles and 1.0 mol/L of NaCl were adjusted to 2-9 with addition of HCl and NaOH solutions. After 24 h, the final pH values of the suspensions were measured again. The pH of PZC was obtained from the intersection of the curve of initial pHs versus final pHs with the diagonal of square [25].

RESULTS AND DISCUSSION

Characterization of nanoparticles

The XRD patterns of the prepared nanoparticles of NiO, NiS, Ni₂O₃, Ni₂S₃, NiO_{0.5}S_{0.5} and Ni₂O_{1.5}S_{1.5} are shown in Fig. 1.

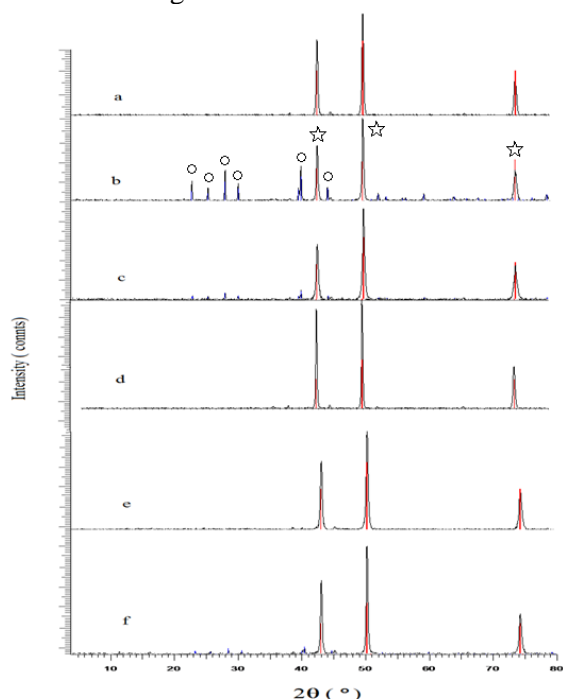


Fig. 1. XRD patterns of nanoparticles of (a) NiO, (b) NiS, (c) NiO_{0.5}S_{0.5}, (d) Ni₂O₃, (e) Ni₂S₃, and (f) Ni₂O_{1.5}S_{1.5} calcined at 700 °C. The signs of star and circle show the peaks of cubic and hexagonal structure, respectively.

The XRD patterns are shown below for comparison. The scale on the vertical axis is the same for all XRD patterns. The nanosized powders were calcined at a temperature of 700 °C. As seen, a cubic structure with diffraction peaks at 2θ of 43, 50 and 74° was observed for NiO, Ni₂O₃ and Ni₂S₃ nanoparticles [26-29]. For nanosized NiS the diffraction peaks at 2θ of 22, 24, 27, 29, 39 and 43° were related to the hexagonal structure and diffraction peaks at 2θ of 43, 50 and 74° were related to the cubic structure [21,22,26,27]. The nanocomposites of Ni₂S₃ NiO_{0.5}S_{0.5} and Ni₂O_{1.5}S_{1.5}, as well as the other oxides and sulfides of Ni(II) and Ni(III) showed a cubic structure with diffraction peaks at 2θ of 43, 50 and 74°.

The crystallite size D of the nanoparticles was estimated by the Scherrer's formula ($D = k\lambda/\beta\cos\theta$), where k is a constant = 0.94, λ is the X-ray wavelength, θ is the Bragg angle of the peak under consideration and β is the full width at half maximum (FWHM) of the diffraction peak [28,29]. The size of the prepared nanoparticles thus obtained was < 25 nm.

The FT-IR spectra of the nanocomposites of NiO_{0.5}S_{0.5} and Ni₂O_{1.5}S_{1.5} calcined at temperature of 700 °C are shown in Fig. 2.

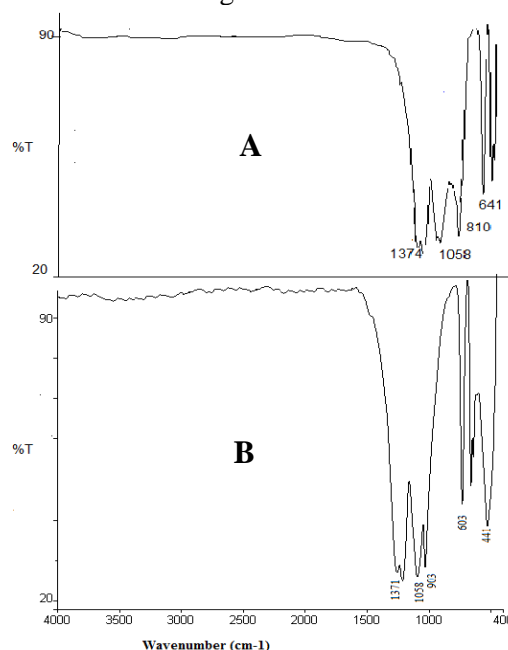


Fig. 2. FT-IR spectra of nanocomposites of NiO_{0.5}S_{0.5} (A) and Ni₂O_{1.5}S_{1.5} (B).

The bands in the range of 1370-800 cm⁻¹ can be attributed to vibrations of stretching and bending of the nitrogen-oxygen, sulfur-oxygen and nitrogen-sulfur bonds. The peaks at 441 and 603 cm⁻¹ were

due to the metal-nonmetal (Ni-S, Ni-O, S-Ni-S and O-Ni-O) stretch [30,31].

It is well known that the photocatalytic activity of a photocatalyst is dependent on the band-gap energy. The UV-Vis absorption bands can be used to determine band-gap energies of semiconductor materials. The DRS UV-Vis spectra of the prepared nanoparticles are shown in Fig. 3.

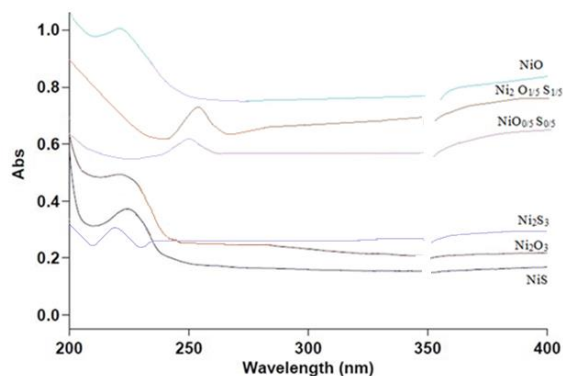


Fig. 3. UV-Vis spectra of the prepared nanoparticles calcined at 700 °C.

The absorption bands show maximum absorption at wavelengths (λ_{\max}) of 214, 217, 220, 225, 250 and 255 nm for Ni_2S_3 , Ni_2O_3 , NiO , NiS , $\text{NiO}_{0.5}\text{S}_{0.5}$ and $\text{Ni}_2\text{O}_{1.5}\text{S}_{1.5}$, respectively. The band-gap was calculated using the Planck's equation (Band-gap, eV = $1240/\lambda_{\max}$, nm) [32]. Band-gap energies of 5.79, 5.71, 5.64, 5.51, 4.96 and 4.86 eV were obtained for Ni_2S_3 , Ni_2O_3 , NiO , NiS , $\text{NiO}_{0.5}\text{S}_{0.5}$ and $\text{Ni}_2\text{O}_{1.5}\text{S}_{1.5}$, respectively. Therefore, the obtained results showed that the nanocomposites of oxides and sulfides of Ni(II) and Ni(III) have a lower band-gap energy in comparison with the Ni_2S_3 , Ni_2O_3 , NiO and NiS nanoparticles. Also, the absorption spectrum of Ni_2S_3 , Ni_2O_3 , NiO and NiS nanoparticles shows an obvious blue shift compared with that of bulk oxides and sulfides of nickel (~2.1 - ~3.9 eV) [26-29,33]. The increase in the surface area of the nanoparticles *versus* bulk materials is an important factor for photocatalysts. The band-gap energy increases with decreasing the size of the prepared particles, so that the increasing in band-gap can be due to a decrease in photocatalytic activity [33,34]. However, the synthesis of nanocomposites can be a solution for excessive perversion of band-gap energy. So, a red shift is seen at the λ_{\max} of the nanocomposites of $\text{NiO}_{0.5}\text{S}_{0.5}$ and $\text{Ni}_2\text{O}_{1.5}\text{S}_{1.5}$ compared with NiO , NiS , Ni_2S_3 and Ni_2O_3 , respectively.

The size of the nanocomposite particles of $\text{Ni}_2\text{O}_{1.5}\text{S}_{1.5}$ was further examined by transmission electron microscopy (TEM). The TEM image of the synthesized $\text{Ni}_2\text{O}_{1.5}\text{S}_{1.5}$ is shown in Fig. 4.

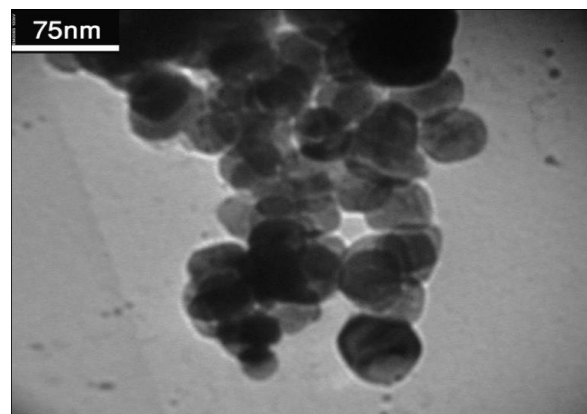


Fig. 4. TEM image of the nanocomposite of $\text{Ni}_2\text{O}_{1.5}\text{S}_{1.5}$ calcined at 700 °C.

The micrograph shows that the nanoparticles are uniformly distributed and are almost spherical in shape. The size of the obtained particles is less than 75 nm.

Energy dispersive spectroscopy (EDS) can be used for qualitative analysis of elements in a composite. Figure 5 shows the EDS spectrum of $\text{Ni}_2\text{O}_{1.5}\text{S}_{1.5}$ nanocomposite that confirms the presence of nickel, oxygen and sulfur in the obtained composite [31].

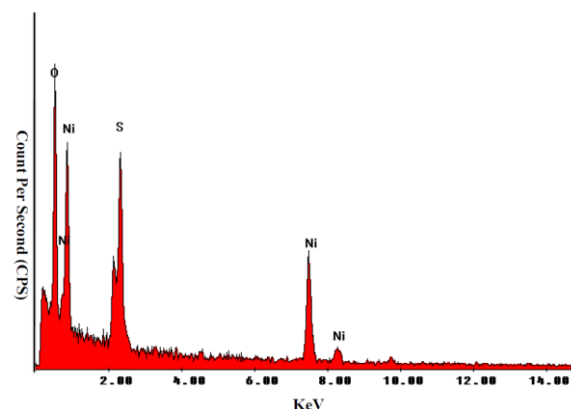


Fig. 5. Energy-dispersive X-ray analysis (EDAX) of the nanocomposite of $\text{Ni}_2\text{O}_{1.5}\text{S}_{1.5}$ calcined at 700 °C.

Photocatalytic activity of nanocomposites

The photocatalytic activity of the prepared nanoparticles was studied in methyl blue photodegradation. The optimized conditions were found by using one-factor-at-a-time method. pH of samples, dose of photocatalysts, initial concentration of dye and irradiation time were the investigated factors.

At first, the pH of the samples was optimized because the surface charge of semiconductors in aqueous samples and the charge of dye molecules are pH-dependent. It is well known that the surface charge of semiconductors is also dependent on the pH of point of zero charge (pH_{PZC}) [35,36]. The

pH_{PZC} of the nanocomposites of $NiO_{0.5}S_{0.5}$ and $Ni_2O_{1.5}S_{1.5}$ has a value of ~ 6 (Fig. 6).

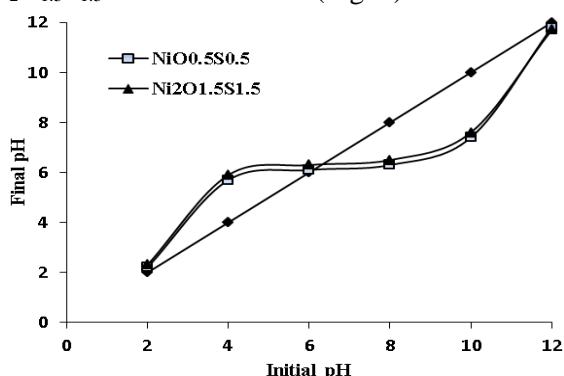


Fig. 6. The pH_{PZC} of nanocomposites of $NiO_{0.5}S_{0.5}$ and $Ni_2O_{1.5}S_{1.5}$.

As a result, the pH_{PZC} of Ni_2S_3 , Ni_2O_3 , NiO and NiS nanoparticles is also ~ 6 . Therefore, the surface charge of semiconductors is positive at $pHs < 6$ and negative at $pHs > 6$. The effect of pH of samples on the reactivity of photocatalysts is indicated in Fig. 7.

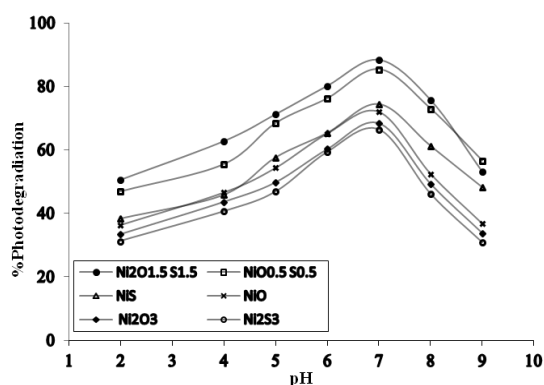


Fig. 7. Effect of pH on the photodegradation efficiency of methyl blue using 0.25 g/L of photocatalyst, 20 mg/L of dye and irradiation time of 60 min.

The highest reactivity was obtained at pH 7. Based on the pH_{PZC} of nanocomposites, the surface of semiconductors is neutral at pH 7. Thus, the pollutant molecules with neutral and/or negative charges are adsorbed on the surface of the catalysts at pH 7. The photodegradation yields decrease at alkaline pHs because there is a repulsion force between the charge of dye molecules and the surface charge of photocatalyst nanoparticles at $pH > 7$.

Fig. 8 shows that the photocatalytic efficiency of the prepared nanoparticles increases with increasing the dose of photocatalysts up to 0.5 g/L and then decreases. The turbidity of the suspension of heterogeneous catalysts at high amounts is due to a decrease in radiation penetration [37].

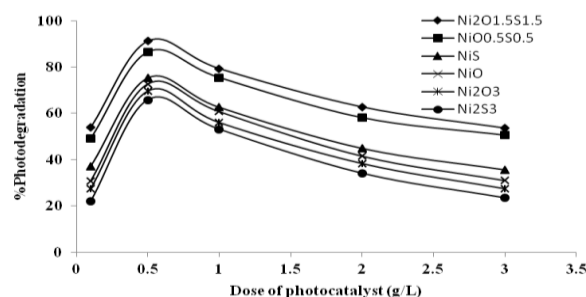


Fig. 8. Effect of photocatalyst dose on the photodegradation efficiency of methyl blue at pH 7, 20 mg/L of dye and irradiation time of 60 min.

The photocatalytic activity was also studied by determining the kinetics of methyl blue photodegradation reaction at initial concentration of 20 mg/L of dye, pH of 7 and 0.5 g/L of photocatalyst. The pseudo-first-order rate constants, k_{obs} (min^{-1}), were obtained using Langmuir–Hinshelwood kinetic expression ($\ln(C_0/C_t) = k_{obs}t$) [38]. The obtained curves are shown in Fig. 9 and the k_{obs} values are collected in Table 1.

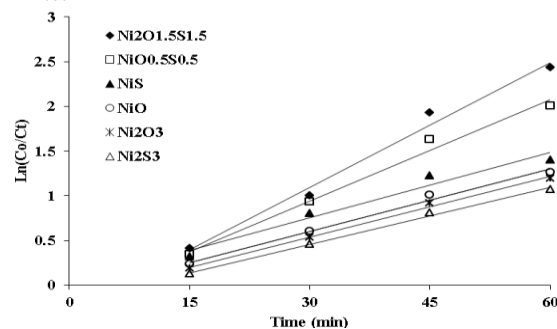


Fig. 9. The variations of $\ln(C_0/C_t)$ versus time for methyl blue photodegradation reaction in presence of different photocatalysts.

The data of Table 1 show that the order of photocatalytic activity of the nanoparticles is: $Ni_2O_{1.5}S_{1.5} > NiO_{0.5}S_{0.5} > NiS > NiO > Ni_2O_3 > Ni_2S_3$.

As mentioned, the band-gap energies of Ni_2S_3 , Ni_2O_3 , NiO , NiS , $NiO_{0.5}S_{0.5}$ and $Ni_2O_{1.5}S_{1.5}$ are: 5.79, 5.71, 5.64, 5.51, 4.96 and 4.86 eV, respectively. Thus, the proposed nanocomposites with lower band-gap energy show higher photocatalytic activity. The new nanocomposites, as well as the nanoparticles of oxides and sulfides of Ni(II) and Ni(III) have higher band-gap energy than their bulk materials. However, the increase in band-gap can be an advantage for a photocatalyst.

Recombination of electrons and holes in a semiconductor is a restricting factor for photocatalytic activity. The lifetime of electrons and holes in conductance and capacitance bands, respectively, increases with addition of band-gap

Table 1. The $k_{\text{obs}} \pm S_D$ values of methyl blue photodegradation reaction catalyzed by the prepared photocatalysts, S_D is standard deviation related to $n=3$.

Photocatalyst	Ni ₂ O _{1.5} S _{1.5}	NiO _{0.5} S _{0.5}	NiS	NiO	Ni ₂ O ₃	Ni ₂ S ₃
k_{obs} (min ⁻¹)	46.6±1.2×10 ⁻³	37.8±1.0×10 ⁻³	24.4±1.1×10 ⁻³	23.3±0.9×10 ⁻³	22.6±1.0×10 ⁻³	21.3±0.7×10 ⁻³

energy. At these conditions, the concentration of active radicals such as •OH radicals increases, thus increasing of the kinetics of degradation reaction is expected. On the other hand, available sites on a heterogeneous catalyst increase with decreasing size of particles. Thus, higher rate for photodegradation of a pollutant is achieved by using the new nanocomposites [39,40].

CONCLUSIONS

A simple precipitation method can be used to prepare new nanocomposites of NiO_{0.5}S_{0.5} and Ni₂O_{1.5}S_{1.5}. The proposed nanosized composites of nickel oxide and sulfide have a narrower band-gap in comparison with nickel oxide and nickel sulfide. The new nanocomposites exhibit higher photocatalytic activity.

REFERENCES

- L.L. Garza-Tovar, L.M. Torres-Martinez, D. B. Rodriguez, R. Gomez, G. del Angel, *J. Mol. Catal.*, **A 247**, 283 (2006).
- V.N. Blaskov, I.D. Stambolova, S.V. Vassilev, *Bulgarian Chem. Commun.* **45**, 263 (2013).
- P. Dhanasekaran, N.M. Gupta, *Intern. J. Hydrogen Energy*, **37**, 4897 (2012).
- H. Hagiwara, M. Nagatomo, C. Seto, S. Ida, T. Ishihara, *J. Photochem. Photobiol.*, **A 272**, 41 (2013).
- N.G. Dhere, A.H. Jahagirdar, *Thin Solid Films*, **480–481**, 462 (2005).
- R. Afeesh, N.A.M. Barakat, S.S. Al-Deyab, A. Yousef, H.Y. Kim, *Colloids Surfaces*, **A 409**, 21 (2012).
- A.L. Linsebigler, G. Lu, J.T. Yates, *Chem. Rev.*, **95**, 735 (1995).
- G. Gyawali, R. Adhikari, B. Joshi, T.H. Kim, V. Rodríguez-González, S.W. Lee, *J. Hazard. Mater.*, **263**, 45 (2013).
- L. Cheng, Y. Kang, *J. Alloy Compd.* **585**, 85 (2014).
- R. Adhikari, G. Gyawali, S. H. Cho, R. Narro-García, T. Sekino, S.W. Lee, *J. Solid State Chem.*, **209**, 74 (2014).
- G. Wu, S. S. Thind, J. Wen, K. Yan, A. Chen, *Appl. Catal.*, **B 142–143**, 590 (2013).
- K. Sridharan, E. Jang, T. J. Park, *Appl. Catal.*, **B 142–143**, 718 (2013).
- Y. Yu, G. Chen, G. Wang, Z. Lv, *Intern. J. Hydrogen Energy*, **38**, 1278 (2013).
- X. Fu, W. Tang, L. Ji, S. Chen, *Chem. Eng. J.*, **180**, 170 (2012).
- X. Pan, Y.-J. Xu, *Appl. Catal.*, **A 459**, 34 (2013).
- J. Chen, G. Li, Y. Huang, H. Zhang, H. Zhao, T. An, *Appl. Catal.*, **B 123–124**, 69 (2012).
- L. Li, K.S. Hui, K.N. Hui, H.W. Parka, D.H. Hwang, S. Cho, S.K. Lee, P.K. Song, Y.R. Cho, H. Lee, Y.G. Son, W. Zhou, *Mater. Lett.*, **68**, 283 (2012).
- A. K. Srivastava, S. Thota, J. Kumar, *J. Nanosci. Nanotechnol.*, **8**, 4111 (2008).
- M. Banerjee, L. Chongad, A. Sharma, *Res. J. Recent Sci.*, **2**, 326 (2013).
- A. Sharma, S. Rastogi, M. Sindal, *Int. J. Chem. Sci.*, **9**, 1569 (2011).
- F. Atay, S. Kose, V. Bilgin, I. Akyuz, *Electrical, Turk. J. Phys.*, **27**, 285 (2003).
- M. Barman, S. Paul, A. Sarkar, *Adv. Appl. Sci. Res.*, **4**, 343 (2013).
- H. R. Pouretedal, M. Tavakkoli, *Desalination Water Treat.* **51**, 4744 (2013).
- H.R. Pouretedal, Z. Tofangsazi, M.H. Keshavarz, *J. Alloy Compd.*, **513**, 359 (2012).
- H. R. Pouretedal, M. Kiyani, *J. Iran. Chem. Soc.*, DOI 10.1007/s13738-013-0297-2.
- H. Zhou, B. Lv, D. Wu, Y. Sun, *Particuology*, **10**, 783 (2012).
- N. Chen, W. Zhang, W. Yu, Y. Qian, *Mater. Lett.*, **55**, 230 (2002).
- A.G. Al-Sehemi, A.S. Al-Shihri, A. Kalam, G. Du, T. Ahmad, *J. Mole. Structure*, **1058**, 56 (2014).
- M.A. Behnajady, S. Bimeghdar, *Chem. Eng. J.* **239**, 105 (2014).
- Q. Li, L.-S. Wang, B.-Y. Hu, C. Yang, L. Zhou, L. Zhang, *Mater. Lett.*, **61**, 1615 (2007).
- M. Salavati-Niasari, F. Davar, H. Emadi, *Chalcogenide Lett.*, **7**, 647 (2010).
- D. Rezaei Ochbelagh, N. Morsali Golboos, Sh. Sohrabnezhad, *Radiation Phys. Chem.*, **87**, 1 (2013).
- N. Li, B. Zhou, P. Guo, J. Zhou, D. Jing, *Int. J. Hydrogen Energy*, **38**, 11268 (2013).
- A. Nezamzadeh Ejhieh, M. Khorsandi, *J. Hazard. Mater.*, **176**, 629 (2010).
- H. R. Pouretedal, A. Shafeie, M. H. Keshavarz, *J. Korean Chem. Soc.*, **56**, 484 (2012).
- G. Zhang, W. Zhang, D. Minakata, Y. Chen, J. Crittenden, P. Wang, *Int. J. Hydrogen Energy*, **38**, 11727 (2013).
- H.R. Pouretedal, S. Basati, *Iran. J. Catal.*, **2**, 50 (2012).
- K. Ullah, S. Ye, L. Zhu, Z.-D. Meng, S. Sarkar, W.-C. Oh, *Mater. Sci. Eng.*, **B 180**, 20 (2014).
- H.R. Pouretedal, H. Motamedi, A. Amiri, *Desalination Water Treat.*, **44**, 92 (2012).
- N. Kaneval, A. Ponomareva, L. Krasteva, D. Dimitrov, A. Bojinova, K. Papazova, G. Suchaneck, V. Moshnikov, *Bulgarian Chem. Commun.*, **45**, 635 (2013).

СИНТЕЗА, ОХАРАКТЕРИЗИРАНЕ И ИЗСЛЕДВАНЕ НА ФОТОКАТАЛИТИЧНАТА АКТИВНОСТ НА НАНОКОМПОЗИТИ ОТ ОКИСИ И СУЛФИДИ НА Ni(II) И Ni(III)

Х.Р. Пуретедал^{1*}, Ф. Момензаде²

¹ Факултет по приложна химия, Технологичен университет Малек-ащар, Шахин Шахр, Иран

² Департамент по химия, Ислямски университет "Азад", Клон Шахреза, Шахреза, Иран

Постъпила на 21 декември, 2013 г.; коригирана на 1 май, 2014 г.

(Резюме)

Синтезирани са наночастици от NiO, NiS, Ni₂O₃, Ni₂S₃, NiO_{0.5}S_{0.5} и Ni₂O_{1.5}S_{1.5} по метода на контролираното утаяване. Пригответените наночастици са калцинирани при 700 °C. Рентгено-дифракционните изследвания показват кубична структура за NiO, Ni₂O₃, Ni₂S₃, NiO_{0.5}S_{0.5} и Ni₂O_{1.5}S_{1.5}, а при наноразмерните частици от NiS се наблюдават както кубична, така и хексагонална структура. Абсорбционните пикове в FT-IR спектрите при вълнови числа 600-400 cm⁻¹ показват наличието на вибрации на връзките S-Ni и S-Ni-S. Наблюдава се червено отместване от 30 nm в DRS UV-Vis – спектрите на наноконпозитите от NiO_{0.5}S_{0.5} и Ni₂O_{1.5}S_{1.5} спрямо наночастиците на оксидите и сулфидите на Ni (II) и Ni(III). Енергийни ями 5.79, 5.71, 5.64, 5.51, 4.96 and 4.86 eV са получени съответно Ni₂S₃, Ni₂O₃, NiO, NiS, NiO_{0.5}S_{0.5} и Ni₂O_{1.5}S_{1.5}. ТЕМ-микроскопски снимки показват, че размерите на наноконпозитите от Ni₂O_{1.5}S_{1.5} са под 70 nm. Съществуването на атоми от Ni, S и O в структурата на наноконпозитите от Ni₂O_{1.5}S_{1.5} е доказано чрез дисперсионен рентгенов анализ. Фотокаталитичната активност на пригответените наночастици е изследвана върху фото-разпадането на метиленово синьо. Фотокаталитичната активност на изследваните наночастици за тази реакция е както следва: Ni₂O_{1.5}S_{1.5} > NiO_{0.5}S_{0.5} > NiS > NiO > Ni₂O₃ > Ni₂S₃. Стойността на pH в точката на нулев товар е ~6.0. Оптимизираните условия за този процес на фотодеградация са: pH 7, 0.5 g L⁻¹ фотокатализатор, 20 mg L⁻¹ багрило и време на облъчване 60 мин.

Hydromagnetic natural convection flow with induced magnetic field and n^{th} order chemical reaction of a heat absorbing fluid past an impulsively moving vertical plate with ramped temperature

G. S. Seth*, S. Sarkar

Department of Applied Mathematics, Indian School of Mines, Dhanbad, India

Received January 3, 2014; Revised August 26, 2014

An investigation of the unsteady hydromagnetic natural convection flow with heat and mass transfer of a viscous, incompressible, electrically conducting and heat absorbing fluid past an impulsively moving vertical plate with ramped temperature embedded in a fluid-saturated porous medium is carried out taking induced magnetic field and n^{th} order chemical reaction into account. Governing equations along with the initial and boundary conditions are solved numerically using the Crank-Nicolson implicit finite difference scheme. The numerical solutions for fluid velocity, induced magnetic field, species concentration and fluid temperature are depicted graphically, whereas the numerical values of skin friction, Sherwood number and Nusselt number are presented in tabular form for various values of the pertinent flow parameters. In order to highlight the influence of ramped temperature distribution within the plate on the flow-field, the fluid flow past a ramped temperature plate is compared with the one past an isothermal plate. Validation of numerical results is also performed to ensure correctness of the results.

Keywords: Induced magnetic field, thermal buoyancy force, concentration buoyancy force, ramped temperature, heat absorption, n^{th} order chemical reaction.

INTRODUCTION

Natural convection flow resulting from the simultaneous action of thermal and concentration buoyancy forces occurs frequently in nature and has significant engineering applications. Atmospheric flows are driven not only by temperature differences but also by concentration differences since in nature air or water are usually contaminated by suspended particulate matter which may be present either naturally or due to industrial emissions. A comprehensive discussion on convective heat and mass transfer was made by Eckert and Drake [1] through their book "Analysis of Heat and Mass Transfer" which included all previous investigations and laid the groundwork for future research. Later, natural convection heat and mass transfer flow through a fluid saturated porous medium has been investigated by several researchers [2-5] because of its varied and wide range of industrial applications such as enhanced recovery of petroleum products and gases (e.g. CBM: coal bed methane and UCG: underground coal gasification), dispersion of chemical contaminants through water-saturated soil, solid matrix heat exchangers, desert coolers, wet bulb thermometers, packed bed reactors, underground disposal of nuclear waste, exploitation of continental geothermal reservoir, etc.

Hydromagnetic flows with heat and mass transfer in porous media have been considered extensively in recent years due to their occurrence in several engineering applications such as in boundary layer flow control, magnetic levitation and casting, filtration of liquid metals, cooling of nuclear reactors, fusion control, prevention of scaling in heat exchangers, etc. Moreover, the study of unsteady hydromagnetic flows is significant from practical point of view because fluid transients may be expected at the start-up time of many industrial processes and devices, *viz.* MHD power generators, MHD pumps, MHD accelerators, MHD flow-meters, controlled thermonuclear reactors, etc. Keeping in view the importance of such study, several researchers [6-10] have investigated unsteady hydromagnetic natural convection heat and mass transfer flow of a viscous, incompressible and electrically conducting fluid past a flat plate embedded in a fluid-saturated porous medium. It is noticed that there may be significant temperature difference between ambient fluid and surface of the solid in a number of fluid flow problems of physical interest, *viz.* fluids undergoing exothermic and/or endothermic chemical reaction, heat removal from nuclear fuel debris, underground disposal of radioactive waste material, storage of food stuffs, dissociating fluids in packed bed reactors, etc. Therefore, it is suitable to consider temperature dependent heat source and/or sink which may have strong influence on heat transfer characteristics. Keeping in view the importance of such study,

* To whom all correspondence should be sent:
E-mail: gsseth.ism@gmail.com

Chamkha and Khaled [11] investigated hydromagnetic natural convection heat and mass transfer flow past a permeable vertical plate embedded in a fluid-saturated porous medium in the presence of heat generation or absorption. Kamel [12] considered unsteady hydromagnetic natural convection flow due to heat and mass transfer through a porous medium bounded by an infinite vertical porous plate with temperature-dependent heat sources/sinks. Chamkha [13] analyzed unsteady hydromagnetic natural convection heat and mass transfer flow past a semi-infinite vertical moving plate with heat absorption.

In chemical and hydrometallurgical industries, the production of polymers, ceramics and glassware often involve processes that require combined heat and mass transfer over surfaces with different geometries where diffusing species can be generated or absorbed due to some kind of chemical reaction with the ambient fluid and can greatly affect the flow characteristics, as well as the quality of the final product. However, the effect of a chemical reaction significantly depends on its order and whether the reaction is heterogeneous or homogenous. In general, a reaction is said to be of n^{th} order if the rate of reaction is proportional to the n^{th} power of concentration itself. Chemical reactions are said to be heterogeneous or homogenous depending on whether they occur at an interface or as a single phase volume reaction. A homogenous reaction occurs uniformly throughout the given phase, whereas a heterogeneous reaction takes place in a restricted region or within the boundary of a phase. Chambre and Young [14] were among the initial investigators to study the diffusion of a chemically reactive species in a laminar boundary layer flow over a flat plate. Das *et al.* [15] studied the effect of homogenous first order chemical reaction on the flow of an impulsively started infinite vertical plate with uniform heat flux and mass transfer. Muthucumarswamy and Ganesan [16] investigated the transient natural convection flow of a viscous and incompressible fluid past an impulsively started vertical plate taking into account homogenous chemical reaction of first order. Another situation which frequently arises in chemical industries is MHD flow through a porous medium in the presence of chemical reaction. In one of the numerous porous media applications, such as in packed pebble bed-based blanket for fission-fusion hybrid reactors, to sustain a given flow rate of the electrically conducting liquid in the bed, the pressure drop and the liquid holdup will be increased under magnetohydrodynamic conditions

compared with the case of non-conducting fluids. Another application is in crystal growth where the use of external magnetic field has been successfully exploited to suppress unsteady flow and reduce non-uniform composition thereby enhancing quality of the crystal. Keeping in view the importance of such study, Singh and Kumar [17] studied the effects of chemical reaction on unsteady MHD heat and mass transfer flow past a hot vertical porous plate embedded in a porous medium in the presence of heat generation or absorption. Postelnicu [18] considered Soret and Dufour effects on natural convection heat and mass transfer flow over a vertical surface embedded in a fluid-saturated porous medium taking into account a homogenous chemical reaction of order n (where n was taken 1, 2, 3). Makinde [19] investigated MHD mixed-convection flow of an optically thin radiating fluid past a vertical porous plate embedded in a porous medium assuming n^{th} order homogenous chemical reaction between the fluid and the diffusing species. Pal and Talukdar [20] analyzed the effects of thermal radiation on unsteady hydromagnetic heat and mass transfer flow past a vertical moving plate embedded in a porous medium in the presence of heat absorption and first order chemical reaction of the species.

In all these investigations, analytical or numerical solution is obtained under different thermal conditions which are continuous and well defined. However, there are numerous practical problems which may require non-uniform or arbitrary thermal conditions. Pioneering work is due to Schetz [21] who developed an approximate model for free convection flow from a vertical plate with discontinuous thermal boundary conditions. Later on, Chandran *et al.* [22] analyzed the unsteady natural convective flow of a viscous and incompressible fluid near a vertical plate with ramped temperature. Patra *et al.* [23] considered the effects of radiation on the natural convection flow of a viscous and incompressible fluid near a stationary vertical flat plate with ramped temperature. Seth and Ansari [24] investigated the hydromagnetic natural convection flow past an impulsively moving vertical plate with ramped temperature in the presence of thermal diffusion and heat absorption. Seth *et al.* [25] also studied the effects of Hall current and rotation on the unsteady hydromagnetic natural convection flow of a viscous, incompressible, electrically conducting and heat absorbing fluid past an impulsively moving vertical plate with ramped temperature in a porous medium taking into account the effects of thermal diffusion. Nandkeolyar *et al.* [26]

considered the unsteady hydromagnetic heat and mass transfer flow of a heat radiating fluid past a flat porous plate with ramped wall temperature taking first order chemical reaction into account. Recently, Nandkeolyar *et al.* [27] presented an exact solution of unsteady MHD free convection heat and mass transfer flow of a heat absorbing fluid past a flat plate with ramped wall temperature.

In all above studies, induced magnetic field produced by the fluid motion is neglected in comparison to the applied one. This assumption is justified for metallic liquids and partially ionized fluids because magnetic Reynolds number is very small for metallic liquids and partially ionized fluids [28]. In contrast, for flows where magnetic Reynolds number is not very small, induced magnetic fields must be considered [29]. It is noticed that there are several astrophysical and geophysical problems in which induced magnetic field plays a vital role in determining flow features of the problem, namely, fluid flow in earth's interior, star formation, sunspots and solar flares in the Sun, rotating magnetic stars and planetary and solar dynamo problems. In addition to it, induced magnetic fields play a significant role in fusion applications with plasma containments [30] and on the performance of large scale pulsed MHD generators [31]. Moreover, induced magnetic fields could be used as an evidence to predict the existence of salty liquid-water subsurface oceans in Europa and Callisto [32]. The classical problem of Glauert [33] presented a seminal analysis for hydromagnetic boundary layer flow past a magnetized flat plate with uniform magnetic field in the stream direction at the plate. He obtained series of expansion solutions considering both large and small values of the electrical conductivity parameter for the velocity and induced magnetic fields. Raptis and Soundalgekar [34] investigated the flow of an electrically conducting fluid past a steadily moving infinite vertical porous plate in the presence of constant heat flux and constant suction taking induced magnetic field into account. Raptis and Masalas [35] considered the effects of induced magnetic field on the unsteady hydromagnetic flow of a viscous, incompressible, electrically conducting and optically thick radiating fluid past an infinite vertical porous plate. Bég *et al.* [36] obtained local non-similarity numerical solutions for the velocity, temperature and induced magnetic field distributions in forced convection liquid metal boundary layer flow past a non-conducting plate for a wide range of magnetic Prandtl numbers. Singh *et al.* [37] investigated the unsteady hydromagnetic natural convection flow between two insulated

infinitely long vertical walls in the presence of induced magnetic field.

In view of the above analysis, the aim of the present study was to investigate the effects of induced magnetic field on the unsteady hydromagnetic natural convection heat and mass transfer flow of a viscous, incompressible, electrically conducting and heat absorbing fluid past an impulsively moving infinite vertical plate with ramped temperature embedded in a fluid-saturated porous medium in the presence of n^{th} order homogenous chemical reaction. To the best of our knowledge, no study has been reported in the literature by any researcher considering natural convection flow with heat and mass transfer of a chemically reacting fluid past a time dependent moving plate with ramped temperature taking induced magnetic field into account. The governing equations are solved using Crank-Nicolson implicit finite difference scheme. The numerical code is validated by comparing the values of the Nusselt number obtained through our present scheme with the earlier published results.

FORMULATION OF THE PROBLEM

Consider a unsteady hydromagnetic natural convection flow with heat and mass transfer of an electrically conducting, viscous, incompressible, chemically reacting and heat absorbing fluid past an infinite vertical plate embedded in a uniform porous medium in the presence of induced magnetic field. Coordinate system is chosen in such a way that x' - axis is considered along the plate in upward direction, y' - axis is perpendicular to the plane of the plate in the fluid and z' -axis is normal to the xy plane. A uniform transverse magnetic field B_0 is applied in a direction which is parallel to the y' - axis. Since induced magnetic field is taken into account, therefore the magnetic field $\vec{B} \equiv (B'_x, B_0, 0)$, where B'_x is the induced magnetic field in x' direction. Initially, i.e. at time $t' \leq 0$, both the fluid and the plate are at rest and are maintained at a uniform temperature T_∞' . Also species concentration within the fluid is maintained at a uniform value C_∞' . At time $t' > 0$, the plate starts moving in x' -direction with uniform velocity U_0 in its own plane. The temperature of the plate is raised or lowered to $T_\infty' + (T_w' - T_\infty')t'/t_0$ when $0 < t' \leq t_0$, and it is maintained at uniform

Initial and boundary conditions (5a) to (5f), in non-dimensional form, become

$$u = 0, B_x = 0, T = 0, C = 0 \text{ for } y \geq 0 \text{ and } t \leq 0, \quad (10a)$$

$$u = 1, B_x = 0, \text{ at } y = 0 \text{ for } t > 0, \quad (10b)$$

$$T = t \text{ at } y = 0 \text{ for } 0 < t \leq 1, \quad (10c)$$

$$T = 1 \text{ at } y = 0 \text{ for } t > 1, \quad (10d)$$

$$C = 1 \text{ at } y = 0 \text{ for } t > 0, \quad (10e)$$

$$u \rightarrow 0, B_x \rightarrow 0, T \rightarrow 0, C \rightarrow 0 \text{ as } y \rightarrow \infty \text{ for } t > 0. \quad (10f)$$

NUMERICAL SOLUTION

Equations (6) to (9) cannot be solved analytically due to the coupled nature of equations (6) and (7) and the presence of a non-linear term in equation (9). Therefore, in order to understand the physical aspect of the problem, we have solved equations (6) to (9) under the initial and boundary conditions (10) by the Crank-Nicolson implicit finite difference scheme. The region under consideration was restricted by a rectangle of finite dimensions with $y_{\text{max}}=6$ (corresponding to $y \rightarrow \infty$) and $t_{\text{max}}=2$. Assumption of $y_{\text{max}} = 6$ was finalized when the boundary condition (10f) was satisfied within tolerance limit of 10^{-4} . The computational domain is divided into 241×801 grid points and the grid refinement check is performed by comparing the results in this case (with mesh size $\Delta y \times \Delta t$ where $\Delta y = 1/40$ and $\Delta t = 1/400$) with the results obtained when mesh size is reduced to 50% of the present case and it is noticed that the difference between these two results is less than half a unity in the fourth decimal place. The finite difference equations for each time step constitute a tridiagonal system of equations which are solved by Thomas algorithm as given in Carnahan *et al.* [38]. The numerical solution is then obtained corresponding to a desired time through iterations. It was found that the absolute difference between the numerical values of species concentration, fluid temperature, fluid velocity and induced magnetic field obtained for two consecutive time steps is less than 10^{-4} . Hence, the scheme designed is stable. Moreover, Crank-Nicolson method has a local truncation error of $O\left\{(\Delta y)^2 + (\Delta t)^2\right\}$ which tends to zero as Δy and Δt tends to zero which justifies consistency (Antia [39], pp. 643-644). Stability and consistency together ensure convergence of the scheme.

Now in order to highlight the effects of ramped temperature distribution within the plate on the flow-field, it is justified to compare such a flow

with the one past an impulsively moving vertical plate with uniform temperature. Taking into account the assumptions made in this paper, the numerical solutions for fluid temperature, fluid velocity and induced magnetic field for the flow past an impulsively moving isothermal vertical plate are obtained in the same manner as above and are displayed graphically along with the solutions obtained in case of ramped temperature plate for a better interpretation of the results.

Meanwhile, by using the computed values of fluid velocity and fluid temperature, the numerical values of skin friction τ and Nusselt number N_u for both ramped temperature and isothermal plates are obtained as follows:

$$\tau = \left. \frac{\partial u}{\partial y} \right|_{y=0}, \quad (11)$$

$$N_u = \left. \frac{\partial T}{\partial y} \right|_{y=0}. \quad (12)$$

The numerical values of Sherwood number S_h are also obtained as:

$$S_h = \left. \frac{\partial C}{\partial y} \right|_{y=0}. \quad (13)$$

The derivatives involved in equations (11) to (13) are evaluated using five point forward difference formula for the first derivative (Antia [39], page 161).

Validation of Numerical Solution

In order to validate our numerical scheme we have presented a comparison in Table 1 of the values of the Nusselt number obtained numerically from (12) with the values of the Nusselt number computed from the exact expression for Nusselt number obtained by Seth *et al.* [41] for various values of ϕ and t for both ramped temperature and isothermal plates taking $P_r = 0.71$. It is evident from Table 1 that the numerical values of the Nusselt number obtained through our numerical scheme are in very good agreement with the exact values of the Nusselt number obtained by Seth *et al.* [41]. This justifies the correctness of the results presented in the paper.

We have also made a comparison in Fig. 2 of the numerical values of species concentration obtained through our scheme with the exact solution presented by Khan *et al.* [42] taking $K_2 = 0$ (i.e. in absence of chemical reaction) in our model. It is observed that there is a very good agreement of the numerical solution with the exact solution.

Table 1. Nusselt number - N_u when $P_r = 0.71$

$t \rightarrow$ $\phi \downarrow$	For ramped temperature plate						For isothermal plate					
	Numerical values obtained by the present scheme			Exact values obtained by Seth <i>et al.</i> [41]			Numerical values obtained by the present scheme			Exact values obtained by Seth <i>et al.</i> [41]		
	0.3	0.5	0.7	0.3	0.5	0.7	0.3	0.5	0.7	0.3	0.5	0.7
1	0.5712	0.7789	0.9691	0.5713	0.7791	0.9693	1.1166	0.9834	0.9255	1.1160	0.9830	0.9253
3	0.6643	0.9666	1.2621	0.6645	0.9670	1.2624	1.5505	1.4881	1.4700	1.5500	1.4879	1.4700
5	0.7485	1.1287	1.5064	0.7490	1.1294	1.5070	1.9211	1.8914	1.8860	1.9209	1.8916	1.8860

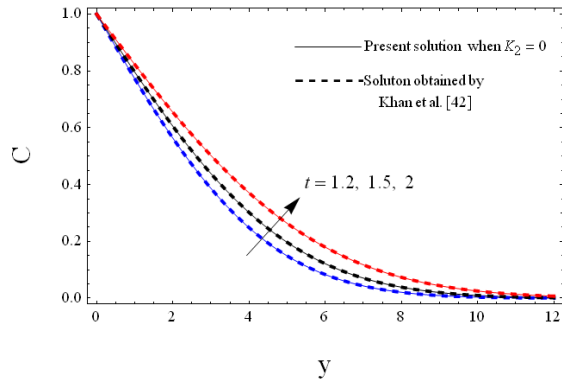


Fig. 2. Concentration profiles for different values of t when $S_c = 0.2$

RESULTS AND DISCUSSION

In order to analyze the effects of magnetic field, thermal buoyancy force, concentration buoyancy force, mass diffusion, chemical reaction, order of chemical reaction, heat absorption and time on the flow-field, the numerical solutions of fluid velocity $u(y,t)$ and induced magnetic field $B_x(y,t)$ in the boundary layer region are displayed graphically *versus* boundary layer coordinate y in Figs. 3 to 18 for various values of magnetic parameter M^2 , thermal Grashof number G_r , solutal Grashof number G_c , Schmidt number S_c , chemical reaction parameter K_2 , order n of chemical reaction, heat absorption parameter ϕ and time t taking $K_1 = 0.4$, $P_r = 0.71$ and $P_m = 0.7$ (ionized hydrogen) [40]. Figs. 3 to 18 reveal that for both

ramped temperature and isothermal plates, fluid velocity and induced magnetic field first increase to a distinctive maximum value and then decrease properly on increasing boundary layer coordinate y to approach free stream value. It is also noticed that fluid velocity is slower in the case of ramped temperature plate than in the case of isothermal plate. Moreover, induced magnetic field is higher in the case of isothermal plate than in the case of ramped temperature plate.

Figure 3 depicts the influence of magnetic field on fluid velocity u for both ramped temperature and isothermal plates. It is evident from Figure 3 that for both ramped temperature and isothermal plates, u decreases in the region near the plate on increasing M^2 while it increases in the region away from the plate on increasing M^2 . This implies that magnetic field tends to retard fluid velocity in the region near the plate whereas it has a reverse effect on fluid velocity in the region away from the plate. This shows that the Lorentz force (a resistive force developed due to the movement of an electrically conducting fluid in the presence of magnetic field) is dominant in the region near the plate and its effectiveness gets diminished by other forces in the region away from the plate. Figures 4 and 5 exhibit the effects of thermal and concentration buoyancy forces on fluid velocity for both ramped temperature and isothermal plates. Figs. 4 and 5 reveal that for both ramped temperature and isothermal

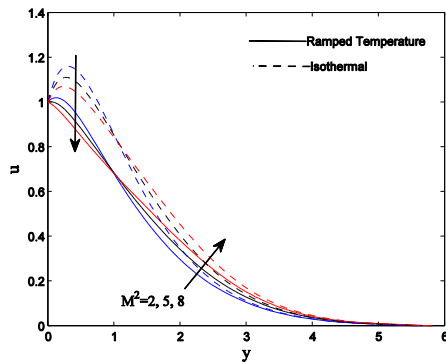


Fig. 3: Velocity profiles when $G_r = 5$, $G_c = 4$, $K_2 = 2.5$, $\phi = 3$, $n = 2$, $t = 0.5$ and $S_c = 0.22$

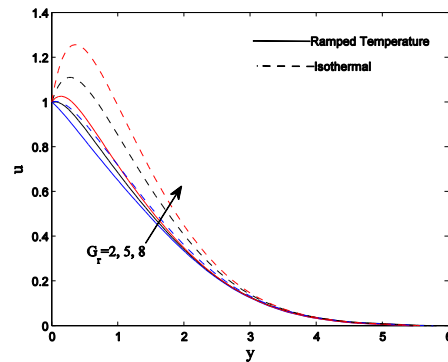


Fig. 4: Velocity profiles when $M^2 = 5$, $G_c = 4$, $K_2 = 2.5$, $\phi = 3$, $n = 2$, $t = 0.5$ and $S_c = 0.22$

plates, u increases on increasing G_r and G_c throughout the boundary layer region. Physically, G_r represents the relative strength of thermal buoyancy force to viscous force and G_c represents the relative strength of concentration buoyancy force to viscous force. Therefore, G_r and G_c increase on increasing the strengths of thermal and concentration buoyancy forces, respectively. In this problem a natural convection flow is induced due to thermal and concentration buoyancy forces, therefore thermal and concentration buoyancy forces tend to accelerate fluid velocity for both ramped temperature and isothermal plates throughout the boundary layer region.

Figures 6 and 7 demonstrate the effects of rate of chemical reaction and heat absorption on fluid

velocity for both ramped temperature and isothermal plates. It is perceived from Figs. 6 and 7 that u decreases on increasing K_2 and ϕ for both ramped temperature and isothermal plates throughout the boundary layer region. This implies that for both ramped temperature and isothermal plates, chemical reaction and heat absorption tend to retard fluid velocity, which is due to the fact that chemical reaction and heat absorption inhibit concentration and thermal buoyancy forces, respectively. Figures 8 and 9 display the influence of the order of chemical reaction and time on fluid velocity for both ramped temperature and isothermal plates. It is depicted in Figs. 8 and 9 that u increases on increasing n and t for

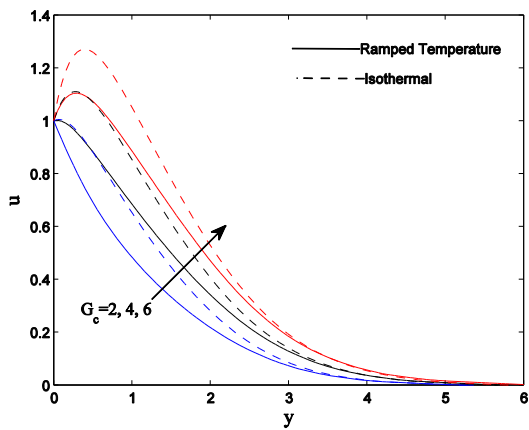


Fig. 5: Velocity profiles when $M^2 = 5$, $G_r = 5$, $K_2 = 2.5$, $\phi = 3$, $n = 2$, $t = 0.5$ and $S_c = 0.22$

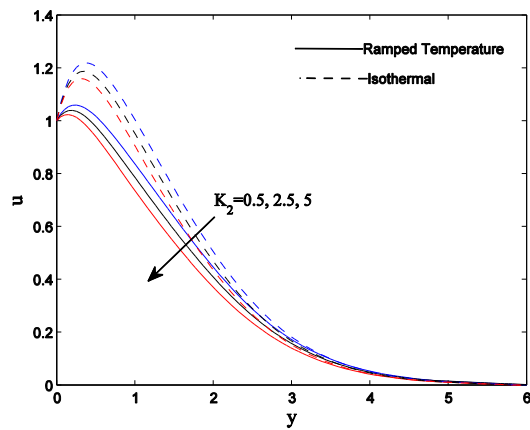


Fig. 6: Velocity profiles when $M^2 = 5$, $G_r = 5$, $G_c = 4$, $\phi = 3$, $n = 2$, $t = 0.5$ and $S_c = 0.22$

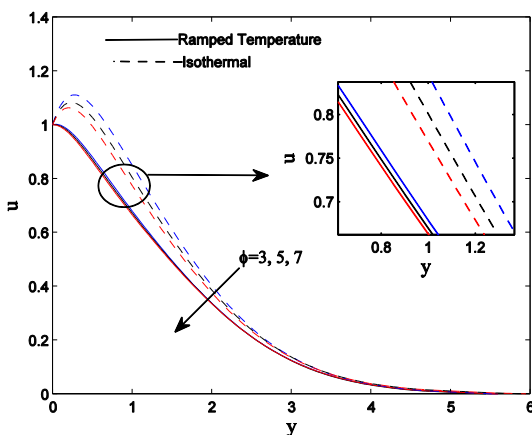


Fig. 7: Velocity profiles when $M^2 = 5$, $G_r = 5$, $G_c = 4$, $K_2 = 2.5$, $n = 2$, $t = 0.5$ and $S_c = 0.22$

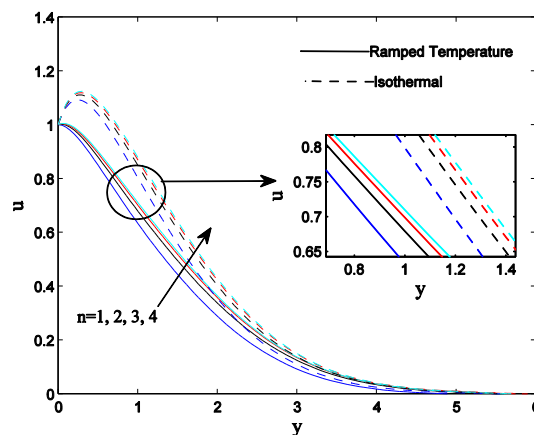


Fig. 8: Velocity profiles when $M^2 = 5$, $G_r = 5$, $G_c = 4$, $K_2 = 2.5$, $\phi = 3$, $t = 0.5$ and $S_c = 0.22$

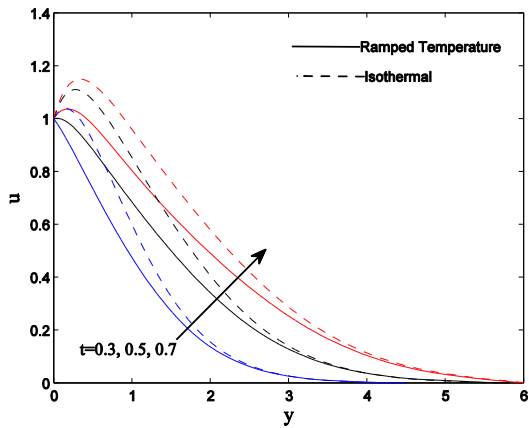


Fig. 9: Velocity profiles when $M^2 = 5, G_r = 5, G_c = 4, K_2 = 2.5, \phi = 3, n = 2$ and $S_c = 0.22$

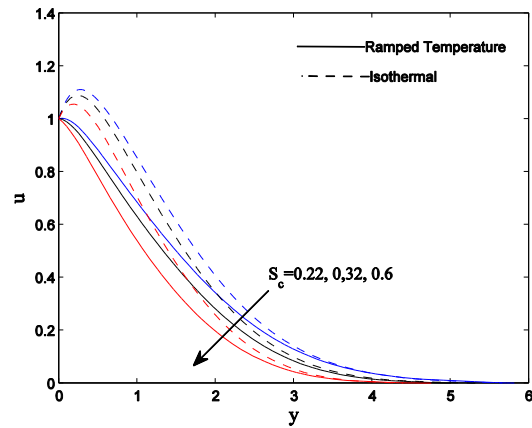


Fig. 10: Velocity profiles when $M^2 = 5, G_r = 5, G_c = 4, K_2 = 2.5, \phi = 3, n = 2$ and $t = 0.5$

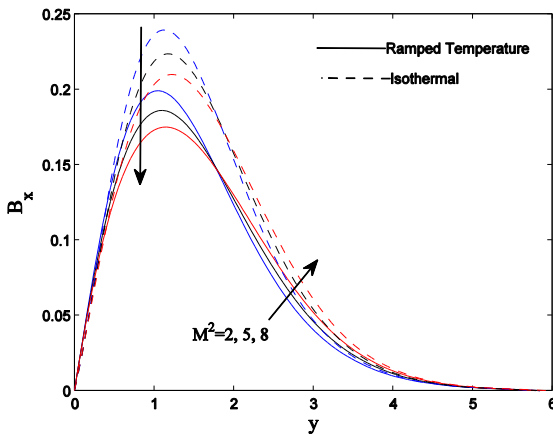


Fig. 11: Induced magnetic field profiles when $G_r = 5, G_c = 4, K_2 = 2.5, \phi = 3, n = 2, t = 0.5$ and $S_c = 0.22$

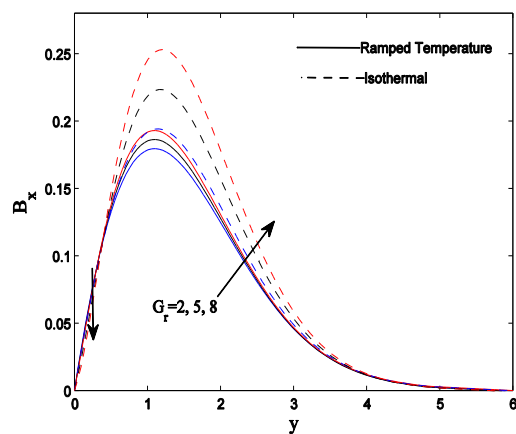


Fig. 12: Induced magnetic field profiles when $M^2 = 5, G_c = 4, K_2 = 2.5, \phi = 3, n = 2, t = 0.5$ and $S_c = 0.22$

both ramped temperature and isothermal plates throughout the boundary layer region. This implies that for both ramped temperature and isothermal plates, the order of the chemical reaction tends to accelerate fluid velocity but the increment almost dies out after a certain level. For both ramped temperature and isothermal plates, fluid velocity is getting accelerated with the progress of time. Figure 10 portrays the effects of mass diffusion on fluid velocity for both ramped temperature and isothermal plates. It is evident from Figure 10 that u decreases on increasing S_c for both ramped temperature and isothermal plates throughout the boundary layer region. Since Schmidt number S_c is a measure of the relative strength of viscosity to molecular (mass) diffusivity of the fluid, S_c decreases on increasing molecular diffusivity

of the fluid. This implies that mass diffusion tends to accelerate fluid velocity for both ramped temperature and isothermal plates. Figure 11 demonstrates the effects of magnetic field on induced magnetic field for both ramped temperature and isothermal plates. It is apparent from Figure 11 that B_x decreases on increasing M^2 in the region near the plate while it increases on increasing M^2 in the region away from the plate for both ramped temperature and isothermal plates. This implies that externally applied magnetic field tends to reduce induced magnetic field in the region near the plate whereas it has a reverse effect on induced magnetic field in the region away from the plate. Figures 12 and 13 illustrate the effects of thermal and concentration buoyancy forces on the induced magnetic field for both ramped temperature and isothermal plates.

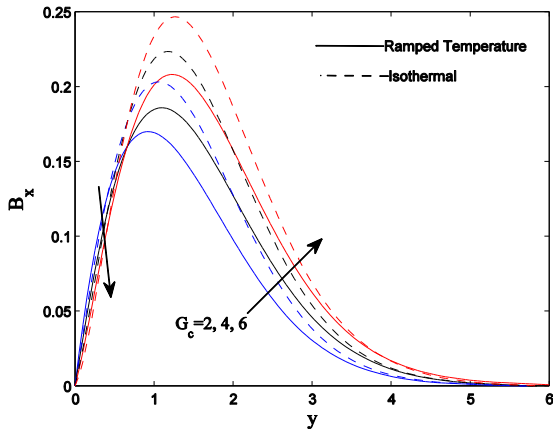


Fig. 13: Induced magnetic field profiles when $M^2 = 5$, $G_r = 5$, $K_2 = 2.5$, $\phi = 3$, $n = 2$, $t = 0.5$ and $S_c = 0.22$

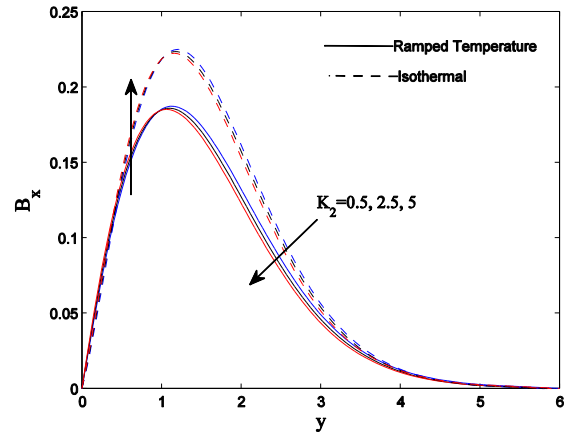


Fig. 14: Induced magnetic field profiles when $M^2 = 5$, $G_r = 5$, $G_c = 4$, $\phi = 3$, $n = 2$, $t = 0.5$ and $S_c = 0.22$

It is seen from Figs. 12 and 13 that B_x decreases on increasing G_r and G_c in the region near the plate while it increases on increasing G_r and G_c in the region away from the plate for both ramped temperature and isothermal plates. This implies that thermal and concentration buoyancy forces tend to reduce induced magnetic field in the region near the plate while they have reverse effect on the induced magnetic field in the region away from the plate. Figures 14 to 16 depict the effects of chemical reaction, heat absorption and mass diffusion on the induced magnetic field

for both ramped temperature and isothermal plates. It is perceived from Figs. 14 to 16 that B_x increases on increasing K_2 , ϕ and S_c in the region near the plate while it decreases on increasing K_2 , ϕ and S_c in the region away from the plate. This implies that chemical reaction and heat absorption tend to enhance the induced magnetic field in the region near the plate while they have reverse effect on the induced magnetic field in the region away from the plate. Mass diffusion tends to reduce the induced magnetic field in the region near the plate while it has a reverse effect on the induced magnetic field in the region away from the plate.

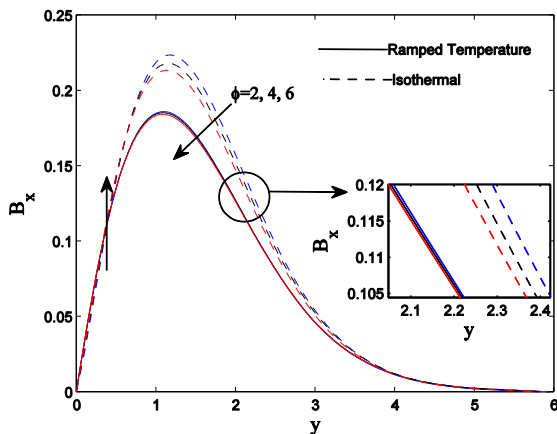


Fig. 15: Induced magnetic field profiles when $M^2 = 5$, $G_r = 5$, $G_c = 4$, $K_2 = 2.5$, $n = 2$, $t = 0.5$ and $S_c = 0.22$

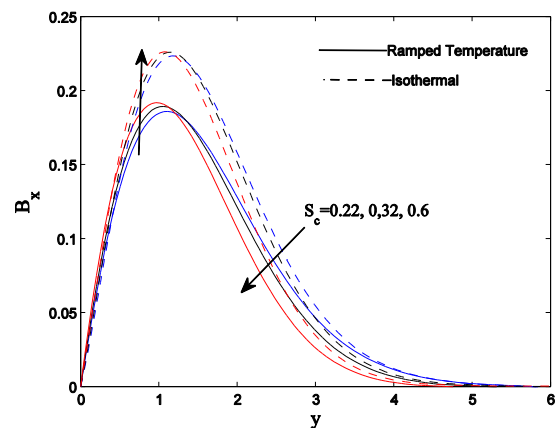


Fig. 16: Induced magnetic field profiles when $M^2 = 5$, $G_r = 5$, $G_c = 4$, $K_2 = 2.5$, $n = 2$, $t = 0.5$ and $\phi = 3$

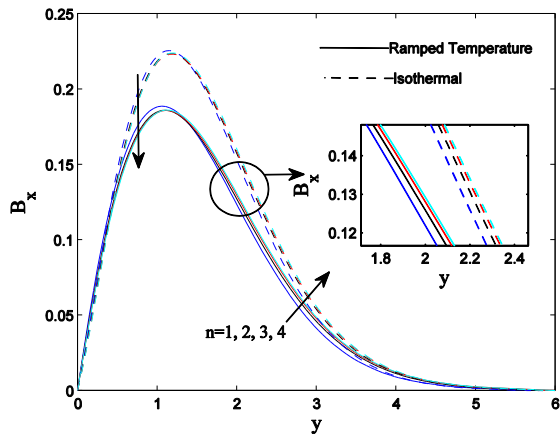


Fig. 17: Induced magnetic field profiles when $M^2 = 5$, $G_r = 5$, $G_c = 4$, $K_2 = 2.5$, $\phi = 3$, $t = 0.5$ and $S_c = 0.22$

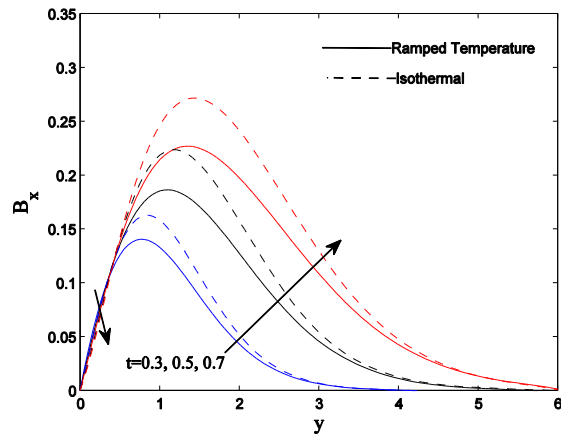


Fig. 18: Induced magnetic field profiles when $M^2 = 5$, $G_r = 5$, $G_c = 4$, $K_2 = 2.5$, $n = 2$, $\phi = 3$ and $S_c = 0.22$

Figures 17 and 18 portray the influence of the order of chemical reaction and time on the induced magnetic field for both ramped temperature and isothermal plates. It is observed from Figs. 17 and 18 that B_x decreases on increasing n and t in a close proximity to the plate while it increases on increasing n and t in the region just away from the plate. This implies that the order of chemical reaction reduces the induced magnetic field in the region near the plate whereas it has a reverse effect on the induced magnetic field in the region away from the plate. Induced magnetic field is getting enhanced with the progress of time in most of the region of the plate.

In order to study the effects of chemical reaction, order of chemical reaction and mass diffusion on species concentration, the numerical

solutions of species concentration C , are presented graphically *versus* boundary layer coordinate y in Figs. 19 to 21 for various values of chemical reaction parameter K_2 , order of chemical reaction n and Schmidt number S_c . It is observed from Figs. 19 to 21 that species concentration attains a distinctive maximum value near the surface of the plate and then decreases properly on increasing boundary layer coordinate y to approach the free stream value. It is evident from Figs. 19 to 21 that species concentration C decreases on increasing either K_2 or S_c while it increases on increasing n . This implies that chemical reaction tends to reduce species concentration whereas mass diffusion has a reverse effect on it. The order of the chemical reaction tends to enhance the species concentration but the incremental effect almost dies out after a certain level.

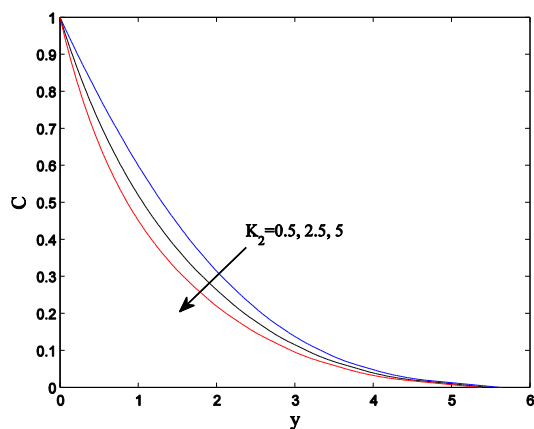


Fig. 19: Concentration profiles when $n = 2$, $t = 0.5$ and $S_c = 0.22$

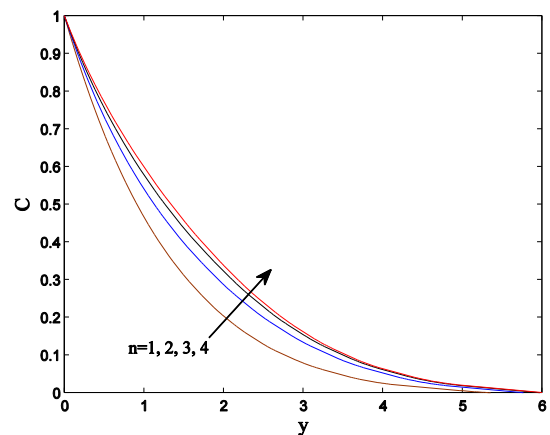


Fig. 20: Concentration profiles when $K_2 = 2.5$, $t = 0.5$ and $S_c = 0.22$

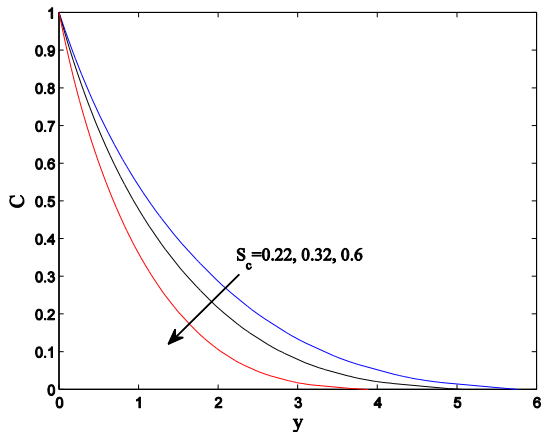


Fig. 21: Concentration profiles when $K_2 = 2.5, t = 0.5$ and $n = 2$

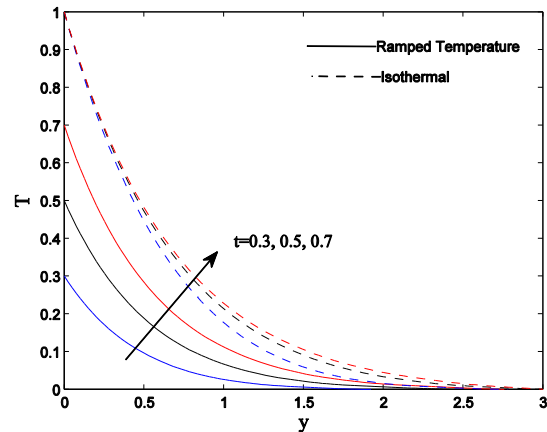


Fig. 22: Temperature profiles when $P_r = 0.71$ and $\phi = 3$

Figure 22 presents the influence of time on fluid temperature T for both ramped temperature and isothermal plates. It is evident from Fig. 22 that T increases on increasing t for both ramped temperature and isothermal plates. This implies that fluid temperature increases with the progress of time for both ramped temperature and isothermal plates.

Skin friction

Numerical values of skin friction τ , for both ramped temperature and isothermal plates, are computed from (11) and are presented in tabular form in Tables 2 and 3 for various values of $M^2, G_r, G_c, S_c, K_2, n, \phi$ and t taking $P_r = 0.71, P_m = 0.7$ [40] and $K_1 = 0.4$. It is observed from Table 2 that for both ramped temperature and isothermal plates, τ increases on increasing M^2, S_c and ϕ . This implies that magnetic field and heat absorption tend to enhance

skin friction whereas mass diffusion has a reverse effect on it. It is also noticed from Table 2 that τ decreases, attains a minimum and then increases on increasing t for both ramped temperature and isothermal plates. It is evident from Table 3 that on increasing G_r , τ decreases for ramped temperature plate and it decreases, attains a minimum and then increases for isothermal plate. τ increases on increasing G_c and n whereas it decreases on increasing K_2 for both ramped temperature and isothermal plates. This implies that thermal buoyancy force tends to reduce skin friction for ramped temperature plate. For both ramped temperature and isothermal plates, the order of the chemical reaction and the concentration buoyancy force tend to enhance skin friction whereas the rate of chemical reaction has a reverse effect on it. It is interesting to note from Tables 2 and 3 that there exists a separation of flow at the plate on increasing either G_r or G_c or t for both ramped temperature and isothermal plates.

Table 2. Skin friction $-\tau$ at ramped temperature and isothermal plates when $G_r = 5, G_c = 4, K_2 = 2.5$ and $n = 2$

M^2	S_c	ϕ	t	Ramped Temperature Plate	Isothermal Plate
2	0.22	3	0.1	1.4009	0.6135
5	0.22	3	0.1	1.5084	0.7261
8	0.22	3	0.1	1.6229	0.8455
5	0.32	3	0.1	1.5626	0.7803
5	0.6	3	0.1	1.6683	0.8860
5	0.6	5	0.1	1.6692	0.9065
5	0.6	7	0.1	1.6701	0.9259
5	0.22	3	0.3	0.4172	-0.5725
5	0.22	3	0.5	-0.0814	-0.9503
5	0.22	3	0.7	-0.4600	-1.0960

Table 3. Skin friction $-\tau$ at ramped temperature and isothermal plates when $M^2 = 5$, $S_c = 0.22$, $\phi = 3$ and $t = 0.5$

G_r	G_c	K_2	n	Ramped Temperature Plate	Isothermal Plate
2	2	0.5	2	1.0021	0.6545
5	2	0.5	2	0.6698	-0.1992
8	2	0.5	2	0.3374	-1.0529
5	4	0.5	2	-0.1708	-1.0397
5	6	0.5	2	-1.0113	-1.8803
5	4	2.5	2	-0.0814	-0.9503
5	4	2.5	3	-0.1175	-0.9864
5	4	2.5	4	-0.1380	-1.0069

Table 4: Sherwood number S_h

t	K_2	S_c	n	$-S_h$
0.1	0.5	0.22	2	0.9795
0.3	0.5	0.22	2	0.5377
0.5	0.5	0.22	2	0.4413
0.5	2.5	0.22	2	0.6619
0.5	2.5	0.32	2	0.7978
0.5	2.5	0.6	2	1.0923
0.5	2.5	0.6	3	1.0004
0.5	2.5	0.6	4	0.9411
0.5	5	0.6	4	1.1960

Sherwood number

Numerical values of Sherwood number which represents the rate of mass transfer at the plate are computed from (13) and are presented in Table 4 for various values of t , K_2 , S_c and n . It is perceived from Table 4 that S_h decreases on increasing t and n whereas it increases on increasing S_c and K_2 . This implies that chemical reaction tends to enhance the rate of mass transfer at the plate whereas mass diffusion and order of chemical reaction have reverse effect on it. The rate of mass transfer at the plate is getting reduced with the progress of time.

CONCLUSION

The present study analyses the effects of induced magnetic field on the unsteady hydromagnetic natural convection heat and mass transfer flow of a viscous, incompressible, electrically conducting and heat absorbing fluid past an impulsively moving infinite vertical plate with ramped temperature embedded in a fluid-saturated porous medium in the presence of n^{th} order homogenous chemical reaction. Significant results are summarized below:

For both ramped temperature and isothermal plates:

Magnetic field tends to retard fluid velocity in the region near the plate whereas it has a reverse

effect on fluid velocity in the region away from the plate.

Throughout the boundary layer region, thermal buoyancy force, concentration buoyancy force, mass diffusion and order of chemical reaction tend to accelerate fluid velocity whereas rate of chemical reaction and heat absorption have reverse effect on it. Fluid velocity is getting accelerated with the progress of time.

Externally applied magnetic field tends to reduce induced magnetic field in the region near the plate whereas it has a reverse effect on induced magnetic field in the region away from the plate.

Thermal buoyancy force, concentration buoyancy force, mass diffusion and order of chemical reaction tend to reduce induced magnetic field in the region near the plate while they have reverse effect on induced magnetic field in the region away from the plate.

Chemical reaction and heat absorption tend to enhance induced magnetic field in the region near the plate while they have reverse effect on induced magnetic field in the region away from the plate.

Magnetic field and heat absorption tend to enhance skin friction whereas mass diffusion has a reverse effect on it. Order of chemical reaction and concentration buoyancy force tend to enhance skin friction whereas rate of chemical reaction has a reverse effect on it. There exists a separation of flow at the plate on increasing either thermal buoyancy force or concentration buoyancy force or with the progress of time.

Acknowledgements: Authors are grateful to the reviewers for their valuable comments and suggestions which helped them to improve the quality of the research paper.

REFERENCES

1. E. R. Eckert, R. M. Drake, Analysis of Heat and Mass Transfer, Mc-Graw Hill, New York, 1972.
2. A. Bejan, K. R. Khair, *Int. J. Heat Mass Transf.*, **28**, 909 (1985).
3. J. Y. Jang, W. J. Chang, *Int. Commun. Heat Mass Transf.*, **15**, 17 (1988).
4. F. C. Lai, F. A. Kulacki, *J. Heat Transf.*, **113**, 252 (1991).
5. A. Nakayama, M. A. Hossain, *Int. J. Heat Mass Transf.*, **38**, 761 (1995).
6. M. A. Hossain, A. C. Mandal, *J. Phys. D: Appl. Phys.*, **18**, 163 (1985).
7. B. K. Jha, *Astrophysics Space Sci.*, **175**, 283 (1991).
8. F. S. Ibrahim, I. A. Hassanien, A. A. Bakr, *Canad. J. Phys.*, **82**, 775 (2004).
9. K. Das, S. Jana, *Bull. Soc. Math. Banja Luka*, **17**, 15 (2010).
10. N. T. M. Eldabe, E. M. A. Elbashbeshy, W. S. A. Hasanin, E. M. Elsaid, *Int. J. Energy Tech.* **3**, 1 (2011).
11. A. J. Chamkha, A. A. Khaled, *Int. J. Numer. Methods Heat Fluid Flow*, **10**, 455 (2000).
12. M. H. Kamel, *Energy Conv. Management*, **42**, 393 (2001).
13. A. J. Chamkha, *Int. J. Engng. Sci.*, **42**, 217 (2004).
14. P. L. Chambré, J. D. Young, *Phys. Fluids*, **1**, 48 (1958).
15. U. N. Das, R. K. Deka, V. M. Soundalgekar, *Forschung im Ingenieurwesen*, **60**, 284 (1994).
16. R. Muthucumarswamy, P. Ganesan, *Forschung im Ingenieurwesen*, **66**, 17 (2000).
17. K. D. Singh, R. Kumar, *Indian J. Phys.*, **84**, 93 (2010).
18. A. Postelnicu, *Heat Mass Transf.*, **43**, 595 (2007).
19. O. D. Makinde, *Chem. Eng. Comm.*, **198**, 590 (2010).
20. D. Pal, B. Talukdar, *Math. Computer Modelling*, **54**, 3016 (2011).
21. J. A. Schetz, *J. Appl. Mech.*, **30**, 263 (1963).
22. P. Chandran, N. C. Sacheti, A. K. Singh, *Heat Mass Transf.*, **41**, 459 (2005).
23. R. R. Patra, S. Das, R. N. Jana, S. K. Ghosh, *J. Appl. Fluid Mech.*, **5**, 9 (2012).
24. G. S. Seth, Md. S. Ansari, *Int. J. Appl. Mech. Eng.*, **15**, 199 (2010).
25. G. S. Seth, G. K. Mahato, S. Sarkar, *Int. J. Energy Tech.*, **5**, 1 (2013).
26. R. Nandkeolyar, M. Das, P. Sibanda, *Math. Problems Eng.* **2013** Article ID 381806 (2013).
27. R. Nandkeolyar, M. Das, P. Sibanda, *Boundary Value Problems*, **2013**, 247 (2013).
28. K. R. Cramer, S. I. Pai, Magnetofluid dynamics for engineers and applied physicists, New York: McGraw Hill, 1973.
29. A. Pantokratoras, *J. Appl. Phys.*, **102**, 076113 (2007).
30. K. Takenouchi, *J. Phys. Soc. Japan*, **54**, 1329 (1985).
31. Y. Koshiha, T. Matsushita, M. Ishikawa *Influence of induced magnetic field on large-scale pulsed MHD generator*, in: AIAA 33rd Plasmadynamics and Lasers Conference, Maui, Hawaii, May 20-23, 2002.
32. K. K. Khurana, M. G. Kivelson, D. J. Stevenson, G. Schubert, C. T. Russell, R. J. Walker, C. Polanskey, *Nature*, **395**, 777 (1998).
33. M. B. Glauert, *J. Fluid Mech.* **10**, 276 (1961).
34. A. Raptis, V. Soundalgekar, *Nuclear Eng. Des.*, **72**(3), 373 (1982).
35. A. Raptis, C. V. Massalas, *Heat Mass Transf.*, **34**, 107 (1998).
36. O. A. Beg, A. Y. Bakier, V. R. Prasad, J. Zueco, S. K. Ghosh, *Int. J. Thermal Sci.*, **48**, 1596 (2009).
37. R. K. Singh, A. K. Singh, N. C. Sacheti, P. Chandran, *Heat Mass Transf.*, **46**, 523 (2010).
38. B. Carnahan, H. A. Luther, J. O. Wilkes, Applied Numerical Methods, New York, John Wiley, 1969.
39. H. M. Antia, Numerical Methods for Scientists and Engineers, New Delhi: Tata McGraw-Hill Publishing Co Ltd, 1991.
40. E. R. Benton, D. E. Loper, *J. Fluid Mech.*, **39**, 561 (1969).
41. G. S. Seth, S. M. Hussain, S. Sarkar, *J. Egyptian Math. Soc.*, **23**, 197 (2015).
42. A. Khan, I. Khan, F. Ali, Samiulhaq, S. Shafie, *Plos One*, **9**(3): e90280. doi:10.1371/journal.pone (2014).

ТЕЧЕНИЕ С ЕСТЕСТВЕНА КОНВЕКЦИЯ В ИНДУЦИРАНО МАГНИТНО ПОЛЕ И ХИМИЧНА РЕАКЦИЯ ОТ n -ТИ ПОРЯДЪК, СЪПРОВОДЕНА С ПОГЛЪЩАНЕ НА ТОПЛИНА ОТ ДВИЖЕЩА СЕ ПЛОСКОСТ С ТЕМПЕРАТУРЕН ПРОФИЛ

Г.С. Сет*, С. Саркар

Департамент по приложна математика, Индийско минно училище, Дханбад 826004, Индия

Постъпила на 3 януари, 2014 г. коригирана на 26 август, 2014 г.

(Резюме)

Изследвано е течение под действие на естествена конвекция в нестационарно магнитно поле, съпроводено от топло- и масопренасяне във вискозен, електропроводящ и топло-поглъщащ флуид зад подвижна вертикална плоскост с температурен профил. Отчетен е ефектът на химична реакция от n -ти порядък. Уравненията на движението и на преноса са решени с използването на крайна диференчна схема по Crank-Nicolson. Численото решение за разпределението на скоростите, индуцираното магнитно поле, концентрациите на веществата и температурата на флуида са представено графично, а стойностите на коефициента на триене и числата на Sherwood и Nusselt са дадени в табличен вид. Влиянието на температурния профил на стената върху течението е сравнено със случая на изотермична стена. Коректността на числените резултати е потвърдена.

Synthesis and characterization of nanohybrid lanthanum oxide doped with polystyrene in electronic devices

S. N. Mousavi-Kani¹, A. Bahari² and Z. Moradinedjad^{3*}

¹ Cellular and Molecular Biology Research Center, Babol University of Medical Sciences, Babol, Iran

² Department of Physics, University of Mazandaran, Babolsar, Iran

³ Sari Second Region, Education Office, Sari, Iran

Received January 4, 2014; Revised July 28, 2014

Organic thin-film transistors (OTFTs) obtained from thin gate dielectrics of organic and inorganic hybrids as thin films have very good electrical properties such as high-K dielectric and low leakage current, and are a very remarkable and practical category in physics-chemistry research. In the present work, we synthesized a polystyrene (PS)/La₂O₃ hybrid by the sol-gel method and studied its properties for replacing silicon oxide as a good gate dielectric material for organic field-effect transistor devices. The structure and morphology of PS/La₂O₃ were studied by using X-ray diffraction (XRD), scanning electron microscopy (SEM) and Fourier transform infrared spectroscopy (FTIR). The effects of different temperatures and concentrations on the size of nanocrystallites were also studied by the X-ray powder method. The dielectric constant (K) and capacity (C) were measured using GPS 132 A technique. The obtained results indicated that PS/La₂O₃ nanocomposite prepared with the highest concentration of PS at the lowest temperature has an amorphous structure which can reduce leakage current and tunneling current due to its high EOT (equivalent oxide thickness). It can be used for future OTFT flexible devices.

Keywords: Dielectric, Nanocomposite, Organic Material, PS/La₂O₃, XRD, Transistor.

INTRUDUCTION:

Nowadays, thin film transistors with an active layer of an organic material have attracted much attention due to their process ability, low cost and flexibility [1-2]. Organic gate dielectrics are favored very much because of their solution process ability and flexibility which can lower process temperature, but polymer gate dielectrics have capability to be used in electronic chipsets due to their low K (dielectric constant) and high current densities [3-5]. On the other hand, the dimensions of microelectronic devices are placed in nano scales. The need for smaller and faster devices made nano electronics of high importance in today's technological world. Use of smaller electronic devices increases processing speed and lowers electricity usage, but this causes problems such as leakage current in Mosfet (metal oxide semiconductor field effect transistor). Correspondingly, one of the solutions is to use nanostructured transistors [6-7]. Organic-inorganic hybrid thin film transistors have good electrical properties such as high dielectric constant, low leakage current density and less than 40 nanometer thickness [8]. We believe that the higher k-gate dielectric materials can be introduced as a better alternative for gate dielectric in future devices [9].

In this case there has been much more literature on organic-inorganic hybrid thin film transistors. Several attempts have been made to get materials with better electrical properties such as PS/TiO₂ [10], PVP/TiO₂ [11], PS/titania [12], PMMA/SiO₂ [13] and this should be continued to get a better hybrid. In this research we tried to synthesize a new PS/La₂O₃ hybrid nanocomposite to get a better structure. Lanthanum oxide nanocrystallite has a lot of attractive properties such as high-k dielectric and energy band gap of 4.3 eV [14]. It has amorphous structure at ≤500°C and can reduce leakage current [15]. These properties make it a good choice for use in future electrical devices as gate dielectric [16]. Polystyrene has good resistance against water absorption and excellent thermal and electrical insulation. So PS/La₂O₃ can be used as a good insulator to lower leakage current in electrical devices [17, 18]. In this work, we used sol-gel methods to synthesize PS/La₂O₃ with different density and temperatures and we studied its structural and electrical properties.

EXPERIMENTAL

The materials used were from Merck; the sets used were: XRD (GBC-MMA-007), SEM (Tescan Vega II) and FTIR (Shimadzu).

PS/La₂O₃ nanocrystallites were prepared by a sol-gel procedure with lanthanum chloride as a raw material. We added 5.9 g of lanthanum chloride (LaCl₃·7H₂O) to 300 ml of distilled water and put it over magnetic stirring at room temperature. We added

* To whom all correspondence should be sent:

E-mail: zm368@yahoo.com

2.7 g of cetyltrimethylammonium bromide (CTAB) into the above solution at room temperature under stirring till the solution became transparent. Then we put 6.0 ml of ammonia into the solution to reach a pH value of 10. After 2 h, polystyrene solution (0.07 g PS in 2 ml o-xylene) was added to this solution. After vigorous stirring for 24 h, the sol solution was dried at 80 °C for 72 h. Finally, the obtained white solid gel was centrifuged, washed with distilled water and ethanol to remove possible ions remaining in the final product and dried it again at 80 °C. As a result, PS/La₂O₃ powder was obtained. The same procedure was performed with two other PS amounts (0.14, 0.28 g) and we calcined at 300 °C and 500°C. We studied the effect of temperature and concentrations on the sample structure. The crystal phases of the product were investigated by XRD technique; morphological analysis was done by SEM technique. The size of the nanocrystallites was determined by the X-powder method. The dielectric constant (K), and the capacity (C) were measured by GPS 132 A technique.

RESULTS AND DISCUSSION

The structure of the PS/ La₂O₃ nanocrystallites was investigated using XRD analysis. Figures 1,2 show the XRD patterns of the PS/ La₂O₃ as-prepared and annealed at temperature 300 °C and 500 °C with different PS amounts: 0.07, 0.14, 0.28 g .

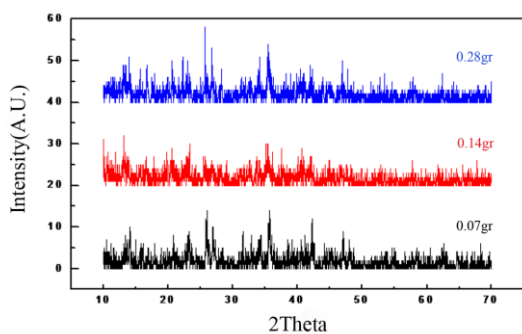


Fig 1. XRD patterns of PS/La₂O₃ nanocrystallites at 300 °C temperature with different PS amounts.

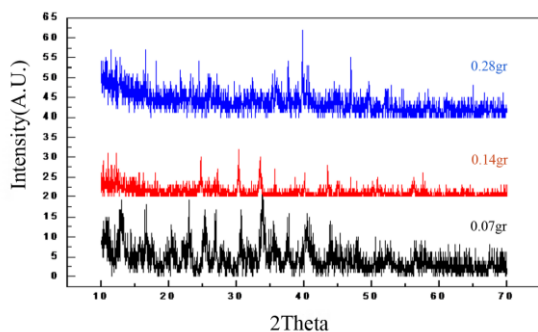


Fig 2. XRD patterns of PS/La₂O₃ nanocrystallites at 500 °C temperature with different PS amounts.

As XRD shows, increasing PS concentration in the PS/La₂O₃ nanocomposite, the peak of PS/ La₂O₃ decreased and the peak width increased. In fact, as the amount of polystyrene increased, it affected the size of nanocrystallites and increasing calcination temperature affected the size and the structure of nano particles. Figure 3 shows the sizes of PS/ La₂O₃ nanocrystallites at 300 °C temperature with different PS concentration.

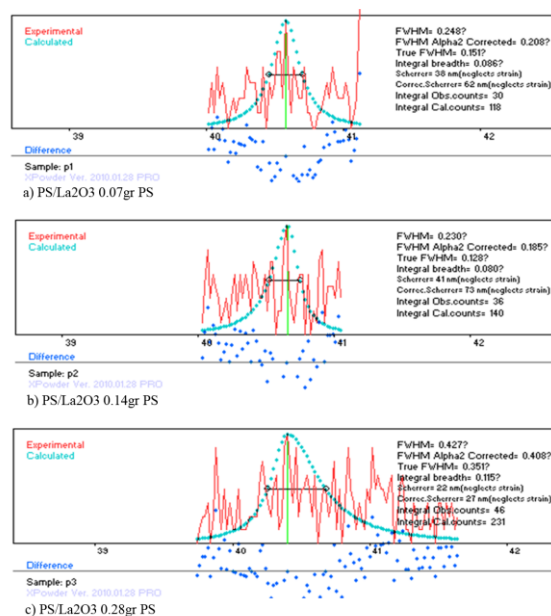


Fig 3. Peaks of nanocrystallites obtained at 300 °C using X-powder method.

X-powder analysis showed that increasing the amount of polystyrene decreased the size of nanocrystallites of PS/ La₂O₃ and the structure of the sample became more amorphous. Increasing the temperature decreased the size of nanocrystallites of PS/ La₂O₃ and the lower size of the nanoparticles is related to the use of 0.028 g of PS and 300 °C (Table 1).

Table 1. Size of nanocrystallites of PS/La₂O₃ at different temperature

Sample	Calcination temperature T/C	Size of nanocrystallites S/nm
0.07 g PS/La ₂ O ₃	300 °C	62 nm
0.14 g PS/La ₂ O ₃	300 °C	73 nm
0.28 g PS/La ₂ O ₃	300 °C	27 nm
0.07 g PS/La ₂ O ₃	500 °C	29 nm
0.14 g PS/La ₂ O ₃	500 °C	52 nm
0.28 g PS/La ₂ O ₃	500 °C	28 nm
Pure La ₂ O ₃	300 °C	51 nm
Pure La ₂ O ₃	500 °C	48 nm

The capacitance measurements were conducted with a Gps 132A precision LCR meter. The dielectric constants were calculated according to the following equation:

$$C = K\epsilon^0 \frac{A}{d}$$

where C is the measured capacitance, ϵ^0 is the permittivity of free space, A is the area of the capacitor, and d is the thickness of the dielectric. According to Table 2, the highest K is related to an amount of 0.028 g of PS at 300 °C.

Table 2. Dielectric constants and capacity of PS/La₂O₃ at different temperatures and different PS amounts. The highest K is registered at 300 °C with 0.28 g of PS.

Sample	Calcination temperature T/ °C	K	C (nf)
0.07 g PS/La ₂ O ₃	300 °C	67.8	0.081F
0.14 g PS/La ₂ O ₃	300 °C	34.6	0.016 F
0.28 g PS/La ₂ O ₃	300 °C	82.67	0.066 F
0.14 g PS/La ₂ O ₃	500 °C	24.7	0.021F
0.28 g PS/La ₂ O ₃	500 °C	57.72	0.027 F

Figure 4 shows the Fourier transform infrared spectrum (FTIR) of PS/La₂O₃ obtained at 300 °C with different PS amounts.

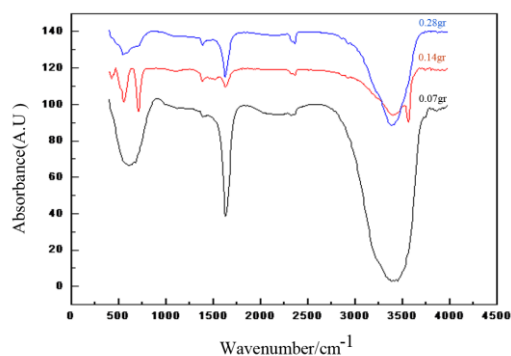


Fig. 4. FTIR spectrum of PS/La₂O₃ at 300 °C temperature with different PS amounts.

The FTIR spectrum in the area of 1650 cm⁻¹ shows that the absorption is due to an aromatic ring and the maximum absorption is about O-H hydrogen bond; the peak at wavenumber 2923 cm⁻¹ is related to the C-H bond of methylene group and the peak at wavenumber 540-601 cm⁻¹ is related to the C-Cl. The FTIR spectrum of the nanocomposite showed that as the concentration and temperature increased, the absorption decreased which results in bonding failure. The morphologies of PS/La₂O₃ hybrid nanocomposites were analyzed using SEM technique (Figures 5, 6, 7).

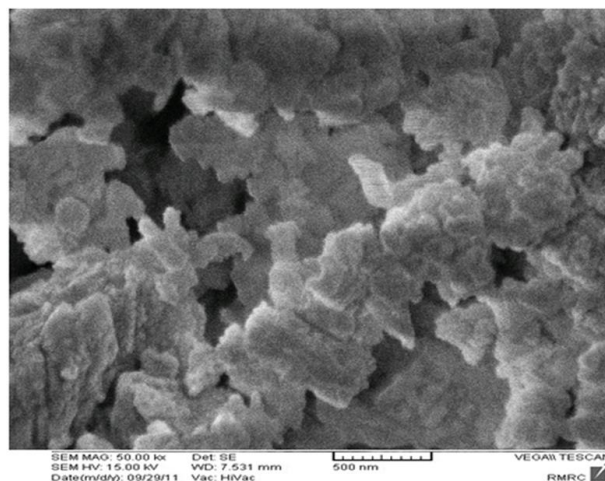


Fig. 5. SEM image of PS/La₂O₃ nanocrystallites obtained at 500 °C with 0/07 g PS

The SEM comparison between PS/La₂O₃ and La₂O₃ showed that adding polystyrene to lanthanum oxide changed its structure and made it uniform and the size of the nanocomposite decreased leading to amorphous PS/La₂O₃. As the SEM image of the nanocomposite obtained with 0.28 g of PS at 300 °C shows, it has uniform structure and lower size of nanoparticles that are more amorphous than other PS/La₂O₃ with different concentration and temperature.

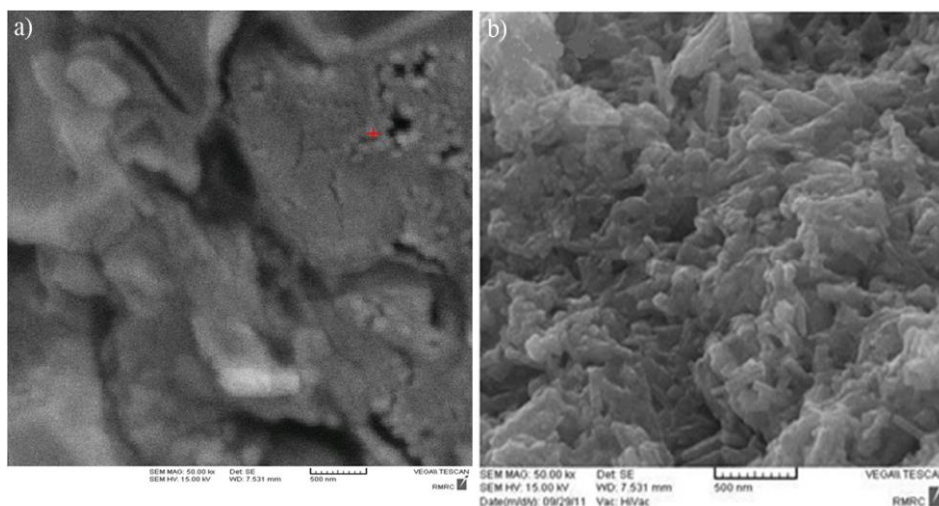


Fig. 6. SEM image of PS/La₂O₃ nanocrystallites obtained: (a) at 300°C with 0.28 g PS (b) SEM image of La₂O₃ at 300°C.

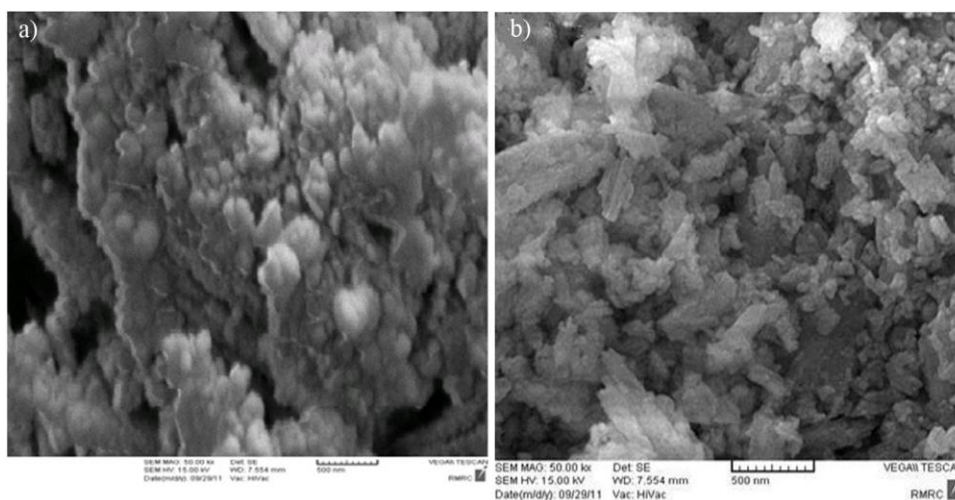


Fig. 7. SEM image of PS/ La₂O₃ nanocrystallites obtained: (a) at 500°C with 0.28 g PS (b) SEM image of La₂O₃ at 500°C.

According to the previous research, La₂O₃ was introduced as a high-K dielectric gate and was used in NVMs [15]. In another study monohybrid TiO₂/PS was investigated and results showed that it can be used as a gate insulator [10]. Conspicuously, the quality of the dielectric surface improved significantly and it reduced the leakage current. According to the above conclusion, we decided to use La₂O₃ instead of TiO₂. The obtained results also showed a very impressive quantity of amorphous phase in the samples and considerably better reduction of leakage current than in previous research.

CONCLUSION

In this work, we studied PS/La₂O₃ with different contents and temperatures using XRD, SEM, FTIR and GPs 132 A techniques. Results showed that the

nanocomposite PS/La₂O₃ with 0.28 g of PS at 300 °C is more amorphous, has a higher K- dielectric constant and can be used as a good insulator in electric devices to prevent tunneling leakage current. It can be used in future OTFT flexible devices.

REFERENCES

1. G. Paasch, S. Scheinert, R. Tecklenburg, Proceedings of the 27th European Solid- state Device Research Conference., 636 (1997).
2. T. W. Kelley, L. D. Boardman, T. D. Dunbar, D. V. Muyres, M. Pellerite, T. P. Smith, *J. Phys. Chem.*, **107**, 5877 (2003).
3. S. H. Kim, S. Y. Yang, K. Shin, H. Jeon, J. W. Lee, K. P. Hong, C. E. Park, *Appl. Phys. Lett.*, **89**, 183516-1 (2006).
4. A. Facchetti, M. H. Yoon and T. J. Marks, *Adv. Mater.*, **17**, 1705 (2005).

5. J. Veres, S. Ogier and G. Lloyd, *Chem. Mater.*, **16**, 4543 (2004).
6. R. W. Siegel, E. Hu and M. C. Roco. International Technology Research Institute World Technology (WTEC), Division Loyola college: Maryland, 1, 1990.
7. A. C. Dillon, P. A. Parilla, J. L. Alleman, J. D. Perkins, M. J. Heben, *Chem. Phys. Lett.*, **316**, 13 (2000).
8. C. G. Choi, B. S. Bae, *Synth. Met.*, **159**, 1288 (2009).
9. A. Bahari, P. Morgen, Z. S. Li, *Surf. Sci.*, **602**, 2315 (2008).
10. Y. Lu, W. H. Lee, H. S. Lee, Y. Jang, K. ChO, *Appl. Phys. Lett.*, **94**, 3303 (2009).
11. F. C. Chen, C. W. Chu, J. He, Y. Yang, *Appl. Phys. Lett.*, **85**, 3295 (2004).
12. J. Park, S. D. Lee, B. J. Park, H. J. Choi, D. W. Kim, J. W. Lee, J. S. Choi, *Mol. Cryst. Liq. Cryst. Sci.*, **519**, 222 (2010).
13. M. D. Morales-Acosta, M. A. Quevedo-López, B. E. Gnade, R. Ramírez-Bon, *J. Sol-Gel Sci. Technol.*, **58**, 218 (2011).
14. A. Bahari, A. Anasari and Z. Rahmani, *J. Eng. Technol. Res.*, **3**, 203 (2011).
15. A. Bahari, Z. Khorshidi Mianaeae, R. Gholipur, T. Taghipoor, A. Rezaeian, *Americ. J. Sci. Res.*, **54**, 19 (2012).
16. P. Pisechny, K. Husekova, K. Frohlich, L. Harmatha, J. Soltys, D. Machajdik, J. P. Espinos, M. Jergel, J. Jakabovic, *Mater. Sci. Semicond. Process.*, **7**, 231 (2004).
17. S. Doroudiani, C. E. Chaffey, M. T. Kortschot, J. Polym. Sci., Part B: *Polym. Phys.*, **40**, 723 (2002).
18. S. Doroudiani, M. T. Kortschot, *J. Thermoplast. Compos. Mater.*, **17**, 13 (2004).

СИНТЕЗА И ОХАРАКТЕРИЗИРАНЕ НА НАНОХИБРИДЕН ЛАНТАНОВ ОКСИД ДОТИРАН С ПОЛИСТИРЕН ЗА ЕЛЕКТРОННИ УРЕДИ

С.Н. Мусави-Кани¹, А. Бахари², З. Морадинеджад^{3*}

¹Изследователски център по клетъчна и молекулярна биология, Медицински университет, Бабол, Иран

²Департамент по физика, Университет Мазандаран, Баболсар, Иран

³Сари-втори регион, Бюро по образовани, Сари, Иран

Постъпила на 4 януари, 2014 г.; коригирана на 28 юли, 2014

(Резюме)

Органични транзистори с тънък филм (OTFTs), получени от тънки диелектрици на органични и неорганични хибриди като тънки слоеве имат много добри електрически свойства като висока диелектрична К и нисък ток на утечка, и са забележително и практическо поле за физико-химични изследвания. В настоящата работа, ние синтезирахме полистирен (PS) / La_2O_3 хибриден по метода на зол-гел и изучихме неговите свойства за заместване на силициев оксид като добър диелектричен материал за органични транзисторни устройства. Структурата и морфологията на (PS) / La_2O_3 бяха изследвани с помощта на рентгенова дифракция (XRD), сканираща електронна микроскопия (SEM) и инфрачервена спектроскопия с трансформация на Фурие (FTIR). Ефектите на различни температури и концентрации върху размера на нанокристалитите също бяха изследвани по метода на рентгенова прахова. Диелектрична константа (К) и капацитет (С) се измерва като се използва GPS 132 А техника. Получените резултати показват, че (PS) / La_2O_3 нанокмпози има аморфна структура, при най-високата концентрация и най-ниската температура, която може да намали изтичането на ток и ток на тунелиране, поради високата си ЕОТ (еквивалентна оксидна дебелина). Той може да се използва за бъдещи OTFT гъвкави устройства.

Statistical analysis of seed oils from melon and pumpkin by using colour parameters

J. Petkova², K. Nikolova^{*1}, D. Boyadzhiev³, A. Aladjadjiyan⁴, G. Antova²

¹ University of Food Technologies, Plovdiv, Bulgaria

² Department of Chemical Technology, PU „Paisii Hilendarski”

³ Department of Applied Mathematics, PU „Paisii Hilendarski”

⁴ Department of Mathematics, Informatics and Physics, Agricultural University

Received November 18, 2013; Revised August 7, 2014

Difference in colour parameters and content of the pigments chlorophyll and β -carotene for different sorts of melon and pumpkin seed oils was proved by applying mathematic statistical analysis. The significance of the different indicators for modeling the oil groups was estimated. Data on different sorts of melon and pumpkin fruit oils were processed by applying discriminant analysis to study the possibility to create discriminatory procedures for modelling the various sorts and their origin.

Keywords: pumpkin and melon seed oils, colorimetry, statistical analysis

INTRODUCTION

Various physical and chemical tests have been used to establish the authenticity of oils and to detect the level of adulterants in it. The most useful are the chromatographic methods. They offer high sensitivity and accuracy, but are time consuming and expensive. For this reason in our study we suggest three fast and cheap physical methods on the base of colorimetric techniques. Different kinds of vegetable oils can be quickly and precisely differentiated by using statistical analysis.

The study aims to analyze a database of colour parameters of seed oils obtained from different varieties of pumpkin and melon grown in Bulgaria, and to explore the possibility for application of mathematical and statistical modeling to different varieties of different origin.

To achieve this objective the following tasks were formulated:

- obtaining and analyzing a database of colorimetric analyses of seed oils of different varieties of pumpkin and melon;
- establishing the differences in the values of the investigated indicators;
- modeling and analysis of the groups representing different varieties.

MATERIALS AND METHODS

The seeds of the pumpkin species *Cucurbita moschata*, *Cucurbita pepo* and *Cucurbita maxima*, and the melon species Honeydew, Desserten 5 and Hybrid 1 from fam. *Cucurbitaceae*, were grown and obtained from the region of South Bulgaria, crop 2013.

Isolation of glyceride oil and determination of oil content.

The seeds (50 g samples) were air-dried and ground to powder and the oil was extracted with n-hexane in a Soxhlet apparatus for 8 h. The solvent was partly removed in a rotary vacuum evaporator, the residue was transferred in a pre-weighed glass vessel and the rest of the solvent was removed under stream of nitrogen to a constant weight to determine the oil content [1].

Colour parameters in two different colorimetric systems - XYZ (for large colour differences) and CIE Lab (for small ones) were obtained using a colorimeter Lovibond PFX 880 (UK) and cuvette with a length of 10 mm [2]. All measurements were carried out at room temperature immediately after oil extraction. Colour coordinates, colour parameters a, b and brightness L of the tested samples were measured. Chlorophyll and β -carotene were calculated by using the transmission spectra in the visible region and the values of the colour parameters - by software program developed specially for Lovibond PFX 880 by the producer. Five replicates of each measurement were performed.

The programme “Statistica” was used for data processing. Data distribution was found to be normal according to the criterion of Kolmogorov - Smirnov [3-4]. To establish statistically significant differences between the characteristics of the studied varieties, the Tukey criterion for multiple comparisons was applied [5]. When modeling the groups per variety discriminant analysis with *a priori* equal probabilities for hit in groups was used [6-7]. Data about Mahalanobis distances were obtained.

* To whom all correspondence should be sent:

E-mail: kr.nikolova@abv.bg

Table 1. Colour parameters and pigments in seed oils of different pumpkin varieties

Parameters	Variety of pumpkin seed oils					
	<i>Cucurbita pepo</i>		<i>Cucurbita moschata</i>		<i>Cucurbita maxima</i>	
	\bar{x}	SD	\bar{x}	SD	\bar{x}	SD
X	4.64	0.07	34.09	2.56	26.02	1.18
Y	3.54	0.12	34.58	2.73	28.36	1.23
Z	0.18	0.02	4.90	0.53	8.32	0.61
Brightness L	22.31	0.02	66.42	0.02	60.80	0.001
<i>a</i>	16.49	0.02	0.61	0.00	-7.31	0.01
<i>b</i>	35.69	0.05	71.63	0.05	48.18	0.02
Chlorophyll, ppm	0.00	0.00	0.00	0.00	0.00	0.00
β - carotene, ppm	62.84	4.78	72.91	2.32	1222.33	0.72

\bar{x} -Average value; SD – standard deviation

RESULTS AND DISCUSSION

Colour parameters of the investigated seed oils from different melon and pumpkin varieties were obtained. Data are presented in Tables 1 and 2. Fisher’s test significance is 0.00.

Unlike the other pumpkin seed oil varieties, the one for the variety *Cucurbita maxima* possesses a negative colour component *a*. This colour parameter means that the green component predominates over the red one in that sample, although none of the pumpkin seed oils contains chlorophyll. The mentioned variety is probably rich in pigments, different from chlorophyll. Similar observation for the same variety has been announced by Leila Rezig [8], who has obtained rather lower values for brightness (44.8) of the seed oil of the same variety of pumpkin grown in Tanzania.

The most pronounced yellow component was observed for pumpkin seed oil of the variety *Cucurbita moschata*; the lowest brightness was obtained for the seed oil of the variety *Cucurbita pepo*. The colour component *b* of the pumpkin seed oils is several times higher than that measured in other vegetable oils such as soybean, sunflower, rapeseed, etc. For the listed vegetable oils this

parameter changes from 9.2 to 10.4 while for pumpkin seed oils it lies between 35 and 72. Similar data for plant oil have been obtained by Hsu and Yu [9].

The brightness for melon seed oils has the highest values for the oil of the variety Desserten 5 and the lowest one for the oil of the variety Hybrid 1. Unlike the pumpkin seed oils, melon seed oils possess a negative colour component *a* for all varieties, which means that in melon oils the green component prevails over the red one. The latter observation can be explained with the presence of chlorophyll in all samples of melon oils. In melon seed oils, with rising the content of β -carotene raises the colour component *b*. The strongest prevalence of the yellow nuance was observed in seed oils of the variety Hybrid 1 – about twice as high as that of the two other varieties.

Tests were made about the homogeneity of dispersions. Tukey test showed differences between the varieties, which were sufficient for modeling. After applying the incremental discriminant analysis with grouping variable "variety of pumpkin or melon" the discriminant functions ensuring 100% recognition of the different varieties were derived.

For each of the sample groups, the mahalanobis distances were calculated and canonical analysis was simultaneously performed because mahalanobis distances provide an insight on the specific features of the examined group in the original space,

Table 2. Colour parameters and pigments in seed oils of different melon varieties

Parameters	Variety of Melon seed oils					
	<i>Medena rossa</i>		<i>Desserten 5</i>		<i>Hybrid 1</i>	
	\bar{x}	SD	\bar{x}	SD	\bar{x}	SD
X	53.17	10.02	75.78	0.50	19.47	0.25
Y	56.74	10.64	80.12	0.43	20.88	0.21
Z	40.88	9.44	64.72	0.37	4.17	0.02
Brightness L	76.70	0.94	91.78	0.06	48.29	1.83
<i>a</i>	-4.04	0.10	-5.21	0.01	-3.51	0.21
<i>b</i>	25.44	0.05	22.05	0.05	49.44	1.22
Chlorophyll, ppm	0.04	0.00	0.02	0.00	0.02	0.00
β - caroten, ppm	8.73	0.71	6.58	0.03	35.97	4.31

\bar{x} -Average value; SD – standard deviation

whereas canonical representations are in a bidimensional space. They serve for better visualization of the particular groups since their canonic variables are linear combinations of the initial physical indices. The existence of differences in the values of the investigated parameters was statistically proven. This makes discriminant analysis an efficient tool for the qualitative distinction of natural pumpkin oil and melon oil from other oils. The models and the associated mahalanobis distances enable the classification of unknown samples.

The parameters involved in the modeling in order of their inclusion in the model for oil of pumpkin seeds are: brightness (L), colour component a and β -carotene. To illustrate the groups designating the studied pumpkin varieties, additionally canonical analysis was made. The result presented in Fig. 1 confirms the distinct varietal differences and ensures 100% recognition.

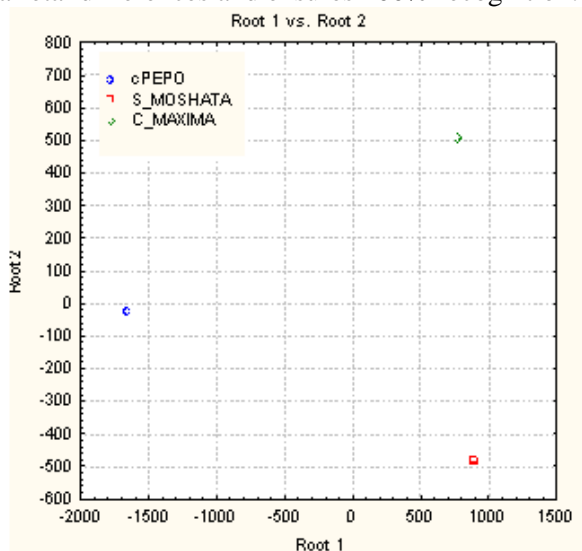


Fig. 1. Location of the varieties of pumpkin seed oil according to the first two canonical variables

For further clarification of these differences the Mahalanobis distances between centroids of the individual groups were identified as well. Results

Table 3. Mahalanobis distances between different varieties of pumpkin seed oils

Pumpkin variety	Mahalanobis distances		
	<i>Cucurbita pepo</i>	<i>Cucurbita moschata</i>	<i>Cucurbita maxima</i>
<i>Cucurbita pepo</i>	0	8966170	8205937
<i>Cucurbita moschata</i>	8966170	0	1332496
<i>Cucurbita maxima</i>	8205937	1332496	0

Table 4 Mahalanobis distances between different varieties of melon seed oils

Melon variety	Mahalanobis distances		
	<i>Medena rossa</i>	<i>Desserten 5</i>	<i>Hybrid 1</i>
<i>Medena rossa</i>	0	38524	985990
<i>Desserten 5</i>	38524.3	0	1409382
<i>Hybrid 1</i>	985990.1	1409382	0

are presented in Table 3. Mahalanobis distances represent individual groups better than canonical variables because they give an idea of the dynamics of the change in the distance between the group centroids.

According to the data on the distances between the centroids of the individual groups, pumpkin oil from the variety *Cucurbita pepo* is relatively equidistant from the varieties *Cucurbita moschata* and *Cucurbita maxima*. Pumpkin seed oil of the variety *Cucurbita moschata* is most distant from the one obtained for the variety *Cucurbita maxima*.

The parameters involved in the modeling of melon seed oils in order of their inclusion in the model for oils of melon seeds are: chlorophyll, colour component a, β -carotene and colour component b. To illustrate the groups designating the studied melon varieties, canonical analysis was made as in the case of pumpkin varieties. Again 100% recognition of the groups was ensured. The latter fact is illustrated on Fig. 2.

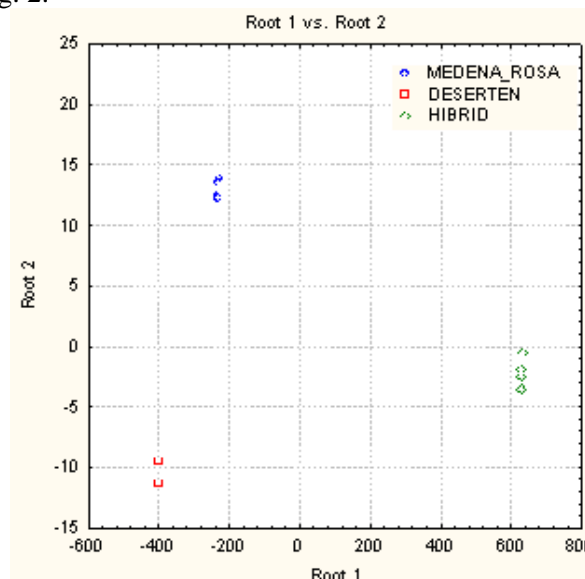


Fig.2. Location of the varieties of melon seed oil according to the first two canonical variables

According to the distances between the centroids of the individual groups the melon seed oil of the variety Medena rossa is closest to that of Desserten 5 and most distant of the oil from variety Hybrid 1. The melon seed oil of variety Hybrid 1 differs most strongly from the melon seed oils of the other two melon varieties.

CONCLUSIONS

The analysis of the database on colour parameters of oils from Bulgarian varieties of pumpkin and melon fruits showed the possibility to characterize certain group varieties by discriminant analysis.

Colour parameters in CIE Lab colorimetric system and pigments (chlorophyll and β - carotene) determine the specificity of oils of different varieties.

Colour indicators in the XYZ colorimetric system are not important in distinguishing oils from pumpkin and melon.

In the case of melon seed oils the oil seed of variety Hybrid 1 differs most strongly in colour parameters and in the case of pumpkin oil - the one of *Cucurbita moschata*.

It was statistically shown that there are differences in the values of the considered parameters for different groups of oils - pumpkin and melon ones. This makes the use of the discriminant analysis efficient for the qualitative differentiation of various oils, non-traditional for food technologies.

Acknowledgments: This work is partly supported by the scientific project SI 13 FMI-002 of the Science Research Department of Plovdiv University "Paisii Hilendarski".

REFERENCES

1. ISO 659:2009. Oilseeds – Determination of oil content (Reference method), 2009, p. 12.
2. Recommendations on uniform color spaces – color - difference equations; Psychometric Color Terms (Commission International de l' Eclairage – CIE). Publication no 15 (F. 1. 3. 1.) 1971. Supplement 2. Bureau Central de la Commission Internationale de l' Eclairage. Vienna, 1978.
3. G. J. McLachlan: In Discriminant Analysis and Statistical Pattern Recognition. John Wiley & Sons. Inc. New York, Chichester, Brisbane, Toronto, Singapore, 1992, p.526.
4. B. M. G. Vandeginste, D. L. Massart, L. M. C. Buydens, S. de Jong, P. J. Lewi, J. Smeyers -Verbeke (ed.) Handbook of Chemometrics and Qualimetrics Part B. Elsevier, Amsterdam, 1998.
5. Kr. Kalinov, Statistical methods in behavioral and social sciences, NBU, Sofia, 2001.
6. A. G. Bondar, G. A. Statjukha, Planning the experiment in the chemical technology, (Principles, examples and tasks). Kiev; Vischaya shkola, 1976. p.184.
7. G. Lakin, Biometrics, Moscow, Higher School, 1990, p.352.
8. L. Rezig, M. Chouaibi, K. Msaada, S. Hamdi, *Industrial Crops and Products*, **37**, 82 (2012).
9. Hsu S. Y., Yu S.H., *Journal of Food Engineering*, **51**, 215 (2002)

МАТЕМАТИКО СТАТИСТИЧЕСКО МОДЕЛИРАНЕ ПО ЦВЕТОВИ ПАРАМЕТРИ НА НЕТРАДИЦИОННИ МАСЛА ОТ СЕМЕ НА ПЪПЕШ И ТИКВА

Ж. Петкова², Кр. Николова¹, Д. Бояджиев³, А. Аладжаджиян⁴, Г. Антова²,

¹ Университет по хранителни технологии, бул. „Марица“ 26, 4002 Пловдив, България.

² Катедра по пимична технология, Пловдивски Университет „Паисий Хилендарски“, ул. „Цар Асен“ 24, 4000 Пловдив, България.

³ Катедра по приложна математика, Пловдивски Университет „Паисий Хилендарски“, ул. „Цар Асен“ 24, 4000 Пловдив, България

⁴ Аграрен Университет, ул. „Менделеев“ 12, Пловдив 4000, България.

Постъпила на 18 ноември, 2013 г.; коригирана на 7 август, 2014 г.

(Резюме)

Чрез прилагане на математико статистически анализ на масла от семена на различни сортове тиква и пъпеш е доказано различие в цветовите параметри и съдържанието на пигменти като хлорофил и β - каротен. Оценена е значимостта на отделните показатели при моделирането на групите при маслата. Чрез дискриминатен анализ са обработени данни за масла, получени от семки на тиква и пъпеш за да се проучи възможността за математико-статистическо моделиране на различни сортове с отделен произход.

Evaluation of thermodynamic properties of long-chain organic compounds using GMA equation of state

A. Morsali *, Z. Alavi, S. A. Beyramabadi

Department of Chemistry, Mashhad Branch, Islamic Azad University, Mashhad, Iran

Received January 8, 2014; Revised May 20, 2014

Concerning the scientific and industrial importance of long-chain organic compounds, endeavors were made in this research to use a simple and accurate equation of state for prediction of thermodynamic properties of these compounds. Using GMA equation of state, different groups of long-chain organic compounds including alkanes, alcohols, ketones and 1-carboxylic acids were studied. It was concluded and ascertained that GMA equation of state is capable of predicting the density of these compounds with a high degree of accuracy. A more sensitive test for any equation of state is the prediction of differential thermodynamic properties, such as internal pressure, isothermal compressibility and thermal expansion coefficient. In such a test, GMA equation of state predicted these properties with an acceptable degree of accuracy.

Keywords: GMA Equation of state; long-chain organic compounds; density; internal pressure; isothermal compressibility

INTRODUCTION

Long-chain organic compounds are of high importance in different branches of chemistry, including chemical industries. For many scientific and industrial purposes, it is necessary to be able to predict the thermodynamic properties of these compounds. It is not always possible to obtain the required thermodynamic data within the intended range of temperature and pressure from articles which have investigated these compounds experimentally. In such cases an accurate and simple equation of state will be very useful. Goharshadi-Morsali-Abbaspour equation of state (GMA EoS) is a simple and accurate equation which has been used for many compounds including polar, nonpolar fluids, refrigerants, hydrogen-bonded fluids, ionic liquids and mixtures [1-17]. In this research, this equation of state has been used to estimate the density and differential thermodynamic properties of a group of long-chain organic compounds.

Some of the equations of state, although successful in predicting the density, confront with difficulties in predicting differential thermodynamic properties such as internal pressure. The GMA EoS predicts these properties with acceptable accuracy in all cases. In the year 2005, Goharshadi *et al.* [1] derived an accurate and simple equation using the average potential energy. In this work, thermodynamic properties of different groups of long-chain organic compounds, including alkanes, alcohols, ketones

and 1-carboxylic acids were studied using GMA EoS.

THEORY

The average potential energy is approximately equal to the sum of contributions from nearest neighbors only, assuming single inverse powers for the effective repulsion and attraction.

The GMA equation of state [1] is based on the average potential energy and is given as:

$$(2Z - 1)V_m^3 = A(T) + B(T)\rho \quad (1)$$

where Z , V_m , and ρ are compressibility factor, molar volume, and molar density, respectively. The intercept and slope of this equation depend on temperature *via* the equations:

$$A(T) = A_0 - 2A_1 / RT + 2A_2 \ln T / R \quad (2)$$

$$B(T) = B_0 - 2B_1 / RT + 2B_2 \ln T / R \quad (3)$$

where A_0 – A_2 and B_0 – B_2 are constants. To use the equation of state for a liquid, the A and B parameters must be known. To find these

parameters, we may plot $(2Z - 1)V_m^3$ against ρ for different isotherms. The slope and intercept of the straight lines can be fitted with Eqs. (2) and (3) from which A_0 – A_2 and B_0 – B_2 can be found, respectively.

RESULTS AND DISCUSSION

We used the experimental PVT data for $C_{18}H_{38}$, $C_{19}H_{40}$ [18], $C_{20}H_{42}$ [19], $C_{23}H_{48}$, $C_{24}H_{50}$ [20], $C_{28}H_{58}$ [21], 1-propanol, 2-propanol, 1-butanol, 2-butanol [22], 1-pentanol, 2-pentanol, 3-pentanol [23], 1-hexanol, 1-octanol, 1-decanol, 1-hexadecanol [24], 1,2-butanediol [25], 2-propanone [26], 2-butanone

* To whom all correspondence should be sent:
E-mail: morsali@mshiau.ac.ir

Table 1. The average of square of correlation coefficient (R^2) of Eq. (1) and the average, minimum, and maximum absolute percent deviations of the calculated densities.

Compound	$T_{\min} - T_{\max}$ (K)	$(P_{\min} - P_{\max})/10^5$ (Pa)	R^2	$(100 \times \rho_{\text{exp}} - \rho_{\text{cal}} / \rho_{\text{exp}})$ Average (min – max)
C ₁₈ H ₃₈	313.15-383.15	0.9998-1475.9437	0.9996	0.0533(0.00094-0.28)
C ₁₉ H ₄₀	313.15-383.15	0.9998-1475.9438	0.9996	0.0532(0.000357-0.27)
C ₂₀ H ₄₂	373-573	0-4934.2105	0.998	0.631(0.0088-4.36)
C ₂₃ H ₄₈	333.15-393.15	0.9869-1475.9437	0.9996	0.0502(0.000262-0.0262)
C ₂₄ H ₅₀	333.15-393.15	0.9869-1475.9438	0.9997	0.0532(0.000357-0.27)
C ₂₈ H ₅₈	353.15-403.15	0.9869-1475.9439	0.9994	0.062(0.00122-0.3)
1-Propanol	283.15-348.15	0.9869-2048.8527	0.9994	0.07(0.001-0.34)
2-Propanol	283.15-348.15	0.9869-1718.2334	0.9994	0.0761(0.00462-0.431)
1-Butanol	283.15-348.15	0.9869-2034.0489	0.999	0.0478(0.0013-0.23)
2-Butanol	283.15-348.15	0.9869-2037.9965	0.9993	0.079(0.00053-0.45)
1-Pentanol	228.8000-433	98.6923-1973.8465	0.9998	0.038(0.000314-0.166)
2-Pentanol	234-433	98.6923-1973.8465	0.994	0.175(0.00418-1.05)
3-Pentanol	233.6-433	98.6923-1973.8465	0.9994	0.0854(0.0020-0.454)
1-Hexanol	298.15-348.15	0.9869-394.9667	0.9999	0.0089(0.000041-0.003)
1-Octanol	298.15-348.15	0.9869-396.5458	0.9999	0.00635(0.000386-0.018)
1-Decanol	298.15-348.15	0.9869-396.7432	0.9999	0.00538(0.00016-0.019)
1-Hexadecanol	348.15	3.3066-3.4087	0.9999	0.0096(0.0051-0.017)
1,2-Butanediol	288.15-308.15	0.9869-592.154	0.9999	0.00796(0.000737-0.0169)
2-Propanone	278.15-298.15	2.5-389.82	0.9997	0.0540(0.00125-0.472)
2-Butanone	278.15-338.15	25.167-3847.2	0.9911	0.143(0.00166-3.9)
3-Pentanone	278.15-338.15	25.166-3847.2243	0.991	0.147(0.00202-3.9)
2-Hexanone	288.15-338.16	25.1369-3755.835	0.9997	0.107(0.00167-4.2)
1-Butanoic acid	293.15-323.15	0.9869-246.7308	0.9995	0.014(0.000235-0.042)
1-Pentanoic acid	293.15-323.15	0.9869-246.7308	0.9984	0.0258(0.0029-0.061)
1-Hexanoic acid	293.15-323.15	0.9869-246.7308	0.9996	0.033(0.0013-0.075)
1-Heptanoic acid	293.15-323.15	0.9869-246.7308	0.996	0.039(0.0052-0.091)
1-Octanoic acid	293.15-323.15	0.9869-246.7308	0.995	0.042(0.0045-0.091)
1-Decanoic acid	343.15-373.1500	0.9869-88.8231	0.9991	0.00816(0.000102-0.0204)
1-Dodecanoic acid	343.15-373.1500	9.6852-871.6707	0.9997	0.058(0.044-0.073)
1-Tetradecanoic acid	353.15-373.15	0.9869-88.8231	0.9994	0.0063(0.00038-0.018)
1-Hexadecanoic acid	353.15-373.15	0.9869-88.8231	0.9996	0.16(0.14-0.18)

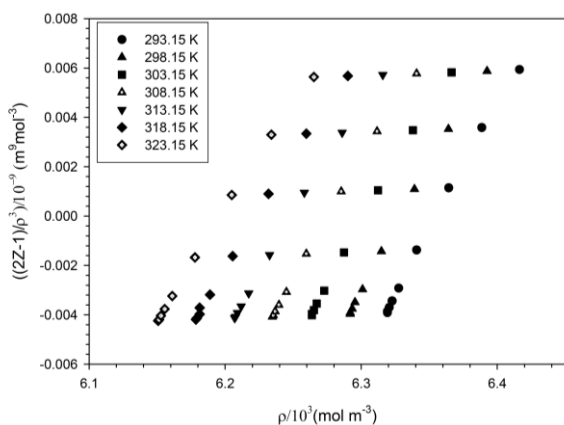


Fig. 1. Isotherms of $(2Z - 1)V_m^3$ versus molar density for 1-octanoic acid

[27], 3-pentanone [28], 2-hexanone [29], 1-butanoic acid, 1-pentanoic acid, 1-hexanoic acid, 1-octanoic acid [30], 1-decanoic acid, 1-dodecanoic acid, 1-tetradecanoic acid and 1-hexadecanoic acid [31] to plot $(2Z - 1)V_m^3$ against ρ for each isotherm. Figure 1 shows

isotherms of $(2Z - 1)V_m^3$ versus ρ for 1-octanoic acid.

The average values of the square of correlation coefficient (R^2) related to 44 compounds are presented in Table 1. As Table 1 shows, the linearity holds very well for all isotherms. Now that the $A(T)$ and $B(T)$ parameters are known, the constants $A0$ – $A2$ and $B0$ – $B2$ can be obtained using Eqs. (2) and (3). These constants are reported in Table 2.

The first test for every equation of state is its ability in prediction of density. The ability of GMA EOS in the prediction of density and other thermodynamic properties can be evaluated by statistical parameter, namely the absolute average deviation (AAD):

$$AAD = \frac{1}{N} \sum_{i=1}^N 100 \left| \frac{\rho_{\text{exp}} - \rho_{\text{cal}}}{\rho_{\text{exp}}} \right| \quad (4)$$

The average, minimum and maximum AADs of the calculated densities are summarized in Table 1, including the pressure and temperature ranges of the data, the minimum and maximum of R^2 . For most cases, the average AAD is within the range of some

hundredth percent and at the highest limit it is below 0.7%. The AAD values confirm the ability of GMA EOS in density evaluation of long-chain organic compounds from low to high pressures.

A more sensitive test for any equation of state is the prediction of differential thermodynamic properties, such as internal pressure, isothermal

compressibility and thermal expansion coefficient. In this research, the differential thermodynamic properties including internal pressure (Pi), isothermal compressibility (κ) and thermal expansion coefficient (α) were calculated within the ranges where experimental data were available and then were compared with experimental values.

Table 2. The constants A₀–A₂ and B₀–B₂ obtained using Eqs. (2) and (3).

Fluid	A ₀ /10 ⁻⁹ (m ⁹ · mol ⁻³)	A ₁ /10 ⁻⁷ (m ¹² · Pa · mol ⁻⁴)	A ₂ /10 ⁻⁷ (m ¹² · Pa · mol ⁻⁴ · K ⁻¹)	B ₀ /10 ⁻⁹ (m ⁹ · mol ⁻³)	B ₁ /10 ⁻⁷ (m ¹² · Pa · mol ⁻⁴)	B ₂ /10 ⁻⁷ (m ¹² · Pa · mol ⁻⁴ · K ⁻¹)
C ₁₈ H ₃₈	-264.324	-354.969	1.61E+00	9.16E+01	1.36E+02	-5.53E-01
C ₁₉ H ₄₀	-256.379	-289.269	1.57E+00	9.43E+01	1.24E+02	-5.71E-01
C ₂₀ H ₄₂	142.715	707.826	-7.67E-01	-4.54E+01	-2.29E+02	2.48E-01
C ₂₃ H ₄₈	-1350.43	-2486.71	8.08E+00	5.79E+02	1103.88	-3.45E+00
C ₂₄ H ₅₀	-1311.42	-2410.37	7.82E+00	6.00E+02	1153.7	-3.56E+00
C ₂₈ H ₅₈	-1223.19	-1573	7.43E+00	6.47E+02	9.43E+02	-3.88E+00
1-Propanol	0.344705	1.13891	-2.03E-03	-0.0245999	-0.0765579	1.48E-04
2-Propanol	0.681687	1.82242	-4.05E-03	-0.0547893	-0.137487	3.30E-04
1-Butanol	0.488254	2.23432	-2.71E-03	-4.49E-02	-0.187895	2.59E-04
2-Butanol	0.510131	2.21884	-2.87E-03	-3.92E-02	-0.170109	2.28E-04
1-Pentanol	-0.928468	0.215877	5.88E-03	9.69E-02	7.70E-03	-5.93E-04
2-Pentanol	-0.63513	0.906193	4.20E-03	6.75E-02	-6.07E-02	-4.23E-04
3-Pentanol	0.283791	2.86804	-1.26E-03	-2.52E-02	-2.56E-01	1.27E-04
1-Hexanol	1.95191	8.36585	-1.09E-02	-2.26E-01	-0.929727	1.30E-03
1-Octanol	2.04706	16.7522	-9.83E-03	-2.29E-01	-2.19718	1.13E-03
1-Decanol	2.30261	31.9335	-0.0087611	-0.201119	-4.932	6.32E-04
1-Hexadecanol	-0.029164	46.4247	-0.0243929	0.420349	-11.4787	0.00568932
1,2-Butanediol	2.60982	6.79975	-1.56E-02	-0.189351	-0.507765	1.13E-03
2-Propanone	1.96592	3.96434	-1.20E-02	-0.135852	-0.269486	8.31E-04
2-Butanone	1.47699	3.54136	-8.96E-03	-0.134251	-0.301789	8.25E-04
3-Pentanone	1.86212	5.15625	-1.12E-02	-0.184425	-0.483184	1.13E-03
2-Hexanone	1.28495	6.1424	-7.09E-03	-0.153793	-0.672011	8.90E-04
1-Butanoic acid	0.696428	2.59141	-3.95E-03	-0.0548807	-0.204206	3.17E-04
1-Pentanoic acid	0.688818	3.71565	-3.68E-03	-0.0569024	-0.332823	3.12E-04
1-Hexanoic acid	5067.59	11140.8	-3.01E+01	-1544.71	-3387.87	9.19E+00
1-Heptanoic acid	0.907951	8.76561	-4.08E-03	-3.42E-02	-0.928789	8.05E-05
1-Octanoic acid	24.9951	58.2755	-1.50E-01	-3.83894	-8.76538	2.32E-02
1-Decanoic acid	-62.1835	-101.671	3.78E-01	13.1378	22.6667	-7.93E-02
1-Dodecanoic acid	-3085.44	-6074.48	18.5005	729.892	1456.89	-4.37E+00
1-Tetradecanoic acid	2425.26	5321.06	-14.4303	-659.077	-1441.59	3.92E+00
1-Hexadecanoic acid	5067.59	11140.8	-30.1299	-1544.71	-3387.87	9.19E+00

The following equations were used for calculating Pi, κ and α :

$$P_i = (B_1 + B_2 T) \rho^5 + (A_1 + A_2 T) \rho^4 \quad (5)$$

$$\alpha_P = \frac{(2B_1 + 2B_2 T) \rho^5 + (2A_1 + 2A_2 T) \rho^4 + 2P}{5\rho^5 (RT^2 B_0 - 2B_1 T + 2T^2 B_2 \ln T) + 4\rho^4 (A_0 RT^2 - 2A_1 T + 2A_2 T^2 \ln T) + RT^2 \rho} \quad (6)$$

$$\kappa_T = 2(\rho RT + 4\rho^4 (RTA_0 - 2A_1 + 2TA_2 \ln T) + 5\rho^5 (B_0 RT - 2B_1 + 2B_2 T \ln T))^{-1} \quad (7)$$

Table 3. Average, minimum and maximum AAD of calculated isothermal compressibility.

Fluid	$T_{\min} - T_{\max}$ (K)	$(P_{\min} - P_{\max})/10^5$ (Pa)	$(\rho_{\min} - \rho_{\max})/10^3$ (mol · m ⁻³)	$(100 \times \kappa_{\text{exp}} - \kappa_{\text{cal}} / \kappa_{\text{exp}})$ Average (min – max)
C ₁₈ H ₃₈	313.15-383.15	0.9998-1475.9437	2.9184-3.2437	2.770809(0.0505358-5.505358)
C ₁₉ H ₄₀	313.15-383.15	0.9998-1475.9438	2.8104-3.0723	2.671265(0.098203-5.3006)
C ₂₃ H ₄₈	333.15-393.15	0.9869-1475.9437	2.2559-2.5475	2.596291(0.0223-5.476841)
C ₂₄ H ₅₀	333.15-393.15	0.9869-1475.9438	2.2090-2.4563	2.353074(0.111-5.426272)
C ₂₈ H ₅₈	353.15-403.15	0.9869-1475.9439	1.9000-2.1024	2.741533(0.00628-5.27943)
2-Butanone	278.15-338.15	25.167-3847.2	10.5481-12.9608	2.501681(0.0423-5.154782)
3-Pentanone	278.15-338.15	25.166-3847.2243	8.9897-11.0177	1.799331(0.0449-5.912318)
2-Hexanone	288.15-338.16	25.1369-3755.835	7.7323-9.6155	2.973575(0.0731-5.455831)

Table 4. Absolute percent deviations of the calculated thermal expansion coefficient

$T(K)$	$\rho/10^3$ (mol · m ⁻³)	$\alpha_{\text{exp}} (K^{-1})$	$\alpha_{\text{cal}} (K^{-1})$	$\left \frac{\alpha_{\text{exp}} - \alpha_{\text{cal}}}{\alpha_{\text{exp}}} \right \times 100$
C ₁₉ H ₄₀				
313.15	2.8807	0.000846	0.00085	0.429
323.15	2.8559	0.000864	0.000845	2.162
333.15	2.8309	0.000881	0.00085	3.533
343.15	2.80597	0.000897	0.000862	3.851
353.15	2.7809	0.000912	0.000883	3.190
363.15	2.7556	0.000926	0.000911	1.616
373.15	2.7301	0.00094	0.000948	0.799
383.15	2.7044	0.000954	0.000993	4.053
2-Butanone				
278.15	11.408	0.00124	0.001211	2.306
288.15	11.267	0.00128	0.001265	1.183
298.15	11.1237	0.00131	0.001301	0.652
313.15	10.9062	0.00137	0.001323	3.406
323.15	10.7631	0.0014	0.001316	5.989
338.15	10.56	0.00145	0.001275	12.05
3-Pentanone				
278.15	9.6464	0.00116	0.001136	2.094
288.15	9.5363	0.00118	0.001159	1.814
298.15	9.4257	0.0012	0.001173	2.278
313.15	9.2609	0.00123	0.001177	4.325
323.15	9.1528	0.00124	0.001168	5.783
338.15	8.996	0.00127	0.001139	10.285
2-Hexanone				
278.15	8.2594	0.00105	0.000958	8.735
288.15	8.179	0.00108	0.001	7.410
313.14	7.967	0.00115	0.001102	4.193
C ₁₈ H ₃₈				
313.15	3.0251	0.000872	0.000866	0.663
323.15	2.998	0.000884	0.000857	3.018
333.15	2.9718	0.000897	0.00086	4.149
343.15	2.9452	0.00091	0.000872	4.166
353.15	2.9184	0.000923	0.000894	3.153
363.15	2.8916	0.000937	0.000926	1.170
373.15	2.8645	0.000951	0.000968	1.775
383.15	2.8372	0.000966	0.00102	5.654

The average, minimum and maximum AAD of calculated isothermal compressibility of some compounds are presented in Table 3. Concerning P_i and α , the calculations were done at points where experimental data were available. Calculated P_i and α are reported in Tables 4 and 5, respectively.

Table 5. Absolute percent deviations of the calculated internal pressure

$T(K)$	$\rho/10^3$ (mol m ⁻³)	$P_{i,\text{exp}}/10^5$ (Pa)	$P_{i,\text{cal}}/10^5$ (Pa)	$\left \frac{P_{i,\text{exp}} - P_{i,\text{cal}}}{P_{i,\text{exp}}} \right \times 100$
C ₁₉ H ₄₀				
313.15	2.8807	2957.978	3140.891	6.183
323.15	2.8559	2934.236	3086.592	5.192
343.15	2.80597	2854.51	3028.287	6.087
333.15	2.8309	2897.931	3049.638	5.232
353.15	2.7809	2802.838	3020.877	7.779
363.15	2.7556	2744.981	3025.849	10.232
373.15	2.7301	2681.091	3041.681	13.449
383.15	2.7044	2617.332	3066.978	17.1795
2-Butanone				
278.15	11.408	3392.789	3816.997	12.503
288.15	11.267	3394.618	3850.865	13.440
298.15	11.1237	3345.098	3832.844	14.580
313.15	10.9062	3263.511	3722.332	14.059
323.15	10.7631	3179.169	3603.864	13.358
338.15	10.56	2982.402	3378.232	13.272
3-Pentanone				
278.15	9.6464	3415.695	3571.506	4.561
288.15	9.5363	3210.216	3531.277	10.001
298.15	9.4257	3289.8	3465.893	5.352
313.15	9.2609	3054.782	3327.996	8.943
323.15	9.1528	3052.805	3214.66	5.301
338.15	8.996	2915.976	3021.22	3.609
C ₁₈ H ₃₈				
313.15	3.0251	2981.571	3126.232	4.851
323.15	2.998	2934.244	3061.715	4.344
333.15	2.9718	2885.551	3019.958	4.657
343.15	2.9452	2830.221	2998.559	5.947
353.15	2.9184	2771.195	2995.318	8.087
363.15	2.8916	2708.795	3008.176	11.051
373.15	2.8645	2643.642	3035.234	14.812
383.15	2.8372	2569.993	3074.648	19.636
2-Hexanone				
278.15	8.2594	3252.268	3088.871	5.0240
288.15	8.179	3201.646	3131.472	2.191
313.14	7.967	3146.949	3173.997	0.859

The average of AAD related to κ is less than 0.03. Concerning P_i and α , the average of AAD for all compounds, for which experimental data were available, is less than 0.07. The AAD values in Tables 3, 4 and 5 show that GMA equation of state is able to predict well the differential thermodynamic properties of long-chain organic compound.

CONCLUSION

The volumetric and other thermodynamic properties of long-chain organic compounds were calculated using GMA EoS over a wide range of temperatures and pressures. The accuracy of GMA EoS in the prediction of density and differential thermodynamic properties was determined using the absolute average deviation (AAD). The results show that GMA EoS can produce the experimental density and differential thermodynamic properties within experimental errors throughout the liquid phase.

Acknowledgment: The authors would like to thank Mr. M. H. Morsali for his assistance in preparing the paper

REFERENCES

1. E. K. Goharshadi, A. Morsali and M. Abbaspour, *Fluid Phase Equilib.*, **230**, 170 (2005).
2. E. K. Goharshadi and A. R. Berenji, *J. Nucl. Mater.*, **348**, 40 (2006).
3. M. Moosavi and E. K. Goharshadi, *Int. J. Thermophys.*, **27**, 1515 (2006).
4. E. K. Goharshadi and F. Moosavi, *Int. J. Refrig.*, **30**, 377 (2007).
5. E. K. Goharshadi and M. Moosavi, *J. Mol. Liq.*, **142**, 41 (2008).
6. E. K. Goharshadi and M. Moosavi, *Ind. Eng. Chem. Res.*, **44**, 6973 (2005).
7. E. K. Goharshadi and M. Moosavi, *Thermochim. Acta*, **447**, 64 (2006).
8. A. R. Berenji and E. K. Goharshadi, *Polymer*, **47**, 4726 (2006).
9. E. K. Goharshadi, M. Moosavi and M. Abareshi, *Int. J. Therm. Sci.*, **46**, 944 (2007).
10. E. K. Goharshadi and M. Abareshi, *Fluid Phase Equilib.*, **268**, 61 (2008).
11. E. K. Goharshadi and M. Moosavi, *J. Mol. Liq.*, **42**, 41 (2008).
12. M. Abareshi, E. K. Goharshadi, and S. M. Zebarjad, *J. Mol. Liq.*, **149**, 66 (2009).
13. E. K. Goharshadi and H. Azizi-Toupkanloo, *J. Mol. Liq.*, **151**, 117 (2010).
14. E. K. Goharshadi, M. Imani, R. Rahimi-Zarei, F. Razghandi, M. Abareshi and A. R. Berenji, *Eur. Polym. J.*, **46**, 587 (2010).
15. M. Moosavi, *Ind. Eng. Chem. Res.*, **49**, 6662 (2010).
16. M. Baniasadi, S. Ghader and H. Hashemipour, *Korean J. Chem. Eng.*, **28**, 939 (2011).
17. F. A. M. M. Goncalves, C.S.M.F. Costa, C. E. Ferreira, J. S. C. Bernardo, I. Johnson, I. M. A. Fonseca and A. G. M. Ferreira, *J. Chem. Thermodyn.*, **43**, 914 (2011).
18. S. Dutour, J. L. Daridon and B. Lagourette, *Int. J. Thermophys.*, **21**, 173 (2000).
19. A. K. Doolittle, *J. Chem. Eng. Data*, **9**, 275 (1964).
20. S. Dutour, J. L. Daridon and B. Lagourette, *J. Chem. Thermodyn.*, **33**, 765 (2001).
21. S. Dutour, J. L. Daridon and B. Lagourette, *J. Chem. Thermodyn.*, **34**, 475 (2002).
22. H. Kubota, Y. Tanaka and T. Makita, *Int. J. Thermophys.*, **8**, 47 (1987).
23. S. Wappmann, N. Karger and H.D. L'udemann, *J. Chem. Eng. Data*, **40**, 233 (1995).
24. S. Matsuo and T. Makita, *Int. J. Thermophys.*, **10**, 885 (1989).
25. H. Geyer, P. Ulbig, M. G'ornert and A. Susanto, *J. Chem. Thermodyn.*, **33**, 987 (2001).
26. R. Malhotra and L. A. Woolf, *J. Chem. Thermodyn.*, **23**, 867 (1991).
27. R. Malhotra and L. A. Woolf, *J. Chem. Thermodyn.*, **24**, 1207 (1992).
28. R. Malhotra, W. E. Price and L.A. Woolf, *J. Chem. Thermodyn.*, **25**, 361 (1993).
29. R. Malhotra and L. A. Woolf, *J. Chem. Thermodyn.*, **28**, 1411 (1996).
30. W.-T. Vong and F.-N. Tsai, *J. Chem. Eng. Data*, **42**, 1116 (1997).
31. T. S. Banipal, S. K. Garg and J. C. Ahluwalia, *J. Chem. Thermodyn.*, **24**, 729 (1992).

ОЦЕНКА НА ТЕРМОДИНАМИЧНИТЕ СВОЙСТВА НА ОРГАНИЧНИ СЪЕДИНЕНИЯ С ДЪЛГИ ВЕРИГИ, ПОСРЕДСТВОМ GMA УРАВНЕНИЕ НА СЪСТОЯНИЕТО

А. Морсали *, З. Алави, С. А. Бейрамабади

Катедра по химия, Клон Маишад, Ислямски университет „Азад“, Маишад, Иран

Получена на 8 януари 2014 г.; Ревизирана на 20 май 2014 г.

(Резюме)

В това изследване бяха направени усилия, за да се използва просто и точно уравнение на състоянието за предсказване на термодинамичните свойства на органични съединения с дълга верига, отчитайки научното и промишлено значение на тези съединения. Използвайки GMA уравнение на състоянието, различни групи от органични съединения с дълга верига, включително алкани, алкохоли, кетони и 1-карбоксилни киселини бяха изучени. Беше заключено и установено, че GMA уравнението на състоянието е способно да предвижда плътността на тези съединения с висока степен на точност. Един по-чувствителен тест за всяко уравнение на състоянието е прогнозата на диференциални термодинамичните свойства, като вътрешно налягане, изотермичната свиваемост и коефициента на топлинно разширение. В такъв тест, GMA уравнението на състоянието прогнозира тези свойства с приемлива степен на точност.

Polymerization shrinkage of UV curable dental composites containing multifunctional methacrylates

Z. Czech*, A. Kowalczyk, P. Ragańska, A. Antosik

Institute of Chemical Organic Technology, West Pomeranian University of Technology, Szczecin, Poland

Received January 16, 2014; Revised March 5, 2014

Dental compositions containing bis-GMA as basic material, multifunctional methacrylates, inorganic filler and photoinitiator were used as a model for dental applications. The main problem in the application and UV-Vis curing process is the shrinkage of dental materials. Total shrinkage of UV-Vis curable dental composites is due to polymerization shrinkage, which is a typical behavior of multifunctional methacrylates during the polymerization process. The important factors for curing dental composites are: kind and concentration of used methacrylates, their functionality, double bond concentration, kind and concentration of added photoinitiator and UV-Vis dose. UV-curable dental compositions based on 2,2-bis-[4-(2-hydroxy-3-methacryloyloxypropyl)phenyl]propane (bis-GMA) containing multifunctional monomers such as 1,3-butanediol dimethacrylate (1,3-BDDMA), diethylene glycol dimethacrylate (DEGDMA), tetraethylene glycol dimethacrylate (T3EGDMA), trimethylolpropane trimethacrylate (TMPTMA), polyethylene glycol 200 dimethacrylate (PEG200DA) were investigated. Reduction of polymerization shrinkage of dental compositions is at the moment a major problem for dental technology.

Keywords: dental compositions, polymerization shrinkage, multifunctional methacrylates, UV-Vis curing

INTRODUCTION

In technology of dental materials, dental compositions can be divided into clinical and technical materials. Clinical materials are mainly used in dental technology for dental surgery, whereas technical materials are mostly applied in dental technology for manufacturing of dentures. Various polymers have been widely used in dental materials for many years [1]. Polymerization shrinkage is one of dental clinicians' main concerns when placing direct, posterior, resin-based composite restorations. Evolving improvements associated with resin-based composite materials, dental adhesives, filling techniques and light curing have improved their predictability, but shrinkage problems remained. The main motivation for the reduction of the shrinkage is the too high shrinkage phenomenon using multifunctional methacrylate monomers in dental UV curable compositions [2]. Radical photopolymerization of dental compositions is usually performed in the UV-visible area (UV-Vis) between 380 and 450 nm [3]. Polymerization shrinkage is influenced by clinical technique and manufacturing of the composite resin. This phenomenon is attributed to the formation of a three-dimensional, covalently crosslinked network during crosslinking, which reduces intermolecular

distances between the monomers used to form the crosslinked network. Before cure, the molecules which form the resin are separated by their characteristic van der Waal's radii. Upon cure, these intermolecular distances are reduced due to the formation of covalent bonds between monomers which produce the desired highly crosslinked polymer material [4-9]. This reduction of intermolecular distances creates internal stress throughout the polymer network, which is manifested by reduced adhesion of the polymer material to both the substrate and the object attached thereto. Shrinkage is a very important criterion in long-term performance of adhesives and inversely affects the adhesion properties. In order to control shrinkage, UV dose, kind of multifunctional methacrylates and concentration play very crucial roles. In radiation curing, free radicals are generated on the molecular chains which come closer to each other and form a crosslinked network. As the molecular chains come closer, shrinkage occurs in the dental compositions, which is detrimental for the performance of the polymer composition. There should be no or minimal shrinkage for good adhesion. Multifunctional methacrylates with the function of photoreactive crosslinkers are generally not incorporated in radiation curing but they have several benefits in improving the physical-mechanical properties of the adhesive. The shrinkage is dependent on the nature and amount of crosslinker and on radiation intensity.

* To whom all correspondence should be sent:
E-mail: psa_czech@wp.pl

It is well known that shrinkage is the main drawback of free radical photopolymerization. When photopolymerization shrinkage is constrained by adhesion to a substrate, in the case of dental compositions by adhesion to the tooth wall, shrinkage stress develops. Excessive stress results in defects such as curling and cracking which impedes the long-time application of UV-curable or UV-polymerizable materials. Besides, shrinkage also plays an important role by affecting the marginal integrity of the photo-curable system [10-16].

EXPERIMENTAL

Materials

The investigated multifunctional methacrylates: 2,2-bis-[4-(2-hydroxy-3-methacryloyloxypropyl)phenyl]propane (bis-GMA), 1,3-butanediol dimethacrylate (1,3-BDDMA), diethylene glycol dimethacrylate (DEGDMA), tetraethylene glycol dimethacrylate (T3EGDMA), trimethylolpropane trimethacrylate (TMPTMA), and polyethylene glycol 200 dimethacrylate (PEG200DA) and bifunctional radical photoinitiator 2-hydroxy-1-[4-[4-(2-hydroxy-2-methyl-propionyl)-benzyl]-phenyl]-2-methyl-propan-1-one (Irgacure 127) are presented in Table 1. All multifunctional methacrylates and

the photoinitiator Irgacure 184 are available from BASF (Germany), and hydroxyapatite is available from Continental Chemical (USA).

Hydroxylapatite in form of white powder is the hydroxyl end member of the complex apatite group and crystallizes in the hexagonal crystal system. Thus, it is commonly used as a filler for restorative dental compositions.

The investigated UV-curable dental composition contained the following raw materials:

Bis-GMA: basic material	40 wt.%
Multifunctional (meth)acrylate	30 wt.%
Hydroxyapatite	28 wt.%
Irgacure 127	2 wt.%

Measurement of shrinkage

The thickness change of the polymer was measured with the reflective laser scanning system to determine the shrinkage. The transparent object mode of the laser displacement sensor was chosen for testing the clear liquid monomers. In this measurement mode, the laser displacement sensor detected and recorded the displacement of the upper surface of monomers caused by photopolymerization shrinkage [15]. A reflective laser scanning method based on a laser displacement sensor was used to directly measure shrinkage due to UV-curing.

Table 1 Multifunctional methacrylates and photoinitiator used in this work

Raw material	Chemical structure	Chemical name
Bis-GMA		2,2-bis[4-(2-hydroxy-3-meth-acryloyloxypropyl)phenyl]propane
1,3-BDDMA		1,3-butanediol dimethacrylate
DEGDMA		diethylene glycol dimethacrylate
T3EGDMA		tetraethylene glycol dimethacrylate
TMPTMA		trimethylolpropane trimethacrylate
PEG200DA		polyethylene glycol 200 dimethacrylate
Irgacure 127		2-hydroxy-1-[4-[4-(2-hydroxy-2-methyl-propionyl)-benzyl]-phenyl]-2-methyl-propan-1-one

The laser displacement sensor Keyence, LK-G10 (Japan) could detect the position of the upper surface of the sample (thickness of the sample). When photopolymerization occurs, the change in the sample thickness was recorded as a function of time. Percentage shrinkage (S) is defined by the dimensional change according to the following equation:

$$S = (H_0 - H_t) / H_0 = (1 - H_t / H_0) \times 100 \text{ [%]}$$

where H_0 is the initial thickness and H_t is the thickness at time t . The measured shrinkage is actually a linear shrinkage. However, as the planar dimensions are much greater than the thickness and constrain planar shrinkage, the linear shrinkage appropriately equals to the volumetric shrinkage. The photopolymerization was conducted in ambient conditions at room temperature. The plane UV source (emitting window: 25×25 mm) used was 395 nm RX Firefly SN 490454 from Phoseon Technology (USA). The radiometer from Hoenle UV Technology (Germany) was used to detect the radiation intensity on the surface of samples. The UV intensity on the sample was adjusted to 5 mW/cm².

RESULTS AND DISCUSSION

Variation of UV-Vis curing time, kind of multifunctional (meth)acrylates and functionality

To compare the UV-behaviour of multifunctional methacrylates with that of acrylates, the photopolymerization of dental compositions containing multifunctional (meth)acrylates: tetraethylene glycol dimethacrylate (T3EGDMA), diethylene glycol dimethacrylate (DEGDMA), 1,3-butanediol dimethacrylate (1,3-BDDMA), trimethylolpropane trimethacrylate (TMPTMA) and polyethylene glycol 200 dimethacrylate (PEG200DMA), was examined. As shown in Table 2 and Figure 1, the irradiation starts at 0 s and there is no shrinkage before. The shrinkage of all tested monomers significantly increased during UV exposure. In the shrinkage profiles of all tested monomers, an obvious

expansion after a very short induction time is observed (Fig. 1).

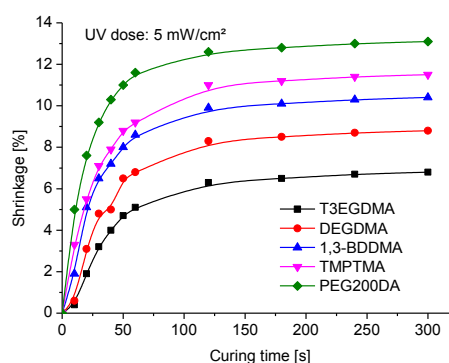


Fig. 1. Shrinkage of dental filling containing the investigated (meth)acrylates versus curing time

This expansion is induced by the accumulated curing, in this case polymerization heat, due to the higher reactivity of acrylates in comparison to methacrylates. The expansion also increases at a very early stage of curing due to auto-acceleration effect. Because of the high reactivity, the acrylate monomer PEG200DA shows much higher shrinkage than the other tested methacrylates and needs less time to reach the maximal measurable shrinkage profile. Beyond this point, the shrinkage rate decreases due to significant reduction of monomers/initiator/radicals (de-acceleration). Thus the shrinkage tends to reach the equilibrium final shrinkage.

There is no doubt that the shrinkage depends on double bonds conversion because the shrinkage phenomenon is a consequence of the polymerization process of the investigated monomers that provides curing of dental filling compositions. The double bond conversion of polymerized monomers can be assessed by comparing the shrinkage plateaus of the investigated monomers. After 240-300 s (4-5 min) shrinkage reaches a maximal level and at this moment the conversion reaction of monomers double bonds is finished.

Table 3 presents molecular weight, density, functionality of investigated monomers, concentration of double bonds in their structure, and maximal shrinkage values after UV curing.

Table 2 Polymerization shrinkage of multifunctional methacrylates as a function of curing time

(Meth)acrylate	Polymerization shrinkage as a function of curing time [%]										
	Curing time [s]										
	0	10	20	30	40	50	60	120	180	240	300
T3EGDMA	0	0.4	1.9	3.2	4	4.7	5.1	6.3	6.5	6.7	6.8
DEGDMA	0	0.6	3.1	4.8	5	6.5	6.8	8.3	8.5	8.7	8.8
1,3-BDDMA	0	1.9	5.1	6.5	7.2	8	8.6	9.9	10.1	10.3	10.4
TMPTMA	0	3.3	5.5	7.1	7.9	8.8	9.2	11	11.2	11.4	11.5
PEG200DA	0	5	7.6	9.2	10.3	11	11.6	12.6	12.8	13	13.1

Table 3 Monomers parameters and shrinkage of tested dental compositions

Monomer	Functionality	Molecular weight [kg/kmol]	Density at 25°C [kg/m ³]	Concentration of double bonds C _{db} [mol/L]	Maximal shrinkage after UV curing [%]
T3EGDMA	2	286	1090	7.6	6.8
DEGDMA	2	242	1070	8.8	8.8
1,3-BDDMA	2	226	1010	8.9	10.4
TMPTMA	3	338	1060	9.4	11.5
PEG200DA	2	308	1110	7.2	13.1

Changing the degree of ethoxylation (1,3-BDDMA, DEGDMA or T3EGDMA) is a convenient way to alter monomer chain lengths (the segment lengths between double bonds in monomers). Two methacrylates with different degrees of ethoxylation, tri (DEGDMA) and four (T3EGDMA) moles of ethoxy groups were used to evaluate the effect of monomer chain lengths on shrinkage. Figure 1 shows that when the degree of ethoxylation is raised, shrinkage obviously decreases. Another dominant factor, the concentration of double bonds (Cdb), should be taken into consideration.

$C_{db} \text{ [mol/L]} = \text{Functionality} \times \text{Monomer density} / \text{Molecular weight}$, where L is the monomer chain length. According to this equation, rising the degree of ethoxylation means reduction of the concentration of double bonds due to the significant increase of the molecular weight. In fact, shrinkage depends on the conversion and by full conversion, on the concentration of double bonds. Because increase of monomer chain lengths has more significant effect on decreasing the concentration of double bonds than on increasing conversion, shrinkage is low even at high conversion. It was also observed that the maximum of shrinkage decreases from 8.8 % to 6.8 % with rising the degree of ethoxylation (Table 3). Thus, the monomer chain lengths effect on the shrinkage is attributed to the change in the concentration of double bonds. Besides, the drop heat expansion shown in Fig. 1 with decreasing the degree of ethoxylation is also due to reduction of the concentration of double bonds. Thus, as shown in Table 3, the maximal shrinkage level moved from the expansion stage to the shrinkage stage when the degree of ethoxylation was increased. The mobility of free radicals and monomeric and pendant double bonds rises due to the formation of less crosslinked networks, and the segmental diffusivity of pendant double bonds rises due to the more flexible pendant double bonds. Thus, the propagation is less diffusion-controlled when the degree of ethoxylation is up.

The ethoxylation is an attractive way to lower shrinkage because the concentration of double

bonds significantly drops with increasing the molecular weight of ethoxylated multifunctional monomers. Likewise, other ways to increase the molecular weight may be promising to solve the shrinkage problem. The influence of the concentration of double bonds in the investigated methacrylate monomers is shown in Fig. 2 (Table 3).

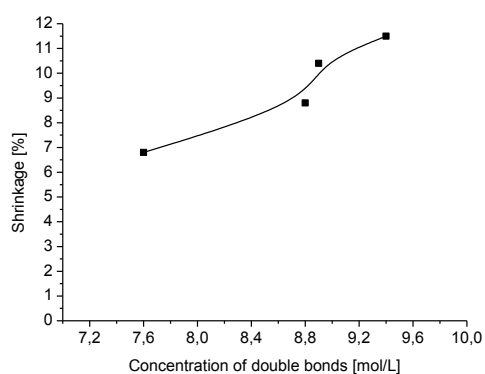


Fig. 2. Shrinkage of a dental composition containing multifunctional methacrylates *versus* concentration of double bonds in the methacrylates

It is widely believed that reduction of functionality lowers the shrinkage. However, the functional effect on shrinkage is very complicated. Functionality obviously affects the conversion and the concentration of double bonds. The concentration of double bonds may not decrease on reducing functionality because changing the functionality is always accompanied by changing both the molecular weight and the density. In this work the difunctional T3EGDMA, DEGDMA and 1,3-BDDMA, and the trifunctional TMPTMA were used to evaluate the functional effect. As shown in Figure 1 and Table 3, the shrinkage level decreases with the increase in monomers functionality, due to the formation of a microgel in the early step. But the shrinkage does not follow this trend. The trifunctional methacrylate TMPTMA has the highest final shrinkage of 11.5 % in comparison with other tested difunctional methacrylates (Table 3).

Influence of the UV dose on shrinkage

Dependencies shown in Fig. 1 point out that the UV dose during curing can influence shrinkage of

the investigated dental filler compositions containing (meth)acrylate monomers. The UV-polymerization effect on the shrinkage of the tested (meth)acrylates, evaluated for UV doses between 10 and 50 mW/cm² and for 3 min UV-crosslinking time, is shown in Table 4 and illustrated in Figs. 3-7.

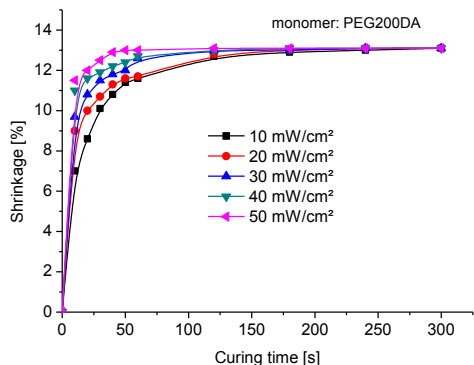


Fig. 3. Shrinkage of dental filling containing the monomer PEG200DA versus curing time and UV curing dose

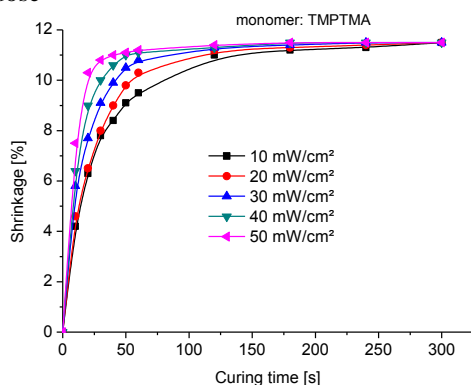


Fig. 4. Shrinkage of dental filling containing the monomer PTMPTMA versus curing time and UV curing dose

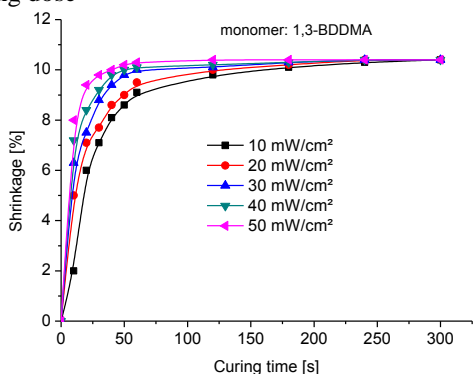


Fig. 5. Shrinkage of dental filling containing the monomer 1,3-BDDMA versus curing time and UV curing dose

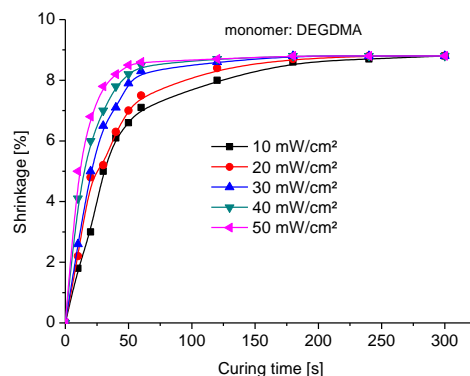


Fig. 6. Shrinkage of dental filling containing monomer DEGDMA versus curing time and UV curing dose

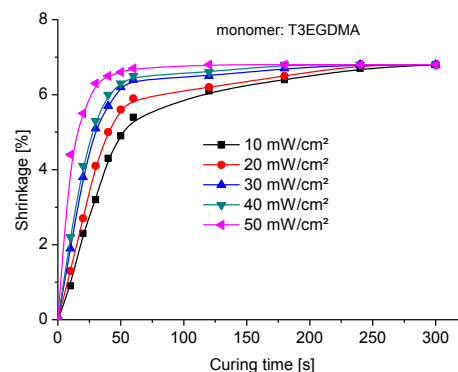


Fig. 7. Shrinkage of dental filling containing the monomer T3EGDMA versus curing time and UV curing dose

The results of the tested dental compositions for shrinkage at different UV doses with variation of multifunctional monomers are given in Figures 3-7 which represent the effect of UV polymerization dose in the range between 10 and 50 mW/cm². It is observed that with increasing the UV dose from 10 to 50 mW/cm² the shrinkage values during UV curing increases and remains at a constant level after 120 s, especially at higher UV doses up to 30-40 mW/cm². This indicates that the UV dose of 50 mW/cm² is sufficient to cure the investigated dental filling compositions. The maximal shrinkage was observed for the bifunctional monomer polyethylene glycol 200 dimethacrylate (PEG200DMA).

CONCLUSION

The polymerization shrinkage of (meth)acrylate monomers was found to depend mainly on the double bonds conversion, concentration of double bonds, UV curing time and UV curing dose. Methacrylate monomers displayed lower shrinkage than acrylate monomers because the low reactivity decreases the conversion as a function of curing time. Increase in chain length of monomers

Table 4. Polymerization shrinkage of monomers as a function of curing time and UV curing dose

Monomer	UV dose [mW/cm ²]	Curing shrinkage [%] as a function of curing time and UV dose										
		Curing time [s]										
		0	10	20	30	40	50	60	120	180	240	300
PEG200DA	10	0	7.0	8.6	10.1	10.8	11.4	11.6	12.7	12.9	13.0	13.1
	20	0	9.0	10.0	10.7	11.3	11.6	11.7	12.8	13.0	13.1	13.1
	30	0	9.7	10.8	11.5	11.8	12.0	12.6	13.0	13.0	13.1	13.1
	40	0	11.0	11.6	11.9	12.2	12.4	12.7	13.0	13.1	13.1	13.1
	50	0	11.5	12.0	12.5	12.9	13.0	13.0	13.1	13.1	13.1	13.1
TMPTMA	10	0	4.2	6.3	7.8	8.4	9.1	9.5	11.0	11.2	11.3	11.5
	20	0	4.6	6.5	8.0	9.0	9.8	10.3	11.2	11.3	11.4	11.5
	30	0	5.8	7.7	9.1	9.9	10.5	10.8	11.3	11.4	11.5	11.5
	40	0	6.4	9.0	10.0	10.6	11.0	11.1	11.3	11.5	11.5	11.5
	50	0	7.5	10.3	10.8	11.0	11.1	11.2	11.4	11.5	11.5	11.5
1,3-BDDMA	10	0	2.0	6.0	7.1	8.1	8.6	9.1	9.8	10.1	10.3	10.4
	20	0	5.0	7.1	7.7	8.6	9.0	9.5	10.0	10.2	10.4	10.4
	30	0	6.3	7.5	8.8	9.4	9.8	10.0	10.1	10.3	10.4	10.4
	40	0	7.2	8.4	9.2	9.8	10.0	10.1	10.2	10.3	10.4	10.4
	50	0	8.0	9.4	9.8	10.0	10.2	10.3	10.4	10.4	10.4	10.4
DEGDMA	10	0	1.8	3.0	5.0	6.1	6.6	7.1	8.0	8.6	8.7	8.8
	20	0	2.2	4.8	5.2	6.3	7.0	7.5	8.4	8.7	8.8	8.8
	30	0	2.6	5.0	6.5	7.1	7.9	8.3	8.6	8.8	8.8	8.8
	40	0	4.1	6.0	7.0	7.8	8.2	8.5	8.7	8.8	8.8	8.8
	50	0	5.0	6.8	7.8	8.2	8.5	8.6	8.7	8.8	8.8	8.8
T3EGDMA	10	0	0.9	2.3	3.2	4.3	4.9	5.4	6.1	6.4	6.7	6.8
	20	0	1.3	2.7	4.1	5.0	5.6	5.9	6.2	6.5	6.8	6.8
	30	0	1.9	3.8	5.1	5.7	6.2	6.4	6.5	6.7	6.8	6.8
	40	0	2.2	4.1	5.3	6.0	6.3	6.5	6.6	6.8	6.8	6.8
	50	0	4.4	5.5	6.3	6.5	6.6	6.7	6.8	6.8	6.8	6.8

(rising the degree of ethoxylation) significantly lowered the shrinkage because the obvious rise of molecular weight decreased the concentration of double bonds. Reduction of functionality was not an attractive way to lower the final shrinkage due to the combined effect of the concentration of double bonds and conversion. The concentration of double bonds also played an important role in the shrinkage rate. When changing the degree of ethoxylation or monomer functionality, it was observed that shrinkage increased with the concentration of double bonds. Besides, heat expansion caused by curing could bring forward a maximal shrinkage rate from the shrinkage stage to the expansion stage. Thus, we believe that a promising way to decrease the shrinkage might be the increase in the molecular weights of photoreactive monomers, if other properties such as viscosity and solubility meet application requirements.

REFERENCES

1. N. Moszner, T. Hirt, *J. Polym. Sci. Part A: Polym. Chem.* **50**, 4369 (2012).
2. A. J. Feilzer, A. J. De Gee, *J. Dent. Res.* **66**, 1636 (1987).
3. N. Moszner, U. Salz, *Macromol. Mater. Eng.* **292**, 245 (2007).
4. C. F. Liu, S. M. Collard, C. D. Armeniades, *Am. J. Dent.* **3**, 44 (1990).
5. J. Luo, J. J. Lannutti, R. R. Seghi, *Dent. Mater.* **14**, 29 (1998).
6. Z. Czech, A special report, *Adv. Polym. Techn.* **20**, 72 (2001).
7. R. Milker, Z. Czech, Removable and Repositionable Pressure-Sensitive Adhesive Products, STICK, 3rd European Congress of Adhesive and Sealant Raw Materials, Nürnberg, Germany, 2003, p. 23
8. R. Labella, P. Lambrechts, B. Van Meerbeek, *Dent. Mater.* **15**, 128 (1999).
9. Z. Czech, *Polish J. Chem. Technol.* **45** (2004).
10. J. R. Condon, J. L. Ferracane, *J. Am Dent. Assoc.* **131**, 497 (2000).
11. Z. Czech, A. Kowalczyk, J. Kabatc, J. Świdarska, *Eur. Polym. J.* **48**, 1446 (2012).
12. C. M. Kemp-Scholte, C. L. Davidson, *J. Dent. Res.* **69**, 1240 (1990).
13. Z. Czech, A. Butwin, J. Kabatc, J. Świdarska, *Polym. Bull.* **69**, 71 (2012).
14. C. L. Davidson, A. J. De Gee, *J. Dent. Res.* **63**, 1396 (1984).
15. Y. Jian, Y. He, T. Jiang et al., *J. Polym. Sci. Part B: Polym. Phys.* **50**, 923 (2012).
16. A. K. Singh, D. S. Mehra, U. K. Niyogi et al. *J. Polym. Mater.* **28**, 525 (2011).

ПОЛИМЕРИЗАЦИОННО СВИВАНЕ НА UV-КАТАЛИЗИРАНИ ЗЪБНИ КОМПОЗИТИ, СЪДЪРЖАЩИ МНОГОФУНКЦИОНАЛНИ МЕТАКРИЛАТИ

З. Чех*, А. Ковалчик, П. Раганска, А. Антошик

*Институт по органична химична технология, Западно-померански технологичен университет, Шчечин 70322,
Полша*

Постъпила на 15 януари 2014 г.; коригирана на 5 март, 2014 г.

(Резюме)

В статията се описват зъбни композиции, съдържащи бис-GMA като основен материал, многофункционални метакрилати, органичен пълнеж и фотоинициатор като модели за приложение за зъбни протези. Главният проблем за приложението и UV-Vis - лечебния процес е свиването на полимерния материал. Пълното свиване на UV-Vis – лечебните зъбни композиции е явлението на свиване при полимеризацията, което е типично за многофункционалните метакрилати. Важни фактори за лечебната употреба на зъбните композиции са: видът и концентрацията на използваните метакрилати, тяхната функционалност, концентрацията на двойни връзки, на добавения фотоинициатор и дозата на UV-Vis – облъчването.

Изследвани са UV-лечебни зъбни композиции, основани на 2,2-бис-[4-(2-хидрокси-3-метакрилоил-оксипропил)фенил]пропан (Bis-GMA) и съдържащи многофункционални мономери, като 1,3-бутандиол диметакрилат (1,3-BDDMA), диетилен гликол диметакрилат (DEGDMA), тетраетилен гликол диметакрилат (T3EGDMA), триметилпропан триметакрилат (TMPTMA), полиетилен гликол 200 диметакрилат (PEG200DA). Намаляването на полимеризационното свиване при зъбните композиции в момента е главният проблем в зъболекарската технология.

Catalytic synthesis of 1,4-dihydropyridine derivatives using hexagonal mesoporous silicate (HMS)

A. Farhadi *, T. Hamoule, M. Ali Takassi, T. Arizavipour

Petroleum University of Technology, Faculty of Science, Ahwaz, Iran

Received January 22, 2014; Revised February 28, 2014

A simple and efficient one-pot synthesis of 1,4-dihydropyridine derivatives was achieved *via* condensation of ethyl acetoacetate with various aryl aldehydes and ammonium acetate in the presence of hexagonal mesoporous silicate (HMS) as a heterogeneous catalyst and EtOH as a solvent under reflux conditions with good to excellent yields.

Keywords: 1,4-Dihydropyridine, EtOH, Hantzsch Condensation, HMS, One-pot, Reflux conditions, mechanisms [23-29].

INTRODUCTION

Six-membered heterocyclic compounds are important materials in organic chemistry. These compounds exhibit diverse biological and medical activities, and may be used as constituents of synthetic compounds of medicinal interest [1,2]. Among them, 1,4-dihydropyridine (1,4-DHP) cores are important classes of drugs because 1,4-DHPs are analogues of NADH coenzymes that are an important class of drugs [3]. These heterocyclic compounds are some of the most important classes of drugs to inhibit the HIV virus [4]. They display neuroprotectant [5] and platelet anti-aggregatory activity [6]. They act as cerebral anti-ischemic agents in the treatment of Alzheimer's disease [7]. 1,4-DHPs have potential as chemo sensitizers in tumor therapy [8]. Some of their derivatives are well known as Ca²⁺ channel blockers [9,10].

The classical method for the synthesis of these compounds is the Hantzsch and Liebig's reaction involving multicomponent condensation of an aldehyde with a 1,3-dicarbonyl compound and NH₃ [11]. In the past, many methods for synthesis of 1,4-DHPs and their derivatives have been reported [12-15].

The synthesis of mesoporous molecular sieves using the templating effect of lyotropic liquid crystal mesophases was first proposed in 1992 [16,17]. Mesoporous structures with high surface area have attracted great interest in chemistry. These compounds have been used as nano-filters, photonic devices, and low-k dielectrics, support materials for catalysts, encapsulation, sensors, etc. [18-22]. So far, various strategies have been proposed to tailor a new class of mesoporous structures, to develop a more convenient route to syntheses and to understand their formation

Therefore, the use of a HMS compound as an efficient catalyst for the one-pot synthesis of some 1,4-dihydropyridines (1,4-DHPs) under thermal conditions was investigated.

The comparison of these data with those of other mesoporous compounds shows that using HMS is a simple and mild method which has advantages such as excellent yields, short reaction time and low cost. The synthesis of HMS is easy [30,31], and this catalyst is very stable in the atmosphere.

RESULTS AND DISCUSSION

Characterization of the catalyst

XRD analysis

The typical XRD pattern for the HMS material shows that it contains an intense diffraction peak at $2\theta = 2.3^\circ$ corresponding to the diffraction of (100) plane, indicating that this sample has a typical characteristic peak of a mesoporous molecular sieve in agreement with the literature [32].

Surface and porosity

The physicochemical properties of HMS are presented in Table 1. The high surface area, the appropriate pore volume and average pore diameter confirm the formation of HMS material, in accordance with the XRD results.

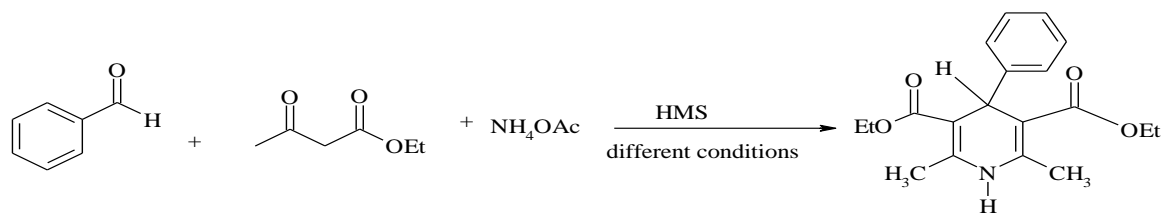
Table 1. Physicochemical characteristics of the mesoporous support

Sample	Surface area (m ² g ⁻¹)	pore volume (cm ³ g ⁻¹)	APD (Å) ^a
HMS	987	1.0	33.0

^a: Average pore diameter

Initially, we studied the Hantzsch-type reaction of benzaldehyde (1a), ethyl acetoacetate, ammonium acetate and HMS as a Lewis acid in different solvents under various conditions (Scheme 1 and Table 2).

* To whom all correspondence should be sent:
E-mail: farhadichem@put.ac.ir



Scheme 1

Table 2. Optimization of reaction conditions

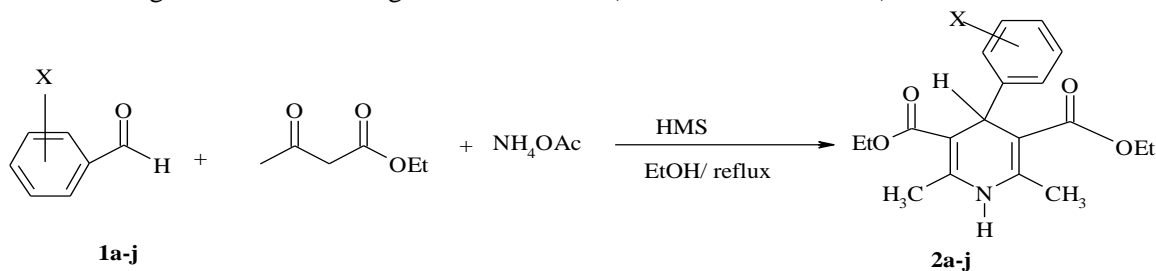
Entry	HMS (g)	Solvent	T (°C)	Time (h) ^a	Yield% ^b
1	0.2	EtOH	90	3	30
2	0.5	EtOH	90	3	30
3	0.8	EtOH	90	3	45
4	0.9	EtOH	90	3	95
5	1.0	EtOH	90	3	60
6	1.1	EtOH	90	3	80
7	0.9	EtOH	70	3	80
9	0.9	EtOH	80	3	85
10	0.9	EtOH	90	3	95
11	0.9	EtOH	100	3	95
12	0.9	EtOH	90	3	95
13	0.9	CH_3CN	90	3	<10
14	0.9	H_2O	90	3	75
15	0.9	Solvent free	90	3.5	<10
16	0.9	EtOH	r.t	3	<10

^a Required time for maximum progress of the reaction. ^b isolated yield.

We have developed a simple methodology for the one-pot synthesis of 1,4-dihydropyridines by HMS as a heterogeneous catalyst to give excellent yields.

Synthesis of 4-phenyl substituted-1,4-dihydropyridine (2a) as a model product was carried out in different solvents (Scheme 1 and Table 2). According to the data presented in Table 2, the use of 0.9 g of HMS at 90°C gave the best

result (Table 2, entry 10). Applying of heat was necessary for the reaction due to failure of reaction when carried out at room temperature. Also, various ethyl 4-substituted-1,4-dihydropyridine 3,5-dicarboxylates (2a-J) were obtained by the reaction of ethyl acetoacetate, different aldehydes and ammonium acetate under the same conditions (Scheme 2 and Table 3).



Scheme 2

Table 3. HMS catalyzed synthesis of substituted 1,4-dihydropyridines in ethanol under reflux conditions

Comp.	R	Time (h) ^a	Yield (%) ^b	m.p.	
				measured	reported
2a	C_6H_5-	3	95	160-161	158-160[33]
2b	4- CH_3 - C_6H_4-	3	80	124-125	122-124[34]
2c	3- CH_3 - C_6H_4-	3	80	124-125	122-124[34]
2d	4-MeO- C_6H_4-	3.5	80	160-161	158-160[33]
2e	4-Cl- C_6H_4-	3.5	80	149-150	147-148[33]
2f	2-Cl- C_6H_4-	3.5	85	122-124	122-126[35]
2g	4-Br- C_6H_4-	3.5	85	163-164	162-164[33]
2h	3-Br- C_6H_4-	3.5	80	116-118	115-117[35]
2i	4- NO_2 - C_6H_4-	2.5	80	130-131	129-131[33]
2j	3- NO_2 - C_6H_4-	2	85	163-164	162-164[33]

^a Required time for maximum progress of the reaction. ^b isolated yield

Table 4. Reuse of HMS in the Hantzsch synthesis of 1,4-DHP (benzaldehyde : ethyl acetoacetate: NH₄ OAc, (1:2 :1.5) in EtOH as solvent at 90°C and 0.9 g HMS)

Run	1	2	3
Isolated yield (%)	95	60	40

Analysis of the data reported in Table 4 shows that the conversion is lower with a reused catalyst. These data suggested that the reaction occurs mainly within the pores of the catalyst.

CONCLUSIONS

We have successfully developed a simple and efficient method for the preparation of a variety of 4-substituted-1,4-dihydropyridines by one-pot three-component reactions of different aromatic aldehydes, β -ketoester and ammonium acetate in the presence of a catalytic amount of HMS catalyst and ethanol under reflux conditions. The main advantages of this methodology are: (a) operational simplicity, (b) short reaction time, (c) high yields of products, and (d) use of relatively non-toxic solvents.

We suggest that the reactivity of this catalyst is related to the number of pores in the HMS catalyst.

EXPERIMENTAL

Melting points were determined in an oil bath and were uncorrected. IR spectra were recorded for solid samples using KBr discs on a Shimadzu FT-IR apparatus Prestige 21. The ¹H NMR spectra (CDCl₃, standard TMS) were recorded with a Bruker 300 MHz instrument. They are reported as follows: chemical shifts, (multiplicity, number of protons, and assignment).

After maximum conversion of the reaction as indicated by TLC, the resultant solid product was washed with EtOH (30 mL). The pure product was obtained by further recrystallization from ethanol, and then washed with n-hexane. The spectral and analytical data for the selected compounds are presented below.

Preparation and characterization of the catalyst

The HMS catalyst was synthesized by a sol-gel method similar to the procedure reported by Tanev and co-worker [32]. The specific surface area, pore volume and average pore diameter of HMS were measured in an ASAP-2010 Micromeritics (USA) apparatus using low temperature N₂ physisorption isotherms. Before analysis, the sample was evacuated at 350 °C under vacuum conditions.

General procedure for the preparation of 1,4-dihydropyridines (2a-j)

The mixture of ethyl acetoacetate (10 mmol), aromatic aldehydes (5.1 mmol), ammonium acetate

(7.5 mmol) and HMS (1 g) in EtOH (6 mL) was refluxed for 3 h. The progress of the reaction was monitored by TLC. A yellow precipitate was obtained and was recrystallized from EtOH. The products were characterized by FT-IR, ¹H and ¹³C NMR spectra.

The catalyst was washed with hot EtOH and dried at 530°C for 5 h. It was available for reuse in further reactions. (Table 4)

Diethyl 2,6-dimethyl-4-phenyl-1,4-dihydro-pyridin-3,5-dicarboxylate (2a)

M.p.: 160-161 °C (lit. [33] m.p. 158-160 °C). FT-IR (KBr): ν 3339.15 (N-H), 2880.44 (C-H), 1694.07-1727.51 (C=O), 1489.15 (C=C), 1274.83 (C-O) cm⁻¹. ¹H NMR (CDCl₃): δ = 1.51 (t, J= 7.1 Hz, 6 H), 2.22 (s, 6 H), 4.0 (q, J= 7.01 Hz, 4 H), 4.93 (s, 1 H), 9.2 (brd s, 1 H), 7.04-7.22 (m, 5 H) ppm. ¹³C NMR (CDCl₃): δ = 14.26, 19.40, 39.63, 59.74, 103.93, 126.1, 127.84, 127.98, 144.23, 147.85, 167.81 ppm.

Diethyl 2,6-dimethyl-4-(3-methylphenyl)-1,4-dihydropyridin-3,5-dicarboxylate (2c)

M.p.: 124-125 °C (lit. [34] M.p. 122-124 °C). FT-IR (KBr): ν 3356.86 (N-H), 2986.39 (C-H), 1650.65-1696.65 (C=O), 1412.39 (C=C), 1273.05 (C-O) cm⁻¹.

Diethyl 4-(4-chlorophenyl)-2,6-dimethyl-1,4-dihydropyridin-3,5-dicarboxylate (2e)

M.p.: 149-150 °C (lit. [33] m.p. 147-148 °C). FT-IR (KBr): ν 3356.89 (N-H), 2986.39 (C-H), 1696.48-1650.65 (C=O), 1487.16 (C=C), 1293.15 (C-O) cm⁻¹. ¹H NMR (CDCl₃): δ = 1.15 (t, J= 7.1 Hz, 6 H), 2.10 (s, 6 H), 3.98 (q, J= 7.0 Hz, 4 H), 4.89 (s, 1 H), 6.2 (brd s, 1 H), 7.03-7.16 (m, 4 H) ppm. ¹³C NMR (CDCl₃): δ = 21.14, 19.47, 39.68, 59.68, 103.50, 126.24, 126.30, 128.23, 129.06, 133.56, 144.45, 149.81, 167.49 ppm.

Diethyl 4-(2-chlorophenyl)-2,6-dimethyl-1,4-dihydropyridin-3,5-dicarboxylate (2f)

M.p.: 122-124 °C (lit. [35] m.p. 122-126 °C). FT-IR (KBr): ν 3351.94 (N-H), 2985.99 (C-H), 1647.58-1695.84 (C=O), 1481.68 (C=C), 1297.71 (C-O) cm⁻¹. ¹H NMR (CDCl₃): δ = 1.13 (t, J=6.9 Hz, 6 H), 2.19 (s, 6 H), 4.01 (q, J=7.0 Hz, 4 H), 4.89 (s, 1 H), 6.30 (brd s, 1 H), 7.06-7.15 (m, 4 H) ppm. ¹³C NMR (CDCl₃): δ : 14.27, 19.31, 39.24, 59.85, 103.50, 127.92, 129.36, 131.66, 144.45, 145.45, 167.68 ppm.

Diethyl 4-(4-bromophenyl)-2,6-dimethyl-1,4-dihydropyridin-3,5-dicarboxylate (2g)

M.p.: 163-164 °C (lit.[33] m.p. 162-164 °C). FT-IR (KBr): ν 3483.32 (N-H), 2933.21 (C-H), 1615.62-1707 (C=O), 3353.24 (C=C), 1202.30 (C-O) cm⁻¹.

Diethyl 2,6-dimethyl-4-(4-nitrophenyl)-1,4-dihydropyridin-3,5-dicarboxylate (2i)

M.p.: 130-131 °C (lit. [33] m.p. 129-131 °C). FT-IR (KBr): ν 3336.19 (N-H), 2995.05 (C-H), 1691.89-1727.86 (C=O), 1480.60 (C=C), 1290.19 (C-O) cm^{-1} .

Diethyl 2,6-dimethyl-4-(3-nitrophenyl)-1,4-dihydropyridin-3,5-dicarboxylate (2j)

M.p.: 163-164 °C (lit. [33] m.p. 162-164 °C). FT-IR (KBr): ν 3360.62 (N-H), 2988.18 (C-H), 1645.61-1691.89 (C=O), 1480.6 (C=C), 1212.72 (C-O) cm^{-1} .

REFERENCES:

1. N. Nakamichi, Y. Kawashita, M. Hayashi, *Org. Lett.*, **4**, 3955 (2002).
2. N. Nakamichi, Y. Kawashita, M. Hayashi, *Synthesis*, 1015 (2004).
3. D. Mauzeral, F.H. Westheimer, *J. Am. Chem. Soc.*, **77**, 2261 (1955).
4. A. Hilgeroth, *Mini Reviews in medicinal chemistry*, **2**, 235 (2002).
5. V. Klusa, *Drugs Fut.*, **20**, 135 (1995).
6. R. G. Bretzel, C. C. Bollen, E. Maeser, K. F. Federlin, *Am. J. Kidney Dis.*, **21**, 53 (1993).
7. R. G. Bretzel, C. C. Bollen, E. Maeser, K. F. Federlin, *Drugs Fut.*, **17**, 465 (1992).
8. R. Boer, V. Gekeler, *Drugs Fut.*, **20**, 499 (1995).
9. F. Bossert, H. Meyer, E. Wehinger, *Angew. Chem. Int. Ed.*, **20**, 762 (1981).
10. H. Nakayama, Y. Kasoaka, *Heterocycles*, **42**, 901 (1996).
11. A. Hantzsch, J. Liebig, *Ann. Chem.*, **215**, 1 (1882).
12. A. Kumar, R. A. Maurya, *Synlett*, **883** (2008).
13. M. Li, Z. Zuo, L. Wen, S. Wang, *J. Combinator. Chem.*, **10**, 436 (2008).
14. H. R. Memarian, M. Abdoli-Senejani, D. Döpp, *Z. Naturforsch.*, **61b**, 50 (2006).
15. M. A. Zolfigol, M. Mokhlesi, *J. Iran. Chem. Soc.*, **5**, S91 (2008).
16. C. T. Kresge, M. E. Leonowicz, W. J. Roth, J. C. Vartuli, J. S. Beck, *Nature*, **359**, 710 (1992).
17. J. S. Beck, J. C. Vartuli, W. J. Roth, M. E. Leonowicz, C. T. Kresge, K. D. Schmitt, C. T. W. Chu, D. H. Olson, E. W. Sheppard, S. B. McCullen, J. B. Higgins, J. L. Schlenker, *J. Am. Chem. Soc.*, **114**, 10834 (1992).
18. H. Yang, N. Coombs, I. Sokolov, G. A. Ozin, *Nature*, **381**, 589 (1996).
19. K. L. Frindell, M. H. Bartl, A. Popitsch, G. D. Stucky, *Angew. Chem. Int. Ed.*, **41**, 960 (2002).
20. C. M. Yang, A. T. Cho, F. M. Pan, T. G. Tsai, K. J. Chao, *Adv. Mater.*, **13**, 1099 (2001).
21. K. M. Coakley, Y. Liu, M. D. McGehee, K. L. Frindell, G. D. Stucky, *Adv. Func. Mater.*, **13**, 301 (2003).
22. K. Y. Kim, W. S. Ahn, D. W. Park, J. H. Oh, C. M. Lee, W. P. Tai, *Bull. Korean Chem. Soc.*, **25**, 634 (2004).
23. C. J. Brinker, Y. Lu, A. Sellinger, H. Fan, *Adv. Mater.*, **11**, 579 (1999).
24. Y. Lu, R. Ganguli, C. A. Drewien, M. T. Anderson, C. J. Brinker, W. Gong, Y. Guo, H. Soyez, B. Dunn, M. H. Huang, J. I. Zink, *Nature*, **389**, 364 (1997).
25. B. Alonso, A. R. Balkenende, P. A. Albouy, H. Amenitsch, M. N. Rager, F. Babonneau, *J. Sol-Gel Sci. Tech.*, **26**, 587 (2003).
26. S. Shen, B. Tian, C. Yu, S. Xie, Z. Zhang, B. Tu, D. Zhao, *Chem. Mater.*, **15**, 4046 (2003).
27. D. Zhao, P. Yang, N. Melosh, J. Feng, B. F. Chmelka, G. D. Stucky, *Adv. Mater.*, **10**, 1380 (1998).
28. S. Besson, C. Ricolleau, T. Gacoin, C. Jacquioid, J. P. Boilot, *J. Phys. Chem. B.*, **104**, 12095 (2000).
29. A. Gibaud, D. Grosso, B. Smarsly, A. Baptiste, J. F. Bardeau, F. Babonneau, D. A. Doshi, Z. Chen, C. J. Brinker, C. Sanchez, *J. Phys. Chem. B.*, **107**, 6114 (2003).
30. S. Ray, M. Brown, A. Bhaumik, A. Duttac, C. Mukhopadhyay, *Green Chem.*, **15**, 1910 (2013).
31. J. Safari, Z. Zarnegar, M. Borjian Borujeni, *Chemical Papers*, **67**, 688 (2013).
32. T. Tanev, T. J. Pinnavaia, *Science*, **267**, 865 (1995).
33. A. Debache, W. Ghalem, R. Boulcina, A. Belfaitah, S. Rhouati, B. Carboni, *Tetrahedron Lett.*, **50**, 5248 (2009).
34. W. Ghalem, R. Boulcina, A. Debache, *Chin. J. Chem.*, **30**, 733 (2012).
35. S. Rostamnia, K. Lamei, *Chinese Chemical Letters.*, **23**, 930 (2012).

КАТАЛИТИЧНА СИНТЕЗА НА 1,4-ДИГИДРОПИРИДИНОВИ ПРОИЗВОДНИ,
ИЗПОЛЗВАЙКИ ХЕКСАГОНАЛЕН МЕЗОПОРЕСТ СИЛИКАТ (HMS)

А. Фархади^{1*}, Т. Хамуле², М.А. Такаси³, Т. Аризавипур⁴

Университет по технология на петрола, Научен факултет, Ахваз, Иран

Постъпила на 22 януари г.; коригирана на 28 февруари, 2014 г.

(Резюме)

Постигната е проста едно-стадийна синтеза на производни на 1,4-дихидропиридина чрез кондензация на етил-ацетоацетат с различни арилови алдехиди и амониев ацетат в присъствие на хексагоналнен мезопорест силикат (HMS) като катализатор. Използван е етанол като разтворител. Постигнати са отлични добиви.

Synthesis, chemical structures elucidation and biological studies on the effect of some vital metal ions on vitamin A: Ca(II), Mg(II), Zn(II), Fe(III) and VO(II) complexes

M. Zaky¹, M. Y. El-Sayed^{1,2}, S. M. El-Megharbel^{1,3}, S. A. Taleb¹, M.S. Refat^{3,4}

¹ Department of Chemistry, Faculty of Science, Zagazig University, Egypt

² Faculty of Applied Medical Science, Al Jouf University-Al Qurayate

³ Department of Chemistry, Faculty of Science, Taif University, 888 Taif, Kingdom Saudi Arabia

⁴ Department of Chemistry, Faculty of Science, Port Said, Port Said University, Egypt

Received January 22, 2014; Revised April 4, 2014

Complexes of vitamin A as a pharmaceutical ligand with Ca(II), Mg(II), Zn(II), Fe(III) and VO(II), were synthesized and characterized by microanalysis, conductance, infrared and thermogravimetric (TG/DTG and DTA) measurements. The ligand can be coordinated as a monodentate ligand *via* the oxygen atom of the deprotonated hydroxyl group. Thermal degradation curves revealed that the uncoordinated water molecules are removed in a first stage while the decomposition of ligand besides coordinated water molecules took place in the second and subsequent steps. Vitamin A ligand, as well as its complexes were checked against some kinds of bacteria and fungi and produced a significant effect. The effect of kinetic thermodynamic parameters (E^* , ΔH^* , ΔS^* and ΔG^*) of the synthesized complexes upon the TG curves was calculated using Coats-Redfern and Horowitz-Metzger equations.

Keywords: Vitamin A complexes, Infrared spectra, Electronic spectra, Thermal analysis, Antimicrobial activity.

INTRODUCTION

Metal ions are required for many critical functions in humans. Scarcity of some metal ions can lead to diseases. Well-known examples include pernicious anemia resulting from iron deficiency, growth retardation arising from insufficient dietary zinc, and heart disease in infants owing to copper deficiency. The ability to recognize, to understand at the molecular level, and to treat diseases caused by inadequate metal ion functions constitutes an important aspect of medicinal bioinorganic chemistry [1-5].

Metals and metal complexes have played a key role in the development of modern chemotherapy [6]. For example, anticancer platinum drugs appear in more chemotherapy regimes than any other class of anticancer agents and have substantially contributed to the success achieved in treating cancer over the past three decades. Metals can play an important role in modifying the pharmacological properties of known drugs coordinated to a metal. This is because the resulting pro-drugs have different physical and pharmacological properties, allowing the drug to be released in a controlled fashion or at specific location [7]. This approach may lead to the rescue of drugs that have failed

because of poor pharmacology or high toxicity. Complexation of non-steroidal anti-inflammatory drugs to copper overcomes some of the gastric side effects of these drugs [8]. The release of cytotoxins such as nitrogen mustards from redox-active metals such as cobalt in the hypoxic regions of solid tumors has the potential to improve drug activity and reduce toxicity [9]. The metal-based drugs are also being used for the treatment of a variety of ailments, *viz.* diabetes, rheumatoid arthritis, inflammatory and cardiovascular diseases, as well as for diagnostics [10-12]. A number of drugs and potential pharmaceutical agents also contain metal-binding or metal-recognition sites, which can bind or interact with metal ions and potentially influence their bioactivities and might also cause damages on their target biomolecules. Numerous examples of these “metallo-drugs” and “metallo-pharmaceuticals” and their actions can be found in the literature, for instance: (a) several anti-inflammatory drugs, such as aspirin and its metabolite salicylglycine [13-16], suprofen [17], and paracetamol [18] are known to bind metal ions and affect their antioxidant and anti-inflammatory activities; (b) the potent histamine-H₂-receptor antagonist cimetidine [19] can form complexes with Cu²⁺ and Fe³⁺, and the histidine blocker antiulcer drug famotidine can also form a stable complex with Cu²⁺ [20,21]; (c) the anthelmintic and fungistatic agent thiabendazole, which is used for the treatment of several parasitic diseases, forms a

* To whom all correspondence should be sent:
E-mail: msrefat@yahoo.com

Co²⁺ complex of 1:2 metal-to-drug ratio [22]; (d) the Ru²⁺ complex of the anti-malaria agent chloroquine exhibits activity two to five times higher than that of the parent drug against drug-resistant strains of *Plasmodium faciparum* [23]. However, it is known that some drugs act *via* chelation or by inhibiting metalloenzymes but most of the drugs act as potential ligands. A lot of studies are being carried out to ascertain how metal binding influences the activities of the drugs [24]. Metal complexes are gaining increasing importance in the design of drugs on coordination with a metal. Metal-organic frameworks are a burgeoning field in the last two decades, which not only stems from their tremendous potential applications in areas such as catalysis, molecular adsorption, magnetism, nonlinear optics, and molecular sensing, but also from their novel topologies and intriguing structural diversities [25-28]. On the other hand, many organic drugs, which possess modified pharmacological and toxicological properties, administered in the form of metallic complexes [29], have the potential to act as ligands and the resulting metal-drug complexes are particularly important both in coordination chemistry and biochemistry [30-34]. However, the study of metal-drug complexes is still in its early stages, thus representing a great challenge in current synthetic chemistry and coordination chemistry.

Vitamin A (Fig. 1) is an essential nutrient for humans because it cannot be synthesized *de novo* within the body. The term "vitamin A" is used generically for all derivatives (other than carotenoids) that have the biological activity of all-trans retinol. Forms of vitamin A include retinol, retinal (also called retinaldehyde), and various retinyl esters [35]. Retinoic acid can perform some but not all of the biological functions of vitamin A.

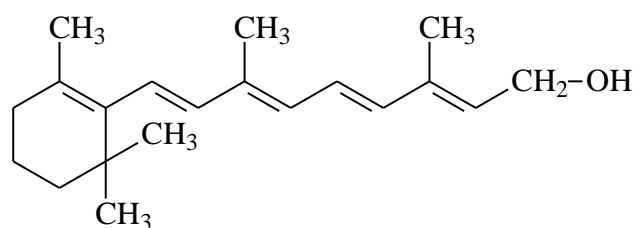


Fig. 1. Structure of vitamin A (Vit. A)

Vitamin A deficiency is a major nutritional disorder in many developing countries. It especially affects young children, in whom it can cause xerophthalmia and lead to blindness, and can also limit growth, weaken innate and acquired host defenses, exacerbate infection and increase the risk

of death [36]. Researchers have succeeded in creating water-soluble forms of vitamin A, which they believed could reduce the potential for toxicity; however a study in 2003 found water-soluble vitamin A approximately 10 times as toxic as the fat-soluble vitamin [37]. Because vitamin A is fat soluble and can be stored primarily in the liver, routine consumption of large amounts of vitamin A over a period of time can result in toxic symptoms, including liver damage, bone abnormalities and joint pain, alopecia, headaches and vomiting, and skin desquamation. Hypervitaminosis A appears to be due to abnormal transport and distribution of vitamin A and retinoids caused by overloading of the plasma transport mechanisms [38]. Recently the interest in the trend of metal drug complexes has increased in order to achieve an enhanced therapeutic effect in combination with decreased toxicity. To the best of our knowledge, little attention has been paid to discuss the interaction between vitamin A and metal ions and the literature is still poor in such spectroscopic characterizations. The interpretations are based on the ability of the cited drug to form complex associations with vital metal ions like Ca(II), Mg(II), Zn(II), Fe(III) and VO(II). The spectral characteristics and the stability of the formed complex associates were also included.

MATERIALS AND METHODS

Materials

All chemicals used in this investigation were of highest purity grade (Merck). Selected metal salts like CaCl₂, MgCl₂.6H₂O, ZnSO₄.H₂O, Fe(NO₃)₃.9H₂O and VOSO₄.H₂O were used. Vitamin A was received from the Egyptian International Pharmaceutical Industrial Company (EIPICO.).

Preparation of solid complexes

The hygroscopic vitamin A complexes with the formulas: [Ca(Vit.A)(Cl)(NH₃)₂(H₂O)₂].13H₂O (I), [Mg(Vit.A)(Cl)(NH₃)₂(H₂O)₂].50H₂O (II), [Zn(Vit.A)(SO₄)(NH₃)₂(NH₄)].20H₂O (III), [Fe(Vit.A)(NO₃)₂(NH₃)(H₂O)₂].16H₂O (IV) and [VO(Vit. A)(SO₄)(NH₄)].2NH₃.20H₂O (V) were prepared, employing a 1:1 (metal : Vit. A) ratio. The complexes were prepared by mixing equal volumes (20 ml) of distilled water solutions of CaCl₂ (0.111 g, 1.0 mmol), MgCl₂.6H₂O (0.203 g, 1.0 mmol), ZnSO₄.H₂O (0.180 g, 1.0 mmol), Fe(NO₃)₃.9H₂O (0.404 g, 1.0 mmol) and VOSO₄.H₂O (0.163 g, 1.0 mmol) with a methanol solution of Vit. A (0.286 g, 1.0 mmol). The mixtures were neutralized by titration against 5% alcoholic ammonia solution to adjust the pH at (7.0–9.0), then warmed at about ~ 60 °C for about 3 h and left overnight to evaporate slowly at

room temperature. The obtained precipitates were filtered off, washed several times with minimum amounts of hot methanol and dried at 60 °C over anhydrous CaCl₂.

Preparations of stock solutions

Barium chloride solution

A 10 g of barium chloride dihydrate, BaCl₂·2H₂O, was weighed and dissolved in a minimum amount of distilled water. The volume was completed to 100 ml in a measuring flask to give a 10% solution.

Silver nitrate solution

A weight of 0.1701 g of AgNO₃ was dissolved in a small amount of distilled water and completed to 100 ml in a dark measuring flask to obtain an approximate 0.01 M solution.

Ammonium hydroxide solution

The stock solution of NH₄OH was prepared by taking 15 ml of concentrated NH₃ (33% v/v) in 35 ml distilled water. The volume was then completed to 100 ml by methanol to give an approximately (5% v/v) solution.

Apparatus and experimental conditions

Carbon, hydrogen and nitrogen content were determined using a Perkin-Elmer CHN Elemental Analyzer model 2400. The metal content was determined gravimetrically by converting the compounds into their corresponding oxides.

The Ca(II), Mg(II), Zn(II), Fe(III) and VO(II) contents were determined gravimetrically by direct ignition of the complexes at 800 °C for 3 h till constant weight. The residues were then weighed in the form of metal oxides. Molar conductivities of freshly prepared 1.0 × 10⁻³ mol/l DMSO solutions of the complexes were measured using a Jenway 4010 conductivity meter. IR spectra were recorded on a Bruker FTIR spectrophotometer (4000 – 400 cm⁻¹) in KBr pellets. The UV-vis spectra were recorded in DMSO solvent with concentration of (1.0×10⁻³ M) for the free ligands and their complexes using a Jenway 6405 spectrophotometer with 1 cm quartz cell, in the range of 200-600 nm. ¹H-NMR spectra of the free ligands and their complexes were recorded on a Varian Gemini 200 MHZ spectrophotometer using DMSO-d₆ as solvent and TMS as internal reference. Thermogravimetric analysis (TGA, DTG and DTA) was carried out in the temperature range from 25 to 800 °C in a steam of nitrogen atmosphere by using a Shimadzu TGA-50 H thermal analyzer. The experimental conditions were: platinum crucible, nitrogen atmosphere with a 30 ml/min flow rate and heating rate of 10 °C/min.

In recent years there has been increasing interest in determining the rate-dependent parameters of solid-state non-isothermal decomposition reactions by analysis of TG curves [39-45]. Most commonly used methods are the differential method of Freeman and Carroll [39], the integral method of Coat and Redfern [40] and the approximation method of Horowitz and Metzger [43]. In the present investigation, the general thermal behavior of the vitamin A complexes in terms of stability ranges, peak temperatures and values of kinetic parameters are discussed. The kinetic parameters were evaluated using the Coats-Redfern equation:

$$\int_0^\alpha \frac{d\alpha}{(1-\alpha)^n} = \frac{A}{\varphi} \int_{T_1}^{T_2} \exp\left(-\frac{E^*}{RT}\right) dt \quad (1)$$

This equation on integration gives:

$$\ln\left[-\frac{\ln(1-\alpha)}{T^2}\right] = -\frac{E^*}{RT} + \ln\left[\frac{AR}{\varphi E^*}\right] \quad (2)$$

A plot of the left-hand side (LHS) against 1/T was drawn. E* is the energy of activation in J mol⁻¹ and is calculated from the slope and A in (s⁻¹) from the intercept value. The entropy of activation ΔS* in (JK⁻¹mol⁻¹) was calculated by using the equation:

$$\Delta S^* = R \ln(Ah/k_B T_s) \quad (3)$$

where k_B is the Boltzmann constant, h is the Plank's constant and T_s is the DTG peak temperature [44].

The Horowitz-Metzger equation is an illustration of the approximation methods.

$$\log\left\{\frac{1-(1-\alpha)^{1-n}}{(1-n)}\right\} = E^*\theta/2.303RT_s^2 \quad \text{for } n \neq 1 \quad (4)$$

When n = 1, the LHS of equation 4 would be log[-log(1-α)]. For a first-order kinetic process the Horowitz-Metzger equation may be written in the form:

$$\log[\log(w_\alpha/w_\gamma)] = E^*\theta/2.303RT_s^2 - \log 2.303$$

where θ = T - T_s, w_γ = w_α - w, w_α = mass loss at completion of the reaction; w = mass loss up to time t. The plot of log[log(w_α/w_γ)] vs θ was drawn and was found to be linear. From its slope E* was calculated. The pre-exponential factor, A, was calculated from the equation:

$$E^*/RT_s^2 = A/[\varphi \exp(-E^*/RT_s)]$$

The entropy of activation, ΔS*, was calculated from equation 3. The enthalpy activation, ΔH*, and Gibbs free energy, ΔG*, were calculated from: ΔH* = E* - RT and ΔG* = ΔH* - TΔS*, respectively.

Microbiological investigation

According to Gupta *et al.* 1995 [46], the hole well method was applied. The investigated isolates of bacteria and fungi were seeded in tubes with nutrient broth (NB) and Dox's broth (DB), respectively. The seeded (NB) for bacteria and (DB) for fungi (1 ml) were homogenized in the tubes with 9 ml of melted

(45 °C) nutrient agar (NA) for bacteria and (DA) for fungi. The homogenous suspensions were poured into Petri dishes. Holes (diameter 0.5 cm) were done in the cool medium. After cooling in these holes, about 100 µl of the investigated compounds were applied using a micropipette. After incubation for 24 h in an incubator at 37 °C and 28 °C for bacteria and fungi, respectively, the inhibition zone diameters were measured and expressed in cm. The antimicrobial activities of the investigated compounds were tested against some kinds of bacteria as *Escherichia coli* (Gram -ve) and *Staph albus* (Gram +ve), and some kinds of fungi as *Aspergillus flavus* and *Aspergillus niger*. In the same time with the antimicrobial investigations of the complexes, the pure solvent was also tested. The concentration of each solution was 1.0×10^{-3} mol/L. Commercial DMSO was employed to dissolve the tested samples.

RESULTS AND DISCUSSION

The reactions of vitamin A with the metal ions Ca(II), Mg(II), Zn(II), Fe(III) and VO(II) gave colored solid complexes in moderate to good yields (65–85 %). The physical and analytical data, colors, percentage (carbon, hydrogen and nitrogen) and melting/decomposition temperatures of the compounds are presented in Table (1).

The found and calculated percentages of elemental analysis CHN are in good agreement and prove the suggested molecular formulas of the

obtained vitamin A complexes. The complexes have low melting points (lower than 100 °C). The molar conductivities of the compounds in DMSO ranged (7–47) $\Omega^{-1} \text{ cm}^2 \text{ mol}^{-1}$, showing that they were of non-electrolytes nature. Vit. A ligand behaves as a monodentate ligand and coordinates to the metal ions through the oxygen of the hydroxyl group upon deprotonation. Isolated Vit. A complexes are in 1:1 molar ratio of (M:Vit. A) where M=Ca(II), Mg(II), Zn(II), Fe(III) and VO(II).

Molar conductivities

Conductivity measurements have frequently been used to predict the structure of metal chelates within the limits of their solubility. They provide a method of testing the degree of ionization of the complexes. The more molecular ions a complex liberates in solution, the higher will be its molar conductivity and *vice versa* [47]. The molar conductivity values for the Ca(II), Mg(II), Zn(II), Fe(III) and VO(II) complexes of vitamin A in DMSO solvent (1.00×10^{-3} M) were found to be in the range (7–47) $\Omega^{-1} \text{ cm}^2 \text{ mol}^{-1}$ at 25°C, suggesting them to be non-electrolytes [48], as shown in Table (1). Hence, the molar conductance values indicate that no ions are present outside the coordination sphere so the Cl^- , SO_4^- and NO_3^- ions may be inside the coordination sphere or absent.

The obtained results were strongly matched with the elemental analysis data where Cl^- , SO_4^- and NO_3^- ions are detected in case of Ca(II), Mg(II), Zn(II), Fe(III) and VO(II) complexes after

Table 1. Elemental analysis and physical data of vitamin A complexes

Complex	M wt. g/mole	m.p./ °C	color	% C		% H		% N		% M		$\Lambda_m (\Omega^{-1} \text{ cm}^2 \text{ mol}^{-1})$
				Calcd.	Found	Calcd.	Found	Calcd.	Found	Calcd.	Found	
[Ca(Vit. A)(Cl)(NH ₃) ₂ (H ₂ O) ₂].13H ₂ O (C ₂₀ H ₆₅ O ₁₆ N ₂ Cl Ca)	664.5	Low melting points < 100 °C	Pale yellow	36.11	35.54	9.78	9.52	4.21	4.01	6.02	5.89	35
[Mg(Vit. A)(Cl)(NH ₃) ₂ (H ₂ O) ₂].50H ₂ O (C ₂₀ H ₁₃₉ O ₅₃ N ₂ Cl Mg)	1314.5		Pale yellow	18.25	18.56	10.57	10.49	2.13	2.48	1.82	1.77	47
[Zn(Vit. A)(SO ₄)(NH ₃) ₂ (NH ₄)].20H ₂ O (C ₂₀ H ₇₉ O ₂₅ N ₃ S Zn)	858.4		Yellow	27.95	27.56	9.20	9.22	4.89	5.07	7.62	7.55	7
[Fe(Vit. A)(NO ₃) ₂ (NH ₃)(H ₂ O) ₂].16H ₂ O (C ₂₀ H ₆₈ O ₂₅ N ₃ Fe)	806		Brown	29.77	30.20	8.43	8.59	5.21	4.82	6.94	6.86	14
[VO(Vit. A)(SO ₄)(NH ₄)].2NH ₃ .20H ₂ O (C ₂₀ H ₇₉ O ₂₅ N ₃ S VO)	860		Dark green	27.90	26.37	9.18	9.05	4.88	5.22	7.79	7.71	11

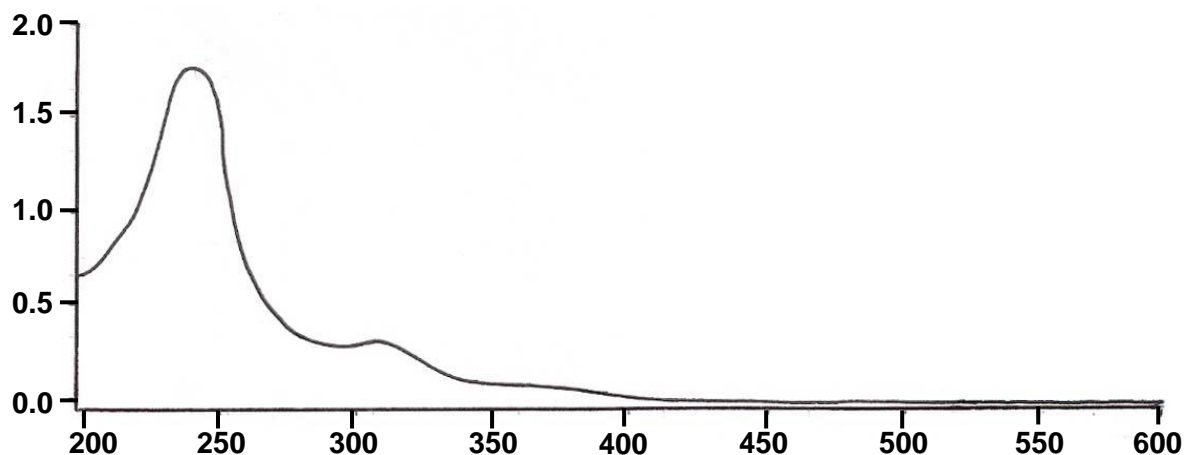


Fig. 2. Uv/vis electronic spectra of the Fe(III)/Vit. A complex.

degradation of these complexes by using nitric acid, and precipitation of Cl^- and SO_4^{2-} by addition of AgNO_3 and BaCl_2 solutions, respectively, to the solutions of the mentioned complexes in nitric acid. NO_3^- ions were also detected using infrared spectral data. The above complexes are hygroscopic, insoluble in water, partially soluble in alcohol and most of organic solvents and soluble in DMSO, DMF and concentrated acids.

Electronic absorption spectra

The formation of the Ca(II), Mg(II), Zn(II), VO(II) and Fe(III) complexes with vitamin A was confirmed by UV-Vis spectra as well. Fig. (2) shows the electronic absorption spectra of the Fe(III) complex in DMSO in the 200–600 nm range.

It can be seen that the free vitamin A has one distinct absorption band at 350 nm which may be attributed to $n \rightarrow \pi^*$ intra-ligand transition. In the spectra of the Fe(III) complex this band is clearly blue shifted to 312 nm, where the Fe(III) complex shows two bands at 241 and 312 nm assigned to $\pi \rightarrow \pi^*$ and $n \rightarrow \pi^*$ respectively, suggesting that the ligand is deprotonated and the lone pair of electrons on the oxygen atom of the OH group participates in the complexation. The electronic absorption spectrum of the Fe(III) complex in DMSO solution has two bands at 375 and 435 nm and a weak band at 480 nm assigned to the charge transfer transition from metal-to-ligand and a d-d transition band, respectively.

Infrared spectra

The infrared spectra of vitamin A free ligand and its complexes are shown in Fig. (3) and Table (2).

The spectra are similar but there are some differences which could give information on the type of coordination. The IR spectrum of vitamin A shows a very strong broad band at 3406 cm^{-1} which is assigned to $\nu(\text{O-H})$ stretching vibration of an alcoholic OH group. Ionization of the alcoholic OH group with subsequent ligation through oxygen atom seems a plausible explanation [49]. It is difficult to distinguish between the $\nu(\text{OH})$ of the alcoholic group of vitamin A and the stretching vibrational bands of water molecules of the complexes due to the overlapping values, and their appearance in one place. To ascertain the involvement of $\nu(\text{OH})$ of the alcoholic group of vitamin A in the coordination process, the stretching vibration bands of $\nu(\text{C-O})$ in all vitamin A complexes were followed. The examination of these complexes showed that the $\nu(\text{C-O})$ is shifted to the lower wavenumbers from 1073 and 1176 cm^{-1} in case of free ligand to $(1035-1084) \text{ cm}^{-1}$ and $(1075-1157) \text{ cm}^{-1}$ in the complexes. This result indicates that the alcoholic group participates in the complexation [50, 51] and vitamin A acts as a monodentate ligand.

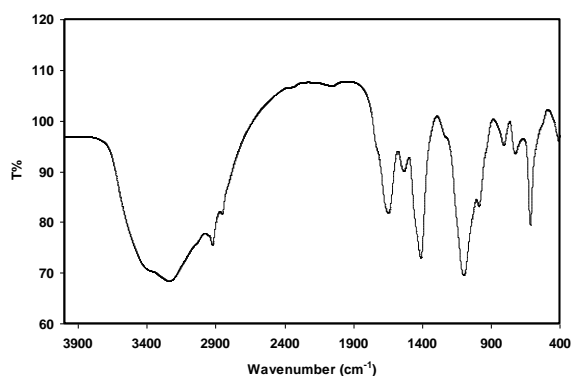


Fig. 3. IR spectrum of the VO(II)/Vit. A complex

Table 2. IR frequencies (cm^{-1}) of vitamin A and its metal complexes

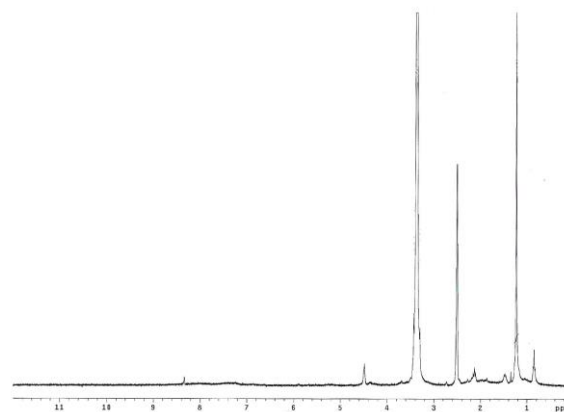
Compound	$\nu(\text{O-H})$	$\nu(\text{NH})$; NH_3 and NH_4	$\delta(\text{NH})$; NH_3 and NH_4	$\nu(\text{C-H})$ aliphatic	$\nu(\text{C-O})$	$\nu(\text{M-O})$	$\nu(\text{M-N})$
Vitamin A	3406	---	---	2955 2929	1176 1073	---	---
[Ca(Vit. A)(Cl)(NH ₃) ₂ (H ₂ O) ₂].13H ₂ O	3423	3230	1640	2925 2900	1157 1038	540	490
[Mg(Vit. A)(Cl)(NH ₃) ₂ (H ₂ O) ₂].50H ₂ O	3410	3220	1637	2923 2857	1075 1035	613	477
[Zn(Vit. A)(SO ₄)(NH ₃) ₂ (NH ₄)].20H ₂ O	3395	3190	1647	2922 2855	1143 1084	520	488
[Fe(Vit. A)(NO ₃) ₂ (NH ₃)(H ₂ O) ₂].16H ₂ O	3383	3170	1652	2924 2900	1150 1037	596	505
[VO(Vit. A)(SO ₄)(NH ₄)].2NH ₃ .20H ₂ O	3410	3160	1649	2926 2857	1101	560	412

The presence of water molecules in the above mentioned complexes is ascertained by the presence of a broad band of strong intensity in the (3383-3423) cm^{-1} region which may be assigned to the OH stretching vibration for the coordinated and uncoordinated water molecules in the vitamin A complexes. The angular deformation motions of the coordinated water can be classified into four types of vibrations: δ_b (bend), δ_r (rock), δ_t (twist) and δ_w (wag). The assignments of these motions in all isolated complexes are as follows, the bending motion, $\delta_b(\text{H}_2\text{O})$ at (1637–1652) cm^{-1} , the rocking motion, $\delta_r(\text{H}_2\text{O})$ at (750–850) cm^{-1} , the wagging motion, $\delta_w(\text{H}_2\text{O})$ at (581–619) cm^{-1} , the twisting motion, $\delta_t(\text{H}_2\text{O})$ at (625–690) cm^{-1} [49]. It should be mentioned here that these assignments for both the bond stretches and angular deformation of the coordinated water molecules fall in the frequency regions reported for related aquo-complexes. The vitamin A complexes show new bands in the range of (3160-3230) cm^{-1} which can be assigned to the stretching vibration of $\nu(\text{N-H})$ of NH_3 and NH_4 groups; the absence of these bands in the spectrum of the free ligand supports our explanation. Also bending motions of $\delta(\text{NH})$ were observed in the range of (1637–1652) cm^{-1} . The $\nu(\text{V=O})$ stretching vibration in the vanadyl complex is observed as an expected band at 989 cm^{-1} , which is in good agreement with those known for many vanadyl complexes [52]. The coordination of a nitrate anion to the Fe(III) ions was also supported by the IR spectrum of the ferric complex, where the nitrate complex displayed two bands due to $\nu_{\text{as}}(\text{NO}_2)$ at 1542 cm^{-1} and $\nu_s(\text{NO}_2)$ at 1381 cm^{-1} assigned to a monodentate group [53]. It is worth mentioning that the test for the presence of sulfato group in the VO(II) and Zn(II) complexes gave a positive result; this conclusion was supported by the two detected infrared frequency bands at about 1100 and 600 cm^{-1}

¹ overlapping with angular deformation motions of the coordinated water molecules. Participation of both oxygen (hydroxyl group) and nitrogen (NH_3 and/or NH_4) is also confirmed by the appearance of new bands in the complexes within the (520-613) and (410-505) cm^{-1} regions which may be assigned to the $\nu(\text{M-O})$ and $\nu(\text{M-N})$ stretching vibrations respectively [54,55].

¹H-NMR spectra

The ¹H-NMR data of vitamin A and its Fe (III) complex are listed in Table (3) and shown in Fig. (4) as an example. ¹H-NMR spectrum of vitamin A shows a signal at $\delta = (\sim 9)$ ppm, which is assigned to the proton of the alcoholic OH group which disappears in the Mg(II) complex.

**Fig. 4.** ¹H-NMR spectrum of the Mg(II)/Vit. A complex

The disappearance of the signal of the proton of the hydroxyl group in the ¹H-NMR spectrum of the complex confirms that the hydroxyl group contributes to the complexation between vitamin A and Mg(II) ion [56]. The proton NMR spectrum for the Mg(II) complex shows singlets at 3.29 and 3.42 ppm. These singlets are not observed in the free ligand spectrum and can be assigned to protons of H₂O molecules, thus supporting the complex formula.

Thermal analysis

The obtained vitamin A complexes were studied by thermogravimetric (TG), differential thermogravimetric (DTG) and DTA analysis from ambient temperature to 800 °C in a N₂ atmosphere. The TG curves were drawn as mg mass loss *versus* temperature and DTG curves were drawn as rate of mass loss *versus* temperature. The thermoanalytical results are summarized in Table (4).

[Ca(Vit. A)(Cl)(NH₃)₂(H₂O)₂].13H₂O complex

The thermal decomposition of the Ca(II) complex of vitamin A with the general formula [Ca(Vit. A)(Cl)(NH₃)₂(H₂O)₂].13H₂O occurs in four steps. The first degradation step takes place within

the temperature range of 25-145 °C at DTG_{max}=59 °C and DTA= 60 °C (endo) and it corresponds to the loss of 8 molecules of hydration water(uncoordinated water) with an observed weight loss of 20.05% (calcd.=21.67%). The activation energy of this step is 20 K J mol⁻¹. The second step occurs within the temperature range of 145-275 °C at DTG_{max}=225 °C which is assigned to the loss of 3 molecules of hydration water (uncoordinated water) with a weight loss (obs =7.99%, calcd.=8.12%). The activation energy of this step is 74 K J mol⁻¹. The third step occurs within the temperature range of 275-440 °C at DTG_{max}=367 °C and DTA=415 °C (exo) which is assigned to the loss of 4 molecules of hydration water

Table 3. 1H-NMR spectral data of vitamin A and its Mg(III) complex

Compound	δ ppm of hydrogen					
	H; <u>CH</u> ₃	H; <u>CH</u> ₂	H; <u>CH</u>	H; <u>H₂O</u>	H; <u>NH</u> ₃	H; <u>OH</u>
Vitamin A	1.0	1.50	1.6-1.65-1.8- 1.9-2.0	---	---	~ 9
Mg(II) complex	1.05 – 0.84	1.23	1.34-1.47- 1.86-2.10-2.13	3.29 - 3.42	4.48	---

Table 4. Thermal data of vitamin A complexes.

Compound	Steps	TG, temp. range (°C)	DTG _{max} (°C)	DTA (°C)	TG weight loss (%)		Assignments
					Calcd.	Found	
[Ca(Vit. A)(Cl)(NH ₃) ₂ (H ₂ O) ₂].13H ₂ O (C ₂₀ H ₆₅ O ₁₆ N ₂ Cl Ca)	1	25-145	59	60	21.67	20.05	8H ₂ O
	2	145-275	225	---	8.12	7.99	3H ₂ O
	3	275-440	367	415	21.44	21.71	4H ₂ O+2NH ₃ +HCl
	4	440-580	511	513	20.46	21.27	C ₉ H ₂₈ (organic moiety)
<i>Final residue = CaO + 11C (found =28.98%, Calcd.=28.29%)</i>							
[Mg(Vit. A)(Cl)(NH ₃) ₂ (H ₂ O) ₂].50H ₂ O (C ₂₀ H ₁₃₉ O ₅₃ N ₂ Cl Mg)	1	30-140	70	71	28.75	28.80	21H ₂ O
	2	140-210	184	---	17.80	18.02	13H ₂ O
	3	300-370	334	---	13.69	12.92	10H ₂ O
	4	370-465	420	440	13.54	13.51	8H ₂ O+2NH ₃
	5	465-580	534	539	14.94	14.80	HCl+C ₁₁ H ₂₈ (organic moiety)
<i>Final residue = MgO + 9C (found =11.95%, Calcd.=11.25%)</i>							
[Zn(Vit. A)(SO ₄)(NH ₃) ₂ (NH ₄)].20H ₂ O (C ₂₀ H ₇₉ O ₂₅ N ₃ S Zn)	1	48-190	81	82	14.67	15.30	7H ₂ O
	2	225-350	292	---	10.48	11.06	5H ₂ O
	3	350-400	345	354	12.58	11.89	6H ₂ O
	4	475-570	537	539	19.57	18.20	2H ₂ O+2NH ₃ +H ₂ SO ₄
	5	700-800	749	---	24.81	23.87	C ₁₃ H ₃₁ N (organic moiety)
<i>Final residue = ZnO + 7C (found =19.68%, Calcd.=19.26%)</i>							
[Fe(Vit. A)(NO ₃) ₂ (NH ₃)(H ₂ O) ₂].16H ₂ O (C ₂₀ H ₆₈ O ₂₅ N ₃ Fe)	1	50-125	80	---	3.34	3.27	1.5H ₂ O
	2	125-220	187	196	17.86	17.51	8H ₂ O
	3	220-325	284	302	28.90	28.67	8.5H ₂ O+NH ₄ NO ₃
	4	325-430	366	372	26.55	26.62	C ₁₁ H ₂₈ N O _{2.5} (organic moiety)
<i>Final residue = FeO_{1.5} + 9C (found =23.93%, Calcd.=23.32%)</i>							
[VO(Vit. A)(SO ₄)(NH ₄)].2NH ₃ .20H ₂ O (C ₂₀ H ₇₉ O ₂₅ N ₃ S VO)	1	45-140	66	---	4.18	3.79	2H ₂ O
	2	140-310	266	262	31.39	30.99	15H ₂ O
	3	310-360	341	339	14.06	14.72	3NH ₄ OH+CH ₄
	4	360-510	454	460	32.32	32.78	C ₁₃ H ₂₆ O ₄ S (organic moiety)
<i>Final residue = VO₂ + 6C (found =17.54%, Calcd.=18.02%)</i>							

exo=exothermic peak, endo=endothermic peak.

(2 uncoordinated and 2 coordinated) +2(NH₃) gas+HCl with a weight loss (obs.=21.71%, calcd.=21.44%). The large number of water molecules can participate in intermolecular hydrogen bonding which in some cases causes an increase in the temperature for weight losses [57]. The activation energy of this step is 99.7 K J mol⁻¹. The fourth step occurs within the temperature range of 440-580 °C at DTG_{max}=511 °C and DTA=513 °C (exo) which is assigned to the loss of C₉H₂₈ (organic moiety) with a weight loss (obs.=21.27%, calcd.=20.46%); the activation energy of this step is 192 K J mol⁻¹. CaO+11C are the products remaining stable till 800 °C as a final residue.

[Mg(Vit. A)(Cl)(NH₃)₂(H₂O)₂].50H₂O complex

The thermal decomposition of the Mg(II) complex of vitamin A with the general formula [Mg(Vit. A)(Cl)(NH₃)₂(H₂O)₂].50H₂O occurs in five steps. The first degradation step takes place within the temperature range of 30-140 °C at DTG_{max}=70 °C and DTA=71 °C (endo) and it corresponds to the loss of 21 molecules of hydration water (uncoordinated water) with an observed weight loss of 28.80% (calcd.=28.75%); the activation energy of this step is 44.1 K J mol⁻¹. The second step occurs within the temperature range of 140-210 °C at DTG_{max}=184 °C which is assigned to the loss of another 13 molecules of hydration water (uncoordinated water) with a weight loss (obs.=18.02%, calcd.=17.80%); the activation energy of this step is 84.5 K J mol⁻¹. The third step occurs within the temperature range of 300-370 °C at DTG_{max}=334 °C which is assigned to the loss of 10 molecules of hydration water (uncoordinated water) with a weight loss (obs.=12.92%, calcd.=13.69%); the activation energy of this step is 164 K J mol⁻¹. The fourth step occurs within the temperature range of 370-465 °C at DTG_{max}=420 °C and DTA=440 °C (exo) which is assigned to the loss of 8 molecules of hydration water (6 uncoordinated and 2 coordinated) +2(NH₃) gas molecules with a weight loss (obs.=13.51%, calcd.=13.54%); the activation energy of this step is 268 K J mol⁻¹. The remaining several water molecules not liberated till higher temperature back to the hydrogen bonding between the water molecules [57]. The fifth step occurs within the temperature range of 465-580 °C at DTG_{max}=534 °C and DTA=539 °C (exo) which is assigned to the loss of HCl+C₁₁H₂₈ (organic moiety) with a weight loss (obs.=14.80%, calcd.=14.94%). MgO+9C are the products remaining stable till 800 °C as a final residue.

[Zn(Vit. A)(SO₄)(NH₃)₂(NH₄)].20H₂O complex

The thermal decomposition of the Zn(II) complex of vitamin A with the general formula [Zn(Vit. A)(SO₄)(NH₃)₂(NH₄)].20H₂O occurs in six steps. The first degradation step takes place within the temperature range of 48-190 °C at DTG_{max}=81 °C and DTA=82 °C (endo) and it corresponds to the loss of 7 molecules of hydration water with an observed weight loss of 15.30% (calcd.=14.67%); the activation energy of this step is 44.9 K J mol⁻¹. The second step occurs within the temperature range of 225-320 °C at DTG_{max}=292 °C which is assigned to the loss of another 5 molecules of hydration water with a weight loss (obs.=11.06%, calcd.=10.48%); the activation energy of this step is 102 K J mol⁻¹. The third step occurs within the temperature range of 320-400 °C at DTG_{max}=345 °C and DTA=354 °C (endo) which is assigned to the loss of 6 molecules of hydration water with a weight loss (obs.=11.89%, calcd.=12.58%); the activation energy of this step is 144 K J mol⁻¹. The fourth step occurs within the temperature range of 475-570 °C at DTG_{max}=537 °C and DTA=539 °C (exo) which is assigned to the loss of 2 molecules of hydration water +2 NH₃ molecules+H₂SO₄ with a weight loss (obs.=18.20%, calcd.=19.57%); the activation energy of this step is 263 K J mol⁻¹. The fifth step occurs within the temperature range of 700-800 °C at DTG_{max}=749 °C which is assigned to the loss of C₁₃H₃₁N (organic moiety) with a weight loss (obs.=23.87%, calcd.=24.81%). ZnO+7C are the products remaining stable till 800 °C as a final residue.

[Fe(Vit. A)(NO₃)₂(NH₃)(H₂O)₂].16H₂O complex

The thermal decomposition of the Fe(III) complex of vitamin A with the general formula [Fe(Vit. A)(NO₃)₂(NH₃)(H₂O)₂].16H₂O occurs in four steps. The first degradation step takes place within the temperature range of 50-125 °C at DTG_{max}=80 °C and it corresponds to the loss of 1.5 molecules of hydration water (uncoordinated water) with an observed weight loss of 3.27% (calcd.=3.34%); the activation energy of this step is 71.4 K J mol⁻¹. The variation from one molecule to one and half water molecules is assigned to the hygroscopic nature of the vitamin A complexes. The second step occurs within the temperature range of 125-220 °C at DTG_{max}=187 °C and DTA=196 °C (exo) which is assigned to the loss of another 8 molecules of hydration water (uncoordinated water) with a weight loss (obs.=17.51%, calcd.=17.86%); the activation energy of this step is 88.4 K J mol⁻¹. The third step occurs within the temperature range of 220-325 °C at DTG_{max}=284 °C and DTA=302 °C (exo) which is assigned to the loss of 8.5 molecules of hydration water+NH₄NO₃ with a weight loss (obs.=28.67%, calcd.=28.90%); the

activation energy of this step is 97.7 K J mol⁻¹. The fourth step occurs within the temperature range of 325-430 °C at DTG_{max}=366 °C and DTA=372 °C (exo) which is assigned to the loss of C₁₁H₂₈NO_{2.5} (organic moiety) with a weight loss (obs.=26.62%, calcd.=26.55%); the activation energy of this step is 123 K J mol⁻¹. FeO_{1.5}+9C are the products remaining stable till 800 °C as a final residue.

[VO(Vit. A)(SO₄)(NH₄)]₂.2NH₃.20H₂O complex

The thermal decomposition of the VO(II) complex of vitamin A with the general formula [VO(Vit. A)(SO₄)(NH₄)]₂.2NH₃.20H₂O occurs in four steps. The first degradation step takes place within the temperature range of 45-140 °C at DTG_{max}=66 °C and it correspond to the loss of 2 molecules of hydration water (uncoordinated water) with an observed weight loss of 3.79% (calcd.=4.18%); the activation energy of this step is 51.6 K J mol⁻¹. The second step occurs within the temperature range of 140-310 °C at DTG_{max}=266 °C and DTA=262 °C (endo) which is assigned to the loss of another 15 molecules of hydration water with a weight loss (obs.=30.99%, calcd.=31.39%); the activation energy of this step is 100 K J mol⁻¹. The third step occurs within the temperature range of 310-360 °C at DTG_{max}=341 °C and DTA=339 °C (endo) which is assigned to the loss of 3 NH₄OH and CH₄ gas with a weight loss (obs.=14.72%, calcd.=14.06%); the activation energy of this step is 181 K J mol⁻¹. Concerning retained ammonia molecules over water till DTG of 341 °C, the combination between water molecules and ammonia to give 3NH₄OH altered to 3NH₃ + 3H₂O. The fourth step occurs within the temperature range of 360-510 °C at DTG_{max}=454 °C and DTA=460 °C (exo) which is assigned to the loss of C₁₃H₂₆O₄S (organic moiety) with a weight loss (obs.=32.78%, calcd.=32.32%); the activation energy of this step is 149 K J mol⁻¹. VO₂+6C are the products remaining stable till 800 °C as a final residue. It can be noted that the increase in the number of water molecules favors the formation of intermolecular hydrogen bonding which pushes up the temperature range for losing water molecules.

Kinetic studies

The kinetic parameters such as activation energy (ΔE^*), enthalpy (ΔH^*), entropy (ΔS^*) and free energy change of the decomposition (ΔG^*) were evaluated graphically, as shown in Figs. (5, 6) by employing the Coats–Redfern and Horwitz–Mitzger relations [43,40].

The calculated values of E^* , A , ΔS^* , ΔH^* and ΔG^* for the decomposition steps of vitamin A complexes are given in Table (5). The most

significant result is the considerable thermal stability of the Ca(II), Mg(II), Zn(II), Fe(III) and VO(II) complexes evidenced by the high values of the activation energy of decomposition. The second essential result is that the entropy change ΔS^* for the formation of the activated complexes from the starting reactants has in most cases negative values. The negative sign of ΔS^* suggests that the thermodynamic behavior of all vitamin A complexes is non-spontaneous (more ordered) and the degree of structural “complexity” (arrangement, “organization”) of the activated complexes is lower than that of the starting reactants, hence the thermodynamic behavior of all complexes is endothermic ($\Delta H > 0$) and endergonic ($\Delta G > 0$), during the reactions. The thermodynamic data obtained with the two methods are in harmony with each other. The correlation coefficients of the Arrhenius plots of the thermal decomposition steps were found to lie in the range from 0.9628 to 0.9999, showing a good fit with the linear function. The thermograms and the calculated thermal parameters for the complexes show that the stability of these complexes depends on the nature of the central metal ion. The thermal stability of the metal complexes was found to increase periodically with the increase in atomic number of the metal and the larger value of charge/radius ratio [58].

Microbiological investigation of the vitamin A complexes

Antibacterial and antifungal activities of vitamin A complexes are carried out against some kinds of bacteria as *Escherichia coli* (Gram -ve) and *Staph albus* (Gram +ve), as well as some kinds of fungi as *Aspergillus niger* and *Aspergillus flavus*. The antimicrobial activity was estimated based on the size of the inhibition zone. The free vitamin A was found to have the lowest activity against the four types of bacteria and fungi, while the Zn(II) complex was found to have the highest activity. The biological activities increase in the following order: Zn(II)/Vit.A > Fe(III)/Vit.A > VO(II)/Vit.A > Mg(II)/Vit.A > Ca(II)/Vit.A. The data are listed in Table (6) and are shown in Fig. (7), the activity is verified with different metal ions containing the respective complexes, thus chelation increases lipophilic character in the complexes and results in enhancement of activity.

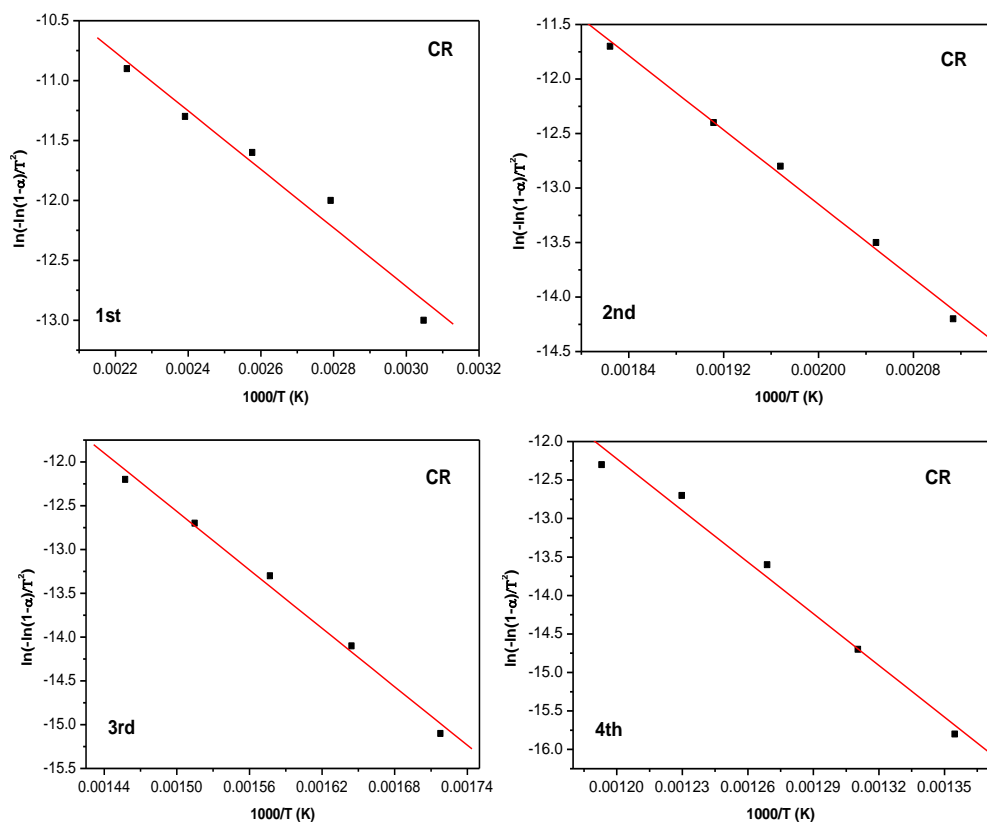


Fig. 5. Coats-Redfern (CR) plots of the first, second, third and fourth thermal decomposition steps of the Ca(II)/Vit. A complex

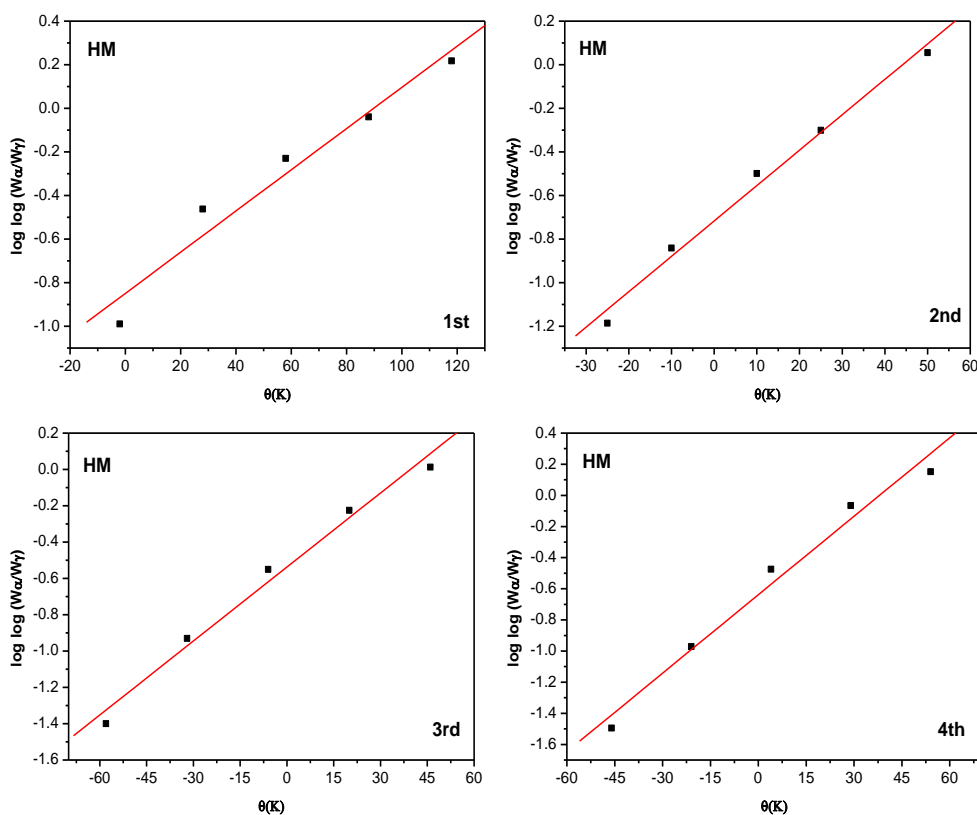


Fig. 6. Horowitz-Metzger (HM) plots of the first, second, third and fourth thermal decomposition steps of the Ca(II)/Vit. A complex

Table (5): Kinetic and thermodynamic parameters of the thermal decomposition of vitamin A complexes

Complex	Stage	Method	Parameter					R
			E (J mol ⁻¹)	A (s ⁻¹)	ΔS (J mol ⁻¹ K ⁻¹)	ΔH (J mol ⁻¹)	ΔG (J mol ⁻¹)	
Ca(II)	1 st	CR	2.03E+04	2.78E+00	-2.37E+02	1.76E+04	9.59E+04	0.98295
		HM	1.97E+04	7.18E+00	-2.29E+02	1.70E+04	9.27E+04	0.9774
	2 nd	CR	7.08E+04	1.04E+05	-1.53E+02	6.67E+04	1.43E+05	0.99746
		HM	7.72E+04	1.15E+06	-1.33E+02	7.30E+04	1.39E+05	0.99991
	3 rd	CR	9.25E+04	1.71E+05	-1.51E+02	8.72E+04	1.84E+05	0.99575
		HM	1.07E+05	3.87E+06	-1.25E+02	1.01E+05	1.81E+05	0.99241
Mg(II)	1 st	CR	1.86E+05	1.26E+10	-5.96E+01	1.80E+05	2.26E+05	0.99221
		HM	1.98E+05	1.45E+11	-3.93E+01	1.91E+05	2.22E+05	0.98946
	2 nd	CR	4.27E+04	1.08E+04	-1.69E+02	3.98E+04	9.78E+04	0.9689
		HM	4.55E+04	9.96E+04	-1.50E+02	4.27E+04	9.43E+04	0.96461
	3 rd	CR	7.86E+04	8.21E+06	-1.16E+02	7.48E+04	1.28E+05	0.99124
		HM	9.05E+04	2.84E+08	-8.67E+01	8.67E+04	1.26E+05	0.99174
Zn(II)	1 st	CR	1.59E+05	3.29E+11	-3.03E+01	1.53E+05	1.72E+05	0.99366
		HM	1.69E+05	4.96E+12	-7.78E+00	1.64E+05	1.69E+05	0.99208
	2 nd	CR	2.62E+05	8.36E+14	3.25E+01	2.56E+05	2.29E+05	0.99963
		HM	2.75E+05	7.73E+15	5.10E+01	2.68E+05	2.27E+05	0.99841
	3 rd	CR	4.41E+04	1.03E+04	-1.70E+02	4.12E+04	1.01E+05	0.9628
		HM	4.57E+04	6.08E+04	-1.55E+02	4.28E+04	9.76E+04	0.96425
Fe(III)	1 st	CR	9.46E+04	4.86E+06	-1.22E+02	8.99E+04	1.59E+05	0.99486
		HM	1.11E+05	1.80E+08	-9.22E+01	1.06E+05	1.58E+05	0.99292
	2 nd	CR	1.42E+05	4.19E+09	-6.68E+01	1.37E+05	1.78E+05	0.99044
		HM	1.47E+05	2.96E+10	-5.05E+01	1.42E+05	1.73E+05	0.98735
	3 rd	CR	2.53E+05	2.04E+14	2.07E+01	2.47E+05	2.30E+05	0.99821
		HM	2.74E+05	6.26E+15	4.92E+01	2.68E+05	2.28E+05	0.99883
VO(II)	1 st	CR	7.02E+04	1.17E+08	-9.19E+01	6.73E+04	9.97E+04	0.98551
		HM	7.26E+04	9.49E+08	-7.45E+01	6.96E+04	9.59E+04	0.97885
	2 nd	CR	8.18E+04	1.52E+07	-1.11E+02	7.80E+04	1.29E+05	0.99895
		HM	9.50E+04	8.10E+08	-7.80E+01	9.11E+04	1.27E+05	0.99717
	3 rd	CR	9.15E+04	2.52E+06	-1.28E+02	8.69E+04	1.58E+05	0.99382
		HM	1.04E+05	5.85E+07	-1.01E+02	9.95E+04	1.56E+05	0.99332
VO(II)	1 st	CR	1.22E+05	5.59E+07	-1.03E+02	1.17E+05	1.83E+05	0.99414
		HM	1.25E+05	1.58E+08	-9.43E+01	1.20E+05	1.80E+05	0.99286
	2 nd	CR	5.11E+04	2.42E+05	-1.43E+02	4.83E+04	9.68E+04	0.97166
		HM	5.21E+04	1.46E+06	-1.28E+02	4.93E+04	9.27E+04	0.9723
	3 rd	CR	9.40E+04	8.39E+06	-1.17E+02	8.95E+04	1.53E+05	0.99492
		HM	1.07E+05	2.59E+08	-8.88E+01	1.03E+05	1.50E+05	0.99333
4 th	CR	1.79E+05	1.11E+13	-1.19E+00	1.74E+05	1.74E+05	0.98955	
	HM	1.84E+05	6.20E+13	1.31E+01	1.79E+05	1.71E+05	0.98833	
4 th	CR	1.42E+05	1.24E+08	-9.74E+01	1.36E+05	2.07E+05	0.99851	
	HM	1.56E+05	1.31E+09	-7.78E+01	1.49E+05	2.06E+05	0.99856	

r = correlation coefficient of the linear plot

Table (6): Antimicrobial data of vitamin A complexes

Compound	Diameter of inhibition zone (cm)			
	<i>E. coli</i>	<i>Staph albus</i>	<i>Aspergillus niger</i>	<i>Aspergillus flavus</i>
Control	0	0	0	0
Vitamin A	0	0	0	0
Ca(II) complex	0	0	0.3	0
Mg(II) complex	0	0	0.5	0.2
Zn(II) complex	0	0.5	0.5	0.5
Fe(III) complex	0	0.2	0.4	0.4
VO(II) complex	0	0.2	0.3	0.4

Structure of the vitamin A complexes

The structures of the complexes of vitamin A with Ca(II), Mg(II), Zn(II), Fe(III) and VO(II) ions were confirmed by the elemental analysis, IR, ¹H-

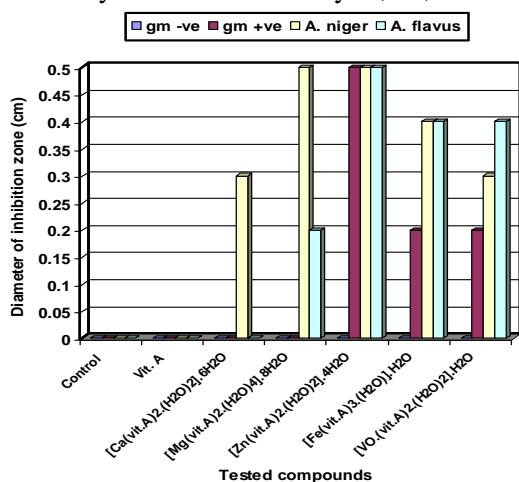


Fig. 7. Statistical representation of the biological activity of Vit. A and its complexes.

NMR, molar conductance, UV-Vis and thermal analysis data. Thus, from the IR spectra, it is concluded that vitamin A behaves as a monodentate ligand coordinated to the metal ions via the deprotonated hydroxyl oxygen atom. The structures of the investigated complexes are shown in Figs. (8-12).

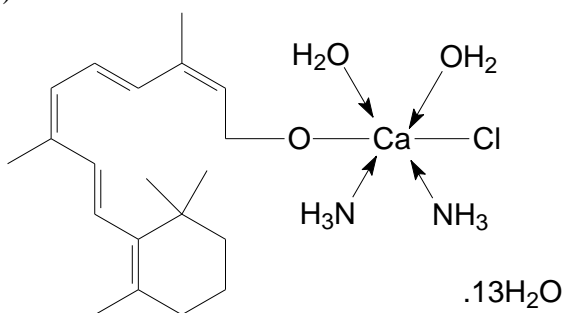


Fig. 8. Suggested structure of the Ca(II) complex of vitamin A

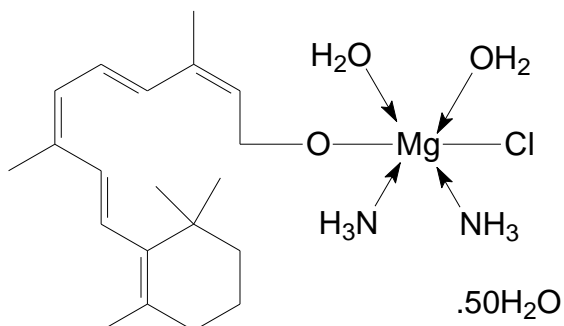


Fig. 9. Suggested structure of the Mg(II) complex of vitamin A

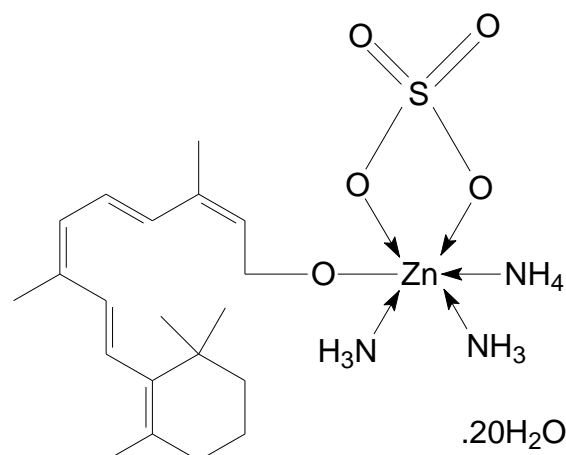


Fig. 10. Suggested structure of the Zn(II) complex of vitamin A

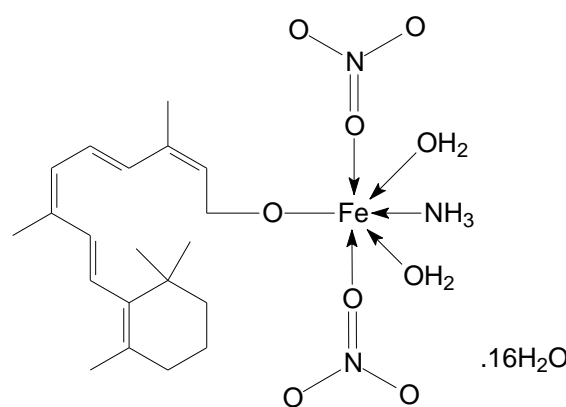


Fig. 11. Suggested structure of the Fe(III) complex of vitamin A

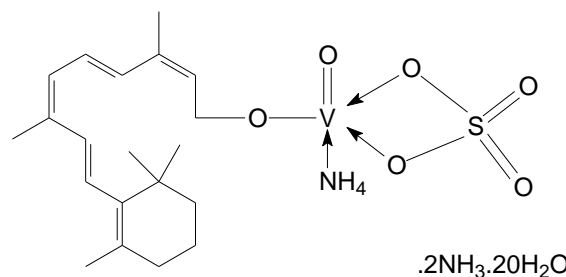


Fig. 12. Suggested structure of the VO(II) complex of vitamin A

REFERENCES

1. R. X. Yuan, R.G. Xiong, B. F. Abrahams, G.H. Lee, S.M. Peng, C. M. Che, and X. Z. You, *J. Chem. Soc. Dalton Trans*, **2071** (2001).
2. D. R. Xiao, E. B. Wang, H.Y. An, Z. M. Su, Y.G. Li, L. Gao, C.Y. Sun and L. Xu, *Chem. Eur. J.*, **11**, 6673 (2005).
3. P. Drevenšek, T. Zupancič, B. ihlar, R. Jerala, U. Kolitsch, A. Plaper, and I. Turel, *J. Inorg. Biochem.*, **99**, 432 (2005).

4. J.H. He, D. R. Xiao, H. Y. Chen, S.W. Yan, D.Z. Sun, X. Wang,, J. Yang, R. Yuan, and E. B. Wang, *Inorg. Chim. Acta*, **385**, 170 (2012).
5. L. Kathawate, S. Sproules, O. Pawar, G. Markad, S. Haram, V. Puranik, S. S. Gawali, *Journal of Molecular Structure* **1048**, 223 (2013).
6. M. Gielen, and E. R. T. Tiekink, Eds., *Metallotherapeutic Drugs and Metal-Based Diagnostic Agents, the Use of Metals in Medicine*, Wiley, Chichester, 2005.
7. Sanjay K. Bharti, Sushil K. Singh, *Metal Based Drugs: Current Use and Future Potential*, *Der Pharmacia Lettre*, 1 (2) 39-51 (2009).
8. J. E. Weder, C. T. Dillon, T. W. Hambley, B.J., Kennedy, P. A. Lay, J. R. Biffin, H. L. Regtop, and N.M. Daview, *Coord. Chem. Rev.* **232**, 95 (2002).
9. D. C. Ware, P. J. Brothers, and G. R. Clark, *J. Chem. Soc. Dalton Trans.*, **925**, (2000).
10. M. Nakai, F. C. Sekiguchi, M. Obata, C. Ohtsuki, Y. Adachi, H. Sakurai, Orvig, D. Rehder, and , S. Yano, *J. Inorg. Biochem.*, **99**, 1275 (2005).
11. T. Chaviara, P. C. Christidis, A. Papageorgiou, Chrysogelou, E., D. J. Hadjipavlou-Litina, and C. A. Bolos, *J. Inorg. Biochem.*, **99**, 2102 (2005).
12. Sadler, P.J. and Guo, Z., *Pure and Appl.Chem.*, **70**, 863 (1998).
13. R. K. Baslas, R. Zamani, and A. A., Nomani, *Experientia*, **35**, 455 (1979).
14. B. E. Gonzalez, N. N. Daeid, K. B. Nolan and E. Farkas, *Polyhedron*, **13**, 1495 (1994).
15. K. B. Nolan and A. A. Soudi, *Inorg. Chim. Acta*, **230**, 209 (1995).
16. J. G. Muller and C. J. Burrows, *Inorg. Chim. Acta*, **275**, 314 (1998).
17. A.E. Underhill, Bougourd, S. A. Flugge, M.L., Gale, S.E. and Gomm, P.S., *J. Inorg. Biochem.*, **52**, 139 (1993).
18. A. Joshua Obaleye, *Biokemistri*, **19**, 9 (2007).
19. M. Kirkova, M. Atanassova, and E. Russanov, *Gen. Pharmacol.*, **33**, 271 (1999).
20. A.M. Duda, T. Kowalik-Jankowska, H. Kozlowski, and T. Kupka, *J. Chem. Soc. Dalton Trans.*, **2909** (1995).
21. M. Kubiak, A.M., Duda, M. L. Ganadu, H. Kozlowski, *J. Chem. Soc. Dalton Trans.*, **1905**, (1996).
22. B. Umadevi, P.T. Muthiah, X. Shui and D. S. Eggleston, *Inorg. Chim. Acta*, **234**, 149 (1995).
23. R. A. Sanchez-del Grado, M. Navarro, H. Perez and J. A. Urbina, *J. Med. Chem.*, **39**, 1095 (1996).
24. N. B. Behrens, G. M. Diaz, and D. M. L. Goodgame, *Inorg. Chim. Acta.*, **125**, 21 (1986).
25. P. J.Hagrman, D. Hagrman and Zubieta, *Angew. Chem. Int. Ed.*, **38**, 2638 (1999).
26. B. M. .Moulton, J. Zaworotko, *Chem. Rev.*, **101**, 1629 (2001).
27. C. D. Wu, C. Z. Lu, H. H. Zhuang and J.S., Huang, *J. Am. Chem. Soc.*, **124**, 3836 (2002).
28. D. N. Dybtsev, H. Chun and K. Kim, *Angew. Chem. Int. Ed.*, **43**, 5033 (2004).
29. M. P. Lpez-Gresa, R., Ortiz, L. Perell, J. Latorre, M. Liu-Gonzalez, S. Garcí'a- Granda, M. Perez-Priede, E. Cantn, *J. Inorg. Biochem.*, **92**, 65 (2002).
30. I.Turel, *Coordination Chemistry Reviews*, **232**, 27 (2002).
31. D. R. Xiao, E. B. Wang, H. Y. An, Y. G. Li, and L. Xu, *Cryst. Growth Des.*, **7**, 506 (2007).
32. D. R. Xiao, J. H. D.Z., HeSun, H. Y. Chen, S. W. Yan, X. Wang, J. Yang, R. Yuan and E. B. Wang, *Eur. J. Inorg. Chem.*, **1783** (2012).
33. M. Palumbo, B. Gatto, G. Zagotto and G. Palu, *Trends. Microbiol.*, **1**, 232 (1993).
34. C. Sissi, M. Andreolli, V. Cecchetti, A. Fravolini, B. Gattoand, M. Palumbo, *Bioorg. Med. Chem.*, **6**, 1555 (1998).
35. H. E.Sauberlich, R. E. J. Hodges, D. L. Wallace, H. Kolder, J. E. Canham, Hood, et al., *Vitamin A metabolism and requirements in the human studies with the use of labeled retinal. Vitamins and Hormones-Advances on Research and Applications*, **32**, 251 (1974).
36. A. Sommer, and K. P. West, *Vitamin A Deficiency: Health, survival, and vision*. New York: Oxford University Press, 1996, p. 100.
37. A. M. Myhre, M. H. Carlsen, S. K. Bøhn, H. L. Wold, P. Laake, and R. Blomhoff, *Water-miscible, emulsified, and solid forms of retinol supplements are more toxic than oil-based preparations.*, *Am. J. Clin. Nutr.*, **78**, 1152 (2003).
38. WHO/CHD Immunisation-Linked Vitamin A Supplementation Study Group., *Randomised trial to assess benefits and safety of vitamin A supplementation linked to mmunization in early infancy. Lancet*, **352**: 1257 (1998).
39. E. S. Freeman, and B. Carroll, *J. Phys. Chem.*, **62**, 394 (1958).
40. A. W. Coats and J. P. Redfern, *Nature*, **201**, 68 (1964).
41. T. Ozawa, *Bull. Chem. Soc. Jpn.*, **38**, 1881 (1965).
42. W. W. Wendlandt, *Thermal Methods of Analysis*, Wiley, New York , 1974.
43. H. W. Horowitz, and G. Metzger, *Anal. Chem.*, **35**, 1464 (1963).
44. J. H. Flynn and L. A. Wall, *Polym. Lett.*, **4**, 323 (1966).
45. P. Kofstad, *Nature*, **179**, 1362 (1957).
46. R. Gupta, , R. K. Saxena, P. Chatarvedi and J. S. Viridi, *J. Appl. Bacteriol.*, **78**, 378 (1995).
47. M.S. Refat, *J. Mol. Struct.*, **842**, 24 (2007).
48. T., Vogel, *Textbook of Practical Organic Chemistry*. 4th Edn., John Wiley Inc., England, 1989, p. 133.
49. K. Nakamoto, *Infrared Spectra of Inorganic and Coordination Compounds*, Wiley Interscience, New York, 1970.
50. G. G. Mohamed, M. A. Zayed, F. A. Nour El-Dien, and R. G. El-Nahas, *Spectrochim. Acta Part A*, **60**, 1775 (2004).
51. A. Soliman, and W. Linert, *Thermochim. Acta*, **338**, 67 (1999).

52. S. Bhattacharyya, S. Mukhopadhyay, S. Samanta, T. J. R. Weakley and M. Chaudhury, *Inorg. Chem.*, **41**, 2433 (2002).
53. G. G. Mohamed, *Spectrochim. Acta Part A*, **57**, 1643 (2001).
54. M.A. Zayed, F. A., Nour El-Dien, G. G. Mohamed and N. E. A. El-Gamel, *Spectrochim. Acta Part A*, **60**, 2843 (2004).
55. E. Santi., M. H. Torre, E. Kremer, S. B. Etcheverry, and E. Baran, *Vib. Spectrosc.*, **5**, 285 (1993).
56. A. Trincherо, S. Bonora, A. Tinti and G. Fini, *Biopolymers*, **74**, 120 (2004).
57. T. Arumuganathan, A. Srinivasarao, T.V. Kumar, S.K. Das, *J. Chem. Sci.*, **120**, 95 (2008).
58. W. Malik, G. D. Tuli and R. D. Madan, Selected topics in inorganic chemistry, New Delhi: Chand and Co. Ltd., 1984.

СИНТЕЗ, ИЗЯСНЯВАНЕ НА ХИМИЧНИТЕ СТРУКТУРИ И БИОЛОГИЧНИ ИЗСЛЕДВАНИЯ ВЪРХУ ЕФЕКТА НА НЯКОИ ВАЖНИ МЕТАЛНИ ЙОНИ НА ВИТАМИН А: Ca (II), Mg (II), Zn (II), Fe(III) И VO(II) КОМПЛЕКСИ

М. Заки¹, М. И. Ел-Саид^{1,2}, С. М. Ел-Мегарбел^{1,3}, С. Або Талел¹, М. S. Refat^{3,4}

1 Катедра по химия, Научен факултет, Университет Загазиг, Египет

2 Факултет за приложни медицински науки, Университет Ал-Джуф-Ал Караят

3 Катедра по химия, Научен факултет, Университет Тауф, 888 Тауф, Кралство Саудитска Арабия

4 Катедра по химия, Научен факултет, Порт Сауд, Университет Порт Сауд, Египет

Получена на 22 януари 2014 г.; ревизирана на 4 април 2014 г.

(Резюме)

Комплекси на витамин А като фармацевтичен лиганд с Ca (II), Mg (II), Zn (II), Fe (III) и VO (II), бяха синтезирани и охарактеризирани с микроанализ, проводимост, инфрачервена спектроскопия и термогравиметрични (TG / DTG и DTA) измервания. Лигандът може да се координира като монодентатен лиганд чрез кислородния атом на депротонирана хидроксилна група. Кривите на термичното разграждане разкриха, че некоординираните водни молекули са премахнати в първия етап, докато разлагането на лиганда, освен координирани водни молекули, намира място при втория и следващите етапи. Витамин А като лиганд, както и неговите комплекси бяха проверени срещу някои видове бактерии и гъбички и показаха значителен ефект. Ефектът от кинетични термодинамични параметри (E^* , AH^* , ΔS^* и ΔG^*) на синтезираните комплексите върху TG кривите бяха изчислени с помощта на уравненията на Coats-Redfern and Horowitz-Metzger.

Multicomponent synthesis of bioactive 1-amidoalkyl-2-naphthols under solvent-free conditions

M. Hajjami*, A. Ghorbani-Choghamarani, F. Gholamian

Department of Chemistry, Faculty of Science, Ilam University, Ilam, Iran

Received January 26, 2014; Revised July 23, 2014

A one-pot condensation reaction of 2-naphthol, aromatic aldehydes, and acetamide or thioacetamide catalyzed by L-pyrrolidine-2-carboxylic acid-4-hydrogen sulfate (supported on silica gel) to afford 1-amidoalkyl-2-naphthols under solvent-free conditions is described. The advantages of this method are good yields, easy work-up, mild and solvent-free conditions and inexpensive catalyst.

Keywords: L-Pyrrolidine-2-carboxylic acid-4-hydrogen sulfate; Multicomponent reaction; Amidoalkyl naphthols; Solvent-free.

INTRODUCTION

Multicomponent reaction (MCR) condensations involve three or more simple substrates reacting in a single event to create structurally complex organic compounds which contain the fundamental parts of all the starting materials [1]. It is considered that multicomponent reactions approach close to the "ideal synthesis" due to atom economy, and high bond forming efficiency [2]. Therefore, chemists have made great efforts to find and develop new MCRs.

Compounds containing 1,3-amino oxygenated functional groups such as 1-amidoalkyl-2-naphthol derivatives are frequently found in a variety of biologically active natural products and potent drugs such as a number of nucleoside antibiotics and HIV protease inhibitors [3-5]. Furthermore, these compounds can be converted to important bioactive 1-aminomethyl-2-naphthols by amide hydrolysis reaction. These compounds exhibit hypotensive, bradycardia effects and Ca²⁺ channel-blocking activities in humans [6,7].

1-amidoalkyl-2-naphthols can be prepared by three-component condensation of 2-naphthol, aldehydes, and different amides in the presence of Brønsted or Lewis acidic catalysts such as PEG-based dicationic acidic ionic liquid [8], Al(HSO₄)₃ [9], Fe(HSO₄)₃ [10], H₃BO₃ [11], [TEBSA][HSO₄] [12], cation exchange resins [13], Cu-exchanged heteropoly acids [14], dodecylphosphonic acid [15], N,N,N',N'-tetrabromobenzene-1,3-disulfonamide [16], RuCl₂(PPh₃)₃ [7], H₃PW₁₂O₄₀ [17], [Bmim]Br

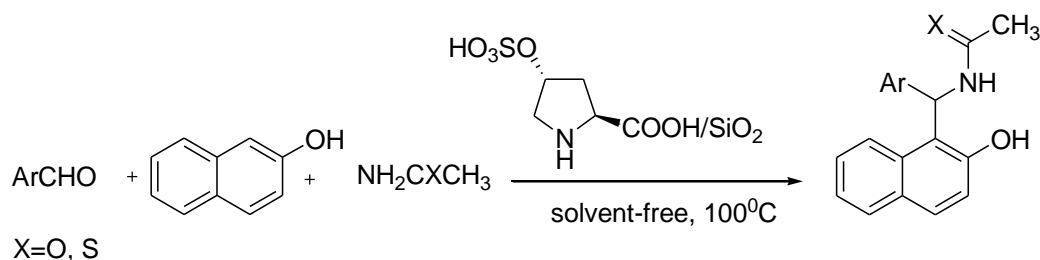
[18], [NMP]⁺HSO₄⁻ [19], molybdophosphoric acid [20], imidazolium salts [21], Cu(ClO₄)₂·6H₂O [22], tin tetrachloride [23], sulfamic acid [24], zinc benzenesulfonate [25], iodine [26], montmorillonite K10 [27], graphite supported perchloric acid [28], trityl chloride [29], MCM-41-*N*-propylsulfamic acid [30]. However, some of the reported methods suffer from disadvantages such as prolonged reaction time, low yields, use of toxic solvent, use of large amount of catalyst, strongly acidic conditions, microwave or ultrasonic irradiation and harsh reaction conditions. Therefore, finding a versatile, green and simple protocol that uses a highly efficient catalyst for preparation of amidoalkyl naphthols is still desirable.

In this paper, we report a simple and efficient procedure for one-pot synthesis of 1-amidoalkyl-2-naphthols from 2-naphthol, aromatic aldehydes and acetamide/thioacetamide in the presence of catalytic amounts of L-pyrrolidine-2-carboxylic acid-4-hydrogen sulfate (supported on silica gel) under solvent-free conditions.

RESULTS AND DISCUSSION

In continuation of our research with heterogeneous catalysts [30-34], herein we report a mild, simple and effective procedure for one-pot synthesis of 1-amidoalkyl-2-naphthol derivatives *via* a multicomponent condensation reaction between aryl aldehydes, 2-naphthol and acetamide or thioacetamide in the presence of L-pyrrolidine-2-carboxylic acid-4-hydrogen sulfate (supported on silica gel) at 100 °C (scheme 1).

* To whom all correspondence should be sent:
E-mail: mhajjami@yahoo.com



Scheme 1. Synthesis of 1-amidoalkyl-2-naphthols

In initial experiments to find the optimum conditions, a model reaction of 4-bromobenzaldehyde (1 mmol), 2-naphthol (1 mmol), and acetamide (1.6 mmol) in the presence of supported L-pyrrolidine-2-carboxylic acid-4-hydrogen sulfate on silica gel was performed under solvent-free conditions at 100 °C (Table 1). In the absence of any catalyst, the yield was low (entry 2), whereas good results were obtained in the presence of 0.1 mmol of catalyst (entry 1). In all cases the amount of the catalyst was crucial to a good yield and reaction rate. Also the scope of acetamide was studied (entry 3 and 4).

Next, to determine the effect of temperature on the reaction, the reaction of 4-bromobenzaldehyde, 2-naphthol, and acetamide in the presence of supported L-pyrrolidine-2-carboxylic acid-4-hydrogen sulfate on silica gel was performed under solvent-free conditions at different temperatures in an oil bath. As shown in table 2 the best result was achieved at 100 °C.

Table 2. Effect of temperature on the synthesis of N-[(4-bromo-phenyl)-(2-hydroxy-naphthalen-1-yl)-methyl]-acetamide in the presence of L-pyrrolidine-2-carboxylic acid-4-hydrogen sulfate (supported on silica gel) under solvent-free conditions

Entry	Temperature (C°)	Yield (%) ^b
1	25	- ^c
2	40	- ^d
3	50	34
4	60	61
5	70	70
6	80	77
7	90	81
8	100	94

^a 4-bromobenzaldehyde/2-naphthol/acetamide/catalyst = 1:1:1.6:0.1 mmol.

^b yields refer to pure isolated products. ^c No reaction. ^d Trace conversion.

In all reactions, good to excellent yields were obtained at appropriate reaction times. Clean and complete conversions leading to the corresponding 1-amidoalkyl-2-naphthols were observed. Aromatic aldehydes carrying either electron-withdrawing

(nitro) or electron-donating (halide, alkyl, alkoxy) groups were all suitable for the reactions.

The proposed mechanism for this acid catalysis condensation reaction *via in situ* generation of ortho-quinone methides (o-QMs), is presented in Scheme 2. The o-QMs have been reacted with acetamide or thioacetamide *via* conjugate addition to form 1-amidoalkyl-2-naphthols as final products.

In comparison with other catalysts employed for the synthesis of N-[(4-methyl-phenyl)-(2-hydroxy-naphthalen-1-yl)-methyl] acetamide from 4-methylbenzaldehyde, 2-naphthol and acetamide, L-pyrrolidine-2-carboxylic acid-4-hydrogen sulfate (supported on silica gel) showed significant catalytic activity in terms of good reaction time, high yield and mild conditions (table 3).

In conclusion, supported L-pyrrolidine-2-carboxylic acid-4-hydrogen sulfate on silica gel as a green and inexpensive catalyst can efficiently catalyze the synthesis of 1-amidoalkyl-2-naphthols *via* one-pot three-component reaction of 2-naphthol, acetamide/thioacetamide and aromatic aldehydes. This solvent-free procedure has advantages such as mild reaction conditions, straightforward workup and purification, excellent yields and environmental benignancy.

EXPERIMENTAL

Materials and Methods

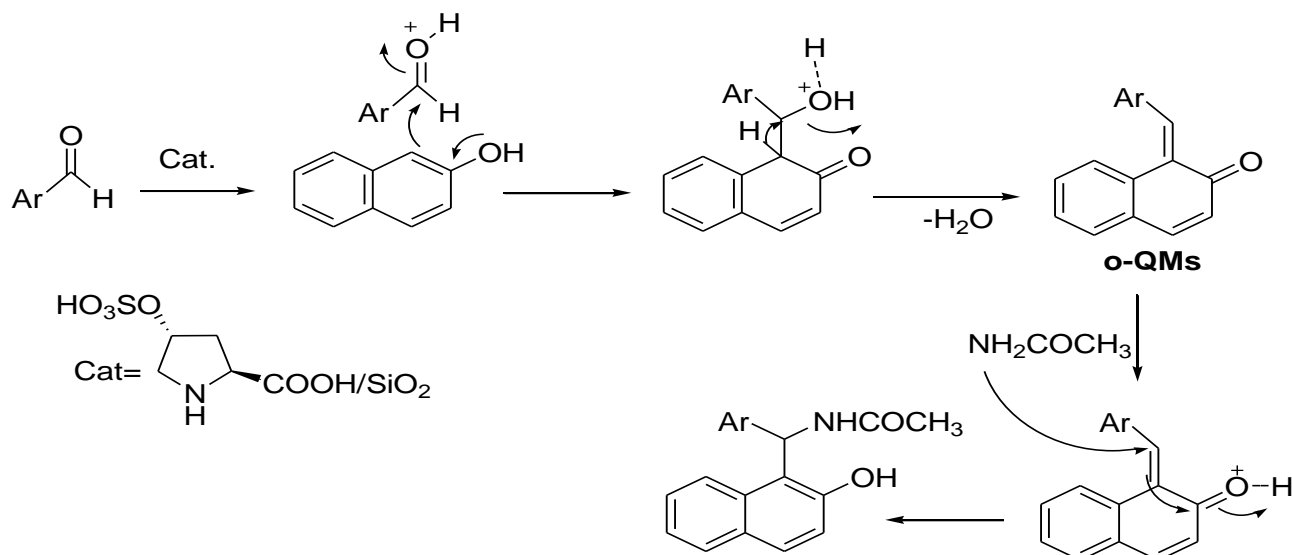
All chemicals were purchased from Fluka, Merck and Aldrich chemical companies. The products were characterized by comparison of their spectral (¹H NMR, and ¹³C NMR) and physical data with those of authentic samples.

Supported L-pyrrolidine-2-carboxylic acid-4-hydrogen sulfate on silica gel as a solid acid catalyst is safe and easy to handle catalyst. This catalyst was prepared by the reaction of L-hydroxyproline with chlorosulfonic acid at room temperature according to the reported procedure [35]. Because of the gummy properties of L-pyrrolidine-2-carboxylic acid-4-hydrogensulfate, it was supported on silica gel.

Table 1. The one-pot three-component reaction of 2-naphthol, acetamide/thioacetamide and aryl aldehydes in the presence of L-pyrrolidine-2-carboxylic acid-4-hydrogen sulfate (supported on silica gel) under solvent-free conditions at 100 °C^a

Entry	Aldehyde	amide	Time(h)	Yield(%) ^b	m.p. (lit. m.p.)	Ref.
1	4-Bromobenzaldehyde	CH ₃ CONH ₂	3	94	235.5-236.7 (229-231)	[12]
2	4-Bromobenzaldehyde	CH ₃ CONH ₂	3	22 ^{c,f}	234-236 (229-231)	[12]
3	4-Bromobenzaldehyde	CH ₃ CONH ₂	5	86 ^d	235-237 (229-231)	[12]
4	4-Bromobenzaldehyde	CH ₃ CONH ₂	5	90 ^e	235-236.5 (229-231)	[12]
5	4-Chlorobenzaldehyde	CH ₃ CONH ₂	2	90	231.5-232.9 (229-230)	[12]
6	4-Flourobenzaldehyde	CH ₃ CONH ₂	6	84	223-224 (230-232)	[9]
7	3-Nitrobenzaldehyde	CH ₃ CONH ₂	1.75	95	241-243 (241-242)	[8]
8	2-Nitrobenzaldehyde	CH ₃ CONH ₂	1.66	91	215-216 (218-219)	[36]
9	4-Methylbenzaldehyde	CH ₃ CONH ₂	2	93	220-221 (221-223)	[8]
10	4-Methoxybenzaldehyde	CH ₃ CONH ₂	5.5	91	182-183 (181-183)	[8]
11	2-Naphthaldehyde	CH ₃ CONH ₂	2.6	94	218-220 (220-222)	[11]
12	4-Hydroxybenzaldehyde	CH ₃ CONH ₂	4	92	224.5-225.5	-
13	5-Bromo-2-hydroxybenzaldehyde	CH ₃ CONH ₂	6	95	212.5-213	-
14	4-Bromobenzaldehyde	CH ₃ CSNH ₂	7	83	214.5-215.5	-
15	4-Chlorobenzaldehyde	CH ₃ CSNH ₂	5.5	89	214-215	-
16	3-Nitrobenzaldehyde	CH ₃ CSNH ₂	6	83	231-232	-
17	4-Methylbenzaldehyde	CH ₃ CSNH ₂	6	84	199-201	-
18	5-Bromo-2-hydroxybenzaldehyde	CH ₃ CSNH ₂	7	45 ^f	216.5-217.5	-

^areaction conditions: aldehyde/2-naphthol/acetamide or thioacetamide/catalyst= 1:1:1.6:0.1 mmol. ^byields refer to pure isolated products. ^c reaction is performed in the absence of catalyst. ^d amount of acetamide was 1.2 mmol. ^e amount of acetamide was 1.4 mmol. ^f yield determined by preparative TLC.



Scheme 2. Plausible mechanism of the one-pot synthesis of 1-amidoalkyl-2 naphthols -

Table 3. Comparative results of L-pyrrolidine-2-carboxylic acid-4-hydrogen sulfate (supported on silica gel) with other catalysts for the synthesis of N-[(4-methyl-phenyl)-(2-hydroxy-naphthalen-1-yl)-methyl]-acetamide

Entry	Catalyst (mol %)	Time (h)	Yield (%)	Ref.
1	Molybdophosphoric acid (0.12 g)	4	92	[20]
2	Al(HSO ₄) ₃ (0.05 g)	9 min	83	[9]
3	Graphite-HClO ₄ (7.5)	2	74	[28]
4	Polymer-supported sulphonic acid (0.17 g)	4	92	[37]
5	Cu-exchanged heteropoly acids (5)	1.5	85	[14]
6	MCM-41-N-propylsulfamic acid (0.1 g)	3	95	[30]
7	L-pyrrolidine-2-carboxylic acid-4-hydrogen sulfate (0.0423 g)	2	93	This work

General procedure: solvent-free synthesis of 1-amidoalkyl-2-naphthols using supported L-pyrrolidine-2-carboxylic acid-4-hydrogen sulfate on silica gel as catalyst at 100 °C

In a typical reaction, to a mixture of 2-naphthol (1 mmol), aldehydes (1 mmol) and acetamide/thioacetamide (1.6 mmol), catalyst (0.1 mmol, 0.0423 g) was added. The mixture was stirred at 100 °C in an oil bath as indicated by thin-layer chromatography (TLC) for a complete reaction. After completion of the reaction, the mixture was cooled to room temperature, then the solid residue was dissolved in boiling EtOH and the mixture was stirred for 10 min. The pure product was obtained by recrystallization from water and ethanol (50:50).

The spectral data of some representative amidoalkyl naphthols are given below:

N-[(5-bromo-2-hydroxy-phenyl)-(2-hydroxy-naphthalen-1-yl)-methyl]-acetamide (Table 1,

Entry 13) ¹H NMR (400 MHz, DMSO-d₆): δ_H = 1.92 (s, 3H), 6.66 (d, *J* = 8.8, 1H), 7.13-7.20 (m, 3H), 7.28 (m, 1H), 7.44 (m, 1H), 7.60 (s, 1H), 7.71 (d, *J* = 8.8, 1H), 7.78 (d, *J* = 8, 1H), 8.20 (d, *J* = 8.4, 1H), 8.45 (d, *J* = 8.4, 1H), 9.73-9.90 (br, 2H) (ppm). ¹H-NMR (400 MHz, DMSO+ D₂O): δ_H = 1.89 (s, 3H), 6.69 (d, *J* = 8.8, 1H), 7.11-7.18 (m, 3H), 7.26 (m, 1H), 7.39-7.42 (m, 1H), 7.47 (s, 1H), 7.70 (d, *J* = 8.8, 1H), 7.76 (d, *J* = 7.6, 1H), 8.10 (d, *J* = 8.4, 1H) (ppm). ¹³C-NMR (100 MHz, DMSO): δ_C = 23.1, 44.9, 110, 117.4, 119, 119.1, 122.7, 123.7, 126.5, 128.6, 128.8, 129.3, 130.3, 131.7, 131.8, 133.1, 153.7, 154.3, 169 (ppm).

N-[(4-bromo-phenyl)-(2-hydroxy-naphthalen-1-yl)-methyl]-acetamide (Table 1, Entry 1) ¹H NMR (400 MHz, DMSO-d₆): δ_H = 2 (s, 3H), 7.10 (m, 3H), 7.23-7.30 (m, 2H), 7.38 (d, *J* = 8, 1H), 7.45 (d, *J* = 8.4, 2H), 7.80 (m, 3H), 8.49 (d, *J* = 8, 1H), 10.07 (s, 1H) (ppm). ¹H-NMR (400 MHz, DMSO+ D₂O): δ_H = 1.98 (s, 3H), 7.07 (m, 3H), 7.20 (d, *J* = 8.8, 1H), 7.26 (m, 1H), 7.38 (m, 3H), 7.77 (m, 3H) (ppm).

N-[(4-chloro-phenyl)-(2-hydroxy-naphthalen-1-yl)-methyl]-acetamide (Table 1, Entry 5) ¹H NMR (400 MHz, DMSO-d₆): δ_H= 2 (s, 3H), 7.10 (d, *J* = 8, 1H), 7.17 (d, *J* = 8.4, 2H), 7.23 (d, *J* = 8.8, 1H), 7.26-7.33 (m, 3H), 7.39 (m, 1H), 7.78-7.83 (m, 3H), 8.48 (d, *J* = 8, 1H), 10.06 (s, 1H) (ppm). ¹³C-NMR (100 MHz, DMSO): δ_C= 23.1, 56.6, 118.9, 119, 123, 123.6, 127, 128.4, 128.9, 129.1, 130, 131.1, 132.7, 142.3, 153.7, 170 (ppm).

N-[(4-fluoro-phenyl)-(2-hydroxy-naphthalen-1-yl)-methyl]-acetamide (Table 1, Entry 6) ¹H NMR (400 MHz, DMSO-d₆): δ_H= 2 (s, 3H), 7.06-7.12 (m, 3H), 7.17-7.3 (m, 4H), 7.39 (m, 1H), 7.77-7.83 (m, 3H), 8.49 (d, *J* = 8.4, 1H), 10.05 (s, 1H) (ppm). ¹³C-NMR (100 MHz, DMSO-d₆): δ_C= 22.6, 47.33, 114.51, 118.2, 122.41, 122.8, 126.38, 128.0, 128.55, 129.54, 132.19, 138.6, 153.12, 159.48, 161.88, 169.26 (ppm)

N-[(3-nitro-phenyl)-(2-hydroxy-naphthalen-1-yl)-methyl]-acetamide (Table 1, Entry 7) ¹H NMR (400 MHz, DMSO-d₆): δ_H= 2.04 (s, 3H), 7.27 (m, 3H), 7.43 (t, *J* = 7.2, 1H), 7.57 (m, 2H), 7.86 (m, 3H), 8.03 (s, 1H) 8.06 (m, 1H), 8.65 (d, *J* = 8, 1H), 10.17 (s, 1H) (ppm). ¹³C-NMR (100 MHz, DMSO): δ_C= 23, 48.1, 118.3, 118.9, 120.9, 121.7, 123.1, 123.3, 127.3, 128.9, 129.2, 130.1, 130.4, 132.6, 133.3, 145.9, 148.2, 153.8, 170.2 (ppm).

N-[(4-methyl-phenyl)-(2-hydroxy-naphthalen-1-yl)-methyl]-acetamide (Table 1, Entry 9) ¹H-NMR (400 MHz, DMSO-d₆): δ_H= 1.99 (s, 3H), 2.24 (s, 3H), 7.1 (s, 1H), 7.23 (d, 1H), 7.24 (d, 4H), 7.26 (m, 1H), 7.75 (m, 1H), 7.78 (d, 1H), 7.79 (d, 1H), 7.82 (d, 1H), 8.44 (s, 1H), 9.98 (s, 1H) (ppm) ¹³C-NMR (100 MHz, DMSO-d₆): δ_C= 47.61, 118.46, 118.98, 122.32, 125.97, 126.21, 129.1, 128.51, 132.3, 134.9, 139.55, 153.07, 169.14 (ppm)

N-[(5-bromo-2-hydroxy-phenyl)-(2-hydroxy-naphthalen-1-yl)-methyl]-thioacetamide (Table 1, Entry 18) ¹H NMR (400 MHz, DMSO-d₆): δ_H= 1.92 (s, 3H), 6.66 (d, *J* = 8.8, 1H), 7.12-7.20 (m, 3H), 7.27 (m, *J* = 14.8, 1H), 7.44 (m, *J* = 14.8, 1H), 7.60 (s, 1H), 7.71 (d, *J* = 8.8, 1H), 7.78 (d, *J* = 8, 1H), 8.20 (d, *J* = 8.8, 1H), 8.44 (d, *J* = 8.4, 1H), 9.70 (s, 1H), 9.91 (s, 1H) (ppm). ¹H-NMR (400 MHz, DMSO+ D₂O): δ_H= 1.88 (s, 3H), 6.68 (d, *J* = 8.8, 1H), 7.10-7.18 (m, 3H), 7.27 (m, 1H), 7.39- 7.46 (m, 2H), 7.71 (d, *J* = 8.8, 1H), 7.76 (d, *J* = 8, 1H), 8.10 (d, *J* = 8.8, 1H) (ppm). ¹³C-NMR(100 MHz, DMSO): δ_C= 23.1, 44.9, 110, 117.4, 119, 119.1, 122.7, 123.7, 126.5, 128.6, 128.8, 129.3, 130.3, 131.7, 131.8, 133.1, 153.7, 154.3, 169 (ppm).

N-[(4-bromo-phenyl)-(2-hydroxy-naphthalen-1-yl)-methyl]-thioacetamide (Table 1, Entry 14) ¹H NMR (400 MHz, DMSO-d₆): δ_H= 2 (s, 3H), 7.10 (m, 3H), 7.23-7.30 (m, 2H), 7.38 (d, *J* = 7.6, 1H),

7.45-7.47 (m, 2H), 7.80 (m, 3H), 8.49 (d, *J* = 8.4, 1H), 10.07 (s, 1H) (ppm). ¹H-NMR (400MHz, DMSO+ D₂O): δ_H= 1.98 (s, 3H), 7.1-7.6 (m, 3H), 7.21 (m, 1H), 7.24-7.28 (m, 1H), 7.39-7.43 (m, 3H), 7.76- 7.80(m, 3H) (ppm). ¹³C-NMR (100 MHz, DMSO): δ_C= 23.1, 47.9, 118.8, 118.9, 119.5, 123, 123.7, 127, 128.8, 129, 129.1, 130, 131.3, 132.7, 142.7, 153.7, 170(ppm).

N-[(3-nitro-phenyl)-(2-hydroxy-naphthalen-1-yl)-methyl]-thioacetamide (Table 1, Entry 14) ¹H NMR (400 MHz, DMSO-d₆): δ_H = 2.04 (s, 3H), 7.19-7.25 (m, 2H), 7.31 (m, 1H), 7.43 (m, 1H), 7.55-7.60 (m, 2H), 7.82-7.86 (m, 4H), 8.03-8.08 (m, 2H), 8.65 (d, *J* = 8, 1H), 10.16 (s, 1H) (ppm). ¹H-NMR (400 MHz, DMSO+D₂O): δ_H= 2.01 (s, 3H), 7.15 (s, 1H), 7.2 (d, *J* = 8.8, 1H), 7.3 (m, 1H), 7.42 (m, 1H), 7.54 (m, 1H), 7.6 (d, *J* = 8, 1H), 7.79- 7.87 (m, 2H), 7.9 (s, 1H), 8.02-8.04 (m, 1H) (ppm). ¹³C-NMR(100 MHz, DMSO): δ_C= 23, 48, 118.3, 118.9, 120.9, 121.7, 123.1, 123.3, 127.2, 128.9, 129.2, 130.1, 130.4, 132.6, 133.3, 145.9, 148.2, 153.8, 170.2 (ppm).

Acknowledgment: Financial support for this work by the Ilam University, Ilam, Iran is gratefully acknowledged.

REFERENCES

1. Y. Rubin, S. S. Lin, C. B. Knobler, J. Anthony, A. M. Boldi, F. Diederich, *J. Am. Chem. Soc.*, **113**, 6943 (1991).
2. V. A. Chebanov, S. M. Desenko, *Chem. Heterocycl. Compd.*, **48**, 566 (2012).
3. Y. -F. Wang, T. Izawa, S. Kobayashi, M. Ohno, *J. Am. Chem. Soc.*, **104**, 6465 (1982).
4. D. Seebach, J. L. Matthews, *Chem. Commun.*, **2015**, (1997).
5. A. Y. Shen, C. L. Chen, C. I. Lin, *Chinese. J. Physiol.*, **35**, 45 (1992).
6. A. Y. Shen, C.T. Tsai, C. L. Chen, *Eur. J. Med. Chem.*, **34**, 877 (1999).
7. X. Zhu, Y. R. Lee, S. H. Kim, *Bull. Korean Chem. Soc.*, **33**, 2799 (2012).
8. J. Luo, Q. Zhang, *Monatsh. Chem.*, 142, 923 (2011).
9. H. R. Shaterian, M. Ghashang, M. Asadi, N. Tajbakhsh Riki, *J. Iran. Chem. Soc.*, **9**, 1 (2012).
10. H. R. Shaterian, H. Yarahmadi, M. Ghashang, *Bioorg. Med. Chem. Lett.*, **18**, 788 (2008).
11. A. Shahrisa, S. Esmati, M. Gholamhosseini Nazari, *J. Chem. Sci.*, **124**, 927 (2012).
12. A. R. Hajipour, Y. Ghayeb, N. Sheikhan, A. E. Ruoho, *Tetrahedron Lett.*, **50**, 5649 (2009).
13. S. B. Patil, P. R. Singh, M. P. Surpur, S. D. Samant, *Synth. Commun.*, **37**, 1659 (2007).
14. H. Khabazzadeh, K. Saidi, N. Seyedi, *J. Chem. Sci.*, **121**, 429 (2009).
15. M. Zandi, A. R. Sardarian, *C. R. Chimie*, **15**, 365 (2012).

16. R. Ghorbani-Vaghei, S. M. Malaekhepour, *Cent. Eur. J. Chem.*, **8**, 1086 (2010).
17. A. Dorehgiraei, H. Khabazzadeh, K. Saidi, *Arkivoc*, (vii), **303** (2009).
18. A. Zare, A. Hasaninejad, A. Salimi Beni, A. R. Moosavi-Zare, M. Merajoddina, E. Kamalia, M. Akbari-Seddigh, Z. Parsaee, *Sci. Iran.*, **18**, 433 (2011).
19. K. M. Deshmukh, Z. S. Qureshi, Y. P. Patil, B. M. Bhanage, *Syn. Commun.*, **42**, 93 (2012).
20. J. Wen-Qing, A. Li-Tao, Z. Jian-Ping, *Chin. J. Chem.*, **26**, 1697 (2008).
21. M. A. Zolfigol, A. Khazaei, A. R. Moosavi-Zare, A. Zare, V. Khakyzadeh, *Appl. Catal. A: Gen.*, **400**, 70 (2011).
22. S. Puri, B. Kaur, A. Parmar, H. Kumar, *Org. Prep. Proced. Int.*, **44**, 91 (2012).
23. M. Wang, Y. Liang, T. T. Zhang, J. J. Gao, *Chem. Nat. Compd.*, **48**, 185 (2012).
24. S. B. Patil, P. R. Singh, M. P. Surpur, S. D. Samant, *Ultrason. Sonochem.*, **14**, 515 (2007).
25. M. Wang, Z. G. Song, Y. Liang, *Synth. Commun.*, **42**, 582 (2012).
26. B. Das, K. Laxminarayana, B. Ravikanth, B. R. Rao, *J. Mol. A. Catal. Chem.*, **261**, 180 (2007).
27. S. Kantevari, S. V. N. Vuppapapati, L. Nagarapu, *Catal. Commun.*, **8**, 1857 (2007).
28. Z.-K. Lei, L. Xiao, X.-Q. Lu, H. Huang, C.-J. Liu, *Molecules*, **18**, 1653 (2013).
29. A. Khazaei, M. A. Zolfigol, A. R. Moosavi-zare, F. Abi, A. Zare, H. Kaveh, V. Khakyzadeh, M. Kazem-Rostami, A. Parhami, H. Torabi-Monfared, *Tetrahedron*, **69**, 212(2013).
30. M. Hajjami, F. Ghorbani, F. Bakhti, *Appl. Catal. A: Gen.*, **470**, 303 (2014).
31. A. Ghorbani-Choghamarani, M. A. Zolfigol, M. Hajjami, K. Darvishi, L. Gholamnia, *Collect. Czech. Chem. Commun.*, **75**, 607 (2010).
32. A. Ghorbani-Choghamarani, M. Hajjami, H. Goudarziafshar, M. Nikoorazm, S. Mallakpour, F. Sadeghizadeh, G. Azadi, *Monatsh. Chem.*, **140**, 607 (2009).
33. A. Ghorbani-Choghamarani, P. Zamani, *J. Iran. Chem. Soc.*, **8**, 142 (2011).
34. A. Ghorbani-Choghamarani, M. A. Zolfigol, R. Ayazi-nasrabadi, *J. Braz. Chem. Soc.*, **21**, 33 (2010).
35. A. Ghorbani-Choghamarani, P. Zamani, *J. Iran. Chem. Soc.*, **9**, 607 (2012).
36. G. C. Nandi, S. Samai, R. Kumar, M. Singh, *Tetrahedron Lett.*, **50**, 7220 (2009).
37. L.-T. An, X.-H. Lu, F.-Q. Ding, W.-Q. Jiang, J.-P. Zou, *Chin. J. Chem.*, **26**, 2117 (2008).

МНОГОКОМПОНЕНТНА СИСТЕМА НА БИОАКТИВНИ 1-АМИДОАЛКИЛ-2-НАФТОЛИ В ОТСЪСТВИЕ НА РАЗТВОРИТЕЛ

М. Хаджджами*, А. Горбани-Чогамарани, Ф. Голамиан

Департамент по химия, Научен факултет, Университет „Илам“, Иран

Постъпила на 26 януари, 2014 г.; коригирана на 23 юли, 2014 г.

(Резюме)

Описана е едностадийна реакция на кондензация на 2-нафтол, ароматни алдехиди с ацетамид или тиацетамид, катализирана от L-пиролидин-2-карбоксилска киселина-4-хидроген сулфат (нанесен върху силикагел) за получаването на 1-амидоалкил-2-нафтоли в отсъствие на разтворител. Предимствата на метода са добрите добиви, лесното изпълнение, меките условия, отсъствието на разтворител и евтиния катализатор.

Solution thermodynamics and solubility of indomethacin in ethanol-water mixtures in the temperature range from 293.15 to 318.15 K

F. Shakeel^{1,2*}, F. K. Alanazi^{1,2}, I. A. Alsarra^{1,2}, N. Haq^{1,2}

¹Center of Excellence in Biotechnology Research, King Saud University, Riyadh, Saudi Arabia

²Kayyali Chair for Pharmaceutical Industry, Department of Pharmaceutics, College of Pharmacy, King Saud University, Riyadh, Saudi Arabia

Received January 26, 2014; Revised March 1, 2014

The aim of this study was to correlate the solubility of indomethacin (IND) in pure solvents and various ethanol-water mixtures in the temperature range from 293.15 to 318.15 K. The solubility of IND was determined by the shake flask method and resulting data correlated with the modified Apelblat equation. The experimental data of IND were found to correlate well with the modified Apelblat model. The solubility of IND was found to increase with increasing temperature in pure solvents, as well as in ethanol-water mixtures. The mole fraction solubility of IND was highest in pure ethanol (2.50×10^{-3} at 298.15 K) as compared to pure water (4.48×10^{-8} at 298.15 K) at each temperature. The values of enthalpy and entropy indicated that the dissolution of IND is an endothermic and entropy-driven process.

Keywords: Ethanol, indomethacin, mole fraction solubility, thermodynamics, modified Apelblat model.

INTRODUCTION

Indomethacin (IND) is an indole derivative: 1-(4-chlorobenzoyl)-5-methoxy-2-methyl-3-indoleacetic acid and its molecular structure is presented in Figure 1 (molecular formula $C_{19}H_{16}ClNO_4$, molecular weight 357.79 g/mol, CAS registry number 53-86-1) [1].

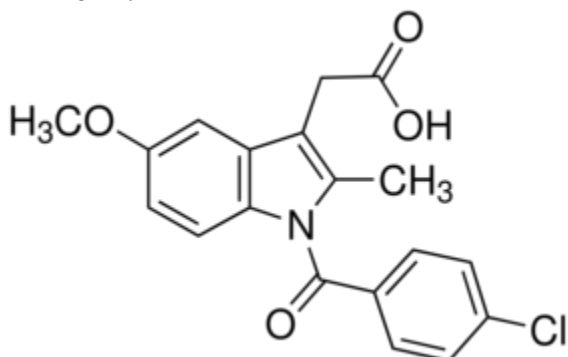


Fig. 1. Molecular structure of indomethacin

It has several pharmacological activities such as anti-inflammatory, analgesic & antipyretic and is commercially available in the form of tablets/capsules, gels and injections [1-4]. It is considered as a practically insoluble drug according to several pharmacopoeias, which is the main obstacle for the formulation development of IND especially for parenteral/liquid dosage forms [1-10]. Therefore, physicochemical data of drugs such as solubility, partition coefficient, dissolution, volume of solvents and other components in the solution are very important for

facilitating formulation/drug development processes [4-7]. The solubility data of drugs in water-cosolvent mixtures have significant importance because they are frequently used in drug release/dissolution studies, drug permeation studies, drug purification, drug crystallization, preformulation studies and formulation/drug development [10-13]. Although various mathematical models/equations have been reported in the literature for calculation of solubility of drugs, no temperature dependent solubility data of drugs could be obtained using all these models [3-19]. Therefore, it is important to determine temperature dependent solubility data of drugs in order to get complete information about their physicochemical data [7]. Ethanol is a commonly used cosolvent in preformulation studies and formulation development process of several poorly soluble drugs due to its nontoxicity, good solubilizing capacity, cost effectiveness, etc. [20]. The modified Apelblat model is the most accurate one and is applied for both polar and nonpolar systems to make correlation between experimental and calculated solubility data [21]. Therefore, the aim of this study was to determine the mole fraction solubility of IND in pure solvents (distilled water and ethanol), as well as in ethanol-water mixtures in order to make correlation between experimental data and the modified Apelblat model in the temperature range from 293.15 to 318.15 K. These preliminary studies on IND solubility could be useful in drug dissolution/permeation studies, purification, preformulation studies and formulation development of IND.

* To whom all correspondence should be sent:
E-mail: faiyazs@fastmail.fm

Table 1 General properties of the materials used in the experiment

Materials	Molecular formula	M.W. (g/mol)	D (g/ml)	Purity (%)	CAS No.
Indomethacin	C ₁₉ H ₁₆ ClNO ₄	357.790	1.320	99.20	53-86-1
Ethanol	C ₂ H ₅ OH	46.068	0.789	99.90	64-17-5
Water	H ₂ O	18.015	1.000	100	7732-18-5

EXPERIMENTAL

Materials

IND (purity 99.20%) was obtained as a gift sample from Alfa Aesar (Ward Hill, MA). Ethanol (purity 99.9%) was purchased from Sigma Aldrich (St. Louis, MO). Distilled water was obtained from a distillation unit. All other chemicals and reagents used were of analytical reagent (AR) grade. The general properties of all materials used in the present study are listed in Table 1.

Measurement of IND solubility

The saturated solubility of IND in pure solvents (distilled water and ethanol) and ethanol-water mixtures (mass fraction [w] from 0.1 to 0.9) was determined by a previously reported shake flask method at atmospheric pressure in the temperature range from 293.15 to 318.15 K [4]. An excess amount of IND was added to 25 g of distilled water, ethanol and ethanol-water mixtures in 50 ml capacity conical flasks in triplicate. Each solid-liquid mixture after proper mixing was kept in an isothermal mechanical shaker bath (Julabo, PA) at a shaking speed of 100 rpm for 72 h to reach equilibrium (shorter and longer time studies were performed and optimum time was observed to be 72 h to reach equilibrium). After 72 h, all samples were removed from the shaker and allowed to

settle the drug particles for 2 h at the bottom of conical flasks. The samples were filtered through 0.45 μm filter paper, the supernatant from each sample was taken and properly diluted with the respective solvent and subjected for analysis of the IND content

spectrophotometrically at 318 nm [2]. The standard uncertainty for the temperatures u(T) was found to be ± 0.20 K. However, the standard uncertainty in solubilities u_r(x_e) was 1.52 %. The experimental mole fraction solubility (x_e) of IND in each sample was calculated using the reported equation 1 [22]:

$$x_e = \frac{m_1/M_1}{m_1/M_1 + m_2/M_2 + m_3/M_3 \dots \dots \dots (1)}$$

where m₁ is the mass of IND (solute) and m₂ and m₃ are the masses of ethanol and distilled water, respectively. M₁ represents the molecular mass of IND; M₂ and M₃ represent the molecular masses of ethanol and distilled water, respectively.

RESULTS AND DISCUSSION

Solubility data of IND

The mole fraction solubility data of IND in neat solvents (distilled water and ethanol) and ethanol-water mixtures in the temperature range from 293.15 to 318.15 K are listed in Table 2.

Table 2 Mole fraction solubility (x_e) of indomethacin in various ethanol-water mixtures in the temperature range from 298.15 to 318.15 K^a

w	10 ³ x _e					
	293.15	298.15	303.15	308.15	313.15	318.15
0.0	4.48 × 10 ⁻⁵	4.73 × 10 ⁻⁵	5.04 × 10 ⁻⁵	5.29 × 10 ⁻⁵	4.54 × 10 ⁻⁵	5.84 × 10 ⁻⁵
0.1	6.43 × 10 ⁻⁴	8.58 × 10 ⁻⁴	1.12 × 10 ⁻³	1.44 × 10 ⁻³	1.87 × 10 ⁻³	2.35 × 10 ⁻³
0.2	2.06 × 10 ⁻³	2.40 × 10 ⁻³	2.98 × 10 ⁻³	3.61 × 10 ⁻³	4.35 × 10 ⁻³	5.10 × 10 ⁻³
0.3	7.39 × 10 ⁻³	8.00 × 10 ⁻³	8.74 × 10 ⁻³	9.48 × 10 ⁻³	1.02 × 10 ⁻²	1.10 × 10 ⁻²
0.4	7.65 × 10 ⁻²	8.65 × 10 ⁻²	9.98 × 10 ⁻²	0.11	0.12	0.13
0.5	0.18	0.21	0.26	0.31	0.36	0.42
0.6	0.26	0.33	0.42	0.53	0.63	0.75
0.7	0.42	0.49	0.56	0.64	0.74	0.85
0.8	0.82	0.88	0.98	1.07	1.17	1.27
0.9	1.66	2.05	2.55	3.11	3.66	4.32
1.0	2.50	3.32	4.26	5.50	6.96	8.87

^aThe relative standard uncertainty for temperature was ± 0.20 K, the uncertainty for solubility was 1.52 % and measurements were recorded at a pressure of 0.1 MPa, mass fraction of ethanol in cosolvent mixtures (w), experimental solubility of indomethacin (x_e), relative deviation between experimental and calculated solubility using Apelblat equation was 0.01-5.57 %.

The solubility of IND was found to increase exponentially with the increase in temperature in pure solvents, as well as in ethanol-water mixtures. The mole fraction solubility of IND was highest in pure ethanol ($w = 1.0$) and lowest in distilled water ($w = 0.0$) at each temperature studied. The mole fraction solubility of IND in pure ethanol was 2.50×10^{-3} at 298.15 K as compared to 4.48×10^{-8} in distilled water (Table 2), i.e., it was significantly higher in ethanol than in water. The effect of mass fraction of ethanol on the mole fraction solubility in the temperature range from 293.15 to 318.15 K is presented in Figure 2.

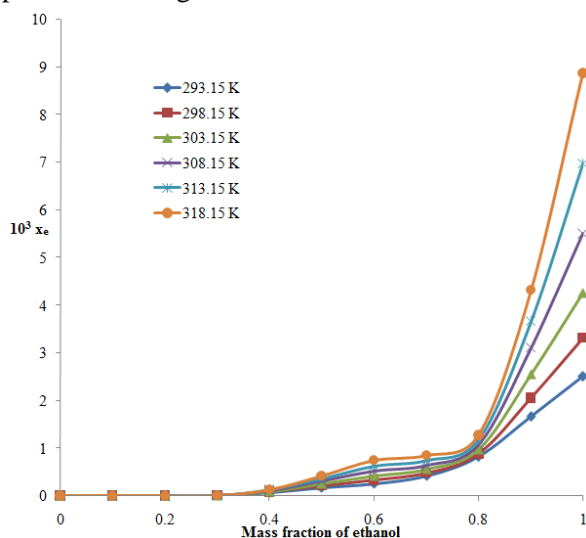


Fig. 2. Impact of mass fraction of ethanol on experimental mole fraction solubility (x_e) of indomethacin at 293.15 - 318.15 K

The mole fraction solubility of IND was found to increase with the increase in mass fraction of ethanol at each temperature studied. It is well known that water is of higher polarity than ethanol because the dielectric constant of water at 298.15 K is 78.36 as compared to 24.30 of ethanol [23]. It has also been reported that the solubility of the solute could be increased by decreasing the polarity of solvents or solvent mixtures [24, 25]. Our results were in good agreement with previous reports of polarities. Moreover, the solubility of IND in ethanol-water mixtures increased by increasing the mass fraction of ethanol that could be due to reduced polarity of the ethanol-water mixtures [23-25]. Therefore, we can conclude that the mole fraction solubility could depend on several factors such as dielectric constant, molecular structure and

molecular masses of the solutes and solvents. These results were in agreement with recently published temperature dependent solubility data of paracetamol and risperidone in Transcutol-water cosolvent mixtures [26, 27]. Based on these results, IND could be considered as soluble in ethanol and practically insoluble in distilled water. In the literature, IND has also been reported as practically insoluble in water and soluble in ethanol [3, 4]. The results of the current study are in agreement with previously published solubility reports [4]. Therefore, ethanol could be utilized as a physiologically compatible cosolvent in preformulation studies and formulation development of IND.

Thermodynamic modeling of IND solubility

As mentioned in the introduction, many equations/models have been used to correlate experimental solubility data with theoretical mole fraction solubility. The modified Apelblat model is the most accurate one and is applied for both polar and nonpolar systems; therefore it was selected in our study to correlate experimental data with calculated solubility data [21, 22, 28]. The temperature-dependent mole fraction solubility of IND can be represented by equation 2 to describe the solid-liquid equilibrium according to the modified Apelblat equation [29]:

$$\ln x_e = A + \frac{B}{T} + C \ln(T) \dots\dots\dots(2)$$

where, x_e is the experimental mole fraction solubility, T is the absolute temperature (K), parameters A , B and C are adjustable equation parameters. Parameters A , B and C were determined by multivariate regression analysis of the experimental data using equation 2. The modified Apelblat solubilities (x_{mAc}) were calculated using the equation parameters A , B and C . The modified Apelblat solubilities were correlated with experimental solubilities of IND and the percentage of absolute relative deviation (% AD) was calculated using equation 3. The correlations between experimental and calculated solubility of IND in various ethanol-water mixtures are presented in Figure 3.

$$AD (\%) = \frac{(x_e - x_c)}{x_e} \times 100 \dots\dots\dots(3)$$

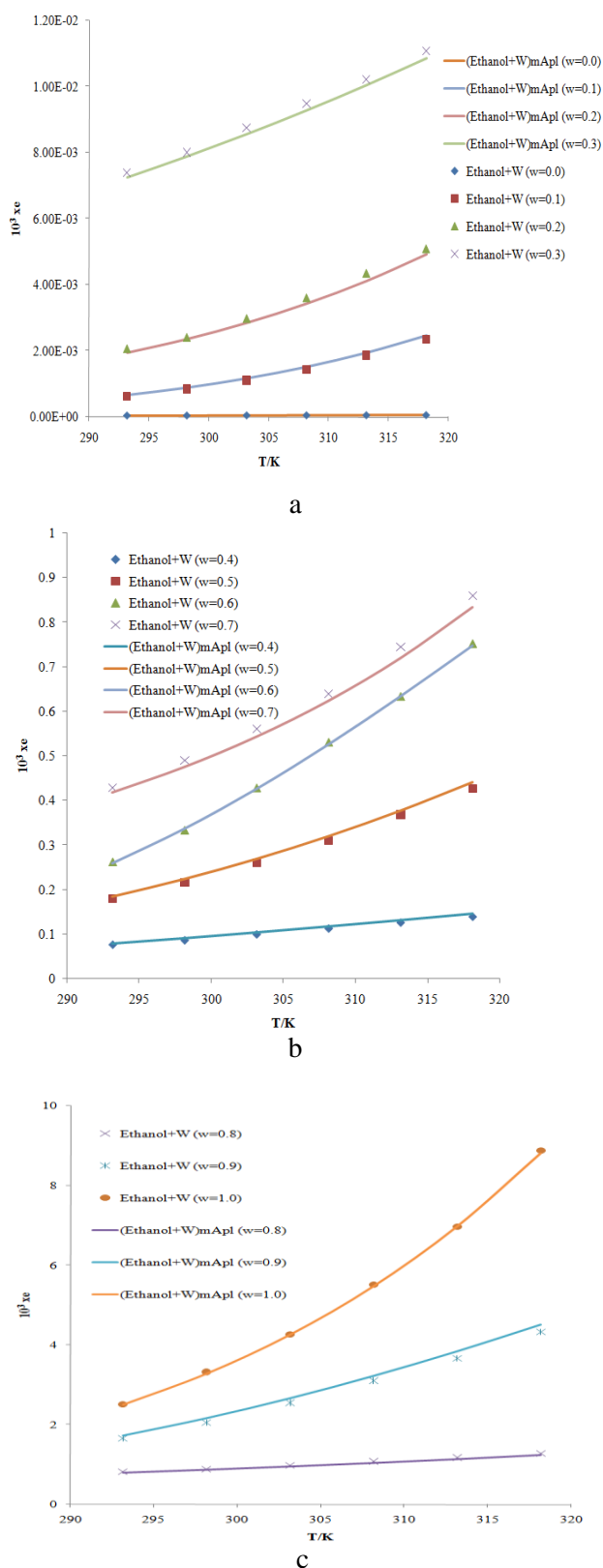


Fig. 3 Correlation and curve fitting of experimental mole fraction solubilities (x_e) with the modified Apelblat solubilities (m_{Apl}) for indomethacin in various ethanol + water mixtures from 293.15 to 318.15 K [a-lower solubility curves, b-low solubility curves and c-high solubility curves]

where, x_e is the experimental mole fraction solubility and x_c is the calculated solubility of IND. The lowest % AD was found in pure ethanol (0.1 to 0.98) at all temperatures studied. However, % AD in the range of 0.03 to 5.57 % was observed in other cosolvent mixtures. The values of regressed parameters A, B and C in distilled water, ethanol and ethanol-water mixtures are listed in Table 3. The values of R^2 for IND in distilled water and ethanol were 0.998 and 0.999, respectively (Table 3).

The R^2 values for IND in various ethanol-water mixtures were in the range from 0.995 to 0.999, indicating a good fit in pure solvents, as well as in cosolvent mixtures.

Thermodynamic parameters for IND dissolution

The dissolution of IND into a liquid can be expressed as [15-17]:

Solid + liquid = solid-liquid at an equilibrium

The molar enthalpy ($\Delta_{sol}H$) and entropy ($\Delta_{sol}S$) of IND dissolution can be calculated using equations 4 and 5, respectively:

$$\Delta_{sol}H = RT \left(C - \frac{B}{T} \right) \dots\dots\dots(4)$$

$$\Delta_{sol}S = R \left(C - \frac{B}{T} \right) \dots\dots\dots(5)$$

where B and C are the adjustable parameters calculated by the modified Apelblat equation. R and T are the universal gas constant and the absolute temperature, respectively. $\Delta_{sol}H$ and $\Delta_{sol}S$ for IND dissolution were calculated using equations 4 and 5, respectively at various temperatures. The $\Delta_{sol}H$ of IND dissolution in distilled water and ethanol at various temperatures ranged from 7.97 to 8.40 kJmol^{-1} and from 38.54 to 39.34 kJmol^{-1} , respectively. However, the $\Delta_{sol}H$ of IND dissolution in various ethanol-water mixtures ranged from 12.19 to 41.91 kJmol^{-1} in the same temperature range. These results indicated that IND dissolution in distilled water, ethanol and various ethanol-water mixtures was endothermic because the values of $\Delta_{sol}H$ were positive in each case. It was considered that the solute is solid and energy is required for the hypothetical melting process before mixing with the solvent. Hence, the positive values of $\Delta_{sol}H$ were probably due to the formation of new bond energy of attraction between IND molecules and the solvent molecules. The $\Delta_{sol}S$ values of IND dissolution in distilled water, ethanol and various ethanol-water mixtures were also positive at each temperature studied which also indicated that IND dissolution is an endothermic and an entropy-driven process.

Table 3 Modified Apelblat model parameters for indomethacin in various ethanol-water mixtures

w	Apelblat parameters			
	A	B	C	R ²
0.0	0.47	-162.68	-2.08	0.998
0.1	110.41	-9755.55	-16.08	0.999
0.2	-62.45	-684.46	9.09	0.998
0.3	-32.15	-356.24	3.79	0.999
0.4	128.20	-8175.47	-19.32	0.997
0.5	86.25	-7036.76	-12.47	0.999
0.6	437.59	-23588.50	-64.32	0.995
0.7	-231.08	7957.44	34.53	0.998
0.8	-53.33	685.40	7.72	0.997
0.9	252.03	-14746.20	-36.63	0.997
1.0	36.01	-5866.89	-3.87	0.999

Mass fraction of ethanol in cosolvent mixtures (w), correlation coefficient (R²)

CONCLUSION

In the present study, the mole fraction solubility of IND in distilled water, ethanol and various ethanol-water mixtures in the temperature range from 293.15 to 318.15 K was measured. The solubilities of IND were found to increase with the increase in temperature in distilled water, ethanol and various ethanol-water mixtures. The solubility of IND in pure ethanol was found to be significantly higher than that in pure distilled water. The solubility data of IND in distilled water, ethanol and various ethanol-water mixtures correlates well with the modified Apelblat equation. Based on solubility data, IND is considered as soluble in ethanol and practically insoluble in distilled water. These preliminary studies indicate that ethanol could be utilized as a green cosolvent in preformulation studies and formulation development of IND.

Acknowledgment: The project was financially supported by King Saud University, Vice Deanship of Research Chairs, Kayyali Chair for Pharmaceutical Industry (Grant no. FN-2015).

REFERENCES

1. E.A. Cantillo, D.R. Delgado, F. Martinez, *J. Mol. Liq.*, **181**, 62 (2013).
2. F. Shakeel, N. Haq, F.K. Alanazi, I.A. Alsarra, *Drug Develop. Ind. Pharm.*, **40**, 1240 (2014).
3. M.A. Ruidiaz, D.R. Delgado, F. Martinez, *Rev. Acad. Colomb. Cienc.*, **35**, 329 (2011).
4. F. Martinez, M.A. Pena, P. Bustamante, *Fluid Phase Equilib.*, **308**, 98 (2011).
5. M.A. Ruidiaz, D.R. Delgado, C.P. Mora, A. Yurquina, F. Martinez, *Rev. Colomb. Cienc. Quim. Farm.*, **39**, 79 (2010).
6. D.C. Pérez, C.C. Guevara, C.A. Cárdenas, J.A. Pinzón, H.J. Barbosa, F. Martínez, *Rev. Colomb. Cienc. Quim. Farm.*, **32**, 116 (2003).

7. J.A. Jimenez, F. Martinez, *J. Braz. Chem. Soc.*, **17**, 125 (2006).
8. A.R. Holguin, D.R. Delgado, F. Martinez, *Lat. Amer. J. Pharm.*, **31**, 720 (2012).
9. A. Nokhodchi, Y. Javadzadeh, M.R. Siahi-Shadbad, M. Barzegar-Jalali, *J. Pharm. Pharm. Sci.*, **8**, 18 (2005).
10. M.A. Ibrahim, G.M. Mahrous, M. El-Badry, F.K. Alanazi, *Farm.*, **59**, 483 (2011).
11. B. Bouillot, S. Teychene, B. Biscans, *Fluid Phase Equilib.*, **309**, 36 (2011).
12. A. Jouyban, S. Soltanpour, S. Soltani, H.K. Chan, W.E. Acree, *J. Pharm. Pharm. Sci.*, **10**, 263 (2007).
13. E. Baka, J.E.A. Comer, K. Takacs-Novak, *J. Pharm. Biomed. Anal.*, **46**, 335 (2008).
14. G.D. Yang, Y.R. Huang, G.J. Nan, H.J. Chen, A.G. Zeng, X.L. Bian, *J. Mol. Liq.*, **180**, 160 (2013).
15. C.L. Zhang, F. Zhao, Y. Wang, *J. Mol. Liq.*, **156**, 191 (2010).
16. C.L. Zhang, F. Zhao, Y. Wang, *J. Mol. Liq.*, **159**, 170 (2011).
17. C.L. Zhang, B.Y. Li, Y. Wang, *Can. J. Chem. Eng.*, **88**, 63 (2010).
18. M. Yang, P. Wang, C. Gogos, *Drug Develop. Ind. Pharm.*, **39**, 102 (2013).
19. S. Soltanpour, A. Jouyban, *J. Mol. Liq.*, **180**, 1 (2013).
20. R.G. Strickley, *Pharm. Res.*, **21**, 201 (2004).
21. Q. Wang, Y. Chen, L. Deng, J. Tang, Z. Zhang, *J. Mol. Liq.*, **180**, 135 (2013).
22. N. Sunandee, M. Hronec, M. Stolcova, N. Leepipatiboon, U. Pancharoen, *J. Mol. Liq.*, **180**, 252 (2013).
23. M. Faraji, A. Farajtabar, F. Gharib, *J. Appl. Chem. Res.*, **9**, 7 (2009).
24. C.S. Mali, S.D. Chavan, K.S. Kanse, A.C. Kumbharkhane, S.C. Mehrotra, *J. Pure Appl. Phys.*, **45**, 476 (2007).
25. J. Chen, S.K. Spear, J.G. Huddleston, R.D. Rogers, *Green Chem.*, **7**, 64 (2005).
26. F. Shakeel, F.K. Alanazi, I.A. Alsarra, N. Haq, *J. Chem. Eng. Data*, **58**, 3551 (2013).
27. F. Shakeel, F.K. Alanazi, I.A. Alsarra, N. Haq, *J. Mol. Liq.*, **191**, 68 (2014).
28. L. Wang, T.T. Lv, *J. Mol. Liq.*, **181**, 29 (2013).
29. A. Apelblat, E. Manzurola, *J. Chem. Thermodyn.*, **31**, 85 (1999).

ТЕРМОДИНАМИКА И РАЗТВОРИМОСТ НА ИНДОМЕТАЦИН В ВОДНО-ЕТАНОЛОВИ СМЕСИ В ТЕМПЕРАТУРНИЯ ИНТЕРВАЛ ОТ 293.15 ДО 318.15 К

Ф. Шакийл^{1,2*}, Ф.К. Аланази^{1,2}, И.А. Алсарра^{1,2}, Н. Хак^{1,2}

¹Център за върхови постижения по биотехнология, Университет «Крал Сауд», Риад 11451, Саудитска Арабия

²Катедра по фармацевтична промишленост “Кайади”, Фармацевтичен департамент, Колеж по фармация, Университет «Крал Сауд», Риад 11451, Саудитска Арабия

Постъпила на 26 януари, 2014 г.; коригирана на 1 март, 2014 г.

(Резюме)

Цел на работата е да се намери корелация между разтворимостта на индометацин (IND) в чисти разтворители и във водно-етанолови смеси в температурния интервал от 293.15 до 318.15) К. Разтворимостите са определяни след разбъркване на клатачна машина, а получените данни са корелирани с модифираното уравнение на Apelblat. Установено е, че разтворимостта на IND нараства с температурата в чисти разтворители, както и във водно-алкохолните смеси. Моларната разтворимост на IND е най-висока в чист етанол (2.50×10^{-3} при 298.15 К) в сравнение с тази в чиста вода (4.48×10^{-8} при 298.15 К) за всяка изследвана температура. Резултатите за енталпиите и ентропиите показват, че разтварянето на IND е ендотермичен и ентропийно обусловен процес.

New, simple and validated UV-spectrophotometric methods for the estimation of pyridoxine hydrochloride in bulk and formulation

A. Z. Mirza^{*1}, F. A. Siddiqui²

¹. Department of Chemistry, University of Karachi, Karachi, Pakistan

². Faculty of Pharmacy, Federal Urdu University of Arts, Science and Technology, Karachi, Pakistan.

Received January 28, 2014; Revised June 30, 2014

In this study, two rapid, simple and accurate spectrophotometric methods for the determination of pyridoxine hydrochloride, in bulk and in pharmaceutical formulations are described. These methods are based on the reaction of pyridoxine hydrochloride with ferric salts, i.e. ferric nitrate and ferric ammonium citrate. The reaction produces a yellowish orange color which absorbs maximally at 445 and 450 nm for ferric nitrate and ferric ammonium citrate, respectively. Beer's law was obeyed in the range of 5-50 $\mu\text{g mL}^{-1}$ for both reagents. The regression analysis of Beer's plot showed a good correlation coefficient ($r^2= 0.9987, 0.9982$). The results were validated analytically and statistically according to International Conference on Harmonization (ICH) guidelines. The proposed methods were applied to the determination of pyridoxine hydrochloride in bulk and pharmaceutical preparations with good results.

Keywords: Pyridoxine, ferric nitrate, ferric ammonium citrate, spectrophotometric methods.

INTRODUCTION

The importance of vitamins in one's diet can be ascertained by the fact that their deficiency leads to different diseases in humans. Therapeutic multivitamins are prescribed in such deficiencies as dietary supplements since the human body is unable to synthesize these vitamins [1], therefore a multivitamin complex is recommended to be used as a dietary supplementation. Pyridoxine hydrochloride (figure 1) is a well-known drug used for the treatment or prophylaxis of depression, pregnancy complications as nausea and vomiting and to overcome vitamin B6 deficiency [2, 3].

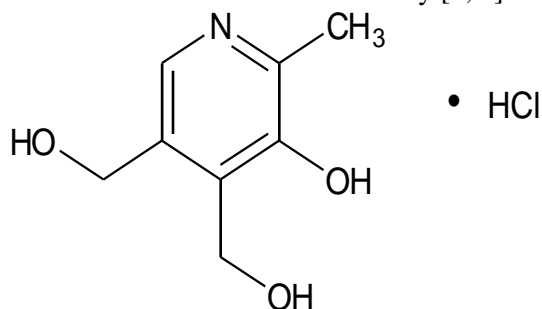


Fig. 1: Pyridoxine hydrochloride

After absorption in the gastrointestinal tract the two active forms, pyridoxal phosphate and pyridoxamine phosphate are released [4]. It helps in the metabolism of amino acids, carbohydrates and fats [5]. A number of methods for the determination of pyridoxine hydrochloride in combination with antihistamine drugs have been reported using HPLC [6-22], capillary electrophoresis [23], planar HPLC

[24] and UV spectrophotometry [25-32].

However, all reported methods are time consuming with extensive use of chemicals. The economical significance of spectrophotometric methods over other methods cannot be overlooked. Several spectrophotometric methods for the estimation of pyridoxine hydrochloride using different complicated techniques and expensive reagents in tablets have been reported. Surmeian [25] reported a method using derivative UV spectrophotometric technique. Dinc and Baleanu [26] reported a method using a one-dimensional wavelet transform. Ozdemir and Dinc [27] reported the estimation of pyridoxine hydrochloride using a genetic algorithm based on multivariate calibration methods. El Gindy [30] estimated pyridoxine hydrochloride by using graphical (second derivative of the ratio spectra) and numerical spectrophotometric methods (principal component regression and partial least squares, applied to the zero order UV spectra of the mixture). Raza *et. al.*, [32] reported a method using chloranil, an expensive reagent.

The present study was designed to develop easy, economical accurate and least time-consuming spectrophotometric methods for the determination of pyridoxine hydrochloride in raw form and in pharmaceutical formulations. In the present methods, pyridoxine hydrochloride was reacted with ferric salts producing a yellow orange colored complex showing absorption in the visible region of the spectrum at 445 and 450 nm for the quantification. The proposed methods were validated according to International Conference on

* To whom all correspondence should be sent:
E-mail: dr.zeeshan80@gmail.com

Harmonization (ICH) guidelines [33]. The two developed methods were found to be convenient, economical and easy for the routine analysis of the drug in laboratories and pharmaceutical industries.

EXPERIMENTAL

Apparatus

A double-beam Shimadzu (Japan) UV-Visible spectrophotometer, model UV-1601 was used. The software was UVPC personal spectroscopy software version 3.91 (Shimadzu) utilized for analysis.

Materials

Pyridoxine hydrochloride was kindly supplied by UCB (Belgium). Commercial pharmaceutical formulation named VITA-6[®] tablets from Chas. A. Mendoza Pharma Karachi containing 50 mg of pyridoxine was obtained from local pharmacies. Ferric salts were purchased from Merck Marker Pakistan. All other chemicals and reagents were of analytical grade and deionized water was used throughout the experiments.

Preparation of standard solutions

Standard stock solution of pyridoxine hydrochloride 100 $\mu\text{g mL}^{-1}$ was prepared in deionized water and diluted to a working range of 5 to 50 $\mu\text{g mL}^{-1}$ in 25 mL volumetric flasks. Then, 3 mL of 1% each of ferric salts solution was added to each flask. The volume was made up to the mark with deionized water and the yellowish orange complexes formed at room temperature were scanned on the spectrophotometer in the visible range of 400-700 nm against the reagent blank.

Analysis of tablets

Twenty tablets of weight equivalent to 100 mg of pyridoxine hydrochloride were crushed, and transferred to a 100 mL volumetric flask. The volume was adjusted to the mark with deionized water. Then, the solution was sonicated for 30 min, filtered and subjected to the proposed procedure for determination.

Study of interferences

Effect of excipients on the method was studied by mixing a known amount of pyridoxine (10 mg) with specified amounts of the excipients such as talc, magnesium stearate, aerosol, etc. in their recommended percentages [3].

RESULTS AND DISCUSSION

Numerous methods for the determination of pyridoxine and its mixtures have been reported in the literature using HPLC and spectrophotometry. It is reported that pyridoxine hydrochloride binds to

ferric chloride [31] in which pyridoxal reacts with the -OH group following a second order rate constant. Ferric salts easily react with -OH groups and the complex thus formed, can be used for detection and quantification of -OH group containing drug molecules [28, 34, 35]. The iron forms a yellowish orange color complex which absorbs radiation in the visible range.

In the present work, the complexes formed by pyridoxine hydrochloride with ferric nitrate and ferric ammonium citrate, displayed the λ_{max} of 445 and 450 nm, respectively (figure 2).

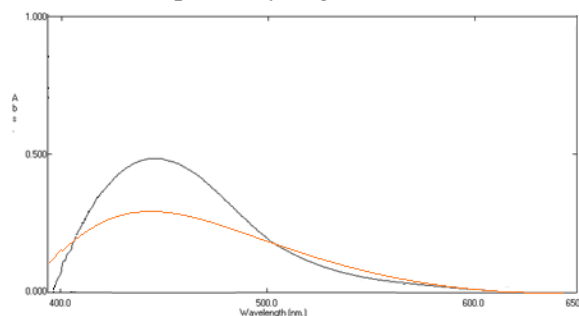


Fig. 2: UV-visible spectra of the complexes of pyridoxine with ferric nitrate (red) and ferric ammonium citrate (black)

These complexes followed Beer's law in the concentration range of 5-50 $\mu\text{g mL}^{-1}$. Regression analysis of pyridoxine hydrochloride-iron complexes formation and linearity of calibration graph was validated by the high value of the correlation coefficient ($r^2 = 0.9987, 0.9982$). Quantitative determination of pyridoxine hydrochloride in tablets using this method was performed according to ICH guidelines and the results were in good agreement with the labeled amount of pyridoxine hydrochloride. In addition, % RSD for the determination of pyridoxine hydrochloride and % recovery showed that the proposed method was accurate, precise and reliable. It was further observed that excipients of the tablet did not interfere with the reaction between pyridoxine hydrochloride and ferric salts. These proposed methods can be used for the determination of pyridoxine hydrochloride in pharmaceutical preparations.

METHOD VALIDATION

Validation of the method was carried out using International Conference on Harmonization Q2B guidelines for linearity, precision, accuracy, limits of detection and quantification [33].

Linearity

In developed UV method, calibration curves were linear in the range from 5-50 $\mu\text{g mL}^{-1}$ for both

Table 1 Linear regression functions and their statistical parameters

Drug complex with	Ferric nitrate	Ferric ammonium citrate
Regression equations	$y = 0.0364x - 0.0094$	$y = 0.0133x + 0.0001$
Beer's law limits ($\mu\text{g mL}^{-1}$)	5-50	5-50
λ_{max} (nm)	445	450
r^2	0.9987	0.9982
LOD ($\mu\text{g mL}^{-1}$)	0.25	0.29
LOQ ($\mu\text{g mL}^{-1}$)	1.10	1.17

complexes. Calibration curves were constructed with 9 different concentrations. Each concentration was analyzed 3 times. Statistical data (Table 1) showed that the methods were linear with correlation coefficient (R^2) 0.9987 and 0.9982 for complexes of pyridoxine with ferric nitrate and ferric ammonium citrate, respectively.

Accuracy and precision

Different levels of drug concentrations were prepared from the stock solution and were analyzed for accuracy determination. Accuracy was assessed as the mean percentage recovery of drug concentrations prepared from the stock solution and analyzed (Table 2).

Table 2 Accuracy of method

Drug with	Added Concentration ($\mu\text{g mL}^{-1}$)	Measured Concentration ($\mu\text{g mL}^{-1}$)	Accuracy %
Ferric nitrate	8	8.01	100.18
(FeNO_3)	10	10.11	101.10
	12	12.11	100.91
Ferric ammonium citrate	8	8.19	102.37
($\text{C}_6\text{H}_8\text{O}_7\text{FeNH}_3$)	10	10.04	100.44
	12	11.98	99.83

Repeatability was determined by using different levels of drug concentrations prepared from the stock solution and analyzed. The relative standard deviation (in %) was taken as precision.

Statistical calculations for the above method are shown in Table 3 which proves the reliability of the method for the determination of pyridoxine hydrochloride in formulations, since no significant effect of excipients was observed.

Limit of detection and quantification

The LOD and LOQ of pyridoxine hydrochloride were determined and were calculated from the equations as $3.3 \delta/S$ and $10 \delta/S$, respectively, where S is the slope of the calibration curve and δ is the standard deviation of y-intercept of the regression equation [33] (Table 1).

Application

The proposed methods were successfully applied to the assay of pyridoxine hydrochloride in their

dosage forms. Excellent recoveries with low RSD (%) values were obtained. The results are tabulated in table 4. Tablet excipients did not interfere and therefore confirming that the developed methods are suitable for routine estimation of pyridoxine hydrochloride in their pharmaceutical preparation.

Table 3 Precision of method

Drug with	Measured concentration ($\mu\text{g mL}^{-1}$)	RSD%
Ferric nitrate	50	1.08
Ferric ammonium citrate	50	1.17

Table 4 Recovery studies

Complex with:	Ferric nitrate	Ferric ammonium citrate		
Concentration ($\mu\text{g mL}^{-1}$)	Found	Recovery %	Found	Recovery %
10	9.89	98.90	10.09	100.90
20	19.88	99.40	19.91	99.55
30	30.09	100.30	29.84	99.47
40	40.11	100.28	39.93	99.83
50	49.73	99.46	50.13	100.26

The methods are based on inexpensive chemicals and a very simple methodology using a common instrument. The sensitivity of the above methods is comparable to that of the HPLC technique and the validation results further prove its application for all drugs containing OH group.

CONCLUSION

Accurate, precise and convenient methods based on ultraviolet spectral data, were developed for the determination of pyridoxine hydrochloride in pharmaceutical dosage forms. The high recovery values of these drugs showed the good reproducibility of the methods. The methods were found to be easy, simple and quick with minimal sample preparation and simple instrumentation. The methods can be used for routine analysis in quality control laboratories. The methods can be applied for stock solution stability tests and for drug quantification in pharmaceutical formulations. Any of these methods may be adopted as an alternative to the existing time consuming methods.

REFERENCES

1. M.K. Enos, J.P. Burton, J. Dols, S. Buhulata, J. Chagalucha, G. Reid *Beneficial Microbes*, **4**, 3 (2013).
2. Dorland's illustrated Medical Dictionary, 28th ed., W.B. Saunders Company, 1994, p.1395.
3. British Pharmacopoeia, 2003, pp.1195, 1595.
4. The Merck Index, An Encyclopedia of Chemical, Drugs and Biologicals, 13th edn., Merck Research Laboratories, 2001, pp.1032, 429.
5. Martindale, The extra pharmacopoeia, Royal Pharmaceutical Society of Great Britain, 1 Lambeth High Street. London SE17 Jn England, 31st edn., 1996. pp.447, 1384.
6. P. Chen and W.R. Wolf, *Anal Bioanal Chem.*, **387**, 2441 (2007).
7. C.K. Markopoulou, K.A. Kagkadis and J.E. Koundourellis, *J. Pharm. Biomed. Anal.*, **30**, 1403 (2002).
8. M. N. Ramos, G. F. Aguirre, D. A. Molina and V. L. F. Capitan, *J. AOAC Int.*, **84**, 676 (2001).
9. P. Moreno and V. Salvado, *J. Chromatogr. A*, **870**, 207 (2000).
10. M. S. Arayne, N. Sultana, F. A. Siddiqui, *Chromatographia.*, **67**, 941 (2008).
11. G. W. Chase, W. O. Jr. Landen, A. G. Soliman and R. Eitenmiller, *J. AOAC Int.*, **76**, 1276 (1993).
12. P. Vinas, C. L. Erroz C, N. Balsalobre and M. H. Cordoba, *J. Chromatogr. A.*, **1007**, 77 (2003).
13. M. M. Sena, Z.F. Chaudhry, C. H. Collins and R. J. Poppi, *J. Pharm. Biomed. Anal.*, **36**, 743 (2004).
14. M. L. Marszall, A. Lebedzinska, W. Czarnowski and P. Szefer, *J. Chromatogr. A.*, **1094**, 91 (2005).
15. G. A. Zafra, A. Garballo, J. C. Morales and A. L. E. Garcia, *J Agric Food Chem.*, **54**, 4531 (2006).
16. A. El-Gindy, F. El-Yazby, A. Mostafa and M. M. Maher, *J. Pharm. Biomed. Anal.*, **35**, 703 (2004).
17. A. Jedlicka and J. Klimes, *Ceska. Slov. Farm.*, **53**, 243 (2004).
18. A. El-Gindy, S. Emara and A. Mostafa, *Farmaco*, **59**, 713 (2004).
19. O. Heudi, T. Kilinic and P. Fontannaz., *J. Chromatogr. A.*, **1070**, 49 (2005).
20. M. R. Hadjmohammadi, F. Momenbeik and J. H. Khorasani, *Ann. Chim.*, **94**, 857 (2004).
21. P. F. Chatzimichalakis, V. F. Samanidou, R. Verpoorte and I. N. Papadoyannis, *J. Sep. Sci.*, **27**, 1181-88 (2004).
22. P. L. Monferrer, P. M. E. Capella, A. M. Gil and R. J. Esteve, *J. Chromatogr. A.*, **984**, 223 (2003).
23. L. Fotsing, M. Fillet, I. Bechet, P. Hubert and J. Crommen, *J. Pharm. Biomed. Anal.*, **15**, 1113-23 (1997).
24. M. Aranda and G. Morlock, *J. Chromatogr. A.*, **1131**, 253 (2006).
25. M. Surmeian, *Drug Dev. Ind. Pharm.*, **24**, 691 (1998).
26. E. Dinc and D. Baleanu, *J. Pharm. Biomed. Anal.*, **31**, 969 (2003).
27. D. Ozdemir and E. Dinc, *Chem. Pharm. Bull.*, **52**, 810-7(2004).
28. M. S. Arayne, N. Sultana, F. A. Siddiqui, M. H. Zuberi and A. Z. Mirza, *Pak. J. Pharm. Sci.*, **20**, 149, (2007).
29. C. S. Suresh, C. S. Satish, R. C. Saxena and K. T. Santosh, *J. Pharm. Biomed. Anal.*, **7**, 321 (1989).
30. A. El-Gindy, *J. Pharm. Biomed. Anal.*, **32**, 277 (2003).
31. L. H. Miao, K. C. Yang and F.L. Yun, *Chemico-Biological Interactions*, **97**, 63 (1995).
32. R. A. Ansari, T. M. Niazi, S. B. Rehman, *Journal of the Chemical Society of Pakistan*, **29**, 33 (2007).
33. International Conference on the Harmonization of Technical for the Registration of Pharmaceuticals for Human Use (ICH) Q2B, Validation of Analytical Procedures, Methodology Requirements, 1996
34. F. A. Siddique, M. S. Arayne, N. Sultana, A. Z. Mirza, M. H. Zuberi and F. Qureshi, *Medicinal Chemistry Research*, **19**, 1259 (2010).
35. M. S. Arayne, N. Sultana, F. A. Siddiqui, A. Z. Mirza and M. H. Zuberi, *Journal of Molecular Structure*, **891**, 475 (2008)

НОВИ, ПРОСТИ И ВАЛИДИРАНИ UV-СПЕКТРОФОТОМЕТРИЧНИ МЕТОДИ ЗА ОПРЕДЕЛЯНЕ НА ПИРИДОКСИН ХИДРОХЛОРИД В РАЗТВОРИ И ПРЕПАРАТИ

А.З. Мирза^{*1}, Ф.А. Сидикуи²

¹Департамент по химия, Университет в Карачи, Пакистан

²Факултет по фармация, Федерален урду университет за изкуства, наука и технология, Карачи, Пакистан

Постъпила на 28 2014 г.; коригирана на 30 юни, 2014 г.

(Резюме)

В тази работа се описват два бързи, прости и точни спектрофотометрични методи за определянето на пиридоксин хидрохлорид в разтвори и фармацевтични препарати. Тези от реакцията на пиридоксин хидрохлорид с ферисоли, т.е. феринитрат и фери-амониев цитрат. Реакцията дава жълто-оранжево съединение, което максимално абсорбира светлина при 445 и 450 nm съответно за феринитрат и фериамониев цитрат. Законът на Beer се спазва в интервала 5-50 $\mu\text{g mL}^{-1}$ за двата реагента. Регресионният анализ дава висок корелационен коефициент за калибровъчната права по закона на Beer ($r^2 = 0.9987$, 0.9982). Резултатите са потвърдени аналитично и статистически по правилата на International Conference on Harmonization (ICH).

Simultaneous analysis of glycyrrhizic acid and preservatives in licorice aqueous extract by HPLC/PDA detection

K. Abu-Shandi¹, A. R. Halawah², AlSayed Sallam³, Gh. Al-Edwan⁴, A. R. Al-Tawaha⁵, Sh. A. Albajawi², E. S. M. Abu-Nameh^{2*}

¹ Department of Chemistry, Faculty of Science, Tafila Technical University, Tafila, Jordan

² Department of Chemistry, Faculty of Science, Al-Balqa Applied University, Al-Salt, Jordan.

³ Al-Taqaddom Pharmaceutical Industries, Amman, Jordan.

⁴ DAD Industries, Amman, Jordan.

⁵ Department of Biological Sciences, Al Hussein Bin Talal University, Maan, Jordan.

Received January 29, 2014; Revised March 13, 2014

A high performance liquid chromatographic (HPLC) analytical method for the assay of glycyrrhizic acid (GLY), sodium benzoate (SB), methyl 4-hydroxybenzoate (MP), and propyl 4-hydroxybenzoate (PP) in licorice aqueous extract was developed. The method employed Lichro CART® Purospher STAR, C18, 5 μm (250 \times 4.6 mm) analytical column with a simple mobile phase of potassium acetate buffer: acetonitrile (68.8: 31.2) v:v ratio. The detection was achieved by PDA detector at a wavelength of 254 nm. The developed method was considered linear within the specified range at concentrations of 80%, 90%, 100%, 110% and 120%. The method was found to be accurate, repeatable and precise. Upon storage in 0.1N HCl for 24 h, 0.1N NaOH for 24 h, and 3% H₂O₂ with exposure to UV for 24 h and heating in water bath at 90 °C for 24 h, methyl paraben (MP) was stable upon changing conditions. The other tested components exhibited different stability properties upon changing conditions.

Keywords: glycyrrhizic acid (GLY), sodium benzoate (SB), methyl 4-hydroxybenzoate (MP), propyl 4-hydroxybenzoate (PP), validation, Arrhenius plots.

INTRODUCTION

Liquorice or licorice [1, 2] is the root of *Glycyrrhiza glabra* from which a somewhat sweet flavor can be extracted. Licorice extract is produced by boiling licorice root and subsequently evaporating most of the water, and is traded both in solid and syrup forms [3, 4, 5]. Its active component is glycyrrhizin known as glycyrrhizic acid (GLY) (Figure 1), a sweetener from 30 to 50 times sweeter than sucrose, which also has pharmaceutical effects [6].

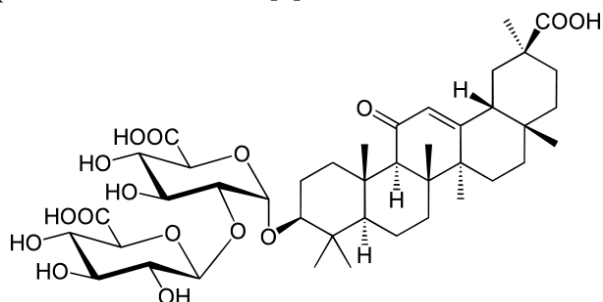


Fig. 1. The chemical structure of glycyrrhizic acid (GLY), the major active component in licorice.

Several studies have investigated the main components in licorice root extract for anti-inflammatory activity [7-10]. The effects of the aqueous extract of *Glycyrrhiza glabra* on the

depression in mice using forced swim test (FST) and tail suspension test (TST) have been investigated [11]. Ethanolic extracts of the dried roots of *Glycyrrhiza glabra* were analyzed for their phytochemical constituents. The analysis showed the presence of various phytochemicals like alkaloids, cardiac glycosides, flavonoids, HCN, indoles, juglones, phenols, saponins, steroids, tannins and terpenoids [12].

An ionic liquid based single-drop microextraction procedure followed by HPLC has been developed and validated for the determination of the components of licorice tablets [13].

Several research studies have been conducted and reported in the literature on the analysis of licorice and its extract. For example, Qiao Xue and coworkers investigated the regulatory effects of licorice on bile acid metabonome in rats using liquid chromatography coupled with tandem mass spectrometry [14]. Also, Farag and coworkers utilized multi-targeted metabolic profiling and fingerprinting techniques to study the *Glycyrrhiza* species components [15]. Moreover, licorice and its extract were quantitatively determined by two-dimensional liquid chromatography [16], inductively coupled plasma atomic emission spectrometry [17], HPLC-ESI-MS/MS [18], high-performance thin-layer chromatography (HPTLC) [19,20], HPLC-UV detector with external standard

* To whom all correspondence should be sent:

E-mail: eyadchem@yahoo.com

[21], graphite furnace atomic absorption spectrometry [22], liquid chromatography coupled with electrospray ionization quadrupole time-of-flight tandem mass spectrometry [23,24], RP-HPLC/DAD method [23-25], UPLC-MS-MS [26], gas chromatography [27], first derivative spectrophotometric and Vierordt's method [28], multi-stage mass spectrometric [29] and HPLC-UV-MS [30].

Literature survey showed that there was no published data related to the routine or/and stability assay of glycyrrhizic acid in the presence of a mixture of preservatives like sodium benzoate, methyl 4-hydroxybenzoate and propyl 4-hydroxybenzoate in licorice aqueous extract by any type of analytical methods. Thus, the main purpose of this study was to develop a novel HPLC analytical method for the assay of these four components in licorice aqueous extract. The study includes the validation of the HPLC method according to FDA and ICH guidelines. The described method can be applied to similar patterns for the identification of low concentrations of extract components. For example, comparable methods were used for identification of anthocyanin derivatives in grape skin extracts [31], identification of polyphenol mixtures and plant extracts [32], identification of phenolic compounds in lemon verbena extracts [33], determination of domoic acid in shellfish [34] and many other extraction products in the field.

EXPERIMENTAL

Chemicals and Materials

Licorice dry aqueous extract EP (*Glycyrrhiza glabra L.*), was purchased from Instituto Farmochimico Fitoterapico (EPO), Milano, Italy. 18-beta-glycyrrhetic acid 98%, glycyrrhizic acid monoammonium salt trihydrate 98%, and acetonitrile HPLC grade were purchased from Acros Organics, USA. Glycyrrhizic acid 100% USP Reference STD was purchased from USP Convention, Rockville, USA. Methyl paraben EP and propyl paraben EP were purchased from KIMIA International Ltd., India. Sodium benzoate EP powder was purchased from VELSICOL, Estonia. Methanol LC grade, was purchased from MERCK, Germany. 1-Octanesulfonic acid sodium salt HPLC grade, potassium acetate reagent grade ACS, and acetic acid glacial analytical grade ACS, were purchased from Sharlau, Spain. Distilled deionized water was prepared in house by STILMAS Pharmastill MS 15045 ultra pure water system (Vaponics, USA). Certification of licorice dry aqueous extract was achieved by the HPLC

analytical method specified in United States pharmacopoeia USP-27 using glycyrrhizic acid USP as a reference standard. The preservatives (methyl paraben, propyl paraben, and sodium benzoate) were certified according to European Pharmacopoeia-7th by the titrimetric analytical methods described there. The determined purity of standards is reported in table 1.

Table 1. Certification of the used working standards

Working standard name	Specifications	Assay (w/w)
Licorice dry aqueous extract (LAE)	≥ 3.0 %	4.0 %
Sodium benzoate (SB)	99.0 -100.5 %	99.3 %
Methyl 4-hydroxy benzoate (MP)	99.0 -100.5 %	100.0 %
Propyl 4-hydroxy benzoate (PP)	99.0 -100.5 %	99.6 %

Instruments

The HPLC system consists of a MERCK-HITACHI gradient pump model L-7100 connected to MERCK "On-Line" Degasser L-7614, MERCK-HITACHI Autosampler L-7200, MERCK Column Oven L-7360, MERCK-HITACHI Diode Array Detector L7455, and MERCK-HITACHI Interface D7000. The HPLC system was connected to DELL PC with hp-DeskJet 845c Printer. The HPLC system was controlled by MERCK-HITACHI D-7000 HPLC system manager (HSM) software. A Purospher® STAR, C18, (250 × 4.6 mm, 5µm) analytical column with C18 guard column was used after several optimization trials. The following helping tools were used to complete the work: Sartorius research analytical balance type R200 D from Germany; pH-meter type Orion Research Expandable ion analyzer EA 940; ultrasonic bath type FRITSCH-laborette 17.002, Germany; water bath type GFL 1003, Germany; magnetic stirrer type Gallenkamp, England; vacuum oven type Gallenkamp A-20011, England; incubator type VISMARA S.R.L F1 480 RS, Italy; oven type Heraeus T 6120, Germany; humidity oven type Heraeus VTRK 150, Germany; and centrifuge type JOUAN MR18-12, France.

Mobile phase preparation

Potassium acetate buffer solution was prepared by dissolving 0.724 g of potassium acetate in 1000 mL of deionized water using a volumetric flask. The pH was adjusted to 3.60 by glacial acetic acid (≈ 4.0 mL) with gentle mixing. Acetonitrile (454 mL) was accurately measured by using a 500-mL measuring cylinder, and mixed well with the potassium acetate buffer solution in a suitable container. The mixture was filtered through a 0.45 µm Nylon membrane filter under vacuum and degassed in a ultrasonic water bath.

Standard solution preparation

Accurately weighed amounts of methyl paraben (MP) and propyl paraben (EP) standardized materials equivalent to 192.4 mg and 28.8 mg, respectively, were dissolved in a 200-mL volumetric flask with the mobile phase. The solution was mixed well and 5 mL were transferred to a 100-mL volumetric flask; an amount of licorice aqueous extract (LAE) dry powder equivalent to 18 mg GLY and accurately weighed amount of sodium benzoate equivalent to 72.1 mg were added and dissolved with the mobile phase. The solution was mixed well by sonication for about 15 min. The obtained solution was centrifuged and the resulted supernatant was filtered through a membrane syringe filter having a porosity of 0.45 μm .

Test sample solution preparation

A 3 mL pipette was rinsed carefully with the mobile phase. The test sample bottle was shaken gently and 3.0 mL of licorice aqueous extract was transferred to a 100 mL volumetric flask. The solution was sonicated for about 5 min, then mixed well and filtered through a membrane syringe filter having a porosity of 0.45 μm .

Methodology of the validation characteristics

Accuracy

The accuracy of the analytical method was assessed by application of the analytical procedure to nine synthetic samples at three concentration levels, namely 80%, 100%, and 120%, three samples for each concentration. The synthetic samples were prepared by adding known quantities of the analytes to a placebo sample. Accuracy was reported as the percent recovery of the assay of known added amounts of the analytes in the synthetic samples.

Precision

Repeatability

Repeatability of the preparation of the standard solution

The repeatability of the preparation of the standard solution was assessed by application of the analytical procedure to nine determinations at three concentration levels, namely 80%, 100%, and 120%, three samples for each concentration. The repeatability of the preparation of the standard solution was reported as relative standard deviation for injections of each prepared standard solution, and for replicates of the preparation of standard solution at each concentration level: 80%, 100%, and 120%.

Repeatability of the preparation of test sample solution

The repeatability of the preparation of the test sample solution was assessed using 6 determinations at 100% of the concentration of the test sample solution; 6 sample solutions from the same container were prepared and injected into the chromatograph. The repeatability of the preparation of the test sample solution was reported as relative standard deviation for injections of each prepared test solution, and for replicates of the preparation of the test solution.

Intermediate precision

The variations that have been studied include days, analysts, and equipment. The same test sample was analyzed in different days by different analysts and equipments. The results obtained from the first and the second assay test were reported and compared.

Linearity and Range

The linearity was evaluated over the range from 80% to 120% of the concentration of the test solution. It was demonstrated by dilution of a standard stock solution. Standard stock solution was prepared in duplicate, then serial dilutions were performed for each one to obtain standard solutions having the following concentrations: 80%, 90%, 100%, 110%, and 120% of the concentration of the test solution.

Selectivity

The selectivity of the analytical method was demonstrated by evaluation of chromatographic peak purity and resolution for the analytes after storing their solutions under relevant severe conditions: light, heat, acid/base hydrolysis and oxidation. Practically, this was performed by preparing the tested samples for each analyte individually using the following media and conditions; 0.1 N NaOH, 0.1 N HCl, 3% H₂O₂, UV-radiation, and heat (90°C).

Accelerated stability study

Container closure system

Accelerated stability testing was conducted on licorice aqueous extract packed in 25 ml-amber glass bottle containers with plastic screw capped closures.

Storage Conditions and testing frequency

The licorice aqueous extract bottles were stored in several storage conditions for 12 weeks, and were frequently tested, as shown in the following table:

Table 2: Stability study storage conditions and frequency of testing

Storage conditions	Frequency of testing (weeks)
RT/DL	1,2,3,4,5,8, and 12
25°C ± 2°C / 60% RH ± 5% RH	1,2,3,4,5, and 8
40°C ± 2°C / 75% RH ± 5% RH	1,2,3, and 4
50 °C ± 2°C	1,2,3,4,5,8, and 12
70 °C ± 2°C	1,2,3,4,5,8, and 12

RESULTS AND DISCUSSION

Wavelength selection

The chemical composition of the sample can provide valuable clues for the best choice of initial conditions for an HPLC separation. In this work, empirical procedures were emphasized in combination with techniques for minimizing the number of required experimental runs. However, theoretical considerations and the chemical composition of the sample were not ignored. Since the analytes have good UV-absorbance and exist in sufficient concentrations, the PDA detector was chosen as the detector. In photodiode array detection glycyrrhizic acid, sodium benzoate, propyl paraben and methyl paraben have λ_{max} of 251 nm, 240 nm, 255 nm and 255 nm, respectively. Depending on the obtained UV-spectra the wavelength was adjusted at 254 nm.

Selection of HPLC conditions

The USP-27 assay method for licorice was tested at the beginning (figure 2A). The peak at 6.39 min consists of two components: sodium benzoate and methyl paraben. The method was considered unsuitable because the separation required further improving. After that the attention was focused on the strength and pH value of the solvent. Increasing of the concentration of

acetonitrile in the eluent led to a decrease in the analytes retention and hence the capacity factor (k') decreased. There was no significant effect by changing the pH of the mobile phase in the investigated experiment for this issue. The results exhibited poor resolution of the analytes. The effect of the column length and the flow rate was tested. The increase in column length did not sufficiently improve the separation of sodium benzoate and methyl paraben peaks. The method was still not selective for sodium benzoate and methyl paraben analytes under the specified conditions of the experiments (Figure 2B). The mobile phase flow rate was increased to 1.0 ml per minute in order to reduce the run time. As the column was increased in length the analytes separated better and were longer retained due to the increase in column plate number (N), so that both k and α values of the analytes increased and the R value improved. Although the increase in the flow rate reduced the run time, it also increased the column pack pressure which was considered unfavorable because it exceeded the specified pressure limit (2000 psi).

Further separation trials were performed by using organic solvents other than acetonitrile, e.g., THF and methanol, in order to improve the selectivity of the chromatographic system. The results are still

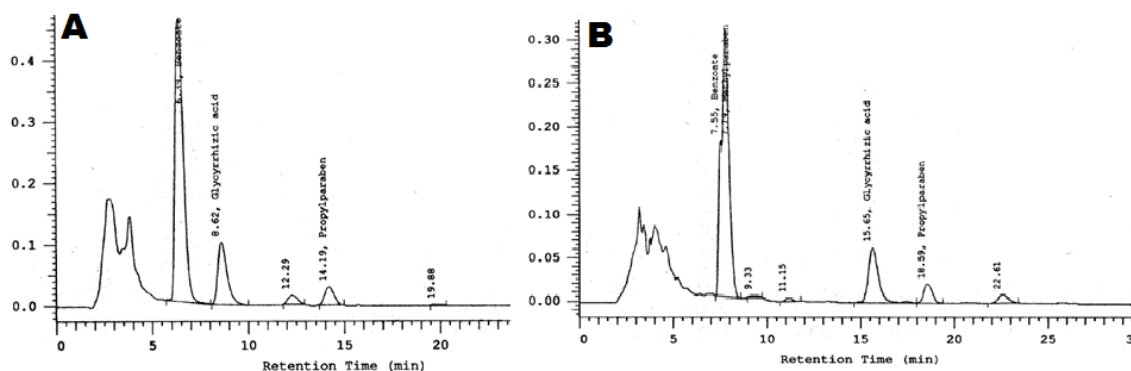


Fig. 2. A) Representative chromatogram of the sample (LAE) using the USP method. B) Representative chromatogram of the sample solution using a 25cm × 4.6mm 5 μ m C₁₈ analytical column (modified USP-method).

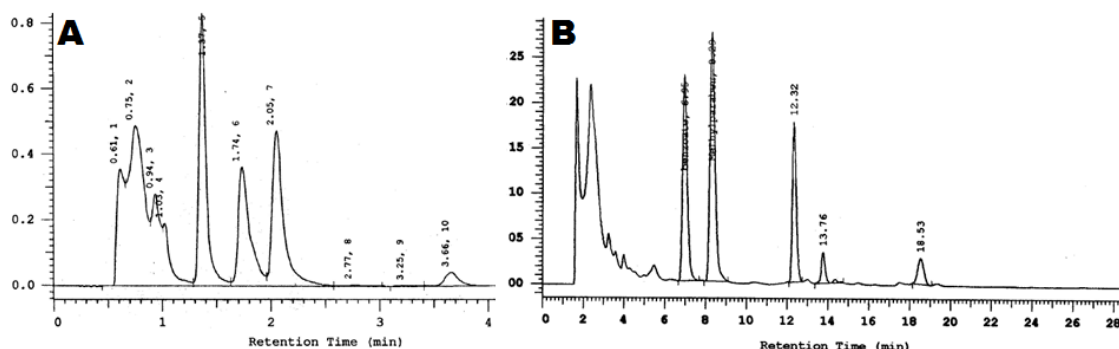


Fig. 3. A) Representative chromatogram with 12.5 cm C₈ column at FR 1.5 ml/min with 30% acetonitrile in system No.3; GLY at 1.4, SB at 1.8 min, MP at 2.0 and PP at 3.7 min. B) Representative chromatogram of gradient: (SB at 7.0 min, MP at 8.3 min, GLY at 12.3 min, and PP at 18.5 min.)

unsatisfactory. Also, packing material such as cyano and C8 columns were tested over C18 (Figure 3A). However, this type of columns did not produce the expected improvement since there was no good separation for the four analytes within the accepted run time.

Gradient elution was employed during the development trials. The most apparent problem during the development of the gradient system was the improper resolution of PP due to its low concentration which made it sensitive to the base line noise and drifts (Figure 3B). Many trials were conducted including changing the parameters mentioned above and other parameters not reported here such as ion pairing and others. The results from these trials are the optimized chromatographic conditions listed in table 3. A representative chromatogram is shown in figure 4. The method provides good values for column plates number (N), capacity factor (k), selectivity α and resolution (R).

ANALYTICAL METHOD VALIDATION

Linearity study

The linearity of the analytical method was statistically evaluated by calculation of a regression line by the method of least squares. The correlation coefficient, y-intercept, and

slope of the regression line are shown in table 4. Plots of the data are included in figure 5. The specified range was derived from the linearity studies and depended on the intended application of the analytical method. It was considered from 80% to 120% of the concentration of the test solution.

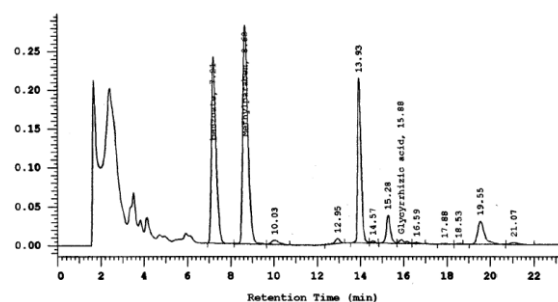


Fig. 4. Representative chromatogram under optimized chromatographic conditions: (SB at 7.2 min, MP at 8.7 min, GLY at 14.0 min, and PP at 19.6 min.)

Based on the tabulated results of the linearity study (Table 5) the developed method was considered linear within its specified range (80-120%: SB [575-865 $\mu\text{g/ml}$], GLY [144-216 $\mu\text{g/ml}$], MP [38.5-57.7 $\mu\text{g/ml}$], and PP [5.8-8.6 $\mu\text{g/ml}$] since the correlation coefficients (r) of the analytes were not less than 0.998.

Table 3: The chromatographic system of the developed method

Mobile phase	Potassium acetate buffer pH 3.60: acetonitrile (68.8: 31.2) V/ V
Column	Purospher® STAR, C ₁₈ , 5 μm (250 \times 4.6 mm), with C ₁₈ guard column.
Temperature	30 $^{\circ}\text{C}$
Detector	254 nm
Flow rate	1.3 ml/min
Injection volume	10.0 μl
Run time	22 min

Table 4: Linearity data of the analytes (average of duplicate)

Analyte Name	Area 80%	Area 90%	Area 100%	Area 110%	Area 120%
Glycyrrhizic acid (GLY)	399985	440764	491201	540321	589441
Na benzoate (SB)	547061	603990	672440	739684	817376
Methyl paraben (MP)	778294	860944	958518	1040691	1157109
Propyl paraben (PP)	97423	109388	120951	128884	141168

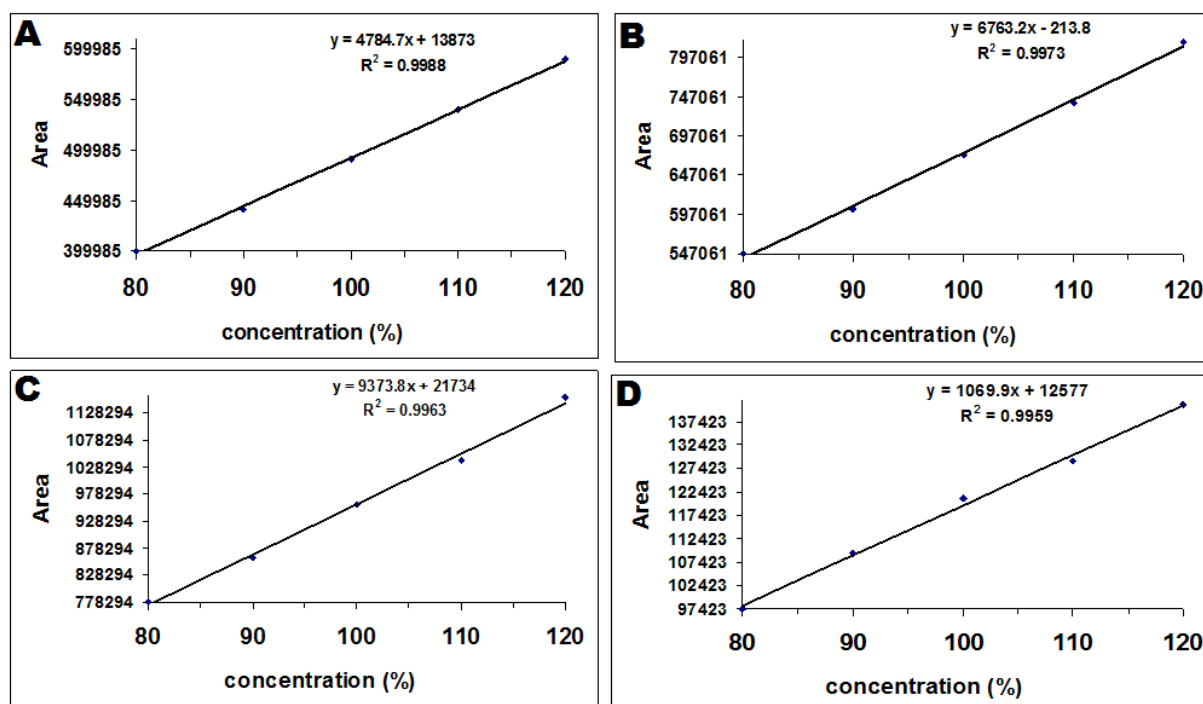


Fig. 5. Calibration curve for A: glycyrrhizic acid, B: sodium benzoate, C: Methyl paraben, D: Propyl paraben. The concentration points are 80%, 90%, 100%, 110% and 120%.

Table 5: Results of the linearity studies for the analytes

Analyte Name	Correlation coefficient (r)	Y-intercept	Slope of the regression line
Glycyrrhizic acid	0.9994	13873	4785
Na benzoate	0.9986	- 214	6763
Methyl Paraben	0.9982	21734	9374
Propyl paraben	0.9980	12577	1070

Table 6: Accuracy study results of glycyrrhizic acid

Target Concentration	Spiked Concentration (mg/mL)	Measured Concentration (mg/mL)	Percentage (%)	Average Recovery (%)	RSD (%)	
80% (144 µg/ml)	S1	0.144	0.1475	102.4	102.0	0.44
	S2	0.144	0.146	101.5		
	S3	0.143	0.146	102.0		
100% (180 µg/ml)	S1	0.179	0.180	100.8	100.7	0.85
	S2	0.179	0.182	101.5		
	S3	0.179	0.179	99.8		
120% (216 µg/ml)	S1	0.2155	0.217	100.7	100.7	0.55
	S2	0.2158	0.216	100.2		
	S3	0.2155	0.218	101.3		

The RSDs for SB, MP and PP are 0.55 to 0.80; 0.53 to 0.94; and 0.94 to 1.84, respectively.

Accuracy study

Based on the tabulated results of the accuracy studies, the method was found to be accurate since the average recovery values of the analytes were 100.0% ± 2.0%. Table 6 shows the results of glycyrrhizic acid; other detailed results for SB, MP and PP are not shown here for space issue.

Precision study

Repeatability

Repeatability of the preparation of the standard solution

Based on the tabulated results of the precision studies the developed method was found to be repeatable and precise since the relative standard deviations for different injections from the same test solution and for different preparations of the test solution were not more than 2.0%.

Table 7: Repeatability precision study results of Glycyrrhizic acid

Target Concentration	Measured Area	Average of Measured Area	SD	RSD (%)
80% (144 µg/ml)	S1	402280	2002	0.50
	S2	398429		
	S3	399402		
100% (180 µg/ml)	S1	491852	4114	0.84
	S2	495208		
	S3	487024		
120% (216 µg/ml)	S1	589643	3311	0.56
	S2	586198		
	S3	592818		

Table 8: Repeatability of the preparation of the test sample solution for the assay

Analyte	Prep. No.1	Prep. No.2	Prep. No.3	Prep. No.4	Prep. No.5	Prep. No.6	Average %	RSD %
GLY	100.5	100.8	99.2	101.3	101.0	100.0	100.5	0.76
SB	99.6	100.8	98.8	99.4	100.3	100.1	99.8	0.71
MP	99.7	99.6	98.7	99.9	99.6	101.3	99.8	0.86
PP	101.2	99.6	98.1	100.5	101.2	100.5	100.2	1.18

Table 7 shows the results of glycyrrhizic acid; other detailed results for SB, MP and PP are not shown here for space issue. The RSDs for SB, MP and PP are 0.50 to 0.94; 0.50 to 0.97; and 1.36 to 1.82, respectively.

Repeatability of the preparation of the test sample solution

Based on the tabulated results of the intra-assay repeatability (Table 8) the developed method was found to be repeatable and precise since the relative standard deviations for different assay preparations from the same test solution were less than 2.0%.

Intermediate precision

As shown in Table 9, the deviations in the assay results for the analytes were less than 2.0% for two separate analyses (A & B) of the same sample bottle by different analysts and instruments at different days, which indicates a good precision of the developed analytical method.

Analysis B was performed by a different analyst using a different instrument at a different day.

Selectivity

Representative chromatograms were run for each tested sample of the analytes and the

chromatographic peak purity and resolution were evaluated.

Table 9: Results of the intermediate precision study

Analyte name	Analysis A (Assay)	Analysis B (Assay)	Deviation %
GLY	99.5 %	100.0 %	0.5
SB	100.6 %	99.7 %	0.9
MP	99.3 %	99.9 %	0.6
PP	100.8 %	99.5 %	1.3

Stability

The analytes under study were put to vigorous conditions, namely, storage in 0.1N HCl for 24 h, storage in 0.1N NaOH for 24 h, heating in water bath at 90 °C for 24 h and storage in 3% H₂O₂ with exposure to UV for 24 h. Table 10 shows the results of the stability experiments. Methyl paraben was not affected by the different conditions. It was found that the degradation products did not interfere with the analytes peaks and their assays were not affected.

Storage conditions

The pH and appearance of the stored extract were evaluated in addition to the assay of the

Table 10: The results of stability tests under different conditions.

Conditions	Storage in 0.1N HCl for 24 h	Storage in 0.1N NaOH for 24 h	Heating in water bath at 90 °C for 24 h	Storage in 3% H ₂ O ₂ with exposure to UV for 24 h
GLY	☑	☒	☑	☑
SB	☒	☒	☑	☒
MP	☒	☒	☒	☒
PP	☒	☑	☒	☑

☑ Degradation products appeared in the chromatogram and/or the analyte peak disappeared

☒ not affected

components of interest. The obtained results of the accelerated stability study for glycyrrhizic acid, sodium benzoate, methyl 4-hydroxybenzoate, and propyl 4-hydroxybenzoate in licorice aqueous extract during 12 weeks showed that there were significant changes in the pH values of the stored samples of LAE at high temperatures (50 °C and 70 °C) and in the assay results of their components of interest. GLY was the most affected analyte while PP was the least affected one.

The data of the analysis of LAE were obtained at the start point (Table 11) and after different time periods at the following conditions:

Table 11: Zero time analysis results of LAE stored samples.

Test	Results at zero time
Appearance	Dark brown liquid
pH	5.32
Assay	
Na-benzoate	101.5 %
Methyl paraben	101.0 %
Propyl paraben	99.6 %
Glycyrrhizic acid	102.3 %

The pH values for LAE samples stored during 1-12 weeks at RT/DL, 25 °C/65%RH, 50 °C and 70 °C were: 5.30-5.25, 5.29-5.24, 5.25-5.13 and 5.18-4.29, respectively. The assay values for GLY samples stored during 1-12 weeks at RT/DL, 25 °C/65%RH, 50 °C and 70 °C were 102.3-91.8%, 101.7-91.0%, 101.3.0-91.6%, 101.3-76.5%. The assay values for SB samples stored during 1-12 weeks at RT/DL, 25 °C/65%RH, 50 °C and 70 °C were 102.4-93.0%, 102.0-91.0%, 100.2.0-93.9%, 101.6-91.7%. The assay values for methyl paraben samples stored during 1-12 weeks at RT/DL, 25 °C/65%RH, 50 °C and 70 °C were 101-91.2%, 101.9-91.1%, 99.3.0-90.6%, 100.2-81.7%. The assay values for propyl paraben samples stored during 1-12 weeks at RT/DL, 25 °C/65%RH, 50 °C and 70 °C were 97.6-88.2%, 101.0-NT%, 94.0.0-87.3%, 96.72-80.1%.

The stability data of LAE samples stored during 4 weeks were obtained at 40 °C /75%RH. The results are not shown here.

CONCLUSIONS:

A high performance liquid chromatographic (HPLC) analytical method using a PDA detector at 254 nm and a Lichro CART® Purospher STAR, C18, 5µm (250 x 4.6 mm) analytical column with a simple mobile phase of potassium acetate buffer pH 3.60: acetonitrile (68.8: 31.2) v:v was successfully developed for the assay of glycyrrhizic acid, sodium benzoate, methyl 4-hydroxybenzoate, and propyl 4-hydroxybenzoate in licorice aqueous extracts.

The method was simple and reliable and did not need long extraction procedures.

The validation of the analytical method indicated its suitability for the intended use. The method could be applied for stability studies of the analytes in licorice aqueous extracts, thus it was considered a stability indicating method. It was selective, accurate, precise, and linear within its specified range (80-120%). The method can be applied in similar patterns for the identification of low concentrations of extract components.

The developed RP-HPLC analytical method for the routine assay of GLY and SB in alcoholic liquid extracts was validated for its intended use.

REFERENCES

- 1.H. Hayashi, N. Hiraoka, Y. Ikeshiro, H. Yamamoto, *Plant Science*, 116(2), 233 (1996)
- 2.L. RenJie *Carbohydrate Polymers*, 74, (4), 858 (2008)
- 3.W. Li, Y. Asada, and T. Yoshikawa, *Phytochemistry*, 55(5), 447-456 (2000)
- 4.V. Gupta, A. Fatima, U. Faridi, A. Negi, K. Shanker, J. Kumar, N. Rahuja, S. Luqman, B. Sisodia, D. Saikia, M. Darokar, S. Khanuja, Jo. *Ethnopharmacology*, 116(2), 377-380 (2008)
- 5.C. Chandrasekaran, K. Sundarajan, A. Gupta, H. Srikanth, J. Edwin, A. Agarwal, *Regulatory Toxicology and Pharmacology*, 61(3),373-380(2011)
- 6.W. Liao, Y. Lin, T. Chang, W. Huang, *Food Chemistry*, 132(4), 2188-2193(2012)
- 7.Z. Jingze, G. Wenyuan, Y. Shuo, Z. Yaxin, *Iranian Journal of Pharmaceutical Research* 11(2), 601-609 (2012)
- 8.L. Siracusa, A. Saija, M. Cristani, F. Cimino, M. D'Arrigo, D. Trombetta, F. Rao, G. Ruberto *Fitoterapia*, 82(4), 546-556 (2011)
- 9.J. Kim, S. Oh, H. Kwon, Y. Oh, S. Lim, H. Shin, *Biochemical and Biophysical Research Communications*, 345(3), 1215-1223 (2006)
- 10.C. Fiore, M. Eisenhut, E. Ragazzi, G. Zanchin, D. Armanini, Jo. *Ethnopharmacology*, 99(3), 317-324 (2005)
- 11.D. Dhingra and A. Sharma, *Neuro-Psychopharmacology and Biological Psychiatry*, 30(3), 449-454 (2006)
- 12.S. Rekha and A. Parvathi, *International Journal of Pharma and Bio Sciences*, 3(2), 357-362 (2012)
- 13.H. Xiaowen, Z. Fucheng, J.Ye, *Chromatographic Science*, 50 (6), 457-463 (2012)
- 14.Q. Xue, Y. Min, X.Cheng, B. Tao, Y.Wen-zhi, L.Chun-fang, M.Wen-juan, G. De-an, *Steroids*, 77(7), 745-755 (2012)
- 15.A. Farag, P. Andrea, A. Wessjohann, L. Farag, *Phytochemistry*, 76, 60-72(2012)
- 16.C. Jingxiang, W. Shaoyan, G. Hong, *Advanced Materials Research*, 455-456, (2012)
- 17.Y. Qinghua, Y. Li, Z. Huirong, N. Liyuan, *Asian Journal of Chemistry*, 24(2), 899-902 (2012)

18. Z. Jing-Ze, G. Wen-Yuan, G. Ying, L. Dai-Lin, H. Lu-Qi, *Acta Physiologiae Plantarum*, 33(6), 2511-2520 (2011)
19. T. Sweta, B. Upendra, S. Laxmi, G. Anand, S. Shailendra, *Asian Journal of Pharmacy & Life Science*, 1(2), 124-127 (2011)
20. K. Deepak, K. Kanchan, P. Nitin, *Liquid Chromatography & Related Technologies*, 34(15), 1502-1517 (2011)
21. L. Hai-yun, X. Yong, Y. Mei-zi, Z. Shu-ping, *Medicinal Plant*, 2(5), 28-29,32 (2011)
22. S. Hanwen and L. Lixin, *American Journal of Analytical Chemistry*, 2(2), 217-222 (2011)
23. L. Yan-Jing, C. Jun, L. Ying, L. Qin, Z. Yun-Feng, F. Yu, L. Ping, *Journal of Chromatography*, 1218(45), 8181-8191 (2011)
24. T. Guangguo, Z. Zhenyu, Z. Hai, Z. Liang, L. Yi, D. Xin, L. Ziyang, Z. Guoqing, C. Yifeng, *Rapid Communications in Mass Spectrometry*, 24(2), 209-218 (2010)
25. Z. Min, W. Meng-Yue, L. Ya-Qian, S. Hai-Ming, L. Xiao-Bo, *Food and Drug Analysis*, 19(2), 131-138 (2011)
26. G. Pingping, H. Xi, Z. Meizuo, S. Ming, Q. Feng, Z. Chunhu, *Medicinal Plants Research*, 4(24), 2615-2621 (2010)
27. Y. Ru-zhen, W. Jin-hua, W. Ming-lin, Z. Rong, L. Xiao-yu, L. Wei-hua, *Journal of Chromatographic Science*, 49(9), 702-708 (2011)
28. H. Mao-qiu, Z. Ming-shi, L. Cun-xiong, Z. Zhi-bing, *Medicinal Plant*, 2(5), 25-27 (2011)
29. G. Abdolmohammad, M. Seyavash, S. Reza, K. Morteza, *Fresenius Environmental Bulletin*, 20(6), 1406-1413 (2011)
30. K. Ibrahim, V. Laurian, L. Doina, C. Andreia, I. Bianca, L. Mihai Ioan, *Farmacologia*, 58(4), 416-421 (2010)
31. I. Revilla, S. Pérez-Magariño, M.L. González-SanJosé, S. Beltrán, *Journal of Chromatography A*, 847(1-2), 83-90 (1999)
32. K. Helmja, M. Vaher, T. Püssa, M. Kaljurand, *Journal of Chromatography A*, 1216(12), 2417-2423 (2009)
33. R. Quirantes-Piné, L. Funes, V. Micol, A. Segura-Carretero, A. Fernández-Gutiérrez, *Journal of Chromatography A*, 1216(28), 5391-5397 (2009)
34. J. Regueiro, E. Martín-Morales, G. Álvarez, J. Blanco, *Food Chemistry*, 129(2), 672-678 (2011)

ЕДНОВРЕМЕНЕН АНАЛИЗ НА ГЛИЦИРОВА КИСЕЛИНА И КОНСЕРВАНТИ ВЪВ ВОДНИ ЕКСТРАКТИ ОТ ЖЕНСКО БИЛЕ ЧРЕЗ HPLC/PDA

Х. Абу-Шанди¹, А.Р. Халауа², А.С. Салам³, Г. Ал-Едуан⁴, А.Р. Ал-Тауаха⁵, Ш.А. Албаджауи², Е.С.М. Абу-Намех^{2*}

¹ Департамент по химия, Научен факултет, Технически университет в Тафила, Йордания

² Департамент по химия, Научен факултет, Приложен университет Ал-Балкха, Ал-Салт, Йордания

³ Фармацевтични индустрии "Ал-Такхадом", Аман, Йордания

⁴ ДАД-индустрии, Аман, Йордания

⁵ Департамент по биологични науки, Университет Ал Хусейн бин Талал, Маан, Йордания

Постъпила на 29 януари 2014 г.; коригирана на 13 март, 2014 г.

(Резюме)

Успешно е разработен аналитичен метод за високо-ефективна течна хроматография (HPLC) за определянето на глицирова киселина (GLY), натриев бензоат (SB), метил 4-хидроксibenзоат (MP), и пропилен 4-хидроксibenзоат (PP) във водни екстракти от женско биле. Методът използва аналитична колона Lichro CART® Purospher STAR, C18, 5µm (250 x 4.6 mm) с проста подвижна фаза от калиев ацетатен буфер:ацетонитрил в обемно съотношение (68.8: 31.2). Анализът се извършва при PDA-детектор при дължина на вълната 254 nm. Методът дава линейна зависимост в интервал от концентрации 80%, 90%, 100%, 110% and 120%. Методът е точен възпроизводим и прецизен. Метил-парабенът (MP) е стабилен при променливи условия при съхранение в 0.1N HCl за 24 часа, 0.1N NaOH за 24 часа и 3% H2O2 и облъчване с ултравиолетова светлина и нагряване на водна баня. Другите изпитани компоненти показват различна стабилност при променящи се условия.

Mannitol as a radiation sensitive material for electron paramagnetic resonance dosimetry

Y. Karakirova*, N. Yordanov

Molecular Catalysis with Centre of EPR spectroscopy, Institute of Catalysis, Bulgarian Academy of Sciences, Sofia, Bulgaria

Received February 6, 2014; Revised March 27, 2014

The possibility of solid state/mannitol ($C_6H_8(OH)_6$) dosimeters as a radiation sensitive material for γ -ray irradiation using electron paramagnetic resonance (EPR) spectroscopy, is reported. The peak-to-peak signal amplitude of the first derivative of the EPR spectrum is used as a dosimetric index. The influence of some EPR parameters, such as the microwave power and modulation amplitude on the peak-to-peak height of the EPR spectra of the irradiated mannitol is studied. The dose response curves for γ irradiated mannitol in two dose ranges (1-20 Gy and 0.5-20kGy) are investigated. It was found that mannitol can be considered as a useful radiation sensitive material in the ranges of 1-20 Gy and 0.5-10 kGy. Sucrose is used for comparison and reference.

Keywords: EPR spectroscopy, irradiation, mannitol, free radicals

INTRODUCTION

Ionizing radiation generates stable free radicals in some materials. For quantitative determination of the radiation-induced free radicals, several methods are used. One of the most popular in this area is the electron paramagnetic resonance (EPR) spectroscopy. The problem for the determination of the absorbed dose of ionizing radiation using solid state/EPR dosimetry has attracted the attention of researchers for about 50 years. The advantages of these dosimeters are: simple and rapid dose evaluation, non-destructive analysis permitting repeated measurements and thus allowing storage for archival purposes.

In the last two decades the alanine-EPR dosimetric system was recognized by the International Atomic Energy Agency (1-3) as a routine, reference and transfer dosimeter for industrial irradiators operating in the kGy range of doses. The radiation sensitivity of alanine is comparatively low and this has prompted the search for alternative materials. In order to increase the sensitivity of the solid state/EPR dosimetric system, up to now several materials as: sucrose (4-8), lithium lactate (9), aspartame (10, 11), xylitol and sorbitol (12,13) have been studied as dosimetric materials. It is well known that ionizing radiation generates stable long-lived free radicals in some saccharides. Recent study shows that among several mono- and disaccharides, sucrose shows the best

dosimetric properties (14). Despite good dosimetric characteristics of alanine and sucrose, the investigators continued to look for others materials, which can be used as dosimeters.

In view of the importance of the problem, mannitol was studied as a possible dosimetric material.

The aim of the present work is to investigate the possibility for estimation of the absorbed dose gamma rays using mannitol/EPR dosimeters. Because of the complex EPR spectrum obtained after irradiation, the important step was to investigate the influence of some EPR spectrometers settings parameter. Mannitol investigated in this work has never before been considered for dosimetric purposes.

EXPERIMENTAL

Materials and preparation of the solid state/EPR dosimeters

Mannitol is a white, crystalline sugar alcohol with the chemical formula $C_6H_8(OH)_6$. It is used in analytical chemistry, medicine, foods and so on. In foods mannitol is used as a sweetener for people with diabetes, in mint candies, chewing gums and dried fruits.

Mannitol, used as a radiation sensitive material, was purchased from Aldrich and paraffin, used as a binding material, from Merck. Both of them were used as obtained.

The solid state/EPR dosimeters (SS/EPR) were prepared from a homogeneous mixture of mannitol (60 % w/w) and paraffin (40 % w/w) (15). Solid

* To whom all correspondence should be sent:
E-mail: daniepr@ic.bas.bg

dosimeters were pressed in the form of cylinders with diameter 4 mm and length of 10 mm.

Irradiation

The dosimeters were irradiated with γ -rays on a "Gamma-1300" irradiator (^{137}Cs) with a dose rate of 200 Gy/h in two dose ranges - 1-20 Gy and 0.5–20 kGy. The irradiation procedure was performed in air at room temperature. After irradiation all samples were kept in closed plastic bags at room temperature and were stored in dark.

In order to avoid all interferences in dose estimations due to any short-living species and transition EPR spectra, all measurements were performed at least 72 h after irradiation.

Isothermal annealing of the free radicals in the dosimeters

After irradiation, part of the mannitol dosimeters were kept for several h at 50°C in a desiccator. EPR spectra were recorded every hour. The aim was to investigate the time dependence of the dosimeters at 50°C.

Instrumentation

The EPR spectra were recorded at room temperature on a JEOL JES-FA 100 EPR spectrometer operating in the X-band, equipped with a standard TE₀₁₁ cylindrical resonator. The dosimeters were placed in quartz tubes and were fixed in the cavity center. The instrumental settings using the above spectrometer were: modulation frequency 100 kHz, magnetic field sweep 10 mT, time constant 0.3 s and sweep time 2 min. Other parameters as microwave power and amplitude of the magnetic field modulation were varied in order to find the most suitable value to record the maximal intensive and non-deformed EPR spectra.

RESULTS AND DISCUSSION

Features of the EPR spectrum of mannitol dosimeters

In a non-irradiated mannitol/EPR dosimeter, no EPR spectrum was recorded. After irradiation all dosimeters exhibited an EPR spectrum with g factor of 2.0170 ± 0.0002 of the most intense peak (Figure 1).

In the X-band it is unresolved and a complex signal contains several overlapped and not well resolved EPR patterns. The nature of these radicals is not cleared up to the moment.

It was found that the EPR spectrum of irradiated mannitol strongly depends on the applied microwave power and modulation amplitude.

Because of that, the first step after irradiation was to study the influence of these instrumental settings. A set of EPR spectra at different magnitudes of the microwave power is given in Figure 2.

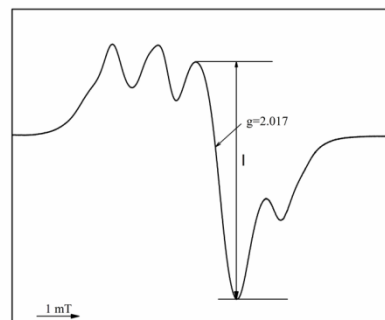


Fig. 1. EPR spectrum of γ irradiated mannitol EPR/dosimeter three days after irradiation with a dose of 10 kGy. The microwave power is 1 mW, modulation amplitude – 0.16 mT.

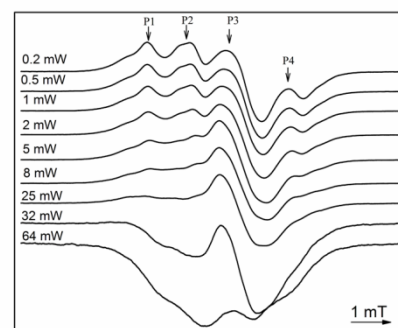


Fig. 2 A set of EPR spectra of γ irradiated mannitol at different microwave powers. Modulation amplitude is 0.05 mT.

It is seen from this figure that the EPR spectrum of the radiation-induced free radicals of mannitol has four peaks (noted as P1, P2, P3 and P4) and they are sensitive to the magnitude of the applied microwave power. It was found that the peaks P1, P2 and P4 have an equal behavior of saturation. They are saturated even at microwave power of ca. 0.2 mW. At a microwave power above 8 mW these peaks disappeared. Because of the same behavior of saturation from the applied microwave power we can conclude that the peaks P1, P2 and P4 are probably due to the one and the same radical. The peak P3 is slightly broadened at a microwave power higher than 1 mW, which unambiguously indicates a saturation effect. Figure 3 shows the dependence of EPR signal intensity as a function of the square root of microwave power.

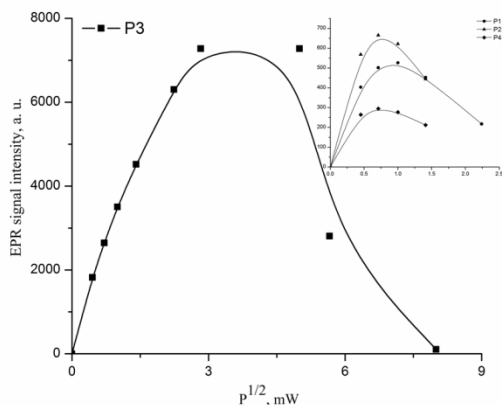


Fig. 3. The peak-to-peak signal intensity as a function of the square root of the applied microwave power. The modulation amplitude is 0.05 mT.

As can be seen, the peak-to-peak signal intensity of P3 strongly increases with the increase of the applied microwave power from 0.2 to 8 mW, reaching a maximum at ca. 25 mW, and decreases at higher microwave power values. At a microwave power of 64 mW the EPR signal reaches a minimum, which means that it is completely saturated. The peak-to-peak signal amplitude of the other peaks increase with microwave power to 0.2 mW and after that decrease because of saturation. In view of that, P3 was further used to study the EPR response of mannitol as a function of the absorbed dose ionizing radiation at a microwave power of 1 mW.

On the other hand, the EPR spectrum of irradiated mannitol depends on the applied modulation amplitude, as was mentioned before. Because of that, the dependence of the shape of the EPR signal to the applied modulation amplitude was studied. Figure 4 shows the dependence of peak-to-peak signal intensity as a function of applied modulation amplitude.

Linearity can be seen to about 0.16 mT; after that over-modulation of the separated EPR lines appears. In view of this, 0.16 mT modulation amplitude was chosen to examine the dose response of mannitol.

Time stability of radiation-induced EPR signals

From dosimetric point of view the time stability of radiation-induced EPR signals is an important feature for every EPR dosimeter. This is because solid state/EPR dosimeters have the advantage of being suitable for estimation of the absorbed dose high energy radiation not only immediately after

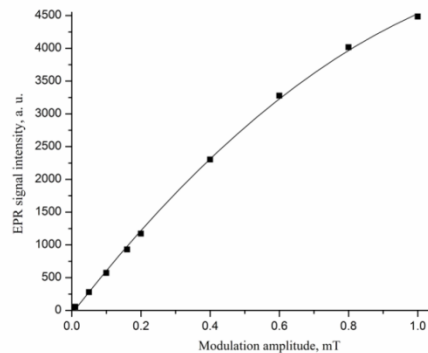


Fig. 4 The EPR signal intensity of γ irradiated mannitol as a function of applied modulation amplitude.

irradiation but also to be archived for future measurements. Previous works [6, 14, 16] show that immediately after irradiation, the shape and the intensity of the EPR spectra of saccharides undergo changes during a certain period of time, characteristic for each material. The EPR spectrum due to the remaining radical species, is then stable for a long time and can be used for dose estimations. The EPR spectrum of irradiated solid sucrose undergoes changes within 72 h after irradiation and then becomes stable [16]. Having this in mind, the EPR spectra of γ -irradiated mannitol were monitored from 3 days up to 3 months after the end of the irradiation (Figure 5).

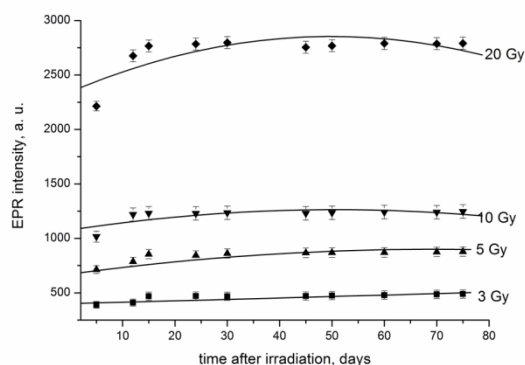


Fig. 5 Time stability of EPR signals intensity

The EPR spectra undergo small transformations in the first days after irradiation. It was found that the peak-to-peak signal intensity and the width of the signal noted as P3 in the EPR spectrum (Figure 2) have changed. As can be seen from Figure 5, the peak-to-peak signal intensity of irradiated mannitol increased with about 25%. The above results show that in mannitol some processes take place during the irradiated and in the first days after irradiation, which lead to broadening of the lines and increasing of the peak-to-peak signal amplitude. These changes could be due to the influence from

more short-lived species fading out during the first 10 days and saturated at a lower microwave power. After 10 days, the line width and the peak-to-peak amplitude became stable. In order to shorten the period to reach a stable EPR spectrum (in view of line width and peak-to-peak amplitude) immediately after irradiation the irradiated samples were kept at 50°C for several h. An EPR spectrum was recorded every h. It was found that heating for 5 h at 50°C is enough to stabilize the EPR spectrum of γ irradiated mannitol. Following this procedure it is not necessary to wait 10 days before starting dosimetric measurements.

EPR response of mannitol to radiation dose

For a dosimeter a linear dose response is required for relative dose measurements, but most dosimeters show such a good behaviour only within a certain dose range. The dependence of the EPR signal intensity of γ irradiated mannitol on the absorbed dose of ionizing radiation in two dose ranges 1-20 Gy and 0.5-20 kGy was investigated (Figure 6).

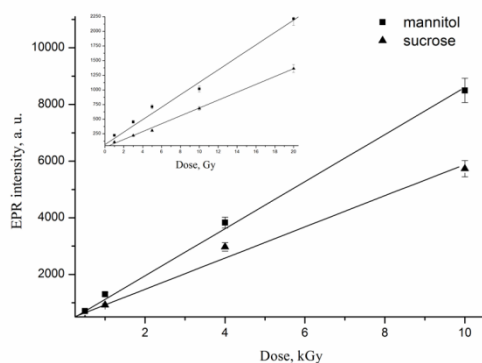


Fig. 6. The dependence of the EPR signal intensity of γ irradiated mannitol and sucrose on the absorbed dose ionizing radiation in two dose ranges: 1 - 20 Gy and 0.5 - 10 kGy.

In the sample irradiated with 1 Gy of γ rays the contribution of the noise to the signal is very large and it is necessary to make more than 35 accumulations to reach $S/N \geq 2$. For samples irradiated with 3 Gy the EPR measurement was repeated 10 times to improve the signal-to-noise ratio. In case of 10 accumulations, the ratio S/N is equal to 2. In view of this, the detection limit was obtained as 1 Gy. It is possible to reach even lower doses, but then more than 100 accumulations should be done. Mannitol shows a linear dose response for doses of 1 to 20 Gy, and from 0.5 to 10 kGy with saturation at higher doses. In comparison with mannitol, sucrose shows a linear dependence of the EPR signal intensity of the

absorbed dose ionizing radiation in the investigated dose range (to 20 kGy). In view of radiation sensitivity, mannitol shows good results comparable with these of sucrose, but it can be used for doses up to 10 kGy.

CONCLUSIONS

Mannitol is a useful dosimetric material for dose ranges of 1 – 20 Gy and 0.5 – 10 kGy. It has the disadvantage that a few days are needed before the assumed unstable short-lived radicals have decayed. This disadvantage can be eliminated with the proposed procedure of isothermal annealing.

On the basis of the microwave power saturation it was found that at least two different radicals are present in the γ irradiated mannitol.

The present studies on the properties of mannitol as a radiation sensitive material show its suitability as an alternative to sucrose, but with some limitations:

- the detection limit is about 1 Gy, whereas it is about 0.5 Gy for sucrose;
- the maximal dose of radiation that can be measured is up to 10 kGy, whereas it is 20 kGy for sucrose.

The obtained results show that mannitol is a promising dosimetric material, but there is still work to be done before it can be taken in routine use as a dosimeter.

Acknowledgements: YK thanks the European Social Fund within the framework of Operating Program Development of Human Resources [Grant BG051PO001-3.3.06-0050] for the financial support.

REFERENCES

1. K. Mehta, R. Girzikowsky, *Appl. Radiat. Isot.*, **47**, 1189 (1996).
2. K. Mehta, Proceedings of the IAEA International Symposium on "Techniques for high Dose dosimetry in Industry, Agriculture and Medicine", IAEA-TECDOC-1070, Vienna, **11** (1999).
3. W. J. Nam, D. F. Regulla, *Appl. Radiat. Isot.*, **40**, 953 (1989).
4. T. Nakajima, *Health Phys.*, **55**, 951 (1988).
5. T. Nakajima, *Appl. Radiat. Isot.*, **46**, 819 (1995).
6. N. Yordanov, V. Gancheva, E. Georgieva, *Radiat. Phys. Chem.*, **65**, 269 (2002).
7. P. Fattibene, T. L. Duckworth, M. F. Desrosiers, *Appl. Radiat. Isot.*, **47**, 1375 (1996).
8. C. Flores, E. B. Cabrera, T. Calderün, E. Muñoz, E. Adem. J. Hernández, J. L. Boldú, P. Ovalle, H. S. Murrieta, *Appl. Radiat. Isot.*, **52**, 1229 (2000).
9. G. M. Hassan, M. Ikeya, S. Toyoda, *Appl. Radiat. Isot.*, **49**, 823 (1998).

10. A. Kinoshita, F. A. Jose, O. Baffa, *Health Phys.*, **98**, 406 (2010).
11. A. Maghraby, E. Salama, *Radiat. Prot. Dos.*, **139**, 505 (2010).
12. E. E. Budzinski, W. R. Potter, H. C. Box, *J. Chem. Phys.*, **72**, 972 (1980).
13. A. Israelsson, H. Gustafsson, E. Lund, *Radiat. Prot. Dos.*, **154**, 133 (2013).
14. Y. Karakirova, N.D. Yordanov, H. DeCooman, H. Vrielinck, F. Callens, *Radiat. Phys. and Chem.*, **79**, 654 (2010).
15. N. D. Yordanov, Y. Karakirova, *Radiat. Meas.*, **42**, 347 (2007).
16. N. Yordanov, E. Georgieva, *Spectrochim. Acta Part A*, **60**, 1307 (2004).

МАНИТОЛ КАТО РАДИАЦИОННО ЧУВСТВИТЕЛЕН МАТЕРИАЛ ЗА ДОЗИМЕТРИЯ С ЕЛЕКТРОН ПАРАМАГНИТЕН РЕЗОНАНС

Й. Каракирова*, Н. Йорданов

Молекулен катализ с център по ЕПР спектрометрия, Институт по катализ, Българска академия на науките, София, България

Постъпила на 16 февруари, 2014 г.; коригирана на 27 март, 2014 г.

(Резюме)

Представена е възможността за използване на твърдо тяло/дозиметри, съдържащи манитол, като радиационно чувствителен материал за гама облъчване, с помощта на електрон парамагнитен резонанс спектроскопията. Като дозиметричен индекс е използвана амплитудата на сигнала от пик до пик на първата производна на ЕПР спектъра. Изследвано е влиянието на апаратурните ЕПР параметри, мощност на микровълновото лъчение и амплитуда на модулация, върху интензитета на ЕПР сигнала на облъчен манитол. Изследван е дозовия отклик на гама облъчен манитол в две области от дози (1 – 20 Gy и 0.5 – 10 kGy). Установено е, че манитолът може да бъде полезен радиационно чувствителен материал в областта от 1 до 20 Gy и от 0.5 до 10 kGy. Като референтен материал е използвана захароза.

Phenolic profile, antimicrobial and anti-inflammatory activity of *Carum copticum* L. essential oil

M. Kazemi

Department of Horticultural Science, Faculty of Agricultural Science and Natural Resources, Science and Research Branch, Islamic Azad University, Tehran, Iran

Received February 7, 2014; Revised March 7, 2014

Ajowan (*Carum copticum*) is an annual herbaceous plant belonging to the *Umbelliferae* family. The seeds of *Carum copticum* have a therapeutic effect on some cutaneous, neural, and urinary tract disorders. The present study reports the chemical composition, antimicrobial activity, antioxidant and anti-inflammatory properties of *Carum copticum* essential oil and its main compounds. The essential oil was obtained from the seeds of the *Carum copticum* by hydrodistillation and analysed by GC/MS. The major components were carvacrol (1%), *p*-cymene (23%), γ -terpinene (23%), β -pinene (5%), α -thujene (3%), sabinene (0.51%), α -phyllanderene (1.6%), α -pinene (1%), terpinene-4-ol (0.1%), thymol (26.03%), β -phyllanderene (1%), myrcene (1%) and limonene (1.05%). The essential oil was also subjected to antifungal and antibacterial tests, using the minimum inhibitory concentration (MIC) and minimal bactericidal concentration (MBC) method. The essential oil was particularly active against *Candida parapsilosis*, with the lowest MIC and MBC value (1.05 mg/ml). Furthermore, the essential oil and its main compounds showed a potent NO scavenging effect and inhibited inducible NO synthase expression. In conclusion, these results support the use of the essential oil and its main compounds for their anti-inflammatory properties and antimicrobial activity.

Keywords: *Carum copticum*, Essential oil, Antimicrobial activity, Antioxidant activity, Anti-inflammatory activity.

INTRODUCTION

In recent years, essential oils have been traditionally used for their antimicrobial, antioxidant, anti-inflammatory and antimicrobial activity. The antimicrobial and anti-inflammatory properties of essential oils and their constituents from a wide variety of plants have been assessed [1]. Antimicrobial and antioxidant properties of certain plant essential oils towards human and animal pathogens have been well documented and reviewed by several authors [2,3]. Chevallier [4] reported that essential oils are used safely in herbal medicine as antimicrobial, antioxidant and anti-inflammatory compounds. Ajowan (*Carum copticum*) is an annual herbaceous plant belonging to the *Umbelliferae* family which grows in India, Iran, and Egypt with white flowers and small, brownish seeds [5]. During the past centuries, several therapeutic effects including anti-vomiting, antiasthma and anti-spasm, are postulated in the Iranian traditional medicine for *Carum Copticum* fruits [6]. The major component of its fruit is essential oil which is composed of γ -terpinene, *p*-cymene, α -pinene, β -pinene, and other substances such as thymol and carvacol [7]. The seeds of *Carum copticum* have a therapeutic effect on some cutaneous, neural, and urinary tract disorders [5].

Thangam and Dhananjayan [8] reported that *Carum copticum* fruit oil has diuretic, carminative, analgesic, anti-dyspnoea and anti-inflammatory properties. Singh *et al.* [9] found that *Carum copticum* is very effective against some bacteria and its effect on the digestive tract may be due to its antibacterial activity. Due to the application of *C. copticum* as an annual herbaceous plant in folk medicine, the purpose of the present work was to evaluate the anti-inflammatory properties, antioxidant and antimicrobial activities of *Carum copticum* essential oil and relate them with the chemical composition, for further application in pharmaceutical industries as natural valuable products.

MATERIALS AND METHODS

Plant material and oil isolation

The plant materials were collected from the mountains at the city of Ilam-Iran in July 2013. The Ajowan seeds were ground and the resulting powder was subjected to hydrodistillation for 3 h in an all glass Clevenger-type apparatus according to the method recommended by the European Pharmacopoeia [10]. The obtained essential oils were dried over anhydrous sodium sulphate and after filtration, were stored at +4 °C until tested.

* To whom all correspondence should be sent:
E-mail: kazemimohsen85@gmail.com

Essential oil analysis

The GC/MS analyses were executed on a Hewlett-Packard 5973N gas chromatograph equipped with a column HP-5MS (30 m length × 0.25 mm i.d., film thickness 0.25 μm) coupled to a Hewlett-Packard 5973N mass spectrometer. The column temperature was programmed at 50 °C as an initial temperature, holding for 6 min, with 3 °C increases per min to a temperature of 240 °C, followed by a temperature enhancement of 15 °C per min up to 300 °C and holding at the mentioned temperature for 3 min. Injector port temperature was 290 °C and helium was used as carrier gas at a flow rate of 1.5 ml/min. The ionization voltage of the mass spectrometer in the EI-mode was 70 eV and ionization source temperature was 250 °C. Linear retention indices for all components were determined by coinjection of the samples with a solution containing a homologous series of C₈-C₂₂ n-alkanes and comparing them and their mass spectra with those of authentic samples or with available library data of the GC/MS system (WILEY 2001 data software) and Adams spectral libraries [11].

Antioxidant activity

The efficacy of the essential oils to scavenge 2,20-diphenyl-1-picrylhydrazyl (DPPH) radicals was evaluated using a spectrophotometric method [12,13] based on the bleaching of the bluish-red or purple color of a DPPH solution as a reagent. Briefly, a 50 ml volume of various dilutions of each sample was mixed with 5 ml of 0.004% methanol solutions of DPPH followed by 30 min incubation at ambient temperature. Thereafter, the sample absorbance was recorded against control at 517 nm. The inhibition percentages were measured using Eq. (1). The antioxidant activity of the test samples at a concentration providing 50% inhibition, were considered as IC₅₀ (g/ml).

$$\text{Inhibition percent} = \frac{\text{Abs}_{\text{control}} - \text{Abs}_{\text{sample}}}{\text{Abs}_{\text{control}}} \times 100 \quad (1)$$

Butylhydroxyanisole (BHA) and ascorbic acid were used as positive controls. All experiments were repeated three times and the average results and standard deviations were calculated.

Antibacterial activity

Gram-positive bacteria: *Bacillus cereus* (ATCC 10876), *Enterobacter cloacae* (ATCC 13047), *Enterococcus faecalis* (ATCC 49452), *Listeria monocytogenes* (ATCC15313), *Staphylococcus aureus* (ATCC 25923). Gram-negative bacteria: *Acinetobacter baumannii* (ATCC 19606),

Escherichia coli (ATCC 25922), *Klebsiella pneumoniae* (ATCC 700603), *Pseudomonas aeruginosa* (ATCC 27853), *Proteus mirabilis* (ATCC 35659), *Salmonella typhimurium* (ATCC 13311), *Citrobacter freundii* (ATCC 8090). Fungal strains: *Candida albicans* (ATCC 10231), *Candida tropicalis* (ATCC 13803), *Candida parapsilosis* (ATCC 90018), *Aspergillus niger* (ATCC 16404) and *Aspergillus fumigatus* (ATCC 46645).

Screening of antimicrobial activity

The agar disc diffusion assay was employed for determination of the antimicrobial activity of the essential oil [14]. Briefly, a suspension of the test organism (2×10^8 CFU/ml) was spread on the solid media plates. Filter paper discs (6 mm in diameter) were individually impregnated with 15 μl of the diluted oil aliquots (200 mg/ml stock), then placed on the inoculated plates for 2 h at 4 °C. The plates were incubated at 37 °C for 24 h for bacteria, and at 30 °C for 48 h for fungal strains, using a spread restraint method for epiphytes at 30 °C for 48 h [15]. The diameters of the inhibition zones (DD) were measured in millimeters. Each test was carried out in triplicate, repeated three times, and the average was calculated for the inhibition zone diameters.

Determination of minimum inhibitory concentration (MIC)

A broth microdilution method was used to determine the MIC and MBC [16,17]. All tests were performed in Mueller Hinton broth and Sabouraud Dextrose broth, both supplemented with ethanol at a final concentration of 0.5% (v/v) for both bacteria and fungi. Serial doubling dilutions of the oils were prepared in a 96-well plate, ranging from 0.05 to 200.00 mg/ml. The final concentration of each strain was adjusted to 5×10^4 CFU/ml. Plates were incubated at 37 °C for 24 h for bacteria. The MIC was defined as the lowest concentration of the essential oil at which the microorganism does not demonstrate visible growth. The microorganism growth was indicated by the turbidity.

Determination of minimum bactericidal concentration (MBC)

To determine MBC, broth was taken from each well and incubated in Mueller Hinton Agar at 37 °C for 24 h for bacteria. The MBC was defined as the lowest concentration of the essential oil at which the incubated microorganism was completely killed [16,17]. Each test was carried out in triplicate and repeated three times.

Anti-inflammatory activity

To evaluate the anti-inflammatory potential of the oils, NO production in lipopolysaccharide (LPS)-stimulated macrophages was used. Exponentially growing macrophages (RAW 264.7 cells) were placed in 24-well microplates at a density of 2×10^5 cells per well in 400 μ l of culture medium and were allowed to adhere for 24 h at 37 °C under 5% CO₂. Cells were then treated with increasing concentrations of essential oil and pure compounds dissolved in DMSO. The final concentration of solvent in the culture medium was maintained at 0.5% (v/v) to avoid solvent toxicity. Cells were then stimulated with 100 μ g/ml LPS and incubated at 37°C under 5% CO₂. After 24 h, cell-free supernatants were collected and NO was measured by the modified method of Green *et al.* [18]. Griess reagent (50 μ l of 1% sulphanilamide and 50 μ l of 0.1% N-1-naphthylethylenediamine dihydrochloride in 2.5% H₃PO₄) was added in equal volume (100 μ l) to cell supernatant and incubated at room temperature for 30 min. N(G)-nitro-L-arginine methyl ester (L-NAME) was used as a positive control. Absorbance was measured using an ELISA automatic microplate reader at 550 nm and the nitrite concentration was determined by regression analysis performed with serial dilutions of sodium nitrite [19].

Statistical analysis

Main effects indicating significant differences were tested using Duncan's multiple range test. Correlation and regression coefficients were

performed using Statistical Package for the Social Sciences (SPSS).

RESULTS AND DISCUSSION

Chemical composition of the essential oil

The chemical composition of *Carum copticum* essential oil is shown in Table 1.

Thirteen compounds representing 97.29 % of *C. copticum* essential oil were identified. The major organic compounds detected in the seeds oils were: carvacrol (1%), *p*-cymene (23%), γ -terpinene (23%), *b*-pinene (5%), α -thujene (3%), sabinene (0.51%), α -phyllanderene (1.6%), α -pinene (1%), terpinene-4-ol (0.1%), thymol (36.03%), *b*-phyllanderene (1%), myrcene (1%) and limonene (1.05%). Thangam and Dhananjayan [8] reported thymol as the main constituent (36.7%) of the *C. copticum* essential oil. A previous report by Rasooli *et al.*, [20] indicated that the major constituent of the essential oil of *C. copticum* was *p*-cymene and in other studies, γ -terpinene was the second most abundant constituent of the oil [5]. Similar to previous studies [21], thymol was found to be the major constituent of the oil *C. copticum*, while others reported carvacrol as the major constituent of this oil [22]. It has been reported that the chemical composition of the essential oil is highly influenced by climatic conditions and geographical factors [2, 23]. The high level of *p*-cymene and thymol in the essential oil could contribute to the valorization of Iranian *C. copticum* species, since this monoterpene is of great importance in industry as intermediate for the synthesis of fragrances, pharmaceuticals and herbicides.

Table 1. Chemical composition of *Carum copticum* essential oil

	Components	%	Retention Index ^a	Identification Methods
1	Carvacrol	1	1306	MS, RI
2	<i>p</i> -cymene	23	1028	MS, RI, CoI
3	γ -terpinene	23	1060	MS, RI, CoI
4	β -pinene	5	948	MS, RI, CoI
5	α -thujene	3	932	MS, RI
6	Sabinene	0.51	981	MS, RI
7	α -phyllanderene	1.6	1000	MS, RI
8	α -pinene	1	941	MS, RI, CoI
9	Terpinene-4-ol	0.1	1177	MS, RI
10	Thymol	36.03	1294	MS, RI, CoI
11	β -phyllanderene	1	1035	MS, RI
12	Myrcene	1	523	MS, RI
13	Limonene	1.05	610	MS, RI
	Total	97.29		

^aThe retention Kovats indices were determined on a capillary column. MS= Mass Spectroscopy, RI= Retention Index, CoI= Co injection with authentic compounds

Table 2. Antimicrobial activity of the essential oils from *C. copticum* using paper disc-diffusion method and microdilution test

Microorganisms	The essential oil of <i>C. copticum</i>			Antibiotic		
	DD ^a	MIC ^b	MBC ^b	DD ^c	MIC ^b	MBC ^b
<i>Bacillus cereus</i>	24	2	2	18	2 ^f	2 ^f
<i>Enterobacter cloacea</i>	14	2.5	2.5	17	5 ^f	3.5 ^f
<i>Enterococcus faecalis</i>	13	4	3.5	15	3 ^f	3 ^f
<i>Listeria monocytogenes</i>	16	4.5	4.5	16	2 ^f	2.5 ^f
<i>Staphylococcus aureus</i>	NA ^e	NA ^e	NA ^e	14	4.25 ^f	6 ^f
<i>Acinetobacter baumannii</i>	16	5	5	14	4 ^f	4 ^f
<i>Escherichia coli</i>	12	5.5	5.5	16	3.5 ^f	3.5 ^f
<i>Klebsiella pneumoniae</i>	23	4	5	19	2.5 ^f	3 ^f
<i>Pseudomonas aeruginosa</i>	NA ^e	NA ^e	NA ^e	20	4 ^f	3.5 ^f
<i>Proteus mirabilis</i>	22	3.5	3.5	20	3 ^f	3 ^f
<i>Salmonella typhimurium</i>	20	2.5	2.5	17	4 ^f	4 ^f
<i>Citrobacter freundii</i>	21	3	3	18	2.5 ^f	4 ^f
<i>Candida albicans</i>	21	2	3	16	5 ^d	5.5 ^d
<i>Candida tropicalis</i>	22	2.5	3	18	4 ^d	3.5 ^d
<i>Candida parapsilosis</i>	27	1.05	1.05	19	2 ^d	3 ^d
<i>Aspergillus niger</i>	20	2.5	2.5	19	3 ^d	3 ^d
<i>Aspergillus fumigatus</i>	23	3.5	4	18	4.5 ^d	4.5 ^d

DD (mm): disc diffusion; a: tested at a concentration of 1.2 mg/disc; b: values given as mg/ml; c: tested at a concentration of 5.0 µg/disc; d: Streptomycin; e: NA. Not Active. f: Netilmycin.

Antimicrobial activity

The *in vitro* antimicrobial activities of *C. copticum* essential oil against the studied microorganisms were qualitatively and quantitatively assessed by the presence or absence of inhibition zones, disc diameters of zone of inhibition (DDs), minimum bactericidal concentrations (MBCs) and minimum inhibitory concentrations (MICs) values (Table 2).

According to the results given in Table 2, *C. copticum* essential oil exhibited moderate to strong and, in few cases, very weak antimicrobial activity against the tested species. However, the essential oil of *C. copticum* failed to show antibacterial activity toward *Staphylococcus aureus* and *Pseudomonas aeruginosa*. Results obtained by disc-diffusion method and microdilution test, followed by measurements of MIC and MBC values indicated that *Candida parapsilosis* is the most sensitive microorganism tested, with the lowest MIC and MBC value (1.05 mg/ml) in the presence of the oil isolated from *C. copticum*. The *C. copticum* oil showed the strongest activity against both types of microorganisms (MIC 2.5–4.5 mg/ml and MBC 2.5–5 mg/ml for bacteria and MIC 1.05–3.5 mg/ml and MBC 1.05–4 mg/ml for fungi). After this, the goal of the present work was to evaluate how the bacteriostatic and bactericidal effectiveness of the *C. copticum* essential oil was affected by the relative concentration of their major volatile compounds. In our study, most of the

antimicrobial activity of the essential oil from *C. copticum* appears to be associated with phenolic compounds (thymol, γ -terpinene and ρ -cymene); these results agree with those reported by other authors [20, 24]. Trombetta *et al.* [25] reported that thymol might induce antimicrobial action by perturbation of the lipid fraction of the microorganism plasma membrane, resulting in alteration of the membrane permeability and leakage of intracellular materials. P -cymene is another major compound identified in *C. copticum* oil that is a hydrophobic molecule and causes swelling of the cytoplasmic membrane [2]. *C. copticum* has shown high antimicrobial activity by incorporating cymene in the lipid bilayer of bacteria, facilitating the transport of phenolic monoterpenes of EOs across the cytoplasmic membrane [26]. The results from the disc diffusion method and microdilution test, followed by measurement of minimum inhibitory concentration (MICs) and minimum bactericidal concentrations (MBCs), indicated that *Bacillus cereus* and *Candida parapsilosis* were the most sensitive microorganisms tested, showing the largest inhibition zones and the lowest MICs and MBCs values. Least activity was exhibited against *Escherichia coli*, with the smallest inhibition zones and the highest MICs and MBCs values. In agreement with our results, Cantore *et al.* [27] reported that the Gram-negative strains of bacteria, especially *Escherichia coli*, have lower sensitivity to essential oils. Food poisoning originating from

foods contaminated by both bacteria (Gram-positive and Gram-negative) and fungi causes concern to society and to industry. A major problem in antimicrobial chemotherapy is the increasing resistance to antibiotics, which leads to insufficiency of the antimicrobial treatment [28]. Spices and herbs have been safely used since ancient times as food flavoring agents and herbal medicines and are now mainly “generally regarded as safe” (GRAS). Recently, there have been considerable emphasis studies involving essential oils and extracts of spices and herbs on inhibiting the growth of microbes [29].

Antioxidant activity

Antioxidant activity is a complex process usually occurring through several mechanisms. Due to its complexity, the evaluation of the antioxidant activity for pure compounds or extracts should be carried out by more than one test method [30]. The lower IC₅₀ value indicates a stronger ability of the extract to act as a DPPH scavenger while the higher IC₅₀ value indicates a lower scavenging activity, as more scavengers were required to achieve 50% scavenging reaction. The results presented in Table 3 reveal that *C. copticum* essential oil and its main constituents exhibit a remarkable activity. In particular, thymol clearly showed higher activity (IC₅₀ = 19.24 ± 0.5 µg/ml) followed by *C. copticum* essential oil (20 µg/ml), γ-terpinene (20.11 ± 0.3 µg/ml) and β-pinene (26.11 ± 0.8 µg/ml) samples (Table 3). BHT and ascorbic acid as positive controls exhibited IC₅₀ values of 15.33 ± 0.7 µg/ml and 5.1 ± 0.4 µg/ml, respectively. It is well-known that oxygenated monoterpenes and monoterpene hydrocarbons are the main antioxidant compounds in plants [31]. The monoterpene hydrocarbons, *p*-cymene and β-pinene were inactive (Table 3), despite previous reports of their *in vitro* antioxidant activities [32].

Table 3. DPPH radical scavenging activity of *C. copticum* seed essential oil and its main constituents. Butylhydroxyanisole (BHA) and ascorbic acid were used as positive controls.

Tested compounds	IC ₅₀ (µg/ml)
<i>C. copticum</i> essential oil	20
<i>p</i> -cymene	25 ± 1.4 µg/ml
γ-terpinene	20.11 ± 0.3 µg/ml
β-pinene	26.11 ± 0.8 µg/ml
Thymol	19.24 ± 0.5 µg/ml
BHA	15.33 ± 0.7 µg/ml
AA	5.1 ± 0.4 µg/ml

Our findings revealed that the presence of oxygenated monoterpenes such as thymol and γ-terpinene could be attributed to strong antioxidant

activity. However, our results indicated that antioxidant activity of the essential oil is mainly due to the action of γ-terpinene and thymol.

Anti-inflammatory activity

The anti-inflammatory activities of *C. copticum* essential oil and its major constituents were evaluated by measuring their capacity to inhibit cellular NO generation. Nitric oxide is an endogenous free radical species that is synthesized from L-arginine by nitric oxide synthase (NOS) in various tissues. The anti-inflammatory activity of *C. copticum* essential oil was evaluated on RAW 264.7 macrophages which were stimulated to induce overproduction of NO. As presented in Table 4, the essential oil showed a strong inhibitory effect on LPS-induced NO secretion with 84.0 ± 0.3% inhibition observed at 45.0 µg/ml. Comparatively, the L-NAME, used as positive control inhibited NO release by 40.31 ± 0.3%. Thymol was found to be the most active compound inhibiting NO production by 88.0 ± 0.7 % at 45.0 µM. The effect of thymol alone was similar to that of the essential oil. Therefore, this compound may be responsible for the anti-inflammatory activity of the oil. Nitric oxide inhibition was also demonstrated at 45.0 µM by β-pinene (43.1 ± 0.1%), γ-terpinene (61.11 ± 0.2 %), γ- and *p*-cymene (39.45 ± 0.5%). The anti-inflammatory potential of the *C. copticum* essential oil or its main compounds may be directly related to its scavenging ability and/or capacity to inhibit iNOS expression, the enzyme responsible for the release of high amounts of NO, during inflammatory conditions. However, our results (Table 4) suggest that the anti-inflammatory capacity of *C. copticum* essential oil could be mediated, at least in part, by its strong direct antioxidant activity as an effective ROS scavenger. Our results are concomitant with literature data indicating the potent anti-inflammatory activity of oxygenated terpenes and thymol [33-35]. It has been shown that the activity of the enzyme NOS is consistent in human cancer and its selective modulation has been suggested as a potential strategy for chemoprevention and reduction of cancer cell proliferation [36-37]. Indeed, inflammatory mediators, such as NO have been reported to contribute to mutagenesis [38]. This radical is an important regulator of physical homeostasis, whereas large amounts have been closely correlated with the pathophysiology of a variety of diseases and inflammations [38]. Therefore, the inhibition of NO production may be a useful strategy for the treatment of various inflammatory disorders [39]. Inflammation is

involved in many chronic diseases and several types of cancers [40]. Essential oils seem to be a good source of antioxidant and anti-inflammatory natural products. In conclusion, the essential oil of *C. copticum* revealed antimicrobial, antioxidant and anti-inflammatory effects and these results support the traditional use of this plant in antimicrobial activity, relieving pain and inflammation.

Table 4. Effects of *C. copticum* seed essential oil (45.0 µg/ml) and its main constituents (45.0 µM) on NO production in LPS-stimulated RAW-264.7 macrophages. Values are mean±S.D. of three replicates.

Tested compounds	NO inhibition (%)
<i>C. copticum</i> seed essential oil	84± 0.3
<i>p</i> - cymene	39.45± 0.5
γ- terpinene	61.11± 0.2
β-pinene	43.1± 0.0
Thymol	88± 0.7
L-NAME	40.31± 0.3

REFERENCES

1. M. Lis-Balchin, S.G. Deans, *Journal of Applied Microbiology*, **82**, 759 (1997).
2. S. Burt, *Int. J. Food Microbiol.*, **94**, 223 (2004).
3. R. González-Lamothe, G. Mitchell, M. Gattuso, M.S. Diarra, F. Malouin, K. Bouarab, *Int. J. Mol. Sci.*, **10**, 3400 (2009).
4. A. Chevallier, *The Encyclopedia of Medicinal Plants*. Dorling Kindersley, London, 2001.
5. M. Khajeh, Y. Yamini, F. Sefidkon, N. Bahramifar, *Food Chemistry*, **86**, 587 (2004).
6. M.H. Boskabady, P. Jandaghi, S. Kiani, L. Hasanzadeh, *J Ethnopharmacol.*, **97**, 79 (2005).
7. R.N. Chopra, *Indigenous Drugs of India*, Calcutta: Academic Publishers, 1982, p. 215.
8. C. Thangam, R. Dhananjayan, *Indian J. Pharmacol.*, **35**, 388 (2003).
9. G. Singh, I.P. Kappor, S.K. Pandey, R.K. Singh, *Phytother Res.*, **16**, 680 (2002).
10. European Pharmacopoeia. Vol. 3, Maisonneuve S. A., Sainte-Ruffine, 1975.
11. R.P. Adams, *Allured*, Carol Stream, IL, 1989, p. 469
12. M. Cuendet, K. Hostettmann, O. Potterat, *Helvetica Chimica Acta.*, **80**, 1144 (1997).
13. A.J. Kirby, R.J. Schmidt, *Journal of Ethnopharmacology*, **56**, 103 (1997).
14. S.Y. Zhu, Y. Yang, H.D. Yu, Y. Ying, G.L. Zou, *J Ethnopharmacol.*, **96**, 151 (2005).
15. A. Uzela, A. Guvensena, E. Cetinb, *J Ethnopharmacol.*, **95**, 151 (2004).
16. J.Q. Yu, J.C. Lei, H. Yu, X. Cai, G.L. Zou, *Phytochemistry*, **65**, 881 (2004).
17. P.H. Chuang, C.W. Lee, J.Y. Chou, M. Murugan, B.J. Shieh, H.M. Chen, *Bioresource Technol.*, **98**, 232 (2007).
18. J. Green, M.S. Meltzer, J.B. Hibbs, C.A. Nacy, *Journal of Immunology*, **144**, 278 (1990).
19. S. Bourgou, A. Pichette, B. Marzouk, J. Legault, *South African Journal of Botany*, **76**, 210 (2010).
20. I. Rasooli, M.H. Fakoor, D. Yadegarinia, L. Gachkar, A. Allameh, M.B. Rezaei, *Int J Food Microbiol.*, **122**, 135 (2008).
21. J. Behravan, M. Ramezani, M.K. Hassanzadeh, S. Ebadi, *JEOBP.*, **10**, 259 (2007).
22. A. Mohagheghzadeh, P. Faridi, Y. Ghasemi, *Food Chem.*, **100**, 1217 (2007).
23. N.S. Sangwan, A.H.A. Farooqi, F.R. Shabih, S. Sangwan, *Plant Growth Regulation*, **34**, 3 (2002).
24. M. Marino, C. Bersani, G. Comi, *J. Food Prot.*, **62**, 1017 (1999).
25. D. Trombetta, F. Castelli, M.G. Sarpietro, V. Venuti, M. Cristani, C. Daniele, A. Saija, G. Mazzanti, G. Bisignano, *Antimicrob. Agents Chemother.*, **49**, 2474 (2005).
26. C. Juliano, A. Mattana, M. Usai, *JEOR.*, **12**, 516 (2000).
27. P.L. Cantore, N.S. Iacobellis, A.D. Marco, F. Capasso, F. Senatore, *J. Agric. Food Chem.*, **52**, 7862 (2004).
28. M. Valero, M.C. Salmeroj, *Int. J. Food Microbiol.*, **85**, 73 (2003).
29. L.M. Falzari, R.C. Menary, RIRDC Publication No. 02/156 RIRDC Project No. UT-28 A, Australia, 2003.
30. O.I. Aruoma, *Mutation Research, Fundamental and Molecular Mechanisms of Mutagenesis*, **523** (2003).
31. L. Cao, J. Y. Si, H. Sun, W. Jin, Z. Li, X. H. Zhao, R. L. Pan, *Food Chemistry*, **115**, 801 (2009).
32. G. Ruberto, M.T. Baratta, *Food Chemistry*, **69**, 167 (2000).
33. P. H. Hart, C. Brand, C. F. Carson, T. V. Riley, R. H. Prager, J. J. Finlay-Jones, *Inflammatory Research*, **49**, 619 (2000).
34. C.S. Lino, P.B. Gomes, D.L. Lucetti, J.P. Diogenes, F.C. Sousa, M.G. Silva, *Phytother Res.*, **19**, 708 (2005).
35. P.C. Braga, M. Dal Sasso, M. Culici, T. Bianchi, L. Bordonni, L. Marabini, *Pharmacology*, **77**, 130 (2006).
36. N. Ahmad, R.C. Srivastava, R. Agarwal, H. Mukhtar, *Biochemical and Biophysical Research Communications*, **232**, 328 (1997).
37. M. Nishikawa, B.J. Chang, M. Inoue, *Carcinogenesis*, **25**, 2101 (2004).
38. M.A. Marletta, *Journal of Biological Chemistry*, **17**, 12231 (1993).
39. C.Y. Choi, K.R. Park, J.H. Lee, Y.J. Jeon, K.H. Liu, S. Oh, D.E. Kim, S.S. Yea, *European Journal of Pharmacology*, **576**, 151 (2007).
40. M.A. Martin-Luengo, M. Yates, M.M.J. Domingo, B. Casal, M. Iglesias, M. Esteban, C. Moro, I. Palacios, M. Lozano, M. D'Arrigo, E. Guillamon, A.S. Villares, *Food Chemistry*, **130**, 350 (2012).

ХИМИЧЕН СЪСТАВ, АНТИМИКРОБНО И ПРОТИВО-ВЪЗПАЛИТЕЛНО ДЕЙСТВИЕ НА ЕТЕРИЧНО МАСЛО ОТ *CARUM COPTICUM* L.

М. Каземи

Департамент по хортикултури, Факултет по земеделски науки и природни източници, Научно-изследователски клон, Ислямски университет "Азад", Техеран, Иран

Постъпила на 7 февруари, 2014 г.; коригирана на 7 март, 2014 г.

(Резюме)

Аджоуан (*Carum copticum*) е едногодишно тревисто растение, принадлежащо към семейство Umbelliferae. Семената на *Carum copticum* имат терапевтично действие при някои кожни, нервни и урологични смущения. Настоящата работа съобщава за химичния състав, антимикробното, антиоксидантното и противовъзпалителното действие на маслото от *Carum copticum* и неговите по-важни съставки. Етеричното масло се добива от семената на *Carum copticum* чрез хидродестилация и е анализирано чрез GC/MS - техника. Основните компоненти са карвакрол (1%), ρ -кимен (23%), γ -терпинен (23%), β -пинен (5%), α -тужен (3%), сабинен (0.51%), α -филандерен (1.6%), α -пинен (1%), терпинен-4-ol (0.1%), тимол (26.03%), β -филандрен (1%), мирцен (1%) и лимонен (1.05%). Етеричното масло е изпитано с тестове за фунгицидно и бактерицидно действие, използвайки метода на минималните концентрации за инхибиране (MIC) и за бактерицидно действие (MBC). Етеричното масло е особено активно спрямо *Candida parapsilosis*, с най-ниски стойности за MIC и MBC (1.05 mg/ml). Освен това, етеричното масло и неговите основни компоненти показват потенциален NO-отстраняващ ефект и инхибират експресията на индуцирана NO-синтаза. В заключение, тези резултати подкрепят употребата на етеричното масло и неговите основни компоненти поради техните противовъзпалителни свойства и антимикробна активност.

Efficient one-pot synthesis of substituted propanamide derivatives by a three-component reaction of 2-oxopropyl benzoate, 1,1,3,3-tetramethylbutyl isocyanide and aromatic carboxylic acids in water

A. Jafari, A. Ramazani*, M. Rouhani

Department of Chemistry, University of Zanjan, Zanjan, Iran

Received February 11, 2014; Revised March 24, 2014

In the present paper, we have performed the synthesis of fully substituted propane dibenzoate derivatives *via* the reactions of 2-oxopropyl benzoate with 1,1,3,3-tetramethylbutyl isocyanide and various aromatic acids in aqueous media in 83–92% yields at room temperature. This procedure provides several advantages such as operational simplicity, high yield, safety and environment friendly protocol. The resulting products were characterized on the basis of ^1H NMR, ^{13}C NMR, IR and mass spectral (in one case) data.

Keywords: 2-oxopropyl benzoate, 1,1,3,3-tetramethylbutyl isocyanide, aromatic acids, aqueous media.

INTRODUCTION

Multicomponent reactions (MCRs) are convergent reactions between three or more reactants in which all or most of the atoms in the starting materials form part of the final product [1]. They are inherently atom-economical processes. Enhanced complex products can be obtained in a one-pot reaction from simple starting materials and thus exemplify many of the desired features of an “ideal synthesis”. Within multicomponent reactions, isocyanide-based multicomponent reactions (IMCRs) have provided a wealth of highly useful sequences for the assembly of compound libraries of particular interest to the pharmaceutical industry. Also products which incorporate amino acid or hydroxyacid motifs through the use of the well known Ugi [2] and Passerini [3] reactions have proven to be very valuable. The replacement of the carbonyl component in these reactions with a cyclic acetal unit could provide access to alternative multicomponent pathways. To date, reactions have been limited to simple isocyanide insertion into one of the C-O bonds [4-7]. However, the application of bis-secondary diamines [8,9], *N,O*-acetals [10] and glycolaldehyde dimer [11-13] in new IMCRs has been reported. In recent years numerous papers on the development and application of isocyanide-based multicomponent reactions provide evidence of the growing interest in this rapidly evolving research area [14-19].

The chemical industry is one of the major

contributors to environmental pollution, owing to the use of hazardous materials, in particular large amounts of volatile, flammable and often toxic organic solvents. With burgeoning interest in green chemistry concept, such toxic organic solvents are being replaced by alternative non-toxic, non-volatile and nonflammable media such as supercritical fluids, ionic liquids and water or the reactions are carried out under solvent free conditions [20]. Water is a safe, readily available, cheap and environmentally benign solvent. Therefore, significant interest has been evinced in the development of organic reactions in water in recent years [21-24].

Multi-component one-pot reactions are always resource effective and environmentally acceptable and, hence, greener as compared to multi-step reactions. They offer significant advantages over conventional linear step syntheses by saving money, energy, raw materials and reducing time, thus resulting in both environmental and economical benefits. Diversity can be achieved for building up libraries by simply varying each component [25-37].

EXPERIMENTAL

Starting materials were obtained from Merck (Germany) and Fluka (Switzerland) and were used without further purification. The methods used to follow the reactions are TLC and NMR. TLC and NMR indicated that there are no side products. IR spectra were measured on a Jasco 6300 FTIR spectrometer. ^1H and ^{13}C NMR spectra were measured (CDCl_3 solution) with a BRUKER DRX-400 AVANCE spectrometer at 400.0 and 100.0 MHz, respectively. Mass spectra were recorded on a FINNIGAN-MATT 8430 mass spectrometer operating at an ionization potential of 70 eV. 2-

* To whom all correspondence should be sent:
E-mail: aliramazani@gmail.com

Oxopropyl benzoate **3** was prepared based on known procedure [28].

General Procedure for the Preparation of Compounds (4)

To a stirred solution of aromatic acid (**2**) (1 mmol) and 2-oxopropyl benzoate (**3**) (1 mmol) in water (7 mL), 1,1,3,3-tetramethylbutyl isocyanide (**1**) (1 mmol) was added dropwise (5 mL) at room temperature over 15 min. The mixture was stirred for 24 h. The solvent was removed under reduced pressure, and the products were obtained without any purification. The characterization data of the compounds are given below:

2-methyl-3-oxo-3-(2,4,4-trimethylpentan-2-ylamino)propane-1,2-diyl dibenzoate (4a). Yellow oil, yield (85%); IR: 710.68, 1274.52, 1451.55, 1601.62, 1686.41, 1727.45, 2953.41, 3447.14 cm^{-1} ; ^1H NMR(CDCl_3) δ : 0.95 (s, 9H, CMe_3), 1.44 and 1.46 (6 H, Me_2CNH), 1.61 and 1.78 (AB quartet, 2H, $^2J_{\text{HH}} = 12$ Hz, CH_2CMe_3), 1.86 (s, 3H CH_3C), 4.84 and 5.04 (AB quartet, 2H, $^2J_{\text{HH}} = 12$ Hz, $\text{CH}_2\text{CO}_2\text{Ph}$), 6.28 (s, 1H, NH), 7.29-8.02 (m, 10 H, CH of arom); ^{13}C NMR (CDCl_3) δ : 19.92 (CH_3C), 28.39 and 28.71 (CMe_2), 31.48 (CMe_3), 31.78 (CMe_3), 55.51 (CH_2CMe_3), 55.94 (Me_2C), 66.37 (CH_2CCH_3), 83.03 (CH_3C), 128.52, 128.91, 129.65, 129.68, 129.91, 130.15, 130.58, 133.21, 133.46, 133.50 (10 CH and C of arom), 164.66 (COPh), 165.66 (COPh), 168.71 (CONH). MS: m/e (%) 439 (M^+ , 5), 408 (45), 252 (85), 145 (20), 119 (100), 91 (23), 57 (55).

3-(benzoyloxy)-2-methyl-1-oxo-1-(2,4,4-trimethylpentan-2-ylamino)propan-2-yl-4-methylbenzoate (4b). Yellow oil, yield (87%); IR: 711.21, 1275.00, 1611.51, 1687.84, 1748.08, 2953.22, 3445 cm^{-1} ; ^1H NMR(CDCl_3) δ : 0.94 (s, 9H, CMe_3), 1.43 and 1.45 (6 H, Me_2CNH), 1.60 and 1.77 (AB quartet, 2H, $^2J_{\text{HH}} = 12$ Hz, CH_2CMe_3), 1.85 (s, 3H CH_3C), 2.41 (Ph CH_3), 4.82 and 5.02 (AB quartet, 2H, $^2J_{\text{HH}} = 12$ Hz, $\text{CH}_2\text{CO}_2\text{Ph}$), 6.30 (s, 1H, NH), 7.24-8.00 (m, 9 H, CH of arom); ^{13}C NMR (CDCl_3) δ : 19.93 (CH_3C), 21.69 (Ph CH_3), 28.39 and 28.71 (CMe_2), 31.48 (CMe_3), 31.75 (CMe_3), 55.45 (CH_2CMe_3), 55.88 (Me_2C), 66.38 (CH_2CCH_3), 82.81 (CH_3C), 127.38, 128.39, 128.50, 128.98, 129.34, 129.56, 129.63, 129.71, 129.88, 130.01, 133.19, 133.47 (9 CH and 3 C of arom), 168.85 (CONH), 165.63 (COPh), 164.69 (COPh).

3-(benzoyloxy)-2-methyl-1-oxo-1-(2,4,4-trimethylpentan-2-ylamino)propan-2-yl-3-methylbenzoate (4c). Pale Yellow oil, yield (86%); IR: 711.56, 1287.22, 1602.75, 1688.70, 1728.08, 2953.27, 3446.83 cm^{-1} ; ^1H NMR(CDCl_3) δ : 0.96 (s, 9H, CMe_3), 1.45 and 1.47 (6 H, Me_2CNH), 1.62

and 1.79 (AB quartet, 2H, $^2J_{\text{HH}} = 12$ Hz, CH_2CMe_3), 1.86 (s, 3H CH_3C), 2.39 (Ph CH_3), 4.82 and 5.06 (AB quartet, 2H, $^2J_{\text{HH}} = 12$ Hz, $\text{CH}_2\text{CO}_2\text{Ph}$), 6.32 (s, 1H, NH), 7.35-8.01 (m, 9 H, CH of arom); ^{13}C NMR (CDCl_3) δ : 19.91 (CH_3C), 21.28 (Ph CH_3), 28.45 and 28.71 (CMe_2), 31.50 (CMe_3), 31.77 (CMe_3), 55.49 (CH_2CMe_3), 55.88 (Me_2C), 66.31 (CH_2CCH_3), 83.00 (CH_3C), 126.65, 127.01, 128.21, 128.39, 128.52, 129.65, 129.71, 130.11, 130.13, 133.21, 134.21, 138.43 (9 CH and 3 C of arom), 168.83 (CONH), 165.65 (COPh), 164.82 (COPh).

3-(benzoyloxy)-2-methyl-1-oxo-1-(2,4,4-trimethylpentan-2-ylamino)propan-2-yl-3,4-dimethylbenzoate (4d). Yellow oil, yield (89%); IR: 759.30, 1278.24, 1603.35, 1687.70, 1733.04, 2923.53, 3445.79 cm^{-1} ; ^1H NMR(CDCl_3) δ : 0.95 (s, 9H, CMe_3), 1.43 and 1.44 (6 H, Me_2CNH), 1.62 and 1.79 (AB quartet, 2H, $^2J_{\text{HH}} = 12$ Hz, CH_2CMe_3), 1.83 (s, 3H CH_3C), 2.28 and 2.32 (2 CH_3 of Ph(CH_3)₂), 4.80 and 5.03 (AB quartet, 2H, $^2J_{\text{HH}} = 12$ Hz, $\text{CH}_2\text{CO}_2\text{Ph}$), 6.30 (s, 1H, NH), 7.07-8.00 (m, 8 H, CH of arom); ^{13}C NMR (CDCl_3) δ : 19.86 (CH_3C), 19.69 and 20.03 (2 CH_3 of Ph(CH_3)₂), 28.44 and 28.70 (CMe_2), 31.57 (CMe_3), 31.78 (CMe_3), 55.40 (CH_2CMe_3), 55.88 (Me_2C), 66.38 (CH_2CCH_3), 82.86 (CH_3C), 127.08, 127.72, 128.23, 128.32, 128.54, 129.65, 129.84, 130.63, 133.09, 133.22, 136.96, 138.42 (8 CH and 4 C of arom), 168.88 (CONH), 165.65 (COPh), 164.82 (COPh).

3-(benzoyloxy)-2-methyl-1-oxo-1-(2,4,4-trimethylpentan-2-ylamino)propan-2-yl-4-tert-butylbenzoate (4e). Yellow oil, yield (88%); IR: 710.43, 1365.85, 1684.05, 1727.87, 2960.30, 3445.93 cm^{-1} ; ^1H NMR(CDCl_3) δ : 0.94 (s, 9H, CMe_3), 1.31 (PhC(CH_3)₃), 1.42 and 1.44 (6 H, Me_2CNH), 1.61 and 1.77 (AB quartet, 2H, $^2J_{\text{HH}} = 12$ Hz, CH_2CMe_3), 1.83 (s, 3H CH_3C), 4.80 and 5.02 (AB quartet, 2H, $^2J_{\text{HH}} = 12$ Hz, $\text{CH}_2\text{CO}_2\text{Ph}$), 6.32 (s, 1H, NH), 7.34-7.97 (m, 9 H, CH of arom); ^{13}C NMR (CDCl_3) δ : 19.93 (CH_3C), 28.57 and 28.80 (CMe_2), 31.30 (PhC(CH_3)₃), 31.56 (CMe_3), 31.72 (CMe_3), 35.12 (PhC(CH_3)₃), 55.41 (CH_2CMe_3), 55.82 (Me_2C), 66.35 (CH_2CCH_3), 82.83 (CH_3C), 125.60, 127.34, 128.21, 128.36, 128.51, 129.44, 129.62, 129.69, 130.19, 133.17, 133.95, 157.21 (9 CH and 3 C of arom), 168.84 (CONH), 165.57 (COPh), 164.62 (COPh).

3-(benzoyloxy)-2-methyl-1-oxo-1-(2,4,4-trimethylpentan-2-ylamino)propan-2-yl-4-chlorobenzoate(4f). Yellow oil, yield (92%); IR: 711.56, 1278.22, 1602.75, 1688.70, 1728.08, 2953.27, 3446.83 cm^{-1} ; ^1H NMR(CDCl_3) δ : 0.92 (s, 9H, CMe_3), 1.42 and 1.44 (6 H, Me_2CNH), 1.60 and 1.75 (AB quartet, 2H, $^2J_{\text{HH}} = 12$ Hz, CH_2CMe_3), 1.83 (s, 3H CH_3C), 4.80 and 4.98 (AB quartet, 2H, $^2J_{\text{HH}} = 12$ Hz, $\text{CH}_2\text{CO}_2\text{Ph}$), 6.14 (s, 1H, NH), 7.37-8.11 (m, 9 H, CH

of arom); ^{13}C NMR (CDCl_3) δ : 19.84 (CH_3C), 28.25 and 28.63 (CMe_2), 31.56 (CMe_3), 31.58 (CMe_3), 55.58 (CH_2CMe_3), 55.83 (Me_2C), 66.36 (CH_2CCH_3), 83.19 (CH_3C), 128.54, 128.76, 128.94, 129.36, 129.61, 129.88, 130.91, 131.48, 131.87, 133.28, 133.46, 139.94 (9 CH and 3 C of arom), 163.82 (COPh), 165.64 (COPh), 168.41 (CONH).

3-(benzoyloxy)-2-methyl-1-oxo-1-(2,4,4-trimethylpentan-2-ylamino)propan-2-yl-3-chlorobenzoate (4g). Pale Yellow oil, yield (89%); IR: 711.21, 1271.62, 1601.79, 1686.27, 1730.43, 2953.48, 3450.30 cm^{-1} ; ^1H NMR(CDCl_3) δ : 0.93 (s, 9H, CMe_3), 1.41 and 1.44 (6 H, Me_2CNH), 1.60 and 1.75 (AB quartet, 2H, $^2J_{\text{HH}} = 12$ Hz, CH_2CMe_3), 1.84 (s, 3H CH_3C), 4.80 and 5.00 (AB quartet, 2H, $^2J_{\text{HH}} = 12$ Hz, $\text{CH}_2\text{CO}_2\text{Ph}$), 6.21 (s, 1H, NH), 7.36-8.01 (m, 9 H, CH of arom); ^{13}C NMR (CDCl_3) δ : 19.88 (CH_3C), 28.34 and 28.62 (CMe_2), 31.47 (CMe_3), 31.73 (CMe_3), 55.61 (CH_2CMe_3), 55.80 (Me_2C), 66.17 (CH_2CCH_3), 83.39 (CH_3C), 127.69, 128.46, 129.52, 129.59, 129.62, 129.87, 129.99, 131.85, 133.32, 133.44, 134.71. (9 CH and 3 C of arom). 163.54 (COPh), 165.62 (COPh), 168.38 (CONH).

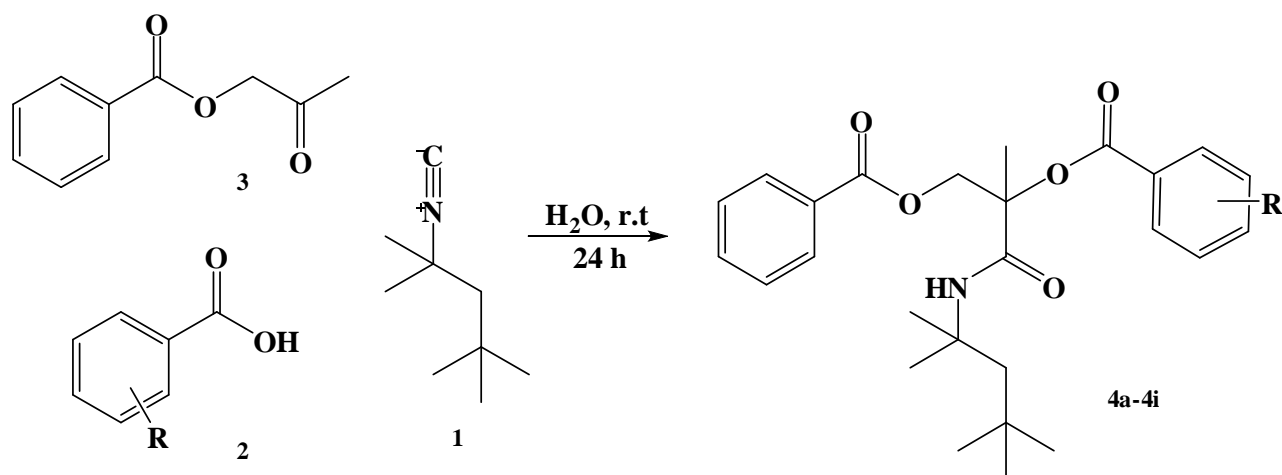
3-(benzoyloxy)-2-methyl-1-oxo-1-(2,4,4-trimethylpentan-2-ylamino)propan-2-yl-1-naphthoate (4h). Yellow oil, yield (83%); IR: 710.57, 1192.28, 1510.76, 1685.15, 1731.44, 2925.00, 3439.82 cm^{-1} ; ^1H NMR(CDCl_3) δ : 0.87 (s, 9H, CMe_3), 1.40 and 1.44 (6 H, Me_2CNH), 1.55 and 1.76 (AB quartet, 2H, $^2J_{\text{HH}} = 12$ Hz, CH_2CMe_3), 1.94 (s, 3H CH_3COCOPh), 4.88 and 5.23 (AB quartet, 2H, $^2J_{\text{HH}} = 12$ Hz, $\text{CH}_2\text{CO}_2\text{Ph}$), 6.39 (s, 1H, NH), 7.43-8.07 (m, 9 H, CH of arom); ^{13}C NMR

(CDCl_3) δ : 20.08 (CH_3C), 28.49 and 28.64 (CMe_2), 31.38 (CMe_3), 31.50 (CMe_3), 55.47 (CH_2CMe_3), 55.78 (Me_2C), 66.14 (CH_2CCH_3), 83.59 (CH_3C), 124.47, 1278.78, 125.38, 126.42, 127.92, 128.35, 128.69, 129.24, 129.67, 129.78, 130.95, 133.16, 133.35, 133.52, 133.81 (11 CH and 4 C of arom), 165.64 (COPh), 165.74 (COPh), 168.80 (CONH).

3-(benzoyloxy)-2-methyl-1-oxo-1-(2,4,4-trimethylpentan-2-ylamino)propan-2-yl-4-fluorobenzoate (4i). Pale Yellow oil, yield (91%); IR: 711.55, 1278.21, 1601.76, 1687.71, 1728.12, 2953.26, 3446.53 cm^{-1} ; ^1H NMR(CDCl_3) δ : 0.89 (s, 9H, CMe_3), 1.39 and 1.41 (6 H, Me_2CNH), 1.57 and 1.71 (AB quartet, 2H, $^2J_{\text{HH}} = 12$ Hz, CH_2CMe_3), 1.81 (s, 3H CH_3COCOPh), 4.79 and 4.95 (AB quartet, 2H, $^2J_{\text{HH}} = 12$ Hz, $\text{CH}_2\text{CO}_2\text{Ph}$), 6.18 (s, 1H, NH), 7.05-7.99 (m, 9 H, CH of arom); ^{13}C NMR (CDCl_3) δ : 19.88 (CH_3C), 28.26 and 28.62 (CMe_2), 31.52 (CMe_3), 31.70 (CMe_3), 55.52 (CH_2CMe_3), 55.83 (Me_2C), 66.36 (CH_2CCH_3), 82.93 (CH_3C), 126.31, 126.34, 128.21, 128.43, 129.57, 129.83, 130.11, 132.08, 132.17, 133.29, 138.43 (9 CH and 3 C of arom), 164.65 (COPh), 165.60 (COPh), 168.50 (CONH).

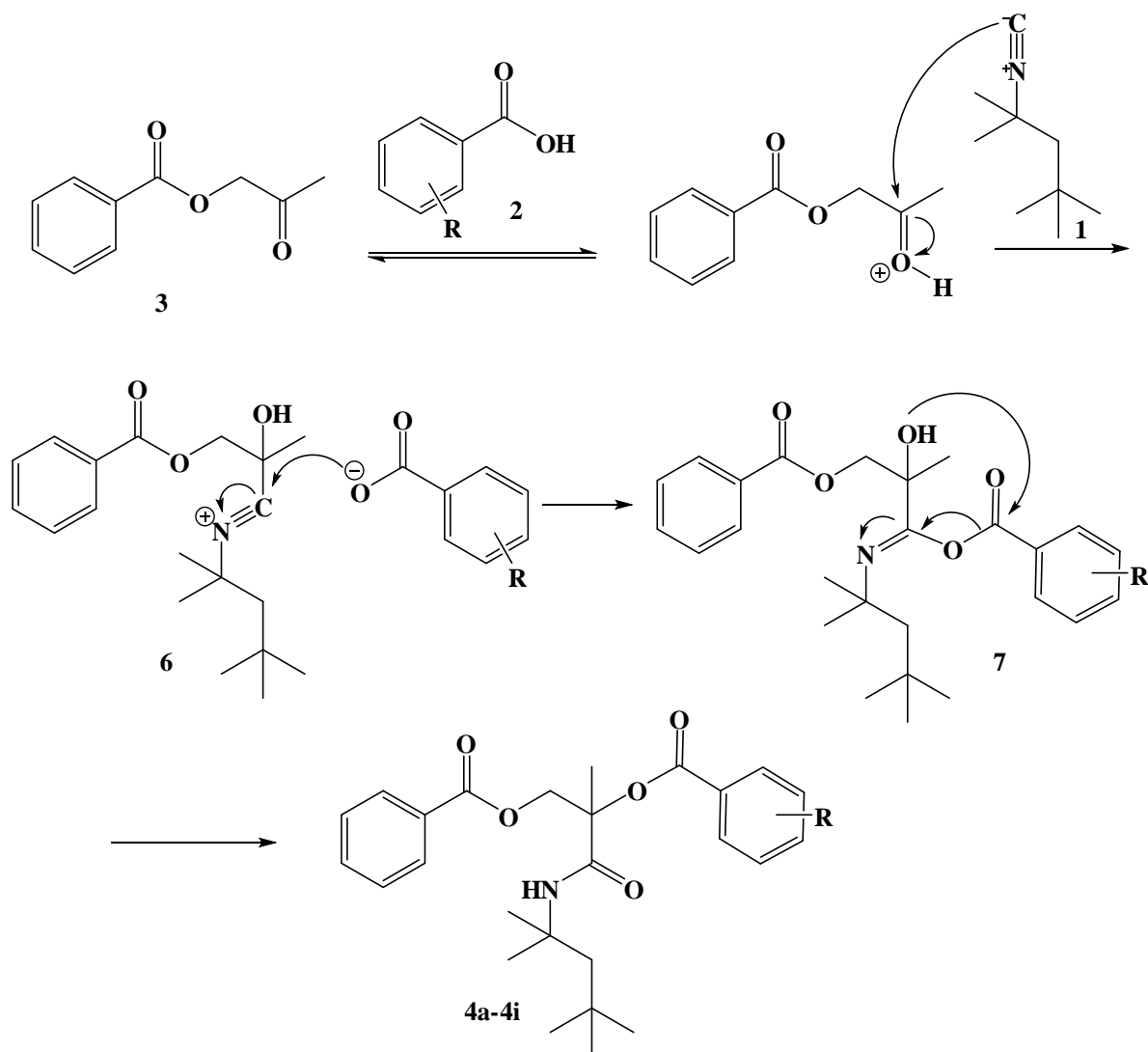
RESULTS AND DISCUSSION

As part of our program aimed at developing new isocyanide-based multi-component reactions [28-37] herein we describe for the first time an efficient synthetic approach to substituted propanamide derivatives preparation by an isocyanide-based three-component reaction between 2-oxopropyl benzoate (**3**), 1,1,3,3-tetramethylbutyl isocyanide (**1**) and various aromatic acids (**2**) in aqueous media at ambient temperature in excellent yields (Scheme 1).



4a: R=H; **4b:** R=4-methyl; **4c:** R= 3-methyl; **4d:** R= 3,4-dimethyl, **4e:** 4-*t*-butyl, **4f:** R= 4-chloro; **4g:** R= 3-chloro; **4h:** 1-naphthyl; **4i:** R= 4-flouro

Scheme 1: Three-component synthesis of substituted propanamide derivatives (**4a-i**).



Scheme 2. Proposed mechanism for the formation of substituted propanamide derivatives (4a-i).

The structures of the products were deduced from their ^1H NMR, ^{13}C NMR, mass and IR spectra. The mass spectra of these compounds displayed molecular ion peaks at the appropriate m/z values. The ^1H NMR spectrum of (**4a**) consists of a singlet at $\delta = 0.95$ ppm for CMe_3 , two peaks at 1.44 and 1.46 for Me_2CNH , an AB-quartet for CH_2 of CH_2CMe_3 at $\delta = 1.61$ ppm and 1.78 ppm ($^2J_{\text{HH}} = 12$ Hz), a singlet at $\delta = 1.86$ ppm for CH_3C , an AB-quartet for CH_2 of $\text{CH}_2\text{CO}_2\text{Ph}$ at $\delta = 4.84$ ppm and 5.04 ppm ($^2J_{\text{HH}} = 12$ Hz), a singlet at $\delta = 6.28$ ppm for NH and a multiplet at $\delta = 7.29$ -8.02 ppm for aromatic protons of phenyls. The ^1H -decoupled ^{13}C NMR spectrum of **4a** is in agreement with the proposed structure. In view of the success of the above-mentioned reaction, we explored the scope of this promising reaction by varying the structure of the carboxylic acid component.

As indicated in Scheme 1, the reaction proceeds very cleanly under mild reaction conditions at room temperature, and no undesirable byproducts are

observed. Owing to the great diversity of substitution patterns, this reaction may be used in the production of combinatorial libraries. A mechanistic rationalization for this reaction is provided in Scheme 2. On the basis of the chemistry of isocyanides, it is reasonable to assume that the first step may involve protonation of 2-oxopropyl benzoate **3** with the acid **2** follows by the nucleophilic addition of the isocyanide **1** to it leading to the nitrilium intermediate **6**. This intermediate may be attacked by a conjugate base of the acid to form the 1:1:1 adduct **7**. This adduct may undergo Mumm rearrangement to afford the isolated sterically congested propanamide derivatives **4** (Scheme 2).

CONCLUSION

In conclusion, an efficient, clean, and simple method for the preparation of fully substituted propane dibenzoate derivatives using readily available starting materials is reported. The advantage of our work is that the reaction proceeds under neutral

conditions with no bases or catalysts in high yield and no purification of the products. The simplicity of the present procedure makes it an interesting alternative to the complex multistep approaches.

Acknowledgment: The authors thank the University of Zanjan for the support and guidance.

REFERENCES

1. J. Zhu, H. Bienayme, (Eds), Multicomponent Reactions, Wiley-VCH, Weinheim, 2005.
2. I. Ugi, *Angew. Chem. Int. Ed. Engl.* **1**, 8 (1962).
3. M. Passerini, *Gazz. Chim. Ital.*, **61**, 964 (1931).
4. H. Pellissier, A. Meou, G. Gil, *Tetrahedron Lett.*, **27**, 2979 (1986).
5. H. Pellissier, G. Gil, *Tetrahedron Lett.* **29**, 6773 (1988).
6. S. Yoshioka, M. Oshita, M. Tobisui, *Org. Lett.*, **7**, 3697 (2005).
7. M. Tobisu, A. Kitakima, S. Yoshioka, *J. Am. Chem. Soc.*, **129**, 11431 (2007).
8. G.B. Giovenzana, G.C. Tron, S. Di Paola, *Angew. Chem. Int. Ed.*, **45**, 1099 (2006).
9. T. Pirali, G. Callipari, E. Ercolano, *Org. Lett.*, **10**, 4199 (2008).
10. L.J. Diorazio, W.B. Motherwell, T.D. Sheppard, R.W. Waller, *Synlett*, **2281** (2006).
11. Y. B. Kim, E. H. Choi, G. Keum, *Org. Lett.*, **3**, 4149 (2001).
12. L. Banfi, A. Basso, G. Guanti, *Mol. Divers.*, **12**, 187 (2008).
13. R. Mossetti, T. Pirali, G.C. Tron *J. Org. Chem.*, **74**, 4890 (2009).
14. A. Ramazani, F. ZeinaliNasrabadi, Z. Karimi, M. Rouhani, *Bull. Korean Chem. Soc.*, **32**, 2700 (2011).
15. A. Ramazani, A. Rezaei, A. Mahyari, *Helv. Chim. Acta.*, **93**, 2033 (2010).
16. A. Ramazani, A. Tofangchi Mahyari, M. Rouhani, *Tetrahedron Lett.*, **50**, 5625 (2009).
17. A. Ramazani, K. Dastanra, F. ZeinaliNasrabadi, *Turk. J. Chem.*, **36**, 467 (2012).
18. A. Ramazani, F. ZeinaliNasrabadi, B. Abdian, M. Rouhani, *Bull. Korean Chem. Soc.* **33**, 453 (2012).
19. A. Ramazani, M. Rouhani, A. Rezaei, *Helv. Chim. Acta.*, **94**, 282 (2011).
20. C. J. Li, *Chem. Rev.* **93**, 2033 (1993) 2023.
21. N. Azizi, F. Aryanasab, L. Torkiyan, *J. Org. Chem.*, **71**, 3634 (2006).
22. U.K. Roy, S. Roy, *Tetrahedron*, **62**, 678 (2006).
23. J. Safaei-ghomi, A. Kakavand-Qalenoee, M.A. Ghasemzadeh, *Turk. J. Chem.*, **36**, 852 (2012).
24. C. Yildirim, C. Yollacan, F. Aydogan, *Turk. J. Chem.*, **36**, 101 (2012).
25. N.K. Terret, M. Gardener, D.W. Gordon, *Tetrahedron*, **51**, 8135 (1995).
26. L. A. Thompson, J. A. Ellman, *Chem. Rev.*, **96**, 555 (1996).
27. J. A. Ellman, *Acc. Chem. Res.*, **29**, 132 (1996).
28. A. Ramazani, Y. Ahmadi, A. Mashhadi Malekzadeh, A. Rezaei, *Heteroat. Chem.*, **22**, 692 (2011).
29. A. Ramazani, A. Souldozi, *Phosphorus Sulfur Silicon Relat. Elem.*, **184**, 2344 (2009).
30. A. Ramazani, A. Souldozi, *Arkivoc* *xvi*, 235 (2008)
31. A. Ramazani, S. Salmanpour, A. Souldozi, *Phosphorus Sulfur Silicon Relat. Elem.*, **18**, 97 (2010).
32. A. Souldozi, A. Ramazani, K. Slepokura, T. Lis, *Z. Naturforsch.*, **62b**, 835 (2007).
33. A. Ramazani, A. Rezaei, *Org. Lett.* **12**, 2852 (2010).
34. A. Ramazani, Z. Karimi, A. Souldozi, Y. Ahmadi, *Turk. J. Chem.*, **36**, 81 (2012).
35. A. Massoudi, I. Amini, A. Ramazani, F. Zeinali-Nasrabadi, *Turk. J. Chem.*, **36**, 537 (2012).
36. M. Valizadeh-Holagh, A.M.O. Maharramov, M.A.O. Allahverdiyev, *Turk. J. Chem.*, **36**, 179 (2012).
37. M. Valizadeh-Holagh, A. M. O. Maharramov, M. A. O. Allahverdiyev, A. Ramazani, Y. Ahmadi, F. Zeinali-Nasrabadi, A. Souldozi, *Turk. J. Chem.*, **36**, 671 (2012).

ЕФЕКТИВНА ЕДНОСТАДИЙНА СИНТЕЗА НА ЗАМЕСТЕНИ ПРОПАНАМИДНИ ПРОИЗВОДНИ ЧРЕЗ ТРИКОМПОНЕНТНА РЕАКЦИЯ НА 2-ОКСОПРОПИЛОВ БЕНЗОАТ, 1,1,3,3-ТЕТРАМЕТИЛБУТИЛ ИЗОЦИАНИД И АРОМАТНИ КАРБОКСИЛНИ КИСЕЛИНИ ВЪВ ВОДА

А. Джафари, А. Рамазани *, М. Рухани

Катедра по химия в Университета на Занджиан, Занджиан, Иран

Получена на 11 февруари, 2014 г.; коригирана на 24 март, 2014 г.

(Резюме)

В настоящата статия, ние извършихме синтеза на напълно заместени пропан дибензоат производни чрез реакции на 2-оксопропил бензоат с 1,1,3,3-тетраметилбутил изоцианид и различни ароматни киселини във водна среда, с добив 83-92% при стайна температура. Тази процедура осигурява няколко предимства, като например оперативна простота, висок добив, безопасност и благоприятен за околната среда протокол. Получените продукти бяха характеризирани на основата на $^1\text{H NMR}$, $^{13}\text{C NMR}$, IR и мас-спектрални (в един случай) данни.

Differences in the mode of thermomechanical processing between white gold alloys to produce semi-finished products

M. B. Miric^{1*}, R. S. Peric², S. P. Dimitrijevic³, S. A. Mladenovic⁴, S. R. Marjanovic⁵

¹Directorate of Measures and Precious Metals, Beograd, Department of the control subjects in precious metals, Nis, Serbia

²PERIC & PERIC & Co. d.o.o., Pozarevac, Serbia

³Innovation center of the Faculty of Technology and Metallurgy, Belgrade, Serbia

⁴Technical Faculty in Bor, University of Belgrade, Bor, Serbia

⁵Technical Faculty in Bor, University of Belgrade, Bor, Serbia

Received February 12, 2014; Revised July 3, 2014

The results of the investigation of the reduction degree on the hardness of a gold sample with chemical composition Au58,5Ag15Cu9,5Ni9Zn5Pd3 for old white gold alloy and Au58,5Ag18Cu10,5Ga8Zn5 (wt %) for new white gold alloy, are shown. The obtained results show that hardness of samples is higher when total reduction is higher, and that it decreases after process annealing. Also, the mechanical properties of the investigated alloys were compared. Alloy without Ni has lower hardness and higher elongation values.

Keywords: white gold; rolling; drawing; hardness; total elongation; nickel; gallium.

INTRODUCTION

With the beginning of the human race evolved an aspiration of the people for beautification and wearing jewelry. The rich and beautiful yellow color, good mechanical properties and relatively easy way of processing, have made gold a major element to use for this purpose [1, 2, 3].

Almost all metals in pure elemental state are very soft, malleable and difficult for mechanical processing [4,5]. This feature happens to be an advantage in the production of contemporary jewelry because it allows mixing pure gold with other appropriate elements to a higher or smaller degree, depending on the production technology and the grade of jewelry you want to get [6]. However, its disadvantages are ductility, wear and susceptibility to mechanical injuries during processing of jewelry [7]. Gold alloys are widely used in jewelry, mostly in the form of wires and thin strips.

White gold alloys were developed as substitutes for platinum and are mainly used for jewellery. The whitening or bleaching of gold is a process of creating a material that is cheaper and easier to alloy and fabricate than platinum. There are two groups of commercial white gold alloys, in one of which the bleaching element is nickel and in the other - palladium. Because of the strong hardening effect of nickel, white gold alloys containing large amounts of nickel do not have the deformation characteristics desired for jewelry manufacture. It is

possible to obtain a better combination of colour and mechanical properties in white golds by bleaching with palladium, but since the price of palladium is about 1 000 times that of nickel, these better alloys are more costly [8,9].

Also, nickel has long been known as a major skin allergen. In an attempt to reduce the occurrence of allergic contact dermatitis caused by nickel, the European Parliament and EU Council passed the Nickel Directive. For products designed for direct and long-term contact with the skin (earrings, necklaces, bracelets, etc.) the rate of release of Ni should not exceed 0.5 $\mu\text{g}\cdot\text{cm}^2$ per week. A more recent measure passed by the Commission, Directive 2004/96/EC, in an attempt at more effective protection of EU citizens and taking into consideration new findings on the toxic properties of nickel, sets a migration limit of 0.2 $\mu\text{g}\cdot\text{cm}^2$ per week. This new limit also applies for earring posts inserted into the pierced ear or into other pierced parts of the human body [10].

The new line of total nickel-free white alloy was created to provide maximum protection for sensitive skin. The Italian company Legor produced new alloy Proderma [11,12]. Proderma was created as a practical response to the growing attention towards phenomena of allergy and skin intolerance in contact with some commonly used metals in the gold industry, including nickel. This brand contains NPF alloys (nickel/palladium free), which do not contain the two most common whitening elements,

that for several reasons may not be acceptable or not compatible. Instead, they contain gallium as a

* To whom all correspondence should be sent:
E-mail: mladenmiric@dmdm.rs

M. Miric et al., Differences in the mode of thermomechanical processing between white gold alloys to produce ... whitening component and a slightly higher percentage of Ag and Cu (REF).

In this study, we performed a comparative analysis of old and new white gold alloy strips obtained from molten pieces of rectangular cross-section. We investigated the influence of rolling, drawing and annealing on the mechanical properties of those two types of white gold strips.

EXPERIMENTAL PROCEDURE

Preparation of the sample

Mixing of gold with purity of 999,9 ‰ and the corresponding master and finished pre-alloys was used to obtain the needed mixtures of white gold for jewelry making. From those two mixtures castings with composition (determined by the FISHERSCOPE X-RAY XAN-DPP unit located at the Directorate of Measures and Precious Metals, Belgrade) 58,5% Au, 15% Ag, 9,5% Cu, 9% Ni, 5% Zn and 3% Pd for old white gold and 58,5% Au, 18% Ag, 10,5% Cu, 8% Ga, 5% Zn (wt %) for new NPF white gold, with dimensions of 92 mm × 28,6 mm × 4,7 mm were effused using a melting procedure at a temperature of 1064°C and fixed periods of mixing.

Rolling process

Prepared castings were passed through working rolls to obtain a thickness of 0.38 mm, which was appropriate for cutting on circled cutting scissors. After each reduction, samples were taken for mechanical investigations. After each fifth reduction the samples were heated in a furnace at a temperature of 650°C for 10 min. Aforementioned samples were cut to the width of 18.5 mm and passed through 4 cylinder plates rolling machine where tubes were obtained. Subsequently, we performed gas brazing of the tubes with tungsten electrodes in argon atmosphere at a current of 10V and 12A.

Drawing process

The obtained tubes were passed through a drawing bench with diamond dies to obtain the diameter most commonly used for making necklaces and bracelets (tables 2 and 4). After each fifth reduction the samples were heated in a furnace at temperature of 650°C for 10 min. Along with the cast samples, samples obtained in rolling and drawing processes were taken for mechanical examination.

RESULTS AND DISCUSSION

The parameters of rolling and drawing for old white gold with Ni alloy are given in Table 1 for rectangular samples, and table 2 for tube samples. Figures 2 and 3 demonstrate the results of hardness

investigation for the same old white gold with Ni alloy.

Table 1. Rolling parameters for the tested old white gold with Ni alloy samples

b, mm	h, mm	Total height reduction, %	Single height reduction, %	F ₀ /F	HV 10
28.6	4.7				153
28.7	4.5	4.25	4.25	1.0444	160
28.8	4.2	10.64	6.67	1.1190	176
28.9	3.6	23.40	14.29	1.3056	206
29.0	3.1	34.04	13.89	1.5161	250
29.1	2.8	40.43	9.68	1.6786	263
29.3	2.2	53.19	21.43	2.1364	275
29.5	1.8	61.70	18.18	2.6111	296
29.7	1.3	72.34/0	27.78	3.6154	314/182*
29.9	0.87	81.49/33.77	33.08	5.4023	245
30.1	0.58	87.66/55.38	33.33	8.1034	279
30.3	0.38	91.91/70.77	34.48	12.3684	311/157*

b - Sample width, HV 10 - Vickers hardness, h - Sample height,

* Hardness after annealing,, F - Cross section area

Table 2. Drawing parameters for the tested white gold alloy

l, mm	Ø, mm	Single elongation, %	Total elongation, %	HV 10
150	6.0			173
153	5.8	2.0	2.0	186
158	5.5	3.27	5.33	207
164	5.0	3.80	9.33	231
169	4.8	3.05	12.67	248/182*
182	4.6	7.69	21.33	200
196	4.3	7.70	30.67	210
214	3.9	9.18	42,67	242

l - Tube length, Ø - Tube diameter, HV 10 - Vickers hardness

* Hardness after annealing

We show that for higher total height reduction the hardness values increase (Figure 1).

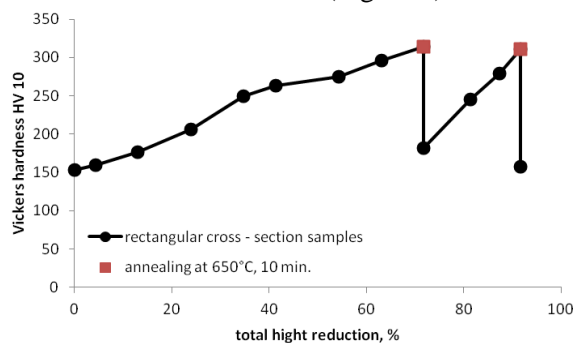


Fig. 1. Dependence of white gold alloy strips hardness on total height reduction

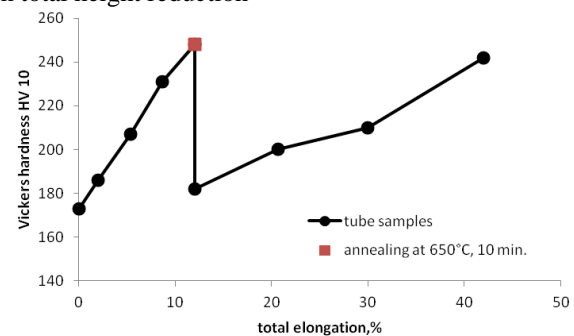


Fig. 2. Dependence of white gold alloy tubes hardness on the total elongation.

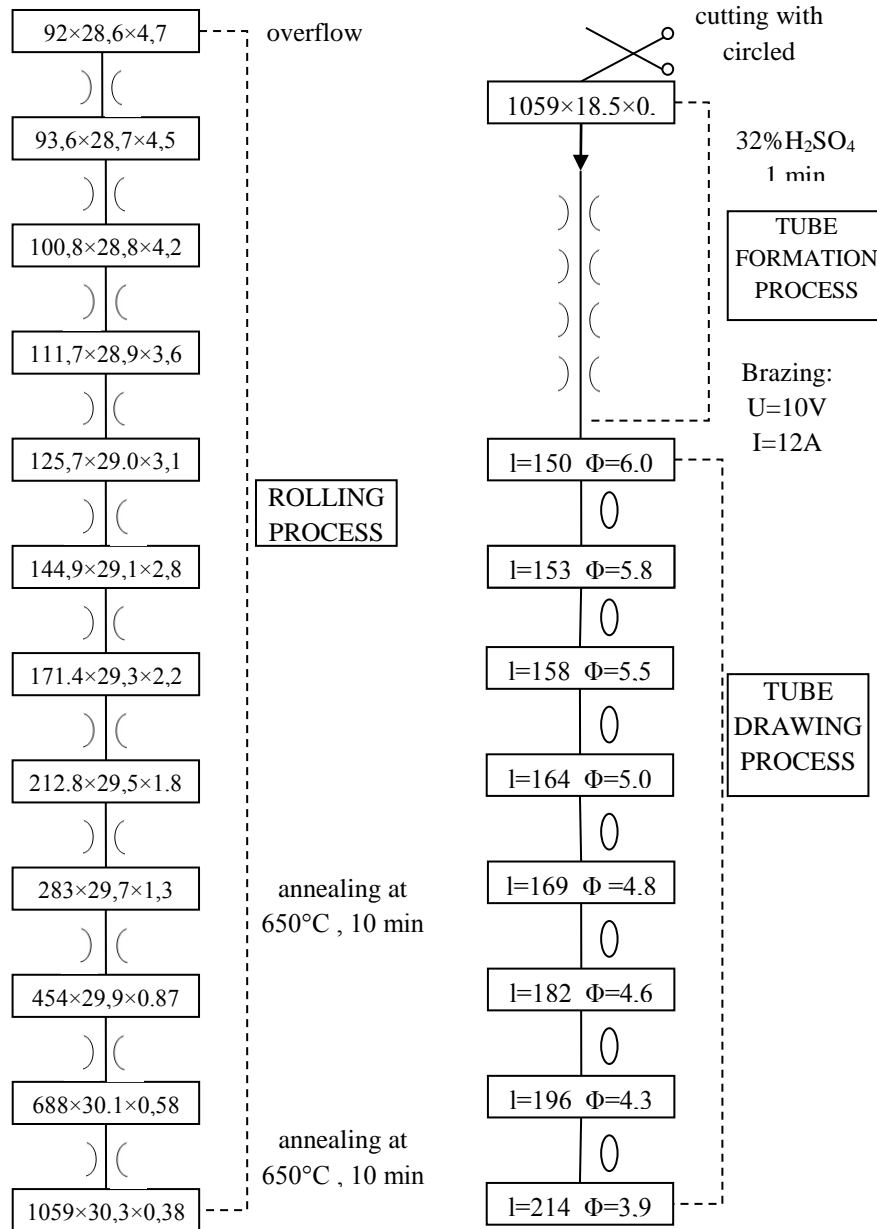


Fig. 3. Schematic view of the study of old white gold alloy with Ni.

After process annealing, the hardness values decrease, and for further total height reduction, hardness increases again.

Our results demonstrate that as total elongation increases, hardness values also increase (Figure 2). After process annealing, values for hardness decrease, and with subsequent increase of percentage of elongation, hardness increases again.

Figure 3 presents a schematic view of the study of old white gold alloy with Ni.

The parameters of rolling and drawing for new white gold NPF alloy are given in tables 3 and 4, for rectangular and tube samples, respectively. Diagrams in figures 2 and 3 represent results of NPF alloy hardness investigation.

Table 3. The parameters of rolling for tested new white gold NPF alloy samples

b mm	h mm	Total hight reduction, ε _{huk}	Single hight reduction, %	F ₀ /F	HV 10
28,6	4,7				146
28,7	4,5	4,25	4,25	1,0444	154
28,9	4,1	12,77	8,88	1,1463	170
29,0	3,5	25,53	14,63	1,3429	201
29,2	2,9	38,30	17,14	1,6207	247
29,4	2,6	44,68	10,34	1,8077	260
29,6	2,1	55,32	19,23	2,2381	270
29,8	1,6	65,96	23,80	2,9375	292
29,9	1,2	74,47/0	25,00	3,9167	310/180*
30,1	0,8	82,98/33,33	33,33	5,8750	240
30,3	0,5	89,36/58,33	37,50	9,4000	275
30,5	0,38	91,91/68,33	24,00	12,3684	305/150*

b-Sample width, h-Sample height, HV 10-Vickers hardness, * Hardness after annealing,, F-Cross section area

Table 4. Drawing parameters for the tested new white gold NPF alloy

l, mm	Ø, mm	Single elongation %	Total elongation, %	HV 10
150	6.0			170
154	5.7	2.66	2.66	182
159	5.4	3.25	6.00	203
165	5.0	3.77	10.00	230
173	4.7	4.85	15.33	242/180*
184	4.5	5.20	22.67	199
197	4.2	7.06	31.33	209
216	3.9	8.80	44.00	240

l- Tube length, Ø- Tube diameter, HV 10 - Vickers hardness

* Hardness after annealing

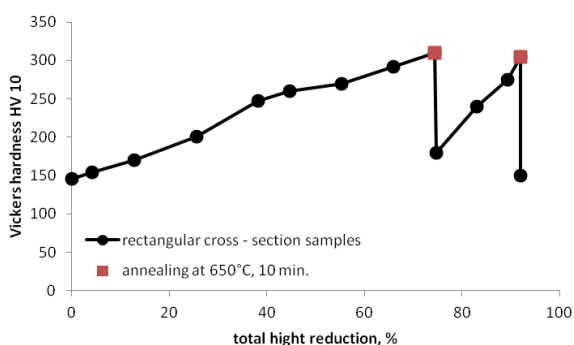


Fig. 4. Dependence of the hardness of white gold alloy strips on total height reduction

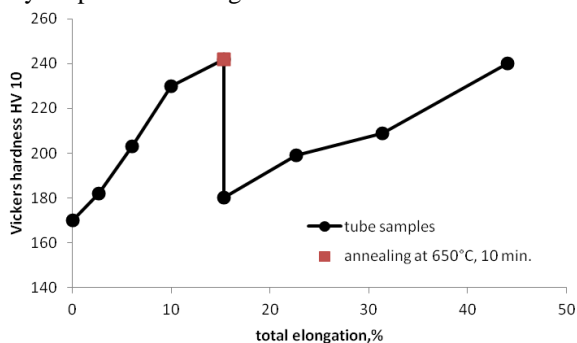


Fig. 5. Dependence of the hardness of white gold alloy tubes on total elongation

Based on the results presented in Tables 1 – 4 the following comparison between the two white gold alloys can be made: regarding the total reduction, the new white gold alloy has a higher value (74.47) than the old white gold alloy (72.34). At the same time, total elongation is higher for the new alloy (15.33) than for old alloy (12.67). These differences in the degree of reduction and elongation are the result of the presence of very dispersive liquid Ga over the macro and micro grain boundaries, since the liquid phase lays over

almost each grain with definite nm or µm dimension.

Vickers hardness for the new alloy with Ga, after annealing process, is almost the same as for the old alloy with Ni (180 vs. 182). For both alloys, permanent hardness increase is consequent to grain fragmentation of solid solutions or intermetallics, under the influence of strains caused by dislocations accumulation on grains boundaries. Such accumulation with short, (only 10 min), annealing process at 650°C, enables dislocations to move drastically lowers Vickers hardness.

CONCLUSION

Based on the experimental research performed and the results obtained, we can conclude the following:

During cold rolling, for higher total height reduction, the hardness values increase for both old and new white gold alloys (slightly more for old white gold alloys, tables 1 and 3). After the annealing process, the hardness values rapidly decrease. Subsequent increase in total height reduction causes an increase in hardness again.

The relative elongation data obtained are in good correlation with literature values [2].

During the drawing process, with an increase in total elongation, the hardness values increase for both old and new white gold alloys (more for old white gold alloys, tables 2 and 4). After the annealing process, the hardness values rapidly decrease. Subsequent increase in reduction results in an increase in hardness again.

These investigations show that using the new alloy NPF, strips and tubes of mechanical properties appropriate for jewelry making, can be obtained by rolling and drawing processes.

Moreover, new alloy NPF showed slightly better thermomechanical properties in comparison to old alloy. Gallium, used instead of nickel, proved to be a good replacement. The only flaw is that its use is not providing the desired white color component of the funds used for the development of modern jewelry. However, this can easily be overcome by coating with a layer of semi-finished rhodium, in order to obtain the desired jewelry white as shown in Picture 1.

Acknowledgement: This work has resulted from the Project funded by the Ministry of Education, Science and Technological Development of the Republic of Serbia, No. 19018, for which the authors on this occasion would like to thank



Picture 1. Products before and after coating with a layer of semi-finished rhodium

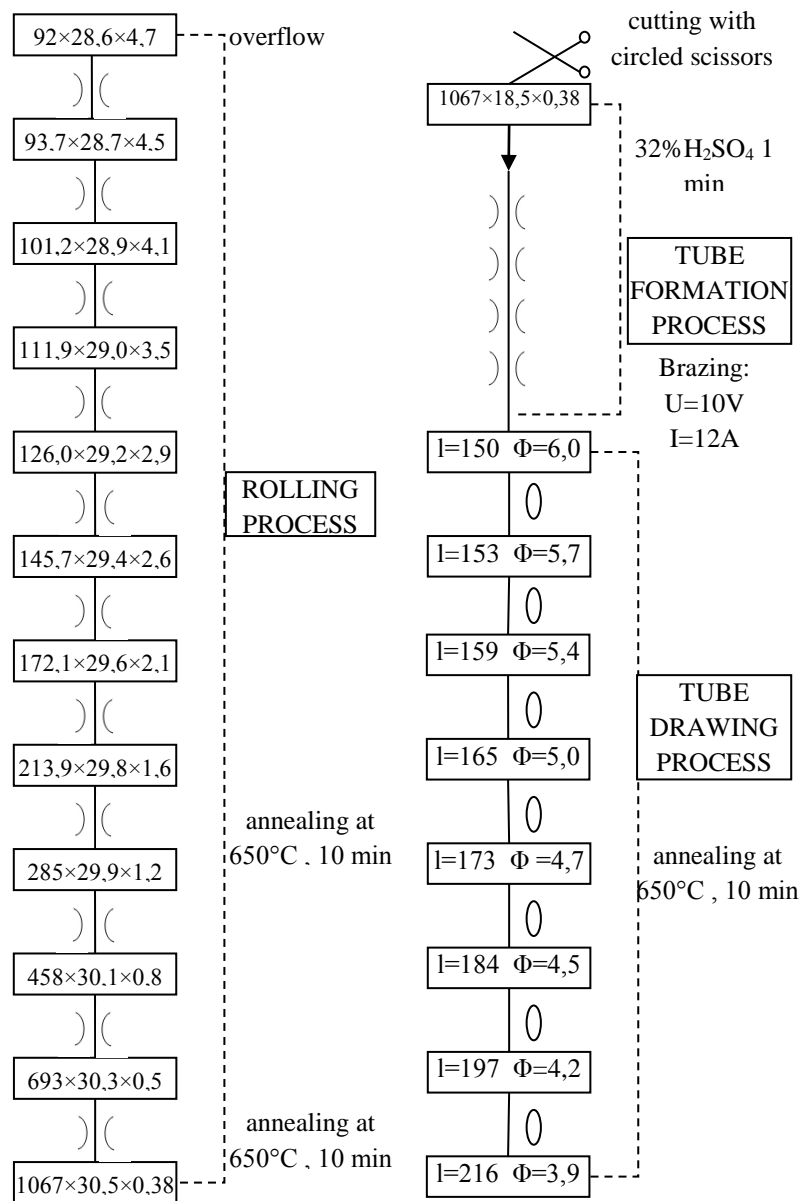


Fig. 6. Schematic presentation of the study of the new white gold NPF alloy

REFERENCES

1. S.Mozgovoy, J.Heinrich, U.E.Klotz, R.Busch, Establishing the process Mineralogy of gold ores, *Intermetallics*, **18**, 2289, (2010).
2. S.Watanabe, L.S.Benner, T.Suzuki, K.Meguero, S.Tanaka, Precious Metals Science and Tecnology, International Precious Metals Institute, Allentown, 1991.
3. P.K.Liaw, G.Wang, J.Schneider, *Advances in bulk metallic glasses, JOM*, **62**, 9 (2010)
4. J.Schroers, B.Lohwongwatana, W.L.Johnson, A.Peker, *Materials Science and Engineering:A*, **449**, 235 (2007).
5. C.Cretu, E.Lingen, Colored Gold Alloys, *Gold Bulletin*, **32**, 115 (1999).
6. Corti, Dr. Christopher W., The Role of Hardness in Jewelry Alloys, Santa Fe Symposium on Jewelry Manufacturing Technology, Albuquerque, New Mexico, USA, May 2008.
7. D.Maggian, S.Bortolamei, M. di Siro, A. Carlotto, D.Bruttomesso, C. Girardi, Characterization of 14-Karat Gold Alloys, 25th Santa Fe Symposium on Jewelry Manufacturing Technology, Albuquerque, New Mexico, USA, May 2011.
8. G. Normandeau, White golds: a review of commercial material characteristics & alloy design alternatives, *Gold Bull.*, **25**, 94 (1992).
9. B. MacCormack, John E. Bowers, New white gold alloys, *Gold Bull.*, **14**, 19 (1981).
10. M. Pouzar, M. Schmidt, A. Krejcova, T. Cernohorsky, Nickel Release from Piercing Jewellery, *SRX Chemistry*, **1-6**, (2010).
11. A.Basso, M.Poliero, A.Frisco, R.Bertoncello, Legor group S.p.A., White-Gold Alloys for Gold Jewelry and the new EN1811:2011 Standard on Nickel: Limitations and Possibilities, 27th Santa Fe Symposium on Jewelry Manufacturing Technology, Albuquerque, New Mexico, USA, May 2013.
12. S.Bezzone, Nickel Release Tests on Current Production Jewelry, 27th Santa Fe Symposium on Jewelry Manufacturing Technology, , Albuquerque, New Mexico, USA, May 2013.

РАЗЛИКИ В НАЧИНА НА ТЕРМОМЕХАНИЧЕСКА ПРЕРАБОТКА МЕЖДУ СПЛАВИ НА БЯЛО ЗЛАТО ЗА ПРОИЗВОДСТВО НА ПОЛУГОТОВИ ПРОДУКТИ

М. В. Мирич¹, Р. С. Перич², С. П. Димитриевич³, С. А. Младенович⁴, С. Р. Марджанович⁵

¹Дирекция за измерания и благородни метали, Белград, катедра законтрolni субекти от благородни метали, Ниш, Сърбия

²Перич & Перич & Съд. ООД, Пожаревац, Сърбия

³Иновационен център към технологичен и металургичен факултет, Белград, Сърбия

⁴Технически факултет в Бор, Белградски университет, Бор, Сърбия

⁵Технически факултет в Бор, Белградски университет, Бор, Сърбия

Получена на 12 Февруари, 2014 г.; ревизирана на 3 юли 2014 г.

(Резюме)

Показани са резултатите от изследването на степента на намаляване на твърдостта на проба злато с химически състав Au58,5Ag15Cu9,5Ni9Zn5Pd3 за стара сплав на бяло злато и Au58,5Ag18Cu10,5Ga8Zn5 (тегловни%) за нова сплав на бяло злато. Получените резултати показват, че твърдостта на пробите е по-висока, когато общото намаление е по-високо, и че тя намалява след процеса отгряване. Също така, са сравнени механичните свойства на изследваните сплави. Сплав без Ni има малка твърдост и по-високи стойности на удължение

Optimization strategies for improved growth, polysaccharide production and storage of the red microalga *Rhodella reticulata*

J. G. Ivanova¹, L. V. Kabaivanova^{2*}, P. D. Petrov³, S. N. Yankova⁴

¹ Institute of Plant Physiology and Genetics, Bulgarian Academy of Sciences, 21, Acad. G. Bonchev Str., Sofia, Bulgaria

² Institute of Microbiology, Bulgarian Academy of Sciences, 26, Acad. G. Bonchev Str., Sofia, Bulgaria

³ Institute of Polymers, Bulgarian Academy of Sciences, 103, Acad. G. Bonchev Str., Sofia, Bulgaria

⁴ Institute of Chemical Engineering, Bulgarian Academy of Sciences, 103, Acad. G. Bonchev Str., Sofia, Bulgaria

Received November 13, 2013; Revised April 14, 2014

To ensure good conditions for growth and heteropolysaccharide production by the red microalga *Rhodella reticulata*, optimization of the medium and conditions was performed. Stimulation of the growth of microalgal cells up to 1.6-fold was achieved with a new medium. Maximal growth rate ($\mu=0.19\text{ d}^{-1}$) was reached at the beginning of stationary phase of growth (72 h), together with the increase in the pigment content. The influence of the great quantity of humic acids and thiamin in the medium (proved by HPLC) on algal growth was also established. The amount of extracellular polysaccharide (0.365 mg ml^{-1}) produced by the algal cells cultivated in the new medium was 1.4-fold higher compared to the quantity in the standard medium. The immobilization of *Rhodella reticulata* cells into super-macroporous cryogel of 2-hydroxyethylcellulose lead to a prolonged period of storage. Algal cells were vital after three months and could be successfully used for the production of extracellular polysaccharide with values for immobilized cells 1.3 –fold higher than those for free cells.

Key words: Algae; Bioactive substances; Growth medium; Immobilization

INTRODUCTION

A successful biotechnological process depends on the selection of a suitable organism capable to produce a desired product at optimal conditions. By 2015, the industrial biotechnology will have a 20% share in total chemical production [1]. The red microalgae of the genus *Rhodophyta* are potential sources of unique bioactive substances [2-3] that can find different applications - in medicine, pharmacy, cosmetics, food industry as food supplements, etc. [4-5]. Typical representative of the genus is the unicellular red microalga *Rhodella reticulata*, which has the ability to synthesize and release part of the polysaccharide material into the culture medium [6-7]. Its functions are mainly protective but its antiviral and antitumor effects are well known [8-9]. The growth of microalgae is primarily affected by abiotic environmental factors. Some biologically active organic compounds, namely vitamins, nucleic acids and organic matter such as humic substances and soil extracts, also stimulate the growth of algal cultures [10]. However, long cultivation of algae in a laboratory usually leads to contamination and decreased growth rates and densities, when cultured in

traditional media [11]. It is suggested that the type of nutrient medium plays a critical role for the algal growth [12]. Therefore, the suitable balancing of the elemental composition of the growth medium is a tool to obtain high-density cultures. Different optimization strategies were applied to the media components in order to increase the productivity of algal cells, pigment synthesis and polysaccharide production [13-14]. An approach to keep the vitality of cells after long-term storage of the algal cultures in the laboratory is the immobilization technique. It is based on finding suitable carriers that can ensure preservation of the algal cultures for a long period under laboratory conditions. Immobilization of different algae had already been performed in alginate beads to increase the period of storage and preserve their physiological activity [15]. At the same time, immobilization facilitates both the extraction of the extracellular polysaccharide from the medium and the handling of the system [16].

Super-macroporous polymer cryogels are an interesting class of materials due to their unique heterogeneous open porous structure, which significantly increases the equilibrium sorption properties and allows unhindered diffusion of solutes, nano-particles and micro-particles. Usually, cryogels possess spongy-like structure of huge pores ($50\text{-}200\text{ }\mu\text{m}$) containing free water surrounded by thin walls and, therefore, they are often used for immobilization

* To whom all correspondence should be sent:
E-mail: lkabaivanova@yahoo.com

of enzymes and cells by entrapment inside the channels of interconnected pores [17].

The aim of the present study was to find the most appropriate conditions for intensive algal growth and increased polysaccharide production of *Rhodella reticulata* by optimizing the components of the nutrient medium and to prolong the storage of the algal culture with the immobilization technique.

EXPERIMENTAL

The red microalga *Rhodella reticulata* (*Rhodophyta*), strain UTEX LB2320 was acquired from the Austin University, Texas, USA. It was isolated from brackish water in the region. It is maintained as a working culture in the laboratory collection of the Department of Experimental Algology of the Institute of Plant Physiology-Bulgarian Academy of Sciences.

Intensive cultivation

To test the effect of culture media and polysaccharide production of free and immobilized algal cells, all culture experiments were conducted at permanent illumination of $150 \mu\text{E m}^{-2} \text{s}^{-1}$ in special vessels (100 ml) for intensive cultivation and 2% CO_2 supply. Temperature was maintained at 29 - 30°C and pH = 7.3. The algae were grown in 5 nutrient media.

Soil extract preparation

The soil was collected from a region with pine trees. Air-dried soil and twice its volume of distilled water were autoclaved together at 15 psi for 15 min. After centrifugation at 3000 g, the supernatant was decanted and then filtered to a final volume of 100 ml.

Dry weight measurement

The growth of the algal culture was estimated following the increase in its weight. For this purpose, 10 ml of the algal suspension were centrifuged at 6000 g for 20 min (Rotofix 32A, Hettich). The supernatant was removed and the cells were dried at 105°C for 16 h. The salts were eliminated by rinsing thrice with tap water. Cell count to evaluate the growth and development of the investigated strain was carried out by using a Burkner counting chamber.

Specific growth rate (μ , d^{-1})

Specific growth rate was calculated from the dry weight: $\mu = \ln(N_2/N_1)/(t_2 - t_1)$, where N_1 and N_2 are the dry weights of algal cells at definite times t_1 and t_2 .

Pigment content

It was estimated spectrophotometrically. The amounts of chlorophyll "a", carotenoids and phycobiliproteins were given according to the absorption spectra, taking into account the absorbances at: 665 nm for chlorophyll "a", 460 nm for carotenoids, 565 nm for phycoerithrin and 620-650 nm for phycocyanin. Pigments content was determined from the absolutely dry weight, employing the equations of Siegelman and Kucia [18].

ICP-OES analysis

The elemental composition in the soil extract was determined by inductively coupled plasma atomic emission spectroscopy (Varian-Vista MPX CCD Simultaneous ICP-OES).

Carbohydrates analysis

The extracellular carbohydrates were analyzed by the phenol-sulphuric method of Dubois [19] using glucose as a standard.

Organic carbon analysis

The determination of soil organic carbon was based on the Walkley-Black chromic acid wet oxidation method. Oxidation matter in the soil is oxidized by 1 N $\text{K}_2\text{Cr}_2\text{O}_7$ solution. The remaining dichromate is titrated with ferrous sulphate. The titre is inversely related to the amount of carbon present in the soil sample [20].

HPLC analysis

The amounts of humic acid and thiamine were determined using a modular HPLC system consisting of a pump Perkin Elmer, Series 10, Liquid chromatograph, chromatography column C18, UV-detector. Mobile phase 9:1, phosphate buffer: methanol, pH = 3, flow rate 1 ml min^{-1} .

Matrix synthesis

HEC cryogels were synthesized by a procedure described elsewhere [21]. Briefly, 2 mass % aqueous solution of HEC (Hercules Inc.; MW 1 300 000 g/mol) and photoinitiator ((4-benzoylbenzyl) trimethylammonium chloride, 2 mass% to HEC) were poured into Teflon dishes (20 mm diameter) forming a 2.5 mm thick layer and kept in a freezer at minus 20 °C for 2 h. The frozen system was irradiated with full spectrum UV-vis light with a "Dymax 5000-EC" UV curing equipment with 400 W metal halide flood lamp for 2 min (dose = 11.4 J/cm^2 ; input power = 93 mW/cm^2). Finally, cryogels were extracted with distilled water and freeze dried. Gel fraction yield = $92 \pm 2\%$.

During cell entrapment the algal suspension was centrifuged and re-suspended, as mentioned above, to

reach a concentration of 5.10^6 cells ml^{-1} . The freeze dried matrices were immersed into the suspension and left under illumination at $25^{\circ}C$ without CO_2 supply for 10 days until the whole surface was abundantly covered with algal cells. Cell count was accomplished by mechanical disruption of one matrix with cells. The experiment was carried out in triplicate and average values were presented.

For each medium the experiments were carried out in 2 replicate flasks and every experiment was repeated 3 times. Values presented in the figures are the means \pm standard deviations of the different experiments.

RESULTS AND DISCUSSION

Growth, pigment content and polysaccharide production in different media

The growth and development of *Rhodella reticulata* were studied in five different media to estimate their influence. Media constituents are presented in Tables 1 and 2.

The initial cell dry weight employed in the experiments was 0.85 mg ml^{-1} and its change was measured for a period of 72 h (Fig. 1). Medium 5, we will call medium C for convenience. The

obtained results after comparison of the 5 different media showed that the most intensive growth of cells was observed for the new medium C.

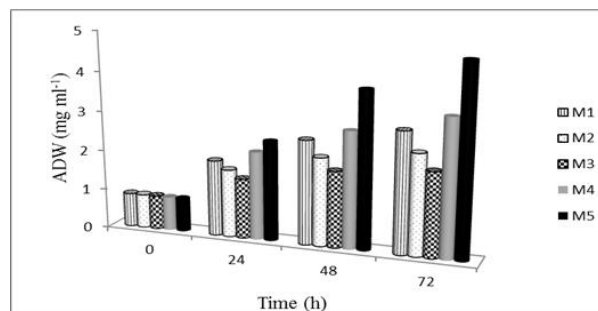


Fig. 1. Development of *Rhodella reticulata* for 72 h using 5 different media. (M-medium)

The optimization of the concentration of the participating nutrients and the addition of soil extract resulted in important quantitative and qualitative differences from the other media used. The growth was worst in medium 3 and medium 2 and best in medium C, in which the algal growth was increased 1.6-fold at the 72nd h compared to the standard medium 1. The new medium C contained 1076 mg l^{-1} nitrogen.

Table 1. Compositions of 5 different types of media used for the cultivation of *Rhodella reticulata*

Media components, (mg l^{-1})	Type of medium				
	1	2	3	4	5
KNO ₃	1240	-	-	620	826
NaNO ₃	-	1250	750	375	250
CaCl ₂ .2H ₂ O	-	2.5	2.5	1.25	0.83
KH ₂ PO ₄	-	175	175	87.5	58.3
K ₂ HPO ₄	620	75	75	347.5	413.3
MgSO ₄ .7H ₂ O	2500	75	75	1287.5	1692
KCl	8000	-	-	4000	5333
NaCl	6260	6260	6260	6260	6260
KI	500	-	-	250	333
KBr	500	-	-	250	333
ME	0.72	0.9	0.9	0.40	0.51
Ca(NO ₃) ₂	170	-	-	85	113
Vitamin B12			5-10.10 ⁶ g l^{-1}		
Soil (soil extract)	-	30000	30000	15000	10000
EDTA	9.3	80	80	45	33
FeSO ₄ .7H ₂ O	-	4.98	4.98	2.49	1.66
H ₃ BO ₃	1.55	11.42	11.42	6.485	4.83
% salinity	0.6	0.6	0.6	0.6	0.6

1. Medium of Pekarkova; 2. Medium of Bold (1985) with 3-fold increase in the nitrogen content and soil extract; 3. Medium of Bold with 2-fold increase in the nitrogen content and soil extract; 4. Combination of (medium 1) + (medium 2) in a ratio of 1:1; 5. Medium C - combination of (medium1) + (medium 2) in a ratio of 2:1.

Table 2. Microelements composition in the Pekarkova, Bold and C media

Trace elements (mg l^{-1})	Pekarkova medium	Bold's Basal medium	Medium C
H ₃ BO ₃	3.09	11.4	7.76
MnSO ₄ .4H ₂ O	1.2	1.44	1.52
CoSO ₄ .7H ₂ O	1.4	0.49	1/17
CuSO ₄ .5H ₂ O	1.24	1.57	1.62
ZnSO ₄ .7H ₂ O	1.43	8.82	5.36
NH ₄ Mo ₇ O ₂₄	1.84	0.71	1.59

In comparison to the standard medium 1, the nitrogen quantity was lower. Although the nitrogen content in medium 2 was increased (1250 mg l⁻¹), no intensification of growth of *Rhodella reticulata* was registered.

This result showed that nitrogen concentration in the different variants of the medium (about 1000 mg l⁻¹) is enough for the culture growth and further addition of nitrogen did not lead to an increase in algal growth. Mn, Cu, B, Zn and Co in trace amounts are capable of inducing the growth of microalgae; at the same time, higher concentrations of these micronutrients hinder the growth of microalgae [22, 23]. The new improved medium C, possessed optimal amounts of these micronutrients which resulted in maximum growth. As cells entered the stationary phase of growth (day 4), medium C provided the highest specific growth rate - 0.19 d⁻¹ (Fig 2). We assume that the highest increase in the algal growth in medium C is probably due to the most suitable balance between the basic components. Approximately the same level of growth rate in a medium specific for *Haematococcus pluvialis* was obtained in an airlift reactor reported by Kaewpintong et al.[24].

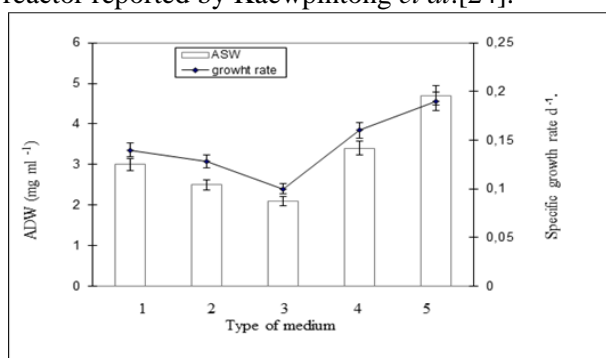


Fig. 2. Absolutely dry weight and specific growth rate of *Rhodella reticulata* obtained during cultivation in the various types of media tested.

Analysis of the elemental composition of the media tested

The main factor for enhanced growth and increase in pigment content and polysaccharide

production appeared to be the choice of the basic components in the medium, together with their most suitable balance. The quantity of some constituents in the combined medium C was reduced as follows: KI, KBr - by 170 mg, MgSO₄ - by 100 mg. The quantity of EDTA was increased 3-fold in the medium C. Important appeared to be the contribution of trace elements in the media (Table 2). Since medium C was based on Pekarkova and Bold's media, a comparison of the trace elements contained in both media showed that the only significant difference was the 6 - fold greater amount of ZnSO₄ and the 3.8 - fold greater amount of H₃BO₃ in the medium. Thus, the Zn concentration seemed to contribute for better growth in the new medium as compared to the standard one.

Pigment content of algae is an important factor that reveals the state of the algal culture. The comparison of the results for pigment quantity at the 72th h of *Rhodella*'s development was carried out. The quantity of pigments was calculated for the medium C and the standard medium. The results showed an increase in the whole pigment quantity by about 1.35-fold compared to the control (Table 3). The pigment content in microalgae is a specific feature for each species. Its evaluation is essential as an indirect measure of cell growth [25]. On the other hand, the pigments can serve as a valuable bioproduct used in different applications: medicine, cosmetics and food industry [26]. In the course of the experiments the production of exopolysaccharide was also followed in the new medium C. The standard "Pekarkova" medium was tested as a control. The polysaccharide production at intensive cultivation was followed with initial algal cell quantity of 1.10⁶ cells ml⁻¹ for 120 h (Fig. 3).

The direct comparison of the results obtained for the standard growth medium used for *Rhodella reticulata* cultivation and the new formulation revealed a more intensive growth of algal cells, increased pigment quantity and higher polysaccharide production.

Table 3. Percent content of pigments from the absolutely dry weight (ADW)

Pigments type	Pigments content (% from ADW)	
	Pekarkova medium	Medium C
Carotenoids	0.46	0.61
Chlorophyll "a"	0.39	0.52
Sum of phycobiliproteins	10.1	13.6

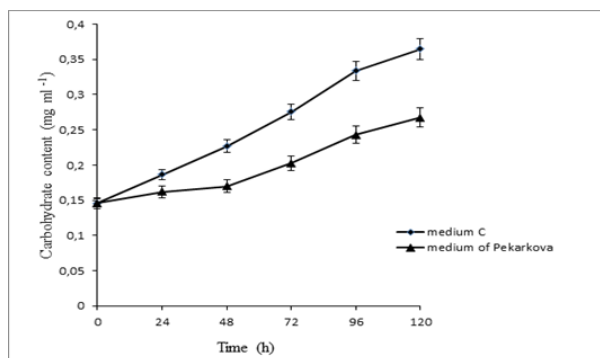


Fig. 3. Production of extracellular polysaccharide by *Rhodella reticulata* cultivated in two media (Pekarkova medium and medium C).

Starting from an equal quantity of polysaccharide in the beginning of the process, at the 120th h, the difference between the carbohydrate contents using the two different media reached about 1.4 - fold. The use of the new medium C led to obtaining of higher values of the polysaccharide quantity - 0.365 mg ml⁻¹, towards 0.267 mg ml⁻¹ for the standard one. Finding the optimal conditions and medium composition for the increased biosynthesis of algal polysaccharides will permit this valuable product to be used in its many applications [27]. This is achieved by the use of the new medium C. This fact could be a prerequisite for a large-scale production of this biopolymer.

Soil extract had been reported to promote the highest increase in dry weight of the marine microalgae *Ulva lactuca* [28]. *Cladophora glomerata*, an attached green alga is a species that grows well on synthetic media supplemented with soil. The same fact was evident from our experiments with *Rhodella*. The exact constituents in the soil extract as an important part of the nutrient medium become essential for the implementation of different physiological experiments [29]. We suggest that the presence of soil extract in the new medium is another factor for growth intensification, which we analyzed precisely. The results did not reveal significant differences in the elemental inorganic constituents of the standard and the new medium, where soil extract was present. Evaluation of the constituents in the soil extract was carried out using ICP-OES analysis (Table 4).

Another survey followed the organic components available in the soil extract. Using the HPLC method and Black chromic acid wet oxidation, the presence of humic acids and thiamine was proved. Their stimulating effect was established by other researchers as well [30].

Table 4. Elemental composition in the aqueous soil extract

N	Elemental composition	Content (mg l ⁻¹)
1	Aluminum	0.2
2	Arsenic	<0.5
3	Calcium	112.8
4	Cadmium	0.011
5	Cobalt	0.015
6	Copper	0.075
7	Iron	0.56
8	Potassium	61.7
9	Magnesium	24.0
10	Manganese	0.555
11	Sodium	28.7
12	Nickel	0.046
13	Phosphorus	9,6
14	Lead	<0.03
15	Sulfur	20.5
16	Zinc	0.743

The values for the quantity of humic acids and thiamine are presented in Figure 4. Retention time of humic acids was 2.435 min and retention time of thiamine was 4.468 min. The amounts of thiamine and humic acids introduced in the new medium C were 40 mg and 85 mg, respectively, obtained from 10 g soil. They are about 30% from the soil organic carbon content. The quantity of organic carbon is about 2.9 % of the soil.

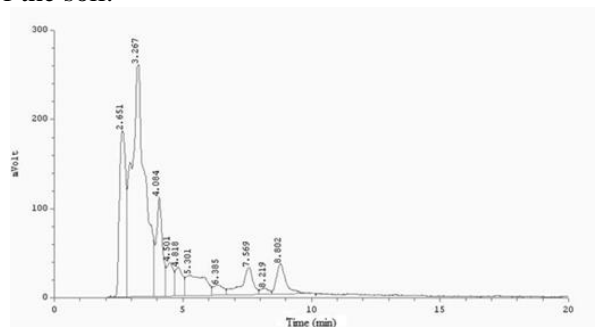


Fig. 4. HPLC determination of thiamine and humic acids content.

Following the HPLC and the ICP-OES analyses, we found that the most important difference of the new medium from the other ones was the presence of thiamine and humic acids. That was the reason for substituting the soil extract with these two components in quantities comparable to those already measured. They appeared to play a major role for the algal growth as organic constituents in the medium with soil extract. To test their effect on algal growth, 3 variants of media were involved, where in addition to the control – standard medium, variant 2 - medium C with humic acids and thiamine, quantity as obtained from the HPLC analysis and 3 - medium C with replaced humic acids and thiamine with soil extract in the same quantity. The results proved that growth was stimulated to the same extent as in the presence of soil extract (Fig. 5).

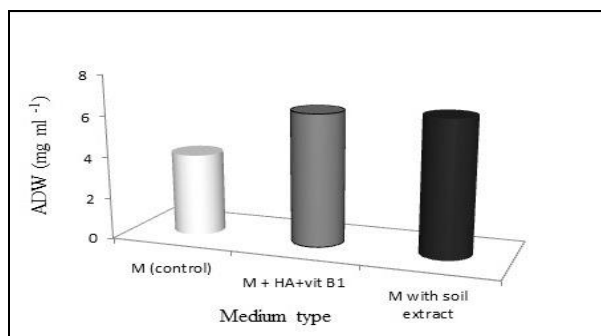


Fig. 5. Influence of humic acids and vitamin B1 on the growth (ADW) of *Rhodella reticulata*

The results obtained proved the significant role of these two organic constituents present together in the medium. When soil extract was included, the values for ADW were 6.55 mg ml⁻¹ compared to 6.4 mg ml⁻¹ when HA and vitamin B1 were added. Literature data also showed that the humic acids and thiamine are capable of enhancing algal production and quality. Only 80-100 mg l⁻¹ of humic acids are required to greatly increase pigment development and growth, influencing the metabolism by their chelating activity [31]. The presence of thiamine is also of major importance for the growth and development of algae. Vitamin B1 is important for primary carbohydrate and amino acid metabolism and likely useful as an anti-oxidant [32]. Depending on the specific conditions, both types of the media (variants 2 and 3) could be appropriate for algae cultivation. If the purpose of the experiment is proving physiological or biochemical characteristics, variant 2 will be more suitable. When we pursue mass cultivation and production of red algae, variant 3 has to be used. In that way the cost of production will be decreased and the biomass yield will be increased. Employing medium C led to significantly higher polysaccharide production and higher pigment content correlated with more intensive growth of the algal strain. As a result from the changes in the nutrient media, during the abundant growth of the algal culture the regulation in its metabolic activity was changed, concerning the pigment and extracellular polysaccharide synthesis.

Cell immobilization

The red microalga *Rhodella reticulata* was cultivated and entrapped for the first time in a HEC cryogel matrix and tested for long-term storage and exopolysaccharide synthesis. The immobilized algae were let to grow on to the polymer matrix for 10 days and then, the cell count was performed. The pure HEC matrix and the matrix with immobilized algal cells are visualized on the digital image (Fig. 6).



Fig. 6. Digital image of the matrix without cells (left) and the matrix with entrapped cells (right)

The good growth and development of the algal culture proved the appropriate choice of matrix for *Rhodella reticulata*. The quantity of immobilized cells was 5.3 10⁶ cells ml⁻¹, which is similar to the free cells cultivation. This result indicates that HEC matrix provides suitable conditions for algal cells growth. In the next step pieces of matrix with immobilized algal cells were transferred to the new medium C and left to develop in flasks under extensive conditions of growth for a period of 15 days. During this period the immobilized *Rhodella* cells started to produce extracellular polysaccharide.

The results showed that starting from a lack of polysaccharide in the beginning because the matrices with cells were transferred into fresh medium, the difference of the carbohydrate content, using free and immobilized cells appeared to be about 1.3-fold at the 20th day. The use of immobilization procedure led to higher values of the exopolysaccharide quantity (Table 5).

The conditions for long-term storage of algal cultures in a laboratory aim to preserve culture vitality. The algal cells immobilized into HEC cryogels were still alive after 90 days. This phenomenon can be attributed to the presence of free water in the macroscopic pores of the cryogel that preserves cells vitality. The survival of immobilized cells after three months storage in a refrigerator in absolute darkness at 4°C without nutrient medium was tested in 30 ml of the new medium C. The estimation of the cell growth was carried out by applying cell count.

Table 5. Content of extracellular polysaccharide produced by immobilized and free algal cells at intensive cultivation.

Time (days)	Polysaccharide (mg ml ⁻¹)	
	Immobilized cells (1.5 10 ⁶ cells ml ⁻¹)	Free cells (1.5 10 ⁶ cells ml ⁻¹)
0	0.0	0.15
24	0.09	0.18
48	0.16	0.19
72	0.25	0.21
96	0.29	0.23
120	0.41	0.26

The matrices were disrupted and immersed into the medium and put at extensive cultivation for 20 days. The initial cell number was $4.6 \cdot 10^6$. The number of cells appeared to be $18.4 \cdot 10^6$ in 30 ml after 20 days, showing the good development of the algal culture.

Immobilization of the red microalga into 2-hydroxyethylcellulose cryogel was performed for the first time. The immobilized cells revealed significantly higher polysaccharide production and more intensive growth. The cells immobilization also led to a prolonged period of storage of vital cells and enhanced production of the desired product, the polysaccharide. The increased quantity of polysaccharide produced was probably due to the new medium that permits good growth and development, and on the other hand, to the suitable conditions provided by the immobilization for the cells. The separation of polysaccharide from the medium was much facilitated when the cells were in an immobilized form. We have to note that the cryogel matrices were synthesized from a low-cost polymer from renewable sources employing a very facile method. Thus, the utilization of HEC cryogels for immobilization and long-term storage of algal cell appears to be an efficient and cheap approach to keep the cells vital and, on the other hand, eliminate the risk of contamination at frequent sifting of the algal cultures.

The isolated polysaccharide was subjected to purification and lyophilization. This ready product is being tested at the moment as a supplement in natural cosmetic products such as gels, creams and serums (data not shown).

CONCLUSION

Algae could significantly contribute to industrial biotechnology. Our experiments proved the increased algal growth by the addition of soil extract to the new medium C as a cheap way for reaching mass production of red algae. Microalgal cultures are recently receiving much attention because of the biotechnological and biomedical production of active biomolecules. A new technological scheme employing immobilization was developed that increased the algal growth and polysaccharide production. For most of the applications, the market is still developing and the biotechnological use of microalgae will extend into new areas.

REFERENCES

1. J. Otero, G. Panagiotou, L. Olsson, *Advances in Biochem. Eng./Biotech.*, **108**, 1 (2007).
2. J. Conquer and B. Holub, *J. Nutr.*, 126, 3032 (1996).

3. Berge J., Debiton E., Dumay J., Durand P., Barthomeuf C., *J. Agr. Food Chem.*, **9 (50/21)**, 6227 (2002).
4. I. Dvir, A. Stark, Ch. Reuven, Z. Madar, S. Arad, *Nutrients*, **1**, 156 (2009).
5. N. Sharma, S. Tiwari, K. Tripathi, A. Rai, *Appl. Phycol.* **23**, 1059 (2011).
6. J. Bermurdez, N. Rosales, C. Loreto, B. Bricen and E. Morales, *World J. Microb. Biot.* **20**, 179 (2004).
7. M. Lapidot, R. Shrestha, Y. Weinstein, S. Arad, *Cell. Orig. Life in Extreme Hab. Astrobiol.* **13 (3)**, 205 (2010).
8. M. Huleihel, V. Ishanu, J. Tal, S. Arad, *J. Appl. Phycol.* **13**, 127-134 (2001).
9. E. Gardeva, R. Toshkova, K. Minkova, L. Gigova, *Biotechnology & Biotech. Equip.* **23**, 783 (2009).
10. S. Mostafa and L. Ali, In: The 4th Conference on Recent Technologies in Agriculture, Proceedings Nov. 3rd-5th, Special Edition of Bull. Fac Agric, Cairo Univ, 918 (2009).
11. T. Toncheva-Panova, J. Ivanova, *J. Appl. Microbiol.* **93 (3)**, 497 (2002).
12. R. Mandalam, B. Palsson, *Biotech. Bioeng.* **59 (5)**, 605 (1998).
13. J. Fábregas, A. Domínguez, M. Regueiro, A. Maseda, A. Otero, *Appl. Microb. Biot.* **53 (5)**, 530 (2000).
14. J. Yim, S. Kim, S. Ahn, H. Lee, *Biomolecular Eng.* **20**, 273 (2003).
15. Y. Chen, *Aquaculture* **263**, 97 (2007).
16. K. Gasljevic, K. Hall, S. Oakes, D. Chapman, E. Matthys, *Eng. Life Sci.* **9 (6)**, 479 (2009).
17. V. Lozinsky, I. Galaev, F. Plieva, I. Savina, H. Jungvid, B. Mattiasson, *Trends Biotechnol.* **21 (10)**, 445 (2003).
18. H. Siegelman and J. Kucia, In: Hellebust, J. and Craisie, J., editors, Handbook of Phycological Methods. Cambridge University Press, UK, **71** (1978).
19. M. DuBois, K. Gilles, J. Hamilton, P. Rebers, F. Smith, *Anal. Chem.* **28 (3)**, 350 (1956).
20. S. McLeod, In: Notes on Soil Technique -Division of Soils, Adelaide, Australia CSIRO 73 (1975).
21. P. Petrov, E. Petrova, B. Tchurbanov, Ch. Tsvetanov, *Polymer* **48 (17)**, 4943 (2007).
22. V. Dembitsky, R. Smoum, A. Aziz Al-Quntar, I. Pergament, M. Srebnik, *Plant Science* **163 (5)**, 931 (2002).
23. A. Ilavarasi, D. Mubarakali, R. Praveenkumar, E. Baldev, N. Thajuddin, *Biotechnology* **10**, 540 (2011).
24. K. Kaewpintong, A. Shotipruk, S. Powtongsook, P. Pavasanta, *Bioresource Technol.* **98**, 288 (2007).
25. M. Henriques, A. Silva, J. Rocha, In: Mendez -Vilaz A. editor. Communicating Current Research and Educational Topics and Trends in Applied Microbiology 1, Badajoz, Spain, Formatex, 586 (2007).
26. P. Spolaore, C. Joannis-Cassan, E. Duran, A. Isambert, *Journal of Bioscience and Bioeng.* **101 (2)**, 86 (2006).
27. S. Geresh, A. Mamontov, J. Weinstein, *J. Biochem. Biophys. Meth.* **50 (2-3)** 179 (2002).
28. A. Nasr, B. Inaam, *Hydrobiologia* **36 (1)**, 53 (1970).

29. P. Harrison, J. Berges, In: R. Andersen, editor. Algal culturing technics. West Boothbay Harbor, ME USA, Elsevier Acad. Press, 21 (2005).
30. H. Bährs and C. Steinberg, *Environ. Sci. Pollut. R.* **19** (2), 335 (2012).
31. R. Haynes, M. Mokolobate, *Agroecosystems* **59**, 47 (2001).
32. E. Bertrand and A. Allen, *Front. Microbiol.* **3**, 375 (2012).

СТРАТЕГИИ ЗА ОПТИМИЗАЦИЯ И УВЕЛИЧАВАНЕ НА РАСТЕЖА, ПРОДУКЦИЯТА НА ПОЛИЗАХАРИД И СЪХРАНЕНИЕ НА ЧЕРВЕНОТО ВОДОРАСЛО *Rhodella reticulata*

Ю. Г. Иванова¹, Л. В. Кабаиванова^{2*}, П. Д. Петров³, С. Н. Янкова⁴

¹Институт по физиология на растенията и генетика, Българска академия на науките, ул. „Акад. Г. Бончев“, бл. 21, 1113 София, България

²Институт по Микробиология, Българска академия на науките, ул. „Акад. Г. Бончев“, бл. 26, 1113 София, България

³Институт по полимери, Българска академия на науките, ул. „Акад. Г. Бончев“, бл. 103, 1113 София, България

⁴Институт по инженерна химия, Българска академия на науките, ул. „Акад. Г. Бончев“, бл. 103, 1113 София, България

(Резюме)

За да се осигурят добри условия за растеж и продукция на хетерополизахарид от червеното микроводорасло *Rhodella reticulata*, е осъществена оптимизация на средата и условията. При използването на нова среда е постигната стимулация на растежа на микроводорасловите клетки до 1.6 пъти. Максимална скорост на растеж ($\mu=0.19 \text{ d}^{-1}$) е достигната в началото на стационарната фаза на растеж (72 h), заедно с увеличаване на пигментното съдържание. Установено е влиянието на голямото количество хуминови киселини и тиамин в средата (доказано с HPLC), върху растежа на водораслото. Получените стойности за количеството екстрацелуларен полизахарид (0.365 mg ml^{-1}), продуциран от водорасловите клетки, култивирани в новата среда са 1.4 пъти по-високи в сравнение с количеството при използване на стандартна среда. Имобилизацията на клетките на *Rhodella reticulata* в супермакропорьозния криогел на основата на 2-хидроксиетилцелулоза доведе до удължителен период на съхранение. Водорасловите клетки са запазили жизнеността си след три месеца и могат успешно да бъдат използвани за продукция на екстрацелуларен полизахарид, като стойностите за количеството му са 1.3 пъти по-високи в сравнение с количеството, синтезирано от свободни клетки.

Low cost fabrication of tandem dye-sensitized solar cells

M. Awais^{1*}, H. Shafeek^{1,2}

¹Department of Industrial Engineering, King Abdulaziz University, Rabigh, Saudi Arabia

²Suez Canal University, Industrial College of Education, Egypt

Received February 14, 2014; Revised July 16, 2014

The overall objective of this research was to deposit metal oxide semiconductor in order to construct dye-sensitized solar cell (DSSC) for converting solar energy into electric energy. It is well known that, TiO₂ is the most common constituent of conventional dye-sensitized solar cell, whereas platinum counter electrode was replaced by *p*-type semiconductor (in this study, NiO) in order to construct tandem dye-sensitized solar cell. The main focus of this research was to prepare NiO electrodes with high surface area in order to increase its photo-conversion efficiency since *p*-type electrode is the limiting factor which was not allowing exploring the potential of tandem cell. In this technique, both NiO and TiO₂ nanoparticles were sprayed onto the conductive glass substrates to prepare loosely adhered particulate coatings. After performing furnace sintering, both NiO and TiO₂ coatings were sensitized with suitable dyes and joined together in order to prepare tandem dye-sensitized solar cells (DSSCs).

Keywords: Dye-sensitized solar cells, TiO₂, *p*-type semiconductor, NiO, sintering

INTRODUCTION

The total power utilized by the world is estimated to be approximately 15 terawatts in one year [1], only 1.6 terawatts of which are produced from renewable energy resources including nuclear fission [2-4]. It is predicted that the fossil fuels, the main ingredient to our energy recipe, may finish in few hundred years (Fig. 1). The diminution of fuel and the global warming, for which the burning of fossil fuels is a major issue, is pushing humanity towards renewable energy resources. The sun is potentially the chief resource of renewable energy as the total power from sunlight striking the earth is a massive of 101,000 terawatts and experts have estimated that if we could harness one hour of that sunlight, it is possible to meet one year energy demands of the world's population.

Bell Laboratories' pioneering work on photovoltaic cells in 1954 [6] helped to carry out solar to electric energy conversion. All three 1st, 2nd and 3rd generations of solar cells are presented in Fig. 2. DSSCs have low efficiencies when compared with other thin film solar cells; however, they offer many advantages over their competitors. They are fabricated through the use of low cost material [7], can be produced more economically and at a lower cost [8]. More importantly, DSSCs can be used in building integrated photovoltaics (BIPV) because of their availability in different color and transparency grades. Lastly, there is a

significant DSSCs market for products which require low power input such as consumer electronics [9, 10].

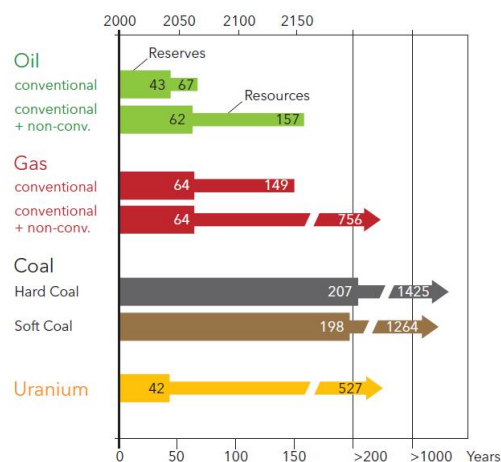


Fig. 1. Range of conventional fuels in years [5]

Types of solar cells	First Generation	Second Generation	Third Generation
Structure			
Efficiency	40%	25%	15%
Materials	Crystalline Silicon	Amorphous Silicon CIGS CdTe	DSSC Perovskite

Fig. 2. Basic structure and current efficiencies of 1st, 2nd and 3rd Gen solar cells

The dye-sensitization process started with the invention of photography back in the 19th century [11]. However, the main credit of converting

* To whom all correspondence should be sent:
E-mail: myunas@kau.edu.sa

photons into an electric current should be given to Tributsch who reported his results with a chlorophyll sensitized zinc oxide (ZnO) electrode [12]. The use of nanoporous metal oxide (TiO₂) electrodes with a roughness factor of ca. 1000 introduced by O'Regan and Grätzel in 1991 [7] transformed the materials from bulk to nano which reduced the size of the material and lead to an increase in surface area [13] (Fig. 3). Because of the higher surface area of TiO₂ nanoparicles resulting in dramatic increase in the light harvesting efficiency, solar cells with an efficiency of 7 % were obtained.

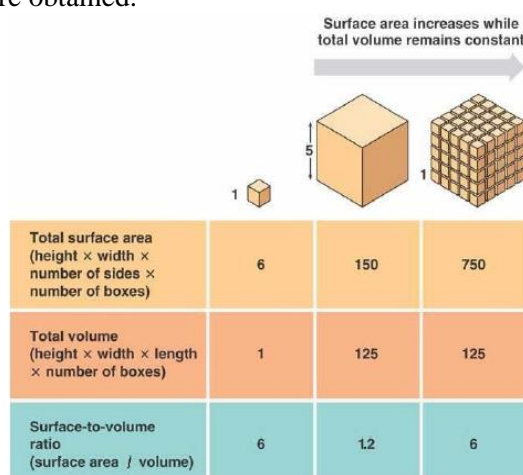


Fig. 3. A cartoon showing the variations in surface-to-volume ratio of bulk vs. nano (adapted from [13]).

With the recent invention of perovskite sensitized solar cells, the efficiencies have gone beyond 11 to 15 % [14-17], which is less than other generations of solar cells [18]. This reduction of efficiency in DSSCs is primarily due to the inefficiency of the dye to absorb all the light from the solar spectrum from visible to near IR region. A method of more effective utilization of the solar spectrum was suggested by He *et al.* [19] in which they substituted the cathode of a conventional DSSC [which is generally a platinum coated fluorine doped tin oxide (FTO) displaying no photoelectrochemical activity] with a dye-sensitized photoactive *p*-type metal oxide, and hence turned the simple cathode into photocathode. By combining this photocathode with a photoanode of a conventional DSSC, a tandem cell is constructed. By using this cell, more visible energy of the solar field could be utilized with the two dyes to complement a wide absorption range. The theoretical upper limit of the efficiency of a cell with two photoactive electrodes is estimated to surpass by 13 % the 32 % theoretical conversion efficiency of the conventional DSSC with one photo-active electrode [19].

In this work, the main requirement was to choose a *p*-type semiconductor surface having high dye adsorption capability. Nickel oxide (NiO) was chosen for these applications in this study, due to its *p*-type nature [20] and remarkable chemical immovability, in addition to good optical and electrical properties [21]. Additionally, NiO wide band-gap energy range from 3.6 to 4.0 eV makes it suitable for tandem solar cell application [20]. NiO coatings have been prepared by spray pyrolysis [22, 23], plasma enhanced chemical vapor deposition [24, 25], pulsed laser deposition [26, 27], electrodeposition [28], chemical bath deposition [22, 29], sol gel [19, 30-34], sputtering [35, 36] and hydrothermal synthesis [28, 37]. Most of the methods involved sintering in order to enhance the packing density of the coatings, to get crystalline structure in the as deposited sputtered coatings [38] and to get rid of the binder in the case of sol-gel prepared coatings. Mostly, heating at 350-550 °C for 30 to 60 min was used [31, 39-41] in conventional furnace treatments.

The purpose of this work was to prepare *n*-type TiO₂ and *p*-type NiO coatings for employing them as electrodes in tandem DSSCs (Fig. 4). The main objective was to prepare coatings displaying meso-structure with improved interconnectivity between the particles and the substrate/electrode interface in order to reduce inherent resistance in the metal oxide structure. The type of structure of the electrode is of extreme importance to obtain the required dye adsorption and charge injection from the dye to the cathode which will eventually enhance the light-to-photocurrent conversion efficiency.

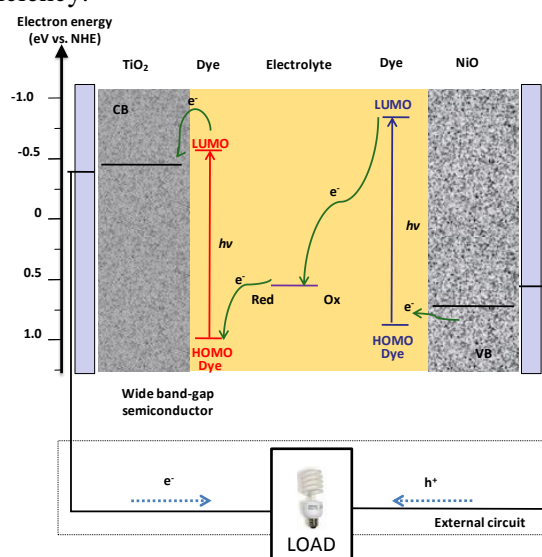


Fig. 4 A schematic showing the working of tandem DSSC

EXPERIMENTAL

NiO coating depositions

The TiO₂ and NiO particulate layers were prepared onto fluorine doped tin oxide (FTO) glass substrates (12 Ω/sq, 3 mm thick) supplied by Solaronix.

The glass substrates (2 × 2 cm) were ultrasonically cleaned in methanol followed by acetone, each for 5 minutes prior to the application of the particulate layers. 50 nm NiO nanoparticles (99.8 %) and 100 nm TiO₂ nanoparticles (99.8 %) supplied by Sigma-Aldrich, were mixed in 2-propanol (20 mg/ml) to make suspension and the particulate layers of TiO₂/NiO were deposited by to-and-fro nebulized spraying [42]. The heat treatments were carried out in air using a Carbolite Furnace (RHF 1200). TiO₂ or NiO samples were treated at temperatures of ~450 °C, for a time of 60 min for TiO₂ and 5 and 30 min for NiO coatings.

Characterizations

The thickness of NiO coatings was measured using step height with WYKO NT1100 optical profilometer in vertical scanning interferometry (VSI) mode. For the morphological analysis and cross sectional investigations, the samples were inspected using a FEI Quanta 3D FEG DualBeam system (FEI Ltd, Hillsboro, USA). X-ray diffraction (XRD) investigations were performed using a Siemens D500 diffractometer operating at 40 kV and 30 mA with Cu Kα radiation in normal diffraction mode at 0.2°/min scan rate in the 2θ range of 40-50°. NiO coatings were sensitized using 0.3 mM Erythrosin B (ERY) dye [19, 39], in a 99.8 % ethanol solution for 1 whole day. The dye adsorption was measured in transmission mode using an Analytik Jena Specord 210 UV-vis spectrophotometer. The wavelength range was 350-700 nm. In order to construct *p*-type DSSCs, the sensitized coatings were sealed face-to-face in a sandwich configuration with a platinum coated FTO counter electrode using 30 μm thick pre-cut Surlyn® thermoplastic frames (6 × 6 mm interior). The device was filled with 0.5M I₂, 0.05M LiI in propylene carbonate electrolyte from a pre-drilled hole made through the counter electrode under reduced pressure. The hole was sealed with Surlyn® and a glass cover-slide. For *J-V* measurements the coatings were masked using a 4 × 4 mm opaque frame and in all cases the cells were illuminated from the NiO working electrode side. The photovoltaic performance (*J-V* characteristics) was measured using a solar simulator AM1.5G, at an intensity of 87 mW cm⁻². The electrochemical investigations were performed

with a three-electrode configuration: NiO coatings and dye sensitized NiO coatings were the working electrodes, whereas two Li rods (Sigma-Aldrich) were utilized as reference and counter electrodes, respectively. Electrolyte was 0.5 M LiClO₄ in anhydrous propylene carbonate (Fisher). The potential values were referred to the Li⁺/Li couple. Cells were prepared in an argon atmosphere inside a glove-box from Innovative Technology (Newbury Port, Massachusetts, USA). In this glove-box the oxygen content was maintained below 10 ppm and water content below 5 ppm. Cyclic voltammeteries were calculated using an electrochemical analyzer (model 604C) from CH Instruments (Austin, Texas, USA).

RESULTS AND DISCUSSION

As shown in Fig. 5, loosely adherent TiO₂ and NiO particulate layers were deposited onto FTO glass substrates, from a metal oxide / 2-propanol slurry using spraying. The coating thickness was maintained at ~2.5 μm by controlling the number of spraying cycles.

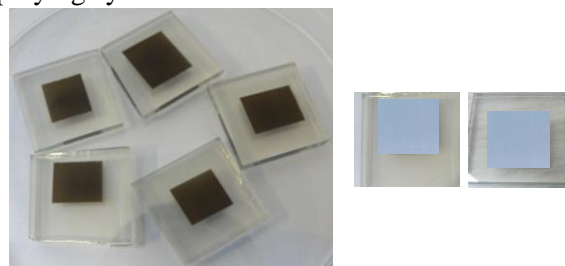


Fig. 5. Approx. 2.5 μm thick NiO (Black) and TiO₂ (White) coatings (1 x 1) cm deposited onto (2 x 2) cm FTO glass substrates using spraying technique.

Thickness was measured using optical profilometry with the help of step height measurements (Fig. 6). In order to enhance the packing density of loosely adhered particles deposited, the conventional furnace treatments of NiO coatings were carried out at 450 °C for 5 min in a box furnace (as described earlier). Heating and cooling rate of 10 °C/min were applied.

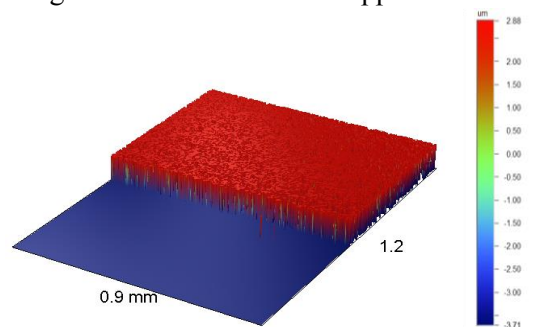


Fig. 6. Approx. 2.5 μm thick NiO coating layer measured via step height measurement using an optical profilometer.

There were already many reported results on TiO₂ based DSSC, thus prior to constructing a tandem DSSC by joining dye-sensitized TiO₂ and NiO electrodes, a comprehensive performance evaluation of NiO *p*-type DSSC was carried out, that included the examination of crystal structure, morphology and dye adsorption properties. The preferred orientation of NiO coatings was found to be (200) with crystallite size of 14 nm using Scherrer equation (*Vide supra*). Enhanced packing density with good interaction between particles and appropriate contact of the particles with the substrates was found on evaluating the morphology/cross sectional investigations of the coatings (Fig. 7). Similar dye absorption was found to correspond to the requirement to construct dye-sensitized solar cells.

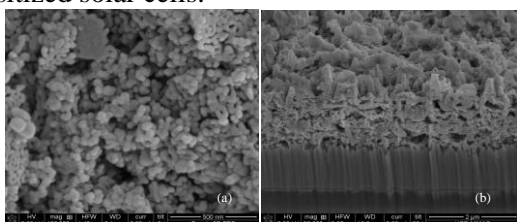


Fig. 7. (a) SEM image of a NiO coating (b) FIB/SEM cross section images of a NiO coating

Finally, *p*-type DSSC were constructed by attaching the sensitized NiO electrodes with platinum counter electrodes and inserting electrolyte between them and their photovoltaic performances were analyzed (Table 1). For 5 min sintering time the results were similar to the reported; however when we increased the sintering time from 5 min to 60 minutes the efficiency, voltage and current density of the solar cells started to decrease. This could be due to convective type of heating that blocks the sensitizer to penetrate into the nanoparticles. Table 1 also includes a literature report for ERY sensitized NiO. These measurements were obtained under the same test methodology as used in this work and quite similar

results were obtained for the case of our sprayed/sintered NiO coatings.

The electrochemical properties of bare NiO coatings and dye-sensitized NiO coatings, were examined in order to evaluate their redox properties [43]. From the integration of the anodic currents observed in the cyclic voltammeteries the sintered coatings were 3.96 mCcm⁻². The NiO oxidation was found to be fully reversible. The integration of the anodic current associated with the oxidation of ERY-sensitized NiO coatings gave a 0.58 mC cm⁻² anodic charge. However, the anodic charges exchanged by the sensitized coatings were generally lower than those exchanged by the unsensitized coatings (0.58 vs.3.96 mCcm⁻² for NiO coatings). This reduction in the charge could be due to a passivation effect of the ERY film in the process of NiO oxidation. In addition, no change in the electrochemical process of oxidation was observed for sensitized NiO coatings when compared with the bare NiO coatings, since ERY did not introduce additional redox processes in the potential window considered here.

A preliminary study was carried out to investigate the performance of NiO coatings in a tandem DSSC configuration. Erythrosin B (ERY) dye [19, 39] was used for sensitizing the NiO electrode to work as a photocathode [19], whereas N719 dye [19, 44, 45] was used to sensitize TiO₂ to work as a photoanode in the tandem DSSC configuration. An 80 mV increase in the open current photovoltage was observed for tandem DSSC when compared with a single photoactive electrode. This value was in close agreement with the reported value (83 mV) in the literature [19]. This preliminary study demonstrated that NiO coatings can be utilized in tandem DSSC configurations. A more detailed investigation is needed in order to optimize properties such as thickness, morphology and open pore structure of the NiO coatings for their use in tandem DSSCs.

Table 1: Photovoltaic performance of *p*-type DSSCs prepared by spraying furnace sintering treatments (compared with reported values in literature).

This study / Reported data	Sintering time (min)	V _{oc} (mV)	J _{sc} (mAcm ⁻²)	FF	Efficiency (η)
In house sprayed and sintered	5	84.00	0.22	25	0.0050
In house sprayed and sintered	30	35.29	0.21	26	0.0023
In house sprayed and sintered	60	25.29	0.20	20	0.0018
He et al. [19] (~1 μm thick)	60	83.00	0.20	27	0.0070

CONCLUSION

In this work, the use of spraying and sintering was investigated for preparing TiO₂ and NiO photoelectrodes for tandem dye-sensitized solar cells. Prior to demonstrate the work of the tandem cell, a standalone *p*-type NiO cell was prepared and its photovoltaic and electrochemical performance was evaluated. The properties of NiO coatings such as crystal structure, morphology and dye adsorption behavior were also investigated in order to relate their performance in solar cells. In this work, tandem DSSC was constructed, however, the potential of NiO in tandem DSSC needs future studies.

Acknowledgment: This work was funded by the Deanship of Scientific Research (DSR), King Abdul Aziz University, Jeddah, under grant number (829-021-D1434). The authors, therefore, acknowledge with thanks DSR technical and financial support.

REFERENCES

1. A. Cho, *Science*, **329**, 786 (2010).
2. N. Lewis, *MRS bulletin*, **32**, 808 (2007).
3. V. Arunachalam, E. Fleischer, *MRS bulletin*, **33**, 264 (2008).
4. D. Ginley, M. Green, R. Collins, *MRS bulletin*, **33**, 355 (2008).
5. www.bgr.bund.de, in, accessed Feb 2014.
6. http://science.nasa.gov/science-news/science-at-nasa/2002/solarcells/, in, accessed Feb 2014.
7. B. O'Regan, M. Grätzel, *Nature*, **353**, 737 (1991).
8. M. Grätzel, *Nature*, **414**, 338. (2001)
9. http://g24i.com/, in, accessed Feb 2014.
10. http://solarprint.ie/, in, accessed Feb 2014.
11. W. West, *Photographic Science and Engineering*, **18**, 35 (1874).
12. H. Tributsch, *Photochemistry and Photobiology*, **16**, 261 (1972).
13. http://chemspace.wordpress.com/nano-properties/capture1/, in, accessed Feb 2014.
14. M.K. Nazeeruddin, F. De Angelis, S. Fantacci, A. Selloni, G. Viscardi, P. Liska, S. Ito, B. Takeru, M. Gratzel, *JACS*, **127**, 16835 (2005).
15. Y. Chiba, A. Islam, Y. Watanabe, R. Komiya, N. Koide, L. Han, *Jap. J. Appl. Physics*, **45**, 638 (2006).
16. J. You, Z. Hong, Y. Yang, Q. Chen, M. Cai, T.-B. Song, C.-C. Chen, S. Lu, Y. Liu, H. Zhou, *ACS Nano*, (2014).
17. J. Burschka, N. Pellet, S.-J. Moon, R. Humphry-Baker, P. Gao, M.K. Nazeeruddin, M. Gratzel, *Nature*, **499**, 316 (2013).
18. M.A. Green, K. Emery, D.L. King, Y. Hishikawa, W. Warta, *Progress in Photovoltaics: Research and Applications*, **14**, 455 (2006).
19. J. He, H. Lindström, A. Hagfeldt, S.-E. Lindquist, *Solar Energy Materials and Solar Cells*, **62**, 265 (2000).
20. H. Sato, T. Minami, S. Takata, T. Yamada, *Thin Solid Films*, **236**, 27 (1993).
21. Y.M. Lu, W.S. Hwang, J.S. Yang, H.C. Chuang, *Thin Solid Films*, **420**, 54 (2002).
22. L. Berkat, L. Cattin, A. Reguig, M. Regragui, J.C. Bernède, *Mater. Chem. and Physics*, **89**, 11 (2005).
23. B.A. Reguig, A. Khelil, L. Cattin, M. Morsli, J.C. Bernède, *Applied Surface Science*, **253**, 4330 (2007).
24. E. Fujii, A. Tomozawa, H. Torii, R. Takayama, *Jap. J. Appl. Physics, Part 2: Letters*, **35** (1996).
25. W.C. Yeh, M. Matsumura, *Jap. J. Appl. Physics, Part 1: Regular Papers and Short Notes and Review Papers*, **36**, 6884 (1997).
26. J. Moscovici, I. Bouessay, A. Rougier, A. Michalowicz, *Physica Scripta*, (2005) 326.
27. B. Sasi, K.G. Gopchandran, *Solar Energy Materials and Solar Cells*, **91**, 1505 (2007).
28. Y.Y. Xi, D. Li, A.B. Djuricic, M.H. Xie, K.Y.K. Man, W.K. Chan, *Electrochem. Solid-State Lett.*, **11**, 56 (2008).
29. X.H. Xia, J.P. Tu, J. Zhang, X.L. Wang, W.K. Zhang, H. Huang, *Electrochimica Acta*, **53**, 5721 (2008).
30. J. He, H. Lindstrom, A. Hagfeldt, S.-E. Lindquist, *The Journal of Physical Chemistry B*, **103**, 8940 (1999).
31. A. Nakasa, H. Usami, S. Sumikura, S. Hasegawa, T. Koyama, E. Suzuki, *Chemistry Letters*, **34**, 500 (2005).
32. E. A. Gibson, A. L. Smeigh, L. Le Pleux, J. Fortage, G. Boschloo, E. Blart, Y. Pellegrin, F. Odobel, A. Hagfeldt, L. Hammarström, *Angewandte Chemie International Edition*, **48**, 4402 (2009).
33. L. Li, E.A. Gibson, P. Qin, G. Boschloo, M. Gorlov, A. Hagfeldt, L. Sun, *Advanced Materials*, **22**, 1759 (2010).
34. P. Qin, J. Wiberg, E.A. Gibson, M. Linder, L. Li, T. Brinck, A. Hagfeldt, B. Albinsson, L. Sun, *The Journal of Physical Chemistry C*, **114**, 4738 (2010).
35. S. Passerini, B. Scrosati, A. Gorenstein, *Journal of the Electrochemical Society*, **137**, 3297 (1990).
36. M. Awais, M. Rahman, J.M. Don MacElroy, N. Coburn, D. Dini, J.G. Vos, D.P. Dowling, *Surface and Coatings Technology*, **204**, 2729 (2010).
37. L. Le pleux, B. Chavillon, Y. Pellegrin, E. Blart, L. Cario, S. Jobic, F. Odobel, *Inorg. Chem.*, **48**, 8245 (2009).
38. K.W. Tan, in: Dept. of Materials Science and Engineering, MIT, 2008.
39. A. Nattestad, M. Ferguson, R. Kerr, Y.-B. Cheng, U. Bach, *Nanotechnology*, **19**, 295 (2008).
40. M. Grätzel, *Journal of Photochemistry and Photobiology A: Chemistry*, **164**, 3 (2004).
41. R. McConnell, *Renewable and Sustainable Energy Reviews*, **6**, 271 (2002).
42. J. Halme, J. Saarinen, P. Lund, *Solar Energy Materials and Solar Cells*, **90**, 887 (2006).
43. G. Boschloo, A. Hagfeldt, *The Journal of Physical Chemistry B*, **105**, 3039 (2001).
44. A. Nattestad, A.J. Mozer, M.K.R. Fischer, Y.B. Cheng, A. Mishra, P. Bauerle, U. Bach, *Nat. Mater.*, **9** (2010) 31-35.
45. F. Odobel, L.c. Le Pleux, Y. Pellegrin, E. Blart, *Accounts of Chemical Research*, **43**, 1063 (2010).

ЕВТИНА ИЗРАБОТКА НА ТАНДЕМНИ ЦВЕТНО-ЧУВСТВИТЕЛНИ СЛЪНЧЕВИ БАТЕРИИ

М. Аваис^{1*}, Х. Шафиик^{1,2}

¹ *Катедра по промишлено инженерство, Университет „Крал Абдулазиз“, Рабигх, Саудитска Арабия*

² *Университет „Суецки канал“, Индустриален колеж, Египет*

Получена на 14 февруари 2014 г.; Ревизирана на 16 юли 2014

(Резюме)

Общата цел на това проучване е да се отложи полупроводник от метален оксид, за да се изградят цветно-чувствителни слънчеви батерии (DSSC) за преобразуване на слънчевата енергия в електрическа енергия. Добре известно е, че TiO_2 е най-честата съставка на конвенционалните цветно-чувствителни слънчеви батерии, докато платиновия противоелектрод е заменен от p -тип полупроводник (в това изследване, NiO), за да се изгради тандемна цветно-чувствителна слънчева батерия. Основната цел на това проучване е да се подготвят NiO електроди с голяма повърхност, за да се повиши тяхната ефективност при фото-преобразуване, тъй като p -тип електрода е ограничаващият фактор, което не позволява разкриването на потенциала на тандемната клетка. В тази техника, покрития от наночастици от NiO и TiO_2 се напръскват върху проводимите стъклени субстрати за получаване на свободно прилепнали покрития от частици. След извършване на синтероване в пещ, NiO и TiO_2 покрития са сенсibiliзирани с подходящи бои и се свързват, за да се подготвят тандемни цветно-чувствителни слънчеви батерии (DSSCs).

Proceedings of the Vth National Crystallographic Symposium

September 25–27, 2014, Sofia, Bulgaria

The Fifth National Crystallographic Symposium with international participation **NCS'14** was held up with the financial support of the **MINISTRY OF EDUCATION AND SCIENCE**
(Project Д-01-239/10.09.2014)

Пети национален кристалографски симпозиум с международно участие **NCS'14** се проведе със съдействието на **МИНИСТЕРСТВОТО НА ОБРАЗОВАНИЕТО И НАУКАТА**
(Договор Д-01-239/10.09.2014)



Preface

Dear reader,

In this issue of Bulgarian Chemical Communications, some studies, presented at the Fifth National Crystallographic Symposium with international participation **NCS'14**, are collected. This most important event, which took place from 25th to 27th September, 2014 at the University of Chemical Technology and Metallurgy – Sofia was organized under the auspices of the Bulgarian Crystallographic Society and was dedicated to the officially proclaimed by the General Assembly of the United Nations International Year of Crystallography. The year 2014 marked the centennial of the birth of modern crystallography and we hope to have used this opportunity to stimulate and ignite an interest in crystallography amongst students, scientists and the general public.

Following the tradition, established during the previous symposia of the Bulgarian Crystallographic Society, the organizers have invited leading researchers from abroad and from Bulgaria. The invited speakers were: Prof. Dr. J. Manuel Perez-Mato (University of Basque Country, Bilbao, Spain), Prof. Dr. Ulrich Bismayer (University of Hamburg, Germany), Prof. Dr. Georgi Kirov (Sofia University “St. Kliment Ohridski”, Bulgaria), Prof. Dr. Ross Angel (University of Padova, Italy), Prof. Dr. Maria Lalia-Kantouri (Aristotle University of Thessaloniki, Greece), Dr. Tonya Vitova (Karlsruhe Institute of Technology, Germany), Dr. Jörg Rothe (Karlsruhe Institute of Technology, Germany), Dr. Emre S. Tasci, (Middle East Technical University, Ankara, Turkey), Dr. Biliانا Gasharova (Karlsruhe Institute of Technology, Germany), Dr. Krassimir Grabev (Karlsruhe Institute of Technology, Germany), Assoc. Prof. Dr. Rossitza Pentcheva (University of Duisburg-Essen, Germany). Their participation made **NCS'14** attractive and useful for a wide range of participants from the scientific community, giving them the chance to become acquainted with the

current research achievements in the field of crystallography, presented in an impressive and interesting way. The invited speakers, showed the audience directions and trends in the development of modern science.

One of the sessions of the Fifth National Crystallographic Symposium, was dedicated to Prof. Georgi Kirov from Sofia University “St. Kl. Ohridski”. He was the first scientist awarded an honorary sign by the Bulgarian Crystallographic Society for his overall activity and his outstanding contribution to the development of crystallography in Bulgaria.

As expected in the International Year of Crystallography and to the delight of the organizers, this edition of the symposium **NCS'14** was marked by the largest number of participants compared to the previous ones. Bulgarian scientists from eight universities, eleven institutes of the Bulgarian Academy of Sciences and scientists from universities and institutes from Germany, Italy, Spain, Turkey, Greece, the Republic of Macedonia, USA and Egypt submitted 27 oral and 90 poster presentations, which involved more than 300 authors. It is our sincere hope that the participation of various representatives of the domestic and foreign scientific institutions as well as the presentation of extremely versatile topics led to fruitful work, interesting and useful encounters for the participants in this scientific forum and thus, the objectives intended during the **NCS'14** were achieved. An important incentive for the **NCS'14** participants was the opportunity to publish in this journal.

Established practice of the organizers of the National Crystallographic Symposia is to encourage and support the scientific progress of young researchers. There were some new and good ideas in this regard last year. It is also a great achievement that over 30% of the participants in **NCS'14** were students, PhD students and young scientists who actively participated in the poster sessions.

Eleven scientific sessions (including two poster sessions) which were conducted within three days were field for lively discussions and exchange of ideas and we expect them to be useful for the future work of the participants. An award for the Best Poster Contribution by young scientist was announced, which was given by the international jury to the students from the University of Chemical Technology and Metallurgy – Sofia: A. Petrova, S. M. Angelova and I. A. Nikolchina.

Between 2009 and 2014, successively the Ist, IInd, IIIrd, IVth and Vth National Crystallographic Symposia (NCS) were successfully held in Sofia. During the years this scientific forum has become an attractive initiative for a wide range of scien-

tists to meet and exchange ideas. We are pleased to announce on the pages of Bulgarian Chemical Communications, that International School on Introduction in the Rietveld Structure Refinement, will be held in Sofia between September, 28th and October, 3rd 2015 as well as the Sixth National Crystallographic Symposium, **NCS'16** to be conducted in 2016. These events, organized by the Bulgarian Crystallographic Society and the studies presented in this issue of Bulgarian Chemical Communications will hopefully provoke a growing interest in crystallography in the Bulgarian scientific community and will show the opportunities it offers to researchers from diverse scientific areas.

Irena Mihailova

Comparison of thermal behaviour of γ - $\text{MnC}_2\text{O}_4 \cdot 2\text{H}_2\text{O}$ in oxidative and inert media

B. Donkova¹, V. Petkova^{2, 3*}

¹ Department of General and Inorganic Chemistry, Faculty of Chemistry and Pharmacy, University of Sofia, 1 J. Bourchier Av., 1164 Sofia, Bulgaria; E-mail: nhbd@inorg.chem-uni.sofia.bg;

² Department Natural Sciences, New Bulgarian University, 21 Montevideo Str., 1618 Sofia, Bulgaria

³ Institute of Mineralogy and Crystallography, Bulgarian Academy of Sciences, Acad. G. Bonchev Str., bl. 107, 1113 Sofia, Bulgaria

Received December, 2014; Revised January, 2015

The aim of the present study is to investigate and compare the decomposition mechanism of the slightly known γ - $\text{MnC}_2\text{O}_4 \cdot 2\text{H}_2\text{O}$ in oxidative and inert media under non-isothermal conditions with analysis of the evolved gases. Pure phase of pinkish orthorhombic dihydrate was obtained and characterized by X-ray diffraction and scanning electron microscopy. The non-isothermal investigation was carried out in static air and dynamic Ar atmosphere (60 ml min^{-1}) at a heating rate of $5 \text{ }^\circ\text{C min}^{-1}$ in the range of $25\text{--}800 \text{ }^\circ\text{C}$, using a coupling system TG-MS – instrument SETSYS2400 combined with a mass-spectrometer. According to TG-DTA-DTG curves, dehydration proceeds in the interval $140\text{--}187 \text{ }^\circ\text{C}$ in Ar and $140\text{--}182 \text{ }^\circ\text{C}$ in air. The corresponding intervals of decomposition are $335\text{--}434 \text{ }^\circ\text{C}$ in Ar and $230\text{--}361 \text{ }^\circ\text{C}$ in air. In inert Ar atmosphere, CO and CO_2 are liberated simultaneously and MnO is obtained as a final product. In oxidative air atmosphere the evolved CO participate in additional oxy-reduction reactions and only CO_2 is detected. The decomposition is accompanied by oxidation of Mn(II) thus leading to formation of manganese oxides in higher and most probably mixed oxidation states.

Keywords: manganese(II) oxalate; decomposition, thermal analyses, XRD, SEM.

INTRODUCTION

Sparingly soluble manganese oxalate is widely used nowadays as a precursor for various nano-sized manganese oxides with a variety of technological applications due to their magnetic, electric and catalytic properties [1, 2, 3]. The widespread use of manganese oxides and the dependence of their properties on composition explain the interest in studying the process of thermal decomposition of manganese oxalate. A specific feature of this system is the simultaneous liberation of CO_2 and CO, the latter being able to reduce the obtained oxide.

Recently, three crystal forms of manganese oxalate are known – monoclinic α - $\text{MnC}_2\text{O}_4 \cdot 2\text{H}_2\text{O}$ (SG C2/c) [4], orthorhombic γ - $\text{MnC}_2\text{O}_4 \cdot 2\text{H}_2\text{O}$ (P2₁2₁2₁) [5] and orthorhombic trihydrate $\text{MnC}_2\text{O}_4 \cdot 3\text{H}_2\text{O}$ (Pcca) [6]. While the mechanism and products of

thermal decomposition of monoclinic dihydrate in air have been extensively studied by various methods [7–12], the literature data for the trihydrate and orthorhombic dihydrate are quite scarce – [12, 13] and [14], respectively, as well as our papers [15, 16]. Our previous investigations [15] revealed that the difference in the crystal lattice of α - $\text{MnC}_2\text{O}_4 \cdot 2\text{H}_2\text{O}$ and $\text{MnC}_2\text{O}_4 \cdot 3\text{H}_2\text{O}$ is responsible for both the **different thermal behavior of the materials** and the different extent of Mn(II) oxidation. In the present study, we focused on the crystal form γ - $\text{MnC}_2\text{O}_4 \cdot 2\text{H}_2\text{O}$. The mechanism of its thermal decomposition is investigated and a comparison between its behavior in air and in Ar atmosphere is performed on the basis of thermal analysis data.

EXPERIMENTAL

Manganese oxalate was synthesized by mixing $\text{Mn}(\text{NO}_3)_2$ and $(\text{NH}_4)_2\text{C}_2\text{O}_4$ solutions at room temperature. The obtained precipitate was kept for 8 hours at $60 \text{ }^\circ\text{C}$ and magnetically steered. The pinkish

* To whom all correspondence should be sent:
E-mail: vpetkova@nbu.bg

product $\gamma\text{-MnC}_2\text{O}_4\cdot 2\text{H}_2\text{O}$ was filtered, washed several times and dried in a desiccator.

Orthorhombic $\gamma\text{-MnC}_2\text{O}_4\cdot 2\text{H}_2\text{O}$ was investigated by X-ray diffraction using a D 500 Siemens powder diffractometer with $\text{Cu K}\alpha$ radiation. The phase identification was performed by the JCPDS data-base. The morphological characterization was carried out by a scanning electron microscope (SEM) JEOL JSM-5510. The thermal investigation was performed in both static air and Ar flow (60 ml min^{-1}) on a sample of mass about 15 mg, with a heating rate of $5\text{ }^\circ\text{C min}^{-1}$ in the range of $25\text{--}800\text{ }^\circ\text{C}$, using a coupling system TG-MS – instrument SETSYS2400 (SETARAM, France) for thermal analysis and OmniStar mass spectrometer.

RESULTS AND DISCUSSION

The X-ray pattern is presented in Fig. 1 (a) and confirms that as synthesized product is a pure phase of $\gamma\text{-MnC}_2\text{O}_4\cdot 2\text{H}_2\text{O}$ (JPCDS 32-0647). The strongest reflections of $\text{MnC}_2\text{O}_4\cdot 3\text{H}_2\text{O}$ (13.323 deg) and of $\alpha\text{-MnC}_2\text{O}_4\cdot 2\text{H}_2\text{O}$ (18.430 deg) were not observed. The high intensities and small FWHM of the diffraction peaks indicate a good crystallinity of the sample. The scanning electron microscope image of the sample (Fig. 1, b) shows a rod-shape of the crystals. Due to the long duration of magnetic stirring, the rods of oxalate are fragmented and with uneven walls, but their prismatic shape is clearly visible.

Figure 2 shows the TG/DTA curves in air and in Ar at a heating rate of $5\text{ }^\circ\text{C}\cdot\text{min}^{-1}$. The evolved

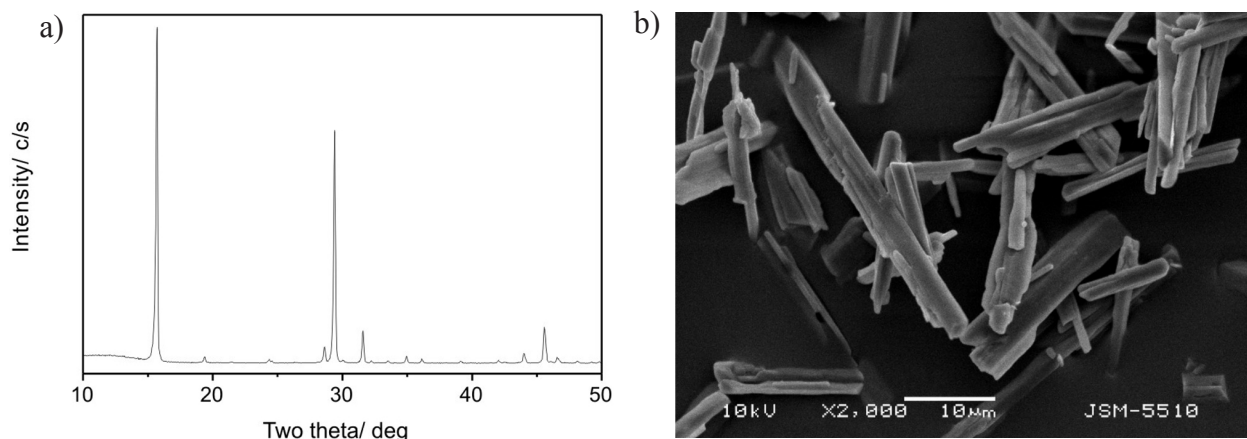


Fig. 1. XRD pattern (a) and scanning electron micrograph of $\gamma\text{-MnC}_2\text{O}_4\cdot 2\text{H}_2\text{O}$ (b)

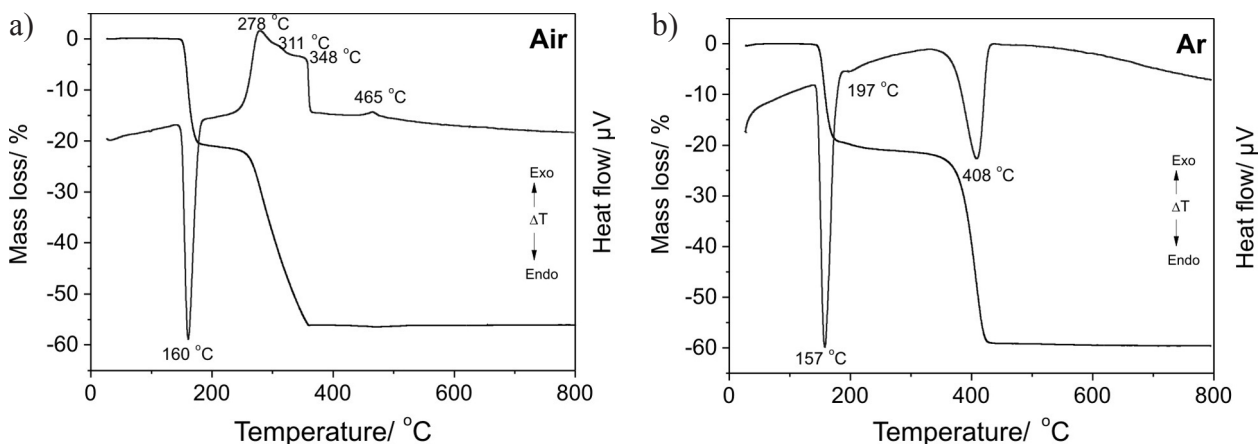


Fig. 2. DTA and TG curves of $\gamma\text{-MnC}_2\text{O}_4\cdot 2\text{H}_2\text{O}$ decomposition in air (a) and Ar (b)

gases are depicted on Fig. 3. As expected, for $\text{MnC}_2\text{O}_4 \cdot 2\text{H}_2\text{O}$ the temperature of dehydration is almost the same in both media, with peaks position at 156 °C in Ar and 160 °C in air. The dehydration occurs in a single step as in the case of monoclinic α - $\text{MnC}_2\text{O}_4 \cdot 2\text{H}_2\text{O}$ [15]. The theoretical mass loss (ML_{th}) is 20% and the observed experimental values (ML_{exp}) at the end of the steep slope of TG-curves in Ar and air are 19,3% and 20,6%, respectively.

The decomposition process is carried out after dehydration and the temperature of decomposition depends on the kind of atmosphere, in which the process is occurred and on the inclination of the Mn(II) to be oxidized. It is known that in air, oxidation of Mn(II) to Mn(III) takes place just before decomposition and catalyzes the latter [7, 8, 11, 17]. Accordingly, the decomposition in Ar starts at 325 °C, a much higher temperature than in air and one narrow endo-thermal peak is observed at 408 °C. In oxidative medium (air), the decomposition starts at 227 °C and results in several exo- and endo-thermal peaks at 278, 311 and 348 °C. The DTA curve is more complicated due to the overlapping of the

processes of decomposition, oxidation of Mn(II) to higher oxidation states Mn^{n+} and a subsequent reduction to Mn^{m+} . The above statements are supported by evolution curves of the liberated during decomposition gases (Fig. 3). In Ar atmosphere CO and CO_2 are liberated simultaneously in the narrow interval of 325 to 449 °C with peaks of the symmetric curves at 408 °C, while in air only CO_2 evolution is observed which starts at much lower temperature. The lack of CO evolution as well as the consumption of O_2 in this region (not shown) indicates that CO oxidation takes place during the decomposition, most probably catalyzed by Mn^{n+} and Mn^{m+} [8] available in the system. This leads to the broad asymmetric curve of CO_2 evolution and implies that the CO oxidation contributes to the complicated trend of the DTA curve.

The experimentally measured mass losses at the end of decomposition in Ar and air are 59,1% and 56,3%, respectively. The theoretical values for obtaining of different manganese oxides are 51,4% (MnO_2), 55,04% (Mn_5O_8), 55,9% (Mn_2O_3), 57,38% (Mn_3O_4), and 60,35% (MnO). Based on the observed

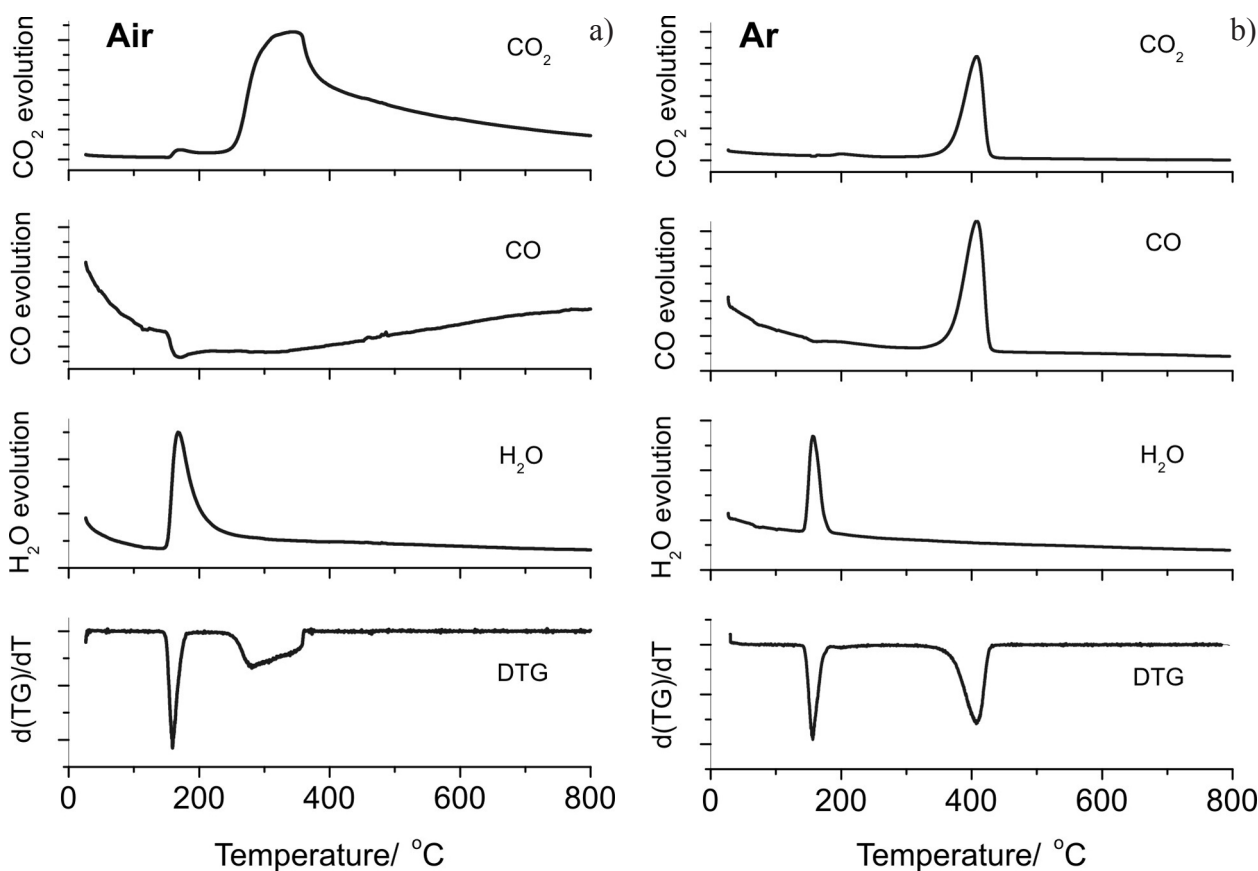


Fig. 3. DTG and evolution curves of H_2O , CO and CO_2 in air (a) and Ar (b)

ML_{exp} and the green color of the final product, one can conclude that in Ar atmosphere the decomposition of γ - $\text{MnC}_2\text{O}_4 \cdot 2\text{H}_2\text{O}$ leads to the formation of MnO. In air probably mixture of oxides Mn_2O_3 and Mn_3O_4 is produced, but it is difficult to define the products only on the basis of TG analysis because of the complexity of the system. For understanding of the phenomena additional studies by other methods are necessary to be performed.

CONCLUSIONS

Thermal decomposition of γ - $\text{MnC}_2\text{O}_4 \cdot 2\text{H}_2\text{O}$ in both air and Ar was investigated and compared. Data for the evolved gases during decomposition of this crystal form of manganese oxalate is reported for the first time. According to TG-DTA-DTG curves, dehydration proceeds in the interval 140–187 °C in Ar and 140–182 °C in air. The corresponding intervals of decomposition are 335–434 °C in Ar and 230–361 °C in air. In Ar atmosphere, CO and CO_2 are liberated simultaneously and MnO is obtained as a final product. In oxidative air atmosphere the evolved CO participate in additional oxy-reduction reactions and only CO_2 is detected. The decomposition is accompanied by oxidation of Mn(II) leading to the formation of manganese oxides in higher and most probably mixed oxidation states. The investigations at other heating rates and calculation of the reaction enthalpy and activation energy of the processes under different atmospheres are in progress.

REFERENCES

1. K.-W. Zhou, W.-W. Wu, Y.N. Li, X.H. Wu, S. Liao, *J. Therm. Anal. Calorim.*, **114**, 205 (2013).
2. K. Muraleedharan, P. Labeeb, *J. Therm. Anal. Calorim.*, **109**, 89 (2012).
3. S. J. Joshi, K. P. Tank, B. B. Parekh, M. J. Joshi, *J. Therm. Anal. Calorim.*, **112**, 761 (2013).
4. R. Deyrieux, C. Berro, A. Peneloux, *Bull. Soc. Chim. Fr.*, **1**, 25 (1973).
5. Z. A. D. Lethbridge, A. F. Congreve, E. Esslemont, A. M. Z. Slawin, P. Lightfoot, *J. Solid State Chem.*, **172**, 212 (2003).
6. W.-Y. Wu, Y. Song, Y.-Z. Li, X.-Z. You, *Inorg. Chem. Commun.*, **8**, 732 (2005).
7. E. D. Macklein, *J. Inorg. Nucl. Chem.*, **30**, 2689 (1968).
8. D. Dollimore, D. L. Griffiths, *J. Therm. Anal.*, **2**, 229 (1970).
9. M. I. Zaki, A. K. Nohman, Ch. Kappenstein, T. M. Wahdan, *J. Mater. Chem.*, **5**, 1081 (1995).
10. A. K. Nikumbh, A. E. Athare, S. K. Pardeshi, *Thermochim. Acta*, **326**, 187 (1999).
11. M. A. Mohamed, A. K. Galwey, S. A. Halawy, *Thermochim. Acta*, **429**, 57 (2005).
12. O. I. Gyrdasova, V. N. Krasil'nikov, G. V. Bazuev, *Russ. J. Inorg. Chem.*, **54**, 1035, (2009).
13. K. B. Zaborenko, Shu-Ch'un Kung, L. L. Melikhov, V. A. Portyanoi, *Radiokhimiya*, **6**, 749 (1966) (*in Russ.*).
14. Z. G. Jia, L. H. Yue, Y. F. Zheng, Z. D. Xu, *Chinese J. Inorg. Chem.*, **23**, 181 (2007).
15. B. Donkova, D. Mehandjiev, *Thermochim. Acta*, **421**, 141 (2004).
16. B. Donkova, D. Mehandjiev, *Compt. Rend. Acad. Bul. Sci.*, **66**, 983 (2013).
17. M. E. Brown, D. Dollimore, A. K. Galwey, *J. Chem. Soc., Faraday Trans.*, **1:70**, 1316 (1974).

СЪПОСТАВЯНЕ НА ТЕРМИЧНОТО ПОВЕДЕНИЕ НА γ -MnC₂O₄·2H₂O В ОКИСЛИТЕЛНА И ИНЕРТНА АТМОСФЕРА

Б. Донкова¹, В. Петкова^{2,3}

¹ Катедра по Обща и Неорганична химия, Факултет по Химия и фармация, СУ „Св. Кл. Охридски“,
бул. „Дж. Баучер“ №1, София 1164, България

² Департамент „Природни науки“, Нов Български Университет, ул. „Монтевидео“ №21,
София 1618, България

³ Институт по минералогия и кристалография, Българска академия на науките,
ул. „Акад. Г. Бончев“, бл. 107, София 1113, България

Постъпила декември, 2014 г.; приета януари, 2015 г.

(Резюме)

Цел на представената работа е изследване и съпоставяне на процеса на неизотермично разлагане на слабо изучения γ -MnC₂O₄·2H₂O в окислителна и инертна атмосфера, съпроводено с анализ на отделените газове. Полученият орторомбичен дихидрат е охарактеризиран посредством рентгенова дифракция и сканираща електронна микроскопия. Изследването при неизотермични условия е проведено в среда от статичен въздух и продухвач Ar (60 ml min⁻¹) в температурен интервал 25–800 °C при скорост на нагряване 5 °C min⁻¹. Използван е TG-MS – апарат SETSYS2400, комбиниран с мас-спектрометър. Съгласно TG-DTA-DTG кривите, в Ar атмосфера дехидратацията протича в интервала 140–187 °C, а разлагането в интервала 335–434 °C. Съответните температурни интервали в среда на въздух са 140–182 °C и 230–361 °C. В инертната Ar среда е установено едновременно отделяне на CO и CO₂ в хода на разлагане на оксалата, като крайният продукт е MnO. В окислителна среда отделяният се при разлагане CO участва в допълнителни окислително-редукционни процеси, поради което се регистрира единствено отделяне на CO₂. Процесът на разлагане на γ -MnC₂O₄·2H₂O в тази среда е съпроводен с окисление на Mn(II), водещо до получаване на оксиди, в които манганът е в по-високи и най-вероятно смесени окислителни състояния.

Comparative study of ZnO photocatalyst samples prepared by different methods

K. I. Milenova^{1*}, A. E. Eliyas¹, V. N. Blaskov², I. A. Avramova², I. D. Stambolova²,
S. V. Vassilev³, P. M. Nikolov⁴, N. A. Kassabova⁴, S. K. Rakovsky¹

¹ Institute of Catalysis, BAS, Acad. G. Bonchev St, bl.11, 1113 Sofia, Bulgaria

² Institute of General and Inorganic Chemistry, BAS, Acad. G. Bonchev St, bl.11, 1113 Sofia, Bulgaria

³ Institute of Electrochemistry and Energy Systems, BAS, Acad. G. Bonchev bl. 10, 1113, Sofia, Bulgaria

⁴ University of Chemical Technology and Metallurgy, 8 Kliment Ohridski, 1756, Sofia, Bulgaria

Received December, 2014; Revised January, 2015

Three different ways of preparation: activation (ZA), precipitation method using two different ingredients (ZP, ZD) were used to obtain nanosize ZnO powders. The photocatalytic activity was tested in the reaction of oxidative discoloration of diazo dye solution. The ZnO nanoparticle powders were obtained and characterized by XRD, IRS, TG – DTA, XPS and BET methods. The XRD analysis of ZnO photocatalysts showed presence of wurtzite ZnO phase, while IRS proves the formation of Zn–O bonds. The specific surface area of the ZnO sample, obtained by the activation method, was higher, compared to the other samples. The photocatalytic properties of the samples were tested in the reaction of oxidative degradation of Reactive Black 5 azo dye in solution. All the three photocatalysts showed high effectiveness in the dye degradation. The best photocatalyst is the activated ZnO powder, prepared by an original patented method. The highest rate constant of degradation of Reactive Black 5 model contaminant is on the ZA sample ($33.8 \times 10^{-3} \text{ min}^{-1}$).

Key words: ZnO; photocatalysis; ultraviolet light; azo dye.

INTRODUCTION

The discharging of waste water from textile industries into waterways is causing a huge environmental problem. The wastewater not only deteriorates the aesthetic view of water, but it is also noxious for aquatic flora and fauna. Among the various dyes, present in wastewaters from textile industries, the azo dyes constitute the largest portion. These dyes are known to be toxic, carcinogenic and they can induce mutations [1]. Different purification technologies such as: biological treatment, adsorption, filtration, ozonation, sedimentation, and UV/visible light/solar photocatalytic processes, etc. have been used for dyes treatment. Among them, the photocatalytic degradation of organic pollutants under UV irradiation has received much attention in view of purifying waste waters [2–8]. When a photocatalyst is irradiated with light having photon energy greater than or equal to the band gap energy, an electron from valence band is excited into the conduction band. The remaining hole oxidizes

water molecules giving OH radicals, while the conduction band electron reduces the adsorbed oxygen molecule to give superoxide radical anion, which further results in the formation of additional OH radicals. The OH radical is a strong oxidizing agent via radical-chain mechanism leading to complete mineralization of the dye [9, 10]. The photocatalytic degradation of dyes was studied using commercial ZnO [9, 11] or ZnO prepared by different techniques such as: thermal evaporation [10–12], thermal decomposition of zinc oxalate [11–14] etc. The degradation of various dyes, such as Mordant Black 11 [11], Methyl Orange [12, 14] and Reactive Red 120 [13] was investigated on ZnO.

In the present study we investigate the phase and chemical composition of ZnO samples prepared in three different ways: activation, precipitation method using two different ingredients. The photocatalytic activity was tested in the reaction of oxidative discoloration of Reactive Black 5 azo dye solution.

EXPERIMENTAL

(1) Activated ZnO powder was obtained by original patented method (*Bulgarian Patent 28915/*

* To whom all correspondence should be sent:
E-mail: kmilenova@ic.bas.bg

1980), described in ref. [15]. The preparation includes dissolution of commercial ZnO in nitric acid, followed by simultaneous treatment using NH_4OH solution and CO_2 bubbling leading to precipitation of $\text{Zn}(\text{OH})\text{CO}_3$ (ZH), which was further thermally decomposed at 500°C for 3h. The so prepared powder sample was denoted as (ZA).

(2) Na_2CO_3 was dissolved in H_2O and added dropwise to solution of $\text{ZnSO}_4 \cdot 7\text{H}_2\text{O}$ under heating and continuous stirring (pH value adjusted to 11). The precipitate was separated by filtration, washed several times with distilled water and dried in air. The corresponding precursor was heated for 3 h at 500°C in air. The so prepared ZnO sample was denoted as (ZP).

(3) The third sample was synthesized in the same way as the second sample, but using different starting materials – this time $\text{Zn}(\text{NO}_3)_2 \cdot 6\text{H}_2\text{O}$ and NH_4HCO_3 . The so prepared powder sample was denoted as (ZD).

For comparison the commercial ZnO sample (denoted as ZC) has also been tested.

All the chemicals, used for the synthesis of the ZnO samples: $\text{Zn}(\text{NO}_3)_2 \cdot 6\text{H}_2\text{O}$, $7\text{NH}_4\text{HCO}_3$, $\text{ZnSO}_4 \cdot 7\text{H}_2\text{O}$ and Na_2CO_3 have been delivered by the Bulgarian branch of Aquachim Merck (at present Aquachim Beckmann Coulter) and are analytical grade of purity, with the exception of ZnO (Chemapol, Praha), which is technical grade of purity.

The phase composition of the samples was studied by X-ray diffraction (XRD) with CuK_α -radiation (Philips PW 1050). The crystallite size, was estimated from the XRD spectra, according to Sherrer's equation.

The DTA and TG curves have been recorded on a LABSYSTEM EVO apparatus SETARAM (France), at a heating rate of $10^\circ/\text{min}$ starting from 25°C until reaching 600°C in alumina crucible in air. The determination of the specific surface area of the samples was carried out by the single point Brunauer-Emmet-Teller (BET) method involving nitrogen adsorption from mixture $30\%\text{N}_2+70\%\text{He}$ at the boiling temperature of liquid nitrogen (77.4K) using a conventional volumetric apparatus. Before measuring the specific surface area the samples were degassed at 423K for 30 min to liberate the entire surface from adsorbed impurities until the residual pressure became lower than $1.333 \cdot 10^{-2}\text{Pa}$. The nitrogen (N_2) monolayer formed was used to evaluate the specific surface area (A_{BET}) using the BET equation.

The IR spectra were recorded in the range of 4000 to 400cm^{-1} on a IFS 25 spectrometer (Bruker) with resolution of less than 2cm^{-1} . The samples were prepared in the form of KBr tablets, containing the investigated samples.

The X-ray photoelectron spectroscopy (XPS) studies were performed in a VG Escalab II electron

spectrometer using $\text{AlK}\alpha$ radiation with energy of 1486.6eV under base pressure 10^{-7}Pa and a total instrumental resolution 1eV . The binding energies (BE) were determined utilizing the C1s line (from an adventitious carbon) as a reference with energy of 285.0eV . The accuracy of measuring the BE values was 0.2eV . The C1s, Zn2p and O1s photoelectron lines were recorded and corrected by subtracting a Shirley-type of background and quantified using the peak area and Scofield's photoionization cross-sections.

Reactive Black 5 (RB5), a toxic azo dye was used as a model pollutant for the evaluation of photocatalytic activity. The absorption of RB 5 on suspended ZnO oxides was measured as follows: 0.15g of sample powder was suspended in 150ml of dye aqueous solution (Reactive Black initial concentration, 20ppm giving $\text{pH}=7$), which was then stirred with a magnetic stirrer at a constant magnetic stirring rate (400rpm) under oxidative conditions (bubbling air through two frits to achieve water saturation in oxygen) at room temperature. The photodegradation of Reactive Black 5 (RB5) was studied under standard reference conditions of 1mg/ml suspension. The photocatalytic degree of oxidative degradation of RB5 has been carried out using polychromatic UV-A lamp (Sylvania BLB, 18W), with wavelength range $315\text{-}400\text{nm}$ (with a maximum of the irradiation at 365nm). The light power density on the sample position was $0.66\text{mW}\cdot\text{cm}^{-2}$. The changing concentration of dye in the course of the reaction was monitored using UV-Vis absorbance single beam spectrophotometer CamSpec M501 (UK) at operating in the wavelength range from 190 to 800nm . After reaching adsorption equilibrium for 30min in the dark, the lamp was switched on to initiate the photocatalytic reactions.

RESULTS AND DISCUSSION

The X-ray diffraction patterns of precursors and zinc oxide powders are represented in Figure 1. The X-ray diffraction analysis of the ZA precursor revealed the formation of phase $\text{Zn}_5(\text{OH})_6(\text{CO}_3)_2$ according to PDF 72-1100. The sizes of crystallites of t_{200} are 21nm , calculated by Debye-Scherrer's equation. The sample ZD precursor show existence of the same phase, but it is amorphous to some extent and a lot of peaks are superimposed. The sizes of crystallites of t_{200} are 6nm . The third sample- ZP precursor shows existence of mixture of ZnO (PDF 36-1451) and $3\text{Zn}(\text{OH})_2 \cdot 2\text{ZnCO}_3$. The X-ray diffraction patterns of investigated zinc oxides synthesized from the above mentioned precursors are also shown in Figure 1. The three of them- ZA, ZD and ZP displayed wurzite ZnO phase (JCPDS 36-

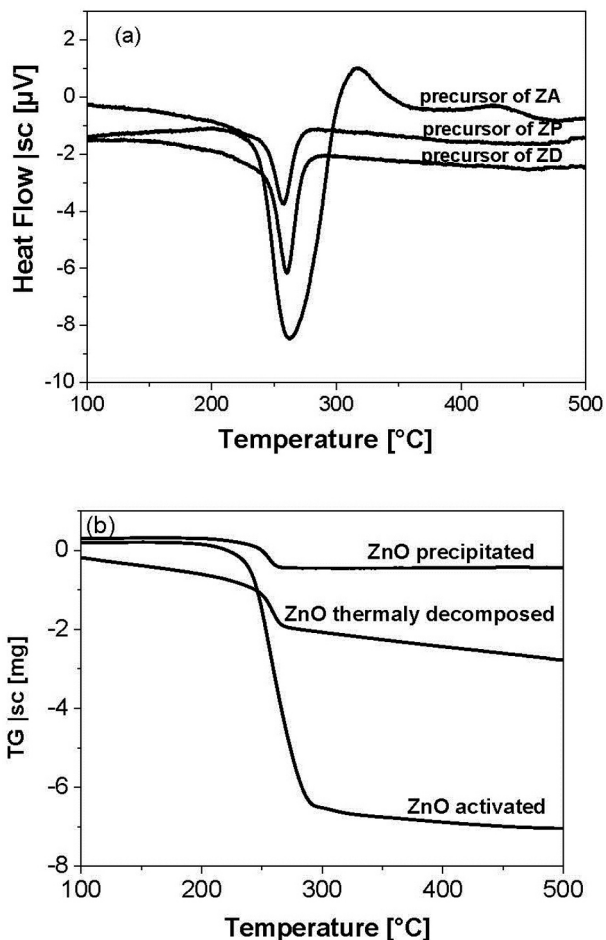


Fig. 1. X-ray diffractograms of ZnO precursors (a) ZA, ZD, ZP and (b) zinc oxides- ZD, ZA and ZP

1451). Crystallites size (D), specific surface area (A_{BET}), lattice constants of ZnO, calculated mass change (Δm) and rate constants (k) are presented in Table 1. The specific surface area of the ZA sample is $40 \text{ m}^2/\text{g}$, i.e. much higher than those of ZP and ZD samples. The crystallites size of ZA, ZP and ZD samples are 67 nm , 28 nm and 31 nm , respectively. This contradiction could be explained by possible agglomeration between the particles of ZP and ZP samples.

Figure 2 represents the DTA (a) and TG (b) patterns of precursors of all samples. A strong endothermic peak has been registered on the DTA curve for the three precursors under $300 \text{ }^\circ\text{C}$, which is the result of zinc hydroxide decomposition. The maximum of the endothermic peak for ZA, ZP and ZD is $258 \text{ }^\circ\text{C}$, $263 \text{ }^\circ\text{C}$ and $260 \text{ }^\circ\text{C}$, respectively. The thermally decomposed ZnO (ZD) showed a max-

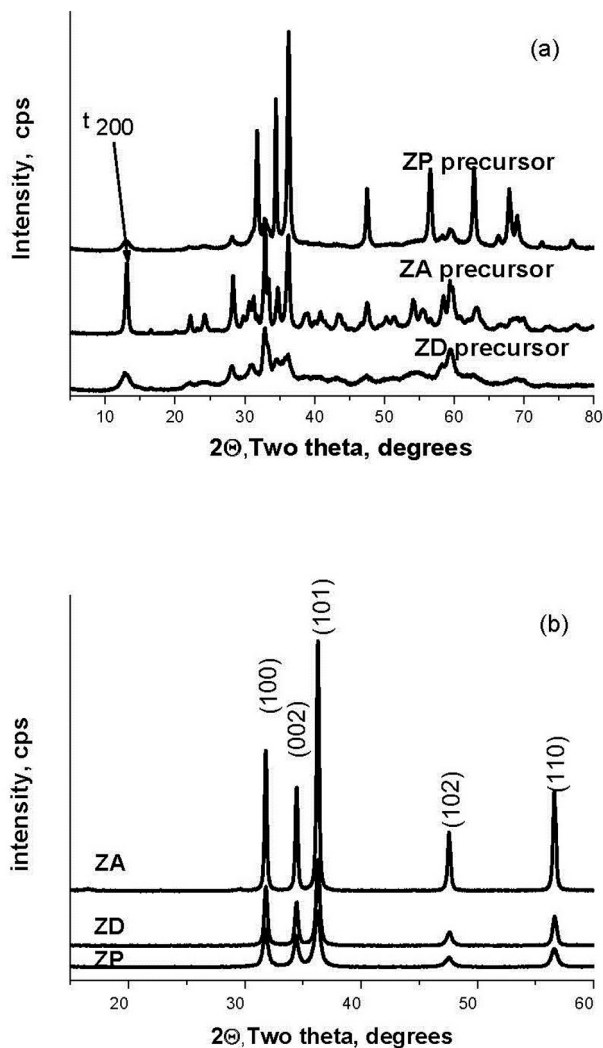


Fig. 2. (a) DTA and (b) TG curve of zinc precursors

Table 1. Specific surface area (A_{BET}), crystallites size (t), lattice constants of ZnO, calculated mass change (Δm) and rate constants (k)

Sample	A_{BET} (m^2/g)	t (nm)	a (Å)	c (Å)	Δm (%)	k ($\times 10^{-3} \text{ min}^{-1}$)
ZA	40	67	3.2484	5.2019	20.251	33.8
ZP	25	28	3.2497	5.2083	7.189	23.6
ZD	22	31	3.2499	5.2076	48.335	12.8

imum at 260 °C, it decomposition begins at 247 °C and it is completed at 273 °C. From DTA-TG analysis we can calculate the mass change (Δm) as $\Delta m = (m_0 - m_t / m_0) \times 100$ (%), where m_0 is initial mass and m_t is mass at the temperature, where the process is finished for investigated samples. The exact values of mass change are given in Table 1.

The ZnO catalysts synthesized in different ways have been subjected to X-ray photoelectron spectroscopy investigation in order to elucidate the influence of preparation procedure on the photocatalytic activity, manifested in a degradation of Reactive Black 5 (RB5) used as a model pollutant. The results of the recorded O1s core level are presented in Figure 3. Due to their complex structure the obtained spectra have been fitted with 3 components. The first sharp peak having binding energy at about 530.0eV shows the existence of Zn-O bonds that belonged to the ZnO lattice. The well pronounced shoulder from the higher binding energy side consisted of two peaks according to the applied fitting procedure. The first one is associated with existing of oxygen vacancies and binding energy is about 531.5 eV, while the second one having binding energy at 532.5 eV belongs to the chemisorbed oxygen or OH- groups on top of the studied catalysts surfaces. The catalytic activities of the studied cata-

lysts depend on the quantity of the formed defects on the surface as it has already been reported by other authors [16]. The calculated percentage of the oxygen vacancies is the following: 24% (ZA), 30% (ZP) and 24% (ZD). Equal quantities of oxygen vacancies are present on the surface of the ZA and ZD catalyst and nevertheless ZA catalyst demonstrates higher activity in a degradation of RB5. Reasonable explanation could be the fact that there is some difference in the relative percentage on the surface of the catalysts due to the OH- groups chemisorbed or dissociated oxygen. Most probably a synergistic effect exists between them playing an important role for the catalytic activity.

The degree of purity and molecular structure of the products were analyzed by the IR spectroscopy (Figure 4). The ZA sample showed strong narrow peak at 437 cm^{-1} , while for the ZD and ZP samples a broad band was observed around 382–602 cm^{-1} , which is typical of ZnO. According to other investigations this peak can be ascribed to Zn–O stretching vibration [13, 17]. The ZnO prepared, by a different method, showed a broad band with two maxima, due to the change in morphology of ZnO [18].

The reaction course as a function of the time interval of illumination (C/C_0) and dye degradation conversion degrees $[(C_0 - C)/C_0]$ of the Reactive

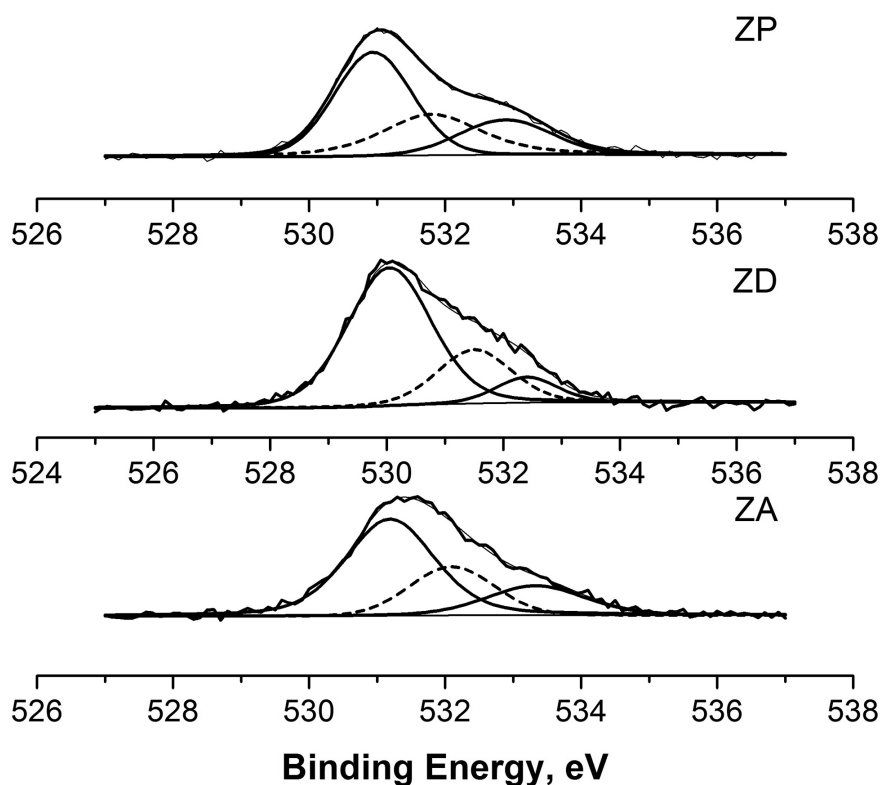


Fig. 3. X-ray photoelectron spectroscopy of ZD, ZA and ZP

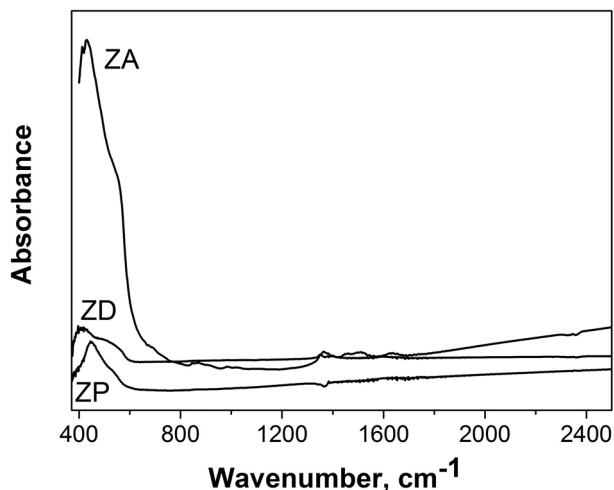


Fig. 4. IR spectroscopy of ZD, ZA and ZP

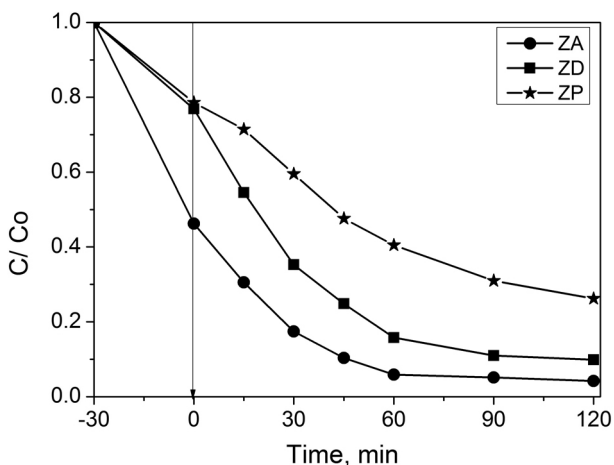


Fig. 5. Reaction course as a function of the time interval of illumination (C/C_0) of ZD, ZA and ZP

Black 5 on ZD, ZA and ZP are shown in Figure 5 and 6 respectively. The ZA sample exhibits highest degradation of the dye (96%) than those of ZP (90%) and ZD (74%). The activated ZnO powder showed the highest adsorption capacity. The rate constants k (min^{-1}) are calculated using logarithmic linear dependence of the concentrations ratio on the time: $-\ln(C/C_0) = k.t$. Their values give the following order of activities: ZA ($33.8 \times 10^{-3} \text{ min}^{-1}$) > ZP ($23.6 \times 10^{-3} \text{ min}^{-1}$) > ZC ($16.1 \times 10^{-3} \text{ min}^{-1}$) > ZD ($12.8 \times 10^{-3} \text{ min}^{-1}$). The activated ZnO possesses the best photocatalytic efficiency due to influence of the following factors: high degree of crystallinity (proved by both XRD and IR spectra) and higher specific surface area. The degradation mechanism

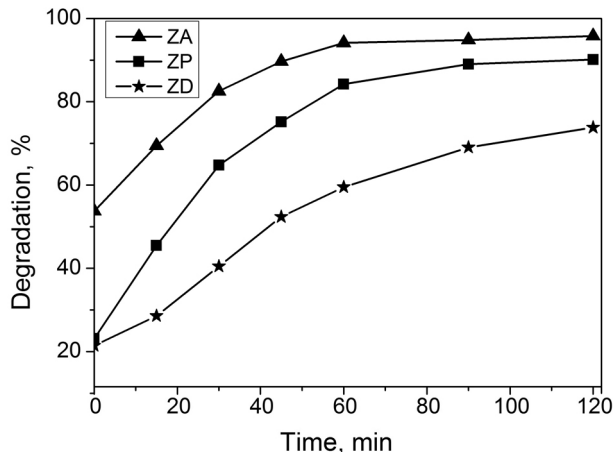


Fig. 6. Dye degradation of ZD, ZA and ZP

is one and the same with all ZnO samples – the active sites (positively charged holes in the valence band) produce the active particles (hydroxyl radicals) by oxidation of adsorbed water molecules. The only difference is the number of the active sites on the surface as a result of the different synthesis procedures. The number of active sites is proportional to the value of the specific surface area. Here we should point out that the role of the sodium ions (ZP sample) is unfavourable, leading to smaller value of the specific surface area in comparison to the case when ammonium carbonate is used (ZA and ZD samples). The difference between the two latter samples can be explained in view of the DTA pattern – there is exothermal peak at about $320 \text{ }^\circ\text{C}$, which is evidence for the formation of intermediate phase, decomposing further into more active ZnO phase. The best photocatalytic sample ZA is superior in its performance to the commercially available ZnO sample.

CONCLUSIONS

ZnO powder was activated using an original patented method and its performance was compared with that of the other two ZnO samples prepared by the precipitation method. According to XRD and IRS data only ZnO is being registered. The photocatalytic properties of the samples were tested in the reaction of oxidative degradation of Reactive Black 5 azo dye used as model waste water pollutant in a semi-batch photo-reactor. All the three investigated photocatalysts, show high effectiveness in the dye decomposition, but the best performance with the highest conversion degree (96%) was observed with the activated ZnO (ZA). The sample ZA per-

formance exceeds that of the other ZnO due to its: (i) higher degree of crystallinity, (ii) higher surface area, (iii) higher adsorption capacity. The order of activities (based on rate constants k) in degradation of Reactive Black 5 model contaminant for the three samples is as follows: ZA > ZP > ZC > ZD, which coincide with the decreasing values of specific surface areas.

Acknowledgements: The authors are grateful to European Science Fund, Project No BG051PO001-3.3.06-0050 and National Science Fund under Contract NSF T 02 16/12.12.2014 for the financial support.

REFERENCES

1. J. Kaur, S. Singhal, *Ceram. Int.*, **40**, 7417 (2014).
2. J. Miao, Z. Jia, H. Lu, D. Habibi, L. Zhang, *Journal of the Taiwan Institute of Chemical Engineers*, **45**, 1636 (2014).
3. N. Tripathy, R. Ahmad, J. Song, H. Ko, Y. Hahn, G. Khang, *Mater. Lett.*, **136**, 171 (2014).
4. K. Enayatzamir, H. Alikhani, B. Yakhchali, F. Tabandeh, S. Rodriguez-Couto, *Environ. Sci. Pollut. Res.*, **17**, 145 (2010).
5. Y. Al-Ani, Y. Li., *Journal of the Taiwan Institute of Chemical Engineers*, **43**, 942 (2012).
6. A. Amani-Ghadim, S. Aber, A. Olad, H. Ashassi-Sorkhabi, *Chemical Engineering and Processing Process Intensification*, **64**, 68 (2013).
7. B. Barragan, C. Costa, M. Marquez, *Dyes Pigments*, **75**, 73 (2007).
8. J. Peralta-Hernandez, Y. Meas-Vong, F. Rodriguez, T. Chapman, M. Maldonado, L. Godinez, *Dyes Pigments*, **76**, 656 (2008).
9. S. Shinde, P. Shinde, C. Bhosale, K. Rajpure, *J Photochem. Photobiol. B Biol.*, **104**, 425 (2011).
10. J. Kaur, S. Singhal, *Ceram. Int.*, **40**, 7417 (2014).
11. J. Miao, Z. Jia, H. Lu, D. Habibi, L. Zhang, *Journal of the Taiwan Institute of Chemical Engineers*, **45**, 1636 (2014).
12. N. Tripathy, R. Ahmad, J. Song, H. Ko, Y. Hahn, G. Khang, *Mater. Lett.*, **136**, 171 (2014).
13. R. Velmurugan, M. Swaminathan, *Sol. Energ. Mater. Sol. Cell.*, **95**, 942 (2011).
14. K. Barick, S. Singh, M. Aslam, D. Bahadur, *Micro-porous and Mesoporous Materials*, **134**, 195 (2010).
15. D. Shishkov, C. Velinova, N. Kassabova, C. Canov, D. Ivanov, D. Klissurski, V. Iordanova, I. Uzunov, *Bulgarian Patent* 28915/1980 (CI C 01 G 9/02) (1980).
16. I. Udom, M. Ram, E. Stefanakos, A. Hepp, D. Goswami, *Mater. Sci. Semicond. Process.*, **16**, 2070 (2013).
17. A. Reddy, M. Kokila, H. Nagabhushana, R. Chakradhar, C. Shivakumara, J. Rao, B. Nagabhushana, *J. Alloy. Comp.*, **509**, 5349 (2011).
18. L. Wu, Y. Wu, W. Lu, *Physica. E*, **28**, 76 (2005).

СРАВНИТЕЛНО ИЗСЛЕДВАНЕ НА ZnO ФОТОКАТАЛИЗАТОРНИ ПРОБИ, ПОЛУЧЕНИ ПО РАЗЛИЧЕН НАЧИН

К. И. Миленова^{1*}, А. Е. Елияс¹, В. Н. Блъсков², И. А. Аврамова², И. Д. Стамболова²,
С. В. Василев³, П. М. Николов⁴, Н. А. Касабова⁴, С. К. Раковски¹

¹ *Институт по катализ, Българска академия на науките, ул. „Акад. Г. Бончев“, бл. 11,
1113 София, България*

² *Институт по обща и неорганична химия, Българска академия на науките, ул. „Акад. Г. Бончев“,
бл. 11, 1113 София, България*

³ *Институт по електрохимия и енергийни Системи, Българска академия на науките,
ул. „Акад. Г. Бончев“, бл. 10, 1113 София, България*

⁴ *Химико-технологичен и металургичен университет, бул. „Св. Климент Охридски“ 8,
1756 София, България*

Постъпила декември, 2014 г.; приета януари, 2015 г.

(Резюме)

За получаването на образци от наноразмерен прахообразен ZnO са използвани три различни подхода: активиране (образец ZA), утаяване чрез използването на два различни реагента (образци ZP и ZD). Измерена е тяхната фотокаталитична активност в реакции на окислително обезцветяване водни разтвори на диазо багрила. Получените наноразмерни прахообразни образци от ZnO са охарактеризирани чрез рентгенофазен анализ (РФА), инфрачервена спектроскопия (ИЧС), термогравиметрия в съчетание с диференциален термичен анализ (ТГ–ДТА), рентгенова фотоелектронна спектроскопия (РФС) и измерване на специфичната площ на повърхността по БЕТ метода. РФА анализа на получените фотокатализатори от ZnO показва наличие на вюрцитна фаза ZnO, докато ИЧС указва формиране на Zn–O връзки. Специфичната площ на повърхността на ZnO, получен по метода на активация е по-висока, в сравнение с другите проби. Фотокаталитичните свойства на образците бяха изпитани в реакцията на окислително разлагане на Реактивно Черно 5 азо-багрило. И трите образца имат висока ефективност за разграждане на багрилото. Най-добрият фотокатализаторен образец е активираният прахообразен ZnO, получен по оригинален патентован метод. Скоростните константи на превръщане на моделния замърсител Реактивно Черно 5 над отделните образци дават следния ред активност: ZA ($33.8 \times 10^{-3} \text{ min}^{-1}$) > ZP ($23.6 \times 10^{-3} \text{ min}^{-1}$) > ZD ($12.8 \times 10^{-3} \text{ min}^{-1}$).

Investigation of the possibility to increase the mechanical properties of ferritic nodular cast iron

R. I. Petkov, R. Vl. Gavrilova*, L. P. Atanasov

University of Chemical Technology and Metallurgy – Sofia, Faculty of Metallurgy and Material Science,
1756 Sofia, blvd. Kl. Ohridski 8

Received December, 2014; Revised January, 2015

The aim of this study is to ensure ferrite structure of the metal base, solid-solution hardening of ferrite and hence higher mechanical performance by additional alloying. For the purpose of the experimental work brand GGG 50 is designated as the base. In its own classic form, this brand has pearlite-ferrite structure. In standard cooling conditions of the cast iron its chemical composition is 3.2–3.7% C; 2.0–2.5% Si; 0.3–0.7% Mn. To study the influence of the chemical composition of the structure and mechanical properties were carried out experiments with alloys with the same carbon equivalent, but the content of Mn up to 0.15% and the silicon content varied in the range from 2.0 to 4.5%.

The analysis of results allows the conclusion, that in the presence of silicon within 3.5–3.7% and about 4.2 carbon equivalent a ferritic ductile cast iron can be obtained which satisfies the brand GGG 50.

Keywords: ductile cast iron, ferrite structure, mechanical properties.

INTRODUCTION

Good technological properties of ductile irons are that they are chemically related to the eutectic iron-carbon alloys, as are ordinary gray irons. Removing to the notch effect of graphitic inclusions as a result from transformation of shape of blade in spheroidal are reasons for higher mechanical properties (comparable and sometimes greater than those of steels) of ductile irons [1, 4]. That is achieved after adding of suitable modifiers into the melt. Specifically – requirements concerning the basic mechanical properties of ductile irons and which are set on the standards in different countries are similar. For various brands of ductile iron they provide:

- specific elongation A from 22 to 2%;
- HBS conditional yield strength $R_{0.2}$ from 220 to 850 MPa;
- Brinell hardness from 140 to 360;
- tensile strength R_m in the range from 350 to 1200 MPa;

At similar chemical composition the difference in mechanical properties of the individual brands is determined by the ratio of ferrite and pearlite in the metal base – it varies from almost 100% ferrite,

wherein the relatively low strength and hardness combined with high ductility, up to 100% pearlite, wherein the high strength and stiffness combined with low ductility [5].

EXPERIMENTAL EQUIPMENT, METHODS AND MATERIALS

As is known, the pearlite is produced by diffusion of austenite decomposition. Pearlite grain structure of iron-carbon alloys are made of a soft and ductile ferrite and a hard and brittle cementite (iron carbide, Fe_3C), and depending on the shape of the cementite is constitute as lamellar pearlite or granular [4]. This heterogeneity in the structure of the pearlite is a cause of great differences in the hardness of the cast iron in the mold (170–230 HB), and as a result, because of the great heterogeneity, the workability is greatly deteriorated - it is not possible to apply high speeds of cutting, the tools take off the edge quickly and it is not possible to achieve high-end roughness on the surface [1, 5].

The aim of this study is to investigate the possibility of using additional alloying of the alloy. The idea is thus to suppress pearlite decomposition of austenite, i.e. to provide complete graphitization in the course of decomposition and obtaining a ferrite structure of the metal base just after casting, while

* To whom all correspondence should be sent:
E-mail: r.gavrilova@abv.bg

achieving the solid solutions hardenability of austenite, which would lead to the achievement of higher values of the mechanical properties of castings. In analyzing the possibilities to use alloying elements, the suggestion is that may be used only those, who meet the above requirements: first – graphitization and solid solution strength effect and second – content of elements, stabilizing pearlite - Ni, Mn, Cu, Sn and carbide-form elements – Cr, Mo, V, Mn should be restricted. Generally two elements meet the conditions – silicon and aluminum. Aluminum has a stronger effect of graphitization, but its ability of alloying is worse because of suppressed spheroidizing effect of magnesium and a marginal strength effect. For this reason, studies have been conducted with the use of silicon.

As noted, the objective of this work is to achieve a high mark ductile iron while maintaining a ferritic structure of the metal base. For this purpose, the most appropriate mark is GGG 50 (500 MPa tensile strength and 7% elongation). In the classic form, this brand has a perlite-ferrite structure (for example see Fig. 3b). For standard conditions of cooling in the casting of iron it has a chemical composition with 3.2–3.7% C; 2.0–2.5% Si; 0.3–0.7% Mn, (i.e. carbon equivalent C_e 4.125).

To study the influence of the chemical composition on the structure, the tensile strength, hardness and elongation are planned and realized experiments with alloys with the same carbon equivalent. Content of Mn up to 0.15%, silicon content was varied in the range of 2.0 to 4.5% at intervals of 0.5%; respectively the carbon content in mass percentage for each alloy is within the limits, shown in Table 1.

From the alloys cylindrical sample bodies are cast with a standard diameter (30 mm) and length of 250 mm. The proportional specimens (tubes) are made to determine the mechanical properties and standard samples are prepared for metallographic analysis of the structure [2].

The hardness is determined to Brinell method (BS ISO 6506), [2, 3]. Measurement is made by a sphere with a diameter 2.5 mm, 187.5 kgf (1840N). The results of hardness and mechanical tests are presented in Fig. 1 and Fig. 2.

RESULTS AND DISCUSSION

The analysis of the results shows:

- Ferrite structure (100%) of the metal base in cast condition is fixed even at the third test – 3% Si and 3.25% C, but the tensile strength is 420 MPa;

Table 1. Variation of the Si content in the experimental alloys

	Content of Mn, %	Content of Si, %	Carbon equivalent
1	≤0.15%	3.5±3.6	4.125
2	≤0.15%	3.3±3.4	4.125
3	≤0.15%	3.2±3.3	4.125
4	≤0.15%	3.0±3.1	4.125
5	≤0.15%	2.9±3.0	4.125
6	≤0.15%	2.7±2.8	4.125

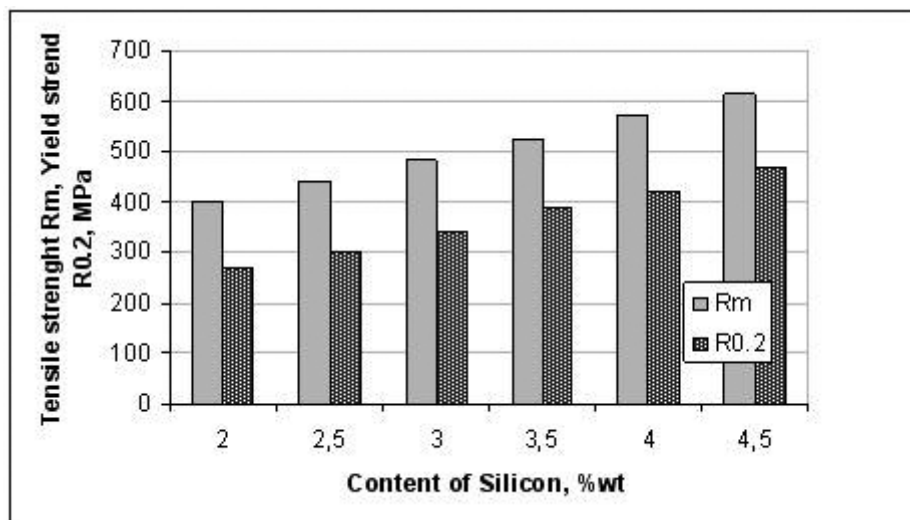


Fig. 1. Changes in tensile strength and yield strength depending on silicon

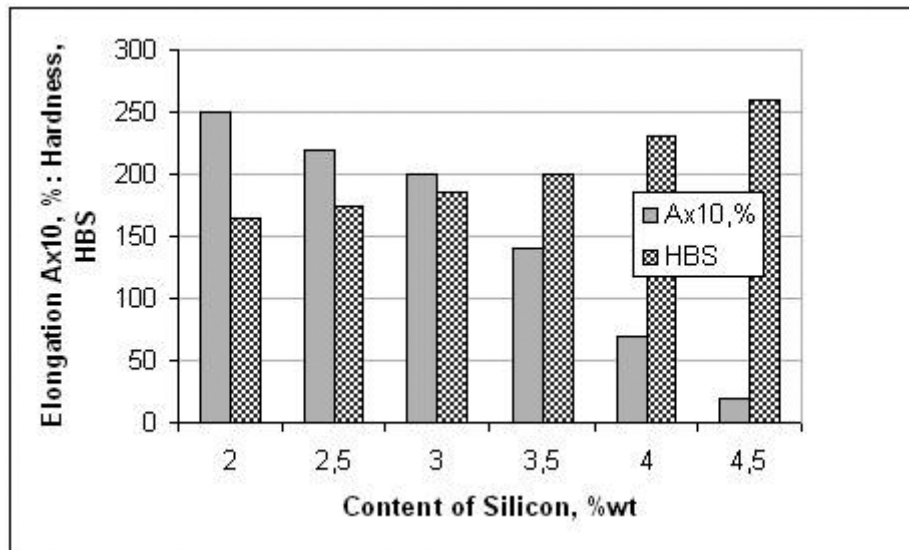


Fig. 2. Changes in elongation and HBS depending on silicon

- By increasing the silicon content, increase the tensile strength. In case of 3.5% Si the tensile strength exceeds 500 MPa in cast condition; in a 4.5% Si the tensile strength reaches 650 MPa;
- With increasing the silicon content elongation gradually decreases from 20% to 3% Si and becomes 8% to 4% Si;
- The hardness increases gradually with increasing the silicon content, as in the pure ferritic structure vary from 185HBS at 3% Si to 240HBS at 4% Si.

CONCLUSIONS

With the results of metallographic analysis and testing of mechanical properties it can be concluded that the silicon content within 3.5÷3.7% and with carbon equivalent about 4.2, ferrite ductile iron can be obtained that meets the requirements of trademark GGG 50.

REFERENCES

1. R. E. Smallman, R. J. Bishop, Modern Physical Metallurgy and Materials Engineering, Science, process, applications, Sixth Edition, Butterworth-Heinemann, Linacre House, Jordan Hill, Oxford OX2

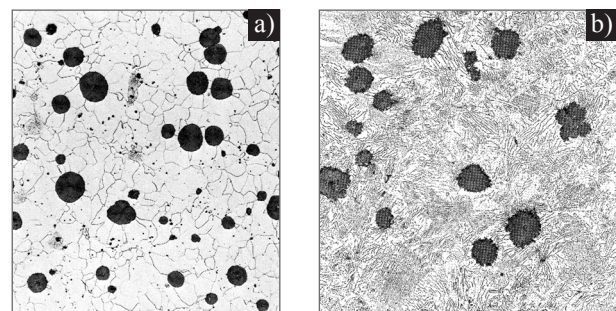


Fig. 3. a) Ferrite structure (100%) of the metal base in cast condition; b) Perlite-ferrite structure with Si content 2.0–2.5%

- 8DP, 225 Wildwood Avenue, Woburn, MA 01801-2041, 1999.
2. H. Schumann, Metallographie, VEB DVG Leipzig 10. Auflage.
3. K. Geels, Metallographic and Materialographic Specimen Preparation, Light Microscopy, Image Analysis and Hardness Testing, Printed in U.S.A., ASTM, No. MNL46, 2007.
4. J. R. Davis, ASM Specialty handbooks – Cast irons, ASM International, Materials Park, Ohio, U.S, 1996, p. 6.
5. Minkoff, The physical metallurgy of cast iron, John Wiley & Sons Ltd., Norwich, 1983, p. 102.

ИЗСЛЕДВАНЕ ВЪЗМОЖНОСТТА ЗА ПОВИШАВАНЕ НА МЕХАНИЧНИТЕ ПОКАЗАТЕЛИ НА ФЕРИТЕН СФЕРОГРАФИТЕН ЧУГУН

Р. И. Петков, Р. Вл. Гаврилова*, Л. И. Атанасов

Химикотехнологичен и металургичен университет – София, Факултет по металургия и материалознание, 1756 София, бул. „Кл. Охридски“ №8

Постъпила декември, 2014 г.; приета януари, 2015 г.

(Резюме)

Както е известно, при сферографитните чугуни високи механични показатели се постигат при перлитна структура на металната основа. Тя е хетерогенна, вследствие на което се получават големи разлики в твърдостта в рамките на отлетия обем, а това води до влошена обработваемост.

В този смисъл, целта на разработката е да се изследва възможността за допълнително легиране на сплавта, чрез което да се подтисне перлитното разпадане на аустенита, т.е. да се осигури пълна графитизация при разпадането му и получаване на феритна структура на металната основа непосредствено след леене. Цели се същевременно да се постигне уякчаване на твърдия разтвор, което би довело до постигане на по-високи стойности на механичните показатели на отлетия метал.

Анализът на възможностите за използване на легиращи елементи показва като най-подходящо добавянето на силиций. Получените резултати показват, че:

- феритна структура (100%) на металната основа в лято състояние се фиксира още при 3% Si и 3,25% C, но якостта на опън е ниска – 420 МПа;
- с повишаване съдържанието на силиций якостта на опън расте и при 3,5% Si надхвърля 500 МПа в лято състояние а при 4,5% Si достига 650 МПа;
- относителното удължение с повишаване съдържанието на силиций плавно намалява от 20% при 3% Si до 8% при 4% Si;
- твърдостта нараства плавно с повишаване съдържанието на Si, като в областта на чисто феритната структура се изменя от 185 НВ при 3% Si до 240 НВ при 4% Si.

От проведения металографски анализ и изпитванията на механичните показатели в настоящето изследване може да се направи заключение, че при съдържание на силиций в рамките 3,5–3,7% и въглероден еквивалент около 4,2 може да се получи феритен сферографитен чугун, който удовлетворява изискванията за марка GGG500-7.

Crystal structure of Ag⁺ exchanged ETS-4 at room temperature and 150 K

L. Tsvetanova^{1*}, N. Petrova¹, S. Ferdov², V. Kostov-Kytin¹, R. Nikolova¹

¹ Institute of Mineralogy and Crystallography, Bulgarian Academy of Sciences, Sofia, 1113, Bulgaria

² Department of Physics, University of Minho, 4800-058 Guimarães, Portugal

Received December, 2014; Revised January, 2015

Single crystals of microporous titanasilicate Na-K-ETS-4 are synthesized and exchanged to Ag⁺ form. Crystal structures of the as-synthesized and ion exchanged samples are analyzed by single crystal X-ray diffraction at room temperature and 150K. The material characterization is supplemented by SEM, DTA/TG-DTA, and powder XRD. Our studies show that Na⁺ and K⁺ ions are completely removed from the ETS-4 structure during the ion exchange procedure and the framework charge is almost entirely compensated by Ag⁺ ions. The occurring structural deformations upon the applied ion exchange have been thoroughly analyzed. The low temperature measurements ensure precise determination of atomic positions and minimize the effects of atomic thermal vibration and positional disorder.

Key words: ETS-4, single crystal X-ray diffraction, low temperature experiment.

INTRODUCTION

ETS-4 (Engelhard titanium silicate-4) is a mixed tetrahedral-octahedral molecular sieve synthesized for the first time in 1990 [1]. Based on ²⁹Si MAS NMR analyses and powder XRD data it was assumed that ETS-4 structure is related to that of the mineral zorite [1–4]. Later on, many authors performed studies on ETS-4 structure in order to clarify the tetrahedral-octahedral arrangement of its “highly faulted framework” [5–7]. The conventional explanation of the ETS-4 structure was proposed by Braunbarth et al. in 2000 who described the framework as a superposition of four hypothetical polymorphs differing in the arrangement of the bridging units [6]. The first single crystal structure solution was reported by Nair et al. in 2001 [7]. The common understanding for the ETS-4 structure is that it exhibits three-dimensional microporous framework built of silicon tetrahedra and titanium octahedra and semioctahedra. Within the framework there are three types of channels: **6-** and **8-**membered ones running parallel to **b** axis and **7-**membered one along **c** axis. It is interesting to note that each of the suggested theoretical polymorphs allows the existence of additional unbroken channels running along **c** axis built up of **12-**membered rings. Unfortunately, the

superposition of the polymorphs within the structure precludes the formation of these potentially very interesting channels. The search of appropriate synthetic conditions for obtaining singular polymorphs still goes on. Anyway, the ETS-4 materials suppose good ion exchange properties, which have been extensively studied by many authors [8–17]. While the exchange capacity of monovalent Li⁺, Na⁺, K⁺, Cs⁺ and Ag⁺ has been reported there is still lack of information concerning the positions of these ions within the ETS-4 channels [12–15]. Recently, we published results on the structural characterization of Cs⁺ exchanged ETS-4 and the elastic behavior of the structure under ion exchange and low temperature conditions [16, 17].

Here we present results on the structure solution of Ag⁺ exchanged ETS-4 and compare the flexibility of the framework before and after the ion exchange. Crystal structures of the as-synthesized and ion exchanged samples were analyzed by single crystal X-ray diffraction at room temperature (RT) and low temperature (LT) conditions. The material characterization has been performed by SEM, DTA/TG-DTA, and powder XRD.

EXPERIMENTAL

Sample preparation: The Na-K-ETS-4 samples were synthesized using the procedure described by Nikolova et al. [16]. In our synthesis, 5 g SiO₂ (Aldrich) were added to a solution of 6.3 g NaOH

* To whom all correspondence should be sent.
E-mail: lilicvetanova79@abv.bg

and 1 g KOH (Aldrich) in 150 ml distilled water. Subsequently, 0.5 ml TiCl₄ (Fluka) hydrolyzed in 40 ml distilled water was added to the above solution. The mixture was homogenized and transferred into Teflon-lined stainless autoclave. The crystallization was performed under static conditions at 200 °C for 24 h. The ion exchange was performed by immersing the as-synthesized ETS-4 in 1 M solutions of AgCl₂ (Aldrich) for 3 days at 80 °C. Finally, the samples were washed with distilled water and dried at room temperature.

SEM analysis of the single crystal samples was performed using a JEOL JSM 6390 scanning electron microscope. The technique was equipped with Oxford INCA Energy 350 – EDS. The device was connected to INCA Energy software for data processing. The data were collected at accelerating voltage 20kV and been current of 65 nA. 30 s of integration time were used to perform EDS analysis on single crystals of as-synthesized NaK ETS-4 and the Ag exchanged ETS-4 samples.

DTA/TG experiments were conducted by Setsys Evolution apparatus (SETERAM, France) in the temperature range from room temperature to 550 °C, in air environment. The rate of heating was 10 °C min⁻¹, and the weight of the measured samples was 10 mg.

Powder XRD experiments were carried on a diffractometer D2 PHASER AXS - Bruker, equipped with Bragg-Brentano horizontal goniometer (2θ) and scintillation counter using Ni-filtred CuKα radiation (λ = 1.5406 Å). The data were recorded at room temperature in the interval of 4–55° 2θ with a step at of 0.05 2θ and scanning time 1s.

Single-crystal X-ray diffraction data were collected for the as-synthesized Na-K-ETS-4 and Ag⁺ exchanged samples. The same crystals were used for the RT and LT experiments. Data collections were performed by ω-scan technique on an Agilent Diffraction SuperNova Dual four-circle diffractometer equipped with Atlas CCD detector using mirror-monochromatized MoKα radiation from micro-focus source (λ = 0.7107 Å). During the LT data collection the samples were kept at 150K with an Oxford Instruments Cobra controller device and in nitrogen atmosphere. The determination of unit cell parameters, data integration, scaling and absorption corrections were carried out using the CrysAlis Pro program package [18]. The structures were solved by direct methods (SHELXS-97/2013) [19] and refined by full-matrix least-square procedures on F² (SHELXL-97/2013) [19]. The structure visualization was performed by Crystal Maker (version 2.6.2, SN2080) [20]. Further details of the crystal structure investigation may be obtained from Fachinformationszentrum Karlsruhe, 76344 Eggenstein-Leopoldshafen, Germany (fax:

(+49)7247 808 666; e-mail: crysdata@fiz-karlsruhe.de, http://www.fizkarlsruhe.de/request_for_deposited_data.html on quoting the CSD-429019, 429026, 429027 and 429028. The structural data obtained at room and low temperature measurements and the structure refinement indicators for the studied compounds are presented in Table 1.

STRUCTURE SOLUTION

The crystal structures have been solved in an orthorhombic space group *Cmmm* and refined using similar procedure for all studied samples. Each of the Si and Ti atoms occupies two crystallographic positions marked as Si1, Si2 and Ti1 and Ti2, respectively. The superposition *Cmmm* model suggests that the framework atoms positions are of two types. First one belongs to the non-bridging units and should be refined as a fully occupied (in our structures Si1, Ti1 and the adjacent O atoms). The second type is of the bridging unit and should be refined with ½ occupancy (Si2, Ti2 and the adjacent O atoms). In addition, the Ti2 atom could lie on the (001) mirror plane and in that case will have exactly ½ occupancy. If Ti2 is slightly outside of the (001) mirror plane, as it has been reported by Nair et al. [7], its position and that of the corresponding oxygen atoms should be refined as ¼ occupied. Following the described conditions, first the atomic positions of the framework atoms with isotropic displacement parameters have been refined. Concerning the Ti2 position, both of the possible arrangements have been observed. In the as synthesized Na-K ETS-4 sample Ti2 lies at a distance of 0.06Å apart from the mirror plane, while in the Ag exchanged sample Ti2 is exactly on the mirror plane. That is why the Ti2 occupancy has been fixed as ¼ in the Na-K ETS-4 sample and ½ in the Ag ETS-4 one. After the refinement of the framework atoms the positions of compensating ions and water oxygens have been found from difference Fourier maps. Their occupancies have been refined simultaneously with the atomic coordinates and isotropic displacement parameters. Subsequently, a refinement of the anisotropic displacement parameters has been performed. The experimental data do not allow anisotropic refinement for all of the atoms. This is because of the disparity between the number of measurable intensities and the number of refinement parameters, which is due to the size and quality of the single crystal samples. For the as-synthesized Na-K-ETS-4 sample the water oxygens (O21, O22, O23) and O4 oxygen (part of the framework bridging unit) have been refined only isotropically at RT while the LT measurement allows refinement of the anisotropic displacement parameters for all of the atoms. In the case of Ag⁺

Table 1. Crystal data and structure refinement parameters for Na-K- ETS-4 and Ag-ETS-4 samples measured at different temperature conditions – 290 K (RT) and 150 K (LT)

Samples	Na-K-ETS-4		Ag-ETS-4	
	290	150	290	150
Space group	Cmmm	Cmmm	Cmmm	Cmmm
a (Å)	23.226(2)	23.2140(18)	23.252(2)	23.235(4)
b (Å)	7.2103(9)	7.1932(6)	7.2477(10)	7.2034(9)
c (Å)	6.9610(8)	6.9584(6)	6.9169(9)	6.9153(9)
V (Å ³)	1165.7(2)	1161.93(17)	1165.6(2)	1157.4(3)
Z	1	1	1	1
Dx [Mg m ⁻³]	2.201	2.208	2.832	2.821
μ [mm ⁻¹]	1.381	1.404	3.634	3.587
Tmin–Tmax	0.1928/1	0.8942/1	0.716/1	0.5499/1
measured reflections	2614	2673	1639	1979
independent reflections	847	844	599	635
parameters	78	88	83	85
reflections with $I > 2\sigma(I)$	554	634	429	447
θmin–θmax	2.926/29.216	2.927/29.521	3.419/26.434	3.421/24.964
F000	759	759	943	933.4
T (K)	290	150	290	150
R [$F^2 > 2\sigma(F^2)$]	0.0772	0.0584	0.0746	0.0876
wR (F ²)	0.2019	0.1575	0.216	0.254
Rint	0.104	0.0539	0.0755	0.0805
S	1.085	1.113	1.073	1.298

exchanged sample water oxygens has been refined isotropically only for both the RT and LT experiments. The two very close to each other positions of water oxygens (O23 and O24) at RT conditions turn into one position at LT conditions. The chemical composition of the studied samples obtained after the structure refinement are presented in Table 2. The bond distances within the framework and the compensating cation coordination environment are summarized in Table 3 and Table 4, respectively.

RESULT AND DISCUSSION

The EDS analysis shows lower Si/Ti ratio than the expected one for the model framework (12/5). The Si deficiency differs from crystal to crystal and is found to be up to 10% for some of the exchanged

samples. This is most likely due to the highly disordered framework of ETS-4. It should be noted that our analyses show chemical composition of isolated single crystals, while the published till now chemical compositions are based on ICP analyses of powder samples. For simplification of the structure refinement we use the ideal Si/Ti ratio of 12/5.

DTA /TG analysis were used for determination of the type and quantity of the water molecules. The results show three types of water molecules for the studied samples – one physisorption and two crystallization ones. The Ag⁺ exchanged ETS-4 sample contains one water molecule less than the as-synthesized one.

Powder XRD analyses of the samples after DTA-TG analyses confirm that the ETS-4 structure has completely been destroyed upon heating it to 350 °C.

Table 2. Chemical composition of Na-K- ETS-4 and Ag-ETS-4 samples calculated after the structure refinement

Sample	Data from structure refinement at 290 K (RT)	Data from structure refinement at 150 K (LT)
Na-K-ETS-4 – as synthesized	Na _{5.92} K _{0.72} H _{2.36} Si ₁₂ Ti ₅ O ₃₈ (OH) x 11.28 H ₂ O	Na _{5.66} K _{0.96} H _{2.38} Si ₁₂ Ti ₅ O ₃₈ (OH) x 11.04 H ₂ O
Ag-ETS-4 – ion exchanged	Ag _{5.83} H _{3.17} Si ₁₂ Ti ₅ O ₃₈ (OH) x 9.92 H ₂ O	Ag _{5.68} H _{3.32} Si ₁₂ Ti ₅ O ₃₈ (OH) x 9.55 H ₂ O

Table 3. Framework interatomic distances (Å) for Na-K- ETS-4 and Ag- ETS-4 samples

Bond length	Na-K-ETS-4 290 K (RT)	Na-K-ETS-4 150 K(LT)	Ag-ETS-4 290 K (RT)	Ag-ETS-4 150 K(LT)
Si1-O1	1.615(2)	1.615(19)	1.612(3)	1.6110(3)
Si1-O2(x2)	1.607(4)	1.610(3)	1.596(6)	1.603(7)
Si1-O3	1.644(6)	1.643(4)	1.620(8)	1.613(10)
Si2-O3(x2)	1.656(6)	1.656(4)	1.649(9)	1.654(10)
Si2-O4	1.635(4)	1.636(3)	1.627(5)	1.608(7)
Si2-O5	1.621(13)	1.611(10)	1.57(3)	1.62(3)
Mean Si-O	1.63(6)	1.63(7)	1.61(6)	1.62(7)
Ti1-O2(x4)	1.965(4)	1.963(3)	1.964(6)	1.9587(7)
Ti1-O6(x2)	1.935(3)	1.931(2)	1.943(4)	1.925(5)
Ti2-O5(x4)	1.964(11)	1.958(9)	1.93(2)	1.87(3)
Ti2-O7	1.69(4)	1.70(3)	2.01(4)(x4)	2.05(5)(x4)
	2.47(4)	2.46(3)		
Mean Ti-O	2.00(5)	2.00(4)	1.96(4)	1.95(5)

Table 4. Selected bond lengths (Å) for Na-K-ETS-4 and Ag-ETS-4 samples

Na-K-ETS-4	Distance 290 K (RT)	Distance 150 K (LT)	Ag-ETS-4	Distance 290 K (RT)	Distance 150 K (LT)
Na1 – O21(x2)	2.429(13)	2.423(11)	Ag1 – O22	2.59(9)	2.38(3)
Na1 – O1(x2)	2.859(6)	2.862(5)	Ag1 – O24	2.13(5)	–
Na1 – O2(x4)	2.495(4)	2.490(3)	Ag1 – O2(x2)	2.669(6)(x1)	2.661(7)
			Ag1 – O5(x2)	2.68(2)(x1)	2.62(19)
Na2/K – O21(x2)	2.539(14)	2.576(12)	Ag1 – O6	2.40(10)	2.380(13)
Na2/K – O22(x2)	2.46(2)	2.447(17)	Ag1 – O7	2.61(4)	2.55(5)
Na2/K – O2(x2)	2.626(6)	2.619(5)			
Na2/K – O5(x2)	2.693(14)	2.682(11)	Ag2 – O22	2.60(9)	2.89(5)
Na2/K – O6	2.479(11)	2.472(8)	Ag2 – O24	2.24(14)	–
			Ag2 – O1	2.872(9)	2.857(10)
			Ag2 – O2(x4)	2.419(7)(x2)	2.393(7)
				2.656(6)(x2)	2.635(7)
			Ag3 – O2(x2)	2.526(12)	2.520(9)
			Ag3 – O6	2.523(25)	2.569(16)

IMPACT OF THE ION EXCHANGE AND LOW TEMPERATURE CONDITIONS ON FRAMEWORK

The elastic properties of ETS-4 structure are manifested by the variations of the unit cell parameters upon ion exchange and upon applying low temperature conditions. The structural parameters of the studied compounds are compared with the previously reported results for Cs⁺ exchanged ETS-4 in order to check how the ionic radii and amount of the compensating ions influence the elasticity [17] (Table 5). The results show that in contrast to Cs⁺ the Ag⁺ exchange does not cause increase of the unit cell volume of ETS-4, most probably because

of the smaller size of Ag⁺ cations (ionic radius of Cs⁺ – 1.85Å and Ag⁺ – 1.22Å). The LT conditions cause structure contraction being more pronounced for the ion exchanged forms than for the as-synthesized one. The framework topology remains stable and only some of the atomic positions are slightly shifted in order to adapt the topology to the temperature conditions (Table 3.) It should be noted that the position of the Ti2 atom remains the same at RT and LT conditions for both of the studied samples. Such a behavior was reported for Mg²⁺ and Cs⁺ exchanged forms, but not for the Ba²⁺ exchanged one, where LT conditions shift the Ti2 atom from outside the mirror plane to exactly the plane itself [16, 17]. It will be interesting to provide more detailed study

Table 5. Unit cell parameters (Å) and volume (Å³) of Na–K-ETS-4, Ag-ETS-4 and Cs-ETS-4 [] samples

Sample	Ionic radii of charge compensating ion [Å]	Unit cell parameters 290 K (RT)	Unit cell parameters 150 K (LT)	Volume 290 K (RT)	Volume 150 K (LT)
Na–K-ETS-4	1.12/1.38	a = 23.226(2) b = 7.210(9) c = 6.961(8)	a = 23.214(9) b = 7.193(6) c = 6.958(6)	1165.7(2)	1161.9(8)
Ag-ETS-4	1.22	a = 23.252(2) b = 7.247(9) c = 6.9169(9)	a = 23.235(4) b = 7.203(9) c = 6.915(9)	1165.6(2)	1157.4(3)
Cs-ETS-4	1.85	a = 23.214(10) b = 7.258(2) c = 6.9416(19)	a = 23.123(2) b = 7.213(4) c = 6.930(3)	1169.6(7)	1156.9(2)

on how the ion exchange and different temperature or pressure conditions influence the Ti2 position in the structure, because exactly the Ti2 position was one of the reasons for Nair et al. to propose five coordinated environment of this atom [7]. According to our results the Ti2 position is more appropriate to expect both five and six coordinated titanium in the

bridging part. Moreover, the refinement of the O7 position (oxygen connected only to Ti2 atom) occupancy indicates that almost half of the Ti2 atoms should be six coordinated.

The framework structure of ETS-4 is presented on Figure 1. The channel systems are built by 6-, 7- and 8-membered rings and are marked as A1 (mixed

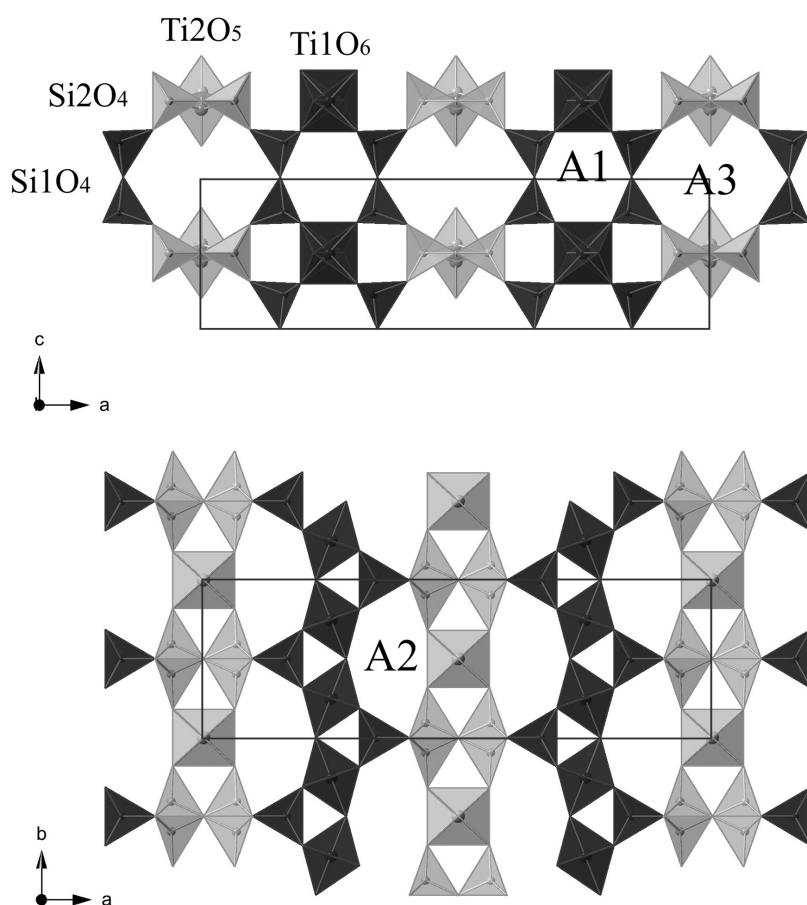


Fig. 1. Model of ETS-4 framework showing the channel systems: a) in direction [010] and b) in direction [001]. The six, seven and eight-membered ring channels are marked as A1, A2, and A3, respectively. The Ti1O₆ and Si1O₄ polyhedrons are dark grey colored. The Ti2O₅ and Si2O₄ bridging units are light grey colored.

terahedra-octahedra 6-membered rings), A2 (mixed tetrahedra-octahedra-semioctahedra 7-membered rings) and A3 (8-membered rings only tetrahedra), respectively. The structure refinement of the Ag⁺ exchanged form shows that all of the Na⁺ and K⁺ ions are released from the structure during the ion exchange procedure. This is also confirmed by the chemical composition based on EDS analysis. The framework charge is entirely compensated by Ag⁺ ions, which occupy three crystallographically non-equivalent positions – one within A1 channel and two within the A2 one. Refinement of the occupancy of the exchangeable cations positions shows that the Ag⁺ ions in A1 channel are less than the released Na⁺ ions, while Ag⁺ ions in A2 channel have almost the same quantity as the sum of K⁺ and Na⁺ ions released during the ion exchange procedure. The A3 channel is occupied only by water molecules similarly to the as-synthesized sample. The coordination spheres of the charge compensating ions are built of framework oxygens and water molecules (Table 3). The polyhedra within the ion exchanged sample are more irregular and distorted comparing to those in the as-synthesized sample.

CONCLUSIONS

The crystal structure of Ag⁺ exchanged ETS-4 was solved using RT and LT single crystal diffraction data. The structure refinement showed that all of the Na⁺ and K⁺ ions are released from the ETS-4 structure during the Ag⁺ ion exchange procedure and the framework charge is almost entirely compensated by Ag⁺ ions. The Ag⁺ exchange does not cause changes of the unit cell parameters of ETS-4. The LT conditions on the other side causes structure contraction of higher degree compared to that of the as-synthesized ETS-4 and the structure deformation affects mainly the bridging units of the framework.

Acknowledgments: This work was supported by the European Social Fund and Republic of Bulgaria, Operational Programme “Human Resources De-

velopment”, 2007-2013 framework, Grant № BG051PO001-3.3.06-0027 from July 2013 and DRNF 02/1 Project.

REFERENCES

1. S. M. Kuznicki, *U.S. I. Patent* 4 938 939 (1990).
2. G. Cruciani, P. D. Luca, A. Nastro, P. Pattison, *Micropor. Mesopor. Mater.*, **21**, 143 (1998).
3. A. Merkov, I. Bussen, E. Goiko, E. Kulchiczka, J. Menshikov, A. Nedorezova, *Zapiski Vses. Mineralog. Obshch.*, **54**, 9 (1973).
4. P. A. Sandomirski, N. V. Belov, *Sov. Phys. Crystallogr.*, **24**, 686 (1979).
5. A. Philippou, M.W. Anderson, *Zeolites*, **16**, 98 (1996).
6. C. Braunbarth, H. W. Hillhouse, S. Nair, M. Tsapatsis, A. Burton, R. F. Lobo, R. M. Jabubinas, S. M. Kuznicki, *Chem. Mater.*, **12**, 1857 (2000).
7. S. Nair, H. K. Jeong, A. Chandrasekaran, C. M. Braunbarth, M. Tsapatsis, S. M. Kuznicki, *Chem. Mater.*, **13**, 4247 (2001).
8. S.W. Park, S. H.Cho, W. S. Ahn, W. J. Kim, *Micropor. Mesopor. Mater.*, **145**, 200 (2011)
9. S. P. Cardoso, C. B. Lopes, E. Pereira, A. C. Duarte, C. M. Silva, *Water, Air, and Soil Pollution*, **224**, 1 (2013).
10. S. Ferdov, E. Shikova, Z. Ivanova, L. T. Dimowa, R. P. Nikolova, Z. Lin, B. L. Shivachev, *RSC Advances*, **3**, 8843 (2013).
11. M. L. Pinto, A. C. Fernandes, J. Rocha, A. Ferreira, F. Antunes, J. Pires, *Journal of Materials Chemistry B*, **2**, 224 (2014).
12. D. Vilarde, P. De Luca, D. Vuono, J. B. Nagy, A. Nastro, *Studies in Surface Science and Catalysis*, **154**, 1929 (2004).
13. G. Guan, K. Kusakabe, Sh. Morooka, *Micropor. Mesopor. Mater.*, **50**, 109 (2001).
14. R. Chakraborty, P. Chattopadhyay, *J Radioanal Nucl. Chem.* **294**, 31 (2012).
15. K. Popa, C. C. Pavel, *Desalination* **293**, 78 (2012).
16. R. P. Nikolova, B. L. Shivahev, S. Ferdov, *Micropor. Mesopor. Mater.*, **165**, 121 (2013).
17. L. Tsvetanova, L. Dimowa, S. Ferdov, R. Nikolova, *Bul. Chem. Commun.*, **45**, 522 (2013).
18. Agilent. CrysAlis PRO (version 1.171.35.15). 9. Agilent Technologies Ltd, Yarnton England, 2010.
19. G. M. Sheldrick, *Acta Cryst., A*, **64**, 112 (2008).
20. Crystal Maker (version 2.6.2, SN2080).

КРИСТАЛНА СТРУКТУРА НА Ag⁺ ЙОНООБМЕНЕНИ
МОНОКРИСТАЛИ НА ETS-4 ПРИ СТАЙНА (290 К)
И НИСКА (150 К) ТЕМПЕРАТУРА

Л. Цветанова^{1*}, Н. Петрова¹, С. Фердов², В. Костов-Китин¹, Р. Николова

¹ *Институт по минералогия и кристалография, Българска академия на науките,
София, 1113, България*

² *Department of Physics, University of Minho, 4800-058 Guimarães, Portugal*

Постъпила декември, 2014 г.; приета януари, 2015 г.

(Резюме)

Синтезиран е микропорест титаносиликат Na-K-ETS-4 във вид на монокристали, които са обменени със Ag⁺ йони. Кристалните структури на изходната и йонно-обменена форми са изследвани чрез монокристална рентгенова дифракция при стайна 290 К и ниска 150 К температура. За допълнителна характеристика на изследваните кристали са използвани методите: SEM, DTA/TG и прахова XRD. Изследването показва, че Na⁺ и K⁺ йони са напълно обменени от Ag⁺ йони. Йонообменът и нискотемпературните условия водят до деформации в структурата на скелета, проявено в промяна на параметрите на елементарната клетка. Нискотемпературните изследвания позволяват по-прецизно уточняване на атомните параметри, минимизиране на ефекта на температурните трептения и позиционната неподреденост на атомите.

Novel 13-membered cyclic dioxatetraaza scaffolds – synthesis, solution and solid state characterization

A. A. Petrova¹, S. M. Angelova¹, I. A. Nikolchina¹, R. I. Russev², V. B. Kurteva^{1*},
B. L. Shivachev^{2*}, R. P. Nikolova²

¹ Institute of Organic Chemistry with Centre of Phytochemistry, Bulgarian Academy of Sciences,
Acad. G. Bonchev str., bl. 9, 1113 Sofia, Bulgaria

² Institute of Mineralogy and Crystallography “Acad. Ivan Kostov”, Bulgarian Academy of Sciences,
Acad. G. Bonchev str., bl. 107, 1113 Sofia, Bulgaria

Received December, 2014; Revised January, 2015

A series of three novel ligands with 1,4,8,11-tetraazacyclotridecine-2,10-dione skeleton, possessing relatively hindered amine fragment and variable substitution pattern at the aryl group in the amide moiety, was designed and obtained *via* an improved synthetic protocol. The macrocycles were analysed by NMR spectra in solution and by single crystal and powder XRD in solid state. The 13-membered ring conformation was discussed and compared with literature data.

Key words: 1,4,8,11-tetraazacyclotridecine-2,10-diones, NMR, single crystal XRD, powder XRD

INTRODUCTION

Macrocyclic polyfunctional molecules are of growing interest as they are widely applied as scaffolds in the combinatorial synthesis of artificial receptors for ions with medical and environmental potential [1–16]. Among the broad variety of synthetic macrocycles [17–26], polyaza ligands have received special attention due to their outstanding coordination abilities [27–34]. In particular, dioxatetraaza macrocycles possess unique properties due to their dual features between oligopeptides and saturated cyclic amines. The characteristics of the amide group and the hydrogen-bonding capability of both NH and C=O moieties [35] determine the amino acid like ligands' properties. The latter instigated the extraordinary research in supramolecular chemistry in last decades on the amide-based receptors for molecule and ion recognition [36–49].

The most widely studied dioxatetraaza macrocycles are built of *o*-phenylene diamine amide fragment and saturated amine unit. The usual protocol for their construction is based on subsequent acylation of *o*-phenylene diamine and reaction with bis-

amine. Among the latter, unsubstituted ethylene and propylene α,ω -diamines are commonly used [42, 46, 49]. The corresponding 12- and 13-membered cyclic products are isolated in low to moderate yields and studied as ligands for metal complexes.

Herein, we report on the synthesis of three new 13-membered cyclic dioxatetraaza ligands, convenient scaffolds for synthetic protein surface receptors, *via* improved protocol and their characterization in solution and solid state.

EXPERIMENTAL

Synthesis

All reagents were purchased from Aldrich, Merck and Fluka and were used without any further purification. Fluka silica gel/TLC-cards 60778 with fluorescent indicator 254 nm were used for TLC chromatography and R_f -values determination. The melting points were determined in capillary tubes on SRS MPA100 OptiMelt (Sunnyvale, CA, USA) automated melting point system with heating rate 1 °C/min. The NMR spectra were recorded on a Bruker Avance II+ 600 spectrometer (Rheinstetten, Germany) at 25 °C; the chemical shifts were quoted in ppm in δ -values against tetramethylsilane (TMS) as an internal standard and the coupling constants were calculated in Hz. The assignment of the sig-

* To whom all correspondence should be sent:
E-mail: vkurteva@orgchm.bas.bg

nals was confirmed by applying 2D techniques. The spectra were recorded as 5×10^{-2} M solutions and were processed with Topspin 2.1 program.

Synthesis of N,N' -(1,2-phenylene)bis(2-chloroacetamides) 2

To a suspension of 1,2-phenylenediamine (5 mmol **1a** x 2HCl, **1b**, or **1c**;) and K_2CO_3 (25 mmol for **2a**, 15 mmol for **2b** and **2c**) in dry CH_2Cl_2 (50 ml) chloroacetyl chloride (11 mmol) was added and the mixture was stirred at room temperature for 3 h. The products were partitioned between water and CH_2Cl_2 . The organic phase was dried over Na_2SO_4 and evaporated to dryness to give the crude product, which was pure enough (TLC, NMR) to be used in the next step without purification.

N,N' -(1,2-phenylene)bis(2-chloroacetamide) 2a: m. p. 200.6-201.2 °C (lit. [50] 204 °C); R_f 0.53 (5% MeOH in DCM); 1H NMR (DMSO- d_6) 4.284 (s, 4H, 2 x CH_2), 7.219 (AA'BB', 2H, CH-4,5), 7.500 (AA'BB', 2H, CH-3,6), 9.786 (bs, 2H, 2 x NH); ^{13}C 43.57 (CH_2), 125.68 (CH-3,6), 126.39 (CH-4,5), 130.59 ($C_{q-1,2}$), 165.93 (C=O); NOESY cross peaks 4.284/9.786, 7.219/7.500, 7.500/9.786; HSQC cross peaks 4.284/43.57, 7.219/126.39, 7.500/125.68.

N,N' -(4-Methyl-1,2-phenylene)bis(2-chloroacetamide) 2b: m. p. 177.8-178.2 °C; R_f 0.55 (5% MeOH in DCM); 1H NMR (DMSO- d_6) 2.285 (s, 3H, CH_3), 4.303 (s, 2H, CH_2), 4.309 (s, 2H, CH_2), 7.030 (dd, 2H, J 1.3, 8.2, CH-5), 7.358 (d, 2H, J 1.3, CH-3), 7.388 (d, 2H, J 8.2, CH-6), 9.625 (s, 1H, NH-1), 9.634 (s, 1H, NH-2); ^{13}C 20.62 (CH_3), 43.28 (CH_2), 43.29 (CH_2), 125.09 (CH-6), 125.34 (CH-3), 126.29 (CH-5), 127.59 (C_{q-1}), 130.14 (C_{q-4}), 135.11 (C_{q-2}), 165.15 (C=O), 165.17 (C=O); NOESY cross peaks 2.285/7.030, 2.285/7.358, 4.303, 4.309/9.625, 9.634, 7.030/7.388, 7.388/9.625, 9.634; HSQC cross peaks 2.285/20.62, 4.303, 4.309/43.28, 43.29, 7.030/126.29, 7.358/125.34, 7.388/125.09; HMBC cross peaks 2.285/125.34, 2.285/126.29, 2.285/135.11, 4.303/165.15, 165.17, 4.309/165.15, 165.17, 7.030/20.62, 7.030/125.34, 7.030/127.59, 7.358/20.62, 7.358/127.59, 7.388/130.14, 7.388/135.11, 9.625, 9.634/165.15, 165.17.

N,N' -(4-Nitro-1,2-phenylene)bis(2-chloroacetamide) 2c: m. p. 145.2-145.6 °C (lit. [51] 142.5-143.5 °C); R_f 0.46 (5 % MeOH in DCM); 1H NMR (DMSO- d_6) 4.381 (s, 2H, CH_2 -2), 4.407 (s, 2H, CH_2 -1), 7.887 (dd, 2H, J 2.7, 9.0, CH-5), 7.963 (d, 2H, J 9.0, CH-6), 8.430 (d, 2H, J 2.7, CH-3), 10.047 (s, 1H, NH-2), 10.067 (s, 1H, NH-1); ^{13}C 43.35 (CH_2 -2), 43.43 (CH_2 -1), 120.90 (CH-3), 123.67 (CH-5), 124.45 (CH-6), 129.73 (C_{q-2}), 136.53 (C_{q-1}), 143.58 (C_{q-4}), 165.63 (C=O-1), 165.78 (C=O-2); NOESY cross peaks 4.381/10.047, 4.407/10.067,

7.887/7.963, 7.963/10.067, 8.430/10.047; HSQC cross peaks 4.381/43.35, 4.407/43.43, 7.887/123.67, 7.963/124.45, 8.430/120.90; HMBC cross peaks 4.381/165.78, 4.407/165.63, 7.887/120.90, 7.887/136.53, 7.963/129.73, 7.963/143.58, 8.430/123.67, 8.430/136.53, 8.430/143.58 (weak), 10.047/120.90, 10.047/165.78, 10.067/124.45, 10.067/165.78.

Synthesis of 6,6-dimethyl-4,5,6,7,8,9-hexahydro-1H-benzo[e][1,4,7,10]tetraazacyclotridecine-2,10(3H,11H)-diones 3

To a solution of crude dichloride **2** (theor. 5 mmol) and Et_3N (10.7 mmol) in dry DMF (10 ml) 2,2-dimethyl-1,3-propanediamine (5 mmol) was added and the mixture was stirred at room temperature for 3–5 h. The reaction mixture was poured in water. The solid phase formed was filtered off, washed with water, and dried in air.

6,6-dimethyl-4,5,6,7,8,9-hexahydro-1H-benzo[e][1,4,7,10]tetraazacyclotridecine-2,10-dione 3a: 64% overall yield; m. p. 283.6-283.9 °C (*i*-PrOH); R_f 0.36 (5% MeOH in DCM); 1H NMR ($CDCl_3$) 0.960 (s, 6H, 2 x CH_3 -6), 1.688 (bs, 2H, NH-4,8), 2.668 (bs, 4H, CH_2 -5,7), 3.416 (bs, 4H, CH_2 -3,9), 7.185 (AA'BB', 2H, CH-13,14), 7.861 (AA'BB', 2H, CH-12,15), 9.506 (bs, 2H, NH-1,11); ^{13}C 24.59 (2 x CH_3 -6), 34.61 (C_{q-6}), 53.00 (CH_2 -3,9), 56.74 (CH_2 -5,7), 123.00 (CH-12,15), 125.32 (CH-13,14), 128.16 ($C_{q-11a,15a}$), 169.44 ($C_{q-2,10}$); NOESY cross peaks 0.960/1.688, 0.960/2.668, 0.960/9.506 (weak), 1.688/2.668 (weak), 1.688/3.416, 1.688/9.506 (exchange), 2.668/3.416, 2.668/9.506, 3.416/9.506, 7.185/7.861, 7.861/9.506; HSQC cross peaks 0.960/24.59, 2.668/56.74, 3.416/53.00, 7.185/125.32, 7.861/123.00; HMBC cross peaks 0.960/24.59, 0.960/34.61, 0.960/56.74, 7.185/123.00, 7.185/128.16, 7.861/125.32, 7.861/128.16, 9.506/123.00, 9.506/128.16 (weak).

6,6,13-trimethyl-4,5,6,7,8,9-hexahydro-1H-benzo[e][1,4,7,10]tetraazacyclotridecine-2,10-dione 3b: 70% overall yield; m. p. 252.4-252.7 °C (EtOH); R_f 0.38 (5% MeOH in DCM); 1H NMR ($CDCl_3$) 0.942 (s, 6H, 2 x CH_3 -6), 1.672 (bs, 2H, NH-4,8), 2.332 (s, 3H, CH_3 -13), 2.642 (bs, 4H, CH_2 -5,7), 3.386 (bs, 4H, CH_2 -3,9), 6.980 (dd, 1H, J 1.3, 8.2, CH-14), 7.671 (d, 1H, J 1.3, CH-12), 7.701 (d, 1H, J 8.2, CH-15), 9.388 (bs, 1H, NH-1), 9.444 (bs, 1H, NH-11); ^{13}C 21.38 (CH_3 -13), 24.68 (2 x CH_3 -6), 34.70 (C_{q-6}), 53.10, 53.12 (CH_2 -3,9), 56.79, 56.84 (CH_2 -5,7), 122.96 (CH-15), 123.43 (CH-12), 125.60 (C_{q-11a}), 126.08 (CH-14), 128.13 (C_{q-15a}), 135.36 (C_{q-13}), 169.53 ($C_{q-2,10}$); NOESY cross peaks 0.942/1.672, 0.942/2.642, 1.672/2.642 (weak), 1.672/9.388, 9.444 (exchange), 1.672/3.386, 2.332/6.980, 2.332/7.671, 2.642/3.386, 6.980/7.701, 7.671/9.444, 7.701/9.388; HSQC cross

peaks 0.942/24.68, 2.332/21.38, 2.642/56.79, 56.84, 3.386/53.10, 53.12, 6.980/126.08, 7.671/123.43, 7.701/122.96; HMBC cross peaks 0.942/24.68, 0.942/34.70, 0.942/56.79, 56.84, 2.332/123.43, 2.332/126.08, 2.332/135.36, 6.980/21.38, 6.980/123.43, 6.980/125.60, 7.671/126.08, 7.671/128.13, 7.701/125.60, 7.701/135.36, 9.388/122.96, 9.444/123.43.

6,6-dimethyl-13-nitro-4,5,6,7,8,9-hexahydro-1H-benzo[e][1,4,7,10]tetraazacyclotridecine-2,10-dione 3c: 61% overall yield; m. p. 284.1–284.3 °C (*i*-PrOH-acetone); R_f 0.40 (5% MeOH in DCM); ^1H NMR (DMSO- d_6) 0.879 (s, 6H, 2 x CH_3 -6), 2.549 (bs, 2H, CH_2 -5,7), 2.585 (bs, 2H, CH_2 -5,7), 3.269 (bs, 4H, CH_2 -3,9), 3.341 (bs, 2H, NH -4,8), 6.530 (bs, >2H, NH -1,11; mixed with H_2O in the solvent), 8.053 (d, 1H, J. 8.9, CH -15), 8.086 (dd, 1H, J. 2.5, 8.9, CH -14), 8.532 (d, 1H, J. 2.5, CH -12); ^{13}C 24.92 (2 x CH_3 -6), 34.54 (C_q -6), 52.68, 52.77 (CH_2 -3,9), 56.31, 56.39 (CH_2 -5,7), 117.82 (CH -12), 120.31 (CH -14), 121.58 (CH -15), 128.85 (C_q -11a), 135.87 (C_q -15a), 142.77 (C_q -13), 170.50 (C_q -2,10), 170.63 (C_q -2,10); NOESY cross peaks 0.879/2.549, 0.879/2.585, 0.879/3.341 (weak), 2.549/3.269, 2.549/3.341, 2.585/3.269, 2.585/3.341, 3.341/6.530 (exchange), 8.053/8.086; HSQC cross peaks 0.879/24.92, 2.549/56.31, 2.585/56.39, 3.269/52.68, 52.77, 8.053/121.58, 8.086/120.31, 8.532/117.82; HMBC cross peaks 0.879/24.92, 0.879/34.54, 0.879/56.39, 2.549/24.92, 2.549/34.54, 2.585/24.92, 2.585/34.54, 3.269/56.39, 3.269/170.50, 3.269/170.63, 3.341/56.39, 8.053/128.85, 8.053/142.77, 8.086/135.87, 8.532/120.31, 8.532/128.85, 8.532/135.87, 8.532/142.77.

Crystallography

The crystals of **3a** and **3b** were mounted on a glass capillary and all geometric and intensity data were taken from these crystals. Crystallographic measurements were taken on an Agilent SupernovaDual diffractometer equipped with an Atlas CCD detector and on an Enraf Nonius CAD4 diffractometer using micro-focus Mo $\text{K}\alpha$ radiation ($\lambda = 0.71073 \text{ \AA}$) at room temperature. The determinations of the unit cell parameters, data collection and reduction were performed with CrysAlispro software [52]. The structures were solved by direct methods and refined by the full-matrix least-squares method on F^2 with ShelxS and ShelxL 2013 programs [53]. All non-hydrogen atoms, including solvent molecules, were located successfully from Fourier maps and were refined anisotropically. Hydrogens adjoining N atoms were positioned from difference Fourier map while H atoms on C atoms were generated geometrically. The methyl moiety of **3b** shows a disorder over two positions and the refinement model revealed that the major component is 65%. Most important crystallographic and refine-

ment indicators are listed in Table 1. Complete crystallographic data for the structure reported in this paper, **3a** and **3b**, have been deposited in the CIF format with the Cambridge Crystallographic Data Center as supplementary publication No. CCDC 1037064 and 1037065, respectively. Copies of the data can be obtained free of charge on application to CCDC, 12 Union Road, Cambridge CB2 1EZ, UK (fax: (44) 1223336-033; e-mail: deposit@ccdc.cam.ac.uk).

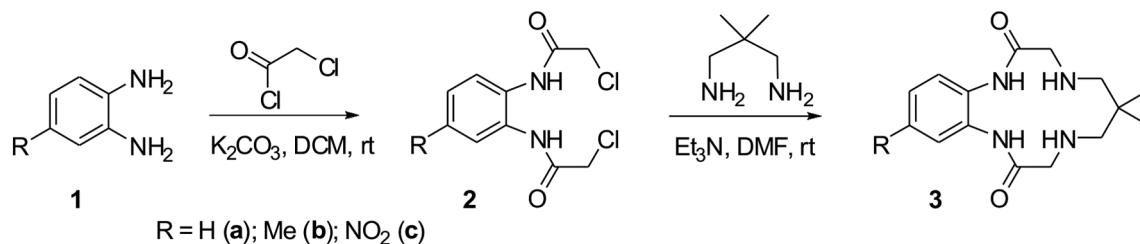
Powder X-ray diffraction data were collected at room temperature on Bruker D2 Phaser diffractometer (Ni-filtered Cu $\text{K}\alpha$ radiation, 30 kV, 10 mA). Data collection was performed in the range 5 to 50° 2θ , step size of 0.02° 2θ with counting time of 10 s per step.

RESULTS AND DISCUSSION

The novel 13-membered benzodioxatetraaza cyclic compounds, 1,4,8,11-tetraazacyclotridecine-2,10-diones **3**, were designed by following two main concepts. First, to replace the flexible propylenediamine unit of an existing scaffold [42, 46] with its 2,2-dimethyl analogue in order to hinder partially the amine fragment, which is expected to have an important impact on our further studies. Second, to obtain the symmetric product **3a** and non-symmetric compounds, possessing either an electron donating (Me, **3b**) or an electron withdrawing (NO_2 , **3c**) substituent at position 13, which will enable to examine the influence of the latter on the amide proton properties.

The target molecules were obtained *via* improved two-step protocol from the cheap commercial sources, *o*-phenylenediamines (**1**), as shown on Scheme 1.

The intermediates **2** were synthesised *via* a standard protocol and were isolated in high to quantitative yields. The compounds were pure enough, as indicated by TLC and NMR, and were submitted to the second step without purification. The conversion of **2** into the target heterocyclic products **3** was performed *via* a modified literature procedure for analogues molecules [42]; the reaction was carried out in DMF instead of acetonitrile, due to the limited solubility of the dichlorides **2**, in the presence of triethylamine as a base instead of heterogeneous potassium carbonate. The macrocyclic compounds **3** were isolated in good yields, 61–70% overall for two steps *vs* 52% for the second step [42], after short reaction times, 3–5 h, at room temperature *vs* 24 h at 40 °C, and simple work-up, water treatment and filtration. Products structures were assigned by 1D and 2D NMR experiments and were confirmed by X-ray diffraction.



Scheme 1. Synthesis of the novel 1,4,8,11-tetraazacyclotridecine-2,10-dione scaffolds **3**.

NMR spectra showed that the symmetrical molecule **3a** gives sharp and well defined signals for aromatic and methyl group protons and broad signals for methylene groups (Fig. 1). This pattern is valid for **3b**, while all signals are sharp in the spectra of **3c**. From the other side, the symmetrical signals in the non-symmetrical analogues **3b** and **3c**, CH-12,15, CH₂-3,9, CH₂-5,7, NH-1,11, and NH-4,8, are

distinguished each other; the effect being more significant in nitro group containing compound **3c**.

Compound **3a** was recrystallized from *iso*-propanol and was analyzed by single crystal diffraction. It crystallized in monoclinic *C2/c* space group (Table 1). Only half of the molecule is observed in the asymmetric unit (ASU) of **3a**. The whole molecule is obtained (e.g the other half of the molecule)

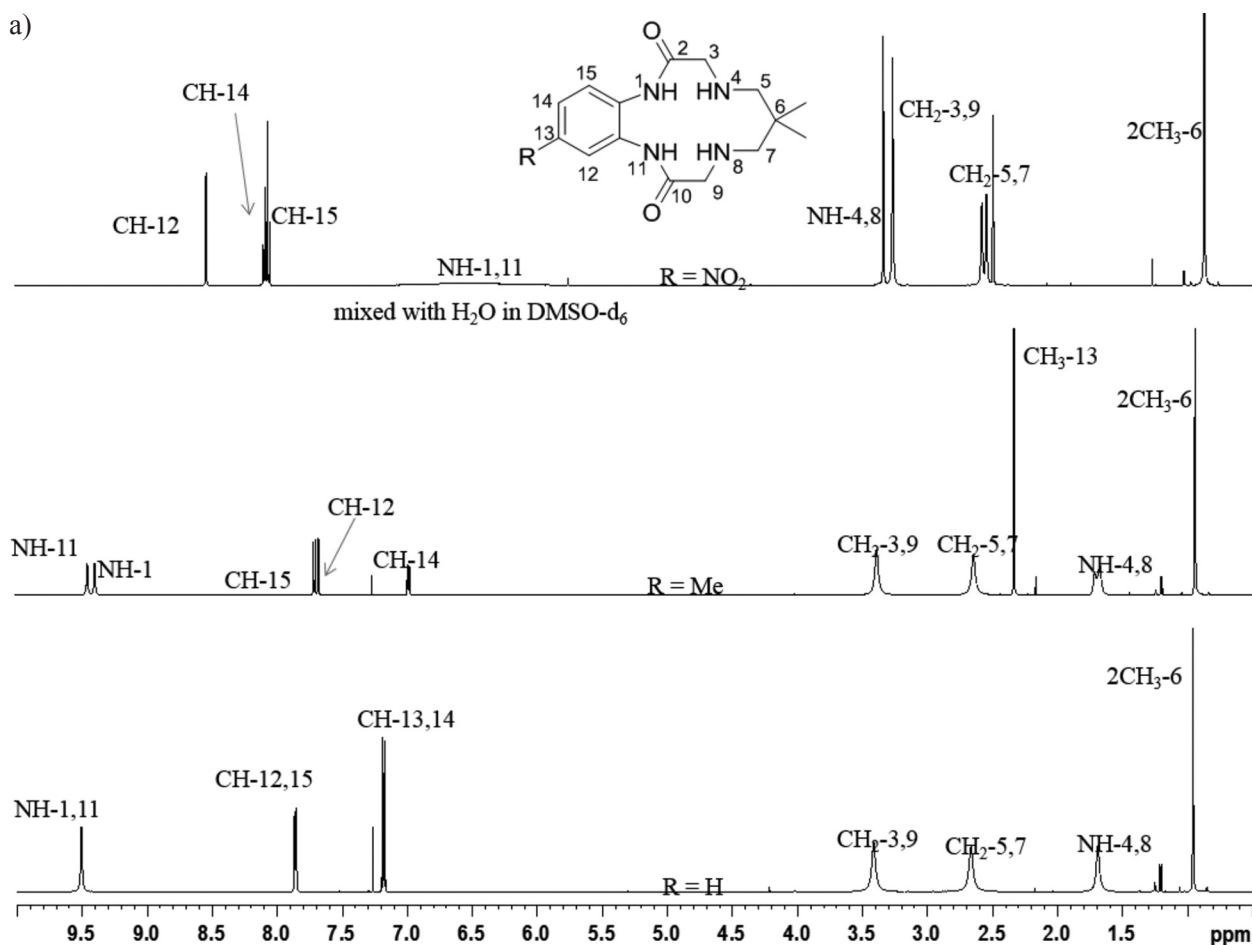


Fig. 1. ¹H NMR spectra of **3a** in CDCl₃ (down), **3b** in CDCl₃ (middle) and **3c** in DMSO-d₆ (up): a) full spectra; b) aromatic protons area

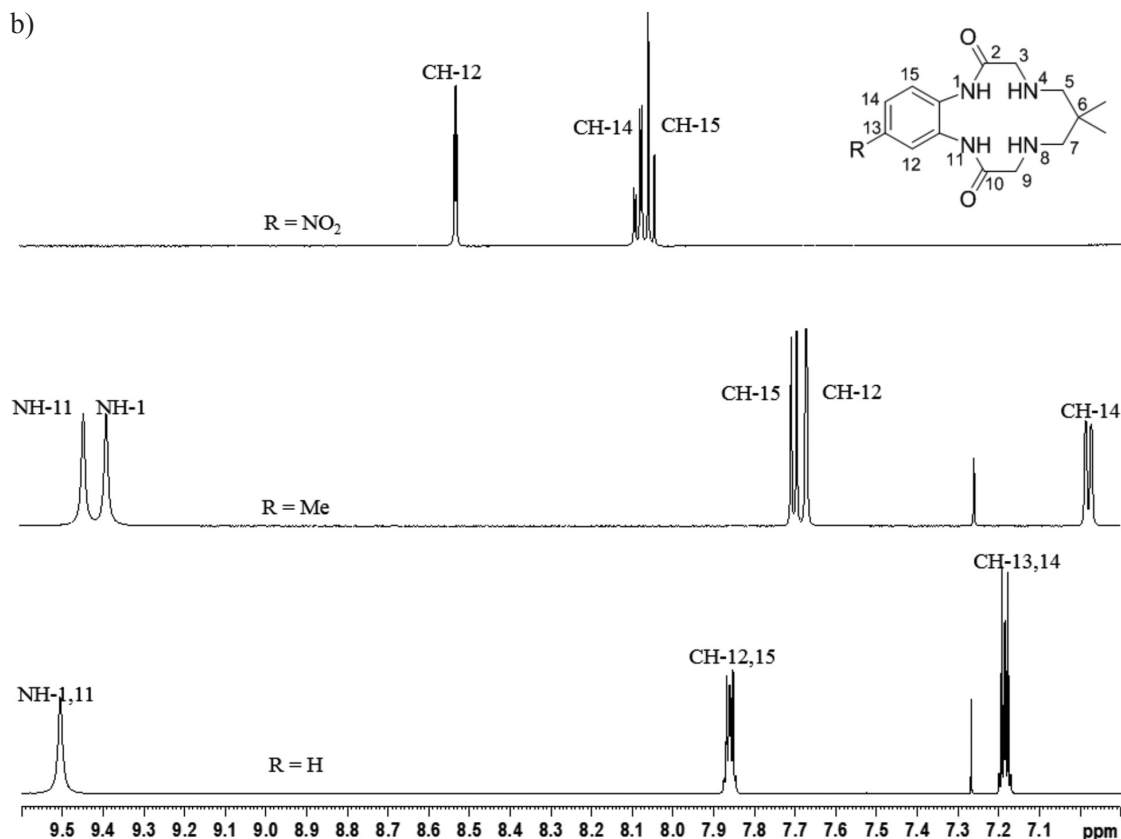
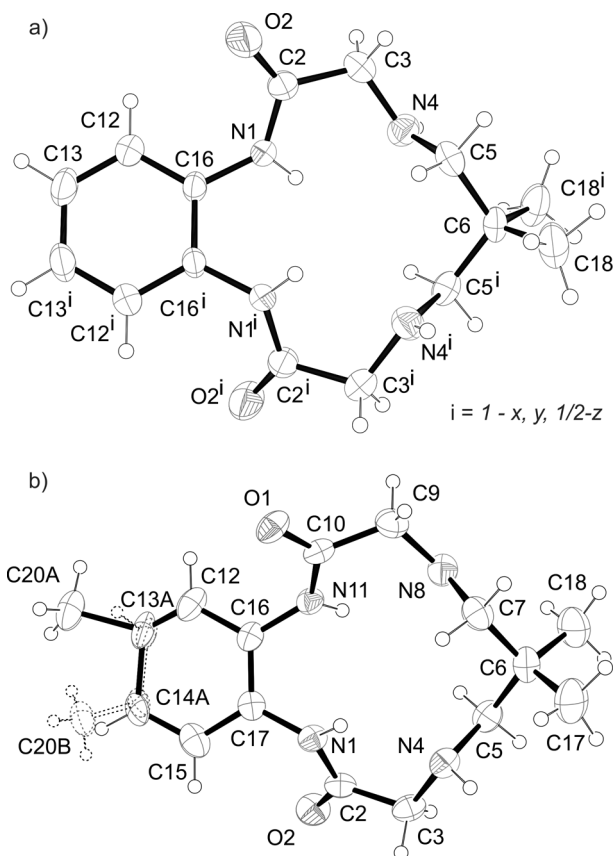


Fig. 1. (continued)

through a 2-fold rotation axis (with direction $[0, 1, 0]$ at $0, y, 1/4$) (Fig. 2a). Quality single crystals of compound **3b**, suitable for data collection, were obtained by the vapor diffusion technique using acetonitrile and diethyl ether. Compound **3b** crystallizes in the triclinic space group $P\bar{1}$, with one molecule per asymmetric unit (for additional details see Table 1 and Fig. 2b). The majority of bond lengths and angles are comparable for **3a** and **3b** (Table 2 and Fig. 3).

The 13 membered ring, [1,4,7,10]tetraazacyclotridecine-2,10-dione, common for **3a-c** is decorated

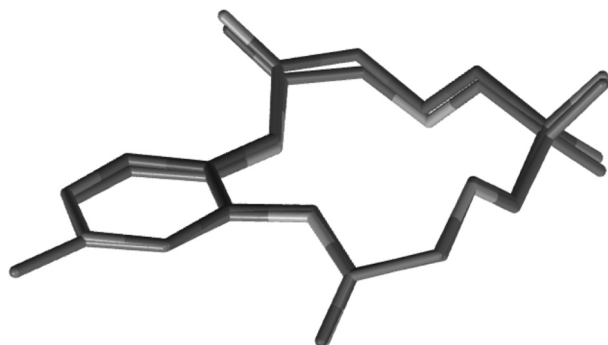


→
Fig. 2. ORTEP (ORTEP-3, v. 2.02) drawing of **3a** (a) and **3b** (b) with the atomic numbering scheme (ellipsoids are at 50% probability), the hydrogen atoms are shown as small spheres of arbitrary radii (Color figure available online). The minor disorder component (33%) in **3b** is shown as dotted lines (atoms C20B, C13B, C14B). The ASU of **3a** contains only half of the molecule while the complete molecule is generated through a 2-fold rotation axis (symmetry operation: $1-x, y, 1/2-z$).

Table 1. Most important crystallographic and refinement details for compounds **3a** and **3b**

Compound reference	3a	3b
Chemical formula	C ₁₅ H ₂₂ N ₄ O ₂	C ₁₆ H ₂₄ N ₄ O ₂
Formula Mass	290.36	304.39
Crystal system	Monoclinic	Triclinic
<i>a</i> /Å	11.584(6)	8.7532(13)
<i>b</i> /Å	12.475(7)	8.960(2)
<i>c</i> /Å	10.089(6)	11.210(7)
α /°	90	101.80(5)
β /°	93.20(3)	91.76(5)
γ /°	90	108.567(19)
Unit cell volume/Å ³	1455.6(14)	811.5(6)
Temperature/K	290(2)	290(2)
Space group	<i>C</i> 2/ <i>c</i>	<i>P</i> $\bar{1}$
No. of formula units per unit cell, <i>Z</i>	4	2
Radiation type	MoK α	MoK α
Absorption coefficient, μ /mm ⁻¹	0.091	0.084
No. of reflections measured	2718	9358
No. of independent reflections	1435	4502
<i>R</i> _{int}	0.2218	0.0282
Final <i>R</i> ₁ values (<i>I</i> > 2 σ (<i>I</i>))	0.093	0.0666
Final <i>wR</i> (<i>F</i> ²) values (<i>I</i> > 2 σ (<i>I</i>))	0.2098	0.2067
Final <i>R</i> ₁ values (all data)	0.2321	0.0881
Final <i>wR</i> (<i>F</i> ²) values (all data)	0.2701	0.2261
Goodness of fit on <i>F</i> ²	0.984	0.949
CCDC number	1037064	1037065

with an aromatic moiety (benzene, toluene and nitrobenzene) and two methyl groups. The aliphatic diamine and aromatic diamide fragments are opposite to each other. The aromatic ring in **3b** is nearly planar [with *rmsd* of 0.00217(2)] while in **3a** it is obtained from three atoms which always lie on a plane. The angle between the mean planes of the aromatic ring and the 13-membered ring system is 5.6(1.1) and 11.7(3)° in **3a** and **3b** respectively.

**Fig. 3.** Relative orientation of the 13-cycle fragment in **3a** vs **3b**.

In **3b**, the Me substituent at position 13 produces a disorder over two positions with major component occupancy of 65% (C20A-C13A-C14A) and 35% (almost one third) for the minor component (C20B-C13B-C14B). The superposition of the molecules **3a** and **3b** shows that the molecular features (bond length and angles) are very similar (Table 2). In the CSD the data base (v.5.35) forty seven structures with the 13-membered cyclic fragment are present (AHUCAI [55], BAYZIL [56], BAYZOR [56], DIGFUW [57], FENMOA [58], FEZMEE [57], FUNPEJ [59], FUNPIN [59], ICUDUG [60], ICUFAO [60], IXISUE [61], JEDZIB [62], JETBUF [63], KAJBIH [64], KAJBON [64], KAPPUO [65], KAPQAV [65], KELXUW [66], KELYAD [66], KELYEH [66], KUXJAP [67], KUXJIX [67], LUGSOW [68], LUGSUC [68], LUGTAJ [68], MOCMAT [69], MTAZNI [70], PUJGIK [71], RASSAF [72], SICVAC [68], UYOVUA [73], UYOWAH [73], VASSOY [74], VASSUE [74], VASTAL [74], VIXTOM [75], VIXTUS [75], VOKFAC [76], VOKFEG [76], WIMVEU [77], XATXIB [78], XATXOH [78], XOWWUB [79], YUTHAW [80], YUTHEA [80], ZUFFIP [81]). From the 47 structures, only in three structures

Table 2. Selected bond lengths, angles and torsions

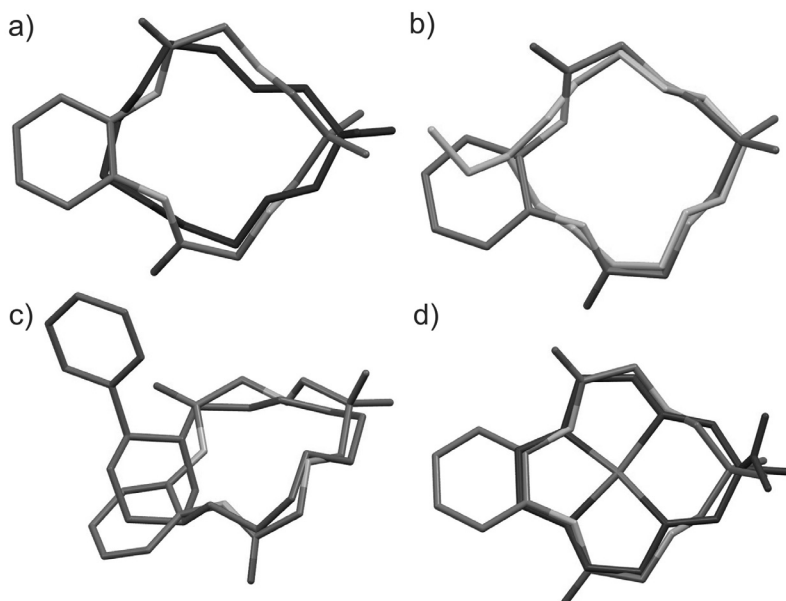
Compound 3a		Compound 3b	
Bond length			
C13—C12	1.365 (8)	C12—C17	1.395 (3)
C13—C13 ⁱ	1.387 (13)	C12—C13B	1.30 (3)
C12—C16	1.380 (8)	C12—C13A	1.430 (12)
C16—C16 ⁱ	1.394 (11)	C17—C16	1.385 (3)
C16—N1	1.412 (7)	C17—N11	1.415 (3)
C2—O2	1.201 (7)	C16—C15	1.390 (3)
C2—N1	1.335 (7)	C16—N1	1.418 (3)
C2—C3	1.506 (9)	C10—O2	1.220 (2)
C3—N4	1.462 (8)	C10—N11	1.347 (3)
C5—N4	1.452 (7)	C10—C9	1.518 (3)
C5—C6	1.516 (7)	C9—N8	1.464 (3)
C6—C17	1.508 (8)	C7—N8	1.465 (3)
C6—C5 ⁱ	1.516 (7)	C2—O1	1.233 (3)
N1—H1	0.8599	C2—N1	1.347 (3)
Bond angle			
C12—C13—C13 ⁱ	120.1 (4)	C16—C17—C12	119.2 (2)
C13—C12—C16	120.4 (6)	C16—C17—N11	118.96 (18)
C12—C16—C16 ⁱ	119.5 (4)	C12—C17—N11	121.8 (2)
C12—C16—N1	122.8 (5)	C17—C16—C15	119.8 (2)
C16 ⁱ —C16—N1	117.6 (3)	C17—C16—N1	118.24 (18)
O2—C2—N1	126.0 (6)	C15—C16—N1	121.9 (2)
O2—C2—C3	120.8 (6)	O2—C10—N11	124.5 (2)
N1—C2—C3	113.1 (5)	O2—C10—C9	120.65 (19)
N4—C3—C2	113.9 (5)	N8—C9—C10	113.79 (18)
N4—C5—C6	114.4 (4)	N8—C7—C6	113.48 (19)
C17—C6—C17 ⁱ	108.3 (7)	C7—C6—C5	111.64 (18)
C17—C6—C5 ⁱ	110.5 (4)	C7—C6—C18	107.9 (2)
C2—N1—H1	116.4	C5—C6—C18	110.7 (2)
C16—N1—H1	117	C7—C6—C19	110.1 (2)
C5—N4—C3	113.7 (5)	N4—C5—C6	114.24 (18)
C5—N4—H4	122.8	N4—C3—C2	114.62 (17)
C2—N1—H1	116.4	O1—C2—N1	124.0 (2)
C16—N1—H1	117	O1—C2—C3	121.45 (19)
Torsion angle			
C13 ⁱ —C13—C12—C16	-0.5 (12)	C12—C17—C16—C15	0.8 (3)
C13—C12—C16—C16 ⁱ	-0.2 (11)	N11—C17—C16—C15	-177.93 (18)
C13—C12—C16—N1	175.4 (6)	C12—C17—C16—N1	-178.60 (18)
O2—C2—C3—N4	163.8 (6)	N11—C17—C16—N1	2.7 (3)
N1—C2—C3—N4	-17.7 (8)	O2—C10—C9—N8	159.8 (2)
N4—C5—C6—C17	172.2 (5)	N11—C10—C9—N8	-21.8 (3)
N4—C5—C6—C17 ⁱ	53.8 (7)	N8—C7—C6—C5	-67.2 (3)
N4—C5—C6—C5	-66.3 (4)	N8—C7—C6—C18	171.0 (2)
O2—C2—N1—C16	-1.7 (10)	N8—C7—C6—C19	52.1 (3)
C3—C2—N1—C16	-180.0 (5)	C7—C6—C5—N4	-65.6 (3)
C12—C16—N1—C2	42.2 (9)	C18—C6—C5—N4	54.6 (3)
C16 ⁱ —C16—N1—C2	-142.1 (7)	C19—C6—C5—N4	173.5 (2)
C6—C5—N4—C3	-180.0 (5)	N4—C3—C2—O1	165.35 (19)
C2—C3—N4—C5	-93.0 (6)	N4—C3—C2—N1	-17.2 (3)

Symmetry code: (i) $-x, y, -z+1/2$.

(KUXJAP, KUXJIX and RASSAF) no metal ion is trapped by the 13-membered ring. Nevertheless the structural variations of the dioxatetraaza scaffolds are conserved and the changes are not significant as one can see from figure Fig. 4.

Thus, one can expect that the metal coordination ability of the cycle will not be significantly affected by the various substituents. On the other hand, specific interactions and/or properties can be achieved by the selection of the 13-cycle “opposite” and

Fig. 4. Fig. XRD3. Relative orientation of the 13-cycle fragment in **3a** vs RASSAF (a), **3a** vs KUXJAP (b), **3a** vs KUXJIH (c) and **3a** vs FUNPEJ (d).



“side” substituents. Undeniably, the obtained scaffolds are very promising building blocks allowing various functionalizations.

The crystal packing of **3a** and **3b** showed that adjacent molecules are alternately oriented; the amide area of one molecule is on the side of the amine fragments of the neighboring molecules.

Thus they are connected by N—H...O=C hydrogen bonds producing identical $R_2^2(14)$ hydrogen bonding topology (Table 3). One should note that amine nitrogen atoms (N4 and N8) are not participating in intermolecular hydrogen bonding interactions. Interestingly the molecular arrangement produces a relatively short distances between the carbonyl atom from different molecules that are somewhat close to the limit distances e.g. O2...O2 3.235 and O1...O1 of 3.511 Å in **3b** and 3.991 Å for O1...O1 in **3a**. Contrary, a similar 12-membered di-

oxatetraaza compound [42] has shown packing of identically oriented molecules (Fig. 5) with both intra and intermolecular H-bonding. This substantial difference is most probably due to the steric hindrance of the CMe₂ fragment of **3**.

The NOESY experiments showed three unexpected features: weak interaction between CH₃ and NH-1,11, which seemed rather distant each other, and weak interactions between NH-1,11 and CH-12,15 and CH₂-3,9, which were expected to be stronger. Moreover, this pattern, which is illustrated on Fig. 6 for **3a**, was valid for all compounds. So, we decided to compare NOESY interactions with crystal structure data (Fig. 7) and found that the distances in the single crystal structure of **3a**, CH₃...NH-1,11 of 4.234 Å, CH-12,15...NH-1,11 of 3.376 Å, and CH₂-3,9...NH-1,11 of 2.907 Å, are in full agreement with the observed cross peaks in

Table 3. Hydrogen-bond geometry (Å, °)

<i>D</i> —H... <i>A</i>	<i>D</i> —H	H... <i>A</i>	<i>D</i> ... <i>A</i>	<i>D</i> —H... <i>A</i>
Compound 3a				
N1—H1...N4	0.86	2.19	2.655 (7)	114
N1—H1...O2 ⁱ	0.86	2.43	3.153 (7)	142
Symmetry codes: (i) <i>x</i> , - <i>y</i> , <i>z</i> +1/2.				
Compound 3b				
N11—H11...N8	0.83	2.32	2.721 (3)	110
N11—H11...O1 ⁱ	0.83	2.37	3.089 (3)	145
N1—H1...N4	0.87	2.17	2.709 (3)	120
N1—H1...O2 ⁱⁱ	0.87	2.42	3.046 (2)	130
Symmetry codes: (i) - <i>x</i> +2, - <i>y</i> +1, - <i>z</i> ; (ii) - <i>x</i> +1, - <i>y</i> , - <i>z</i> .				

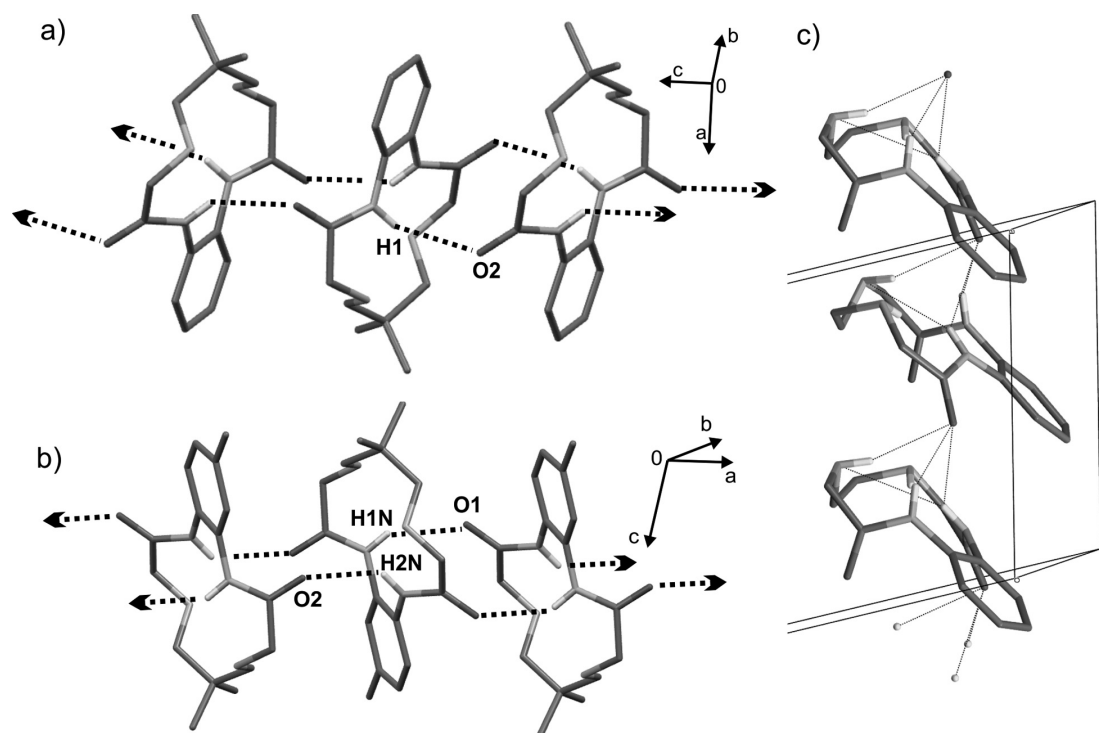


Fig. 5. Relative orientation of the molecules (amide area of one molecule is on the side of the amine fragments) and hydrogen bonding interactions in a) **3a**, b) **3b** and c) ref. 43.

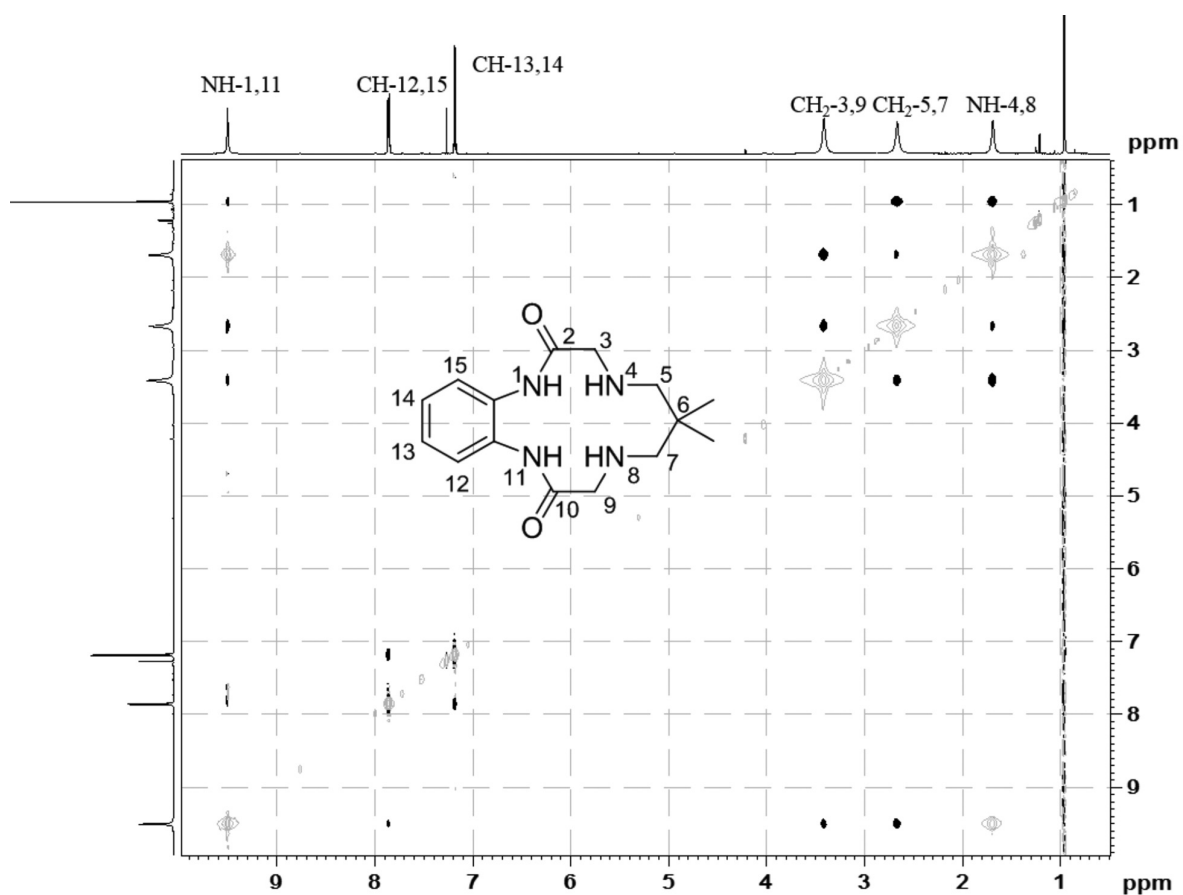


Fig. 6. ^1H - ^1H NOESY spectrum of **3a** in CDCl_3 .

NOESY experiment. Similarly, the unsymmetrical ligand **3b** showed CH₃...NH-1 of 4.280 Å, CH₃...NH-11 of 4.213 Å, CH-12...NH-11 of 3.269 Å, CH-15...NH-1 of 3.308 Å, CH₂-3...NH-1 of 2.946 Å, and CH₂-9...NH-11 of 2.902 Å distances in the crystal phase. These results indicate that the ligands possess similar conformations in solution and in solid state.

As well as in NMR spectra the powder X-ray diffraction data of the three new compounds (Fig. 8) show that no parasite phases are present and that they crystallize with different unit cell parameters. In addition one can speculate that the crystal packing of **3a** and **3b** is comparable. While suitable single crystals were obtained for **3a** and **3b**, large crystals could not be grown for **3c**. Thus indexing, structure solution and refinement were attempted from powder diffraction data.

CONCLUSIONS

Three new ligands with 1,4,8,11-tetraazacyclo-tridecine-2,10-dione skeleton, a symmetric product **3a** and non-symmetric compounds possessing either an electron donating (Me, **3b**) or an electron withdrawing (NO₂, **3c**) substituent at position 13, were obtained *via* an improved two-steps protocol in good overall yields, 61–70%. The products were fully characterized by 1D and 2D NMR spectra and

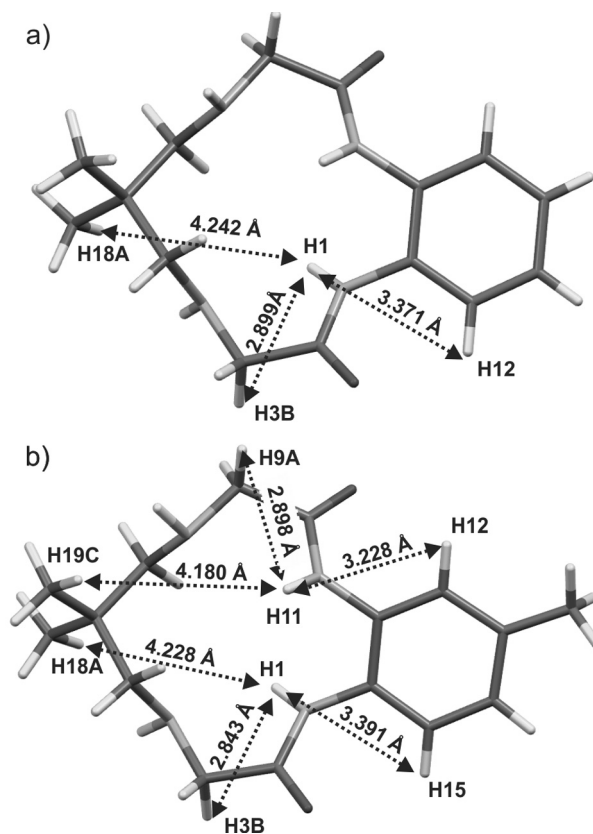


Fig. 7. Weak intramolecular interaction observed in NOESY experiments and the distances for molecules of (a) **3a** and (b) **3b** from X-ray.

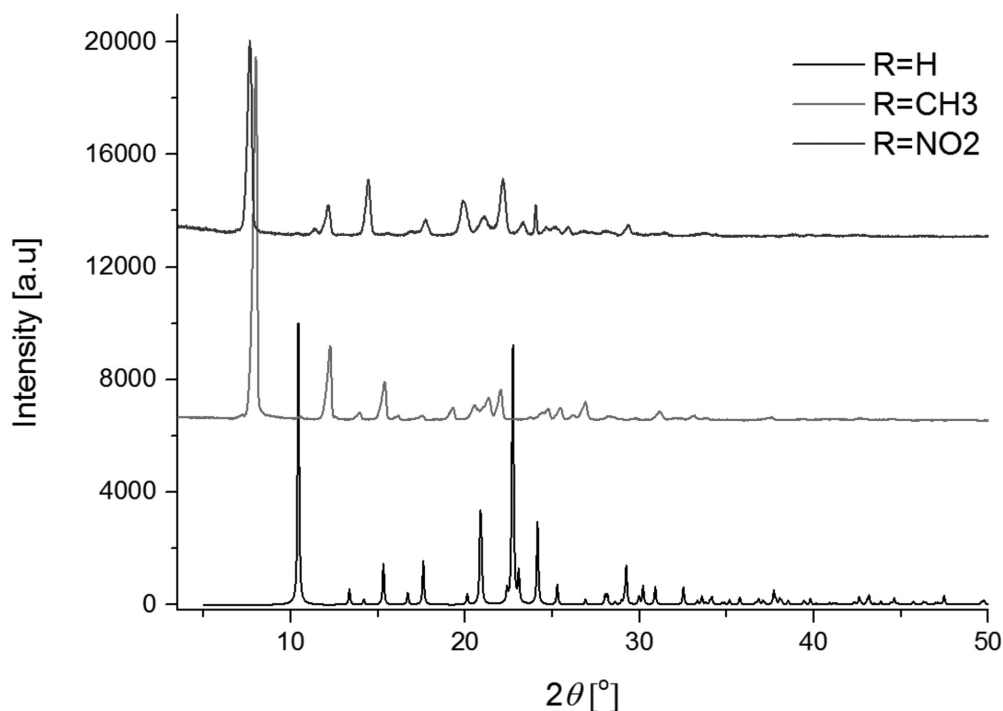


Fig. 8. Powder XRD of **3a** (black), **3b** (red) and **3c** (blue).

single crystal and powder X-ray diffraction. The crystal packing of **3a** and **3b** showed that adjacent molecules are alternately oriented; the amide area of one molecule is on the side of the amine fragments of the neighboring molecules. A juxtaposition with literature data indicated that the metal coordination ability of the cycle is not significantly affected by the substitution pattern in aryl unit. From the other side, specific interactions and/or properties can be achieved by the selection of the 13-cycle “opposite” and “side” substituents. A comparison between NOESY interactions and distances in crystal phases was performed and was found that the ligands possess similar conformations in solution and in solid state.

The obtained products **3** offer unlimited possibilities for derivatization. The preparation of a series of compounds, possessing variable spacers and type of substituents at N-4,8, and investigation of their efficiency as protein surface receptors is in progress.

Acknowledgement: The financial support by The Bulgarian Science Fund, projects UNA-17/2005, DRNF-02-13/2009, and DRNF-02/01, is gratefully acknowledged.

REFERENCES

- Co-ordination Chemistry of Macrocyclic Compounds, G. A. Melson (Ed.), Plenum, New York, 1979.
- J.-M. Lehn, *Supramolecular Chemistry*, VCH, Weinheim, 1995.
- Supramolecular Chemistry of Anions*, E. Bianchi, K. Bowman-James, E. García-España (Eds.), Wiley-VCH, New York, 1997.
- J. P. Desvergne, A. W. Czarnik, *Chemosensors for Ion and Molecule Recognition*; NATO Asi Series, Series C, Kluwer Academic Publishers, London, 1997.
- F. P. Schmidtchen, M. Berger, *Chem. Rev.*, **97**, 1609 (1997).
- K. P. Wainwright, *Coord. Chem. Rev.*, **166**, 35 (1997).
- P. A. Gale, *Coord. Chem. Rev.*, **199**, 181 (2000).
- P. D. Beer, P. A. Gale, *Angew. Chem., Int. Ed.*, **40**, 486 (2001).
- P. A. Gale, *Coord. Chem. Rev.*, **213**, 79 (2001).
- R. Martínez-Máñez, F. Sancenón, *Chem. Rev.*, **103**, 4419 (2003).
- C. Suksai, T. Tuntulani, *Chem. Soc. Rev.*, **32**, 192 (2003).
- Anion Receptor Chemistry*, J. F. Stoddart (Ed.), RSC Publishing, 2006.
- T. Gunnlaugsson, M. Glynn, G. M. Tocci, P. E. Kruger, F. M. Pfeffer, *Coord. Chem. Rev.*, **250**, 3094 (2006).
- J. W. Steed, J. L. Atwood, *Supramolecular Chemistry*, Second Edition, John Wiley & Sons, Ltd, Chichester, UK, 2009.
- P. J. Cragg, *Supramolecular Chemistry, From Biological Inspiration to Biomedical Applications*, Springer Science+Business Media B.V., 2010.
- Applications of Supramolecular Chemistry*, H.-J. Schneider (Ed.), CRC Press, Boca Raton, 2012.
- V. Alexander, *Chem. Rev.*, **95**, 273 (1995).
- Macrocyclic Synthesis, A Practical Approach*, D. Parker (Ed.), Oxford University Press, 1996.
- J. A. Semlyen, *Large Ring Molecules*; John Wiley & Sons, Chichester, 1996.
- Z. R. Laughrey, B. C. Gibb, *Top. Curr. Chem.*, **249**, 67 (2005).
- Modern Supramolecular Chemistry: Strategies for Macrocyclic Synthesis*, F. Diederich, P. J. Stang, R. R. Tykwinski (Eds.), Wiley-VCH Verlag GmbH & Co. KGaA, 2008.
- N. K. Terrett, *Drug Discovery Today: Technologies*, **7**, e97 (2010).
- F. Davis, S. Higson, *Macrocycles*, John Wiley & Sons, Ltd., 2011.
- J. C. Collins, K. James, *Med. Chem. Commun.*, **3**, 1489 (2012).
- X. Yu, D. Sun, *Molecules*, **18**, 6230 (2013).
- L. Xu, Y. Li, Y. Li, *Asian J. Org. Chem.*, **3**, 582 (2014).
- J. S. Bradshaw, K. E. Krakowiak, R. M. Izatt, *Azacrown Macrocycles, The Chemistry of Heterocyclic Compounds Series*, Volume 51, E. C. Taylor, A. Weissberger (Eds.), John Wiley&Sons, Inc., 1993.
- A. P. de Silva, H. Q. N. Gunaratne, T. Gunnlaugsson, A. J. M. Huxley, C. P. McCoy, J. T. Rademacher, T. E. Rice, *Chem. Rev.*, **97**, 1515 (1997).
- L. Cronin, *Annu. Rep. Prog. Chem., Sect. A*, **101**, 319 (2005).
- K. Bowman-James, *Macrocyclic Ligands. Encyclopedia of Inorganic and Bioinorganic Chemistry*, John Wiley & Sons, Ltd., 2006.
- A. Chaudhary, R.V. Singh, *Rev. Inorg. Chem.*, **28**, 35 (2008).
- T.-B. Lu, in: *Macrocyclic Chemistry: New Research Developments*, D. W. Fitzpatrick, H. J. Ulrich (Eds.), Nova Science Publishers, Inc., 2009, Chapter 15.
- K. Bowman-James, *Macrocyclic Ligands. Encyclopedia of Inorganic and Bioinorganic Chemistry*, John Wiley & Sons, Ltd., 2006.
- Rajni, L. Singh, *Int. J. Adv. Eng. Appl.*, **6**, 74 (2013).
- L. Pauling, *The Nature of the Chemical Bond*, 3rd ed., Cornell University Press, New York, 1960.
- Molecular Recognition: Receptors for Molecular Guests*, F. Vögtle (Ed.), *Comprehensive Supramolecular Chemistry*, Vol. 2, Pergamon, New York, 1996.
- L. Fabbrizzi, M. Licchelli, G. Rabaioli, A. Taglietti, *Coord. Chem. Rev.*, **205**, 85 (2000).
- M. B. Inoue, L. Machi, I. C. Muñoz, S. Rojas-Rivas, M. Inoue, Q. Fernando, *Inorg. Chim. Acta*, **324**, 73 (2001).
- G. Cooke, V. M. Rotello, *Chem. Soc. Rev.*, **31**, 275 (2002).
- R. Martinez-Manez, F. Sancenon, *Chem. Rev.*, **103**, 4419 (2003).
- J. L. Sessler, P. A. Gale, W. S. Cho, *Anion Receptor Chemistry*, J. F. Stoddart (Ed.), Royal Society of Chemistry, Cambridge, 2006.

42. P. Antunes, R. Delgado, M. G. B. Drew, V. Félix, H. Maecke, *Inorg. Chem.*, **46**, 3144 (2007).
43. S. Carvalho, R. Delgado, M. G. B. Drew, V. Calisto, V. Félix, *Tetrahedron*, **64**, 5392 (2008).
44. H. M. Betts, P. J. Barnard, S. R. Bayly, J. R. Dilworth, A. D. Gee, J. P. Holland, *Angew. Chem., Int. Ed.*, **47**, 8416 (2008).
45. R. E. Navarro, D. Aguilera-Márquez, C. Virués, M. Inoue, *Supramol. Chem.*, **20**, 737 (2008).
46. P. J. Barnard, J. P. Holland, S. R. Bayly, T. J. Wadas, C. J. Anderson, J. R. Dilworth, *Inorg. Chem.*, **48**, 7117 (2009).
47. S. Kumar, S. Vaidya, M. Pissas, Y. Sanakis, R. Gupta, *Eur. J. Inorg. Chem.*, 5525 (2012).
48. S. K. Sharma, R. Gupta, *Inorg. Chim. Acta*, **376**, 95 (2011).
49. P. Comba, M. Kubeil, J. Pietzsch, H. Rudolf, H. Stephan, K. Zarschler, *Inorg. Chem.*, **53**, 6698 (2014).
50. J. L. Everett, W. C. J. Ross, *J. Chem. Soc.*, 1972 (1949).
51. W. Ozegowski, D. Krebs, M. Wunderwald, *J. Prakt. Chem.*, **20**, 166 (1963).
52. CrysAlis PRO, Agilent Technologies, UK Ltd, Yarn-ton, England, 2011.
53. G. M. Sheldrick, *Acta Cryst. A*, **64**, 112 (2008).
54. L. Farrugia, *J. Appl. Crystallogr.*, **45**, 849 (2012).
55. J. Annaraj, J. Cho, Y.-M. Lee, S. Y. Kim, R. Latifi, S. P. de Visser, W. Nam, *Angew. Chem. Int. Ed.*, **48**, 4150 (2009).
56. X. Zhou, A. I. Day, A. C. Willis, W. G. Jackson, *Chem. Commun.*, 2386 (2003).
57. J. Cho, H. Y. Kang, L. V. Liu, R. Sarangi, E. I. Solomon, W. Nam, *Chem. Sci.*, **4**, 1502 (2013).
58. C. G. Miller, S. W. Gordon-Wylie, C. P. Horwitz, S. A. Strazisar, D. K. Peraino, G. R. Clark, S. T. Weintraub, T. J. Collins, *J. Am. Chem. Soc.*, **120**, 11540 (1998).
59. P. Comba, N. F. Curtis, G. A. Lawrance, M. A. O'Leary, B. W. Skelton, A. H. White, *J. Chem Soc, Dalton Trans*, 2145 (1988).
60. J. Notni, H. Görls, E. Anders, *Eur. J. Inorg. Chem.*, **2006**, 1444 (2006).
61. A. Ghosh, P. Ramidi, S. Pulla, S. Sullivan, S. Col-lom, Y. Gartia, P. Munshi, A. Biris, B. Noll, B. Berry, *Catal. Lett.*, **137**, 1 (2010).
62. T. J. Collins, R. D. Powell, C. Slebodnick, E. S. Uffelman, *J. Am. Chem. Soc.*, **112**, 899 (1990).
63. T. J. Collins, C. Slebodnick, E. S. Uffelman, *Inorg. Chem.*, **29**, 3433 (1990).
64. A. Ghosh, F. Tiago de Oliveira, T. Yano, T. Nishioka, E. S. Beach, I. Kinoshita, E. Münck, A. D. Ryabov, C. P. Horwitz, T. J. Collins, *J. Am. Chem. Soc.*, **127**, 2505 (2005).
65. S. Kumar, R. Gupta, *Indian J. Chem., Sect. A: Inorg., Bio-inorg., Phys., Theor. Anal. Chem.*, **50**, 1369 (2011).
66. S. Kumar, S. Vaidya, M. Pissas, Y. Sanakis, R. Gupta, *Eur. J. Inorg. Chem.*, **2012**, 5525 (2012).
67. Y. Rousselin, N. Sok, F. Boschetti, R. Guillard, F. Denat, *Eur. J. Org. Chem.*, **2010**, 1688 (2010).
68. P. J. Barnard, J. P. Holland, S. R. Bayly, T. J. Wadas, C. J. Anderson, J. R. Dilworth, *Inorg. Chem.*, **48**, 7117 (2009).
69. V. Polshin, D.-L. Popescu, A. Fischer, A. Chanda, D. C. Horner, E. S. Beach, J. Henry, Y.-L. Qian, C. P. Horwitz, G. Lente, I. Fabian, E. Münck, E. L. Bominaar, A. D. Ryabov, T. J. Collins, *J. Am. Chem. Soc.*, **130**, 4497 (2008).
70. J. M. Waters, K. R. Whittle, *J. Inorg. Nucl. Chem.*, **34**, 155 (1972).
71. R. E. Patterson, S. W. Gordon-Wylie, C. G. Woome, R. E. Norman, S. T. Weintraub, C. P. Horwitz, T. J. Collins, *Inorg. Chem.*, **37**, 4748 (1998).
72. O. P. Gladkikh, N. F. Curtis, M. M. Turnbull, *Acta Crystallogr. Sect. C*, **53**, 586 (1997).
73. S. K. Sharma, R. Gupta, *Inorg. Chim. Acta*, **376**, 95 (2011).
74. A. Ghosh, A. D. Ryabov, S. M. Mayer, D. C. Horner, D. E. Prasuhn, S. Sen Gupta, L. Vuocolo, C. Culver, M. P. Hendrich, C. E. F. Rickard, R. E. Norman, C. P. Horwitz, T. J. Collins, *J. Am. Chem. Soc.*, **125**, 12378 (2003).
75. J. Notni, S. Schenk, H. Görls, H. Breitzke, E. Anders, *Inorg. Chem.*, **47**, 1382 (2008).
76. T. J. Collins, R. D. Powell, C. Slebodnick, E. S. Uffelman, *J. Am. Chem. Soc.*, **113**, 8419 (1991).
77. G. Berggren, F. B. Kaynak, M. F. Anderlund, L. Eriksson, B. Akermark, *Acta Crystallogr. Sect. E*, **63**, m2672 (2007).
78. J. Cho, R. Sarangi, H. Y. Kang, J. Y. Lee, M. Kubo, T. Ogura, E. I. Solomon, W. Nam, *J. Am. Chem. Soc.*, **132**, 16977 (2010).
79. C. P. Horwitz, S. W. Gordon-Wylie, Y. Leychkis, D. M. Flynn, S. T. Weintraub, G. R. Clark, T. J. Collins, *J. Phys. Chem. B*, **105**, 8821 (2001).
80. M. J. Bartos, C. Kidwell, K. E. Kauffmann, S. W. Gordon-Wylie, T. J. Collins, G. C. Clark, E. Münck, S. T. Weintraub, *Angew. Chem. Int. Ed.*, **34**, 1216 (1995).
81. E. Joseph Billo, P. J. Connolly, D. J. Sardella, J. P. Jasinski, R. J. Butcher, *Inorg. Chim. Acta*, **230**, 19 (1995).

НОВИ 13-ЧЛЕННИ ЦИКЛИЧНИ ДИОКСАТЕТРААЗА
ПЛАТФОРМИ – СИНТЕЗ И ОХАРАКТЕРИЗИРАНЕ В РАЗТВОР
И ТВЪРДО СЪСТОЯНИЕ

А. А. Петрова¹, С. М. Ангелова¹, И. А. Николчина¹, Р. И. Русев²,
В. Б. Куртева^{1*}, Б. Л. Шивачев^{2*}, Р. Н. Петрова²

¹ *Институт по Органична Химия с Център по Фитохимия, Българска Академия на Науките,
ул. Акад. Г. Бончев, бл. 9, 1113 София, България*

² *Институт по Минералогия и Кристалография „Акад. Иван Костов“, Българска Академия на Науките,
ул. Акад. Г. Бончев, бл. 107, 1113 София, България*

Постъпила декември, 2014 г.; приета януари, 2015 г.

(Резюме)

Серия от три нови лиганда с 1,4,8,11-тетраазациклотридецин-2,10-дионон скелет, притежаващи относително запречен аминен фрагмент и разнообразен модел на заместване в ароматното ядро на амидната единица, са моделирани и получени по подобрен синтетичен протокол. Макроциклите са анализирани с ЯМР спектри в разтвор и с монокристална и прахова рентгенова дифракция в твърдо състояние. Дискутирана е конформацията на 13-членния пръстен и е сравнена с литературни данни.

The use of high-temperature superconducting cuprate as a dopant to the negative electrode in Ni-Zn batteries

A. K. Stoyanova-Ivanova^{1*}, S. D. Terzieva¹, G. D. Ivanova², M. A. Mladenov²,
D. G. Kovacheva³, R. G. Raicheff², S. I. Georgieva⁴, B. S. Blagoev⁵,
A. J. Zaleski⁶, V. Mikli⁷

¹ Institute of Solid State Physics – Bulgarian Academy of Sciences,
Tzarigradsko Chaussee 72 Blvd., 1784 Sofia, Bulgaria

² Institute of Electrochemistry and Energy Systems – BAS Bulgarian Academy of Sciences,
G. Bonchev Street, bl.10, 1113 Sofia, Bulgaria

³ Institute of General and Inorganic Chemistry – Bulgarian Academy of Sciences,
G. Bonchev Street, bl.11, 1113 Sofia, Bulgaria

⁴ University of Chemical Technology and Metallurgy, 8 Kl. Ohridski Blvd., 1756 Sofia, Bulgaria

⁵ Institute of Electronics – Bulgarian Academy of Sciences, 72 Tzarigradsko Chaussee Blvd.,
1784 Sofia, Bulgaria

⁶ Institute of Low Temperature and Structure Research, Polish Academy of Sciences,
2 Okolna Str., 50-422 Wrocław, Poland

⁷ Centre for Materials Research, Tallinn University of Technology, 5 Ehitajate Str.,
19086 Tallinn, Estonia

Received December, 2014; Revised January, 2015

The chemical stability of YBCO ($Y_1Ba_2Cu_3O_{7-x}$) and GdBCO ($Gd_1Ba_2Cu_3O_{7-x}$) superconducting ceramics in an alkaline medium was studied by analyzing polycrystalline samples of the ceramics before and after exposure to an alkaline solution (7M KOH), normally used as a basic electrolyte in alkaline batteries. The high chemical resistance of the ceramics to the alkaline medium was confirmed by structural observations and magnetic measurements. The powder of YBCO ceramics was also used as a conducting additive to the active mass of zinc electrodes in an experimental nickel-zinc alkaline battery. The electrochemical studies were carried out by a specially designed electrochemical cell with demountable “coin” type zinc and nickel electrodes. The tests showed that the cells with an YBCO superconducting ceramic additive to the zinc electrode exhibited good cyclic operation ability and a capacity stability, as well as a higher specific capacity (by about 30%) than the cells with a zinc electrode with carbon as a conducting additive to the active mass. The results obtained suggest a possible application of these structural type superconducting ceramics as additives to the electrode material of zinc electrodes for alkaline battery systems.

Key words: Superconducting ceramics; alkaline battery; microstructure; stability

INTRODUCTION

Since the discovery of the high-temperature superconductors (HTS) in the late 1980s, the technological research has been focused on producing HTS materials in sufficient quantities to make their use economically viable and on optimizing their properties in relation to a wide range of advanced applications. The basic areas of applications of the

high-temperature superconductors are divided into three general purposes [1]: bulk superconductors, superconducting tapes and wires. Bulk HTS have been developed for electronic power application as well as for magnetic separation in water cleaning systems [2].

The chemical stability and the interaction of the HTS with the environment is one of the important factors that can hinder or support their application. The deterioration of the superconducting properties of the YBCO ($Y_1Ba_2Cu_3O_{7-x}$) and BSCCO ($Bi_2Sr_2Ca_2Cu_3O_{7-x}$) systems due to the reaction with water has been studied intensively [3, 4]; it was shown that the superconductors are destroyed in a

* To whom all correspondence should be sent:
E-mail: e-mail: aksi_bg@abv.bg

few minutes by boiling water [5]. The first electrochemical investigations on the dissolution behavior of superconducting oxides were published by Rosamilia et al. [6]. The corrosion behavior of the HTS in different aqueous solutions has also been studied by cyclic voltammetry at temperatures higher than T_c in order to determine the effective exposure “lifetimes” [7]. Applying electrochemical dc and ac methods, Bachtler and Lorentz [8] found that the high temperature superconductor $\text{YBa}_2\text{Cu}_3\text{O}_{7-x}$ does not act as a special electrocatalyst for anodic oxygen evolution reaction. Moreover, the surface structure and composition of the semiconductors were found to depend strongly on the polarization conditions and the contact time with the solution.

Along with the development of zinc electrodes for alkaline battery systems, the application of different conducting powders as additives to the active electrode mass based on zinc oxide have come into consideration because of their low electronic conductivity [9]. In this respect, it is interesting to investigate the possibilities of application of different superconducting ceramic materials as additives to the electrode mass of the zinc electrodes in alkaline rechargeable battery systems, thus contributing to a longer battery life by improving the conductivity and electrochemical homogeneity of the anode mass and reducing gas evolution problems during charging of the cell.

In the present work, the changes of elemental and phase composition, as well as of the superconducting properties of samples of superconducting ceramics $\text{YBa}_2\text{Cu}_3\text{O}_{7-x}$ (YBCO) and $\text{GdBa}_2\text{Cu}_3\text{O}_{7-x}$ (GdBCO) after exposure to a concentrated alkaline solution, were first studied in order to evaluate the stability of the ceramic materials in electrolytes normally used in the alkaline batteries. Second, the behavior of the conducting ceramic powder of the high temperature superconducting system $\text{YBa}_2\text{Cu}_3\text{O}_{7-x}$ was also studied as an additive to the zinc anode mass of nickel-zinc alkaline rechargeable batteries to form a highly conducting network between the particles of the electrode mass thus improving the electrochemical contact in the power generation material in the system.

MATERIALS AND METHODS

Samples preparation

YBCO and GdBCO samples were prepared by the standard solid state synthesis. The appropriate amounts of high purity (all 99.99% pure) powders of Y_2O_3 , Gd_2O_3 , BaCO_3 and CuO were mixed, ground, pressed into pellets and subjected to sintering in three stages in an oxygen atmosphere. The

first sintering was performed at 900 °C for 21h in flowing oxygen. After grinding, the powder was sintered for a second time at 930 °C under the same conditions, followed by a slow cooling and an additional annealing at 450 °C for 2h. The pellets were then pressed at 6 MPa and sintered for the third time at 950 °C for 23h, and subsequently annealed at 450 °C for 23 h.

The pellets of the sintered ceramics (10 mm diameter, 2 mm thick) were first soaked in a model alkaline solution (7M KOH) and then exposed to the same solution for 24, 48, 72 or 96 hours. After the exposure, the samples were removed from the solution, dried at room temperature and studied. Since the properties of all samples varied practically negligibly with the exposure period, further in the paper results from the longest soaking time (96 hours) are only presented and discussed

Pasted zinc electrodes and battery assembling

The pasted zinc electrodes used in the present study were prepared by inserting a preliminarily prepared zinc paste on a metal support and current collector (copper mesh). The paste was composed by powder ZnO (average particle size 30–40 nm, 88 wt.%), a conducting additive – superconducting ceramic powder YBCO (particle size 5–10 μm , 7 wt.%) and binding agents – polytetrafluorethylene (PTFE, 4 wt.%) and carboxymethylcellulose (CMC, 1 wt.%). The paste was uniformly spread on the preliminarily configured copper support (15 mm diameter). The pasted electrode was dried at 90 °C for 2 hours, then pressed under 30 MPa for 2 min and sintered at 320 °C for 10 min. For comparison, similar zinc electrodes with an active paste composed by the same nanosized ZnO (93 wt.%), the same binding agents – polytetrafluorethylene (PTFE, 4 wt.%) and carboxymethylcellulose (CMC, 1 wt.%), but with a conducting carbon additive – acetylene black (AB, 2 wt.%) were also fabricated applying the same technological procedure.

Sintered-type nickel electrodes with a nominal capacity twice as high as the capacity of the zinc electrodes were used as cathodes in the experimental nickel-zinc battery cells. A solution of 7M KOH saturated with ZnO was used as a battery electrolyte. Before assembling the cell, the electrodes were soaked under vacuum with the electrolyte for 10 min. The cell package consisted of two disk-type zinc and nickel electrodes with a diameter of 15 mm, separated by a micro porous separator (Celgard 3501). The electrode package was assembled into a coin-type cell container made of transparent material and soaked with the electrolyte. The zinc electrodes were characterized by the charge-discharge cycling behavior and the cycling life.

Methods for analysis

The X-ray diffraction patterns of the superconducting powder samples were obtained within the range 5.3 to $80^\circ 2\theta$ at a constant step of $0.02^\circ 2\theta$ on a Bruker D8 Advance Diffractometer with Cu $K\alpha$ radiation and a LynxEye Detector. The phase identification was performed by a Diffracplus EVA v. 15 program using the ICDD-PDF2 (2009) Database. The mean crystallite size was determined by the Topas v.4.2 software package using the fundamental parameters peak shape description including appropriate corrections for the instrumental broadening and diffractometer geometry [10].

The microstructure of the samples was studied by means of a Zeiss EVO MA-15 scanning electron microscope (SEM) with a LaB_6 cathode on the polished cross-section of the samples. The chemical composition was determined by X-ray microanalysis using energy dispersive spectroscopy (EDS) on an Oxford Instruments INCA Energy system. The qualitative and quantitative analyses were carried out at an accelerating voltage of 20 kV.

The non-stoichiometric oxygen coefficient δ was determined by spectrophotometry based on the absorbance measurement of colored Cu(II)-EDTA and Co(III)-EDTA complexes [11]. The samples were dissolved in the presence of chloride ions, Co(II) and EDTA without removing the air from the solution ($pH = 2.5$). Co(III)-EDTA and Cu(II)-EDTA complexes were formed in a medium of sodium acetate-acetic acid buffer ($pH = 4.9$) and their absorbance was measured. The δ non-stoichiometric oxygen coefficient was calculated as the ratio of the concentrations of Co(III)-EDTA and Cu(II)-EDTA complexes using salts CoF_3 and $CuSO_4$ as standards for calibration.

The magnetic measurements of bulk polycrystalline superconducting samples were performed using a PPMS (Physical Property Measurement System – Quantum Design) as follows: 1) magnetization vs. magnetic field ($-9 \div 9$ T) $M(H)$ measurements at a temperature of 10 K; and 2) AC magnetization (ACM) vs. temperature ($10 \div 200$ K) measurements in an applied AC magnetic field with a frequency of 3333 Hz and an amplitude of 0.5 mT. For the ACM measurements, the sample was first cooled down to 10 K without a magnetic field.

The electrochemical investigation of the zinc electrodes was carried out on a specialized electrochemical equipment (Arbin Instrument) allowing a galvanostatic mode charge/discharge cycling, as well as a mixed mode constant current/constant voltage cycling. The charge/discharge cycling tests were performed at room temperature. The cells were charged at 20 mA ($C/5$, where $C = 100$ mAh is the nominal capacity of the zinc electrode) for 6 h, and

then discharged at the same current load down to 1.3 V cut-off, recording the cell voltage as a function of time. Both the charge and discharge specific capacities were automatically calculated so that the important dependency of the discharge capacity of both type zinc electrodes on the number of the cycles was thus obtained.

EXPERIMENTAL RESULTS AND DISCUSSION

The X-ray diffraction patterns showed that the single-phase well-crystallized samples formed superconductive 123 systems (YBCO and GdBCO). The refined unit cell parameters were $a = 3.8209(5)$ Å; $b = 3.8938(8)$ Å; $c = 11.675(2)$ Å for YBCO (SG: Pmmm) and $a = 3.8439(5)$ Å; $b = 3.8923(7)$ Å; $c = 11.712(1)$ Å for GdBCO (SG: Pmmm) respectively, leading to a unit cell volume V_m (YBCO) = $173.70(5)$ Å³ and V_m (GdBCO) = $175.35(5)$ Å³. After the treatment with the alkaline solution, all peaks of the 123-type phase remained and no impurity phases related to sample deterioration or products of reaction with potassium hydroxide were found (Fig. 1). No significant changes of the unit cell parameters and the volume after the alkaline treatment were registered; however, the XRD pattern of the treated GdBCO samples showed the presence of an amorphous component, probably due to some surface structure deterioration.

It is well known that the oxygen content is crucial for the phase stability of the cuprate superconductors. Its precise control, as well as the determination of the oxygen non-stoichiometry, provides important information on the phase relation, structural defects and fundamental material properties [12, 13]. In order to obtain more detailed information about the stability of the superconducting phases of the samples treated, the oxygen content was also determined.

The average results for the non-stoichiometric coefficient δ of all (as synthesized and after exposure to the alkaline solution) YBCO and GdBCO samples obtained by spectrophotometry are listed in Table 1. Each result is the mean value of at least three independent determinations, the standard deviation being within ± 0.002 . The spectrophotometric method based on the absorbance measurement of the I_3^- – starch compound was used for comparison [14]. The results obtained by the two methods practically did not differ.

Figure 2 presents SEM images of YBCO and GdBCO samples before and after alkaline treatment. It is seen that a highly homogeneous ceramics was produced after sintering the YBCO bulk sample. The grains were relatively large ($5-10$ μm) without

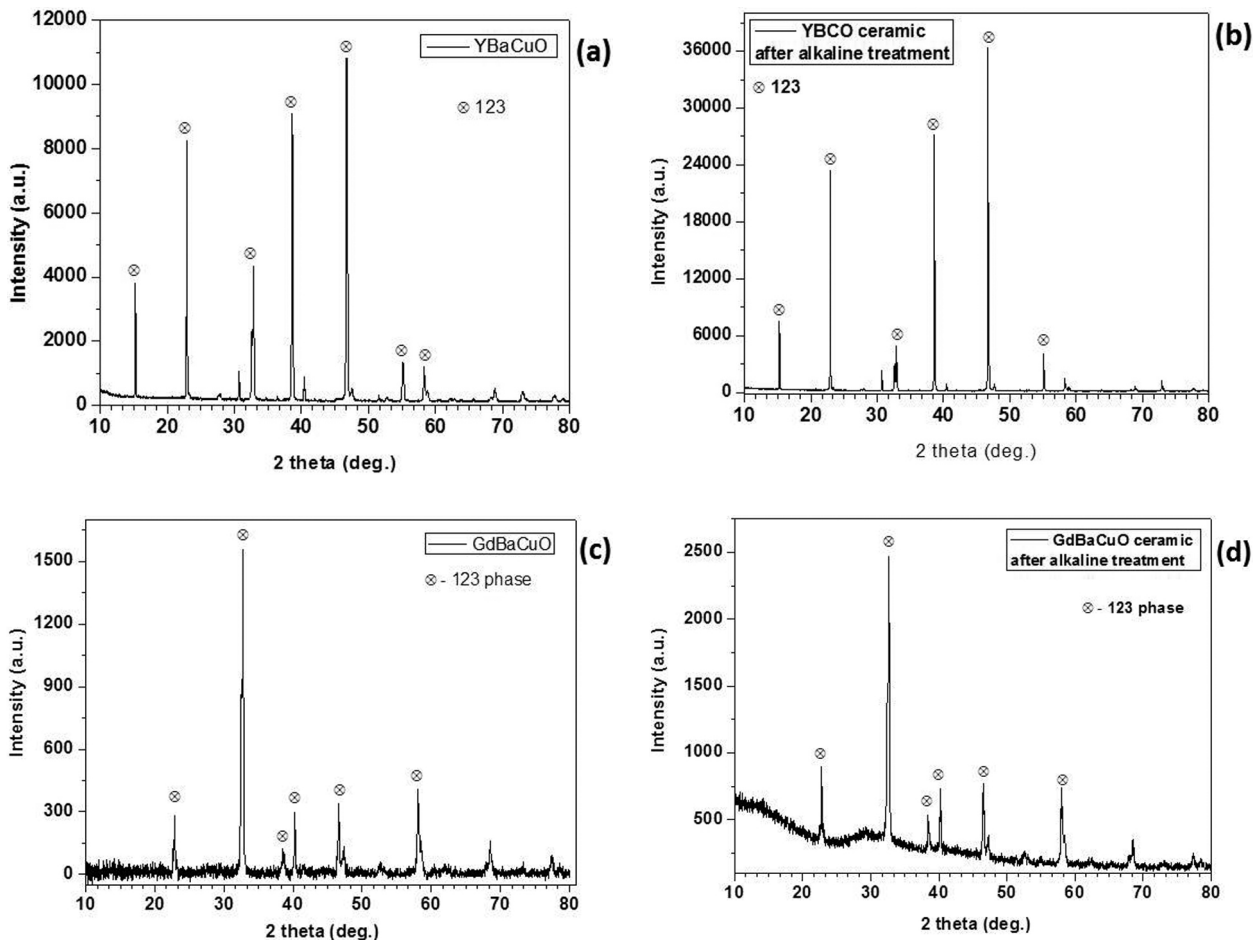


Fig. 1. Powder X-ray diffraction patterns of YBCO and GdBCO ceramic samples before (a, b) and after (c, d) alkaline treatment

Table 1. Values of oxygen coefficients “ δ ” and “ y ” as determined by spectrophotometry.

Sample	oxygen coefficient δ^*	oxygen coefficient $y = 6.5 + \delta$
YBCO	0.450	6.950
YBCO* (alkaline treatment)	0.498	6.998
GdBCO	0.376	6.876
GdBCO* (alkaline treatment)	0.387	6.887

*Each result is a mean value of at least three parallel determinations. The confidence interval with $P=0.95$ for each sample is ± 0.004 .

a specific shape. In contrast, despite that the synthesis regime was the same for both powders, the polycrystalline GdBCO sample exhibited larger grains than the YBCO sample. After the alkaline treatment

of the ceramics, no significant changes of the bulk morphology were observed, as seen in Fig. 2.

Figure 3 shows the surface of the YBCO sample after the alkaline treatment. It is seen that this sample endured well the alkaline treatment and only small spots on the surface were changed. On the contrary, the SEM micrographs of GdBCO sample show a modified surface morphology as a result of interaction with the KOH solution. It should be mentioned that the surface changes observed concerned only a thin surface layer of the sample, while preserving the sample volume unchanged. This observation is confirmed well by the EDX results of both samples, as summarized in Table 2 and Table 3 for the YBCO and GdBCO ceramics, respectively.

The results in Table 2 indicated that YBCO samples remained stable after alkaline treatment and the stoichiometry of superconducting phase was unchanged. Only traces of potassium, originating from the solution, were detected on the sample surface.

The results of the EDX analyses of the GdBCO samples showed generally that the Gd-

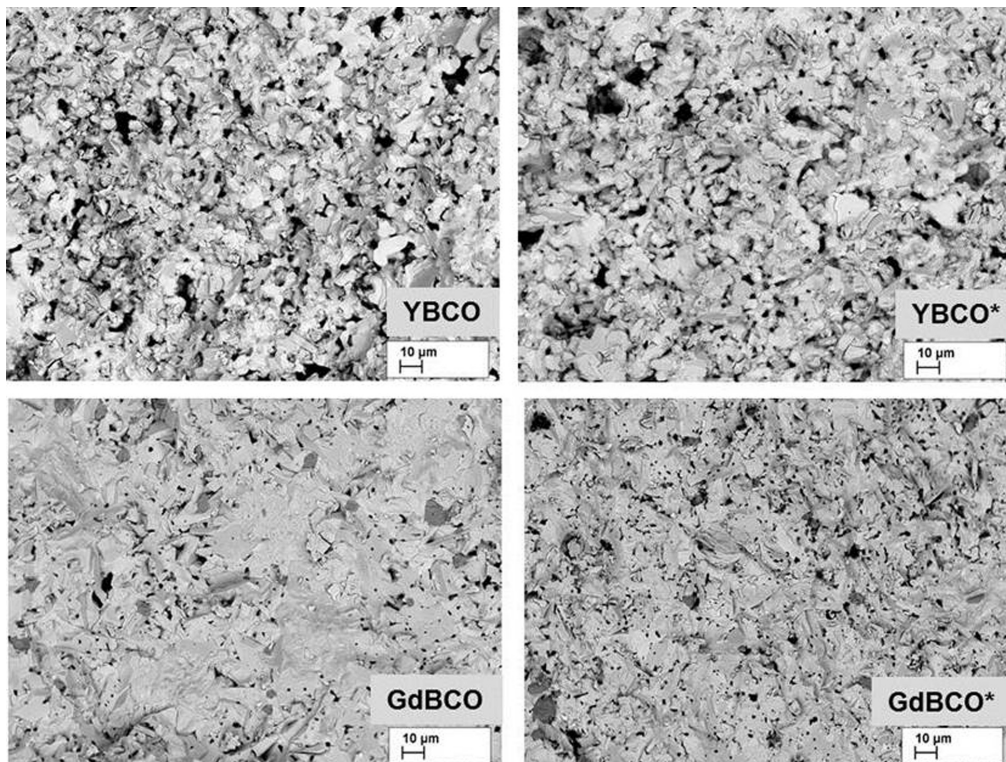


Fig. 2. SEM micrographs of YBCO and GdBCO ceramics before and after (*) alkaline treatment

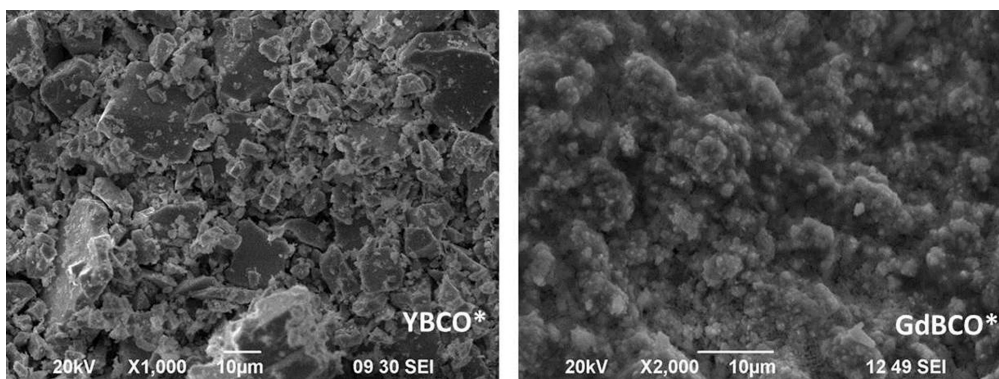


Fig. 3. SEM micrographs of YBCO and GdBCO ceramics surfaces after alkaline treatment

superconducting phase was not as stable in a highly alkaline medium as the Y-containing superconducting ceramics. The slight change of the stoichiometry observed indicated a reaction with the KOH solution and, as a result of such a reaction, parts of the barium and copper contents of the sample were lost. The changes in the chemical composition of the Gd-ceramics probably affected some physical properties of this material, as can be seen below.

The superconducting properties of the ceramics samples were studied using the AC susceptibil-

ity method. The YBCO samples (as sintered and treated in the alkaline solution) were typical superconductors with a critical temperatures $T_c = 91.3$ K. The transition behavior of the treated sample almost overlapped the original sintered one, as is seen in Fig. 4a. The complete hysteresis loop (magnetization vs. applied magnetic field – $M(H)$) was typical for superconductors without any essential difference between the treated and untreated samples (Fig. 4b). The critical fields determined were $H_1 = 0.25$ T and $H_2 > 9$ T.

Table 2. EDX results for elements content of the samples before and after (*) alkaline treatment for YBCO.

	Y at. %	Ba at. %	Cu at. %	O at. %	K at. %
Before alkaline treatment EDX (integral) YBCO	7.21	12.39	21.02	59.38	0
After alkaline treatment EDX (integral) YBCO*	7.18	12.67	20.90	59.12	0.13

Table 3. EDX results for elements content of the samples before and after (*) alkaline treatment for GdBCO

	Gd at. %	Ba at. %	Cu at. %	O at. %	K at. %
Before alkaline treatment EDX (integral) GdBCO	6.45	15.22	22.09	56.24	0
After alkaline treatment EDX (integral) GdBCO*	6.73	14.67	20.54	58.06	0

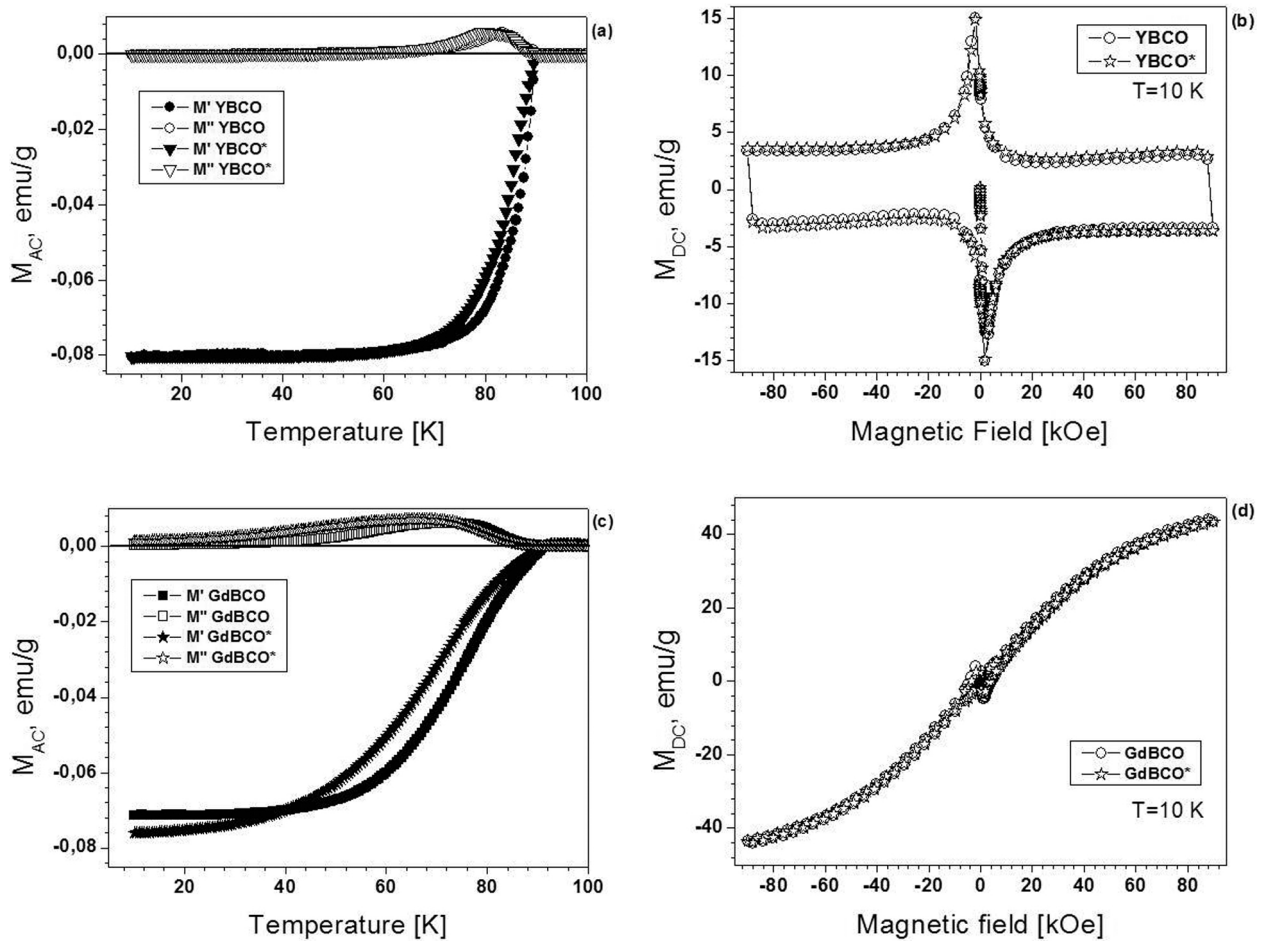


Fig. 4. The real (in-phase) and imaginary (out-of-phase) parts of the complex magnetization (ACM) vs. temperature for YBCO (a) and GdBCO (c). The hysteresis loop (magnetization vs. applied magnetic field – $M(H)$) for YBCO (b) and GdBCO (d)

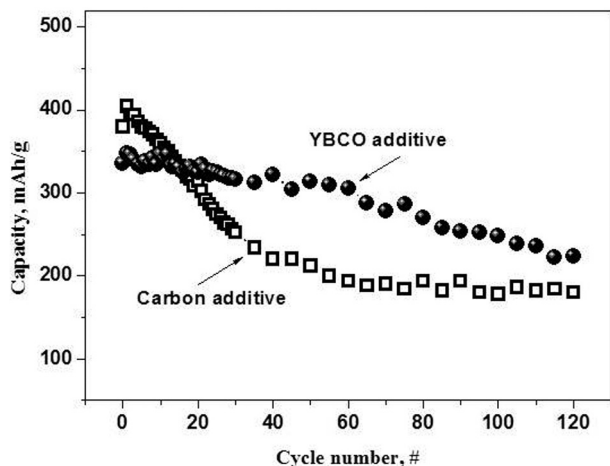


Fig. 5. Dependence discharge capacity – number of the cycles for nickel-zinc cells with zinc electrode paste containing $\text{YBa}_2\text{Cu}_3\text{O}_{7-x}$ superconducting ceramics and zinc electrode paste with carbon additive

The magnetic behavior of the sintered and alkaline-treated GdBCO samples followed the curve loops characteristic for systems with a considerable magnetic moment [15, 16]. In the case of the critical temperature measurements, some difference were observed, which could be related to a non-constant stoichiometry and the appearance of a Gd excess in the alkaline-treated sample. On the other hand, the critical parameters determined for the GdBCO ceramics were not affected significantly – only a slight decrease of the critical temperature of the alkaline treated GdBCO sample was measured as compared to the untreated one ($T_c = 91.5$ K for the untreated, and 91 K for the alkaline-treated sample).

Figure 5 presents typical plots of the specific discharge capacity vs. the number of cycles of the electrochemical cells with the zinc electrode paste containing carbon or $\text{YBa}_2\text{Cu}_3\text{O}_{7-x}$ superconducting ceramics as a conducting additive during the cycling test. Comparing the capacity of the cell with a zinc electrode containing superconducting ceramics with that of the cell with a zinc electrode containing a carbon additive leads to the conclusion that adding superconducting ceramics to the electrode mass maintains the cell capacity to higher values after an extended cycling.

The discharge capacity of the cell with a zinc electrode containing carbon as a conducting additive is lower (up to 30%) than the capacity of the cell with a zinc electrode containing $\text{YBa}_2\text{Cu}_3\text{O}_{7-x}$ superconducting ceramics. To summarize, the results of the electrochemical investigation showed that the nickel-zinc cell with superconducting ceramics in the zinc electrode mass exhibited gener-

ally good cyclic operation ability and a performance stability. In our opinion, the superconducting ceramic powder forms a highly-conducting network between the particles of the zinc electrode mass thus improving the electrochemical contact in the power generation material.

CONCLUSIONS

The stability of YBCO and GdBCO superconducting ceramics was investigated by analyzing polycrystalline samples before and after exposure to an alkaline solution that is normally used as a basic electrolyte in the alkaline batteries. The high chemical resistance of the ceramics to the alkaline medium was confirmed by structural observations and magnetic measurements. The study revealed that the YBCO samples are remarkably stable, while the GdBCO ceramics showed only a slight decrease of the critical temperature T_c , thus leaving the superconducting properties of the 123-type phase unchanged after the alkaline treatment.

The possibility was also studied of using the superconducting YBCO ceramics as a conducting additive to the zinc electrode mass of nickel-zinc alkaline rechargeable batteries. The electrochemical tests showed that the battery cells with an YBCO superconducting ceramic additive in the zinc electrode exhibited a good cyclic operation ability and a capacity stability, as well as a higher (by about 30%) specific capacity than the cells with zinc electrode with a “classic” carbon conducting additive to the zinc electrode mass.

The electrochemical characteristics of the experimental nickel-zinc battery cells obtained suggest that adding superconducting ceramics to the electrode mass improves the retention of the cell capacity to higher values after prolonged cycling and thus may contribute to extending the battery life.

Acknowledgments: The research was conducted within a scholarship project funded by the World Federation of Scientists. The work was a part of an inter-academic collaboration project between the Bulgarian Academy of Sciences and the Institute of Low Temperature and Structure Research, Polish Academy of Sciences, and of the Erasmus Mobility Teaching Program.

REFERENCES

1. Narlikar, A.V; High Temperature Superconductivity 2 – Engineering Applications, Application fields of high-temperature superconductors, Roland Hott, Springer, Berlin, 35 (2004).

2. S. Nishijima, S. Eckroad, A. Marian, K. Choi, W. Seok Kim, M. Terai, Z. Deng, J. Zheng, J. Wang, K. Umemoto, J. Du, P. Febvre, S. Keenan, O. Mukhanov, L. D. Cooley, C. P. Foley, W. V. Hassenzahl, M. Izumi, *Supercond. Sci. Technol.*, **26**, 113001 (2013).
3. J. Dominec, L. Smrčka, P. Vašek, S. Geurten, O. Smrčková, and D. Sýkorová, *Sol. State Commun.*, **65**, 373 (1988).
4. P. Vašek, P. Svoboda, O. Smrčková, and D. Sýkorová, *Sol. State Commun.*, **71**, 403 (1989).
5. O. Smrčková, D. Sýkorová, P. Svoboda, P. Vašek, *Collect. Czech. Chem. Commun.*, **58**, 1548 (1993).
6. J. M. Rosamilia, B. Miller, L.F. Schneemeyer, J.V. Waszczak and H. M. O'Bryan, Jr., *J. Electrochem. Soc.*, **134**, 1863(1987).
7. J. T. McDevitt et al., *J. Electroanal. Chem.*, **243**, 465(1988).
8. M. Bachtler, W. J. Lorentz, W. Schindler and G. Saemann-Ischenko, *Mod. Phys. Lett. B* **2**, 6, 819 (1988).
9. H. Huang, L. Zhang, W. K. Zhang, Y. Gan, H. Shao, *Journal of Power Sources*, **184**, 663 (2008).
10. TOPAS V4: General profile and structure analysis software for powder diffraction data, *User's Manual*, Bruker AXS, Karlsruhe, Germany Bruker AXS (2008).
11. S. I. Georgieva, T. K. Nedeltcheva, L. K. Vladimirova, A. K. Stoyanova-Ivanova, *CEJC*, **11**(3), 381 (2013).
12. D. C. Harris, T. A. Hewson, *J. Solid State Chem.*, **69**, 182 (1987).
13. M. Karppinen, L. Niinisto, *Supercond. Sci. Technol.*, **4**, 334 (1991).
14. T. Nedelcheva, St. Georgieva, L. Vladimirova, A. Stoyanova-Ivanova, *Talanta*, **77**, 1745 (2009).
15. Hong Zhang, Guang Li, Tao-fei Zhou, Yong Liu, Xiao-guang Li, Yu Chen, *Chinese Journal of Chemical Physics.*, **20**, 324 (2007).
16. C. H. Cheng, Chang Chun Hsieh, Chuan Ke, H. Zhang, C. C. Sorrell, *Journal of Modern Transportation*, **19**, 104 (2011).

ПРИЛОЖЕНИЕ НА ВИСОКОТЕМПЕРАТУРНИ СВРЪХПРОВОДИМИ КУПРАТИ КАТО ДОБАВКА КЪМ ОТРИЦАТЕЛНИЯ ЕЛЕКТРОД В Ni-Zn БАТЕРИИ

А. К. Стоянова-Иванова^{1*}, С. Д. Терзиева¹, Г. Д. Иванова², М. А. Младенов², Д. Г. Ковачева³, Р. Г. Райчев², С. И. Георгиева⁴, Б. С. Благоев⁵, А. J. Zaleski⁶, V. Mikli⁷

¹ *Институт по Физика на Твърдото Тяло „Акад. Георги Наджаков“, Българска Академия на Науките, бул. Цариградско шосе 72, 1784 София, България*

² *Институт по Електрохимия и Енергийни Системи – Българска Академия на Науките, ул. „Акад. Георги Бончев“, бл.10, 1113 София, България*

³ *Институт по Обща и Неорганична Химия – Българска Академия на Науките, ул. „Акад. Георги Бончев“, бл. 11, 1113 София, България*

⁴ *Химикотехнологичен и Металургичен Университет, бул. „Кл. Охридски“ 8, 1756 София, България*

⁵ *Институт по Електроника – Българска Академия на Науките, бул. „Цариградско шосе“ 72, 1784 София, България*

⁶ *Институт по ниски температури и структурни изследвания, Полска Академия на Науките, ул. Околна 2, 50-422 Вроцлав, Полша*

⁷ *Център за изследване на материали към Талински Технологичен Университет – Талин, Ehitajate 5, 19086 Талин, Естония*

Постъпила декември, 2014 г.; приета януари, 2015 г.

(Резюме)

Химическата устойчивост на $YBCO(Y_1Ba_2Cu_3O_{7-x})$ и $GdBCO(Gd_1Ba_2Cu_3O_{7-x})$ поликристални свръхпроводими керамики в алкална среда е изследвана преди и след третиране в 7М КОН разтвор, който обикновено се използва като електролит в алкалните батерии. Високата химическа устойчивост на керамиката в алкална среда е потвърдена от структурни изследвания и магнитни измервания. Керамика от вида $YBCO$ е използвана като добавка към активната маса на цинков електрод на никел-цинкова алкална батерия. Електрохимичните изследвания са проведени в специално конструирана електрохимична клетка тип „копче“ с разглюбеми цинков и никелов електрод. Установено е, че батерийна клетка с добавка от $YBCO$ свръхпроводима керамика подобрява стабилността на капацитета при циклиране (с около 40%) спрямо батерийна клетка с въглеродна добавка. Получените резултати дават възможност за приложение на свръхпроводими керамики като добавка към електродния материал на цинковия електрод за алкални батерии.

Analysis of elemental composition of a heat activated, multi-force, nickel titanium orthodontic archwire

V. I. Petrunov^{1*}, L. S. Andreeva¹, S. I. Karatodorov², V. I. Mihailov², S. D. Terzieva²,
I. Ilievska², A. K. Stoyanova-Ivanova², V. G. Tumbalev³, V. Mikli⁴

¹ Faculty of Dental Medicine, Medical University Sofia, 1 St. St. Georgi Sofijski Blvd., 1431 Sofia, Bulgaria

² Georgi Nadjakov Institute of Solid State Physics, Bulgarian Academy of Sciences,
72 Tzarigradsko Chaussee Blvd., 1784 Sofia, Bulgaria

³ Institute of General and Inorganic Chemistry, Bulgarian Academy of Sciences,
“Acad. Georgi Bonchev” str. bld.11, 1113 Sofia, Bulgaria

⁴ Centre for Materials Research, Tallinn University of Technology, Ehitajate 5, Tallinn 19086, Estonia

Received December, 2014; Revised January, 2015

The heat activated, multi-force, nickel-titanium archwire have three distinct force regions. This archwire places the correct force to the appropriate region (anterior, bicuspid and posterior) of the arch to quickly torque, level and align, without sacrificing patient comfort. In this work, analysis of such archwire (cross section 0.41×0.56 mm.) with variable longitudinal elasticity is done. The elemental composition is obtained by different wire's regions with 5 mm separation by Laser-Induced Breakdown Spectroscopy (LIBS) and two other independent methods such as X-ray diffraction analysis (XRD) and Energy Dispersive X-ray method (EDX). The large area of application of LIBS is due to its ability to perform microprobe elemental analysis of wide variety of samples with no preliminary sample preparation. Pulsed Nd:YAG laser (λ 1,064 μm , pulse duration 8 ns) is focused on the sample surface, causing ablation and formation of laser-induced plasma plume. Collecting and processing the plasma emission gives us information of the sample elemental composition. The obtained results of unused wire provide useful knowledge needs for further investigations on the wire changes during the treatment.

Key words: thermo activated orthodontic archwire, XRD, SEM-EDX, elemental composition.

INTRODUCTION

Orthodontic arch wires are one of the main and most important components of the treatment with fixed appliances. They have evolved tremendously due to the major advances in materials science and metallurgy. During the different phases of treatment arch wires with specific qualities are used, which explains the vast choice of alloys and sizes. Arch wires are required to preserve their chemical and physical characteristics [1]. In the early phases of treatment, during teeth levelling, the most important characteristics of the selected wire are its elasticity and the amount of force, generated after the initial deflection. At first stainless steel arch wires were used, but because of their small elastic range [2, 3] they delivered very high forces. Soon they were

replaced by Ni-Ti archwires [4, 5] and superelastic Ni-Ti archwires [6, 7]. These wires deliver an almost constant force, regardless of the initial bending of the wire [8, 9]. The next step in the development of the aligning archwires was the heat activated wires. As a function of temperature these wires alter their austenitic structure to martensite and vice versa and thus the amount of force can be regulated [10, 11].

When an archwire with uniform qualities is deflected it generates an equal amount of force along its whole length although it acts on teeth with different root surface. This has led to one of the latest inventions in orthodontic material science – the invention of thermodynamic wires that deliver differential forces. The characteristics of these wires allow the ratio of delivered force/surface area to be almost equal for all teeth. This allows a shortening of the aligning phase of the treatment. Despite their improved elastic properties, it is interesting to analyze their chemical composition and structure in the different areas of elasticity.

* To whom all correspondence should be sent:
E-mail: e-mail: dr.petrunov@mail.bg

The aim of this work is to analyze the composition and structure of a heat-activated wire with differential force delivery.

MATERIAL AND METHODS

In this work, analysis of heat activated nickel-titanium orthodontic archwire (cross section 0.41×0.56 mm) with variable longitudinal elasticity is done. The archwire has 3 regions of elasticity – anterior (A), bicuspid (B) and posterior segment (C). According to the manufacturer the ratio of the delivered force in the three segments is approximately 1:1,5:2.

The studied wires were analyzed by X-ray powder diffraction method, scanning electron microscopy (SEM), X-ray dispersive analysis (EDX). The technique of Laser-Induced Breakdown Spectroscopy (LIBS), also was used as an independent method for elemental composition obtained by different wire’s regions with 5 mm separation.

Powder X-ray diffraction patterns were collected within the range from 5.3 to $80^\circ 2\theta$ with a constant step $0.02^\circ 2\theta$ on Bruker D8 Advance diffractometer with $\text{CuK}\alpha$ radiation and LynxEye position sensitive detector. Phase identification was performed by the program DiffracPlus EVA using ICDD PDF-2 (2009) database. The microstructure of the wires surface was studied by means of Zeiss EVO MA-15 scanning electron microscope (SEM) with LaB_6 cathode on the polished cross-section samples. The chemical composition was determined by the X-ray microanalysis using the energy dispersive spectroscopy (EDS) method and Oxford Instruments INCA Energy system. The qualitative and quantitative

analyses were carried out at an accelerating voltage 20 kV, an optimal condition for these samples.

In this work, we perform LIBS analysis on the studied orthodontic archwire for verifying the elemental composition obtained by XRD analysis. Laser-induced breakdown spectroscopy (LIBS) is widely applied for elemental composition determination because it can perform fast, preparation-free, microprobe analysis of solid samples [12, 13]. In LIBS technique, powerful pulsed laser is focused on the sample surface, causing ablation and formation of laser-induced plasma plume. Collecting and processing the plasma emission gives us information of the sample elemental composition. LIBS is capable of qualitative and in some conditions of quantitative analysis. The setup we use consists of pulsed Nd:YAG Quanta Ray GCR3 laser ($\lambda 1,064 \mu\text{m}$, pulse duration 8 ns), focused with a 15 cm lens on the archwire surface. The emission is collected with optical fiber (50 μm core) coupled to Mechelle 5000 spectrograph equipped with iStar DH734 iCCD camera which is controlled by PC. Each spectrum is accumulated from 30 laser pulses and registered in 300–800 nm spectral region. Under these experimental conditions the spectra of the pure Ti and pure Ni samples also are measured.

EXPERIMENTAL RESULTS AND DISCUSSION

The results obtained by XRD X-ray diffraction analysis (XRD analysis done at room temperature) show peaks typical for cubic austenite-type phase, Fig. 1. The position of the peaks of samples taken from different part of the archwire does not show

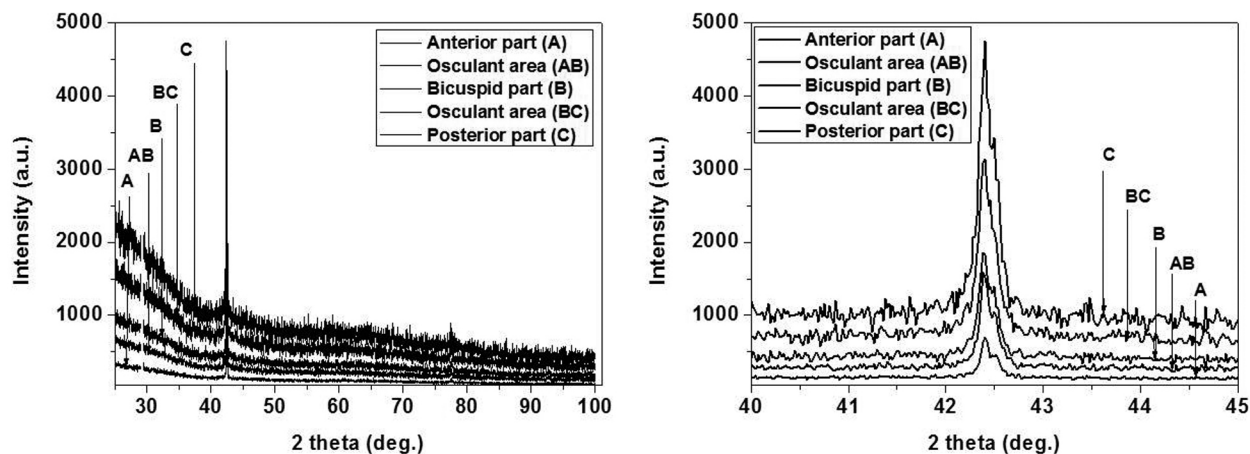


Fig. 1. XRD patterns of the main regions of orthodontic Variable Force 3 Archwire

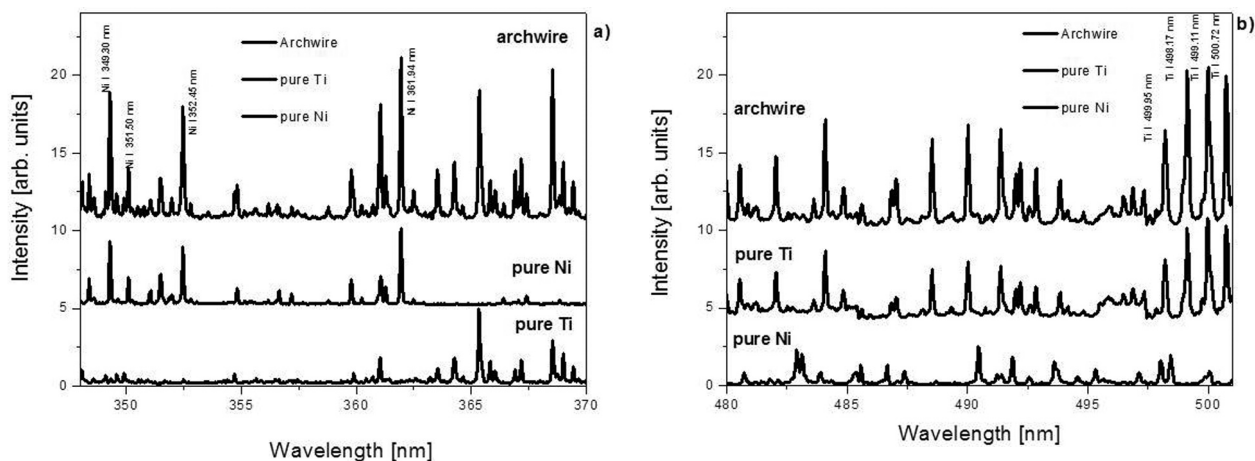


Fig. 2. Laser-induced plasma emission spectra from orthodontic archwire, pure Ti and pure Ni samples

differences of unit cell parameters which lead us to the conclusion that the phase composition of arc is constant all along the wire.

The measured orthodontic archwire spectrum by LIBS is plotted against the spectra of pure Ti and pure Ni. In Fig. 2a is shown part of the spectra (348–370 nm) in which analytical Ni I lines (361.94 nm, 352.45 nm, 351.50 nm and 349.30 nm) [14, 15] are present. Similarly, Fig. 2b displays portion of the spectra (480–501 nm) with analytical Ti I lines (500.72 nm, 499.95 nm, 499.11 nm, 498.17 nm) [14, 15]. It is seen in the figures that the analytical lines of both pure elements are clearly observable in the spectrum of the orthodontic archwire. This verifies that only Ni and Ti are present in the elemental composition of the archwire.

The presented scanning microscopically pictures (Fig. 3) are of main areas of the wires’ surface, where a point element analysis is made as well.

Table 1. Elements content of selected points of orthodontic archwire

Spectrum №	1	2	3	4
Elements				
Titanium, Ti (wt.%)	63.24	64.20	46.37	46.35
Nickel, Ni (wt.%)	36.76	35.80	53.63	53.65
Total, %	100	100	100	100

Wire is not coated with any layer and the average values of the element composition is approximately Ti 46.28 wt.% and Ni 53.72 wt.%. The surface microstructure is identical for all different parts of wires, which were confirmed by (Energy Dispersive X-Ray method (EDX), Table 1.

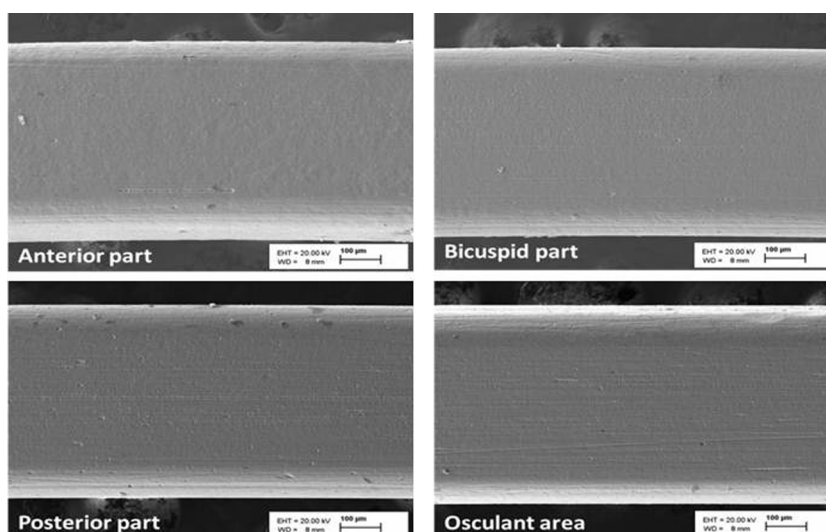


Fig. 3. Scanning electron microscopy images of the main regions surface of orthodontic archwire

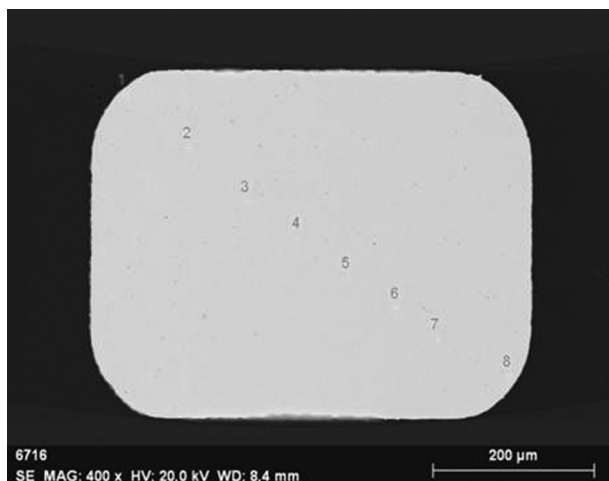


Fig. 4. Scanning electron microscopy image of the cross-section of Posterior part of orthodontic archwire

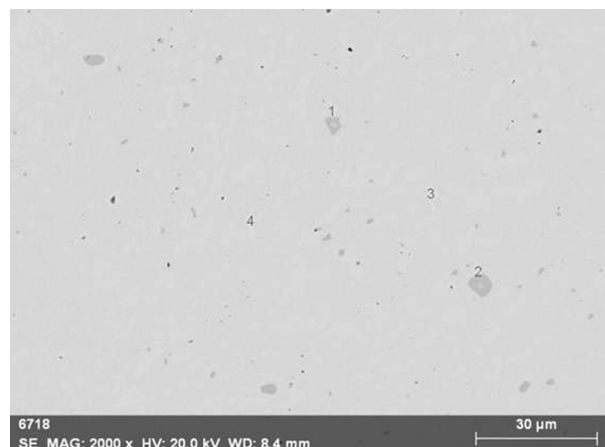


Fig. 5. SEM image on the surface of orthodontic archwire

Table 2. Elements content of investigated points of orthodontic archwire

Spectrum №	1	2	3	4	5	6	7	8
Elements								
Titanium, Ti (wt. %)	46.44	46.48	46.57	46.04	46.65	46.69	46.05	46.50
Nickel, Ni (wt. %)	53.66	53.52	53.43	53.96	53.35	53.31	53.95	53.50
Total, %	100	100	100	100	100	100	100	100

The analyzed cross-section of the end part (Posterior part) wire by Energy Dispersive X-Ray method (EDX) shows good homogeneity of the proportion of elements (Fig. 4, Table 2). There are small inclusions (2–5 μm) inside the compound, which composition is similar to Ti₂Ni (Fig. 5, Table 2), which could be result of producing process (exp. different annealing process).

CONCLUSION

From the carried out tests it is established that there are no significant changes in the chemical composition of the surface of the thermally activated wires with variable longitudinal elasticity. The obtained results of unused wire provide useful knowledge needs for further investigations on the mechanical properties of the wire as well as for structure changes during the treatment period.

REFERENCES

1. V. Petrov et al., *Bulgarian Chemical Communications*, **4**, 455 (2013).
2. W. A. Brantley, in: *Orthodontic Materials: Scientific and Clinical Aspects*. W. A. Brantley, T. Eliades (eds), Thieme, Stuttgart, 2001, p. 77.
3. R. P. Kusy, G. J. Dilley, J. Q. Whitley, *Clin Mater.*, **33**, 41 (1988).
4. G. F. Andreasen, T. B. Hilleman, *JADA*, **82**, 1373 (1971).
5. G. F. Andreasen, P. R. Brady, *Angle Orthod.*, **42**, 172 (1972).
6. Y. Oshida, R. C. L. Sachdeva, S. Miyazaki, *Bio-Medical Materials and Engineering*, **2**, 51 (1992).
7. K. Otsubo, *J. Jpn. Orthod. Soc.*, **53**, 641 (1994).
8. S. E. Khier, W. A. Brantley, R. A. Fournelle, *Am. J. Orthod. Dentofacial Orthop.*, **99**, 310 (1991).
9. F. Miura et al., *Am. J. Orthod. Dentofac. Orthop.*, **90**, 1 (1986).
10. G. Airoldi, G. Bellini, C. Di Francesco, *J. Physics F: Metal Physics*, **14**, 1983 (1984).

11. T. W. Duerig, R. Zadno, Engineering aspects of shape memory alloys, Butterworth-Heinemann, London, 1990, p. 369.
12. D. W. Hahn, N. Omenetto, *Appl. Spectr.*, **64**, 335 A (2010).
13. D. W. Hahn, N. Omenetto, *Appl. Spectr.*, **66**, 347 (2012).
14. А. Н. Зайдель, В. К. Прокофьев, С. М. Райский, В. А. Славнин, Е. Я. Шрейдер, Таблицы спектральных линий, изд. Наука, Москва, 1977, (in Russian).
15. A. Kramida, Yu. Ralchenko, J. Reader and NIST ASD Team, NIST Atomic Spectra Database (version 5.2), <http://physics.nist.gov/asd>, 2014.

ИЗСЛЕДВАНЕ НА ТЕРМОАКТИВИРАЩА НИКЕЛ-ТИТАНОВА ОРТОДОНТСКА ДЪГА С ДИФЕРЕНЦИРАНО ОСВОБОЖДАВАНЕ НА СИЛА

В. Г. Петрунов^{1*}, Л. С. Андреева¹, С. И. Каратодоров², В. И. Михайлов²,
С. Д. Терзиева², И. Илиева², А. К. Стоянова-Иванова²,
В. Г. Тумбалев³, В. Микли⁴

¹ Факултет по Дентална Медицина, Медицински Университет – София,
бул. „Св. Св. Георги Софийски“ 1, 1431 София, България

² Институт по физика на твърдото тяло „Акад. Георги Наджакон“, Българска Академия на Науките,
бул. „Цариградско шосе“ 72, 1784 София, България

³ Институт по обща и неорганична химия, Българска Академия на Науките,
ул. „Акад. Георги Бончев“, бл. 11, 1113 София, България

⁴ Център за изследване на материали към Талински Технологичен Университет – Талин,
Ehitajate 5, 19086 Талин, Естония

Постъпила декември, 2014 г.; приета януари, 2015 г.

(Резюме)

Термоактивиращата никел-титанова дъга е с диференцирано освобождаване на сила в три различни зони. Дъгата освобождава подходяща сила в различните сегменти (фронтален, премоларен и дистален) на зъбната дъга, което позволява бърза изява на торка, вертикално и хоризонтално нивелиране, без да се нарушава комфорта на пациента. В настоящото изследване е анализирана такава дъга с променлива по дължината си еластичност и сечение $0,41 \times 0,56$ mm. Проследен е елементният състав в различните участъци на дъгата през интервал от 5 mm с помощта на Laser-Induced Breakdown Spectroscopy (LIBS) и два други независими метода като X-ray diffraction analysis (XRD) and Energy Dispersive X-ray method (EDX). Широката област на приложение на LIBS се дължи на възможността му да извършва елементен анализ на микропроби в широк спектър на образци без предварителната им подготовка. Импулс от Nd:YAG laser (λ 1,064 μ m, импулс с продължителност 8 ns) се фокусира върху повърхността на образеца, предизвиквайки аблация и образуване на лазерно-индуциран облак. Улавянето и обработката на плазмените емисии дават информация за елементния състав на образеца. Получените резултати от анализа на неизползвана дъга са необходими като основа за бъдещи изследвания на промените в дъгите при използването им в лечебния процес.

Influence of the treatment period on the morphology and the chemical composition of the thermally activated orthodontic archwires

V. G. Petrov¹, S. D. Terzieva^{2*}, V. G. Tumbalev³, V. Mikli⁴, L. S. Andreeva¹,
A. K. Stoyanova-Ivanova²

¹ Faculty of Dental Medicine, Medical University Sofia, 1 St. St. Georgi Sofijski Blvd., 1431 Sofia, Bulgaria

² Georgi Nadjakov Institute of Solid State Physics, Bulgarian Academy of Sciences,
72 Tzarigradsko Chaussee Blvd., 1784 Sofia, Bulgaria

³ Institute of General and Inorganic Chemistry, Bulgarian Academy of Sciences,
„Acad. Georgi Bonchev“ str. bld. 11, 1113 Sofia, Bulgaria

⁴ Centre for Materials Research, Tallinn University of Technology, Ehitajate 5,
Tallinn 19086, Estonia

Received December, 2014; Revised January, 2015

The thermally activated nickel-titanium archwires are widely employed in orthodontics because they present shape memory effect and super elasticity. The addition of copper to nickel-titanium alloy enhances the thermal properties of the wire while maintaining precise control of forces, comparing to “pure” nickel-titanium alloy. The purpose of this study is to investigate the chemical composition of the surface of thermally activated copper-nickel-titanium archwires with different cross sections (round – 0.33 mm and rectangular – 0.41 × 0.56 mm). For the purpose of comparison, the origin wires (unused and sterilized ones) are also investigated as a control group. All studied orthodontic wires have transition temperature range at 35 °C. The analyses are carried out by three independent methods as X-ray diffraction analysis (XRD), Scanning Electronic Microscope (SEM) and by an Energy Dispersive X-Ray method (EDX).

The obtained results show that the processes of sterilizations of the investigated orthodontic archwires have no adverse effects on their properties. From the carried out tests it is established that there are no significant changes in the chemical composition of the surface of the thermally activated wires after treatment period up to 6 and after 8 weeks. This period covers the average time of residence of the orthodontic wires in the mouth of the patient.

Key words: thermally activated orthodontic wires, XRD, SEM-EDX, surface influence.

INTRODUCTION

The copper-nickel-titanium shape-memory alloys are applied in many areas, due to their unique thermal and mechanical properties [1]. One of the successful applications of the archwires made from these alloys is in orthodontics because of their characteristics, such as low hardness, flexibility, large stored energy, biocompatibility, the thermoelastic shape-memory effects and super-elasticity [2]. The orthodontic shape-memory archwires are also called martensite active, because they can be deformed in the martensitic phase, but when exposed in the oral cavity they are transformed into austenite, allowing the arch to regain its original shape [3].

During the initial placing of the orthodontic arch into the slot of the bracket it bends according to the dental arch when passing into austenitic phase orthodontic the orthodontic archwire is able to “remember” its pre-established form [4, 5]. Thus the orthodontic arch begins to influence and to move the teeth in the direction where they take the correct position, set by the shape of the arch. When lowering the temperature, the alloy is converted into martensite and becomes flexible and easily deformable.

Thermally activated arches were created in 1994 by Ormco Corporation. They are provided to the orthodontists in three temperature options: 27 °C, 40 °C and 35 °C, corresponding to the upper austenitic temperatures that finalize the transformation from martensite to austenite [6]. The element's analysis carried out by EDX shows that the variants of the three thermally activated archwires have similar composition of approximately 44 wt.% nickel, 51 wt.% titanium, small quantities of copper

* To whom all correspondence should be sent:
E-mail: e-mail: mirolina@abv.bg

– 5 wt.%, and according [7] 0.2 wt.% to 0.3 wt.% chromium instead of titanium quantity. Kusy [8] reports that these arches contain at least 5–6% weight percentage of copper and 0.2% to 0.5% weight percentage of chromium. The archwire with transition of 27 °C contains 0.5% weight percentage of chromium in order to balance the influence of copper on the increase of the transition temperature over this in the mouth, and the 40 °C variant contains 0.2 wt.% chromium.

Regardless of the type of the alloys from which the arches are made, they are subject to the ongoing mouth chemical and electrochemical reactions resulting in degradation of the existing and formation of new chemical compounds. The conditions in the oral cavity are very aggressive, causing corrosion of metal alloys. All these factors suggest a rapid aging of the metal orthodontic materials, affecting the morphology, structure and their mechanical properties.

The objective of the present study is to trace the influence of the residence period in the patient’s mouth on the morphology and chemical composition of the copper-nickel-titanium orthodontic arches with two different profiles (round – 0.33 mm and rectangular – 0.41 × 0.56 mm). The results are compared with those obtained for unused (factory) and autoclaved unused archwires in order to establish the changes occurring in their properties after a prolonged stay in the oral cavity.

MATERIAL AND METHODOLOGY

The present study is on the selected orthodontic archwires with two different cross sections used for the treatment that stayed in the patient’s mouth, respectively up to 6 and after 8 weeks. This period covers the average time of residence of the orthodontic wires in the mouth of the patient in order to perform a certain stage of orthodontic treatment. The type D0 wires are with round cross section 0.33 mm,

and the second D1 have a rectangular cross section – 0.41 × 0.56 mm, Table 1. Two wires are used of each type, and are compared with the corresponding starting wires, called as-received.

The studied wires were analyzed by X-ray powder diffraction (XRD), X-ray dispersive analysis (EDX) and scanning electron microscopy (SEM). Powder X-ray diffraction patterns were collected within the range from 5.3 to 80° 2θ with a constant step 0.02° 2θ on Bruker D8 Advance diffractometer with CuKα radiation and LynxEye position sensitive detector. Phase identification was performed by the program DiffracPlus EVA using ICDD-PDF-2 (2009) database. The microstructure of the wires surface was studied by means of Zeiss EVO MA-15 scanning electron microscope (SEM) with LaB₆ cathode on the polished cross-section samples. The chemical composition was determined by the X-ray microanalysis using the energy dispersive spectroscopy (EDS) method and Oxford Instruments INCA Energy system. The qualitative and quantitative analyzes were carried out at an accelerating voltage 20 kV, an optimal condition for these samples.

RESULTS AND DISCUSSION

For the purpose of comparison, the origin wires (control group) were also analysed before and after avtoclave sterilization process. The specific requirements for the prevention and control of the healthcare associated infections require every orthodontist not to allow contaminated orthodontic archwires to be placed in the patient’s mouth. Most of the leading companies offer their products in individual sealed packages suitable for autoclaving. The autoclaving was carried out in an autoclave type B at 121 °C for 21 min.

After the analysis done by XRD Scanning Electronic Microscope and by an Energy Dispersive X-Ray method (EDX) it is established that there are no significant changes in the chemical composition

Table 1. Characteristics of investigated cooper –nickel –titanium orthodontic wires

Type of orthodontic wires	Cross section [mm]	Time of residence in the mouth
D0 – round thermal activated cooper-nickel-titanium	0.33	D0_as-received
		D0_6 – up to 6 weeks
		D0_8 – after 8 weeks
D1 – rectangular thermal activated cooper-nickel-titanium	0.41 × 0.56	D1_as-received
		D1_6 – up to 6 weeks
		B1_8 – after 8 weeks

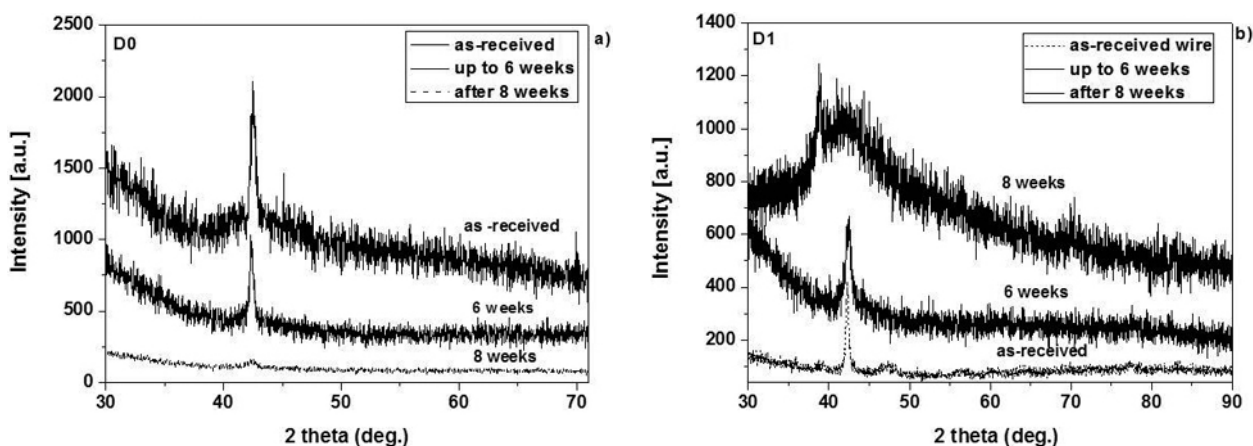


Fig. 1. a) XRD patterns of the orthodontic archwires type D0 at different stages of treatment; **b)** XRD patterns of the orthodontic archwires type D1 at different stages of treatment

of the surface of the autoclaved wires. There are also no changes in the surface characteristics of the archwires made of the investigated alloys. The obtained results show that the processes of autoclaving of the investigated orthodontic archwires have no adverse effects on their properties [9].

Thermally active orthodontic archwires have shape-memory property and are called martensite active. They can be deformed in their martensitic phase, as when increasing the temperature in the mouth a phase transformation to the austenitic phase is induced, and the corresponding restoring of the arch's to the original. The copper-containing thermally activating archwires have constant and weak forces when activating and deactivating in comparison with Ni-Ti arches. Adding copper to the nickel-titanium alloy is effective to stabilize the thermal transformation and to narrow the temperature hysteresis between the formation of the austenite during heating and martensite during cooling. Furthermore, the copper affects the mechanical properties of nickel-titanium alloy. Powder diffraction patterns obtained at room temperature for the

two profiles of arches studied (round or rectangular) show peaks typical for cubic austenite phase (Fig. 1a and Fig. 1b). With the gradual increase of the residence's period in the mouth, it is noticed the formation of amorphous "humps" in the diffraction patterns of both wire profiles which probably is a result of two occurring phenomena: first – an increase in defectiveness of the structure (micro-deformations and strains) as a result of deformation effects and second increase in defectiveness of the structure due to the corrosive processes starting from the surface of the material as a result of the chemical interaction with environment during treatment. The latter is more visible in bends of rectangular section (SEM Fig. 3).

The information about the change in the surface morphology of the orthodontic wires is obtained by scanning electron microscopy (SEM), Fig. 2. The presented scanning microscopical pictures are of unused wire and after treatment period up to 6 and after 8 weeks correspondingly.

The results indicate that the wire's surface does not change for the examined period of treatment. On

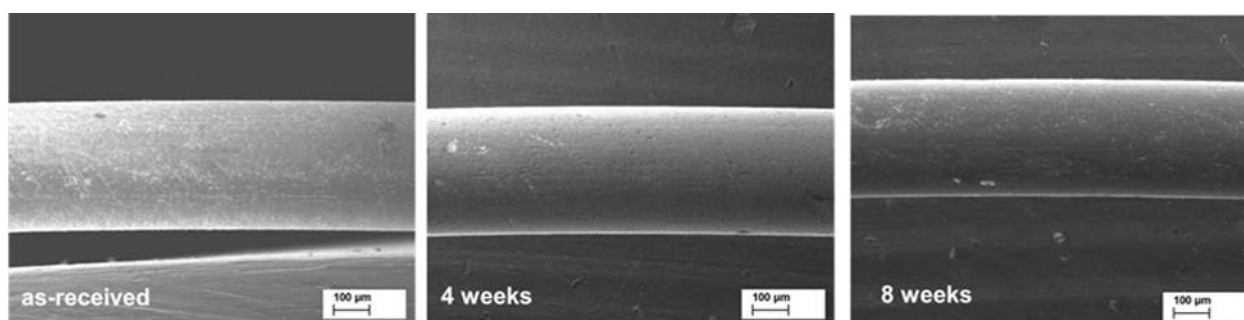


Fig. 2. Scanning electron microscopy images of copper –nickel –titanium with round cross-section 0.33 mm

Table 2. Elements content of investigated D0-cooper–nickel–titanium orthodontic wires with round cross-section 0.33 mm

Round thermal activated cooper-nickel-titanium (0.33 mm)	Elements, weight %			
	Cu	Ni	Ti	Cr
Industrial data (information)	6.5	50	43	0.50
<i>D0_as-received</i>	5.51	48.75	45.18	0.23
D0_6 – up to 6 weeks	5.49	48.60	45.66	0.25
D0_8 – after 8 weeks	5.47	48.58	45.67	0.28

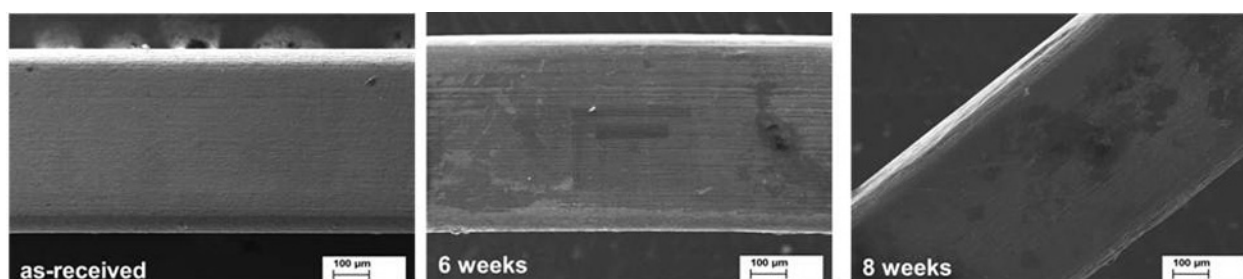


Fig. 3. Scanning electron microscopy images of cooper–nickel–titanium with cross section 0.41×0.56 mm

the wires’ surface that has stayed in for 8 weeks surface irregularities are observed, which we assume to appear as a result of mechanical deformation effects. Additionally, the surface of the archwires was studied in details by means of energy dispersion technique (EDX).

The method used allows quantitative identification of the chemical composition by elements and focuses on the corrosion changes of the alloy rather than commenting on the complex oral flora. The average values of the element composition are shown in Table 2. The period of residence in the mouth has no significant effect on the proportion of elements in the tested orthodontic wires.

The obtained results of the second type studied orthodontic wires (rectangular cross-section) show similar behaviour. As a result of the carried out analyses by SEM was established that small changes have occurred in the structure on the surface of the rectangular wires after treatment process, Fig. 3. The determined chemical composition by EDX analysis is presented in Table 3.

The analysis confirms the presents only of the main components composition. The observed changes of the surface of the material could be as a result of the chemical environment during treatment. It is difficult to trace and investigate the corrosion according to the treatment’s time stage and

Table 3. Elements content of investigated cooper–nickel–titanium orthodontic wires with cross section 0.41×0.56 mm

Rectangular thermal activated cooper-nickel-titanium (0.41×0.56 mm)	Elements, weight %			
	Cu	Ni	Ti	Cr
Industrial data (information)	6.5	50	43	0.50
<i>D1_as-received</i>	5.47	48.29	45.58	0.31
D1_6 – up to 6 weeks	5.41	48.55	46.05	–
D1_8 – after 8 weeks	5.75	48.11	45.82	0.27

the wires' residence in the mouth due to the individuality of each patient (type of food, hygiene, age, gender, etc.).

CONCLUSION

Thermally active orthodontic archwires have shape-memory property and are called martensite active. Regardless of the type of the alloys from which the arches are made, they are subject to the ongoing mouth chemical and electrochemical reactions resulting in degradation of the existing and formation of new chemical compounds. From the carried out tests it is established that there are no significant changes in the chemical composition of the surface of the thermally activated wires (both – round and rectangular cross section) after treatment period up to 6 and after 8 weeks. The period covers the average time of residence of the orthodontic wires in-the patient's mouth.

REFERENCES

1. F. Miura, M. Mogi, Y. Okamoto, *J. Clin. Orthod.*, **242**, 544 (1990).
2. S. M. Seyyed Aghamiri, M. N. Ahmadabadi, Sh. Raygan, *Journal of the mechanical behavior of bio-medical materials*, **4**, 298 (2010).
3. C. L. Hurst, M. G. Duncanson, R. S. Nanda, P. V. Angolkar, *Am. J. Orthod. Dentofacial Orthop.*, **98**, 72 (1990).
4. M. C. Biermann, D. W. Berzins, T. G. Bradley, *Angle Orthod* **77**, 499–503 (2007).
5. W. A. Brantley, M. Iijima, T. H. Grentzer, *Thermochim. Acta*, **37**, 329 (2002).
6. M. Santoro, O. F. Nicolay, T. I. Cangialosi, *Am. J. Orthod. Dentofacial Orthop.*, **119**, 587 (2001).
7. W. A. Brantley, W. Guo, W. A. Clark, Iijima M., *Dent. Mater.*, **24**, 204 (2008).
8. R. P. Kusy, *Angle Orthod.*, **67**, 197 (1997).
9. V. Petrov, S. Terzieva, L. Andreeva, V. Mikli, A. Stoyanova-Ivanova, *Book of Abstracts of the 19th Congress of Balkan Stomatological Society – BaSS*, Belgrade, Serbia, 443 (2014).

ВЛИЯНИЕ НА ВРЕМЕТО НА ПРЕСТОЙ В УСТАТА НА ПАЦИЕНТА ВЪРХУ МОРФОЛОГИЯТА И ХИМИЧНИЯ СЪСТАВ НА МЕД-НИКЕЛ-ТИТАНОВИТЕ ОРТОДОНТСКИ ДЪГИ

В. Г. Петров^{1*}, С. Д. Терзиева², В. Г. Тумбалев³, В. Микли⁴, Л. С. Андреева¹,
А. К. Стоянова-Иванова²

¹ Факултет по дентална медицина, Медицински Университет – София, Бул. „Св.Св. Георги Софийски“ 1,
1431 София, България, vpetrov@dentist.bg

² Институт по физика на твърдото тяло „Акад. Георги Наджакон“, Българска Академия на Науките,
Бул. „Цариградско шосе“ 72, 1784 София, България, mirolina@abv.bg; aksi_bg@abv.bg

³ Институт по обща и неорганична химия, Българска Академия на Науките,
ул. „Акад. Георги Бончев“, бл. 11, 1113 София, България

⁴ Център за изследване на материали към Талински Технологичен Университет – Талин,
Ehitajate 5, 19086 Талин, Естония

Постъпила декември, 2014 г.; приета януари, 2015 г.

(Резюме)

Топлоактивиращите никел-титанови дъги са широко използвани в ортодонтията заради свойството памет на формата, което притежават и голямата им еластичност. Добавянето на мед към никел-титановата сплав подобрява температурните трансформации в дъгата и поддържа по-постоянни и по-слаби връзки при активиране и деактивиране в сравнение с дъгите от „чиста“ никел-титанова сплав. Целта на настоящата работа е да изследва химичният състав по повърхността на топлоактивиращи мед-никел-титанови ортодонтски дъги с две различни сечения (кръгли – 0,33 mm и правоъгълни 0,41 × 0,56 mm) използвани за лечение. Получените резултати са сравнени с изследвания направени и на неизползвани и неизползвани автоклавиращи дъги, споменати като контролна група. Всички изследвани топлоактивиращи дъги се характеризират с температура на преход 35 °С. За проведените анализи са използвани три независими метода: Рентгеноструктурен анализ (XRD), Сканиращ електронен микроскоп (SEM) и Енергийно-дисперсионен анализ (EDX).

Резултатите показват, че процесите на стерилизация не променят свойствата на дъгите. От проведените структурни изследвания е установено, че основният химичен състав на топлоактивиращите дъги не се променя в периода на лечение от до 6 и над 8 седмици.

Comparative study of the phase formation and interaction with water of calcium-silicate cements with dental applications

Y. I. Kouzmanova¹, I. V. Dimitrova¹, G. D. Gentsheva², L. I. Aleksandrov²,
M. G. Markova-Velichkova², D. G. Kovacheva^{2*}

¹ Medical University-Sofia, Faculty of Dentistry, Department of Conservative dentistry,
1 George Sofiiski Str., Sofia, Bulgaria

² Institute of General and Inorganic Chemistry, Bulgarian Academy of Sciences,
Acad. G. Bontchev Str. Bl. 11, 1113 Sofia, Bulgaria

Received December, 2014; Revised January, 2015

Mineral trioxide aggregate (MTA) is based on plain Portland cement and is composed of tricalcium silicate, dicalcium silicate, tricalcium aluminate, and tetracalcium aluminoferrite. This cement is used for various dental clinical applications. The degree of solubility of calcium-silicate based cements is an object of debate among investigators. The present study was designed to compare the phase formation and evolution, as well as solubility of five different commercial calcium-silicate cements. X-ray diffraction (XRD) analysis was applied to determine the phase composition of the initial powder mix, cement compositions, and cement compositions evolution after aging the material in distilled water. Thermal analyses (TG-DTA) were also performed to confirm the XRD results. The concentrations of Ca, Na, Mg, Al, K, Fe, Ti, Bi, Ta and Zr ions passed into the solution were determined by means of ICP-MS and FAAS. The changes of elemental and phase composition were discussed.

Biodentine seems an alternative to MTA. It releases significant amounts of Ca ions and therefore stimulates tissue mineralization. The concentration of radiopaque elements in the soaking water is at trace levels in all materials studied, which makes them safe for dental applications. The obtained good results do not cancel regular safety checks.

Key words: calcium-silicate cements, dental application, phase evolution, solubility.

INTRODUCTION

Calcium-silicate cements were first introduced to dentistry in 1993 by Torabinejad and co-workers [1]. Based on plain Portland cement they are composed of tricalcium silicate, dicalcium silicate, tricalcium aluminate, and tetracalcium aluminoferrite. Bismuth oxide is added as a radiopaque for clinical applications since mineral trioxide aggregate (MTA) is used as endodontic material and should be more radiopaque than its surrounding structures. According to Parirokh and Torabinejad [2] the addition of bismuth oxide affects the hydration mechanism of MTA. It must be insoluble to avoid leakage and should be as hard as possible to avoid dislodgement from the dentine wall [3]. The main requirement to this group of materials is hermetic sealing. The hermetic mechanism comes as a complex result

of several factors – marginal adaptation, adhesion, solubility and volume changes [4].

During the last years many producers developed production of calcium silicate- based cements for dental applications. Despite similar constituents, due to the variations of manufacturing processes the purity of their constituents and hydration products their behavior can be different.

The degree of solubility of calcium-silicate based cements is an object of debate among investigators. Most authors reported low solubility or solubility has not been observed, however increased solubility was reported in a long-term study. According to Frindland et al [5] calcium as hydroxide was the main chemical compound released by MTA in water. Bodanezi et al [6] reported that, in an aqueous environment MTA is more soluble than Portland cement. Calcium silicate materials *MTA Plus gel* and *MTA Angelus* showed the highest values of porosity, water sorption and solubility, according to Gandolfi [7]. Based on the findings of Saghiri and Asgar [8] storage temperature appears to play an important

* To whom all correspondence should be sent:
E-mail: e-mail: didka@svr.igic.bas.bg

role in the properties and hence clinical outcomes of MTA. According to Gandolfi [9] solubility of *MTA Plus* is higher than that of *ProRoot MTA*. Grech [10] reported that *Biodentine* demonstrates a high wash-out, low fluid uptake and sorption values, low setting time and superior mechanical properties.

Regarding the solubility test of Vivan [11], the white *MTA-Angelus* and *MTA-Bio* cements had higher solubility than Portland cement. It is important to explain that the solubility testing standards recommend immersion of the materials only after complete setting, which is impossible to be achieved in a clinical situation, where the materials are immediately in contact with fluids and blood. Therefore, solubility values are probably even higher under clinical conditions.

The aim of the present study is to compare the phase formation and evolution as well as solubility of five different commercial calcium-silicate cements after aging the material in distilled water.

EXPERIMENTAL

Samples notation

The following cements were chosen for the study:

Sample I – white *ProRoot MTA* (*Dentsply, Tulsa, Johnson City, TN*)

Sample II – gray *MTA-Angelus* (*Angelus, Londrina, Brazil*)

Sample III – white *MTA-Angelus* (*Angelus, Londrina, Brazil*)

Sample IV – *BioAggregate* (*Innovative Bioceramix, Vancouver, Canada*)

Sample V – *Biodentine* (*Septodont, Saint-Maur-des-Fossés, France*)

Samples preparation

MTA ProRoot, *MTA-Angelus* и *BioAggregate* were mixed according to the manufacturer's instructions on a glass slab with cement spatula to produce homogeneous paste, the mixture exhibited putty like consistency after about 30 s mixing time. The cements were prepared according to the manufacturer's recommendations in the proportion of 1 g of powder to 0.21 mL of distilled water. Powder and liquid of *Biodentine* are mixed for 30 s in a capsule in a high-speed amalgamator (*Amalga Mix 2, Gnatus, Brazil*) at 4000–4200 rpm. The test materials were placed into a cylindrical polyethylene tube (12 mm in diameter and 2 mm in height). All cements were placed on a tissue soaked with saline gauze and kept at 100% relative humidity for 24 h. After that the samples were left in open air for 48 hours and placed in desiccators till obtaining constant weight.

After drying (to constant weight) the samples were placed in a 30 ml polypropylene containers and 20 ml of de-ionized water (pH=6.3) were added. The samples were kept for 28 days at room temperature (22 ± 1 °C), after which the samples were filtered and the filtrate was used for element content determination.

Analyses

Powder X-ray diffraction (XRD) analysis was applied to determine the phase composition of the initial powder mix, cement compositions, and cement compositions evolution after aging the material in distilled water. The XRD patterns were collected within the range from 5 to 80° 2 θ with a constant step 0.02° 2 θ on Bruker D8 Advance diffractometer with Cu K α radiation and LynxEye detector. Phase identification was performed with the *DiffraPlus* EVA using ICDD-PDF2 Database.

Thermal analyses (TG-DTA) were also performed to confirm the XRD results. Thermal analyses were carried out using the computerized combined thermal analysis apparatus LABSYSEvo, SETARAM Company (France) at atmospheric pressure in a flow of synthetic air (MESSER CHIMCO GAS – OOH 1056, ADR 2, 1A) in the temperature range 25–1000 °C with heating rate 10 °C min⁻¹. Corundum crucibles with a volume of 100 μ l were used.

Inductively coupled plasma-mass spectrometer “X SERIES 2” – Thermo Scientific with 3 channel peristaltic pump, concentric nebulizer, Peltier-cooled spray chamber (4 °C), Xt interface option, Ni cones and forward plasma power of 1400 W was used for the determination of Ca, Na, Mg, Al, K, Fe, Ti, Bi, Ta and Zr.

Thermo SOLAAR M5 Flame Atomic Absorption spectrometer with deuterium background correction was used for the determination of Ca, Na, Mg and K.

Multi-element standard solution V for ICP (Fluka, Sigma-Aldrich); 1000 mg L⁻¹ Ti (Fluka, Sigma-Aldrich); 1000 mg L⁻¹ Ta (Fluka, Sigma-Aldrich) and 1000 mg L⁻¹ Zr (Fluka, Sigma-Aldrich) were used for the preparation of diluted working standard solutions for calibration for ICP-MS measurements. Stock standard solutions of Ca, Na, Mg and K (1.000 g L⁻¹ (Merck)) were used for the preparation of diluted working standards for calibration for flame AAS.

RESULTS AND DISCUSSION

The powder XRD patterns of five cements, currently used in dental practice are shown in Figure 1. Each figure represents initial dry mixture of calcium

silicates, the cement after hydrolysis, prepared according to the manufacturer instruction and the same cement soaked for 28 days in distilled water. The initial composition (Fig. 1, a) contains phases typical for Portland cements, such as tricalcium silicate

(C_3S) – main phase, usually within 50–70% mass of the composition, dicalcium silicate (C_2S), calcium carbonate, traces of calcium hydroxide (portlandite), apatite and, depending on the manufacturer, bismuth oxide (Samples I, II and III), tantalum ox-

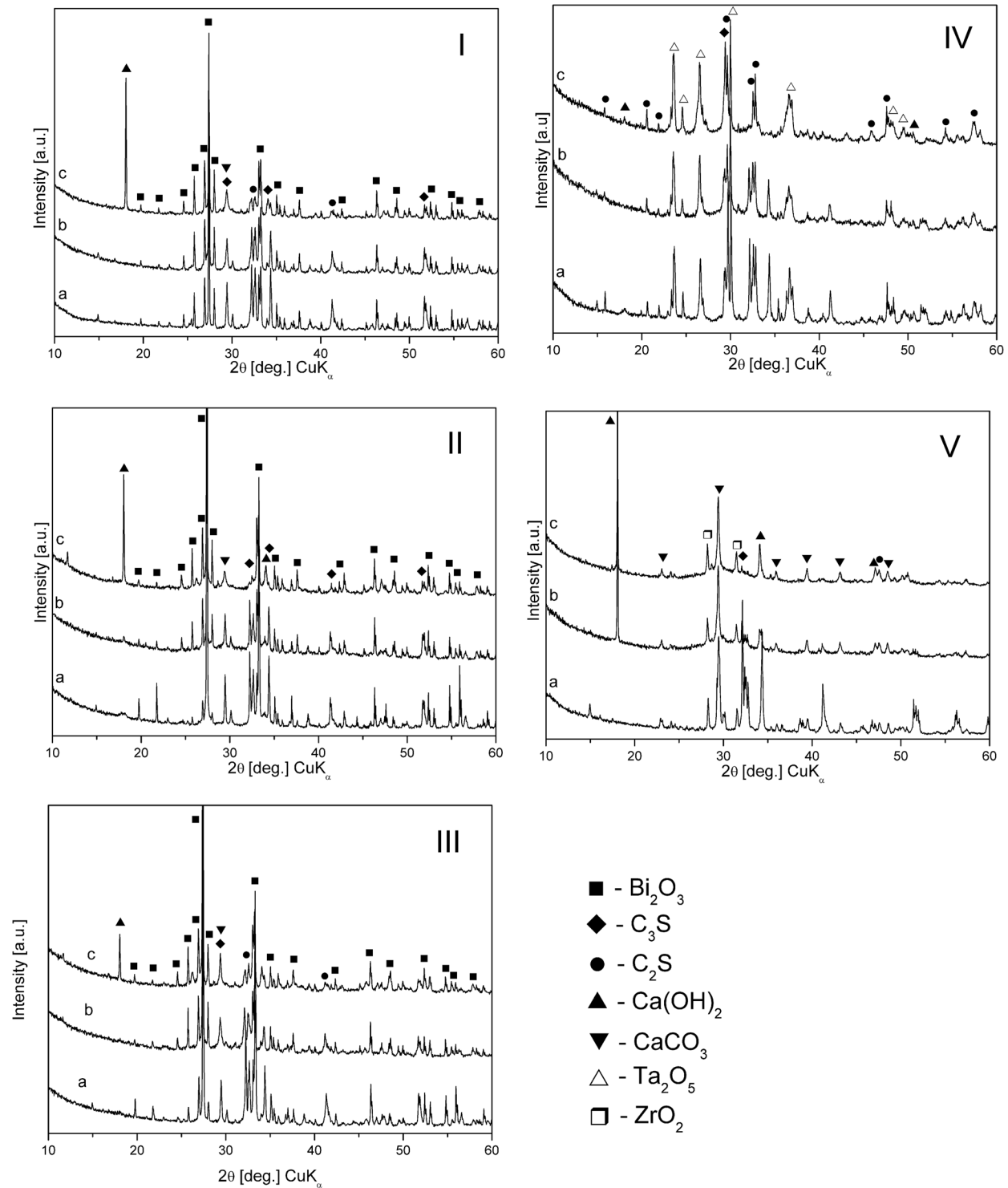


Fig. 1. Powder XRD patterns of the initial dry mixture (a), the cements after setting (b) and the cements after soaking for 28 days in distilled water (c). The different samples are denoted as: I – *ProRooth*, II – *Angelus gray*, III – *Angelus white*, IV – *Bio Aggregate*, V – *Biodentine*

ide (Sample IV) or zirconium oxide (Sample V) as a radiopaquer. The setting reaction i.e. the hydration process of the initial dry cement mixture results in increasing the mass% of the radiopaquer in the crystalline part due to the formation of amorphous calcium silicate hydrates. Increased amount of portlandite is also observed. It should be mentioned that the hydration is not complete for all samples. For some of them part of initial non-hydrated calcium silicates can be detected (Fig. 1, b). According to

the literature amorphous calcium silicate hydrates are formed on the surface of non-hydrated calcium silicates, thus providing a matrix for colloidal-type material. The matrix binds the non-hydrated calcium silicate particles. Calcium portlandite usually remains in the pores of the cement matrix [12, 13]. The soaking process for 28 days results in increased amount of portlandite for all samples with the exception of sample IV (Fig. 1, c). What is interesting is that for the hydrated and soaked samples the

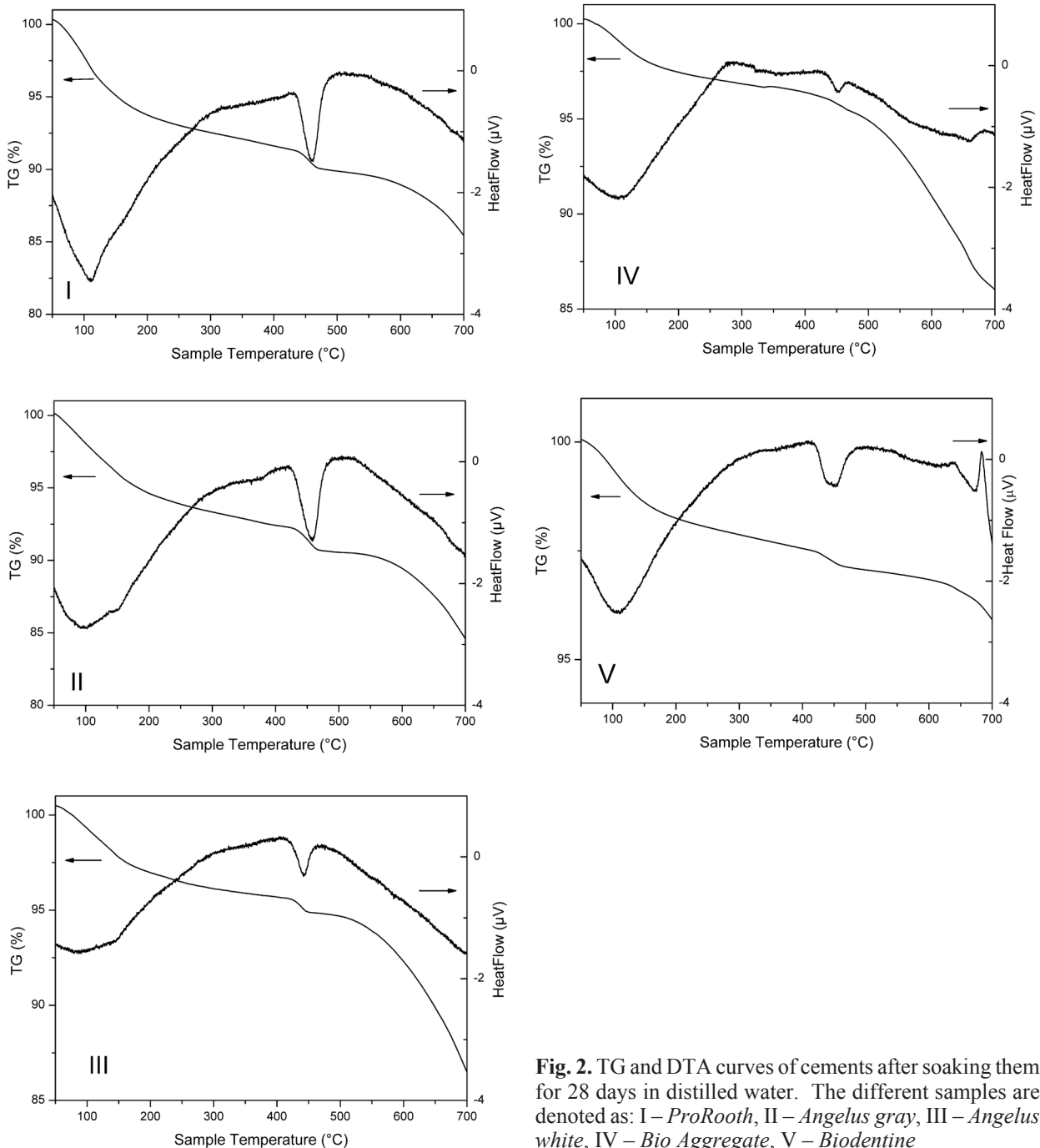


Fig. 2. TG and DTA curves of cements after soaking them for 28 days in distilled water. The different samples are denoted as: I – *ProRoot*, II – *Angelus gray*, III – *Angelus white*, IV – *Bio Aggregate*, V – *Biodentine*

Table 1. Weight loss calculated from TG curves for different temperature regions for cements after soaking for 28 days in distilled water

Sample	Weight loss below 200 °C (%)	Weight loss at 450 °C (%)
I	7.65	1.6
II	8.16	1.8
III	2.81	0.83
IV	3.02	0.85
V	9.24	1.93

amount of calcium carbonate remains almost constant, indicating that this constituent of the cements is independent of treatment.

An important feature of calcium silicate-based cements is the ability to release ions, mainly calcium ions within the tooth tissue, which facilitates the dentin–restoration process. It is assumed that ion release depends on several factors such as the nature of the compositional and matrix structure related to water sorption and solubility as well as the porosity of the material, which is related to water diffusion. To investigate this type of properties thermal analyses were performed. The TG-DTA curves of the samples are presented on Fig 2. All samples show well defined weight loss below 200 °C, which is related to the amount of the adsorbed water. For all samples, an endothermic peak situated at about 450 °C is also observed accompanied by a mass loss. This peak is associated with the decomposition of portlandite presented in the samples. Table 1 represents the values of mass loss for these two cases.

The elements determined by chemical analyses of the soaking liquid were those announced by the manufacturers (Table 2). Analysis of the soaking liquid after 28 days showed that Mg, Al, Ti, Fe, Bi, Zr, and Ta concentrations are at trace levels i.e. less than 1×10^{-5} g. It should be mentioned that oxides used as radiopaquer (Bi_2O_3 , Ta_2O_5 and ZrO_2) do not dissolve in distilled water under the conditions described above. A certain part of the Na ions in the samples comes from the manipulation during sample preparation. In this case the content of dissolution of sodium could not be commented.

The main importance of the analyses is the calcium ions behavior during cement setting and soaking, since it is a key factor for successful endodontic and pulp capping therapies because of the action of calcium on the mineralizing cells. Gandolfi at all [14] in recent study determined the concentration of Ca ions released from *ProRoot MTA* and *Biodentine* cements within 28-day soaking in distilled water. Our results are in good agreement with the results obtained by them. *Biodentine* (Sample V) showed a markedly higher release of free calcium ions than all other cements. This may be due to the fact that calcium is presented not only in the cement powder, but it is also contained in the liquid provided by manufacturer of this cement in a form of CaCl_2 solution.

CONCLUSION

Biodentine seems an alternative to MTA. It releases significant amounts of Ca ions and therefore stimulates tissue mineralization. The concentration of radiopaquer elements in the soaking water is at trace levels in all materials studied, which makes them safe for dental applications. The obtained good results do not cancel regular safety checks.

Table 2. Contents of Na, Mg, Al, K, Ca, Ti, Fe, Bi, Zr and Ta in the solution obtained after 28 days soaking of the samples in distilled water

Elements	Sample I	Sample II	Sample III	Sample IV	Sample V
Na, $\mu\text{g g}^{-1}$	418±20	422±20	756±30		
Mg, $\mu\text{g g}^{-1}$	0.35±0.1	0.20±0.1	0.17±0.1	0.46±0.1	0.20±0.1
Al, $\mu\text{g g}^{-1}$	14.2±0.3	5.91±0.3	15.6±0.3		
K, $\mu\text{g g}^{-1}$		1575±50			
Ca, $\mu\text{g g}^{-1}$	2815±80	10300±440	25.0±1.0	955±30	22830±590
Ti, $\mu\text{g g}^{-1}$	<0.01	<0.01			
Fe, $\mu\text{g g}^{-1}$	<1.0	<1.0	<1.0		<1.0
Bi, $\mu\text{g g}^{-1}$	0.45±0.03	0.55±0.06	0.10±0.01		
Zr, $\mu\text{g g}^{-1}$					<0.01
Ta, $\mu\text{g g}^{-1}$				<0.01	

REFERENCES

1. S. J. Lee, M. Monsef, M. Torabinejad, *J. Endod.*, **19**, 541 (1993).
2. M. Parirokh., M. Torabinejad. *J. Endod.*, **36**, 16 (2010).
3. G. Danesh, T. Dammaschke, H. U. V. Gerth, T. Zandbiglari, E. Schafer, *International Endodontic Journal*, **39**, 213 (2006).
4. M. Torabinejad, C.U. Hong, F. McDonald, T.R. Pitt Ford, *J. Endod.*, **21**, 349, 1995a.
5. M. Fridland, R. Rosado, *J. Endod.*, **29**, 814 (2003).
6. A. Bodanezi, N. Carvalho, D. Silva, N. Bernardineli, C.M. Bramante, R.B. Garcia, I. G. de Moraes, *J. Appl Oral Sci.*, **16**, 127 (2008).
7. M.G. Gandolfi, F. Siboni, T. Botero, M. Bossù, F. Riccitiello, C. Prati, *J. Appl Biomater Funct Mater.* 2014, doi: 10.5301/jabfm.5000201 [Epub ahead of print].
8. M. A. Saghiri, K. Asgar, M. Lotfi, A. Nazari, K. Karamifar, P. Neelakantan, J. L. Gutmann, *Acta Odontologica Scandinavica*, **70**, 536 (2012).
9. M. Gandolfi, F. Siboni, C. M. Primus, C. Prati. *J. Endod.*, **40**, 1632 (2014).
10. L. Grech, B. Mallia, J. Camilleri, *Dental Materials*, **29**, e20 (2013).
11. R. R. Vivan, R. O. Zapata, M. A. Zeferino, C. M. Bramante, N. Bernardineli, R. B. Garcia, M. A. Hungaro Duarte, M. Tanomaru Filho, I. Gomes de Moraes. *Oral Surg. Oral Med. Oral Pathol. Oral Radiol. Endod.*, **110**, 250 (2010).
12. H. F. W. Taylor, *Cement chemistry*, Thomas Telford Ltd., London, 1997.
13. Kjellsen K, H. Justnes, *Cement and Concrete Composites*, **26**, 947 (2004).
14. M. G. Gandolfi, F. Siboni, A. Polimeni, M. Bossù, F. Riccitiello, S. Rengo, C. Prati, *Dent. J.*, **1**, 41 (2013).

СРАВНИТЕЛНО ИЗСЛЕДВАНЕ НА ФАЗООБРАЗУВАНЕТО И ВЗАИМОДЕЙСТВИЕТО С ВОДА НА КАЛЦИЕВО-СИЛИКАТНИ ЦИМЕНТИ С ПРИЛОЖЕНИЕ В ДЕНТАЛНАТА МЕДИЦИНА

Я. И. Кузманова¹, И. В. Димитрова¹, Г. Д. Генчева², Л. И. Александров²,
М. Г. Маркова-Величкова², Д. Г. Ковачева^{2*}

¹ Медицински университет-София, Стоматологичен факултет, катедра Консервативно зъболечение, ул. „Георги Софийски“ 1, гр. София, България

² Институт по обща и неорганична химия, Българска академия на науките, ул. „Акад. Г. Бончев“, Бл. 11, 1113 София, България

Постъпила декември, 2014 г.; приета януари, 2015 г.

(Резюме)

Минералният триоксид агрегат (МТА) е базиран на стандартния Портланд цимент и е съставен от трикалциев силикат, дикалциев силикат, трикалциев алуминат и тетракалциев алумоферит. Като контрастен материал за денталната рентгенография към цимента се добавя бисмутов оксид. Степента на разтворимост на калциево-силикатните дентални цименти е обект на дискусия между изследователите. Настоящата работа изследва фазообразуването и еволюцията на фазите, както и разтворимостта на пет различни търговски калциево-силикатни цименти. Рентгенодифракционният анализ (XRD) е използван за определяне на първоначалния фазов състав на изходната смес, състава на пригответените цименти, и развитието на фазите в циментовите състави след престой на материала в дестилирана вода. Извършени бяха и термични анализи (TG-DTA) чиито резултати корелират добре с резултатите от рентгеновата дифракция. Концентрациите на Ca, Na, Mg, Al, K, Fe, Ti, Bi, Ta и Zr йони преминали в разтвора са определени с помощта на ICP-MS и FAAS. Обсъдени са промените на елементния и фазовия състави на денталните цименти при стареене във водна среда. Установено е, че материалът Biodentine е алтернатива за МТА, защото отдава значително количество Ca йони като по този начин стимулира тъканната минерализация. Концентрацията на контрастните елементи за денталната рентгенография в разтвора е под формата на следи във всички изследвани материали, което ги прави безопасни за стоматологични приложения. Получените добри резултати не анулират редовни проверки за безопасност.

Influence of Y-ion substitution on structural and electrochemical characteristics of $\text{YCo}_{0.5}\text{Fe}_{0.5}\text{O}_3$

S. Dimitrovska-Lazova^{1*}, S. Aleksovska^{1,2,4}, P. Tzvetkov³,
V. Mirčeski^{1,4}, D. Kovacheva³

¹ University “Sts. Cyril & Methodius”, Institute of Chemistry, Faculty of Natural Sciences and Mathematics, Arhimedova 5, 1000 Skopje, Republic of Macedonia

² Research Center for Environment and Materials, Macedonian Academy of Sciences and Arts, Bul. “Krstе Misirkov” 2, P.O. Box 428, 1000 Skopje, Republic of Macedonia

³ Institute of General and Inorganic Chemistry, Bulgarian Academy of Science, “Acad. Georgi Bonchev”, bl. 11, 1113 Sofia, Bulgaria

⁴ Faculty of Medical Sciences, Goce Delcev University, Stip, R. Macedonia

Received December, 2014; Revised January, 2015

The influence of partial substitution of Y^{3+} with Ca^{2+} in $\text{YCo}_{0.5}\text{Fe}_{0.5}\text{O}_3$ perovskite on the crystallochemical and electrocatalytic properties is presented. The perovskites $\text{YCo}_{0.5}\text{Fe}_{0.5}\text{O}_3$ and $\text{Y}_{0.8}\text{Ca}_{0.2}\text{Co}_{0.5}\text{Fe}_{0.5}\text{O}_{3-\delta}$ were synthesized by solution combustion method with citric acid as a fuel. The obtained perovskites were analyzed with powder XRD and cyclic voltammetry. The crystal structures of both compounds were determined by Rietveld refinement method. The XRD patterns showed that both perovskites are orthorhombic and crystallize in space group $Pnma$. In aim to obtain a clearer picture for the influence of substitution of Y^{3+} ion with Ca^{2+} ion on the structural characteristics, the lattice parameters and distances and angles were used to calculate several crystallochemical parameters such as, cell distortion, orthorhombic distortion, bond and angle deformation, the tilting angles, bond valences, and global instability index. It was found that the distortion indices and tilting angles are lower for $\text{Y}_{0.8}\text{Ca}_{0.2}\text{Co}_{0.5}\text{Fe}_{0.5}\text{O}_{3-\delta}$ in comparison with $\text{YCo}_{0.5}\text{Fe}_{0.5}\text{O}_3$ indicating more stable structure. Taking into consideration the possible application of these compounds as catalysts in direct methanol fuel cells, their catalytic properties towards oxidation of methanol in basic solutions were studied by cyclic voltammetry. The electrocatalytic activity towards oxidation of chloride ions and oxidation of H_2O_2 in phosphate buffer were also investigated.

Key words: perovskites, crystal structure, crystallochemical parameters, electrocatalytic properties.

INTRODUCTION

The perovskite-type oxides (ABO_3) have attracted great scientific attention due to number of specific and important physical and chemical properties. Among the numerous different perovskites, rare-earth cobalt containing perovskites (LnCoO_3 ; $\text{Ln} = \text{Y}$ or lanthanide) are of prominent scientific interest since they exhibit interesting properties such as high electronic conductivity, metal to insulator transition with increasing temperature, significant catalytic activity, specific magnetic properties, etc. [1–5]. Their properties are tightly connected with some characteristics of cobalt ions such as the possibility to change the oxidation state (Co^{4+} , Co^{3+} , Co^{2+})

and also the possibility of altering the spin state of the Co^{3+} ion. Thus, it was found that in LnCoO_3 perovskites, Co^{3+} ion could undergo temperature driven spin-state changes from non-magnetic low-spin (t_{2g}^6) to paramagnetic intermediate-spin ($t_{2g}^5e_g^1$) and finally to paramagnetic high-spin state ($t_{2g}^4e_g^2$), or it could exist in mixed spin state [6–9]. The intermediate-spin state Co^{3+} ion in LnCoO_3 is Jahn-Teller active, which is associated with distortion of the CoO_6 octahedra.

Another well investigated and from applicative point of view the most promising cobalt-containing perovskites, are the systems of general formula $\text{Ln}_{1-x}\text{M}_x\text{CoO}_3$. In these perovskites, the partial substitution of rare-earth elements with divalent cations leads to formation of Co^{4+} ions or oxygen deficiencies [10–13]. A typical example is $\text{Y}_{1/4}\text{Sr}_{3/4}\text{CoO}_{3-\delta}$ which could be prepared as A-site ordered or disordered structure. The A-site ordering leads also

* To whom all correspondence should be sent:
E-mail: sandra@iunona.pmf.ukim.edu.mk

to oxygen vacancies ordering (and *vice versa*), which is connected with modifications of the electronic phases and ferromagnetic transitions [11]. It has been recognized that the physical properties of ABO_3 -perovskites are largely dependent on the oxygen deficiency [11]. The mixed conductivity can be enhanced through the substitution of La^{3+} by Sr^{2+} at A-sites and the substitution of B-cation by other transition metal. The charge imbalance and overall charge neutrality can be maintained by the presence of charged oxygen vacancies and mixed valence state ions at the B sites. These point defects are the origin of the mixed electronic and oxygen ion conductivity [11].

Perovskites with partial substitution of Co^{3+} have also been investigated. Thus, Co^{3+} ions could be partially substituted by Ni [14], by Mn [15] or by Cr^{3+} , which was also a subject of our previous investigations [16–20]. It was found that the magnetic and electrical properties of this type of complex perovskites depends on the spin state of the Co^{3+} ion [14, 15, 21] and the cation–anion–cation overlap [14, 15, 18, 21].

However, the literature data for substituents both in A- and B-sites in Co-containing perovskites are very rare. Therefore, following the trend of investigation of different cobalt containing perovskite compounds, in this work $YCo_{0.5}Fe_{0.5}O_3$ and $Y_{0.8}Ca_{0.2}Co_{0.5}Fe_{0.5}O_{3-\delta}$ were synthesized. The main aim of this work was to compare the crystallochemical and catalytic properties of these perovskites and the influence of aliovalent substitution in A-position.

EXPERIMENTAL

The studied perovskites ($YCo_{0.5}Fe_{0.5}O_3$ and $Y_{0.8}Ca_{0.2}Co_{0.5}Fe_{0.5}O_{3-\delta}$) were synthesized by solution combustion method using citric acid as a fuel. The quantity of the fuel was calculated according to the fuel-to-oxidizer ratio, which was set to 1 in order to obtain the highest possible temperature during the reaction. The starting solutions were prepared by dissolving the nitrate salts of constituent metal ions in small quantity of distilled water and the dissolved citric acid was slowly added to this solution. The pH of the reaction solution was adjusted to 7 with addition of NH_4OH . The reaction mixture was placed on magnetic stirrer and it was heated at 80 °C until the evaporation of water. Then the glass baker was transferred on hot plate preheated at ~350 °C when vigorous reaction took place resulting in formation of black spongy powders. The obtained powders were additionally heated for 4 h at 800 °C. In aim to remove the possible impurities and to improve the crystallinity, the resulting powders were washed with diluted HCl and heated at 6 h at 950 °C.

The characterization and structural investigation of the obtained powders were analyzed by powder X-ray diffraction. The XRD patterns were recorded at room temperature on *Bruker D8 Advance* with $CuK\alpha$ radiation and Sol-X detector within the range 10–120° 2θ with step-scanning of 0.02°. The crystal structures were refined by the method of Rietveld [22] using the Fullprof program [23].

The electrocatalytic properties of $YCo_{0.5}Fe_{0.5}O_3$ and $Y_{0.8}Ca_{0.2}Co_{0.5}Fe_{0.5}O_{3-\delta}$ perovskites were investigated using cyclic voltammetry. The investigations were performed on μ AUTOLAB, model III. The cyclic voltammograms were recorded on a specially designed parafine impregnated graphite electrode (PIGE) [24]. The electrochemical cell consisted of three electrodes: PIGE as a working electrode, Ag/AgCl (sat. KCl) as reference electrode, and a platinum wire as auxiliary electrode. The microcrystals of $YCo_{0.5}Fe_{0.5}O_3$ and $Y_{0.8}Ca_{0.2}Co_{0.5}Fe_{0.5}O_{3-\delta}$ were deposited on the surface of PIGE by abrasion. The electrochemical activity was investigated at room temperature, in aqueous solutions of different electrolytes: LiCl, KCl, NaCl, $(CH_3)_4NCl$ (all with concentrations 0.5 mol/dm³), HCl (0.3 mol/dm³), KOH (0.1 and 1 mol/dm³), phosphate buffer (pH = 7.35) and buffer in which H_2O_2 (10^{-1} – 10^{-3} mol/dm³) was added. In aim to investigate the possible application of these compounds as catalysts in direct methanol fuel cells (DMFC), the electrocatalytic activity in basic solutions of 1 mol/dm³ methanol was studied.

RESULTS AND DISCUSSION

Crystal structure

The XRD patterns of the synthesized compounds were completely indexed in orthorhombic $Pnma$ space group. Their purity and the crystallinity were improved by subsequent additional heating (Fig. 1).

The results of crystal structure refinements by Rietveld method of the studied perovskites are presented in Table 1 and selected distances and angles are given in Table 2. Both compounds crystallize in $Pnma$ space group with $Z = 4$. The unit cell parameters and fractional atomic coordinates of $Y_{0.8}Ca_{0.2}Co_{0.5}Fe_{0.5}O_{3-\delta}$ are close to the values of $YCo_{0.5}Fe_{0.5}O_3$.

The relationships between the unit cell parameters in both compounds are $a > c$ and $a > b/\sqrt{2} > c$, which is typical for *O*-type perovskites, where the main reason for the deformation of the structure, in comparison with the ideal one, is the tilting of the octahedra. As it is well known, the ideal perovskite structure is cubic ($Pm\bar{3}m$) in which the B-cations are surrounded by six anions arranged in corner-

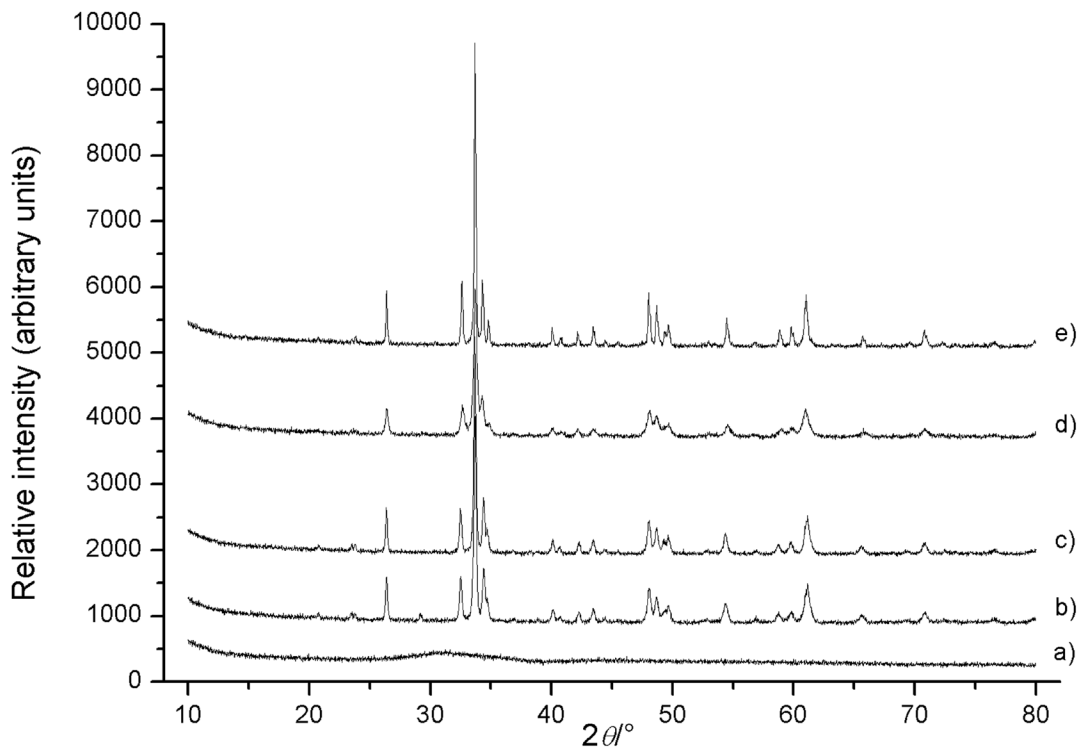


Fig. 1. Powder XRD patterns of: a) as-synthesized $YCo_{0.5}Fe_{0.5}O_3$; b) $YCo_{0.5}Fe_{0.5}O_3$ heated 4h at 800 °C; c) $YCo_{0.5}Fe_{0.5}O_3$ heated 6h at 950 °C; d) $Y_{0.8}Ca_{0.2}Co_{0.5}Fe_{0.5}O_{3-\delta}$ heated 4h at 800 °C and e) $Y_{0.8}Ca_{0.2}Co_{0.5}Fe_{0.5}O_{3-\delta}$ heated 6 h at 950 °C

Table 1. Unit cell parameters, fractional atomic coordinates and discrepancy factors of the synthesized perovskites

Atoms	Par.	$YCo_{0.5}Fe_{0.5}O_3$	$Y_{0.8}Ca_{0.2}Co_{0.5}Fe_{0.5}O_{3-\delta}$
	$a/\text{Å}$	5.5087(2)	5.49338(13)
	$b/\text{Å}$	7.4807(3)	7.47863(17)
	$c/\text{Å}$	5.2133(2)	5.22684(13)
Y/Ca	x	0.06816(14)	0.06591(15)
	z	0.9829(3)	0.9842(3)
	B	0.47(3)	0.45(3)
Co/Fe	B	0.19(4)	0.51(4)
O1	x	0.4663(9)	0.4674(9)
	z	0.0999(9)	0.1008(10)
	B	1.18(16)	1.95(16)
O2	x	0.3041(7)	0.3010(8)
	y	0.0539(5)	0.0537(6)
	z	0.6959(8)	0.6978(8)
	B	0.85(14)	1.29(13)
R_1	R_p	15.1	18.8
	R_{wp}	10.9	12.3
	R_{exp}	9.95	10.65
	χ^2	1.21	1.33
	R_B	2.83	4.31

sharing octahedral geometry. This arrangement forms cubooctahedral cavity in which the A-cation is placed [25]. The ideal cubic perovskite structure is not very common and most of the perovskites are of lower symmetry due to the mismatch of the ionic radii ratio with the one in the ideal perovskite struc-

Table 2. Selected distances and angles for $YCo_{0.5}Fe_{0.5}O_3$ and $Y_{0.8}Ca_{0.2}Co_{0.5}Fe_{0.5}O_{3-\delta}$

	$YCo_{0.5}Fe_{0.5}O_3$	$Y_{0.8}Ca_{0.2}Co_{0.5}Fe_{0.5}O_{3-\delta}$
Y-O1/Å	3.371	3.344
	2.276	2.288
	3.09	3.105
	2.246	2.236
Y-O2/Å x2	2.466	2.463
	2.266	2.275
	3.49	3.462
	2.626	2.634
B-O1/Å x2	1.9502	1.9507
B-O2/Å x2	2.003	1.991
	1.960	1.962
B-O1-B/°	146.06	146.85
B-O2-B/° x2	146.27	147.06

Table 3. Some crystallochemical parameters of the studied compounds

Crystall. param.	$YCo_{0.5}Fe_{0.5}O_3$	$Y_{0.8}Ca_{0.2}Co_{0.5}Fe_{0.5}O_{3-\delta}$
Δ_8	4.014	4.042
Δ_{12}	30.64	29.31
Δ_6	0.135	0.074
s	0.055	0.050
d	5.503	4.564
$dist_{orth}$	0.041	0.037
$\theta/^\circ$	16.47	16.57
$\varphi/^\circ$	12.21	11.66
$\Phi/^\circ$	20.40	20.17
BV(Y/Ca)	3.05	3.144/2.431
BV(Co)	2.438	2.456
BV(Fe)	3.39	3.415
GII	0.205	0.178

ture. The distortion of the ideal perovskite structure is manifested by (1) tilting of the BO_6 octahedra; (2) deformation of the BO_6 octahedra and (3) displacement of the B-cation from the center of the octahedra [25]. As was previously mentioned, in the investigated compounds, the tilting of the octahedra distorts the ideal cubic structure to orthorhombic one. Furthermore, considering the ionic radii of calcium and yttrium ions, which are close to each other ($r(Y^{3+}) = 1.109 \text{ \AA}$ and $r(Ca^{2+}) = 1.12 \text{ \AA}$), it would be expected that both compounds will give similar value for the pseudo-cubic unit cell calculated as $a_p = (V/Z)^{1/3}$ [25]. Thus, a_p for $YCo_{0.5}Fe_{0.5}O_3$ is 3.7729 and for $Y_{0.8}Ca_{0.2}Co_{0.5}Fe_{0.5}O_{3-\delta}$ is 3.7723.

In order to estimate the influence of the partial substitution of Y with Ca ions on the stability of the perovskite structure, some important crystallographic parameters were calculated (Table 3). Some of these parameters were calculated using the cell parameters, such as: spontaneous strain (s) [26], unit cell distortion (d) [27] and orthorhombic distortion ($dist_{orth}$) [28]. The values of these three parameters show that there is some strain and distortion in the unit cells in both investigated structures. However, the obtained values for $Y_{0.8}Ca_{0.2}Co_{0.5}Fe_{0.5}O_{3-\delta}$ are lower, indicating less distortion in its structure.

According to the values of Y-O distances the coordination number of yttrium in these perovskites is 8. This could be also concluded taking into consideration the calculated deformation indices [29] for the coordination polyhedron of the A-cation, which are significantly lower for coordination number of 8 in comparison with one of coordination number of 12. The B-O distances show deformed octahedral

coordination but the values of the deformation indices of the octahedra (Δ_6) indicates that the insertion of calcium ion in the position of Y^{3+} leads towards more regular octahedron (Table 3).

As previously mentioned both perovskites are of O-type, pointing out to the tilting of the octahedra as main reason for deviation of ideal perovskite structure. Therefore, the tilt angles of the octahedra were calculated on the basis of the displacement of the fractional atomic coordinates of the anions from the positions in the ideal cubic structure [25]. It was found that the calculated tilt angles (θ , φ , Φ) in $Y_{0.8}Ca_{0.2}Co_{0.5}Fe_{0.5}O_{3-\delta}$ are similar (but lower) with the ones obtained for $YCo_{0.5}Fe_{0.5}O_3$. Finally in aim to obtain clearer comparison between the general stability of the investigated compound, the global instability index (GII) was calculated [30] taking into account the bond valences model [31]. The obtained value for $Y_{0.8}Ca_{0.2}Co_{0.5}Fe_{0.5}O_{3-\delta}$ is significantly lower than that for $YCo_{0.5}Fe_{0.5}O_3$, which means that the partial substitution of Y by Ca, leads to perovskite structure with decreased internal stress.

Electrocatalytic properties

Our previous investigations on electrocatalytic properties of some perovskites [20] showed that they can catalyze some redox processes such as oxidation of chloride ions, hydrogen peroxide and methanol. Therefore the electrocatalytic properties of $YCo_{0.5}Fe_{0.5}O_3$ and $Y_{0.8}Ca_{0.2}Co_{0.5}Fe_{0.5}O_{3-\delta}$ were investigated by applying cyclic voltammetry at PIGE modified for microcrystals of the perovskite. Firstly, the electrochemical behavior was investigated in contact with the aqueous solutions of chloride ions mentioned in the experimental part. The voltammograms (Fig. 2) were recorded starting from the potential of -1.0 V in a positive potential direction up to 1.5 V , with three different electrodes: blank PIGE electrode, PIGE modified with microcrystals of $YCo_{0.5}Fe_{0.5}O_3$ and PIGE modified with microcrystals of $Y_{0.8}Ca_{0.2}Co_{0.5}Fe_{0.5}O_{3-\delta}$. As can be seen (Fig. 2), a well defined reduction pick at potentials around 0.6 V may be noticed obtained with blank, as well as, with modified PIGE electrode. This reduction pick is preceded by strong oxidation current manifested as an anodic tail on the voltammogram, because the oxidation current is so intensive that it is out of the measuring range of the instrument. It was noticed that if the anodic potential is less than 1.00 V i.e. the value where the oxidation current starts, then the reduction peak disappears. This result points out that the reducible reactant is “*in situ*” formed during the process of oxidation, which is represented by the anodic tail in the voltammogram. Also, the experiments performed with chloride salts of different cations (K^+ , Li^+ , Na^+ or $(CH_3)_4N^+$) but

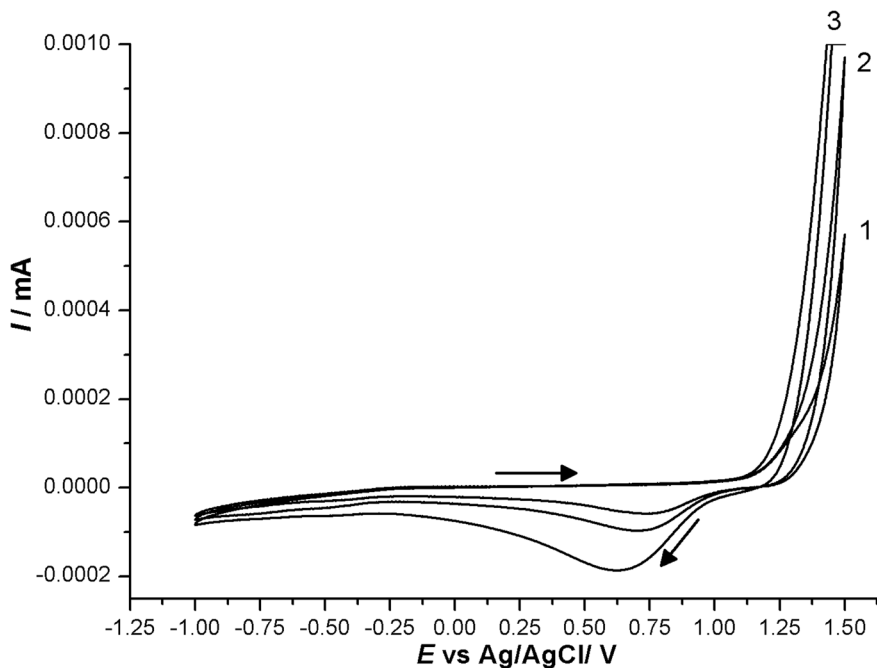


Fig. 2. Cyclic voltammograms in 0.5 mol/dm^3 KCl. 1 – blanc PIGE electrode; 2 – PIGE modified with $YCo_{0.5}Fe_{0.5}O_3$ and 3 – PIGE modified with $Y_{0.8}Ca_{0.2}Co_{0.5}Fe_{0.5}O_{3-\delta}$

of same concentration, gave the same voltammetric response, which means that only the chloride anions are involved in the electrochemical redox reaction.

The analysis of voltammograms clearly shows shifting of the reduction peaks obtained with the perovskite-modified PIGEs towards more negative potentials in comparison with the blank PIGE, due to the catalytic effect of both of the investigated perovskites. Furthermore, according to the positions of the reduction peaks, it could be concluded that $Y_{0.8}Ca_{0.2}Co_{0.5}Fe_{0.5}O_{3-\delta}$ has more pronounced catalytic properties than $YCo_{0.5}Fe_{0.5}O_3$. Another clue to this conclusion is the increasing of the cathodic peak ($I_{p,c}$), which is most intensive in the case of calcium containing perovskite. These results are confirming that the oxidized chlorine species are *in situ* formed during the anodic process. The oxidation process of chlorides yields, most probably, atomic chlorine or some other chlorine containing species that are adsorbed on the electrode, which afterwards give raise to the reductive voltammetric peak in the corresponding cathodic potential sweep. Thus, because of the catalytic effect of perovskite-modified PIGE (especially in the case of $Y_{0.8}Ca_{0.2}Co_{0.5}Fe_{0.5}O_{3-\delta}$), the quantity of the oxidation products increases and as a consequence the $I_{p,c}$ also increases.

The electrocatalytic properties of the investigated perovskites were also analyzed for oxidation of methanol in basic solution (KOH). This reaction

is of special interest since it takes place in so-called direct methanol fuel cells. In order to investigate the possible application of the studied perovskites as catalysts in this type of fuel cells cyclic voltammograms with modified PIGE were recorded (Fig. 3) in the range of 0.0 to 0.8 V. As electrolyte in these experiments basic solution (1 mol/dm^3 KOH) of methanol (1 mol/dm^3) was used. The comparison of the obtained voltammograms of the blank and of the perovskite-modified PIGEs shows clear electrocatalytic effect. Thus, when the electrode process (oxidation of methanol) is performed with perovskite-modified PIGEs, the onset anodic potential is shifted towards less positive potentials in comparison when it is performed with blank electrode (see the inset, Fig. 3). Again, $Y_{0.8}Ca_{0.2}Co_{0.5}Fe_{0.5}O_{3-\delta}$ showed better catalytic activity than $YCo_{0.5}Fe_{0.5}O_3$, which could be also concluded according to the increased $I_{p,a}$.

Finally, the electrocatalytic activity of $Y_{0.8}Ca_{0.2}Co_{0.5}Fe_{0.5}O_{3-\delta}$ and $YCo_{0.5}Fe_{0.5}O_3$ towards oxidation of H_2O_2 in phosphate buffer (pH = 7.35) was investigated in the range of -1.0 to 1.5 V. For this purpose, firstly cyclic voltammograms of $YCo_{0.5}Fe_{0.5}O_3$ and $Y_{0.8}Ca_{0.2}Co_{0.5}Fe_{0.5}O_{3-\delta}$ -modified PIGE in phosphate buffer were recorded. Afterwards, H_2O_2 was added to the solutions of phosphate buffer and its concentration was subsequently increased from 10^{-3} to 10^{-1} mol/dm^3 (Fig. 4a and 4b).

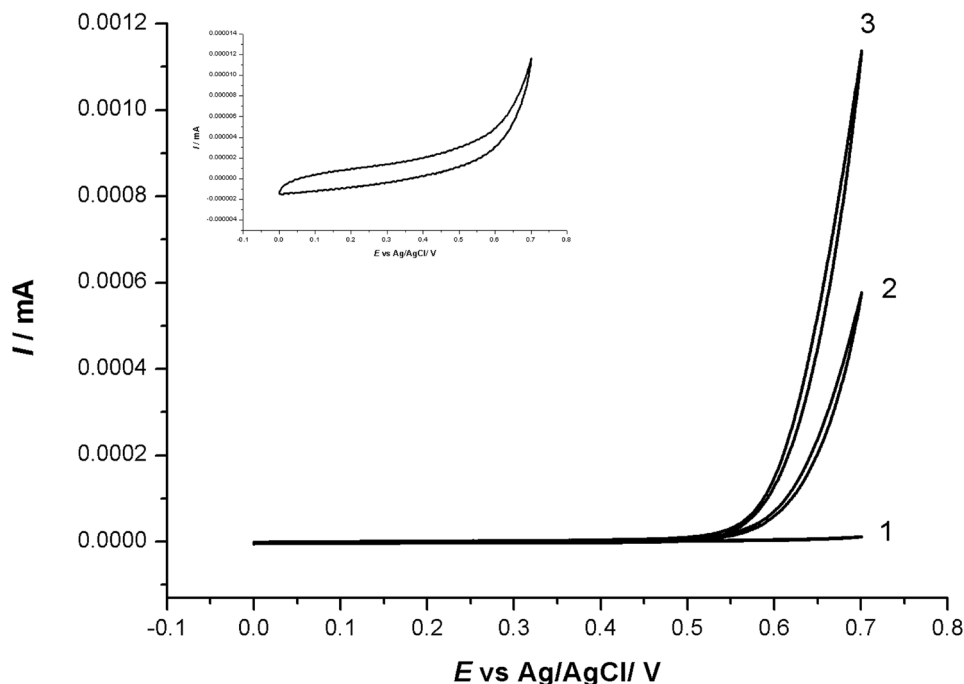


Fig. 3. Cyclic voltammograms in 1 mol/dm³ KOH + 1 mol/dm³ CH₃OH. **1** – blank PIGE electrode; **2** – PIGE modified with $YCo_{0.5}Fe_{0.5}O_3$ and **3** – PIGE modified with $Y_{0.8}Ca_{0.2}Co_{0.5}Fe_{0.5}O_{3-\delta}$. Inset: Enlarged voltammogram of blank PIGE electrode

As can be seen, both investigated perovskites show catalytic activity towards oxidation of H_2O_2 in phosphate buffer. Again, this can be concluded on the basis of the onset starting anodic potential when formation and liberation of O_2 starts. This potential is shifted towards less positive potentials when perovskite-modified PIGEs were used in comparison with blank electrode. Obviously, the Ca-substituted perovskite shows more pronounced electrocatalytic

effect than $YCo_{0.5}Fe_{0.5}O_3$. The repeated experiments with different concentrations of H_2O_2 confirmed this conclusion.

It was previously found that Co-containing perovskites are very good catalysts for number of reactions [4]. However, in all three electrolyte solutions $Y_{0.8}Ca_{0.2}Co_{0.5}Fe_{0.5}O_{3-\delta}$ showed better catalytic activity than $YCo_{0.5}Fe_{0.5}O_3$. The possible explanation for the better electrocatalytic activity of

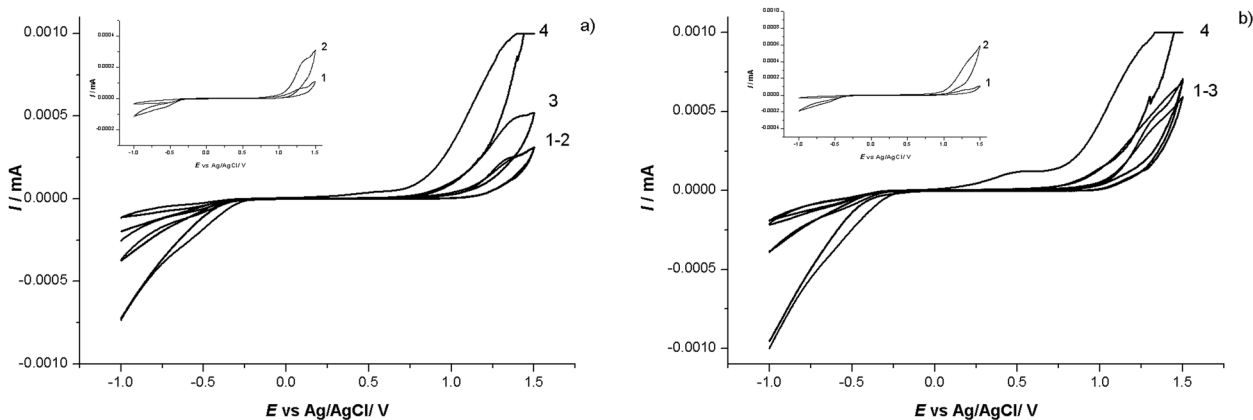


Fig. 4. Cyclic voltammograms of a) $YCo_{0.5}Fe_{0.5}O_3$ and b) $Y_{0.8}Ca_{0.2}Co_{0.5}Fe_{0.5}O_{3-\delta}$ in: **1** – 0.1 M phosphate buffer; **2** – phosphate buffer + 10^{-3} M H_2O_2 ; **3** – phosphate buffer + 10^{-2} M H_2O_2 ; **4** – phosphate buffer + 10^{-1} M H_2O_2 . Inset: **1** – blank PIGE electrode in phosphate buffer + 10^{-3} M H_2O_2 and **2** – modified PIGE in phosphate buffer + 10^{-3} M H_2O_2

$Y_{0.8}Ca_{0.2}Co_{0.5}Fe_{0.5}O_{3-\delta}$ in the investigated electrolyte systems in comparison with $YCo_{0.5}Fe_{0.5}O_3$, is connected with the structure of Ca-containing perovskite. Namely, the partial substitution of Y^{3+} -ions with Ca^{2+} ions leads to oxygen vacancies in the structure. It is supposed that the point defects in the structure, lead to mixed type of conductivity – electronic and ionic – of the modified electrode that facilitates the electrocatalytic process.

CONCLUSION

The perovskites $YCo_{0.5}Fe_{0.5}O_3$ and $Y_{0.8}Ca_{0.2}Co_{0.5}Fe_{0.5}O_{3-\delta}$ were successfully obtained by solution combustion method using citric acid as a fuel. The refinement of crystal structure using the Rietveld method showed that the unit cell parameters and the fractional atomic coordinates of the two compounds are very similar. Calculated crystallochemical parameters revealed that insertion of calcium ion in the position of Y^{3+} leads toward smaller deformation of octahedron. Also, the calculated tilting angles are a little bit lower for $Y_{0.8}Ca_{0.2}Co_{0.5}Fe_{0.5}O_{3-\delta}$. This distortion of the unit cell (d and $dist_{orth}$) is also lower in Ca-containing perovskite, as well as, the value of global instability index.

The investigation of the electrocatalytic properties of the studied compounds with cyclic voltammetry revealed that both compounds catalyze the reaction of oxidation of chloride ions; the oxidation of methanol in basic solution and the oxidation of H_2O_2 in phosphate buffer. It was found that in all three investigated systems, $Y_{0.8}Ca_{0.2}Co_{0.5}Fe_{0.5}O_{3-\delta}$ showed better catalytic activity than $YCo_{0.5}Fe_{0.5}O_3$. This could be explained by the formation of oxygen vacancies in this structure, which probably lead to mixed type of conductivity (electronic and ionic) of the modified electrode that facilitates the electrocatalytic process.

Acknowledgement: The financial support of the BAS-MANU Collaborative Project “Structural characterization and investigation of electrical and catalytic properties of new synthesized complex perovskites” is gratefully acknowledged.

REFERENCES

- Z. Shao, S. M. Haile, *Nature* (London), **431**, 170 (2004).
- Y. Wang, N. S. Rogado, R. J. Cava, N. P. Ong, *Nature* (London) **423**, 425 (2003).
- W. Kobayashi, S. Ishiwata, I. Terasaki, M. Takano, I. Grigoroviciute, H. Yamauchi, M. Karppinen, *Phys. Rev. B* **72**, 104408 (2005).
- M. A. Peña, J. L. G. Fierro, *Chem. Rev.*, **101**, 1981 (2001).
- S. Yáñez-Vilar, A. Castro-Couceiro, B. Rivas-Murias, A. Fondado, J. Mira, J. Rivas, M. A. Señaris-Rodríguez, *Z. Anorg. Allg. Chem.*, **631**, 2265 (2005).
- K. Knížek, Z. Jiráček, J. Hejtmánek, M. Veverka, M. Maryško, G. Maris, T. T. M. Palstra, *Eur. Phys. J. B*, **47**, 213 (2005).
- J.-Q. Yan, J.-S. Zhou, J. B. Goodenough, *Phys. Rev. B*, **69**, 134409 (2004).
- F. H. M. Cavalcante, A. W. Carbonari, R. F. L. Malavasi, G. A. Cabrera-Pasca, R. N. Saxena, J. Mestnik-Filho, *J. Magn. Magn. Mater.*, **320**, e32–e35 (2008).
- J.-S. Zhou, J.-Q. Yan, J. B. Goodenough, *Phys. Rev. B*, **71**, 220103R (2005).
- S. Fukushima, T. Sato, D. Akahoshi, H. Kuwahara, *J. Appl. Phys.*, **103**, 7 (2008).
- Y. Liu, X. Y. Qin, *J. Phys. Chem. Solids*, **67**, 1893 (2006).
- G. Ch. Kostoglou, N. Vasilakos, Ch. Ftikos, *Solid State Ionics*, **106**, 207 (1998).
- A. J. Barón-González, C. Frontera, J. L. García-Muñoz, J. Blasco, C. Ritter, S. Valencia, R. Feyerherm, E. Dudzik, *Physics Procedia*, **8**, 73 (2010).
- R. Z. Yarbay, H. E. Figenand S. Z. Baykara, *Acta Phys. Polonica A*, **121**, 44 (2012).
- M. M. Farhoudi, X. L. Wang, *IEEE Transactions on Magnetics*, **41**(10), 3493 (2005).
- S. Dimitrovska-Lazova, D. Kovacheva, S. Aleksovska, M. Marinšek, P. Tzvetkov, *Bulg. Chem. Comm.*, **44**, 235 (2012).
- S. Dimitrovska-Lazova, D. Kovacheva, P. Tzvetkov, *Bulg. Chem. Comm.*, **44**, 245 (2012).
- M. Pecovska Gjorgjevich, S. Aleksovska, M. Marinšek, S. Dimitrovska-Lazova, *J. Am. Ceram. Soc.*, **97**(12) 3864 (2014).
- M. Pecovska Gjorgjevich, S. Aleksovska, S. Dimitrovska-Lazova, *Physica Macedonica*, **61**, 21 (2012).
- S. Dimitrovska-Lazova, V. Mirčeski, D. Kovacheva, S. Aleksovska, *J. Solid State Electrochem.*, **16**, 219 (2012).
- H. Taguchi, *J. Solid State Chem.*, **122**, 297 (1996).
- H. M. Rietveld, *J. Appl. Crystallogr.*, **2**, 65 (1969).
- J. Rodriguez-Carvajal, *Physica B*, **192**, 55 (1993).
- F. Scholz, U. Schröder, R. Gulaboski, *Electrochemistry of immobilized particles and droplets*, Springer, Berlin, 2005.
- R. H. Mitchell, *Perovskites: Modern and Ancient*, Almaz press – Thunder Bay, 2002.
- J. A. Alonso, M. J. Martínez-Lope, C. de la Calle, V. Pomjakushin, *J. Mater. Chem.*, **16**, 1555 (2006).
- S. Sasaki, C. Prewitt, R. Liebermann, *Am. Mineral.*, **68**, 1189 (1983).
- G. Huo, D. Song, Q. Yang, F. Dong, *Ceram. Int.*, **34**, 497 (2008).
- R. D. Shannon, *Acta Crystallogr.*, **A32**, 751 (1976).
- A. Salinas-Sanchez, J. L. Garcia-Muniz, J. Rodriguez-Carvajal, R. Saez-Puche, J. L. Martinez, *J. Solid State Chem.*, **100**, 201 (1992).
- I. D. Brown, *Acta Crystallogr.*, **B53**, 381 (1997).

ВЛИЯНИЕ НА ЗАМЕСТВАНЕТО НА Y-ЙОНИ ВЪРХУ СТРУКТУРНИТЕ И ЕЛЕКТРОХИМИЧНИ ХАРАКТЕРИСТИКИ НА $YCo_{0.5}Fe_{0.5}O_3$

С. Димитровска-Лазова^{1*}, С. Алексовска^{1,2,4}, П. Цветков³,
В. Мирчески^{1,4}, Д. Ковачева³

¹ Университет „Св. Кирил и Методий“, Институт по химия, Факултет Природни науки и математика, Архимедова 5, 1000 Скопие, Република Македонија

² Изследователски център за околна среда и материали, Македонска академия на науките и изкуствата, Бул. „Кръсте Мисирков“ 2, п.к. 428, 1000 Скопие, Република Македонија

³ Институт по обща и неорганична химия, Българска академия на науките, „Акад. Георги Бончев“, бл. 11, 1113 София, България

⁴ Медицински факултет, Университет „Гоце Делчев“, Щип, Република Македонија

Постъпила декември, 2014 г.; приета януари, 2015 г.

(Резюме)

Представено е влиянието на частично заместване на Y^{3+} от Ca^{2+} в структурата на $YCo_{0.5}Fe_{0.5}O_3$ върху кристалохимичните и електрокаталитични свойства. Съединенията с химичен състав $YCo_{0.5}Fe_{0.5}O_3$ и $Y_{0.8}Ca_{0.2}Co_{0.5}Fe_{0.5}O_{3-\delta}$ имат перовскитова структура и бяха получени по метода на изгаряне от разтвор с използване на лимонена киселина за гориво. Получените фази бяха характеризирани с прахова рентгенова дифракция (XRD) и циклична волтаметрия. Кристалната структура и на двете съединения беше уточнена по метода на Ритвелд. Праховите дифрактограми показват, че двете съединения кристализират в орторомбична пространствена група $Pnma$. С цел да се получи по-ясна представа за влиянието на заместването на Y^{3+} от Ca^{2+} йони върху структурните характеристики, параметрите на елементарната клетка и разстоянията и ъглите в структурата бяха използвани за изчисляване на няколко кристалохимични параметъра като деформация на клетката, орторомбично изкривяване, деформация на дължината на връзки и ъгли, наклон на октаедрите, сума от валентните връзки и глобален индекс на нестабилност. Беше установено, че пресметнатите индекси на деформация и ъгли на наклон между октаедрите са по-малки за $Y_{0.8}Ca_{0.2}Co_{0.5}Fe_{0.5}O_{3-\delta}$ в сравнение с $YCo_{0.5}Fe_{0.5}O_3$, което е показател за по-стабилна структура. Като се има предвид възможното прилагане на тези съединения като катализатори в директни горивни клетки, работещи с метанол, техните каталитични свойства по отношение на окисление на метанол в алкални разтвори бяха изучени с циклична волтаметрия. Беше изпитана също тяхната електрокаталитичната активност спрямо окисление на хлорни йони и H_2O_2 в разтвори на фосфатен буфер.

Novel merwinite/akermanite ceramics: *in vitro* bioactivity

I. K. Mihailova^{1*}, L. Radev¹, V. A. Aleksandrova¹, I. V. Colova¹,
I. M. M. Salvado², M. H. V. Fernandes²

¹ University of Chemical Technology and Metallurgy, 8 St. Kl. Ohridski Blvd., Sofia 1756, Bulgaria

² University of Aveiro and CICECO, Aveiro, Portugal

Received December, 2014; Revised January, 2015

The ceramics in the system CaO–MgO–SiO₂ has recently received a great deal of attention because they exhibit good *in vitro* bioactivity and have potential use as bone implants. Biphasic calcium-magnesium-silicate ceramics was prepared by a sol-gel method. The dried gel with chemical composition 3CaO.MgO.2SiO₂ was thermally treated at 1300 °C for 2 h. The structural behavior of the synthesized ceramics was examined by means of X-ray diffraction (XRD), Fourier Transform Infrared Spectroscopy (FTIR) and Scanning Electron Microscopy (SEM). Merwinite, as the main crystalline phase, and akermanite, as the minor phase, were identified. The *in vitro* bioactivity of the synthesized ceramic samples was recorded in Simulated Body Fluid (SBF) for different times of soaking. The apatite formation on the surface of the immersed samples was detected by FTIR, SEM and Energy Dispersive Spectroscopy (EDS) techniques. The ion concentrations in the SBF solutions after the *in vitro* test were evaluated by Inductively Coupled Plasma Optical Emission Spectrometry (ICP-OES).

On the basis of the results obtained, the ability of the biphasic ceramics to deposit apatite layer was found. The peculiarities of the formation of apatite layer depending on the phase composition were analyzed and discussed.

Key words: CaO–MgO–SiO₂, ceramics, merwinite, akermanite, *in vitro* bioactivity.

INTRODUCTION

It is quite natural important societal issues and topics related to health and quality of life to attract serious scientific interest. Thus, intensive research has been conducted in recent decades to produce new biomaterials for various applications.

Biomaterials can be classified as bioinert, bioactive and bioresorbable, based on their chemical surface reactivity. Bioactive glasses and ceramics are considered as potential materials for bone substitutes, because they can form a direct bond with the living bone. Important requirement for bioactive material is that in the presence of biological fluids, an apatite layer is produced on their surfaces, which provides the bonding interface with living hard tissues [1].

Mg-containing silicate ceramics, glass-ceramics and glasses have proven to be bioactive and exhibit numerous advantages for biomedical applications [2, 3]. Their mechanical properties, bioactivity and bio-

compatibility make them promising candidates for bone tissue regeneration which explains the growing interest in these materials [3, 4]. The effects of MgO contents on the structure, crystallization, degradability and bioactivity of glasses [5], glass-ceramics [6] and ceramics [7] in the MgO–CaO–SiO₂–P₂O₅ system were investigated. Some authors reported that the crystallization of the glasses decreased their apatite-formation ability [8]. Various studies have investigated ceramics and glass-ceramics in the CaO–MgO–SiO₂ system for biomedical applications, including merwinite [4, 9–13], akermanite [14–16], diopside [1, 17, 18] and monticellite [19, 20] ceramics and glass-ceramics. Diba *et al.* [3] summarize and discuss the most relevant studies carried out in the field of Mg-containing bioactive silicate ceramics and glass-ceramics.

Research carried out so far on materials containing merwinite as the main phase reveals their promising properties for use as biomaterials [4, 9–13, 21]. The properties of three single-phase (merwinite, akermanite, and monticellite) ceramics with different MgO contents were compared and the relationship between the chemical composition and the mechanical and biological properties was investigated [20]. The results obtained by Chen *et al.* [21]

* To whom all correspondence should be sent:
E-mail: irena@uctm.edu

showed that the mechanical properties of bioceramics in the MgO–CaO–SiO₂ system were improved from merwinite to akermanite and monticellite ceramics with the increase of MgO contents, whereas the apatite-formation ability in SBF and cell proliferation decreased. Their results indicated that the MgO content was one of the important factors, which distinctly affected the mechanical properties and biological performances of bioceramics.

Despite the positive results of merwinite ceramics bioactivity, the publications related to this phase are much less than the ones dedicated to other calcium magnesium silicates as diopside, akermanite and more [3]. Furthermore, in a series of publications dedicated to nanocrystalline merwinite, the phase is synthesized using the sol-gel molar ratio of TEOS: Mg(NO₃)₂·6H₂O:Ca(NO₃)₂·4H₂O = 1:1.44:0.85 [1, 8–13]. This composition of the gel is significantly different from the stoichiometry of merwinite and the obtained and tested materials are obviously quite a specific case of merwinite bioceramics. In the present study, the composition of the initial gel was selected corresponding to the stoichiometry of merwinite 3CaO·MgO·2SiO₂ to synthesize ceramics, wherein merwinite is prevalent and to examine its structure and bioactive properties.

EXPERIMENTAL

Sample preparation

Ceramics was prepared by sol-gel method using tetraethyl orthosilicate ((C₂H₅O)₄Si, TEOS), magnesium nitrate hexahydrate (Mg(NO₃)₂·6H₂O) and calcium nitrate tetrahydrate (Ca(NO₃)₂·4H₂O) as raw materials. Nitric acid (HNO₃, 2 N) was used to catalyze the hydrolysis of TEOS. The TEOS was mixed with absolute ethanol, water and 2N HNO₃ (molar ratio: TEOS/H₂O/HNO₃=1:8:0.16) and hydrolyzed for 1 h. under stirring. Then, the solutions of Ca(NO₃)₂·4H₂O and Mg₂(NO₃)₂·6H₂O were added into the mixture (molar ratio: TEOS/Mg(NO₃)₂·6H₂O/Ca(NO₃)₂·4H₂O = 2:1:3), and reactants were stirred for 6 h at room temperature. After mixing, the solution was dried at 100 °C for 2 days to obtain the dry gel. The dried gel was calcined at 700 °C for 2 h. Finally, the powders were thermally treated at 1300 °C for 2 h.

Characterization techniques

X-ray powder diffraction (XRD) analysis was applied for phase identification. An X-ray diffractometer Philips at Cu K α radiation was used in the range from 8° to 90° 2 θ (step size: 0.05°, counting time per step: 1 s). The crystalline phases were identified using the powder diffraction files JCPDS:

35-0591 and JCPDS: 35-0592 from database JCPDS – International Centre for Diffraction Data PCPDFWIN v.2.2. (2001). The quantitative phase analysis and the determination of unit cell parameters of crystalline phases was performed with the PowderCell 2.4 software [22].

FTIR spectroscopy was applied. Infrared transmittance spectra were recorded by using the pressed-pellet technique in KBr. KBr pellets were prepared by mixing of ~1 mg of the sample with 300 mg KBr. The measurements were made with a FTIR spectrometer Bruker Tensor 27 in the frequency range from 4000 to 400 cm⁻¹.

The morphology of the surface and chemical composition were analyzed using Scanning Electron Microscopy SEM Hitachi SU-70 equipped with energy dispersive spectrometer (EDS).

SBF in vitro test

In order to estimate the *in vitro* bioactivity (potential of apatite formation) of the sample, we used the Simulated Body Fluid (SBF) proposed by Kokubo et al. [23], the Tris-buffered SBF (Na⁺ 142.0, K⁺ 5.0, Mg²⁺ 1.5, Ca²⁺ 2.5, Cl⁻ 147.8, HCO₃⁻ 4.2, HPO₄²⁻ 1.0 and SO₄²⁻ 0.5 mol m⁻³; 7.4 pH). The concentration of various ions in the SBF was adjusted to be similar to those in human blood plasma.

0.3 g of the homogenized ceramic powders were uniaxially pressed to obtain pellets 2 mm in thickness and 10 mm in diameter. The pellets were placed in polyethylene bottles containing 20 ml of SBF at 37 ± 0.5 °C. The sample surface area to SBF volume (SA/V) ratio was equal to 0.1 cm⁻¹.

Pellets were removed after 7 and 14 days of soaking, gently rinsed with deionized water and acetone, and dried at room temperature.

Sample surfaces and cross-sections, before and after SBF treatment, were examined by SEM and EDS. The changes in the samples during the *in vitro* test were also registered by FTIR spectroscopy.

The SBF was removed after several periods of immersion and calcium, magnesium, phosphorus, and silicon ion concentration in the removed SBF was determined by inductively coupled plasma optical emission spectrometry (Prodigy High Dispersion ICP-OES Spectrometer from Teledyne Leeman Labs – USA).

RESULTS AND DISCUSSION

Phase composition and microstructure of ceramic

XRD data corresponding to the synthesized sample are shown in Fig. 1. Merwinite Ca₃MgSi₂O₈ (JCPDS: 35-0591), as the main crystalline phase,

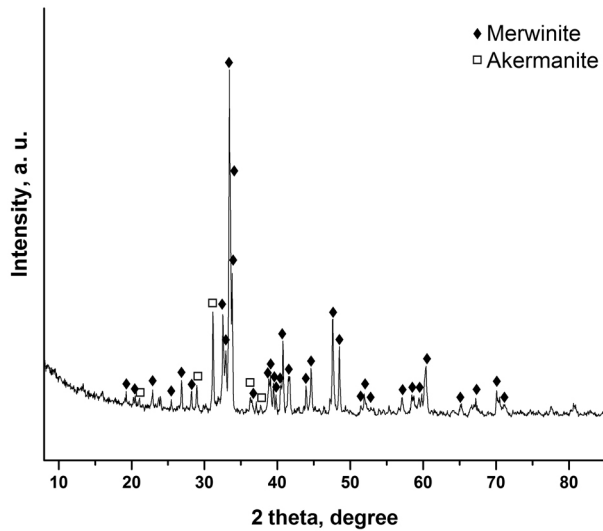


Fig. 1. X-ray diffraction patterns of merwinite-akermanite ceramics

and akermanite $\text{Ca}_2\text{MgSi}_2\text{O}_7$ (JCPDS: 35-0592), as the minor phase, were identified in ceramic sample sintered at 1300 °C for 2 h. The phase composition and lattice parameters for crystalline phases are presented in Table 1. The quantitative phase analysis and calculation of the lattice parameters were performed with the PowderCell 2.4 software. The values of lattice parameters observed for merwinite and akermanite in the ceramic were very close to those of the standard JCPDS and thus no difference in their crystal structures was detected.

As it can be seen, on Fig. 2, the presented FTIR spectrum corresponds to the spectrum of merwinite [24, 25]. The intensive bands posited in the range 850–1050 cm^{-1} correspond to internal antisymmetric and symmetric stretching vibrations of SiO_4 tetrahedra in merwinite [25]. In the same range the most intensive band, posited at 936 cm^{-1} is related to the non-bridging oxygen (NBO) bonds of Si-O-

Ca [26]. The other intensive bands in the region 450 to 550 cm^{-1} could be assigned to Si-O-Si bending vibration [25]. In the FTIR spectrum of the thermally treated sample (Fig. 2), the peaks near 1022, 936, 885, 530 and 515 cm^{-1} confirm merwinite as a dominant phase, while the peaks near 975, 905, 681, 635 and 472 cm^{-1} as well as low frequency shoulder around 850 cm^{-1} could be related to akermanite [24–28]. Both phases reveal peaks near 936 and 587 cm^{-1} . The presented FTIR results are in good agreement with XRD analysis.

SEM images of the thermally treated ceramic sample before *in vitro* test are given in Fig. 3. From the depicted SEM images of the sample before immersion in SBF it was observed that the surface was well crystallized. The euhedral crystals do not exceed 3 μm (Fig. 3 b).

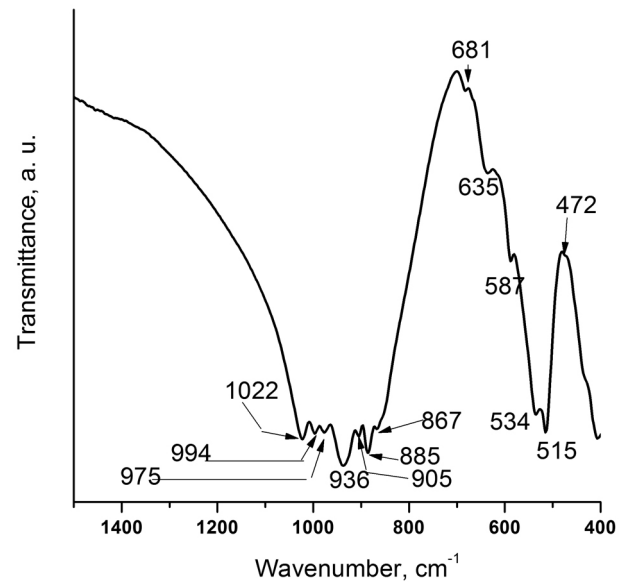


Fig. 2. FTIR spectra of thermally treated at 1300 °C for 2 hours ceramics

Table 1. Phase composition and lattice parameters for crystalline phases in the ceramics

Crystalline phases	Concentration (vol. %)	Lattice parameters			
		a (Å)	b (Å)	c (Å)	β (°)
Merwinite	–	a	b	c	β
Standard JCPDS: 35-0591	–	13.29	5.304	9.352	92.09
Merwinite in ceramics	85	13.28	5.304	9.336	92.14
Akermanite	–	a	b		
Standard JCPDS: 35-0592	–	7.833	5.006		
Akermanite in ceramics	15	7.829	5.006		

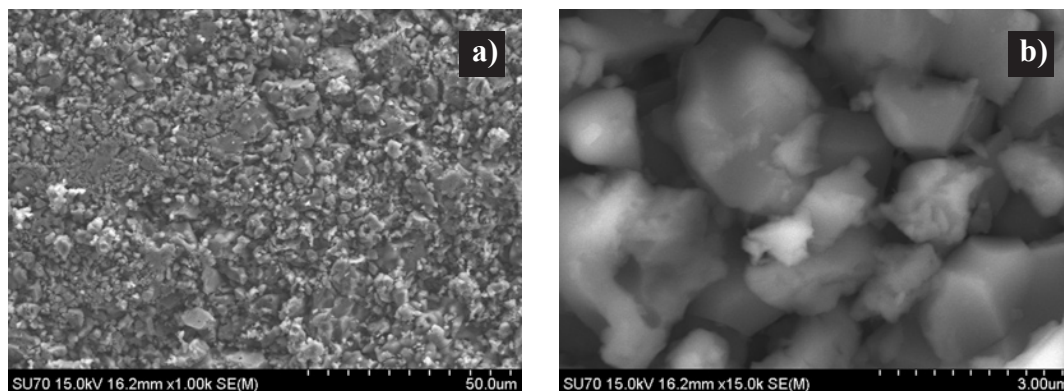


Fig. 3. SEM micrographs of the ceramic surface, after thermal treatment at 1300 °C for 2 hours

In vitro bioactivity of merwinite-akermanite ceramic

FTIR spectra of the ceramic samples after soaking in SBF solution for 7 and 14 days in static conditions are presented at Fig. 4. Four vibrational modes are visible for the PO_4^{3-} ions in apatite: $\nu_1\text{PO}_4^{3-}$ at 960–966 cm^{-1} , $\nu_2\text{PO}_4^{3-}$ at 460 cm^{-1} , $\nu_3\text{PO}_4^{3-}$ at 1190–980 cm^{-1} , and $\nu_4\text{PO}_4^{3-}$ at 660–520 cm^{-1} [29, 30]. The most intensive peak in the infrared spectra should be the peak arising from antisymmetric stretching ν_3 of phosphate group. After SBF soaking a gradual change in the intensity ratio of the peaks in the spectral range 850–1050 cm^{-1} occurred which could be an indication for increased amount of apatite on the surface.

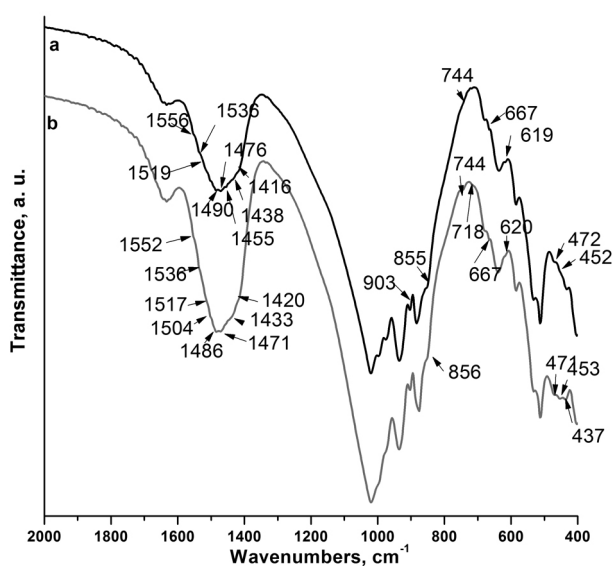


Fig. 4. FTIR of the prepared ceramics, after immersion in SBF solution for 7 (a) and 14 (b) days in static conditions

In our FTIR results, presented in Fig. 4 some new peaks can be observed. These new peaks were posited at 452 (453) cm^{-1} , and 472 (471) cm^{-1} . They could be ascribed to $\nu_2\text{PO}_4^{3-}$ [31, 32]. The additional peaks at 619 (620) cm^{-1} and 667 cm^{-1} (for the two samples) were assigned to $\nu_4\text{PO}_4^{3-}$ [33, 34]. On the other hand, the peak centered at 667 cm^{-1} could be related also to OH^- [35]. The peak at 903 (906) cm^{-1} was characteristic of $\nu_1\text{PO}_4^{3-}$ [36]. In FTIR spectra for the sample after soaking for 7 days (Fig. 4, a) one additional peak at 996 was visible, which could be assigned to $\nu_1\text{PO}_4^{3-}$ [37].

Furthermore, in the presented FTIR spectra we were able to observe the presence of a series of peaks, centered at 718 cm^{-1} , 744 cm^{-1} , and 856 (855) cm^{-1} , which were assigned to $\nu_4\text{CO}_3^{2-}$ and $\nu_2\text{CO}_3^{2-}$ vibrational modes [38, 39].

From the presented infrared results we could assume that the presence of ν_1 - $\nu_4\text{PO}_4^{3-}$ could be related to the crystalline calcium phosphates formed on the surface of the immersed samples. Moreover, CaCO_3 was also formed on the soaked samples.

In addition, on the basis of the depicted results four types of regions of $\nu_3\text{CO}_3^{2-}$ could be detected: 1410–1430 cm^{-1} , 1430–1460 cm^{-1} , 1460–1500 cm^{-1} , and 1500–1560 cm^{-1} . In the case of our samples, the peaks' position can be related as follows:

- For B-type carbonate-containing apatites in which CO_3^{2-} replaced PO_4^{3-} at 1416 cm^{-1} [40], 1420 cm^{-1} [41], 1438 (1433) cm^{-1} [42], 1455 cm^{-1} [43], 1471 (1476) cm^{-1} [41], 1486 cm^{-1} [44], and 1490 cm^{-1} [44]. We must note that the peaks at 1420 and 1490 cm^{-1} could be also related to vaterite [39]. The peak centered at 1476 cm^{-1} was assigned to aragonite, and the one at 1438 cm^{-1} to calcite [39].
- For A-type carbonate-containing apatites in which CO_3^{2-} replaced OH^- at 1504 cm^{-1} [31], 1517 (1519) cm^{-1} [45], 1533 (1536) cm^{-1} [46], and 1552 (1556) cm^{-1} was found.

On the basis of the results related to the presence of CO_3^{2-} bands we can conclude that B-type and A-type carbonate-containing apatites were formed on the immersed ceramics. B-type was a predominant type for carbonate-containing apatites on the ceramics after *in vitro* test in SBF for 7 and 14 days in static conditions.

SEM micrographs of the ceramic sample, after immersion in SBF for 7 and 14 days in static conditions are presented in Fig. 5. After 7 days of immersion in SBF the surface was fully covered by the multiple sphere-like particles (typical size 0.5–1 μm) due to the interaction of the ceramic surface with the SBF solution (Fig. 5a, b). The surface of the sample after a longer test period (14 days) was completely covered by spherical aggregates. On the micrograph (Fig. 5d) the crystals that make up the spherical shapes are easier to distinguish. This type of morphology is typical of carbonate-containing apatites formations.

The detected changes on the sample surface and the identification of the morphology typical of the apatite crystalline aggregates made it necessary to conduct an EDS analysis and the obtained data is shown in Fig. 6. In this context, EDS analysis proved the presence of large amount of Ca

(15.05 at.%) and P (7.43 at.%). The quantity of Si was 2.92 at.%. Moreover, EDS revealed the presence of small amount of Mg (0.91 at.%). On the basis of the results obtained $(\text{Ca}+\text{Mg})/(\text{Si}+\text{P})=1.54$. This ratio was less than the stoichiometric value of 1.67 for pure apatite, i.e. calcium deficient apatite was formed on the surface of the immersed ceramics.

On the other hand, after soaking for 14 days (Fig. 6, b), EDS proved the presence of Ca (21.58 at.%), P (11.22 at.%), Si (2.09 at.%), and Mg (0.60 at.%), i. e. $(\text{Ca}+\text{Mg})/(\text{Si}+\text{P})=1.67$. As it can be seen, apatite layer was formed on the surface of the immersed glass-ceramics after 14 days of soaking.

On the basis of the results obtained we can suppose that two types of substitutions can be produced: (i) $\text{Mg}^{2+} \rightarrow \text{Ca}^{2+}$ and/or (ii) $\text{CO}_3^{2-} \rightarrow \text{PO}_4^{3-}$ and $\text{SiO}_4^{4-} \rightarrow \text{PO}_4^{3-}$ [34].

The release profiles of Si, Ca, Mg and P ions in SBF at 37 °C for ceramic samples are shown on Fig. 7. The ceramic material released Ca and Si ions, and removed P ions from SBF. The concentration of Ca in SBF increased from 116 (for SBF solution) to 952 mg/l for ceramics, when soaked at 37 ± 0.5 °C for 14 days. The continuous Ca^{2+} ion dissolution of the ceramics contributed to generate an increase in the Ca^{2+} ion concentration in the SBF de-

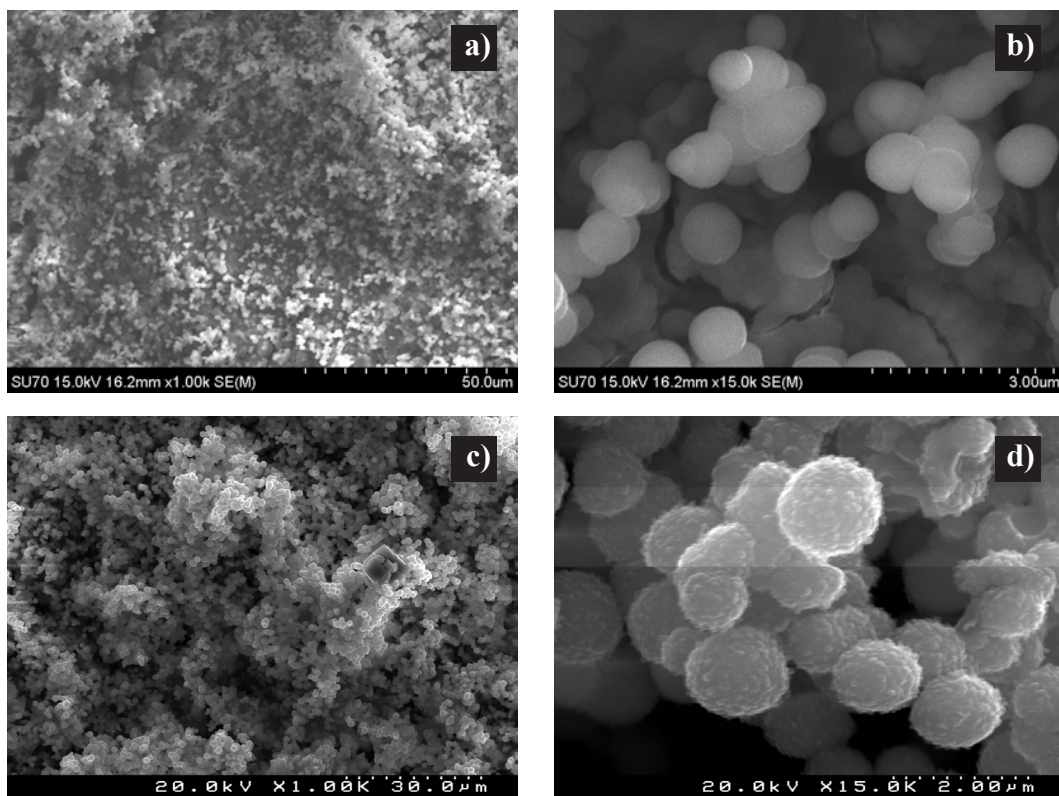


Fig. 5. SEM micrographs of the ceramic surface after immersion in SBF for 7 (a, b), and 14 days (c, d)

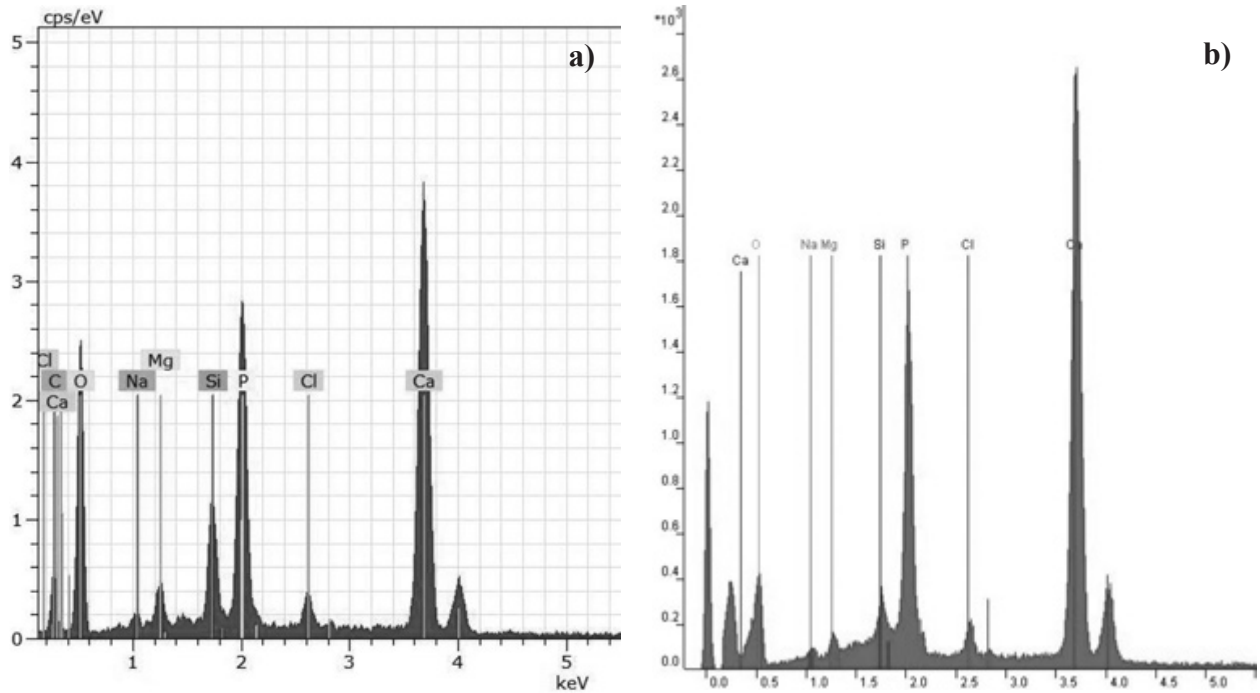


Fig. 6. EDS data for the ceramic surface, after soaking in SBF for 7 (a) and 14 (b) days in static conditions

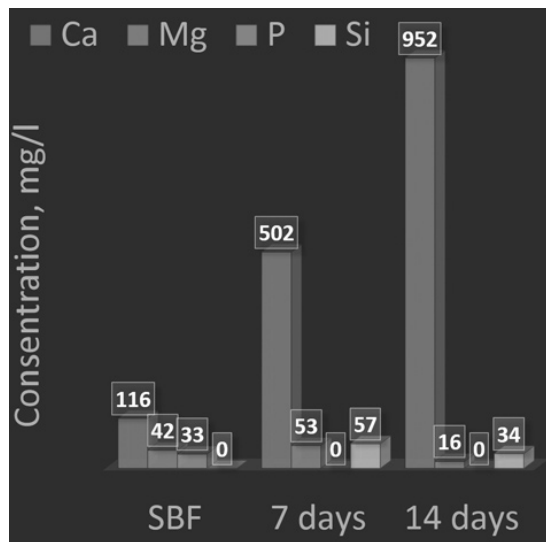


Fig. 7. Evolution of elemental concentrations of Ca, Mg, Si, and P in SBF solution measured by ICP-OES for different soaking times

spite the formation of apatite phase. During the first and second week, the concentration of Ca in SBF increased rapidly and evenly. After 7 days phosphorous ions were fully removed from SBF by the ceramics, because of the formation of apatite phase on the surfaces. In addition, SBF was enriched in Si^{4+}

up to a value of 57 mg/l for 7 days. After 14 days, a relatively lower concentration of Si was detected.

After 7 days of soaking, the concentration of Mg in SBF increased slightly from 42 to 53 mg/l but after 14 days the concentration decreased and Mg^{2+} ions were removed from SBF by the ceramics. On the one hand, the obtained results suggested low partial dissolution of Mg^{2+} and Si^{4+} ions of merwinite-akermanite ceramics, on the other hand, the decrease in their concentration during the second week of immersion may be due to their inclusion in the formation of the surface apatite layer.

After 7 days of soaking a depletion of P ion concentration from the SBF solution was found. However, this did not delay the apatite-like formation process. The obtained SEM and EDS data indicated that the crystallization and growth of the apatite layer continued. Furthermore, with the increase of soaking time, the release of Ca^{2+} led to supersaturation of the Ca ions in the solution and aided the formation of apatite like layer.

The release profile of Ca was similar to the data published by Radev [34] for $\text{CaO-SiO}_2\text{-P}_2\text{O}_5$ glass-ceramics containing $\beta\text{-Ca}_2\text{SiO}_4$ and $\text{Ca}_{15}(\text{PO}_4)_2(\text{SiO}_4)_6$. The microstructural characteristics of the surface after 14 days in SBF were also similar.

In accordance with Diba *et al.* [3] the bioactivity mechanism of the Mg-containing silicate ceramics is similar to those suggested for Mg-containing bio-

active silicate glasses. Studies have shown a relationship between the degradation rate and bioactivity of the ceramics in the CaO–MgO–SiO₂ system [21]. The key role of degradation in the bioactivity process of these materials is correlated to the ion exchange rate of the ceramics/media interface which affects the formation of a silica-rich layer on the ceramic surface [1, 3, 47]. The silanol groups formed on the surface induce heterogeneous nucleation of apatite, and the released calcium ions increase the ionic activity product of apatite, enhancing apatite nucleation. The dissolution behavior of merwinite-akermanite ceramics was generally in accordance with the previously established apatite-forming mechanism. Therefore, the mechanism of apatite formation on the merwinite-akermanite ceramics might be similar to that of the CaO–SiO₂–MgO based bioactive ceramics.

CONCLUSION

In conclusion, biphasic merwinite-akermanite bioceramics in the MgO – CaO – SiO₂ system was prepared first, and then their structural properties and *in vitro* bioactivity were evaluated. After 7 days of immersion of the ceramic samples in SBF, sphere-like Ca-P particles were formed on the surface and continued to grow during the 14 days of immersion. The results indicated that the merwinite-akermanite ceramics had high reactivity in SBF, ability to form an apatite-like layer and potentially it might be used as bioactive implant material. The dissolution behavior of ceramics was generally in accordance with the previously established apatite-forming mechanism on the surface of CaO–SiO₂–MgO based bioactive ceramics in SBF.

Acknowledgements: This work was funded by University of Chemical Technology and Metallurgy – Sofia, Bulgaria through research projects № 11308 and № 11167.

REFERENCES

- M. A. Sainz, P. Pena, S. Serena, A. Caballero, *Acta Biomaterialia*, **6**, 2797 (2010).
- M. Diba, F. Tapia, A. R. Boccaccini, L.A. Strobel, *Int. J. Appl. Glass. Sci.*, **3**, 221 (2012).
- M. Diba, O.-M. Goudouri, F. Tapia, A. R. Boccaccini, *Current Opinion in Solid State and Mater. Sci.*, **18**, 147 (2014).
- A. Nadernezhad, F. Moztarzadeh, M. Hafezi, H. Barzegar-Bafrooei, *J. Eur. Ceram. Soc.*, **34**, 4001 (2014).
- J. Ma, C. Z. Chen, D. G. Wang, Y. Jiao, J. Z. Shi, *Colloids and Surfaces B: Biointerfaces*, **81**, 87 (2010).
- J. Ma, C. Z. Chen, D. G. Wang, X. Shao, C. Z. Wang, H. M. Zhang *Ceram. Int.*, **38**, 6677 (2012).
- J. Ma, C. Z. Chen, D. G. Wang, J. H. Hu, *Materials Letters*, **65**, 130 (2011).
- J. Ma, C. Z. Chen, D. G. Wang, J. H. Hu, *Ceram. Int.*, **37** 1637 (2011).
- J. Ou, Y. Kang, Z. Huang, X. Chen, J. Wu, R. Xiao, G. Yin, *Biomed. Mater.*, **3**, 015015 (2008).
- M. Hafezi-Ardakani, F. Moztarzadeh, M. Rabiee, A. R. Talebi, M. Abasi-shahni, F. Fesahat and F. Sadeghian, *J. Ceram. Process. Res.*, **11**, 765 (2010).
- M. Hafezi-Ardakani, F. Moztarzadeh, M. Rabiee, A. R. Talebi, *Ceram. Int.*, **37**, 175 (2011).
- M. Hafezi, A. R. Talebi, S. M. Miresmaeili, F. Sadeghian, F. Fesahat, *Ceram. Int.*, **39**, 4575 (2013).
- M. Razavi, M. Fathi, O. Savabi, B. H. Beni, D. Vashae, L. Tayebi, *Ceram. Int.*, **40**, 9473 (2014).
- R. K. Singh, A. Srinivasan, *Ceram. Int.*, **36**, 283 (2010).
- M. Razavi, M. Fathi O. Savabi, S. M. Razavi, B. H. Beni, D. Vashae, L. Tayebi, *Ceram. Int.*, **40**, 3865 (2014).
- X. Hou, G. Yin, X. Chen, X. Liao, Y. Yao, Z. Huang, *Appl. Surf. Sci.*, **257**, 3417 (2011).
- C. Wu, Y. Ramaswamy, H. Zreiqat, *Acta Biomaterialia*, **6**, 2237 (2010).
- C. P. Yoganand, V. Selvarajan, L. Lusvardi, O. M. Goudouri, K. M. Paraskevopoulos, M. Rouabhia, *Mater. Sci. Eng. C*, **29**, 1759 (2009).
- S. Ni, L. Chou, J. Chang, *Ceram. Int.*, **33**, 83 (2007).
- S. Ni, J. Chang, L. Chou, *J. Mater. Sci.: Mater. Med.*, **19**, 359 (2008).
- X. Chen, J. Ou, Y. Wei, Z. Huang, Y. Kang, G. Yin, *J. Mater. Sci.: Mater. Med.*, **21**, 1463 (2010).
- W. Kraus, G. Nolze, Powdercell2.4, Federal 19. Institute for materials Research and Testing Rudower Chaussee 512485 Berlin, Germany.
- T. Kokubo, H. Kushitani, S. Sakka, T. Kitsugi and T. Yamamuro, *J. Biomed. Mater. Res.*, **24**, 721 (1990).
- RRUFF Database: Raman, X-ray, Infrared and Chemistry, RRUFF ID R070195.1
- В. С. Горшков, В. В. Тимашев, В. Г. Савельев, Методы физико-химического анализа вяжущих веществ, Высшая школа, Москва, 1981.
- S. R. Federman, V. C. Costa, D. C. L. Vasconcelos, V. L. Vasconcelos, *Mater. Res.*, **10**, 177 (2007).
- M. Kimata, *N. Jb. Miner. Abh.*, **139**, 43 (1980).
- O. M. Goudouri, E. Theodosoglou, E. Kontonasaki, J. Will, K. Chrissafis, P., Kiodis, K. M., Paraskevopoulos, A. R. Boccaccini, *Mater. Res. Bull.*, **49**, 399 (2014).
- I. Rehman, W. Bonfield., *J. Mater. Sci.: Mater. Med.*, **8**, 1 (1997).
- I. R. Gibson, I. Rehman, S. M. Best, W. Bonfield. *J. Mater. Sci.: Mater. Med.*, **12**, 799 (2000).
- S. Agathopoulos, D. U. Tulyaganov, J. M. G. Ventura, S. Kannan, M. A. Karakassides, and J. M. F. Ferreira, *Biomaterials*, **27**, 1832 (2006).
- A. Mateus, C. Barrias, C. Ribeiro, M. P. Ferraz, F. J. Monteiro, *J. Biomed. Mater. Res.*, **86A**, 483 (2008).
- J. Guerrero, R. Unabia, R. M. Vequizo, J. E. Gambe, M. Odarve, and B. B. Sambo, *J. Appl. Sci. Agriculture*, **9**, 321 (2014).

34. L. Radev, *Proc. Appl. Ceram.*, **8**, 155 (2014).
35. I. Fadeeva, V. Komlev, A. Gurin, A. Fomin, S. Barinov, *Powder Metallurgy Progress*, **14**, 181 (2014).
36. R. Singh, A. Srivinasan, *Ceram. Int.*, **36**, 283 (2010).
37. T. Bistey, I. Nagy, A. Simo, C. Hegedus, *J. Dent.*, **35**, 325 (2007).
38. N. Vagenas, A. Gatsouli, C. G. Kontoyannis, *Talanta*, **59**, 831 (2003).
39. M. Sato, S. Matsuda. *Zeitschrift fur Kristallographie*, **120**, 405 (1969).
40. A. Słószarczyk, Z. Paszkiewicz, A. Zima, *Ceram. Int.*, **36**, 577 (2010).
41. S. V. Dorozhkin, *J. Am. Ceram. Soc.*, **90**, 244 (2007).
42. Z. Hong, A. Liu, L. Chen, X. Chen, X. Jing, *J. Non-Cryst. Solids*, **355**, 368 (2009).
43. Y. Zhang, J. Lu, *J. Nanoparticle Res.*, **9**, 589 (2007).
44. G. S. Pappas, P. Liatsi, I. A. Kartsonakis, I. Danilidis, G. Kordas, *J. Non-Cryst. Solids*, **354**, 755 (2008).
45. L. Radev, T. Gerganov, H. Georgiev, A. Kolev, V. Vassileva, R. Iankova, E. Cholakova, *Int. J. Mater. Chem.*, **3A**, 8 (2013).
46. M. Fleet, X. Liu, *Biomaterials*, **28**, 916 (2007).
47. M. Kharaziha, M. H. Fathi, *Ceram. Int.*, **35**, 2449 (2009).

НОВА МЕРВИНИТ/АКЕРМАНИТОВА КЕРАМИКА: IN VITRO БИОАКТИВНОСТ

И. К. Михайлова^{1*}, Л. Радев¹, В. А. Александрова¹, И. В. Цолова¹,
И. М. М. Салвадо², М. Х. В. Фернандес²

¹ Химикотехнологичен и металургичен университет, бул. „Св. Климент Охридски“ № 8,
София, 1756, България

² Авейро Университет и CICECO, Авейро, Португалия

Постъпила декември, 2014 г.; приета януари, 2015 г.

(Резюме)

Керамиката в системата CaO–MgO–SiO₂ напоследък е обект на засилен интерес, защото проявява добра *in vitro* биоактивност и може да се използва за костни импланти. Двухазна калциево-магнезиево-силикатна керамика е получена по зол-гелен метод. Сухият гел с химичен състав 3CaO.MgO.2SiO₂ е термично третиран при 1300 °C за 2 ч. Структурата на синтезираната керамика е изследвана с рентгенофазов анализ, инфрачервена спектроскопия с Фурие трансформация (ИЧ) и сканираща електронна микроскопия (СЕМ). Установени са мервинит, като основна фаза и акерманит – като съпътстваща. Биоактивността *in vitro* на синтезираните керамични образци е определена в симулирана телесна течност (SBF) за различно време на потапяне. Образуването на апатит на повърхността на потапяните образци е регистрирано с ИЧ, СЕМ и енергийно дисперсивна спектроскопия. Промените в концентрацията на йони в SBF след *in vitro* тестовете е определена с оптична емисионна спектроскопия с индуктивно свързана плазма.

На база на получените резултати добра *in vitro* биоактивност е установена за двухазната керамика. Анализирани и дискутирани са особеностите на образуване на апатитов слой в зависимост от фазовия състав на керамиката.

Impact of chemical composition on preparation of nanodimensional spinel ferrites

K. L. Zaharieva^{1*}, Z. P. Cherkezova-Zheleva¹, B. N. Kunev¹,
I. G. Mitov¹, S. S. Dimova²

¹ Institute of Catalysis, Bulgarian Academy of Sciences, "Acad. G. Bonchev" St.,
Bl.11, 1113 Sofia, Bulgaria, E-mail address:zaharieva@ic.bas.bg

² Institute of Polymers, Bulgarian Academy of Sciences, "Acad. G. Bonchev" St.,
Bl.103A, 1113 Sofia, Bulgaria

Received December, 2014; Revised January, 2015

The nanostructured manganese and zinc ferrite-type materials were synthesized using preparation methods such as co-precipitation or co-precipitation and mechanochemical treatment. The physicochemical techniques – Powder X-ray diffraction analysis (PXRD), Mössbauer and Fourier transform infrared (FTIR) spectroscopy were performed in order to establish the phase composition, structure and magnetic behavior of prepared nanodimensional ferrite-type samples. The PXRD results determined that single non-stoichiometric ferrite phase ($Zn_xFe_{3-x}O_4$, $x=0.25$) as well as ferrite ($Zn_xFe_{3-x}O_4$, $x=0.5;1$, $Mn_xFe_{3-x}O_4$, $x=0.25;0.5;1$) and additional akaganeite phases were obtained by co-precipitation procedure. The presence of ferrite and iron phases and elimination of akaganeite was achieved using high-energy ball milling. The synthesized nanosized manganese and zinc ferrite-type materials possess the mean crystallite size about 7–13 nm and 6–13 nm respectively. The superparamagnetic (SPM) and collective magnetic excitations (CME) behavior of the obtained nanodimensional manganese and zinc ferrite-type samples was confirmed by Mössbauer study. In our investigations was determined the relationship on the chemical composition of obtained manganese and zinc ferrites and used methods – co-precipitation and mechanochemical treatment.

Key words: mechanochemical treatment, nanodimensional manganese and zinc ferrite-type materials.

INTRODUCTION

Presently, many researchers have focused their studies on the preparation of nanomaterials, such as spinel ferrite nanocrystals. These materials are interesting for investigations because of their surface effect (large surface-to-volume ratio) and quantum confinement effects (size-dependent properties). These factors influence their chemical and physical properties [1]. Magnetic mixed oxides with structural formula MFe_2O_4 (M = divalent ion, Co, Mg, Mn, Ni), are distinguished to be technologically important materials, because of their controllable properties such as high corrosion resistance, high thermodynamic stability, low magnetic transition temperature, low melting point, high specific heating and high electrical conductivity [2].

Nanocrystalline spinel ferrites can be broadly used in various fields, such as switching and magnetic devices, magnetic refrigeration, catalyst, permanent magnets, ferrofluids, targeted drug delivery, microwave and biomedical applications and sensor technology [3–8]. The attention is directed to the development and use of new approaches to control the morphologies of nanomaterials in order to find the better solution of environmental and health problems [9]. The controllable production of nanodimensional materials including magnetic nanomaterials is the basis for more detailed study of nanoscience and technology because the size, shape and structure of the materials are of great importance determining their catalytic, optical, mechanic or magnetic properties [10]. The synthesis methods for obtaining of nanoparticles which are more environmentally friendly, faster, and more energy efficient have attracted more attention. In this sense, the precipitation technique in aqueous chemistry could find a solution [11]. Mechanical milling is a simple, effective and energy saving method for preparation of nanostructures [12].

* To whom all correspondence should be sent:
E-mail: zaharieva@ic.bas.bg

The aim of the present paper is to investigate the impact of chemical composition on preparation of nanodimensional spinel ferrites. Therefore the series of manganese and zinc ferrite-type samples were obtained by different synthesis methods as co-precipitation or co-precipitation and mechanochemical treatment. The Powder X-ray diffraction analysis, Mössbauer and FTIR spectroscopy were used to study the changes in a chemical composition of ferrite materials.

EXPERIMENTAL

The co-precipitation procedure was carried out for preparation of manganese and zinc [13] ferrite-type materials *Sample A* – $\text{Mn}_{0.25}\text{Fe}_{2.75}\text{O}_4$, *Sample B* – $\text{Mn}_{0.5}\text{Fe}_{2.5}\text{O}_4$, *Sample C* – MnFe_2O_4 , *Sample D* – $\text{Zn}_{0.25}\text{Fe}_{2.75}\text{O}_4$, *Sample E* – $\text{Zn}_{0.5}\text{Fe}_{2.5}\text{O}_4$ and *Sample F* – ZnFe_2O_4 . The starting 0.03 M aqueous solutions of $\text{FeCl}_2 \cdot 4\text{H}_2\text{O}$, $\text{FeCl}_3 \cdot 6\text{H}_2\text{O}$ and $\text{MnCl}_2 \cdot 4\text{H}_2\text{O}$ or ZnCl_2 were prepared and mixed in a ratio of 3:8:1, 1:4:1, 0:2:1. The pH values of mixtures were reached 12.5 and 13 by dropping a precipitant 0.3 M NaOH at continuous stirring. After co-precipitation procedure the mixtures was stirred for one hour. The prepared brown precipitates were centrifuged and washed with distilled water up to neutral reaction (pH=7). The products were dried at 35 °C. The co-precipitated *Sample A*, *Sample B*, *Sample C*, *Sample E* and *Sample F* were mechanochemically treated in order to obtain *Sample G* – $\text{Mn}_{0.25}\text{Fe}_{2.75}\text{O}_4$, *Sample H* – $\text{Mn}_{0.5}\text{Fe}_{2.5}\text{O}_4$, *Sample I* – MnFe_2O_4 , *Sample J* – $\text{Zn}_{0.5}\text{Fe}_{2.5}\text{O}_4$ and *Sample K* – ZnFe_2O_4 . The milling process was performed in argon (*Sample A* and *Sample B*), helium (*Sample E*) or air (*Sample C* and *Sample F*) atmosphere for 1 (*Sample F*) or 2 (*Sample A*, *Sample B*, *Sample C* and *Sample E*) hours and rotation speed 500 rpm. The weight ratio between sample and balls was 1:30. The Highenergy planetary ball mill type PM 100, Retsch, Germany and stainless steel grinding jar of 50 ml volume was used for mechanochemical treatment. The phase composition and magnetic behavior of obtained manganese and zinc ferrite-type materials were physicochemically characterized by Powder X-ray diffraction analysis, Mössbauer and FTIR spectroscopy. The PXRD spectra of manganese and zinc ferrite-type samples during the preparation were recorded on a TUR M62 apparatus with computer management and data collection, working with HZG-4 goniometer and $\text{CoK}\alpha$ radiation. The JCPDS database (Powder Diffraction Files, Joint Committee on Powder Diffraction Standards, Philadelphia PA, USA, 1997) was used to establish the phases. The average crystallite size, lattice microstrain parameter and unit cell parameter of the

ferrite materials were estimated by Williamson-Hall diagram [14].

Mössbauer investigations were performed with apparatus Wissenschaftliche Elektronik GmbH, working with a constant acceleration mode, $^{57}\text{Co}/\text{Rh}$ source (activity ≈ 50 mCi) and $\alpha\text{-Fe}$ standard. The mössbauer parameters of hyperfine interactions of spectral components: isomer shift (IS), quadrupole splitting (QS), hyperfine effective magnetic field in the site of iron nuclei (H_{eff}), line widths (FWHM) and component relative weights (G) were determined by computer fitting. FTIR measurements were collected with a Fourier infrared spectrometers: Bruker-Vector 22 and IRAffinity-1 “Shimadzu”.

RESULTS AND DISCUSSION

On the Figures 1 and 2 are presented PXRD spectra of obtained nanostructured manganese and zinc ferrite-type materials. The co-precipitated *Samples A*, *B* and *C* contain manganese ferrite (PDF-73-1964) and additional akaganeite (PDF-34-1266) phases (Fig. 1). Powder X-ray diffractograms of zinc ferrite-type samples registered the presence of single non-stoichiometric zinc ferrite phase $\text{Zn}_x\text{Fe}_{3-x}\text{O}_4$ (PDF-01-1109; 75-0449) for *Sample D*. The ferrite $\text{Zn}_x\text{Fe}_{3-x}\text{O}_4$ (PDF-01-1109) and different amount of intermediate akaganeite (PDF-34-1266) phases are determined in co-precipitated *Samples E* and *F* (Fig. 2) [13]. The mechanochemical treatment of co-precipitated manganese and zinc ferrite-type materials after one or two hours in inert media (argon, helium) or air initiate the formation of spinel ferrite $\text{Zn}_x\text{Fe}_{3-x}\text{O}_4$ or $\text{Mn}_x\text{Fe}_{3-x}\text{O}_4$ and iron (Fe) (PDF-87-0721) phases in *Samples G*, *H*, *I*, *J* and *K*. The presence of iron phase in samples is due to contamination during the milling process. The additional akaganeite phase disappeared during the high-energy ball milling process. The calculated average crystallite size, lattice microstrain parameter and unit cell parameter of studied spinel ferrite phases are illustrated in Table 1. The determined values correspond to the prepared nanodimensional manganese and zinc ferrite materials with mean crystallite size about 7–13 nm and 6–13 nm.

The Mössbauer spectra at room temperature of obtained nanostructured manganese and zinc ferrite-type samples are shown on Figures 3 and 4. The spectra of *Samples A*, *B*, *D*, *G*, *I*, *J* and *K* are superposition of sextet and doublet components. The doublet lines only are registered in Mössbauer spectra of the other three co-precipitated *Samples C*, *E* and *F*. The calculated Mössbauer parameters after the best computer fitting of spectra with respective components are presented in Table 2. The calculated hyperfine parameters of sextet components can

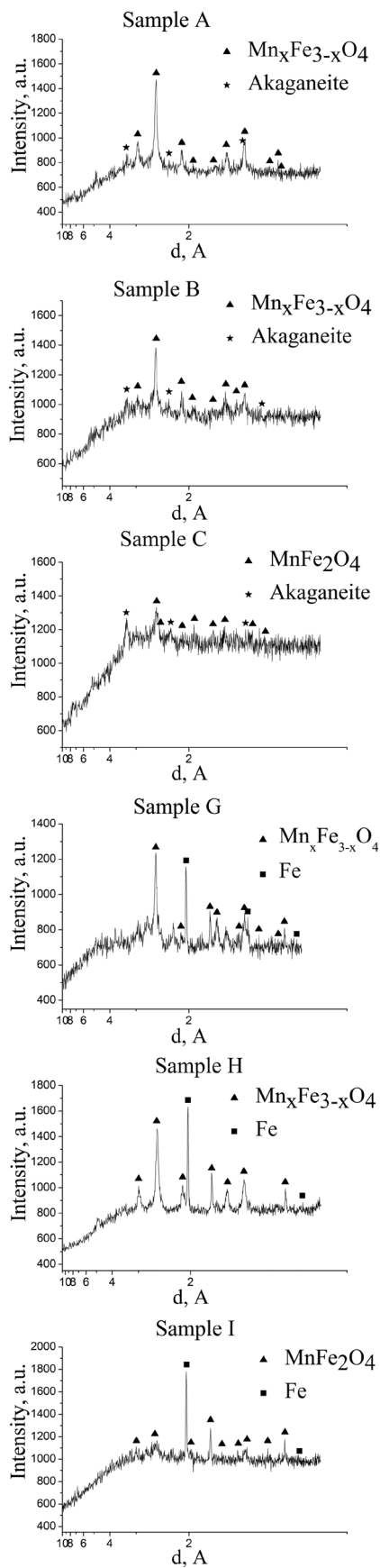


Fig. 1. PXR patterns of synthesized nanosized manganese ferrite-type samples

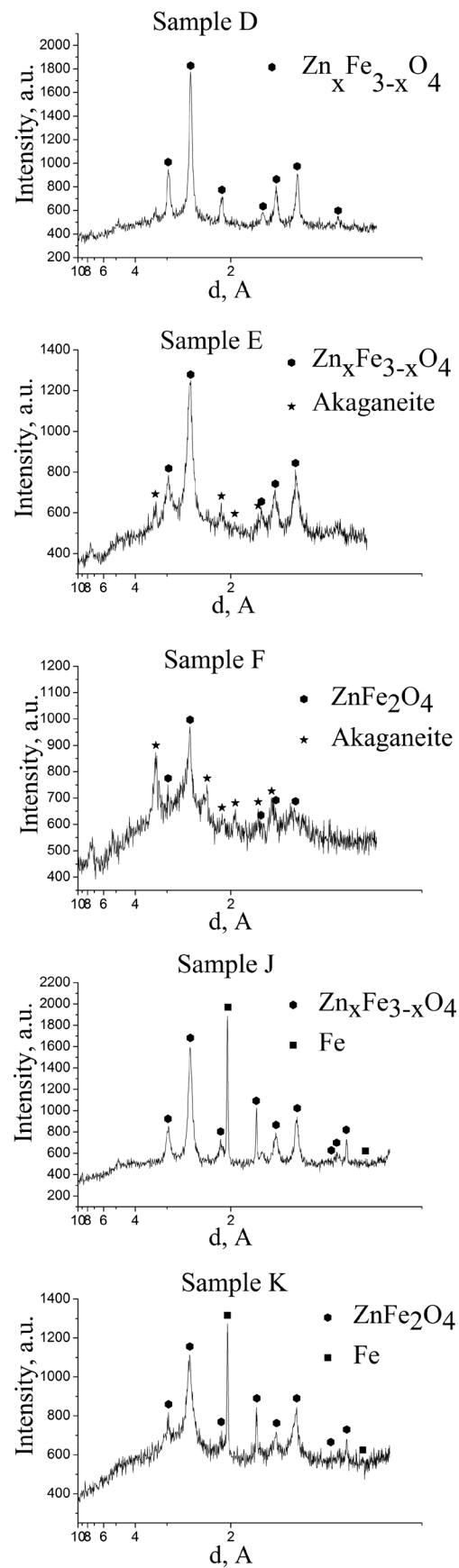


Fig. 2. PXR patterns of synthesized nanosized zinc ferrite-type samples

Table 1. Calculated values of mean crystallite size (D), lattice strain (ϵ) and unit cell parameter (a) of ferrite phases

Sample	D, nm	ϵ , a.u	a, Å
Sample A	9.5	$4.2 \cdot 10^{-3}$	8.485
Sample B	9.3	$3.7 \cdot 10^{-3}$	8.489
Sample C	7.8	$4.1 \cdot 10^{-3}$	8.497
Sample D	12.8	$5.9 \cdot 10^{-3}$	8.412
Sample E	6.8	$4.2 \cdot 10^{-3}$	8.421
Sample F	6.9	$4.2 \cdot 10^{-3}$	8.447
Sample G	12.5	$4.3 \cdot 10^{-3}$	8.415
Sample H	9.5	$4.3 \cdot 10^{-3}$	8.486
Sample I	7.8	$4.1 \cdot 10^{-3}$	8.496
Sample J	7.8	$4.1 \cdot 10^{-3}$	8.383
Sample K	7.8	$4.1 \cdot 10^{-3}$	8.382

be related to tetrahedrally coordinated Fe^{3+} ions in a spinel phase – Sxt1 and octahedrally coordinated $Fe^{2.5+}$ ions in a spinel phase – Sxt2 for *Sample D* [13]. The sextet component Sxt1 corresponds to iron ions show collective magnetic excitations (CME) behavior in RT spectra of *Samples A* and *B*. The

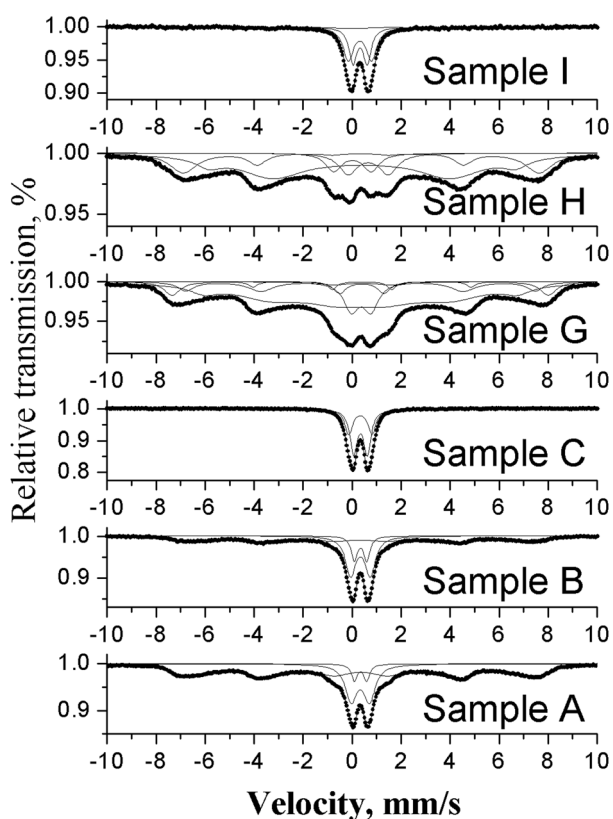


Fig. 3. Mössbauer spectra at room temperature of obtained nanodimensional manganese ferrite-type materials

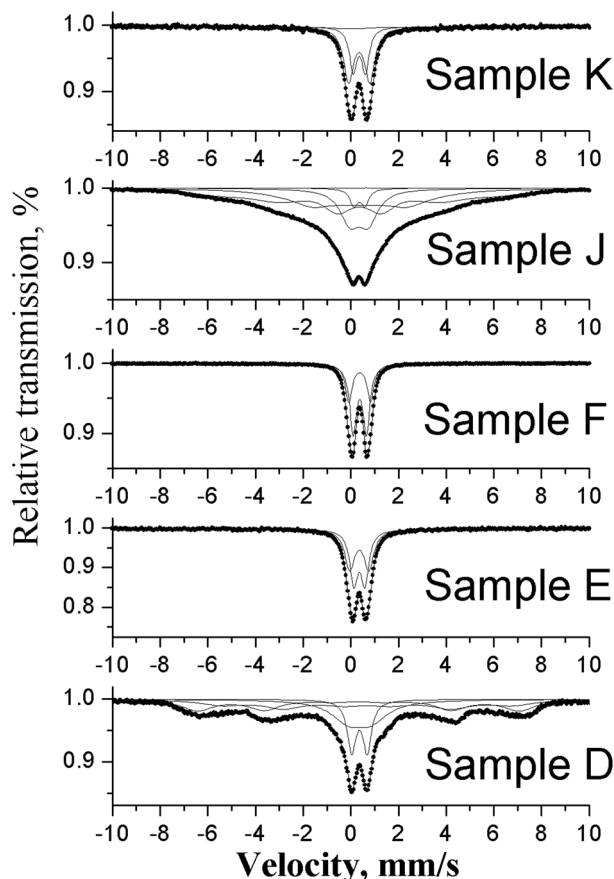


Fig. 4. Mössbauer spectra at room temperature of obtained nanodimensional zinc ferrite-type materials

calculated hyperfine parameters of doublet components in Mössbauer spectrum of *Sample D* could be attributed to the presence of ferrite particles with superparamagnetic (SPM) behaviour [13]. On the other hand the doublet components partially include also the existence of some iron ions in intermediate akaganeite phase (*Samples A, B, C, E* and *F*). The characteristic components for nanosized metal iron phase are registered in the spectra of mechanochemically treated manganese and zinc ferrite-type materials as doublet (Db1), singlet (Sng) or sextet (Sxt) components belonging to iron rich and Mn or Zn rich regions [15]. In the Mössbauer spectra of *Samples G, I, J* and *K* after mechanochemical process are observed two superparamagnetic doublets attributed to the presence of ferrite particles with superparamagnetic (SPM) behavior. The determined hyperfine parameters of three (Sxt1, Sxt2 and Sxt3) or two (Sxt1 and Sxt2) sextet components can be attributed to iron ions show collective magnetic excitations (CME) behavior for *Samples G* and *H*. The presence of spinel phase presented by two sextet components – Sxt 1 due to tetrahedrally coordinated

Table 2. Mössbauer parameters of nanostructured manganese and zinc ferrite-type samples at RT

Sample	Components	IS, mm/s	QS, mm/s	H _{eff} , T	FWHM, mm/s	G, %
Sample A	Sxt 1 – Fe – spinel, CME	0.35	0	43.2	1.72	70
	Dbl 1 – SPM, core/Akaganeite	0.35	0.50	–	0.28	6
	Dbl 2 – SPM, shell/Akaganeite	0.34	0.75	–	0.57	24
Sample B	Sxt 1 – Fe – spinel, CME	0.35	0.03	42.6	1.85	52
	Dbl 1 – SPM, core/Akaganeite	0.35	0.51	–	0.30	13
	Dbl 2 – SPM, shell/Akaganeite	0.34	0.80	–	0.50	35
Sample C	Dbl 1 – SPM, core/Akaganeite	0.34	0.56	–	0.35	61
	Dbl 2 – SPM, shell/Akaganeite	0.34	0.95	–	0.39	39
Sample D	Sxt 1 – Fe ³⁺ -tetra, spinel	0.29	0.01	42.0	1.61	29
	Sxt 2 – Fe ^{2.5+} -octa, spinel	0.69	0	37.8	2.02	58
	Dbl 1 – SPM, core	0.36	0.66	–	0.44	21
	Dbl 2 – SPM, shell	0.36	0.97	–	1.62	22
Sample E	Dbl 1 – SPM, core/Akaganeite	0.36	0.47	–	0.39	51
	Dbl 2 – SPM, shell/Akaganeite	0.36	0.81	–	0.49	49
Sample F	Dbl 1 – SPM, core/Akaganeite	0.37	0.56	–	0.34	64
	Dbl 2 – SPM, shell/Akaganeite	0.37	0.92	–	0.33	36
Sample G	Sxt 1 – Fe – spinel, CME	0.36	–0.08	47.7	0.81	10
	Sxt 2 – Fe – spinel, CME	0.37	–0.06	44.3	0.82	13
	Sxt 3 – Fe – spinel, CME	0.35	0	39.7	1.34	61
	Dbl 1 – SPM, shell	0.37	0.80	–	0.74	12
	Dbl 2 – SPM, core	0.39	1.80	–	0.63	4
Sample H	Sxt 1 – Fe – spinel, CME	0.35	0.03	45.1	1.35	23
	Sxt 2 – Fe – spinel, CME	0.39	0.02	39.1	1.26	57
	Dbl – Fe – metal phase	0.01	1.53	–	0.81	19
	Sng – Fe – metal phase	–0.01	–	–	0.34	1
Sample I	Sxt – Fe – metal phase	0	–	10.2	6.1	14
	Dbl 1 – SPM, core	0.32	0.95	–	0.50	47
	Dbl 2 – SPM, shell	0.33	0.58	–	0.38	39
Sample J	Sxt – Fe – metal phase	0	0	24.8	0.57	1
	Sxt 1 – Fe ³⁺ – tetra, spinel	0.36	–0.01	35.8	0.11	42
	Sxt 2 – Fe ³⁺ – octa, spinel	0.38	–	21.3	3.04	33
	Dbl 1 – SPM, core	0.36	0.46	–	0.40	4
	Dbl 2 – SPM, shell	0.35	0.77	–	0.99	20
Sample K	Sxt – Fe – metal phase	0	0	10.6	5.04	12
	Dbl 1 – SPM, core	0.36	0.51	–	0.37	33
	Dbl 2 – SPM, shell	0.35	0.89	–	0.51	55

Fe³⁺ ions and Sxt 2 due to octahedrally coordinated Fe³⁺ ions are registered in the Mössbauer spectrum at RT of *Sample J*. The obtained Mössbauer results confirm the powder X-ray diffraction investigations about registered phases in synthesized ferrite samples. The FTIR spectra of co-precipitated and mechanochemically treated nanosized ferrite-type materials are displayed on Figure 5. The vibrations observed in the region 423–563 cm⁻¹ are characteristic of the metal-oxygen bonds in the tetrahedral and octahedral sites of the spinel manganese and zinc ferrites [1, 4, 16]. The registered absorption bands at about 3423–3426 cm⁻¹ and 1630–1637 cm⁻¹ correspond to the stretching and bending vibrations of the OH groups [10]. The absorption bands at about 1195 cm⁻¹ could be attributed to the stretch-

ing vibrations of Fe³⁺–O²⁻ [17]. The FTIR spectra of co-precipitated nanostructured zinc ferrite-type samples are discussed in our previous study [13] in full. The FTIR investigations are in very good agreement with presented Powder X-ray diffraction and Mössbauer data.

CONCLUSIONS

The nanodimensional manganese and zinc ferrite-type materials were successfully obtained by co-precipitation or co-precipitation and mechanochemical treatment. The prepared ferrite-type samples have a high dispersity and average crystallite size between 7–13 nm and 6–13 nm. The relation

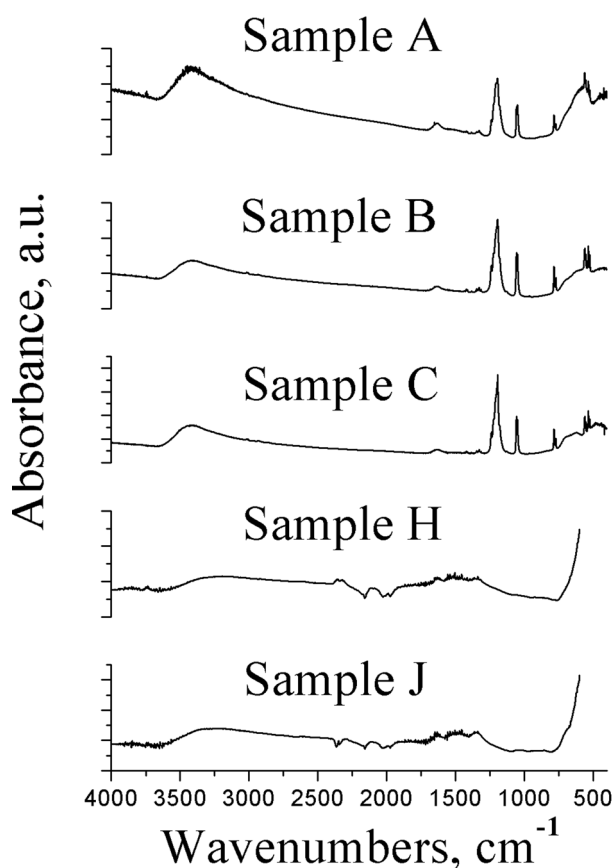


Fig. 5. FTIR spectra of prepared manganese ferrite-type and zinc ferrite-type nanopowders

between chemical composition of obtained manganese and zinc ferrite-type materials and different synthesis methods as co-precipitation and mechanochemical treatment was found. The presence of pure spinel ferrite phase is established in the case of an obtained nanosized $Zn_xFe_{3-x}O_4$, $x=0.25$ by chemical co-precipitation method. The additional intermediate phase as akaganeite is observed in other co-precipitated manganese and zinc containing ferrite samples. The removal of additional akaganeite phase in manganese and zinc ferrite-type materials was realized by the mechanochemical treatment. The formation of spinel ferrite and iron phases is observed during the milling process. The Mössbauer studies at room temperature established that synthesized manganese and zinc containing ferrite materials possess superparamagnetic (SPM) and collective magnetic excitations (CME) behavior.

Acknowledgements: This research work was supported by European Social Fund within the framework of Operating Program "Development of Human Resources" (Grant BG051PO001-3.3.06-0050). The authors from IC-BAS appreciate the financial support of the Bulgarian Science Fund of the Bulgarian Ministry of Education and Science by Project FNI-E02/17/2014.

REFERENCES

1. M. Goodarz Naseri, E. Bin Saion, H. Abbastabar Ahangar, M. Hashim, A.H. Shaari, *Journal of Magnetism and Magnetic Materials*, **323**, 1745 (2011).
2. D. Gherca, N. Cornei, O. Mentré, H. Kabbour, S. Daviero-Minaud, A. Pui, *Applied Surface Science*, **287**, 490 (2013).
3. D. Chen, H.-Y. Liu, L. Li, *Materials Chemistry and Physics*, **134**, 921 (2012).
4. S. Mohapatra, S. R. Rout, A. B. Panda, *Colloids and Surfaces A: Physicochem. Eng. Aspects*, **384**, 453 (2011).
5. Z. Ž. Lazarević, Č. Jovalekić, A. Recnik, V. N. Ivanovski, M. Mitrić, M. J. Romčević, N. Paunović, B.P. Cekić, N. Ž. Romčević, *Journal of Alloys and Compounds*, **509**, 9977 (2011).
6. D. Gherca, A. Pui, V. Nica, O. Caltun, N. Cornei, *Ceramics International*, **40**, 9599 (2014).
7. N. M. Deraz, S. Shaban, *J. Anal. Appl. Pyrolysis*, **86**, 173 (2009).
8. D. Chen, Y. Zhang, Z. Kang, *Chemical Engineering Journal*, **215–216**, 235 (2013).
9. H. Chen, P. K. Chu, J. He, T. Hu, M. Yang, *Journal of Colloid and Interface Science*, **359**, 68 (2011).
10. P. Guo, G. Zhang, J. Yu, H. Li, X. S. Zhao, *Colloids and Surfaces A: Physicochem. Eng. Aspects*, **395**, 168 (2012).
11. F. Giovannelli, C. Autret-Lambert, C. Mathieu, T. Chartier, F. Delorme, A. Seron, *Journal of Solid State Chemistry*, **192**, 109 (2012).
12. T. Şimşek, S. Akansel, Ş. Özcan, A. Ceylan, *Ceramics International*, **40**, 7953 (2014).
13. K. Zaharieva, Z. Cherkezova-Zheleva, B. Kunev, M. Shopska, V. Petkova, J. Krstić, I. Mitov, *Nanoscience and Nanotechnology* **14** (Eds. E. Balabanova, E. Mileva), (2014), 39-42.
14. G. K. Williamson, W. H. Hall, *Acta Metallurgica*, **1** (1), 22 (1953).
15. O. G. Sokhalov, A. V. Katsov, G. V. Karpenko, Superplasticity and corrosion strength of two phase Fe-Mn alloy, Naukova Dumka, Kiev, 1977.
16. G. Fan, Z. Gu, L. Yang, F. Li, *Chemical Engineering Journal*, **155**, 534 (2009).
17. K. Ahalya, N. Suriyanarayanan, V. Ranjithkumar, *Journal of Magnetism and Magnetic Materials*, **372**, 208 (2014).

ВЛИЯНИЕ НА ХИМИЧНИЯ СЪСТАВ ВЪРХУ ПОЛУЧАВАНЕТО НА НАНОРАЗМЕРНИ ШПИНЕЛНИ ФЕРИТИ

К. Л. Захариева^{1*}, З. П. Черкезова-Желева¹, Б. Н. Кунев¹,
И. Г. Митов¹, С. С. Димова²

¹ *Институт по катализ, Българска академия на науките, ул. „Акад. Г. Бончев“,
бл. 11, 1113 София, България, имейл: zaharieva@ic.bas.bg*

² *Институт по полимери, Българска академия на науките, ул. „Акад. Г. Бончев“,
бл. 103А, 1113 София, България*

Постъпила декември, 2014 г.; приета януари, 2015 г.

(Резюме)

Наноструктурирани манганови и цинкови феритен тип материали бяха синтезирани чрез използване на методи като съутаяване или съутаяване и механохимична обработка. Бяха използвани физикохимични техники – рентгенофазов анализ, мьосбауерова и инфрачервена спектроскопия с фурие трансформация с цел да бъде установен фазовия състав, структура и магнитното поведение на получените наноразмерни феритен тип проби. Резултатите от рентгенофазовия анализ показаха, че еднофазен нестехиометричен ферит ($Zn_xFe_{3-x}O_4$, $x=0,25$), а също така ферит ($Zn_xFe_{3-x}O_4$, $x=0,5; 1$, $Mn_xFe_{3-x}O_4$, $x=0,25; 0,5; 1$) и допълнителна фаза акагенит бяха получени чрез процедура на съутаяване. Присъствието на феритна и желязна фаза и премахването на акаганеита беше постигнато чрез използване на високоенергийно мелене. Синтезираните наноразмерни манганови и цинкови феритен тип материали имат съответно среден размер на кристалита 7–13 nm и 6–13 nm. Суперпарамагнитното поведение и колективното магнитно възбуждане на получените наноразмерни манганови и цинкови феритен тип проби беше потвърдено от Мьосбауеровите изследвания. В нашите изследвания беше намерена връзка между химичния състав на получените манганови и цинкови ферити и използваните методи – съутаяване и механохимична обработка.

Synthesis and characterization of silica hybrid materials applicable for defect remediation of concrete

E. V. Todorova, G. E. Chernev*, St. P. Djambazov

*Department of Silicate technology, University of Chemical Technology and Metallurgy,
8 Kl. Ohridski Blvd., 1756, Sofia, Bulgaria*

Received December, 2014; Revised January, 2015

Application of silica hybrids in concrete field, in particular remediation of the defects is a new area for these materials. It is well known that the concrete variety is the most used and also threatened by destruction material. Formation of defects during the exploitation period is a normal process and remediation via materials, which can block the defects, is the optimal way for preventing their further distribution.

In the present work silica hybrid materials applicable for defect remediation of concrete were synthesized via sol-gel technique. Inorganic network obtained via transformation from liquid to dense material after drying was obtained via tetraethyl orthosilicate. Flexibility and reactivity of silica network is achieved by addition of two organic monomers, known as biocompatible and high reactive – chitosan and polyethylene glycol. After preparation of inorganic – organic solution in a different ratio, CaCl_2 , as a source of calcium ions were added. The structural results presented formation of amorphous, smooth, high reactive structures. The important factor for application of the hybrid is surface microstructure, as the results showed formation of homogeneous surface on which particles (5 nm – 1 μm) are evenly distributed. Particle size and improvement of the roughness increase with increasing the organic components value.

Compatibility and possibility of prepared hybrids to form CaCO_3 was investigated by immobilization of bacterial cells, which synthesized enzyme urease. The biocompatibility and favorable effect of the obtained materials showed, that they can be used for defect remediation of concrete and the treatment can prevent the destruction for a long period.

Key words: Silica hybrid materials, bacterial cells, concrete remediation.

INTRODUCTION

Concrete materials are one of the most used and distributed materials, which are characterized with high resistance, stability and long term durability. During their exploitation period formation of micro cracks is a normal process. During their exploitation period formation of micro cracks is a normal process, as their size increase and can lead to gradually destruction of concrete [1]. The prevention of destruction via chemical way can successfully reduce distribution and growth of the cracks and extend the workability of concrete materials [2]. This type of concrete is called self – healing concrete, as their development and optimization represent interest for many researcher groups [3]. Generally, self – heal-

ing effect of concrete implemented by formation of CaCO_3 and $\text{Ca}(\text{OH})_2$ or after second hydration of unreacted cement on the place of formed cracks. Unfortunately, the mentioned processes are less achievable, for example the second hydration of cement particles is possible for concrete materials up to 7 days after their formation [4]. These problems can be overcome via using of innovative materials, which exhibit self – healing property. They can be added in the concrete mixture or applied as coating for external treatment of micro cracks. Mineral additives, hollow fibers/tubes, microcapsules and living cells are proven as potential self – healing agents [5, 6].

Sahmaran et al. [7] investigated the self – healing effect of three mineral mixtures, based on fly ash with low and high concentration of calcium as well as slag. The permeability of chlorine ions in the structure of concrete samples is investigated and it is established, that low permeability exhibit the sample with slag, as mineral additive. This is

* To whom all correspondence should be sent:
E-mail: georgi_chernev@yahoo.com

due to the chemical composition of the slag, as well as small size of the particles [8]. The authors also established that prepared self – healing concrete showed improve properties in moist media. The disadvantage of these self – healing materials is connected with formation of dense structures, which do not prevent formation of cracks and their further distribution [9].

Another opportunity for obtaining self – healing concrete is addition of hollow fibers/tubes in the volume, as their remediation ability is due to material, which is inside [10]. After formation of crack, these materials are released from the fiber/tube and filled the crack. Kim et al. [11] investigated the self – healing effect on concrete cracks using ceramic and glass fibers filled with two type's polyurethane. The polyurethane is chosen, because of its low viscosity and ability to shrink after polymerization. Based on the obtained experimental results the authors established that the ceramic fibers exhibit higher efficiency than glass ones. The efficiency of polyurethane as crack filler depends of position of fibers. The development of correct position of fibers/tubes in concrete sample plays unfavorable effect on their potential application [12].

One of the effective methods for defect remediation of concrete is incorporation of bacterial cells [13]. The compatible cells for that purpose are these, which synthesized enzyme urease, which can provide formation of calcium carbonate [14]. The mechanism of CaCO_3 formation is connected with enzyme hydrolysis of urea, as a result of which NH_4 and CO_3 ions are obtained. As a result of high pH and presence of calcium ions, they can easily interact with CO_3 units and formed calcium carbonate as a precipitate. Sources of calcium ions can be organic components and salts. Calcium lactate is a salt, which exhibit good compatibility with bacterial cells and favor further formation of CaCO_3 . Furthermore, it is established that incorporation of calcium lactate and bacterial cells do not reduce mechanical stability of concrete. The limitation of this type self – healing method is correlated with low stress resistance of the cells and alkali media. Jonckers et al. [15] used for that purpose bacterial cells which exhibit high alkali resistance. Based on the obtained results this researcher group established, that the enzyme activity of cells is kept up to 7 days after addition in the concrete mixture in combination with calcium lactate. After this period the biological activity is slightly reduced, because of the reduce pore size in the concrete sample. Wiktor et al. [16] also investigated the self – healing effect of bacterial cells *Bacillus alkalinitrilicus* and calcium lactate, as they import them in clay particles for cell protection. The clay particles are chosen, because of their ability to expand after addition in concrete

mixture, as this behavior ensures the maintenance of contact surface area for the cells. After preparation of self – healing concrete, the samples are crushed and dipped in water at ambient conditions. After 100 days, the authors established that the formed cracks are filled with white material. The analysis of formed material showed that it is based on calcium, oxygen and carbon, which proved the success formation of CaCO_3 .

For remediation of concrete via self – healing process is possible via development of material, containing bacterial cells and used as (and applied as) external treatment agent. Mink et al. [17] observed the self – healing effect of solution applied on the surface of concrete samples. The solution contains bacterial cells and calcium salt, which favor formation of calcium carbonate. The experimental results established the optimal quantity of initial components for self – healing of concrete. The used solution easy penetrates in the concrete volume, as a result of which it functionality is reduced. The reduce activity of bacterial cells play unfavorable effect on potential application of this solution. The problem can be solved as development of material, in the role of carrier for bacterial cells. Also in the structure it should contain calcium ions for facilitated formation of calcium carbonate.

Wang et al. [18] treat the concrete cracks with a mixture of silica gel and bacterial cells. The self – healing mixture based on silica sol and bacteria suspension (bacterial cells and NaCl) is poured on the crack place. After transformation of silica sol in a dense material, due to condensation and drying process, the treat concrete sample is immersed in a water solution of urea and calcium ions. The result from the test showed, that the crack is filled with calcium carbonate. Furthermore, it is established that the treat concrete sample exhibit better water resistance than untreated one. The disadvantages of silica materials are connected with their reduce reactivity, as well as reduce reactivity and free surface area during the condensation and drying process, which play unfavorable effect on the efficiency of bacterial cells.

Hybrid materials based on silica, which exhibit affinity to bacterial cells, synthesized enzyme urease are good candidate for development of agent for remediation of concrete defects. The silica component guarantees the stability and durability of self – healing material [19]. Furthermore, this type of materials can easily formed strong interactions with concrete after application. On the other hand, the organic components, which are used, should exhibit affinity to bacterial cells and improve their enzyme activity [20]. The enzyme activity depends of organic biocompatibility, as the cell affinity to the hybrid structure is determined by organic reactivity.

Chitosan is organic component, which exhibit favorable effect to different living cells. The broad application of this polysaccharide is due to free reactive amino and hydroxyl groups, which contains. In acidic media the amino groups can be easily transformed in positive groups, which can form strong interactions with negative biological cells. On the other hand hydroxyl groups can interact with positive cells [21, 22]. Combination of chitosan and silica in one hybrid material lead to formation of structures which are applicable in different fields, where the biotechnology play important role – pharmacy, medicine, food industry, environmental safety and others. This type of hybrid materials are characterized with improve biocompatibility, stability and reactivity [23, 24].

For improving the quantity of reactive centers for possible contact and interaction of hybrid material and bacterial cells combination of chitosan with another organic component is preferred. Polyethylene glycol is synthetic organic component, which can be used for that purpose, because of its biocompatibility, non toxicity and reactivity. This type of material is applicable in different fields from medicine, biotechnology and food industry to technical industry [25]. Tanuma et al. [26] investigated the properties of materials on the based on cross linked polyethylene glycol and chitosan. From the obtained results the authors established that these materials change their structure with pH variation – they expand or reduce the volume if the pH is below 7 the crosslinked organic chains expand, due to specific behavior of chitosan, and opposite situation is observed if the pH is higher than 7.

On the other hand the addition of polyethylene glycol improves the reactivity and hydrophilicity of the hybrid structure due to hydroxyl end groups. The authors also investigated the influence of molecular weight of PEG and established that the mentioned properties are reduced with increasing molecular weight.

The aims of the present study are synthesis, structural characterization and biological application of silica hybrid materials with participation of chitosan and polyethylene glycol, applicable as carrier for bacterial cells and further application for remediation of concrete defects.

EXPERIMENTAL

Synthesis

The silica hybrid materials applicable for external treatment of concrete defects are synthesized via sol-gel technique at ambient conditions, as initial components are used: tetraethyl orthosilicate (TEOS,

98%, Sigma Aldrich), chitosan (CS, DD – 75%, Fluka), acetic acid (99.8%, Valerus), polyethylene glycol (PEG, MW 400, Valerus), calcium chloride (CaCl_2 , 98% Valerus), buffer solution (FICAL, pH = 7, containing $\text{Na}_2\text{HPO}_4 \cdot 2\text{H}_2\text{O} - \text{KH}_2\text{PO}_4$, HISTM), hydrochloric acid (HCl, 37%, Merck), distilled water (dH_2O).

The first stage of synthesis is connected with hydrolysis of TEOS using dH_2O and HCl, as initiator of process, as the ratio of these three components is $\text{TEOS}/\text{dH}_2\text{O}/\text{HCl} = 1/0.4/0.4$. The organic component CS is previously dissolved in acetic acid solution for better distribution in the silica matrix. After fully dissolution of CS, calculate amount is mixed with the other organic component PEG. Calcium chloride is also previously dissolved in dH_2O , as the ratio is $\text{H}_2\text{O}/\text{CaCl}_2 = 1/0.1125$.

Second stage of synthesis is correlated with mixing of silica sol and organic components, as for preparation of homogeneous structures the hybrid solution is stirred for 30 min via magnetic stirrer. After that the solution of calcium ions with concentration 0.25 g/ml, as well as buffer solution are added for development of mixture compatible for immobilization of bacterial cells. It is established, that the buffer solution led to increasing of pH from 2 to 5. Obtained hybrid mixtures are dried at room temperature in Petri dishes. For establishment of the influence of nature and quantity of organic components the inorganic/organic ratio is varied as follows:

- $\text{TEOS}/\text{buffer solution} = 1/1$ (SiCa)
- $\text{TEOS}/\text{CS}/\text{PEG}/\text{buffer solution} = 1/0.056/0.056/1.11$ (SiCSPCa1)
- $\text{TEOS}/\text{CS}/\text{PEG}/\text{buffer solution} = 1/0.214/0.214/1.43$ (SiCSPCa3)

Structural Characterization

The structural characterization is made using four different methods for analysis: X-ray diffraction (XRD, Bruker D8 Advance, $\text{CuK}\alpha$ radiation with scan rate of $0.02^\circ \cdot \text{min}^{-1}$ in 2θ range between 10 and 80°), Fourier Transforming InfraRed spectrometer (FTIR, MATSON 7000, KBr pellet's, scanning range $300\text{--}400 \text{ cm}^{-1}$), Scanning Electron Microscopy (SEM, Philips 515) and Atomic Force Microscopy (AFM, Nano Scope Tapping Mode TM). The pH of hybrid solutions is measured via pH meter (Scott, handylab pH 11/SET, Germany).

Biological test

Application of synthesized silica hybrid materials for concrete remediation is investigated via immobilization of bacterial cells *Bacillus sphaericus*. The used cells produced enzyme urease, which favors

formation of calcium carbonate. The hybrid materials are dipped in bacterial suspension for achievement of immobilization process. After that obtained system material (as a carrier) with the bacterial cells are putted in a urea solution for initiating formation of CaCO_3 . For establishment of compatibility of obtained hybrid materials, the biological activity of cells, which are immobilized, is measured.

RESULTS AND DISCUSSION

The FTIR spectra (Fig. 1) showed characteristic peaks of silica network formed via sol-gel technique at room temperature, in the role of backbone inorganic component of hybrids (Si-O-Si asymmetric and symmetric vibrations – 1080 and 450, 560, 790 cm^{-1} ;

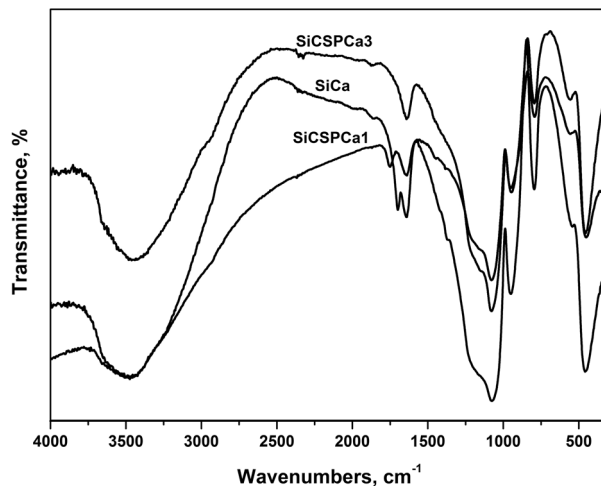


Fig. 1. FTIR spectra of obtained silica hybrid materials

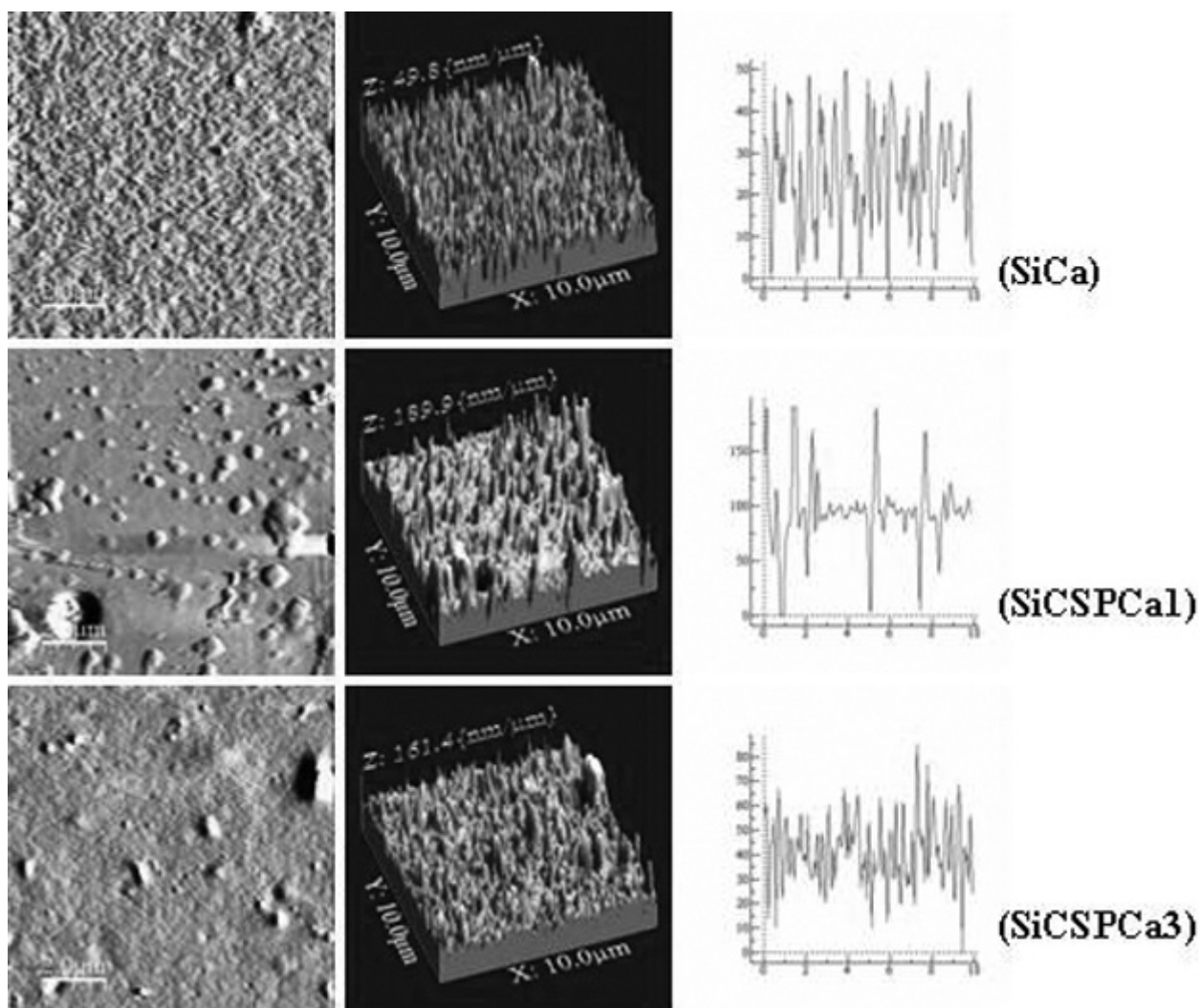


Fig. 2. AFM 2d, 3d topography and roughness profile of obtained hybrid materials

Si-OH – 950 cm^{-1} , Si-O-C – 1000–1200 cm^{-1} , H-OH – 1640 and 3400 cm^{-1}) [27].

The wide range peak around 1100 cm^{-1} is also corresponding to C-C structural units of CS and PEG. The existence of hydroxyl and amino peaks, which play important role for interaction with bacterial cells and incorporate in the hybrid structure due to used organic components are associated with the peaks at 950, 1640 and 3400 cm^{-1} [28].

The surface microstructure is investigated via AFM analysis, because it plays important role for contact area of cells (Fig. 2). The 2d and 3d images of sample SiCa showed formation of rough surface, as the z-coordinate is 49.5 $\text{nm}\cdot\mu\text{m}$. The third micrograph, which presented roughness profile, showed formation of particles, which are closely relative to each other. The dense distributions of the particles lead to limitation of contact surface area for bacterial cells.

The results for sample SiCSPCa1 showed formation of homogeneous silica network into which the particles are evenly distributed. The successful preparation of ordered, amorphous hybrid struc-

tures, established from AFM results is confirmed via obtained XRD patterns. The z-coordinate increase up to 159.9 $\text{nm}\cdot\mu\text{m}$, and the distribution profile showed improvement of contact surface area. Optimal results for roughness and contact surface area presented sample SiCSPCa3.

The possibility of obtained hybrid materials to be applied as self – healing agents for concrete defects is connected with compatibility of them with bacterial cells, synthesized enzyme urease, as well as further formation of calcium carbonate. Model schema of obtained hybrid structure, based on obtained FTIR spectra, showed successful formation of silica network, distribution of CS, PEG and calcium ions in it. The possible reactive centers, reactive groups on cell walls, as well as their potential interaction are also presented on the Figure 3.

The biocompatibility is established via measurement of biological activity of immobilized cells. The obtained results, which presented the activity for a period of time are shown on Figure 4. The activity is measured every 12 h. The result for sample SiCa showed, that the Initial activity of immobilized

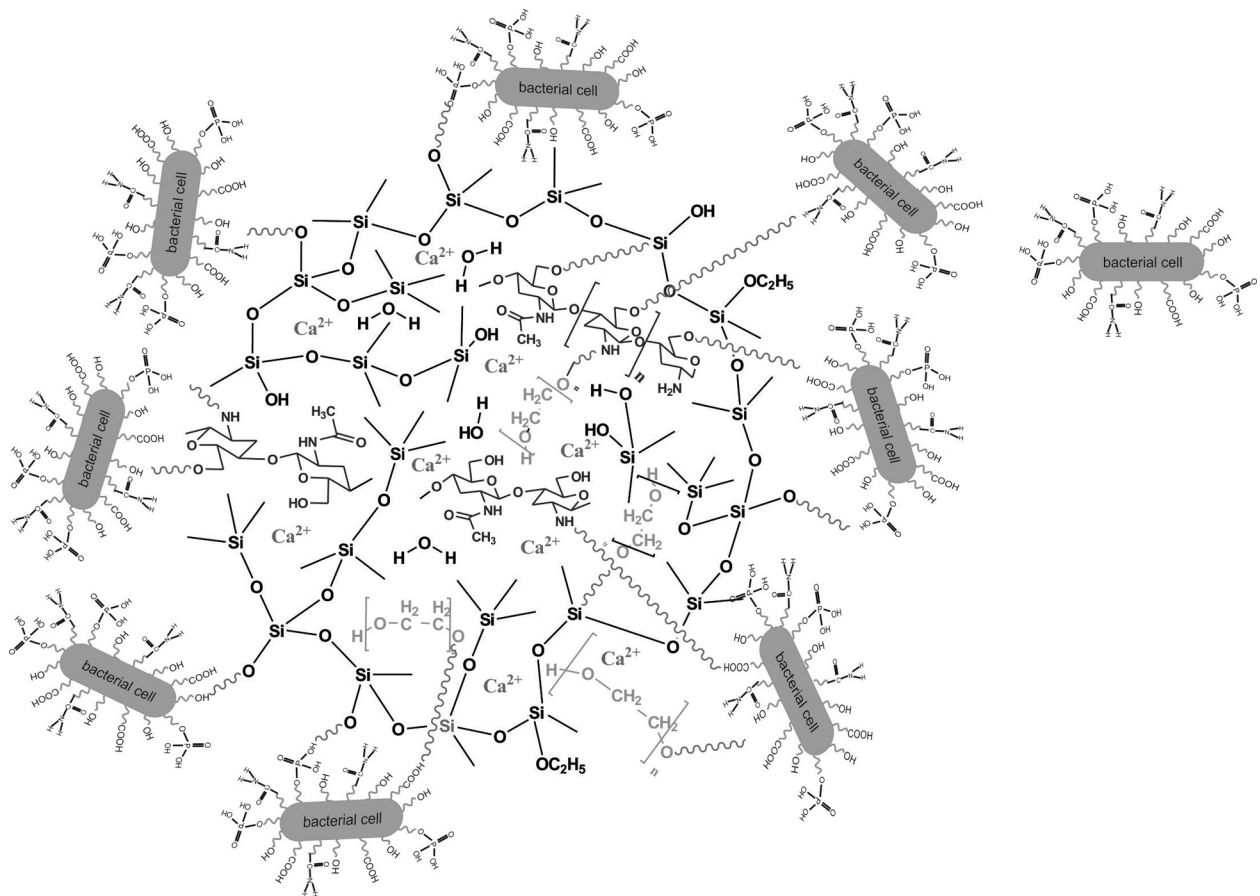
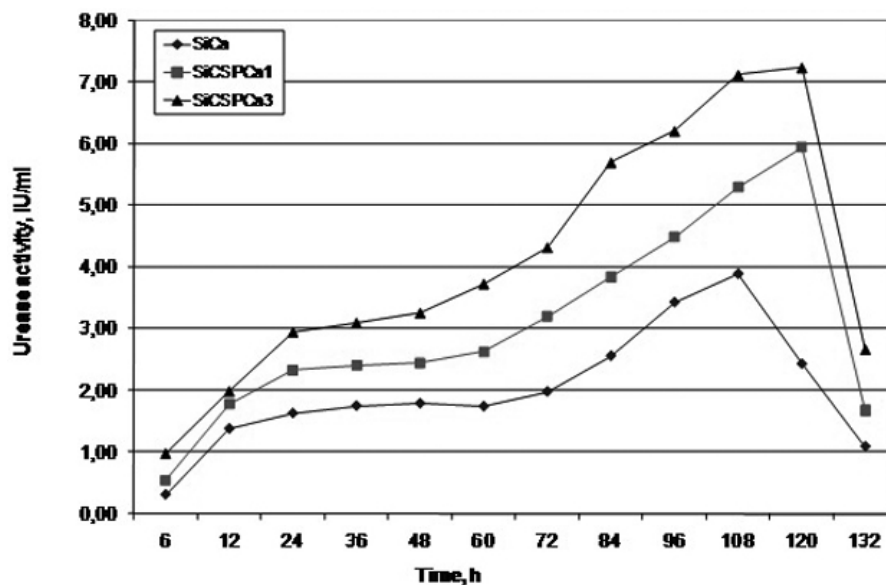


Fig. 3. Model schema of potential interaction between reactive groups of hybrid material and bacterial cells

Fig. 4. Urease activity of immobilized bacterial cells to obtained silica hybrid materials



bacterial cells is below 1IU/ml, after which slightly increase up to 3.9 IU/ml on the 102 h.

With addition of CS and PEG, the urease activity increase, as on 112 h reached to 5.9 IU/ml. The higher values are due to improve reactive and contact centers of silica structure. These results showed the favorable effect of used organic components to bacterial cells. Highest value of bacterial activity presented hybrids with composition SiCSPCa3 (7.2 IU/ml on 112h). The enzyme activity result for the third sample showed, that this hybrid structure exhibits improve functionality and reactivity. The evenly distribution of organic particles (established from AFM analysis) led to improve contact sur-

face area with the bacterial cells. Furthermore, it is proven that, the used inorganic/organic ratio ensure compatibility and favorable effect on the long efficiency of the cells.

Based on the obtained results for enzyme activity, the surface of sample SiCSPCa3 after biological cells is investigated via SEM analysis.

The micrograph (Fig. 5) showed existence of crystal particles. The formation of these particles showed successful formation of a product after interaction of hybrid material and bacterial cells in the presence of urea solution, which can be associated with calcium carbonate, as bioprecipitate. Based on this result can be concluded, that obtained hybrid materials in combination with bacterial cells can be applied for self – healing agents for concrete, which can filled the cracks with bio calcium carbonate.

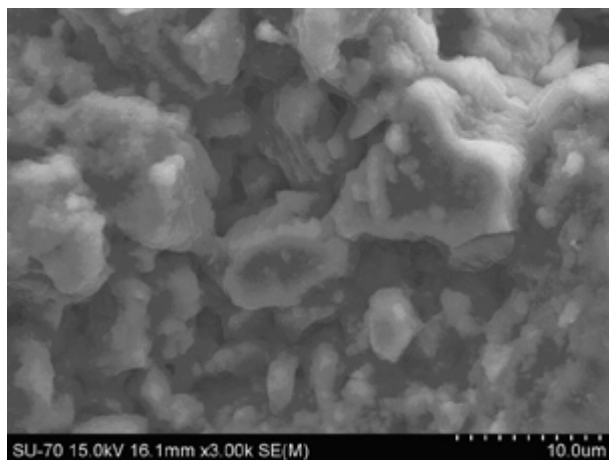


Fig. 5. SEM micrograph of SiCSPCa3 surface after immobilization with bacterial cells and immersion of urea after 24 h

CONCLUSION

Silica hybrid materials with participation of CS and PEG applicable for self – healing of concrete defects are synthesized by sol-gel method. The results from structural characterization showed, that obtained hybrids are amorphous, homogeneous and reactive structures. The results from biological test proved their biocompatibility and favorable effect on enzyme activity of immobilized calls. The SEM micrograph for the sample with higher quantity CS and PEG (SiCSPCa3) showed formation of crystals on the surface, which can be correlated to bio calcium carbonate. The investigations proved that the synthesized silica hybrid materials can be applied as self – healing agents for concrete.

REFERENCES

1. C. In, R. B. Holland, J. Kim, K. E. Kurtis, L. F. Kahn, L. J. Jacobs, *NDT and E Int.*, **57**, 36 (2013).
2. M. Sahmaran, S. B. Keskin, G. Ozerkan, I. O. Yaman, *Cement Concrete Comp.*, **30**, 872 (2008).
3. E. Schlangen, S. Sangadji, *Procedia Eng.*, **54**, 39 (2013).
4. S. Granger, A. Loukili, G. Pijaudier-Cabot, G. Chanvillard, *Cement Concrete Res.*, **37**, 519 (2007).
5. M. Wu, B. Johannesson, M. Geiker, *Constr. Build. Mater.*, **28**, 571 (2012).
6. Sw. K. Ghosh, *Self-healing Materials Fundamentals, Design Strategies, and Applications*, WILEY-VCH Verlag GmbH & Co. KGaA, Weinheim, 2009.
7. M. Sahmaran, G. Yildirim, T. Erdem, *Cement Concrete Comp.*, **35**, 89 (2013).
8. Z. Zhang, S. Qian, H. Ma, *Constr. Build. Mater.*, **52**, 17 (2014).
9. P. Heede, M. Maers, N. Belie, *Constr. Build. Mater.*, (2013) in press.
10. C. Desmettre, J.-P. Charron, *Cement Concrete Res.*, **42**, 945 (2012).
11. K. Tittelboom, N. De Belie, D. Loo, P. Jacobs, *Cement Concrete Comp.*, **33**, 497 (2011).
12. D. Snoeck, N. Belie, *Biosyst. Eng.*, **111**, 325 (2012).
13. V. Achal, A. Mukerjee, M. S. Reddy, *Constr. Build. Mater.*, **48**, 1 (2013).
14. W. Muynck, N. Belie, W. Verstraete, *Ecol. Eng.*, **36**, 118 (2010).
15. H. Jonkers, A. Thijssen, G. Muyzer, O. Copuroglu, E. Schlangen, *Ecol. Eng.*, **36**, 230 (2010).
16. V. Wiktor, H. Jonkers, *Cement Concrete Comp.*, **33**, 763 (2011).
17. W. Muynck, K. Verbeken, N. De Belie, W. Verstraete, *Ecol. Eng.*, **36**, 99 (2010).
18. J. Wang, K. V. Tittelboom, N. Belie, W. Verstraete, *Constr. Build. Mater.*, **26**, 532 (2012).
19. J. A. Toledo-Fernandez, R. Mendoza-Serna, V. Morales, N. Rosa-Fox, M. Pintero, A. Santos, L. Esquivias, *J. Mater. Sci.: Mater. Med.*, **19**, 2207 (2008).
20. M. Bucko, A. Vikartovska, I. Lacik, G. Kollarikova, P. Gemeiner, V. Patoprsty, M. Brygin, *Enzyme Microb. Tech.*, **36**, 118 (2005).
21. C. Le-Tien, M. Millette, M. Mateescu, M. Lacroix, *Biotechnol. Appl. Biochem.*, **39**, 347 (2004).
22. D. Odaci, S. Timur, A. Telefoncu, *Sensor. Actuator. B*, **134**, 89 (2008).
23. D. Avnir, T. Coradin, O. Lev, J. Livage, *J. Mater. Chem.*, **16**, 1013 (2006).
24. Pr. R. Solanki, A. Kaushik, A. A. Ansari, A. Tiwari, B. D. Malhotra, *Sensor. Actuator. B*, **137**, 727 (2009).
25. R. Song, R. Xue, L. He, Y. Liu, Q. Xiao, *Chinese J. Polym. Sci.*, **26**, 621 (2008).
26. H. Tanuma, T. Saito, K. Nishikawa, T. Dong, K. Yazawa, Y. Inoue, *Carbohydr. Polym.*, **80**, 260 (2010).
27. P. Innocenzi, *J. Non-Cryst. Solids*, **316**, 309 (2003).
28. N. Rodkate, U. Wichai, B. Boontha, M. Rutnakornpituk, *Carbohydr. Polym.*, **81**, 617 (2010).

СИНТЕЗ И ОХАРАКТЕРИЗИРАНЕ НА СИЛИКАТНИ ХИБРИДНИ МАТЕРИАЛИ, ПРИЛОЖИМИ ЗА ОТСТРАНЯВАНЕ НА БЕТОННИ ДЕФЕКТИ

Е. В. Тодорова, Г. Е. Чернев, Ст. П. Джамбазов

*Катедра „Технология на силикатите“, Химикотехнологичен и Металургичен Университет,
бул. „Кл. Охридски“ 8, София, България*

Постъпила декември, 2014 г.; приета януари, 2015 г.

(Резюме)

Приложението на силикатните хибриди в областта на бетоните и в частност отстраняване на дефектите им е нова сфера за тези материали. Известно е, че бетонните изделия са едни от най-използваните и предразположени на разрушаване материали. Формирането на дефекти по време на експлоатационния им период е нормален процес, като отстраняването им чрез материали, които могат да блокират дефектите, е оптималният подход за предотвратяване на тяхното последващо разрушаване.

Настоящата работа е свързана със синтез на силикатни хибридни материали, приложими за отстраняване на дефекти на бетонни изделия посредством зол-гелната технология. Неорганичната матрица, получена чрез трансформирането на течност в плътен материал след сушене, е синтезирана посредством тетраетил ортосиликат. Пластичността и реактивоспособността на силикатната матрица е подобрена чрез добавянето на два органични мономера, известни като биосъвместими и реактивоспособни – хитозан и полиетилен гликол. След получаването на неорганично-органичният разтвор в различни съотношения, е добавен CaCl_2 , като източник на калциеви йони. Структурните изследвания показват формирането на аморфни, гладки и реактивоспособни структури. Важен фактор за приложимостта на хибридите е повърхностната микроструктура, като резултатите показват формирането на хомогенна повърхност, на която равномерно са разпределени частици (5 nm – 1 μm). С повишаване на количеството органичен компонент се наблюдава нарастване на размера на частиците, както и подобряване на грапавостта.

Съвместимостта и възможността на получените хибриди да формират CaCO_3 е изследвана чрез имобилизиране на бактериални клетки, които синтезират ензим уреаза. Биосъвместимостта и благоприятният ефект на получените материали показват, че те могат да бъдат използвани за отстраняване на дефекти на бетонни изделия и обработката може да предотврати разрушаването им за дълъг период от време.

Synthesis and characterization of poly sulfide-functionalized hybrid mesoporous silica

M. Abdallah*, N. Velikova, Y. Ivanova, Y. Dimitriev

Department of Silicate Technology, University of Chemical Technology and Metallurgy, Sofia, Bulgaria

Received December, 2014; Revised January, 2015

Poly sulfide-functionalized materials were synthesized by co-condensations of bis[3-(triethoxysilyl)propyl]tetrasulfide (BTPTS) and 1,2-bis(triethoxysilyl)ethane (BTESE) in the presence of the non-ionic surfactant triblock copolymer poly(ethylene glycol)-block-poly(propylene glycol)-block-poly(ethylene glycol) (EO₂₀PO₇₀EO₂₀), Pluronic P123. The surfactant was used as a template for improving the porosity of the hybrid gels. Samples were synthesized with different amounts of BTPTS in acidic media. The final materials were soaked for 24 hours in ethanol and HCl for removing P123. In this work we investigated the influence of the BTPTS amounts on the structure and morphology of the materials after extraction of the surfactant. Samples were characterized by thermo gravimetric analysis (DTA/TG), Fourier-transform infrared spectroscopy (FT-IR), Nitrogen adsorption-desorption measurement (BET), Scanning electron microscopy (SEM), ¹³C CP MAS NMR, ²⁹Si MAS NMR analysis and elemental analysis. The results from ¹³C CP MAS NMR, ²⁹Si MAS NMR, and FT-IR showed that the materials are hybrid organic-inorganic materials. BET and SEM results showed that BTPTS amounts have a significant influence on the morphology and texture parameters of the final materials. The surface area and pore volume decreased by increasing BTPTS amounts; which make the hybrid network to be more flexible and resistant against degradation. DTA/TG results showed that, increasing the amount of BTPTS, the thermal stability of the gel materials decreased.

Key words: Hybrid material, Mesoporous, Template, Thioether bridging group.

INTRODUCTION

Development of organic-inorganic mesoporous hybrid materials is currently an area of extensive research, particularly with regard to potential applications such as adsorption, biotechnology, host-guest chemistry, chromatography, catalysis, sensor technology and gas storage [1–5]. The use of hybrid materials comprised of organic and inorganic building blocks aims to combine the advantages of both components within the solid, making possible production of materials with high mechanical, structural and hydrothermal stability of inorganic materials, with the flexibility and functionality typical of organic compounds. Many different precursors and synthetic routes have been used to prepare hybrid mesoporous materials [5, 6–11]. Organic chain bridging groups originating from methane, ethane, ethylene, as well as small organic aromatic ones

such as thiophene, xylene, benzene and biphenylene have successfully been incorporated into the periodic mesoporous organosilicas (PMOs) [12]. The materials synthesize with thioether functionalized precursor exhibit high adsorption affinity for heavy metal ions [13]. Hydrophobic alkyl chains of thioether functionality may not only provide extra anchoring sites for the adsorption of organic pollutants such phenol, but also endow mesoporous material with high hydrothermal stability [8]. The presence of ethylene bridges in the framework has a high impact on the structure-adsorption characteristics properties of the final materials [14]. Properties and structures of the final mesoporous materials depend on synthesis conditions, such as temperature, acidity of the media, reagents and nature of organic groups as well as the homogenous distribution of organic groups in the silica framework [15]. In the meantime, the variability of PMOs was further extended by the construction of bi-functional PMOs through co-condensation reactions of either bridged bis-(trialkoxysilyl)-organo-silanes [(R'O)₃Si-R-Si(O')₃] and terminal organotrialkoxysilanes [(R'O)₃SiR'] in the presence of an appropriate structural directing agent (SDA),

* To whom all correspondence should be sent:
E-mail: mohammed_abdla@yahoo.com

or by using a mixture of two or more bridged bis-(trialkoxysilyl) precursors which will co-condense also in the presence of a SDA. In the first case, the resulting bi-functional PMOs consist of a combination of bridging organic units and terminal organic units, their end groups inside the pores can be used for further chemical reactions. In the latter case, the PMOs consist of two (or more) different organic bridges that are incorporated within the framework of the pore walls [16]. On basis of the literature data our motivation is to synthesize bifunctional hybrid materials by co-condensation between BTPTE and BTESE precursors, and to study the influence of BTPTS on the structure and morphology characteristic of the final hybrid gel materials. Most of previous research presented the results about hybrid materials synthesized with low amount of BTPTS precursor [8, 13, 17, 18, 25, 28]. From a practical point of view it is interesting to investigate the influence of high concentration of BTPTS on the homogeneity and the final materials structure.

EXPERIMENTAL

Materials

Bis-[3-(triethoxysilyl)propyl]tetrasulfide BTPTS 90% ($(\text{CH}_3\text{CH}_2\text{O})_3\text{Si}(\text{CH}_2)_3\text{S}-\text{S}-\text{S}-\text{S}(\text{CH}_2)_3\text{Si}-(\text{OCH}_2\text{CH}_3)_3$), and 1,2-bis(triethoxysilyl)ethane BTESE 96% [$-\text{CH}_2\text{Si}(\text{OC}_2\text{H}_5)_3$]₂, were purchased from Aldrich. They were used as the bridged organosilica sources. Pluronic P123 ($\text{EO}_{20}\text{PO}_{70}\text{EO}_{20}$) ($M_w=5800$) (Aldrich), HCl (aqueous, 36%), KCl and Xylene and Ethanol were used as the structure-directing agent, acid source, pore improving, swelling agent and template extraction respectively all chemicals used without further purification.

Method of Preparation

The way of preparing of the samples was described in the previous work [19]. The samples were prepared as follow: 1.2 g of P123 and 3.5 g of

KCl were dissolved in 10 ml of distilled water and 52 ml of 2M hydrochloric acid and then magnetically stirred at room temperature until complete dissolution to obtain a homogenous solution. 2.64 ml of Xylene were added into the surfactant solution with stirring for 1 hour followed by addition of 2.64 ml of BTESE and again stirring for 1h. Finally, different quantities of BTPTS were added with continuous stirring at 40 ± 1 °C for 1h as shown in Table 1. The resultant slurry was dried at 100 °C for 24 h; the surfactant was extracted by soaking 1.0 g of the dried gel in 150 ml ethanol, containing 1.7 ml of HCl 36%, at 50 °C for 24h. The way of extraction of P123 was preferred than the knowing approaches in the literature [20, 21, 25, 30] because the approach save the organic functional group in the final materials [19].

Characterization

The thermo gravimetric analysis (TGA) was performed on (PT1600 TG-DTA/DSC (STA Simultaneous Thermal Analysis) LINESIS Messgerat GmbH, Germany Instrument with a heating rate of 10 °C min⁻¹, under a flow of air. Fourier-transformation infrared spectroscopy (FT-IR) of KBr powder pressed pellets was recorded on (Varian 660-IR spectrometer). The sulfur content of the extracted samples was analyzed quantitatively by elemental analyses (Elemental analyzer SPA Euro Vector EA 3000). The morphology of the samples was observed by scanning electron microscopy (SEM) the images were recorded on a Hitachi S-4100 scanning electron microscope with an acceleration voltage of 15 kV. ¹³C (100.61MHz) cross-polarization magic angle spinning (CP MAS) and ²⁹Si (79.49 MHz) MAS solid-state NMR experiments were recorded on a (9.4 T) Bruker Avance 400 spectrometer. The experimental parameters for ¹³C CP MAS NMR experiments: 9 kHz spin rate, 5 s pulse delay, for ²⁹Si MAS NMR experiments: 5 kHz spin rate, 60s pulse delay. Pore size distributions were determined based on the Barrett-Joyner-Halenda (BJH) desorption curve [22].

Table 1. Samples composition of (M1, M2, M3 and M4)

Sample	P123 [g]	H ₂ O [ml]	KCl [g]	2M HCl [ml]	Xylene [ml]	BTESE [Mol%]	BTPTS [Mol%]
M1	1.2	10	3.5	52	2.64	75.4	24.6
M2	1.2	10	3.5	52	2.64	47.7	52.3
M3	1.2	10	3.5	52	2.64	38	62
M4	1.2	10	3.5	52	2.64	31.3	68.7

RESULTS AND DISCUSSION

FT-IR spectrum of samples in Fig. 1 showed the absorption bands at 3458 and 1635 cm^{-1} are assigned to OH groups due to the surface silanol groups and the remaining adsorbed water molecules. The band at 911 cm^{-1} is assigned to Si–OH stretching. The absorption bands at 2927 and 1411 cm^{-1} are assigned to CH_2 groups of BTPTS and BTESE or residual amounts of P123 after extraction [23]. A broad peak noted at 1105 cm^{-1} and 465 cm^{-1} , due to the siloxane vibrations and bending vibrations of Si-O-Si groups [24]. The presence of –S–S– and –S–C– bonds are attributed to the vibration bands at 694 cm^{-1} and at 580 cm^{-1} respectively [25], indicating that BTPTS has been successfully incorporated into organic silica based framework.

Table 2 shows the elemental analysis. All samples have sulfur which confirms FT-IR analysis, by increasing the amounts of BTPTS the amounts of sulfur content increase and the co-condensation reaction with BTESE occurs successfully.

^{29}Si MAS NMR measurements are shown in Fig. 2. The signals at –58.5, –66.0 ppm are assigned as T^2 ((C–Si(OSi) $_2$ (OH)), and T^3 (C– Si(OSi) $_3$), respectively, [26]. Results strongly support the pres-

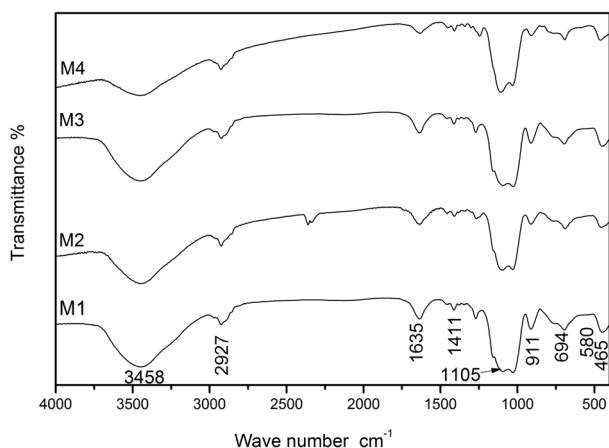


Fig. 1. Infrared spectrum of synthesized samples(M1, M2, M3 and M4)

Table 2. Elemental analysis of samples (M1, M2, M3 and M4)

Sample	Weight (mg)	Sulfur (Wt. %)
M1	1.18	1.47
M2	1.41	21.88
M3	0.70	23.40
M4	2.10	25.83

ence of Si-C in silica framework, also the absence of $\text{Q}^n[\text{Si}(\text{OH})_4(\text{OSi})_{4-n}]$ whose signals are usually observed in the range of –92 and –110 ppm, confirms that the C–Si bond cleavage of the BTESE and BTPTS precursors as material has not occurred during co condensation processes and the extraction process of P123 [27]. These results are in a good agreement with FT-IR analysis.

^{13}C CP MAS NMR analysis for sample M1 presented in Fig. 3. The resonances at 12.3, 22.6 and 42.5 ppm in the ^{13}C CP MAS NMR spectrum of sample M1 assign to the ^1C , ^2C , and ^3C carbon atoms of $\text{Si}-^1\text{CH}_2-^2\text{CH}_2-^3\text{CH}_2-\text{S}-\text{S}-\text{S}-^3\text{CH}_2-^2\text{CH}_2-^1\text{CH}_2-\text{Si}$, respectively [28], as tetrasulfide bridging groups are incorporated in the framework. The resonance at 5 ppm assign to ethane carbon atoms in BTESE [29],

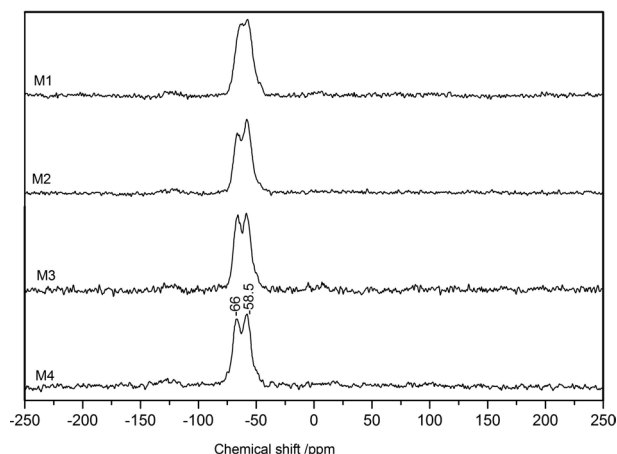


Fig. 2. ^{29}Si MAS NMR spectra of synthesized samples (M1, M2, M3 and M4)

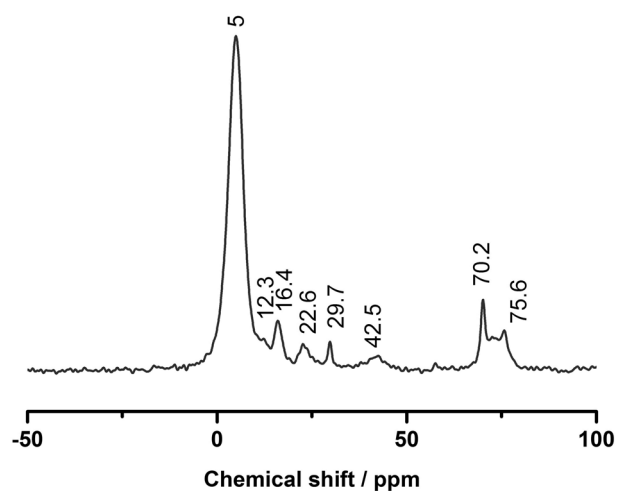


Fig. 3. ^{13}C MAS NMR spectra of the sample M1

which confirm the presence of both bridging groups in the hybrid materials and successful co-condensation process between BTESE and BTPTS. The resonance at 16.4 ppm is attributing to the side-chain carbons of methyl groups of P123, additionally; it could also be assign to carbons of ethoxy groups formed during surfactant extraction [30]. The signals at 70.5 and 75.6 ppm are due to the main-chain carbons of ethylene oxide (EO) and propylene oxide segments of P123 respectively, suggesting incomplete surfactant removal during the extraction process [12].

The thermo-gravimetric analysis was performed under air atmosphere. The weight loss below 150 °C is mainly due to the removal of physically adsorbed water from the materials Fig. 4. The weight loss decrease by increasing the BTPTS amounts. Decomposition of bridging organic group occurs between 300 and 600 °C [31]. Samples M1, M2, M3 and M4 show weight loss 25 wt.%, 42 wt.%, 45 wt.% and 47 wt.% respectively, the weight loss increases as a result of increasing amounts of tetrasulfide functionalized precursor which confirm the incorporation of tetrasulfide organic functional group in silica framework at high BTPTS amount. Weight loss is observed above 600°C, may be at-

tributed to the combustion of residual organic material and/or to the desorption of water resulting from silanol condensation [23].

The N₂ adsorption–desorption isotherms of the materials are presented in Fig. 5. According to IUPAC classification the hysteresis can be clas-

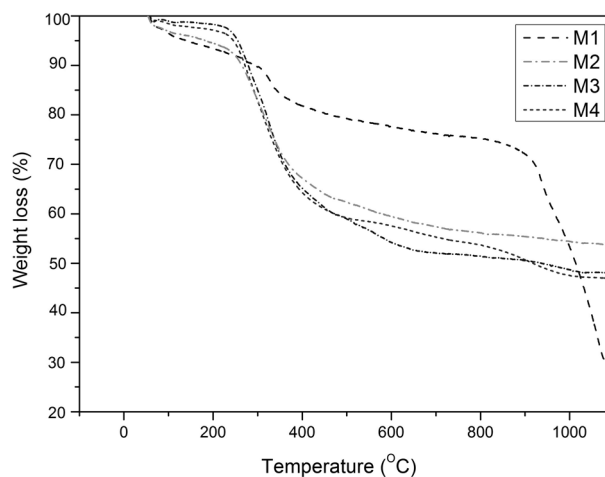


Fig. 4. DTG profiles of synthesized samples (M1, M2, M3 and M4)

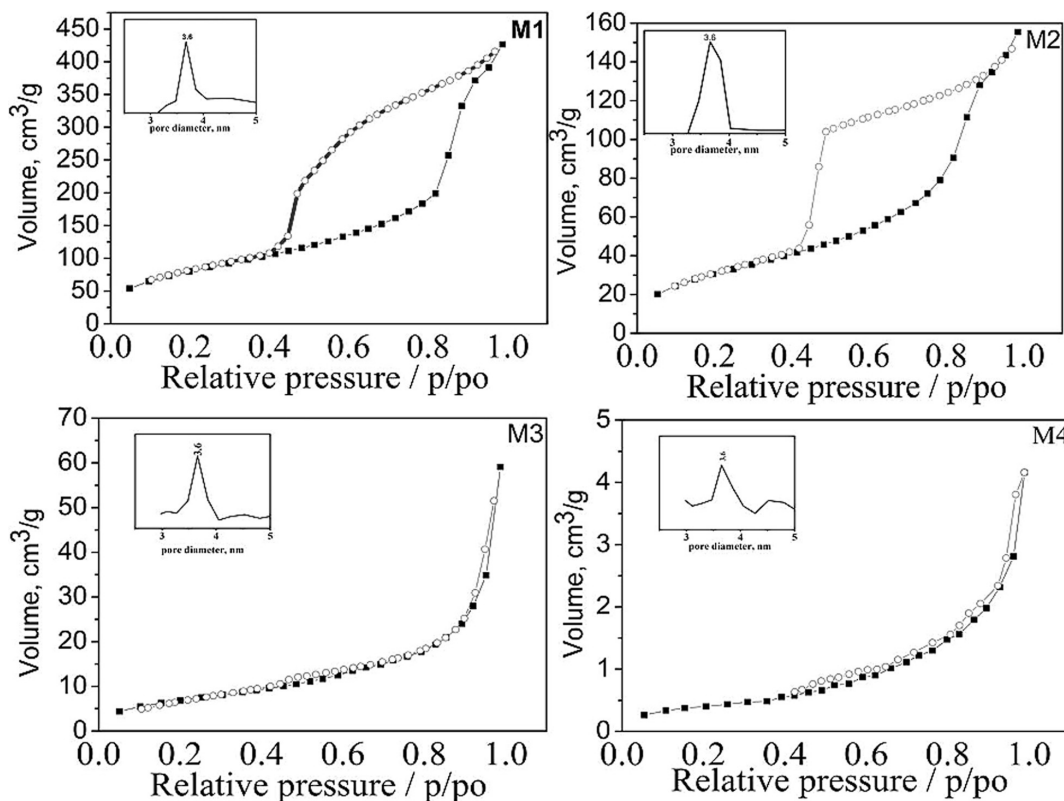


Fig. 5. Nitrogen adsorption–desorption isotherms and BJH pore-size distribution profiles (insets) of samples (M1, M2, M3 and M4)

Table 3. Physical and textural properties of samples (M1, M2, M3 and M4)

Sample	S_{BET} [m ² /g]	V_{total} [cm ³ /g]	D_{average} [nm]
M1	294	0.61	3.7
M2	114	0.22	3.7
M3	26	0.05	3.7
M4	2	0.005	3.6

sified as type IV which is typical for mesoporous structure. Sample M1 and M2 show hysteresis loop type H2 which is typical for ink bottle like pores. The type of hysteresis loop of sample M3 and M4 is H3 characteristic for slit like pores [32]. These results show that increasing the BTPTS amount lead to changes in the pore shapes. The textural parameters are shown in Table 3. By increasing the content of tetrasulfide functionalized precursor occur significant changes in surface area and pore volume, whereas the pore size for all samples almost the same. This can be explained by the flexibility of the silica network with increasing the amount of BTPTS, which prevent the hybrid framework from

collapse during the surfactant extraction and during the drying process. The presence of residuals amount of P123 in the pores which was confirm by ¹³C CP MAS NMR is the main reason for the close values of the pore size.

SEM images of samples presented in Fig. 6 display homogenous structure. The images show significant change in the morphology of the materials with increasing amount of BTPTS. Sample M1 shows particle like structure with particle size between 100–200 nm. Sample M2 shows the formation of smoother surface with particle size around 300 nm. Sample M3 shows particles aggregate with size around 500 nm. Sample M4 shows the smoothest surface than the other. These results confirm the results from BET analyses which show the decreasing of the textural characteristic with increasing the BTPTS amount.

CONCLUSION

Co-condensation reaction with high amount of BTPTS precursor are carried out successfully and the materials are homogeneous, the synthesized gels are tetrasulfide functionalized organic-inorganic hybrid mesoporous materials. The presence of the bands at 694 and 580 cm⁻¹ in FT-IR spectra confirm the

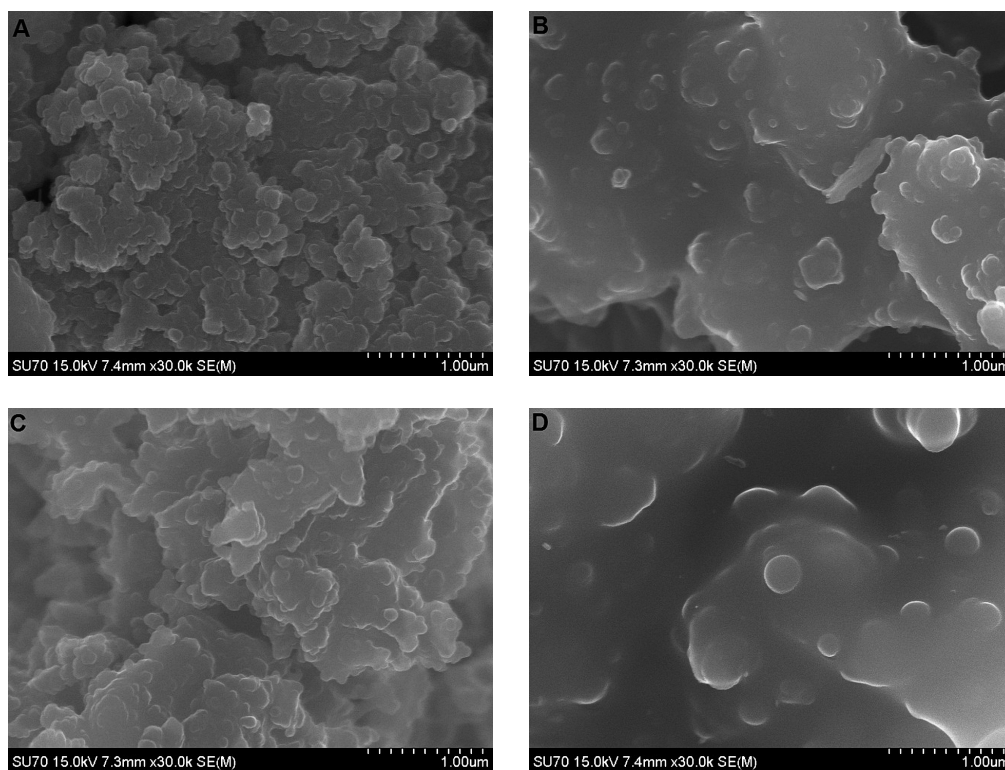


Fig. 6. SEM images of samples (M1, M2, M3 and M4) were A=M1, B=M2, C=M3, D=M4

incorporation of sulfur in the final hybrid structure and also the bands at 2927 and 1411 cm⁻¹ confirm the incorporation of bridging groups in silica network without occurrence decomposition during drying and extraction processes. ¹³C CP MAS NMR confirms the presence of the bridging groups CH₂-CH₂ and -CH₂-CH₂-CH₂-S-S-S-S-CH₂-CH₂-CH₂- from both precursors in the final structure. Surface of gels become smoother, by increasing BTPTS amounts, surface area and pore volume decrease and pore size almost the same. The shape of the pores is changing from type H2 typical for ink-bottle to H3 typical for slit-like shape. These observed changes are result of increased flexibility of the final hybrid network with the increasing the amount of BTPTS. The final hybrid materials show characteristic applications as adsorbent of organic pollutants and dyes from waste water.

Acknowledgements: This study was financially supported by the Erasmus Mundus MEDASTAR (Project Number: 2011-405/001-002-EMA2). And the silicate technology department of the University of Chemical Technology and Metallurgy Sofia, Bulgaria.

REFERENCES

1. A. Stein, *Adv. Mater.*, **15**, 763, (2003).
2. G. Kickelbick, *Angew. Chem. Int. Ed.*, **43**, 3102 (2004).
3. B. Hatton, K. Landskron, W. Hhitnall, D. Perovic, G. A. Ozin, *Acc. Chem. Res.*, **38**, 305 (2005).
4. W. J. Huncks, G. A. Ozin, *J. Mater. Chem.*, **15**, 3716 (2005).
5. A. Sayari, S. Hamoudi, *Chem. Mater.*, **13**, 3151 (2001).
6. M. E. Davis, *Nature*, **417**, 813 (2002).
7. S. Guan, S. Inagaki, T. Ohsuna, O. Terasaki, *J. Am. Chem. Soc.*, **122**, 5660 (2000).
8. J. Liu, J. Yang, Q. Yang, G. Wang, Y. Li, *Adv. Funct. Mater.*, **15**, 1297 (2005)
9. B. Park, J. Park, W. Guo, I. Kim, C.-S. Ha, *Micropor. Mesopor. Mater.*, **66**, 229 (2003).
10. W. Guo, I. Kim, C.-S. Ha, *Chem. Commun.*, **21**, 2692 (2003).
11. S. Thomas, B. Stefan, B. Stefan, R. S. Renata, A. Klaus, S. Stefan, P. Eric, M. Ahmad, R. Catherine, R. J. P. Corriu, *Adv. Funct. Mater.*, **12**, 134 (2002).
12. N. Hao, L. Han, Y. Yang, H. Wang, P. Webley, D. Zhao, *Appl. Surf. Sci.*, **256**, 5334 (2010).
13. X. Chen, Q. Cai, L. Sun, W. Zhang, X. Yujiang, *Front. Mater. Sci.*, **6**, 278 (2012).
14. M. Barczak, P. Borowski, A. Dabrowski, *Colloid Surfaces A*, **347**, 114 (2009).
15. Y. C. Liang, E. S. Erichsen, M. Hanzilk, R. Anwander, *Chem. Mater.*, **20**, 1451 (2008).
16. K. Rurack, R. Martínez-Mañez, *The Supramolecular Chemistry of Organic-Inorganic Hybrid Materials*, John Wiley & Sons: Hoboken, NJ., p. 59, 2010.
17. N. Meeks, S. Rankin, D. Bhattacharyya, *Ind. Eng. Chem. Res.*, **49**, 4687 (2010).
18. K. Johari, N. Saman, H. Mat, *Can. J. Chem. Eng.*, **9999**, 1 (2013).
19. M. Abdallah, N. Velikova, Y. Ivanova, Y. Dimitriev, *J. Chem. Tech. Metall.*, **48**, 571 (2013).
20. W. Guo, I. Kim, C.-S. Ha, *Chem. Mater.*, **15**, 2295 (2003).
21. J. Liu, Q. Yang, L. Zhang, D. Jiang, X. Shi, J. Yang, H. Zhong, C. Li, *Adv. Funct. Mater.*, **17**, 569 (2007).
22. J. Kooyman, M. J. Verhoef, E. Proozet, *Stud. Surf. Sci. Catal.*, **129**, 535 (2000).
23. H. Tao Fan, Z. Jie Su, X. Lei Fan, M-Meng Guo, J. Wang, S. Gao, T. Sun, *J. Sol-Gel Sci. Technol.*, **64**, 418 (2012).
24. D. Liu, J. Lei, L. Guo, X. Di Du, K. Zeng, *Micropor. Mesopor. Mater.*, **11**, 767 (2009).
25. M. Teng, H. Wang, F. Li, B. Zhang, *J. Colloid Interface Sci.*, **355**, 23 (2011).
26. W. Huang, N. Chu Lai, L. Chang, C. Yang, *Micropor. Mesopor. Mater.*, **151**, 411 (2012).
27. M. A. Wahab, I. Kim, C. S. Ha, *Micropor. Mesopor. Mater.*, **69**, 19 (2004).
28. J. Kim, B. Fang, M. Song, J. Sung Yu, *Chem. Mater.*, **24**, 2256 (2012).
29. H. Wua, C. Liao, Y. Pan, C. Yeh, H.-Ming Kao, *Micropor. Mesopor. Mater.*, **119**, 109 (2009).
30. W. Zhang, X. Zhang, Z. Hua, P. Harish, F. Schroeder, S. Hermes, T. Cadenbach, J. Shi, R. Fischer, *Chem. Mater.*, **19**, 2663 (2007).
31. H. Tao Fan, J. Wuc, X. Lei Fan, D. Zhang, Z. Jie Su, F. Yan, T. Sun, *Chem. Eng. J.*, **198-199**, 355 (2012).
32. K. S. W. SING, *Pure Appl. Chem.*, **54**, 2201 (1982).

СИНТЕЗ И ХАРАКТЕРИЗИРАНЕ НА ПОЛИСУЛФИД ФУНКЦИОНАЛИЗИРАНИ ХИБРИДНИ МЕЗОПОРЕСТИ СИЛИЦИЕВО-ДИОКСИДНИ МАТЕРИАЛИ

М. Абдала*, Н. Великова, Й. Иванова, Ян. Димитриев

*Катедра Технология на силикатите, Химикотехнологичен
и металургичен университет, София, България.*

Постъпила декември, 2014 г.; приета януари, 2015 г.

(Резюме)

Синтезирани са полисулфид функционализирани материали чрез съкондензация на бис[3-(триетоксисилил)пропил]тетрасулфид (ВТРТС) и 1,2-бис(триетоксисилил)етан (ВТЕСЕ), в присъствие на нейонно повърхностно активно вещество (ПАВ) триблок съполимер полиетилен гликол-блок-полипропилен гликол-блок-полиетилен гликол ($\text{EO}_{20}\text{PO}_{70}\text{EO}_{20}$), Pluronic P123. ПАВ е използвано като шаблон за подобряване порестостта на хибридните гели. Образците са синтезирани с различни количества ВТРТС в кисела среда. Крайните материали са накснати за 24 часа в разтвор на етанол и HCl за отстраняване на Pluronic P123.

В настоящата работа ние изследваме влиянието на количеството на ВТРТС прекурсора върху структурата и морфологията на материалите след екстракция на ПАВ. Образците са охарактеризирани с Диференциално термичен и Термогравиметричен анализи (DTA/TG), Инфрачервена спектроскопия с Фурие трансформация (FT-IR), Азот адсорбционно-десорбционен анализ (БЕТ), Сканираща електронна микроскопия (СЕМ), Ядрено магнитен резонанс на ядра ^{13}C (^{13}C CP MAS NMR) и ^{29}Si (^{29}Si MAS NMR) и елементен анализ. Резултатите от ^{13}C CP MAS NMR, ^{29}Si MAS NMR и FT-IR показаха, че материалите са хибридни органично-неорганични. БЕТ и СЕМ резултатите показаха, че количеството на ВТРТС оказва съществено влияние върху морфологията и стойностите на текстуралните характеристики на крайните материали. Стойностите на свободната повърхност и обемът на порите се понижават с повишаване количеството на ВТРТС прекурсора, придаващ на хибридната мрежа по-голяма гъвкавост и устойчивост на разрушаване. Резултатите от DTA/TG показаха, че с повишаване количеството на ВТРТС термичната стабилност на гелните материали се понижават.

Silica supported copper and cobalt oxide catalysts for methanol decomposition: Effect of preparation procedure

T. S. Tsoncheva^{1*}, I. G. Genova¹, N. Scotti², M. D. Dimitrov¹, A. Gallo^{2#},
D. G. Kovacheva³, N. Ravasio²

¹ Institute of Organic Chemistry with Centre of Phytochemistry, Bulgarian Academy of Sciences, Sofia, Bulgaria

² Institute of Molecular Sciences and Technologies of the National Research Council, ISTM-CNR, Milano, Italy

³ Institute of General and Inorganic Chemistry, Bulgarian Academy of Sciences, Sofia, Bulgaria

[#] Current address: Department of Chemical Engineering, University of California,
Santa Barbara, USA 93106-5080

Received December, 2014; Revised January, 2015

Novel “chemisorption-hydrolysis” method was developed for preparation of supported on SiO₂ mixed copper and cobalt oxides. For comparison, similar materials were prepared by conventional impregnation technique. The state of loaded metal oxide species was studied by XRD, FTIR-KBr, FTIR-pyridine, UV-Vis, XPS and TPR techniques. The catalytic properties of the samples were tested in methanol decomposition. The variation in the preparation procedure provides the deposition of different metal oxide species and it is considered as simple approach to control the surface and catalytic properties in copper and cobalt oxide bi-component system.

Key words: copper and cobalt mixed oxides, “chemisorption–hydrolysis” method, methanol decomposition.

INTRODUCTION

Complex oxides with spinel structure, such as cobaltites, are of intensive investigation because of their remarkable optical, electrical, magnetic and catalytic properties [1 and refs. therein]. Their normal and inverse structure can be represented by a general formulas A[B]₂O₄ (normal spinel) and B[AB]O₄ (inverse spinel) respectively, where elements A and B denote divalent and trivalent metallic cations, which are octahedrally (inside the parenthesis) and tetrahedrally (outside the parenthesis) coordinated with oxygen ions [2]. In case of normal Co₃O₄ spinel structure, the Co³⁺ ions occupy the octahedral sites, while Co²⁺ is situated on the tetrahedral sites. For copper spinel materials, Cu_xCo_{3-x}O₄, transition to inverse spinel structure was established when x>0.2 [3]. In the inverse CuCo₂O₄ spinel, Co³⁺ ions occupy the tetrahedral and half of octahedral sites, while Cu²⁺ ions situate at the octahedral sites. It was reported that different synthetic procedures, such as

nitrate decomposition, urea combustion, co-precipitation, sol-gel, hydrothermal or mechanotechnical methods provide the formation of Cu_xCo_{3-x}O₄ spinel particles with different dispersion, shape, stoichiometry and cations distribution [1 and refs. therein]. Due to the more significant contribution of metal ions in octahedral position to surface activity rather than tetrahedral ions [4, 5], the preparation procedure seems to be easy and powerful way to control the cobaltite properties. Recently, the synthesis of metals or metal oxides in nanoscale form with well defined size, shape and crystallinity has gain significant attention because of their unique physico-chemical properties with a potential in many technological applications. However, the control and stabilization of nanoparticle size is still a matter of challenge and nowadays, the development of novel preparation procedures is in a focus of interest. In our previous studies we applied a new “chemisorption-hydrolysis” strategy to modify mesoporous silicas with copper [6] or cobalt [7] metal and metal oxide particles. The key step during this procedure was the formation of metal ammonia complexes, which interacted selectively with the surface silanol groups. As a result, formation of copper oxide nanoparticles with predominantly oligomeric and highly disordered crystal structure as well as hardly reduc-

* To whom all correspondence should be sent:
E-mail: tsoncheva@orgchm.bas.bg

ible cobalt species strongly interacting with the support were produced.

The aim of the current study is to apply the novel “chemisorption-hydrolysis” (CH) strategy for preparation of silica-supported copper and cobalt oxide bi-component materials. The samples were characterized by XRD, UV-Vis, XPS, TPR, FTIR, FTIR of adsorbed pyridine, and compared with the similar materials obtained by conventional incipient wetness impregnation (WI) technique. All materials were tested as catalysts in methanol decomposition.

Recently, methanol, and in particular bio-methanol, has been overlooked as efficient energy source [8 and refs. therein]. It can be directly used in internal combustion engine, as well as successfully converted onboard into hydrogen for fuel cells electric cars. Methanol is a feasible alternative for cheap and safe hydrogen storage and supply, especially in case of small scale devices. Decomposed methanol could be also used as a source of synthesis gas for number of catalytic processes.

EXPERIMENTAL

Materials

A commercial mesoporous silica (SiO_2 , Grace, BET – $300 \text{ m}^2\text{g}^{-1}$; pore volume – $1.43 \text{ cm}^3\text{g}^{-1}$) was used as a support for the preparation of mono- and bi-component copper and cobalt oxide materials. The modified “chemisorption-hydrolysis” procedure was applied for SiO_2 modification as was described in [6, 7]. $\text{Cu/SiO}_2\text{-CH}$ sample was prepared by addition of silica support to aqueous solution of $\text{Cu}(\text{NO}_3)_2 \cdot 3\text{H}_2\text{O}$ and NH_4OH (pH 9). After 20 min under stirring the slurry held in ice bath at 273 K, it was slowly diluted. The solid was separated by filtration, washed with water, dried and calcined at 773 K for 4 h. The sample, denoted as $\text{Co/SiO}_2\text{-CH}$ was obtained from $\text{Co}(\text{NO}_3)_2 \cdot 6\text{H}_2\text{O}$, which was dissolved into a water solution containing NH_4NO_3 (mol NH_4NO_3 /mol Co =10/1) under stirring. The

solution was cooled at 273 K and slowly a 30% solution of H_2O_2 and NH_4OH were added. Finally, the temperature was increased to 333 K and after 2.5 hours the solution was cooled down to room temperature and the pH was adjusted to 9 with 28% solution of NH_4OH , before adding the support (SiO_2). The silica suspension was kept under stirring for 0.5 or 24 h and then it was diluted with water at 273 K and filtered. The solid was washed with water, dried and calcined in air at 773 K for 4 h. The bi-component $\text{CuCo/SiO}_2\text{-CH}$ material was prepared following the same procedure, using a mixture of $\text{Co}(\text{NO}_3)_2 \cdot 6\text{H}_2\text{O}$ and $\text{Cu}(\text{NO}_3)_2 \cdot 3\text{H}_2\text{O}$ in NH_4OH (pH=9). Similar $\text{Cu/SiO}_2\text{-WI}$, $\text{Co/SiO}_2\text{-WI}$ and $\text{CuCo/SiO}_2\text{-WI}$ materials were prepared by impregnation technique from nitrate precursors and their decomposition in air at 773 K for 4 h. The samples composition is presented in Table 1.

Methods of investigation

Cobalt content in the samples was determined by Atomic Absorption Spectroscopy on Atomic Absorption Spectrometer 3100 – Perkin Elmer; flame: acetylene/air. Powder X-ray diffraction patterns were collected within the range from 5.3 to $80^\circ 2\theta$ with a constant step $0.02^\circ 2\theta$ on Bruker D8 Advance diffractometer with Cu K_α radiation and LynxEye detector. Phase identification was performed with the Diffracplus EVA using ICDD-PDF2 Database. The IR spectra (KBr pellets) were recorded on a Bruker Vector 22 FTIR spectrometer at a resolution of $1\text{--}2 \text{ cm}^{-1}$, accumulating 64–128 scans. The UV–Vis spectra were recorded on the powder samples using a Jasco V-650 UV-Vis spectrophotometer equipped with a diffuse reflectance unit. The FTIR studies of pyridine adsorption were carried out with a BioRad FTS40 spectrophotometer equipped with mid-IR DTGS detector. The measurements were performed after activation of the samples at 773 K in air for 20 minutes followed by evacuation for 40 minutes and eventual reduction in hydrogen at the same temperature for 40 minutes.

Table 1. Samples composition and reduction degree, determined by TPR-TG analyses

Sample	Preparation procedure	Cu content (wt%)	Co content (wt%)	Reduction degree (wt%)
$\text{Cu/SiO}_2\text{-WI}$	WI	7.6	0.0	100
$\text{Co/SiO}_2\text{-WI}$	WI	0.0	7.6	96
$\text{CuCo/SiO}_2\text{-WI}$	WI	3.8	3.8	100
$\text{Cu/SiO}_2\text{-CH}$	CH	7.6	0.0	88
$\text{Co/SiO}_2\text{-CH}$	CH	0.0	6.3	50
$\text{CuCo/SiO}_2\text{-CH}$	CH	2.7	2.6	67

The absorption of pyridine was performed at room temperature and all spectra were recorded at room temperature after pyridine desorption at selected temperatures. The XPS analyses were performed on a SSX 100/206 photoelectron spectrometer from Surface Science Instruments (USA) equipped with a monochromatized micro focused Al X-ray source (powered at 20 mA and 10 kV). The TPR/TG (temperature-programmed reduction/ thermogravimetric) analyses were performed in a Setaram TG92 instrument in a flow of 50 vol% H₂ in Ar (100 cm³.min⁻¹) and heating rate – 5 K.min⁻¹.

Catalytic experiments

Methanol conversion was carried out in a fixed bed flow reactor (0.055 g of catalyst, three times diluted with grounded glass), argon being used as a carrier gas (50 ml min⁻¹). The methanol partial pressure was 1.57 kPa. The catalysts were tested under conditions of a temperature-programmed regime within the range of 350–770 K with heating rate of 1 K.min⁻¹. On-line gas chromatographic analyses were performed on HP apparatus equipped with flame ionization and thermo-conductivity detectors, on a PLOT Q column, using an absolute calibration method and a carbon based material balance. Before the catalytic experiments the samples were activated *in situ* in air at 773 K for two hours. The products selectivity was calculated as $X_i/X \cdot 100$, where X_i is the current yield of the product i and X is methanol conversion

RESULTS AND DISCUSSION

X-ray diffraction patterns (Fig. 1) of the samples prepared by different procedures are performed to identify the presence of crystalline phase. The absence of any diffraction peaks in the patterns of all CH samples indicates that this procedure provides the formation of very finely dispersed metal oxide phase despite the samples composition. Just the opposite, well defined reflections are visible in the patterns of all materials prepared by WI procedure. The reflections at 35.5, 38.7 and 48.7° 2θ in the pattern of Cu/SiO₂_WI could be indexed to pure monoclinic (Tenorite, space group C2/c) crystallites of CuO [9]. The diffraction peaks at 2θ = 31.2, 36.8, 44.8, 59.4 and 65.3° in the pattern of Co/SiO₂_WI can be indexed to a pure face centered cubic (fcc) structure (space group Fd3m) of Co₃O₄ normal spinel [10]. The XRD reflections for the bi-component CuCo/SiO₂_WI sample are wider and less intensive, indicating formation of mixture of more finely dispersed metal oxide phase as compared to the mono-component materials, which parameters are well

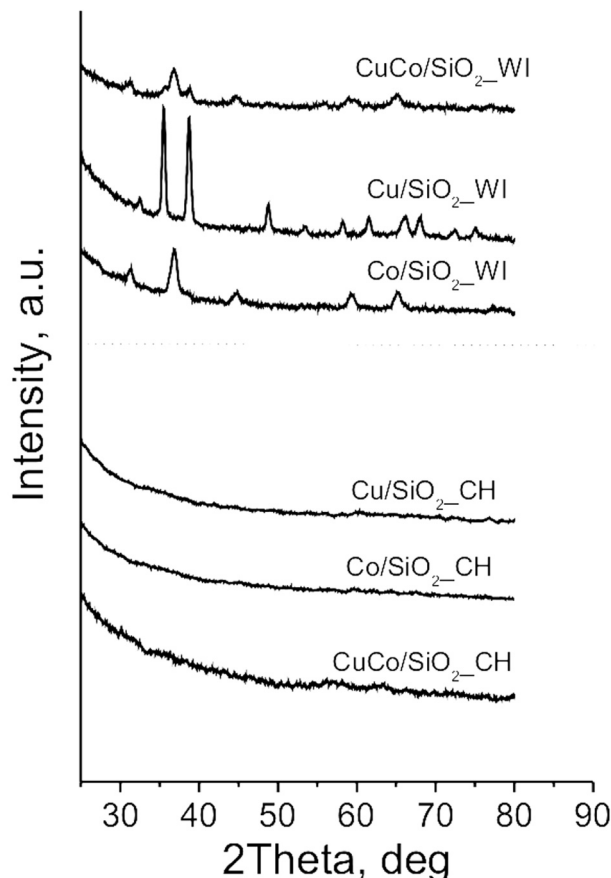


Fig. 1. XRD patterns of mono- and bi-component copper and cobalt oxide silica modifications prepared by CH and WI technique

fitted with the cubic (fcc) structure (space group Fd3m) of Cu_xCo_{3-x}O₄ spinel oxide and monoclinic CuO. The slight changes in the lattice parameters for the spinel phase in bi-component material are due to partial replacement of Co²⁺ ions in octahedral position (ionic radii 52.5 pm) by larger Cu²⁺ ions (ionic radii 73 pm) [11].

More information for the state of loaded metal oxide phases was obtained by combined UV-Vis, FTIR and XPS spectroscopic study. The UV-Vis spectra (Fig. 2) of both mono-component copper materials represent absorption band at about 240 nm and a broad band in a 600–800 nm region which could be assigned to the absorption of Cu²⁺ ions in CuO crystallites [12 and refs. therein]. The absorption in the 300–400 nm region indicates presence of small Cu-O-Cu oligomeric species, which fraction seems to be larger in the case of Cu/SiO₂_CH. (Fig. 1). The broad band at around 215 nm in the spectrum of Co/SiO₂_WI can be assigned to charge transfer from O²⁻ to Co³⁺. The two broad bands at 400–550 nm and 650–800 nm are typical of

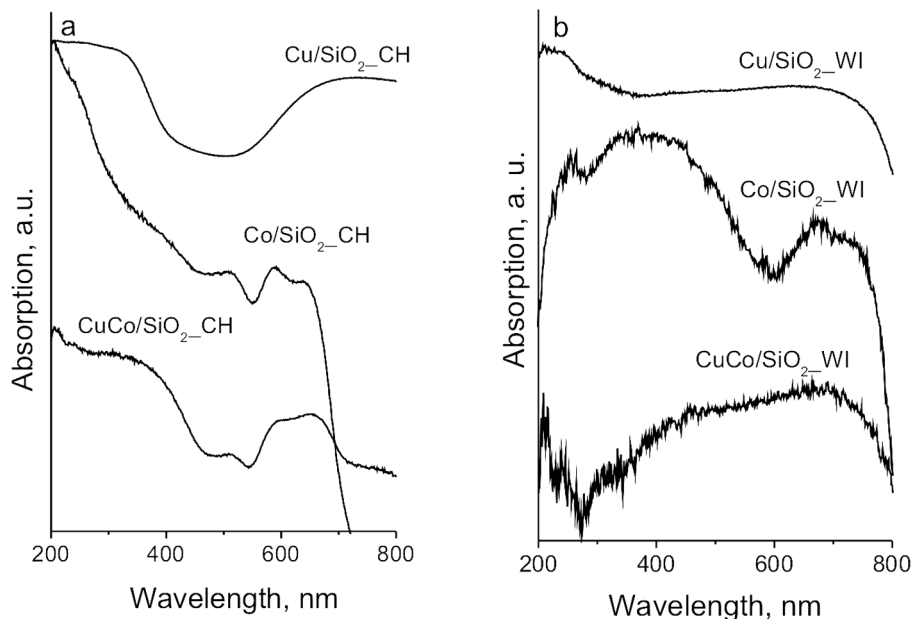


Fig. 2. UV-Vis spectra of copper and cobalt modifications obtained by CH (a) and WI (b) methods

4T1(F)→4T1(P) transitions of octahedrally coordinated Co^{3+} and electronic ligand-field $4A_2$ (F)→ $4T_1$ (p) transition in tetrahedrally coordinated Co^{2+} , respectively. In accordance with the XRD data, (Fig. 1) this evidences presence of well crystallized Co_3O_4 phase. These bands are less resolved in the spectrum of $\text{Co/SiO}_2\text{-CH}$ sample, but the appearance of well pronounced peaks triplet at 525 nm, 583 nm and 654 nm is detected. According to [13] it could be attributed to Co^{2+} species in tetrahedral coordination in CoO_4 units, which includes oxygen ligands from the silica matrix due to strong interaction with it. The changes in the position and relative part of the main absorption peaks for Co_3O_4 in the UV-Vis

spectrum of $\text{CuCo/SiO}_2\text{-WI}$ indicate changes in the distribution of cobalt ions probably due to their partial substitution with copper ones and formation of $\text{Co}_x\text{O}_{3-x}\text{O}_4$ spinel oxide. The UV-Vis spectrum of $\text{CuCo/SiO}_2\text{-CH}$ differs significantly from the spectrum of $\text{CuCo/SiO}_2\text{-WI}$. It could be interpreted as superposition of the spectra of both $\text{Cu/SiO}_2\text{-CH}$ and $\text{Co/SiO}_2\text{-CH}$ mono-component materials, but the small changes in the position and intensity of the main peaks do not excluded also slight interaction between individual oxides.

The formation of well crystallized Co_3O_4 phase in $\text{Co/SiO}_2\text{-WI}$ sample is also evidences by FTIR spectroscopy (Fig. 3a) with the appearance of well

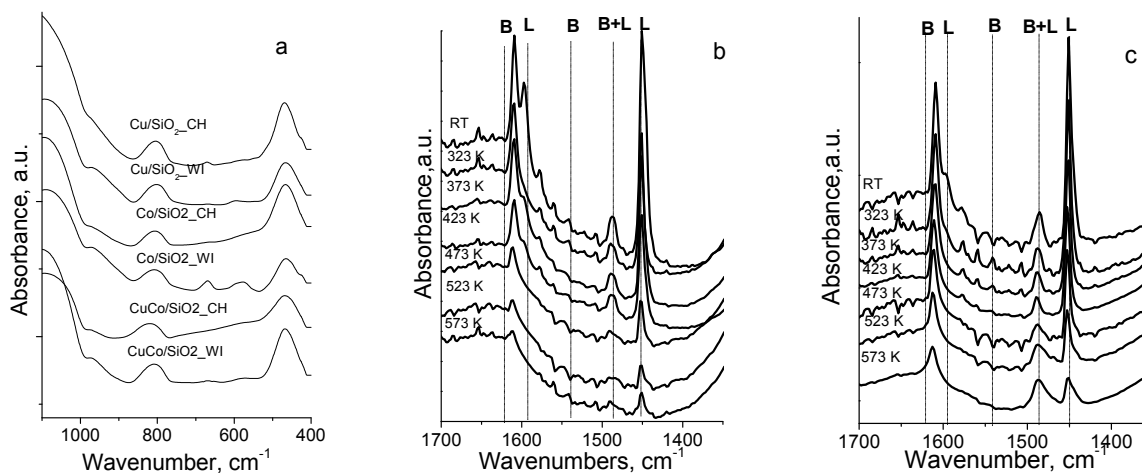


Fig. 3. FTIR spectra of copper and cobalt modifications obtained by different procedures (a) and FTIR of adsorbed pyridine for $\text{CuCo/SiO}_2\text{-CH}$ treated in oxidative (b) and reduction (c) atmosphere

Table 2. XPS data for selected modifications

	Element	BE, (eV)	Concentration (at %)	M/Si Ratio
Cu/SiO ₂ _CH	Cu 2p	933.0	5.34	0.21
	Si 2p	103.4	25.35	
Co/SiO ₂ _CH	Co 2p	781.7	3.78	0.15
	Si 2p	103.5	25.80	
CuCo/SiO ₂ _CH	Co 2p	781.2	1.41	0.05
	Cu 2p	933.0	0.85	0.03
	Si 2p	103.3	26.29	
CuCo/SiO ₂ _WI	Co 2p	778.8	0.68	0.03
	Cu 2p	932.6	1.10	0.05
	Si 2p	103.4	22.35	

resolved bands at 580 cm⁻¹ and 665 cm⁻¹. According to [1] they could be assigned to Co-O stretching vibration mode of Co³⁺ ions in octahedral hole or Co²⁺ ions in tetrahedral hole, respectively. These peaks are less pronounced in the spectrum of Co/SiO₂_CH sample, which is in a good correlation with the UV-Vis and XRD data, indicated very low extent of crystallization of spinel Co₃O₄ phase. The broad band at around 590 cm⁻¹ in the spectrum of Cu/SiO₂_WI is due to stretching vibrations in CuO particles. It is red shifted for Cu/SiO₂_CH probably due to strong interaction of CuO oligomers with the silica support. The observed simultaneous decrease in intensity of the bands at about 665 cm⁻¹ and 580 cm⁻¹ with a tendency of red shifting of the latter in the spectrum of CuCo/SiO₂_WI as compared to the spectra of the corresponding individual oxides could be assigned to the appearance of new type of Co-O stretching vibration mode of Co³⁺ and Cu²⁺ ions in tetrahedral and octahedral coordination, respectively [1]. This spectroscopic data indicate that the loaded metal oxide phase in this sample is not a simple mixture of individual CuO and Co₃O₄ oxides. This conclusion is not valid for CuCo/SiO₂_CH sample where a continuous adsorption in the whole 800–600 cm⁻¹ region is observed. Selected samples were studied by XPS method and data from the analyses are listed in Table 2. The Co 2p_{3/2} peaks in Co/SiO₂_CH and CuCo/SiO₂_CH are observed at ca. 781.7 eV and 781.2 eV, respectively, with the appearance of satellite peak at ca. 5.5 eV higher energy aside from the Co 2p_{3/2} peak. According to the literature data [14], these BEs do not correspond to the BEs typical of polycrystalline Co₃O₄ and CoO phase. So, in accordance with UV-Vis and FTIR measurements, the observed XPS data could be assigned to presence of species with unknown stoichiometry, which are in strong interaction with the silica support. In agreement with [15], the higher values of

BE for Co/SiO₂_CH could be assigned to presence of cobalt silicate Co₂SiO₄ phase as well. This interaction seems to decrease in CuCo/SiO₂_CH, probably due to the appearance of additional interaction with copper species. The higher values of BEs of Cu 2p in Cu/SiO₂_CH and CuCo/SiO₂_CH correspond to Cu²⁺ in highly dispersed oxide species. For comparison, in case of CuCo/SiO₂_WI, BE of Cu 2p is lower, while BE of Co 2p is below the reported for Co₃O₄. Thus, XPS spectra confirm slight interaction between copper and cobalt species when they are supported by CH method, contrary to the WI obtained materials. We should stress on higher surface concentration of Cu ions in case of CuCo/SiO₂_WI as compared to CuCo/SiO₂_CH, which in agreement with the XRD, UV-Vis and FTIR data, confirms their different location, probably in more exposed (octahedral) position in Cu_xCo_{3-x}O₄ spinel for the former material.

Generally, the optimization of surface acid-base and redox properties is of key importance to control the catalytic behavior of solid catalysts, in particular in conversion of methanol molecule, which can be very flexible in presence of different catalytic sites [16]. In our study more information for these characteristics was obtained by FTIR of adsorbed pyridine and TPR study. Selected FTIR data are presented in Fig. 2b, c. The observed intensive peak at 1450 cm⁻¹ and the small ones at 1488 cm⁻¹ and 1610 cm⁻¹ in the spectra of CuCo/SiO₂_CH (Fig. 2b) could be assigned to the adsorbed on Lewis acidic sites pyridine, while no bands corresponding to Brønsted acid sites (1550 cm⁻¹, 1620 cm⁻¹ and 1640 cm⁻¹) are registered [17]. The amount of adsorbed pyridine is 0.057 mmol.g⁻¹ and 0.187 mmol.g⁻¹ for Co/SiO₂_CH and CuCo/SiO₂_CH, respectively, indicating much higher acidity for the bi-component material. The preservation of the FTIR spectra (Fig. 2c) and the amount of adsorbed pyridine (0.189 mmol.g⁻¹)

for the CuCo/SiO₂-CH sample after the reduction treatment (similar reductive conditions are created during the catalytic test) confirms the stability of these acidic sites. For comparison, their changes are more pronounced for pure Co/SiO₂-CH sample, where after reduction the adsorbed amount of pyridine was reduced to 0.041 mmol.g⁻¹.

TPR-DTG profiles for all studied materials are shown in Fig. 4. For both pure copper modifications the main reduction effect is observed in 400–550 K region. The weight loss corresponds to one step Cu²⁺ → Cu⁰ reduction transition. The shifting of this effect to lower temperature for Cu/SiO₂-CH indicates easily reducible and highly dispersed copper phase compared to the IW material though the lower reduction degree (Table 1) suggest also the presence of a small fraction of unreducible copper species. Rather different are the TPR profiles for mono-component cobalt modifications. Taking into account the data from the physicochemical study (see above), step-wise reduction of Co₃O₄ to CoO and then to Co of particles with different dispersion occurs on Co/SiO₂-WI, while reduction of strongly interacted with the silica, mainly

Co²⁺ species is assumed for Co/SiO₂-CH (Fig. 4, Table 1). TPR profiles for bi-component materials reveal different state of metal oxide phase in them. Single effect, which is slightly shifted to lower temperature than the one registered for Cu/SiO₂-WI, is observed for CuCo/SiO₂-WI. In accordance with XRD and spectroscopic data it corresponds to reduction of Cu_xCo_{3-x}O₄ spinel phase. The reduction behaviour of CuCo/SiO₂-CH (Fig. 4, Table 1) confirms the assumption done above, that the strong interaction of different metal oxide species with silica matrix renders difficult their interaction.

Figs. 5a,c represent data for the catalytic activity of the samples in methanol decomposition after their pretreatment in oxidative or reductive atmosphere, respectively. The selectivity to CO, which formation is directly related to hydrogen production from methanol, is shown in Figs. 5b, d. Methane, carbon dioxide, dimethyl ether and C₂-C₃ hydrocarbons are also registered as by-products. Despite the method of samples preparation, well defined tendency for catalytic activity increase for bi-component materials as compared to their mono-component analogues, is registered. This effect is better pronounced for the sample obtained by WI method, where higher selectivity to CO is also found. Note, that bi-component materials preserve their higher activity also after the treatment in reductive atmosphere (Fig. 5c).

So, the incipient wetness impregnation of silica with copper and cobalt nitrates and their further treatment in air promote the formation of finely dispersed, but well crystallized Cu_xCo_{3-x}O₄ spinel particles. Here, the Cu²⁺ ions incorporated into the octahedral sites share the oxygen with adjacent Co²⁺, leading to the formation of Cu-O-Co surface species. The TPR and FTIR of adsorbed pyridine clearly demonstrated that the Cu-Co interaction provides an increase in redox activity and Lewis acidity as compared to the individual oxides and facilitates methanol decomposition in synergistic manner [16]. The combined XRD, UV-Vis, FTIR, XPS and TPR study indicates that “chemisorption-hydrolysis” method leads to the formation of strongly interacted with the support copper and cobalt species, where metal ions exist also in lower oxidative state. This renders difficult the formation of mixed oxide species and, as was well illustrated by FTIR (pyridine) and TPR measurements, and changes the proportion between the acidic and redox functionality. Thus, the prevailing acidic functionality over the redox one for the bi-component materials obtained by CH procedure provides relatively lower catalytic activity and lower selectivity to CO formation. Note, that despite the method of preparation and contrary to individual oxides, bi-component samples exhibit high catalytic activity even after the reduction treatment. We assign this phenomenon to the

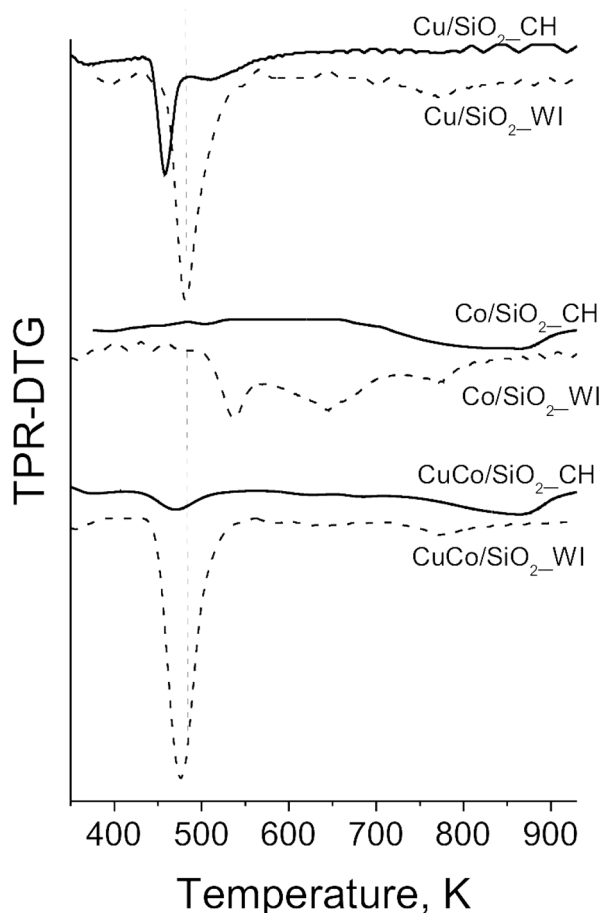


Fig. 4. TPR-DTG profiles of different modifications

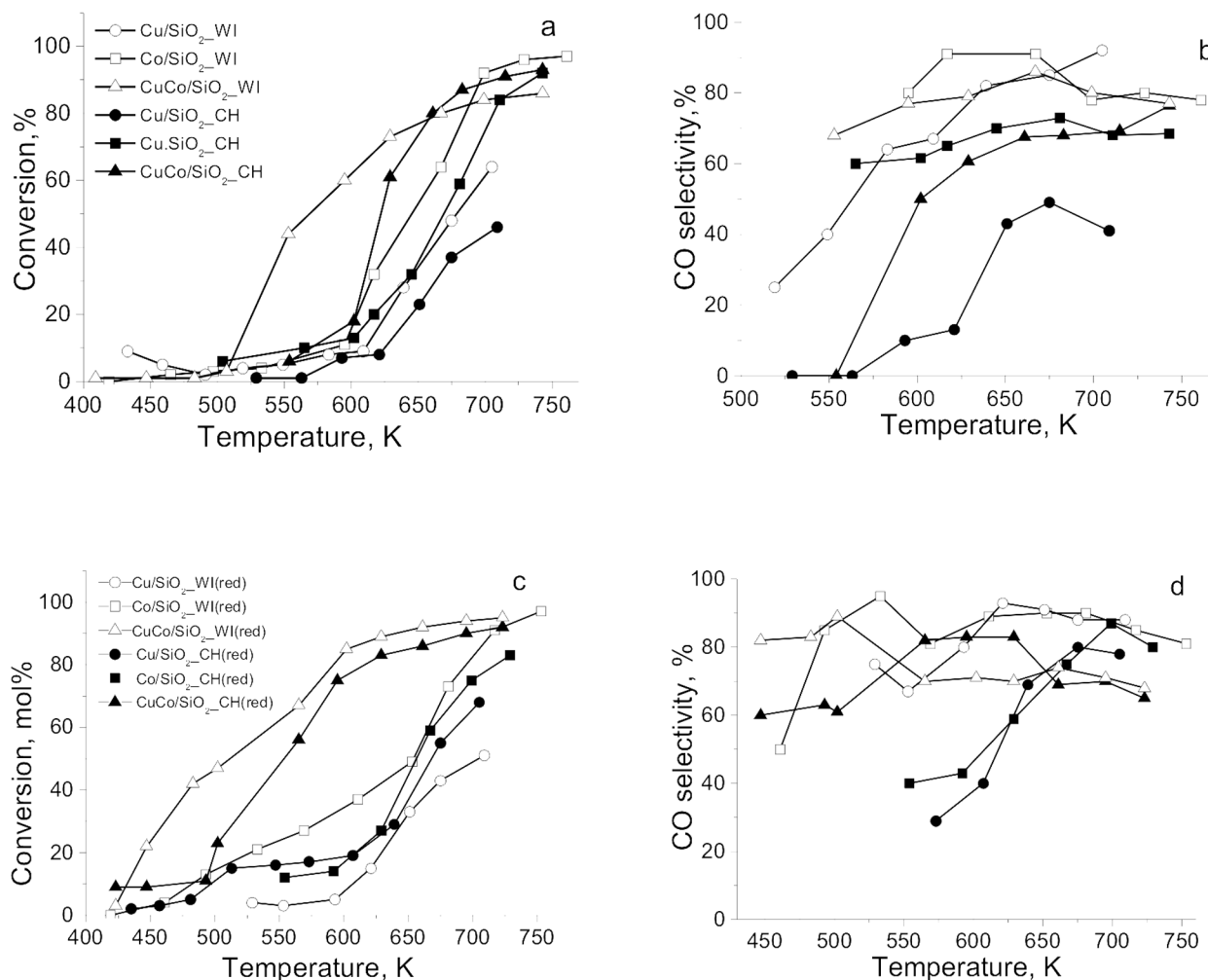


Fig. 5. Methanol conversion (a, c) and CO selectivity (b, d) for the materials treated in air (up) and hydrogen (down) materials

reduction of metal ions, which were stabilized in ordered spinel structure, providing the formation of highly dispersed metal phase. Further investigations are in progress.

CONCLUSION

The modification procedure is a powerful strategy to control the formation of copper cobaltite on SiO₂. The strong interaction of individual metal oxide species with silica support, which realizes during the “chemisorption-hydrolysis” method renders difficult the formation of well crystallized spinel phase, which leads to the formation of less active methanol decomposition catalysts as compared to the conventional incipient wet impregnation technique.

Acknowledgements: Financial support project DFNI-E02/2/12.12.2014 and Bulgarian-Italian

BAS-CNR bilateral project is acknowledged. The authors thank Dr. R. Delaigle and Dr. E. Gaigneaux for the XPS measurements.

REFERENCES

1. E. A.-Gheshlaghi, B. Shaabani, A. Khodayari, Y. A. Kalandaragh, R. Rahimi, *Powder Technol.*, **217**, 330 (2012).
2. M. S.-Niasari, N. Mir, F. Davar, *J. Phys. Chem. Solids*, **70**, 847 (2009).
3. S. Angelov, E. Zhecheva, K. Petrov, D. Menandjiev, *Mat. Res. Bull.*, **17**, 235 (1982).
4. J. Xu, P. Gao, T.S. Zhao, *Energy Env. Sci.*, 5333 (2012).
5. P. Shelke, Y. Kholam, K. Patil, S. Gunjal, S. Jadkar, M. Takwale, K. Mohite, *J. Nano- Electron. Phys.*, **3**, 486 (2011).
6. T. Tsoncheva, V. Dal Santo, A. Gallo, N. Scotti, M. Dimitrov, D. Kovacheva, *Appl. Catal. A: Gen.*, **406**, 13 (2011).

7. T. Tsoncheva, A. Gallo, N. Scotti, M. Dimitrov, R. Delaigle, E. M. Gaigneaux, D. Kovacheva, V. Dal Santo, N. Ravasio, *Appl. Catal. A: Gen.*, **417–418**, 209 (2012).
8. G. Marbán, A. López, I. López, T. V.-Solís, *Appl. Catal. B: Env.*, **99**, 257 (2010).
9. M. Y. Li, W. S. Dong, C. L. Liu, Z. Liu, F. Q. Lin, *J. Cryst. Growth*, **310**, 4628 (2008).
10. G. Laugel, J. Arichi, P. Bernhardt, M. Molière, A. Kiennemann, F. Garin, B. Louis, *CR. Chim.*, **12**, 731 (2009).
11. B. Chi, H. Lin, J. Li, *Int. J. Hydrogen Energy*, **33**, 4763 (2008).
12. L. Liu, Y. Chen, L. Dong, J. Zhu, H. Wan, B. Liu, B. Zhao, H. Zhu, K. Sun, L. Dong, Y. Chen, *Appl. Catal. B: Env.*, **90**, 105 (2009).
13. K. Kojima, H. Taguchi, J. Matsuda, *J. Phys. Chem.*, **95**, 7595 (1991).
14. T. Mochizuki, T. Hara, N. Koizumi, M. Yamada, *Appl. Catal. A: Gen.*, **317**, 97 (2007).
15. H. Ming, B.G. Baker, *Appl. Catal. A: Gen.*, **123**, 23 (1995).
16. T. Tsoncheva, I. Genova, M. Dimitrov, E. Sarcadi-Priboczki, A. M. Venezia, D. Kovacheva, N. Scotti, V. D. Santo, *Appl. Catal. B: Env.*, **165**, 599 (2015).
17. A. Gervasini, S. Bennici, A. Auroux, C. Guimon, *Appl. Catal. A: Gen.*, **331**, 129 (2007).

МЕД И КОБАЛТ МОДИФИЦИРАНИ СИЛИЦИЕВООКСИДНИ КАТАЛИЗАТОРИ ЗА РАЗЛАГАНЕ НА МЕТАНОЛ: ВЛИЯНИЕ НА МЕТОДА НА ПОЛУЧАВАНЕ

Т. С. Цончева^{1*}, И. Г. Генова¹, Н. Скоти², М. Д. Димитров¹,
А. Гало^{2#}, Д. Г. Ковачева³, Н. Равазио²

¹ *Институт по органична химия с Център по фитохимия, Българска Академия на Науките, София, България*

² *Институт по молекулярни изследвания и технологии, ISTM-CNR, Милано, Италия*

³ *Институт по обща и неорганична химия, Българска Академия на Науките, София, България*

[#] *Настоящ адрес: Факултет по химично инженерство, Калифорнийски университет, Санта Барбара, САЩ 93106-5080*

Постъпила декември, 2014 г.; приета януари, 2015 г.

(Резюме)

Разработен е нов метод, наречен „хемосорбция-хидролиза“, за получаване на нанесени върху SiO₂ смесени мед-кобалт оксидни катализатори. За сравнение, аналогични материали са получени чрез използването на традиционен метод на импрегниране. Състоянието на нанесените металооксидни частици е характеризирано чрез Рентгенова дифракция, ИЧ-КВг, ИЧ на адсорбиран пиридин, УВ и Рентгенова фотоелектронна спектроскопия, Температурно програмирана редукция с водород. Каталитичните свойства на образците са изследвани в реакция на разлагане на метанол. Промените в процедурата на модифициране води до формирането на различни металооксидни частици, което предоставя лесен подход за контрол на повърхностните и каталитични свойства на мед-кобалт оксидната би-компонентна система.

Structural analysis of reduced graphene oxide by transmission electron microscopy

A. Shalaby^{1,2*}, D. Nihtianova^{3,4}, P. Markov⁴, A. D. Staneva²,
R. S. Iordanova⁴, Y. B. Dimitriev²

¹ Science and Technology Center of Excellence, Cairo-Egypt

² University of Chemical Technology and Metallurgy, 8 Kl. Ohridski blvd., 1756 Sofia,
Bulgaria, E-mail: yanko@uctm.edu

³ Institute of Mineralogy and Crystallography, Bulgarian Academy of Sciences, Acad. G. Bonchev Str.,
bl. 107, 1113 Sofia, Bulgaria

⁴ Institute of General and Inorganic Chemistry, Bulgarian Academy of Sciences, G. Bonchev str.,
bld. 11, 1113 Sofia, Bulgaria

Received December, 2014; Revised January, 2015

Graphene has attracted scientific interest in recent years due to its unique properties. Reduced graphene oxide (RGO) was prepared by chemical oxidation of purified natural graphite to obtain graphite oxide then the material was exfoliated to reduced graphene nanosheets by ultrasonication and reduction process using sodium borohydride (NaBH_4). The transmission electron microscopy (TEM) investigations were performed on a TEM JEOL 2100 instrument at an accelerating voltage of 200 KV. The measurements of lattice-fringe spacing recorded in High Resolution Transmission Electron Microscopy (HRTEM) micrographs were made using digital image analysis of reciprocal space parameters. The analysis was carried out by the Digital Micrograph software. The obtained selected area electron diffraction (SAED) data show unambiguously that the sample RGO is different from Graphite 2H PDF 75-1621 and has typical interplanar distance d_{002} from 3.586 Å up to 4.016 Å. Lattice fringes obtained by HRTEM method also give additional information about interplanar distance d_{002} for RGO materials where the value is 3.850 Å. It was established that the main phase is RGO but some impurities of Graphite is also found.

Key words: Reduced Graphene Oxide, Structural analysis, TEM analysis.

INTRODUCTION

Reduced graphene oxide (RGO) is one of the exciting topics in many research fields especially in the field of nanotechnology during the last few years. It has different names such as chemically modified graphene, functionalized graphene, chemically converted graphene, or simply graphene. RGO has excellent electrical, thermal and mechanical properties [1, 2]. It is a very promising material for many applications, such as in the development of energy-storage capacitors [3–5], field-effect transistors [6], energy-related materials [7], sensors [8], heavy metal removal [9], drug delivery [10] and biomedical applications [11]. Generally graphene can be produced by top-down or bottom-up approaches. The common methods include mechanical or

chemical exfoliation of graphite, epitaxial growth on SiC and chemical vapor deposition on metal surfaces [12–15]. These methods can produce graphene with a relatively perfect structure and excellent properties. The most popular method which considered a promising route to achieve mass production with low cost is the chemical method for producing graphene sheets from natural graphite [16]. Graphite is available in large quantities from natural sources and consists of a stack of flat graphene sheets held together by weak van der Waals forces [17]. By using highly oxidizing reagents these stack sheets of graphite exfoliated to be graphite oxide. The carbon atoms plane in graphite oxide is heavily decorated by oxygen-containing groups, which expand the interlayer distance and make the atomic-thick layers hydrophilic [18]. These oxidized layers can be exfoliated in water under moderate ultrasonication. Reduction of graphene oxide sheets using reductive reagents such as sodium borohydride [19, 20] removes the oxygen-containing groups to produce

* To whom all correspondence should be sent:
E-mail: ashalaby2011@gmail.com

graphene-like sheets named reduced graphene oxide. There is a general consensus that it is very difficult to remove all the oxygen-containing groups from the graphene oxide layers by chemical reduction. Obviously, the electrical performance of RGO depends on the strength of the reducing agents and the amount of residual functional groups remaining after reduction. The conductivity of graphene oxide can be increased more than 4 orders of magnitude after reduction [21–22]. Generally, a detailed study of the atomic structure of RGO is considered as an important step to understand the properties of this material. The specific atomic scale features in chemically derived graphene monolayers has been already studied in details by Gomez-Navarro [23]. They contribute to the better understanding of effects of the defects which has to be taken into account for any comprehensive study of the RGO properties. There are a few papers concerning the structural analysis of RGO obtained by different methods such as chemical graphitization using a novel reducing agent system hydriodic acid with acetic acid [24], hot pressing [25], thermocatalytic decomposition of methane [26]. Up to now, there is no sufficient data on the structural analysis with lattice-fringe spacing measurements made by HRTEM of chemically derived RGO. This motivates our study.

Recently, we studied the thermal stability of RGO and RGO/SiO₂ nanocomposite prepared by sol-gel technique [20]. This paper is a continuation of our previous investigations and an attempt to present a structural analysis of chemically derived RGO using HRTEM and Powder X-ray Diffraction (XRD) is made.

EXPERIMENTAL

RGO nanosheets are obtained from purified natural graphite powder 99.9% (Alfa Aesar Co.) by different chemical treatments. First step comprises oxidation of graphite powder to graphite oxide by using a modified Hummer's method [27, 28]. In the next step, the graphite oxide is ultrasonicated in order to obtain graphene oxide which is subsequently reduced by using sodium borohydride 98% (Alfa Aesar Co.) to reduced graphene oxide (RGO). A detailed scheme describing each step of the synthesis method is given in our previous paper [20].

The phase formation was studied by XRD technique (Bruker D8 Advance, Cu K α radiation) while the microstructure and morphology of the as-obtained products were observed by Scanning Electron Microscopy (SEM, Philips 525M). TEM investigations were performed on a JEOL JEM 2100 instrument at an accelerating voltage of 200 kV. The specimens were prepared by grinding and dispers-

ing them in ethanol by ultrasonic treatment for 6 min. The suspensions were dripped on standard carbon/Cu grids. The measurements of lattice-fringe spacing recorded in HRTEM micrographs were made using digital image analysis of reciprocal space parameters. The analysis was carried out by the Digital Micrograph software.

RESULTS AND DISCUSSION

Figure 1 shows the XRD patterns of graphite, graphite oxide (GO) and reduced graphene oxide (RGO). Pristine graphite exhibits a basal reflection (002) sharp peak at $2\theta = 26.37$ degree corresponding to d spacing of 3.370 Å which is compatible with the literature data (JCPDS 75-2078, 3.347 Å). Upon oxidation of pristine graphite, the (002) reflection peak shifts to the lower angle at $2\theta = 12.43$ degree (d spacing = 7.110 Å) and a small peak remains closed to the position $2\theta = 26.26$ degree (d spacing = 3.390 Å). The increase in d spacing is due to the intercalation of water molecules and the formation of oxygen containing functional groups between the layers of the graphite [29]. In contrast to GO, all RGO have a broad peak centered at $2\theta = 26.29$ degree corresponding to d spacing of 3.380 Å which might be attributed to very thin RGO layers due to high degree of exfoliation. The close d-spacing of RGO to pristine graphite and disappearance of peak at $2\theta = 12.43$ degree indicate that the oxygen containing group of graphite oxide have been efficiently removed. There are published data which report that the graphene nanosheets are exfoliated into a monolayer or few-layers and it results in new lattice structure, which is significantly different from the pristine graphite flakes and graphite oxide

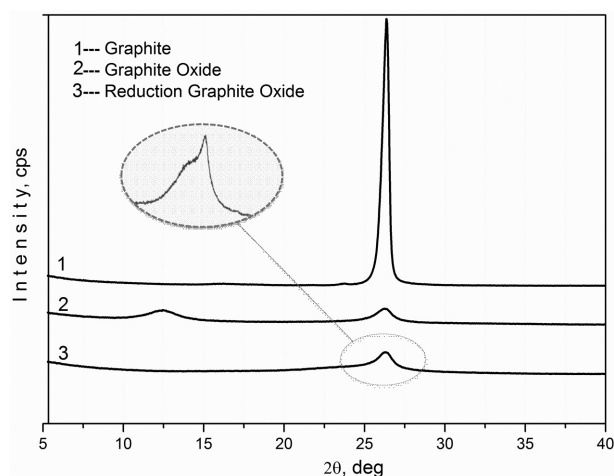


Fig. 1. XRD patterns of graphite, graphite oxide and reduced graphene oxide

sheets [30, 31]. As it is seen on Figure 1 a presence of amorphous halo at $2\theta = 23\text{--}25$ degree is observed. According to S. Huh [30] this is amorphous-like carbon which comprises many defects, folding

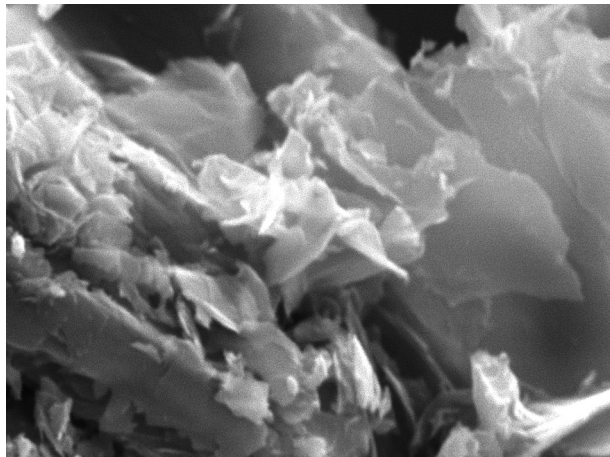


Fig. 2. SEM image of reduced graphene oxide sheets

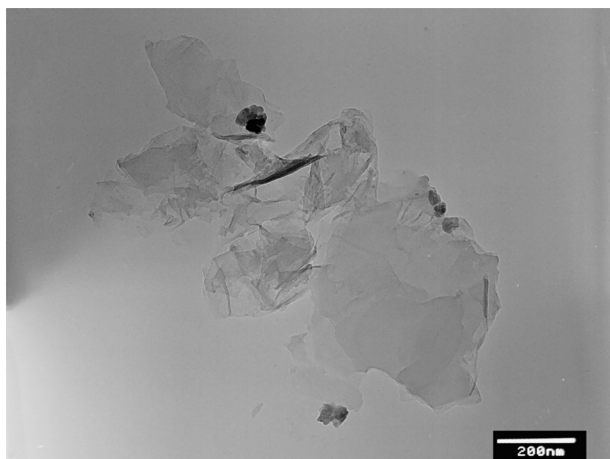


Fig. 3. TEM image of reduced graphene oxide sheets

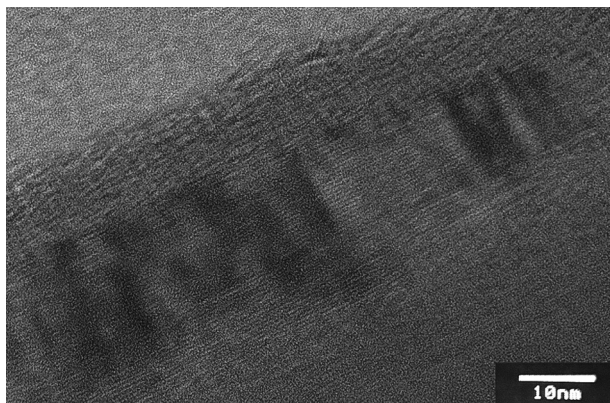


Fig. 4. HRTEM micrograph of reduced graphene oxide sheets

structures, impurities, sp^1 , sp^2 , and sp^3 hybridization structures.

Figure 2 presents SEM image of RGO sheets which appeared as similar thin sheets randomly aggregated, with distinct edges, wrinkled surfaces, and folding. The mean sheets dimension was about $10 \times 20 \mu\text{m}$.

The TEM investigations at lower resolutions are shown on Figure 3 and the obtained data exhibit that RGO sheets consist of few layers ($n < 6$) stacked each other with less wrinkles and folding. Figure 4 represents a HRTEM micrograph of RGO sheets and it clearly shows the lattice fringes of graphene. This gives additional information about the interplanar distance d_{002} for RGO material which value is 3.850 \AA . The crystallographic structure of the graphene sheets was characterized by SAED method. The previous studies mentioned that most of the graphene sheets exhibited a single set of hexagonal diffraction pattern with sharp and clear diffraction spots [32]. Figure 5 shows SAED pattern of reduced graphene oxide. The obtained SAED data show unambiguously that the sample RGO differs from Graphite 2H PDF 75-1621 and has typical interplanar distance d_{002} from 3.586 \AA up to 4.016 \AA for three different RGO samples. For comparison, the



Fig. 5. SAED of reduced graphene oxide

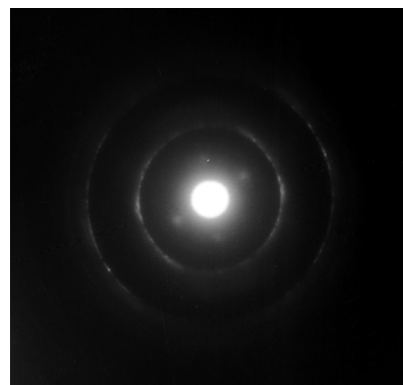


Fig. 6. SAED of graphite flakes

interplanar distance d_{002} of the graphite layers was measured to be about 3.400 Å as shown in Figure 6 and this data are in good accordance with the literature data [33].

CONCLUSIONS

The electron diffraction data established that the chemically derived RGO has interplanar distance d_{002} from 3.586 Å to 4.016 Å. Lattice fringes obtained by HRTEM method also give additional information about interplanar distance d_{002} where the value of RGO material was 3.850 Å.

REFERENCES

1. S. Pei, H.-M. Cheng, *Carbon*, **50**, 3210 (2012).
2. K.T. Das, S. Prusty, *Int. J. Chem. Sci. Appl.*, **4**, 39 (2013).
3. M. Liang, L. Zhi, *J. Mater. Chem.*, **19**, 5871 (2009).
4. M.D. Stoller, S. Park, Y. Zhu, J. An, R.S. Ruoff, *Nano Lett.*, **8**, 3498 (2008).
5. E. Yoo, J. Kim, E. Hosono, H.S. Zhou, T. Kudo, I. Honma, *Nano Lett.*, **8**, 2277 (2008).
6. L. Wang, Y. Park, P. Cui, S. Bak, H. Lee, S. M. Lee, H. Lee, *Chem. Commun.*, **50**, 1224 (2014).
7. Y. Zhu, S. Murali, W. Cai, X. Li, J. W. Suk, J. R. Potts, R. S. Ruoff, *Adv. Mater.*, **22**, 3906 (2010).
8. J. T. Robinson, F. K. Perkins, E. S. Snow, Z. Wei, P. E. Sheehan, *Nano Lett.*, **8**, 3137 (2008).
9. D. Fialova, M. Kremplova, L. Melichar, P. Kopel, D. Hynek, V. Adam, R. Kizek, *Materials.*, **7**, 2242 (2014).
10. G. Wei, R. Dong, D. Wang, L. Feng, S. Dong, A. Song, and J. Hao, *New J. Chem.*, **38**, 140 (2014).
11. L. Cardenas, J. MacLeod, J. Lipton-Duffin, D. G. Seifu, F. Popescu, M. Sijaj, D. Mantovani, and F. Rosei, *Nanoscale*, **6**, 8664 (2014).
12. C. N. R. Rao, K. S. Subrahmanyam, H. S. S. R. Matte, B. Abdulhakeem, A. Govindaraj, B. Das, P. Kumar, A. Ghosh, D. J. Late, *Sci. Technol. Adv. Mater.* **11**, 054502 (2010).
13. C. Berger, Z. Song, X. Li, X. Wu, N. Brown, C. Naud, D. Mayou, T. Li, J. Hass, A. N. Marchenkov, E. H. Conrad, P. N. First, W. A. de Heer, *Science*, **312**, 1191 (2006).
14. X. Li, W. Cai, J. An, S. Kim, J. Nah, D. Yang, R. Piner, A. Velamakanni, I. Jung, E. Tutuc, S. K. Banerjee, L. Colombo, R. S. Ruoff, *Science*, **324**, 1312 (2009).
15. A. Reina, X. Jia, J. Ho, D. Nezich, H. Son, V. Bulovic, M. S. Dresselhaus, J. Kong, *Nano Lett.*, **9**, 30 (2009).
16. D. R. Dreyer, S. Park, C. W. Bielawski, R. S. Ruoff, *Chem. Soc. Rev.*, **39**, 228 (2010).
17. L.-Y. Meng, S.-J. Park, *Bull. Korean Chem. Soc.*, **33**, 209 (2012).
18. F. Bing-Bing, G. Huan-Huan, Z. Rui, J. Yu, and S. Chun-Yan, *Chinese Phys. Lett.*, **31**, 078102 (2014).
19. Y. Si, E.T. Samulski, *Nano Lett.*, **8**, 1679 (2008).
20. A. Shalaby, V. Yaneva, A. Staneva, L. Aleksandrov, R. Iordanova, Y. Dimitriev, In: Nanoscience & Nanotechnology (Proc. 15th Inter. workshop on Nanoscience and Nanotechnology, Sofia, 2013), E. Balabanova, E. Mileva (eds.), vol. 14, Sofia, Bulgaria, 2014, p 120.
21. S. Park, R. S. Ruoff, *Nat. Nano.*, **4**, 217 (2009).
22. C. Vallés, J. D. Núñez, A. M. Benito, W. K. Maser, *Carbon*, **50**, 835 (2012).
23. C. Gomez-Navarro, J. C. Meyer, R. S. Sundaram, A. Chuvilin, S. Kurasch, M. Burghard, K. Kern, U. Kaiser, *Nano Lett.*, **10**, 1144 (2010).
24. I. K. Moon, J. Lee, R. S. Ruoff, H. Lee, *Nat Commun.*, **1**, 73 (2010).
25. Y. Zhang, D. Li, X. Tan, B. Zhang, X. Ruan, H. Liu, C. Pan, L. Liao, T. Zhai, Y. Bando, S. Chen, W. Cai, R. S. Ruoff, *Carbon*, **54**, 143 (2013).
26. Y. Shen, A. C. Lua, *Sci. Rep.*, **3**, 3037 (2013).
27. W. S. Hummers, R. E. Offeman, *J. Am. Chem. Soc.*, **80**, 1339 (1958).
28. D. C. Marcano, D. V. Kosynkin, J. M. Berlin, A. Sinitskii, Z. Sun, A. Slesarev, L. B. Alemany, W. Lu, J. M. Tour, *ACS Nano.*, **4**, 4806 (2010).
29. J. I. Paredes, S. Villar-Rodil, A. Martínez-Alonso, J. M. D. Tascón, *Langmuir*, **24**, 10560 (2008).
30. S. H. Huh, in Physics and Applications of Graphene – Experiments, S. Mikhailov (Ed.), InTech Europe, Croatia, 2011, p. 73.
31. S. Thakur, N. Karak, *Carbon*, **50**, 5331 (2012).
32. N. R. Wilson, P. A. Pandey, R. Beanland, R. J. Young, I. A. Kinloch, L. Gong, Z. Liu, K. Suenaga, J. P. Rourke, S. J. York, J. Sloan, *ACS Nano.*, **3**, 2547 (2009).
33. C. H. Kiang, M. Endo, P. M. Ajayan, G. Dresselhaus, M. S. Dresselhaus, *Phys. Rev. Lett.*, **81**, 1869 (1998).

СТРУКТУРЕН АНАЛИЗ НА РЕДУЦИРАН ГРАФЕНОВ ОКСИД ЧРЕЗ ТРАНСМИСИОННА ЕЛЕКТРОННА МИКРОСКОПИЯ

А. Шалаби^{1,2*}, Д. Нихтянова^{3,4}, П. Марков⁴, А. Д. Станева²,
Р. С. Йорданова⁴, Я. Б. Димитриев²

¹ Наука и технологии, Център за върхови постижения, Кайро, Египет

² Химикотехнологичен и металургичен университет, бул. „Кл. Охридски“, 1756 София,
България, Е-мейл: uanko@uctm.edu

³ Институт по минералогия и кристалография, Българска академия на науките,
ул. „Акад. Г. Бончев“, Бл. 107, 1113 София, България

⁴ Институт по обща и неорганична химия, Българска академия на науките,
ул. „Акад. Г. Бончев“, бл. 11, 1113 София, България

Постъпила декември, 2014 г.; приета януари, 2015 г.

(Резюме)

През последните години графенът е интересен обект за научни изследвания преди всичко заради специфичните си свойства. В настоящата работа редуцираният графенов оксид (РГО) е синтезиран чрез химична реакция от графит и последваща екслоиация до редуцирани графенови наноплоскости чрез ултразвуков метод и редукция чрез натриев борен хидрид (NaBH_4). Изследванията с трансмисионна електронна микроскопия (ТЕМ) са извършени с апарат ТЕМ JEOL 2100 и ускоряващо напрежение 200 кV. Структурните измервания са записани на HRTEM микрографии, използвайки дигитален анализ на реципрочните пространствени параметри. Анализът е направен чрез “Digital Micrograph” софтуер. Получените данни за избрани области на електрона дифракция (SAED) ясно показваха, че образецът РГО се различава от графита 2H PDF 75-1621 и има характерно междуплоскостно разстояние d_{002} от 3.586 Å до 4.016 Å. Допълнителната информация, получена чрез HRTEM метода, също показва, че междуплоскостното разстояние d_{002} за РГО има стойност 3.850 Å. Установено бе, че основната фаза е РГО, но малки замърсявания от графит също бяха регистрирани.

Cu(II)-imprinted copolymer microparticles: effect of the porogen solvents on particle size, morphology and sorption efficiency

I. G. Dakova^{1*}, V. A. Dakov², M. Karadjov³, I. B. Karadjova¹

¹ Faculty of Chemistry and Pharmacy, Sofia University "St. Kliment Ohridski",
1 James Bourchier Blvd., Sofia, Bulgaria

² University Laboratory of Ecology and Environmental Protection, University of Forestry,
10 Kliment Ohridsky Blvd., Sofia, Bulgaria

³ Geological Institute, Bulgarian Academy of Science, Acad. G. Bonchev St. Bl. 24,
Sofia 1113, Bulgaria

Received December, 2014; Revised January, 2015

New Cu(II)-imprinted poly(hydroxyethyl methacrylate-co-trimethylolpropane tri-methacrylate) copolymer gels (Cu-IIPs) were prepared by precipitation copolymerization for the selective solid phase extraction of Cu(II). The Cu-IIPs were characterized by elemental analysis, Fourier transform infrared spectroscopy, scanning electron microscopy and nitrogen physisorption. The effect of the porogen solvents acetonitrile, toluene and their mixtures on particle size and morphology was presented. The adsorption properties of the synthesized copolymers were determined using batch experiments. At optimal chemical parameters the Cu-IIPs show fast sorption/desorption kinetics, high selectivity and satisfied adsorption capacity for adsorption of Cu(II). Finally, the prepared in acetonitrile Cu-IIPs were successfully applied to the selective recognition and determination of copper ions in surface waters.

Key words: Cu(II)-imprinted copolymer microparticles, copper ions, solid phase extraction.

INTRODUCTION

Copper is an essential micronutrient and participates in the cell growth, metabolism and enzyme activities, but slightly above the background concentrations copper can be highly toxic in surface waters to invertebrates and fish [1]. In natural surface waters the concentrations of Cu(II) are usually low with an average concentration of 2 µg/L [2]. Due to the influences of coexisting substances in real water samples, development of analytical procedures for reliable and accurate determination of Cu(II) in surface waters is still an analytical challenge [3]. A great variety of analytical procedures for Cu(II) separation and enrichment are proposed, based mainly on liquid–liquid extraction and micro-extraction [4–6], cloud point extraction [7, 8], coprecipitation [9] and solid phase extraction (SPE) [10–13]. However, SPE is preferred among them because of its significant advantages such as simplicity of performance, low solvent consumption, fast separation of phases without emulsion forma-

tion, high enrichment factor, good reproducibility and flexibility [14, 15]. Relatively low selectivity of conventional sorbents used is the main disadvantage of this approach. It could be significantly improved by using ion-imprinted polymers (IIPs) as sorbents. Generally, IIPs are a new generation of materials with ionic recognition sites having high affinity towards the analytes of interest as compared to the competing species which may also be found in the same matrices [16]. Properties of IIP are remarkable because of their high selectivity towards the target ion due to a memory effect resulting from their preparation process [17]. The general procedure for IIP preparation consists in the formation of a ligand-metal complex and its copolymerization with a cross-linker in order to create three dimensional recognition cavities inside the polymer network. Two main factors are responsible for their high selectivity: the affinity of the ligand toward the imprinted metal ion and the suitable size and shape of the generated cavities [18, 19]. Although polymer matrix is accepted as inert support its binding and sorption properties could influence sorption characteristics and efficiency of synthesized sorbents. Various types of functional monomers have been used in the synthesis of Cu(II) imprinted co-

* To whom all correspondence should be sent:
E-mail: ahid@chem.uni-sofia.bg

polymer gel matrixes: new-synthesized vinylated chelating agents [20, 21], acrylamide [22], N-vinyl-2-pyrrolidone [23], styrene [24], and 4-vinylpyridine (4-VP) [25, 26]. Recently, our group reported a simple procedure for synthesis of microspheric Cu-IIPs via precipitation copolymerization using methacrylic acid (MAA), 4-VP or their mixtures as functional monomers, trimethylolpropane trimethacrylate (TMPTMA) as a cross-linking agent and 4-(2-pyridylazo)resorcinol (RAR) as a specific Cu(II) ligand [27, 28]. However, the carboxylic and pyridine groups in MAA and 4-VP, respectively, are deprotonated in neutral and alkali solutions and this leads to decreased selectivity due to non-specific interactions with other cations. Replacement of MAA (acidic monomer) and 4-VP (basic monomer) with 2-hydroxyethyl methacrylate (HEMA) as neutral functional monomer could improve polymer selectivity. According to authors' knowledge, the Cu-IIPs containing HEMA as a functional monomer have not been synthesized and studied.

In this study, new Cu-IIPs was prepared via precipitation copolymerization using HEMA as a functional monomer, TMPTMA as a crosslinking agent and PAR as a specific for Cu(II) ligand in the presence of different porogen solvents. The synthesized Cu-IIPs were further characterized by scanning electron microscopy (SEM), nitrogen adsorption-desorption isotherms, Fourier transform infrared spectroscopy (FTIR) and elemental analysis. The effect of the type of porogen_solvents used on the morphology and the sizes of polymer particles were defined. The extraction efficiency and selectivity of synthesized Cu-IIPs and non-imprinted polymer gels toward Cu(II) were compared and most suitable of them proposed and applied for Cu(II) determination in surface water samples.

EXPERIMENTAL

Materials

All reagents were of analytical-reagent grade and in all experiments deionized water (DW) (Millipore Corp., Milford, MA, USA) was used. The stock standard solutions of Cu(II), Cd(II), Ni(II) and Pb(II) (1000 µg/mL) were Titrisol, Merck (Germany), in 2 % HNO₃. Working standard solutions were daily prepared by appropriate dilution with DW. PAR (as Na salt, Koch-Light Laboratories Ltd, England), HEMA, TMPTMA, 2,2'-azo-bis-isobutyronitrile (AIBN) (Merck, Germany), acetonitrile (ACN) and toluene (T) (Labscan, Ireland) were used without further purification. The pH was adjusted with the following buffer solutions: CH₃COONa/CH₃COOH for pH 4–6; KH₂PO₄/NaOH for pH 7 and 8.

Apparatus

Electrothermal atomic absorption spectrometric (ETAAS) measurements were carried out on a Perkin Elmer Zeeman 3030 spectrometer (Uberlinden, Germany) with an HGA-600 atomizer. The light source used was a hollow cathode lamp for Cu. The spectral bandpass was 0.7 nm. Pyrolytic graphite-coated graphite tubes were used as atomizers. Solutions (20 µL) were introduced into the graphite atomizer using an AS-60 autosampler. Only peak areas were used for quantification. The IR-spectra (4000–400 cm⁻¹) in KBr disks were recorded on a Nicolet 6700 FTIR spectrometer (Thermo Scientific, USA). A scanning electron microscope (SEM, JEOL JSM-5500, Japan) was used for the determination of the microparticles shape and size. Elemental analysis was carried out with an universal CHNOS elemental analyzer Vario EL III (Elementar Analysen systeme GmbH, Germany). Specific surface area and pore size distribution were measured through nitrogen adsorption-desorption isotherms at 77 K using a Quantachrome NOVA 1200 apparatus (Quantachrome UK Ltd, England). A microprocessor pH meter (Hanna Instruments, Portugal) was used for pH measurements. A centrifuge EBA-20 (DJB Labcare Ltd, England) was used to separate microparticles and extracted metal ion solution in batch experiments.

Preparation of Cu(II)-IIPs

The synthesis of Cu(II) ion-imprinted and non-imprinted polymer gels was adapted from the procedure reported by Dakova et al. [27]. The Cu-IIPs (called P(Cu-PAR-HEMA)) were prepared via a precipitation copolymerization using HEMA (0.57 mmol) as a functional monomer, TMPTMA (0.93 mmol) as a cross-linking agent, AIBN (0.10 mmol) as an initiator, complex of the imprinted ion (Cu(II)) with PAR (0.08 mmol) as a template. Various porogen solvents: ACN, toluene, mixtures of ACN with toluene (25 mL) were tested. Briefly the solution was saturated with dry nitrogen for 15 min and copolymerization was carried out at T = 60 °C for 24 h. The polymer particles obtained were recovered by centrifugation, washed with ACN to remove unreacted monomers and other ingredients. Copper was removed from the sorbent by several, sequential elution steps using 2 M HNO₃. This procedure was repeated until the Cu concentration (template ions) in the eluate solution is below the limit of quantification (LOQ, 10σ criteria) as measured by ETAAS. Non-imprinted polymer sorbent (called P(HEMA)) was synthesized in the same way as described above, in the absence of Cu(II)-PAR complex. Cu(II) ion-imprinted polymer gels and

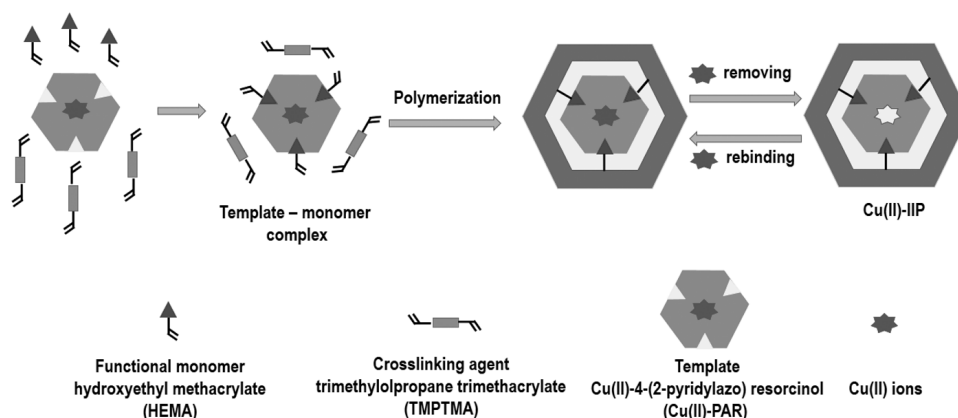


Fig. 1. Schematic representation of ion imprinting process

P(HEMA) were dried in a vacuum oven at 60 °C. The preparation of IIPs is presented schematically in Fig. 1.

Sorption experiments

The effect of pH on the sorption of Cu(II) was tested by equilibrating 50 mg of the prepared imprinted and non-imprinted polymer gels with 10 mL of the buffer solutions containing 0.1 µg of Cu(II) under different pH conditions for 30 min. The sample was centrifuged (5000 rpm), supernatant removed and polymer particles washed twice with DW. The Cu(II) was eluted from the sorbent with 1 mL 2 M HNO₃. Copper content in the effluente (supernatant after sorption) and eluate solutions was determined by ETAAS measurements. The kinetics of the Cu(II) sorption and desorption were investigated in a batch system by adding 50 mg of the P(Cu-PAR-HEMA) particles to 10 mL of Cu(II) solution at pH 7 for 5–40 min. Samples were regularly collected at appropriate time intervals, separated and analyzed for Cu(II) content. To measure the sorption capacity, 50 mg of P(Cu-PAR-HEMA) and P(HEMA) were equilibrated with 10 mL Cu(II) containing solutions with increasing initial concentrations (50–450 µmol/L) under optimum conditions at room temperature. Competitive loading of Cd(II), Cu(II), Ni(II) and Pb(II) by Cu(II)-imprinted and non-imprinted polymer gels was examined in aqueous solutions containing 0.1 µg/mL Cu(II), 0.1 µg/mL Cd(II), 0.3 µg/mL Ni(II) and 0.3 µg/mL Pb(II) at pH 7.

Sorption characteristics of the polymer particles

The degree of sorption (E%), distribution ratio (D), selectivity coefficient ($S_{Cu/Me}$) and relative se-

lectivity coefficient (k') were calculated by the following equations:

$$E \% = [(A_i - A_{eff}) / A_i] \cdot 100 \quad S_{Cu/Me} = D_{Cu} / D_{Me}$$

$$D = (A_i - A_{eff}) / A_{eff} \quad k' = S_{imprinted} / S_{non-imprinted}$$

where A_{eff} (µg) is the cation amount in the effluente solution after sorption from a solution with an initial cation amount A_i (µg); D_{Cu} and D_{Me} are the distribution ratios for Cu(II) and Cd(II), Ni(II) or Pb(II), respectively.

RESULTS AND DISCUSSION

Synthesis of Cu(II)-IIP and characterization studies

Cu-IIPs were synthesized by “trapping” technique, i.e. complexes between target metal ion and non-vinylated chelating agent get trapped inside the polymer matrix during the polymer formation. In this case, preparation of Cu(II)-IIPs included several steps (Fig. 1). Firstly, the template-monomer (prepolymerization) complex was formed by non-covalent interactions between the functional monomer (HEMA) and the template molecule (Cu(II)-PAR complex). Secondly, the copolymer network was formed by the precipitation copolymerization of the prepolymerization complex with TMPTMA as a cross-linker. Finally, Cu(II) ions were removed from copolymer network prepared leaving behind some specific binding sites with functional groups in a predetermined orientation and cavities with special size of templates.

In the present investigation, initially four types of Cu-IIPs were synthesized using varying solvent composition: ACN, toluene and mixture of ACN-toluene (80:20 and 60:40, v/v) to observe

the solvent effect on the morphology of the polymer gels. The SEM micrographs of prepared P(Cu-PAR-HEMA)s are presented in the Fig. 2. It is seen that spherical particles with mean diameters of about 3 μm and about 1 μm were obtained when ACN and ACN-toluene (80:20) were used as porogen solvents (P_{ACN} (Cu-PAR-HEMA) and ($P_{\text{ACN-T(80:20)}}$ (Cu-PAR-HEMA)), respectively (Fig. 2, A and B). Irregular shaped and agglomerated particles can be seen in the SEM images of Cu-IIPs synthesized in the presence of mixture of ACN-toluene (60:40) ($P_{\text{ACN-T(60:40)}}$ (Cu-PAR-HEMA)) (Fig. 2, C). It might be concluded that when the quantities of toluene in the ACN-toluene mixture were low (0% or 20%), large spherical Cu-IIPs particles with relative uniformity and monodispersity were obtained. However, as the percentage of toluene in the solvent mixture increased to about 40%, the particle shape changed from globular to agglomerates formed by smaller particles (Fig. 2, C). A similar influence of the quantity of toluene in the ACN-toluene mixture on the size of molecularly imprinted microspheres prepared by precipitation polymerization was also found by Pardeshi et al. [29]. The SEM micrographs of the particles P_{T} (Cu-PAR-HEMA) prepared in toluene showed irregular aggregates of bigger particles packed together with a smoothly spherical surface (Fig. 2, D).

The specific surface area, total pore volume and average pore diameter, for the Cu-IIPs and non-imprinted P(HEMA) were determined from nitrogen adsorption-desorption isotherms. Both P_{ACN} (Cu-PAR-HEMA) and P_{T} (Cu-PAR-HEMA), have similar surface areas (4 m^2/g and 3 m^2/g) and average pore diameters (15 nm and 12 nm), while P(HEMA) has higher surface area (9 m^2/g) and average pore diameters (18 nm). As it is evident, all the polymer gels studied present a mesoporous structures. The imprinted P_{ACN} (Cu-PAR-HEMA) shows more narrow pore size distribution than non-imprinted P(HEMA) particles (Fig. 3, A and B).

To evaluate the degree of PAR incorporation, the elemental analysis of the Cu-IIPs and non-imprinted P(HEMA) were performed. The nitrogen content in all synthesized Cu-IIPs was in the range from 2.25 wt% to 2.15 wt%. This increase in nitrogen content for imprinted gels compared to P(HEMA) (0.02 wt%) suggests that the PAR molecules are successful incorporated into copolymer network of imprinted sorbents.

FTIR spectroscopy was used to prove the presence of HEMA, TMPTMA and PAR in the chemical structure of the imprinted and non-imprinted copolymer gels. FTIR spectra of Cu-IIPs and P(HEMA) have the characteristic C=O stretching bands which

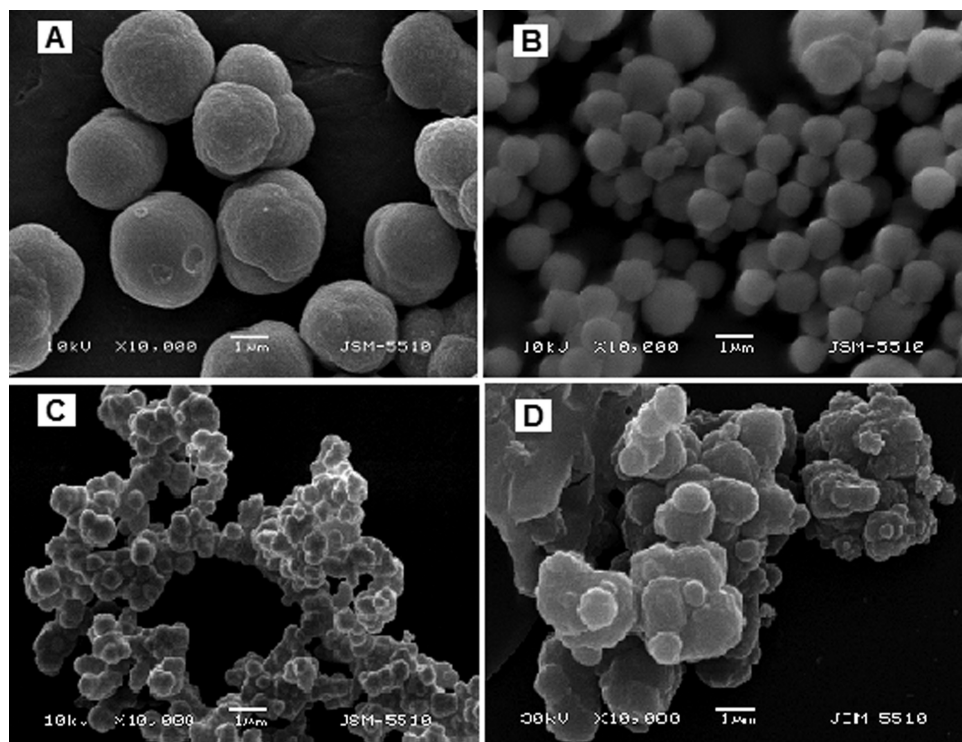


Fig. 2. Scanning electron micrographs of Cu-IIPs: (A) – P_{ACN} (Cu-PAR-HEMA); (B) – $P_{\text{ACN:T(80:20)}}$ (Cu-PAR-HEMA); (C) – $P_{\text{ACN:T(60:40)}}$ (Cu-PAR-HEMA); (D) – P_{T} (Cu-PAR-HEMA)

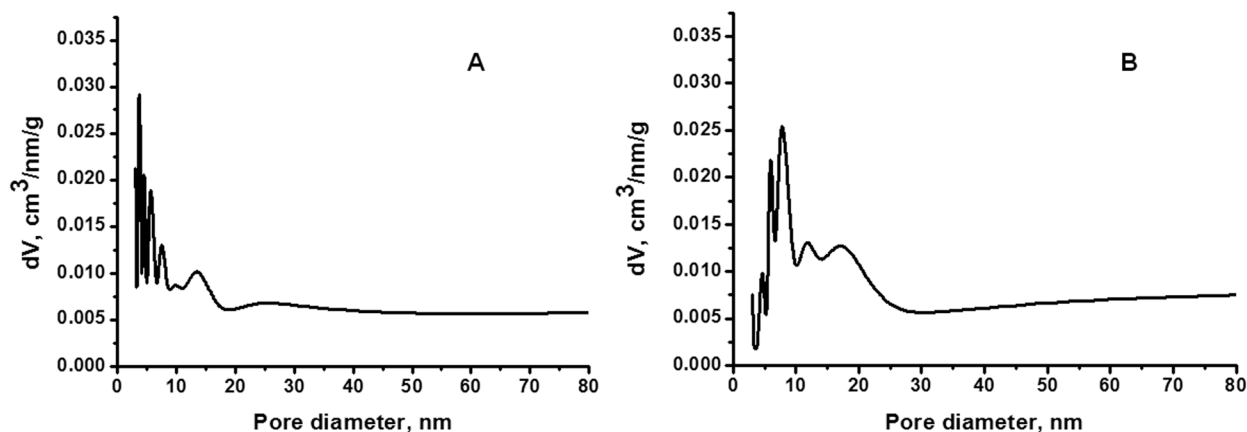


Fig. 3. Pore-size distributions for the imprinted $P_{ACN}(Cu-PAR-HEMA)$ (A) and non-imprinted $P(HEMA)$ (B) prepared in ACN

belongs to the ester functional group of TMPTMA (observed at 1730 cm^{-1} and 1728 cm^{-1} for $Cu(II)$ -IIP and $P(HEMA)$ cm^{-1} , respectively). The four ring stretching bands of pyridine were observed in the $1650\text{--}1450\text{ cm}^{-1}$ region (1640 cm^{-1} , 1596 cm^{-1} , 1560 cm^{-1} and 1465 cm^{-1}) [30, 31]. These data confirmed the presence of PAR in the synthesized Cu-imprinted copolymer gels.

The practical application of any sorbent depends from one side on its chemical properties and from other side on its particles shapes and size and their size distribution. The results obtained for the Cu-IIPs synthesized in the presence of various porogen solvents showed that $P_{ACN}(Cu-PAR-HEMA)$ is the most suitable material for routine application in the analytical practice.

Extraction efficiency of $P_{ACN}(Cu-PAR-HEMA)$ in comparison with $P(HEMA)$

The pH value plays an important role in the adsorption performance of the IIPs toward different ions since it affects on the interaction of the metal ions with the “trapped” chelating agents and functional groups of the polymer matrix. The pH-dependence (in the range 3–9) on the degree of sorption (E , %) of $P_{ACN}(Cu-PAR-HEMA)$ and non-imprinted ($P(HEMA)$) sorbents is presented in Fig. 4. The results show that the E values achieved for imprinted polymer gel are well above those for the non-imprinted $P(HEMA)$ sorbent. The quantitative sorption of $Cu(II)$ ions on the $P_{ACN}(Cu-PAR-HEMA)$ was achieved at pH 7, while the maximal degree of sorption on $P(HEMA)$ was 51%. Evidently, the specific interaction between chelating agent PAR and $Cu(II)$ ions does not take place in the case of $P(HEMA)$, thus explaining the observed lower degree of sorption. The degree of sorption for both

studied sorbents decreased at $pH > 7$, most probably this is related to the $Cu(II)$ ability to form stable complexes with hydroxide groups ($Cu(OH)_4^{2-}$). The formation of these complexes prevents quantitative sorption of $Cu(II)$ ions and reduces $Cu(II)$ sorption on $P_{ACN}(Cu-PAR-HEMA)$ and $P(HEMA)$ as a whole (Fig. 4) at pH 7–9.

Quantitative elution of $Cu(II)$ retained on both sorbents was achieved using 2 M HNO_3 with minimum volume of 1 mL. The kinetic investigations of both processes of sorption and desorption of $Cu(II)$ showed that quantitative sorption was reached for 20 min while for quantitative desorption 30 min has to be used for both sorbents. The average maximum adsorption capacities were $57.8\text{ }\mu\text{mol/g}$ and $21.5\text{ }\mu\text{mol/g}$ for $P_{ACN}(Cu-PAR-HEMA)$ and $P(HEMA)$, respectively. As it might be expected the adsorption capacity of $P_{ACN}(Cu-PAR-HEMA)$ was higher versus the non-imprinted polymer particles $P(HEMA)$, indicating that the cavities created after

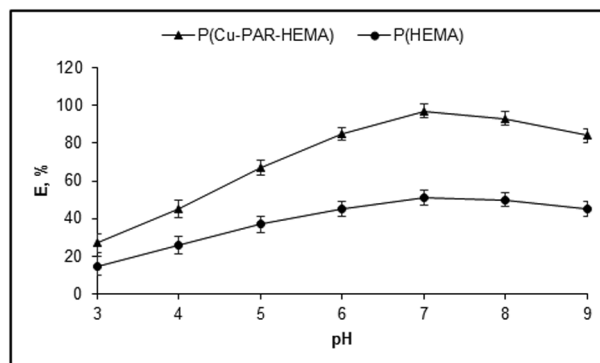


Fig. 4. pH-dependence of the degree of sorption (E , %) of $Cu(II)$ ions with $P_{ACN}(Cu-PAR-HEMA)$ and $P(HEMA)$

Table 1. Degree of sorption (E, %), distribution ratios (D), selectivity coefficients ($S_{Cu/Me}$) and relative selectivity coefficients (k') of $P_{ACN}(Cu-PAR-HEMA)$ and $P(HEMA)$ for Cu(II)

Metal Ion	P(Cu-PAR-HEMA)			P(HEMA)			k'
	E	D	$S_{Cu/Me}$	E	D	$S_{Cu/Me}$	
Cu(II)	97±1	32.3		51±1	1.0		
Cd(II)	42±2	0.5	60.5	31±2	0.4	2.3	26.1
Ni(II)	49±2	0.7	47.1	35±2	0.5	1.9	24.4
Pb(II)	53±1	1.1	28.7	42±2	0.7	1.4	19.9

removal of template ions ensures higher affinity of Cu(II) toward the $P_{ACN}(Cu-PAR-HEMA)$ than to the $P(HEMA)$ confirming the imprinting effect.

In order to examine the selectivity of the imprinted $P_{ACN}(Cu-PAR-HEMA)$ and $P(HEMA)$ sorbents toward Cu(II) ions, competitive adsorption of Cd(II), Cu(II), Ni(II) and Pb(II) from their model mixture was studied. The Cd(II), Ni(II) and Pb(II) ions were chosen as the competitor species because these ions often coexisted in environmental water samples. Although these ions have similar chemical properties and ionic radii ((Cd(II)=0.109, Cu(II) = 0.080, Ni=0.083 and Pb=0.133 nm [32]), significant differences were observed in their extraction characteristics (Table 1). Results presented in Table 1 could be summarized as follows: higher extraction efficiency for Cu(II) than those for Cd(II), Ni(II) and Pb(II); higher $S_{Cu/Me}$ values for $P_{ACN}(Cu-PAR-HEMA)$ compared to $P(HEMA)$; high values of the relative selectivity coefficients (k') which confirmed the selectivity of the imprinted $P_{ACN}(Cu-PAR-HEMA)$.

Application of the method

The applicability of $P_{ACN}(Cu-PAR-HEMA)$ for Cu(II) determination in surface waters was tested for sea and river water samples. Samples of Black sea water and water from river Iskar were spiked with known amounts of Cu(II) in the range (1 and 5 µg/L) and passed through the procedure: 50 mL water sample with pH adjusted to 7, was stirred with 50 mg $P_{ACN}(Cu-PAR-HEMA)$ for 20 mins. After centrifugation supernatant was removed, sorbent washed with 10 mL DW and finally eluted with 1 mL 2 M HNO_3 . The concentration of Cu(II) in the eluate was determined by ETAAS. Results obtained showed that Cu(II) recoveries achieved varied between 94–95% and 95–97% for sea water and river water, respectively. Relative standard deviations are in the range 5–9% for both types of water. Overall $P_{ACN}(Cu-PAR-HEMA)$ could be successfully applied for Cu determination in surface waters.

CONCLUSIONS

In the present paper new Cu(II) imprinted copolymer gels were successfully synthesized by a precipitation copolymerization with HEMA as a functional monomer. It was shown that the polymer particles size and morphology depend on porogen solvent used and ACN was proposed as more suitable reagent which ensures their better uniformity and monodispersity. The prepared $P_{ACN}(Cu-PAR-HEMA)$ sorbent is characterized with good binding properties, fast sorption/desorption kinetics and high selectivity toward Cu(II).

Acknowledgements: The authors gratefully acknowledge financial support by the Bulgarian National Science Fund (Grant No. DFNI-T01/5 NANOSORBLAB).

REFERENCES

1. D. McKnight, *Limnol. Oceanogr.* **26**, 518 (1981).
2. W. Stumm, J. J. Morgan, *Aquatic Chemistry*, John Wiley & Sons, 3rd. ed., New York, 1996.
3. T.R. Crompton, *Analysis of Seawater*, Springer-Verlag, Berlin, 2006.
4. M. C. T. Diniz, O. F. Filho, J. J. R. Rohwedder, *Anal. Chim. Acta*, **525**, 281 (2004).
5. L. Ma, X. Zhu, W. Wang, *J. Mol. Liq.*, **178**, 20 (2013).
6. S. Kagaya, T. Yoshimori, *Anal. Methods*, **4**, 4378 (2012).
7. A. A. Gouda, A. S. Amin, *Spectrochim. Acta A–M*, **120**, 88 (2014).
8. H. Shoaee, M. Roshdi, N. Khanlarzadeh, A. Beiraghi, *Spectrochim. Acta A–M*, **98**, 70 (2012).
9. M. Tuzen, M. Soylak, *J. Hazard. Mater.*, **162**, 724 (2009).
10. V. A. Lemos, P. X. Baliza, *Talanta*, **67**, 564 (2005).
11. A. Tobiasz, S. Walas, A. S. Hernández, H. Mrowiec, *Talanta*, **96**, 89 (2012).
12. R. Saxena, P. L. Meena. *RSC Adv.*, **4**, 20216 (2014).

13. S. Soriano, R. J. Cassella, *J. Braz. Chem. Soc.*, **24**, 1172 (2013).
14. V. Camel, *Spectrochim. Acta B*, **58**, 1177 (2003).
15. D. Das, U. Gupta, A.K. Das, *Trends Anal. Chem.*, **38**, 163 (2012).
16. L. D. Mafu, T. A. M. Msagati, B. B. Mamba, *Environ. Sci. Pollut. Res.*, **20**, 790 (2013).
17. C. Branger, W. Meouche, A. Margaillan, *React. Funct. Polym.*, **73**, 859 (2013).
18. T. Prasada Rao, R. Kala, S. Daniel, *Anal. Chim. Acta*, **578**, 105 (2006).
19. A. N. Pustam, S. D. Alexandratos, *React. Funct. Polym.*, **70**, 545 (2010).
20. R. Say, E. Birlik, A. Ersöz, F. Yılmaz, T. Gedikbey, A. Denizli, *Anal. Chim. Acta.*, **480**, 251 (2003).
21. A. Bhaskarapillai, S. V. Narasimhan, *RSC Adv.*, **3**, 13178 (2013).
22. T. O. Germiniano, M. Z. Corazza, M. G. Segatelli, E. S. Ribeiro, M. J. S. Yabe, E. Galunin, C. R. T. Tarley, *React. Funct. Polym.*, **82**, 72 (2014).
23. S. Z. Bajwa, P. A. Lieberzeit, *Sensor. Actuat. B-Chem.*, **207**, 976 (2015).
24. A. Tobiasz, S. Walas, B. Trzewik, P. Grzybek, M. M. Zaitz, M. Gawin, H. Mrowiec, *Microchem. J.*, **93**, 87 (2009).
25. M. Khajeh, E. Sanchooli, *Environ. Chem. Lett.*, **9**, 177 (2011).
26. H. Hashemi, M. Khajeh, M. Kaykhahi, *Anal. Methods*, **5**, 2778 (2013).
27. I. Dakova, I. Karadjova, I. Ivanov, V. Georgieva, B. Evtimova, G. Georgiev, *Anal. Chim. Acta*, **584**, 196 (2007).
28. I. Dakova, I. Karadjova, V. Georgieva, G. Georgiev, *J. Sep. Sci.*, **35**, 2805 (2012).
29. S. Pardeshi, R. Dhodapkar, A. Kumar, *Food Chem.*, **146**, 385 (2014).
30. B. Gao, D. Kong, Y. Zhang, *J. Mol. Catal. A: Chem.*, **286**, 143 (2008).
31. Y. Zhai, X. Chang, Y. Cui, N. Lian, S. Lai, H. Zhen, Q. He, *Microchim. Acta*, **154**, 253 (2006).
32. J. J. Lurye, *Handbook of Analytical Chemistry*, Khimiya, Moscow 1989.

CU(II)-ОТПЕЧАТАНИ СЪПОЛИМЕРНИ МИКРОЧАСТИЦИ: ВЛИЯНИЕ НА РАЗТВОРИТЕЛЯ ВЪРХУ РАЗМЕРА И МОРФОЛОГИЯТА НА ЧАСТИЦИТЕ И СОРБЦИОННАТА ИМ ЕФЕКТИВНОСТ

И. Г. Дакова^{1*}, В. А. Даков², М. Караджов³, И. Б. Караджова¹

¹ Факултет по химия и фармация, СУ „Св. Климент охридски“, бул. „Джейм Баучер“ 1, София, България

² Университетска лаборатория по екология и опазване на околната среда, Лесотехнически университет бул. „Климент Охридски“ 10, София, България

³ Геологически институт, Българска академия на науките, ул. „Акад. Г. Бончев“, бл. 24, София 1113, България

Постъпила декември, 2014 г.; приета януари, 2015 г.

(Резюме)

Нови Cu(II)-отпечатани поли(хидроксиетилметакрилат-съ-триметилпропан триметакрилат) съполимерни гелове (Cu-IPs) са получени чрез утайтелна съполимеризация и са използвани за селективна твърдофазна екстракция на Cu(II). Cu-IPs са охарактеризирани чрез елементарен анализ, инфрачервена спектроскопия с Фурие преобразуване, сканираща електронна микроскопия и нискотемпературна сорбция на азот. Представено е влиянието на порогени разтворители като ацетонитрил, толуен и техни смеси върху размера и морфологията на частиците. Адсорбционните свойства на получените съполимери са определени чрез експерименти в статичен режим. При оптимални химични условия Cu-IPs показват бърза кинетика на сорбция/десорбция на Cu(II), висока селективност и адсорбционен капацитет. Получените в ацетонитрил Cu-IPs са успешно приложени за селективно определяне на медни йони в повърхностни води.

Silver nanoparticles embedded in biocompatible polymers: extraction efficiency toward metals

L. Djerahov^{1,2}, P. Vasileva^{1*}, I. Karadjova², I. Dakova², R. M. Kurakalva³

¹ Department of General and Inorganic Chemistry, Faculty of Chemistry and Pharmacy, University of Sofia “St. Kliment Ohridski”, 1 James Bourchier blvd., Sofia, Bulgaria

² Department of Analytical Chemistry, Faculty of Chemistry and Pharmacy, University of Sofia “St. Kliment Ohridski”, 1 James Bourchier blvd., Sofia, Bulgaria

³ Environmental Geochemistry Division, CSIR-National Geophysical Research Institute, Uppal Road, Hyderabad-500007, Andhra Pradesh, India

Received December, 2014; Revised January, 2015

The nanocomposite films of chitosan (CS) or polyvinyl alcohol (PVA) loaded down with pre-synthesized silver nanoparticles (AgNPs) were prepared by green chemical approach and studied as an efficient sorbents for solid phase extraction of various chemical elements. Film synthesis is simple and consists of two steps: preparation of AgNPs dispersion and solutions of biocompatible polymers, mixing under stirring of these solutions and final drying at controlled temperature. Nanocomposite films with very good chemical and mechanical properties were obtained; films are stable for at least 3 months and could be used in any time without further treatment. The optical properties, structure and morphology of AgNPs and nanocomposite films were characterized by UV-Vis, TEM and SEM. The extraction efficiency of nanocomposite films prepared toward the most of frequently determined chemical elements was studied. Results obtained showed that under optimal chemical parameters nanocomposite films CS-AgNPs ensured quantitative separation and concentration of Al, Cd, Ni and Pb. Solid phase extraction procedures were developed for the determination of priority pollutants Cd, Pb and Ni in surface waters and Al, Cd and Pb in hemodialysis solutions. Determination limits achieved satisfied accepted permissible limits which makes proposed analytical procedures and new nanocomposite sorbent suitable for routine laboratory practice.

Key words: silver nanoparticles, biocompatible polymers, nanocomposite films, extraction efficiency, toxic metal pollutants.

1. INTRODUCTION

Chemical elements are ubiquitous in the environment. They are derived from both natural and anthropogenic processes. Toxic elements have been recognized as harmful for human health when present above certain levels and could cause various diseases [1]. Reliable control of concentrations of these elements in the environment or human daily life is an important analytical task. Direct instrumental methods are preferable and have been conventionally used for the determination of low levels of chemical elements however matrix interferences observed in some cases still required application of separation and concentration procedures.

Nanomaterials and nanotechnology provide powerful capabilities for determination and treatment of trace pollutants in the environment. Macro-, micro-, and nanomaterial-based tools and strategies have been successfully used for detection of chemical elements and their species in the environment [2]. Substantial progress on detection and treatment of organic and toxic metal pollutants has been achieved by using nanomaterials and analytical nanotechnology [3]. The use of metallic nanoparticles and composite materials for fast and simple quantification of toxic elements has exponentially increased in the past decade due to their unique physical and chemical properties such as surface plasmon resonance (SPR) band, surface enhancement of Raman scattering, nonlinear optical properties, high thermal and electrical conductivity, chemical stability and catalytic activity [4, 5, 6]. Colorimetric sensors for determination of Hg(II), Pb(II), Cu(II) based on metal nanoparticles are very

* To whom all correspondence should be sent:
E-mail: pvasileva@chem.uni-sofia.bg

attractive, because they are rapid, low-cost and can be easily read out with the naked eye [7, 8]. The activity of silver nanoparticles (AgNPs) has been utilized to remove a number of toxic contaminants found in drinking water including pesticides, heavy metals and micro-organisms. Noble metal nanoparticles have been used for ultra low concentration detection of toxic elements in drinking waters [8]. The use of nanoparticles in sample preparation step has noted as a topic of growing interest in analytical sciences [9]. Biocompatible polymers with embedded noble metal nanoparticles have been applied as effective new materials for removal of metals from aqueous solutions [10] or applied as antimicrobial packaging materials and wound dressings, or also grafted onto various implants [11].

The aims of this study were (i) synthesis and characterization of nanocomposite films which consists of AgNPs incorporated in biocompatible polymer (chitosan (CS) or polyvinyl alcohol (PVA)) (ii) investigations on the possibilities to apply them as sorbents in solid phase extraction procedures for the separation and concentration of trace elements and (iii) development of analytical procedure for the determination of priority pollutants Cd, Pb and Ni in surface waters and Al, Cd and Pb in solutions for hemodialysis.

2. EXPERIMENTAL

2.1. Materials

Silver nitrate (AgNO_3 , 99.8%, Merck, Germany), D-(+) raffinose pentahydrate (Alfa Aesar, Germany), and sodium hydroxide (NaOH , 99%, Merck, Germany) were used to prepare aqueous dispersions of silver nanoparticles. Chitosan (low molecular weight, 75–85% deacetylated), polyvinyl alcohol (molecular weight 72000) and acetic acid (CH_3COOH) were purchased from Sigma–Aldrich, Germany. The stock standard solutions for Al(III), Cd(II), Ni(II) and Pb(II) (1,000 $\mu\text{g}/\text{ml}$) were Titrisol, Merck (Germany) in 2% HNO_3 . Working standard solutions were prepared daily by appropriate dilution. Doubly distilled water was used in all experiments.

2.2. Methods and apparatus

Ultraviolet-visible (UV–Vis) absorption spectra were recorded on an Evolution 300 spectrometer (Thermo Scientific, USA). The optical spectra of the solutions were recorded using doubly distilled water as a reference. The morphology and particle sizes of silver nanoparticles in colloidal solutions and in nanocomposite films were examined using

a transmission electron microscope (TEM, JEM-2100) operating at accelerating voltage of 200 kV. The pure polymer films (without AgNPs) and nanocomposite films with incorporated AgNPs were studied for surface morphological variations using a scanning electron microscope (SEM, JEOL JSM 5510). Zeta (ζ) potential of silver nanoparticles was measured with a Zetasizer Nano ZS (Malvern) instrument. Ultrasonic bath UST2.4-150 (Siel, Bulgaria) was used.

2.3. Synthesis

2.3.1. Synthesis of AgNPs

Raffinose-stabilized AgNPs were prepared according to method previously described [12]. The one-step, one-phase “green” synthesis of silver nanoparticles in aqueous solution is based on chemical reduction of Ag^+ (AgNO_3 , 0.1 M) using D-(+) raffinose (0.1 M) as both reducing and stabilizing agent, and sodium hydroxide (0.1 M) as a reaction catalyst. The as-synthesized dispersion of AgNPs (with Ag concentration of 1.0×10^{-3} mol/L) were kept in closed container at room temperature and were stable for at least 2 months. They were used in any further experiments after homogenization by an ultrasonic bath for 30 min.

2.3.2. Preparation CS-AgNPs and PVA-AgNPs films

Transparent nanocomposite films were prepared by: mixing under stirring (15 min at room temperature) of 1% (w/V), chitosan solution in 1% (V/V) CH_3COOH or 4% (w/V) PVA solution in distilled water with AgNPs aqueous dispersion in a different volume ratios. 7.5 ml of mixtures obtained were transferred in 25 ml glass beaker and dried in a controlled environment at 50 °C. Depending on the polymer/AgNPs ratios nanocomposite films with different amounts of AgNPs were obtained. The formed CS-AgNPs films were then immersed for 1 h in 1 mol/L NaOH at room temperature in order to neutralize the excess of acid and finally were washed twice with doubly distilled water. For comparison, pure polymer films of CS or PVA were also prepared by drying the respective aqueous solutions of pure polymers. The thickness of the nanocomposite films was optimized taking into account their mechanical stability during process of sorption – the aim was to keep the integrity of the film.

2.4. General procedure

A model solution of 20 ml with pH adjusted in the range from 7–9 containing 500 $\mu\text{g}/\text{L}$ Al(III),

Cd(II), Ni(II) and Pb(II) was placed in a beaker with nanocomposite film. After sorption time of 24 h, the supernatant was carefully decanted; the film was washed twice with doubly distilled water and eluted with 2 ml 1–4 mol/L HNO₃ or dissolved in 0.4 ml of conc. HNO₃ at 80 °C and diluted to 2 ml with doubly distilled water. Metal content in the supernatant and in the eluate solutions was measured by Electrothermal Atomic Absorption Spectrometry (ETAAS). Matrix matched standards were used for calibration of ETAAS measurements. They were obtained by additions of known amounts of analytes to the blank composite film, dissolved according to the same dissolution procedure.

2.5. Sorption characteristics

The degree of sorption of the investigated pollutants is presented as

$$Ds (\%) = [(A_i - A_{\text{eff}})/A_i] \cdot 100,$$

where A_{eff} (μg) is the mass of metal in the supernatant after sorption from a solution with a total metal mass A_i (μg).

The kinetics of the analytes sorption was investigated in a batch system for 0.5–24 hours. Sample aliquots were analyzed by ETAAS (to maintain constant sample volume) and it was established that the saturation values (i.e., equilibrium extraction efficiency) were gradually reached within 24 hours.

2.6. Analytical procedures

2.6.1. Analysis of surface waters: 30 ml water sample with pH (8–8.5) was placed in a beaker with a nanocomposite film. After 24 h sample solution is decanted, film washed twice, dissolved with 0.4 ml of conc. HNO₃ and diluted to 2 ml with doubly distilled water. Priority pollutants Cd(II), Pb(II) and Ni(II) content was quantified in this solution by ETAAS.

2.6.2. Analysis of solutions for hemodialysis: 20 ml 15% (w/w) saline hemodialysis solution was placed in a beaker with a nanocomposite film. After 24 h sample solution is decanted, film washed twice, dissolved with 0.4 ml of conc. HNO₃ at 80 °C and diluted to 2 ml with doubly distilled water. The content of trace elements Al, Cd and Pb was quantified in this solution by ETAAS.

3. RESULTS AND DISCUSSION

3.1. Characterization of silver nanoparticles and nanocomposite CS-AgNPs and PVA-AgNPs films

UV-Vis absorption measurements of the primary yellow orange solution of raffinose-stabilized AgNPs showed UV-Vis spectrum with SPR band at λ_{max} 412 nm (Fig. 1a). The shape of the plasmon band is symmetrical and quite narrow, suggesting

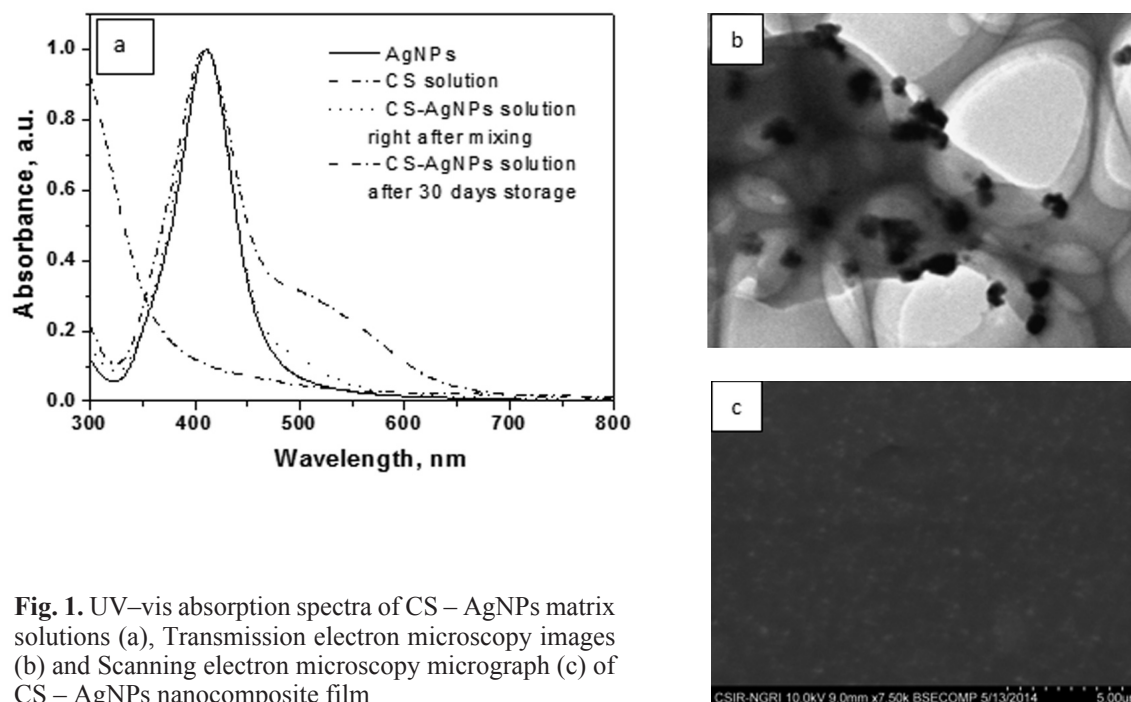


Fig. 1. UV-vis absorption spectra of CS – AgNPs matrix solutions (a), Transmission electron microscopy images (b) and Scanning electron microscopy micrograph (c) of CS – AgNPs nanocomposite film

that AgNPs are mainly spherical with narrow size distribution [13]. The raffinose-stabilized AgNPs were observed to be stable in solution even 2 months after their preparation. The high colloidal stability of raffinose-stabilized AgNPs was confirmed by the ζ potential value of -47.2 ± 1.1 mV measured in 1 mmol/L KCl at pH 6.8. The CS-AgNPs mixed solution exhibits slightly broadened main SPR band peaking at the same wavelength as AgNPs colloidal solution. The asymmetric broadening toward long wavelengths in the spectrum is a sign for some degree of agglomeration in CS-AgNPs solution. It is worth noting that the intensity of this broad band increases with the increase of storage time, most probably due to the attraction forces between the nanoparticles inside the chitosan matrix, making them to move, agglomerate, and form the crystal structures. The TEM observation of CS-AgNPs film (Fig. 1b) indicates that some agglomeration of part of AgNPs takes place during their incorporation into the chitosan matrix and reveals the presence of quasi-spherical silver nanoparticles with an average diameter of about 25 nm. Despite the observed partially agglomeration of nanoparticles, CS-AgNPs films maintain optical clarity. An even distribution of the agglomerates and individual silver nanoparticles into the CS-AgNPs film was clearly observed in SEM image shown on Fig. 1c.

The absorption spectra of the colloidal solution containing Ag nanoparticles and the corresponding PVA-AgNPs film matrix solution are shown in Figure 2a. It can be seen that the PVA-AgNPs solution exhibits the same symmetrical and narrow surface plasmon absorption band as colloidal solution of AgNPs, however, located at 420 nm. The

shift to the longer wavelengths upon incorporation of Ag nanoparticles into PVA can be explained by the change of the dielectric properties of the surrounding environment [14]. The absence of any band broadening clearly indicates that the Ag nanoparticles are not agglomerated and are well distributed within the polymer matrix. TEM measurement showed that the resulting film mainly contains individual quasi-spherical silver nanoparticles with average diameter of 25 nm (Fig 2b). In addition to the nanospheres, some typical polyhedral nanoparticles (multiple twined nanocrystals) can be easily observed (Fig. 2b: inset).

The CS film (Fig. 3b) exhibited a dense and uniform plain microstructure. As far as AgNPs are anchored by chitosan functional groups, the homogeneity of surface morphology is maintained in CS-AgNPs film (Fig. 3d) [15]. CS-AgNPs film showed the presence of nanoparticles in the entire film (white dots in Fig. 1c), confirming the good dispersion of AgNPs within the polymer matrix. In the case of PVA based films, inhomogeneous rough surface with aggregates of polymer submicroparticles was observed for PVA film (Fig. 3a), whereas PVA-Ag NPs film showed homogeneous surface morphology (Fig. 3c).

3.2. Effect of chemical parameters on the extraction efficiency of CS-AgNPs and PVA-AgNPs composite films toward Al(III), Cd(II), Ni(II) and Pb(II)

The effect of various parameters such as pH, sorption medium and sorbent amount (Ag content

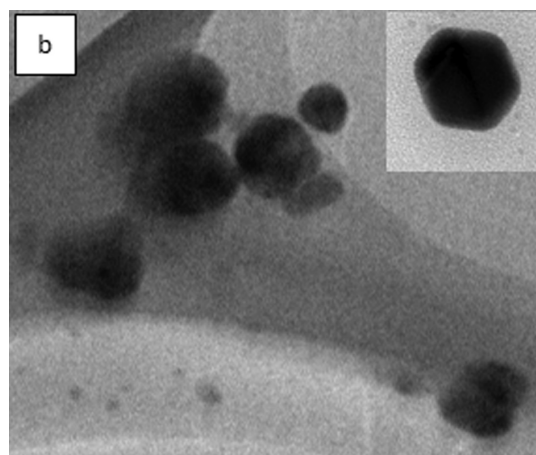
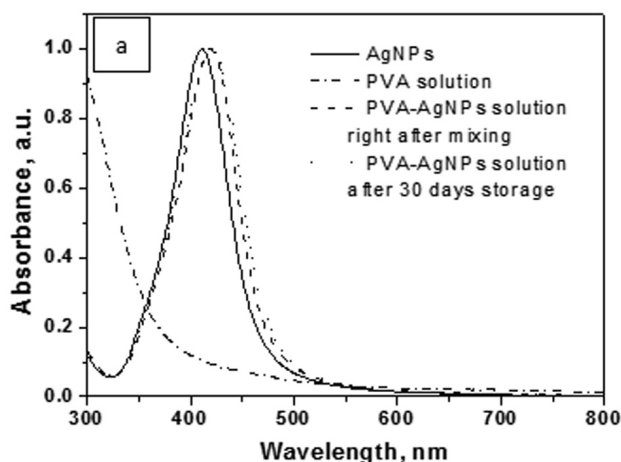


Fig. 2. UV-vis absorption spectra of PVA – AgNPs matrix solutions (a), Transmission electron microscopy image of PVA – AgNPs nanocomposite film (b)

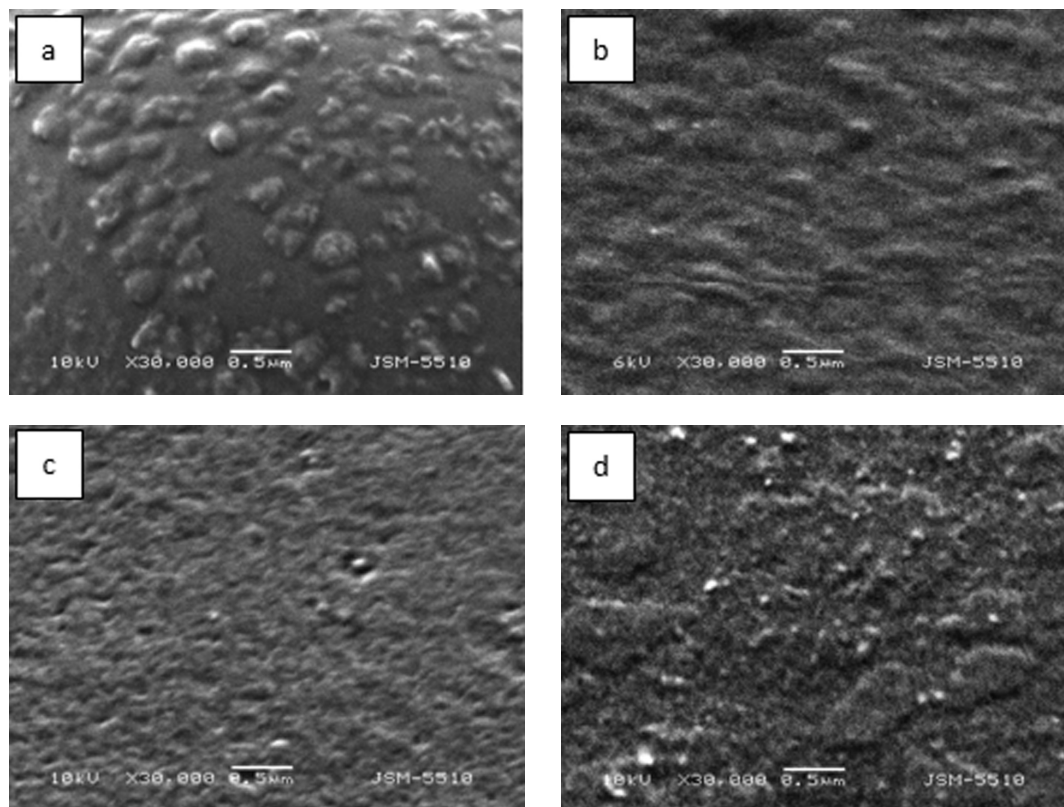


Fig. 3. Scanning electron microscopy micrographs of PVA (a), PVA – AgNPs (b), CS (c) and CS – AgNPs (d) films

in nanocomposite film) on the extraction efficiency of nanocomposite films toward Al(III), Cd(II), Ni(II) and Pb(II) was studied.

3.2.1. Effect of pH and sorption medium on the degree of sorption of Al(III), Cd(II), Ni(II) and Pb(II). Sorption behaviour of elements depends on a number of experimental parameters and sorbent properties and are related mainly to (i) presence of a large number of functional groups (acetamido, primary amino and hydroxyl groups) in the chitosan and degree of their protonation/deprotonation (pKa varies between 6.3 and 6.8 [17]); (ii) surface properties of AgNPs (negatively charged particle surface confirmed by highly negative ζ -potential measured) and (iii) metal speciation in solution. The results obtained for the influence of pH which was varied in the range 7–9 and achieved by using NH_4OH or NaOH on the degree of sorption of elements studied are presented in Figure 4.

The trend observed is an increased sorption for each metal ion with increasing pH of the solution. Quantitative sorption for Al(III), Cd(II), Ni(II) and Pb(II) is achieved at pH 8–9 in the presence of NH_4OH (Fig. 4a). This is due to a favorable combination of several factors resulting in high values of the extraction efficiency. First, amino groups of chitosan are in the non-protonated form, and become

available for interaction with metal cations through the pair of electrons disposed by nitrogen, leading to an increase on the degree of adsorption. Second, hydroxyl groups of chitosan are partially deprotonated, as well and available for complex formation. Third, the negatively charged surface of AgNPs attracts positively charged metal species (free metal ions or metal complexes with NH_3). When the pH of the solution was adjusted with NaOH, maximum extraction efficiencies varied between 50% (for Al(III) and Pb(II)) and 80% (for Cd(II) and Ni(II)) at pH 9 (Fig. 5b). This could be related to the ability of Al(III) and Pb(II) to form stable negatively charged hydroxocomplexes. Finally, pH 8–8.5 adjusted with NH_4OH could be accepted as an optimal for simultaneous quantitative sorption of Al(III), Cd(II), Ni(II) and Pb(II) on CS-AgNPs nanocomposite films. Analogous experiments carried out with PVA-AgNPs showed much lower degree of sorption especially for Cd(II) and Pb(II), most probably due to the much lower sorption activity of PVA film itself and absence of N-containing functional groups.

In order to prove hypothesis that the sorption efficiency of nanocomposite film CS-AgNPs is due to the combined chemical activities of CS film and incorporated AgNPs, experiments were performed

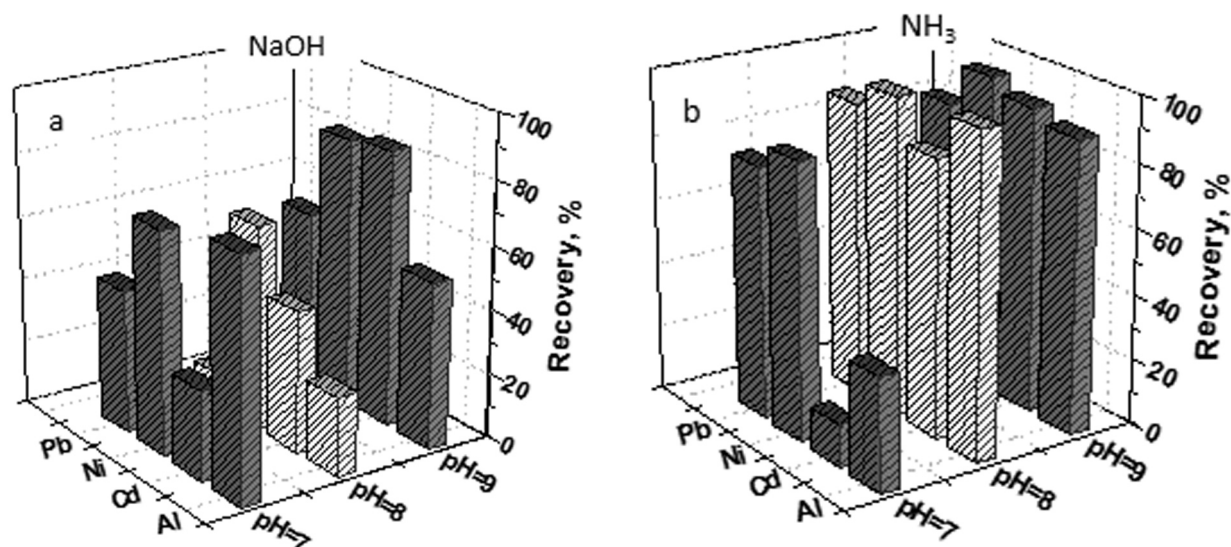


Fig. 4. Effect of pH on Al(III), Cd(II), Ni(II) and Pb(II) sorption by CS-AgNPs nanocomposite film in (a) NaOH and (b) NH₃

for degree of sorption (at optimal sorption conditions pH 8–8.5, NH₄OH) achieved with each one of CS/PVA films and AgNPs. Results presented in Table 1 undoubtedly showed synergetic sorption effect of nanocomposite material CS-AgNPs which ensures quantitative sorption for all tested analytes over CS film (extraction efficiencies 39–59%) and AgNPs (extraction efficiencies 83–93%). Analogous results were found for PVA film and composite sorbent PVA-AgNPs. The sorption of analytes on PVA membrane is due to the partial deprotonation of hydroxyl groups and their interaction with positively charged metal species. The degree of sorption is increased on PVA-AgNPs composite film, yet not quantitative due to the absence of amino groups on the film surface.

Table 1. Comparative results for the degree of sorption of Al(III), Cd(II), Ni(II) and Pb(II) ions with sorbents: upon solid ph CS-AgNPs nanocomposite film, PVA-AgNPs composite film, CS film, PVA film and AgNPs (pH 8–8.5, NH₄OH), three parallel experiments

Sorbents	Degree of sorption, %			
	Al(III)	Cd(II)	Ni(II)	Pb(II)
CS-AgNPs	99±3	94±3	98±2	85±4
CS	39±5	59±5	47±4	53±5
AgNPs	83± 4	30±5	93±3	90±3
PVA-AgNPs	73±4	32±6	39±6	88±4
PVA	75±4	27±5	41±5	78±4

3.2.2. Effect of the AgNPs content in the nanocomposite films. The chemical activity of AgNPs in the nanocomposite film requires optimization of their content. The experiments were carried out with films containing from 540 to 1080 µg Ag and constant CS mass of 25 mg in the film matrix. The results showed that 540 µg Ag was sufficient for the quantitative sorption of all studied analytes. Lower AgNPs amount were not tested as far as they play also role of crosslinker for CS ensuring a good mechanical stability of the nanocomposite films.

3.2.3. Effect of elution parameters. The CS-AgNPs nanocomposite films demonstrate very good mechanical stability, so it was attempted to elute sorbed analytes with relatively low concentrations of HNO₃ (2–4 mol/L). Unfortunately results obtained showed that process of elution is relatively long (more than 4 h), degree of elution is in the range 50–70% for all studied analytes and composite film is not suitable for next sorption cycle. That is why complete film dissolution with minimum amount of conc. HNO₃ was accepted as more efficient procedure for quantitative recovery of retained analytes. The process of film dissolution is accelerated at elevated temperatures (80 °C was accepted as optimal) and could be finalized in 4–5 min.

Brief conclusion – CS-AgNPs composite film is an efficient sorbent, ensures quantitative sorption of Al(III), Cd(II), Ni(II) and Pb(II) for 24 h at pH 8–8.5 (adjusted with NH₄OH), elution of retained analytes is achieved by complete dissolution with small amount HNO₃. The whole separation and concentration procedure could be performed in one analytical vessel (in which the composite film is synthesized).

3.3. Analytical application

3.3.1. Determination of Cd(II), Ni(II) and Pb(II) in surface waters. Samples of 30 ml sea water (Black sea, Bourgas) and river water (Iskar) are spiked with known amounts (ranged between 0.01–0.1 µg/L) of Cd(II), Ni(II) and Pb(II) and passed through the optimized procedure described in Paragraph 2.6. Recoveries achieved varied in the range 94–97%, 95–98% and 93–96% for Cd(II), Ni(II) and Pb(II), respectively. Relative standard deviation is between 5 and 11% for all studied elements in this concentration range. Detection limits achieved are 0.002 µg/L, 0.02 µg/L and 0.04 µg/L for Cd(II), Ni(II) and Pb(II) respectively and completely satisfy requirements of European legislation (Directive 2008/105/EO) for priority pollutants in surface waters.

3.3.2. Determination of Al(III), Cd(II) and Pb(II) in solutions for hemodialysis. The solution for hemodialysis usually contained high concentrations of alkali chlorides and direct instrumental determination of controlled by European Pharmacopoeia elements concentrations is difficult. Separation procedure in this case is required for elimination of matrix interferences. Model saline hemodialysis solutions with matrix concentrations: 10% w/w, 15% w/w and 20% w/w were spiked with known amounts (ranged between 0.1–0.2 µg/L) of Al(III), Cd(II), and Pb(II) are passed through the optimized procedure described in Paragraph 2.6. Recoveries achieved for 10% w/w and 15% w/w saline solutions varied in the range 91–95%, 93–96% and 92–95% for Al(III), Cd(II) and Pb(II) respectively. Recoveries for 20% w/w saline solution were below 85%, most probably due to the slow diffusion of analytes to the film surface in this highly saline solution. Optimized analytical procedure for the determination of Al(III), Cd(II) and Pb(II) in hemodialysis solutions is characterized with detection limits: 0.01 µg/g for Al, 0.001 µg/g for Cd and 0.05 µg/g for Pb and fulfils the requirements of European Pharmacopoeia.

4. CONCLUSION

Cast nanocomposite film of biocompatible polymer CS with embedded AgNPs was prepared and

characterized for its optical and structural properties. The extraction efficiency of nanocomposite film toward Al, Pb, Cd and Ni was studied and analytical procedures for determination of Cd, Ni and Pb in surface waters and Al, Cd and Pb in hemodialysis solutions were proposed.

REFERENCES

1. R. Goyer, T. Clarkson, in: Casarett & Doull's Toxicology: The Basic Science of Poisons 6th edition, C. Klaassen (eds), McGraw-Hill Professional, 2001, p. 811.
2. G. Aragay, J. Pons, A. Merkoç, *Chem. Rev.*, **111**, 3433 (2011).
3. L. Zhang, M. Fang, *Nano Today*, **5**, 128 (2010).
4. B. Ferreira da Silva, S. Perez, P. Gardinalli, R.K. Singhal, A. Mozeto, D. Barcelo, *Trends Anal. Chem.*, **30**, 528 (2011).
5. Y. Liu, X. Wang, *Anal. Methods*, **5**, 1442 (2013).
6. Adnan Haider, Inn-Kyu Kang, *Adv. Mater. Sci. Eng.*, in press, (2014).
7. X.Wu, Y. Xu, Y. Dong, X. Jiang, N. Zhu, *Anal. Methods*, **5**, 560 (2013).
8. T. Pradeep, Anshup, *Thin Solid Films*, **517**, 6441 (2009).
9. R. Lucena, B. M. Simonet, S. Cardenas, M. Valcarcel, *J. Chromatogr. A*, **1218**, 620 (2011).
10. R. Bryaskova, N. Georgieva, D. Pencheva, Z. Todorova, N. Lazarova, T. Kantardjiev, *Colloids Surf. A: Physicochem. Eng. Aspects*, **444**, 114, (2014).
11. V. Thomas, M. Yallapu, B. Sreedhar, S. Bajpai, *J. Biomater. Sci., Polym. Ed.*, **20**, 2129, (2009).
12. M. Chichova, M. Shkodrova, P. Vasileva, K. Kirilova, D. Doncheva-Stoimenova, *Journal of Nanoparticle Research*, **16**, 1 (2014).
13. E. Hutter, J. H. Fendler, *Advanced Materials*, **16**, 1685 (2004).
14. A. N. Krkljes, M. T. Marinovic-Cincovic, Z. M. Kacarevic-Popovic, J. M. Nedeljkovic, *European Polymer Journal*, **43**, 2171 (2007).
15. K. Vimala, Y. Murali Mohana, K. Samba Sivudu, K. Varaprasad, S. Ravindra, N. Narayana Reddy, Y. Padma, B. Sreedhar, K. MohanaRaju, *Colloids Surf. B: Biointerfaces*, **76**, 248 (2010).
16. H. Hristov, P. Vasileva, M. Nedialkova, in: *Nanoscience&Nanotechnology*, Vol. **12**, E. Balabanova, E. Mileva (eds.), Sofia, 2012, p. 47.
17. E. Guibal, T. Vincent, R. Navarro, *J. Mater. Sci.*, **49**, 5505 (2014).

СРЕБЪРНИ НАНОЧАСТИЦИ, ВГРАДЕНИ В БИОСЪВМЕСТИМИ ПОЛИМЕРИ: ЕКСТРАКЦИОННА ЕФЕКТИВНОСТ СПРЯМО МЕТАЛИ

Л. Джерахов^{1,2}, П. Василева^{1,*}, И. Караджова², И. Дакова², Р. М. Куракалва³

¹ *Катедра Обща и Неорганична химия, Факултет по Химия и Фармация, Софийски университет „Свети Климент Охридски“, бул. „Джеймс Баучер“, 1, София, България*

² *Катедра Аналитична химия, Факултет по Химия и Фармация, Софийски университет „Свети Климент Охридски“, бул. „Джеймс Баучер“, 1, София, България*

³ *Лаборатория по Околна среда и Геохимия, Национален институт за геофизични изследвания, Хайдерабад-500007, Индия*

Постъпила декември, 2014 г.; приета януари, 2015 г.

(Резюме)

Нанокмпозитни филми от (CS) или поливинилол алкохол (PVA), с вградени в тях предварително синтезирани сребърни наночастици (AgNPs), са получени с помощта на „зелен“ химичен подход и са приложени като ефективни сорбенти за твърдофазна екстракция на различни метали. Процедурата за получаване на филмите се състои от два етапа: **получаване на дисперсия от AgNPs и разтвори на биосъвместими полимери, смесването им при разбъркване и следващо изпаряване на разтворителя при контролирана температура.** Получените нанокмпозитни филми са с много добри химични и механични свойства; филмите са стабилни поне три месеца след получаването им и могат да се използват без допълнително третиране. Оптичните свойства, структурата и морфологията на AgNPs и нанокмпозитните филми са охарактеризирани с UV-Vis, TEM и SEM. Изследвана е тяхната екстракционна ефективност спрямо често определяни метали. Резултатите показват, че при оптимални условия нанокмпозитният филм CS-AgNPs **осигурява количествено разделяне и концентриране на Al, Cd, Ni и Pb.** Разработени са процедури за твърдофазна екстракция и определяне на приоритетните замърсители Cd, Pb и Ni в повърхностни води, и Al, Cd и Pb в разтвори за хемодиализа. Постигнатите граници на определяне удовлетворяват допустимите концентрации за тези метали, което прави предложените аналитични процедури и новия нанокмпозитен сорбент подходящи за рутинната аналитична практика.

Solvothermal synthesis of theophylline and *N,N'*-(ethane-1,2-diyl)diformamide co-crystals from DMF decomposition and N-formylation through catalytic effect of 3-carboxyphenylboronic acid and cadmium acetate

V. M. Dyulgerov*, L. T. Dimowa, K. Kossev, R. P. Nikolova, B. L. Shivachev

Institute of Mineralogy and Crystallography, Bulgarian Academy of Sciences, 1113 Sofia, Bulgaria

Received December, 2014; Revised January, 2015

Here we present the unexpected production of *N,N'*-(ethane-1,2-diyl)diformamide. The solvothermal reaction was conducted in DMF at 100 °C with starting compounds cadmium acetate, 3-carboxyphenylboronic acid and aminophylline (2:1 mixture of theophylline and ethylenediamine). The *N,N'*-(ethane-1,2-diyl)diformamide is obtained as a result of a formylation reaction, catalyzed by Cd^{2+} and the high temperature. The *N,N'*-(ethane-1,2-diyl)diformamide co-crystallized with theophylline in the triclinic space group $P\bar{1}$, with unit cell parameters $a = 6.7437(8)$, $b = 8.7847(14)$, $c = 9.4656(15)$, $\alpha = 91.825(13)^\circ$, $\beta = 103.313(12)^\circ$, $\gamma = 98.054(12)^\circ$, and $Z = 2$. The co-crystal structure is stabilized by intermolecular hydrogen bonds between the *N,N'*-(ethane-1,2-diyl)diformamide and theophylline. The excesses of theophylline crystallized in a new polymorphic form in space group Pn , with unit cell parameters $a = 3.8744(4)$, $b = 12.8898(9)$, $c = 8.1167(6)$, $\beta = 98.965(8)^\circ$ and $Z = 2$.

Key words: theophylline, polymorphism, single crystal, isotopically, N-formylation.

INTRODUCTION

Formamides are extensively used in organic synthesis as intermediates in the preparation of pharmaceuticals, as protecting groups in peptides synthesis, Lewis base catalysts in organic transformations, for Vilsmeier formylation etc. [1–6]. Nowadays, formylation methods are dependent on the used formylating reagent [7–11] the most common being formyl acetate [12]. Many of these methods suffer from different drawbacks such as the use of a costly and harmful formylating agents or catalysts, long reaction times accompanied by high temperatures and the formation of side products. More recent investigations on N-formylation of amines have been focused on the use of inorganic solid oxides as catalysts [13–15], the reaction media and conditions [16]. The studies are needed in order to minimize the unwanted drawbacks and to reduce the costs. We report herein the unexpected synthesis of *N,N'*-(ethane-1,2-diyl)diformamide from ethylenediamine (**en**) and *N,N'*-dimethylformamide using

cadmium acetate and 4-carboxyphenylboronic acid as catalysts (Scheme 1).

EXPERIMENTAL SECTION

Synthesis of the title compounds

The Aminophylline was kindly provided by Sopharma AD, (Bulgaria) while all other chemicals were commercially available and used without additional purification. Co-crystals of *N,N'*-(ethane-1,2-diyl)diformamide (**edd**), and theophylline (**teo**) were obtained by solvothermal method. Aminophylline (126 mg, 0.3 mmol), 4-carboxyphenylboronic acid (49 mg, 0.3 mmol), $\text{Cd}(\text{CH}_3\text{CO}_2)_2 \times 2\text{H}_2\text{O}$ (40 mg, 0.15 mmol), were dissolved in 8 ml *N,N'*-dimethylformamide (DMF), 2 ml methanol and 0.5 ml of $\text{d}_4\text{H}_2\text{O}$ (double distilled water) and reacted in 20 ml Teflon lined autoclaves at 100 °C for 24 h. The autoclaves were quenched to room temperature in a water bath and the solution was collected by filtration. A mixture of prismatic (plate like) colorless crystals was obtained by slow evaporation of the solution. Single crystal studies revealed the presence of two new crystal phases. Theophylline and a co-crystal of theophylline and *N,N'*-(ethane-1,2-diyl)diformamide.

* To whom all correspondence should be sent:
E-mail: silver@mail.bg

X-ray data collection and structure determination

Crystallographic measurements and data collection were performed on an Agilent SupernovaDual diffractometer equipped with an Atlas CCD detector using micro-focus Mo $K\alpha$ radiation ($\lambda = 0.71073 \text{ \AA}$) at 290 K. The determinations of the unit cell parameters, data collection and reduction were performed with CrysAlis-Pro software [17]. The structures were solved by direct methods ShelxS [18] and refined by the full-matrix least-squares method with the ShelxL-2013 programs [18]. All non-hydrogen atoms, were located successfully from Fourier maps and were refined anisotropically. H atoms on C and N atoms were generated geometrically and their positional parameters were refined with $C-H = 0.9600$, $N-H = 0.9300 \text{ \AA}$ with $U_{iso}(H) = 1.2U_{eq}(C \text{ or } N)$. Most important crystallographic and refinement indicators are listed in Table 1. Complete crystallographic data for the structure reported in this paper have been deposited in the CIF format with the Cambridge Crystallographic Data Center as supplementary publication No. CCDC 1039797 and 1039798. Copies of these data can be obtained free of charge from The Cambridge

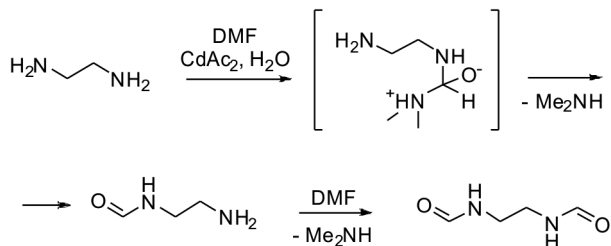
Crystallographic Data Centre via www.ccdc.cam.ac.uk/data_request/cif.

RESULTS AND DISCUSSION

The initial intention was to produce a new metal organic framework (MOF) assembled in the same way as the reported metal-adenine bio-MOFs [19]. The concept was to employ the structural similarity of theophylline (**teo**) and adenine and to replace the dimethylcarbamate and pyridine by 3-carboxyphenylboronic acid and ethylene diamine (all three compounds coordinate Zn through NH- and COOH moieties). The target was to obtain a “free” (e.g. not involved in Zn coordination) NH_2 and/or $R-B(OH)_2$ group, oriented towards the pores of the MOF. Thus an active center that could potentially trap CO_2 or other molecules and gases would be present in the framework. Although, the conducted solvothermal synthesis produced two new crystal phases, single crystal data collection showed that the envisaged porous material was not produced. Instead, a co-crystal between theophylline and *N,N'*-(ethane-1,2-diyl)diformamide a new polymorph of theophylline were obtained. As **edd** was not one of the starting

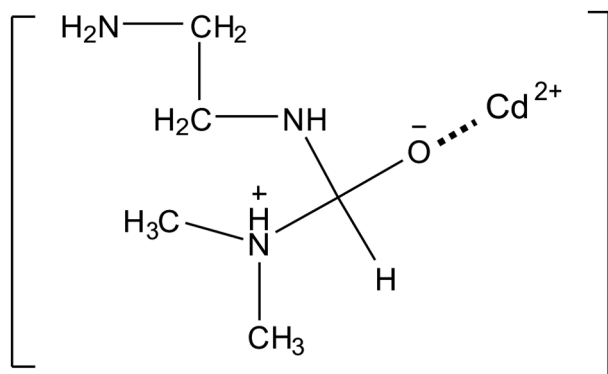
Table 1. Most important crystallographic and refinement details for compounds **1** and **2**

Compound reference	teo:edd	teo
Chemical formula	$C_9H_{12}N_5O_3$	$C_7H_8N_4O_2$
Formula Mass	238.24	176.17
Crystal system	Triclinic	Monoclinic
$a/\text{\AA}$	6.7441(6)	3.8744(4)
$b/\text{\AA}$	8.7826(11)	12.8898(9)
$c/\text{\AA}$	9.4653(11)	8.1167(6)
$\alpha/^\circ$	91.834(10)	90
$\beta/^\circ$	103.319(9)	98.965(8)
$\gamma/^\circ$	98.035(9)	90
Unit cell volume/ \AA^3	539.00(11)	400.40(5)
Temperature/K	290(2)	290(2)
Space group	$P1-$	Pn
No. of formula units per unit cell, Z	2	2
Radiation type	MoK α	MoK α
Absorption coefficient, μ/mm^{-1}	0.114	0.106
No. of reflections measured	2543	2386
No. of independent reflections	1959	1499
R_{int}	0.0218	0.0240
Final R_i values ($I > 2\sigma(I)$)	0.0578	0.0633
Final $wR(F^2)$ values ($I > 2\sigma(I)$)	0.1452	0.1644
Final R_i values (all data)	0.0816	0.0828
Final $wR(F^2)$ values (all data)	0.1663	0.1786
Goodness of fit on F^2	1.152	1.068
CCDC number	1039797	1039798



Scheme 1.

compounds it has to be produced during the synthesis. A plausible mechanism for **edd** production is the N-formylation of **en** through Cd^{2+} catalysis shown in Scheme 1. The reaction implicates the breakdown of DMF and thus the existence of a possible Cd^{2+} intermediate shown on Scheme 2. The DMF breakdown is supported by the occurrence of dimethyl ammonium (CH_3) $_2\text{NH}^{2+}$ cations in several MOF structures [20–30] also obtained by solvothermal method and featuring Cd^{2+} , Zn^{2+} , In^{3+} , La^{3+} etc. as metal centers. One should note that in those cases the presence of boric or boronic acid is lacking. The use of boric acid as catalyst for the formation of primary, secondary and tertiary amides is not so common but is not unknown [31–33]. Interestingly in [31], nei-



Scheme 2.

ther boric acid nor polyethylene glycol (PEG) 400 showed catalytic activity alone, e.g. without the help of each other. Thus one may envisage a synergy catalytic influence Metal and $\text{R}-\text{B}(\text{OH})_2$.

The **teo:edd** ration in the obtained co-crystals is 1:1 vs. 2:1 in aminophylline (Fig. 1). The molecular geometry (bond lengths and angles) of **teo** and **edd** are similar to those in the crystal structures of the compounds reported alone (Fig. 2). As one can expect the **teo:edd** co-crystal is successfully achieved through hydrogen bonding of **teo**

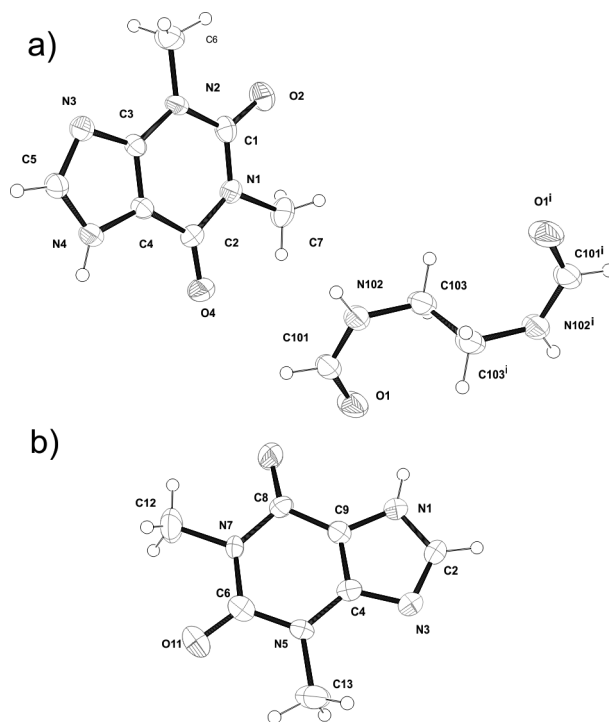


Fig. 1. ORTEP view of molecules present in the asymmetric unit of a) **teo:edd** co-crystal and b) **teo**; displacement ellipsoids are at 50% probability and hydrogen atoms are shown as spheres with arbitrary radii

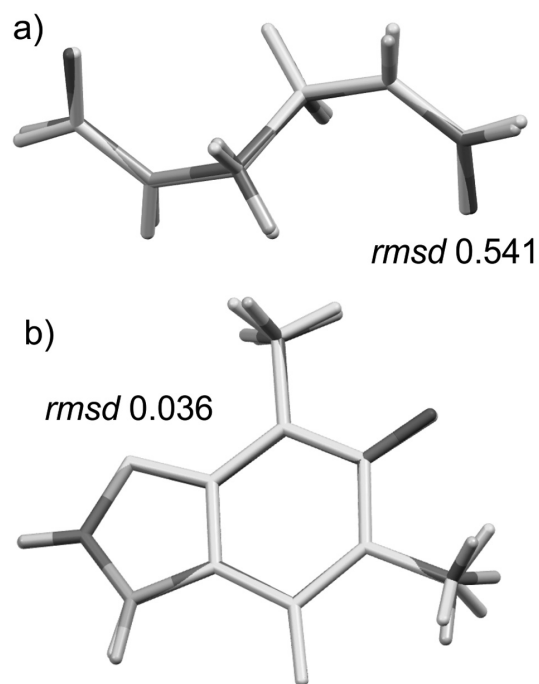


Fig. 2. Overlay of the molecules of a) **edd** and b) **teo** from co-crystal with those of compounds alone; the light (green) molecules are **enn** ref. [37] and **teo** ref. [35]

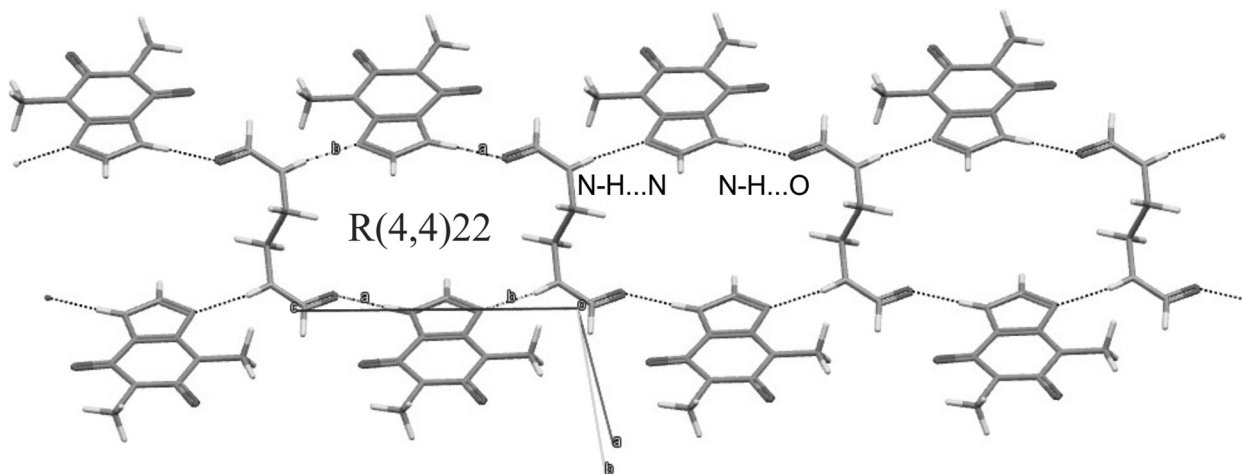


Fig. 3. Hydrogen bonding interactions (for details see Table 2) stabilizing the three-dimensional arrangement in **teo:edd** co-crystal

Table 2. Hydrogen-bond and $\text{CH}_3, \dots, \text{O}$ geometry ($\text{\AA}, ^\circ$)

$D-H \cdots A$	$D-H$	$H \cdots A$	$D \cdots A$	$D-H \cdots A$
teo : edd				
$\text{N4}-\text{H4} \cdots \text{O6}^i$	0.93 (4)	1.78 (4)	2.708 (3)	177 (3)
$\text{N11}-\text{H11} \cdots \text{N7}$	0.88 (4)	2.10 (4)	2.967 (3)	173 (4)
$\text{CH}_3, \dots, \text{O}$				
$\text{C16}-\text{H16B} \cdots \text{O6}^{ii}$	0.93 (3)	3.254 (4)	3.882 (5)	125 (2)
Symmetry codes: (i) $x, y, z+1$; (ii) $x, y-1, z$.				
teo				
$\text{N1}-\text{H1} \cdots \text{N3}^i$	1.07 (9)	1.82 (9)	2.850 (6)	160 (7)
$\text{C2}-\text{H2} \cdots \text{O10}^{ii}$	0.93	2.42	3.179 (7)	139 (5)
Symmetry codes: (i) $x-1/2, -y+2, z+1/2$; (ii) $x+1/2, -y+2, z-1/2$.				

and **edd** – resulting in a $R(4,4)22$ ring motif that extends into $C(4,4)22$ chains along c (Fig. 3 and Table 2). The two **teo** carbonyl oxygens are not involved in hydrogen bonding interaction and do not contribute to the three-dimensional stabilization of the structure. This is probably due to the molecular packing bringing in close proximity CH_3 and CH_2 groups and thus hindering the carbonyl oxygens. As **teo** is a purine it is not unexpected that weak $\pi \dots \pi$ and $\text{CH}_3 \dots \pi$ interactions additionally stabilize the crystal packing (Fig. 4). The excess of **teo** (the initially used Aminophylline is a **teo:en** in a 2:1 ratio) crystallizes in as a new polymorphic form (Fig. 1b). The structure features a pseudo-center of symmetry but the attempts to solve and refine the structure in a higher symmetry were not successful. As the bond

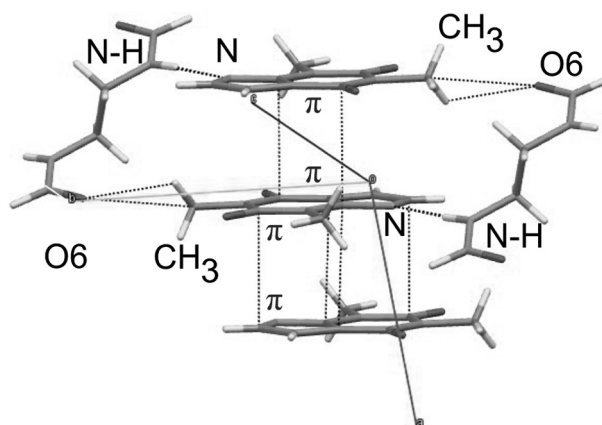


Fig. 4. Observed weak interactions ($\pi \dots \pi$ and $\text{CH}_3 \dots \pi$) in the crystal structure of **teo:edd** co-crystal

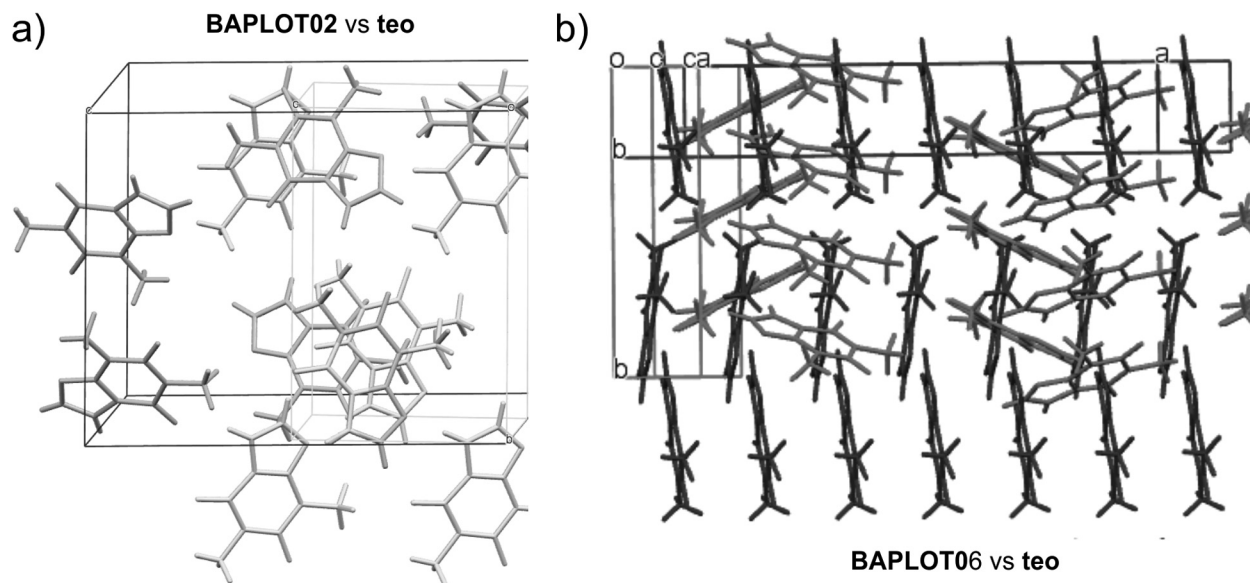


Fig. 5. The dissimilar molecular arrangement observed in the different polymorphic forms of Theophylline a) **teo** vs BAPLOT2 [34, 35] and b) **teo** and BAPLOT6 [36]

lengths and angles of the reported here polymorph and the already know modifications [34–36] are conserved, the differences between the three polymorphic forms (two monoclinic and one orthorhombic) are in the three-dimensional arrangement of the molecules (Fig. 5). This different three-dimensional packing is probably influenced by the presence of additional suitable hydrogen bonding partners as **edd** and 3-carboxyphenylboonic acid.

We have obtained a co-crystal of **teo**: **edd** and a new polymorph modification of theophylline. The N,N'-(ethane-1,2-diyl)diformamide (**edd**) is produced from ethylenediamine and DMF using cadmium acetate and 4-carboxyphenylboronic acid as catalysts. The breakup of DMF occurs in the presence of metal as catalyst while the N-formylation requires the presence of R-B(OH)₂.

Acknowledgments: This work was supported by ESF Grant BG051PO001-3.3.06-0027 and NSFB grant DRNF02/1.

REFERENCES

- H.-Q. Liu, J. Liu, Y.-H. Zhang, C.-D. Shao, J.-X. Yu, *Chin. Chem. Lett.* **26**, 11 (2015).
- H. Lundberg, F. Tinnis, N. Selander, H. Adolfsson, *Chem. Soc. Rev.* **43**, 2714 (2014).
- H. Miyamura, S. Kobayashi, *Acc. Chem. Res.* **47**, 1054 (2014).
- V. R. Pattabiraman, J. W. Bode, *Nature* **480**, 471 (2011).
- N. V. Reddy, K. R. Prasad, P. S. Reddy, M. L. Kantam, K. R. Reddy, *Org. Biomol. Chem.* **12**, 2172 (2014).
- K. Kobayashi, S. Nagato, M. Kawakita, O. Morikawa, H. Konishi, *Chem. Lett.* **24**, 575 (1995).
- F. F. Blicke, C.-J. Lu, *J. Am. Chem. Soc.* **74**, 3933 (1952).
- F. M. F. Chen, N. L. Benoiton, *Synthesis* **1979**, 709 (1979).
- H. Yale, *J. Org. Chem.* **36**, 3238 (1971).
- B. Das, M. Krishnaiah, P. Balasubramanyam, B. Veeranjanyulu, D. Nandan Kumar, *Tetrahedron Lett.* **49**, 2225 (2008).
- T. V. Pratap, S. Baskaran, *Tetrahedron Lett.* **42**, 1983 (2001).
- P. Strazzolini, A. G. Giumanini, S. Cauci, *Tetrahedron* **46**, 1081 (1990).
- M. Sridhar, B. C. Ramanaiah, C. Narsaiah, B. Mahesh, M. Kumaraswamy, K. K. R. Mallu, V. M. Ankathi, P. Shanthan Rao, *Tetrahedron Lett.* **50**, 3897 (2009).
- M. Hosseini-Sarvari, H. Sharghi, *J. Org. Chem.* **71**, 6652 (2006).
- T. Kondo, S. Kotachi, Y. Tsuji, Y. Watanabe, T.-a. Mitsudo, *Organometallics* **16**, 2562 (1997).
- B. Desai, T. N. Danks, G. Wagner, *Tetrahedron Lett.* **46**, 955 (2005).
- CrysAlis PRO, Agilent Technologies, UK Ltd, Yarnton, England, 2011.
- G. M. Sheldrick, *Acta Cryst. A* **64**, 112 (2008).
- J. An, R. P. Fiorella, S. J. Geib, N. L. Rosi, *J. Am. Chem. Soc.* **131**, 8401 (2009).
- R. Patra, H. M. Titi, I. Goldberg, *New J. Chem.* **37**, 1494 (2013).

21. X.-F. Wang, Y.-B. Zhang, Y.-Y. Lin, *CrystEngComm* **15**, 3470 (2013).
22. C. Zou, T. Zhang, M.-H. Xie, L. Yan, G.-Q. Kong, X.-L. Yang, A. Ma, C.-D. Wu, *Inorg. Chem.* **52**, 3620 (2013).
23. Z.-J. Lin, L.-W. Han, D.-S. Wu, Y.-B. Huang, R. Cao, *Cryst. Growth Des.* **13**, 255 (2012).
24. W. W. Lestari, P. Lonneck, M. B. Sarosi, H. C. Streit, M. Adlung, C. Wickleder, M. Handke, W.-D. Einicke, R. Glaser, E. Hey-Hawkins, *CrystEngComm* **15**, 3874 (2013).
25. W. Ouellette, K. Darling, A. Prosvirin, K. Whitenack, K. R. Dunbar, J. Zubietta, *Dalton Trans.* **40**, 12288 (2011).
26. A. D. Burrows, K. Cassar, T. Duren, R. M. W. Friend, M. F. Mahon, S. P. Rigby, T. L. Savarese, *Dalton Trans.* **18**, 2465 (2008).
27. J. Zhang, R. Liu, P. Feng, X. Bu, *Angew. Chem. Int. Ed.* **46**, 8388 (2007).
28. J.-D. Lin, X.-F. Long, P. Lin, S.-W. Du, *Cryst. Growth Des.* **10**, 146 (2009).
29. C. Ma, Y. Wu, J. Zhang, Y. Xu, B. Tu, Y. Zhou, M. Fang, H.-K. Liu, *CrystEngComm* **14**, 5166 (2012).
30. A. K. Chaudhari, S. Mukherjee, S. S. Nagarkar, B. Joarder, S. K. Ghosh, *CrystEngComm* **15**, 9465 (2013).
31. P. Tang, *Org. Synth.* **81**, 262 (2005).
32. L. Y. Shteinberg, *Russ. J. Org. Chem.* **39**, 972 (2003).
33. P. Starkov T. D. Sheppard, *Org. Biomol. Chem.* **9**, 1320 (2011).
34. K. Fucke, G. J. McIntyre, C. Wilkinson, M. Henry, J. A. K. Howard, J. W. Steed, *Cryst. Growth Des.* **12**, 1395 (2012).
35. D. Khamar, R. G. Pritchard, I. J. Bradshaw, G. A. Hutcheon, L. Seton, *Acta Crystallogr. C* **67**, o496 (2011).
36. S. Zhang, A. Fischer, *Acta Crystallogr. E* **67**, o3357 (2011).
37. Jin-hui Yang, Yan-xue Chen, Shao-hui Wang, Jian-lei Wang, *Acta Crystallogr. E* **64**, o2418 (2008).

СОЛВОТЕРМАЛЕН СИНТЕЗ НА СЪКРИСТАЛИ НА ТЕОФИЛИН
И N,N'-(ЕТАН-1,2-ДИИЛ) ДИФОРМАМИД ЧРЕЗ РАЗЛАГАНЕ
НА ДМФ И N-ФОРМИЛИРАНЕ ПРИ КАТАЛИТИЧНО ДЕЙСТВИЕ
НА 3-CARBOXYHENYLBORONIC КИСЕЛИНА
И КАДМИЕВ АЦЕТАТ

В. Дюлгеров*, Л. Т. Димова, К. Косев, Р. П. Николова, Б. Шивачев

*Институт по минералогия и кристалография „Акад. Иван Костов“,
Българска академия на науките, ул. „Акад. Георги Бончев“,
бл. 107, 1113 София*

Постъпила декември, 2014 г.; приета януари, 2015 г.

(Резюме)

Представяме неочакваното получаване на N,N'-(етан-1,2-диил)диформаид. Реакцията е проведена в ДМФ на 100 °С и изходните съединения са кадмиев ацетат, 3-карбоксифенилборна киселина и аминофилин (2:1 смес от 1,3-диметилксантин и етилендиамин). N,N'-(етан-1,2-диил)диформаид се получава в резултат на реакция на формилиране, катализирана от кадмий и висока температура. N,N'-(етан-1,2-диил)диформаид съкрисотализира с теофилин в триклинната пространствена група P1-, с параметри на единичната клетка $a = 6.7437$ (8), $b = 8.7847$ (14), $c = 9.4656$ (15), $\alpha = 91.825$ (13)°, $\beta = 103.313$ (12)°, $\gamma = 98.054$ (12)°, и $Z = 2$. Структурата на съкрисотала е стабилизирана от между-молекулни водородни връзки. Останалият теофилин кристализира в нова полиморфна форма в пространствената група Pn, с параметри на елементарна клетка $a = 3.8744$ (4), $b = 12.8898$ (9), $c = 8.1167$ (6), $\beta = 98.965$ (8) и $Z = 2$.

TiO₂ obtained from mechanically activated ilmenite and its photocatalytic properties

N. G. Kostova^{1*}, M. Achimovičová^{2,3}, A. Eliyas¹, N. Velinov¹, V. Blaskov⁴,
I. Stambolova⁴, E. Gock³

¹ Institute of Catalysis, Bulgarian Academy of Sciences, 1113 Sofia, Bulgaria

² Institute of Geotechnics, Slovak Academy of Sciences, 04001 Košice, Slovakia

³ Institute of Mineral and Waste Processing, Waste Disposal and Geomechanics, Technical University – Clausthal, 38678, Clausthal, Germany

⁴ Institute of General and Inorganic Chemistry, Bulgarian Academy of Sciences, 1113 Sofia, Bulgaria

Received December, 2014; Revised January, 2015

Mechanically activated FeTiO₃ concentrate, and TiO₂-the product after autoclave leaching of mechanically activated FeTiO₃ were characterized by XRD, specific surface area measurement (BET method) and Mössbauer spectroscopy (MS). The photocatalytic properties of the so obtained titania sample were evaluated in the oxidation reaction of photo-discoloring of Methyl Orange aqueous solution. The mechanical activation accelerated the dissolution of FeTiO₃ in sulfuric acid due to decreasing of the crystallite size and revealing the inner surface available for contact with the acid. A well-crystallized anatase TiO₂ phase was obtained with low content of impurities. The specific surface area was 28 m²g⁻¹. The photocatalytic activity of TiO₂ obtained from mechanically activated ilmenite ore was found to be slightly lower than that of the commercially available TiO₂ P 25 Degussa photocatalyst.

Key words: mechanical activation, ilmenite, leaching, TiO₂, photocatalyst.

INTRODUCTION

Ilmenite (FeTiO₃) is an important material for the production of metallic titanium, titanium dioxide, titanium carbide and other titanium-based compounds. There are two industrial methods, that have been developed for the preparation of titania from ilmenite mineral: the pyrometallurgical and the hydrometallurgical one. The pyrometallurgical production of rutile includes some processes which are all extremely energy consuming processes [1]. The direct hydrometallurgical treatment of ilmenite ore produces synthetic rutile using hydrochloric acid [2]. The chlorination process involves high reaction temperature of above 1000 °C, which is also highly consuming process. The application of the industrial hydrometallurgical method leads mainly to rutile formation. In the present paper an envi-

ronmentally friendly process is proposed based on mechanical activation of ilmenite ore concentrate. Mechanical activation generally increases the reactivity of solids and subsequent can induces chemical reactions, which take place spontaneously in activated systems and may appear even during milling or after milling are completed [3]. Milling operation changes the crystalline structure of mineral. The breakage of mineral crystal may cause defects on the crystal faces and increase in the reactivity of mineral [4]. The mechanically driven chemical process has a number of advantages over the conventional metal processing techniques [5]. The reaction kinetic conditions for the processing of mechanically activated ilmenite by means of direct hydrometallurgical conversion in autoclave to synthetic anatase at 150 °C with 30% H₂SO₄ were investigated by Achimovičová et al. [6].

In the following, we will study textural and structural properties of as-received and mechanically activated ilmenite and structural and photocatalytic properties of TiO₂-product after autoclave leaching of mechanically activated ilmenite.

* To whom all correspondence should be sent:
E-mail: nkostova@ic.bas.bg

EXPERIMENTALS

Material

The investigations were carried out with ilmenite ore concentrate (>95% FeTiO₃, <5% SiO₂) of Russian origin (GMD, Mineral Trade Company). The chemical composition was as follows: 34.43% Fe, 30.02% Ti, 0.76% Si, 0.47% Mg, 0.42% Al, 0.34% Mn, 0.11% Zn, 0.09% Ca, 0.07% Cr, 0.06% Co, 0.03% Ba, 31.63% O and 1.57% insoluble residual.

Mechanical activation and leaching

The mechanical activation of ilmenite FeTiO₃ was performed in an industrial eccentric vibratory ball mill ESM 656-0,5 ks (Siebtechnik, Germany) in the air atmosphere and room temperature for 15 min with 300 g of FeTiO₃ per charge. The following conditions were: 5 L steel satellite milling chamber, steel balls having a diameter of 30 mm with a total mass of 17 kg, rotational speed of the eccentric 960 rpm. This type of mill was developed by Gock and Kurrer and is currently used in industry [7, 8].

Mechanically activated FeTiO₃ was leached in 2 L autoclave (Deutsch&Neumann, Germany) in air atmosphere under the following conditions: 200 g of FeTiO₃/L, 30% H₂SO₄, leaching time 60 min, temperature 150 °C, 16 w% of Fe-powder was added because of Fe³⁺ reduction in FeTiO₃ concentrate.

Characterization techniques

The specific surface area was measured by the low temperature nitrogen adsorption method using a NOVA Station A surface area analyzer (Quantachrome Instruments, USA). The phase composition identification was performed by X-ray diffractometry (XRD) with an X'Pert PW 3040 MPD diffractometer (Phillips, Germany) operating in the 2θ geometry with CuK_α radiation.

The Mössbauer measurements were performed with a Wissel (Wissenschaftliche Elektronik GmbH, Germany) electromechanical spectrometer operating in a constant acceleration mode. A ⁵⁷Co/Rh source and a α-Fe standard were used for this purpose. The experimentally obtained spectra were fitted with CONFIT2000 software. The parameters of hyperfine interaction such as isomeric shift (δ), quadrupole splitting (Δ), effective internal magnetic field (B), line widths (Γ_{exp}), and relative weight (G) of the partial components in the spectra were determined.

The photocatalytic experiments were carried out on a semi-batch photoreactor (fixed charge of photocatalyst and dye solution + continuous air flow)

with magnetic stirring (400 rpm). The suspension was prepared by adding the photocatalyst sample (100 mg) to 100 mL of MO solution (1x10⁻⁵ M). In order to form slurry the mixture was sonicated for 5 min. The air flow was bubbled through the suspension by 2 frits forming tiny bubbles to ensure oxygen saturation. The suspension was stirred in the dark for 30 min to achieve an adsorption-desorption equilibrium under ideal mixing conditions and the illumination was switched on. This was considered to be the initial moment (t=0) of the reaction, occurring at room temperature. The suspension was irradiated by Philips 4 Watt TUV lamp (cold illumination). The UV-C monochromatic radiation has wavelength λ=254nm. The concentration of MO during the photocatalytic reaction was determined by monitoring the changes of the maximal absorbance peak of MO by fixed point measurement at wavelength 463 nm.

RESULTS AND DISCUSSION

The X-ray diffraction patterns revealed that the major phase of ilmenite concentrate was non-stoichiometric ilmenite FeTiO_{3+x}. The XRD patterns of the as-received and mechanically activated ilmenite concentrate demonstrate that the milling process causes the broadening and weakening of peaks (Fig. 1). The broadening and decrease in the intensity of the peaks can be related to decrease in the degree of crystallinity during the mechanical activation leading to rapid dissolution of milled ilmenite in diluted H₂SO₄ and formation of TiO₂ during hydrolytic reaction in the autoclave according to the reactions 1a) and 1b) summarized as reaction 2.

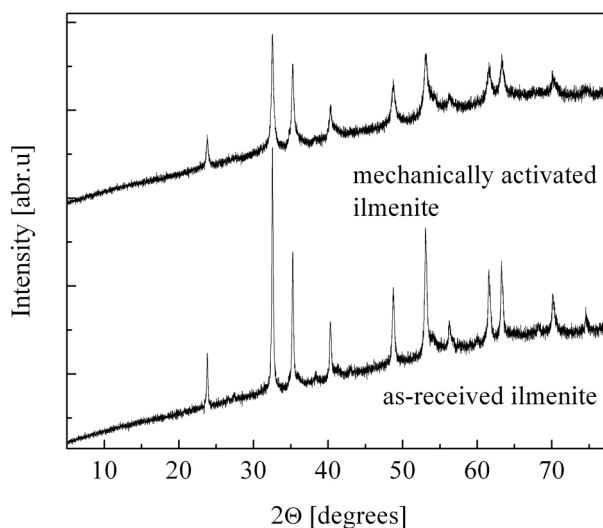


Fig. 1. XRD-patterns of as-received and mechanically activated ilmenite concentrate

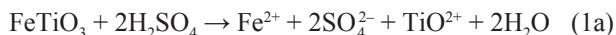


Fig. 2 illustrates that the TiO₂ contains anatase (JCPDS PDF 021-1272) and minor amount of rutile phase (JCPDS PDF 021-1276). The chemical composition of TiO₂ is the following: 52,1% Ti; 2,9% Fe; 0,86% Ca; 0,78% Si; 0,18% Al; 0,03% P; 0,03% Zr and 3,1% insoluble residual.

Leaching of mechanically activated ilmenite with 30% H₂SO₄ lowers the flue gas pollution due to the low reaction temperature and it also reduces

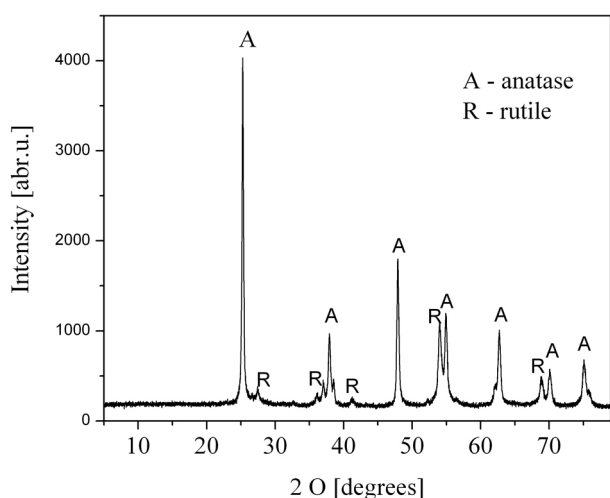


Fig. 2. XRD-pattern of the product after leaching of mechanically activated ilmenite concentrate

the waste acid release by partially recycling the diluted acid. The mechanical activation carried out by energetic milling in vibrational industrial mill accelerates the dissolution rate of ilmenite concentrate by increasing its chemical reactivity. The specific surface area of prepared anatase by leaching of mechanically activated ilmenite increases from 2 m²/g for ilmenite concentrate to 13 m²/g for mechanically activated ilmenite ore and 28 m²/g for titania.

Mössbauer spectroscopy is a very sensitive and versatile technique that can be used to supply information about the chemical, structural, magnetic and time-dependent properties of a material and is widely used to supplement the XRD analysis. The experimentally obtained Mössbauer spectra of the samples represent combinations of doublets or doublets and a sextet. The ⁵⁷Fe Mössbauer spectrum of as-received ilmenite concentrate is fitted with two doublets model. The results of fitting (Table 1) evidently have shown the presence of Fe ions in oxida-

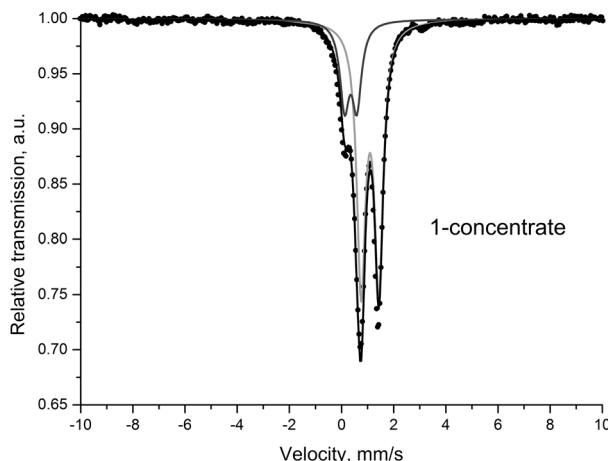


Fig. 3. Mössbauer spectrum of ilmenite concentrate

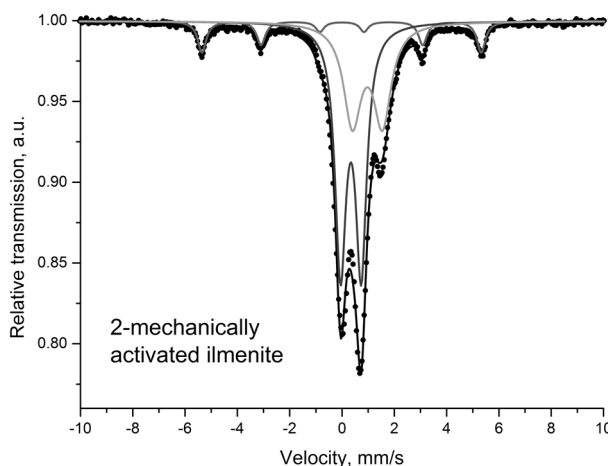


Fig. 4. Mössbauer spectrum of mechanically activated ilmenite concentrate

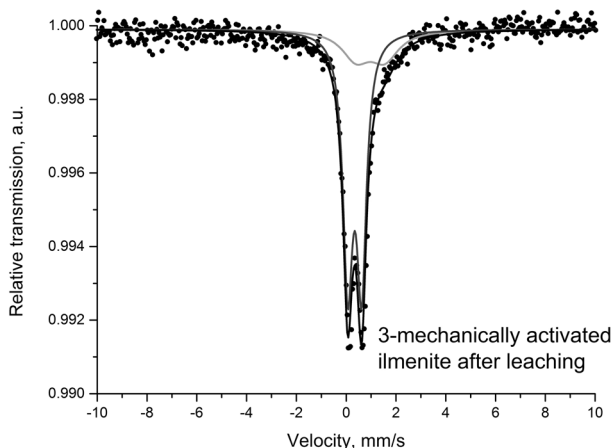


Fig. 5. Mössbauer spectrum of TiO₂ – product after leaching of mechanically activated ilmenite

Table 1. Calculated parameters of Mössbauer spectra of the investigated samples

Sample	Components	δ , mm/s	Δ , mm/s	B, T	Γ_{exp} , mm/s	G, %
Ilmenite concentrate	Db1 – Fe _{1+x} Ti _{1-x} O ₃ – Fe ³⁺	0.35	0.47	–	0.43	25
	Db2 – Fe _{1+x} Ti _{1-x} O ₃ – Fe ²⁺	1.09	0.68	–	0.40	75
	S _x – α -Fe – Fe ⁰	0.00	0.00	33.2	0.39	11
Mechanically activated ilmenite	Db1 – Fe _{1+x} Ti _{1-x} O ₃ – Fe ³⁺	0.34	0.79	–	0.51	54
	Db2 – Fe _{1+x} Ti _{1-x} O ₃ – Fe ²⁺	0.97	1.15	–	0.81	35
TiO ₂ – product after leaching of mechanically activated ilmenite	Db1 – Fe _{1+x} Ti _{1-x} O ₃ – Fe ³⁺	0.34	0.56	–	0.47	75
	Db2 – Fe _{1+x} Ti _{1-x} O ₃ – Fe ²⁺	0.97	1.15	–	1.36	25

tion states Fe³⁺ and Fe²⁺. The calculated parameters of doublets correspond to nonstoichiometric ilmenite Fe_{1+x}Ti_{1-x}O₃. The relative weight of Fe³⁺ component (G) is 25%.

The spectrum of the mechanically activated concentrated ilmenite ore is fitted with a model comprising two doublets and one sextet. The hyperfine parameters of the components, obtained as a result of the processing (Table 1), are indicative of the presence of Fe in various oxidation states: Fe⁰, Fe²⁺ and Fe³⁺. The parameters of the sextet component are corresponding to the phase of α -Fe and it has a relative weight of 11%. The parameters of the two doublet components of the spectra are in correspondence with those of the non-stoichiometrical ilmenite. The Mössbauer spectrum of mechanically activated ilmenite after extraction of the iron represents a doublet having very low intensities of the absorption lines. The parameters of the doublet components, are in correspondence with those of the non-stoichiometric ilmenite, however the ratio Fe³⁺/Fe²⁺ is 3/1. Quite lower values are noticeable for the quadrupole splitting of the component Db1 – Fe³⁺, which is due to a residual of less defective particles of ilmenite in the sample after the treatment for leaching of iron.

Methyl orange (MO), a representative of the azo dye family, is a source of pollution, which releases toxic and potentially carcinogenic substance into the waterways. The photocatalytic activity of sample in MO reaction of oxidative degradation was studied in solution using anatase, prepared by leaching of mechanically activated ilmenite. The photocatalytic degradation of MO was investigated by determining the remaining concentration of MO at various time intervals (Fig. 6). The C/C₀ vs irradiation time curves showed differences. 93% of MO was removed after 120 min irradiation of TiO₂ – product after leaching of mechanically activated ilmenite. Under the same conditions, the mechanical activated ilmenite sample can degrade MO over 38%, which could be expected in advance due to its lower surface area

(Table 2). 99% of the MO removal is obtained using P 25 Degussa TiO₂ photocatalyst. The TiO₂ – product after leaching of mechanically activated ilmenite showed slightly lower photocatalytic activity than that of commercially available P 25 Degussa TiO₂ photocatalyst. A smaller particle size and a larger surface area would facilitate the increase of

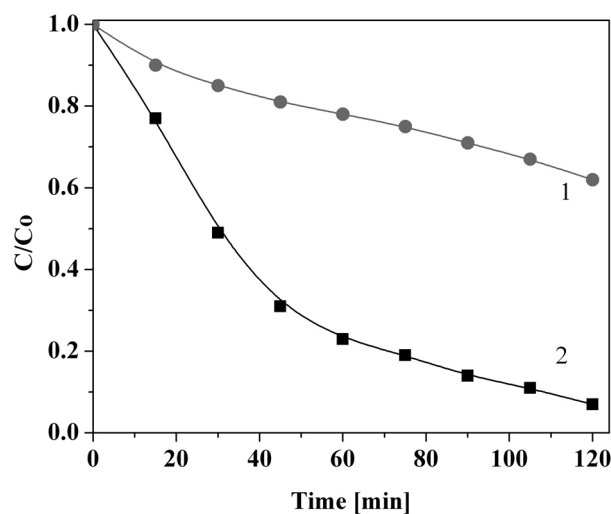


Fig. 6. The UV-C light photocatalytic oxidative degradation of Methyl Orange with mechanically activated ilmenite (1) and TiO₂ – product after leaching of mechanically activated ilmenite (2)

Table 2. Textural properties of samples

Sample	Surface area, m ² g ⁻¹	Pore volume cc g ⁻¹
Ilmenite concentrate	2	
Mechanically activated ilmenite	13	0,0087
TiO ₂	29	0.0187

the photogenerated electrons [9]. The mechanical activation of ilmenite increased the surface area, which provided greater number of adsorption sites for MO. The highly crystalline anatase shows high activity due to the reduced number of defect sites which minimizes the electron-hole recombination.

CONCLUSIONS

(i) The mechanical activation of ilmenite ore concentrate reduces the crystallite size as the lattice strain increased due to a slight compression of the unit cell. The combination of these factors resulted in a much more reactive surface than bulk ilmenite in the leaching process.

(ii) A substantial increase in the quadrupole shift in the Mössbauer spectrum of mechanically activated concentrate is observed as well as an increase in the width of the line of Db-Fe²⁺, that is probably due to increase in the number of crystalline defects as a result of the milling.

(iii) The photocatalytic activity of anatase prepared by leaching of mechanically activated ilmenite ore concentrate was found to be slightly lower than that of the commercially available TiO₂ nanoparticles powder Degussa P 25 but it is also is high.

Acknowledgments: *The present investigations are financially supported by the Bulgarian National*

Science Research Fund under contract DNTS/SLOVAKIA 01/3, bilateral cooperation project between the Bulgarian Academy of Sciences and Slovak Academy of Sciences and project VEGA 2/0027/14.

REFERENCES

1. R. G. Becher, Improved process for the beneficiation of ores containing contaminating iron, Australian Patent 247110, 1963.
2. M. R. Lanyon, T. Lwin, R. R. Merritt, *Hydrometallurgy*, **51**, 299-323 (1999).
3. P. Baláž, *Mechanochemistry in Nanoscience and Minerals Engineering*, DOI: 10.1007/978-3-540-74855-7 Springer, Berlin Heidelberg, 2008.
4. C. Li, B. Liang, L.-H. Guo, Z.-B. Wu, *Minerals Engineering*, **19**, 1430 (2006).
5. N. J. Welham, J. S. Williams, *Metall. Mater. Trans. B*, **30**, 1075 (1999).
6. M. Achimovičová, S. Hassan-Pour, E. Gock, V. Vogt, P. Baláž, B. Friedrich, *Metall. Mater. Eng.*, **20**, 141 (2014).
7. E. Gock, K. E. Kurrer, *Erzmetall*, **49**, 434 (1996).
8. E. Gock, K. E. Kurrer, *Powder Technol.*, **105**, 302 (1999).
9. R. Anpo, T. Shima, S. Kodama, Y. Kubokawa, *J. Phys. Chem.*, **91**, 4305 (1987).

ТiO₂, ПОЛУЧЕН ОТ МЕХАНИЧНО АКТИВИРАН ИЛМЕНИТ И НЕГОВИТЕ ФОТОКАТАЛИТИЧНИ СВОЙСТВА

Н. Г. Костова^{1*}, М. Ахимовичова^{2,3}, А. Елияс¹, Н. Велинов¹,
В. Блъсков⁴, И. Стамболова⁴, Е. Гок³

¹ *Институт по катализ, Българска академия на науките ул. „Акад. Г. Бончев“, бл. 11,
1113 София, България*

² *Институт по геотехника, Словацка академия на науките, Кошице, Словакия*

³ *Институт по минерали и отпадъци, изхвърляне на отпадъци и геомеханика,
Технически университет – Клаустал, 38678, Клаустал, Германия*

⁴ *Институт по обща и неорганична химия, Българска академия на науките,
ул. „Акад. Г. Бончев“, бл. 11, 1113 София, България*

Постъпила декември, 2014 г.; приета януари, 2015 г.

(Резюме)

Механично активиран FeTiO₃ концентрат и TiO₂ – продукт, получен след автоклавно извличане на механично активиран илменит са характеризирани с рентгенофазов анализ, измерване на специфичната повърхност (метод БЕТ) и Мьосбауерова спектроскопия. Фотокаталитичните свойства на получения титанов диоксид бяха определени в окислителната реакция на фотообезцветяване на воден разтвор на метил оранж. Механичното активиране ускорява разтварянето на FeTiO₃ в сярна киселина, дължащо се на понижаване размера на кристалитите и разкриване на вътрешната повърхност за контакт с киселината. Беше получена добре изкристализирана фаза анатаз с ниско съдържание на примеси. Специфичната повърхност на получения продукт беше 28 m²g⁻¹. Фотокаталитичната активност на TiO₂, получен от механично активиран минерал илменит, беше малко по-ниска от тази на комерсиално достъпен TiO₂ P 25 Degussa фотокатализатор.

Optimization of CeO₂-ZrO₂ mixed oxide catalysts for ethyl acetate combustion

M. D. Dimitrov^{1*}, R. N. Ivanova¹, V. Štengl², J. Henych²,
D. G. Kovacheva³, T. S. Tsoncheva¹

¹ Institute of Organic Chemistry with Centre of Phytochemistry, BAS, Sofia, Bulgaria

² Institute of Inorganic Chemistry AS CR v.v.i, Husinec-Rez, Czech Republic

³ Institute of General and Inorganic Chemistry, BAS, Sofia, Bulgaria

Received December, 2014; Revised January, 2015

Nanosized ceria-zirconia mixed oxides were prepared using template-assisted co-precipitation approach followed by a hydrothermal treatment step. Some synthesis parameters (Ce/Zr ratio, presence of template and hydrothermal treatment temperature) were varied in order to get highly active mixed oxide catalysts for ethyl acetate combustion. The performed physicochemical characterization evidenced the presence of a single cubic phase for the samples with lower Ce content (Ce/Zr < 5:5 mol ratio). Surprisingly, formation of separate tetragonal zirconia phase along with the cubic one was registered for the mixed oxide samples with lower Zr amount (Ce/Zr ≥ 5:5 mol ratio). The variation of the other two synthesis parameters had an effect mostly on the textural characteristics of the final materials. The most significant effect on the catalytic properties of mixed Ce-Zr oxide samples comes from varying Ce-Zr ratio. Highest catalytic activity showed 3Ce7Zr(CTAB, HT373) sample due to the complete integration of both metal oxides into one mixed phase with a disturbed cubic lattice structure.

Key words: nanosized CeO₂-ZrO₂, mixed oxide phase, ethyl acetate combustion.

INTRODUCTION

CeO₂ is a rare-earth metal oxide with important applications in areas of catalysis, electrochemistry, photochemistry, and materials science [1] due to both its acidity and ability to undergo a facile conversion between “+4” and “+3” formal oxidation states. That can be enhanced by decreasing ceria particle size in the nanoscale. Another possibility is the addition of zirconia which results in the formation of solid solutions of the Ce_{1-x}Zr_xO₂ type with improved thermal stability [2]. Besides, the fluorite-type structure of ceria, particularly the cation sublattice, could be maintained up to a high level of doping [3, 4]. The consequence is the presence of perturbations in the Me-O coordination sphere, which are responsible for the high oxygen mobility seen in ceria-zirconia mixed oxides thus

enhancing the overall redox capability of the mixed oxide system [5–8]. The enhanced reducibility is likely to lead to improved catalytic properties for some reactions such as volatile organic compounds (VOC) combustion [9]. At the same time, the textural characteristics are very important features for a given porous material. Their optimization could have a significant influence on the catalytic behavior of this material with regard to active sites accessibility and the facile transportation of reactants and products to and from them. In case of nanosized mixed metal oxides usually the surface to volume ratio is high and large part of the surface is exposed, however, the presence of additional porosity coming from either the use of template or some specific treatment during synthesis could have a beneficial effect on the overall catalytic activity of the obtained materials.

The aim of the investigation is to obtain highly active nanostructured Ce_{1-x}Zr_xO₂ mixed oxides catalysts for VOCs elimination using template-assisted hydrothermal approach. The effect of synthesis parameters is in the focus of investigation and ethyl acetate was used as a representative VOC.

* To whom all correspondence should be sent:
E-mail: md2@abv.bg

EXPERIMENTAL

Materials

Mono- and bi-component oxide samples were synthesized using template-assisted precipitation technique followed by hydrothermal treatment step according to a procedure reported by Tsoncheva et al. [10]. In principle, 12.0 g N-Hexadecyl-N,N,N-trimethylammoniumbromide (CTAB) were dissolved in 100 ml distilled water. After that, a second solution of ZrCl₄ (6.80 g) or CeCl₃·7H₂O (10.8 g) in 50 ml distilled water was added slowly and under vigorous stirring. In the case of the mixed oxide samples the second solution contains a mixture of ZrCl₄ and CeCl₃·7H₂O according to the corresponding Ce/Zr mol ratio. Then the temperature was raised to 50 °C and stirred for 30 min before adding dropwise 40 ml NH₃ (12.5%). The resulting mixture was stirred overnight at 50 °C. Then it was transferred into a polypropylene container and treated at 100 °C or 140 °C for 24 h. The next step is filtration of the solution and washing with distilled water, then drying at room temperature and calcination up to 300 °C with a ramp of 1 degree per minute and dwelling time of 15 hours at the final temperature. Selected mixed oxide samples were prepared by varying certain synthesis parameters – the presence/absence of template as well as the temperature of hydrothermal treatment. The obtained samples are designated as follows: *x*Ce_{*y*}Zr(*a*,*T*) where *x* and *y* represent the mol ratio between Ce and Zr, *a* is the organic template molecule and *T* is the temperature of hydrothermal treatment.

Methods of characterization

Powder X-ray diffraction patterns were collected within the range of 10–80° 2θ with a constant step of 0.02° 2θ and counting time of 1 s/step on Bruker D8 Advance diffractometer equipped with Cu Kα radiation and LynxEye detector. The size of the crystalline domains in the samples was determined using Topas 4.2 software with Rietveld quantification refinement. Nitrogen sorption measurements were recorded on a Quantachrome NOVA 1200e instrument at 77 K. Before the physisorption measurements the samples were outgassed at 423 K overnight under vacuum. The UV–Vis spectra were recorded on a Jasco V-650 UV-Vis spectrophotometer equipped with a diffuse reflectance unit. The Raman spectra were recorded on a DXR Raman microscope (Thermo Fisher Scientific, Waltham, Massachusetts, USA). A 532 nm laser was used at a power of 3 mW. The powdered samples were scanned at a 15 point mapping mode under a 10× objective lens with an automated autofocus at each

point to get 15 random measurements. The catalytic experiments were performed in a flow type reactor (0.030 g of catalyst) with a mixture of ethyl acetate (1.21 mol%) in air with WHSV – 335 h⁻¹. Gas chromatographic (GC) analyses were carried out on HP5850 apparatus using carbon-based calibration. The samples were pretreated in Ar at 423 °K for 1 h and then the temperature was raised with a rate of 2 K/min in the range of 423–773 °K for the temperature-programmed regime experiments.

RESULTS AND DISCUSSION

Some physicochemical characteristics of the obtained samples are presented in Table 1. X-ray diffraction technique has been used for determination of samples crystallinity and phase composition (Fig. 1). The XRD pattern of pure zirconia (Fig. 1a) shows low degree of crystallinity due to the presence of very small zirconia particles (Table 1). The obtained broad reflections to zirconia clusters are best fitted with the parameters of tetragonal zirconia phase. This is consistent with literature data where stabilization of zirconia phase with high symmetry (tetragonal or cubic) is the preferred phase for zirconia samples with particles below 10 nm [11, 12]. At the same time, pure ceria sample shows well defined reflections of cubic fluorite-like structure with particle sizes of about 12 nm (Fig. 1a, Table 1). In case of mixed oxides samples, with the increase of Zr content up to Ce/Zr ≥ 5:5 mol ratio, the XRD reflections became asymmetrical and a presence of separate zirconia phase is assumed while in case of the samples with higher Zr content (Ce/Zr < 5:5 mol ratio) the fitting of the obtained XRD reflections shows the presence of only one cubic fluorite-like Fm-3m phase (Fig. 1). The observed significant shift of the reflections for the latter samples indicates a decrease in their unit cell parameter in comparison to the pure ceria material that could be attributed to the complete integration of both metal oxides into one single cubic lattice (Fig. 1a). On the basis of XRD results we chose the two compositions (5:5 and 3:7) that differ structurally most from the pure ceria material and prepared two more samples for each composition where we varied the synthesis conditions (Table 1). The XRD patterns for the samples prepared without template or by hydrothermal treatment at 413 °K do not differ from their analogues obtained by the main synthesis procedure (Fig. 1b). Hence, it seems that the Ce/Zr ratio is the only factor responsible for the final phase composition of the mixed oxide samples when using the present synthesis procedure.

Nitrogen physisorption measurements were conducted in order to elucidate the textural properties

of the studied samples (Fig. 2, Table 1). All isotherms are of type IV that is characteristic of mesoporous materials. Pure zirconia adsorbs nitrogen in the whole pressure interval. It is characterized with

the highest specific surface area and pore volume (Table 1). The pore size distribution is bimodal due to both interparticle mesoporosity and mesoporosity due to the organic template. On the other hand,

Table 1. Some physicochemical characteristics of the studied samples

Sample	Mol ratio Ce:Zr	Template	S _{BET} , m ² /g	V _{tot} , cm ³ /g	Space group	Particle size, nm
Zr(CTAB, HT373)	–	CTAB	296	0.42	P4 ₂ /nmc	1.2
1Ce9Zr(CTAB, HT373)	1:9	CTAB	196	0.16	Fm $\bar{3}$ m	5.1
3Ce7Zr(CTAB, HT373)	3:7	CTAB	167	0.14	Fm $\bar{3}$ m	3.5
3Ce7Zr(CTAB, HT413)	3:7	CTAB	180	0.15	Fm $\bar{3}$ m	4.0
3Ce7Zr(HT373)	3:7	–	150	0.10	Fm $\bar{3}$ m	5.3
5Ce5Zr(CTAB, HT373)	5:5	CTAB	150	0.14	Fm $\bar{3}$ m	9.7
5Ce5Zr(CTAB, HT413)	5:5	CTAB	154	0.17	P4 ₂ /nmc	5.8
5Ce5Zr(HT373)573	5:5	–	131	0.08	Fm $\bar{3}$ m	13.1
7Ce3Zr(CTAB, HT373)	7:3	CTAB	118	0.14	P4 ₂ /nmc	5.0
9Ce1Zr(CTAB, HT373)	9:1	CTAB	93	0.20	P4 ₂ /nmc	4.3
Ce(CTAB, HT373)573	–	CTAB	58	0.27	Fm $\bar{3}$ m	11.7

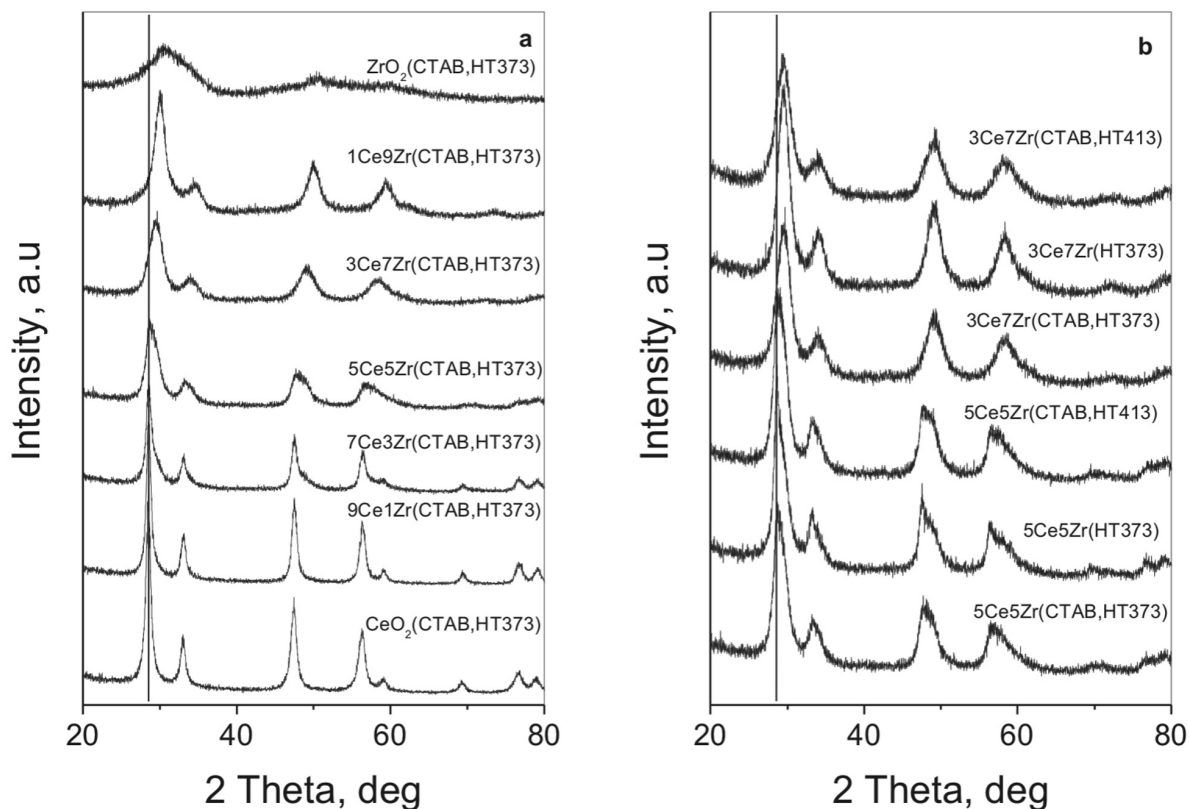


Fig. 1. XRD patterns of the studied samples obtained by the main synthesis procedure (a) and after varying some synthesis parameters (b)

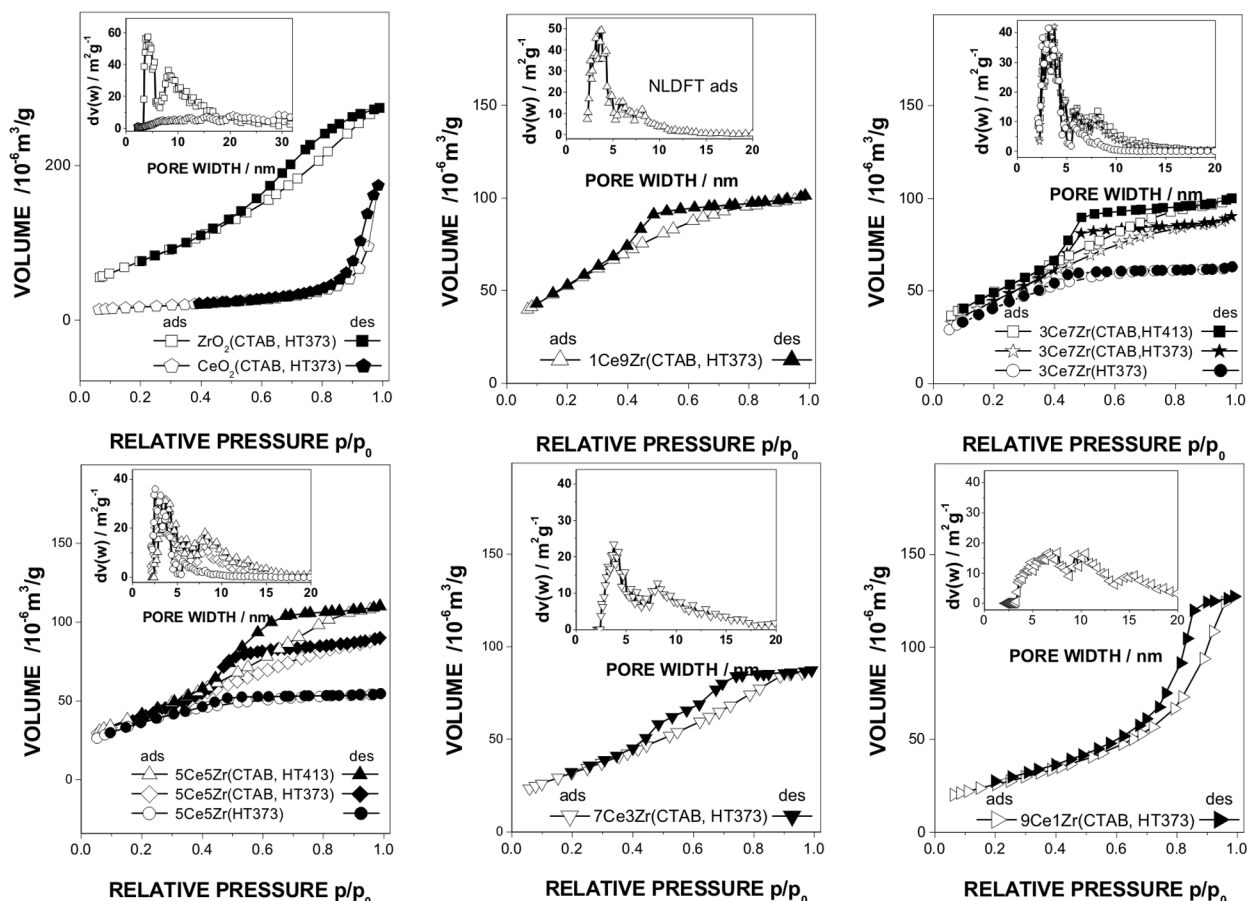


Fig. 2. Nitrogen physisorption isotherms with pore size distributions as insets for the studied pure and mixed metal oxide samples

pure ceria sample show a step step in the adsorption of nitrogen just above 0.8 relative pressure that characterizes it with very broad pore size distribution and predominant presence of large mesopores (Fig. 2). This sample has the lowest specific surface area but the presence of larger mesopores ensures relatively high pore volume (Table 1). In case of mixed oxide samples the shape of the isotherm is in-between those of the pure metal oxides (Fig. 2). With the increase of Zr content the specific surface area increases, the main pore diameter decreases, while the total pore volume goes through a minimum in case of Ce/Zr mol ratio of 5:5 (Table 1). The higher HT temperature leads to samples with slightly higher specific surface area and pore volumes. The samples prepared without template show deteriorated mesoporosity characterised with lower specific surface area and total pore volume due to the presence of slit-like pores only.

UV-vis diffuse-reflectance spectroscopy has been used to study various metal oxides to obtain information on surface coordination and different oxidation states of the metal ions. The measured

UV-Vis spectra exhibit broad and poorly resolved peaks. UV-vis spectra of pure zirconia sample showed strong absorption at about 210 and 230 nm due to the band gap energy of zirconia and weaker broad absorption with maximum at about 300 nm that arises from transitions involving extrinsic states such as surface trap states and/or defect states (Fig. 3). The presence of the latter band could be attributed to the presence of very small zirconia particles [13]. For pure ceria, the strong absorption with maximum at about 315 nm is ascribed to O²⁻→Ce⁴⁺ charge transfer (CT) transitions, while the one at about 250 nm – to O²⁻→Ce³⁺ CT transitions (Fig. 3). In case of the mixed oxides samples these bands are preserved and the registered increased absorption in the 350–500 nm range could be ascribed to both particle size decrease in comparison to pure ceria sample and to disturbances in the ceria lattice and appearance of additional defects due to incorporation of Zr.

Raman spectroscopy is a good technique sensitive to both distortions of oxygen sublattice and defects in the structure. The Raman spectra of se-

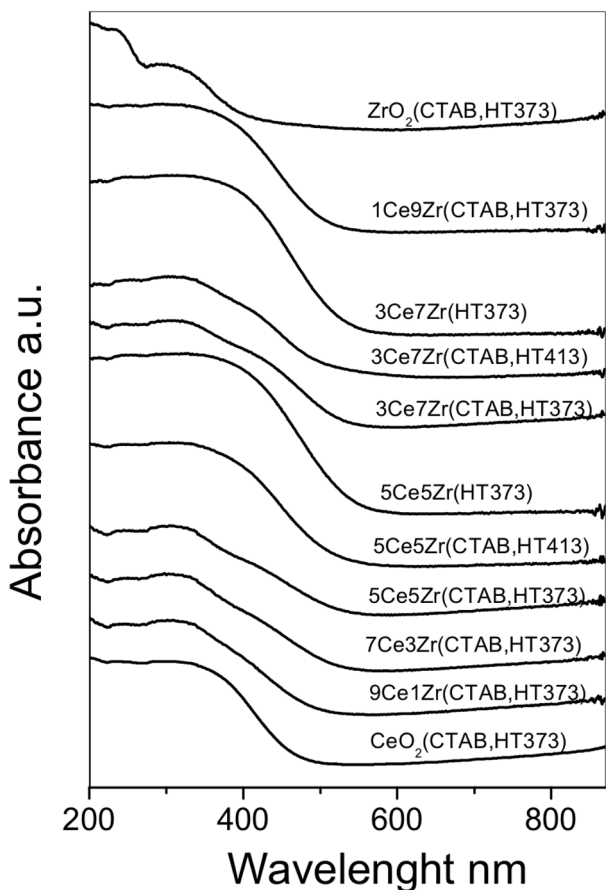


Fig. 3. UV-Vis spectra of pure and mixed metal oxide samples

lected samples are presented in Figure 4. The spectrum of CeO₂ is characterized by one strong band at 462 cm⁻¹ which is due to the F_{2g} vibration mode of the cubic fluorite structure [14]. In addition, it also exhibits two weak bands at about 250 and 600 cm⁻¹ which can be attributed to the non-degenerate transverse and longitudinal optical phonon modes of CeO₂, respectively [15]. Normally, these modes should not be observed by Raman spectroscopy but the presence of some defects, in particular oxygen vacancies in the ceria lattice, can be the reason for their appearance due to relaxation of symmetry rules [16]. At the same time, the spectrum profile of pure zirconia sample remains featureless (not shown) and we carefully could assign the lack of bands to the presence of only very small cluster-like particles in this sample. The obtained Raman spectra for selected mixed oxide samples do not possess bands due to zirconia phase (Fig. 4). The shift in the registered band positions to higher wave numbers in comparison with pure ceria sample (Fig. 4) signifies the changes in bond energies as a consequence of the substitution of zirconium into ceria

lattice. Besides, the appearance of a weak band at about 305 cm⁻¹ can be attributed to displacement of oxygen atoms from their ideal fluorite lattice positions [17]. The found effects are most evident for 3Ce7Zr(CTAB, HT373) sample and we assign this to the found complete integration of ceria and zirconia into a single cubic phase. The observed considerable broadening of the bands for this sample could be attributed to the reduction of phonon lifetime due to the observed significant decrease in the grain size (Fig. 4, Table 1).

The catalytic activity of the studied samples is presented in Figure 5. Pure zirconia starts to convert ethyl acetate just above 600 °K (Fig. 5a). At the same time pure ceria sample is much more active and the conversion of ethyl acetate starts around 550 °K due to the presence of a certain amount of Ce³⁺-ions and oxygen defects within CeO₂(CTAB, HT373) sample as was shown by UV-Vis and Raman spectra. In case of the mixed oxide samples, the increase of Ce:Zr ratio leads to increase in the conversion ability in comparison with the pure zirconia sample (Fig. 5a). However, this activity increase is not linear with the increase of the Ce:Zr ratio but goes through a maximum at Ce:Zr=3:7. The observed

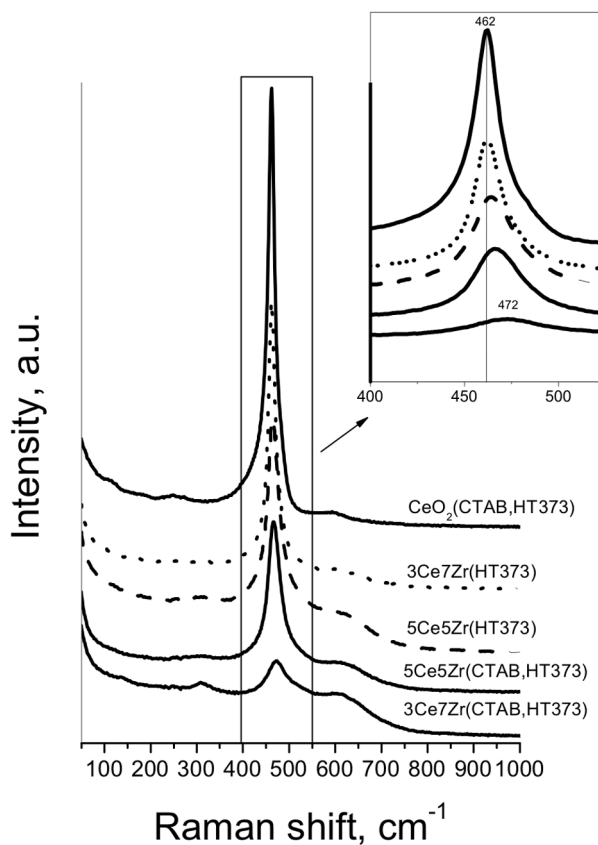


Fig. 4. Raman spectra of selected samples

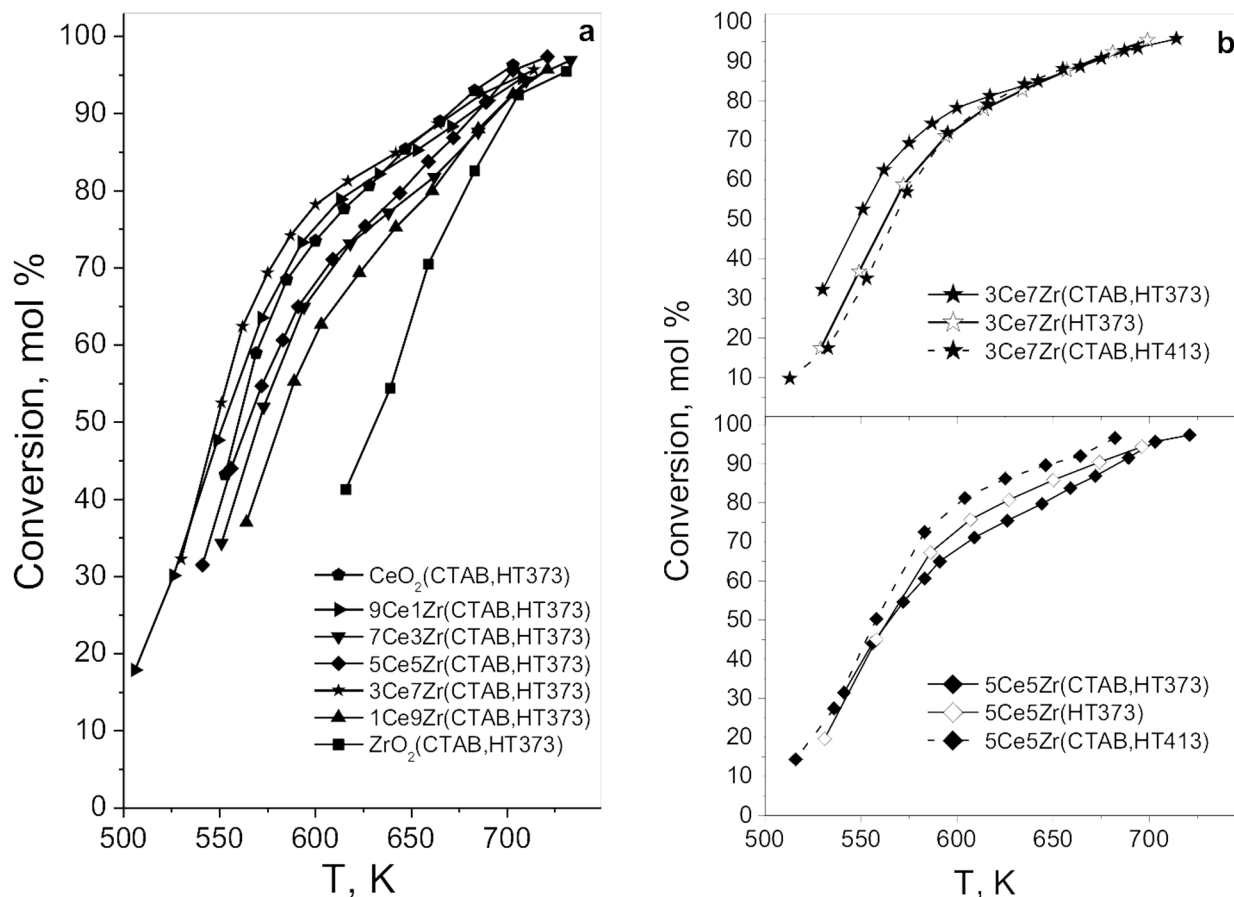


Fig. 5. Temperature dependency of ethyl acetate conversion for the samples obtained (a) by the main synthesis procedure and (b) after varying some synthesis parameters

highest activity for $3\text{Ce}7\text{Zr}(\text{CTAB}, \text{HT}373)$ could be ascribed to the complete integration of both metal oxides into one mixed phase containing a disturbed cubic lattice structure with a lot of defects that act as active sites for the studied reaction. The change in the textural characteristics of the two selected mixed oxide sample does not lead to significant change in the catalytic activity (Fig. 5b). However, in case of $\text{Ce}:\text{Zr}=3:7$ series of samples, both the increase in the temperature of hydrothermal treatment or the absence of organic template during the synthesis procedure have a negative effect on the catalytic activity, while a slight positive effect of the latter synthesis parameters was registered for the $\text{Ce}:\text{Zr}=5:5$ series of samples (Fig. 5b).

CONCLUSION

A series of CeO_2 - ZrO_2 mixed oxide nanocomposites have been prepared by template-assisted

co-precipitation approach followed by hydrothermal treatment step. By varying some synthesis parameters (Ce/Zr ratio, presence/absence of organic template and temperature of hydrothermal treatment) both textural and structural properties of the obtained nanomaterials can be significantly modified. However, the $\text{Ce}-\text{Zr}$ ratio is the key parameter that affects most the catalytic properties of mixed oxide samples. The changes in the other synthesis parameters lead to changes mainly in the textural parameters of a given sample, but have either slight or negative effect on its catalytic activity. Highest catalytic activity possesses $3\text{Ce}7\text{Zr}(\text{CTAB}, \text{HT}373)$ due to the found complete integration of both metal oxides into one mixed phase containing a disturbed cubic lattice structure with a lot of defects.

Acknowledgements: Financial support from BAS-ASCR bilateral project and Bulgarian National Science Fund (Project DFNI-E02/2/12.12.2014) is gratefully acknowledged.

REFERENCES

1. M. Boaro, M. Vicario, C. Leitenburg, G. Dolcetti, A. Trovarelli, *Catal. Today*, **77**, 407 (2003).
2. Q. Yuan, H.-H. Duan, L.-L. Li, L.-D. Sun, Y.-W. Zhang, C.-H. Yan, *J. Coll. Int. Sci.*, **335**, 151 (2009).
3. Q. Fu, H. Saltsburg, M. Flytzani-Stephanopoulos, *Science*, **301**, 935 (2003).
4. M. Fernández-García, A. Martínez-Arias, A. Guerrero-Ruiz, J. C. Conesa, J. Soria, *J. Catal.*, **211**, 326 (2002).
5. S. Arai, S. Muto, J. Murai, T. Sasaki, Y. Ukyo, K. Kuroda, H. Saka, *Mater. Trans.*, **45**, 2951 (2004).
6. P. Fang, J. Lu, X. Xiao, M. Luo, *J. Rare Earth*, **26**, 250 (2008).
7. H. Kaneko, S. Taku, Y. Tamaura, *Sol. Energy*, **85**, 2321 (2011).
8. Y. Nagai, T. Yamamoto, T. Tanaka, S. Yoshida, T. Nonaka, T. Okamoto, A. Suda, M. Sugiura, *Catal. Today*, **74**, 225 (2002).
9. M.V. Ganduglia-Pirovano, A. Hofmann, J. Sauer, *Surf. Sci. Rep.*, **62**, 219 (2007).
10. T. Tsoncheva, L. Ivanova, D. Paneva, I. Mitov, C. Minchev, M. Fröba, *Micropor. Mesopor. Mat.*, **120**, 389 (2009).
11. N. L. Wu, T. F. Wu, I. A. Rusakova, *J. Mater. Res.*, **16**, 666 (2001).
12. V. G. Zavodinsky, A. N. Chibisov, *J. Phys.: Conf. Ser.*, **29**, 173 (2006).
13. M. R. Loghman-Estarki, R. S. Razavi, H. Edris, *Curr. Nanosci.*, **8**, 767 (2012).
14. A. Martinez-Arias, M. Fernandez-Garcia, L. N. Salamanca, R. X. Valenzuela, J. C. Conesa, J. Soria, *J. Phys. Chem. B*, **104**, 4038 (2000).
15. J. Z. Shyu, W. H. Weber, H. S. Gandhi, *J. Phys. Chem.*, **92**, 4964 (1988).
16. X.-M. Lin, L.-P. Li, G.-S. Li, W.-H. Su, *Mater. Chem. Phys.*, **69**, 236 (2001).
17. V. S. Escribano, E. F. Lopez, M. Panizza, C. Resini, J. M. G. Amores, G. Busca, *Solid State Sci.*, **5**, 1369 (2003).

ОПТИМИЗИРАНЕ НА СМЕСЕНИ CeO₂-ZrO₂ КАТАЛИЗАТОРИ ЗА ИЗГАРЯНЕ НА ЕТИЛАЦЕТАТ

М. Д. Димитров¹, Р. Н. Иванова¹, В. Штенгъл², И. Хених²,
Д. Г. Ковачева³, Т. С. Цончева¹

¹ *Институт по органична химия с Център по фитохимия, Българска Академия на Науките,
ул. „Акад. Г. Бончев“, бл. 9, 1113 София, България*

² *Институт по неорганична химия, Академия на Науките на Чешка Република,
Хузинец-Рез, Чешка Република*

³ *Институт по обща и неорганична химия, Българска Академия на Науките,
ул. „Акад. Г. Бончев“, бл. 11, 1113 София, България*

Постъпила декември, 2014 г.; приета януари, 2015 г.

(Резюме)

Получени са наноразмени церий-цирконий смесени оксиди по метода на сътавяването в присъствие на органичен темплейт и последваща хидротермална обработка. Варирани са някои от параметрите на синтеза (съотношението Ce/Zr, присъствие/отсъствие на органичен темплейт и температурата на хидротермална обработка) с цел получаване на високо-активни смесенооксидни катализатори за изгаряне на етилацетат. Проведеното физикохимично характеризирание доказва присъствието само на една кубична фаза за образците с ниско съдържание на Ce (Ce/Zr < 5:5 молно съотношение). Изненадващ резултат е формирането на отделна тетрагонална циркониевооксидна фаза едновременно с кубичната за смесенооксидните образци с ниско съдържание на Zr (Ce/Zr > 5:5 молно съотношение). Варирането на другите два параметъра оказва влияние основно на текстурните характеристики на получените материали. Най-значителен ефект върху каталитичните свойства на смесените Ce-Zr оксиди оказва варирането на Ce/Zr съотношението. Най-висока каталитична активност показва 3Ce7Zr (СТАВ, НТ373) образецът, поради наличието в него на пълно интегриране на двата метални оксида в една смесено оксидна фаза, при която структурата на кубичната решетка е силно деформирана.

Synthesis and photocatalytic performance of Fe (III), N co-doped TiO₂ nanoparticles

A. M. Stoyanova^{1*}, N. K. Ivanova¹, A. D. Bachvarova-Nedelcheva²,
R. S. Iordanova²

¹Medical University-Pleven, 5800 Pleven, Bulgaria

²Institute of General and Inorganic Chemistry, Bulgarian Academy of Sciences,
1113 Sofia, Bulgaria

Received December, 2014; Revised January, 2015

Fe(III), N-TiO₂ nanoparticles were synthesized at low temperature via nonhydrolytic sol-gel method. The present work continues our investigations on the synthesis of nanosized TiO₂ powders with improved photocatalytic activity. The structure and morphology of the obtained samples was characterized by XRD, IR and UV-Vis spectroscopy. The average crystallite size of as prepared Fe and N co-doped TiO₂ was about 15–20 nm. The photocatalytic activity of doped TiO₂ powders was studied in UV and visible light and was evaluated by the degradation of Malachite Green (MG) as model pollutant. The relationship between dopant concentration and photocatalytic activity has been revealed.

Key words: Fe, N-co-doped titanium dioxide, sol-gel, photocatalytic activity.

INTRODUCTION

The application of titanium dioxide photocatalyst for degradation of pollutants has been extensively studied during the past decades owing to its ability to mineralize harmful organic compounds to CO₂ and H₂O under UV (Vis) irradiation. An important drawback of pure TiO₂ is its wide band gap, which allows photoactivation only under UV light irradiation, and quick recombination of electron-hole pairs.

In order to improve the photocatalytic functionality, many attempts have been made by doping of TiO₂ with transition metals.

Among various metal ions, Fe(III) ion has been known to be an effective dopant. Our investigations on the photocatalytic behavior of iron-doped titanium dioxide, prepared by a nonhydrolytic sol-gel method, showed beneficial effect of doping with small amounts of iron [1, 2].

Recently, doping with p-block (N, F, C, S) elements has attracted much attention because it is suggested that the introducing of such elements in

the crystal lattice can improve the photo-absorption properties of TiO₂ under visible light illumination [3–5].

On the other hand, it has been reported, that the photocatalytic activity of TiO₂ doped with elements such as sulfur and nitrogen can be further increased by the presence of Fe(III) as a co-dopant [6–10]. Nanocomposite Fe-N-TiO₂ was synthesized and successfully used for inactivation of tumor cells [11].

The present work reports on synthesis of nitrogen- and iron-nitrogen co-doped TiO₂ powders at low temperature using non-hydrolytic sol-gel method. The structure of the obtained samples was characterized by XRD, IR and UV-Vis spectroscopy. The photocatalytic activity of doped TiO₂ powders was studied under both UV and visible light and was evaluated by the degradation of Malachite Green (MG) as a model pollutant.

EXPERIMENTAL

Materials

Titanium(IV) chloride (purity $\geq 99.0\%$) was purchased from Fluka, benzyl alcohol ($\geq 99.5\%$) from Merck, iron(III) nitrate, Malachite Green oxalate (C₄₆H₅₀N₄·3C₂H₂O₄), absolute ethanol and diethyl

* To whom all correspondence should be sent:
E-mail: a.stoyanova@mu-pleven.bg

ether were supplied by Sigma-Aldrich. All the chemicals were used without further purification.

Preparation and characterization of titania catalysts

It is well known that the doping effect depends on many factors such as synthesis conditions, doping method and the dopant concentration [12, 13]. Pure and doped by Fe and N nanosized TiO₂ were synthesized by a nonhydrolytic sol-gel route from TiCl₄ and benzyl alcohol at moderate temperature. In a typical procedure, at first, the dopants were introduced to benzyl alcohol by adding proper amount iron (III) nitrate and urea (1.3 mol%), dissolved in ethanol (Fig. 1). Then, titanium tetrachloride was slowly added to a beaker containing the above mentioned mixture under vigorous stirring. The resulting sols were heated at 60 °C under continuous stirring. The reaction mixtures were left for aging at room temperature until white precipitate was observed. The resulting white thick suspensions were centrifuged at 5000 rpm for 15 min and the supernatant was discarded by decantation. The precipitates

were then washed with absolute ethanol and diethyl ether. After every washing step, the solvent was separated by centrifugation. The collected material was dried in air overnight and then ground into a fine powder. The obtained powders were calcinated at 500 °C for 2 hours. The as-prepared samples are denoted as TiO₂/N for N-doped and TiO₂/x%Fe/N for Fe,N-co-doped titania, where *x* represents the Fe/Ti mol ratio.

The phase transformations and structure of the resulting particles were characterized by X-ray diffraction (XRD, Bruker D8 Advance X-ray apparatus) and infrared (IR, using the KBr pellets method (Nicolet-320, FTIR spectrometer with a resolution of ±1cm⁻¹, by collecting 64 scans in the range 1000–400 cm⁻¹). The optical absorption spectra of the powdered samples in the wavelength range 200–500 nm were recorded by a UV–VIS diffused reflectance Spectrophotometer “Evolution 300” using a magnesium oxide reflectance standard as the baseline. The absorption edge and the optical band gap were determined following Dharma et al. instructions [14]. The bandgap energies (*E_g*) of the samples were calculated by the Planck’s equation:

$$E_g = \frac{h \cdot c}{\lambda} = \frac{1240}{\lambda},$$

where *E_g* is the bandgap energy (eV), *h* is the Planck’s constant, *c* is the light velocity (m/s), and *λ* is the wavelength (nm).

Photocatalytic activity experiments

The photocatalytic performance of the synthesized powders was evaluated by degradation of a model aqueous solution of Malachite Green (MG) under UV-Vis irradiation. The initial concentration of MG aqueous solution was 5 ppm. The photocatalyst sample (100 mg) was added to 150 ml dye solution to form slurry. After that, the suspension was magnetically stirred in the dark for 30 min to ensure the establishment of an adsorption-desorption equilibrium. The UV-irradiation source was a black light blue UV-lamp (Sylvania BLB 50 Hz 8W T5) with the major fraction of irradiation occurring at 365 nm. The intensity of UV-light reaching the surface of the suspension was measured with a numeric Luxmeter (LM 37, Dostmann electronic). The mean value of the radiation power impinging on the reacting suspension was estimated to be about 150 Lx.

The visible light source was a 500 W halogen lamp (Sylvania) fixed at 40 cm above the treated solution. The mean value of the radiation power reaching on the suspension was estimated to be about 14000 Lx.

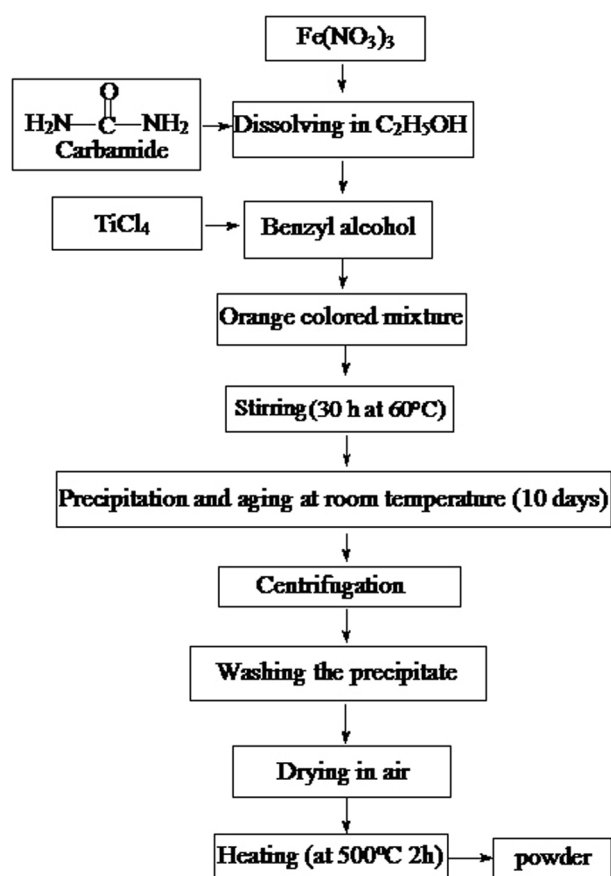


Fig. 1. Scheme of the nonhydrolytic sol-gel synthesis

All photocatalytic tests were performed at constant stirring (400 rpm) at room temperature of 25 °C. Aliquot samples (3 mL) of the mixture were taken at regular time intervals and the catalyst was separated through centrifugation (5000 rpm, 15 min). The absorbances of clear aliquots were measured by a Jenway 6505 UV-Vis spectrophotometer at 618 nm, the maximum absorption wavelength of MG.

RESULTS AND DISCUSSION

Characterization of titania samples

The XRD patterns of the Fe and N co-doped TiO₂ are shown in Figure 2. As is seen in the figure, dominate crystalline phase detected in the XRD patterns is anatase (TiO₂) (JCPDS 78-2486). It is noteworthy that in the XRD patterns of samples TiO₂/0%Fe/N, TiO₂/0.5%Fe/N and TiO₂/2%Fe/N small amount of rutile was observed as well. Obviously, the Fe and N co-doping enhances the crystallization of rutile and as a result it appears at lower temperatures (500 °C). It has to be noticed that iron was

not found in the XRD patterns of the investigated samples. For comparison, our results are in good accordance with those obtained by other authors [15]. The average crystallite size of as prepared Fe and N co-doped TiO₂ calculated from the broadening of the diffraction line using Sherrer's formula is about 15–20 nm. Obviously, the Fe/N co-doping of TiO₂ did not influence on the particles size. For comparison, the particle size of pure TiO₂ obtained by non-hydrolytic sol-gel method is ~20 nm [1]. Our results differ from those obtained by Songkhum et al. [15], where they established that Fe, N co-doping led to increasing of the crystallite size of the obtained products. Probably, the reason of this discrepancy is due to the used precursors; experimental conditions as well as to the applied non-hydrolytic sol-gel method of synthesis.

The short range order of the obtained Fe/N co-doped TiO₂ submicron powders as well as of undoped TiO₂ is investigated by IR spectroscopy in the range 1000–400 cm⁻¹ (Fig. 3). Vibrations of the inorganic building units only were recognized. Bands in the range 470–420 cm⁻¹ and 700–600 cm⁻¹ are observed which could be related to the vibrations

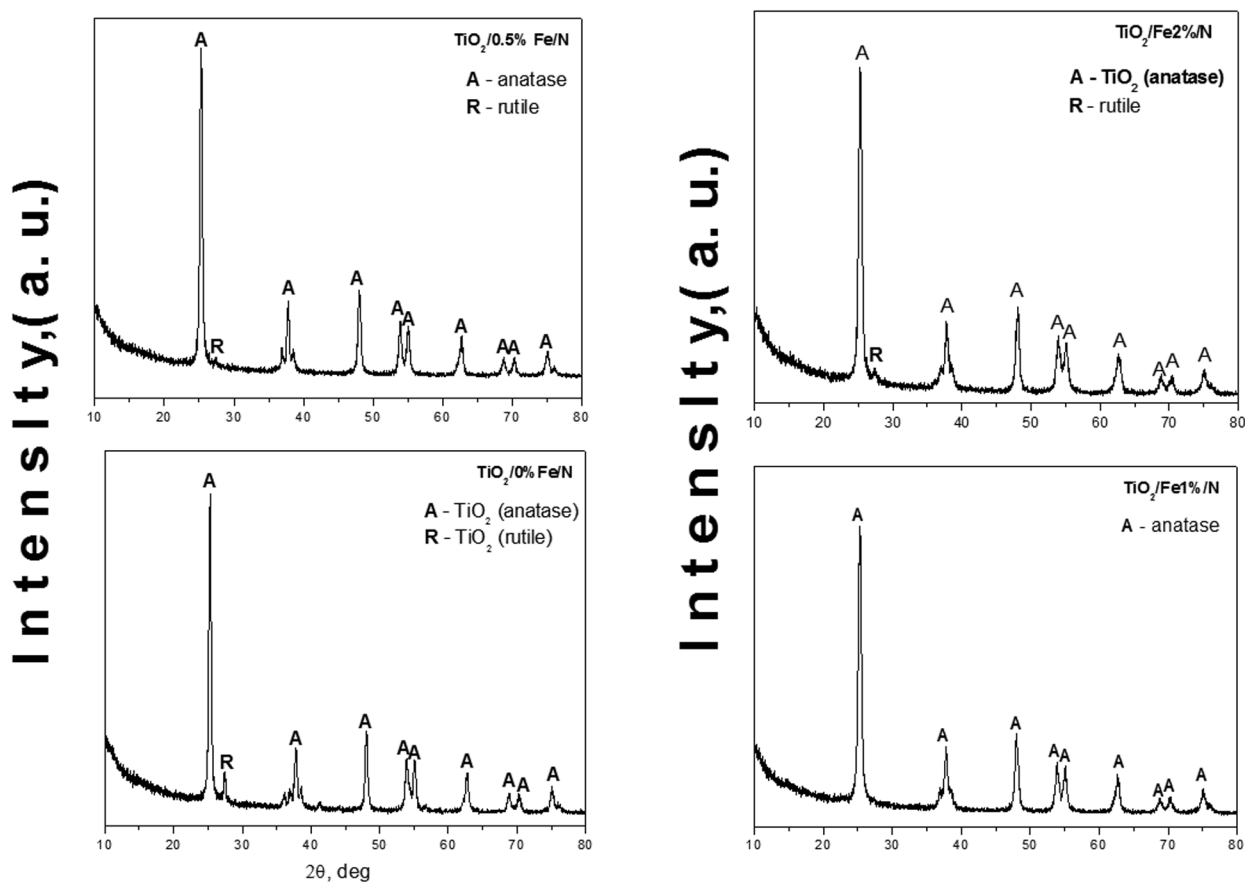


Fig. 2. XRD patterns of Fe/N co-doped TiO₂

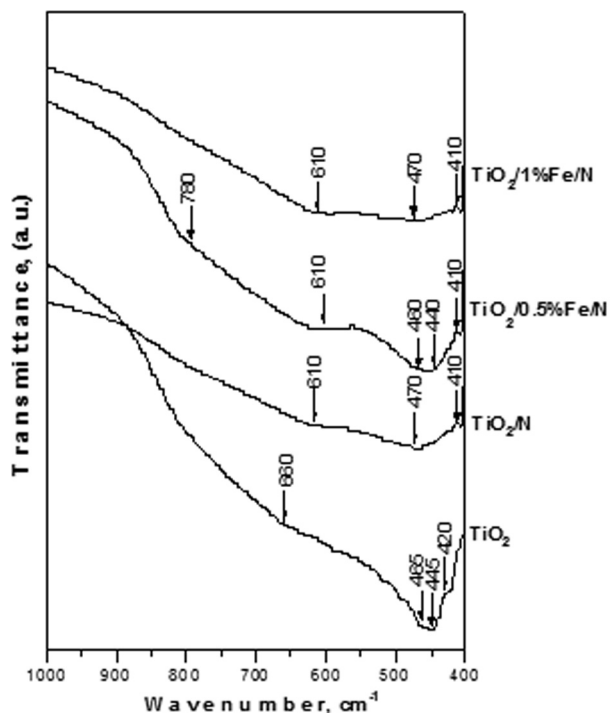


Fig. 3. IR spectra of Fe/N co-doped TiO₂ samples

of TiO₆ units [16, 17]. Despite the fact that iron was not detected in the XRD patterns, its presence was registered by IR spectroscopy (bands in the range 680–470 cm⁻¹). The doping with iron and nitrogen resulted to the appearance of a broad band centred at about 610 cm⁻¹, that could be assigned to the vibrations of FeO_n structural units [18]. Obviously, it is difficult to distinguish the vibrations of TiO₆ and FeO_n structural units due to their overlapping.

UV-Visible spectra of the synthesized samples show an absorption edge in the 388–403 nm region. Figure 4 shows the UV-visible absorption of the modified TiO₂ compared to that of the undoped and obtained by a nonhydrolytic sol-gel method TiO₂. The absorption spectra of the sample TiO₂/0.5%Fe/N exhibited a blue shift (Table 1). Obviously, N and/or Fe doping did not lead to a significant shift of the absorption edge or change in energy band gap compared to those of the synthesized pure TiO₂. Our results are in accordance with the data obtained by other authors [18]. The calculated energy band gaps of all samples are also shown in Table 1.

Photocatalytic activity

The prepared TiO₂ photocatalysts were used to degrade Malachite Green (MG) as a model pollutant under UV-Vis light irradiation and the results were presented in Figures 5a and 5b. The dye MG is widely used in food and textile industries, but it can

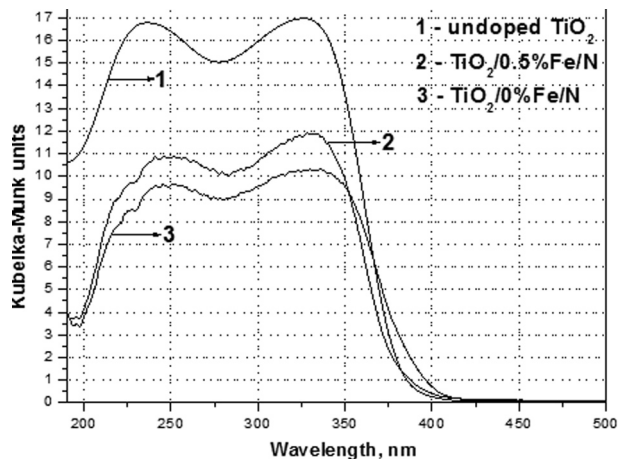


Fig. 4. UV-Vis spectra of Fe/N co-doped TiO₂ samples

Table 1. Cut-off and optical band gap values for obtained compositions

N	Sample	Cut-off, nm	E _g , eV
1.	undoped TiO ₂	388.33	3.19
2.	TiO ₂ /0%Fe/N	403.26	3.07
3.	TiO ₂ /0.5%Fe/N	386.95	3.2

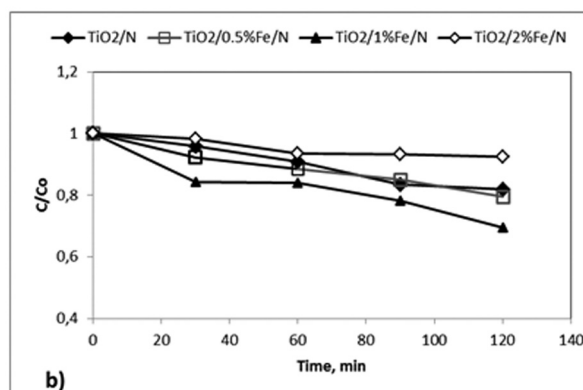
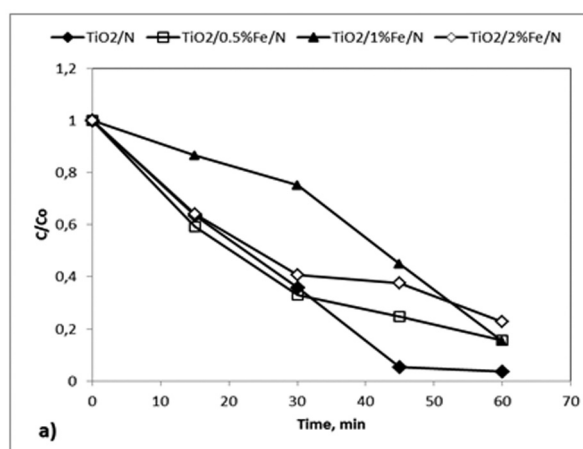


Fig. 5. Photocatalytic activity of Fe/N-modified samples under a) UV irradiation and b) Vis irradiation

cause carcinogenic and genotoxic effects on living organisms [19].

Only 6.2% of MG under UV irradiation and 4.7% under visible light irradiation were removed after 180 min photolysis in the absence of catalyst, determining that decoloration was conducted primarily by the photocatalytic process.

As can be seen (Fig. 5), the photocatalytic activity of Fe, N-modified samples under UV irradiation was not improved, comparing to N-modified TiO₂. In the presence of visible light the highest photo-sensitivity showed TiO₂ modified with 1 mol% Fe and N (Fig. 5). According to the literature, the doped Fe ions can form new energy level below the conduction band of TiO₂ and the N doping either decreases the band gap or creates an N-induced mid-gap level, which can improve the utilization of visible light by the TiO₂ [20].

CONCLUSIONS

Pure and doped by Fe and N nanosized TiO₂ powders (15–20 nm) were synthesized by a nonhydrolytic sol-gel route. According to XRD patterns, mainly TiO₂ (anatase) crystallized. The short range order was verified by IR spectroscopy and presence of TiO₆ (470-420 cm⁻¹), and FeO_n (610 cm⁻¹) building units was proved. Co-doping with Fe and N did not change photocatalytic activity under UV light illumination, comparing to N-modified TiO₂. In the presence of visible light, the highest photo-sensitivity showed the TiO₂ modified with 1% Fe and N.

Acknowledgements: Authors are grateful to the financial support of Medical University-Pleven, Contract No 7/2014.

REFERENCES

1. A. M. Stoyanova, H. Y. Hitkova, N. K. Ivanova, A. D. Bachvarova-Nedelcheva, R. S. Iordanova, M. P. Sredkova, *Bulg. Chem. Commun.*, **45**(4), 497 (2013).

2. A. Stoyanova, N. Ivanova, R. Iordanova, A. Bachvarova-Nedelcheva, *Nanosci. & Nanotechnol.*, **13**, 166 (2013).
3. F. Han, V. S. R. Kambala, M. Srinivasan, D. Rajarathnam, R. Naidu, *Appl. Catal. A*, **359**, 25 (2009).
4. U. G. Akpan, B.H. Hameed, *Appl. Catal. A*, **375**, 1 (2010).
5. M. V. Dozzi, E. Selli, *J. Photochem. Photobiol. C: Photochem. Rev.*, **14**, 13 (2013).
6. P. Xu, T. Xu, J. Lu, S. Gao, N.S. Hosmane, B. Huang, Y. Dai, Y. Wang, *Energy Environ. Sci.*, **9**, 1128 (2010).
7. Y. Cong, J. Zhang, F. Chen, M. Anpo, D. He, *J. Phys. Chem. C*, **111**, 10618 (2007).
8. J. Zhang, Y. Wu, M. Xing, S. A. K. Leghari, S. Sajjad, *Energy Environ. Sci.*, **3**(6), 715 (2010).
9. X. Qiu, Y. Zhao, C. Burda, *Adv. Mater.*, **19**(22), 3995 (2007).
10. X. H. Li, J. B. Lu, Y. Dai, M. Guo, B.B. Huang, *Int. J. Photoenergy*, **2012**, 8 (2012).
11. K. Huang, L. Chen, J. Xiong, M. Liao, *Int. J. Photoenergy*, 2012, 9 (2012).
12. P. Yang, C. Lu, N. Hua, Y. Du, *Mat. Lett.*, **57**(4), 794 (2002).
13. W. K. Choi, A. Termin, M. R. Hoffmann, *J. Phys. Chem.*, **98**(51), 13669 (1994).
14. J. Dharma, A. Pisal, Perkin Elmer Inc., Application note.
15. P. Songkhum, J. Tantirungrotechai, *Pure and Applied Chemistry International Conference (PACCON2011)*, 437 (2011).
16. A. N. Murashkevich, A. S. Lavitskaya, T. I. Barannikova, I. M. Zharskii, *J. Appl. Spectr.*, **75**(5), 730 (2008).
17. A. M. Stoyanova, H. Y. Hitkova, A. D. Bachvarova-Nedelcheva, R. S. Iordanova, N. K. Ivanova, M.P. Sredkova, *J. Univ. Chem. Techn. Metall.*, **48**(2), 154 (2013).
18. K. Marinaga, Y. Suginoara, Y. Yanagase, *J. Jpn. Inst. Met.*, **40**, 775 (1976).
19. S. Srivastava, R. Sinha, D. Roy, *Aquatic Toxicology*, **66**, 319 (2004).
20. W.-X. Liu, J. Ma, X.-G. Qu, W.-B. Cao, *Res. Chem. Intermed.*, **35**, 321 (2009).

СИНТЕЗ И ФОТОКАТАЛИТИЧНА АКТИВНОСТ
НА Fe (III), N КО-ДОТИРАНИ
TiO₂ НАНОЧАСТИЦИ

А. М. Стоянова^{1*}, Н. К. Иванова¹, А. Д. Бъчварова-Неделчева²,
Р. С. Йорданова²

¹ Медицински Университет-Плевен, 5800 Плевен, България

² Институт по Обща и Неорганична Химия, Българска Академия на Науките,
1113 София, България

Постъпила декември, 2014 г.; приета януари, 2015 г.

(Резюме)

Дотирани с Fe(III) и N-TiO₂-наночастици са синтезирани при ниска температура по не-хидролитичен зол-гел метод. Настоящата работа е продължение на нашите изследвания върху синтеза на наноразмерни TiO₂ прахове с подобрена фотокаталитична активност. Структурата и морфологията на получените проби е характеризирани с помощта на РФА, ИЧ и УВ-Вис спектроскопия. Дотирането с Fe и N не повлиява върху размера на частиците. Фотокаталитичната активност на дотираните прахове TiO₂ е изследвана в присъствие на УВ и видима светлина при фотодеградацията на Malachite Green като моделен замърсител. Посочена е зависимостта между концентрацията на допанта и фотокаталитичната активност.

Copper doped zinc oxide nanopowders used for degradation of residual azo dyes in wastewaters

K. I. Milenova^{1*}, A. E. Elias¹, V. N. Blaskov², I. A. Avramova²,
I. D. Stambolova², Y. G. Karakirova¹, S. V. Vassilev³, P. M. Nikolov⁴,
N. A. Kasabova⁴, S. K. Rakovsky¹

¹ Institute of Catalysis, Acad. G. Bonchev St, bl.11, 1113 Sofia, Bulgaria

² Institute of General and Inorganic Chemistry, Acad. G. Bonchev St, bl.11, 1113 Sofia, Bulgaria

³ Institute of Electrochemistry and Energy Systems, BAS, Acad. G. Bonchev bl. 10, 1113, Sofia, Bulgaria

⁴ University of Chemical Technology and Metallurgy, 8 Kliment Ohridski, 1756, Sofia, Bulgaria

Received December, 2014; Revised January, 2015

The influence of copper doping (1.5 wt%) on the structural and on the photocatalytic properties of two different types of ZnO nanopowders (commercial one and ZnO activated by an original patented procedure) was studied. The crystallite size and the oxidation state of the dopant were investigated respectively by X-ray diffractometer (XRD), Electron paramagnetic resonance (EPR) and X-ray photoelectron spectroscopy (XPS) methods. The EPR spectra registered isolated Cu²⁺ ions in both samples. The photocatalytic efficiency of the prepared nanosized samples was examined in the reaction of oxidative degradation of Reactive Black 5 (RB5) dye under UV light. Examined powders have shown significant degree of degradation of the investigated textile dye pollutant, the maximum value of the rate constant ($35.9 \times 10^{-3} \text{ min}^{-1}$) was obtained for the activated Cu/ZnO. The higher photodegradation activity for Reactive Black 5 of the activated Cu/ZnO sample (99.5%) than that of the commercial copper doped ZnO (98.0%) could be explained by the presence of a second phase of CuO clusters in the former. The present research study established that activated copper-doped ZnO can be used as an effective photocatalyst for the removal of azo dyes in wastewaters.

Key words: Cu-doping, ZnO, photocatalytic activity, azo dye pollutant.

INTRODUCTION

During the last decade, photocatalysts have been developed and applied to the removal of dyes from industrial effluents [1, 2]. One of the most efficient ways of reducing contaminations of water is by photocatalytic treatment [3]. The intrinsic defects of ZnO are beneficial for setting up catalytic systems and also changes of surface properties such as surface defects [4]. The photocatalytic activity of ZnO can be improved by control of the designed shape [5], incorporating another atom into the lattice [6, 7], increase of surface area [8] and so on. Transition metal doped ZnO is attracting the attention of most researchers. The efficiency of the dopant element to the changes of electrical properties depends on its ionic radius and it is also strongly influenced by the synthesis method. Recent inves-

tigations on Cu doped ZnO have reported that Cu exists in 2+ oxidation state in the host lattice [9, 10]. The substitution of Cu into the ZnO lattice improves the photocatalytic activity [11]. Cu-doped ZnO nanopowders have been synthesized by sonochemical method [12, 13], sol-gel method [14], hydrothermal method [15, 16], vapor transport method [17], solution combustion method [18] and co-precipitation method [19, 20]. Photocatalytic activities of copper doped zinc oxides have been investigated by the degradation of Methylene Blue dye [14], resazurin dye [17], Methyl Orange [20, 21].

In the present work copper-doped ZnO samples were prepared by modified deposition method. Two types of ZnO samples were used: ZnO powders activated by an original procedure and commercial – delivered by Chemapol, doped with 1.5 wt.% Cu. The aim was to investigate the influence of copper doping on the structural and on the photocatalytic properties of ZnO nanopowders toward degradation of textile azo dye Reactive Black 5 (RB5) under UV light.

* To whom all correspondence should be sent:
E-mail: kmilenova@ic.bas.bg

EXPERIMENTAL

Two types of Cu/ZnO samples were prepared: commercial – delivered by Chemapol and Cu/ZnO powders activated by an original patented procedure, described in [22]. The preparation includes dissolution of the technical purity grade ZnO in NH_4OH , then simultaneous treatment by adding NH_4OH and bubbling CO_2 , leading to precipitation of $(\text{Zn}_5(\text{OH})_6(\text{CO}_3)_2)$. Then it is filtered, washed and dried at 90°C . Both the so activated zinc hydroxide carbonate precursor and the commercial ZnO were impregnated with definite quantities of the aqueous solutions of $\text{Cu}(\text{NO}_3)_2 \cdot 3\text{H}_2\text{O}$. The concentration of metal dopant was so calculated as to give 1.5 wt.% Cu (with respect to the Zn amount). These suspensions were stirred continuously at temperature 70°C under reflux for a short period of time. After that was dried at 100°C for 6 h. Finally, the resulted powder was calcinated for 3 h at 350°C in air. The so prepared samples were denoted as Cu/ZnO commercial and Cu/ZnO activated.

The phase composition of the samples was studied by X-ray diffraction (XRD) with CuK_α -radiation (Philips PW 1050). The crystallite size was estimated from the XRD spectra, according to Scherrer's equation.

The EPR spectra were recorded on JEOL JES-FA 100 EPR spectrometer operating in the X-band with standard TE_{011} cylindrical resonator at room temperature. The sample was put in special EPR cuvette and was positioned in the center of the EPR cavity.

The X-ray photoelectron spectroscopy (XPS) studies were performed on a VG Escalab II electron spectrometer using $\text{AlK}\alpha$ radiation with binding energy (BE) of 1486.6 eV under base pressure 10^{-7} Pa and a total instrumental resolution 1 eV. The BE values were determined utilizing the C1s line (from an adventitious carbon) as a reference with energy of 285.0 eV. The accuracy of the measured BE value was 0.2 eV. The C1s, Zn2p, O1s and Cu2p photoelectron lines were recorded and corrected by subtracting a Shirley-type of background and quantified using the peak area and Scofield's photoionization cross-sections.

The photocatalytic activities of the prepared nanosized samples were measured in the reaction of photocatalytic oxidative degradation of Reactive Black 5 (RB5) dye in slurry semi-batch reactor under UV light. The photocatalytic studies were performed using UV-Vis absorbance spectrophotometer in the wavelength range from 200 to 800 nm and a polychromatic UV-A lamp illumination (18W) with maximum of the emission at 365 nm and intensity of illumination was $0.66 \text{ mW}\cdot\text{cm}^{-2}$. The initial concentration of the used RB5 dye so-

lution was 20 ppm. The investigated systems were equilibrated in the dark period about 30 min before UV irradiation.

RESULTS AND DISCUSSION

The XRD patterns of both Cu doped ZnO samples – the ZnO activated by an original patented procedure and the commercial one are shown in Figure 1. The X-ray diffraction analysis revealed the formation of hexagonal wurtzite ZnO phase (JCPDS 36-1451). There is no indication of peaks of CuO phase, because of the low content of used dopant. CuO/ZnO commercial sample showed higher degree of crystallinity than the CuO/ZnO activated powder. The crystallites size of the CuO-doped ZnO samples and unit cell parameter (a) and (c) of ZnO phase are represented in Table 1. The CuO/ZnO activated samples show drastic decrease in crystallites size, compared to the commercial CuO/ZnO sample.

The EPR spectra of the Cu/ZnO commercial sample and the Cu/ZnO activated sample at room temperature are presented in Figure 2. Hyperfine

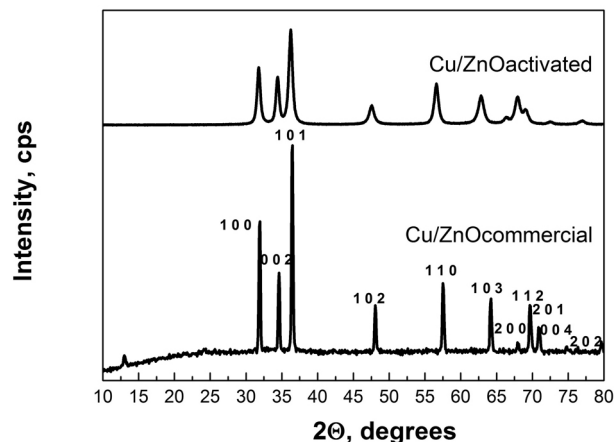


Fig. 1. XRD patterns of: Cu/ZnO activated and Cu/ZnO commercial photocatalyst samples

Table 1. Calculated values of mean crystallite size (D), and unit cell parameter (a) and (c) of ZnO phase

Sample	D, nm	a, Å	c, Å
Ref. JCPDS 36-1451	–	3.2440	5.2050
Cu/ZnO activated	16	3.2519	5.2103
Cu/ZnO commercial	40	3.2174	5.1550

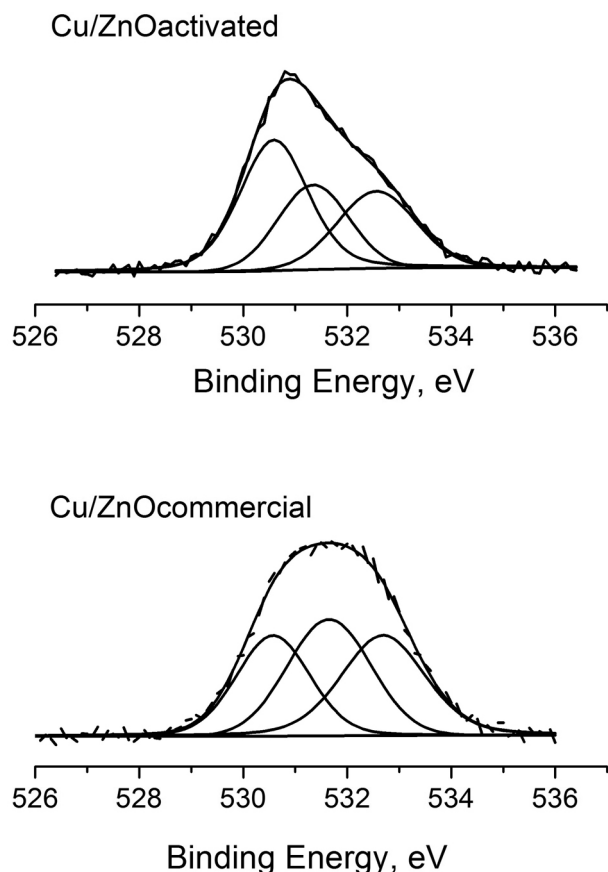


Fig. 2. EPR spectra of: Cu/ZnO activated and Cu/ZnO commercial photocatalysts

structure due to $I=3/2$ of Cu^{2+} ion in parallel components can be seen in both spectra.

There is an EPR line with $g_{\parallel} = 2.3845$ и $g_{\perp} = 2.0959$ observed in the spectrum of commercial Cu/ZnO sample. The resolved hyperfine structure in parallel region suggests the presence of isolated octahedrally coordinated Cu^{2+} ions [23, 24].

In the spectra corresponding to activated Cu/ZnO there are at least two different Cu^{2+} species with the values for parallel components $g_{\parallel} = 2.3845$ и $g_{\parallel} = 2.3262$, both having $A_{\parallel} \approx 12$ mT hyperfine splitting. The value for the normal component of g-tensor is found to be $g_{\perp} = 2.0959$ and it is not resolved for the two Cu^{2+} ions present in the catalyst. The component having resonance parameters $g_{\parallel} = 2.3845$ и $g_{\perp} = 2.0959$ can be assigned to Cu^{2+} ions substituting the Zn^{2+} cations in the ZnO crystal lattice. The interchangeable substitution is possible due to similar ionic radii. These g values of the copper species have been interpreted as existence of Cu^{2+} occupying sites vacated by lattice Zn^{2+} ions [25]. The other component with parameters $g_{\parallel} = 2.3262$ и $g_{\perp} = 2.0959$ have more poorly defined hyperfine splitting and corresponds to the Cu^{2+} ions in CuO clusters

[26]. This is probably due to increasing of dipolar interaction between Cu^{2+} ions. In conclusion in both cases the values of g_{\parallel} и g_{\perp} satisfy the relation $g_{\parallel} > g_{\perp} > g_e = 2.0023$ (g_e represents the g factor for a free electron) indicating that the Cu^{2+} ions are coordinated by six ligand atoms in an axially distorted octahedron [24].

Figure 3 shows the O1s core level spectra of CuO/ZnO activated as well as CuO/ZnO commercial catalysts. Both spectra are completely different, which is an indication of the different oxygen bonds existing on their surfaces. The spectra were subjected to the fitting procedure, which allows making a detailed analysis of the influence of the activation process over ZnO support and further deposition of the active copper phase. The first oxygen component at 530.0 eV corresponds to oxygen bonded to Zn atom in the ZnO lattice. The second (~531.5 eV) and third (~532.5 eV) components belonged to the oxygen vacancies and to adsorbed oxygen, OH- groups or dissociated oxygen, respectively on the surface of the catalysts. The relative intensity of the second component is proportional to the oxygen vacancies concentrations [27]. The

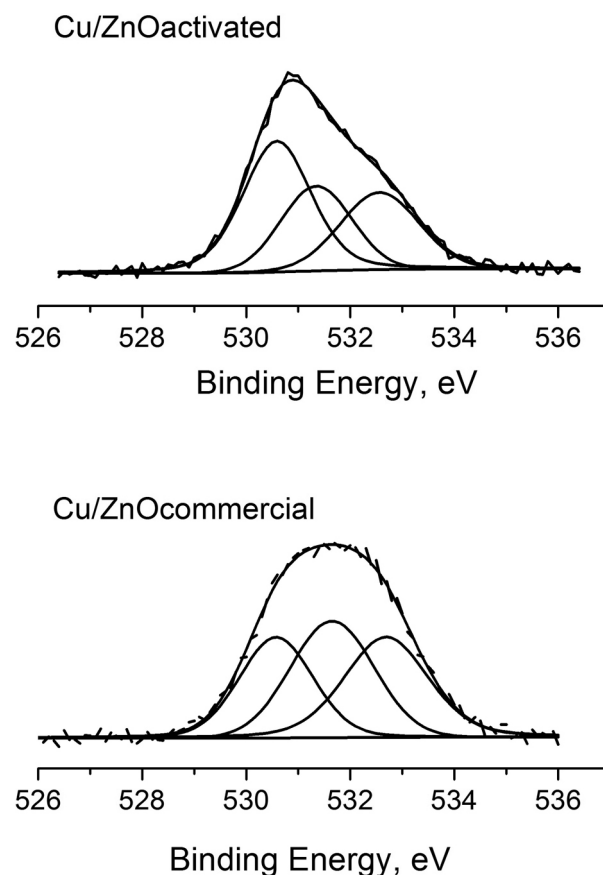


Fig. 3. XPS spectra of: Cu/ZnO activated and Cu/ZnO commercial photocatalysts

relative percentage of the component associated to the oxygen vacancies within ZnO matrix for the studied CuO/ZnO activated and CuO/ZnO commercial catalysts are 27% and 36% of the total oxygen, respectively. Nevertheless the calculated percentage of third type of oxygen present on the surface is the same as that associated with oxygen vacancies for both catalysts. The simultaneous formation of the oxygen vacancies and chemisorbed oxygen is observed and this did not depend of the way of preparation of catalysts. Even so the quantity of the formed defects on the surface of the Cu/ZnO commercial catalyst is more than for the catalyst synthesized by us. The Cu^{2+} chemical states of copper were estimated from the Cu2p core level for both investigated catalysts.

Figure 4 presents concentration changes, degradation degree and dependence of $-\ln(C/C_0)$ with time of UV light illumination of the solution of Reactive Black 5 on two examined catalysts. The sample CuO/ZnO activated exhibits stronger absorption capacity towards RB dye and only after 30 minutes interval in the dark, the concentration of the dye drops down with almost 80%. In the case of CuO/ZnO commercial the adsorption is weaker and after switching on the UV lamp the photocatalytic degradation is initiated. The possible explanation of this could be the fact that the activated sample has higher content of CuO clusters. The photocatalytic efficiencies of both CuO/ZnO activated and Cu/ZnO commercial photocatalysts are almost similar and really high reaching 99.5% on CuO/ZnO activated. Rate constants were calculated using the equation $-\ln(C/C_0) = kt$ on the basis of the slope of the linear logarithmic function. This photodegradation on

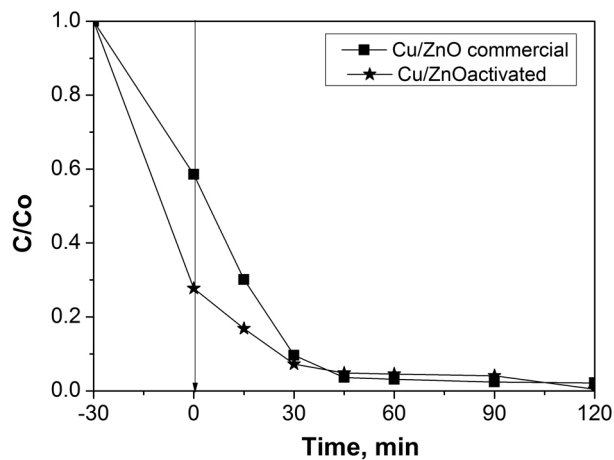


Fig. 4. Dye solution concentration decrease in the course of time of illumination by Cu/ZnO activated and Cu/ZnO commercial photocatalysts

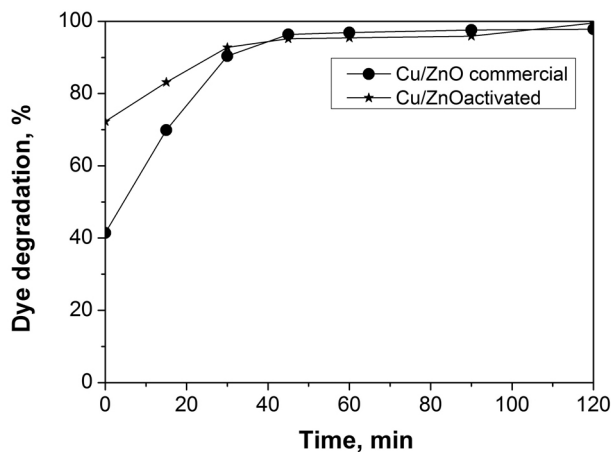


Fig. 5. Oxidative conversion degrees over Cu/ZnO activated and Cu/ZnO commercial photocatalysts

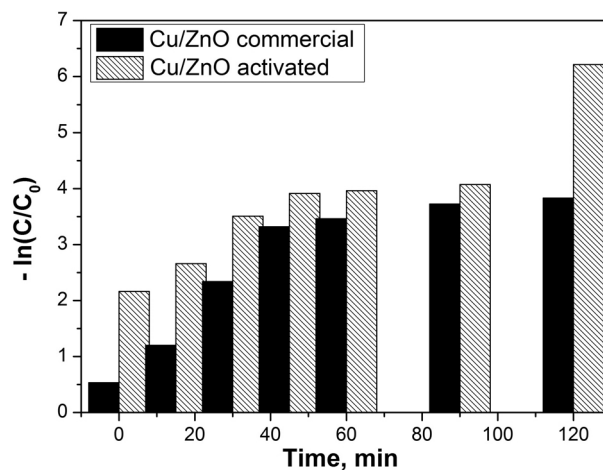


Fig. 6. Dependence of $-\ln(C/C_0)$ on the time of illumination over Cu/ZnO activated and Cu/ZnO commercial photocatalysts

CuO/ZnO powders followed the pseudo-first-order reaction kinetics. Rate constants for two compared catalysts CuO/ZnO commercial and CuO/ZnO activated are: $35.0 \times 10^{-3} \text{ min}^{-1}$ and $35.9 \times 10^{-3} \text{ min}^{-1}$ respectively.

It is known from literature that, various behaviors of ZnO are due to the presence of native defects, such as oxygen vacancies and zinc vacancies. With EPR measurements are confirmed defect structures due to presence of Cu^{2+} ion in the ZnO crystal lattice [18, 28]. The increased photocatalytic activity of Cu-doped ZnO is attributed to intrinsic oxygen vacancies due to high surface to volume ratio in nanoparticles and extrinsic defect due to Cu doping [17].

CONCLUSIONS

The influence of copper doping on the structural and on the photocatalytic properties of ZnO nanopowders was studied. Copper-doped ZnO samples with dopant content of 1.5 wt% were prepared by modified deposition method. Two types of ZnO samples were used – commercial one and ZnO activated by an original patented procedure. The EPR spectra registered two types of Cu²⁺ ions: isolated Cu²⁺ (both in commercial Cu/ZnO and ZnO activated) and Cu²⁺ ions in CuO clusters (ZnO activated). The photocatalytic efficiencies of the prepared nanosized samples were tested in the photocatalytic oxidation of Reactive Black 5 (RB5) dye under UV light illumination. Examined powders have shown significant degree of degradation of the investigated textile dye pollutant, the maximum value of the rate constant ($35.9 \times 10^{-3} \text{ min}^{-1}$) was obtained for the activated CuO/ZnO. The photodegradation conversion for Reactive Black 5 of activated CuO/ZnO is 99.5% and 98.0% for commercial copper doped ZnO. The possible explanation of this difference could be the fact that the activated sample has an additional phase of CuO clusters and smaller ZnO crystallite size. The present research study established that activated copper-doped ZnO can be used as an effective photocatalyst for the removal of azo dyes in wastewaters.

Acknowledgements: Sponsorship by National Science Fund under Contract NSF T 02 16/12.12. 2014 is gratefully acknowledged.

REFERENCES

1. J. Yun, D. Jin, Y.S. Lee, H.I. Kim, *Mater. Lett.*, **64**, 2431 (2010).
2. S. Gelover, P. Mondragón, A. Jiménez, *J. Photochem. Photobiol. Chem.*, **165**, 241 (2004).
3. M. Hoffmann, S. Martin, W. Choi, D. Bahnemann, *Chem. Rev.*, **95**, 69 (1995).
4. R. Mohan, K. Krishnamoorthy, S-J. Kim., *Solid State Comm.*, **152**, 375 (2012).
5. L. Yang, S. Dong, J. Sun, J. Feng, Q. Wu, S. Sun, *J. Hazard. Mater.*, **179**, 438 (2010).
6. J. Sun, S. Dong, J. Feng, X. Yin, X. Zhao, *J. Mol. Catal. Chem.*, **335**, 145 (2011).
7. J. Kong, A. Li, X. Li, H. Zhai, W. Zhang, Y. Gong, H. Li, D. Wu, *J. Solid State Chem.*, **183**, 1359 (2010).
8. W. Chiu, P. Khiew, M. Cloke, D. Isa, T. Tan, S. Radiman, R. Abd-Shukor, M. Hamid, N. Huang, H. Lim, C. Chia, *Chem. Eng. J.*, **158**, 345 (2010).
9. T. Heng, S. Lau, S. Yu, J. Chen, K. Teng, *J. Magn. Magn. Mater.*, **315**, 107 (2007).
10. C. Chien, S. Chiou, G. Gao, Y. Yao, *J. Magn. Magn. Mater.*, **282**, 275 (2004).
11. Y. Sonawane, K. Kanade, B. Kale, R. Aiyer, *Mater. Res. Bull.*, **43**, 2719 (2008).
12. B. Babu, T. Aswani, G. T. Rao, R. J. Stella, B. Jayaraja, R. V. Ravikumar, *J. Magn. Magn. Mater.*, **355**, 76 (2014).
13. D. Sahu, N. Panda, B. Acharya, A. Panda, *Ceram. Int.*, **140**, 11041 (2014).
14. P. Jongnavakit, P. Amornpitoksuk, S. Suwanboon, N. Ndiege, *Appl. Surf. Sci.*, **258**, 8192 (2012).
15. J. Huang, Y. Dai, C. Gu, Y. Sun, J. Liu, *J. Alloy. Comp.*, **575**, 115 (2013).
16. S. Lam, J. Sin, A. Abdullah, A. Mohamed, *Separ. Purif. Tech.*, **132**, 378 (2014).
17. R. Mohan, K. Krishnamoorthy, S-J. Kim, *Solid State Comm.*, **152**, 375 (2012).
18. A. Reddy, M. Kokila, H. Nagabhushana, R. Chakradhar, C. Shivakumara, J. Rao, B. Nagabhushana, *J. Alloy. Comp.*, **509**, 5349 (2011).
19. M. Ashokkumar, S. Muthukumar, *Opt. Mater.*, **37**, 671 (2014).
20. Z. Liu, J. Deng, J. Deng, F. Li, *Mater. Sci. Eng. B*, **150**, 99 (2008).
21. M. Ahmad, E. Ahmed, Z. Hong, X. Jiao, T. Abbas, N. R. Khalid, *Appl. Surf. Sci.*, **285P**, 702 (2013).
22. D. Shishkov, C. Velinova, N. Kassabova, C. Canov, D. Ivanov, D Klissurski, V Iordanova, I. Uzunov, Bulgarian Patent 28915/1980, C I: C 01 G 9/02, 1980.
23. P. Ratnasamy, D. Srinivas, C. V. V. Satyanarayana, P. Manikandan, R. Senthil Kumaran, M. Sachin, *J. Catal.*, **221**, 455 (2004).
24. G. Li, N. M. Dimitrijevic, L. Chen, T. Rajh, K. A. Gray, *J. Phys. Chem. C*, **112**, 19040 (2008).
25. N. C. Giles, N. Y. Garces, L. Wang, L. E. Halliburton, in: Quantum Sensing and Nanophotonic Devices (Proc. of SPIE, Bellingham, WA, 2004), Manijeh Razeghi, Gail J. Brown (eds.), Bellingham, 267, 2004, p. 5359.
26. I. Ardelean, M. Peteanu, R. Ciceo-Lucacel, I. Bratu, *J. Mater. Sci. Mater. Electron.*, **11**, 11 (2000).
27. S.-M. Park, T. Ikegami, K. Ebihara, *Thin Solid Films*, **513**, 90 (2006).
28. Y. Mei, W.-C. Zheng, L. Zhang, *Opt. Mater.*, **36**, 535 (2013).

ЦИНКОВО ОКСИДНИ ПРАХОВЕ, ДОТИРАНИ С Cu,
ИЗПОЛЗВАНИ ЗА РАЗЛАГАНЕ НА ОСТАТЪЧНИ
АЗОБАГРИЛА В ОТПАДНИ ВОДИ

К. И. Миленова^{1*}, А. Е. Елияс¹, В. Н. Блъсков², И. А. Аврамова²,
И. Д. Стамболова², С. В. Василев³, П. М. Николов⁴, Й. Г. Каракирова,
Н. А. Касабова⁴, С. К. Раковски¹

¹ *Институт по катализ, Българска академия на науките, ул. „Акад. Г. Бончев“,
бл. 11, 1113 София, България*

² *Институт по обща и неорганична химия, Българска академия на науките,
ул. „Акад. Г. Бончев“, бл. 11, 1113 София, България*

³ *Институт по Електрохимия и Енергийни Системи, Българска академия на науките,
ул. „Акад. Г. Бончев“, бл. 10, 1113 София, България*

⁴ *Химико-технологичен и металургичен университет, бул. „Св. Климент Охридски“ 8,
1756 София, България*

Постъпила декември, 2014 г.; приета януари, 2015 г.

(Резюме)

Изучено е влиянието на дотирането с мед (1.5 wt%) върху структурните и фотокаталитични свойства на два различни вида ZnO нанопрахове (търговски и ZnO, активиран чрез оригинална патентована процедура). Размерът на кристалитите и степента на окисление на допанта бяха изследвани съответно с рентгенофазов анализ (XRD), електронен парамагнитен резонанс (EPR) и рентгенова фотоелектронна спектроскопия (XPS). От EPR спектрите са регистрирани изолирани Cu²⁺ йони и в двете проби. Фотокаталитичната ефективност на получените наноразмерни проби е изследвана за окислително разграждане на багрилото – Реактивно Черно 5 (RB5), под действието на ултравиолетова светлина. Изследваните прахове показаха значителна степен на разграждане на изследвания замърсител (текстилно багрило), като максимална стойност на скоростната константа ($35.9 \times 10^{-3} \text{ min}^{-1}$) е получена за активирания Cu/ZnO. По-високата активност за фоторазграждане на Реактивно Черно 5 за проба – активиран Cu/ZnO (99.5%), от тази на мед, дотиран търговски ZnO (98.0%), може да бъде обяснена с наличието на CuO клъстери в първия. Настоящото научно изследване установи, че активираният Cu/ZnO може да се използва като ефективен фотокатализатор за отстраняване на азобагрила в отпадни води.

Effect of the duration of mechanochemical treatment on the photocatalytic activity under UV light irradiation of nano-sized zinc oxide synthesized by precipitation

K. L. Zaharieva^{1*}, K. I. Milenova¹, Z. P. Cherkezova-Zheleva¹, S. S. Dimova²,
B. N. Kunev¹, A. E. Eliyas¹, I. G. Mitov¹, I. D. Stambolova³, V. N. Blaskov³

¹ Institute of Catalysis, Bulgarian Academy of Sciences, "Acad. G. Bonchev" St.,
Bl. 11, 1113 Sofia, Bulgaria

² Institute of Polymers, Bulgarian Academy of Sciences, "Acad. G. Bonchev" St.,
Bl.103A, 1113 Sofia, Bulgaria

³ Institute of General and Inorganic Chemistry, Bulgarian Academy of Sciences,
"Acad. G. Bonchev" St., Bl. 11, 1113 Sofia, Bulgaria

Received December, 2014; Revised January, 2015

The influence of mechanochemical treatment on the photocatalytic properties under UV light irradiation of nano-sized zinc oxide is investigated in the present paper. The zinc oxide was synthesized by classical precipitation procedure with starting reagents ZnCl₂, NaOH and following thermal treatment. As-prepared zinc oxide was mechanochemically treated under different milling conditions. The phase composition and structure of the initial and of the mechanochemically activated nanodimensional zinc oxide samples were determined by X-ray diffraction analysis (XRD) and Fourier transform infrared spectroscopy (FTIR). The photocatalytic properties of all prepared zinc oxide samples were tested in the reaction of oxidative photocatalytic degradation of Reactive Black 5 dye as model pollutant under UV light irradiation. Calculations were performed using XRD data establishing that the mechanochemically treated ZnO photocatalysts were ground to smaller average crystallite size (9.9 nm) than that of the starting zinc oxide (14.6 nm). The obtained results show that the photocatalytic activities (rate constants) of precipitated and mechanochemically treated nano-sized zinc oxides decrease in the following order: ZnO (15 min) ($35.5 \times 10^{-3} \text{min}^{-1}$) > ZnO (30.4 $\times 10^{-3} \text{min}^{-1}$) > ZnO (30 min) ($26.4 \times 10^{-3} \text{min}^{-1}$) > ZnO (4 h) ($19 \times 10^{-3} \text{min}^{-1}$). The milling time interval of 15 min is optimal for obtaining nanostructured zinc oxide photocatalyst with the highest photocatalytic activity ($k=35.5 \times 10^{-3} \text{min}^{-1}$) compared to the other investigated samples.

Key words: mechanochemical treatment, nanodimensional zinc oxide, photocatalytic activity, Reactive Black 5.

INTRODUCTION

ZnO is a semiconductor with a wide band gap (3.37 eV) at room temperature, and a large exciton binding energy of 60 meV [1–3]. Zinc oxide finds application in production of rubber, inks, cosmetics, pharmaceutical, ceramic industry, etc due to its electronic and surface properties [3]. In particular, nano-sized ZnO possesses excellent optical, photoelectric and piezoelectric properties, which can be applied in the design of varistors, solar cells, gas sensors and acoustic wave resonators [2]. The dif-

ferent synthetic methods have been described in literature for preparation of ZnO such as precipitation [4–6], sol-gel technique [7], sonochemical method [8], hydrothermal procedure [9, 10], using microwave irradiation [11], spray pyrolysis [12], mechanochemical treatment [13, 14] and others. The precipitation is one of the most often used preparation methods and plays an important role in the field of bulk nanoparticle synthesis because of its high degree of flexibility enabling the possibility to create pure materials with homogeneous distributions [15]. Zinc oxide (ZnO) is highly efficient photocatalysts in degradation of organic pollutants dissolved in water and other solvents because of its impressive catalytic activity and quantum efficiency compared to widely used TiO₂ nanomaterials [16, 17]. Investigations on the use of ZnO as photocat-

* To whom all correspondence should be sent:
E-mail: zaharieva@ic.bas.bg

lyst for photodegradation of different dyes such as Methylene Blue [18–21], Methyl Orange [22, 23], Reactive Black 5 [24], Pararosaniline chloride [25], Mordant Black 11 [26], Reactive Orange 4 [27], Rhodamine B [28], Acid Bright Yellow G [29] have been carried out.

The study on the effect of the duration of mechanochemical treatment on the photocatalytic activity under UV light irradiation of nano-sized zinc oxide is the main aim of the present work. For this purpose the nanodimensional zinc oxide, prepared by precipitation procedure, followed by thermal treatment, was mechanochemically treated using different milling conditions. The physicochemical characterization of the so prepared zinc oxide samples was done by X-ray diffraction analysis and FTIR spectroscopy. In order to determine the changes in the photocatalytic activity of precipitated and mechanochemically treated ZnO, all the prepared samples were tested in the reaction of oxidative degradation of Reactive Black 5 dye (RB5) under UV irradiation.

EXPERIMENTAL

The ZnO, was synthesized by the well-known classical precipitation procedure using aqueous solutions of 1M ZnCl₂ and 4.6M NaOH as precipitating agent. The sodium hydroxide was slowly added drop-by-drop. After the precipitation procedure the residual was filtered. The obtained white precipitate was washed with distilled water several times and then heated at 150 °C. The prepared ZnO was then treated mechanochemically to obtain nano-sized ZnO particles. The mechanochemical treatment was performed on a high-energy planetary ball mill model PM 100, Retsch, Germany. The milling time interval was varied for the different samples – 15, 30 min or 4 hours using agate or stainless steel milling container at rotational velocity of 300 or 600 rpm and mass ratio sample : balls = 1:6 or 1:13.

The physicochemical methods X-ray diffraction (XRD) and FTIR were used to characterize the structural properties of precipitated and mechanochemically treated zinc oxides. The XRD analysis was performed on a TUR M62 apparatus with PC control and data acquisition, using HZG-4 goniometer and CoK α radiation. JCPDS database (Powder Diffraction Files, Joint Committee on Powder Diffraction Standards, Philadelphia PA, USA, 1997) was used to identify the present phases. FTIR spectra were recorded with a Fourier infrared spectrometer Bruker-Vector 22 in the range 400–4000 cm⁻¹. The KBr tablets were used to register the spectra of zinc oxide samples.

Reactive Black 5 (RB5), a toxic azo dye was used as a model waste water pollutant for the evalu-

ation of the photocatalytic activity. The course of the photodegradation oxidative reaction of Reactive Black 5 (RB5) was monitored in the photoreactor using 150 mg of ZnO sample and 150 ml of dye aqueous solution (Reactive Black 5 initial concentration, 20 ppm giving pH=7), which was then stirred continuously with a magnetic stirrer at a constant magnetic stirring rate (400 rpm) under oxidative conditions (bubbling air through two frits to achieve water saturation in oxygen) to form suspension at room temperature. The degree of photocatalytic oxidative degradation of RB5 has been carried out using polychromatic UV-A lamp (Sylvania BLB, 18 W), with wavelength range 315–400 nm (with a maximum of the irradiation at wavelength 365 nm). The light power density at 2 cm distance of illumination was 0.66 mW.cm⁻². The concentrations of dye after regular time intervals were determined, after the powder was separated from the suspension by centrifugation, using a UV-Vis absorbance single beam spectrophotometer CamSpec M501 (UK) on the basis of the absorbances operating in the wavelength range from 190 to 800 nm. After dark adsorption 30 min, the lamp was switched on to initiate the photocatalytic reactions.

RESULTS AND DISCUSSION

The X-ray diffractograms of prepared zinc oxide photocatalysts are represented in Figure 1. As it can be seen the presence of single zinc oxide (ZnO) phase (PDF-89-0510) is registered in the XRD spectra of precipitated and mechanochemically treated ZnO samples for 15 and 30 minutes. The mechanochemical treatment of ZnO sample for 4 hours leads to formation of ZnO and additional iron nickel (Ni, Fe) (PDF-12-0736) phase. The content of iron nickel phase in sample is due to the continuous vigorous contact between stainless steel milling container, balls and ZnO sample during the mechanochemical process of milling. The average crystallite size, the lattice microstrain parameter and the unit cell parameter of investigated ZnO phases were determined using PowderCell for Windows Version 2.4 program [30]. The calculated values are given in Table 1. The precipitated and mechanochemically treated ZnO samples possess mean crystallite size about 11.1 nm. The obtained results show that the mechanochemical process of milling reduces the average partical size (9.9 nm) compared to the initially prepared ZnO (14.6 nm).

The presence of ZnO is also confirmed by FTIR measurements. Figure 2 illustrates the FTIR spectra of the investigated ZnO samples. In the mid-infrared spectral region absorption peaks are registered at about 422–536 cm⁻¹, characteristic of the Zn-O

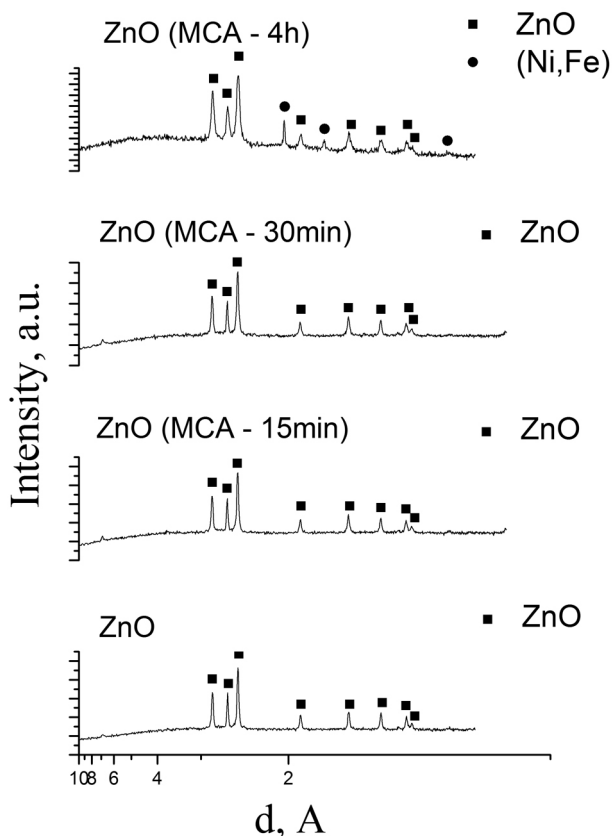


Fig. 1. XRD patterns of obtained ZnO powders

Table 1. Calculated values of mean crystallite size (D), lattice strain (ϵ) and unit cell parameter (a) of ZnO phase

Sample	D, nm	ϵ , a.u	a, Å
ZnO	14.6	$2.7 \cdot 10^{-3}$	3.2493
ZnO (MCA – 15 min)	9.9	$2.9 \cdot 10^{-3}$	3.2511
ZnO (MCA – 30 min)	9.9	$2.9 \cdot 10^{-3}$	3.2503
ZnO (MCA – 4 h)	9.9	$3 \cdot 10^{-3}$	3.2495

bond stretching vibrations [31–34]. According to the literature data the broad band at frequencies about 3440 cm^{-1} , 3422 cm^{-1} and 3429 cm^{-1} , observed in the spectra, can be attributed to the O-H vibration mode of water molecules, adsorbed on the zinc oxide surface [11, 25, 33–35]. The bending vibrations of the two OH groups in the adsorbed water molecule are corresponding to the peaks at 563 cm^{-1} and the band of low intensity positioned at 1638 cm^{-1} [7, 36]. The vibration bands at wave numbers about 785 cm^{-1} , 832 cm^{-1} , $1045\text{--}1051 \text{ cm}^{-1}$, 1058 cm^{-1} , 1196 cm^{-1} , 1384 cm^{-1} , $1507\text{--}1511 \text{ cm}^{-1}$ and 1551 cm^{-1} could be the result from the presence of carbonate (CO_3^{2-}) and hydrocarbonate (HCO_3^-) groups,

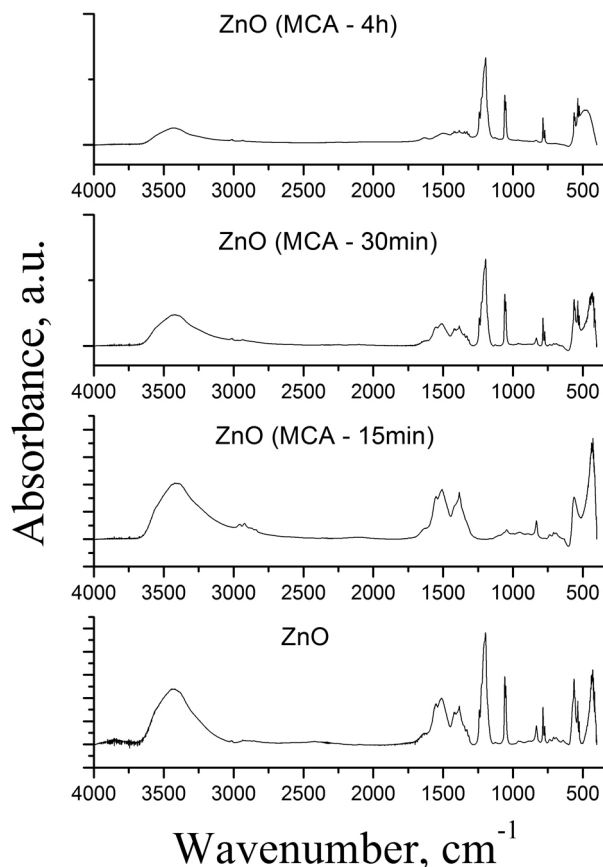


Fig. 2. FTIR spectra of prepared ZnO powders

respectively [37, 38]. The existence of (hydro)carbonates is possibly due to carbonization of prepared samples, when exposed to the air. The FTIR results are in agreement with obtained XRD data.

The concentration changes (C/C_0) and degree of degradation (%) of Reactive Black 5 dye during the photocatalytic process under UV light using precipitated and mechanochemically treated zinc oxide photocatalysts are displayed in Figures 3 and 4. The obtained experimental data show that the highest photocatalytic efficiency, based on conversion, is reaching up to 96% for the mechanochemically activated ZnO powder for 15 minutes. Similar values for the photocatalytic degradation (95%) and (94%) for RB5 dye were established for the mechanochemically treated for 30 minutes and precipitated ZnO materials. The lowest degree of degradation (82%) for Reactive Black 5 dye is observed in the presence of ZnO photocatalyst mechanochemically treated for 4 hours.

The rate constants of all studied zinc oxide photocatalysts are determined using logarithmic linear dependence of the rate constant k (min^{-1}): $-\ln(C/C_0) = k \cdot t$ [27]. The changes in photocatalytic activities of precipitated and mechanochemically treated for dif-

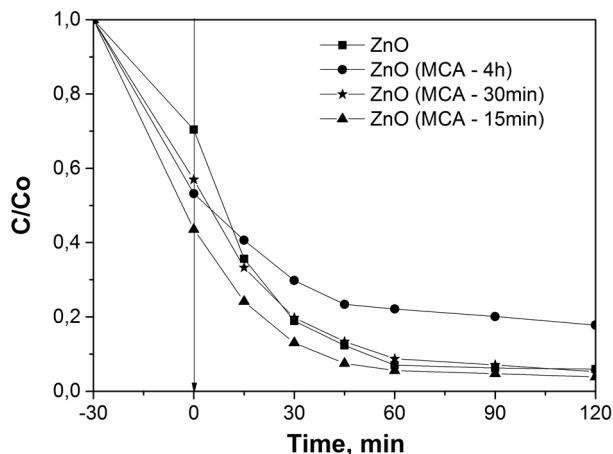


Fig. 3. Concentration decrease in the course of photocatalytic oxidative degradation of a starting solution concentration (C_0) of RB5 dye, observed as changes in the intensity of the absorption peak, corresponding to azo bond ($-N=N-$) at 599 nm as a dependence of the time interval of UV illumination.

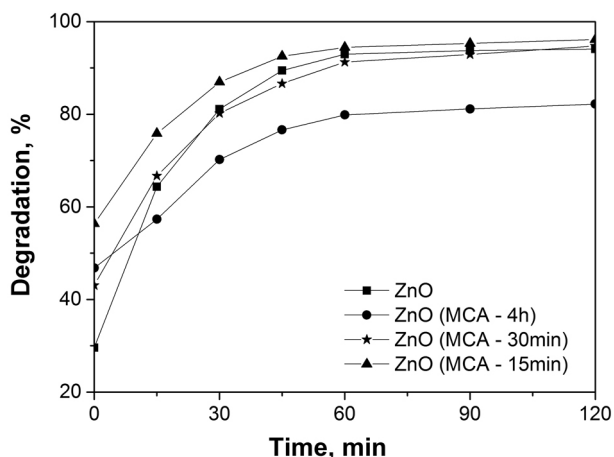


Fig. 4. Degree of degradation of the RB5 dye expressed as $[(C_0-C)/C_0] \times 100, \%$ (where C_0 and C are initial concentration before switching on the illumination and current concentration of the solution based on changes in the intensity of the peak, corresponding to azo bond ($-N=N-$) at 599 nm with the course of time

ferent milling time intervals, nano-sized ZnO photocatalysts are shown in Figure 5. The calculations established that the mechanochemical activation of ZnO photocatalyst for 15 minutes shows the highest photocatalytic activity ($k=35.5 \times 10^{-3} \text{ min}^{-1}$). The precipitated nanodimensional ZnO powder possesses a higher rate constant ($k=30.4 \times 10^{-3} \text{ min}^{-1}$) than that of ZnO (MCA - 30min) ($k=26.4 \times 10^{-3} \text{ min}^{-1}$) and of ZnO (MCA - 4 h) ($k=19 \times 10^{-3} \text{ min}^{-1}$). The photocatalytic investigation established that 15 min-

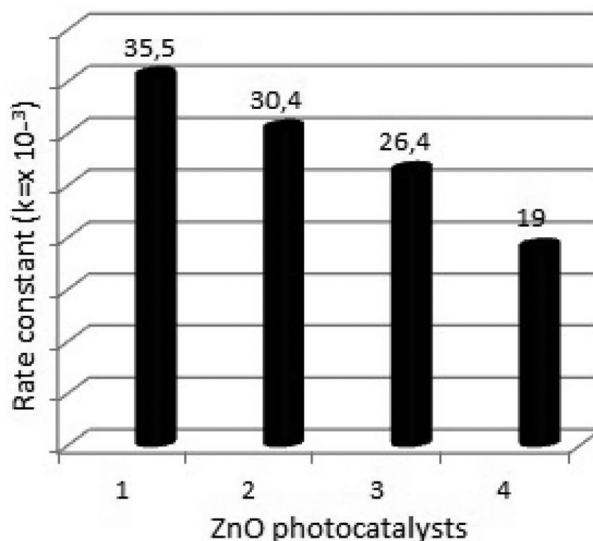


Fig. 5. Comparison data of calculated rate constants of precipitated and mechanochemically treated for different milling time intervals nano-sized zinc oxide photocatalysts in photodegradation of RB5 dye under UV irradiation, 1 - ZnO (MCA - 15 min); 2 - ZnO; 3 - ZnO (MCA - 30 min); 4 - ZnO (MCA - 4h)

utes is optimal milling time interval for activation of ZnO photocatalyst. The longer milling intervals - 30 minutes and 4 hours decrease the photocatalytic activity of ZnO photocatalysts, compared to that of initially precipitated ZnO.

According to Panthi et.al. [39] the photocatalytic activity of ZnO tested in photodegradation of dye pollutants can be explained by the following sequence of four principal steps as the generation of the charge carrier (1), the trapping of the charge-carrier (2), the recombination of the charge carrier (3), and the decomposition of the dye pollutants (4) [39].

CONCLUSIONS

The effect of duration of mechanochemical treatment on the photocatalytic properties of precipitated ZnO powders was investigated. The mechanochemical treatment leads to a decrease in the mean crystallite size of ZnO phase (9.9 nm), compared to the initially obtained nanostructured ZnO (14.6 nm). The so prepared precipitated and mechanochemically treated ZnO powders were tested successfully as photocatalysts in the photocatalytic oxidative degradation of Reactive Black 5 dye under UV irradiation. The obtained results give evidence that the time interval of mechanochemical treatment causes some changes in the photocatalytic

activity of ZnO samples due to size changes. The ZnO treated mechanochemically for 15 min manifests the highest rate constant, based on the slope of the linear dependence $-\ln(C/C_0)=kt$ compared to those of the others samples decreasing in the following order of photocatalytic activities: ZnO (15 min) ($35.5 \times 10^{-3} \text{min}^{-1}$) > ZnO (30.4 $\times 10^{-3} \text{min}^{-1}$) > ZnO (30 min) ($26.4 \times 10^{-3} \text{min}^{-1}$) > ZnO (4 h) ($19 \times 10^{-3} \text{min}^{-1}$). The conversion degree of RB5 dye degradation over the ZnO samples after 120 minutes of illumination is varying within the range 82–96%. The photocatalytic studies show that precipitated and mechanochemically treated zinc oxides are promising photocatalysts for degradation of textile azodyes under UV irradiation especially the mechanochemically treated ZnO powder after optimal mechanochemical activation for 15 min.

Acknowledgements: This research work was supported by European Social Fund within the framework of Operating Program “Development of Human Resources” (Grant BG051PO001-3.3.06-0050). The authors from IC-BAS thank the Bulgarian Science Fund of the Bulgarian Ministry of Education and Science for the financial support under Project DFNI-E01/7/2012.

REFERENCES

- S. Suwanboon, P. Amornpitoksuk, P. Bangrak, C. Randorn, *Ceramics International*, **40**, 975 (2014).
- A.-Q. Zhang, L. Zhang, L. Sui, D.-J. Qian, M. Chen, *Cryst. Res. Technol.*, **48** (11), 947 (2013).
- O. W. Perez-Lopez, A. C. Farias, N. R. Marcilio, J.M.C. Bueno, *Materials Research Bulletin*, **40**, 2089 (2005).
- A. O. Awodugba, A.-M. O. Ilyas, *Asian Journal of Natural & Applied Sciences*, **2** (2), 41 (2013).
- Dr. S. Shanthi, V. Padmavathi, *International Journal of Chemistry and Applications*, **4** (4), 351 (2012).
- A. A. Hassan, M. E. Howayda, H. H. Mahmoud, *Studies in Chemical Process Technology (SCPT)*, **1** (4), 66 (2013).
- S. Suwanboon, *ScienceAsia*, **34**, 031 (2008).
- P. Banerjee, S. Chakrabarti, S. Maitra, B. K. Dutta, *Ultrasonics Sonochemistry*, **19**, 85 (2012).
- C. Y. Chee, K. Nadarajah, M. K. Siddiqui, Y. Wong, *Ceramics International*, **40**, 9997 (2014).
- D. Chen, X. Jiao, G. Cheng, *Solid State Communications*, **113**, 363 (2000).
- N. Faal Hamedani, F. Farzaneh, *Journal of Sciences, Islamic Republic of Iran*, **17** (3), 231 (2006).
- S. D. Lee, S.-H. Nam, M.-H. Kim, J.-H. Boo, *Physics Procedia*, **32**, 320 (2012).
- Y. Dimitriev, M. Gancheva, R. Iordanova, *Journal of the University of Chemical Technology and Metallurgy*, **46** (3), 243 (2011).
- W. Ao, J. Li, H. Yang, X. Zeng, X. Ma, *Powder Technology*, **168**, 148 (2006).
- M. Shamsipur, S. M. Pourmortazavi, S. S. Hajimirsadeghi, M. M. Zahedi, M. Rahimi-Nasrabadi, *Ceramics International*, **39**, 819 (2013).
- R. Shidpour, A. Simchi, F. Ghanbari, M. Vossoughi, *Applied Catalysis A: General*, **472**, 198 (2014).
- Q. I. Rahman, M. Ahmad, S. K. Misra, M. Lohani, *Materials Letters*, **91**, 170 (2013).
- P. Sujaridworakun, K. Natrchalayuth, *Advanced Powder Technology*, **25** (4), 1266 (2014).
- S. B. Gajbhiye, *International Journal of Modern Engineering Research (IJMER)*, **2** (3), 1204 (2012).
- M. Bora Akin, M. Oner, *Ceramics International*, **39**, 9759 (2013).
- C. Kittisittipong, S. Larpiattaworn, P. Sujaridworakun, *Suranaree J. Sci. Technol.*, **21** (1), 35 (2014).
- J. Kaur, S. Singhal, *Ceramics International*, **40**, 7417 (2014).
- N. Elamin, A. Elsanousi, *Journal of Applied and Industrial Sciences*, **1** (1), 32 (2013).
- M. Muruganandham, N. Sobana, M. Swaminathan, *Journal of Hazardous Materials*, **B137**, 1371 (2006).
- S. K. Kansal, A. H. Ali, S. Kapoor, D. W. Bahnemann, *Separation and Purification Technology*, **80**, 125 (2011).
- J. Miao, Z. Jia, H.-B. Lu, D. Habibi, L.-C. Zhang, *Journal of the Taiwan Institute of Chemical Engineers*, **45**, 1636 (2014).
- S. K. Kansal, N. Kaur, S. Singh, *Nanoscale Res Lett.*, **4**, 709 (2009).
- M. A. Ali, M. R. Idris, M. E. Quayum, *Journal Of Nanostructure in Chemistry*, **3**, 36 (2013).
- M. Li, H. Xu, T. Yu, *Journal of Chemical and Pharmaceutical Research*, **6** (2), 625 (2014).
- W. Kraus, G. Nolze, PowderCell for Windows, Federal Institute for Materials Research and Testing, Berlin, 2000.
- S. Anandhavelu, S. Thambidurai, *Materials Chemistry and Physics*, **131**, 449 (2011).
- Z. Khan, M. Khan, M. Zulfequar, M. Shahid Khan, *Materials Sciences and Applications*, **2** (5), 340 (2011).
- R. Viswanatha, T. G. Venkatesh, C. C. Vidyasagar, Y. Arthoba Nayaka, *Arch. Appl. Sci. Res.*, **4** (1), 480 (2012).
- N. Uma Sangari, S. Chitra Devi, *Journal of Solid State Chemistry*, **197**, 483 (2013).
- P. Ma, Y. Wu, Z. Fu, W. Wang, *Journal of Alloys and Compounds*, **509**, 3576 (2011).
- B. J. Saikia, G. Parthasarathy, *J. Mod. Phys.*, **1**, 206 (2010).
- F. A. Miller, C. H. Wilkins, *Analytical Chemistry*, **24** (8), 1253 (1952).
- R. L. Frost, W. N. Martens, D. L. Wain, M. C. Hales, *Spectrochimica Acta Part A*, **70**, 1120 (2008).
- G. Panthi, M. Park, H.-Y. Kim, S.-Y. Lee, S.-J. Park, *Journal of Industrial and Engineering Chemistry*, (2014) in press.

ВЛИЯНИЕ НА ПРОДЪЛЖИТЕЛНОСТТА НА МЕХАНОХИМИЧНА
ОБРАБОТКА ВЪРХУ ФОТОКАТАЛИТИЧНАТА АКТИВНОСТ
ПРИ ОБЛЪЧВАНЕ С УВ СВЕТЛИНА НА НАНОРАЗМЕРЕН
ЦИНКОВ ОКСИД, ПОЛУЧЕН ЧРЕЗ УТАЯВАНЕ

К. Л. Захариева^{1*}, К. И. Миленова¹, З. П. Черкезова-Желева¹,
С. С. Димова², Б. Н. Кунев¹, А. Е. Елияс¹, И. Г. Митов¹,
И. Д. Стамболова³, В. Н. Блъсков³

¹ *Институт по катализ, Българска академия на науките, ул. „Акад. Г. Бончев“,
бл. 11, 1113 София, България*

² *Институт по полимери, Българска академия на науките, ул. „Акад. Г. Бончев“,
бл. 103А, 1113 София, България*

³ *Институт по обща и неорганична химия, Българска академия на науките,
ул. „Акад. Г. Бончев“, бл. 11, 1113 София, България*

Постъпила декември, 2014 г.; приета януари, 2015 г.

(Резюме)

В настоящата статия е изследвано влиянието на времетраенето на механохимичната обработка върху фотокаталитичните свойства при облъчване с УВ-светлина на наноразмерен цинков оксид. Цинковият оксид е синтезиран чрез класическа процедура на утаяване, с изходни реагенти $ZnCl_2$, $NaOH$ и последваща термична обработка. Полученият цинков оксид е механохимично обработен при различни условия на смилане. Фазовият състав и структурата на изходния и механохимично активираният проби на наноразмерен цинков оксид бяха определени чрез рентгенофазов анализ и инфрачервена спектроскопия с Фурие трансформация. Фотокаталитичните свойства на всички приготвени проби на цинков оксид бяха тествани във фотокаталитичното окислително разграждане при облъчване с УВ-светлина на багрилото Реактивно Черно 5 като моделен замърсител. Направените изчисления, използвайки данните от рентгенофазовия анализ, установиха, че механохимично третираните ZnO фотокатализатори са с по малък среден размер на кристалитите (9,9 nm) в сравнение с изходния цинков оксид (14,6 nm). Получените резултати показват, че фотокаталитичните активности (скоростни константи) на утаения и механохимично третираните наноразмерни цинкови оксиди намалява в следния ред: ZnO (15 min) ($35,5 \times 10^{-3} \text{min}^{-1}$) > ZnO (30,4x10⁻³min⁻¹) > ZnO (30 min) ($26,4 \times 10^{-3} \text{min}^{-1}$) > ZnO (4 h) ($19 \times 10^{-3} \text{min}^{-1}$). Оптималното времетраене на смилане, при което се получава наноструктурен ZnO фотокатализатор с най-висока фотокаталитична активност ($k=35,5 \times 10^{-3} \text{min}^{-1}$) в сравнение с другите изследвани образци, е 15 минути.

Preparation, structure and catalytic properties of copper-zinc ferrites

K. V. Koleva¹, N. I. Velinov^{1*}, T. S. Tsoncheva², I. G. Mitov¹

¹ Institute of Catalysis, BAS, Sofia, 1113, Bulgaria

² Institute of Organic Chemistry with Centre of Phytochemistry, BAS, Sofia, 1113, Bulgaria

Received December, 2014; Revised January, 2015

Well crystallized $\text{Cu}_{1-x}\text{Zn}_x\text{Fe}_2\text{O}_4$ ferrites with different composition were prepared and tested as catalysts in methanol decomposition to CO and hydrogen. The influence of cation distribution in ferrites on their catalytic behaviour and phase transitions under the reaction medium was in the focus of the study. It was established that $\text{Cu}_{0.8}\text{Zn}_{0.2}\text{Fe}_2\text{O}_4$ ferrite exhibits the highest catalytic activity and good selectivity in methanol decomposition to H_2 and CO. Mössbauer study of samples after the catalytic test reveals transformation of the initial ferrite phase with the formation of Zn-substituted magnetite, iron carbide, wuestite and α -Fe in different ratio.

Key words: copper-zinc ferrite, Mössbauer spectroscopy, methanol decomposition.

INTRODUCTION

Ferrite materials are object of many scientific investigations because of their potential application in biology [1], electronics [2–4] and catalysis [5–13]. The spinel ferrites are usually denoted with general formula AB_2O_4 . The distribution of metal ions in the spinel crystal lattice determines ferrite structure as normal, inverse and partial inverse spinel type. In the ZnFe_2O_4 ferrite the tetrahedral (A)-sites are occupied by only one type of cations. This is because of the preferences of Zn^{2+} to occupy the tetrahedral spinel sites forming normal spinel, while Cu^{2+} occupies mainly the octahedral [B]-sites, and thus, the tetrahedral sites are occupied by half of Fe^{3+} and CuFe_2O_4 describes as inverse spinel. In the case of $\text{Cu}_{1-x}\text{Zn}_x\text{Fe}_2\text{O}_4$, where $0 < x < 1$, the tetrahedral sites are occupied both by Zn^{2+} and Fe^{3+} cations and its spinel structure are denoted as partially inverse. The cation distribution in crystal structure is important for various properties of materials as magnetic, catalytic etc.

The effect of synthesis temperature on ferrite formation and catalytic properties in reaction of methanol decomposition has been studied for ZnFe_2O_4 composition [14]. It has been established that the crystallite size increases from 6 nm to 46 nm with

increasing of synthesis temperature from 300 °C to 700 °C. The catalytic activity of nanocrystalline $\text{Cu}_{1-x}\text{Zn}_x\text{Fe}_2\text{O}_4$ synthesized at low temperature has been studied in [15]. It has been established that the mixed ferrite materials exhibit high catalytic activity in methanol decomposition and the catalytic behaviour of ferrites strongly depends on the phase transformations that occur by the influence of the reaction medium.

The aim of present work is to prepare well crystallized $\text{Cu}_{1-x}\text{Zn}_x\text{Fe}_2\text{O}_4$ ferrites with different composition and to test their catalytic behaviour in methanol decomposition to CO and hydrogen. The influence of cation distribution in ferrites on the phase transformations under the reductive reaction medium and the relation with their catalytic properties was in the focus of the study.

EXPERIMENTAL

Ferrite samples with compositions $\text{Cu}_{1-x}\text{Zn}_x\text{Fe}_2\text{O}_4$ ($x = 0.2, 0.5, 0.8$ or 1.0) were prepared by co precipitation method. The solution of $\text{Cu}(\text{NO}_3)_2 \cdot 3\text{H}_2\text{O}$, $\text{Zn}(\text{NO}_3)_2 \cdot 6\text{H}_2\text{O}$ and $\text{Fe}(\text{NO}_3)_3 \cdot 9\text{H}_2\text{O}$ was precipitated with drop wise addition of 1 M Na_2CO_3 up to $\text{pH} = 9$ and continuous stirring. The obtained precipitate was washed with distilled water, dried at room temperature and treated at 973 K for 4 hours.

The powder XRD patterns were recorded using a TUR M62 diffractometer with Co K α radiation. The average crystallite size (D), the degree of microstrain and the lattice parameters were determined

* To whom all correspondence should be sent:
E-mail: nikivelinov@ic.bas.bg

by using the PowderCell-2.4 software [16]. The Transmission Mössbauer spectra (TMS) were obtained with a Wissel (Wissenschaftliche Elektronik GmbH, Germany) electromechanical spectrometer working in a constant acceleration mode. A $^{57}\text{Co}/\text{Rh}$ source and a $\alpha\text{-Fe}$ standard were used. The parameters of hyperfine interaction such as isomer shift (IS), quadrupole splitting (QS), effective internal magnetic field (H_{eff}), line widths (FWHM), and relative weight (G) of the partial components in the spectra were determined using the Confit2000 software [17]. Methanol decomposition was carried out in a flow reactor at methanol partial pressure of 1.57 kPa and argon as a carrier gas (50 ml/min). The catalysts (0.055 g of catalyst) were tested under temperature-programmed regime within the range of 350–770 K and heating rate of 1 K/min. On-line gas chromatographic analyses were performed on a PLOT Q column using flame ionization and thermo-conductivity detectors.

RESULTS AND DISCUSSION

The XRD data for the obtained $\text{Cu}_{1-x}\text{Zn}_x\text{Fe}_2\text{O}_4$ ferrites (Fig. 1) revealed formation of well crystallized structure of cubic spinel phase at temperature used. A secondary phase identified as hematite was observed in the samples with high Cu content. The average crystallites size (D), degree of microstrain (e) and lattice parameters determined from XRD patterns are presented in Table 1. The calculated crystalline size is in the range from 43 nm to 60 nm. The lattice parameters decrease from 8.43 to 8.39 Å when x in $\text{Cu}_{1-x}\text{Zn}_x\text{Fe}_2\text{O}_4$ ferrites decreases from 1 to 0.2.

Mössbauer spectra of synthesized samples are presented in Fig. 2. The spectrum of pure ZnFe_2O_4 exhibits of doublet corresponding to paramagnetic behaviour of zinc ferrite where all amount of Fe^{3+} ions are located in [B]-site of unit cell, while Zn^{2+} ions strongly prefer (A)-site position, determining

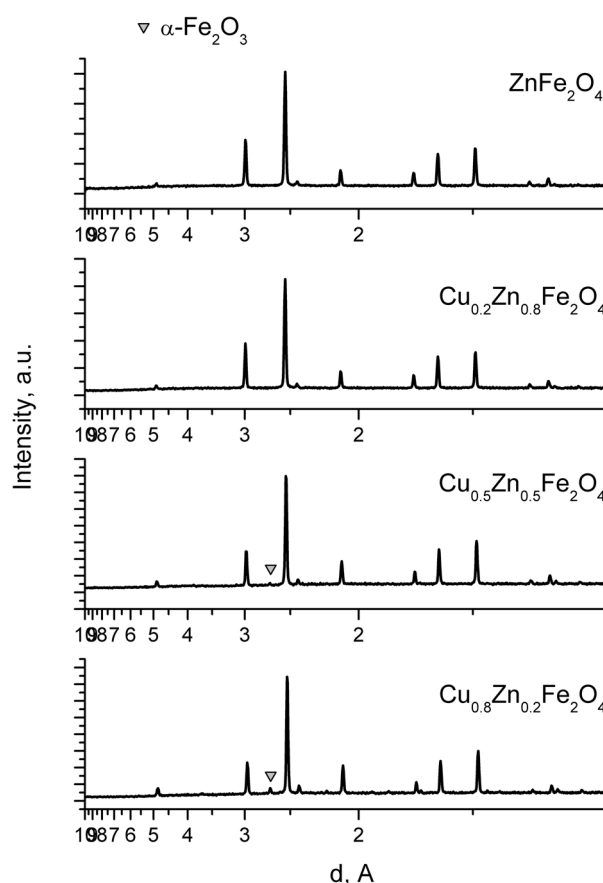


Fig. 1. X-ray diffraction patterns of synthesized samples

zinc ferrite as a normal spinel. The Mössbauer parameters show no significant difference of magnetic structure when $x=0.8$ and existence of paramagnetic phase was also observed. Mössbauer spectra exhibit sextet magnetic components with copper content increase in samples $\text{Cu}_{0.5}\text{Zn}_{0.5}\text{Fe}_2\text{O}_4$ and $\text{Cu}_{0.8}\text{Zn}_{0.2}\text{Fe}_2\text{O}_4$. In this case acceptable fitting of the experimental data could be obtained when the [B]-

Table 1. Average crystallite size (D), degree of microstrain (e) and lattice parameters (a, c) determined from experimental XRD profiles

Sample	Phase	D, nm	e.10 ³ , a.u	a, c, Å	%
ZnFe_2O_4	Fd3m(227) – cubic	45.84	1.187	8,43	100
$\text{Cu}_{0.2}\text{Zn}_{0.8}\text{Fe}_2\text{O}_4$	Fd3m(227) – cubic	59.82	1.684	8.42	100
$\text{Cu}_{0.5}\text{Zn}_{0.5}\text{Fe}_2\text{O}_4$	Fd3m(227) – cubic	42.80	0.352	8.41	98.6
	Fe_2O_3			a=5.04, c=13.77	1.4
$\text{Cu}_{0.8}\text{Zn}_{0.2}\text{Fe}_2\text{O}_4$	Fd3m(227) – cubic	45.24	0.997	8.39	91.3
	Fe_2O_3			a=5.03, c=13.77	8.7

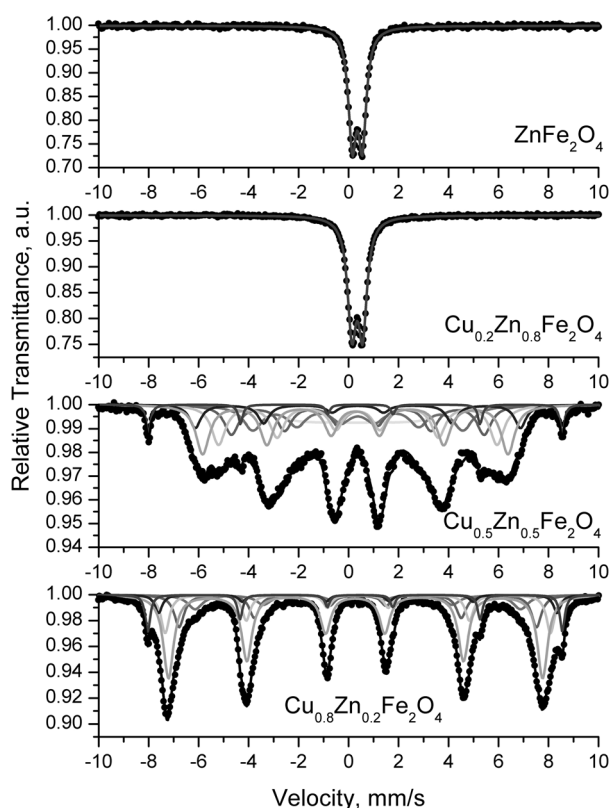


Fig. 2. Mössbauer spectra of synthesized samples

site pattern is assumed as superposition of more than one sextet. The binomial formula is used to calculate a probability $P(n, x)$ of an octahedral site having n nearest-neighbor zinc atoms in order to define the

number of sextet components that have to use in the fitting model, as it has been used in [18]. Mössbauer spectra of one sextet referred to tetrahedral coordination of Fe^{3+} ions (A)-site and five sextets for $x=0.5$ and four sextet for $x=0.2$ with parameters of Fe^{3+} ions in octahedral position. The existence of number of sextet components with different hyperfine field can be explain with random occupancy of tetrahedral positions by Fe^{3+} and diamagnetic Zn^{2+} ions, results in existence of different (A)-site nearest neighbors of [B]-site Fe^{3+} i.e. 6Fe, 5Fe and 1Zn, 4Fe and 2Zn and etc. (A)-site neighbors (corresponding sextet components are shown in Table 2, as B0, B1, B2 and etc., followed by calculated probability in parenthesis). Additional sextet with parameters typical for hematite was determined in Cu- rich samples, as its relative weight is 4% and 8% for $x=0.5$ for $x=0.2$ samples respectively.

Temperature dependencies of methanol conversion and CO selectivity for various ferrite materials are presented in Fig. 3. The main registered by-products during the decomposition are CO_2 (up to 20–30%) and CH_4 (up to 2–10%). Note that the catalytic activity of the samples is in complex relation with their initial composition. The replacement of Zn with small amount of Cu leads to a decrease in the catalytic activity as compared to pure ZnFe_2O_4 . However, the conversion curve of the sample with the highest copper content, $\text{Cu}_{0.8}\text{Zn}_{0.2}\text{Fe}_2\text{O}_4$, is shifted to 80–100 K lower temperature, indicating much higher catalytic activity. Mössbauer study of the samples after the catalytic test was carried out. For all materials significant phase transformations under the reaction medium are established. Formation

Table 2. Parameters of Mössbauer spectra of the investigated samples

Sample	Components	IS mm/s	QS mm/s	H_{eff} , T	FWHM mm/s	G, %
ZnFe_2O_4	Db	0.35	0.40	–	0.38	100
$\text{Cu}_{0.2}\text{Zn}_{0.8}\text{Fe}_2\text{O}_4$	Db	0.35	0.43	–	0.42	100
$\text{Cu}_{0.5}\text{Zn}_{0.5}\text{Fe}_2\text{O}_4$	Sx1- Fe_2O_3	0.37	-0.20	51.4	0.22	4
	Sx2-tetra, A	0.27	0.00	37.0	0.65	23
	Sx3-octa, B1(0.09)	0.37	0.00	40.4	0.55	8
	Sx4-octa, B2(0.23)	0.37	0.00	34.6	0.68	19
	Sx5-octa, B3(0.31)	0.37	0.00	31.4	0.70	15
	Sx6-octa, B4(0.23)	0.37	0.00	26.1	0.93	16
	Sx7-octa, B5(0.09)	0.37	0.00	15.4	0.02	14
$\text{Cu}_{0.8}\text{Zn}_{0.2}\text{Fe}_2\text{O}_4$	Sx1- Fe_2O_3	0.36	-0.20	51.5	0.24	8
	Sx2-tetra, A	0.272	0.02	46.5	0.50	46
	Sx3-octa, B0(0.26)	0.37	0.00	49.5	0.36	6
	Sx4-octa, B1(0.39)	0.37	0.00	47.9	0.40	15
	Sx5-octa, B2(0.25)	0.37	0.00	44.4	0.47	15
	Sx6-octa, B3(0.08)	0.37	0.00	40.5	0.71	10

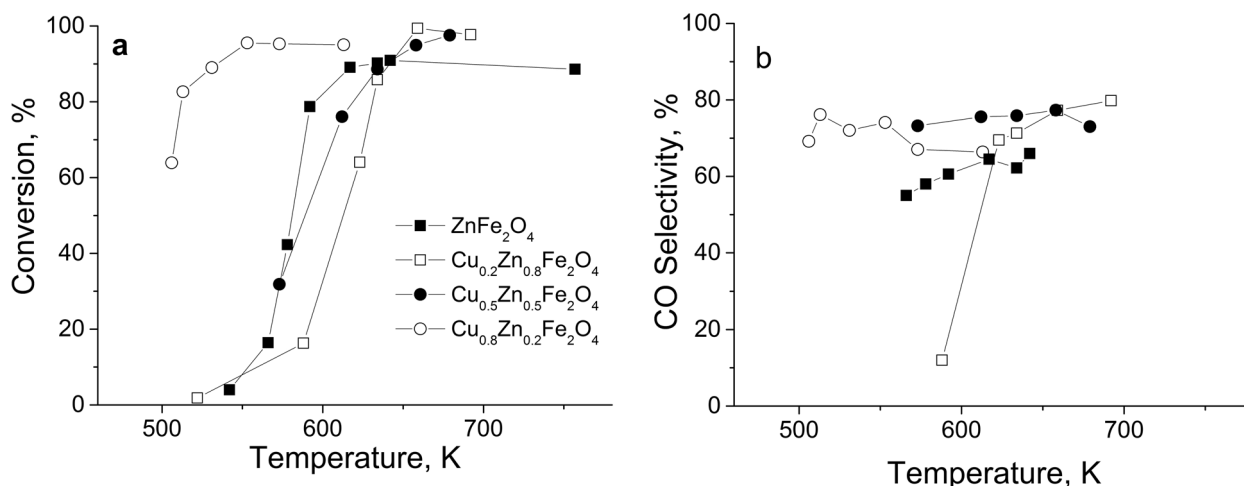


Fig. 3. Methanol conversion (a) and CO selectivity (b) vs. temperature of investigated ferrite materials

of metallic Fe and FeO is typical for pure $ZnFe_2O_4$, while metal-substituted magnetite ($Me_xFe_{3-x}O_4$, $Me = Cu, Zn$) and χ - Fe_5C_2 and θ - Fe_3C carbides in different ratio are observed for all bi-component ferrites (Fig. 4, Table 3). The relative part of θ - Fe_3C is the highest for the sample with minimum copper content, $Cu_{0.2}Zn_{0.8}Fe_2O_4$. Formation of χ - Fe_5C_2 and

$Me_xFe_{3-x}O_4$, with the increase of the relative part of the latter is observed with copper content increase in ferrites. We assume that the highest catalytic activity of $Cu_{0.8}Zn_{0.2}Fe_2O_4$ could be related to the formation of metal-substituted magnetite. A synergistic activity of this magnetite and finely dispersed copper particles is not excluded as well.

Table 3. Parameters of Mössbauer spectra of the investigated samples after catalytic test

Sample	Components	IS, mm/s	QS, mm/s	Heff, T	FWHM, mm/s	G, %
$ZnFe_2O_4$ -MD	Sx1 – $Me_xFe_{3-x}O_4$	0.28	-0.02	48.2	0.26	11
	Sx2 – $Me_xFe_{3-x}O_4$	0.63	0.00	44.6	0.63	28
	Sx3 – α -Fe	0.00	0.01	32.7	0.27	23
	Sx4 – θ - Fe_3C	0.17	0.07	20.4	0.36	8
	Db – FeO	0.88	0.73	–	0.60	30
$Cu_{0.2}Zn_{0.8}Fe_2O_4$ -MD	Sx1 – $Me_xFe_{3-x}O_4$	0.26	-0.01	47.8	0.34	7
	Sx2 – $Me_xFe_{3-x}O_4$	0.57	0.00	42.8	1.13	20
	Sx3 – θ - Fe_3C	0.19	0.03	20.8	0.45	60
	Db – $ZnFe_2O_4$	0.36	0.36	–	0.39	13
$Cu_{0.5}Zn_{0.5}Fe_2O_4$ -MD	Sx1 – $Me_xFe_{3-x}O_4$	0.30	0.07	46.9	0.56	8
	Sx2 – $Me_xFe_{3-x}O_4$	0.62	0.00	42.5	0.85	12
	Sx3 – χ - Fe_5C_2	0.21	0.05	21.0	0.50	44
	Sx4 – χ - Fe_5C_2	0.18	-0.00	18.8	0.49	15
	Sx5 – χ - Fe_5C_2	0.17	0.01	11.5	0.36	7
	Sx6 – $Cu_{0.5}Zn_{0.5}Fe_2$	0.38	0.00	37.9	0.59	6
	Sx7 – $Cu_{0.5}Zn_{0.5}Fe_2$	0.28	0.00	32.2	1.06	8
$Cu_{0.8}Zn_{0.2}Fe_2O_4$ -MD	Sx1 – $Me_xFe_{3-x}O_4$	0.28	-0.01	48.0	0.32	15
	Sx2 – $Me_xFe_{3-x}O_4$	0.60	-0.01	43.8	0.94	44
	Sx3 – χ - Fe_5C_2	0.23	0.09	21.4	0.50	23
	Sx4 – χ - Fe_5C_2	0.17	0.03	18.8	0.44	15
	Sx5 – χ - Fe_5C_2	0.16	0.01	10.8	0.32	3

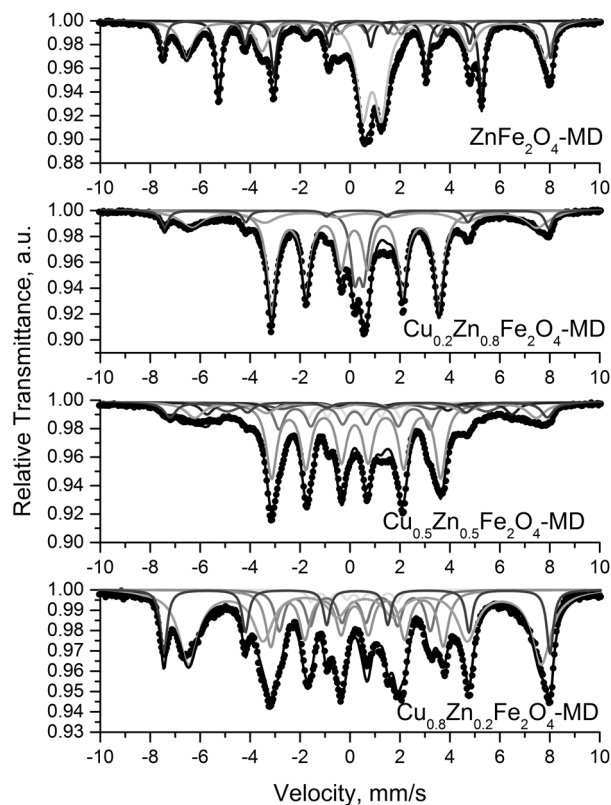


Fig. 4. Mössbauer spectra of samples after catalytic test

CONCLUSIONS

Well crystallized $\text{Cu}_{1-x}\text{Zn}_x\text{Fe}_2\text{O}_4$ ferrites with different composition were synthesized using co-precipitation method. The ferrite samples with higher Cu content exhibit better catalytic activity in methanol decomposition. Mössbauer study of the samples after the catalytic test reveals significant changes in the initial ferrite phase with the formation of metal-substituted magnetite, iron carbide, wuestite and $\alpha\text{-Fe}$ in different ratio. The catalytic activity of ferrites correlates with their phase transformations by the influence of the reaction medium and facilitated effect of the formation of metal-substituted magnetite is established.

Acknowledgements: *The present work is financially supported by the Bulgarian National Science Fund under Projects DFNI-E01/7/2012 and FNI-E02/17/2014.*

REFERENCES

1. K. E. Scarberry, E. B. Dickerson, Z. J. Zhang, B. B. Benigno, J. F. McDonald, *Nanomedicine: Nanotechnology, Biology, and Medicine*, **6**, 399 (2010).
2. M. N. Ashiq, F. Naz, M. A. Malana, R. S. Gohar, Z. Ahmad, *Mater. Res. Bull.*, **47**, 683 (2012).
3. K. Mukherjee, S. B. Majumder, *Sensor Actuator B-Chem*, **162**, 229 (2012).
4. A. Goldman, *Electronic Ceramics*, L. Levenson (ed.), Marcel Dekker, New York, 1988, p. 170.
5. C. Fauteux-Lefebvre, N. Abatzoglou, J. Blanchard, F. Gitzhofer, *J. Power Sources*, **195**, 3275 (2010).
6. R. Benrabaa, H. Boukhlof, S. Barama, E. Bordes-Richard, R. N. Vannier, A. Barama, *Catal. Lett.*, **142**, 42, (2012).
7. A. S. Albuquerque, M. V.C. Tolentino, J. D. Ardisson, F. C. C. Moura, R. de Mendonca, W. A. A. Macedo, *Ceram. Int.*, **38**, 2225 (2012).
8. X. Tana, G. Li, Y. Zhao, C. Hu, *J. Alloy. Compd.*, **493**, 55 (2010).
9. M. Mokhtar, S. N. Basahel, Y. O. Al-Angary, *J. Alloy. Compd.*, **493**, 376 (2010).
10. N. van Vegten, T. Baidya, F. Krumeich, W. Kleist, A. Baiker, *Appl. Catal. B- Environ.*, **97**, 398 (2010).
11. J. Chen, W. Shi, J. Li, *Catal. Today*, **175**, 216 (2011).
12. M. Massa, R. Häggblad, A. Andersson, *Top. Catal.*, **54**, 685 (2011).
13. B. Jäger, A. Stolle, P. Scholz, M. Müller, B. Ondruschka, *Appl. Catal. A-Gen.*, **403**, 152 (2011).
14. K. Koleva, N. Velinov, T. Tsoncheva, I. Mitov, B. Kunev, *Bulg. Chem. Commun.*, **45**, 434 (2013).
15. K. Koleva, N. Velinov, T. Tsoncheva, I. Mitov, Mössbauer study of $\text{Cu}_{1-x}\text{Zn}_x\text{Fe}_2\text{O}_4$ catalytic materials, *Hyperfine Interact.*, **226**, 89 (2014).
16. W. Kraus, G. Nolze, *PowderCell for Windows*, Federal Institute for Materials Research and Testing, Berlin, 2000.
17. T. Žák, Y. Jirásková, CONFIT: Mössbauer spectra fitting program, *Surf. and Interface Anal.*, **38**, 710 (2006).
18. N. Velinov, E. Manova, T. Tsoncheva, Cl. Estournès, D. Paneva, K. Tenchev, V. Petkova, K. Koleva, B. Kunev, I. Mitov, *Solid State Sci.*, **14**, 1092 (2012).

ПОЛУЧАВАНЕ, СТРУКТУРА И КАТАЛИТИЧНИ СВОЙСТВА НА МЕД-ЦИНКОВИ ФЕРИТИ

К. В. Колева¹, Н. И. Велинов^{1*}, Т. С. Цончева², И. Г. Митов¹

¹ *Институт по катализ, Българска академия на науките, ул. Акад. Г. Бончев,
бл. 11, 1113 София, България*

² *Институт по органична химия с център по фитохимия, Българска академия на науките,
ул. Акад. Г. Бончев, бл. 9, 1113 София, България*

Постъпила декември, 2014 г.; приета януари, 2015 г.

(Резюме)

Добре кристализирани ферити със състав $\text{Cu}_{1-x}\text{Zn}_x\text{Fe}_2\text{O}_4$ са получени и тествани като катализатори в реакцията на разлагане на метанол до СО и водород. Във фокуса на изследването са изучаването на влиянието на катионното разпределение във феритите върху каталитичното поведение и фазовите превръщания под влияние на реакционната среда. Установено беше, че феритът със състав $\text{Cu}_{0.8}\text{Zn}_{0.2}\text{Fe}_2\text{O}_4$ проявява най-висока каталитична активност и добра селективност при разлагане на метанол до H_2 и СО. Мьосбауеровият анализ на образците след каталитичен тест показва превръщане на първоначалната феритна фаза в следните фази: Zn-заместен магнетит, железен карбид, вюстит и α -Fe.

Photocatalytic activity of nanostructure zinc ferrite-type catalysts in degradation of Malachite green under UV-light

M. P. Tsvetkov^{1*}, K. L. Zaharieva², Z. P. Cherkezova-Zheleva²,
M. M. Milanova¹, I. G. Mitov²

¹ Sofia University, Faculty of Chemistry and Pharmacy, 1, J. Bourchier Blvd.,
Sofia 1164, Bulgaria

² Institute of Catalysis, Bulgarian Academy of Sciences, "Acad. G. Bonchev" St.,
Bl. 11, 1113 Sofia, Bulgaria

Received December, 2014; Revised January, 2015

Series of nanostructured zinc ferrite-type materials $Zn_xFe_{3-x}O_4$ ($x=0.25, 0.5, 1$) with average crystallite size about 8 nm prepared by co-precipitation or co-precipitation and mechanochemical treatment were tested for photocatalytic degradation of Malachite green oxalate as model contaminant in aqueous solution under UV-light. The performed experiments determined that co-precipitated zinc ferrite-type powders show the higher photocatalytic activity than the mechanochemically treated samples: $ZnFe_2O_4$ ($k=13.7 \times 10^{-3} \text{min}^{-1}$) > $Zn_{0.5}Fe_{2.5}O_4$ ($k=10.7 \times 10^{-3} \text{min}^{-1}$) > $Zn_{0.25}Fe_{2.75}O_4$ ($k=9.4 \times 10^{-3} \text{min}^{-1}$) > $Zn_{0.5}Fe_{2.5}O_4$ (MCT-2hours) ($k=8.1 \times 10^{-3} \text{min}^{-1}$) > $ZnFe_2O_4$ (MCT-1hour) ($k=6.3 \times 10^{-3} \text{min}^{-1}$). The results established that the increase in the degree of substitution of iron ions by zinc ones leads to higher photocatalytic activities for the synthesized ferrite-type samples by co-precipitation. The mechanochemical treatment of co-precipitated zinc ferrite-type materials leads to obtaining of catalyst with higher photocatalytic activity $Zn_{0.5}Fe_{2.5}O_4$ (MCT-2hours) ($k=8.1 \times 10^{-3} \text{min}^{-1}$) with increasing the milling time and decrease the content of zinc ions incorporated in magnetite host structure. Mössbauer spectroscopy was performed in order to study the changes in catalytic behavior of used zinc ferrite-type photocatalysts during the photodegradation process of the dye.

Key words: zinc ferrite-type materials, photocatalysis, Malachite Green.

INTRODUCTION

Photocatalysis find application in various fields including purification of contaminants from water [1]. The presence of industrial wastewater containing dyes in environment generate significant problems due to its high toxicity and possible accumulation in the environment. The most dangerous pollutants in water are synthetic dyes. The presence of even very low concentrations of dyes in water reduces light penetration through the water surface, precluding photosynthesis of the aqueous flora. A large number of these dyes are mutagenic, teratogenic and carcinogenic. These pollutants are toxic to human beings, microorganisms, and fish species and therefore their removal from polluted waters is essential for environmental protection [2]. Many investigations are

carried out about obtaining of effective photocatalyst for degradation of organic contaminants in the past decades [3]. Iron oxides possess catalytic properties for different reactions such as decomposition of hydrogen peroxide and discoloration of synthetic dyes, decomposition of alcohols, selective oxidation of carbon monoxide. The environmental applications of these oxides are widely investigated [4]. The photocatalysts with semiconductor properties are extensively used for degradation of the organic contaminants for the remediation of hazardous wastes and polluted groundwater, and the control of toxic air pollutants [5]. The advantages of using the spinel $ZnFe_2O_4$ in photocatalysis are displaying the desirable optical absorption for the narrow band gap of $\sim 1.9 \text{eV}$, electronic structure, outstanding photochemical stability, strong magnetism and low cost [6, 7]. The zinc ferrite ($ZnFe_2O_4$) photocatalyst was used for degradation of different dyes such as Brilliant Red M5B under UV irradiation [1], methyl orange under UV-irradiation [8], methylene blue under real sunlight irradiation [9] or visible light ir-

* To whom all correspondence should be sent:
E-mail: mptsvetkov@gmail.com

radiation [10], Rhodamine B under the irradiation of simulated solar light [11] or visible light irradiation [6, 12, 13], Acid Orange II in H_2O_2 /visible light system [14], Procion red dye in the presence of H_2O_2 /visible irradiation [15], Reactive Red 198 and Reactive Red 120 in the presence of H_2O_2 and UV-light [16].

The present paper is focused on the investigations of photocatalytic activity of nanosized zinc ferrite-type materials obtained by different methods as co-precipitation or co-precipitation and mechanochemical activation. The catalytic activity of prepared ferrite-type materials is tested about photocatalytic degradation of Malachite green dye as model contaminant in aqueous solution under UV-light at different irradiation intervals. The sorption ability of ferrite materials are studied also. The Mössbauer spectroscopy was used to study the behavior of nanodimensional zinc ferrite-type photocatalysts after photocatalytic reaction.

EXPERIMENTAL

The zinc ferrite-type samples *Sample 1* – $Zn_{0.25}Fe_{2.75}O_4$, *Sample 2* – $Zn_{0.5}Fe_{2.5}O_4$, *Sample 3* – $ZnFe_2O_4$ were prepared by co-precipitation procedure using initial materials $ZnCl_2$, $FeCl_2 \cdot 4H_2O$ and/or $FeCl_3 \cdot 6H_2O$ represented to [17]. The other zinc ferrite-type materials as *Sample 4* – $Zn_{0.5}Fe_{2.5}O_4$ and *Sample 5* – $ZnFe_2O_4$ were synthesized using co-precipitation and mechanochemical treatment for 2 and 1 hours. The mechanochemical activation process was carried out on Highenergy planetary ball mill type PM 100, Retsch, Germany. The phase composition, structure and magnetic behavior of co-precipitated and mechanochemically activated zinc ferrite-type materials were investigated and determined by various physicochemical techniques such as Powder X-ray diffraction analysis, Mössbauer and FT-IR spectroscopy [17].

The photocatalytic tests were performed in a slurry containing 1g zinc ferrite-type catalyst/l and using a $10^{-5}M$, aqueous solution of Malachite green dye as model pollutant. After 60 min “dark”-period in order to establish the equilibrium of the sorption process, the system was UV-illuminated by lamp (Sylvania 18 W BLB T8, emission in the 345–400 nm region with maximum at 365 nm) situated at 9.5 cm distance above the slurry, under continuous magnetic stirring (350 min^{-1}) and bubbling with air (45 l/h). Periodically 7 ml aliquot was taken from the solution and filtered through a 20 μm HPLC filter membranes. The dye concentration was determined spectrophotometrically using Specol 11 by the band at 622 nm. The data obtained were plotted in coordinates $(C/C_0)/t$ and $-\ln(C/C_0)/t$ (where C_0

is the concentration after the “dark” period and C is the concentration after t min of irradiation), and apparent rate constants were determined assuming pseudo first-order kinetic.

In order to investigate the behavior of zinc ferrite-type catalysts after photocatalytic reaction, the Mössbauer spectra were recorded using apparatus Wissenschaftliche Elektronik GmbH, working with a constant acceleration mode, $^{57}Co/Rh$ source (activity $\approx 50 \text{ mCi}$) and α -Fe standard. The computer fitting of the Mössbauer spectra was made to determine the Mössbauer parameters of hyperfine interactions of spectral components: isomer shift (IS), quadrupole splitting (QS), hyperfine effective magnetic field in the site of iron nuclei (H_{eff}), line widths (FWHM) and component relative weights (G).

RESULTS AND DISCUSSION

The Powder X-ray diffraction investigations determined the presence of the single non-stoichiometric spinel zinc ferrite phase $Zn_xFe_{3-x}O_4$ (PDF-01-1109) for *Sample 1* – $Zn_{0.25}Fe_{2.75}O_4$. The ferrite and additional akaganeite phase (PDF-34-1266) were observed in co-precipitated *Sample 2* – $Zn_{0.5}Fe_{2.5}O_4$, *Sample 3* – $ZnFe_2O_4$. The mechanochemical treated *Sample 4* – $Zn_{0.5}Fe_{2.5}O_4$ and *Sample 5* – $ZnFe_2O_4$ contain ferrite phase (PDF-01-1109) and metal iron (PDF-87-0721). The PXRD patterns are presented in study [17]. The calculated mean crystallite size of obtained nanodimensional zinc ferrite-type materials is about 8 nm.

The catalytic results for photocatalytic degradation of Malachite green oxalate as model pollutant in aqueous solution under UV-light irradiation are shown on Figures 1 and 2. The highest decrease

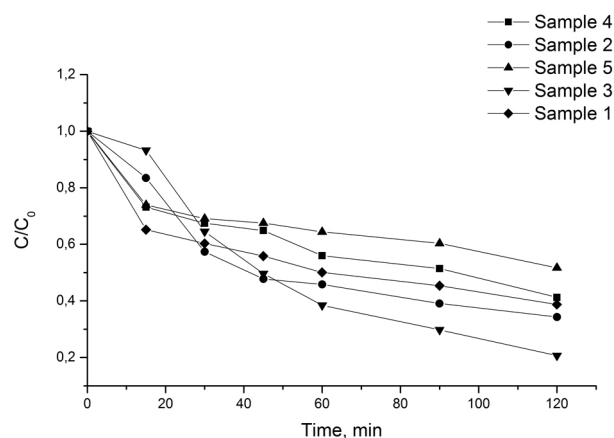


Fig. 1. Concentration changes of Malachite green dye under UV irradiation time using different zinc ferrite-type photocatalysts

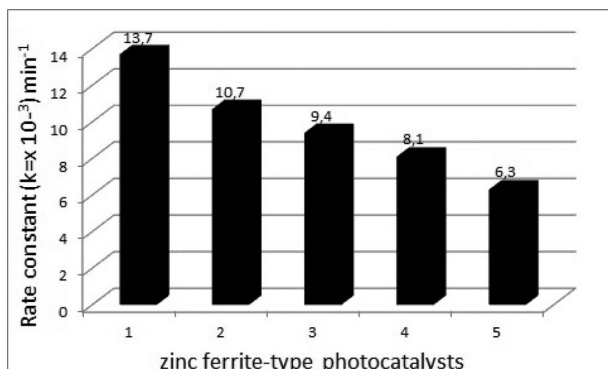


Fig. 2. Apparent rate constants of obtained zinc containing ferrites: 1 – Sample 3; 2 – Sample 2; 3 – Sample 1; 4 – Sample 4; 5 – Sample 5.

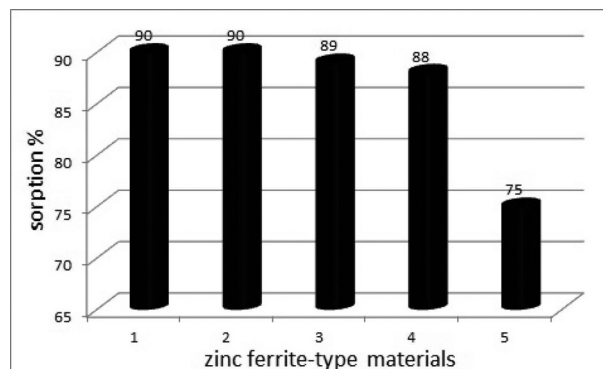


Fig. 3. Sorption abilities of obtained zinc ferrite-type materials: 1 – Sample 3; 2 – Sample 4; 3 – Sample 2; 4 – Sample 1; 5 – Sample 5

ing of initial concentration of Malachite green dye solution during photocatalytic degradation process using UV-illumination was achieved by using co-precipitated *Sample 3* – ZnFe_2O_4 photocatalyst (see Figure 1). The apparent rate constants of prepared nanosized zinc ferrite-type materials were determined by linear slopes using pseudo-first-order kinetic equation $-\ln(C/C_0) = k.t$. The comparison of calculated rate constants is presented on the Figure 2. As can be seen the co-precipitation method leads to formation of zinc ferrite-type catalysts with the higher photocatalytic activity than that of the mechanochemically treated ferrite samples: ZnFe_2O_4 ($k=13.7 \times 10^{-3} \text{ min}^{-1}$) > $\text{Zn}_{0.5}\text{Fe}_{2.5}\text{O}_4$ ($k=10.7 \times 10^{-3} \text{ min}^{-1}$) > $\text{Zn}_{0.25}\text{Fe}_{2.75}\text{O}_4$ ($k=9.4 \times 10^{-3} \text{ min}^{-1}$) > $\text{Zn}_{0.5}\text{Fe}_{2.5}\text{O}_4$ (MCT-2hours) ($k=8.1 \times 10^{-3} \text{ min}^{-1}$) > ZnFe_2O_4 (MCT-1hour) ($k=6.3 \times 10^{-3} \text{ min}^{-1}$). The photocatalytic investigations show that photocatalytic activity of zinc ferrite-type materials depends on the preparation technique, milling time of mechanochemical treatment and degree of substitution of iron ions by zinc ones in magnetite host structure. The increase in the degree of substitution of iron ions by zinc ones leads to the enhancement of photocatalytic activities for the co-precipitated ferrite-type samples. The increase of activation time during the milling treatment of nanostructured zinc ferrite-type photocatalysts and decreasing amount of Zn^{2+} ions incorporated in magnetite host lattice leads to obtaining of mechanochemically treated zinc-ferrite-type catalyst with the higher photocatalytic activity as $\text{Zn}_{0.5}\text{Fe}_{2.5}\text{O}_4$ (MCT-2 hours) ($k=8.1 \times 10^{-3} \text{ min}^{-1}$).

The prepared nanodimensional zinc ferrite-type samples demonstrate good sorption ability of the dye after the dark period varying in the range 75–90% and such materials could be used as sorbents for organic dye pollutants (Figure 3). The sorption abilities of investigated zinc containing ferrite photocatalysts increase in the following order: *Sam-*

ple 5 – ZnFe_2O_4 (75%) < *Sample 1* – $\text{Zn}_{0.25}\text{Fe}_{2.75}\text{O}_4$ (88%) < *Sample 2* – $\text{Zn}_{0.5}\text{Fe}_{2.5}\text{O}_4$ (89%) < *Sample 4* – $\text{Zn}_{0.5}\text{Fe}_{2.5}\text{O}_4$ (90%) ~ *Sample 3* – ZnFe_2O_4 (90%).

In present investigations the structural changes of nanosized zinc ferrite-type materials, after the photocatalytic degradation of Malachite green

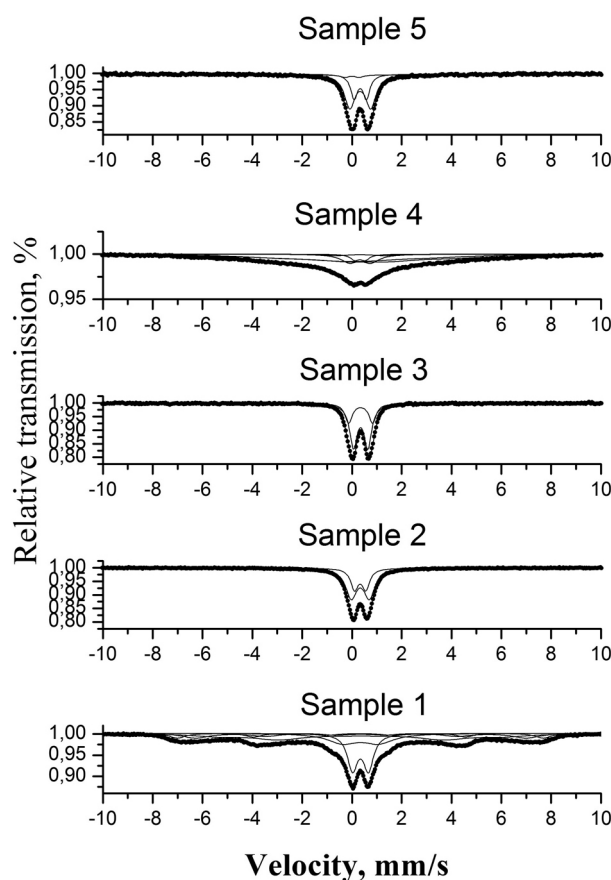


Fig. 4. Mössbauer spectra of synthesized nanosized zinc ferrite-type catalysts after photocatalytic tests

Table 1. Mössbauer parameters of nanodimensional zinc ferrite-type samples at RT after photocatalytic tests

Sample	Components	IS, mm/s	QS, mm/s	H _{eff} , T	FWHM, mm/s	G, %
Sample 1	Sxt 1 – Fe ³⁺ -tetra, spinel	0.32	0.03	45.6	0.77	10
	Sxt 2 – Fe ³⁺ -octa, spinel	0.36	–0.01	41.2	1.27	16
	Sxt 3 – Fe ions spinel	0.36	0	35.4	2.45	31
	Dbl 1 – SPM, core	0.34	0.65	0	0.49	24
	Dbl 2 – SPM, shell	0.35	1.46	0	1.46	19
Sample 2	Dbl 1 – SPM, core	0.33	0.46	0	0.37	33
	Dbl 2 – SPM, shell	0.34	0.73	0	0.54	67
Sample 3	Dbl 1 – SPM, core	0.35	0.58	0	0.37	70
	Dbl 2 – SPM, shell	0.35	0.97	0	0.35	30
Sample 4	Sxt 1 – Fe-Me	0	0	21	3.66	37
	Sxt 2 – Fe ^{2.5+} -octa, spinel	0.62	0	36	3.28	44
	Sxt 3 – Fe ³⁺ -tetra, spinel	0.33	0	37.3	0.89	3
	Dbl 1 – SPM, shell	0.33	0.86	0	0.83	12
	Dbl 2 – SPM, core	0.32	0.42	0	0.43	4
Sample 5	Sxt 1 – Fe-Me	0	0	11.7	4.80	15
	Dbl 1 – SPM, core	0.33	0.50	0	0.33	27
	Dbl 2 – SPM, shell	0.33	0.85	0	0.51	58

dye are studied with Mössbauer spectroscopy. The Mössbauer results determined nonsignificant changes of the materials when compared with the Mössbauer study of the initial nanostructure zinc ferrite-type samples Zn_xFe_{3-x}O₄ (x=0.25, 0.5, 1) discussed in [17]. As it is known the stationary composition of the catalyst is formed during the reaction so that it is possible to observe changes in the composition before and after the reaction. The Mössbauer spectra at room temperature (RT) of the ferrite samples after the catalytic tests are displayed on the Figure 4. The spectrum of *Sample 1* is superposition of three sextet and two doublet components. The doublet lines only are registered in Mössbauer spectra of *Samples 2* and *3*. The calculated Mössbauer parameters of hyperfine interactions after the best computer fitting of spectra are given in Table 1. The calculated hyperfine parameters of *Sample 1* established that sextet components can be related to tetrahedrally coordinated Fe³⁺ ions in a spinel phase – Sxt1, octahedrally coordinated Fe³⁺ in a spinel phase – Sxt2 and iron ions in a spinel phase with smaller size – Sxt3. The doublet components could be assigned the presence of ferrite particles with superparamagnetic (SPM) behaviour and sized below 10 nm for *Sample 1*. In the Mössbauer spectra at RT of *Samples 2* and *3* contain two superparamagnetic doublets attributed to the presence of ferrite particles with superparamagnetic (SPM) behaviour and intermediate phase (akaganeite) are observed. The

superposition of three or one sextet and two doublet components was registered in the Mössbauer spectra of mechanochemically treated nanodimensional zinc ferrite-type photocatalysts *4* and *5*. The calculated hyperfine parameters of doublet components could be relate to the presence of ferrite particles with superparamagnetic (SPM) behaviour. The Sxt 1 component belonging to the metal iron phase, Sxt 2 and Sxt 3 to the octahedrally coordinated Fe^{2.5+} and tetrahedrally coordinated Fe³⁺ in a spinel structure respectively.

CONCLUSIONS

The synthesized zinc ferrite-type materials used about photodegradation of Malachite green oxalate dye under UV irradiation showed good photocatalytic activity especially co-precipitated ZnFe₂O₄ (k=13.7x10⁻³min⁻¹). The investigated zinc ferrite-type photocatalysts possess good sorption ability of the dye after the dark period in the range 75–90%. The performed study determined that photocatalytic activity of zinc ferrite-type materials depends on the degree of incorporation of Zn²⁺ ions in magnetite host structure, preparation method and milling time of mechanochemical treatment. The increasing of Zn²⁺ content in magnetite host structure of powder synthesized by co-precipitation leads to formation of photocata-

lyst with higher rate constant than the other coprecipitated ferrite-type materials. The photocatalytic tests about mechanochemically treated zinc ferrite-type samples determined that photocatalytic activity increase with activation time and decreasing amount of Zn²⁺ ions incorporated in magnetite host lattice. The presence of superparamagnetic nanodimensional zinc-ferrite particles and stable catalytic behavior of tested ferrite-type materials was confirmed by Mössbauer study made after photocatalytic measurements.

Acknowledgements: The authors from IC-BAS thank the Bulgarian Science Fund of the Bulgarian Ministry of Education and Science for the financial support under Project DFNI-E01/7/2012.

REFERENCES

1. M. H. Habibi, A. H. Habibi, *Journal of Industrial and Engineering Chemistry*, **20**, 2964 (2014).
2. W. Konicki, D. Sibera, E. Mijowska, Z. Lenzion-Bieluń, U. Narkiewicz, *Journal of Colloid and Interface Science*, **398**, 152 (2013).
3. G.-Y. Zhang, Y.-Q. Sun, D.-Z. Gao, Y.-Y. Xu, *Materials Research Bulletin*, **45**, 755 (2010).
4. A. S. Albuquerque, M. V. C. Tolentino, J. D. Ardisson, F. C. C. Moura, R. Mendonça, W. A. A. Macedo, *Ceramics International*, **38**, 2225 (2012).
5. G. Fan, Z. Gu, L. Yang, F. Li, *Chemical Engineering Journal*, **155**, 534 (2009).
6. S. Sun, X. Yang, Y. Zhang, F. Zhang, J. Ding, J. Bao, C. Gao, *Progress in Natural Science: Materials International*, **22**(6), 639 (2012).
7. R. Shao, L. Sun, L. Tang, Z. Chen, *Chemical Engineering Journal*, **217**, 185 (2013).
8. S. D. Jadhav, P. P. Hankare, R. P. Patil, R. Sasikala, *Materials Letters*, **65**, 371 (2011).
9. Z. Jia, D. Ren, Y. Liang, R. Zhu, *Materials Letters*, **65**, 3116 (2011).
10. T. Xie, L. Xu, C. Liu, Y. Wang, *Applied Surface Science*, **273**, 684 (2013).
11. Y. Sun, W. Wang, L. Zhang, S. Sun, E. Gao, *Materials Letters*, **98**, 124 (2013).
12. X. Li, Y. Hou, Q. Zhao, L. Wang, *Journal of Colloid and Interface Science*, **358**, 102 (2011).
13. L. Han, X. Zhou, L. Wan, Y. Deng, S. Zhan, *Journal of Environmental Chemical Engineering*, **2**, 123 (2014).
14. M. Su, C. He, V. K. Sharma, M. A. Asi, D. Xia, X.-Z. Li, H. Deng, Y. Xiong, *Journal of Hazardous Materials*, **211–212**, 95 (2012).
15. C. G. Anchieta, A. Cancelier, M. A. Mazutti, S. L. Jahn, R. C. Kuhn, A. Gündel, O. Chiavone-Filho, E. L. Foletto, *Materials*, **7**, 6281 (2014).
16. N. M. Mahmoodi, *Materials Research Bulletin*, **48**, 4255 (2013).
17. K. Zaharieva, Z. Cherkezova-Zheleva, B. Kunev, M. Shopska, V. Petkova, J. Krstić, I. Mitov, in: Nanoscience and Nanotechnology, E. Balabanova, E. Mileva (eds.), vol. 14, 2014, p. 39.

ФОТОКАТАЛИТИЧНА АКТИВНОСТ НА НАНОСТРУКТУРИРАНИ ЦИНКОВИ ФЕРИТЕН ТИП КАТАЛИЗАТОРИ ПРИ РАЗГРАЖДАНЕ НА МАЛАХИТОВО ЗЕЛЕНО ПОД УВ-СВЕТЛИНА

М. П. Цветков^{1*}, К. Л. Захариева², З. П. Черкезова-Желева²,
М. М. Миланова¹, И. Г. Митов²

¹ Факултет по химия и фармация - Софийски университет „Св. Климент Охридски“,
бул. Джеймс Баучър 1, 1164 София, България

² Институт по катализ, Българска академия на науките, ул. „Акад. Г. Бончев“,
бл. 11, 1113 София, България

Постъпила декември, 2014 г.; приета януари, 2015 г.

(Резюме)

Серия наноструктурирани цинкови феритен тип материали $Zn_xFe_{3-x}O_4$ ($x=0,25, 0,5, 1$) със среден размер на кристалита 8 nm, получени чрез съутаяване или съутаяване и механохимична обработка, бяха тествани за фотокаталитичното разграждане на Малахитово зелено оксалат като моделен замърсител във воден разтвор при облъчване с УВ светлина. Проведените експерименти установиха, че сътаените цинкови феритен тип прахове показват по-висока фотокаталитична активност в сравнение с механохимично обработените проби: $ZnFe_2O_4$ ($k=13.7 \times 10^{-3} \text{min}^{-1}$) > $Zn_{0.5}Fe_{2.5}O_4$ ($k=10.7 \times 10^{-3} \text{min}^{-1}$) > $Zn_{0.25}Fe_{2.75}O_4$ ($k=9.4 \times 10^{-3} \text{min}^{-1}$) > $Zn_{0.5}Fe_{2.5}O_4$ (МХТ-2hours) ($k=8.1 \times 10^{-3} \text{min}^{-1}$) > $ZnFe_2O_4$ (МХТ-1hour) ($k=6.3 \times 10^{-3} \text{min}^{-1}$). Резултатите установиха, че нарастването на степента на заместване на железните йони с цинкови води до по-високи фотокаталитични активности на синтезираните феритен тип проби чрез съутаяване. Механохимичната обработка на сътаените цинкови феритен тип материали води до получаване на катализатор с по-висока фотокаталитична активност $Zn_{0.5}Fe_{2.5}O_4$ (МХТ-2часа) ($k=8.1 \times 10^{-3} \text{min}^{-1}$) с увеличаване на времето на мелене и намаляване на съдържанието на цинкови йони, включени в магнетитовата структура. Мьосбауерова спектроскопия беше извършена с цел изследване на промените в каталитичното поведение на използваните цинк феритен тип фотокатализатори при процеса на фоторазграждане на багрилото.

Compositional and structural study of partially exchanged on Na⁺, K⁺, Mg²⁺ and Ca²⁺ natural heulandite

L. Dimowa^{1*}, I. Piroeva², S. Atanasova-Vladimirova², B. Shivachev¹, S. Petrov³

¹ Institute of Mineralogy and Crystallography, Bulgarian Academy of Sciences,
“Acad. Georgi Bonchev” str. building 107, Sofia 1113, Bulgaria

² Academician Rostislav Kaishev Institute of Physical Chemistry, Bulgarian Academy of Sciences,
Acad. Georgi Bonchev str., building 11, Sofia 1113, Bulgaria

³ Department of Chemistry, University of Toronto, 80 St. George Street,
Toronto, ON, M5S 3H6 (Canada)

Received December, 2014; Revised January, 2015

Single crystals of natural heulandite (HEU) from Iskra deposit (Bulgaria) are the initial material for this study. Four parts of this material were selected and were subject to partial ion-exchange on Na⁺, K⁺, Mg²⁺ and Ca²⁺ ions. The chemical composition of the natural and the exchanged samples was obtained by EDS analysis and the derived crystal chemical formula for this HEU is Na_{1.05}K_{1.20}Ca_{1.90}Sr_{1.18})Al_{8.35}Si_{27.65}O₇₂·nH₂O. Weight losses associated with zeolitic H₂O in the channels were obtained by TG. The single crystal X-ray structural refinement revealed the topology of the framework and located the positions and site occupancies of the exchanging cations and water molecules in the channels A and B running along [010] and channel C along [001]. Initial heulandite crystals (natural HEU from Iskra deposit) contain predominantly Ca²⁺ as framework counter ion and some amounts of Na⁺, K⁺ and Sr²⁺. Sodium and strontium ions are positioned Sr and Na/Sr positions in channel A. It was found out that in this early stage of Ca-exchange that Ca²⁺ replaces Na⁺ from their mixed Na/Sr position. The K⁺-exchange leads to surplus of the positive charge, which removes indirectly Na⁺ without affecting Sr²⁺. In the Na⁺-exchanged form the sodium content increases in the mixed Na/Sr and Na position and small amount of Na⁺ is detected in the calcium position in channel B. The data obtained from EDS and structural refinement show that for the employed procedure Mg²⁺ ion exchange is not observed and its position at the center of the large channel A remains empty.

Key words: Heulandite, ion exchange, structure refinement, EDS.

INTRODUCTION

Natural zeolites are porous crystalline materials (aluminosilicates) obtained either by hydrothermal processes most commonly in cavities of basaltic lava flows, or through sedimentation and zeolitization of volcanic tuffs, etc. [1, 2]. The description of their crystal structure generally refers to two distinctive parts: a rigid negatively charged alumino-silicate framework producing two- and three-dimensional channels [3] and extraframework cations and water molecules residing in the channels. The latter are metal cations compensating the negative charge of the framework and H₂O molecules that may com-

plete the cation coordination, or can be trapped in the zeolites pores.

The capability of zeolites to exchange the extraframework cations with other cations (e.g. ion-exchange) is their most important feature for practical applications [4]. The exchange capacity and selectivity of zeolites are function of the Si/Al ratio and the types of framework pores. The HEU group includes heulandite and clinoptilolite (CPT). The crystal structures of the two zeolites are monoclinic, *C2/m*, with iso-structural spatial arrangement of the Si/Al framework. They differ between each other by Si/Al ratio, which is < 4 for HEU and > 4 for CPT. Because of this, both structures have different amount of charge balancing cations and water molecules located into the framework channels. The most common positions occupied by different extraframework cations have been described in several studies [5–8 and references within]. As heulandite

* To whom all correspondence should be sent:
E-mail: Louiza.Dimova@gmail.com

very often contains Na and Ca charge balancing cations their positions are named C1 (channel A) and C2 (channel B) respectively [5]. Potassium is also frequently detected and its position is named by Khobaer et al., 2008 [7] as K3 (in channel C). The general positions (C1, C2, K3) may be occupied simultaneously by different cations and their location within the channels can vary (be shifted) depending on the type of cation (bigger, smaller etc.). As a prominent illustration in full exchanged strontium heulandite [8] Sr is distributed in positions close to the C1 and C2 [10].

The crystal structure of HEU [9] features three sets of intersecting channels. Two of the channels are parallel to the *c*-axis as follow: the larger A channels are formed by strongly compressed ten-membered tetrahedra rings (aperture 3.0 x 7.6 Å) and the smaller B channels are confined by eight-membered tetrahedra rings (aperture 3.3 x 4.6 Å). The C channels are parallel to the *a*-axis and are also formed by eight-membered tetrahedra rings (aperture 2.6 x 4.7 Å). Thus, the structure is a pseudo-layered with layers in *ac*-plane, parallel to (010) [10–13]. The ion-exchange properties of HEU have been studied theoretically [14, 15] and were experimentally confirmed [16–24]. However, most of the research work was focused on kinetic aspects. Our opinion is that there is an insufficient knowledge on the process of cation exchange and the structural features and chemical composition of exchanged forms of HEU and CPT minerals. In this study we purposely performed a partial exchange of natural HEU with four cations: Na, K, Ca and Mg in an attempt to investigate its initial stage and to assess the structural and compositional characteristics of the exchanged forms.

EXPERIMENTAL

Ion exchange

Heulandite crystals from Iskra deposit, Haskovo, Eastern Rhodopes, were exchanged with Na⁺, Ca²⁺, K⁺ and Mg²⁺ ions. The crystals with size around 1 mm³ were selected and gently crushed to sizes of approx. 100–500 μm. Four portions of the crystals (each one of ~100 mg) were placed in Teflon autoclaves and mixed with 20 ml 1M solution of relevant metal nitrates: Na-, K-, Ca- and Mg. The autoclaves were agitated four times per day with frequently refreshed solutions. The pH of the used solution (before refreshing) was > 4.7. The exchange procedure was carried out for seven days. The exchanged crystals were thoroughly washed with distilled water and dried at room temperature.

X-ray single crystal structural refinement

The data collection was carried out on an Agilent SupernovaDual diffractometer equipped with Atlas CCD detector using micro-focus Mo/K α radiation ($\lambda = 0.71073$ Å) at 290 K. The determinations of the unit cell parameters, data collection and reduction were performed with CrysAlisPro software [25]. The structure was solved by direct methods ShelxS [26] and refined by the full-matrix least-squares method with the ShelxL-2013 programs [26]. All non-hydrogen atoms, including water molecules, were located successfully from Fourier maps and were refined anisotropically. Complete crystallographic data for the structure reported in this paper have been deposited in the CIF format with the FIZ Karlsruhe as supplementary publication No. CSD: 428990 (natural-HEU) for natural heulandite, 428991(Na-HEU) for Na⁺ exchanged heulandite, 428992(K-HEU) for K⁺-exchanged and 428993(Ca-HEU)* for Ca²⁺ exchanged.

Scanning and transmission electron microscopy (SEM)

SEM analyses were performed on a JSM 6390 electron microscope (Japan) in conjunction with energy dispersive X-ray spectroscopy (EDS, Oxford INCA Energy 350) equipped with ultrahigh resolution scanning system (ASID-3D) in regimes of secondary electron image (SEI) and back scattered electrons (BEC) mode. All samples were cleaned and completely dried before attempting SEM characterization. The samples were Carbon coated with time of coating ~20 sec. The accelerating voltage was 20 kV, I ~65 μA. The pressure was of the order of 10⁻⁴ Pa.

Differential scanning calorimetry (DSC) and thermo-gravimetric (TG) analyses

The thermal effects and mass losses were obtained by DSC/TGA analyses in a temperature range of the 20–420 °C. Small amount (10 ±0.2 mg) of the crystals from each sample were placed in alumina crucibles and the data were collected at constant heating rate of 10° min⁻¹ in an air flow of ~35 ml/min on a SETARAM, LABSYS EVO.

* Further details on the investigated cation-exchanged HEU-structures can be obtained from Fachinformationszentrum Karlsruhe, 76344 Eggenstein-Leopoldshafen, Germany (fax: (+49)7247-808-666; e-mail: crysdata@fiz-karlsruhe.de; http://www.fiz-karlsruhe.de/request_for_deposited_data.html).

RESULTS AND DISCUSSION

The DSC-TGA curves of the samples (Fig. 1) disclose the typical thermal behavior of HEU with expected release of the extra-framework water at relatively wide temperature range (70–170 °C). The amounts of released water vary slightly around 8.1 wt.% (natural-HEU), 7.1 wt.% (Na-HEU), 5.7 wt. (K-HEU) and 8.5% wt. (Ca-HEU). The destruction of the Si/A framework occurs at about 350 °C and is not associated with weight losses as the related high-temperature Al-Si-O compounds are stable at this temperature.

The chemical composition for all samples was calculated based on 72 framework oxygen. The results are given in Table 1. The composition of natural HEU shows that it is dominantly Ca-form containing some Na⁺, K⁺ and Sr²⁺ as well.

The chemical composition of the natural and partially exchanged HEU obtained from single crystal structures refinement (for the exchanging cations)

Table 1. Chemical composition of natural and exchanged heulandite (EDS)

Sample	Crystal-chemical formulae
natural HEU	(Na _{1.05} K _{1.2} Ca _{1.9} Sr _{1.18})Al _{8.35} Si _{27.65} O ₇₂
Na-HEU	(Na _{2.1} K _{0.32} Ca _{1.8} Sr _{1.08})Al _{8.4} Si _{27.60} O ₇₂
K-HEU	(Na _{0.35} K _{2.05} Ca _{1.75} Sr _{1.18})Al _{8.28} Si _{27.72} O ₇₂
Ca-HEU	(K _{1.0} Ca _{2.55} Sr _{1.1})Al _{8.46} Si _{27.54} O ₇₂

and by EDS (for Si and Al) are given in Table 2. It is worth to note that the cations amounts evaluated by EDS are lower than the ones assessed from single crystal structural data. Given the intrinsic limitations of EDS analysis due to its local sample probing and shallow surface penetration (1–2 μm), we choose to use the cations contents and their site occupancies derived from single crystal structural refinement.

The chemistry of the other three ion-exchanged samples shows different degree of partial ion exchange for Na⁺, K⁺ and Ca²⁺, which will be discussed below.

The purpose of the single crystal structure refinement was to review and compare the structural features of ion-exchanged HEU samples to these of the natural one. The crystal structures of all 4 samples with located positions of the cations and H₂O molecules are displayed on Fig. 3, while Table 3 show the evaluated site occupancies for all participating exchanging cations.

In the natural HEU, which is dominantly a calcium form, almost all amount of Ca²⁺ cations is located in the split Ca-position Ca2 (C2 according to Alberti, 1973 [5]) in the smaller channel B. Potassium is located in its usual position K (K3 according to Khobaer et al., 2008 [7]) at the intersection of channels A and C (Fig. 3 and Table 3).

It is interesting that the regular Na-position (C1 according to Alberti, 1973 [5]) in channel A in the structure of the natural-HEU is transformed to one mixed Na/Sr and one – Sr. In fact, they are located so close to each other that could be considered as a single crystallographic site with a complex cation occupancy. A clear separation of the two sub-sites is visible on Fig. 3 due to the difference in their ionic radii and scattering power. This complex cation site accommodates the initial amounts of Sr²⁺ and Na⁺ and even some extra Ca²⁺.

The detected water molecules are distributed amongst five positions. Three of the positions are located in channel A: Ow1, Ow2 and Ow3 [6, 7]. Water molecules are in positions (Ow1, Ow2) sitting on the mirror plane coordinating Na and Sr

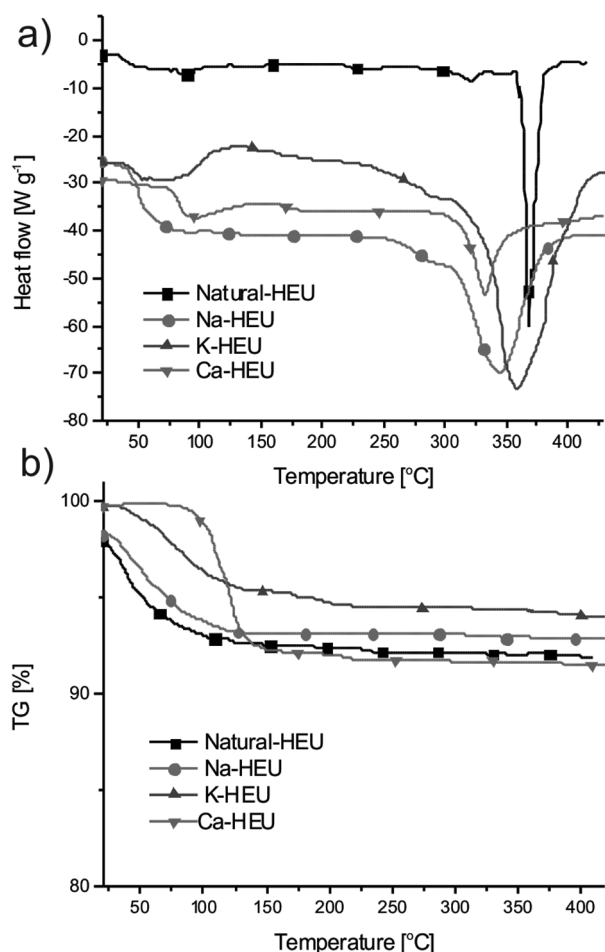


Fig. 1. DSC and TG curves of natural heulandite and exchanged forms

Table 2. Compositional and structural data obtained from single crystal structure refinement of native and cation exchanged forms of heulandite

Compound reference	Natural-HEU	Na-HEU	K-HEU	Ca-HEU
Chemical formula	(Na _{1.18} K _{1.44} Ca _{1.89} Sr _{1.43}) [*] Al _{8.35} Si _{27.65} O ₇₂ ·H ₂ O _{20.99}	(Na _{2.54} K _{0.40} Ca _{1.80} Sr _{1.28}) [*] Al _{8.35} Si _{27.65} O ₇₂ ·H ₂ O _{22.48}	(Na _{0.37} K _{2.18} Ca _{1.81} Sr _{1.43}) [*] Al _{8.3} Si _{27.7} O ₇₂ ·H ₂ O _{20.77}	(K _{1.30} Ca _{2.60} Sr _{1.28}) [*] Al _{8.46} Si _{27.54} O ₇₂ ·H ₂ O _{20.45}
a/Å	17.7671(9)	17.7207(11)	17.7378(11)	17.7176(7)
b/Å	17.8308(7)	17.8236(8)	17.8568(8)	17.9418(6)
c/Å	7.4340(4)	7.4352(4)	7.4247(5)	7.4277(3)
α/°	90	90	90	90
β/°	116.458(6)	116.484(8)	116.560(8)	116.490(5)
γ/°	90	90	90	90
Unit cell volume/Å ³	2108.4(2)	2101.9(2)	2103.5(2)	2113.27(16)
Temperature/K	290(2)	290(2)	290(2)	290(2)
Space group	C2/m	C2/m	C2/m	C2/m
No. of formula units per unit cell, Z	1	1	1	1
Radiation type	MoKα	MoKα	MoKα	MoKα
Absorption coefficient, μ/mm ⁻¹	1.73	1.59	1.76	1.66
No. of reflections measured	7510	9420	9729	9697
No. of independent reflections	3053	3406	3415	3441
No. of reflections with I > 2σ(I)	2587	2917	2980	3062
θ _{max} /θ _{min} , °	30.7/3.4	31.7/3.0	32.1/3.0	32.0/3.0
Parameters	182	198	179	183
Refinement/Least-squares matrix	F ² /full	F ² /full	F ² /full	F ² /full
R _{int}	0.0328	0.0333	0.0395	0.0322
Final R ₁ values (I > 2σ(I))	0.0577	0.0441	0.054	0.0589
Final wR(F ²) values (I > 2σ(I))	0.1336	0.1504	0.1347	0.1466
Final R ₁ values (all data)	0.0685	0.0531	0.0626	0.0659
Final wR(F ²) values (all data)	0.1386	0.1599	0.1393	0.1501
Goodness of fit on F ²	1.181	1.155	1.195	1.233

* The amount of the cations is calculated based on their site occupancies from structure refinement, while Al and Si contents are obtained from EDS analysis.

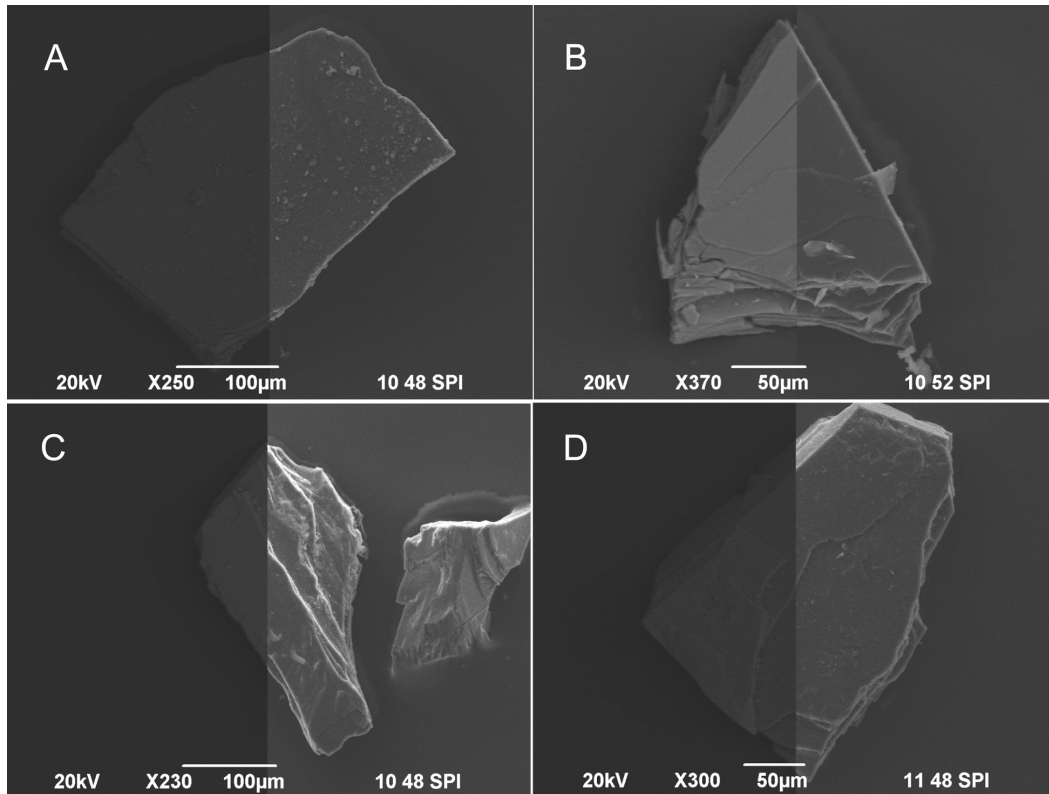


Fig. 2. SEM morphology of A) natural HEU, B) Ca-HEU, C) K-HEU and D) Na-HEU

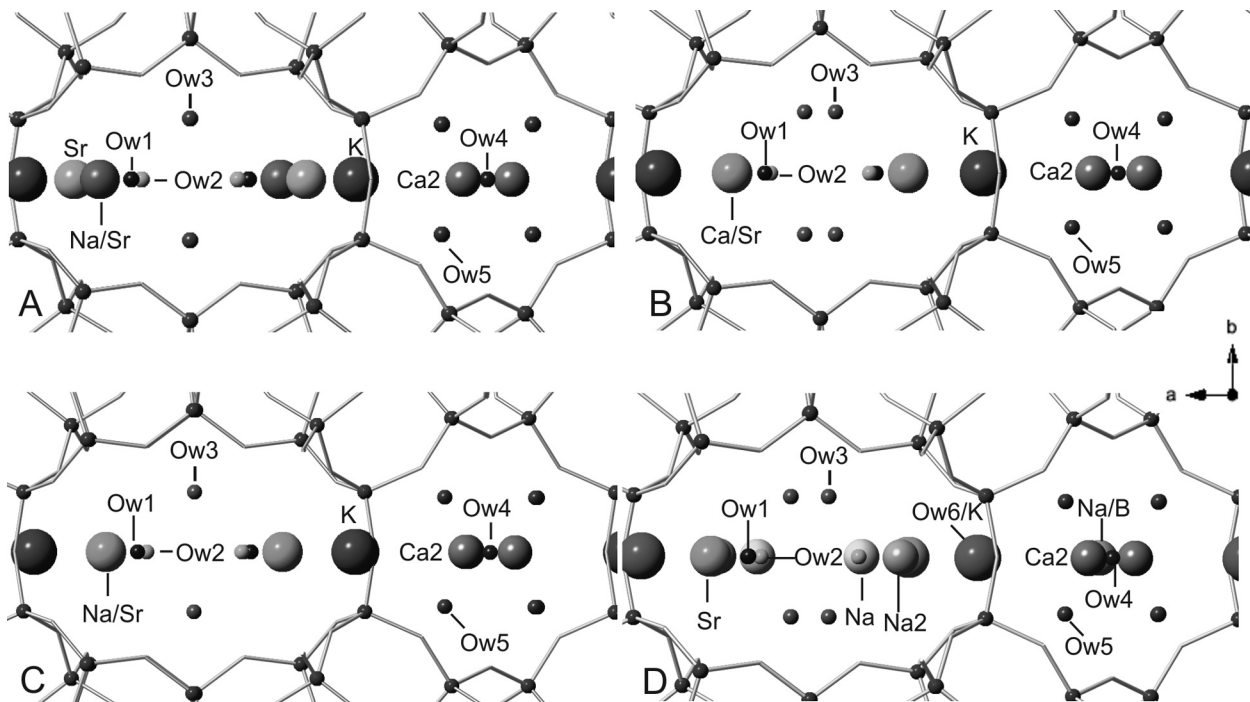


Fig. 3. Cation and H₂O positions in natural heulandite end exchanged forms. A) natural-HEU, B) Ca-HEU, C) K-HEU and D) Na-HEU

Table 3. Occupancy of the cation positions as displayed on Fig. 3

Channel	Cation positions (references)	Cation positions (Fig. 3)	Occupancy of the cation positions			
			nat-HEU	Ca-HEU	Na-HEU	K-HEU
A	C1[5]	Na/SrCa/SrNa	0.29/0.3	0.18/0.32	0.4	0.09/0.36
A	C1[5]	Na			0.18	
A	C1[5]	Sr	0.05		0.32	
B	C2[5]	Ca ²⁺	0.47	0.47	0.45	0.45
B	C2[5]	Na			0.06	
C	K3[7]	K	0.36	0.32	0.1	0.54

cations. Water molecule Ow3 is positioned on two folder axis and coordinate Na/Sr position. Waters molecules Ow4 and Ow5 [6, 7] are located in channel B participating in Ca coordination (position C2).

It was found out that at this early stage of cation exchange, Ca-HEU (Fig. 3-B) does not provide significant changes in the structure. As expected, the Ca content increases twice and because the occupancies of the Ca-sites in channel B are almost full (0.47), the excess of Ca²⁺ completely replaces Na in the mixed Na/Sr position as it is transformed to a Ca/Sr one. The located in the channels water molecules (positions Ow1, Ow2, Ow4 and Ow5) remain at the same positions as in the natural HEU, while Ow3 is split in two causing a decrease of occupancy from ~1 to 0.5 apu. Probably the split is due to the presence of two bivalent cations in the mixed Ca/Sr position.

The partial exchange on K in the K-HEU (Fig. 3-C) increases the K⁺ content in the unit cell from 1.3–1.4 to 2.18 apu. While the contents of Ca²⁺ in Ca2 position and Sr²⁺ in the mixed Na/Sr position are not quite affected, the extra K⁺ ions are filling up to the limit the position in channel C (K3 according to Khobaer 2008 [7]). Due to the requirement that the sum of K, Sr and Na should not exceed 1, this leads to indirect displacement of Na⁺ from its Na/Sr position decreasing 3 times of its content in the unit cell. The five water positions (Ow1-5) remain unchanged.

In the Na-HEU, Na⁺ increased its content in the unit cell twice. Na and Sr cations are distributed in three disordered positions close to the Na one (C1 according to Alberti, 1973 [5]). These positions are indicated as Na, Na2 and Sr on Fig. 3 and their combined occupancies are close to 1 (full occupancy). This causes an indirect displacement of K⁺ in its position in channel C, which content dropped down more than 3 times – from 1.44 to 0.4 apu. Ow3 water position is splitting by two

creating 4 crystallographic sites positioned closer to the two Na-enriched positions in channel A. Potassium shared its position with H₂O molecule named Ow6. (Table 3-D and Fig. 3). Small amount of Na⁺ is detected in Ca position in channel B. Small amount of Na⁺ is detected in Ca position in channel B.

Finally, both EDS and structural refinement of Mg-HEU, could not register the presence of Mg²⁺. The refinement of the so called Mg-HEU samples (two single crystal experiments on different crystals were performed) established that the assumed Mg position M4 [13] located in the center of the A channel is empty. This finding correlates with the results from EDS analysis and ultimately proves that the Mg²⁺ ions do not participate in the exchange under the applied exchanging conditions.

CONCLUSIONS

The performed DSC/TGA analyses, chemical analyses (EDS) and single crystal structure refinements presented in this study aimed to bring some light on the effect of partial cation exchange with K⁺, Na⁺, Ca²⁺ and Mg²⁺ of natural heulandite from Iskra deposit. The natural HEU is Ca-HEU form although some amounts of Na, K and Sr cations are also detected in its structure. It was found out that for the employed conditions no Mg ion-exchange is observed. The single crystal structural refinement of the Na- K- and Ca-exchanged HEU-forms shows that at the early stage of ion-exchange (up to seven (7) days) only cations located in the large channel A are affected except the Sr²⁺ one. The amounts of Ca²⁺ in channel B remain almost unchanged.

Acknowledgments: This work was supported by ESF Grant BG051PO001-3.3.06-0027 and NSFB grant DRNF02/1.

REFERENCES

1. E. M. Flanigen, L. B. Sand, American Chemical Society, Division of Colloid and Surface Chemistry, Molecular sieve zeolites, American Chemical Society, Washington, Advances in chemistry series, 1971, p. 101.
2. P. A. Wright, Royal Society of Chemistry (Great Britain), Microporous framework solids, RSC Publishing, Cambridge, U.K., RSC materials monographs, 2008.
3. R. Xu, Chemistry of zeolites and related porous materials: synthesis and structure (John Wiley & Sons (Asia), Singapore; Hoboken, N. J., 2007.
4. A. A. Zagorodni, Ion exchange materials: properties and applications (Elsevier, Amsterdam; Boston, 2007), 1st edn.
5. A. Alberti, *Tschermaks Min. Petr. Mitt.* **19**, 173 (1973).
6. A. O. Larsen, F. S. Nordrum, N. Döbelin, T. Armbruster, O. V. Ptersen, M. Erambert, *Eur. J. Mineral.*, **17**, 143 (2005).
7. T. M. Khobaer, T. Kuribayashi, K. Komatsu, Y. Kudoh, *Journal Of Mineralogical And Petrological Sciences*, **103**, 2, 61 (2008).
8. N. Döbelin, T. Armbruster, *American Mineralogist*, **88**, 527 (2003).
9. C. Baerlocher, L. B. McCusker, D. H. Olson, Atlas of zeolite framework types, Elsevier B.V., 2007, 7-th edn.
10. A. Alberti, *Tschermaks mineralogische und petrographische Mitteilungen*, **18**, 129 (1972).
11. A. Alberti, *Tschermaks mineralogische und petrographische Mitteilungen*, **22**, 25 (1975).
12. A. Alberti, G. Vezzalini, *Tschermaks mineralogische und petrographische Mitteilungen*, **31**, 259 (1983).
13. K. Koyama, Y. Takéuchi, *Zeitschrift für Kristallographie*, **45**, 216 (1977).
14. A. Galarneau, Zeolites and mesoporous materials at the dawn of the 21st century (Proceedings of the 13th International Zeolite Conference, Montpellier, France, 8-13 July 2001), Elsevier, Amsterdam; New York, 1st edn., Stud. Surf. Sci. Catal., 2001, p. 135.
15. G. Eisenman, *Biophys. J.*, **2**, 259 (1962).
16. L. Dimova, O. Petrov, M. Kadiyski, N. Lihareva, A. Stoyanova-Ivanova, V. Mikli, *Clay Minerals*, **46**, 205 (2011).
17. L. Dimova, B. L. Shivachev, R. P. Nikolova, *Bulg. Chem. Comm.*, **43**, 217 (2011).
18. H. Faghihian, M. G. Marageh, H. Kazemian, *Appl. Radiat. Isot.*, **50**, 655 (1999).
19. V. J. Inglezakis, H. P. Grigoropoulou, *Microporous Mesoporous Mater.*, **61**, 273 (2003).
20. V. J. Inglezakis, M. D. Loizidou, H. P. Grigoropoulou, *J. Colloid Interface Sci.*, **261**, 49 (2003).
21. V. J. Inglezakis, A. A. Zorpas, M. D. Loizidou, H. P. Grigoropoulou, *Microporous Mesoporous Mater.*, **61**, 167 (2003).
22. A. Langella, M. Pansini, P. Cappelletti, B. de Gennaro, M. de' Gennaro, C. Colella, *Microporous Mesoporous Mater.*, **37**, 337 (2000).
23. K. Margeta, N. Z. Logar, M. Љbiljeg, A. Farkaљ, Natural Zeolites in Water Treatment – How Effective is Their Use, 2013, Water Treatment.
24. S. K. Oukiand M. Kavannagh, *Water Sci. Technol.*, **39**, 115 (1999).
25. CrysAlis PRO, Agilent Technologies, UK Ltd, Yarnton, England, 2011.
26. G. M. Sheldrick, *Acta Cryst. A*, **64**, 112 (2008).

СЪСТАВ И СТРУКТУРА НА ЧАСТИЧНО ОБМЕНЕН НА Na⁺, K⁺, Mg²⁺ И Ca²⁺ ПРИРОДЕН ХЕЙЛАНДИТ

Л. Димова^{1*}, И. Пироева², С. Атанасова-Владиминова²,
Б. Шивачев¹, С. Петров³

¹ *Институт по Минералогия и Кристалография, Българска Академия на Науките,
ул. „Акад. Георги Бончев“, бл. 107, София 1113, България*

² *Институт по физикохимия, Българска Академия на Науките, ул. „Акад. Георги Бончев“,
бл. 11, София 1113, България*

³ *Химически факултет, Университет в Торонто, ул. „Сейнт Джордж“ 80,
Торонто, ОН, М5S 3Н6 Канада*

Постъпила декември, 2014 г.; приета януари, 2015 г.

(Резюме)

Използваният материал е монокристален природен хейландит от находище Искра (България). Изходните монокристали са разделени на четири части и е осъществен йонообмен на Na⁺, K⁺, Mg²⁺ и Ca²⁺. Химичният състав на изходния природен и йонообменените хейландитни форми е направен чрез енергийно дисперсионна рентгенова спектроскопия като получената кристалохимична формула за природния хейландит е (Na_{1.05}K_{1.20}Ca_{1.90}Sr_{1.18})Al_{8.35}Si_{27.65}O₇₂·nH₂O. Тегловните загуби, свързани със зеолитната вода в каналите, са получени чрез термо-гравиметричен анализ. Монокристалният рентгеноструктурен анализ разкрива топологията на зеолитния скелет, позициите и заетостта на намиращите се в каналите катиони, водни молекули на природната и обменени форми. Кристалите на природния хейландит (от находище Искра) съдържат предимно Ca²⁺ и по-малки количества от Na⁺, K⁺ и Sr²⁺ катиони, които компенсират негативния заряд на Al/Si скелет. Натриевите и стронциевите йони са позиционирани в канал А. Частичният Ca-обмен показва, че в първоначално Ca²⁺ измества Na⁺ от общата Na/Sr позиция в канал А. Калиевият йонообмен води до излишък на положителния заряд, като това води до индиректно изместване на Na⁺, без да се засяга количеството на Sr²⁺. При натриевия йонообмен се увеличава съдържанието на натрий в общата Na/Sr позиция като Na⁺ се позиционира и в канал В, допълвайки Ca²⁺. Данните, получени от енергийно дисперсионната рентгенова спектроскопия и от структурната разшифровка на магнезиево обменен природен монокристал от находище Искра, показват, че йонообменът с Mg²⁺ не се наблюдава, като позицията в центъра на „големия А канал“ остава празна.

Intensity and SAR dependent changes in conformation of frog skeletal muscle total protein content after irradiation with 2.45 GHz electromagnetic field

T. I. Apostolova*

*Department of excitable structures, Institute of Biophysics and Biomedical engineering,
Bulgarian Academy of Sciences, Sofia, Bulgaria*

Received December, 2014; Revised January, 2015

A study of the influence of 2.45 GHz electromagnetic field with high (20 mW/cm²) and low (10 mW/cm²) intensities on frog skeletal muscle protein conformation was engaged. Two different fractions (centrifuged at 900 g and 9600 g respectively) were preliminary exposed with the electromagnetic field and others were sham exposed. The same ones were lyophilized after that and processed with Fourier transform infrared spectroscopy using Bruker IFS 113 v. Specific absorption rate was calculated for both fractions and field intensities. The water mask was removed mathematically. The characteristic peaks and shoulders from Amid I and Amid II bands (descriptive for protein secondary structures) were decomposed and the area under them was calculated. The percentage decrease of α -helices after irradiation with the two intensity fields and in both fractions was observed. The changes of β -sheets, parallel β -structures, turns, bends and random coils were intensity and specific absorption rate dependent. Because of the temperature controlled conditions during the whole time of irradiation, we argue that these conformational changes are specific, non-thermal.

Key words: electromagnetic field, protein conformation, infrared spectroscopy, frog skeletal muscle.

INTRODUCTION

The investigations of microwave electromagnetic fields (EMF) and their influence on different biological structures exponentially increased during the last 30 years. This fact is due to the increased use and hence increasing exposure of different human groups. At the same time, the therapeutic use of EMFs in medical practice has increased markedly.

The cellular and sub-cellular mechanisms of the EMF effects are not yet well understood. There are different hypothesis and model investigations, but still there is no agreement achieved about the common mechanisms of EMF action on biological systems. The effects of microwaves (MMW) are usually classified as thermal (heat-producing) and non-thermal (specific, below the thermal noise at physiological temperatures). Many authors accept that the effects of MMW are due only to the temperature rising in the irradiated object [1–9]. In the

case of large molecules the energy shares out in the whole molecule and not enough quantity remains to cause covalent bonds breaking. The energy is taking out from the system with oscillating atoms and converts to heat. In the biological systems the absorbed microwave energy transforms to the increasing kinetic energy, which in that way causes common heating of the different tissues. This heating is a result from ion conductance and vibration of dipole water molecules and peptides [10, 11]. The MMW absorption depends on the medium electrical properties – dielectric constant, electrical conductance and hence wave penetration depth. These properties are changing with EMF frequency [12]. On the basis of these properties one can define the depth of penetration of the EMF of particular frequency. In tissues with low water content (like adipose tissue) the penetration of EMF is vastly higher than in these with high water content (like muscle tissue). At the same time the depth of penetration decreases with frequency growth.

The interaction between MMW and living creatures depends on characteristics like field oscillation frequency and field intensity. Relative boundary between low- and high-intensity EMF is accepted to

* To whom all correspondence should be sent:
E-mail: tivukova@bio.bas.bg

be 10 mW/cm² [13]. At sub-cellular level the action of EMF is connected with dielectric properties of biomacromolecules and macromolecule aggregates, as enzyme complexes, membrane receptors and ion channels [14]. If one applies conventional heating, the kinetic energy is introduced in all molecules, while after EMF irradiation the influence is on polarized and charged molecules, and ions. As the water molecules possess large polar moment they absorb the microwave energy with priority, and hence become more mobile and probably more reactive [15].

There are no controversial opinions observed concerning the nonspecific – temperature effects of MMWs up to this moment. With regard to the specific – non-temperature effects of MMWs consensus is not achieved presently. Despite all that, we can find out in literature the increasingly experimental and model data about these effects. Recently published experimental data argues about specific effect on protein conformation of EMF field with frequency 1765 MHz and 800 mW/m² power density on myoglobin structure through increasing of β -sheet content with respect to α -helix content decreasing [16]. The same authors [17] observed similar effects on bovine ground meet after irradiation with 2.45 GHz MMW.

We were inspired by these data to further investigate whether there is any specific (non-thermal) effect of 2.45 GHz electromagnetic field with low (10 mW/cm²) and high (20 mW/cm²) power densities on compound protein, derived from frog skeletal muscle.

EXPERIMENTAL

Object and methods of investigation

Striated muscles from summer and autumn frogs (*Rana ridibunda*) was homogenized with 0.5 M Na/P buffer pH 7.6 for 1 minute. The homogenate was centrifuged after that for 15 minutes at 900 g (3600 ob./min) at 4° C. The supernatant was centrifuged after that for 30 min at 9600 g (12000 ob./min). At this stage nuclei and mitochondria were removed. The obtained fractions were divided into two equal quantities of a 15 ml and were placed in two Petri dishes with 96 mm diameter, making thin films of a 2 mm on the bottom of the dishes. The Petri dishes after that were placed at 25 °C temperature. One of the dishes was irradiated for 30 min with 2.45 GHz electromagnetic field (10 and 20 mW/cm² power density), whereas the other was sham exposed at this time. Two probes were placed on ice in order to maintain constant temperature. At the end of irradiation the temperature changes were between 1.8–2 °C.

The fractions were then lyophilized with USIFROID SMH50 for 44 hrs. at a temperature 45 °C and 180 μ Bar pressure. The lyophilized probes were analyzed by Fourier transform infrared spectroscopy (FTIRS) in order to analyze the conformational changes of compound proteins in lyophilized probes. FTIRS was made at three reiterations in KBr tablets in absorption interval of 1800–1400 cm⁻¹ with accuracy 0.1–0.2 cm⁻¹ on Bruker IFS 113 V apparatus.

Computation and statistical analysis

Structural information and quantity information about the protein secondary structures is obtained by decomposition of Amid I and Amid II bands at the interval of 1800–1400 cm⁻¹ using the method of Arrondo et al. [18, 19]. The procedure is based on deconvolution of the curve of infrared spectre and its compounds in boundaries of Amid I and Amid II bonds. The first step is evaluation of the characteristic shoulders and peaks and rough assessment of their shape (width and height). This operation is necessary for the start of the iterative procedure with Gaussian functions. After this operation the area under the peaks and shoulders is determined. The information from Amid I (1600–1700 cm⁻¹) band is due to vibrational stretching of C=O peptide groups (nearly 80%), whereas the Amid II band (1510–1580 cm⁻¹) is characteristic for β -sheets movement. The calculation procedure was made by MATLAB package.

The data for the secondary structures were presented as mean values \pm standard deviation (SD). One-way ANOVA was used to evaluate the statistically significant differences between exposed and sham exposed groups with high- and low-intensity fields (with 20 and 10 mW/cm² intensities respectively). In all four groups of experiments the number of reiterations were eight (n=8) in order to achieve Gaussian distribution.

The specific absorption rate (SAR) calculation

The magnetic permeability of most tissues is practically equal to that of free space, and all known and anticipated interactions at higher radio frequencies occur through mechanisms involving the electrical (E) field (including the currents induced by the magnetic (H) field). Therefore, the E-field vector, or its distribution throughout the exposed object, fully describes the exposure field-tissue interactions. A dosimetric measure that has been widely adopted is the specific absorption rate (SAR) defined as “the time derivative of the incremental energy absorbed by, or dissipated in an incremental mass contained in a volume element of a given density” and is cal-

culated using the Poynting vector theorem for sinusoidal varying electromagnetic fields [20].

The model of SAR calculation was based on the assessment of the energy across a plane section of the flux, formed by a cone with a vertex in the amplitude centre. Homogenous electrical field represented the flux in the cone. The average SAR, defined as a ratio between the total energy absorbed in the exposed object (E_t) and its mass (m_t), is:

$$SAR = \frac{E_t}{m_t}$$

The energy was defined from the densities of the electric components of the generated electromagnetic field and the characteristic parameters of the exposed object. The average SAR was calculated according to the mathematical model described earlier [21]. SAR values for the fraction centrifuged at 900 g was: for low intensity field (10 mW/cm²) – 4.92 mW/mg; for high intensity field (20 mW/cm²) – 9.83 mW/mg. SAR values for the fraction centrifuged at 9600 g was 5.08 mW/mg and 10.2 mW/mg respectively.

RESULTS

Changes of secondary structures in membrane fraction centrifuged at 900 g after irradiation

The Amid I band is localised between 1600 cm⁻¹ and 1800 cm⁻¹ and Amid II band is localised be-

tween 1510 cm⁻¹ and 1580 cm⁻¹. The peaks and shoulders content is characteristic for the secondary protein conformation.

The data from FTRIS show changes of the absorption maximum compared to the control at 1653 cm⁻¹ in all groups observed. Additional absorption peaks were observed at 1695 cm⁻¹, 1683 cm⁻¹, 1645 cm⁻¹ and 1635 cm⁻¹, as well as weak shoulders at 1657 cm⁻¹ and 1617 cm⁻¹ (Figs 1 and 2). The maximum of the peak in Amid II band is at 1599 cm⁻¹ with additional absorption peaks at 1576 cm⁻¹, 1559 cm⁻¹, 1719 cm⁻¹, and 1507 cm⁻¹ and a shoulder at 1521 cm⁻¹ (Figs 1 and 2 down curves). Out of the characteristic Amid I and Amid II curves was observed one more characteristic peak at 1733 cm⁻¹ which depicts weak lipid-protein interactions.

After irradiation with low-intensity field (10 mW/cm²) (Fig. 1 upper curve) the maximum in Amid I band is once again at 1653 cm⁻¹, but there are additional shoulders at 1695 cm⁻¹ and 1657 cm⁻¹. In Amid II band the peak at 1549 cm⁻¹ is shifted at 1547 cm⁻¹ with additional absorptions at 1576 cm⁻¹, 1540 cm⁻¹ and 1505 cm⁻¹.

The irradiation of probes with high intensity EMF (20 mW/cm²) (Fig. 2, down curve) the absorption peaks of Amid I band are at 1695 cm⁻¹, 1685 cm⁻¹, 1643 cm⁻¹, 1635 cm⁻¹, 1617 cm⁻¹ and 1602 cm⁻¹ with maximum peak at 1653 cm⁻¹. In Amid II band the maximums are at 1559 cm⁻¹ and 1540 cm⁻¹, with additional absorption shoulders at 1576 cm⁻¹, 1571 cm⁻¹, 1554 cm⁻¹, 1547 cm⁻¹, 1521 cm⁻¹, and 1508 cm⁻¹.

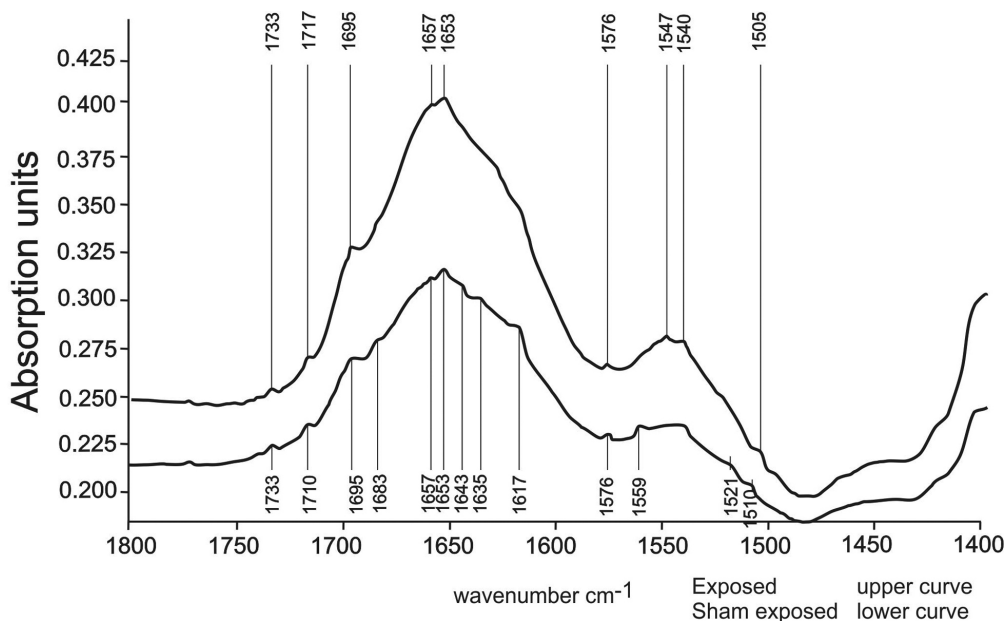


Fig. 1. Example of infrared spectra from sham exposed (lower curve) lyophilised homogenates of frog skeletal muscle, centrifuged at 900 g, and from exposed ones (upper curve) with low intensity field (10 mW/cm²)

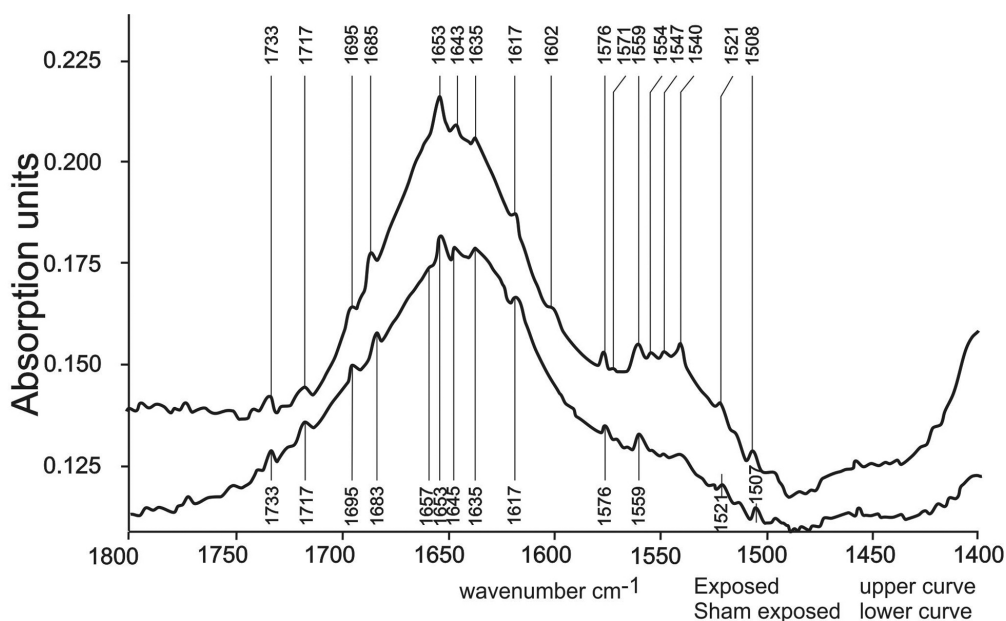


Fig. 2. Example of infrared spectra from sham exposed (lower curve) lyophilised homogenates of frog skeletal muscle, centrifuged at 900 g, and from exposed ones (upper curve) with high intensity field (20 mW/cm²)

The percentage changes of the basic secondary structures of low intensity (Table 1) and high intensity-field was calculated (Table 2) on the basis of these characteristic peaks and shoulders. I observed statistical significant changes of α -helices after irradiation with both intensities (Table 1 and 2). The

low intensity field influenced statistically significant unordered structures (turns, bends and coils) (Table 1). The high intensity field caused statistically significant lowering of parallel β -structures, as well as statistically significant increasing of unordered structures (Table 2).

Table 1. Quantification of secondary peptide structure derived from peaks and shoulders obtained from FTIRS of sham exposed and exposed with low intensity field (10 mW/cm²) homogenates of frog skeletal muscle, centrifuged at 900 g (first column). Second column – the quantity in percentage of corresponding peaks and shoulders

Sham exposed		Exposed	
(1)	(2)	(1)	(2)
α -helices 1653 cm ⁻¹ 1557 cm ⁻¹	Total 38%±3.9%	α -helices 1653 cm ⁻¹ 1557 cm ⁻¹	Total 29%±3.6%*
β -sheets 1695 cm ⁻¹ 1683 cm ⁻¹ 1617 cm ⁻¹ 1576 cm ⁻¹	Total 22 %±1.8%	β -sheets 1695 cm ⁻¹ 1683 cm ⁻¹ 1617 cm ⁻¹ 1576 cm ⁻¹	Total 23%±2.54%
parallel β -structures 1643 cm ⁻¹ 1635 cm ⁻¹	Total 10%±1.13%	parallel β -structures 1643 cm ⁻¹ 1635 cm ⁻¹	Total 9%±1.73%
Turns, bends and random coils 1626 cm ⁻¹ 1521 cm ⁻¹	Total 30%±3.5%	Turns, bends and random coils 1626 cm ⁻¹ 1521 cm ⁻¹ 1505 cm ⁻¹	Total 39%±2.28%*

Table 2. Quantification of secondary peptide structure derived from peaks and shoulders obtained from FTIRS of sham exposed and exposed with high intensity field (20 mW/cm²) homogenates of frog skeletal muscle, centrifuged at 900 g (first column). Second column – the quantity in percentage of corresponding peaks and shoulders

Sham exposed		Exposed	
(1)	(2)	(1)	(2)
α -helices 1653 cm ⁻¹ 1559 cm ⁻¹	Total 38%±2%	α -helices 1653 cm ⁻¹ 1559 cm ⁻¹	Total 30%±2.91%*
β -sheets 1695 cm ⁻¹ 1683 cm ⁻¹ 1617 cm ⁻¹ 1507 cm ⁻¹	Total 22 %±2.33%	β -sheets 1695 cm ⁻¹ 1683 →1685cm ⁻¹ 1617 cm ⁻¹ 1507→1508 cm ⁻¹	Total 21 %±2.07%
parallel β -structures 1643 cm ⁻¹ 1635 cm ⁻¹	Total 10%±1.6%	parallel β -structures 1643 cm ⁻¹ 1635 cm ⁻¹	Total 35%±3.76%***
Turns, bends and random coils 1626 cm ⁻¹ 1521 cm ⁻¹	Total 30%±2.56%	Turns, bends and random coils 1602 cm ⁻¹ 1521 cm ⁻¹	Total 14%±1.03%***

Changes of secondary structures in fraction centrifuged at 9600 g

The absorptions of the probes irradiated with low- and high-intensity fields in comparison to their sham exposed controls are shown on Figs. 3 and 4. The data from sham exposed preparation showed main absorption maximum at 1653 cm⁻¹ in Amid I band. Additional absorption peaks are observed at

1695 cm⁻¹, 1684 cm⁻¹, 1635 cm⁻¹, as well as weak shoulders at 1626 cm⁻¹ and 1617 cm⁻¹ (Figs 3 and 4, lower curves). For Amid II band the maximum is localised at 1558 cm⁻¹ and there are additional absorption peaks at 1576 cm⁻¹, 1533 cm⁻¹, 1516 cm⁻¹ and 1507 cm⁻¹ with absorption shoulder at 1521 cm⁻¹ (Figs 3 and 4, down curves).

After irradiation with both intensity fields, the maximums are shifted from 1653 cm⁻¹ to 1657 cm⁻¹

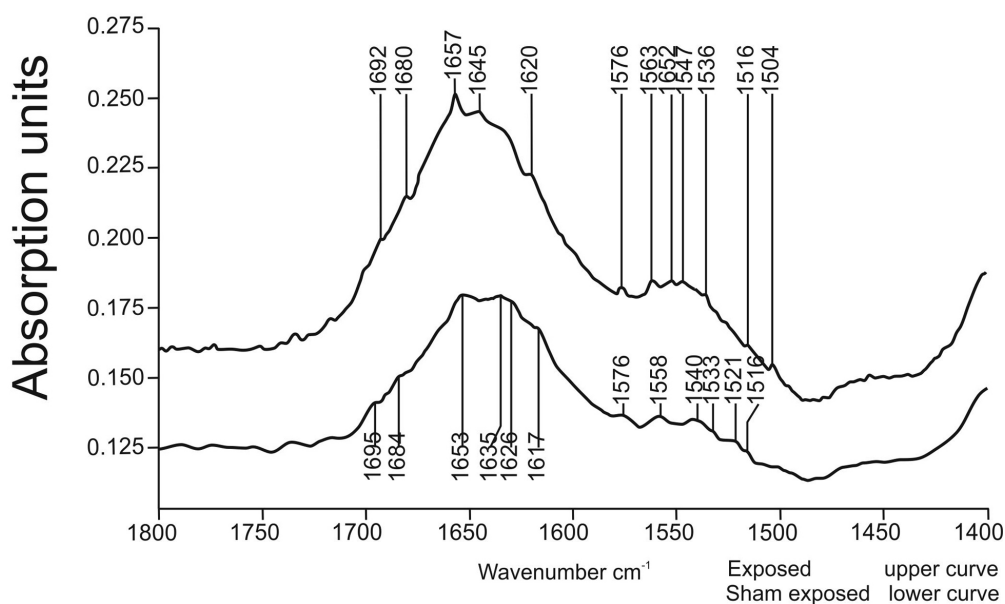


Fig. 3. Example of infrared spectra from sham exposed (lower curve) lyophilised homogenates of frog skeletal muscle, centrifuged at 9600 g, and from exposed ones (upper curve) with low intensity field (10 mW/cm²)

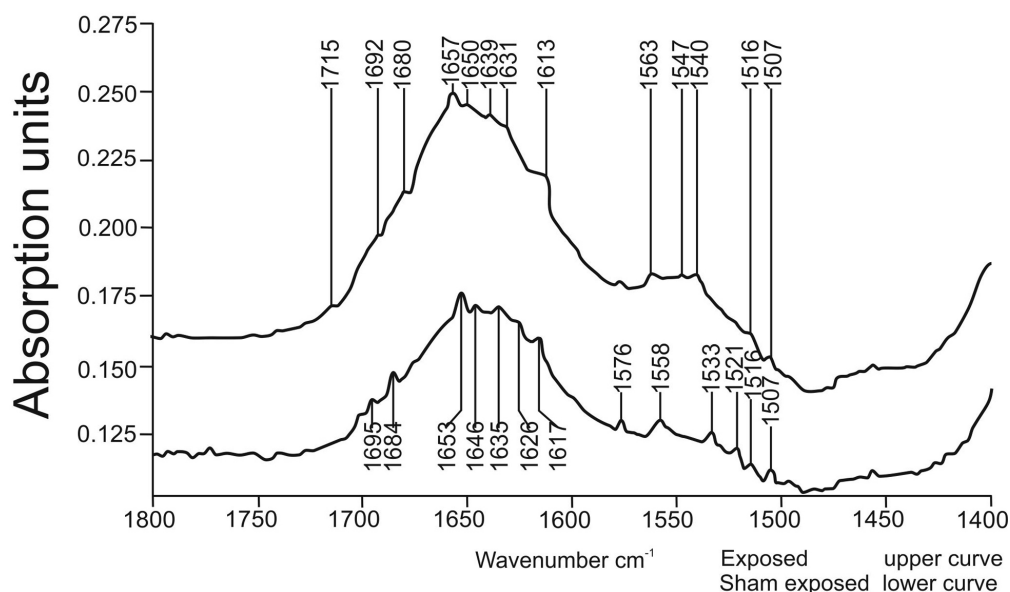


Fig. 4. Example of infrared spectra from sham exposed (lower curve) lyophilised homogenates of frog skeletal muscle, centrifuged at 9600 g, and from exposed ones (upper curve) with high intensity field (20 mW/cm²)

Table 3. Quantification of secondary peptide structure derived from peaks and shoulders obtained from FTIRS of sham exposed and exposed with low intensity field (10 mW/cm²) homogenates of frog skeletal muscle, centrifuged at 9600 g (first column). Second column – the quantity in percentage of corresponding peaks and shoulders

Sham exposed		Exposed	
(1)	(2)	(1)	(2)
α -helices 1653 cm ⁻¹ 1558 cm ⁻¹	Total 31%±3.5%	α -helices 1653→1557 cm ⁻¹ 1558→1563 cm ⁻¹	Total 16.14%±2.4%*
antiparallel β -forms 1695 cm ⁻¹ 1684 cm ⁻¹ 1617 cm ⁻¹ 1516 cm ⁻¹ 1507 cm ⁻¹	Total 11.65%±2.4%	antiparallel β -forms 1695→1692 cm ⁻¹ 1684→1680 cm ⁻¹ 1617→1620 cm ⁻¹ 1516 cm ⁻¹ 1507→1504 cm ⁻¹	Total 41.21%±1.52%
parallel β -forms 1646 cm ⁻¹ 1635 cm ⁻¹	Total 23.22%±1.4%	parallel β -forms 1645 cm ⁻¹ 1635 cm ⁻¹	Total 14.1%±3.4%
turns, coils, bends 1626 cm ⁻¹ 1521 cm ⁻¹	Total 14.6%±1.7%	turns, coils, bends 1626 cm ⁻¹ 1521 cm ⁻¹ 1504 cm ⁻¹	Total 48.1%±1.6%*

and additional peaks at 1680 cm⁻¹ and 1692 cm⁻¹ are observed. The irradiation with low-intensity field caused the appearance of two additional shoulders at 1645 cm⁻¹ and 1620 cm⁻¹. Additional shoulders after high intensity field irradiation are observed at 1650 cm⁻¹, 1639 cm⁻¹, 1631 cm⁻¹ and 1613 cm⁻¹

(Figs 3 and 4). There was observed additional shoulder out of Amid I and Amid II ranges at 1715 cm⁻¹ after irradiation with 20 mW/cm² field (Fig. 4, down curve).

In Amid II band the maximum was shifted from 1558 cm⁻¹ to 1563 cm⁻¹ after irradiation with both

Table 4. Quantification of secondary peptide structure derived from peaks and shoulders obtained from FTIRS of sham exposed and exposed with high intensity field (20 mW/cm²) homogenates of frog skeletal muscle, centrifuged at 9600 g (first column). Second column – the quantity in percentage of corresponding peaks and shoulders

Sham exposed		Exposed	
(1)	(2)	(1)	(2)
α -helices 1653 cm ⁻¹ 1558 cm ⁻¹	Total 33.3%±2.6%	α -helices 1653→1557 cm ⁻¹ 1558→1563 cm ⁻¹	Total 15.26%±2.2%**
antiparallel β -forms 1695 cm ⁻¹ 1684 cm ⁻¹ 1617 cm ⁻¹ 1516 cm ⁻¹ 1507 cm ⁻¹	Total 8.43%±1.73%	antiparallel β -forms 1695→1692 cm ⁻¹ 1684 →1680cm ⁻¹ 1617→1613 cm ⁻¹ 1516 cm ⁻¹ 1507 cm ⁻¹	Total 10.33%±1.69%*
parallel β -forms 1646 cm ⁻¹ 1635 cm ⁻¹	Total 17.9%±1.3%	parallel β -forms 1646→1650 cm ⁻¹ 1635→1639 cm ⁻¹	Total 20.6%±2%
turns, coils, bends 1626 cm ⁻¹ 1521 cm ⁻¹	Total 40.37%±1.8%	turns, coils, bends 1626→1631 cm ⁻¹ 1521 cm ⁻¹	Total 53.81%±1.75%**

fields. The low-intensity field provoked additional shoulders at 1552 cm⁻¹, 1547 cm⁻¹, 1536 cm⁻¹ and 1504 cm⁻¹ (Fig. 3, upper curve).

On the basis of peaks position changes and changes in the area under them, secondary structures alteration after the irradiation was calculated (Tables 3 and 4). After low intensity field exposure was observed statistically significant lowering of α -helices and structures (Table 3). After high-intensity field irradiation was observed statistically significant decreasing of α -helices and β -sheets, as well as a growth of percentage content of turns, bends and coils (Table 4).

DISCUSSION

A number of authors presumed that the EMF irradiation influences the activity of an exact protein through the influence of its conformation. The ability of microwave irradiation to cause changes in protein conformation is largely debated by several teams [22–27].

Böhr and Böhr [24, 25] suggested that after irradiation of protein molecule vibrational stations of little moving parts of the molecule decrease their vibrational frequency and increase their axis length respectively, which is in agreement with Fröhlich [28] hypothesis. They supposed that these preconditions may lead to conformational changes in these proteins and hence to different biological effects of EMF on certain structure. The authors observed

conformational changes of different proteins in solution after irradiation with MMW with 2.45 GHz frequency and 800 W power density.

The effects of impulse EMF with very low densities on protein conformation were observed by Neshev and Kirilova, [29]. They assume that the cell reacts on irradiation by stress answer. This answer acts by Hsp-proteins and it is very important for the normal cell function. Hsp-proteins act as “molecule companions”, which bind and stabilise damaged protein conformation. In that way they defend the cell from outward stress factors.

Laurence et al. [23] discuss the theoretical opportunity low intensity impulse EMFs to influence specifically protein conformation. They compare different characteristics of the fields and protein molecule interactions like irradiation time, characteristic time of protein cooling in water solution, characteristic time of energy diffusion in macromolecule vibrational regime, characteristic time of protein unfolding. In the light of these comparisons they conclude that EMF with low intensity (10 mW/cm²) and of the order of GHz frequency theoretically influences protein conformation. The authors suggest that the mechanism of protein conformation changes is resonance absorption of the field energy with afterward energy diffusion in water surrounded, or vice versa. After irradiation with very low intensity fields, it is supposed that they resonance with a few amino acid groups in proteins, so they can change the action of the corresponding enzyme active centre [30]. This hypothesis can explain the observation of

the so called “intensity windows”. Small conformational changes after exposure to low intensity EMFs can greatly affect protein functionality in comparison to those after exposure with high intensity field, where the functionality can be lost because of the appearance of stronger changes in protein conformation [21].

Conformational changes after irradiation presume functional alteration of membrane ion channels, receptors, enzymes (membrane bonded or free). Thompson et al. [32] hypothesised changes in Ca²⁺-binding after irradiation. They assumed that conformational changes of Ca²⁺-binding proteins are due to the increased amount of ordinary structures responsible for binding this ion. The authors suggest that this mechanism agrees with the postulate of the so called “intensity windows”.

Batanov et al [33] observed increasing of α -helices in albumin after irradiation with MMW. At the same time they did not observe breaking polypeptide chains or protein oligomerization. Changes of albumin's secondary structure is linearly connected with the field power.

Protein molecules possess high surface potential energy and non-harmonic dynamics [34]. As it is considered that protein biological function is connected with non-harmonic dynamics, the mechanism of binding between protein motion and its function is on the basis of interaction between EMFs and these large molecules. This protein dynamics is based on the following: 1) Globular proteins have vigorously packed structures and their conformational changes require common motion of most of the protein atoms; 2) For a molecule to undergo a conformational change from one structure to another, general vibrational regimes must be excited to jump over the energy barrier.

In our previous study [35] decreasing of α -helices quantity and increasing of unordered structures and β -sheets as a whole was shown. As the shift of amino acid activity in catalytic centre is vulnerable in rate of angstroms in order to be functional in biological systems we can speculate that the appearance of “intensity windows” connected with MMW irradiation is far more common. An interesting point is that after irradiation with low intensity field the changes in secondary protein structures are more pronounced. I suppose that the influence is specific (non-temperature), because the experiments were carried out in controlled temperature conditions. This suggestion is in congruence with the hypothesis of Böhr and Böhr [24, 25] which postulate that after irradiation the vibrational modes of little particles of the protein molecule decrease their vibrational frequencies, and is also in agreement with Fröhlich's [36, 37] hypothesis that the energy of EMFs does not disseminate like heat, but is stored in vibrational

modes of large protein molecules. I can infer that in my case after irradiation with 10 mW/cm² and 20 mW/cm² EMFs the energy was sufficient to arouse common vibrational modes of protein molecule in such a way as to nip over the energy barrier.

In our investigations the information from characteristic Amid I and II bands confirmed lowering of α -helices quantity in two fractions estimated, exposed with EMF with two power densities [35]. This phenomenon was more pronounced in “rough membrane fraction”. This is in accordance with the presence of the so called “intensity windows” referred to by other authors. Additional absorption peak is observed in “rough membrane fraction” which is out of the two Amid bands at 1733 cm⁻¹. It is characteristic of lipid-peptide hydrophobic interactions. Interestingly, the samples irradiated with low intensity field exhibit relatively more pronounced changes of protein secondary structure. We propose that the effect is specific (non-temperature) due to controlled temperature conditions of the experiment. This is in accordance with Böhr and Böhr [24, 25] hypothesis which states that if a peptide molecule is irradiated with microwave EMF the vibrational modes of little moving parts decrease their vibrational frequency. Another hypothesis that matches well our findings states that the energy from EMF entered the cells does not transform in thermal energy but is stored in peptide molecules and macromolecule vibrational modes. We can assume that in our case the energy from exposure was sufficient to excite general vibrational modes of peptide molecules to a level suitable for jumping over the energy barrier, leading to observed conformational changes.

In conclusion the EMF irradiation with two intensities influences statistically significant protein conformation in the direction of diminishing of α -helices and increasing of β -sheets and unordinary structures. In fraction centrifuged at 900 g there were observed changes of hydrophobic lipid-peptide interactions.

Acknowledgement: The author expresses his acknowledgement to Ilina Amer for her kind assistance in stylistically editing and formatting of this article, and to d-r Nikolina Radicheva for her methodological support.

REFERENCES

1. M. Boon, L. P. Kok, Microwave cookbook of pathology. Coulomb Press Leyden, Leiden, The Netherlands, 1987.
2. E. Marani, P. Bolhuis, M. E. Boon, *Histochem. J.*, **20**, 658 (1988).
3. Z. Wang, R. Van Dorp, A. F. Weidema, D. L. Yepsey, *Eur. J. Morphol.*, **29**(3), 198 (1991).

4. E. C. Pollard, *Amer. Sci.*, **57**, 206 (1969).
5. C. K. Chou, H. Bassen, J. Osepchuk J, Q. Balzano, R. Petersen, M. Meltz, R. Cleveland, J. C. Lin, L. Heynick, (1998): *Bioelectromagnetics*, **17**(3), 195 (1998).
6. E. M. Czerska, E. C. Elson, C. C. Davis, M. L. Swicord, P. Czerski P, *Bioelectromagnetics*, **13**(4), 247 (1992).
7. L. P. Kok, M. E. Boon, Microwave cookbook for microscopists. Art and science of visualization, Coloumb press, Leyden, The Netherlands, 1992.
8. E. Marani, H. K. Feirabend, *Eur. J. Morphol.*, **32**(2-4), 330 (1994).
9. R. Van Dorp, E. Marani, M. E. Boon, *Methods*, **15**(2), 151 (1998).
10. C. C. Johnson, A. W. Gui, *Proc TEEE*, **60**, 692 (1972).
11. L. J. Challis, *Bioelectromagnetics Suppl*, **7**, S98 (2005).
12. H. P. Schwan, K. Li, *Proc. IRE*, **41**, 1735 (1953).
13. N. D. Devyatkov, O. V. Betskii eds., Biological aspects of low intensity millimeter fields, Moscow, 1994.
14. P. P. Bernardi, D'Inzeo, in: Electromagnetic bio-interaction: mechanisms, safety standarts, protection guide, Franceschetti G, Gandhi M, Gandolfo M (eds.), Plenum Press, New York, 1989, p. 27.
15. J. M. Ruijgrok, M. E. Boon, H. Feirabend, S. Ploeger S, *Eur. J. Morphol.*, **31**(4), 290 (1993).
16. E. Calabro, S. Magazu, *Spectroscopy letters: An international Journal of Rapid Communication*, **46**(8), 583 (2013).
17. Calabro, S. Magazu, *Spectroscopy letters: An international Journal of Rapid Communication*, **47**(8), 649 (2014).
18. J. L. Arrondo, M. G. Felix, *Progress in Biophys. and Molecular Biol.*, **72**, 367 (1999).
19. J. L. Arrondo, A. Muga, J. Castresana, F. M. Goni, *Prog. Biophys. Mol. Biol.*, **59**, 23 (1993).
20. C. Polk, E. Postow, CRC Handbook of biological effects of electromagnetic fields, CRC Press, Inc, 1996.
21. N. Radicheva, K. Mileva, T. Vukova, B. Georgieva, I. Kristev, *Arch of Physiol and Biochem*, **110**(3), 203 (2002).
22. J. A. Laurence, P. W. French, R. A. Lindner, D. R. McKenzie, *J. Theor. Biol.*, **206**, 291 (2000).
23. J. A. Laurence, D. R. McKenzie, K. R. Foster, *J. Theor. Biol.*, **222**, 403 (2003).
24. H. Böhr, J. Böhr, *Bioelectromagnetics*, **21**, 68 (2000a).
25. H. Böhr, J. Böhr, *Phys Rev*, **E61**, 312 (2000b).
26. R. D. Astumian, *Phys. Rev. Lett.*, **11**, 118202 (2003).
27. J. Neumann, K. E. Gottschalk, R. D. Astumian, *ACS Nano*, **6**(6), 5242 (2012).
28. H. Fröhlich, *Adv. Electr. And Electr. Phys.*, **53**, 85 (1980).
29. N. N. Neshev, E. I. Kirilova, *Rev. Environ. Health*, **11**, 85 (1996).
30. S. K. Chattopadhyay, K. A. Toews, S. Butt, R. Barlett, H. D. Brown, *Cancer Biochem. Biophys.*, **15**, 245 (1997).
31. D. E. Koshland, *Nature medicine*, **4**(10), 1112 (1998).
32. C. J. Thompson, Y. S. Yang, V. Anderson, A. W. Wood, *Bioelectromagnetics*, **21**, 455 (2000).
33. A. Batanov, A. Volkov, V. M. Govorun, A. I. Demin, A. B. Kapitanov, S. V. Timofeev, V. B. Fleurov, Preprint IOFAN (Institute of general physics, Moscow), 3: (in Russian), 1989.
34. H. Frauenfelder, S. G. Sligar, P. G. Wolynes, *Science*, **254**, 1598 (1991).
35. T. Vukova, A. Atanassov, R. Ivanov, N. Radicheva, *MSM*, **11**(2), BR50 (2005).
36. H. Fröhlich, Biological coherence and response to external stimuli, Berlin, Springer-Verlag, 1988, p. 265.
37. H. Fröhlich H, *Proceedings of the Natural Academic Sciences of the USA*, **72**, 4211 (1975).

ПРОМЕНИ В БЕЛТЪЧНАТА КОНФОРМАЦИЯ НА ОБЩ БЕЛТЪК
ОТ ЖАБЕШКИ СКЕЛЕТЕН МУСКУЛ СЛЕД ОБЛЪЧВАНЕ С 2.45 GHz
ЕЛЕКТРОМАГНИТНО ПОЛЕ, В ЗАВИСИМОСТ ОТ ИНТЕНЗИТЕТА
НА ПОЛЕТО И ОТ ПОГЪЛНАТАТА МОЩНОСТ

Т. И. Апостолова*

*Секция „Възбудими Структури, Институт по Биофизика и Биомедицинско инженерство,
Българска Академия на Науките, София, България*

Постъпила декември, 2014 г.; приета януари, 2015 г.

(Резюме)

Беше направено проучване върху влиянието на електромагнитно поле с честота 2.45 GHz и два интензитета – висок (20 mW/cm^2) и нисък (10 mW/cm^2) съответно. Две различни фракции (центрифугирани на 900 и на 9000 g съответно) бяха подложени на облъчване а другите бяха оставени като контрола (необлъчени) върху лед. По-късно същите фракции бяха лиофилизирани и подложени на инфрачервена спектроскопия. Беше изчислена погълнатата мощност (specific absorption rate, SAR) за двете фракции, облъчени с полета и с двете мощности. Пикът, отговарящ за наличието на вода в лиофилизатите беше премахнат математически. Бяха изчислени площите под характеристичните пикове и рамена, намиращи се в АмидI и АмидII ивиците (характеристични за вторичните белтъчни структури). Наблюдавано беше процентно намаление на α -спиралите и при двете фракции, облъчени с полета и с двата интензитета. Наблюдаваните промени на β -листовете, паралелните β -структури, огъванията и неподредените структури бяха зависими от интензитета на полето и от SAR. Смятаме, че промените във вторичната белтъчна структура са специфични (нетемпературни), тъй като през цялото време се работеше при контролирани температурни условия.

Synthesis and crystallization of gels in the $\text{TiO}_2\text{--TeO}_2\text{--ZnO}$ system

R. D. Gegova¹, A. D. Bachvarova-Nedelcheva^{1*},
R. S. Iordanova¹, Y. B. Dimitriev²

¹ Institute of General and Inorganic Chemistry, BAS, "Acad. G. Bonchev" str.,
bld. 11, 1113 Sofia, Bulgaria

² University of Chemical Technology and Metallurgy – Sofia, "Kl. Ohridski" blvd, 8,
1756 Sofia, Bulgaria

Received December, 2014; Revised January, 2015

Transparent and monolithic gels were obtained in the ternary $\text{TeO}_2\text{--TiO}_2\text{--ZnO}$ system. The gel formation region is situated between 10–100 mol% TiO_2 , up to 65 mol% TeO_2 and up to 90 mol% ZnO . Tellurium alkoxides, the telluric (VI) acid (H_6TeO_6) along with zinc acetate and titanium butoxide were used as a combination of precursors during the synthesis. The phase transformations of the gels in the temperature range 200–700 °C were investigated by XRD method. It was established that above 200 °C composites were obtained and they contain an amorphous phase and different crystalline phases: TiO_2 (anatase), $\alpha\text{-TeO}_2$, TiTe_3O_8 , ZnTeO_3 , ZnTiO_3 и Zn_2TiO_4 depending on composition and heating temperature. The IR results showed that the short range order of the amorphous phases which are part of the composite materials consist of TiO_6 , ZnO_4 and TeO_4 structural units.

Key words: sol-gel, telluric (VI) acid, crystallization.

INTRODUCTION

It is well known that amorphous tellurite materials possess good physical and chemical properties which make them good candidates for new optical devices due to their high refractive index, high dielectric constant, wide band infrared transmittance and large third order non-linear optical susceptibility [1]. Pure TeO_2 is well known conditional network-former although it does not form glass alone, even at high cooling rates [2]. Binary and multicomponent TeO_2 -based glasses were studied and summarized in El-Mallawany's book [1]. The sol-gel method is an attractive alternative to the melt quenching method that may be used to extend application of new tellurite compositions. Powders and films in the $\text{TiO}_2\text{--TeO}_2$ and $\text{TeO}_2\text{--PbO--TiO}_2$ systems were reported in several papers irrespective of the high hydrolysis rate of the Te (VI) alkoxides [3–5]. It was established that sol-gel derived tellurite coatings and glasses exhibit greater resistance to devitrification than melt quenched glasses [3–5]. On the other hand, TiO_2 -based materials have always been of primary research interest for materials chemistry.

This interest is mostly driven by the unique properties of TiO_2 and its ability to create high surface area structures suitable for photo catalysis and sensors [6]. ZnO is an intermediate oxide and in the past years it is the preferred one for obtaining of transparent glass-ceramics applying conventional melt-quenching method. These materials combine the unique properties of ZnO as well as its good network formation ability.

As mentioned above the binary $\text{TiO}_2\text{--TeO}_2$ system is of special interest, as it has been shown that TiO_2 inhibits structural changes of the Te polyhedra and maintains a continuous glass network [7, 8]. Moreover, it was found that the addition of TiO_2 increases the thermal stability of TeO_2 -based glasses by replacing Te-O-Te linkages by more rigid Te-O-Ti ones [9]. The glass forming tendency in the binary ZnO--TeO_2 system was also studied and the corresponding glasses were found to be stable [10]. Structural investigations on the $\text{TeO}_2\text{--ZnO}$ binary glasses were also reported [11–15]. Recently, the structure of the binary $(100-x)\text{TeO}_2\text{--}x\text{ZnO}$ glass was studied using EXAFS data [16]. Several investigations on the refractive index and the optical band gap for binary and ternary zinc tellurite glass system have been published [17–20]. A large number of investigations are devoted to the sol-gel productions of composite materials in the binary $\text{TiO}_2\text{--ZnO}$.

* To whom all correspondence should be sent:
E-mail: albenadb@svr.igic.bas.bg

Coupled semiconductor photocatalyst of TiO_2/ZnO has been investigated to enhance the photodegradation efficiency of TiO_2 catalyst by a number of researchers and its effect for improving photocatalytic efficiency was reported [21–22]. The results showed that the photocatalytic activity of ZnO/TiO_2 coupled photocatalysts was higher than that of the single phase [23].

Up to now the thermal, optical and structural properties of glasses in the ternary $\text{TiO}_2\text{-TeO}_2\text{-ZnO}$ system have been studied by Kabalci et al. [24] as well as by N. Ghribi et al. [25]. But there is no data for gel formation in this ternary system.

The main purpose of this paper is to study the gel formation tendency in the three-component $\text{TiO}_2\text{-TeO}_2\text{-ZnO}$ system, to identify the phases and structural evolution of the gels upon heating as well as to verify the compatibility of the structural units in the amorphous phase.

were used. Telluric acid (H_6TeO_6) is selected to overcome the problem with the high hydrolysis rate of tellurium (VI) alkoxide that has been reported in several papers [26–28]. The precursor solutions were subjected to 5–30 min intensive stirring at room temperature in order to achieve complete dissolution. No direct addition of water was made to the precursors' solutions. Sol-gel hydrolysis reaction was acquired from absorbed atmospheric moisture. The measured pH is 4–5 depending on composition. The gelation time for the investigated compositions was from 1 to 5 min. The aging of gels was performed in air for several days (~ one week) to complete the processes. The obtained gels were subjected to the stepwise heating from 200 to 700 °C in air. The heat treatment at 200 °C was performed in order to hydrolyze any unreacted OR groups. Further increasing of temperatures (300–700 °C) was conducted to verify the phase and structural transformations of the gels. Selected gels, containing a constant TiO_2 amount (40 mol%) were subjected to more detailed phase analysis (Figs. 4 and 7, Table 1).

EXPERIMENTAL

Samples preparation

The scheme for sol-gel synthesis of $\text{TiO}_2/\text{TeO}_2/\text{ZnO}$ compositions is presented in Figure 1. A combination of Te(VI) acid (Aldrich) along with Ti butoxide (Fluka AG), Zn acetate (Merck) precursors dissolved in ethylene glycol ($\text{C}_2\text{H}_6\text{O}_2$) (99% Aldrich)

Samples characterization

Powder XRD patterns were registered at room temperature with a Bruker D8 Advance diffractometer using Cu-K_α radiation. The morphology of the samples was examined by scanning electron microscopy (SEM) using a JEOL JSM 6390 elec-

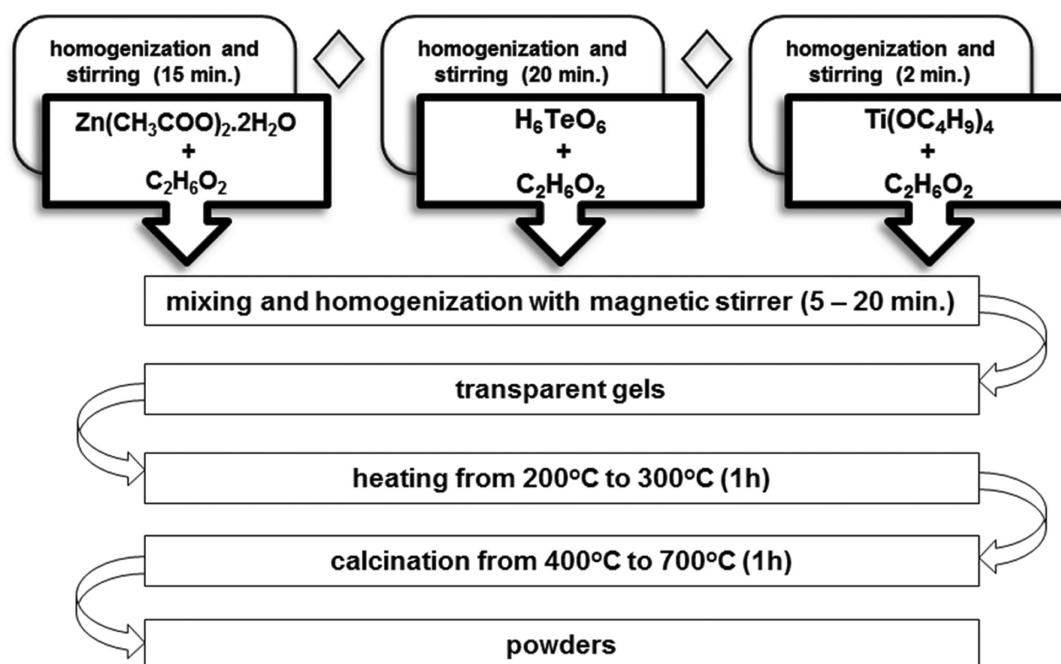


Fig. 1. Scheme for the sol-gel synthesis of $\text{TiO}_2/\text{TeO}_2/\text{ZnO}$ gels

tron microscope (Japan), equipped with ultrahigh resolution scanning system (ASID-3D). The optical absorption spectra of the powdered samples in the wavelength range 200–1000 nm were recorded by a UV–VIS diffused reflectance Spectrophotometer “Evolution 300” using a magnesium oxide reflectance standard as the baseline. The absorption edge and the optical band gap were determined following Dharma et al. instructions [29]. The band gap energies (E_g) of the samples were calculated by the Planck’s equation:

$$E_g = \frac{h.c}{\lambda} = \frac{1240}{\lambda} \quad (eq. 1),$$

where E_g is the band gap energy (eV), h is the Planck’s constant, c is the light velocity (m/s), and λ is the wavelength (nm). The infrared spectra were

registered in the range 1600–400 cm⁻¹ using the KBr pellet technique on a Nicolet-320 FTIR spectrometer with 64 scans and a resolution of ±1 cm⁻¹.

RESULTS AND DISCUSSION

Phase transformations

Transparent and monolithic gels were obtained applying the scheme shown in Fig. 1 and their images are given on Fig. 2. The gel formation region determined at room temperature is situated between 10–100 mol% TiO₂, up to 65 mol% TeO₂ and 90 mol% ZnO (Fig. 3). In the binary ZnO–TeO₂ system, gels are not obtained at given experimental conditions using H₆TeO₆ and Zinc acetate as precursors.

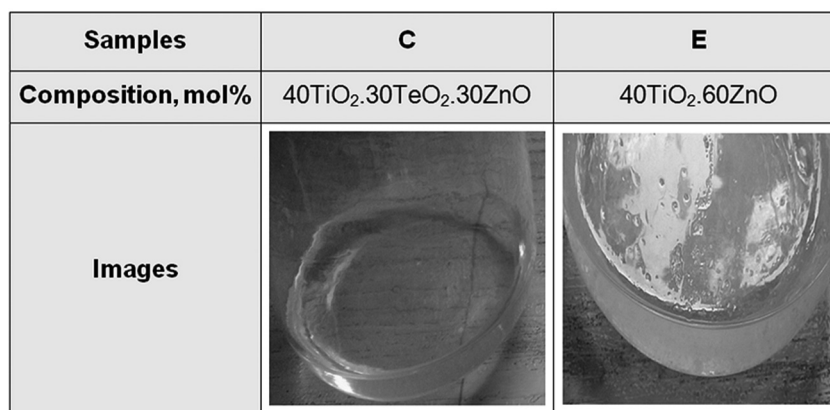


Fig. 2. Gel formation region in the investigated TiO₂-TeO₂-ZnO system

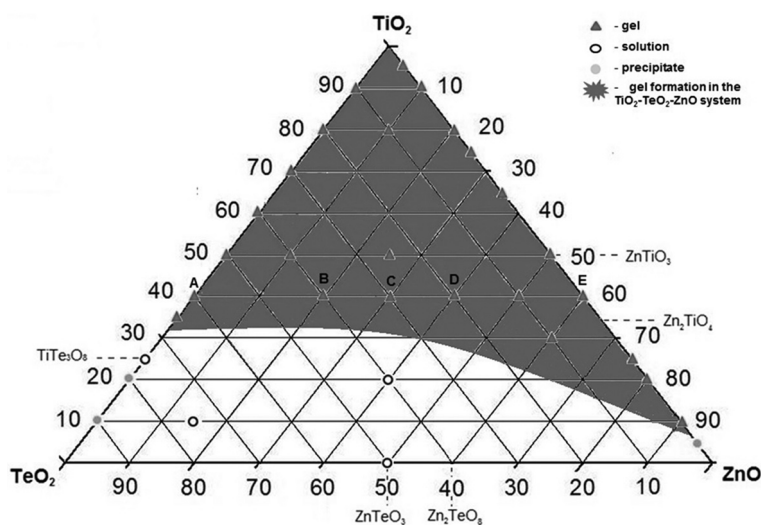


Fig. 3. Images of selected gels

According to the X-ray diffraction patterns in the temperature range 200–500 °C composite materials containing an amorphous phase and different crystalline phases {metallic Te (JCPDS 78-2312), $\alpha\text{-TeO}_2$ (JCPDS 42-1365), anatase (JCPDS 78-2486), rutile (JCPDS 21-1276), ZnTeO_3 (JCPDS 44-0240), ZnTiO_3 (cubic, JCPDS 39-0190) and Zn_2TiO_4 (JCPDS 25-1164)} are prepared. As one can see at 200 and 300 °C the amorphous phase co-exists with metallic tellurium while at 400 °C simultaneous presence of amorphous phase and metallic tellurium, $\alpha\text{-TeO}_2$, anatase or ZnO (JCPDS 78-2486) is observed (Fig. 4, samples A, B, C, D and E). The oxidation of tellurium starts at 400 °C and it is fully oxidized to TeO_2 about 500 °C. In the binary composition $40\text{TiO}_2\cdot 60\text{ZnO}$ (sample E) (Fig. 4) ZnO appears even at 200 °C. In sample D ($40\text{TiO}_2\cdot 20\text{TeO}_2\cdot 40\text{ZnO}$), ZnO remains in the amorphous phase in the temperature range 200–500 °C. The anatase appears at lower temperature (400 °C) in sample D ($40\text{TiO}_2\cdot 20\text{TeO}_2\cdot 40\text{ZnO}$) and conversion to rutile is observed at 600 °C. In the binary sample A ($40\text{TiO}_2\cdot 60\text{TeO}_2$), anatase appears at 500 °C and a small amount is converted to rutile at 700 °C, while in the sample E ($40\text{TiO}_2\cdot 60\text{ZnO}$), anatase did

not appeared in the XRD patterns. At 400 °C the average crystallite size (calculated using Sherrer's equation) of TiO_2 (anatase) in the powdered sample D is about 58 nm (Fig. 4). At higher temperatures (600–700 °C) crystalline phases only (anatase, rutile, $\alpha\text{-TeO}_2$, TiTe_3O_8 (JCPDS 50-0250), ZnTeO_3 and Zn_2TiO_4) were found in the prepared composite materials (Fig. 4).

SEM observations of a representative sample with nominal composition $50\text{TiO}_2\cdot 25\text{TeO}_2\cdot 25\text{ZnO}$, heat treated at 400 °C were performed (Fig. 5). As one can see the morphology is a result from the crashing of the monolithic gels during the drying process. The microprobe analysis in different points of the sample showed that the obtained weight ratio of $\text{TiO}_2\text{:TeO}_2\text{:ZnO}$ ($49\text{:}22\text{:}29 \approx 2\text{:}1\text{:}1$) is similar as in the initial nominal composition.

Optical properties and structural transformations

The diffuse reflectance absorption spectra of selected binary and ternary $\text{TiO}_2\text{/TeO}_2\text{/ZnO}$ gels (aged at room temperature) as well as of pure Ti butoxide gel are illustrated in Figure 6 a, b. The observed

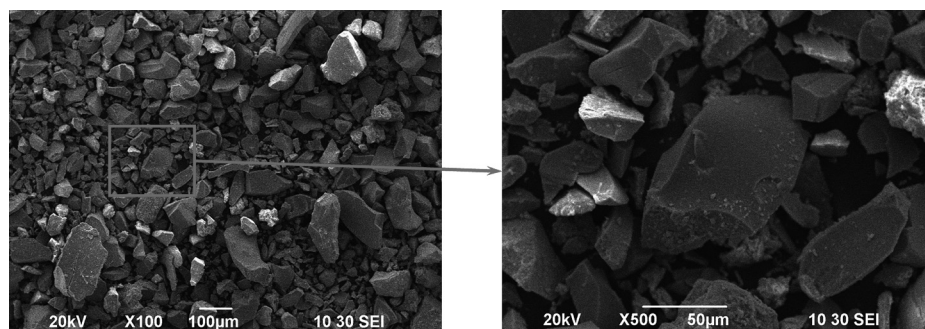


Fig. 5. SEM images of composition $50\text{TiO}_2\cdot 25\text{TeO}_2\cdot 25\text{ZnO}$ heat treated at 400 °C

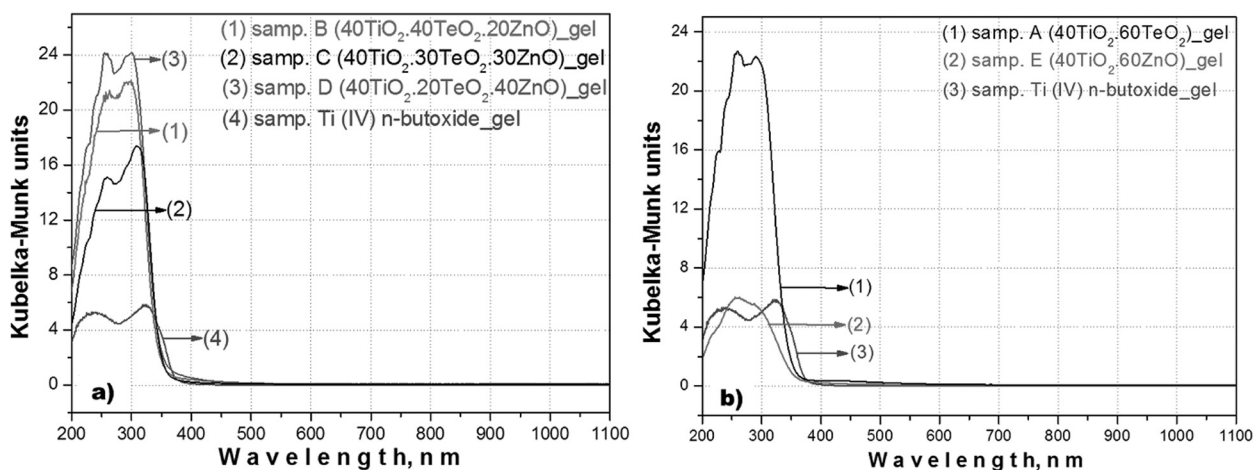


Fig. 6. UV-Vis spectra of: a) binary and b) ternary gels in the investigated ternary system

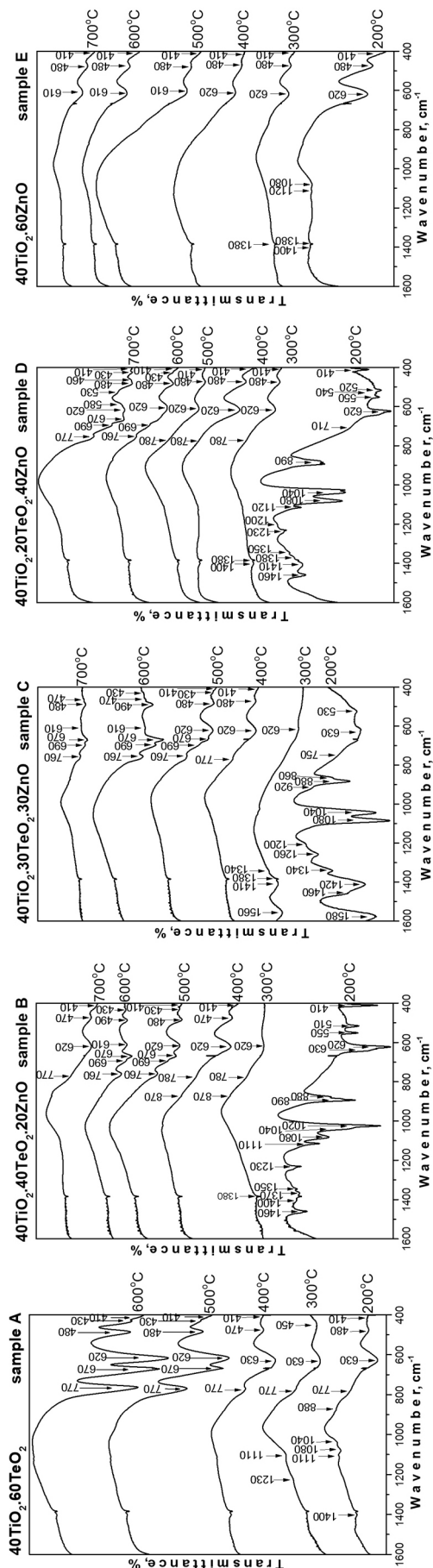
Table 1. Investigated binary and ternary gels, observed cut-off and calculated optical band gap values (Eg)

Samples	Compositions, mol. %	Cut-off, nm	Eg, eV
	Ti (IV) n-butoxide gel	389.71	3.18
A	40TiO ₂ .60TeO ₂	348.07	3.56
B	40TiO ₂ .40TeO ₂ .20ZnO	347.36	3.57
C	40TiO ₂ .30TeO ₂ .30ZnO	348.90	3.55
D	40TiO ₂ .20TeO ₂ .40ZnO	366.89	3.38
E	40TiO ₂ .60ZnO	386.82	3.21

absorption edges and calculated optical band gap values are pointed out in Table 1. It is evident that the ternary gels containing TiO₂, TeO₂ and ZnO exhibit higher absorption in the UV region in comparison to pure Ti butoxide gel. Another peculiarity is the appearance of two absorption bands below and above 300 nm, the so called charge transfer bands. For the isolated TiO₄ units, the ligand to metal charge transfer band is in the region 200–260 nm, while in a titania network (anatase) the charge transfer in TiO₆ is above 300 nm [30–32]. The TiO₄ groups are the main building units in the unhydrolyzed Ti butoxide and the coordination geometry is changed to TiO₆ as a result of polymerized Ti species (Ti-O-Ti links between TiO₆ units) [32]. For the three component gels, the observed more intensive absorption peak about 300–340 nm is associated with an increase of the polymerization degree of Ti atoms in comparison to pure Ti butoxide gel. Similar data was obtained by Klein et al. [32] which investigated the UV-Vis spectra of TiO₂/SiO₂ gels. The UV-Vis spectra of the binary 40TiO₂.60ZnO gel (with high ZnO content) (Fig. 6a) is different from those of sample A (40TiO₂.60TeO₂) and pure Ti butoxide. The charge transfer of O → Ti is in the range 260–300 nm but it is known that the exciton absorption peak of bulk ZnO exists in the same region (300–360 nm, Eg ~3.24 eV) [33]. Due to the overlapping of these absorption bands it is difficult to obtain more precise information for the influence of ZnO on the polymerization ability of Ti. The absorption edge of our gels varies between 348.07 to 386.82 nm (± 0.01 precision). According to several authors [24, 25] TiO₂/TeO₂/ZnO glasses (containing up to 35 mol% ZnO) exhibit optical band gap value about 2.94–3.00 eV. Our values obtained for gels are higher (3.2–3.28 eV) than those pointed out in the literature but lower than the value of melted bulk tellurite glass (~3.79 eV).

The phase transformations during the heat treatment (in the temperature range 200–700 °C) were monitored also by IR spectroscopy (Fig. 7). The as-

signments of the vibrational bands of the separate structural units are made on the basis of well-known spectral data of the precursors (Ti (IV) n-butoxide, H₆TeO₆ and zinc acetate) and crystalline phases existing in the system [8, 34–35]. In the obtained by us IR spectra of samples heat treated up to 200 °C the absorption bands in the 1120–1040 cm⁻¹ region (Ti-O-C stretching vibrations) are very weak in the binary 40TiO₂.60TeO₂ and 40TiO₂.60ZnO compositions (Fig. 7, samples A, E) while in the ternary ones these bands are very intensive (Fig. 7, samples B, C, D). This observation could be explained by the greater degree of hydrolysis and condensation processes in the binary samples. The bands above 1000 cm⁻¹, characteristic for the organic groups are not visible above 300 °C and the spectra in the temperature range 300–500 °C are characterized mainly with bands below 900 cm⁻¹ typical for the inorganic units. At 300 and 400 °C these bands are broadened, with low intensity that is a peculiarity of the disordered systems. According to the XRD data at these temperatures (300 and 400 °C) the obtained composite materials contain mainly an amorphous phase along with elementary tellurium. An exception is the sample E (40TiO₂.60ZnO), where the composite contains an amorphous phase and ZnO. Basis on the IR and XRD results the observed absorption bands in the IR spectra of samples heated at 300 and 400 °C could be related to the vibrations of structural units building up the amorphous network: TeO₄ (780–770 cm⁻¹; 630–620 cm⁻¹; TiO₆ and ZnO₄ (630–620 cm⁻¹, 480 and 410 cm⁻¹) [36–44]. It is well known that the elementary tellurium does not exhibit absorption bands in the IR spectral region. At higher temperatures (above 500 °C) the content of the amorphous phase decreases (it is negligible at 500 °C). In this case the observed absorption bands in the IR spectra are assigned to the vibrations of inorganic structural units building up the crystalline phases (TiTe₃O₈, ZnTeO₃, Zn₂TiO₄ and ZnTiO₃). It is difficult to distinguish the vibrations of TiO₆ and ZnO₄ structural units due to their strong over-



←
Fig. 7. IR spectra of the investigated samples

lapping. The obtained IR spectra proved the phase transition established by XRD (Fig. 4).

CONCLUSIONS

The gel formation region in the ternary $\text{TiO}_2\text{-TeO}_2\text{-ZnO}$ system was determined. New original gel derived composite materials consisting of amorphous and different crystalline phases: TiO_2 (anatase), ZnTiO_3 , TiTe_3O_8 and ZnTeO_3 were obtained depending on composition. The decrease in the TeO_2 content (20 mol%, sample D) stimulates the crystallization of TiO_2 (anatase) at lower temperatures (400 °C). At constant TiO_2 content (40 mol%) and define TeO_2/ZnO ratios 2:1 and 1:1 (samples B, C), the anatase → rutile transition occurred at 500 °C. By IR spectroscopy was established that organic and OH groups participate in the amorphous organic–inorganic structure below 300 °C. At higher temperatures (300–400 °C) the inorganic amorphous phases consist of TiO_6 , ZnO_4 and TeO_4 structural units.

Acknowledgements: The study was performed with financial support of The Ministry of Education and Science of Bulgaria, Operational Program “Human Resources Development”, co-financed by the European Social Fund of the European Union, contracts: BGO51PO001-3-306-0050. The first author R. Gegova thanks also for the financial support of the project T-01-239/10.09.2014, Ministry of Education Youth and Science (co-financing of a scientific event “V-th National Crystallographic Symposium NCS2014”).

REFERENCES

1. R. A. H. El-Mallawany, *Tellurite Glasses Handbook: Physical Properties and Data*. CRC Press, 2001.
2. P. Sarjeant, R. Roy, *J. Am. Ceram. Soc.*, **51**, 500 (1967).
3. L. Weng, S. Hodgson, X. Bao & K. Sagoe-Crentsil, *Mater. Sci. Eng. B*, **107**, 89 (2004).
4. S. N. B. Hodgson & L. Weng, *J. Mater. Sci.: Mater. Electron.*, **17**, 723 (2006).
5. T. Hayakawa, H. Koyama, M. Nogami, & Ph. Thomas, *J. Univ. Chem. Techn. Metall.*, **47**, 381 (2012).
6. Arrachart, G., Cassidy, D. J., Karatchevtseva, I. & Triani, G., *J. Am. Ceram. Soc.*, **92**, 2109 (2009).

7. M. Arnaudov, V. Dimitrov, Y. Dimitriev & L. Markova, *Mater. Res. Bull.*, **17**, 1121 (1982).
8. R. Iordanova, R. Gegova, A. Bachvarova-Nedelcheva, Y. Dimitriev, *Europ. J. Glass Sc. Techn., Part B: Phys. Chem. Glasses*, (2014) (accepted).
9. M. Udovic, P. Thomas, A. Mirgorodsky, O. Durand, M. Soulis, O. Masson, T. Merle-Méjean, J. C. Champarnaud-Mesjard, *J. Solid State Chem.*, **179**, 3252 (2006).
10. S. K. Ahmed, M. A. Sameea, A. Edukondalu, et S. Rahman, *Results Phys.*, **2**, 175 (2012).
11. T. Sekiya, N. Mochida, A. Ohtsuka, *J. Non-Cryst. Sol.*, **168**, 106 (1994).
12. H. Burger, K. Kneipp, H. Hobert, W. Vogel, V. Kozhukharov, S. Neov, *J. Non-Cryst. Sol.*, **151**, 134 (1992).
13. C. Duverger, M. Bouazaoui, S. Turrell, *J. Non-Cryst. Sol.*, **220**, 169 (1997).
14. U. Hoppe, E. Yousef, C. Rüssel, A. C. Hannon, *J. Phys. Condens. Matter.*, **16**, 1645 (2004).
15. V. Kozhukharov, H. Bürger, S. Neov, B. Sidzhimov, *Polyhedron*, **5**, 771 (1986).
16. J. G. Thorbahn, J. W. Zwanziger, *J. Non-Cryst. Sol.*, **381**, 48 (2013).
17. N. I. T. Komatsu, *Solid State Sci.*, **14**, 1419 (2012).
18. M. Soulis, J.-R. Duclère, T. Hayakawa, V. Couderc, M. Dutreilh-Colas, P. Thomas, *Mater. Res. Bull.*, **45**, 551 (2010).
19. A. R. N Manikandan A. Rysanyanskiy, J. Toulouse, *J. Non-Cryst. Solids*, **358**, 947 (2012).
20. G. Yankov, L. Dimova, N. Petrova, M. Tarassov, K. Dimitrov, T. Petrov, B. L. Shivachev, *Opt. Mater.*, **35** (2), 248 (2012).
21. G. Marci, V. Augugliaro, M.J. Lopez-Munoz, C. Martin, L. Palmisano, V. Rives, M. Schiavello, M., R. J. D. Tilley, A. M. Venezia, *J. Phys. Chem. B*, **105**, 1026 (2001).
22. X. Xu, J. Wang, J. Tian, X. Wang, J. Dai, X. Liu, *Ceramics International*, **37**, 2201 (2011).
23. C. Shifu, Z. Wei, L. Wei, Z. Sujuan, *Appl. Surf. Sci.*, **255**, 2478 (2008).
24. I. Kabalci, N. Öztürk Körpe, T. Duran, M. Özdemir, *Phys. Status Solidi*, **8**, 2629 (2011).
25. N. Ghribi, M. Dutreilh-Colas, J.-R. Duclère, T. Hayakawa, J. Carraud, R. Karray, A. Kabadou, P. Thomas, *Journal of Alloys and Compounds* (2014), doi: <http://dx.doi.org/10.1016/j.jallcom.2014.10.063>
26. S. N. B. Hodgson & L. Weng, *J. Mater. Sci: Mater. Electron.*, **17**, 723 (2006).
27. A. Lecomte, F. Bamiere, S. Coste & P. Thomas, J. C. Champarnaud-Mesjard, *J. Europ. Cer. Soc.*, **27**, 1151 (2007).
28. L. Weng & S. Hodgson, *Mater. Sci. Engineer*, **B 87**, 77 (2001).
29. J. Dharma & A. Pisal, Perkin Elmer, Inc, Application note.
30. R. S. Singh, & S. P. Singh, *J. Mater. Sci.*, **36**, 1555 (2001).
31. R. J. H. Clarck, "Chemistry of titanium and vanadium", Elsevier, Amsterdam, 1968.
32. S. Klein, B. M. Weckhuysent, J. Martens, W. Maier, & P. Jacobs, *J. Catal.*, **163**, 489 (1996).
33. D. W. Bahnemann, C. Kormann, and M. R. Hoffmann, *J. Phys. Chem*, **91**, 3789 (1987).
34. A. Bachvarova-Nedelcheva, R. Gegova, R. Iordanova, A. Stoyanova, Y. Dimitriev, and N. Ivanova, *Nanoscience and Nanotechnology*, **13**, 56 (2013).
35. R. Iordanova, A. Bachvarova-Nedelcheva, R. Gegova, and Y. Dimitriev, *Bulg. Chem. Commun.*, **45** (4) 485 (2013).
36. Ahmed Shalaby, Y. Dimitriev, R. Iordanova, A. Bachvarova-Nedelcheva and Tz. Iliev, *J. Univ. Chem. Techn. Metall.*, **46** (2), 137 (2011).
37. A. Stoyanova, H. Hitkova, A. Bachvarova-Nedelcheva, R. Iordanova, N. Ivanova, M. Sredkova, *J. Chem. Techn. Metall.*, **48** (2) 154 (2013).
38. A. Murashkevich, A. Lavitkaya, T. Barannikova et al., *J. Appl. Spectr.*, **75** (5) 730 (2008).
39. E. Yurchenko, G. Kustova, S. Bacanov, "Vibratioanal spectroscopy of inorganic compounds", izd. "Nauka", (1981) (in Russian).
40. O. Yamaguchi, M. Morimi, H. Kawabata et al., *J. Amer. Ceram. Soc.*, **70**, c97 (1987).
41. B. G. Shabalin, *Mineral. Zh.*, **4**, 54 (1982).
42. M. Mancheva, R. Iordanova, Y. Dimitriev, *J. Alloys Compd.*, **509** (1), 15 (2011).
43. M. Andres-Verges, M. Martinez-Gailego, *J. Mater. Sci.*, **27**, 3756 (1992).
44. Y. Dimitriev, Y. Ivanova, A. Staneva, L. Alexandrov, M. Mancheva, R. Yordanova, C. Dushkin, N. Kaneva, C. Iliev, *J. Univ. Chem. Tech. Metall.*, **44** (3), 235 (2009).

СИНТЕЗ И КРИСТАЛИЗАЦИЯ НА ГЕЛИ В СИСТЕМАТА TeO₂-TiO₂-ZnO

Р. Д. Гегова¹, А. Д. Бъчварова-Неделчева^{1*}, Р. С. Йорданова¹,
Я. Б. Димитриев²

¹ *Институт по Обща и Неорганична Химия, БАН, ул. „Акад. Г. Бончев“,
бл. 11, София, 1113, България*

² *Химикотехнологичен и Металургичен Университет, бул. „Кл. Охридски“,
1756 София, България*

Постъпила декември, 2014 г.; приета януари, 2015 г.

(Резюме)

Прозрачни и монолитни гели са получени в трикомпонентната система TeO₂-TiO₂-ZnO и е установено, че областта на гелообразуване е разположена между 10–100 mol% TiO₂, до 65 mol% TeO₂ и 90 mol% ZnO. Телурова киселина (H₆TeO₆), цинков ацетат и титанов бутоксид са използвани като прекурсори за синтеза. Фазовите промени на гелите са изследвани в температурния интервал 200–700 °C. Чрез РФА е установено, че получените композити съдържат аморфна фаза и различни кристални фази – TiO₂ (анатаз), α-TeO₂, TiTe₃O₈, ZnTeO₃, ZnTiO₃ и Zn₂TiO₄, в зависимост от състава и температурата на нагряване. С ИЧ спектроскопия е установено, че близкият порядък на аморфните фази, които са част от композитните материали, са изградени от TiO₆, ZnO₄ и TeO₄ структурни единици.

Study of medieval ceramics excavated at the monastery of Karaachteke (Varna, Bulgaria)

A. Yoleva, S. Djambazov*, P. Djambazov

Department of Silicate Tehcnology, University of Chemical Technology and Metallurgy, Sofia, Bulgaria

Received December, 2014; Revised January, 2015

The study of medieval ceramics is important in order to obtain information for development of ceramic production during this period. Various medieval unglazed and glazed ceramic artifacts discovered during archaeological excavations in the monastery of Karaachteke near Varna (Bulgaria) were chemically and structurally characterized by ICP-AES, XRD, SEM-EDS and Archimedes method to understand the technology of medieval ceramics production. Water absorption of unglazed artifacts is ranging from 10 to 15 wt.%, which indicates that the ceramics is good sintered and possibly is fired at a high temperature, around 950–1050 °C. The phase composition of the ceramic artifacts indicates the presence of crystalline phases of quartz and plagioclase, the amount of which varies in different samples. SEM proves the presence of coarse quartz grains having a size of 0.05 to 0.3 mm in the sintered ceramic body. This leads to the conclusion that it is used or highly sandy clay or ceramic body, consisting of red firing clay and coarse grain quartz sand.

The study of glazed artifacts proves that a transparent lead glaze with firing temperature about 950–1050 °C was widely used in the Middle Ages. Part of glazed artifacts is typical sgraffito pottery. Other part of glazed artifacts is of the type of the famous Preslav ceramics of a white ceramic body and transparent green glaze with the Seger formula $\text{PbO} \cdot 0,16\text{Al}_2\text{O}_3 \cdot 2\text{SiO}_2$ and firing temperature above 1000 °C.

Key words: medieval ceramics, SEM, structure, glazes.

INTRODUCTION

The most common and significant material as volume found by archaeological excavation is the ceramics. With its forms and decoration, chemical and mineral composition it is among the main elements, that in multilateral study give information on the organization of production, business and trade relations, cultural influences and differences between ages and regions. The overall knowledge of a ceramic material and its properties requires knowing the relationship composition-structure-properties that are strictly dependent on the applied technology.

Subject of research are various unglazed and glazed ceramic artifacts found during archaeological excavations in the monastery Karaachteke by prof. Casimir Popkonstantinov (University of Veliko Tarnovo), assoc. prof. Rosina Kostova (University

of Veliko Tarnovo) and Valentine Pletnyov (Regional Museum Varna) in the period from 2011 to 2013. Extensive excavation and research begin only in 1995, and with some interruptions, continue also today, as in a large scale they are in the recent years. The monastery of Karaachteke near Varna (Bulgaria) is one of the largest monasteries in the Balkans. The found ceramics is varied – without ornaments or decorated with relief and parallel or grid cross lines, with green transparent glaze, so called sgraffito ceramic of XII–XIV century and ceramic from the Ottoman period – XV–XVIII century. A sign of the intense life in the monastery is the found textured and painted pottery from white clay. Some of the dishes are imported from Byzantium, and others are in the style of “Preslav painted ceramics” from the end of IX and the beginning of the Xth century [1–2].

At present is interesting the study of medieval pottery in order to meet the level of development of ceramics during this period. The authors of this research have a big experience in the field of ceramic glazed and bodies, frits and decoration [3–10].

The aim of the present study is a chemical and structural characterization of unglazed and glazed

* To whom all correspondence should be sent:
E-mail: djam@uctm.edu

medieval pottery found during archaeological excavations in Karaachteke monastery near Varna (Bulgaria).

EXPERIMENTAL PROCEDURE

Studied artifacts

Unglazed ceramic artifacts are shown in Fig. 1. The ceramic artifacts, indicated by UG1 are found at depth of 1.0 to 1.2 m. The ceramic artifacts, labeled UG2 are discovered at depth of 1 m, others ceramic artifacts, labeled UG3 and UG4 – at depth from 0.60 to 0.80 m. The glazed ceramic artifacts are found at depth of 1 m and are shown in Fig. 2, indicated by G1, G2, G3 and G4.

Analytical methods for study of the ceramic artifacts

– Chemical analysis – ICP – AES after alkali fusion and dissolved in acid and the classical silicate analysis.

– XRD – Diffractometer “TUR-M62”, CoK_α radiation in the range of 2θ from 5 to 60° .

– SEM – Scanning electron microscopy SEM 525 M, Philips with Energy Dispersive Spectrometer EDS – EDAX 9900.

– Archimedes method for determination of water absorption of ceramic artifacts.

RESULTS AND DISCUSSION

The results from the chemical analysis of the composition of the unglazed artifacts are given in Table 1. SiO_2 and Al_2O_3 are the most important oxides in the ceramic body of unglazed ceramic artifacts. The coloring oxides ($\text{Fe}_2\text{O}_3 + \text{TiO}_2$) cause the slightly red color in the ceramic body of the unglazed artifacts. The artifacts contain more than 3 wt.% alkali oxides as K_2O and Na_2O . The water absorption of unglazed artifacts is varied from 10 to 15 wt.%, which gives reason to believe that the artifacts are well sintered probably at high temperature around $950\text{--}1050^\circ\text{C}$. The phase composition of the ceramic artifacts, established by XRD and shown in Fig. 3, indicates the presence of crystalline phases of quartz and plagioclase, which amount is varied in the different samples.

The chemical composition and the microstructure of the glazed ceramic artifacts was characterized by SEM-EDS. Fig. 4 shows a scanning microscope photograph and local chemical analysis from EDS of glazed ceramic artifact denoted in Fig. 2 with G1. In the ceramic body are clearly vis-

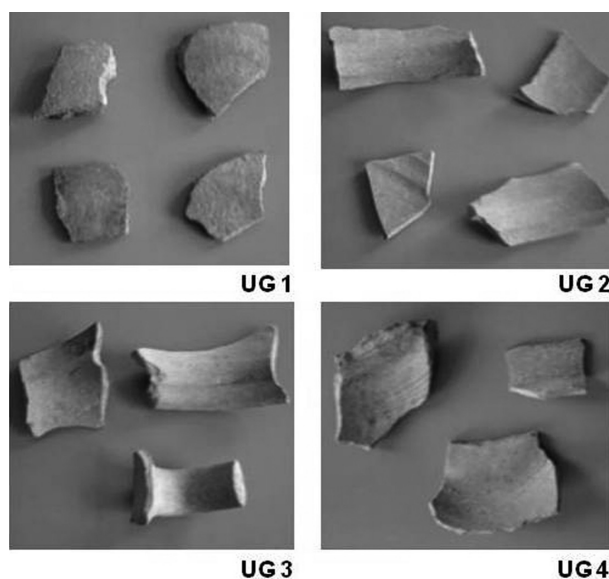


Fig. 1. Unglazed medieval ceramic artifacts from Monastery Karaachteke (Varna, Bulgaria)

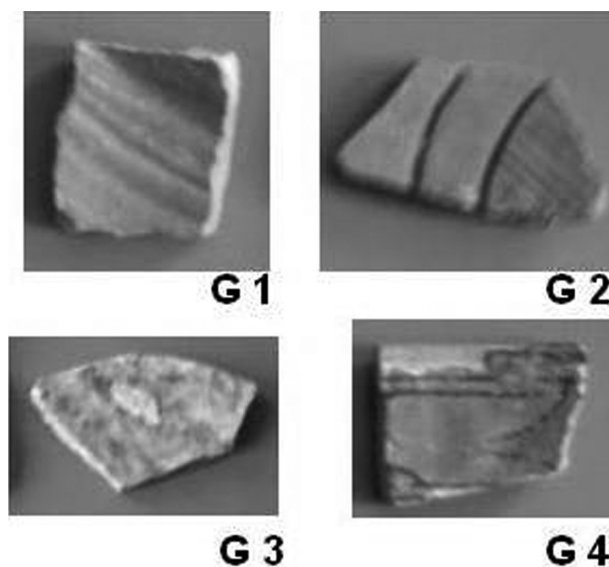


Fig. 2. Glazed medieval ceramic artifacts from Monastery Karaachteke (Varna, Bulgaria)

ible coarse quartz grains having a size of 0.05 to 0.30 mm, immersed in a sintered ceramic matrix. The average chemical composition of the ceramic matrix surrounding the quartz grains is shown in Fig. 4. The presence of coloring oxides explains light red color of the ceramic body of the artifact G1. These results show that is used very sandy clay, which apparently was not digested, but only passed through a sieve of 0.5 mm or used in the form in

Table 1. Chemical compositions of unglazed ceramic artifacts

Artifacts	SiO ₂	Al ₂ O ₃	Fe ₂ O ₃	MgO	CaO	TiO ₂	MnO	Na ₂ O	K ₂ O	SO ₃	P ₂ O ₅	LI
UG1	70.55	15.47	5.60	1.43	1.40	0.78	0.05	1.05	2.57	1.38	0.09	0.26
UG2	70.75	13.57	5.0	1.54	3.14	0.69	0.07	0.74	2.54	<0.03	0.11	1.06
UG3	66.41	17.54	5.91	1.38	1.65	0.74	0.05	0.73	3.54	<0.03	0.14	1.06
UG4	65.3	18.56	5.89	1.46	2.05	0.86	0.05	0.83	3.09	<0.03	0.06	1.28

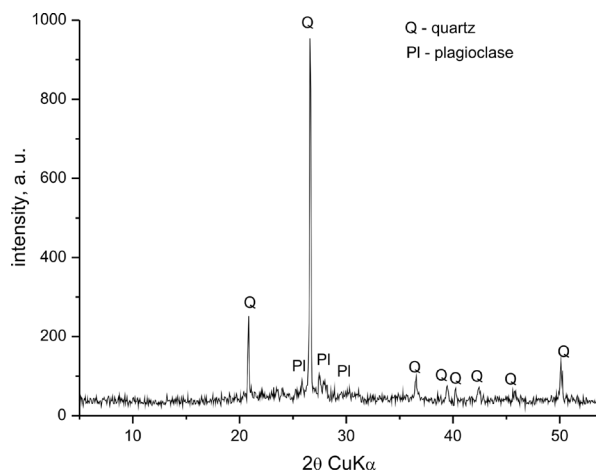


Fig. 3. XRD patterns of unglazed medieval ceramic artifact UG3

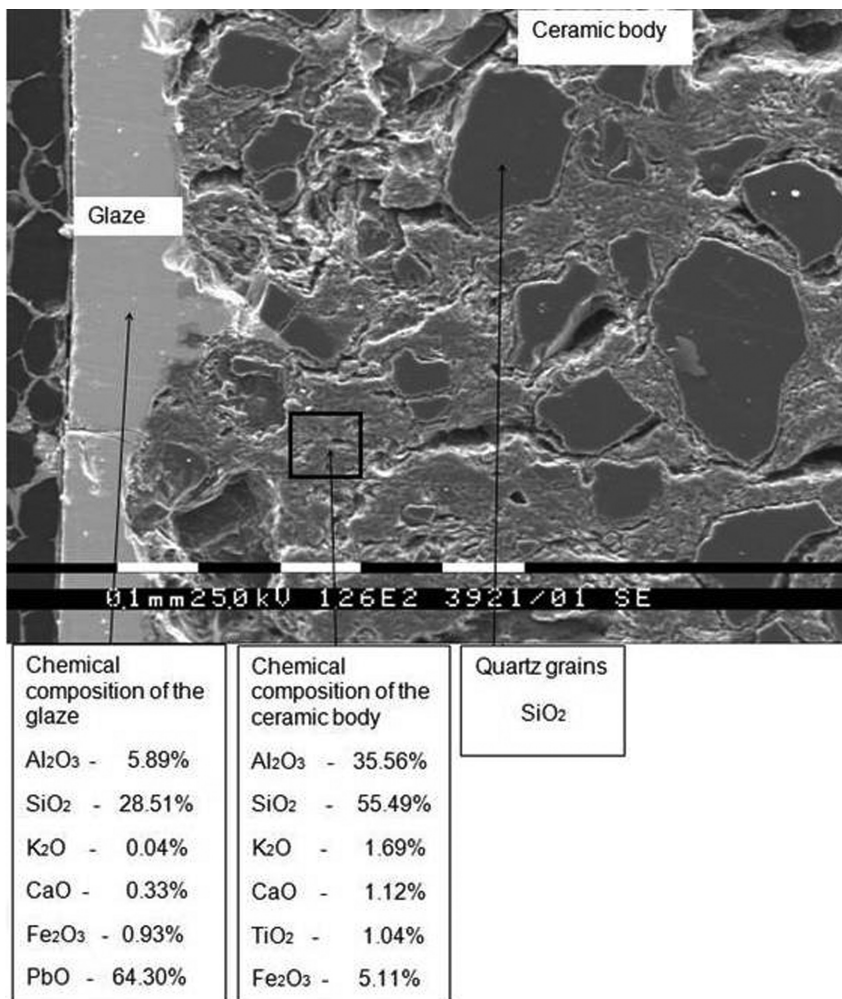


Fig. 4. SEM and local chemical analysis by EDS of the glaze and ceramic body of glazed ceramic denoted G1

which it is extracted. The content of grains of quartz sand in the ceramic body is needed from the presence of lead glaze having a high thermal expansion coefficient. The glaze on the ceramic body is a transparent lead glaze. This glaze probably is prepared by two raw materials: PbO – 70% and clay – 30%. The glaze is applied by dipping of the green ceramic body in the glaze following single firing or on a biscuit ceramic body on at double firing. Assumed, that the artifact is obtained by double firing, because it has relatively good water absorption, which shows good sintering of the ceramic body at about 950–1050 °C. The high percent of the lead oxide (64.30%) in the glaze notes that the temperature of the second glaze firing is lower with 50–100 °C and is done in a strongly oxidizing environment, otherwise the lead would be reduced. The oxidizing environment affects on the glaze color, which is yellowish-brown due to the lead glaze,

to brick-red with an effect of bleed of the ceramic body through the glaze.

Fig. 5 shows a scanning microscope image and local chemical analysis of the glazed ceramic artifact marked on Fig. 2 with G2. SEM analysis shows the presence of two layers on the ceramic body – glaze and engobe. There is a relief decoration of dark red lines and the color of the artifact is yellowish brown. This artifact, visual and as a result of the carried out analyzes, can be referred as a typical sgraffito pottery. SEM of artifact G2 shows that the ceramic body comprises open pores and grains of quartz, which are smaller compared with the previous artifact G1. The ceramic body has a higher content of Fe₂O₃, compared with the engobe and glaze, which explains the dark red color of the relief ornaments, in which the engobe is removed at the manufacture of the product and there is direct contact between the reactive lead glaze and the ceramic

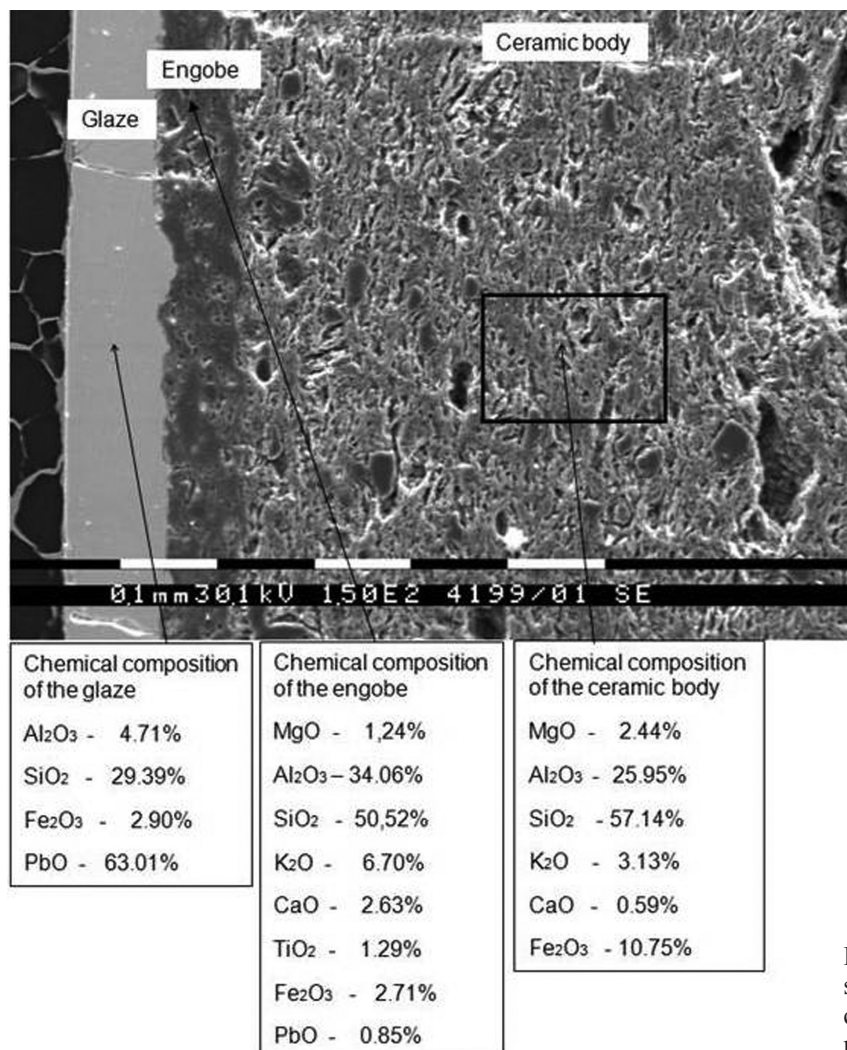


Fig. 5. SEM and local chemical analysis by EDS of the glaze, engobe and ceramic body of glazed ceramic denoted G2

body. This interaction leads to dark red coloration of the medium layer. Unlike the previous artifact G1, in this artefact is observed also the presence of engobe with chemical composition shown in Fig. 5, which relatively more sintered of the ceramic body. It can be argued that it is composed of fireclay, potassium feldspar, quartz sand and dolomite, i.e. during this period of ceramic development, ceramic bodies, glazes and glazes for recipe composition have been known and made. The role of the engobe is to cover the ceramic body and to prevent reaction between the glaze and the ceramic body or if such one exists it to be controlled only if it is necessary to obtain decoration ornaments with specific color. The lead glaze is transparent with Seger formula $PbO.0,13Al_2O_3.1,3SiO_2$ and firing temperature 940–960 °C. Such ceramics can be produced by a single firing or by double firing [9, 10].

SEM of glazed ceramic artifact G3 (Fig. 6) with white ceramic body and green transparent glaze

shows that this artifact is glazed with also typical lead glaze. The composition of the ceramic body reveals that it is prepared from quite pure white fireclay – possibly washed, which requires high firing temperature. The ceramic body has closed pores and 15.0% water absorption. The lead glaze is transparent with Seger formula $PbO.0,16Al_2O_3.2SiO_2$ and firing temperature above 1000 °C. Apparently this ceramic artifact belongs to the famous Preslav ceramics.

SEM of the glazed ceramic artifact labeled as G4 shown in Fig. 2 with red ceramic body, green glaze and black lines ornaments is presented in Fig. 7. The picture also reveals that it contains glaze, engobe and ceramic body. Distinctively for this artifact is that these black decorative ornaments are made by engraving the body after the application of the engobe, so in the ornaments between the glaze and the body there is not engobe, which makes the thickness of the glaze larger. There is again a di-

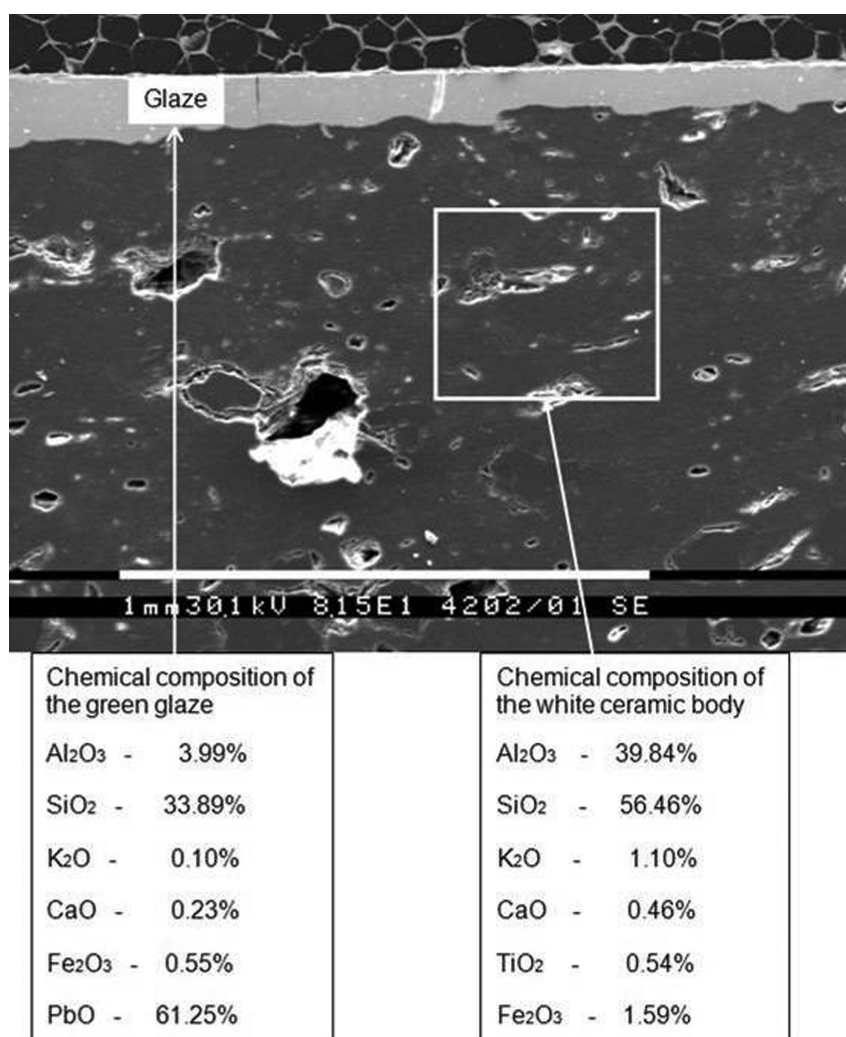


Fig. 6. SEM and local chemical analysis by EDS of the green transparent glaze, engobe and white ceramic body of glazed ceramic denoted G3

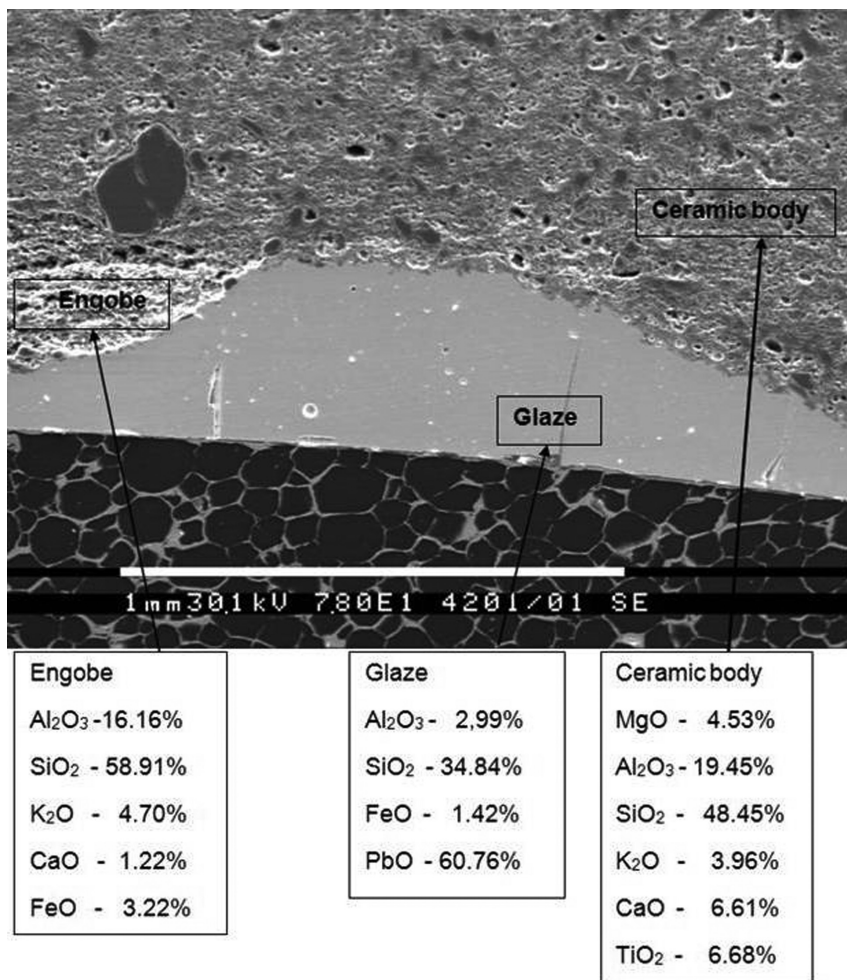


Fig. 7. SEM and local chemical analysis by EDS of the engobe, green transparent glaze and red ceramic body of glazed ceramic artifact denoted G4

rect contact between the reactive lead glaze and the ceramic body containing Fe₂O₃ – 10 wt.%, a concentration at which the carved ornament gets this black color. This is shown on Fig. 7. SEM observes more porous engobe compared to the ceramic body, which is more sintered. In recipe composition of the engobe, in addition to clay, quartz sand and potassium feldspar PbO is included too, as probably the engobe is only homogenized without grinding. The reaction between the glaze and the engobe gives green color which can be obtained in reducing conditions at that content of Fe₂O₃. The glaze has a Seger formula PbO.0,15Al₂O₃.1,9SiO₂ and firing temperature 1000–1020 °C [9, 10].

Figure 8 shows the chemical composition of the boundary of the engobe and the glaze, the chemical composition in the black line, the chemical composition of the boundary between the black line and the ceramic body and the chemical composition of the glaze. Areas near the contact between the engobe and glaze, glaze and ceramic body were studied By SEM – EDS. It has been found that chemical components migrate in both directions. The lead from

the glaze enters in the engobe and body, and K, Ca, and Fe dissolve in the reactive lead glaze.

CONCLUSION

It has been established that the main oxides in the ceramic body of the medieval pottery are SiO₂ and Al₂O₃. The artifacts contain also a certain amount of coloring oxides (Fe₂O₃ + TiO₂), which cause the slightly red color. The water absorption of the medieval pottery is in the range 10–15 wt.%, which gives reason to believe that the artifacts are well sintered, probably at high temperature around 950–1050 °C. The phase composition of the artifacts is represented by quartz and plagioclase, which amount varies by the samples. SEM proves the presence of coarse quartz grains having a size of 0.05 to 0.3 mm in a sintered ceramic body. This leads to the conclusion that it is used either highly sandy clay or ceramic body, consisting of red firing clay and quartz sand with dimensions of 0.05 to 0.3 mm, providing the high thermal expansion coefficient of the ceramic

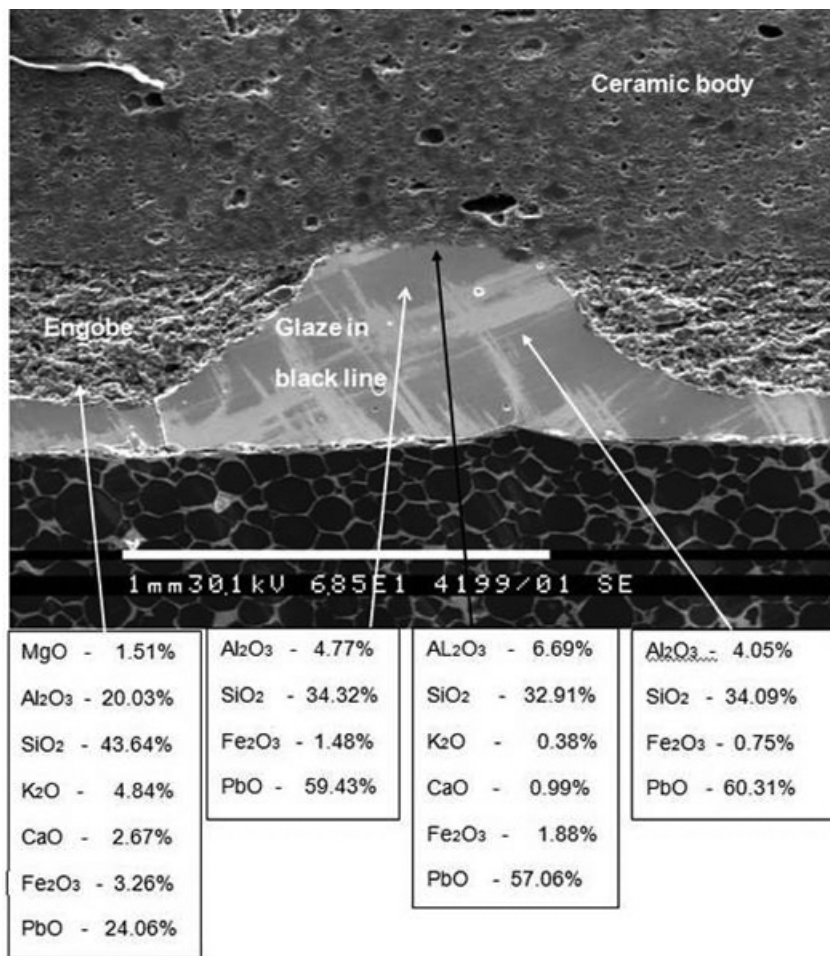


Fig. 8. Chemical composition of the boundary between engobe and glaze, of the black line, of the boundary between the black line and the ceramic body and of the glaze of glazed ceramic denoted G4

body after firing, necessary for the coordination of transparent lead glaze, also having a high thermal expansion coefficient.

The study of the glazed artifacts indicates that transparent lead glaze with firing temperature around 950–1050 °C is widely used in the Middle Ages. The sintered ceramic body of the glazed artifacts is obtained from ceramic body involving clay with a high content of Fe₂O₃, quartz sand and potassium feldspar. The conclusion is that the glazed artifacts G2 and G4 are typical sgraffito pottery, a fact indicating that during this period of ceramic development, when these products have been created (middle ages), the ceramic masters knew and made ceramic bodies, engobes and glazes in recipe composition from different raw materials.

It is proven that the artifact G4 is of the type of the famous Preslav ceramics with a white ceramic body and transparent green glaze, with the Seger formula $PbO \cdot 0.16Al_2O_3 \cdot 2SiO_2$ and firing temperature above 1000 °C. It has been found that the chemical elements are migrating in both directions within the contact layers: engobe–glaze and glaze–

ceramic body. The lead from the glaze enters in the engobe and body, and K, Ca, and Fe dissolve in the reactive lead glaze.

REFERENCE

1. K. Popkonstantinov, R. Kostova, V. Pletnyov, in: Bulgarian lands during the Middle Ages VII–XVIII century, International Conference honor of Prof. Al. Kuzev. Acta Musei Varnaensis III-2, Varna, 2005, p. 107.
2. R. Kostova, *Archaeologia Bulgarica*, **3**, 120 (1998).
3. Y. Dimitriev, E. Kashchieva, St. Djambazov, in: Proc. 4th European Conference on Advanced Materials and Processes, 25–28 Sept. Padua/Venice, Italy, 1995, p. 613.
4. St. Djambazov, Y. Dimitriev, E. Kashchieva, A. Yoleva, in: Proc. International symposium on glass problems, 4–6 September, Istanbul, Turkey, 1996, vol. 2, p. 178.
5. St. Djambazov, N. Nedelchev, Y. Ivanova, A. Yoleva, E. Kashchieva, Y. Dimitriev, in: Proc. IV World Congress on Ceramic Tile Quality, QUALICER’ 96, Castellon, Spain, 1996, p. 445.

6. St. Djambazov, Y. Ivanova, E. Kashchieva, A. Yoleva, in: Proc. Second International Conf. on Borates Glasses, Crystals and Melts, Abingdon, U.K., 1997, p. 1.
7. S. Djambazov, A. Yoleva, in: Proceedings of the First Balkan Conference on Glass Science & Technology, G. Kordas and N. Vlachos (eds.), Volos, Greece, 9–10.10.2000, 2000, p. 449.
8. M. Semmoto, T. Kannari, T. Shibata, H. Kamuro, St. Djambazov, A. Yoleva, O. Malinov, in: The 29th Annual Meeting of the Japan Society for Scientific Studies on Cultural Property 23–24.06.2012.
9. A. Gerasimov et al, Technology of ceramic materials, Sarasvati, Sofia, 2003.
10. St. Bachvarov, S. Stefanov, Ceramic Glazes, Technika, Sofia, 1985.

ИЗСЛЕДВАНЕ НА СРЕДНОВЕКОВНА КЕРАМИКА ОТКРИТА В МАНАСТИРА КАРААЧТЕКЕ КРАЙ ВАРНА, БЪЛГАРИЯ

А. Йолева, С. Джамбазов, П. Джамбазов

*Катедра Технология на силикатите, Химикотехнологичен и металургичен университет,
София, България*

Постъпила декември, 2014 г.; приета януари, 2015 г.

(Резюме)

Изследването на средновековни керамики е важно, за да се получи информация за развитието на технологията на производство на керамиката през този период. Различни средновековни неглазирани и глазирани керамични артефакти, открити при археологически разкопки в манастира Караachteke близо до Варна (България) са химически и структурно охарактеризирани с РФА и СЕМ за установяване на технологията на производство на средновековната керамика. Водопоглъщаемостта на неглазираните артефакти, определена по метода на Архимед, е в интервала от 10 до 15 тегл.%, което показва, че керамиката е добре спечена и вероятно е изпичана при висока температура около 950–1050 °С. Фазовият състав на керамичните артефакти показва наличието на кристални фази от кварц и плагиоклаз, количеството на които варира в различните проби. СЕМ доказва присъствието на едри кварцови зърна, имащи размер от 0,05 до 0,3 mm в спеченото керамично тяло. Това води до заключението, че за получаване на керамиката се е използвала или силно пясъклива глина или керамична маса, състояща се от червено изпичаща се глина и едрозърнест кварцов пясък.

Изследването на глазираните керамични артефакти доказва, че през Средновековието широко е била използвана прозрачна оловна глазура и керамиката е изпичана при температура около 950–1050 °С. Част от глазираните артефакти са типична сграфито керамика. Друга част от глазираните артефакти е от типа на известната Преславска керамика, характеризираща се с бял керамичен череп и прозрачна зелена глазура с Зегерова формула $PbO \cdot 0,16Al_2O_3 \cdot 2SiO_2$ и температурата изпичане над 1000 °С.

Effect of thickness on the photocatalytic properties of ZnO thin films

N. Kaneva^{1*}, A. Bojinova¹, K. Papazova¹, D. Dimitrov¹,
I. Svinyarov², M. Bogdanov²

¹ Laboratory of Nanoparticle Science and Technology, Department of General and Inorganic Chemistry, Faculty of Chemistry and Pharmacy, University of Sofia, 1 James Bourchier Blvd., 1164 Sofia, Bulgaria

² Laboratory of Heterocyclic compounds, Faculty of Chemistry and Pharmacy, University of Sofia, 1 James Bourchier Blvd., 1164 Sofia, Bulgaria

Received December, 2014; Revised January, 2015

Nanostructured zinc oxide films are prepared by sol-gel method using dip-coating technique. The thin films are deposited on glass substrates with different thickness (1, 3, 5 and 7 coats). The samples are characterized by means of XRD, SEM and UV-visible analyses. The aim of our investigations is photocatalytic degradation of the organic dyes – *Malachite Green* (MG, triarylmethane azo dye) and *Methylene Blue* (MB, heterocyclic aromatic dye) under UV-light illumination.

The photocatalytic results show that the thickest films on glass exhibit the highest efficiency under UV-light. The thin films with one coating have lowest rate constants in comparison with the other samples. The ZnO films with 7 coats have better photocatalytic efficiency and faster degradation of MG compared to MB, reasoned by the formation of stable intermediates in the reaction of OH radicals with triarylmethane dye (C=C bond) during the photocatalysis.

Key words: ZnO, thin films, thickness, photocatalysis, sol-gel, organic dyes.

INTRODUCTION

In the past decades, environmental problems have been increasingly serious with the development of the industry of human society. Eradication of toxic compounds from water and wastewater has become the focus of research recently.

Textile dyes are of environmental interest because of their widespread use and their potential for forming toxic aromatic amines. Among the synthetic dyes, which are widely used for textile dyeing and other industrial applications, those containing an azo chromophore constitute the largest class [1]. Azo dyes are a class of dyes, which are widely used in a variety of products, such as textiles, paper, foodstuffs or leather. However, these compounds and degradation products can be hazardous because their toxicity and carcinogenicity. Excess use of various dyes in the textile industry has led to the severe surface water and groundwater contamination by releasing the toxic and colored effluents [2].

It is important for the sake of increasing amount, its variety and resistance to biological destruction [3].

Many dye pollutants can be degraded effectively and ultimately mineralized using Advanced Oxidation Processes[®] (AOP). Heterogeneous photocatalysis as an advanced oxidation process [4] for wastewater treatment involves degradation of organic pollutants from wastewater using semiconductor oxides powders or suspensions. The catalytic materials applied in such studies have drawbacks like catalyst agglomeration, difficulty in post operation recovery and reuse as well as environmentally safe disposal. To circumvent these limitations, immobilizing the photocatalyst as thin films over large transparent supports is a viable option. ZnO thin films can be prepared by a number of methods including chemical vapor deposition (CVD) [5, 6], spin coating [7, 8], magnetron sputtering [9, 10], sol-gel method [11–13], pulsed laser deposition (PLD) [14, 15] and plasma-assisted molecular beam epitaxy (P-MBE) [16]. The sol-gel process is very attractive low-cost and versatile method for deposition of homogeneous thin films with desired thickness and nanostructure.

ZnO has a competitive photocatalytic activity greater in some cases than TiO₂; for example,

* To whom all correspondence should be sent:
E-mail: nina_k@abv.bg

on the discoloration of Reactive Blue 19, a textile anthraquinone dye, in aqueous suspension [17]. Furthermore, ZnO thin films have been found to decompose aqueous solutions of azo [18] and textile dyes [19], as well as phenol [20] and pharmaceutical drugs [21, 22]. Despite the importance of ZnO in the photocatalytic processes, little work has been done on ZnO thin films and their photocatalytic properties.

In this study, low cost sol-gel method is used to synthesize ZnO films over glass substrate via dip-coating technique. The thin films are obtained with different thickness and used as catalysts for photodegradation of *Malachite Green* and *Methylene Blue*.

MATERIALS AND METHODS

Materials

All reagents were used as received and purchased from Fluka. Zinc acetate dihydrate ($\text{Zn}(\text{CH}_3\text{COO})_2 \cdot 2\text{H}_2\text{O}$, $\geq 99.5\%$ purity) was used as a zinc source. As a dispersing medium, 2-methoxyethanol ($\text{C}_3\text{H}_8\text{O}_2$, $\geq 99.5\%$ purity) has an important role as the solvent and monoethanolamine (MEA, $\text{HOCH}_2\text{C}_2\text{NH}_2$, $\geq 99.0\%$ purity) as stabilizer. The glass slides (ca. 76×26 mm) for substrates of ZnO films were from ISO-LAB (Germany). *Malachite Green* ($\text{C}_{52}\text{H}_{54}\text{N}_4\text{O}_{12}$, $\lambda_{\text{max}} = 615$ nm, Chroma-Gesellschaft mbH&Co) and *Methylene Blue* ($\text{C}_{16}\text{H}_{18}\text{ClN}_3\text{S}$, $\lambda_{\text{max}} = 660$ nm, Fluka) were model pollutants and representatives of the most important impurities in the textile industry wastewater. Distilled water was used in the preparation of dye solutions.

Methods

Synthesis and characterization of ZnO films

The method of preparing sols and thin films was the same as procedure, carried out in previous works and was described briefly as following [18, 23]: In order to prepare the samples, zinc acetate dihydrate was dissolved in 2-methoxyethanol under vigorous magnetic stirring for a few minutes at room temperature to obtain a homogeneous medium. The equimolar quantity mole of monoethanolamine was added to the solution (molar ratio of zinc acetate to MEA was 1:1). The reaction mixture solution was stirred by a magnetic stirrer at 500 rpm to yield homogeneous solution and heated at 60°C for 1 h. Afterwards the solution was kept in a covered for 24 h at room temperature. No visible changes were observed in the sol upon storing of the precursor for at least 2 months. The glass substrates were rinsed

in distilled water. The thin films were prepared by dip-coating technique with withdrawal speeds of 0.9 cm/min at room temperature. After dip-coating process, the samples were dried at 80°C for 15 min. This coating procedure was repeated 1, 3, 5 and 7 times. Finally, the films were annealed at 500°C for 1 hour in order to obtain the ZnO films for photocatalytic experiments. The mass of ZnO deposited on films prepared with a single and seven coatings was 2.06 mg ($\pm 8\%$) and 7.88 mg ($\pm 6\%$), respectively. The film area was about 14.5 cm² on each side of the glass plate.

The obtained ZnO thin films were characterized by powder X-ray diffraction (XRD) and Scanning Electron Microscopy (SEM). The XRD spectra were recorded at room temperature by powder diffractometer (Siemens D500 with $\text{CuK}\alpha$ radiation within 2θ range 30 – 70 deg at a step of 0.05 deg 2θ and counting time 2 s/step). The average size of crystallites is calculated by the Scherer's equation:

$$d_{hkl} = k\lambda/\beta \cos(2\theta) \quad (1)$$

where d_{hkl} is the average crystallite size (nm), λ is the wavelength of $\text{CuK}\alpha$ radiation applied ($\lambda = 0.154056$ nm), θ is the Bragg's angle of diffraction, β is the full-width at half maximum intensity of the most intensive 101 peak observed at $2\theta = 36.2^\circ$ (converted to radians) and k is a constant usually chosen ~ 0.9 .

The SEM images were obtained by scanning electron microscope JSM-5510 (JEOL) operated at 10 kV of acceleration voltage. The investigated samples were coated with a thin film of gold by fine coater JFC-1200 (JEOL) before observation.

Photocatalytic experiment

The photocatalytic activity of the sol-gel films with different thickness were evaluated by the photocatalytic purification of model pollutants: *Malachite Green* (MG) and *Methylene Blue* (MB) were used as organic materials to be mineralized under UV-light illumination. The light power density at the sample position was 0.66 mW/cm² measured with research radiometer (Ealing Electro-optics, Inc.). The lamp was fixed at 15 cm above the treated solution. The initial concentration of MG and MB were 10 ppm. All photocatalytic experiments were performed at ambient temperature ($23 \pm 2^\circ\text{C}$).

The ZnO films were placed in glass reactor containing 150 mL 10 ppm dyes solution and were then irradiated with light source (Sylvania 18 W BLB T8). The films were placed at 0.5 cm below the surface of the investigated solution. This tube emits UVA in the range of 315 – 400 nm. After irradiating for 4 h, the concentration of the residual MG and

MB were determined by a UV–Vis spectrophotometer (Evolution 300 Thermo Scientific) at $\lambda_{\max} = 615$ nm and $\lambda_{\max} = 660$ nm. The rate of decolorization was observed in terms of change in intensity at λ_{\max} of the dyes. The decolorization efficiency (D %) was calculated using the equation:

$$D\% = \frac{C_0 - C_t}{C_t} \times 100 \quad (2)$$

where C_0 and C_t were initial and instantaneous concentrations of MG and MB.

RESULTS AND DISCUSSION

Structure and morphology of ZnO films

The phase structure and orientation of the ZnO films with 1 and 7 coats on glass substrate are determined by X-ray diffraction (XRD) and the diffractogram is presented in Fig. 1. The films produced are polycrystalline, showing the wurtzite ZnO hexagonal structure, while there is no evidence for the presence of other phases. All the diffraction peaks of the ZnO thin films can be indexed to (100), (002), (101), (102), (110), (103), (200), (112) and (201) diffraction planes at $2\theta = 31.77^\circ$, 34.42° , 36.25° , 47.54° , 56.60° , 62.86° , 66.37° , 67.96° and 69.09° , respectively. The most intensive (101) peak is observed at $2\theta = 36.2^\circ$. The size of crystallites of the all thin films, calculated by Scherer (Eq. 1) from the (101) peak is ~ 30 nm.

SEM image of the surface of the samples with one and seven coatings synthesized via sol-gel method is presented in Fig. 2. As seen in the figure, the investigated films has homogeneous surface with different ganglia-like hills. The morphology is

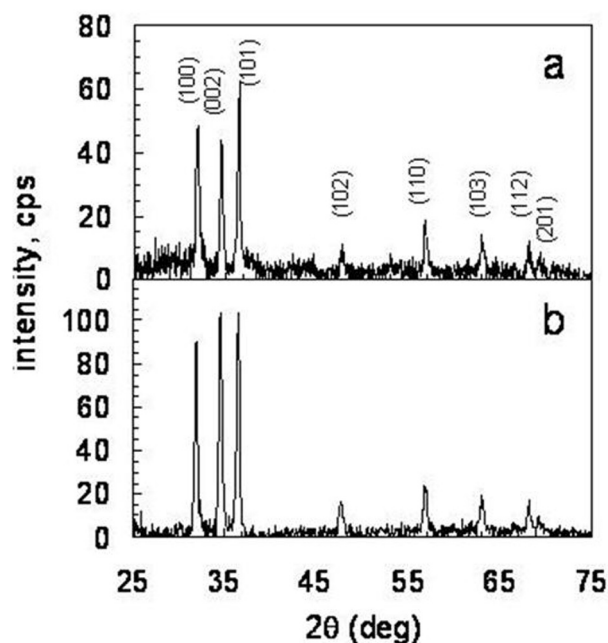


Fig. 1. XRD pattern of sol-gel film with one (a) and seven (b) coats

homogenous with the wrinkles, which are located on the films surface. Their shape, size and thickness are changed, depending of number of coats (Fig. 2a). The surface of films with seven coats is much more developed (Fig. 2b). The wrinkles are bigger (typical height about $2.5\text{--}3\mu\text{m}$, width $1\mu\text{m}$ and length from 5 to $15\mu\text{m}$) and the morphology is homogenous. The thin films show much better adhesion of the layers and higher density, compared to films with one coat. They are reproducible irrespective on the conditions of film deposition (with

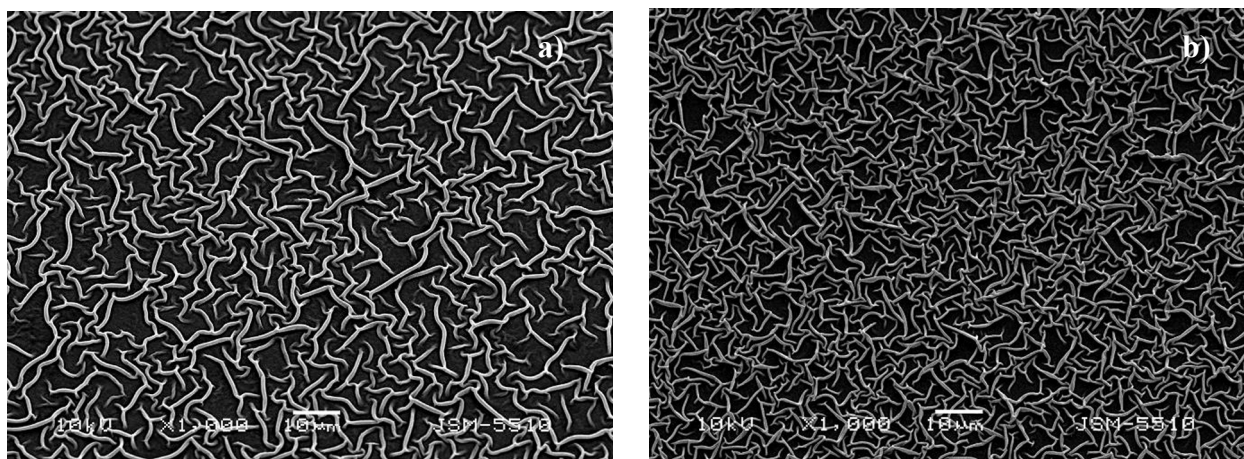
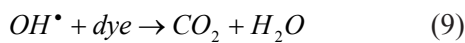
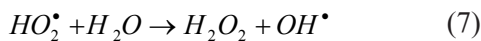
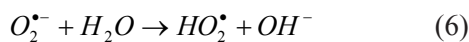
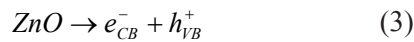


Fig. 2. SEM image of ZnO film with one (a) and seven (b) coats

different thickness) and we can see them in always different films [18, 23].

Photocatalytic properties

The photocatalytic efficiency depends on many parameters such as the distance between light source and organic compound, light intensity, initial concentration of dyes, doped and pure photocatalysts, different thickness of materials, pH and so on. In this work, the effect of thickness on the photocatalytic activity of ZnO films is studied for degradation of Malachite Green and Methylene Blue. The photocatalytic activity of the ZnO sol-gel films with different thickness are evaluated by the photocatalytic degradation of MG and MB as representative dye pollutants. The photocatalytic decolorization of dyes is believed to take place according to the following mechanism [24]:



where h_{vb}^+ and e_{cb}^- are the electron vacancies in the valence band and the electron in the conduction band, respectively.

Several reports claim that the rate of photocatalytic degradation of various dyes fitted a pseudo first order kinetic model [25, 26]:

$$r = -\frac{dC}{dt} = k \quad (10)$$

Integrates Eq. (10), giving

$$-Ln \frac{C_t}{C_0} = k \quad (11)$$

where C_0 is the initial concentration of MG and MB, C_t is the concentration of dyes at irradiation time t , t is the irradiation time and k is the apparent pseudo first order rate constant. The photocatalytic degradation of the dye solutions over all illuminated ZnO thin films with different thickness obeyed pseudo first order kinetics. Figure 3 shows the pseudo first order reaction with respect to the change of dyes concentration under UV-light illumination. The relationship between thickness and photocatalytic properties of ZnO films is summarized and compared for the both dyes in Fig. 4. As seen from figure, the thickest films have the highest rate constants and photocatalytic properties. This dependence is observed in the mineralization of the two dyes. The photocatalytic degradation is highest for the films obtained by seven coatings, which is probably due to the largest amount of ZnO catalyst. The films with three layers have higher efficiency than those, prepared with one. The rate constants

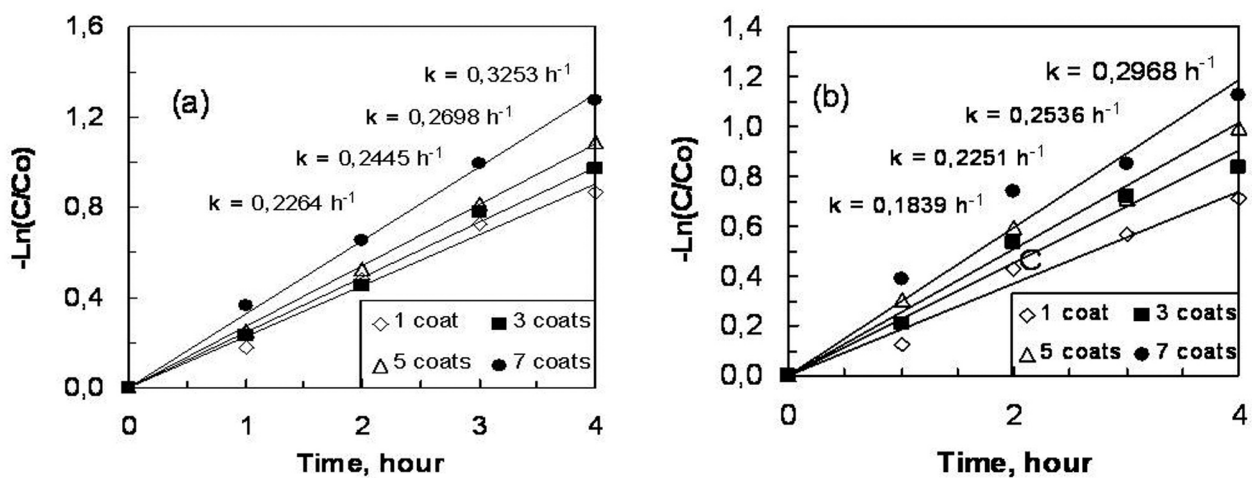


Fig. 3. Kinetic study on the photocatalytic degradation Malachite Green (a) and Methylene Blue (b) using ZnO thin films with different thickness (1, 3, 5 and 7 coats)

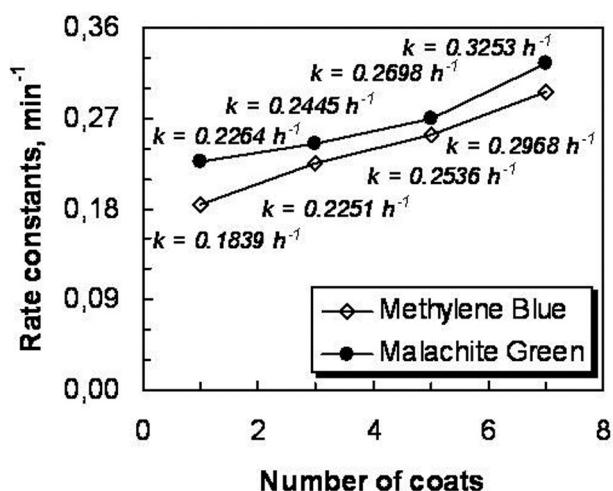


Fig. 4. Relation between rate constants and different thickness of ZnO films for the degradation of dyes under UV-light illumination

are increased in the intermediate thickness – 3 and 5 coats. These results confirm that the rise in thickness of ZnO films leads to increases of the activity. The observed faster degradation of MG compared to MB most probably is due to the formation of a stable intermediates in the reaction of OH radicals with triarylmethane dye (C=C bond) during the photocatalysis [26, 27]. The values k of the rate constants are confirmed by rate of degradation of the organic dyes. The degradation is calculated using Eq. 2.

Nanostructured films with 7 layers have a better photocatalytic activity and faster degradation MG ($D\% = 72.11\%$ for four hours) in comparison with

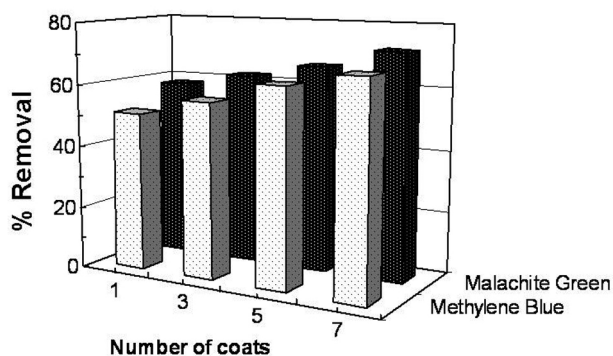


Fig. 5. Effect of the thin films with different thickness on photocatalytic mineralization of Malachite Green and Methylene Blue

MB ($D\% = 67.43\%$ for four hours) (Fig. 5). The photocatalytic activity is highest for the films obtained by seven coats, while samples obtained with one layer have a lowest activity ($D\%_{MG} = 58.04\%$ and $D\%_{MB} = 50.84\%$, Fig. 5). The reason is probably due to the larger amount of ZnO catalyst – 0.230 mg/cm^2 compared to 0.175 mg/cm^2 (film with 5 coats), 0.126 mg/cm^2 (film with 3 coats) and 0.058 mg/cm^2 (film with 1 coat).

Probable mechanisms of degradation of MB and MG, induced by a reaction with hydroxyl radicals, have been reported in the literature [27, 28]. Regarding MB, Houas et al. [26] suggested that in the initial step $HO\cdot$ radical cleavages S+=C double bond, which in turn induces ring-opening reaction of the central heterocyclic moiety, thereby leading to decolourization of the solution (Fig. 6a). In an-

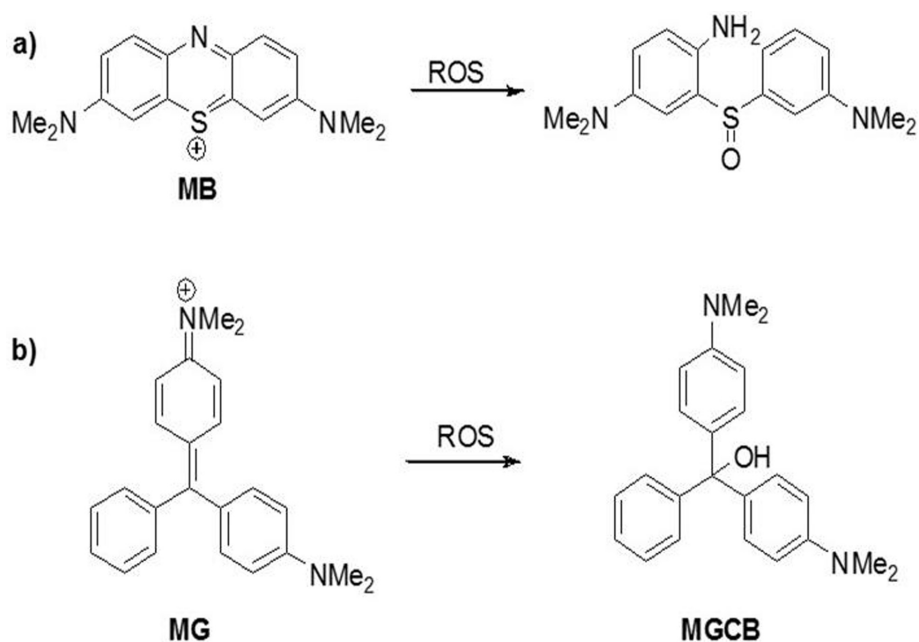


Fig. 6. First step of decomposition of: a) Methylene Blue (MB) and b) Malachite Green (MG)

other study, Ju et al. [28] showed that the initial step of MG degradation includes radical attack on the central carbon of MG, which transforms it into malachite green carbinol base (MGCB) and again leads to decolorization of the solution (Fig. 6b). Taking into account the above reasoning, it can be concluded that the faster degradation of MG, observed in the present study, can be attributed to the facilitated attack of HO• radical toward the sulfur atom, the latter being due to its enhanced electron density.

CONCLUSION

Nanostructure ZnO films are obtained by sol-gel method from zinc acetate dehydrate dissolved in 2-methoxyethanol and monoethanolamine. The samples onto glass substrates are deposited with different thickness (1, 3, 5 and 7 coats) via dip-coating technique. The film thickness plays an important role in the degradation performance of *Malachite Green* and *Methylene Blue*. The photocatalytic results show that the films with seven coats show better efficiency and faster degradation MG compared to MB under UV-light. The thin films with one layer have lowest photocatalytic behavior for mineralization of dyes in comparison with the other samples. The optimal thickness of films is experimentally established. A 72% of MG and 67% of MB decolorization is reached with the thickest ZnO photocatalysts under UV-light irradiation. The photocatalytic processes show that ZnO films with different thickness are attractive for application in wastewaters.

Acknowledgments: This research is financially supported by project DFNIT0216, FP7 project Beyond Everest and Russian Presidential Program of engineer advanced training.

REFERENCES

- H. Zollinger, Wiley-VCH, New York, 1987, p. 92.
- I. Salem, M. El-Maazawi, *Chemosphere*, **41**, 1173 (2000).
- M. Sohrabi, M. Ghavamia, *J. Hazard. Mater.*, **153**, 1235 (2008).
- M. Simonsen, *Chemistry of Advanced Environmental Purification Processes of Water*, 2014, p. 135.
- L. Fanni, B. Aebersold, D. Alexander, L. Ding, M. Morales Masis, S. Nicolay, C. Ballif, *Thin Solid Films*, **565**, 1 (2014).
- Zh. Li, Z. Hu, L. Jiang, H. Huang, F. Liu, X. Zhang, Y. Wang, P. Yin, L. Guo, *Applied Surface Science*, **258**, 10175 (2012).
- V. Kumar, V. Kumar, S. Som, A. Yousif, N. Singh, O. Ntwaeaborwa, A. Kapoor, H. Swart, *Journal of Colloid and Interface Science*, **428**, 8 (2014).
- A. Nalbant, Ö. Ertek, İ. Okur, *Materials Science and Engineering: B*, **178**, 368 (2013).
- Ch. Zhang, X. Chen, X. Geng, C. Tian, Q. Huang, Y. Zhao, X. Zhang, *Applied Surface Science*, **274**, 371 (2013).
- I. Soumahoro, S. Colis, G. Schmerber, C. Leuvrey, S. Barre, C. Ulhaq-Bouillet, D. Muller, M. Abd-lefdil, N. Hassanain, J. Petersen, A. Berrada, A. Slaoui, A. Dinia, *Thin Solid Films*, **566**, 61 (2014).
- M. Addonizio, A. Aronne, S. Daliento, O. Tari, E. Fanelli, P. Pernice, *Applied Surface Science*, **305**, 194 (2014); Ch. Li, Ch. Hsu, Y. Li, *Journal of Alloys and Compounds*, **606**, 27 (2014).
- M. Popa, R. Mereu, M. Filip, M. Gabor, T. Petrisor, L. Ciontea, T. Petrisor, *Materials Letters*, **92**, 267 (2013).
- N. Kaneva, A. Bojinova, K. Papazova, D. Dimitrov, *Journal of the University of Chemical Technology and Metallurgy*, **49**, 149 (2014).
- R. Jamal, M. Hameed, K. Adem, *Materials Letters*, **132**, 31 (2014).
- S. Huang, Y. Chou, C. Chou, V. Hsiao, *Applied Surface Science*, **266**, 194 (2013).
- P. Ding, X. Pan, J. Huang, H. He, B. Lu, H. Zhang, Z. Ye, *Journal of Crystal Growth*, **331**, 15 (2011).
- C. Lizama, J. Freer, J. Baeza, H. Mansilla, *Catalysis Today*, **76**, 235 (2002).
- N. Kaneva, D. Dimitrov, C. Dushkin, *Applied Surface Science*, **257**, 8113 (2011).
- R. Saravanan, S. Karthikeyan, V.K. Gupta, G. Sekaran, V. Narayanan, A. Stephen, *Materials Science and Engineering: C*, **33**, 91 (2013).
- I. Prabha, S. Lathasree, *Materials Science in Semiconductor Processing*, **26**, 603 (2014).
- D. Mohapatra, S. K. Brar, R. Dagher, R. Tyagi, P. Picard, R. Surampalli, P. Drogui, *Science of The Total Environment*, **485–486**, 263 (2014).
- I. Pronin, N. Kaneva, A. Bozhinova, I. Averin, K. Papazova, D. Dimitrov, V. A. Moshnikov, *Kinetics and Catalysis*, **55**, 167 (2014).
- N. Kaneva, A. Bojinova, K. Papazova, D. Dimitrov, *Journal of the University of Chemical Technology and Metallurgy*, **49**, 149 (2014).
- S. Kumar, K. Rao, *Royal Science of Chemistry (Advances)*, **5**, 3306 (2015).
- J. Xu, Y. Ao, D. Fu, C. Yuan, *Applied Surface Science*, **254**, 3033 (2008).
- A. Valentine Rupa, D. Manikandan, D. Divakar, T. Sivakumar, *Journal of Hazardous Materials*, **147**, 906 (2007).
- A. Houas, H. Lachheb, M. Ksib, E. Elaloui, C. Guillard, J.-M. Herrmann, *Applied Catalysis B: Environmental*, **31**, 145 (2001).
- Y. Ju, J. Qiao, X. Peng, Z. Xu, J. Fang, S. Yang, C. Sun, *Chemical Engineering Journal*, **221**, 353 (2013).

ЕФЕКТ НА ДЕБЕЛИНАТА ВЪРХУ ФОТОКАТАЛИТИЧНИТЕ СВОЙСТВА НА ZnO ТЪНКИ ФИЛМИ

Н. Кънева^{1*}, А. Божинова¹, К. Папазова¹, Д. Димитров¹,
И. Свиняров², М. Богданов²

¹ Лаборатория по Наука и Технология на Наночастиците, Катедра по Обща и неорганична химия,
Факултет по Химия и Фармация, Софийски университет,
бул. "Джеймс Баучер" 1, 1164, София, България

² Лаборатория по Хетероциклени съединения, Факултет по Химия и Фармация,
Софийски университет, бул. "Джеймс Баучер" 1, 1164, София, България

Постъпила декември, 2014 г.; приета януари, 2015 г.

(Резюме)

Наноструктурираните цинк оксидни филми са получени чрез зол-гел метод използвайки метода на потапящата подложка. Тънките филми са отложени върху стъклени подложки с различна дебелина (1, 3, 5 и 7 покрития). Пробите са характеризирани основно чрез XRD, SEM и UV-visible анализи. Целта на нашите изследвания са фотокаталитично разграждане на органични багрила– *Малахитово Зелено* (МЗ, триарилметаново азо багрило) и *Метиленово Синьо* (МС, хетероциклено ароматно багрило) под действието на ултравиолетова светлина.

Фотокаталитичните резултати показват, че най-дебелите филми върху стъкло притежават най-висока ефективност под ултравиолетова светлина. Тънките филми с едно покритие имат най-ниска скоростна константа в сравнение с останалите проби. ZnO филми със седем слоя има по-висока фотокаталитична ефективност и по-бързо разграждат МЗ в сравнение с МС, доказано чрез образуването на стабилни междинни продукти в реакцията на ОН радикали с триарилметановото багрило (С=С връзка) по време на фотокатализата.

Sol aging effect on the structure and photocatalytic action of ZnO films for pharmaceutical drugs degradation

N. Kaneva*, A. Bojinova, K. Papazova, D. Dimitrov

Laboratory of Nanoparticle Science and Technology, Department of General and Inorganic Chemistry, Faculty of Chemistry and Pharmacy, University of Sofia, 1164 Sofia, Bulgaria

Received December, 2014; Revised January, 2015

In this work, ZnO thin films are prepared by sol–gel method and the effect of aging time of the ZnO sol on the structural and photocatalytic properties of the films is studied. ZnO sol is aged for different periods (0, 30 and 60 days). Nanocrystalline thin films with different thickness (one or five coats) are deposited on glass substrates via dip-coating technique. The structural properties of samples are analyzed by Scanning Electron Microscopy and X-ray diffractometer. The effect of aging time of the starting sol in respect to photocatalytic degradation of the pharmaceutical drugs (*Paracetamol (PCA)* and *Chloramphenicol (CA)*) is studied by UV-vis spectroscopy. The experiments are conducted under UV and visible light irradiation. The results show that the increased aging time of the starting ZnO solution generally promotes photocatalytic activity. The films with one coating have lower rate constants of degradation with comparison to the other samples. The thin films with five coats obtained from ZnO sol, aged 60 days exhibit highest photocatalytic degradation of the drugs (*PCA*: UV – 84.57% and Vis – 65.66%; *CA*: UV – 67.2% and Vis – 52.2%) in comparison to the freshly prepared ones (*PCA*: UV – 29.60% and Vis – 18.62 %; *CA*: UV – 18.43% and Vis – 14.12%).

Key words: ZnO sol-gel films, aging time, photocatalysis, UV-visible, pharmaceutical drugs.

INTRODUCTION

In the recent years the interest in wide band gap oxide semiconductor materials such as zinc oxide (ZnO) [1], indium oxide (In₂O₃) [2], tin oxide (SnO₂) [3] and titanium oxide (TiO₂) [4] has notably increased. These materials in form of thin film present transport and optical properties that make them good candidates for modern applications. ZnO is a well known, chemically stable material, commonly used as coating material in optical thin films and has been applied in many other fields [5–7]. ZnO has also received extensive attention due to its excellent photocatalytic properties [8–10]. By photocatalytic processes in polluted air and water, using of UV irradiated inorganic oxides, contaminants such as textile dyes, pesticides and pharmaceutical drugs have been degraded [11–14].

Although pharmaceuticals have been consumed for many decades, only during the last few years their fate and release in the aquatic environment have

been recognized as one of the most urgent problems of environmental chemistry. Pharmaceutically active compounds such as analgesics, antibiotics, steroids, hormones, etc., have been detected in several public water systems in Europe, USA and Australia as a result of human, animal and plant activities [15, 16]. Mass balance of the input and output of pharmaceuticals in sewage treatment plants indicates that during sewage treatment not all pharmaceuticals are removed quantitatively [17] from the surface and underground water. Their environmental presence gains importance because they are related to abnormal physiological processes in reproduction, increased incidences of cancer, development of antibiotic-resistant bacteria and potential increased toxicity of chemical mixtures. Therefore, the photocatalytic decomposition of pharmaceutical products of environmental concern has been studied extensively and it has been demonstrated that heterogeneous photocatalysis using ZnO (nanowires, nanoparticles, thin films, etc.) as catalyst can be an alternative to conventional methods for their removal from water [13].

Different chemical and physical methods have been employed to prepare ZnO films including sputtering [18], chemical bath deposition [19],

* To whom all correspondence should be sent:
E-mail: nina_k@abv.bg

pulsed laser deposition [20], sol–gel [10, 21, 22] and spray pyrolysis [23]. The chemical methods present advantages as low cost, safety and easy handling equipments. The sol–gel process is one of the most appropriate methods to prepare thin oxide coatings due to some advantages, such as depositions are with good homogeneity, low processing temperature, low equipment cost and good optical properties. The preparation conditions of ZnO thin films by sol–gel method can influence the physical properties of the film [16, 17].

In this work we report ZnO thin films deposited on glass substrates by sol–gel technique, using zinc acetate dehydrate as a starting reagent. The ZnO sol is aged for different period – 0, 30 and 60 days. The deposited films with dip-coating technique are characterized using SEM, XRD and UV–vis analysis. The effect of the aging time of the starting solution as well as the number of coatings (1 and 5 coatings) is investigated for the photocatalytic degradation of *Paracetamol* (PCA) and *Chloramphenicol* (CA). *Paracetamol* (PCA) and *Chloramphenicol* (CA) are common drugs used extensively in variety medical applications. Therefore, they are chosen as model pollutants to test the activity of ZnO films with different aging time of the starting solution.

EXPERIMENTAL

Precursor sol preparation

Zinc acetate dihydrate ($\text{Zn}(\text{CH}_3\text{COO})_2 \cdot 2\text{H}_2\text{O}$, $\geq 99.5\%$ purity, Fluka) was chosen as Zn precursor. The zinc compound was dissolved in a solution containing 2-methoxyethanol ($\text{C}_3\text{H}_8\text{O}_2$, $\geq 99.5\%$ purity, Fluka) and monoethanolamine (MEA, $\text{HOCH}_2\text{C}_2\text{NH}_2$, $\geq 99.0\%$ purity, Fluka) used as a solvent and stabilizer, respectively. The mixture was continuously stirred at room temperature until a clear and homogeneous solution was reached. The obtained solution was heated up at $60\text{ }^\circ\text{C}$ upon magnetic stirring for 1 hour. The final solutions were kept at room temperature in darkness, in order to avoid some light-assisted reaction, and to limit the variables that may affect the solution. No visible changes were observed in the precursor when stored in darkness at room temperature for at least 2 months. An aliquot was taken each 0, 30 and 60 days for the films deposition.

ZnO films deposition and characterization

The thin films were deposited onto cleaned and dried glass substrates (ca. $76 \times 26\text{ mm}$, ISO-LAB Germany) by dip-coating technique. The films deposition consists in a dipping process of the sub-

strate into the starting solution and then pulling out at a constant velocity at room temperature. It was experimentally found out that best film quality was obtained at rates of 0.9 cm/min . The dipping process can be repeated until the desirable number of coatings or immersions is reached. The film thickness can be controlled by the number of coating cycles. Films were deposited with one and five coats from sols aged for different times. After each dipping process, the films were thermally treated at $80\text{ }^\circ\text{C}$ for 10 min, in order to remove the remaining solvents. The films were cooled at atmospheric conditions. As a final step, the films were subjected to another thermal treatment at $500\text{ }^\circ\text{C}$ for 1 h, in order to synthesize the final compound (ZnO) for photocatalytic tests.

The surface morphology of the ZnO films obtained from sols of different aging times was characterized by Scanning Electron Microscope (SEM, JEOL JSM-5510). The crystallinity and size of crystallites were determined by X-Ray Diffraction (XRD) at room temperature by powder diffractometer (Siemens D500 with $\text{CuK}\alpha$ radiation within 2θ range $30\text{--}70\text{ deg}$ at a step of $0.05\text{ deg } 2\theta$ and counting time 2 s/step). Drug concentrations in the aqueous solution after 4 h UV or visible irradiation and the optical absorbance spectra were measured by spectrophotometer Evaluation 3000 Thermo Science in the wavelength range from 200 to 600 nm.

Photocatalysis

The photocatalytic efficiency was measured in a glass reactor (250 ml), equipped with magnetic stirrer (rotating speed controlled by stroboscope), UV (maximum emission at 370 nm ; the light power density at the sample position was 0.66 mW/cm^2 as measured with Research Radiometer of Ealing Electro-optics, Inc.). The distance between the glass reactor and UV lamp was 15 cm. The mineralization of pharmaceutical drugs was monitored by UV-vis absorbance spectroscopy after aliquot sampling at regular time intervals. The sample was fixed at 0.5 cm bellow the drugs solution surface. The mineralization has been calculated as:

$$D\% = \left[\frac{C_0 - C}{C_0} \right] \times 100 \quad (1)$$

where C_0 is the initial concentration of drugs and C is the concentration of drugs after irradiation in selected time interval.

Experiments were carried out with six series of samples: nanostructured ZnO films obtained at different aging time of the starting solution (0, 30 and 60 days), prepared with 1 and 5 layers. The drugs solution volume was 150 mL. The initial concentra-

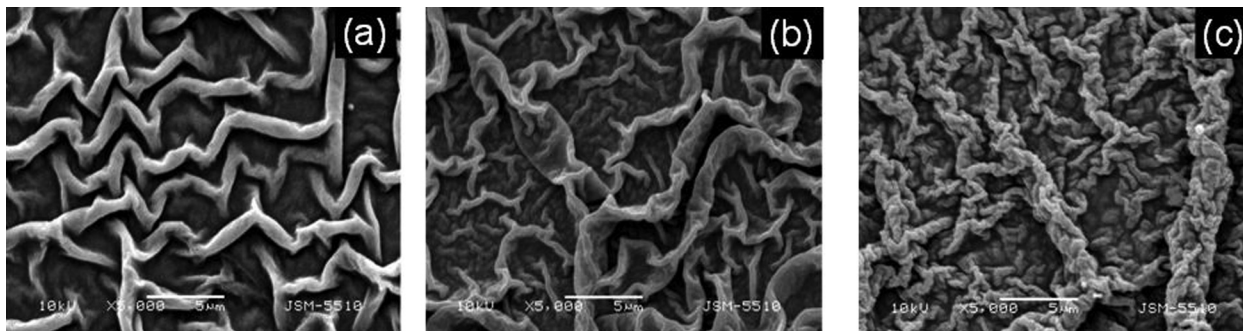


Fig. 1. SEM images of ZnO films with five coats obtained from sols aged (a) 0, (b) 30 and (c) 60 days

tion of PCA and CA was 20 ppm. All photocatalytic tests were performed at constant stirring rate (500 rpm) at room temperature (23 ± 2 °C).

RESULTS AND DISCUSSION

Structure analysis of ZnO films

The SEM images of the surface of ZnO films deposited at different aging time with 5 coats are shown in Fig. 1. These micrographs clearly show that there are changes in the morphology of the thin films with the aging time. The surface on the nanostructure films (ZnO starting sol, stayed 0 day) is homogeneous with typical ganglia-like structure. Their shape, size and thickness are changed, depending of the aging time of the starting solution. The increase of aging time of ZnO sol increases the volume and size of ganglia-like hills (Fig. 1 b, c), which are looking more branched and developed at their ends. The sol-gel films, sol aged 60 days, are more uniform and show much better adhesion of the layers and the highest density of the film. In this case the inorganic polymer-oxide network is uniformly built up. The ganglia-like structure seems reproducible irrespective on the conditions of films deposition and annealing.

The XRD patterns of ZnO films at 0, 30 and 60 day aged solution with 5 coats are presented in Fig. 2. The wurtzite-like structured ZnO is registered as only crystalline phase. The samples obtained at 500 °C by 0, 30 day-aged solution (Fig. 2a, b) show more intensive diffraction peak (002) at 34.4° which suggests a preferential orientation along the c-axis. But the films deposited by the starting solution with aging time 60 days are preferentially oriented along the (101) direction in turn (Fig. 2c). This result is similar to that reported by Guerra et al. [24] and Rozati et al. [25] describing ZnO thin films obtained by spray pyrolysis. The authors found that the aging time of the starting solution has a great effect on the

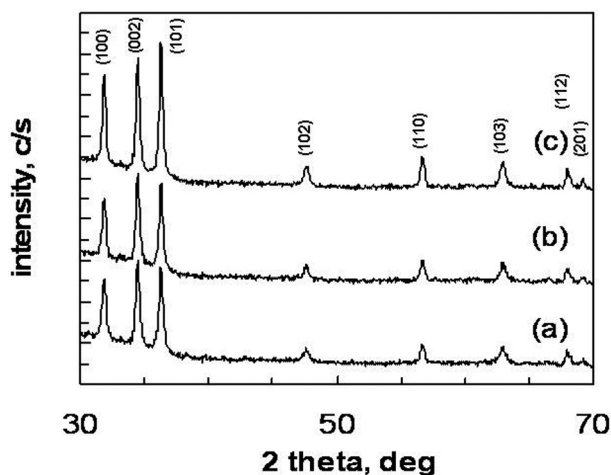


Fig. 2. XRD patterns of ZnO films with five coats obtained from sols aged (a) 0, (b) 30 and (c) 60 days

crystal growth orientation, which is in a good agreement with the literature data [24, 25].

The sizes of ZnO crystallites estimated along the (101) direction (the main peak of the 60 days sample with 5 coats) by Sherrer's formula are about 8, 30 and 60 nm for the films from sols aged for 0, 30 and 60 days. The longer aging time makes the diffraction peaks (100, 002, 101) better pronounced with higher intensity and increases the size of crystallites (see Fig. 3).

Photocatalytic activity

The relationship between morphology and photocatalytic performance of synthesized ZnO films is studied as model reaction for photodegradation of pharmaceutical drugs (*Paracetamol* and *Chloramphenicol*). The photocatalytic efficiency can be influenced by two factors – one of them is aging time of the ZnO sol itself and the other factor is the influence of the PCA and CA solutions. It is

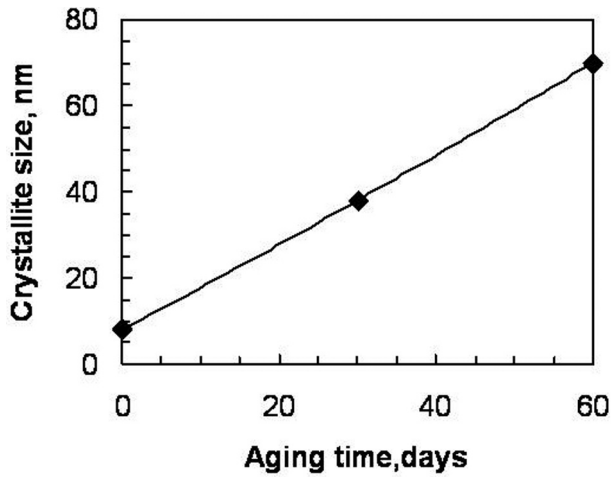


Fig. 3. Relationship between crystallite size and aging time

obvious, that these factors can not be separated completely, as the photocatalytic efficiency is measured by decomposition of the drugs.

The relationship between apparent rate constants of drugs degradation and irradiation time are presented in Fig. 4 (UV light, 4h) and Fig. 5 (visible light, 4h). The values of rate constants, k , are calculated from the corresponding $\ln(C/C_0)$ versus irradiation time:

$$\ln(C/C_0) = -kt \quad (2)$$

where C is the initial concentration of PCA and CA at each irradiation time interval at the wavelength of 243 nm and 278 nm, C_0 is the initial concentration before the irradiation, when the adsorption – desorption equilibrium between the drug molecules and the photocatalysts nanoparticles is achieved.

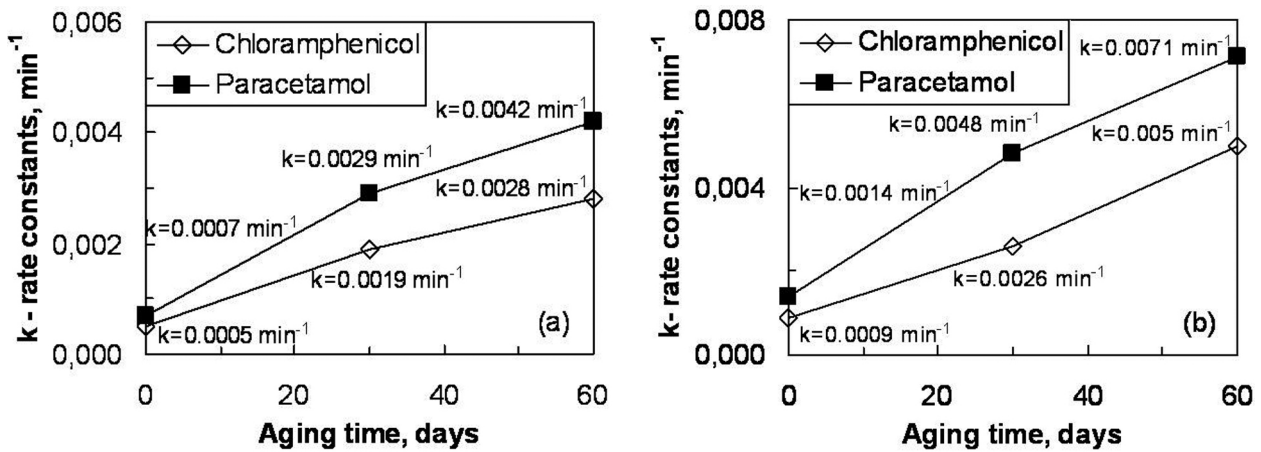


Fig. 4. Kinetic study on the photocatalytic degradation of drugs using ZnO films with 1 (a) and 5 (b) coats under UV-light illumination

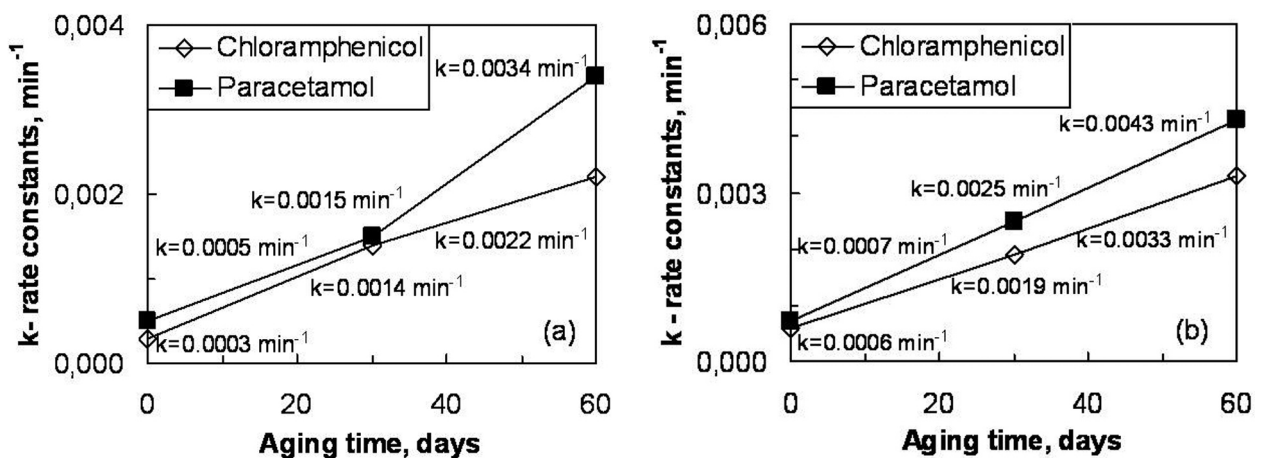


Fig. 5. Kinetic study on the photocatalytic degradation of drugs using ZnO films with 1 (a) and 5 (b) coats under visible illumination

The degradation of drugs obeys pseudo first order kinetics according to the Langmuir-Hinshelwood (L-H) model [26]. The apparent rate constant (k) is calculated by equation (2). As can be seen from Figures 4 and 5 the apparent rate constant increases with the increased aging time (in the range 0–60 days) and number of layers.

Nanostructure ZnO films deposited from 60 day aged solution have highest photocatalytic activity for degradation of the drugs under UV and visible light illumination. The samples with ZnO starting sol, aged 30 days show faster degradation of pharmaceutical products in comparison with these prepared from 0 day aged solution (Fig. 4 and 5). It is found that increasing the aging time of the starting sol increased the photocatalytic activity and the surface morphology of the samples is more developed.

The sol-gel films with five coats have higher efficiency than those prepared with one, which is probably due to the larger amount of ZnO catalyst in this case – 0.175 mg/cm², compared to 0.058 mg/cm² for the film with one coat. The largest ZnO amount is located as more developed surface of the catalysts, prepared with 5 coats. ZnO films have better photocatalytic efficiency and faster degrade PCA compared to CA. The reason for this fact is the smaller

molecule of the analgesic. As confirmation of the values of rate constants is the degree of degradation of the drugs. The degradation of drugs is calculated by Eq. (1) and the results are presented in Fig. 6.

The removal (%) of PCA and CA as a function of the light exposure time for the 1 (Fig. 6 a, b) and 5 (Fig. 6 c, d) ZnO immersions, deposited from starting solutions aged at different times, namely, 0, 30, and 60 days as can be seen. From these graphs a slight degradation of drugs increasing as the number of coats increases as well can be observed. In the case of Fig. 6c, d, corresponding to the film deposited with 5 coats from a 60-day aged solution, the most significant change occurs at PCA – under UV exposure time. A low removal of analgesic and antibiotic are reached at the not optimized conditions (0 day).

When more aged solution is used, the films present a higher photocatalytic activity, as can be observed in Figures 4–6. According to our results, the ZnO films with a very rough surface present a better degradation of drugs than those with a smoother surface. The more developed surface increases the total illuminated surface area, thus increasing the number of active surface sites and enhancing the catalytic activity of the films, as has been also established by Aprile et al. [27]. Taking this into account, we

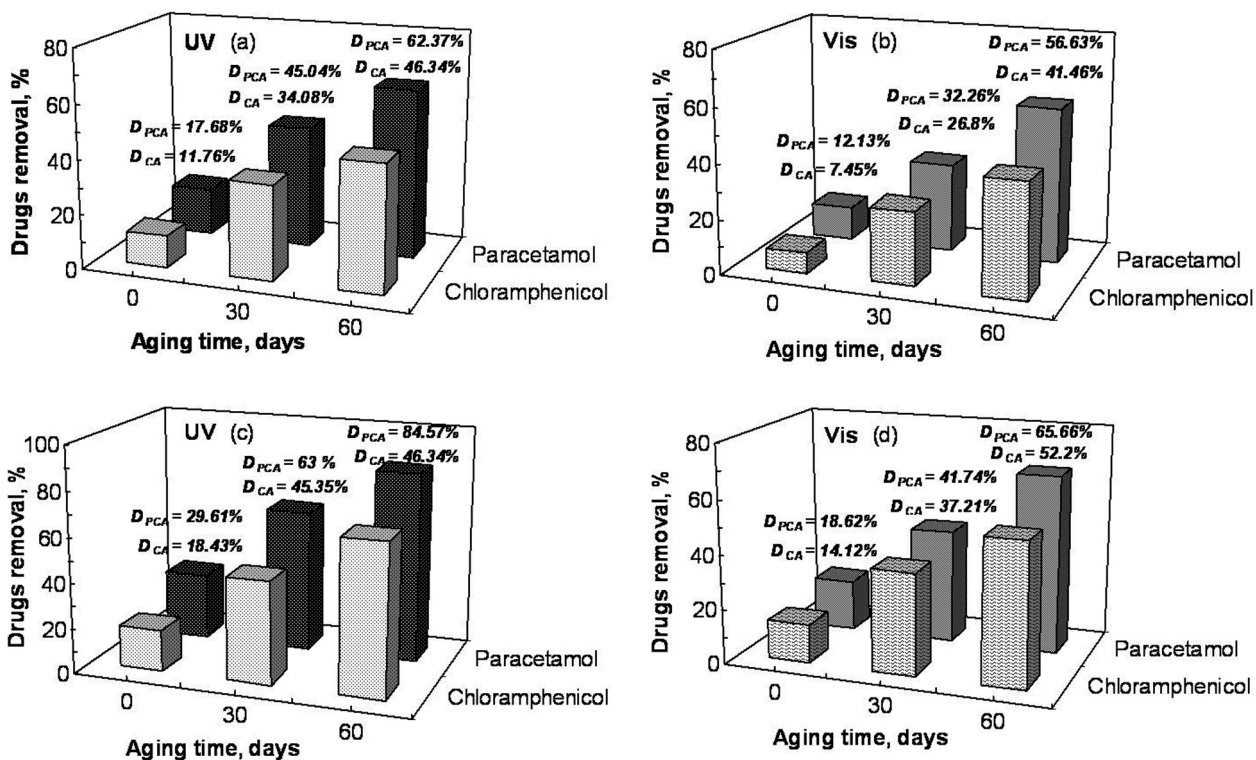


Fig. 6. Photocatalytic mineralization of Paracetamol and Chloramphenicol under UV and visible illumination using ZnO films with 1 (a, b) and 5 (c, d) coats

can consider that the formation of spatial structures promote the photocatalytic activity by increasing the exposed area and enhancing the mean life of the photo-generated holes

CONCLUSIONS

ZnO thin films on glass substrates are deposited by sol-gel technique starting from zinc acetate dehydrate dissolved in 2-methoxyethanol and monoethanoamine. The samples with different aging time (ZnO sol, stored 0, 30 and 60 days) have a ganglia-like surface, which are obtained by this simple and economical method. The film thickness and the aging time of the starting solution play an important role in the degradation performance of *Paracetamol* and *Chloramphenicol*. A 85% of analgesic and 67% of antibiotic degradation is reached using ZnO thin films with five coats, starting sol stayed 60 day, under UV-irradiation. Our investigation shows that aging time and thickness of ZnO thin films play significant role in the photocatalytic process.

Acknowledgements: This research is financially supported by project DFNIT0216, FP7 project Beyond Everest and Russian Presidential Program of engineer advanced training.

REFERENCES

1. Y. Zhu, D. Fan, Y. Dong, G. Zhou, *Superlattices and Microstructures*, **74**, 261 (2014).
2. Sh. Wang, Y. Zhang, J. Yu, X. Song, Sh. Ge, M. Yan, *Sensors and Actuators B: Chemical*, **171–172**, 891 (2012).
3. J. Tawale, G. Gupta, A. Mohan, A. Kumar, A. Srivastava, *Sensors and Actuators B: Chemical*, **201**, 369 (2014).
4. V. Belessi, D. Petridis, The Role of Colloidal Systems in Environmental Protection, **121**, 289 (2014).
5. N. Chaturvedi, S. Swami, A. Kumar, V. Dutta, *Solar Energy Materials and Solar Cells*, **126**, 74 (2014).
6. J. Rouhi, M. Alimanesh, R. Dalvand, C. Ooi, Sh. Mahmud, M. Mahmood, *Ceramics International*, **40**, 11193 (2014).
7. G.-C. Yi, T. Yatsui, M. Ohtsu, *Comprehensive Nano-science and Technology*, **1**, 335 (2011).
8. L. Fang, B. Zhang, W. Li, Xiangjie Li, T. Xin, Q. Zhang, *Superlattices and Microstructures*, **75**, 324 (2014).
9. Y. Fang, Zh. Li, S. Xu, D. Han, D. Lu, *Journal of Alloys and Compounds*, **575**, 359 (2013).
10. N. V. Kaneva, C. D. Dushkin, A. S. Bojinova, *Bulgarian Chemical Communication*, **44**, 261 (2012).
11. B. Jeong, D. Kim, E. Park, M. Jeong, K. Kim, Hyun Ook Seo, Y. Kim, S. Uhm, *Applied Surface Science*, **307**, 468 (2014).
12. S. Navarro, J. Fenoll, N. Vela, E. Ruiz, G. Navarro, *Journal of Hazardous Materials*, **172**, 1303 (2009).
13. T. Ivetić, M. Dimitrievska, N. Finčur, Lj. Đaćanin, I. Gúth, B. Abramović, S. Lukić-Petrović, *Ceramics International*, **40**, 1545 (2014).
14. L. Haroune, M. Salaun, A. Ménard, C. Legault, J. Bellenger, *Science of The Total Environment*, **475**, 16 (2014).
15. K. Ajit, A. Sarmah, M. Meyer, A.B.A. Boxall, *Chemosphere*, **65**, 725 (2006).
16. D. Kolpin, E. Furlong, M. Meyer, E. Thurman, S. Zaugg, L. Barber, H. Buxton, *Environ. Sci. Technol.*, **36**, 1202 (2002).
17. T. Heberer, *Toxicol. Lett.*, **131**, 5 (2002).
18. H. Chen, J. Ding, W. Guo, *Ceramics International*, **40**, 4847 (2014).
19. H. Wang, Sh. Dong, Y. Chang, X. Zhou, X. Hu, *Applied Surface Science*, **258**, 4288 (2012).
20. G. Kenanakis, M. Pervolaraki, J. Giapintzakis, N. Katsarakis, *Applied Catalysis A: General*, **467**, 559 (2013).
21. K. Thongsuriwong, P. Amornpitoksuk, S. Suwanboon, *Advanced Powder Technology*, **24**, 275 (2013).
22. N. Kaneva, D. Dimitrov, C. Dushkin, *Applied Surface Science*, **257**, 8113 (2011).
23. M. Duta, D. Perniu, A. Duta, *Applied Surface Science*, **306**, 80 (2014).
24. S. Guerra, M. de la, L. Olvera, A. Maldonado, L. Castaneda, *Sol. Energy Mater. Sol. Cells*, **90**, 2346 (2006).
25. S. Rozati, S. Moradi, S. Golshahi, R. Martins, E. Fortunato, *Thin Solid Films*, **9**, 1279 (2009).
26. F. Hussein, M. Obies, A. Dreua, *Int. J. Chem. Sci.*, **8**, 2736 (2010).
27. C. Aprile, A. Corma, H. García, *Phys. Chem. Chem. Phys.*, **10**, 769 (2008).

ЕФЕКТ НА СТАРЕЕНЕ НА ЗОЛ ВЪРХУ СТРУКТУРАТА И ФОТОКАТАЛИТИЧНАТА АКТИВНОСТ НА ZnO ФИЛМИ ЗА РАЗГРАЖДАНЕ НА ФАРМАЦЕВТИЧНИ ЛЕКАРСТВА

Н. Кънева*, А. Божинова, К. Папазова, Д. Димитров

*Лаборатория по Наука и Технология на Наночастиците, Катедра по Обща
и неорганична химия, Факултет по Химия и Фармация, Софийски университет,
бул. "Джеймс Баучер" 1, 1164, София, България*

Постъпила декември, 2014 г.; приета януари, 2015 г.

(Резюме)

В тази работа, ZnO тънки филми са получени чрез зол-гел метод и ефекта на стареене на ZnO зол е изследван върху структурата и фотокаталитичните свойства на филмите. ZnO зол е престоял различно време (0, 30 и 60 дни). Нанокристалните тънки филми с различна дебелина (едно и пет покрития) са отложени върху стъклени подложки чрез метода на потапящата подложка. Структурните свойства на пробите са анализирани чрез Сканиращ Електронен Микроскоп и Рентгенова дифракция. Ефектът на стареене на изходния зол е изследван за фотокаталитичното разграждане на фармацевтични лекарства (*Парацетамол (ПЦА)* и *Хлорамфеникол (ХА)*) посредством УВ-вис спектроскопия. Експериментите са проведени под действието на ултравиолетова и видима светлина. Резултатите показват, че с повишаване времето на стареене на изходния ZnO разтвор обикновено се увеличава фотокаталитичната активност. Филмите с едно покритие имат по-ниски скоростни константи при разграждането в сравнение с останалите проби. Тънките филми с пет слоя получени от ZnO зол, престоял 60 дни показват най-високо фотокаталитично разграждане на лекарствата (*ПЦА*: УВ – 84.57% и Видима – 65.66%; *ХА*: УВ – 67.2% и Видима – 52.2%) в сравнение с тези получени с едно (*ПЦА*: УВ – 29.60% и Видима – 18.62%; *ХА*: УВ – 18.43% и Видима – 14.12%).

Seed-mediated approach to size-controlled synthesis of a mordenite type zeolite from organic template free initial gel

T. D. Todorova, Yu. A. Kalvachev*

*Institute of Mineralogy and Crystallography, Bulgarian Academy of Sciences,
Acad. G. Bonchev St., bl.107, 1113 Sofia, Bulgaria*

Received December, 2014; Revised January, 2015

This study reports on the hydrothermal synthesis of mordenite crystals without an organic template and on the characterization of resulting crystals, as the ultimate goal has been to decrease the crystal size. Two synthesis approaches have been applied. The first one involved subjecting a standard initial gel $18\text{SiO}_2 : \text{Al}_2\text{O}_3 : 1.24\text{K}_2\text{O} : 1.21\text{Na}_2\text{O} : x\text{H}_2\text{O}$ to hydrothermal crystallization for a period of 2 to 7 days ($x=600, 280$ and 22.5). The second approach included the usage of seeds employing the same initial gel composition. The crystals growth kinetics of mordenite at a different seed content (1, 2 and 5 wt.%) has been studied. The seed-assisted process enabled us to synthesize mordenite crystals of submicrometric range. Particle size distribution of the resulting products strongly depends on the water content in the initial gel and on the amount of added seed. It has been found that seed concentration and water content in the initial gel are the key factors influencing the crystallization time and the physicochemical properties of crystalline products. All products have been characterized by X-ray, scanning electron microscopy (SEM), dynamic light scattering (DLS), and infrared spectroscopy (FTIR).

Key words: Nanozeolites, mordenite, hydrothermal synthesis, seed-mediated synthesis.

INTRODUCTION

Zeolites are crystalline hydrated aluminosilicates containing cavities and channels. Their structure consists of three-dimensional frameworks of $[\text{SiO}_4]^{4-}$ and $[\text{AlO}_4]^{5-}$ tetrahedra linked through the shared oxygen atoms. Pure silicon structures are neutral. While isomorphic substitution of silicon tetrahedra with aluminum tetrahedra takes place the structure has a negative charge, which can be compensated by a number of cations – ions of the alkali and alkaline earth metals, protons, and certain organic cations. Being a combination of unique structure and composition of high efficiency makes zeolites useful in a wide range of areas. Due to the pore system zeolites may block various molecules and allow a smooth passage of the smaller molecules. Therefore they have also been referred to as “molecular sieves”. Many properties depend on Si/Al ratio in the framework of zeolites. With an increase in Si/Al ratio from 1 to infinity an increase

in the thermal stability of the zeolite framework is observed. The structural selectivity also changes and from hydrophilic becomes more hydrophobic, the acid stability enhances and the ion-exchange capacity is reduced within the zeolite structure. Some zeolites are found in nature as natural minerals, but the more widely used are synthetic materials due to the large number of application areas - chemical industry, cosmetics, building materials, purification and separation of liquids, gasses and many other fields. Another significant advantage of synthetic zeolite materials is their purity since parameters such as Si/Al ratio and purity of the phase can be controlled during the synthesis [1]. The shape-selectivity, the potential acidic properties and high active surface area are among the parameters which make zeolites widely applicable. Taking into account the industrial importance of zeolite materials many of scientists' efforts have been focused on the synthesis of new zeolite materials and on improving the characteristics of already existing zeolites. Size reduction of zeolite crystals to submicrometric and nanometric scale has a significant impact on their physical and chemical properties. The widespread use of nanosized zeolites, mainly in the applied fields of catalysis and adsorption, is due to their

* To whom all correspondence should be sent:
E-mail: kalvachev@clmc.bas.bg

having a higher external surface area, a high surface energy and shorter channels. These surface properties provide new possibilities to explore adsorption and reaction of bulky molecules that do not normally interact with the micropore volume of the zeolites [2–4]. In the recent years, the number of zeolites synthesized as nanosized materials has increased significantly owing to the new areas of applications – preparation of zeolite films, membranes, other composite materials, hierarchical structures, etc. They are also used for obtaining colloidal suspensions of nanosized zeolites. New approaches to the synthesis and modification of zeolite materials have been implemented in order to achieve the desired size and morphology [5–7].

One of the widely used zeolite minerals mordenite has the chemical formula $[\text{Na}_8(\text{H}_2\text{O})_{24} | \text{Al}_8\text{Si}_{40}\text{O}_{96}]$. This high-silica representative was first found in Canada (Nova Scotia) and its crystal structure was reported by How in 1864 [8–10]. Mordenite has an orthorhombic structure with a space group symmetry Cmc m ($a = 18.3 \text{ \AA}$; $b = 20.5 \text{ \AA}$ and $c = 7.5 \text{ \AA}$). Its structure is composed of five-membered rings interconnected by four ring members, each corner of which is composed of silicon or aluminum shared tetrahedra forming properly arranged channels. The channel system is one-dimensional running parallel to [001]. There are two types of channels, namely, the twelve-membered channel system and the eight-membered channel system. In the direction (010) there is only a eight-membered channel system. Since the eight-membered channels are inaccessible for many molecules, it is often said that mordenite has a one-dimensional channel system taking into account only the twelve-member channels [11]. Because of the extensive channel system in combination with a high thermal and acidic stability mordenite is widely used as a catalyst in reactions such as hydrocracking, isomerization, hydroisomerization, alkylation, reforming, and for the production of dimethylamine [12]. In addition, mordenite is used for adsorption and separation of gaseous and liquid mixtures, in photochemistry, electrochemistry, as thin films and zeolite membranes. For its wide application in catalysis it has been a great challenge to obtain nanosized crystals possessing a high active surface area and facilitating both diffusion and an easy access to the active sites of the zeolite. Nanosized mordenite crystals are used preferably in the area of supramolecular catalysis, photochemistry, optoelectronics, for developing zeolite membranes as well [13, 14].

The synthesis of zeolite materials is carried out under hydrothermal conditions with the silicate or aluminosilicate gels at alkaline pH and at a temperature ranging from 40 to 200 °C. Basically there four sources for the formation of the gel, namely:

(i) reagents forming the frame and comprising SiO_2 , Al_2O_3 ; (ii) structure directing agents (SDA) – that are mostly organic molecules; (iii) mineralizing agents – OH^- or F^- and (iv) a synthetic medium, which is usually water. Although most of the applications of zeolites are aimed at protecting the environment, their synthesis is not fully ecological, due to the use of SDA during their synthesis. The usage of SDA facilitates the synthesis process, i.e. it aids/guides the polymerization and organizes the anionic building blocks that form the zeolite framework. To make the zeolite useful, SDA trapped in its crystal micropores should be removed via calcination at 500–550 °C. Besides, the organic templates used in the conventional synthesis of zeolites are often poisonous and expensive for massive industrially production. Moreover, removing them at high temperature induces inevitable energetic and environmental pollution [15]. That is the main reason for the scientists to focus their efforts on the synthesis of zeolites from starting gels without organic templates.

The aim of the work is to carry out a hydrothermal seed-assisted synthesis of pure mordenite from an initial gel free of organic template. Varying the water content in the initial gel and the amount of seeds used during the hydrothermal synthesis one can control the size of zeolite crystals.

EXPERIMENTAL

SDA-free synthesis of mordenite

Mordenite was prepared under hydrothermal conditions using seeds from the initial gel with molar composition: $18\text{SiO}_2 : \text{Al}_2\text{O}_3 : 1.24\text{K}_2\text{O} : 1.21\text{Na}_2\text{O} : x\text{H}_2\text{O}$ ($x = 600, 280$ and 22.5). The seed amount was adjusted to be 1, 2 and 5 wt % of the total silica amount in the gel. The initial gel was aged for 24 hours at room temperature and then the synthesis was carried out at 160 °C and 180 °C for a period between 6 and 168 hours.

The seeds were synthesized from a starting gel having molar composition: $18\text{SiO}_2 : \text{Al}_2\text{O}_3 : 1.24\text{K}_2\text{O} : 1.21\text{Na}_2\text{O} : 280\text{H}_2\text{O}$. The crystallization of seeds was performed under static conditions at 180 °C for 120 hours.

The starting reagents were: highly dispersed extra pure silicon dioxide – Merck; Aluminium 99.97% – Acros Organics; NaOH pellets 98% – Sigma Aldrich, KOH pellets 85% – Sigma Aldrich and distilled water. The suspension preparation procedure started with dissolution of sodium and potassium hydroxide into water, followed by adding of aluminium powder under constant stirring till a clear solution was obtained. After the silica source and seeds were added the initial suspension

was stirred at room temperature for 60 min and then aged at room temperature for 24 hours. In order to obtain a gel with low water content (22.5 moles H₂O) and have the water distributed evenly in the gel, a freeze-dryer and a desiccator were employed sequentially. The crystallization was performed in stainless steel Teflon-lined autoclaves under autogenous static conditions at two different temperatures of 160 °C and 180 °C for a period of 6–168 hours. After the synthesis the autoclaves were quenched in cold water. The solid was purified by four consecutive steps of centrifugation and re-dispersion in distilled water and then dried at 60 °C overnight.

Characterization

The X-ray powder diffraction patterns were recorded on a D2 Phaser (Bruker) diffractometer with CuK α radiation, working at 30 kV acceleration and 10 mA current. The 2 θ scanned range was 4–50 with a step of 0.05° and 1 s acquisition time. FTIR spectra were taken on a Bruker Tensor 37 spectrometer using KBr pellet technique. For each sample, 64 scans were collected at a resolution of 2 cm⁻¹ over the 4000–400 cm⁻¹ wavenumber region. The scanning electron microscope (SEM) analyses were obtained on a Philips 515 apparatus, working at 20 kV accelerating voltage. The samples were covered with gold before investigation. Dynamic light scattering (DLS) particle size distribution measurements were performed on a Brookhaven Instrument 90Plus by suspension of the samples in water.

RESULTS AND DISCUSSION

The results from the hydrothermal synthesis of mordenite from different molar composition of the initial gel are listed in Table 1. The crystallinity and purity of the phases has been investigated by X-ray at various amounts of water and seeds in the initial gel at two temperatures – 160 °C and 180 °C. In almost all systems synthesized from the initial gel containing a large amount of water (600 moles) the product is a mixture of two phases – mordenite and ferrierite. The presence of a ferrierite phase is evidenced by the appearance of peaks at 9.30 and 12.50 2 θ in X-ray diffraction patterns obtained. An exception is when the synthesis is carried out at 160 °C in the presence of 5 wt% mordenite seed crystals. In this case after 72 hours the product is a pure mordenite phase. SEM investigations show aggregates with slab morphology whose average size is about 8–10 μ m. Decreasing the water amount in the gel leads to an alkalinity increase. As a result, the crystallization time is shorter and the only product formed is mordenite.

Series of syntheses with starting gel 18SiO₂ : Al₂O₃ : 1,24K₂O : 1.21Na₂O : 280H₂O at two temperatures 160 °C and 180 °C has been carried out. X-ray diffraction patterns of the samples prepared from gels with 280 moles of water are shown in Fig. 1. In all cases mordenite of high crystallinity has been observed. With increasing the amount of seeds added to the initial gel, crystallization time is shortened. The same effect, but much less pro-

Table 1. List of used initial gel compositions, crystallization conditions and products of synthesis

Gel Composition	Seeds (%)	160 °C		180 °C	
		Time (hours)	Product	Time (hours)	Product
18SiO ₂ :Al ₂ O ₃ :1,24K ₂ O:1.21Na ₂ O:600H ₂ O	–	120 h	Mor. / Fer.	72 h	Mor. / Fer.
18SiO ₂ :Al ₂ O ₃ :1,24K ₂ O:1.21Na ₂ O:600H ₂ O	1%	96 h	Mor. / Fer.	48 h	Mor. / Fer.
18SiO ₂ :Al ₂ O ₃ :1,24K ₂ O:1.21Na ₂ O:600H ₂ O	2%	96 h	Mor. / Fer.	48 h	Mor. / Fer.
18SiO ₂ :Al ₂ O ₃ :1,24K ₂ O:1.21Na ₂ O:600H ₂ O	5%	72 h	Mor.	48 h	Mor. / Fer.
18SiO ₂ :Al ₂ O ₃ :1,24K ₂ O:1.21Na ₂ O:280H ₂ O	–	144 h	Mor.	96 h	Mor.
18SiO ₂ :Al ₂ O ₃ :1,24K ₂ O:1.21Na ₂ O:280H ₂ O	1%	96 h	Mor.	72 h	Mor.
18SiO ₂ :Al ₂ O ₃ :1,24K ₂ O:1.21Na ₂ O:280H ₂ O	2%	72 h	Mor.	72 h	Mor.
18SiO ₂ :Al ₂ O ₃ :1,24K ₂ O:1.21Na ₂ O:280H ₂ O	5%	48 h	Mor.	48 h	Mor.
18SiO ₂ :Al ₂ O ₃ :1,24K ₂ O:1.21Na ₂ O:22.5H ₂ O	–	96 h	Mor.	72 h	Mor.
18SiO ₂ :Al ₂ O ₃ :1,24K ₂ O:1.21Na ₂ O:22.5H ₂ O	1%	24 h	Mor.	48 h	Mor.
18SiO ₂ :Al ₂ O ₃ :1,24K ₂ O:1.21Na ₂ O:22.5H ₂ O	2%	24 h	Mor.	18 h	Mor.
18SiO ₂ :Al ₂ O ₃ :1,24K ₂ O:1.21Na ₂ O:22.5H ₂ O	5%	18 h	Mor.	6 h	Mor.

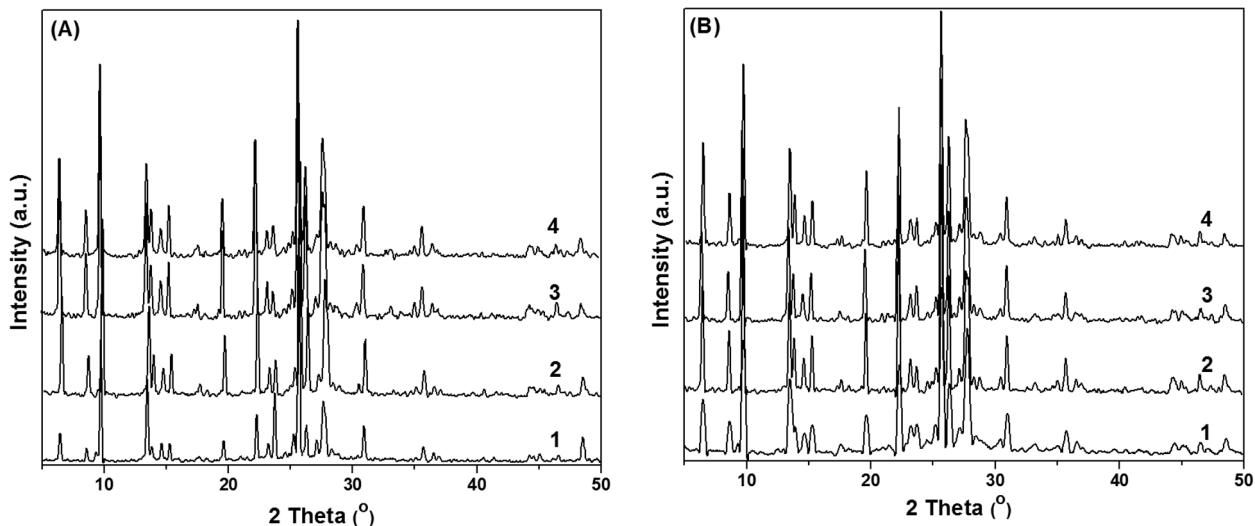


Fig. 1. XRD patterns of samples prepared from gels with 280 moles of water contents at 160 °C (A) and 180 °C (B) wherein: 1 – a gel composition without seeds, 2 – a gel composition with 1% seeds, 3 – a gel composition with 2% seeds and 4 – gel composition with 5% seeds

nounced has the increasing of temperature (Fig. 1, Table 1). Further extension of the crystallization time does not improve X-ray crystallinity of the material. The series of samples has been further examined by IR spectroscopy, thus complementing the information of the long-range (XRD) with short-range (IR) order analysis. Bands, characteristic for the zeolite framework at 1209, 1075, 806, 566 and 480 cm^{-1} have been observed in FTIR spectra what demonstrates the formation of the zeolite phase (Fig. 2). The shoulder at 1209 cm^{-1} and the band at 566 cm^{-1} are assigned to external linkage modes, i.e. their observation is associated with the presence of secondary building units in the mordenite structure.

The SEM inspection of mordenite has been performed to investigate the size and morphology of the crystals. The product is uniform in size (Fig. 3) comprising crystals of slab and slab-like morphology. As known, the increase in the synthesis temperature results into the formation of larger particles. However, in the presence of seeds this effect is less pronounced. Thus, the particles synthesized at 180 °C (Fig. 3B) are similar in size to those obtained at 160 °C (Fig. 3A). Obviously, the number of crystals in the systems is determined by the number of seeds per gel unit and the effect of other factors controlling zeolite crystal size is negligible. As seen from Fig. 3 the average size of the product synthesized without seeds is about 50 μm . The addition of seeds leads to a significant reduction of the crystal size. When 1 wt % of seeds (calculated as a percent of the total silica amount in the gel) is added, the size of the resulting crystals is about 15 μm , 2% seeds – 10 μm and 5% seeds – 7 μm , respec-

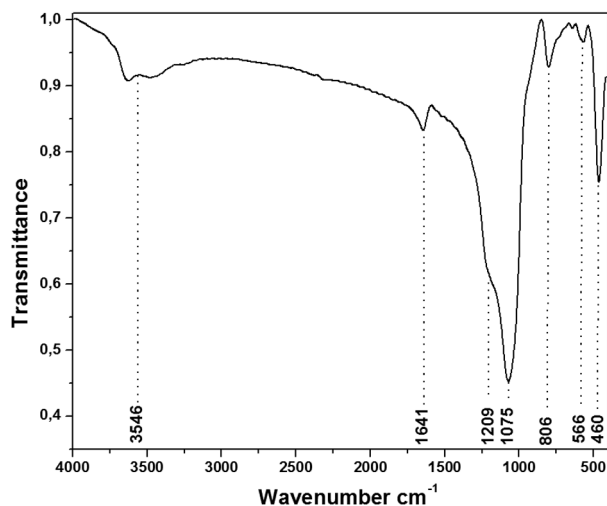


Fig. 2. FTIR spectrum of sample synthesized from gel containing 280 moles water at 160 °C without seeds

tively (Fig. 3). The results are confirmed by DLS investigations performed using a suspension of the samples in water. Crystal size distributions at both temperatures are similar. Increasing the amount of seed added to the initial gel results in shrinking the particle size of the product obtained.

Reductions of water content and seed-assisted methods are known for the synthesis of other zeolites and zeolite-like systems [16]. In order to obtain smaller mordenite crystals, water content in the initial gel has been further reduced up to 22.5 moles. That water amount has been achieved by sequential

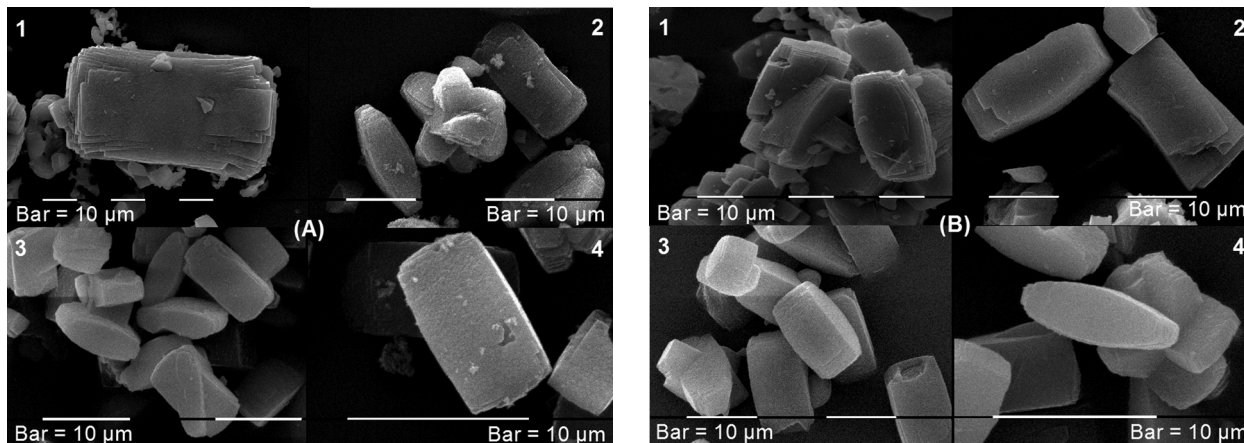


Fig. 3. SEM images of crystals synthesized from gels with 280 moles of water contents at 160 °C (A) and 180 °C (B) wherein: 1 is a gel composition without seeds, 2 is a gel composition with 1% seeds, 3 is a gel composition with 2% seeds and 4 gel composition 5% seeds

lyophilization of the initial gel and humidification in the desiccator, where together with the sample a plate with 1 M of NH_4Cl solution is placed. Thus the small amount of water is distributed evenly in the gel. The procedure then follows the conventional hydrothermal synthesis in an autoclave.

X-ray diffraction patterns of the products are shown in Fig. 4. Despite the large reduction of water in the initial gel, X-ray diffraction analysis indicates that the products are highly crystallized zeolite mordenite. The dependence of the yield on crystallization time at the two temperatures used – 160 °C

and 180 °C is presented in Fig. 5. The syntheses carried out at 160 °C show clearly the influence of seeds. The system without seeds gives a crystalline product for 96 hours while with the addition of 1% or 2% of seeds, the crystallization time is shortened to 24 hours. By increasing the seed content to 5%, the time for obtaining of pure zeolite phase mordenite is cut to 18 hours. Raising the temperature with 20 °C reduces the crystallization time. For the system without seeds it is 72 hours. The crystallization time is 6 hours for the system with 5% of seeds. Crystallization kinetics plotted in Fig. 5

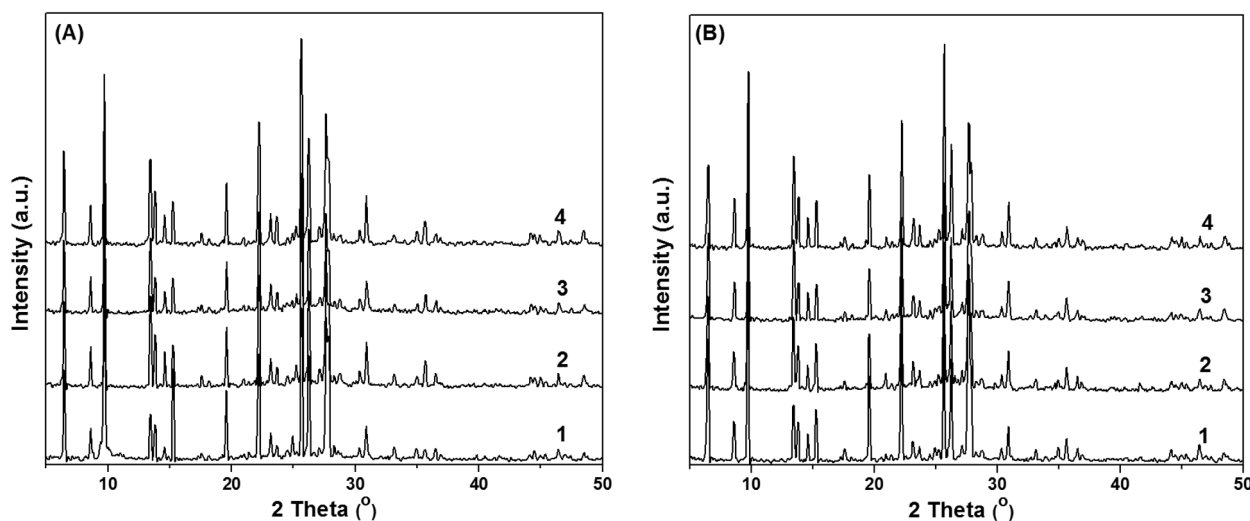


Fig. 4. XRD patterns of samples prepared from gels with 22.5 moles of water contents at 160 °C (A) and 180 °C (B) wherein: 1 is a gel composition without seeds, 2 is a gel composition with 1% seeds, 3 is a gel composition with 2% seeds and 4 gel composition 5% seeds

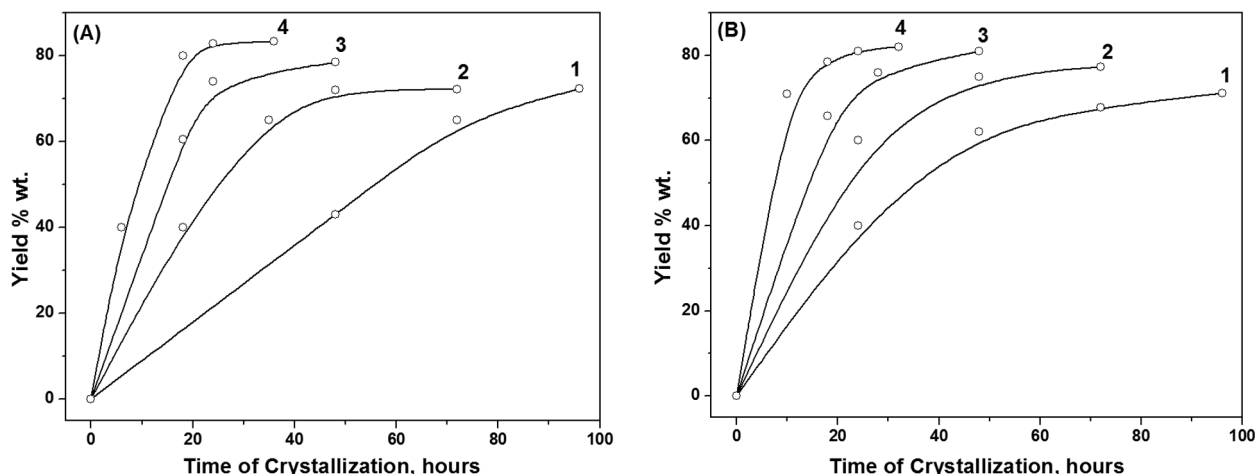


Fig. 5. Crystallization kinetics of samples prepared from gels with 22.5 moles of water contents at 160 °C (A) and 180 °C (B) wherein: 1 is a gel composition without seeds, 2 is a gel composition with 1% seeds, 3 is a gel composition with 2% seeds and 4 gel composition 5% seeds

shows clearly the effect that temperature and addition of seeds to the initial gel have upon the crystallization time.

SEM micrographs of the samples synthesized with 22.5 moles of water in the initial gel with a different amount of seeds in the system at two temperatures are presented in Fig. 6. The sample synthesized at 160 °C without seeds consists of large aggregates of slab morphology whose average size is 40 μm (Fig. 6 A1). The addition of seeds decreases the particle size, as seen from Fig. 6. The particle size of the sample synthesized with 1% of seed is 15 μm , of the

one with 2% – 6 μm . The particles synthesized with 5% of seeds are relatively uniform in size and shape with average crystals size of about 1–2 μm . The results concerning the size and morphology of the particles obtained at 180 °C (Fig. 6B) are similar, just uniformity is less pronounced because of the higher synthesis rate. The particle size distribution obtained by DLS analysis of all samples confirms these results. The narrowest distribution is for the samples synthesized with 5% of seeds. Thus, by adding a different amount of seeds to the synthesis system the size of the crystal particles obtained is controlled.

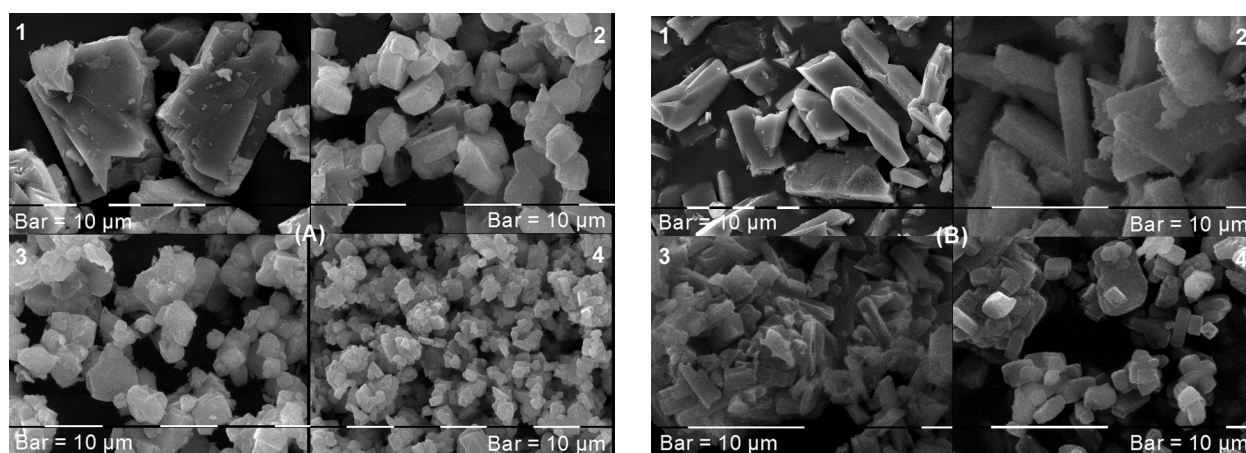


Fig. 6. SEM images of crystals synthesized from gels with 22.5 moles of water contents at 160 °C (A) and 180 °C (B) wherein: 1 is a gel composition without seeds, 2 is a gel composition with 1% seeds, 3 is a gel composition with 2% seeds and 4 gel composition 5% seeds

The seed crystals added to a synthesis system introduce crystallites into it and act as nuclei over which the crystals grow. The higher the number of crystallites in the initial gel is, the smaller is the size of the particles obtained. Adding seed crystals to a crystallization system has resulted in increased crystallization rates. The enhanced crystallization rate might be caused by an increase in the rate at which the solute is integrated into the solid phase of the solution due to the enlarged available surface area.

CONCLUSIONS

Hydrothermal syntheses of mordenite without using organic SDAs in the system $18\text{SiO}_2 : \text{Al}_2\text{O}_3 : 1.24 \text{K}_2\text{O} : 1.21\text{Na}_2\text{O} : x\text{H}_2\text{O}$ ($x=600, 280$ and 22.5) are reported. The resulting product has uniform particles of high crystallinity. Two synthesis approaches have been utilized. In the first one a standard initial gel is subjected to hydrothermal crystallization for a period ranging between 2 and 7 days. The second approach includes the use of seeds while the same initial gel composition is employed. The crystals growth kinetics of mordenite at different seed content (1, 2 and 5 wt.%) has been studied. Implementing the seed-assisted process we were able to synthesize mordenite crystals of sub-micrometric range. The water content in the initial gel and the amount of added seed are the parameters which strongly influence the particle size of the resulting products. Changing those parameters one can control the size of zeolite particles. It has been found the seed concentration and water content in the initial gel to be the key factors affecting the crystallization time and the physicochemical properties of crystalline products. Six hours is the established shortest time for obtaining zeolite mordenite of high crystallinity.

Acknowledgments: The authors acknowledge the financial support from the operational programme "Human Resources Development" within project BG051PO001-3.3-06-0027.

REFERENCES

1. C. Cundy, P. Cox, *J. Am. Chem. Soc.*, **103**, 663 (2003).
2. S. Mintova, J. P. Gilson, V. Valtchev, *Nanoscale*, **5**, 6693 (2013).
3. F. Adam, J.-T. Wong, E.-P. Ng, *Chem. Eng. J.*, **214**, 63 (2013).
4. S. Van Donk, A. Janseen, J. Bitter, K. De Jong, *Cat. Rev. Sci. Eng.*, **45**, 297 (2003).
5. L. Tosheva, V. Valtchev, *J. Am. Chem. Soc.*, **17**, 2494 (2005).
6. M. Ackley, S. Rege, H. Saxena, *Microp. Mesopor. Mater.*, **61**, 25 (2003).
7. Yu. Kalvachev, M. Jaber, V. Mavrodinova, L. Dimitrov, D. Nihtianova, V. Valtchev, *Microp. Mesopor. Mater.*, **177**, 127 (2013).
8. H. How, *J. Chem. Soc.*, **17**, 100 (1864).
9. P. Sharma, P. Rajaram, R. Tomar, *J. Colloid Interface Sci.*, **325**, 547 (2008).
10. P. Simoncic, Th. Armbruster, *Am. Mineral.*, **89**, 421 (2004).
11. C. Oprea, V. Popescu, *Romanian J. Phys.*, **53**, 231 (2008).
12. Kh. Minachev, V. Garanin, V. Kharlamov, T. Isakova, E. Senderov, *Russ. Chem. Bull.*, **18**, 1737 (1969).
13. M. Matsukata, K. Sawamura, Ts. Shirai, M. Takada, Ya. Sekine, E. Kikuchi, *J. Membr. Sci.*, **316**, 18 (2008).
14. H. Aly, M. Moustafa, E. Abdelrahman, *Adv. Powder Technol.*, **23**, 757 (2012).
15. X. Meng, F. Xiao, *Chem. Rev.*, **114**, 1521 (2014).
16. V. Valtchev, S. Mintova, in: *Encyclopedia of Inorganic Chemistry*, R. C. M. Lukehart (ed), vol. 380, John Wiley & Sons, Ltd, 2008, p. 543.

КОНТРОЛИРАНЕ РАЗМЕРА НА ЧАСТИЦИТЕ НА МОРДЕНИТ
ЧРЕЗ СИНТЕЗ С ИЗПОЛЗВАНЕ НА ЗАРОДИШИ
И БЕЗ ОРГАНИЧЕН ТЕМПЛЕЙТ

Т. Тодорова, Ю. Кълвачев*

*Институт по минералогия и кристалография, Българска Академия на Науките,
ул. „Акад. Г. Бончев“, бл. 107, 1113 София, България*

Постъпила декември, 2014 г.; приета януари, 2015 г.

(Резюме)

Тази работа докладва успешен хидротермален синтез на морденит без използване на органичен темплейт, като крайната цел е да се получат кристали с намалени размери. При синтеза са приложени два подхода. При първия, се използва стандартен първоначален гел 18SiO_2 гел: Al_2O_3 : $1.24\text{K}_2\text{O}$: $1.21\text{Na}_2\text{O}$: $x\text{H}_2\text{O}$ ($X = 600, 280$ и 22.5) и време на хидротермална кристализация от 2 до 7 дни. Вторият подход включва използването на зародиши, добавени към същия първоначален гел. Проучена е кинетиката на растеж на морденитните кристали при използване на различно съдържание на зародиши (1, 2 и 5 %). Използването на зародиши прави възможен синтез на морденитните кристали с размери в субмикронния регион. Разпределението на частиците по размер силно зависи от съдържанието на вода в първоначалния гел и от количеството на добавените зародиши. Установено е, че концентрацията на зародишите и съдържанието на вода в първоначалния гел са основните фактори, които влияят върху времето на кристализация и физикохимичните свойства на кристалните продукти. Всички продукти се характеризирани с рентгенова дифракция, сканиращ електронен микроскоп, динамично разсейване на светлина и инфрачервена спектроскопия.

Influence of the content of samarium on the structure and the optical properties of zinc borophosphate materials

G. Patronov*, I. Kostova, D. Tonchev

Dept. Chem. Technology, Plovdiv University "Paisii Hilendarski", 4000 Plovdiv, Bulgaria

Received December, 2014; Revised January, 2015

Glasses, glass ceramics and polycrystalline compositions based on ZnO, P₂O₅ and B₂O₃ have both scientific and technological importance because of their useful applications. Doping with rare earth elements not only leads to a rearrangement in the structure, but also to variation in the optical, magnetic and electrical properties.

We have synthesized samarium doped ZnO-rich borophosphate materials of composition xSm₂O₃ – (72.31–x)ZnO – 9.69P₂O₅ – 18B₂O₃, where x = 0, 0.25, 0.5, 0.75, 1 mol%. Samarium doped ZnO-rich borophosphate compositions were annealed with a target to obtain nanocrystalline structures. Materials were characterized by x-ray powder diffraction (XRD), differential scanning calorimetry (DSC), scanning electron microscopy (SEM) and photoluminescence (PL) measurements.

The results obtained show that synthesized materials are predominantly amorphous, with the presence of nano and polycrystalline structures in heat-treated samples. The structure and morphology of the obtained materials were evidenced by powder XRD data, SEM imaging and thermal DSC analysis. All different content Sm doped samples show PL peaks in the range of 550–650 nm belonging to Sm³⁺ ions.

Key words: zinc borophosphates, samarium doping, nanocrystallization, x-ray powder diffraction, differential scanning calorimetry, scanning electron microscopy.

INTRODUCTION

Recently, there is a significant interest in the synthesis and characterization of rare earth doped glasses and glass ceramics. These comparatively novel materials have been developed for a variety of applications. Rare earth ions play an important role in modern technology as active ions in many optical materials due to photoluminescence, X-ray scintillating etc. Glasses doped with rare-earth ions are attracting great interest regarding fibre amplifiers, up conversion lasers and optical devices for three-dimensional displays. Also samarium doped materials are widely used in different optical devices (high-density optical storage, under sea communication, colour display) [1–4].

The functionality of optically active glasses can be modified by appropriate doping and post synthesis thermal processing. Samarium ions fluorescence in glassy materials has attracted a lot of attention.

Borate glasses are good candidates as a host matrix material for rare earths ions like ions of samarium since these glasses can offer high optical transparency and are also robust and inexpensive [5–8].

On the other hand the materials with nanocrystals have immense potential for a variety of applications, by virtue of their electrical, magnetic, and optical properties. They are attractive not only for their potential for technological applications, but also the feasibility which they provide to engineer their structures at atomic levels to generate solids with novel properties [2, 5, 9]. It was specially emphasized that optical properties are depending on nano and polycrystalline formation into similar materials especially for high resolution and dosimetric X-ray detectors [10]. With constantly increasing demand for various optical devices, further studies of rare earth doped materials and especially these containing nanocrystals in the glass matrix are becoming more significant.

The purpose of this study is to synthesize stable, transparent samarium doped ZnO-rich borophosphate glassy materials and to form optically active nanocrystalline structures by annealing. We studied the effect of samarium content on the structure and

* To whom all correspondence should be sent:
E-mail: patron@uni-plovdiv.bg

the optical properties of Sm doped ZnO-rich borophosphate materials with composition $x\text{Sm}_2\text{O}_3 - (72.31-x)\text{ZnO} - 9.69\text{P}_2\text{O}_5 - 18\text{B}_2\text{O}_3$, where $x = 0, 0.25, 0.5, 0.75, 1$ mol%. The obtained compositions were characterized by x-ray powder diffraction (XRD), differential scanning calorimetry (DSC), scanning electron microscopy (SEM) and photoluminescence (PL) measurements.

EXPERIMENTAL

Sample preparation

All samples were prepared by high-temperature melt-quenching method using ZnO, P_2O_5 , B_2O_3 and Sm_2O_3 as starting materials. The reagents were thoroughly mixed, placed in alumina crucibles and heated at 950 °C for 3 hours in a muffle furnace. Samples were quenched out of the melt to room temperatures. The ratio between the main components – ZnO, P_2O_5 , B_2O_3 , the amount of dopant – Sm_2O_3 and conditions of the synthesis are based on our previous research in this area [11]. The synthesized compositions were heat-treated at 600 °C for three hours with a target to obtain nanocrystalline structures. We obtained homogeneous, non hygroscopic transparent and easily reproducible glasses. List of the zinc borophosphate compositions is presented in Table 1, where samples 2A–4A and 5A are heat-treated.

Powder X-ray diffraction analysis

Powder X-ray diffraction data were collected on Bruker diffractometer operating with a $\text{CuK}\alpha$ radiation source ($\lambda = 1.5406$ nm), in steps of 0.02° over the range of $10\text{--}80^\circ 2\theta$, with a time per step of 2.8 sec. The crystalline phases were identified using the powder diffraction files PDF 01-083-0655 (SmPO_4 – Monazite-(Sm)) from ICSD using POWD – 12++ (2004) [12], PDF 19-1455 ($\alpha\text{-Zn}_5\text{B}_4\text{O}_{11}$ – Zinc Borate) and PDF 86-2017 ($\text{Zn}_3(\text{BO}_3)(\text{PO}_4)$ – Zinc Borate Phosphate) from da-

tabase JCPDS – International Centre for Diffraction Data PCPDFWIN v.2.2 (2001) [13, 14].

Differential Scanning Calorimetry

DSC measurements were performed using TA Instruments DSC Q100 with attached Fast Air Cooling System (FACS). The samples (20–22 mg) were placed in aluminium hermetic pans. A heating rate of 10 K/min was used to scan all samples.

Scanning electron microscopy analysis

Scanning electron microscopy (SEM) was performed using a JEOL scanning microscope JSM-5510 operating at 10 kV with magnification of 1000, 5000 and 10000. The surfaces of the samples were gold sputtered using a JEOL fine coater JFC-1200.

Photoluminescence measurements

The photoluminescence spectra were measured by optical CCD Avantes spectrometer Avaspec 2048, operating at 25 MW in the range 250–1100 nm at room temperature. The light source was a semiconductor light emitting diode, emitting at 395 nm wavelength to pump directly the sample under study for photoluminescence measurements.

RESULTS AND DISCUSSION

The X-ray diffraction pattern of the synthesized and heat-treated Sm^{3+} -doped Zn-B-phosphate glasses are presented in Fig. 1. No diffraction peak appears for the Sm^{3+} -doped samples (2–5) which indicate that these materials are amorphous (glass structure). The main crystallization phases that are indexed in some areas of nondoped sample 1 are zinc borate phosphate $\text{Zn}_3(\text{BO}_3)(\text{PO}_4)$ (JCPDS file 86-2017 – [13]) and zinc borate $\alpha\text{-Zn}_5\text{B}_4\text{O}_{11}$ (JCPDS file 19-1455 – [14]). These XRD results were presented in our previous investigations [11].

Table 1. List of the samarium doped zinc borophosphate samples

Sample, No	ZnO, mol%	B_2O_3 , mol%	P_2O_5 , mol%	Sm_2O_3 , mol%
1	72.31	18.00	9.69	–
2, 2A	72.06	18.00	9.69	0.25
3, 3A	71.81	18.00	9.69	0.50
4, 4A	71.56	18.00	9.69	0.75
5, 5A	71.31	18.00	9.69	1.00

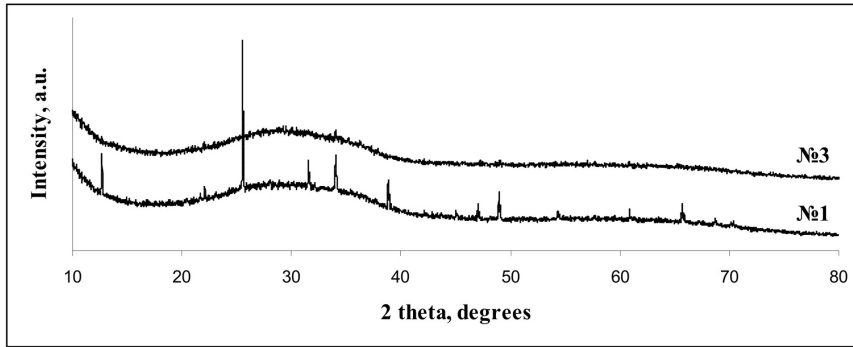


Fig. 1a. Powder X-ray diffraction patterns for samples № 1, 3

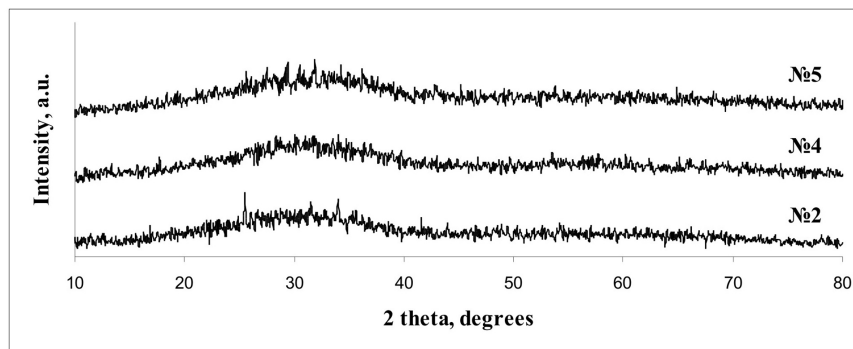


Fig. 1b. Powder X-ray diffraction patterns for samples № 2, 4, 5

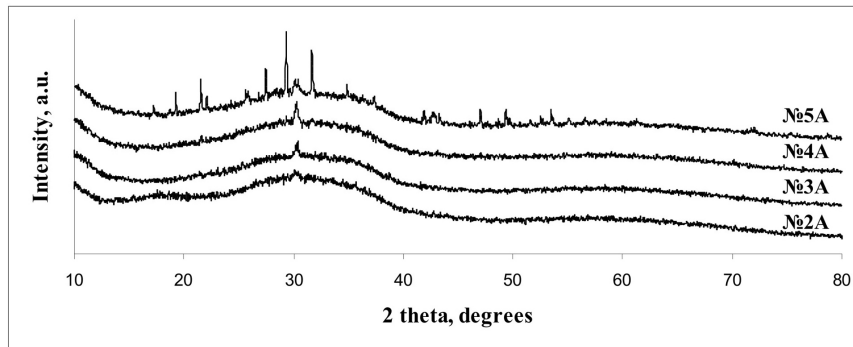


Fig. 1c. Powder X-ray diffraction patterns for heat-treated samples № 2A, 3A, 4A, 5A

Fig. 1. Powder X-ray diffraction patterns for the synthesized and heat-treated samples

Looking at XRD figure of heat-treated samples it is possible to observe nano crystallization in samples 2A, 3A, 4A (0.25, 0.5 and 0.75 mol% Sm). Only sample 5A (1% Sm) is showing an evidence of nano and poly crystallization mixed structure. Crystalline phase identified in heat-treated samples is indexed as samarium phosphate SmPO_4 – Monazite-(Sm) (ICSD file 01-083-0655 – [12, 15]). The appearance of phosphate in the crystallization products shows the important role of PO_4 structural units in the structural network of borophosphate glasses.

The average crystallite size (diameter, d) is calculated by using the Scherer's equation [16]:

$$d = \frac{0.89\lambda}{\beta \cos \theta}, \quad (1)$$

where λ is the wavelength of X-ray radiation, β is the full width at half maximum of the diffraction peak and θ is the diffraction angle. The average calculated crystallite size of SmPO_4 nanocrystals was found to be in the range 80–120 nm.

DSC analysis of annealed and non-annealed glass samples are in accordance with XRD results. The presented thermograms show that partially crystallized samples keep showing an amorphous phase (i.e. it is possible to evaluate glass transition T_g but with reduced relaxation) as shown in the Figure 2.

However in Figure 3 almost full crystallization can be observed after annealing. It is not possible to observe T_g and there is no any other transitions that could be evaluated. This result is confirmed by XRD data. The sample 5A is also opaque (non transparent).

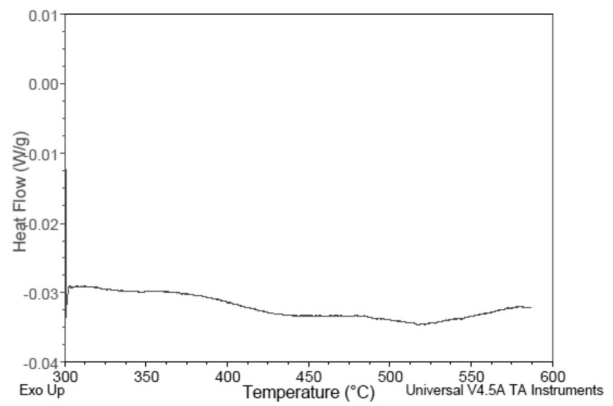
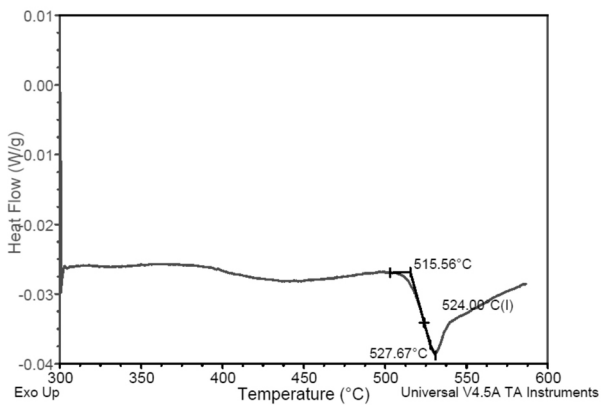
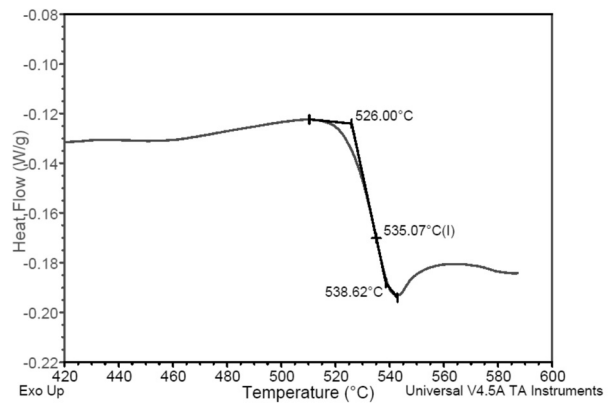
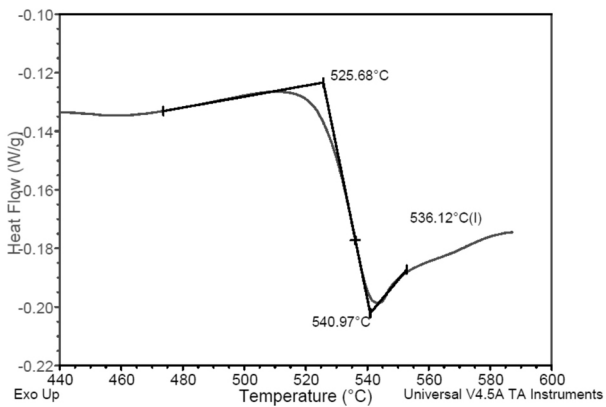


Fig. 2. DSC data of the samples No 2 and No 2A (0.25% Sm)

Fig. 3. DSC data of the samples No 5 and No 5A (1% Sm)

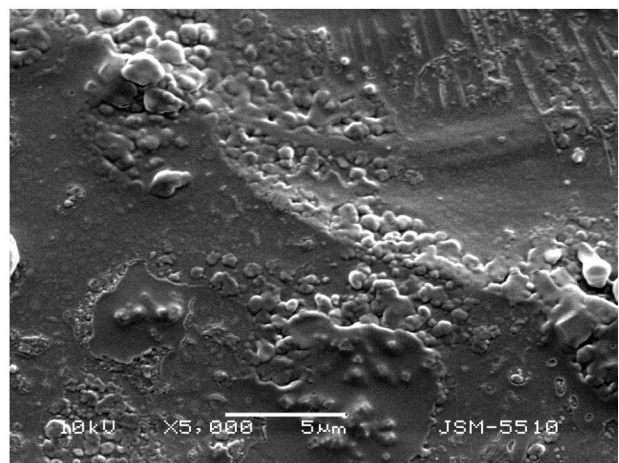
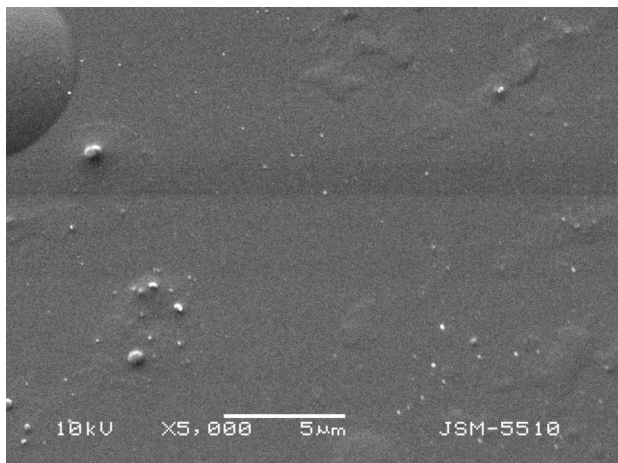


Fig. 4. SEM images of the microstructure for the samples No 2 and 2A (0.25% Sm)

Scanning electron microscopy analysis was performed to study the particles size, shape and morphology of Sm-doped Zn-B-phosphate glasses. SEM images of the fractured surface of synthesized and heat-treated samples are presented in Fig. 4 (samples 2 and 2A – 0.25% Sm) and Fig. 5 (sample 5A with highest content of Sm – 1%). The SEM micrographs are clearly showing that the synthesized non annealed samples are homogeneous. A spontaneous formation of defined crystallites takes place in all annealed samples. The nanocrystallites are spherical in shapes and joined each other to form clusters. The size of these clusters increases with an increase of samarium content. The size of nanocrystallites is over 100 nm and corresponds to results obtained from the XRD data as presented above. A polycrystalline material for the sample with highest content of Sm (Fig. 5) is formed.

According to our previous research [17] the most efficient LED for pumping the glasses is the one at 395 nm. In all of the presented spectra, we can observe three peaks at correspondingly 560, 600 and 645 nm. The band at 600 nm, which corresponds to orange emission, is the most intense [18]. In addition, a fourth peak at 704 nm is observed which is considerably weaker than the former. These peaks are characteristic for Sm^{3+} . The photoluminescence spectra of synthesized samples are illustrated in Fig. 6.

CONCLUSIONS

ZnO-rich borophosphate compositions doped with different content of Sm (0.25, 0.5, 0.75 and 1.0 mol%) were synthesized, annealed and inves-

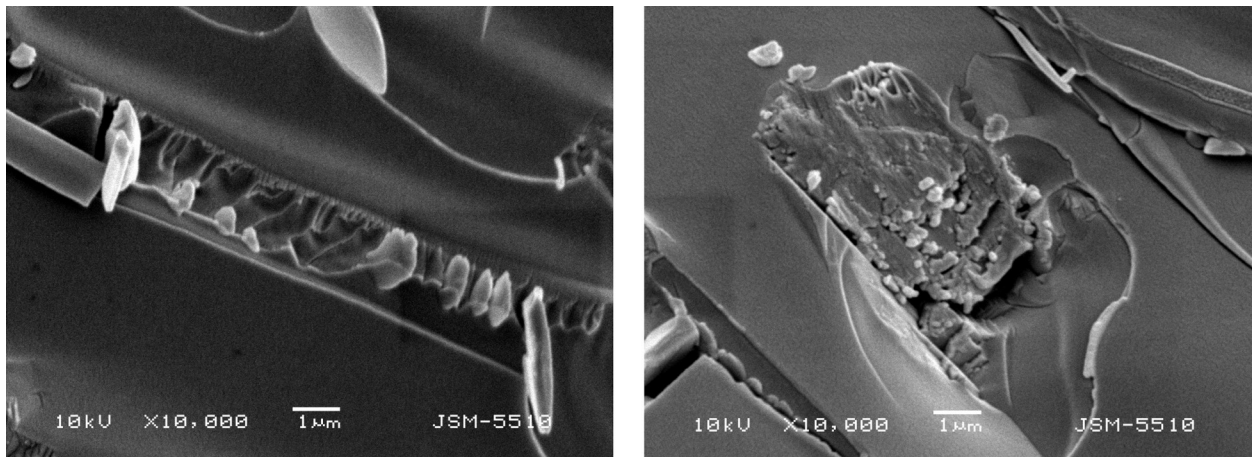


Fig. 5. SEM images of the microstructure for heat-treated sample No 5A (1% Sm)

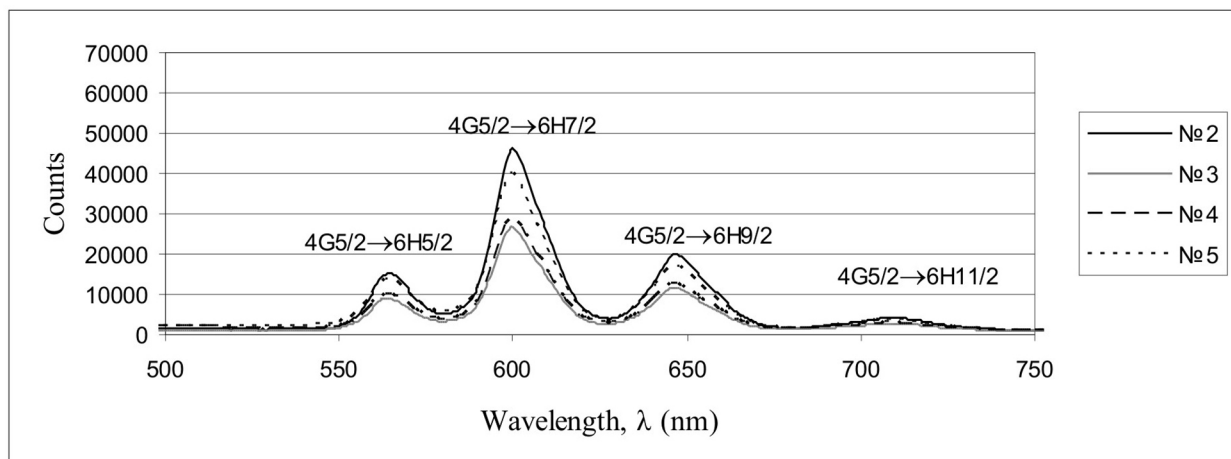


Fig. 6. Photoluminescence spectra for samples No 2–5 at an excitation wavelength 395 nm

tigated by powder X-ray diffraction, SEM analysis, differential scanning calorimetry (DSC) and photoluminescence spectroscopy.

The results show that synthesized samples are predominantly amorphous, with the presence of nano (samples % 2–4) and polycrystalline structures (sample % 5) in heat-treated samples. The crystalline phase identified in all heat-treated samples is indexed as samarium phosphate SmPO_4 . The average XRD calculated crystallite size of SmPO_4 nanocrystals is in the range of 80–120 nm. This result is confirmed by SEM images.

Thermal analysis (DSC) is showing that obtained materials are stable (T_g is over 500 °C) and materials transformations are in accordance to XRD and SEM data.

All doped samples with different content of Sm are optically active with a photoluminescence signal out of Sm^{3+} ions.

Acknowledgments: We are grateful to Assist. Prof. Dr P. Tzvetkov of Institute of General and Inorganic Chemistry (BAS) for the powder X-ray diffraction measurements, Prof. Eftimov and T. Pashova of the Faculty of Physics and Engineering Technologies at Plovdiv University for the optical analysis and also N. Dimitrov of the Faculty of Chemistry at Sofia University for the SEM analysis.

REFERENCES

1. Q. Sheng, Y. Shen, S. Liu, W. Li and D. Chen, *Applied Physics Letters*, **101**, 061904 (2012).
2. G. Lakshminarayana, R. Yang, M. Mao, J. Qiu, I. Kityk, *Journal of Non-Crystalline Solids* **355**, 2668 (2009).
3. M. Elfayoumi, M. Farouk, M.G. Brik, M.M. Elokr, *Journal of Alloys and Compounds*, **492**, 712 (2010).
4. M. Elisa, B.A. Sava, I.C. Vasiliu, R. Monteiro, J.P. Veiga, L. Ghervase, I. Feraru, R. Iordanescu, *Journal of Non-Crystalline Solids*, **369**, 55 (2013).
5. A. Tarafder, A. R. Molla, S. Mukhopadhyay, B. Karmakar, *Optical Materials*, **36**, 1463 (2014).
6. C. Smith, R. Brow, L. Montagne, B. Revel, *Journal of Non-Crystalline Solids*, **386**, 105 (2014).
7. M. Dyrba, P.-T. Miclea, S. Schweizer, *Radiation Measurements*, **45**, 314 (2010).
8. S. Krause, C. Pfau, M. Dyrba, P.-T. Miclea, S. Schweizer, *Journal of Luminescence*, **151**, 29 (2014).
9. B. H. Venkataraman, T. Fujiwara, T. Komatsu, *Journal of Solid State Chemistry*, **182**, 1538 (2009).
10. Go Okada, J. Ueda, S. Tanabe, G. Belev, T. Wysockinski, D. Chapman, D. Tonchev and S. Kasap, *J. Am. Ceram. Soc.*, **97**, 2147 (2014).
11. G. Patronov, I. Kostova, D. Tonchev, *Bulgarian Chemical Communications*, **45(4)**, 536 (2013).
12. K. Bluhm., C.H. Park, *Z. Naturforsch. B: Chem. Sci.*, **52**, 102 (1997).
13. Petzoldt, *Glastech. Ber.*, **39**, 130 (1966).
14. Y.-X. Ni, J. M. Hughes, A.N. Mariano, *Am. Mineral.*, **80**, 21 (1995).
15. N. Clavier, R. Podor, N. Dacheux, *Journal of the European Ceramic Society*, **31**, 941 (2011).
16. M. Ermrich, D. Opper, XRD for the analyst, PANalytical B.V., Almelo, The Netherlands, 2013.
17. I. Kostova, T. Pashova, G. Patronov, D. Tonchev, T. Eftimov, *Proceedings of ICYS 2013 Plovdiv, Scientific researches of the Union of Scientists in Bulgaria – Plovdiv, Series C. Natural Sciences and Humanities*, **16**, 231 (2013).
18. G. Lakshminarayana, H. Yang, Y. Teng, J. Qiu, *J. Luminesc.*, **129**, 59 (2009).

ВЛИЯНИЕ НА СЪДЪРЖАНИЕТО НА САМАРИЙ ВЪРХУ СТРУКТУРАТА И ОПТИЧНИТЕ СВОЙСТВА НА ЦИНК-БОР-ФОСФАТНИ МАТЕРИАЛИ

Г. И. Патронов, И. П. Костова, Д. Т. Тончев

Катедра Химична технология, Пловдивски Университет „Паисий Хилендарски“, 4000 Пловдив, България

Постъпила декември, 2014 г.; приета януари, 2015 г.

(Резюме)

Материалите на основата на ZnO, P₂O₅ и B₂O₃ (стъкла, стъклокерамики и полукристални композиции) имат важно значение, както от научна, така и от технологична гледна точка поради техните полезни приложения. Дотирането с редкоземни елементи води не само до промяна в структурата, но и до вариране на оптичните, магнитните и електричните им свойства.

Настоящото изследване представя синтез и характеристика на богати на ZnO борфосфатни материали, дотирани със Sm със състав $x\text{Sm}_2\text{O}_3 - (72,31-x)\text{ZnO} - 9,69\text{P}_2\text{O}_5 - 18\text{B}_2\text{O}_3$, където $x = 0, 0,25, 0,5, 0,75, 1 \text{ mol}\%$. Синтезираните композиции са отгreti с цел получаване на нанокристална структура. Материалите са охарактеризирани чрез рентгеноструктурен анализ, диференциално сканираща калориметрия, сканираща електронна микроскопия и фотолуминесцентни измервания.

Получените резултати показват, че синтезираните материали са основно аморфни с присъствие на нано- и поликристална структура в отгretите проби. Всички дотирани с различно съдържание на Sm проби дават фотолуминесцентни пикове в интервала 550–650 nm отнасящи се за Sm³⁺ йони.

Nano-sized iron oxide with controlled size modified with Pd for purification processes

S. Zh. Todorova^{1*}, Z. P. Cherkezova-Zheleva¹, I. D. Yordanova¹, A. Ganguly⁴,
H. G. Kolev¹, S. Mondal², M. G. Shopska¹, K. K. Tenchev, N. I. Velinov¹,
A. K. Ganguli^{2,3,4}, G. B. Kadinov¹

¹ Institute of Catalysis, Bulgarian Academy of Sciences, Acad. G. Bonchev St.,
Block 11, 1113 Sofia, Bulgaria

² Department of Chemistry, Indian Institute of Technology, Hauz Khas, New Delhi 110016, India

³ Nanoscale Research Facility, Indian Institute of Technology, Hauz Khas, New Delhi 110016, India

⁴ Institute of Nano Science & Technology, Habitat Centre, Phase – X, Mohali, Punjab, 160062, India

Received December, 2014; Revised January, 2015

Fe₃O₄ nano-oxide was prepared by wet chemical procedure and it was modified with palladium. The catalysts were characterized by X-ray diffraction (XRD), X-ray photoelectron spectroscopy (XPS), transmission electron microscopy (TEM), temperature programmed reduction (TPR) and diffuse reflectance infrared spectroscopy (DRIRS).

The catalytic performance of Fe₂O₃ and Pd/Fe₂O₃ was examined in the reaction of CO oxidation. Strong interaction between palladium and the nano-sized oxide was established leading to the formation of finely divided PdO on the surface. Remarkable increase in the catalytic activity was found after Fe₂O₃ modification with Pd. This feature was explained with the ability of the iron oxide, located in the close proximity to palladium, to provide active oxygen species that can subsequently react with CO molecules adsorbed on adjacent Pd. The Langmuir–Hinshelwood reaction mechanism of CO oxidation was suggested to proceed up to 100 °C over Pd/Fe₂O₃ catalyst including both the linear and bridge-bonded CO.

Key words: iron nano-oxide, palladium modified iron oxide, CO oxidation.

INTRODUCTION

The iron oxide nano-particles are of considerable interest due to their wide range of applications in chemical industries, magnetic storage materials, medicine and environmental protection [1]. Considering numerous applications of the iron oxides in various emerging fields, remarkable efforts on the synthesis of nano-dispersed particles are continuing. The biggest challenge in this field is to economically produce iron oxide nano particles of desired characteristics for specific application in large scale. There is a lot of progress in understanding the basic science of the nano-iron oxides but the evaluation of their catalytic properties and industrial application needs much more attention [2]. The application of the nano-sized iron oxides can be

attributed to the difference in properties of the particles in nano scale as compared to their bulk counterparts. The iron oxide materials have been found to be good candidates as cheap and efficient catalysts, especially in environmental processes [3, 4]. The magnetite and hematite are the most applied iron oxides as catalysts for oxidation/reduction and acid/base reactions. The nano-particle iron oxide is significantly more effective than conventional micron-sized iron oxide for the oxidation of CO [5]. These effects could be derived from the high activity of the nano-particles that have high BET surface area and more coordination unsaturated sites on the surfaces. Chemical and electronic properties, such as phase changes, OH content, band gap changes etc., could also contribute to their high reactivity [4]. Fe₂O₃ based nano-materials have been developed for the selective catalytic reduction (SCR) of NO_x by NH₃ in diesel exhaust [6]. The catalytic activity of nano-sized Pd/Fe₂O₃ and Au/Fe₂O₃ at low temperatures in a CO oxidation reaction has been investigated [7, 8]. The activity of Pd/Au in the reaction of CO oxidation depends of the active phases' particle size,

* To whom all correspondence should be sent:
E-mail: todorova@ic.bas.bg

morphology, and Pd (Au)–support interactions. On the other hand Pd supported catalysts are widely accepted as the most active catalysts for catalytic combustion of methane and the low temperature oxidation of CO [7].

The present work aimed development of highly active and stable catalysts for CO oxidation by appropriate combination of Pd and iron nano-oxide with controlled size, shape and morphology.

2. EXPERIMENTAL

2.1. Samples preparation

The iron oxide was prepared according to the procedure described in [9]. Before Pd deposition the metal oxide was calcined 2 h at 450 °C in air. The as-prepared iron oxide was modified with Pd (~0.5% wt. Pd) by impregnation with aqueous solution of Pd(NO₃)₂·2H₂O. The quick evaporation of the solvent after the impregnation step was applied [10]. Thus the oxide particles were coated by a thin layer of Pd. The sample was calcined additionally for 2 h at 450 °C in air.

2.2. Catalysts characterization

The XRD patterns were obtained on TUR M62 apparatus, HZG-4 goniometer with Bragg-Brentano geometry, Co K α radiation and Fe filter. XRD data processing was performed by using the X'Pert HighScore program. The HRTEM studies were carried out using FEI Technai G2 20 (200 kV). The TEM samples were prepared by loading an ethanol suspension of the sample on a holey copper grid. The specific surface area of supported catalyst samples have been determined by low temperature adsorption of nitrogen according to the B.E.T. method using Nova 1200 (Quantachrome) apparatus. The samples were degassed for 4–6 hours between 70–150 °C prior to the measurement. Temperature-programmed reduction (TPR) was carried out using a flow mixture of 10% H₂ in Ar at 10 ml/min, temperature rate of 10 °C/min up to 700 °C. Prior to the TPR experiment, the samples were treated in Ar for 1 hour at 150 °C.

The Mössbauer spectra were obtained at room temperature with an electromechanical spectrometer (Wissenschaftliche Elektronik GMBN, Germany) working in a constant acceleration mode. A ⁵⁷Co/Rh source (activity \approx 50 mCi) and α -Fe standard were used. The experimentally obtained spectra were subjected to mathematical processing according to the least squares method. The parameters of hyperfine interaction such as isomer shift (IS), quadrupole splitting (QS) and magnetic hyperfine field

(H_{hf}) as well as the line widths (FWHM) and the relative spectral area (G) of the partial components of the spectra were determined.

X-ray photoelectron measurements were carried out on the ESCALAB MkII (VG Scientific) electron spectrometer at a base pressure in the analysis chamber of 5x10⁻¹⁰ mbar using twin anode MgK α /AlK α X-ray source with excitation energies of 1253.6 and 1486.6 eV, respectively. The spectra were recorded at the total instrumental resolution (as it was measured with the FWHM of Ag3d_{5/2} photoelectron line) of 1.06 and 1.18 eV for MgK α and AlK α excitation sources, respectively. The energy scale was calibrated by normalizing the C1s line of adsorbed adventitious hydrocarbons to 285.0 eV. The processing of the measured spectra includes a subtraction of X-ray satellites and Shirley-type background. The peak positions and areas were evaluated by a symmetrical Gaussian-Lorentzian curve fitting. The relative concentrations of the different chemical species were determined based on normalization of the peak areas to their photoionization cross-sections, calculated by Scofield [11].

The adsorption of CO on Pd/Fe₂O₃ catalyst was studied by *in situ* diffuse reflectance infrared Fourier transform (DRIFT) spectroscopy, using a Nicolet 6700 spectrometer equipped with a high temperature/vacuum chamber installed in the Collector II accessory (Thermo Spectra-Tech). The CO was adsorbed from CO+N₂ or CO+O₂+N₂ flow mixture at room temperature. Experiments were carried out on oxidized (“as-prepared”, pretreated in N₂ for 1 h at 350°) surface.

2.3. Catalytic activity measurements

The catalytic tests were carried out in a flow type glass reactor at atmospheric pressure with a catalyst loading of about 0.5 cm³ (fraction 0.25–0.31 mm). The gas mixture consisted of 1700 ppm CO, 2 vol.% O₂ and He for balance to 100 vol.%. External mass transfer limitations were minimized by working at high GHSV (60 00 h⁻¹). The reaction temperature was measured by an internal thermocouple. The gas analysis was performed by a HP5890 series II gas chromatograph equipped with a thermal conductivity detector and Carboxen-1000 column. Helium was used as a carrier gas.

3. RESULTS AND DISCUSSION

The powder X-ray diffraction studies of the oxide nanoparticles show the formation of a cubic phase for iron oxide (PDF 01-080-153 9) (Figs 1 and 2).

The size and morphology of the oxide nanoparticles were found out from the TEM images of

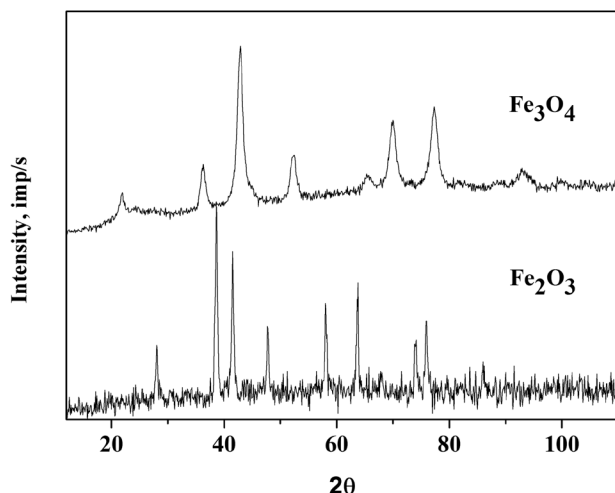


Fig. 1. XRD pattern of non calcinated Fe_3O_4 and after calcination

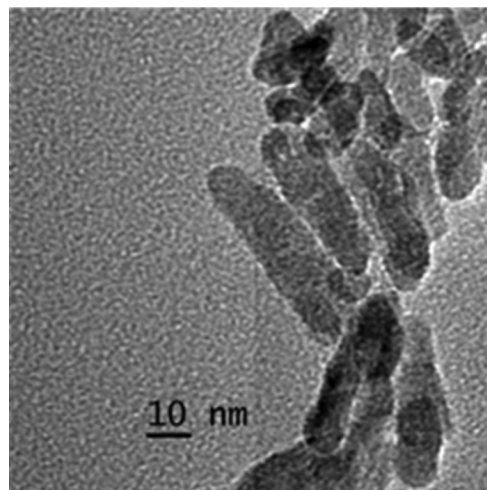


Fig. 2. TEM image of Fe_3O_4 before calcination

the oxide sample, the formation of particles of size elongated nanostructures of iron oxide with diameter ~ 12 nm and length ~ 50 nm. This oxide material is characterized by high surface area of $97 \text{ m}^2/\text{g}$.

According to the XRD data, the calcination in air leads to transformation of Fe_3O_4 to Fe_2O_3 and to an increase in the particles mean diameter about two times. The palladium deposition and following calcination do not increase the particle size additionally (Table 1). Decrease in the specific surface area was observed for an iron oxide sample after treatment in air for 2 h at 450°C . Palladium or palladium oxide

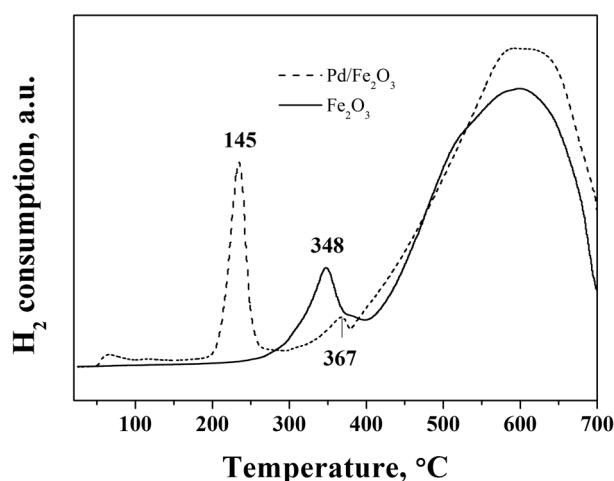


Fig. 3. TPR profile of Fe_2O_3 and $\text{Pd}/\text{Fe}_2\text{O}_3$

Table 1. Samples characterization after calcination

Sample	D_{MeOx} [nm]	S_{BET} [m^2/g]
Fe_2O_3	22	28.8
$0.5\text{Pd}/\text{Fe}_2\text{O}_3$	22	27

were not detected in XRD spectrum of Pd modified sample revealing finely divided phase of palladium (XRD data are not given).

TPR spectra of Fe_2O_3 after calcination and of the oxide after Pd loading are presented on the Figure 3.

TPR profile of the Fe_2O_3 (Fig. 3) shows sharp reduction peak at 348°C , attributed to the reduction of Fe_2O_3 to Fe_3O_4 , and a broad peak in the temperature interval $450\text{--}700^\circ\text{C}$, assigned to the subsequent reduction of Fe_3O_4 to FeO and Fe [12]. The reduction of Fe_2O_3 to Fe_3O_4 in $\text{Pd}/\text{Fe}_2\text{O}_3$ takes place at signifi-

cantly lower temperature. It is well known that addition of a noble metal to oxide catalysts accelerates the reduction of the oxides by supplying hydrogen via spillover from the pre-reduced noble metal particles to the oxides [13]. Three major reduction peaks are detected during the reduction of the $\text{Pd}/\text{Fe}_2\text{O}_3$ sample. The peak located at lower temperature is attributed to the reduction of the metal oxide in contact with the Pd metal particles, and the peak located at higher temperature is assigned to the reduction of the large oxide particles apart from the noble metal particles [14]. Since PdO can be reduced at very low temperature, it should be noted that a separate peak corresponding to the reduction of Pd oxide, only, was not observed in our experiments. This is due to the low Pd content (high FeOx/Pd ratio) in our cata-

lysts leading to very small hydrogen consumption by palladium compared to that one for the reduction of iron oxide.

Moessbauer spectra of prepared ferrite powders registered at room temperature are presented on Figure 4. The spectrum A of the initial material (Fe_3O_4) is superposition of sextet and doublet components. Sextet lines, only, are registered in Mössbauer spectra of the other two samples Fe_2O_3 (spectrum B) and Pd/ Fe_2O_3 (spectrum C) which are thermally treated iron oxide powder and that after Pd deposition, respectively. The calculated Moessbauer parameters after the best computer fitting of the spectra with respective components are given in Table 2. The calculated hyperfine parameters of the sextet components in the spectrum of the initial material (spectrum A) could be attributed to the presence of highly disperse ferrite phase with particle size below 20 nm showing collective magnetic excitation (CME) behaviour [1, 15, 16].

In this spectrum (of Fe_3O_4) iron ions in octahedral and tetrahedral position in spinel particles are distinguished. The calculated hyperfine parameters of doublet components could be attributed to the presence of ferrite particles with superparamagnetic (SPM) behaviour and ultra-disperse size below 10 nm [1, 15, 16]. The calculated hyperfine parameters of the sextet components in the other two spectra (Fe_2O_3 (spectrum B) and Pd/ Fe_2O_3 (spectrum C)) could be attributed to the presence of bulk hematite particles and (compare G column 66/72%) and hematite particles with lower size (compare G column 33/28%) (see Table 2).

The oxidation states of Pd and Fe on the catalytic surface were studied by X-ray photoelectron spectroscopy.

The Pd3d and Fe2p XP spectra of 0.5%Pd/ Fe_2O_3 are shown in Fig. 5. The line form, position of the peak and the position of satellite structures for Fe2p XP spectra were compared with previously reg-

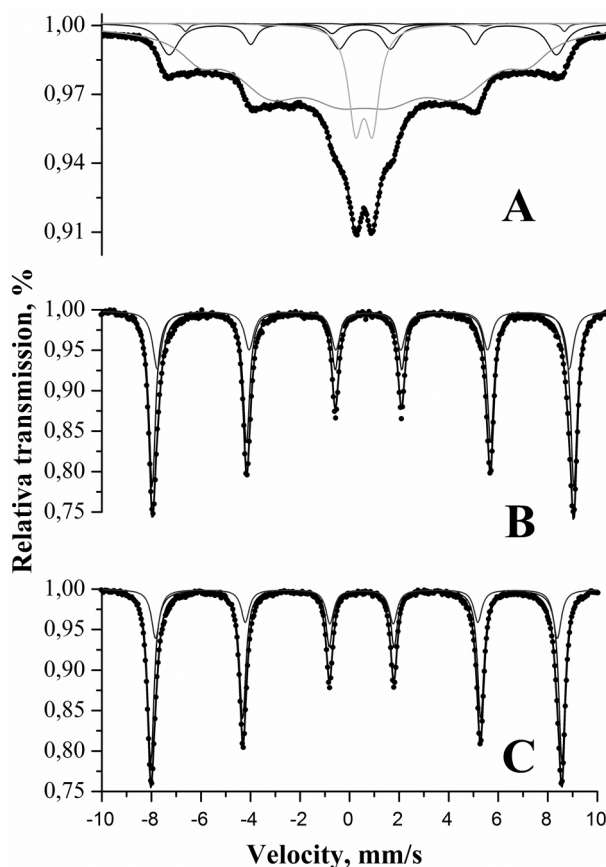


Fig. 4. Moessbauer spectra of synthesized materials. A – Fe_3O_4 – as synthesized initial sample; B – Fe_2O_3 – calcined initial sample; C – 0.5%Pd/ Fe_2O_3

istered iron oxide spectra and with literature data also. Base on this we suggest the presence of Fe_2O_3 as a main phase [17]. Very weak satellite structure at binding energies about 719 eV (typical for Fe^{3+}) and $\text{Fe}2p_{3/2}$ peak at about 710.5 eV are characteristic for Fe^{3+} . The broadening of $\text{Fe}2p_{3/2}$ peak corre-

Table 2. Moessbauer parameters of the samples

Sample	Components	IS, mm/s	QS, mm/s	H_{eff} , T	FMHW, mm/s	G, %
Fe_3O_4 (A)	Sxt 1 – $\text{Fe}^{3+}_{\text{tetra}}$ spinel	0.27	0	47.3	0.75	9
	Sxt 2 – $\text{Fe}^{2.5+}_{\text{octa}}$ spinel	0.74	0	46.3	0.51	10
	Sxt 3 – Fe^{3+} – spinel CME	0.32	0	40.1	2.20	65
	Dbl 1 – Fe in spinel SPM	0.34	0.67	–	0.75	11
	Dbl 1 – Fe in spinel SPM	0.32	1.2	–	0.63	5
Fe_2O_3 (B)	Sxt 1 – Fe^{3+} in hematite	0.38	–0.21	51.5	0.32	66
	Sxt 2 – Fe^{3+} in hematite	0.37	–0.20	50.3	0.42	34
Pd/ Fe_2O_3 (C)	Sxt 1 – Fe^{3+} in hematite	0.38	–0.21	51.5	0.31	72
	Sxt 2 – Fe^{3+} in hematite	0.37	–0.20	50.4	0.38	28

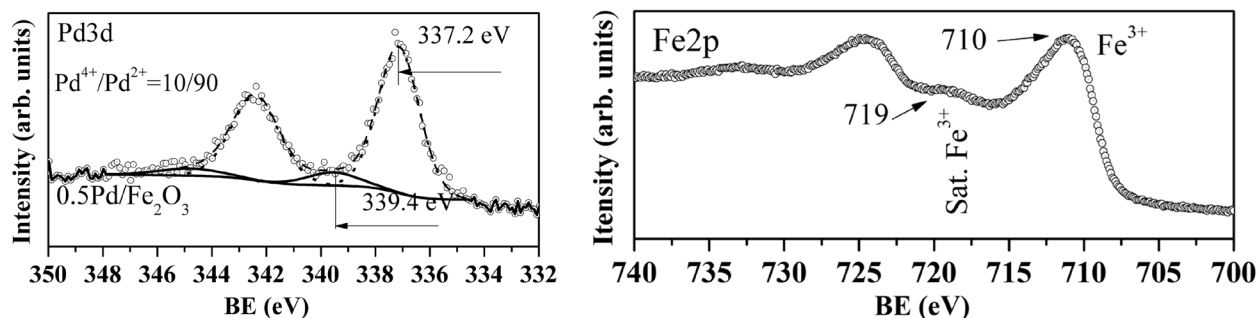


Fig. 5. XPS spectra of Pd 3p and Fe 2p of 0.5%Pd/Fe₂O₃ after calcination 2 h at 450 °C

sponds to the presence of nano-sized particles. The surface atomic concentrations obtained from the normalized peak area divided by the cross section of the elements presented are as follow: Pd – 2 at.%; Fe – 33 at.%; and O – 65 at.%.

The binding energies in the range of 337.2–337.6 eV for Pd modified sample indicate the presence of PdO [18, 19]. A third component at 339.4 eV was observed. It is smaller than the other component detected and contributes with 10 % of the total Pd signals. This peak may be associated with Pd⁴⁺ from PdO₂ [19]. Pd⁴⁺ from PdO₂ is highly unstable, but according to Barr [20] Pd metal particles exposed long enough to air form on their surface PdO oxide with outermost layers of PdO₂ or Pd(OH)₄.

Figure 6 shows the CO conversion vs. temperature on the samples of iron oxide and iron oxide modified with palladium. The pure Fe₂O₃ demonstrate activity in CO oxidation. The addition of Pd results in remarkable displacement of the conver-

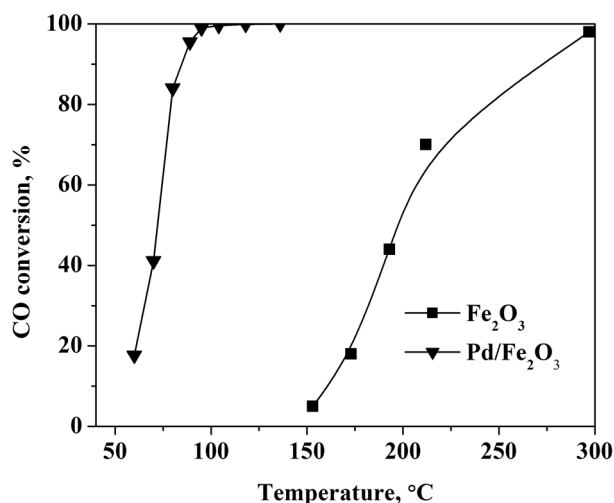


Fig. 6. Catalytic activity of the samples in the reaction of CO oxidation

sion curve to lower temperature, indicating better catalytic activity (Fig. 6).

As it was mentioned above palladium presents at the catalyst surface as finely divided particles (there were no diffraction peaks for Pd nor PdO in the XRD spectrum) and palladium and iron oxide are supposed to interact strongly. According to Liu *et al.* [21] the promoting effect of iron oxide in the case of Pt-FeO_x catalysts is related to the ability of the iron oxide species, located in close proximity to the palladium, to provide adsorption sites for oxygen that can subsequently react with CO molecules adsorbed on adjacent Pd sites. Thus, we can conclude that because of the high dispersion of Pd and close interaction between Pd and Fe₂O₃ in Pd/Fe₂O₃ sample, more surface oxygen species are provided to the palladium, thus improving its catalytic activity.

In situ DRIFT spectroscopy was used as one of the most powerful methods to obtain information about the type of the active sites, their stability and reactivity, chemical state of the surface under static and dynamic conditions in a wide temperature interval and after different pretreatments. DRIFT experiments on CO adsorption and reaction in O₂ – containing flow mixture were carried out to shed some light on the reaction mechanism.

The bridge-bonded CO band (at 1984 cm⁻¹) and linearly bonded CO on Pd¹⁺ (at 2124 cm⁻¹) and Pd⁰ (at 2089 cm⁻¹) are visible in the IR spectrum of Pd/Fe₂O₃ at T_{room} (Fig. 7). The decrease in intensity of the bands of gas phase CO indicates activity in the CO oxidation even at ambient temperature. The bands of linearly and bridge-bonded CO are seen in the spectra collected up to 100 °C. The Langmuir–Hinshelwood mechanism (L-H) between adsorbed CO and oxygen species was well established as the dominant reaction pathway in the reaction of CO oxidation on noble metals [22]. Based on this it is possible to suggest that the reaction mechanism is L-H includes these two types of adsorption species. The so-called bi-functional reaction path involv-

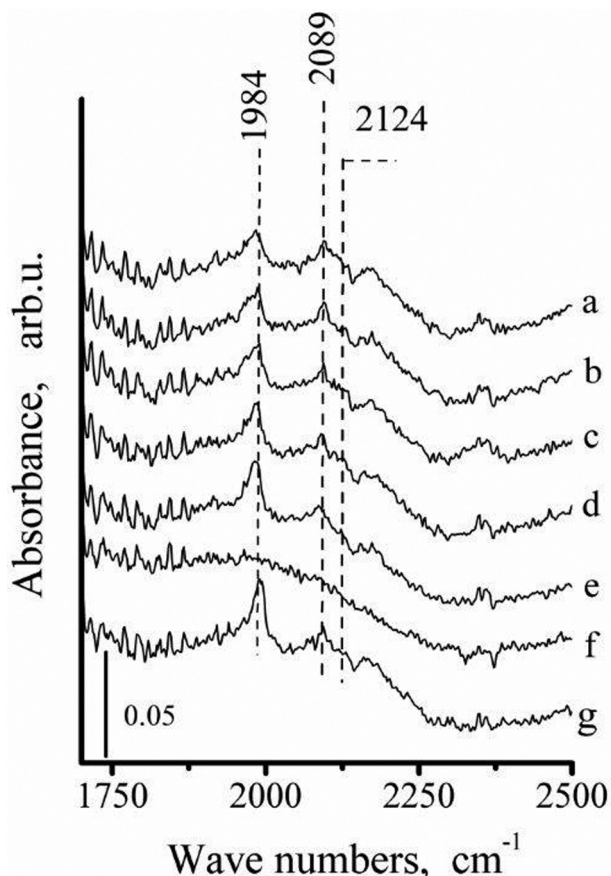


Fig. 7. DRIFT spectra of CO adsorption in (1% CO + 10% O₂)/N₂ flow on Pd/Fe₂O₃ at different temperatures: **a.** N₂-O₂ flow at T_{room}; **b.** after 10 min, T_{room}; **c.** at 50 °C; **d.** at 70 °C; **e.** at 100 °C; **f.** at 150 °C; **g.** after cooling the sample in the reaction flow mixture at T_{room}

ing the reaction between CO adsorbed on the noble metal and oxygen from oxides is possible as well.

CONCLUSIONS

Strong interaction between the palladium and the nano-sized Fe₂O₃ oxide was established in a Pd/Fe₂O₃ catalyst leading to the formation of finely divided PdO on the surface. The high catalytic activity was established for Pd/Fe₂O₃ and it was explain with the ability of the iron oxide, located in close proximity to the palladium, to provide adsorption sites oxygen that can subsequently react with CO molecules adsorbed on the adjacent Pd.

Based on DR IRS investigations the Langmuir–Hinshelwood reaction mechanism was suggested for CO oxidation up to 100 °C over Pd/Fe₂O₃. The linear and bridge-bonded CO take part in the reaction on the surface of Pd/Fe₂O₃.

Acknowledgements: The authors thank the National Science Fund of Bulgaria for the financial support under the Contract No DFNI/India 01/8. I. Yordanova and M. Shopska gratefully acknowledge the European Social Fund within the framework of Operating Program – Development of Human Resources (BG051PO001-3.3.06-0050).

REFERENCES

1. U. Schwertmann, R. Cornell, Iron Oxides in the Laboratory, Weinheim, New York-Basel-Cambridge, 1991.
2. Anil K. Kandalam, B. Chatterjee, S.N. Khanna, B. K. Rao, P. Jena, B. V. Reddy, *Surf. Sci.*, **601**, 4873 (2007).
3. M. Mohapatra, S. Anand, *Int. J. Eng. Sci. Technol.*, **2**, 127 (2010).
4. S. C. Kwon, M. Fan, T. D. Wheelock, B. Saha, *Sep. Purif. Technol.*, **58**, 40 (2007).
5. J. S. Walker, G. I. Stragauzzi, W. H. Manogue, G. C.A. Schuit, *J. Catal.*, **110**, 298 (1988).
6. N. Apostolescu, B. Geiger, K. Hizbullah, M. Jan, S. Kureti, D. Reichert, F. Schott, W. Weisweiler, *Appl. Catal. B: Environ.*, **62**(1-2), 104 (2001).
7. M. Jin, J.-N. Parka, J. Shona, J. Kima, Z. Li, Y. Park, J. Kima, *Catal. Today*, **185**, 183 (2012).
8. R. A. Searles, *Stud. Surf. Sci. Catal.*, **116**, 23 (1998)
9. Z. H. Zhou, J. Wang, X. Liu, H. S. O. Chan, *J. Mater. Chem.*, **11**, 1704 (2001)
10. J. Hagen, *Industrial Catalysis. A Practical Approach*, Wiley-VCH Verlag GmbH & Co. KGaA, Weinheim, Germany, 2006, p. 227.
11. J. H. Scofield, *J. Electron Spectrosc. Relat. Phenom.*, **8**, 129 (1976)
12. W. K. Jozwiak, E. Kaczmarek, T. P. Maniecki, W. Ignaczak, W. Maniukiewicz, *Appl. Catal.*, A, **326**, 17 (2007).
13. Cl. Bianchi, *Catal. Lett.*, **76**, 155 (2001).
14. H. Duan, D. Xu, W. Li, H. Xu, *Catal. Lett.*, **124**, 318 (2008).
15. B. S. Randhawa, H. S. Dosanjh, M. Kaur, *Ceram. Int.*, **35**, 1045 (2009).
16. B. G. Toksha, S. E. Shirsath, S. M. Patange, K. M. Jadhav, *Solid State Commun.*, **147**, 479 (2008).
17. S. Gota, E. Guiot, M. Henriot, M. Gautier-Soyer., *Phys. Rev. B*, **60**, 14387 (1999).
18. A. de la Peña, M. C. Alvarez-Galvan, J. L. G. Fierro, P. L. Arias, *Appl. Catal. B*, **57**, 191 (2005).
19. V. A. de la Peña O’Shea, M. C. Alvarez-Galvan, J. Requies, V. L. Barrio, P. L. Arias, J. F. Cambra, M. B. Güemez, J. L. G. Fierro, *Catal. Commun.*, **8**, 1287 (2007).
20. T. L. Barr, *J. Phys. Chem.*, **82** 1801 (1978).
21. L. Liu, F. Zhou, L. Wang, X. Qi, F. Shi, Y. Deng, *J. Catal.*, **274**, 1–10 (2010).
22. T. Engel, G. Ertl, Oxidation of Carbon Monoxide, in: *The Chemical Physics of Solid Surfaces and Heterogeneous Catalysis*, D. A. King, D. P. Woodruff (eds.), Elsevier, Amsterdam-Oxford-New York, 1983, vol. 2.

НАНОРАЗМЕРЕН ЖЕЛЕЗЕН ОКСИД С КОНТРОЛИРАН РАЗМЕР, МОДИФИЦИРАН С Pd ЗА ПРОЦЕСИ НА ОЧИСТВАНЕ

С. Ж. Годорова^{1*}, З. П. Черкезова-Желева¹, Ил. Д. Йорданова¹,
А. Гангули⁴, Х. Г. Колев¹, С. Мондал², М. Г. Шопска¹, К. К. Тенчев¹,
Н. Ив. Велинов¹, А. К. Гангули^{2,3,4}, Г. Б. Кадинов¹

¹ *Институт по катализ, Българска академия на науките, ул. „Акад. Г. Бончев“,
бл. 11, 1113 София, България*

² *Факултет по химия, Индийски технологичен институт, Хаус Кназ, Нью Делхи, 110016, Индия*

³ *Факултет за разработки и изследвания на нанотехнологии, Индийски технологичен институт,
Хаус Кназ, Нью Делхи, 110016, Индия*

⁴ *Институт по нанонауки и технологии, Мохали, Пенджаб, 160062, Индия*

Постъпила декември, 2014 г.; приета януари, 2015 г.

(Резюме)

Получен е наноразмерен Fe₃O₄ от водни разтвори на железни соли посредством утаяване. Така приготвеният оксид е накален и модифициран с паладий. Получените образци са характеризирани чрез методите на рентгеновата дифракция, рентгеновата фотоелектронна спектроскопия, трансмисионната електронна микроскопия, температурно-програмираната редукция и дифузно-отражателната инфрачервена спектроскопия.

Каталитичното поведение на получените материали е изследвано в реакцията на окисление на СО. Установено е силно взаимодействие между паладия и наноразмерния оксид, което води до формирането на финодисперсен PdO на повърхността на образеца. Pd/Fe₂O₃ показва висока каталитична активност в изследваната реакция. Това се обяснява със способността на железния оксид, намиращ се в непосредствена близост до паладия, да доставя активен кислород, който в последствие да реагира с адсорбираните върху Pd молекули СО. Предполага се, че окислението на СО при температури до 100 °С в присъствие на катализатор Pd/Fe₂O₃ протича по механизма на Лангмюир-Хиншелвуд включващ линейно и мостово свързани с паладия молекули СО.

Urbach's rule of Ni doped Mn_3O_4 thin films

P. Petkova^{1*}, K. Boubaker², P. Vasilev¹,
M. Mustafa¹, T. Larbi³

¹ Shumen University "Konstantin Preslavsky", 115 Universitetska street,
9712 Shumen, Bulgaria

² École Supérieure de Sciences et Techniques de Tunis (ESSTT), Université de Tunis/63
Rue Sidi Jabeur, 5100, Mahdia, Tunisia

³ Unité de Physique des Dispositifs à Semi-conducteurs (U.P.D.S), Faculté des sciences de Tunis,
Tunis El Manar University, 2092 Tunis, Tunisia

Received December, 2014; Revised January, 2015

The absorption spectra of Ni doped manganese oxide thin films are measured in the spectral region 1.65–2.7 eV at room temperature. The slope parameter of absorption coefficient and the dynamic disorder in Urbach's rule region are calculated. The behavior of transition metal ions is also reported. The effective mass of $Mn_3O_4:Ni$ has been determined in the investigated spectral region.

Key words: doped thin films, Urbach's rule, Urbach's energy, effective mass.

INTRODUCTION

During the past few decades, manganese oxides have been widely exploited because of their potential applications in many fields, such as catalysis [1], super capacitors [2], ion exchange [3], molecular adsorption [4], magnetic applications [5] and secondary batteries [6].

Among these manganese oxides, hausmannite Mn_3O_4 is most stable at high temperature relative to other oxides. Hausmannite Mn_3O_4 has high catalytic activity for many reactions, such as selective reduction of nitrobenzene [7], oxidation of methane and carbon monoxide [8], decomposition of waste gases [9] and combustion of organic compounds at temperature of the order of 373–773 K [10]. The aim of this work is connected with the explanation of: 1) the structural disorder in Ni doped Mn_3O_4 at the absorption edge region; 2) the width of the impurity localized states at the same investigated region; 3) the change of the form of the valence and conduction bands of doped hausmannite in the vicinity of absorption edge.

EXPERIMENTAL

Nickel doped manganese oxide ($Mn_3O_4:Ni$) or Hausmannite thin films were grown at 350 °C on 1×2 cm² glass substrate by the spray pyrolysis technique (Fig. 1). The substrate temperature was fixed using a digital temperature controller with a k-type thermocouple. The aqueous solution with a flow rate of about 4ml/min contains Manganese chloride ($MnCl_2 \cdot 6H_2O$) 0.1M as precursor. Nickel chloride

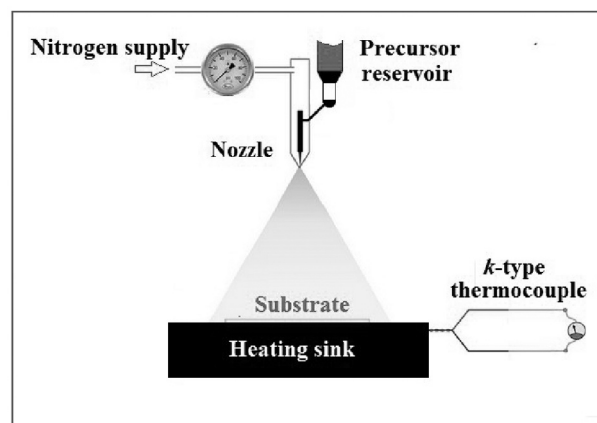


Fig. 1. The experimental set up for the spray pyrolysis technique

* To whom all correspondence should be sent:
E-mail: Petya232@abv.bg

(NiCl₂·6H₂O) was used as doping agent and added to the starting solution at [Ni]/[Mn] concentration ratios: 1, 2 and 3 at.%. The distance between nozzle and substrate was about 27 cm. The filtered compressed nitrogen was used as gas carrier at a flow rate of 4L.mn⁻¹. The total deposition time was maintained at 20 min. After deposition, the coated substrates were allowed to cool down naturally to room temperature. X-ray diffraction (XRD) measurements were performed using a Siemens D500 X-ray diffractometer with a Cu K α radiation ($\lambda = 1.54056 \text{ \AA}$). Morphological observations were performed by means of an atomic force microscope (AFM, VEECO digital instrument 3A). The rms surface roughness and grain size are obtained from a scan area of 5 $\mu\text{m} \times 5\mu\text{m}$ of the samples [11]. The experimental set up for measurement of the absorption coefficient in the visible and near IR region consists of the following: a halogen lamp with a stabilized 3H-7 rectifier, a SPM-2 monochromator, a system of quartz lenses, Glan–Taylor prism which is used as a polarizer, sample holder, and a Hamamatsu S2281-01 detector.

RESULTS AND DISCUSSION

The energy gap E_g of the investigated samples shifts to the small energies with increasing of Ni concentration (Fig. 2). The behaviour of the absorption coefficient α has been investigated at the absorption edge using the Urbach's formula $\ln\alpha = -A + (B/T) \cdot \hbar\omega$, where A and B are the constants, $\hbar\omega$ is the energy of photons, T is the temperature (Fig. 3). The function $y(x)$ corresponds to $\ln\alpha$ and the variable $x = \hbar\omega$. Thus, the ratio B/T has three different values respectively 3.9796, 3.77 and 2.3319 (Fig. 3a,b and c). The constant B is expressed by the dependence $B = \sigma(T)/k_B$, where $\sigma(T)$ is the parameter characterizing the slope of the absorption edge, k_B is the Boltzmann constant. The tangent of the angle between $y = \ln\alpha$ and $x = \lambda$ is equal to $\sigma(T)$. In the case of Mn₃O₄:Ni 1% and Mn₃O₄:Ni 2%, the slope of absorption edge is the same $\sigma_1(T) = \sigma_2(T) = 0.0005 \cdot 10^{-3}$ (Fig. 3a, b). $\sigma_3(T) = 0.0004 \cdot 10^{-3}$ for the sample Mn₃O₄:Ni 3% (Fig. 3c). The magnitude W_d describes the broadening of the absorption edge due to the dynamic disorder. When the temperature is higher, the absorption edge is wider due to the dynamic disorder in the structure of thin film. The equation $W_d = k_B T / \sigma$ [12] describes the connection between W_d and $\sigma(T)$. The dynamic disorder for the samples with the concentration of Ni 1% and 2% has the same values: $W_d^1 = W_d^2 = 0.0518 \text{ eV}$. For the third investigated thin film $W_d^3 = 0.0648 \text{ eV}$. Urbach's energy is connected with the carrier impurity interaction, the carrier-phonon interaction and

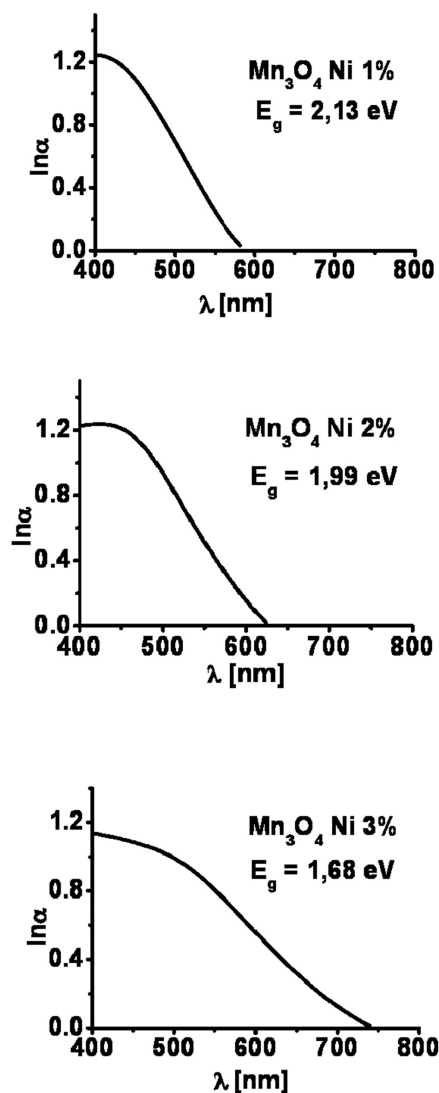


Fig. 2. The energy gap of Ni doped Mn₃O₄

the structural disorder [13]. In a previous study [14] and in order to understand Urbach tailing alteration following doping agent insertion in host structures, Urbach energy E_u has been determined, for doped and un-doped samples through the equations:

$$\ln(\alpha(h\nu)) = \ln(\alpha_0) + (h\nu)/E_u$$

$$E_u = \alpha(h\nu)(d[\alpha(h\nu)]/d[h\nu])^{-1} = h[d/d\nu(\ln\alpha(\nu))]^{-1},$$

where $\alpha(h\nu)$ represents, for each sample, the experimentally deduced optical absorption profile.

Urbach energy E_u is a measure of the unhomogeneous disorder and atomic scale dispersion inside structures as it indicates the width of the band tails of the localized states in presence of defects. Its analytical formulation deduced by taking into account three components: structural disorder, carrier-pho-

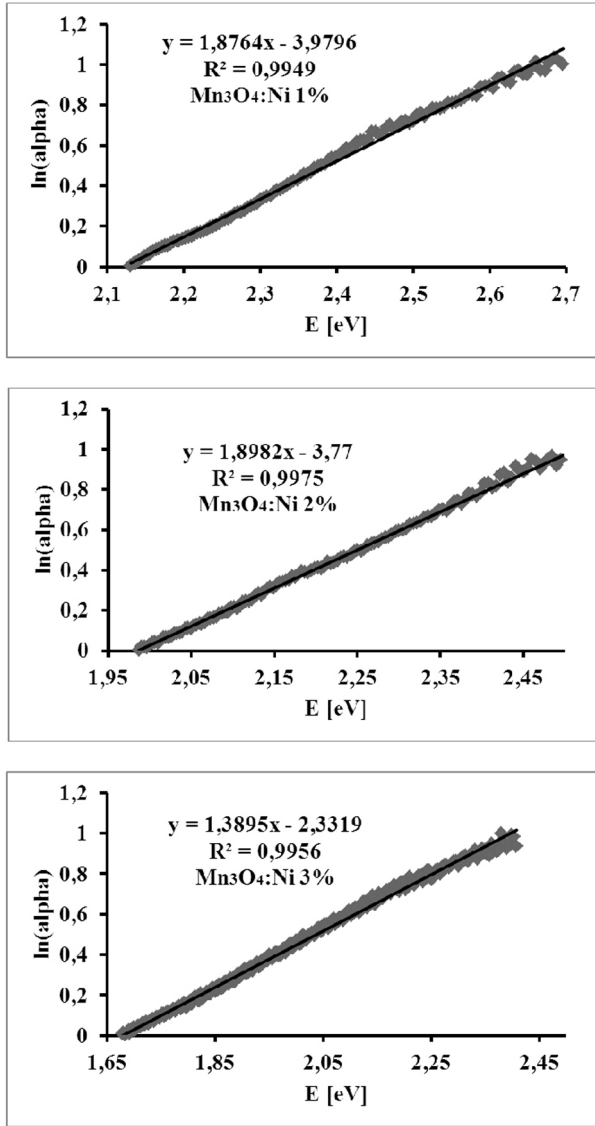


Fig. 3. The Urbach's rule region of the Ni doped Mn₃O₄

non interaction and carrier-impurity which are presented in the next equation:

$$E_U = \frac{1}{2} k_B U \theta_D + \Omega_1 \frac{4\pi^2 Z^2 q^4 m^* L_D^3}{9\sqrt{3}\epsilon^2 \hbar^2} + \Omega_2 \coth\left(\frac{\Omega_3}{2k_B T}\right)$$

where Ω_1 , Ω_2 and Ω_3 are constants, k_B is Boltzmann constant, U is lattice strain related with the structural disorder, θ_D is Debye temperature, L_D is Debye length, m^* is carrier effective mass, Z is impurity charge, q is electron charge, ϵ is static dielectric permittivity and \hbar is Planck's constant. The width of the localized states (band tail energy or Urbach energy E_U) is then estimated from the slopes of the plots of $(\ln\alpha(h\nu))$ versus energy $E = h\nu$.

The Urbach's energy curve as a function of $E = h\nu$ has different form for each different concentration of nickel impurity (Fig. 4). This means that carrier-phonon interaction depends of the concentration of Ni²⁺ ions in the investigated sample. The effective mass of electrons of doping elements can be calculated by the next formula: $m^* = \hbar^2 / (d^2E/dk^2)$, where $\hbar = h/2\pi$ (h is Planck constant) and $k = \alpha\lambda/4\pi$ is the extinction coefficient. The experimental dependence $m^*(E)$ for Ni doped Mn₃O₄ is presented on Fig. 5 in the Urbach's rule region. Most values of m^* for Ni doped manganese oxide thin films are less than $2 \cdot 10^{-28}$ kg (Fig. 5). This means that the

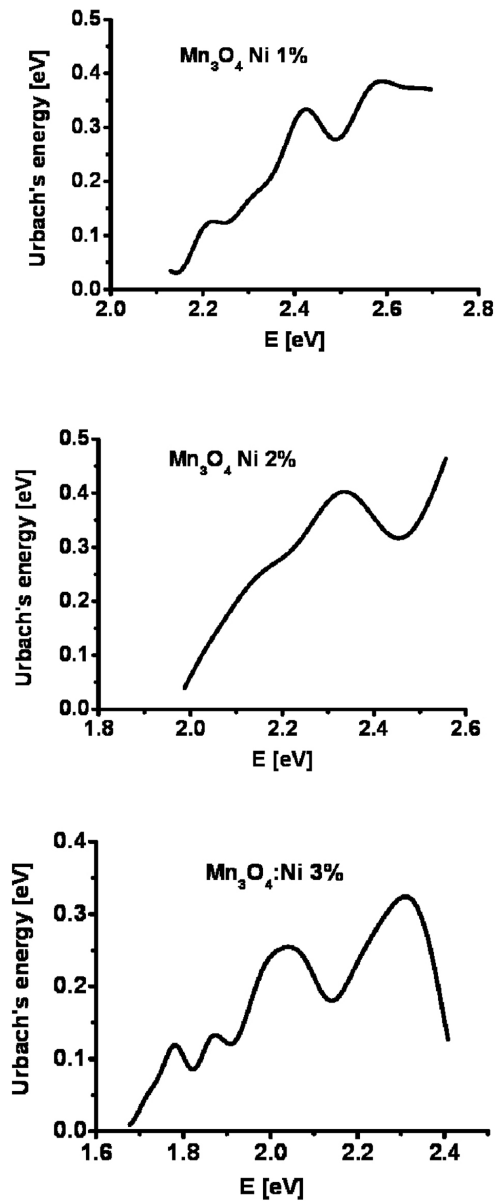


Fig. 4. Urbach's energy as a function of $E = h\nu$ in the spectral region 1.68–2.7 eV

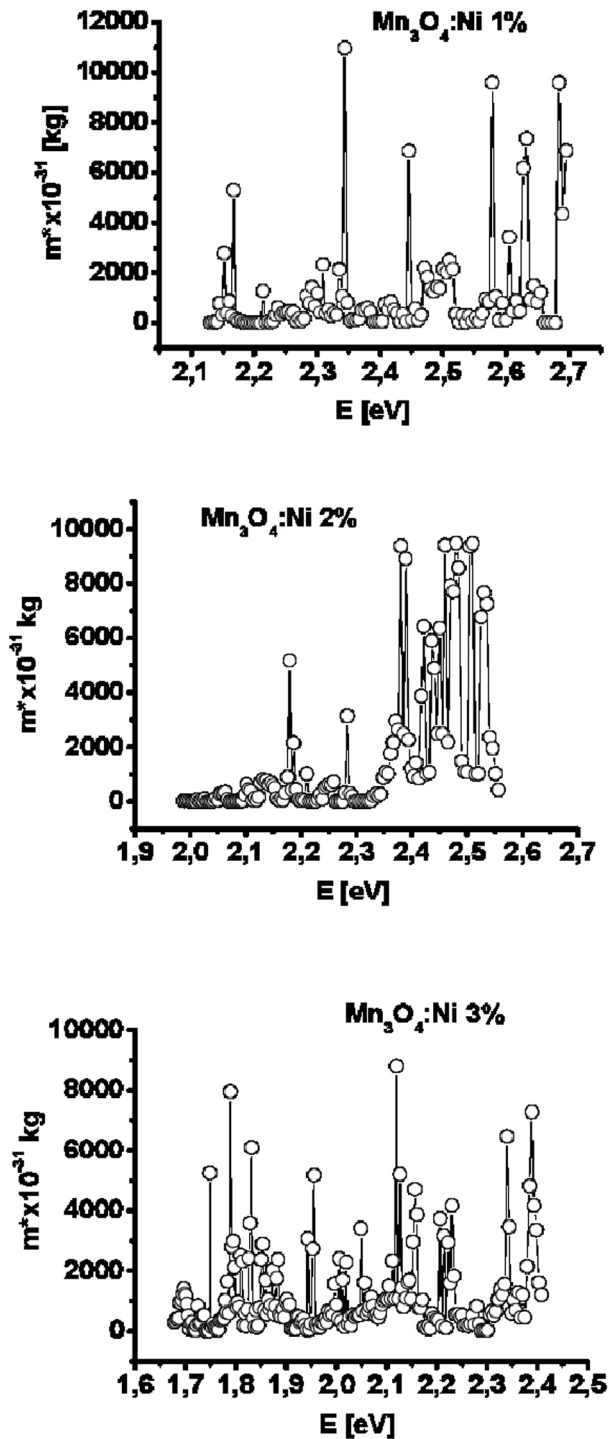


Fig. 5. Effective mass m^* of Ni doped Mn_3O_4

nickel ions narrow the parabolic form of valence and conduction band of doped Mn_3O_4 thin film.

CONCLUSION

The final conclusion for Mn_3O_4 :Ni thin films is that all determined optical characteristics in the vicinity of the absorption edge show good possibility of the application of hausmannite as optoelectronic and photocatalytic devices.

Acknowledgements: The financial support by the project of Shumen University (2015) is gratefully acknowledged.

REFERENCES

1. H. Ginaga, S. Futamura, *J. Catal.*, **227**, 304 (2004).
2. C. C. Hu, T. W. Tsou, *Electrochem. Commun.*, **4**, 105 (2002).
3. O. Giraldo, S. L. Brock, W. S. Willis, M. Marquez, S.L. Suib, S. Ching, *J. Am. Chem. Soc.*, **122**, 9330 (2000).
4. Y. F. Shen, R. P. Zenger, R. N. Deguzman, S. L. Suib, L. Mccurdy, D. I. Potter, C. L. Oyoung, *Science*, **206**, 511 (1993).
5. A. R. Armstrong, P. G. Bruce, *Nature*, **381**, 499 (1996).
6. K. S. Park, M. H. Cho, S. H. Park, K. S. Nahm, Y.K. Sun, Y. S. Lee, M. Yoshio, *Electrochim. Acta*, **47**, 2937 (2002).
7. E. Grootendorst, Y. Verbeek, V. Ponce, *J. Catal.*, **157**, 706 (1995).
8. E. R. Stobhe, B. A. D. Boer, J. W. Geus, *Catal. Today*, **47**, 161 (1999).
9. T. Yamashita, A. Vannice, *J. Catal.*, **163**, 158 (1996).
10. M. Baldi, E. Finocchio, F. Milella, G. Busca, *Appl. Catal. B*, **16**, 43 (1998).
11. T. Larbi, M. H. Lakhdar, A. Amara, B. Ouni, A. Boukhachem, A. Mater, M. Amlouk, *Journal of Alloys and Compounds*, **626**, 93 (2015).
12. V. Kunets, N. Kulish, V. Kunets and M. Lisitsa, *Semiconductor Physics, Quantum Electronics & Optoelectronics*, **5**, 9 (2002).
13. Sk.F. Ahmed, M. Myoung-Woon and L. Kwang-Ryeol *Thin Solid Films*, **517**, 4035 (2009).
14. P. Petkova and K. Boubaker, *Journal of Alloys and Compounds*, **546**, 176 (2013).

ПРАВИЛО НА УРБАХ ЗА ЛЕГИРАНИ С НИКЕЛ
ТЪНКИ ФИЛМИ ОТ Mn₃O₄

П. Петкова^{1*}, К. Боубакер², П. Василев¹,
М. Мустафа¹, Т. Ларби³

¹ Шуменски университет *Shumen „Епископ Константин Преславски“*,
ул. „Университетска“ № 115, 9712 Шумен, България

² Висше училище за наука и технологии, 63 Rue Sidi Jabeur, 5100, Махдия, Тунис

³ Физика на полупроводниковите елементи, Факултет на науките,
Университет El Manar, 2092 Тунис

Постъпила декември, 2014 г.; приета януари, 2015 г.

(Резюме)

Измерени са спектрите на поглъщане на легираните с никел тънки филми от Mn₃O₄ в спектралната област 1.65–2.7 eV при стайна температура. Изчислени са параметрите, определящи наклона при ръба на поглъщане и динамичния безпорядък в областта на Урбах. Определено е и влиянието на йоните на преходните метали. Направена е оценка на ефективната маса на Mn₃O₄:Ni в изследвания спектрален диапазон.

Investigation on the proliferation of Gram negative bacterial cells onto sol-gel carriers

D. Marinkova^{1*}, M. Michel², R. Raykova¹, D. Danalev¹, S. Yaneva¹,
L. Yotova¹, P. Griesmar²

¹ Department of Biotechnology, University of Chemical Technology and Metallurgy,
“Kliment Ohridski” blvd. 8, Sofia 1756, Bulgaria

² Laboratory for Systems and Applications in Information and Energy Technologies
(SATIE), University of Cergy Pontoise, ENS Cachan, UMR CNRS 8029,
Cergy-Pontoise, F-95000, France

Received December, 2014; Revised January, 2015

This work is related to the synthesis and characterization of new hybrid sol-gel materials. Several carriers based on poly (N-acryloylglycine) (NAGly) composed of poly (ethylene glycol) dimethacrylate (PEGDM) were prepared. The effectiveness of biofilms formation of bacterial strains *Escherichia coli* and *Pseudomonas fluorescens* on the matrices was investigated by biochemical methods.

Two types of hybrid gels were synthesized based on PEGDM, 2-hydroxyethyl acrylate (HEA) and N-acryloxysuccinimide ester (NAS) with incorporation of inorganic precursors. The rheological properties of the gels and formed biofilms were investigated by quartz crystal microbalance (QCM).

The experimental results demonstrated that the obtained matrices are appropriate for biofilms formation.

Key words: biofilms, matrices, hybrid gels.

INTRODUCTION

Biofilms are defined as microbial communities adhered to surfaces and encased within an extracellular polymeric substance (EPS) produced by the microbial cells themselves. Biofilms may form on a wide variety of surfaces, including natural aquatic systems living tissues, indwelling medical devices and industrial/potable water system piping [1].

A major fact influencing the biofilm development in water treatment system is the surface area. Industrial water systems, unlike most natural environments (lakes and rivers), offer a tremendous amount of surface area for attachment. Different polymeric membranes, resins, storage tanks, cartridge filters, and piping systems all provide surfaces suitable for bacterial attachment and growth [2]. The topography of the surface to which a microbial cell attaches is also fundamental to biofilm formation. Generally, as the roughness of a surface

increases, bacterial adhesion will also increase [3]. In addition, the physicochemical properties of the surface effects bacterial adhesion. Microorganisms attach more rapidly to hydrophobic, non-polar surfaces such as teflon and other plastics than to hydrophilic materials such as glass or metals [4–6].

Hybrid materials obtained by the sol-gel method are effective carriers of enzymes, cells, amino acids, etc. Development of a good biocompatible matrix for immobilization of cells is very crucial for improving the performance of functional biohybrids. Synthesis of solid inorganic materials from alkoxide, aqueous and polyol-modified silanes routes, as well as the incorporation of organic polymers, is further areas being developed to improve the viability of encapsulated cells [7]. Depending on the precursor (SiO₂, TiO₂, SnO₂, etc.) introduced in the system, the matrices obtained by the sol-gel technology possess different physical and mechanical properties. These multifunctional materials are used in different fields, including construction of chemical and biological sensors, in optics and catalysis [8–10].

According to type of bonding between organic and inorganic part, the hybrid materials can be clas-

* To whom all correspondence should be sent:
E-mail: dmarinkova@yahoo.com

sified in two groups: Class I includes matrices based on non-covalent bonding (donor-acceptor, H-bonds, etc.) between organic and inorganic parts. They are quite simple to obtain because they consist of a mixture of two different types of polymers. Class II requires covalent bonds between the two parts [11].

In order to investigate the rheological properties of obtained sol-hybrid materials and biofilms, thickness shear mode (TSM) resonators was used. (TSM) resonators use transversal waves in the ultrasound range for investigation of the properties of complex materials and nanostructures at different scale [12–15]. The Quartz Crystal Microbalance (QCM) TSM resonator, is a simple, low cost effective, high-resolution mass sensing technique, based upon the piezoelectric effect. The QCM can be applied for solution measurements mainly in analytical chemistry and in electrochemistry due to its sensitive solution–surface interface measurement capability. The technique possesses a wide detection range [16–18]. At the low mass end, it can detect monolayer surface coverage by small molecules or polymer films. At the upper end, it is able to detect a larger masses bound to the surface. Such kind of masses can be complex arrays of biopolymers and bio-macromolecules, or even whole cells. This model and technique have been used to characterize the micro-viscoelastic properties of gels and biomaterials particularly during their formation [19]. The efficiency of this new micro-rheometer is sufficiently high to ensure a complete and a reliable on-line follow-up of the intrinsic characteristics at microscopic scale of both organic and inorganic materials [20, 21].

Hybrid organic-inorganic materials are deeply investigated as host substrate for bioapplication. Innovative applications of microorganisms embedded in sol-gel hybrid materials have strongly increased. One of those applications is the assessment of water quality to detect traces of chemical or biological pollution [22]. To increase the efficiency of these tests, it is important to carry out early detection of the different microorganisms involved. One can note the interest of the early detection of bacteria such as *Escherichia coli* involved in pathogenic human diseases such as gastroenteritis, urinary tract infections, or meningitis [23–25] or *Pseudomonas aeruginosa* presents in septicemia or nosocomial infections [26].

Several microbial strains which can form biofilms onto various matrices are well known: *Bacillus cereus*, *Bacillus licheniformis*, *Halomonas salina*, *Bacillus pumilus*, *Pseudomonas aeruginosa*, *Pseudomonas putida*, *Pseudomonas species*, *Candida albicans*, *E.coli* [27–32].

Although current knowledge of bacterial biology owes much to work done on planktonic cul-

tures of laboratory strains of *E. coli*, many isolates also have the capacity to form biofilm structures *in vivo* and *in vitro*. Indeed, *E. coli* is a predominant species among facultative anaerobic bacteria of the gastrointestinal tract, where it thrives in an environment with structural characteristics of a multispecies biofilm [33, 34]. Biofilm formation of *E.coli* has mainly studied with non-pathogenic laboratory strains. The authors demonstrate that *E. coli* forms biofilms on multiple abiotic surfaces in a nutrient-dependent fashion [35–39].

Pseudomonas fluorescens is known to form biofilms and consequently the surface adhesion of a number of isolates has been investigated. *Pseudomonas fluorescens* is a ubiquitous, Gram-negative, motile, biofilm-forming bacterium commonly-encountered in soil and water habitats. The organism plays an important role in food spoilage, drinking water quality and plant disease [40]. Cossard et al. determined that the adherence properties of four *Pseudomonas fluorescens* isolates were independent of their ecological habitat [41].

A biofilm formation from cells of *Pseudomonas aeruginosa* and *Pseudomonas fluorescens* on different surfaces: glass, copolymers of cellulose, poly-dimethylsiloxane, etc. was reported [42].

This study is devoted to the synthesis and characterization of different hybrid materials based on pure organic material N-acryloylglycine (NAGly). Two microorganisms *Escherichia coli* 52170 and *Pseudomonas fluorescens* FFD16 were selected to be involved in the formation of biofilms on newly synthesized hybrid matrices as follows. The dynamics of proteins and polysaccharides production of biofilms were examined. Two types of gels based on poly(ethylene glycol) dimethacrylate with incorporation of inorganic precursor was also synthesized and characterized.

EXPERIMENTS AND EQUIPMENT

Reagents

2,2'-azobis(2-methyl propanitrile) (AIBN) and glycine were provided by Acros Organics. Poly(ethylene glycol)dimethacrylate (PEGDM 550, Mw= 550 g/mol), N, N-dimethylacetamide (DMAc) acryloylchloride, 2-hydroxyethyl acrylate (HEA), tetramethylorthosilicate (TMOS), 3-(dimethylamino) propionitrile (DMAPN), sodium persulfate (PSS), 2-hydroxy succinimide (NHC), Triethylamine (TEA), hydrochinon, ethyl acetate and hexane were purchased by Sigma-Aldrich. All products were used without any further purification. N-acryloxysuccinimide ester (NAS) was synthesized in Laboratory for Systems

and Applications in Information and Energy Technologies (SATIE), University of Cergy Pontoise.

Escherichia coli 52170 and *Pseudomonas fluorescens* FFD16 microbial strains were supplied by the Collection of Pasteur Institute of France. Salts for nutrient medium were obtained from Merck (Germany). Glucose and bovine serum albumin (BSA) were obtained from Fluka (Switzerland). Agar and LB for nutrient microbial growth mediums were obtained from Sigma-Aldrich.

Carriers for biofilm formation

The following four different polymeric matrices and hybrid gels were used for biofilm formation during the experiments:

The matrices were synthesized by co-polymerization between NAGly and PEGDM-like organic crosslinker. For biofilms formation we used four matrices with different ratio of NAGly and PEGDM as follows: NAGly/ PEGDM: 10/90, 20/80, 30/70, 50/50 wt%. Polymerization was obtained using 25 mg AIBN.

Preparation of NAGly

The polymer carriers for biofilms formation were synthesized according to Ringear et al. [43].

NAGly was prepared by adapted method of Bentolila et al. [44]. It was synthesized by a Schotten-Baumann reaction in aqueous phase as follows: 4.50 g of glycine (60 mmol) were dissolved in 60 ml of 2M solution of potassium hydroxide. The mixture was cooled at 4°C in water ice bath for about 10 minutes. 6 ml of acryloyl chloride (73.6 mmol) were added to the mixture drop wise using a dropping funnel. At the end of the reaction (TLC monitoring) the solution was washed with 2x40 ml of diethyl ether and the separated aqueous phase was acidified to pH = 2. The aimed product was extracted by 3x40ml ethyl acetate. After drying the organic phase over MgSO₄, the residue was concentrated using a rotary evaporator. The yield of this synthesis is 74%. mp 130 °C (lit. 132 °C) [45]; H NMR (250 MHz, dimethyl sulfoxide [DMSO]-d₆, (δ): 6.25 (dd, 1H, C(γ)H), 6.08 (dd, 1H; C(β)H), 5.67 (dd, 1H; C(α)H), 3.95 (s, 2H, Et); infrared (IR) (ATR): ν=3350 (s), 1740 (s), 1650 (s), 1600 (s), and 1530 (s) cm⁻¹ [43].

Preparation of matrices based on NAGly/PEGDM

Four different types of matrices based on NAGly were synthesized according to the methodology described above [43]. The overall composition of the networks was varied between 10/90, 20/80, 30/70

and 50/50 wt% of NAGly and PEGDM. All investigated co-networks were reported as PNAGly/PEGDM (x/y). The numbers between brackets (x/y) correspond to the PNAGly and crosslinker weight proportions, respectively. For example, a co-network obtained from a mixture of 450 mg of NAGly and 50 mg PEGDM was noted PNAGly/PEGDM (90/10 wt%). The synthesis of co-network is performed in a flask containing x wt% of NAGly, y wt% of crosslinker and 600 μl of DMAc. The mixture was stirred and degassed to remove all traces of oxygen (radical inhibitor). Finally, 25 mg of AIBN were added at the last moment to avoid the rapid decomposition of the initiator. The content of the flask was taken with a pipette and placed between two glass plates separated by a teflon film (e=500 μm) and held together by a clamp system to ensure the sealing of the experimental device. The purpose was to achieve the shape of thin polymer membranes. The device was placed in an oven and treated according to the following thermal program: 2,5 h at 60 °C to complete polymerization and then one hour at 120 °C to achieve a post-curing. After polymerization, the cross linked polymer was detached from the device and vacuum dried at 60 °C [43].

Preparation of hybrid gels based on PEGDM and NAS

In the experiments for biofilms formation from two bacterial strains were used gels without NAS and with NAS synthesized in laboratory SATIE according the following procedure:

In 250ml two-necked flask in water ice bath (4 °C) were added 11,5 g NHC, 11 g TEA (three ethyl amine) and 10 g acryloylchloride. Further 150 ml chloforme was added drop wise using a dropping funnel during 20 minutes. After stirring the reaction mixture was washed three times with 80 ml cold water. The organic phase was dried over MgSO₄. After filtration it was added 50 mg hydrochinone. The solvent was removed to obtain 25 ml volume. The traces of hydrochinone were removed by filtration. Ethyl acetate and hexane 1.5ml/10ml respectively were added to the mixture. The aimed product was precipitated after several hours in ice bath conditions. The sediment (white precipitate) was recovered by washing with solution of hexane/ethyl acetate (9:1 V/V).

Two types of gels were synthesized based on PEGDM and HEA. 60.48 mg – 2-hydroxyethyl acrylate (HEA) and 10.27 mg poly(ethylene glycol)dimethacrylate (PEGDM) were dissolved in 1059.5μl H₂O. 79.75 mg TMOS was added to the mixture. 10% DMAPN and 7% PSS were used as gelling agents. To synthesize gel with NAS to the mixture was added 8.46 mg NAS.

Cell culture

Escherichia coli 52170 and *Pseudomonas fluorescens* FFD16 were cultivated on solid agar nutrient medium containing yeast extract, peptone, glucose, NaCl at 30 °C for 24 h. After incubation the colonies were picked up and suspended in liquid nutrient medium containing LB and 10% glucose for 24h in bath shaker at 30 °C, pH 7. Further the cells were suspended in fresh liquid medium, containing LB and 10% glucose and the biomass was used for formation of biofilms onto different matrices.

Formation of biofilm

The obtained matrices were autoclaved for 20 min in 0.8 atm then placed in cell suspension with nutrient medium containing LB and 10% glucose to form biofilms with cell adhesion. The binding of cells was carried out at pH 7 and temperature 30 °C under continuous stirring in bath shaker (220 rpm). Biofilms formation was studied at 24, 72, and 120 h. Every 24 h the matrices were washed up by 0.9% NaCl and suspended in the fresh nutrient medium.

Methods

Biochemical analyses

The absorbance of the biomass of free cells and this produced by biofilms was measured at 590 nm with a "Biochrom, Libra S12", (Germany). The renovation of the biofilm was monitored microscopically as well as by means of the turbidity (OD-590) of the effluent.

The extracellular protein content attach to the matrices was measured using a modification of the Lowry method [46] according to Raunkjaer et al. [47]. The exopolysaccharide content was measured using the reaction with 3,5-dinitrosalicylic acid [48].

Thickness shear mode (TSM) resonators and Quartz Crystal Device (QCM)

It was observed the rheological properties of synthesized hybrid gels and formed biofilms by quartz crystal microbalance (QCM).

The experimental setup was presented in details according to Ould Ehssein et al. [19]. An AT-cut quartz crystal sensor resonating at 6 MHz was loaded on one side with the polymer gel. The other side was in contact with air. The polymer gel and the quartz were kept during the gelation at the desired temperature. The admittance of the quartz was measured within a 7 kHz band width near the resonance frequency using aHP4195A network ana-

lyzer. In order to observe the gelation process, the total admittance of the quartz was saved every 30s. The viscoelastic parameters are then computed online using an appropriate model developed in laboratory SATIE, University of Cergy Pontoise, Paris, France [19].

RESULTS AND DISCUSSION

The formation of biofilm from *Escherichia coli* and *Pseudomonas fluorescens* onto different polymer matrices has been shown by the determination of the extracellular polymeric substance (EPS) concentration. It was followed by measuring of extracellular proteins and exopolysaccharides present in the biofilm.

Initially, we started with investigation of biochemical properties of formed biofilms onto synthesized hybrid membranes. The dynamics of proteins and extracellular polysaccharides production by biofilms were studied.

Dynamics of extracellular proteins production from biofilms of *Escherichia coli* and *Pseudomonas fluorescens* onto different polymer matrices

After the culture was developed and a biomass was accumulated, the sterilized polymer carriers were added to the cell suspension for biofilms formation. The kinetics of proteins and polysaccharides produced by biofilms formed on four different types of polymer carriers based on NAGly/PEGDM in different ratio for 5 days was tracked and the 24th hour was assumed as initial period for the incubation. The quantity of proteins synthesized from biofilms of *Escherichia coli* and *Pseudomonas fluorescens* on four different types of matrices after 24, 72 and 120 h of incubation time is shown on Figures 1, 2 and 3. A biofilm is constituted of a mixture of polymeric compounds, primarily polysaccharides, generally referred to as EPS. These substances are characteristic of the formation of a biofilm formed by bacteria.

The figures show that a larger quantity of proteins is produced from biofilms formed on NAGly/PEGDM matrix in 50/50 wt% ratio of the components during the incubation time.

The concentration of proteins from biofilms increased proportionally to the quantity of NAGly in the matrices.

The figures also reveal that considering the produced proteins, the polymer matrix based on NAGly/PEGDM in 50/50wt% ratio is a better carrier for biofilm formation. The most quantity of proteins

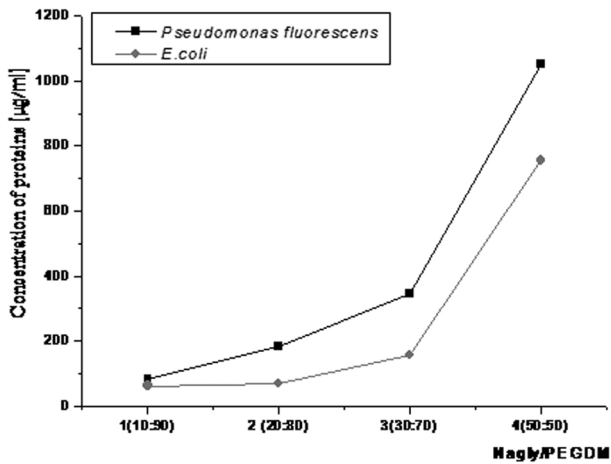


Fig. 1. Kinetics of proteins production from biofilms formed on NAGly/PEGDM matrices after 24 h

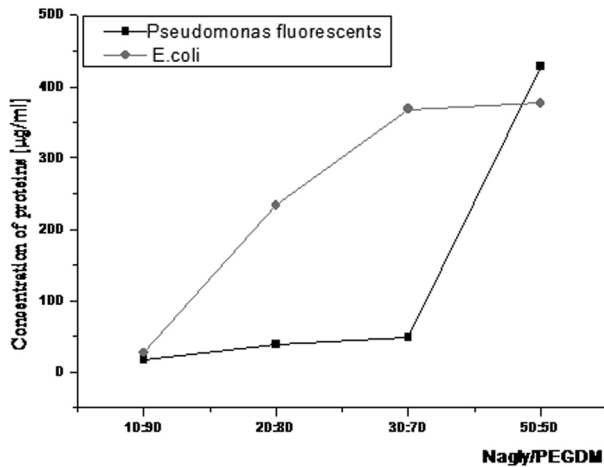


Fig. 2. Kinetics of proteins production from biofilms formed on NAGly/PEGDM matrices after 72 h

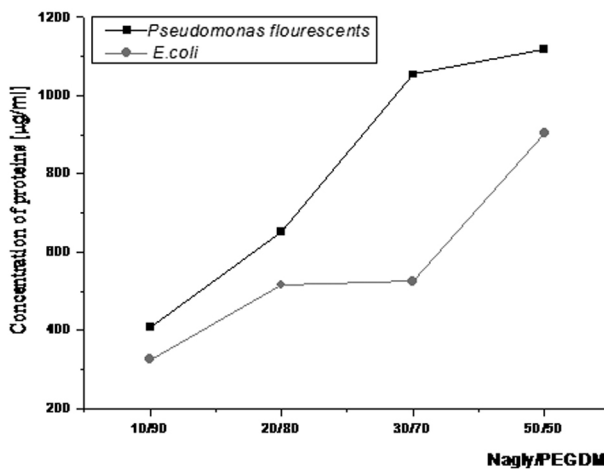


Fig. 3. Kinetics of proteins production from biofilms formed on NAGly/PEGDM matrices after 120

is produced of biofilm formed from *Pseudomonas fluorescens* cells.

Dynamics of extracellular polysaccharides production from biofilms of Pseudomonas fluorescens and Escherichia coli formed onto different polymer matrices

Kinetics of polysaccharides production from the formed biofilms is presented on Figures 4, 5 and 6.

The figures show that the quantity of polysaccharides produced from biofilms formed on a matrix of NAGly/PEGDM in 50/50 wt% ratio is higher.

It can be clearly observed that polysaccharides production of biofilms formed onto NAGly/PEGDM matrix is increased proportional of the concentration of NAGly in the matrices. These results can

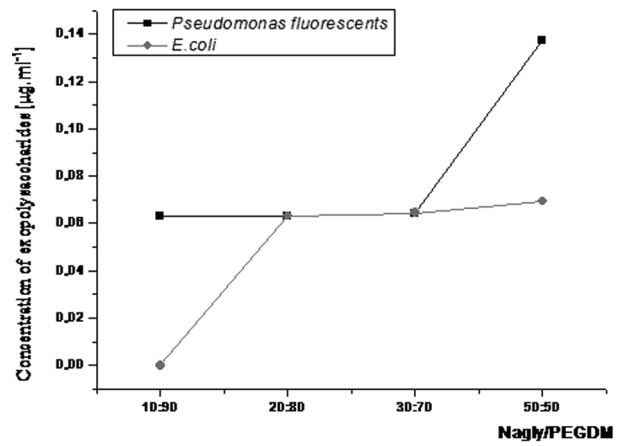


Fig. 4. Kinetics of the polysaccharides production from biofilms formed on NAGly/PEGDM matrix after 24 h

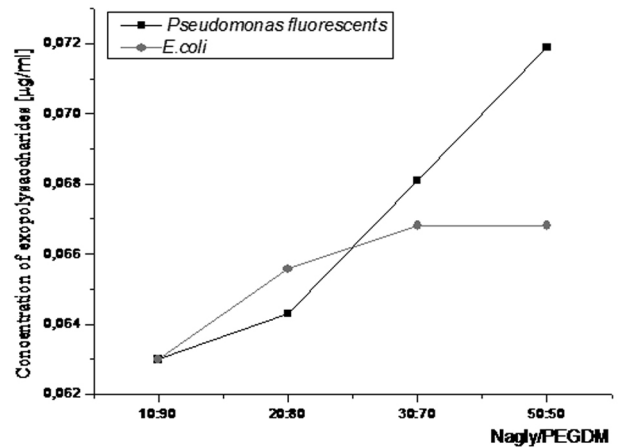


Fig. 5. Kinetics of the polysaccharides production from biofilms formed on NAGly/PEGDM matrix after 72 h

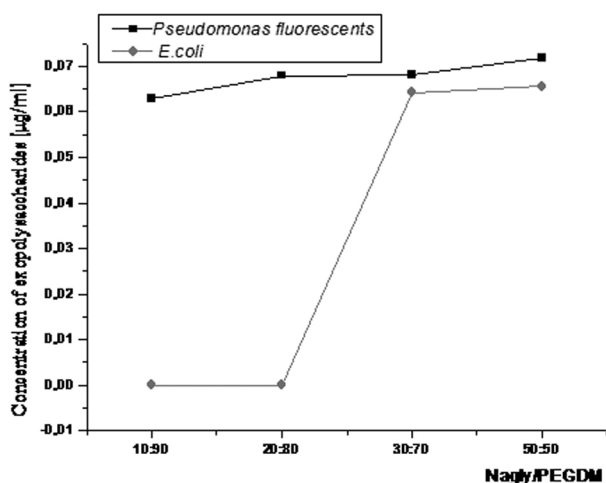


Fig. 6. Kinetics of the polysaccharides production from biofilms formed on NAGly/PEGDM matrix after 120 h

be explained by the preference of bacteria to form biofilms in the presence of higher concentration of NAGly. The production of extracellular substances is more significant for *Pseudomonas fluorescens* compared to *Escherichia coli*.

Comparing the proteins and polysaccharides production from biofilms on the four types of carriers we could conclude that the most appropriate matrix for biofilm formation is NAGly/PEGDM in 50/50 wt% ratio. The adhesion of bacterial cells is expected to be higher for conetworks with a large amount of NAGly due to the increase of interactions between glycine function and bacterial cells.

Visualization of biofilms by optical microscopy

Some representative images of the formation of biofilms from *Pseudomonas fluorescens* and

Escherichia coli on NAGly/PEGDM (50/50 wt%) are shown in Figures 7 and 8 (a and b), respectively. The composition for NAGly/PEGDM (50/50 wt%) has been chosen to promote interactions between microorganisms and materials, as already explained. These images are representative of the whole sample. They demonstrate that the formed biofilm are concentrated on the surfaces of matrices based on NAGly and the growth is more efficient for NAGly/PEGDM (50/50wt%).

Microscopic images show that *Pseudomonas fluorescens* and *Escherichia coli* cells are visible in biofilms onto matrices uniformly onto surfaces. The microscopic analysis presents that the cells from *Pseudomonas fluorescens* are more onto the surface than cells of *Escherichia coli*.

Rheological properties of formed biofilms by QCM

The results obtained by QCM analysis of the starting organic materials based on gel HEA/TMOS

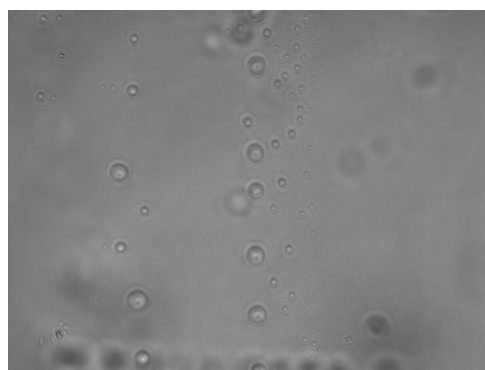


Fig. 7. Optical microscopy image of empty matrix from NAGly/PEGDM (50/50wt%), magnification 100x(oil)

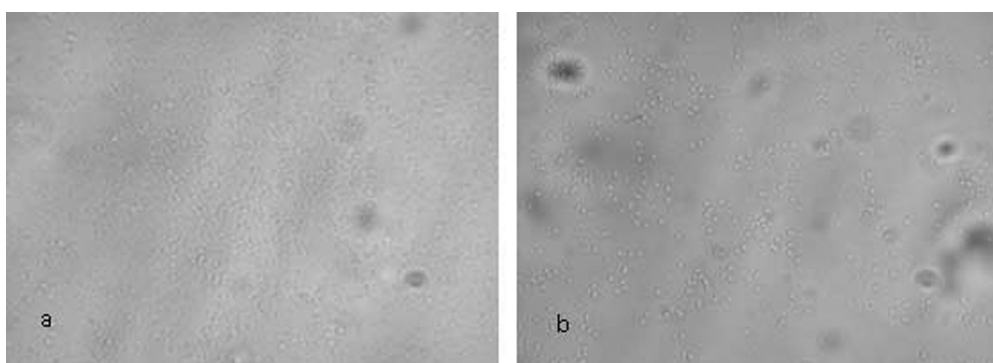


Fig. 8. Optical microscopic image of biofilm after 5 days from *Pseudomonas fluorescens* (a) and *Escherichia coli* (b) onto matrix NAGly/PEGDM (50/50wt%), magnification 100x(oil)

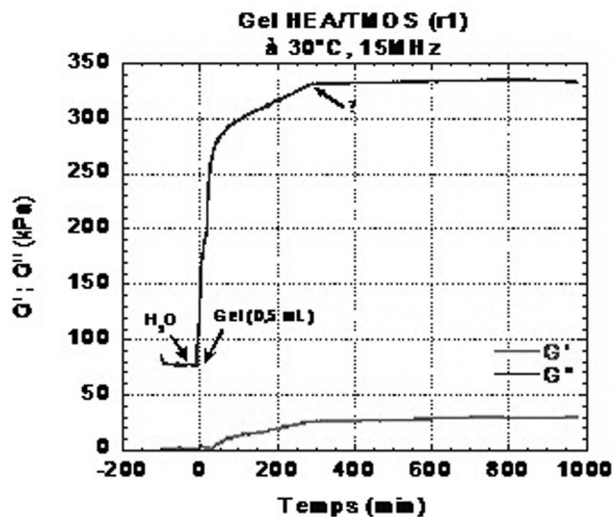


Fig. 9. Rheological properties of formed gels without microorganisms

and rheological properties of the formed biofilms are shown on the next figures. Figure 9 shows that the starting mixture presents a low elasticity evolution (G' is almost constant with time) but the viscosity (G'') increases with time due to the incorporation of two parts of materials.

The QCM analyses (Figure 10 a and b) show that the viscosity of the formed biofilms from *E.coli* onto the gel without NAS, is lower than the biofilms formed from *Pseudomonas fluorescens* cells. The elasticity is higher in biofilm formed from *E. coli* cells than *Pseudomonas fluorescens* biofilm.

Concerning the viscosity of the biofilm from *E. coli* cells formed onto gel with NAS is significantly higher comparing with the other biofilm viscosity. In this case the elasticity profiles are the same for both biofilms.

According to the rheological properties it can be concluded that both biofilms possess more defined viscosity properties than elastic. This can be explained by viscose properties of extracellular polymeric substances (EPS) of formed biofilms.

CONCLUSIONS

Our study reveals that it is possible to preserve microbial adhesion of *Pseudomonas fluorescens* and *E.coli* in newly obtained matrices. Additionally, the obtained results show that the most appropriate carrier for biofilm formation is the matrix based on NAGly/PEGDM in 50/50 wt% for both bacterial strains. Finally our results from rheological properties reveal that the matrices obtained by gel with and without NAS are also appropriate for biofilm formation.

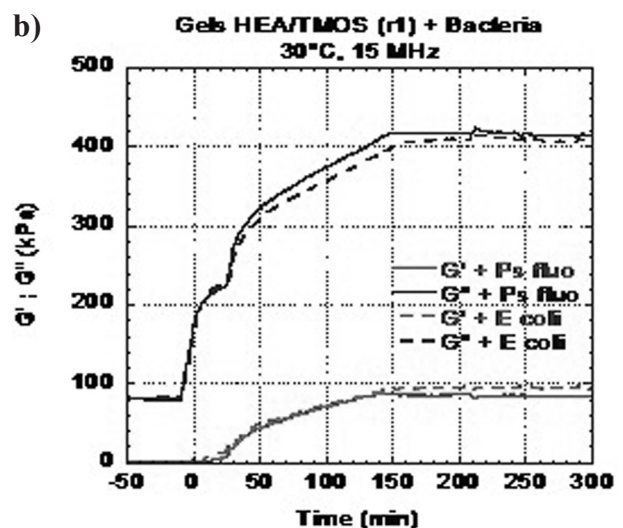
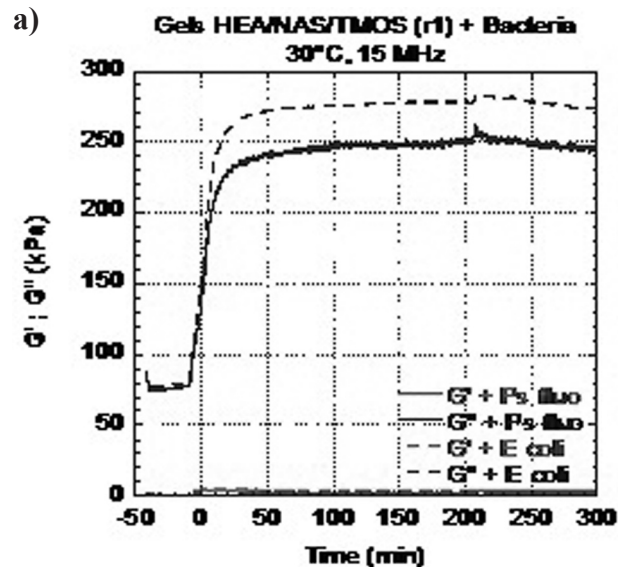


Fig. 10. Rheological properties of biofilms formed from *E.coli* and *Pseudomonas fluorescens* onto two kinds of gels (a-gel with NAS) and (b-gel without NAS)

Acknowledgments: This study was supported by "Ministry of Education and Science", Bulgaria, project "Science and Business": BG051PO001-3.3.05-0001, 2014.

REFERENCES

1. S. L. Percival, S. Malic, H. Cruz, D.W. Williams, *Biofilms and Veterinary Medicine, Springer Series on Biofilms*, 6, p. 41 (2011).
2. M. W. Mittelman, *Microcontamination*, 3, 51 (1985).
3. W. G. Characklis, G.A McFeters, K.C Marshall, Physiological ecology of biofilm systems, in: Characklis WG, Marshall KC (eds.) *Biofilms*, Wiley, New York, 1990, p. 341.

4. J. H. Pringle, M. Fletcher, *Appl. Environ. Microbiol.*, **45**, 811 (1983).
5. B. Bendinger, H. H. M. Rijnaarts, K. Altendorf, A. J. B. Zehnder, *Appl. Environ. Microbiol.*, **59**, 3973 (1993).
6. S. L. Percival, J. G. Thomas, *Water Health*, **7**, 469 (2009).
7. M. F. Desimone., G. S. Alvarez., M. L. Foglia, L. E. Diaz, *Recent Pat. Biotechnol.*, **3**, 55 (2009).
8. A. Lukowiak, W. Streck, *J. Sol-Gel Sci. Techn.*, **50**, 201 (2009).
9. C. Sanchez, B. Julian, P. Belleville, M. Popall, *J. Mater. Chem.*, **15**, 3559 (2005).
10. A. Walcarius, D. Mandler, A. J. Cox, M. Collinson, O. Lev, *J. Mater. Chem.*, **15**, 3663 (2005).
11. Y. Shoichiro, I. Keisuke, K. Kimio, *Mater. Sci. Eng.*, **C6**, 75 (1998).
12. C. Ould Ehssein, S. Serfaty, P. Griesmar, J.-Y. Le Hu'rou, L. Martinez, E. Caplain, N. Wilkie Chancellier, M. Gindre, G. Gouedard, P. Figuiere, *Ultrasonics*, **44**, 881 (2006).
13. N. Wilkie-Chancellier, L. Martinez, S. Serfaty, P. Griesmar, E. Caplain, J.-Y. Le Hu'rou, M. Gindre, *Ultrasonics*, **44**, 863 (2006).
14. N. Wilkie-Chancellier, L. Martinez, S. Serfaty, P. Griesmar, *IEEE Sens. J.*, **9**, 1142 (2009).
15. L. Martinez, N. Wilkie-Chancellier, C. Glorieux, B. Sarens, E. Caplain, *J. Phys. Conf. Ser.*, **195**, 1 (2009).
16. R. W. Cernosek, S. J. Martin, A. R. Hillman, H. L. Bandey, *IEEE Trans. Ultrason. Ferr. Freq. Contr.*, **45**, 1399 (1998).
17. H. L. Bandey, S. J. Martin, R. W. Cernosek, *Anal. Chem.*, **71**, 2205 (1999).
18. A. Janshoff, H.-J. Galla, C. Steinem, *Angew. Chem. Int. Ed.*, **39**, 4004 (2000).
19. C. Ould Ehssein, S. Serfaty, P. Griesmar, J.-Y. Le Huerou, L. Martinez, E. Caplain, N. Wilkie-Chancellier, M. Gindre, *Ultrasonics*, **44**, 875 (2006).
20. S. Serfaty, E. Caplain, P. Griesmar, J.-Y. Le Hu'rou, M. Gindre, Effects of materials conductivity on the viscosity measurement using a QCM. Paper presented at the 2nd ASA EAA Congress on Acoustics, Paris, France, June 29–July 4, 2008.
21. P. Banet, P. Griesmar, S. Serfaty, F. Vidal, V. Jaouen, J.-Y. Le Huerou, *J. Phys. Chem.*, **B113**, 14914 (2009).
22. T. E. Cloete, L. Jacobset, V. S. Brozel, *Biodegradation*, **9**, 23 (1998).
23. L. Brousse, *Sens. Actuat. B*, **34**, 270 (1996).
24. T. Vo-Dinh, B. Cullum, *J. Anal. Chem.*, **366**, 540 (2000).
25. P. Janknecht, L. F. Melo, *Environ. Sci. Biotechnol.*, **2**, 269 (2003).
26. N. Hoiby, B. Frederiksen, T. Pressler, *J. Cyst. Fibros*, **4**, 49 (2005).
27. A. M. Al-Fattani, J. L. Douglas, *J. Med. Microbiol.*, **55**, 999 (2006).
28. G. S. Baillie and L.J., *J. Antimicrob. Chemother.*, **46**, 397 (2000).
29. M. M. Cowan, T. M. Warren, M. Fletcher, *Biofouling*, **3**, 23 (1991).
30. K.V. Gayathri, N. Vasudevan, *J. Bioremed. Biodegrade.*, **1**, 1 (2010).
31. M. Krug, H. Ziegler, *J. Basic. Microbiol.*, **25**, 103 (1985).
32. C. Beloin, A. Roux, J.-M. Ghigo, *Curr. Top. Microbiol. Immunol.*, **322**, 249 (2008).
33. J. W. Costerton, Z. Lewandowski, D. E. Caldwell, D. R. Korber, H. M. Lappin-Scott, *Annu. Rev. Microbiol.*, **49**, 711 (1995).
34. H. M. Probert, G. R. Gibson., *Curr. Issues Intest. Microbiol.*, **3**, 23 (2002).
35. L. A. Pratt, R. Kolter, *Mol. Microbiol.*, **30**, 285 (1998).
36. C. Prigent-Combaret, O. Vidal, C. Dorel, P. Lejeune, *J. Bacteriol.*, **181**, 5993 (1999).
37. J. M. Ghigo, *Nature*, **412**, 442 (2001).
38. P. Di Martino, H. Gagnière, H. Berry, L. Bret, *Microbes and Infection*, **4**, 613 (2002).
39. A. Reisner, J. A. J. Haagensen, M. A. Schembrei, E. L. Zechner, S. Molin, *Mol. Microbiol.*, **48**, 933 (2003).
40. M. M. Baum, A. Kainović, T. O'Keeffe, R. Pandita, K. McDonald, S. Wu, P. Webster, *BMC Microbiology*, **9**, 103 (2009).
41. E. Cossard, O. Gallet, P. Di Martino, *Can. J. Microbiol.*, **51**(9), 811 (2005).
42. Contribution a l'étude de l'organisation et des propriétés mécaniques d'exopolymères de matrice de biofilms modèles, Pierre Lembre, PhD thesis, 2013.
43. J.-M. Ringeard, E. Caplain, M. Michiel, D. Marinkova, L. Yotova, S. Serfaty, J.-Y. Le Huerou, P. Griesmar, *J. Appl. Polym. Sci.*, **130**, 835 (2013).
44. A. Bentolila, I. Vlodaysky, C. Haloun, A. Domb, *J. Polym. Adv. Technol.*, **11**, 377 (2000).
45. T. Seki, I. Yajima, T. Yabu, M. Ooguri, J. Nakanishi, R. Furuya, E. Yagi, Y. Nakayama, *Cosmet. Toiletries*, **120**, 87 (2005).
46. O. H. Lowry, N. L. Rosenbrough, A. L. Farr, R. J. Randall, *J. Biol. Chem.*, **193**, 265 (1951).
47. K. T. Raunkjær, Jacobsen Hvitved, P. H. Nielsen, *Water Res.*, **28**, 251 (1994).
48. L. Yotova, I. Dobrev, I. Ivanov, Diagnosis Press, Practical exercises of biochemistry, ISBN 954-8436-06-X, 2000, (in Bulgarian).

ИЗСЛЕДВАНИЯ ВЪРХУ ПРОЛИФЕРАЦИЯТА
НА ГРАМ-ОТРИЦАТЕЛНИ БАКТЕРИАЛНИ КЛЕТКИ
ВЪРХУ ЗОЛ-ГЕЛНИ ХИБРИДНИ НОСИТЕЛИ

Д. Маринкова^{1*}, М. Мишел², Р. Райкова¹, Д. Даналев¹, С. Янева¹,
Л. Йотова¹, П. Гриесмар²

¹ Катедра Биотехнология, Химикотехнологичен и Металургичен Университет,
бул. „Кл. Охридски“ 8, 1756 София, България

² Университет на Сержи Понтоаз, ENS, UMR CNRS 8029, SATIE, F-95000,
Сержи Понтоаз, Париж, Франция

Постъпила декември, 2014 г.; приета януари, 2015 г.

(Резюме)

Представената статия е свързана със синтез и характеристика на нови хибридни зол-гелни материали. Приготвени са няколко носителя на основата на поли (N-акрилоилглицин) (NAGly), съдържащи поли (етилен гликол) диметакрилат (PEGDM). Чрез биохимични методи е изследвано формирането на биофилми от клетки на щамовете *Escherichia coli* и *Pseudomonas fluorescens* върху синтезираните матрици.

Синтезирани са два вида хибридни гелове на основата на 2-хидроксиетил акрилат и поли (етилен гликол) диметакрилат с инкорпорирането на неорганични прекурсори. Чрез кварцово-кристална микро везна са изследвани реологичните свойства на получените гелове и формираните биофилми.

Експерименталните резултати показваха, че получените матрици са подходящи за формиране на биофилми.

Design of optical biosensors for detection of pharmaceutical products

A. Hassaan^{1*}, S. Yaneva², L. Yotova¹

¹ University of Chemical Technology and Metallurgy, Department of Biotechnology

² University of Chemical Technology and Metallurgy, Department of Fundamentals of Chemical Technologies, blvd. Kl. Ohridski 8, Sofia, Bulgaria, 1756

Received December, 2014; Revised January, 2015

Sol-gel approach has rapidly become a fascinating new field of research in materials science. The use of some organic molecules in the gel formation process that may influence the dimensions of the forming pores represents another way to increase the immobilized enzyme activity.

The aim of our work is a design of optical biosensors for detection of pharmaceutical products. We synthesized by sol-gel methods hybrid matrices contained silica precursors, cellulose derivatives and Poly (amido amine) dendrimers (PAMAM) as perspective carriers for covalent immobilization. Horseradish peroxidase (HRP) was used as a model enzyme. Conditions were optimized, kinetic parameters, pH and temperature optimums were determined. Constructed biosensors were implemented to detect resorcinol, pirogallol, epinephrine and etc.

These biosensors can be potentially applied in medical, pharmaceutical, food and environmental monitoring fields.

Key words: optical biosensors, hybrid materials, toxic compounds detection.

INTRODUCTION

Demands for developing biosensors like amperometric [1], potentiometric [2] and optical sensors [3] for controlling the quality of food [4], pharmaceuticals [5], environmental activities [6, 7] and industrial processes [8] have encountered an enormous increase over the last decade. A lot of effort was devoted to design highly sensitive and selective methods for that purpose [9, 10]. Biosensors are self-contained analytical devices that associate a biological sensing element and a transducer to respond selectively to chemical species in the monitored samples and are considered a powerful tool compared to the existing traditional techniques; this is because of their high specificity, efficiency, direct use, reliability and cost effectiveness. [11, 12, 13]

Using enzymes as a promising biological sensing element because of their specificities is limited by their low stability, low availability and high cost. Immobilizing enzymes enhances their stability [14, 15, 16], reduces the required amounts by recovering them [3] so optimizes operational costs, while maintaining activity and signal of detection [17, 14].

Using peroxidases to catalyze oxygenation of different substrates in presence of hydrogen peroxide was reported [18, 19]. Horseradish peroxidase (HRP) was used for analytical purposes [20] to produce signals that could be based on colorimetry [15], chemiluminescence, fluorescence [21] or amperometric measurements [1].

An optical biosensor was developed by covalent immobilization of horseradish peroxidase onto prefabricated matrices. Matrices were constructed by sol-gel method; to be mainly composed of cellulose acetate butyrate (CAB) and Poly (amido-amine) (PAMAM) dendrimers as the organic part and prepared SiO₂ nanoparticles with precisely controlled size as the inorganic part that were optimized and mixed for developing the matrices to construct the optical biosensor. The system response to substrate, catalytic properties and other parameters like pH, temperature, sensitivity and stability were examined.

EXPERIMENTAL

Reagents

Peroxidase isolated from horseradish (E.C.1.11.1.7) purchased from Sigma–Aldrich; trimethoxysilane (TMOS) from Merck; cellulose acetate butyrate

* To whom all correspondence should be sent:
E-mail: ahmed.hassaan@ymail.com

(CAB), Polyamidoamine (PAMAM) dendrimers second generation from Sigma–Aldrich; phenol, hydrogen peroxide solution (35%) and chloroform from Merck. Other chemicals were of analytical reagent grade. Double-distilled and deionized water was utilized.

Synthesis of hybrid matrices by sol-gel method

Preparation was done via two separate steps, by separating the organic part preparation (PAMAM/CAB) and inorganic component (SiO_2). This was followed by optimized mixing of the two components to prepare the matrices.

Methods

Transmission electron microscopy (TEM). High Resolution Transmission Electron Microscope: JEM-2100 with 200kV/ Cu grids was used for characterizing the size and morphology of prepared SiO_2 nanoparticles used within the study.

Fourier transform-infrared (FTIR) Spectroscopy. Structure and covalent immobilization were investigated using JASCO FTIR-5300, on free HRP, free matrices, TMOS/CAB/PAMAM/A and TMOS/CAB/PAMAM/B.

SiO_2 nanoparticles preparation. SiO_2 were synthesized by the modified Stöber method; 0.6 mL of trimethoxysilane (TMOS) was hydrolysed and condensed to give SiO_2 in two mixed alcohol solutions of ethanol and methanol (A and B) with a basic catalyst of ammonia solution (1 mL of water and 3 mL of 30% NH_4OH in 50 mL of total alcoholic solution used). The relative volume ratio of methanol: ethanol was 8:1 (a) and 4:1 (b) while all the other factors were fixed.

Cellulose acetate butyrate (CAB) was used as the organic component, with PAMAM dendrimers as a source of active groups for covalent immobilization of HRP as being done before by our team [22].

Chloroform was used as a solvent for CAB, 50 μl PAMAM dispersed in chloroform was added, and then the mixture was stirred at room temperature for 3 hours.

Previously prepared SiO_2 particles were added in a percentage of 3% of the total cellulose acetate butyrate added. Mixture was then stirred well followed by membrane casting in the desired shape and drying at room temperature to induce phase separation yielding a microporous structure [23].

Oxidation of HRP. Oxidation of carbohydrate residues of horseradish peroxidase was done according to Zaborsky and Ogletree's procedure [24]. The oxidized HRP was dialyzed by dialysis membrane from Serva, Germany, through submerging

for 24 hours in 50 mmol/L acetate buffer with pH 5.6. Conditions utilized for oxidation of carbohydrate residues of HRP and that for immobilization were used to preserve HRP activity and having high immobilization efficiency [25].

Covalent immobilization of peroxidase onto hybrid matrices. HRP covalent immobilization onto matrices was done using Zaborsky and Ogletree approach, via covalent linkage between amide groups flanking onto the prefabricated matrices and the carbohydrate residues of HRP [24]. HRP covalent immobilization was carried out as follow: 1.0 g of the hybrid matrices was added to 10 ml of the oxidized dialyzed solution of HRP. Immobilization was done by continuous stirring for 24 h at 4 °C.

Determination of enzyme activity. HRP activity was measured spectrophotometrically by measuring the increase of absorbance ($\lambda = 510 \text{ nm}$) for the solution of oxidized 4-APP (4-aminoantipyrin), as being converted to the reduced form by HRP. The assay was done within phosphate buffer (PBS, 100 mM, pH 6.5) having 4-APP (1.4 mL/2.5 mM), H_2O_2 (1.4 mL/1.7 mM), at 25 °C.

Total protein determination. Total free and immobilized protein was determined via modified Lowry method taking bovine serum albumin as a standard [26].

pH and temperature optimum

The optimum operational pH for immobilized HRP was determined using 100 mM phosphatic buffer within the pH range 4.0–8.5 using 100 μM solution of hydrogen peroxide. Temperature optimum was determined in the range from 20 °C to 65 °C.

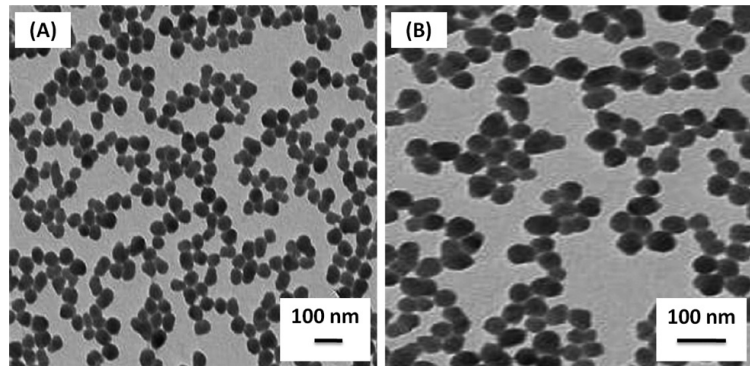
Drying time (Drying characteristics). This is done by recording the amount of evaporated solvent from the system with respect to time. Matrices were weighed immediately after the application of the coating, and then the weight loss was recorded until constant weight was reached.

RESULTS AND DISCUSSION

The constructed hybrid matrices exhibited enhanced uniformity, flexibility, transparency and surface properties, which is desirable properties for sensing applications and for enzyme immobilization. Both used organic and inorganic exhibits biocompatibility, while matrices exhibit inertness towards the enzyme, in addition to the low preparation cost, simplicity, and versatility of the used sol-gel process [25, 27].

Figure 1 shows the Transmission Electron Microscopy (TEM) of SiO_2 nanoparticles, SiO_2 nano-

Fig. 1. TEM images of SiO₂ particles prepared in the mixtures of methanol: ethanol (v/v); (a) 8:1, and (b) 4:1



particles appeared to be of spherical shape, with estimated average size around 50 nm and 65 nm. It is believed that the changes of the size of SiO₂ particles in the mixed alcohol solvent might due to the average effect of polarity, hydrogen bonding and viscosity of two used alcohols [28].

Optimized addition of silica nanoparticles around 3% contributes in enhancing mechanical properties while the integrated silica within the cellulosic matrix forms hydrogen bonding and so founding a connection between both organic and inorganic phases while decreasing the internal pressure gradients dur-

ing membrane drying [29]. Using PAMAMs which is a polymeric material is believed to affect the inorganic condensation-polymerization process and that of the sol-gel material [30].

Fourier transform infrared spectroscopy studies

As shown by FT-IR measurements for free HRP, matrices before immobilization, TMOS/CAB/PAMAM/A and TMOS/CAB/PAMAM/B (Figures 2a, b, c and d respectively), the sharp band

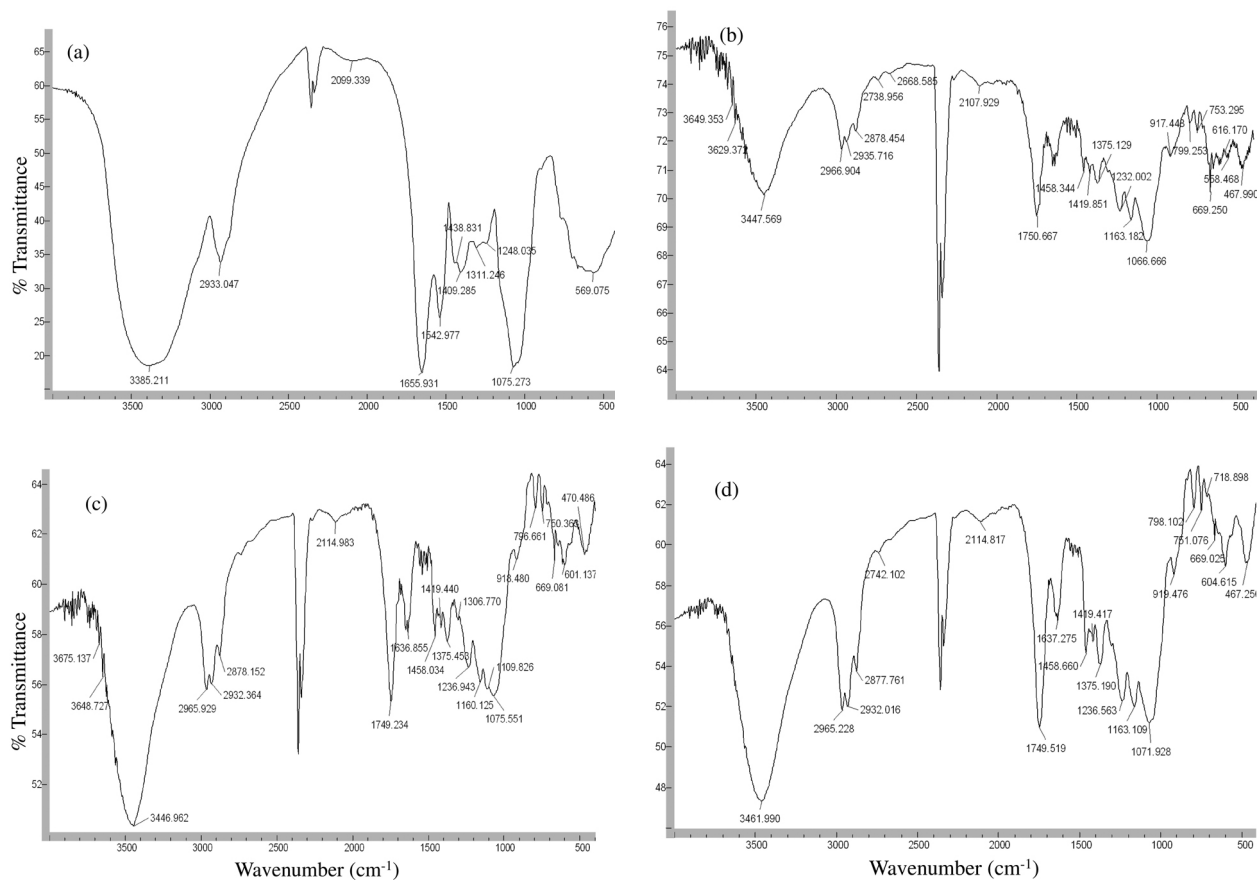


Fig. 2. FT-IR (JASCO FTIR-5300) spectrum (a) Free HRP, (b) Only matrices, (c) TMOS/CAB/PAMAM/A and (d) TMOS/CAB/PAMAM/B

Table 1. Catalytic properties of free and immobilized HRP

Sample	Abs. dry wt. [mg/g]	Specific activity [U/mg]	Relative activity [%]	pH optimum	Temp. optimum [°C]
Free HRP	–	31.7		6	30
TMOS/CAB/PAMAM (A)	2.48	29.8	94	6.5	40
TMOS/CAB/PAMAM (B)	2.5	28.7	90	6.5	45

at 1071 cm^{-1} corresponds to Si-O-Si stretching vibrations, indicating SiO_2 existence within matrices. The appearance of a broad peak within the range of 3100–3550 cm^{-1} might be corresponding to the -NH- of HRP protein, beside the clear increase with the intensities of the sharp peaks at 1637 cm^{-1} , 1458 cm^{-1} , and 1236 cm^{-1} that is attributed to amide I (-CONH-) (the C=O stretching vibration of the peptide linkage in the protein background), amide II and C-N stretching of the amide III respectively. Appearance and enhancements of these peaks may be also attributed to the HRP protein, so matrices with immobilized HRP displaying these bands, indicating successful covalent immobilization of HRP.

Catalytic properties of free and immobilized HRP

As shown in Table 1, catalytic properties for immobilized HRP showed high values compared to the free HRP. This goes with previous reports about CAB matrices with its high surface area and open structure at the end [31]. TMOS/CAB/PAMAM (A) showed better catalytic properties, with the highest relative activity recording 94%, while TMOS/CAB/PAMAM (B) relative activity was 90%. On the other hand, under pH 7.0 TMOS/CAB/PAMAM (A) and TMOS/CAB/PAMAM (B) recorded close levels of the bounded HRP recording 2.48 mg and 2.5 mg bounded protein per gram absolute dry weight respectively.

Enhanced catalytic properties and amount of bounded protein might be due to optimized addition of SiO_2 nanoparticles; SiO_2 act as a surface modifying molecules that optimized the formation of more graded pore sublayer structure with higher porosity which resulted in an enhanced permeation rate through the membrane [33, 32], providing more surface area for higher quantity of HRP immobilization and better substrate penetration into the membrane and the products out by decreasing substrate diffusion limitation [34] as well as offering higher protection from the environment, explaining the resulted increase in the activity [35].

Table 2 is comparing kinetic parameters of immobilized HRP against parameters of free HRP.

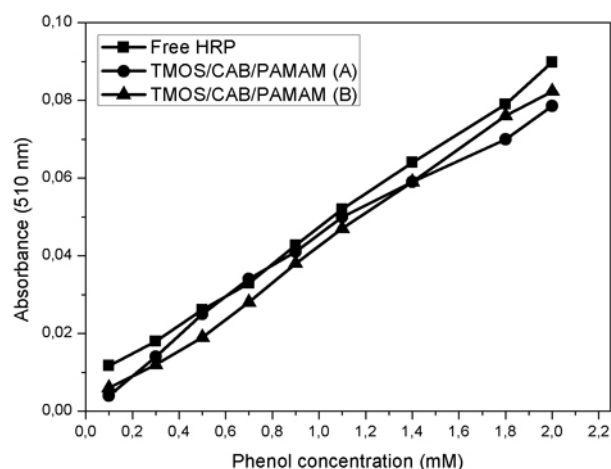
Table 2. Kinetic parameters for free and immobilized HRP onto hybrid matrices

Sample	Km [μM]	Vmax [$\mu\text{M}/\text{min}$]	R ²
Free HRP	0.96	18.5	0.998
TMOS/CAB/PAMAM (A)	3.24	27	0.997
TMOS/CAB/PAMAM (B)	0.94	13	0.971

Using Lineweaver-Burk plotting for characterization of our immobilized HRP allowed calculation of apparent Michaelis constants and maximum reaction velocity.

Immobilized and free HRP exhibited response to the reduction of phenol concentration with a recorded range from 0.09 mM/L till 2 mM/L for phenol. For immobilized and free HRP Km values obtained were found varying between 0.94×10^{-3} and 3.24×10^{-3} . Kinetic parameters results corresponded with results reported by Mohamed and co-authors [36].

Figure 3 shows the dependence of the steady state of immobilized HRP on the concentrations of phenol, the increase in response was linear up

**Fig. 3.** Dependence of the absorbance on concentration of phenol

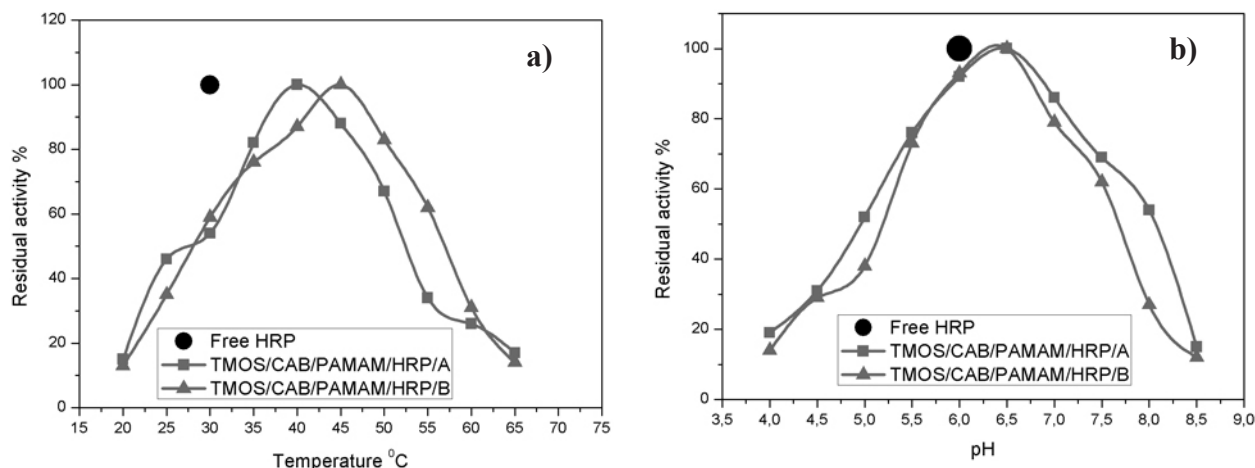


Fig. 4. (a) Temperature effect on residual activity of Immobilized HRP at pH 6.0; (b) pH effect on residual activity of HRP at room temperature

to 2.0 mM/L for free HRP, 1.4 mM/L for TMOS/CAB/PAMAM (A) and 2 mM/L for TMOS/CAB/PAMAM (B). Results coincide with previously reported data by Arzum et al [1].

Figure 4 (A) shows the residual activity of free and immobilized HRP as a function of temperature, results showed higher thermal stability for immobilized HRP onto the two matrices through shifting of temperature optimum from 30 °C for free HRP to 40 °C for TMOS/CAB/PAMAM/HRP/A, and 45 °C for TMOS/CAB/PAMAM/HRP/B.

Matrices were believed to provide better environment and protection for HRP that affected temperature optimums and enzyme stability, These observations corresponds with work done by Yotova et al [15].

Figure 4 (B) shows the optimum operational pH, pH shift was recorded for the two matrices having 100% residual activity around pH 6.5, compared with optimum pH for free HRP that was around 6.0. Immobilized HRP curves showed relatively high residual activity over a wider pH range, which goes with previously reported results [37].

After the measurements were done, the matrices with the immobilized HRP were stored in the phosphate buffer solution (0.01 M, pH 6.0) at 4 °C. As shown in Figure 5 (a), results show that immobilized HRP retained about 80% of the initial enzyme activity after 10 successive cycles of application. the other hand, Figure 5 (b) shows that the system with Immobilized HRP retained about 85% of the initial activity 60 days after enzyme immobiliza-

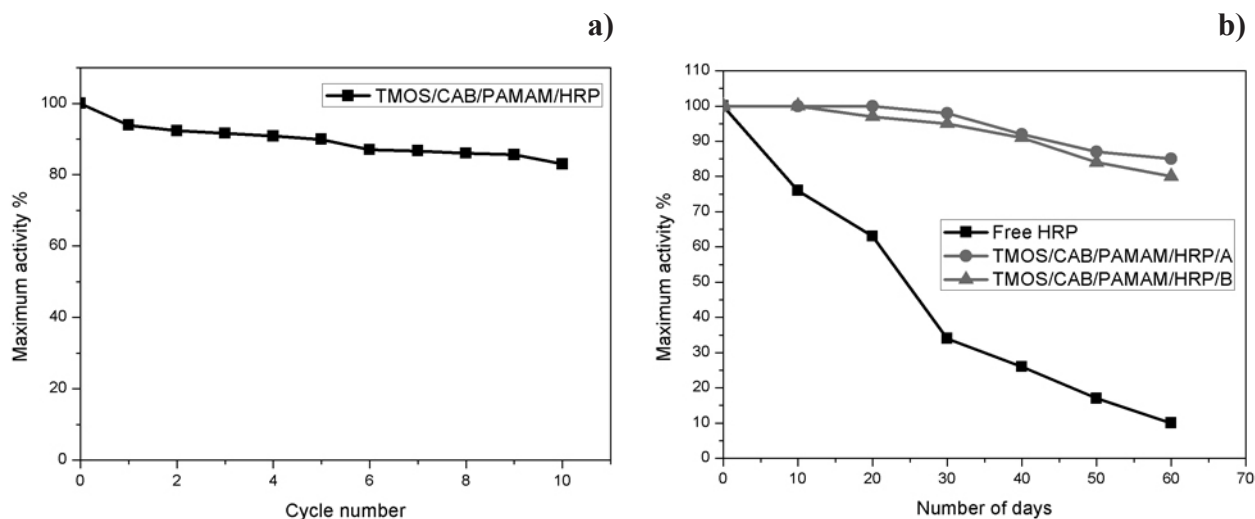


Fig. 5. Maximum activity retained versus (a) number of cycles, (b) storage period

tion compared to the free HRP that retained about 10–15% after this period.

Drying behavior

Drying process is considered critical step in membrane casting which significantly affects the final membrane morphology [38]. On solidification polymer rich phase precipitated forming solid matrix that includes the polymer phase which is rich in solvent [39]. In general drying membranes using higher temperature can leads to shrinkage of the surface pore size, and as cellulose acetate membranes demonstrates low resistance to shrinkage it was important to optimize the drying step.

The silicate nano-fillers used had an impact on accelerating the drying process while avoiding shrinkage and deterioration of matrices; Drying was accomplished at 25 °C overnight with final residual solvent less than 10%. It is believed that by introducing SiO₂ nanoparticles, they acted as a surface modifying molecules that optimized the evaporation rate at optimum room temperature within shorter period of time, forming more graded pore sub-layer structure with higher porosity which resulted in an enhanced removal of residual solvent and higher permeation rate through matrices that affected the final behavior of the constructed biosensor [38, 40, 41].

CONCLUSIONS

The paper demonstrates enhanced protocol for construction of hybrid matrices based on sol-gel technology; with optimized addition of prepared SiO₂ particles of precise size in the nano-range at an addition rate of 3% W/W. Immobilized HRP was used as biocatalyst for detection of phenol in presence of hydrogen peroxide. Spectrophotometric analysis was carried out in phosphate buffer (pH 6.0) in the presence of hydrogen peroxide. Results showed that immobilized HRP responds rapidly to changes in substrate addition while having a wide range of detection in our experiments from 0.1 mM till 0.002 M. The resulted signals obtained were proportional to the substrate concentration in samples. Different parameters like pH and temperature were discussed. The stability of immobilized HRP was also demonstrated, about 80% of the initial enzyme activity was retained after 10 successive cycles of application and about 85% of the initial activity 60 days after enzyme immobilization compared to the free HRP that retained about 10–15% after this period. Relative activity for TMOS/CAB/PAMAM (A) and TMOS/CAB/PAMAM (B) were 94% and 90% respectively. The constructed system based on the

optimized co-immobilization of HRP demonstrated enhanced operational potential towards further construction of immunosensor.

Acknowledgements: The presented work is supported by ERASMUS MUNDUS MEDASTAR project.

REFERENCES

1. A. Erdemi, A. Pabuccuoglu, B. Meric, K. Kerman, M. Ozsoz, *Turk. J. Med. Sc.*, 349 (2000).
2. J. Yu, H. Ju, *Electroanalysis*, **16**, 1305 (2003).
3. J. Abdullah, M. Ahmad, Y. L. Heng, N. Karuppiah, H. Sidek, *Talanta*, **70**, 527 (2006).
4. M. Ozsoz and J. Wang, *Electroanalysis*, **3**, 655 (1991).
5. M. V. Deshpande and E. A. Hall, *Biosens. Bioelectron.*, **5**, 431 (1990).
6. A. Erdem, N. Altinine, Kilinç E, Gokgunec L, Dalbasti T, Ozsoz, *Pharmaceutical Society of Ankara.*, **23**, 1 (1998).
7. M. Ozsoz, A. Erdem, E. Kilinc and L. Gokgunec, *Electroanalysis*, **8**, 147 (1996).
8. E. Kilinc, A. Erdem, L. Gokgunec, T. Dalbast, M. A. Karaoglan, M. Ozsoz, *Electroanalysis* **10**, 273 (1998).
9. C. Apetrei, M. L. Mendez -Rodríguez, J. A. De Saja, *Electrochim. Acta*, **56**, 8919 (2011).
10. De Quan, Y. Kim, W. Shin, *Bull. Korean chem. Soc.*, **25**, 1195 (2004).
11. P. R. Coulet, *Marcel Dekker Inc. New York, Basel, Hong Kong*, 1 (1991).
12. K. Ajeet, K. Sunil, V. Abhay, B. Shekhar, *Open Journal of Applied Biosensor*, **2**, 1 (2013).
13. J. M. Banuls, R. Puchades, A. Maquieira, *Analitica Chimica Acta*, **777**, 1 (2013).
14. K. Jungbae, W. G. Jay, W. Ping, *Chemical Engineering Science*, **61**, 1017 (2006).
15. L. Yotova, S. Yaneva, D. Marinkova, S. Serfaty, *Biotechnology & Biotechnological Equipment*, **27**(3), 3885 (2013).
16. J. Yangyang, G. Chen, X. Hansong, M. Iram, L. Chunzhao, L. Huizhou, *Journal of Molecular Catalysis B: Enzymatic*, **58**, 103 (2009).
17. L. Xianqiao, X. Jianmin, G. Yueping, S. Guobin, L. Huizhou, *Physicochem. Eng. Aspects*, **238**, 127 (2004).
18. P. D. Sánchez, A. J. M. Ordieres, A. C. García and P. T. Blanco, *Electroanalysis*, **3**, 281 (1991).
19. U. Wollenberger, J. Wang, M. Ozsoz, E. Gonzalez-Romero, F. Scheller, *Bioelectrochem and Bioenergetics*, **26**, 287 (1991).
20. P. Buddhalee, M. Amatatongchai, *Int. J. Electrochem. Sci.*, **8**, 10250 (2013).
21. O. Ryan, M. R. Smyth, C. O. Fágáin, *Essays in Biochemistry*, **28**, 129 (1994).
22. S. Yaneva, D. Marinkova, L. Yotova, B. Samuneva, *Bioautomation*, **8**, 172 (2007).
23. M. Teramoto, S. Kitada, N. Ohnishi, H. Matsuyama and N. Matsumiya, *Journal of Membrane Science*, **234**, 83 (2004).

24. O. Zaborsky, R. Ogletree, *Biochem. Bioph. Res. Co.*, **61**, 210 (1974).
25. M. Trevan, *Immobilized Enzymes. An Introduction and Applications in Biotechnology*, (Trevan, M., ed.), Wiley, Chichester-New York, 1980, p. 1.
26. O. H. Lowry, N. J. Rosebrough, A. L. Farr, R. J. Randall, *J. Biol. Chem.*, **193**, 265 (1951).
27. P. Brodelius and K. Mosbach, in: *Methods in Enzymology*, **135**, Academic Press, London, 1987, p. 173.
28. J. Lim, S. Ha and J. Lee, *Bull. Korean Chem. Soc.*, **1067** (2012).
29. K. Xie, Y. Yu, Y. Shi, **78**, 799 (2009).
30. R. Gupta, N. K. Chaudhury, *Biosensors and Bioelectronics*, **2387** (2007).
31. C. S. Manuela, J. S. Abilio, J. T. Guthrie, M. H. Gil, *J Mater Sci Mater Med*, **677** (2008).
32. S. L. Boor, K. Victor, H. Raed, H. Nidal, *Desalination*, **326**, 77 (2013).
33. L. Y. Lafreniere, F. D. F. Talbot, T. Matsuura, S. Sourirajan, *Ind. Eng. Chem. Res.*, **26**, 2385 (1987).
34. G. Bayramoglu, A. Akbulut, Y. M. Arica, 2013, *Journal of Hazardous Materials*, **245**, 528 (2013).
35. M. B. Beatriz and B. V. Francisco, *Methods in Biotechnology*, **15** (2006).
36. S. A. Mohamed, S. A. Aly, T. M. Mohamed, H. A. Salah, *Appl. Biochem. Biotechnol.*, **144**, 169 (2008).
37. H. Yin, S. Ai, W. Sha, L. Zhu, *Sensor. Actuator. B-chem.*, **137**, 747 (2009).
38. R. K. Arya, *International Journal of Scientific & Technology Research*, **1**, 48 (2012).
39. T. H. Young, J. H. Huang, W. Y. Chuang, *European Polymer Journal*, **38**, 63 (2002).
40. B. S. Laliaa, V. Kochkodanb, R. Hashaikeha, N. Hilala, *Desalination*, **326**, 77 (2013).
41. L. Y. Lafreniere, F. D. F. Talbot, T. Matsuura, S. Sourirajan, *In d.Eng. Chem. Res.*, **26**, 2385 (1987).

ДИЗАЙН НА ОПТИЧНИ БИО-СЕНЗОРИ ЗА ОТКРИВАНЕ НА ФАРМАЦЕВТИЧНИ ПРОДУКТИ

А. Хасан^{1*}, С. Янева², Л. Йотова¹

¹ Химикотехнологичен и металургичен университет, Катедра по биотехнологии,
бул. „Кл. Охридски“ 8, 1756 София, България

² Химикотехнологичен и металургичен университет, катедра Основи на химичните
технологии, бул. „Кл. Охридски“ 8, 1756 София, България

Постъпила декември, 2014 г.; приета януари, 2015 г.

(Резюме)

„Зол-гел“ синтезът бързо се превърна в завладяваща нова област на изследвания за науката за материалите. Използването на органични молекули в процеса на образуване на гел, може да повлияе на размерите на порите, което представлява друг начин за увеличаване на активността на мобилизирания ензим.

Целта на тази работа е дизайнът на оптични био-сензори за откриване на фармацевтични продукти. Чрез зол-гел методи синтезирахме хибридни матрици, съдържащи силициев диоксид, целулозни производни и поли (амидо/амин) дендримери (РАМАМ), като перспективен носители за ковалентна имобилизация. Пероксидазата от *Armoracia rusticana* (HRP) бе използвана като моделен ензим. Условиата, които бяха оптимизирани и за които бе определен максимален ефект, са: кинетичните параметри, рН и температурата. Получените био-сензори бяха използвани за детекция на резорцин, pirogallol, епинефрин и т.н. Такива биосензори имат потенциално приложение в медицинската, фармацевтичната, хранителната сфера и за мониторинг на околната среда.

BULGARIAN CHEMICAL COMMUNICATIONS

Instructions about Preparation of Manuscripts

General remarks: Manuscripts are submitted in English by e-mail or by mail (in duplicate). The text must be typed double-spaced, on A4 format paper using Times New Roman font size 12, normal character spacing. The manuscript should not exceed 15 pages (about 3500 words), including photographs, tables, drawings, formulae, etc. Authors are requested to use margins of 3 cm on all sides. For mail submission hard copies, made by a clearly legible duplication process, are requested. Manuscripts should be subdivided into labelled sections, e.g. **Introduction, Experimental, Results and Discussion, etc.**

The **title page** comprises headline, author's names and affiliations, abstract and key words.

Attention is drawn to the following:

a) **The title** of the manuscript should reflect concisely the purpose and findings of the work. Abbreviations, symbols, chemical formulas, references and footnotes should be avoided. If indispensable, abbreviations and formulas should be given in parentheses immediately after the respective full form.

b) **The author's** first and middle name initials, and family name in full should be given, followed by the address (or addresses) of the contributing laboratory (laboratories). **The affiliation** of the author(s) should be listed in detail (no abbreviations!). The author to whom correspondence and/or inquiries should be sent should be indicated by asterisk (*).

The abstract should be self-explanatory and intelligible without any references to the text and containing not more than 250 words. It should be followed by key words (not more than six).

References should be numbered sequentially in the order, in which they are cited in the text. The numbers in the text should be enclosed in brackets [2], [5, 6], [9–12], etc., set on the text line. References, typed with double spacing, are to be listed in numerical order on a separate sheet. All references are to be given in Latin letters. The names of the authors are given without inversion. Titles of journals must be abbreviated according to Chemical Abstracts and given in italics, the volume is typed in bold, the initial page is given and the year in parentheses. Attention is drawn to the following conventions:

a) The names of all authors of a certain publications should be given. The use of “*et al.*” in the list of references is not acceptable.

b) Only the initials of the first and middle names should be given.

In the manuscripts, the reference to author(s) of cited works should be made without giving initials, e.g. “Bush and Smith [7] pioneered...”. If the reference carries the names of three or more authors it should be quoted as “Bush *et al.* [7]”, if Bush is the first author, or as “Bush and co-workers [7]”, if Bush is the senior author.

Footnotes should be reduced to a minimum. Each footnote should be typed double-spaced at the bottom of the page, on which its subject is first mentioned.

Tables are numbered with Arabic numerals on the left-hand top. Each table should be referred to in the text. Column headings should be as short as possible but they must define units unambiguously. The units are to be separated from the preceding symbols by a comma or brackets.

Note: The following format should be used when figures, equations, *etc.* are referred to the text (followed by the respective numbers): Fig., Eqns., Table, Scheme.

Schemes and figures. Each manuscript (hard copy) should contain or be accompanied by the respective illustrative material as well as by the respective figure captions in a separate file (sheet). As far as presentation of units is concerned, SI units are to be used. However, some non-SI units are also acceptable, such as °C, ml, l, etc.

The author(s) name(s), the title of the manuscript, the number of drawings, photographs, diagrams, etc., should be written in black pencil on the back of the illustrative material (hard copies) in accordance with the list enclosed. Avoid using more than 6 (12 for reviews, respectively) figures in the manuscript. Since most of the illustrative materials are to be presented as 8-cm wide pictures, attention should be paid that all axis titles, numerals, legend(s) and texts are legible.

The authors are asked to submit **the final text** (after the manuscript has been accepted for publication) in electronic form either by e-mail or mail

on a 3.5" diskette (CD) using a PC Word-processor. The main text, list of references, tables and figure captions should be saved in separate files (as *.rtf or *.doc) with clearly identifiable file names. It is essential that the name and version of the word-processing program and the format of the text files is clearly indicated. It is recommended that the pictures are presented in *.tif, *.jpg, *.cdr or *.bmp format, the equations are written using "Equation

Editor" and chemical reaction schemes are written using ISIS Draw or ChemDraw programme.

The authors are required to submit the final text with a list **three individuals and their e-mail addresses** that can be considered by the Editors as potential reviewers. Please, note that the reviewers should be outside the authors' own institution or organization. The Editorial Board of the journal is not obliged to accept these proposals.

EXAMPLES FOR PRESENTATION OF REFERENCES

REFERENCES

1. D. S. Newsome, *Catal. Rev.-Sci. Eng.*, **21**, 275 (1980).
2. C.-H. Lin, C.-Y. Hsu, *J. Chem. Soc. Chem. Commun.*, 1479 (1992).
3. R. G. Parr, W. Yang, *Density Functional Theory of Atoms and Molecules*, Oxford Univ. Press, New York, 1989.
4. V. Ponec, G. C. Bond, *Catalysis by Metals and Alloys (Stud. Surf. Sci. Catal., vol. 95)*, Elsevier, Amsterdam, 1995.
5. G. Kadinov, S. Todorova, A. Palazov, in: *New Frontiers in Catalysis (Proc. 10th Int. Congr. Catal., Budapest, 1992)*, L. Gucci, F. Solymosi, P. Tetenyi (eds.), Akademiai Kiado, Budapest, 1993, Part C, p. 2817.
6. G. L. C. Maire, F. Garin, in: *Catalysis. Science and Technology*, J. R. Anderson, M. Boudart (eds), vol. 6, Springer-Verlag, Berlin, 1984, p. 161.
7. D. Pocknell, *GB Patent 2 207 355* (1949).
8. G. Angelov, PhD Thesis, UCTM, Sofia, 2001.
9. JCPDS International Center for Diffraction Data, *Power Diffraction File*, Swarthmore, PA, 1991.
10. *CA* **127**, 184 762, (1998).
11. P. Hou, H. Wise, *J. Catal.*, in press.
12. M. Sinev, private communication.
13. <http://www.chemweb.com/alchem/articles/1051611477211.html>.

CONTENTS

80 th Anniversary for Prof. Ivan Schopov, DSc	5
<i>M. H. Moemeni, M. A. Amrollahi, F. Tamaddon</i> , A facile catalyst-free Knoevenagel condensation of pyridinecarbaldehydes and active methylene compounds	7
<i>R. Venkata Nadh, M. Sireesha</i> , Kinetics and mechanism of Ru (III) catalysed and uncatalysed oxidation of DL-alanine by N-bromosuccinimide	13
<i>H. Zhang, H. Xue, J. Yang, L. Liang</i> , Determination of complex 12-grade phytic acid dissociation constants	22
<i>S. Hina, M. Mustafa, T. Hayat</i> , On the exact solution for peristaltic flow of couple-stress fluid with wall properties	30
<i>J. Mladenović, A. Radovanović, R. Pavlović, B. Radovanović, J. Zdravković, G. Aćamović-Doković</i> , Cytotoxicity, antimicrobial and antioxidant activity of <i>Daucus carota</i> L., <i>Lycopersicon esculentum</i> Mill. and <i>Capsicum annum</i> L.	38
<i>R. A. Girchev, P. P. Markova, P. T. Todorov, E. D. Naydenova</i> , Sympathovagal balance after application of N-modified nociceptin analogues	45
<i>S. Murugavel, D. Lakshmanan, Sangaraiah Nagarajan, Alagusundaram Ponnuswamy</i> , Synthesis and crystal structure of 6-(1-benzyl-5-methyl-1H-1,2,3-triazol-4-yl)-4-(2-methoxyphenyl)-3,4-dihydropyrimidine-2(1H)-thione activity	50
<i>G. Mohammadi Ziarani, M. Shakiba Nahad, N. Lashgari</i> , Green synthesis of 2-substituted benzothiazole derivatives under solvent-free conditions	55
<i>H. R. Pourtedal, F. Momenzadeh</i> , Synthesis, characterization and study of photocatalytic activity of nanocomposites of oxides and sulfides of Ni(II) and Ni(III)	59
<i>G. S. Seth, S. Sarkar</i> , Hydromagnetic natural convection flow with induced magnetic field and n th order chemical reaction of a heat absorbing fluid past an impulsively moving vertical plate with ramped temperature	66
<i>S. N. Mousavi-Kani, A. Bahari, Z. Moradinedjad</i> , Synthesis and characterization of nanohybrid lanthanum oxide doped with polystyrene in electronic devices	80
<i>J. Petkova, K. Nikolova, D. Boyadzhiev, A. Aladjadjian, G. Antova</i> , Statistical analysis of seed oils from melon and pumpkin by using colour parameters	85
<i>A. Morsali, Z. Alavi, S. A. Beyramabadi</i> , Evaluation of thermodynamic properties of long-chain organic compounds using GMA equation of state	89
<i>Z. Czech, A. Kowalczyk, P. Ragańska, A. Antosik</i> , Polymerization shrinkage of UV curable dental composites containing multifunctional methacrylates	94
<i>A. Farhadi, T. Hamoule, M. Ali Takassi, T. Arizavipour</i> , Catalytic synthesis of 1,4-dihydropyridine derivatives using hexagonal mesoporous silicate (HMS)	101
<i>M. Zaky, M. Y. El-Sayed, S. M. El-Megharbel, S. A. Taleb, M.S. Refat</i> , Synthesis, chemical structures elucidation and biological studies on the effect of some vital metal ions on vitamin A: Ca(II), Mg(II), Zn(II), Fe(III) and VO(II) complexes	105
<i>M. Hajjami, A. Ghorbani-Choghamarani, F. Gholamian</i> , Multicomponent synthesis of bioactive 1-amidoalkyl-2-naphtols under solvent-free conditions	119
<i>F. Shakeel, F. K. Alanazi, I. A. Alsarra, N. Haq</i> , Solution thermodynamics and solubility of indomethacin in ethanol-water mixtures in the temperature range from 293.15 to 318.15 K	125
<i>A. Z. Mirza, F. A. Siddiqui</i> , New, simple and validated UV-spectrophotometric methods for the estimation of pyridoxine hydrochloride in bulk and formulation	131
<i>K. Abu-Shandi, A. R. Halawah, AlSayed Sallam, Gh. Al-Edwan, A. R. Al-Tawaha, Sh. A. Albajawi, E. S. M. Abu-Nameh</i> , Simultaneous analysis of glycyrrhizic acid and preservatives in licorice aqueous extract by HPLC/PDA detection	135
<i>Y. Karakirova, N. Yordanov</i> , Mannitol as a radiation sensitive material for electron paramagnetic resonance dosimetry	144

M. Kazemi, Phenolic profile, antimicrobial and anti-inflammatory activity of <i>Carum copticum</i> L. essential oil	149
A. Jafari, A. Ramazani, M. Rouhani, Efficient one-pot synthesis of substituted propanamide derivatives by a three-component reaction of 2-oxopropyl benzoate, 1,1,3,3-tetramethylbutyl isocyanide and aromatic carboxylic acids in water	156
M. B. Miric, R. S. Peric, S. P. Dimitrijevic, S. A. Mladenovic, S. R. Marjanovic, Differences in the mode of thermomechanical processing between white gold alloys to produce semi-finished products.....	161
J. G. Ivanova, L. V. Kabaivanova, P. D. Petrov, S. N. Yankova, Optimization strategies for improved growth, polysaccharide production and storage of the red microalga <i>Rhodella reticulat</i>	167
M. Awais, H. Shafeek, Low cost fabrication of tandem dye-sensitized solar cells	175
<i>Proceedings of the Vth National Crystallographic Symposium – Preface</i>	183
B. Donkova, V. Petkova, Comparison of thermal behaviour of γ -MnC ₂ O ₄ ·2H ₂ O in oxidative and inert media	185
K. I. Milenova, A. E. Eliyas, V. N. Blaskov, I. A. Avramova, I. D. Stambolova, S. V. Vassilev, P. M. Nikolov, N. A. Kassabova, S. K. Rakovsky, Comparative study of ZnO photocatalyst samples prepared by different methods.....	190
R. I. Petkov, R. Vl. Gavrilova, L. P. Atanasov, Investigation of the possibility to increase the mechanical properties of ferritic nodular cast iron.....	197
L. Tsvetanova, N. Petrova, S. Ferdov, V. Kostov-Kytin, R. Nikolova, Crystal structure of Ag ⁺ exchanged ETS-4 at room temperature and 150 K	201
A. A. Petrova, S. M. Angelova, I. A. Nikolchina, R. I. Russev, V. B. Kurteva, B. L. Shivachev, R. P. Nikolova, Novel 13-membered cyclic dioxatetraaza scaffolds – synthesis, solution and solid state characterization	208
A. K. Stoyanova-Ivanova, S. D. Terzieva, G. D. Ivanova, M. A. Mladenov, D. G. Kovacheva, R. G. Raicheff, S. I. Georgieva, B. S. Blagoev, A. J. Zaleski, V. Mikli, The use of high-temperature superconducting cuprate as a dopant to the negative electrode in Ni-Zn batteries	221
V. I. Petrunov, L. S. Andreeva, S. I. Karatodorov, V. I. Mihailov, S. D. Terzieva, I. Ilievska, A. K. Stoyanova-Ivanova, V. G. Tumbalev, V. Mikli, Analysis of elemental composition of a heat activated, multi-force, nickel titanium orthodontic archwire	229
V. G. Petrov, S. D. Terzieva, V. G. Tumbalev, V. Mikli, L. S. Andreeva, A. K. Stoyanova-Ivanova, Influence of the treatment period on the morphology and the chemical composition of the thermally activated orthodontic archwires.....	234
Y. I. Kouzmanova, I. V. Dimitrova, G. D. Gentscheva, L. I. Aleksandrov, M. G. Markova-Velichkova, D. G. Kovacheva, Comparative study of the phase formation and interaction with water of calcium-silicate cements with dental applications	239
S. Dimitrovska-Lazova, S. Aleksovska, P. Tzvetkov, V. Mirčeski, D. Kovacheva, Influence of Y-ion substitution on structural and electrochemical characteristics of YCo _{0.5} Fe _{0.5} O ₃	245
I. K. Mihailova, L. Radev, V. A. Aleksandrova, I. V. Colova, I. M. M. Salvado, M. H. V. Fernandes, Novel merwinite/akermanite ceramics: <i>in vitro</i> bioactivity	253
K. L. Zaharieva, Z. P. Cherkezova-Zheleva, B. N. Kunev, I. G. Mitov, S. S. Dimova, Impact of chemical composition on preparation of nanodimensional spinel ferrites	261
E. V. Todorova, G. E. Chernev, St. P. Djambazov, Synthesis and characterization of silica hybrid materials applicable for defect remediation of concrete	268
M. Abdallah, N. Velikova, Y. Ivanova, Y. Dimitriev, Synthesis and characterization of poly sulfide-functionalized hybrid mesoporous silica.....	276
T. S. Tsoncheva, I. G. Genova, N. Scotti, M. D. Dimitrov, A. Gallo, D. G. Kovacheva, N. Ravasio, Silica supported copper and cobalt oxide catalysts for methanol decomposition: Effect of preparation procedure	283
A. Shalaby, D. Nihtianova, P. Markov, A. D. Staneva, R. S. Iordanova, Y. B. Dimitriev, Structural analysis of reduced graphene oxide by transmission electron microscopy	291

<i>I. G. Dakova, V. A. Dakov, M. Karadjov, I. B. Karadjova</i> , Cu(II)-imprinted copolymer microparticles: effect of the porogen solvents on particle size, morphology and sorption efficiency	296
<i>L. Djerahov, P. Vasileva, I. Karadjova, I. Dakova, R. M. Kurakalva</i> , Silver nanoparticles embedded in biocompatible polymers: extraction efficiency toward metals.....	303
<i>V. M. Dyulgerov, L. T. Dimowa, K. Kossev, R. P. Nikolova, B. L. Shivachev</i> , Solvothermal synthesis of theophylline and <i>N,N'</i> -(ethane-1,2-diyl)diformamide co-crystals from DMF decomposition and N-formylation through catalytic effect of 3-carboxyphenylboronic acid and cadmium acetate.....	311
<i>N. G. Kostova, M. Achimovičová, A. Eliyas, N. Velinov, V. Blaskov, I. Stambolova, E. Gock</i> , TiO ₂ obtained from mechanically activated ilmenite and its photocatalytic properties	317
<i>M. D. Dimitrov, R. N. Ivanova, V. Štengl, J. Henych, D. G. Kovacheva, T. S. Tsoncheva</i> , Optimization of CeO ₂ -ZrO ₂ mixed oxide catalysts for ethyl acetate combustion	323
<i>A. M. Stoyanova, N. K. Ivanova, A. D. Bachvarova-Nedelcheva, R. S. Iordanova</i> , Synthesis and photocatalytic performance of Fe (III), N co-doped TiO ₂ nanoparticles.....	330
<i>K. I. Milenova, A. E. Eliyas, V. N. Blaskov, I. A. Avramova, I. D. Stambolova, Y. G. Karakirova, S. V. Vassilev, P. M. Nikolov, N. A. Kasabova, S. K. Rakovsky</i> , Copper doped zinc oxide nanopowders used for degradation of residual azo dyes in wastewaters	336
<i>K. L. Zaharieva, K. I. Milenova, Z. P. Cherkezova-Zheleva, S. S. Dimova, B. N. Kunev, A. E. Eliyas, I. G. Mitov, I. D. Stambolova, V. N. Blaskov</i> , Effect of the duration of mechanochemical treatment on the photocatalytic activity under UV light irradiation of nano-sized zinc oxide synthesized by precipitation.....	342
<i>K. V. Koleva, N. I. Velinov, T. S. Tsoncheva, I. G. Mitov</i> , Preparation, structure and catalytic properties of copper-zinc ferrites	348
<i>M. P. Tsvetkov, K. L. Zaharieva, Z. P. Cherkezova-Zheleva, M. M. Milanova, I. G. Mitov</i> , Photocatalytic activity of nanostructure zinc ferrite-type catalysts in degradation of Malachite green under UV-light.....	354
<i>L. Dimowa, I. Piroeva, S. Atanasova-Vladimirova, B. Shivachev, S. Petrov</i> , Compositional and structural study of partially exchanged on Na ⁺ , K ⁺ , Mg ²⁺ and Ca ²⁺ natural heulandite.....	360
<i>T. I. Apostolova</i> , Intensity and SAR dependent changes in conformation of frog skeletal muscle total protein content after irradiation with 2.45 GHz electromagnetic field	368
<i>R. D. Gegova, A. D. Bachvarova-Nedelcheva, R. S. Iordanova, Y. B. Dimitriev</i> , Synthesis and crystallization of gels in the TiO ₂ -TeO ₂ -ZnO system.....	378
<i>A. Yoleva, S. Djambazov, P. Djambazov</i> , Study of medieval ceramics excavated at the monastery of Karaachteke (Varna, Bulgaria)	387
<i>N. Kaneva, A. Bojinova, K. Papazova, D. Dimitrov, I. Svinjarov, M. Bogdanov</i> , Effect of thickness on the photocatalytic properties of ZnO thin films	395
<i>N. Kaneva, A. Bojinova, K. Papazova, D. Dimitrov</i> , Sol aging effect on the structure and photocatalytic action of ZnO films for pharmaceutical drugs degradation	402
<i>T. D. Todorova, Yu. A. Kalvachev</i> , Seed-mediated approach to size-controlled synthesis of a mordenite type zeolite from organic template free initial gel	409
<i>G. Patronov, I. Kostova, D. Tonchev</i> , Influence of the content of samarium on the structure and the optical properties of zinc borophosphate materials.....	417
<i>S. Zh. Todorova, Z. P. Cherkezova-Zheleva, I. D. Yordanova, A. Ganguly, H. G. Kolev, S. Mondal, M. G. Shopska, K. K. Tenchev, N. I. Velinov, A. K. Ganguli, G. B. Kadinov</i> , Nano-sized iron oxide with controlled size modified with Pd for purification processes.....	424
<i>P. Petkova, K. Boubaker, P. Vasilev, M. Mustafa, T. Larbi</i> , Urbach's rule of Ni doped Mn ₃ O ₄ thin films.....	431
<i>D. Marinkova, M. Michel, R. Raykova, D. Danalev, S. Yaneva, L. Yotova, P. Griesmar</i> , Investigation on the proliferation of Gram negative bacterial cells onto sol-gel carriers	436
<i>A. Hassaan, S. Yaneva, L. Yotova</i> , Design of optical biosensors for detection of pharmaceutical products	445
INSTRUCTIONS TO THE AUTHORS	452

СЪДЪРЖАНИЕ

<i>М. Х. Моемени, М. А. Амротахи, Ф. Тамадон</i> , Проста Knoevenagel'ова кондензация на пиридин-карбалдехиди и активни метиленови съединения без катализатор	12
<i>Р. Венката Надх, М. Сирееша</i> , Кинетика и механизъм на окислението на DL-аланин с N-бромосукцинимид с и без рутениев Ru (III)-катализатор	21
<i>Х. Жанг, Х. Ксюе, Дж. Янг, Л. Лианг</i> , Определяне на сложна, дванадесестепенна дисоциационна константа на фитинова киселина	29
<i>С. Хина, М. Мустафа, Т. Хаят</i> , Относно точното решение за перисталтично течение на флуид със спрегнати напрежения и променливи свойства на стената	37
<i>Дж. Младенович, А. Радованович, Р. Павлович, Б. Радованович, Дж. Здравкович, Г. Ачанович-Джокович</i> , Цитотоксичност, антимиembroно и антиоксидантно действие на <i>Daucus carota</i> L., <i>Lycopersicon esculentum</i> Mill. and <i>Capsicum annuum</i> L.	44
<i>Р. А. Гърчев, П. П. Маркова, П. Т. Тодоров, Е. Д. Найденова</i> , Симпатико-вагусов баланс след приложение на N-модифицирани ноцицептинови аналози	49
<i>С. Муругавел, Д. Лакшманан, С. Нагараджан, А. Понусвами</i> , Синтез и кристална структура на 6-(1-бензил-5-метил-1H-1, 2, 3-триазол-4-ил)-4-(2-метоксифенил)-3,4-дихидропиримидин-2 (1H) - тион	54
<i>Г. Мохамеди Зиарани, М. Шакива Нахад, Н. Лаишгари</i> , Зелена синтеза на 2-субституирани производни на бензотшозгла в отсъствие на разтворител	58
<i>Х. Р. Пуретедал, Ф. Момензаде</i> , Синтеза, охарактеризиране и изследване на фотокаталитичната активност на нанокompозити от окиси и сулфиди на Ni(II) и Ni(III)	65
<i>Г. С. Сет, С. Саркар</i> , Течение с естествена конвекция в индуцирано магнитно поле и химична реакция от n-ти порядък, съпроводена с поглъщане на топлина от движеща се плоскост с температурен профил	79
<i>С. Н. Мусави-Кани, А. Бахари, З. Морадинеджад</i> , Синтеза и охарактеризиране на нанохибриден лантанов оксид дотиран с полистирен за електронни уреди	84
<i>Ж. Петкова, Кр. Николова, Д. Бояджиев, А. Аладжаджиян, Г. Антова, Д. Бухалова, Ил. Томова, Й. Алексиева</i> , Математико статистическо моделиране по цветови параметри на нетрадиционни масла от семе на пьпеш и тиква	88
<i>А. Морсали, З. Алави, С. А. Бейрамабади</i> , Оценка на термодинамичните свойства на органични съединения с дълги вериги, посредством GMA уравнение на състоянието	93
<i>З. Чех, А. Ковалчик, П. Раганска, А. Антошик</i> , Полимеризационно свиване на UV-катализирани зъбни композити, съдържащи многофункционални метакрилати	100
<i>А. Фархади, Т. Хамуле, М. А. Такаси, Т. Аризавитур</i> , Каталитична синтеза на 1,4 дихидропиридинови производни, използвайки хексагонален мезопорест силикат (HMS)	104
<i>М. Заки, М. И. Ел-Сауд, С. М. Ел-Мегарбел, С. Або Талеб, М. С. Рефат</i> , Синтез, изясняване на химичните структури и биологични изследвания върху ефекта на някои важни метални йони на витамин А: Ca (II), Mg (II), Zn (II), Fe(III) и VO(II) комплекси	118
<i>М. Хаджеджиами, А. Горбани-Чогамарани, Ф. Голамиан</i> , Многокомпонентна система на биоактивни 1-амидоалкил-2-нафтоли в отсъствие на разтворител	124
<i>Ф. Шакийл, Ф.К. Аланази, И.А. Алсарра, Н. Хак</i> , Термодинамика и разтворимост на индометацин в водно-етанолови смеси в температурния интервал от 293.15 до 318.15 K	130
<i>А. З. Мирза, Ф. А. Сидикуи</i> , Нови, прости и валидирани UV-спектрофотометрични методи за определяне на пиридоксин хидрохлорид в разтвори и препарати	134
<i>Х. Абу-Шанди, А. Р. Халауа, А. С. Салам, Г. Ал-Едуан, А. Р. Ал-Тауаха, Ш. А. Албаджауи, Е. С. М. Абу-Намех</i> , Едновременен анализ на глицирова киселина и консерванти във водни екстракти от женско биле чрез HPLC/PDA	143

Й. Каракирова, Н. Йорданов, Манитол като радиационно чувствителен материал за дозиметрия с електрон парамагнитен резонанс	148
М. Каземи, Химичен състав, антимикробно и противо-възпалително действие на етерично масло от <i>Carum copticum</i> L.	155
А. Джафари, А. Рамазани, М. Рухани, Ефективна едностадийна синтеза на заместени пропанамидни производни чрез трикомпонентна реакция на 2-оксопропилов бензоат, 1,1,3,3-тетраметилбутил изоцианид и ароматни карбоксилни киселини във вода	160
М. В. Мирич, Р. С. Перич, С. П. Димитриевич, С. А. Младенович, С. Р. Марджанович, Разлики в начина на термомеханическа преработка между сплави на бяло злато за производство на полуготови продукти.....	166
Ю. Г. Иванова, Л. В. Кабаиванова, П. Д. Петров, С. Н. Янкова, Стратегии за оптимизация и увеличаване на растежа, продукцията на полизахарид и съхранение на червеното водорасло <i>Rhodella reticulata</i>	174
М. Аваис, Х. Шафиш, Евтина изработка на тандемни цветно-чувствителни слънчеви батерии	180
Пети национален кристалографски симпозиум – Предговор.....	183
Б. Донкова, В. Петкова, Съпоставяне на термичното поведение на γ - $MnC_2O_4 \cdot 2H_2O$ в окислителна и инертна атмосфера	189
К. И. Миленова, А. Е. Елияс, В. Н. Блъсков, И. А. Аврамова, И. Д. Стамболова, С. В. Василев, П. М. Николов, Н. А. Касабова, С. К. Раковски, Сравнително изследване на ZnO фотокатализаторни проби, получени по различен начин	186
Р. И. Петков, Р. Вл. Гаврилова, Л. И. Атанасов, Изследване възможността за повишаване на механичните показатели на феритен сферографитен чугун	200
Л. Цветанова, Н. Петрова, С. Фердов, В. Костов-Китин, Р. Николова, Кристална структура на Ag^+ йонообменени монокристали на ETS-4 при стайна (290 K) и ниска (150 K) температура.....	207
А. А. Петрова, С. М. Ангелова, И. А. Николчина, Р. И. Русев, В. Б. Куртева, Б. Л. Шивачев, Р. Н. Петрова, Нови 13-членни циклични диоксатетрааза платформи – синтез и охарактеризиране в разтвор и твърдо състояние.....	220
А. К. Стоянова-Иванова, С. Д. Терзиева, Г. Д. Иванова, М. А. Младенов, Д. Г. Ковачева, Р. Г. Райчев, С. И. Георгиева, Б. С. Благоев, А. J. Zaleski, V. Mikli, Приложение на високотемпературни свръхпроводими купрати като добавка към отрицателния електрод в Ni-Zn батерии.....	228
В. Г. Петрунов, Л. С. Андреева, С. И. Каратодоров, В. И. Михайлов, С. Д. Терзиева, И. Илиева, А. К. Стоянова-Иванова, В. Г. Тумбалева, В. Микли, Изследване на термоактивираща никел-титанова ортодонтска дъга с диференцирано освобождаване на сила	233
В. Г. Петров, С. Д. Терзиева, В. Г. Тумбалева, В. Микли, Л. С. Андреева, А. К. Стоянова-Иванова, Влияние на времето на престой в устата на пациента върху морфологията и химичния състав на мед-никел-титановите ортодонтски дъги.....	238
Я. И. Кузманова, И. В. Димитрова, Г. Д. Генчева, Л. И. Александров, М. Г. Маркова-Величкова, Д. Г. Ковачева, Сравнително изследване на фазообразуването и взаимодействието с вода на калциево-силикатни цименти с приложение в денталната медицина.....	244
С. Димитровска-Лазова, С. Алексовска, П. Цветков, В. Мирчески, Д. Ковачева, Влияние на заместването на Y-йони върху структурните и електрохимични характеристики на $YCo_{0.5}Fe_{0.5}O_3$	252
И. К. Михайлова, Л. Радев, В. А. Александрова, И. В. Цолова, И. М. М. Салвадо, М. Х. В. Фернандес, Нова мервинит/акерманитова керамика: <i>in vitro</i> биоактивност	260
К. Л. Захариева, З. П. Черкезова-Желева, Б. Н. Кунев, И. Г. Митов, С. С. Димова, Влияние на химичния състав върху получаването на наноразмерни шпинелни ферити	267
Е. В. Тодорова, Г. Е. Чернев, Ст. П. Джамбазов, Синтез и охарактеризиране на силикатни хибридни материали, приложими за отстраняване на бетонни дефекти	275

<i>М. Абдала, Н. Великова, Й. Иванова, Ян. Димитриев</i> , Синтез и характеризиране на полисулфид функционализирани хибридни мезопорести силициево-диоксидни материали.....	282
<i>Т. С. Цончева, И. Г. Генова, Н. Скоти, М. Д. Димитров, А. Гало, Д. Г. Ковачева, Н. Равазио</i> , Мед и кобалт модифицирани силициевооксидни катализатори за разлагане на метанол: Влияние на метода на получаване	290
<i>А. Шалаби, Д. Нихтянова, П. Марков, А. Д. Станева, Р. С. Йорданова, Я. Б. Димитриев</i> , Структурен анализ на редуциран графенов оксид чрез трансмисионна електронна микроскопия	295
<i>И. Г. Дакова, В. А. Даков, М. Караджов, И. Б. Караджова</i> , Cu(II)-отпечатани съполимерни микрочастици: влияние на разтворителя върху размера и морфологията на частиците и сорбционната им ефективност	302
<i>Л. Джерахов, П. Василева, И. Караджова, И. Дакова, Р. М. Куракалва</i> , Сребърни наночастици, вградени в биосъвместими полимери: екстракционна ефективност спрямо метали	310
<i>В. Дюлгеров, Л. Т. Димова, К. Косев, Р. П. Николова, Б. Шивачев</i> , Солвотермален синтез на съкристали на теофилин и N,N'-(етан-1,2-диил) диформаид чрез разлагане на ДМФ и N-формиране при каталитично действие на 3-carboxyphenylboronic киселина и кадмиев ацетат	316
<i>Н. Г. Костова, М. Ахимовичова, А. Елияс, Н. Велинов, В. Блъсков, И. Стамболова, Е. Гок</i> , TiO ₂ , получен от механично активиран илменит и неговите фотокаталитични свойства	322
<i>М. Д. Димитров, Р. Н. Иванова, В. Штенгъл, И. Хених, Д. Г. Ковачева, Т. С. Цончева</i> , Оптимизиране на смесени CeO ₂ -ZrO ₂ катализатори за изгаряне на етилацетат	329
<i>А. М. Стоянова, Н. К. Иванова, А. Д. Бъчварова-Неделчева, Р. С. Йорданова</i> , Синтез и фотокаталитична активност на Fe (III), N ко-дотирани TiO ₂ наночастици.....	335
<i>К. И. Миленова, А. Е. Елияс, В. Н. Блъсков, И. А. Аврамова, И. Д. Стамболова, С. В. Василев, П. М. Николов, Й. Г. Каракирова, Н. А. Касабова, С. К. Раковски</i> , Цинково оксидни прахове, дотирани с Cu, използвани за разлагане на остатъчни азобагрила в отпадни води	341
<i>К. Л. Захариева, К. И. Миленова, З. П. Черкезова-Желева, С. С. Димова, Б. Н. Кунев, А. Е. Елияс, И. Г. Митов, И. Д. Стамболова, В. Н. Блъсков</i> , Влияние на продължителността на механохимична обработка върху фотокаталитичната активност при облъчване с УВ светлина на наноразмерен цинков оксид, получен чрез утаяване	347
<i>К. В. Колева, Н. И. Велинов, Т. С. Цончева, И. Г. Митов</i> , Получаване, структура и каталитични свойства на мед-цинкови ферити.....	353
<i>М. П. Цветков, К. Л. Захариева, З. П. Черкезова-Желева, М. М. Миланова, И. Г. Митов</i> , Фотокаталитична активност на наноструктурирани цинкови феритен тип катализатори при разграждане на Малахитово зелено под УВ-светлина	359
<i>Л. Димова, И. Пироева, С. Атанасова-Владимирова, Б. Шивачев, С. Петров</i> , Състав и структура на частично обменен на Na ⁺ , K ⁺ , Mg ²⁺ и Ca ²⁺ природен хейландит	367
<i>Т. И. Апостолова</i> , Промени в белтъчната конформация на общ белтък от жабешки скелетен мускул след облъчване с 2.45 GHz електромагнитно поле, в зависимост от интензитета на полето и от погълнатата мощност	377
<i>Р. Д. Гегова, А. Д. Бъчварова-Неделчева, Р. С. Йорданова, Я. Б. Димитриев</i> , Синтез и кристализация на гели в системата TeO ₂ -TiO ₂ -ZnO.....	386
<i>А. Йолева, С. Джамбазов, П. Джамбазов</i> , Изследване на средновековна керамика открита в манастира Караачтеке край Варна, България	394
<i>Н. Кънева, А. Божинова, К. Папазова, Д. Димитров, И. Свињаров, М. Богданов</i> , Ефект на дебелината върху фотокаталитичните свойства на ZnO тънки филми	401
<i>Н. Кънева, А. Божинова, К. Папазова, Д. Димитров</i> , Ефект на стареене на зол върху структурата и фотокаталитичната активност на ZnO филми за разграждане на фармацевтични лекарства	408
<i>Т. Тодорова, Ю. Кълвачев</i> , Контролиране размера на частиците на морденит чрез синтез с използване на зародиши и без органичен темплейт.....	416

<i>Г. И. Патронов, И. П. Костова, Д. Т. Тончев, Влияние на съдържанието на самарий върху структурата и оптичните свойства на цинк-бор-фосфатни материали</i>	<i>423</i>
<i>С. Ж. Тодорова, З. П. Черкезова-Желева, Ил. Д. Йорданова, А. Гангули, Х. Г. Колев, С. Мондал, М. Г. Шопска, К. К. Тенчев, Н. Ив. Велинов, А. К. Гангули, Г. Б. Кадинов, Наноразмерен железен оксид с контролиран размер, модифициран с Pd за процеси на почистване</i>	<i>430</i>
<i>П. Петкова, К. Боубакер, П. Василев, М. Мустафа, Т. Ларби, Правило на Урбах за легирани с никел тънки филми от Mn_3O_4</i>	<i>435</i>
<i>Д. Маринкова, М. Мишел, Р. Райкова, Д. Даналев, С. Янева, Л. Йотова, П. Гриесмар, Изследвания върху пролиферацията на Грам-отрицателни бактериални клетки върху зол-гелни хибридни носители</i>	<i>444</i>
<i>А. Хасан, С. Янева, Л. Йотова, Дизайн на оптични био-сензори за откриване на фармацевтични продукти</i>	<i>451</i>
ИНСТРУКЦИЯ ЗА АВТОРИТЕ	452